

Frontiers
in
Artificial
Intelligence
and
Applications

PROCEEDINGS OF CECNET 2022

**The 12th International Conference
on Electronics, Communications
and Networks (CECNet 2022),
4-7 November 2022**



IOS Press

Edited by
Antonio J. Tallón-Ballesteros

PROCEEDINGS OF CECNET 2022

Electronics, communication and networks coexist, and it is not possible to conceive of our current society without them. Within the next decade we will probably see the consolidation of 6G-based technology, accompanied by many compatible devices, and fiber-optic is already an advanced technology with many applications.

This book presents the proceedings of CECNet 2022, the 12th International Conference on Electronics, Communications and Networks, held as a virtual event with no face-to-face participation in Xiamen, China, from 4 to 7 November 2022. CECNet is held annually, and covers many interrelated groups of topics such as electronics technology, communication engineering and technology, wireless communications engineering and technology and computer engineering and technology. This year the conference committee received 313 submissions. All papers were carefully reviewed by program committee members, taking into consideration the breadth and depth of research topics falling within the scope of the conference, and after further discussion, 79 papers were selected for presentation at the conference and for publication in this book. This represents an acceptance rate of about 25%.

The book offers an overview of the latest research and developments in these rapidly evolving fields, and will be of interest to all those working with electronics, communication and networks.



ISBN 978-1-64368-368-3 (print)
ISBN 978-1-64368-369-0 (online)
ISSN 0922-6389 (print)
ISSN 1879-8314 (online)

PROCEEDINGS OF CECNet 2022

Frontiers in Artificial Intelligence and Applications

The book series Frontiers in Artificial Intelligence and Applications (FAIA) covers all aspects of theoretical and applied Artificial Intelligence research in the form of monographs, selected doctoral dissertations, handbooks and proceedings volumes. The FAIA series contains several sub-series, including 'Information Modelling and Knowledge Bases' and 'Knowledge-Based Intelligent Engineering Systems'. It also includes the biennial European Conference on Artificial Intelligence (ECAI) proceedings volumes, and other EurAI (European Association for Artificial Intelligence, formerly ECCAI) sponsored publications. The series has become a highly visible platform for the publication and dissemination of original research in this field. Volumes are selected for inclusion by an international editorial board of well-known scholars in the field of AI. All contributions to the volumes in the series have been peer reviewed.

The FAIA series is indexed in ACM Digital Library; DBLP; EI Compendex; Google Scholar; Scopus; Web of Science: Conference Proceedings Citation Index – Science (CPCI-S) and Book Citation Index – Science (BKCI-S); Zentralblatt MATH.

Series Editors:

Nicola Guarino, Pascal Hitzler, Joost N. Kok, Jiming Liu, Ramon López de Mántaras,
Riichiro Mizoguchi, Mark Musen, Sankar K. Pal, Ning Zhong

Volume 363

Recently published in this series

- Vol. 362. E. Francesconi, G. Borges and C. Sorge (Eds.), Legal Knowledge and Information Systems – JURIX 2022: The Thirty-fifth Annual Conference, Saarbrücken, Germany, 14–16 December 2022
- Vol. 361. A.M. Metelli, Exploiting Environment Configurability in Reinforcement Learning
- Vol. 360. J.-L. Kim (Ed.), Machine Learning and Artificial Intelligence – Proceedings of MLIS 2022
- Vol. 359. M. Hecher, Advanced Tools and Methods for Treewidth-Based Problem Solving
- Vol. 358. A.J. Tallón-Ballesteros (Ed.), Fuzzy Systems and Data Mining VIII – Proceedings of FSDM 2022
- Vol. 357. G. Šír, Deep Learning with Relational Logic Representations
- Vol. 356. A. Cortés, F. Grimaldo and T. Flaminio (Eds.), Artificial Intelligence Research and Development – Proceedings of the 24th International Conference of the Catalan Association for Artificial Intelligence
- Vol. 355. H. Fujita, Y. Watanobe and T. Azumi (Eds.), New Trends in Intelligent Software Methodologies, Tools and Techniques – Proceedings of the 21st International Conference on New Trends in Intelligent Software Methodologies, Tools and Techniques (SoMeT_22)

ISSN 0922-6389 (print)
ISSN 1879-8314 (online)

Proceedings of CECNet 2022

The 12th International Conference on Electronics,
Communications and Networks (CECNet 2022),
4–7 November 2022

Edited by

Antonio J. Tallón-Ballesteros

University of Huelva, Huelva City, Spain



IOS Press

Amsterdam • Berlin • Washington, DC

© 2022 The authors and IOS Press.

This book is published online with Open Access and distributed under the terms of the Creative Commons Attribution Non-Commercial License 4.0 (CC BY-NC 4.0).

ISBN 978-1-64368-368-3 (print)
ISBN 978-1-64368-369-0 (online)
doi: 10.3233/FAIA363

Publisher

IOS Press BV
Nieuwe Hemweg 6B
1013 BG Amsterdam
Netherlands
fax: +31 20 687 0019
e-mail: order@iospress.nl

For book sales in the USA and Canada:

IOS Press, Inc.
6751 Tepper Drive
Clifton, VA 20124
USA
Tel.: +1 703 830 6300
Fax: +1 703 830 2300
sales@iospress.com

LEGAL NOTICE

The publisher is not responsible for the use which might be made of the following information.

PRINTED IN THE NETHERLANDS

Preface

After more than a decade of existence, the Conference on Electronics, Communications and Networks (CECNet) series has become established as a mature event. CECNet is held annually, and covers many interrelated groups of topics such as electronics technology, communication engineering and technology, wireless communications engineering and technology and computer engineering and technology.

Electronics, communication and networks coexist, and it is not possible to conceive of the current society without them. The next decade will probably see the consolidation of 6G-based technology, accompanied by many compatible devices. On a different topic, data centers are on the rise, and fiber-optic is now the most advanced technology, with many applications such as fiber to the home, fiber to the desktop, fiber for business and fiber to the node. As regards speed, we may soon have 100 Gb/s passive optical networks operating at a symmetrical mode. Going beyond this, 400 Gb/s may be achieved for long hauls with compact optical transceivers, and rates of 800 Gb/s for short hauls are possible. The trend is to have a hybrid coax-fiber material to take advantage of both technologies. TDSL (Terabit DSL) is not a new concept, and performance of about 2 Tb/s at a distance of 200 meters is also possible. Circular data centers are the future trend, with the idea that the heat generated by a data center could be used in, for example, a greenhouse.

This book contains the papers accepted and presented at the 12th International Conference on Electronics, Communications and Networks (CECNet 2022), held from 4–7 November 2022 as a virtual event with no face-to-face participation in Xiamen, China. All papers were carefully reviewed by program committee members, who took into consideration the breadth and depth of the research topic that fall within the scope of CECNet. CECNet 2022 was also a reference conference, and attracted many remarkable keynote speakers, such as Prof. Lyudmila Mihaylova, Department of Automatic Control and Systems Engineering, University of Sheffield, United Kingdom; Prof. Xiangjie Kong, College of Computer Science & Technology, Zhejiang University of Technology, China; and Prof. Victor Chang, Aston Business School, Aston University, United Kingdom.

CECNet 2022 received 313 submissions, and after a lively discussion stage, the committee decided to accept 79 papers, which represents an acceptance rate of about 25%.

I would like to thank all the keynote speakers and authors for their efforts in preparing a contribution for this leading international conference. Moreover, I am very grateful to all those, especially the program committee members and reviewers, who devoted their time to evaluate the papers. It is a great honour to continue with the publication of these proceedings in the prestigious series *Frontiers in Artificial Intelligence and Applications (FAIA)* from IOS Press.

Finally, although I hope you enjoy your virtual visit to Xiamen, I also hope we will be able to attend the conference face-to-face in the very near future.

October 2022

Antonio J. Tallón-Ballesteros
Huelva city (Spain)
University of Huelva (Spain)

This page intentionally left blank

About the Conference

With the support of Huaqiao University, the 12th International Conference on Electronics, Communications and Networks (CECNet 2022) was held online via Microsoft Teams during November 4–7, 2022 instead of offline in Xiamen, China as originally scheduled because of the global pandemic of COVID-19. It is held annually to provide a comprehensive global forum for experts and participants from academia to exchange ideas and present results of ongoing research in the most state-of-the-art areas of electronics technology, communication engineering and technology, wireless communications engineering and technology, computer engineering and technology.

All accepted full papers were carefully reviewed by technical program members, after a vibrant and vivid discussion stage, 79 papers were finally accepted by the committee from 313 submissions this year, which are qualified and fell into the scope of conference topics.

General Chair

Prof. Hui Tian, Deputy Dean, College of Computer Science and Technology, Huaqiao University, China

Technical Program Committee

Dr. Ahmed Moumena, Associate professor, University of Hassiba Benbouali of Chlef, Algeria

Dr. Ali Shahidinejad, University of the West of England Bristol Branch, Oman

Dr. Antonio J. Tallón-Ballesteros, Department of Electronic, Computer Systems and Automation Engineering, University of Huelva, Spain

Dr. Aounallah Naceur, Associate Professor, University of Ouargla, Algeria

Dr. Apurva Kumari, Associate Professor, Department of Electronics and Communication Engineering, BVRIT, Narsapur Campus, India

Dr. Arslan Khalid, Sirindhorn International Institute of Technology, Thammasat University, Thailand

Dr. Balasubramanian Padmanabhan, Hardware and Embedded Systems Lab, School of Computer Science and Engineering, Nanyang Technological University, Singapore

Dr. Bhagyashri R Hanji, Professor, Computer Science and Engineering, Global Academy of Technology, India

Dr. Bin Chen, Associate Professor, Tourism and Cultural College, Yunnan University, China

Dr. Chia Chao Kang, Xiamen University Malaysia, Malaysia

Dr. Dagang Jiang, Associate Professor, School of Astronautics and Aeronautics, University of Electronic Science and Technology of China, China

Dr. Daming Feng, CGG, USA

Dr. Daniele Giusto, Professor, Department of Telecommunications, University of Cagliari, Italy

Dr. Di Yuan, Harbin Institute of Technology, Shenzhen, China

- Dr. Do Duy Tan, Computer and Communication Engineering Department, Ho Chi Minh City University of Technology and Education, Vietnam
- Dr. Fabi Zhang, Professor, Guangxi Key Laboratory of Precision Navigation and Application, Guilin University of Electronic Technology, China
- Dr. Feng Shen, University at Buffalo, The State University of New York, USA
- Dr. Globa Larysa, Professor, National Technical University of Ukraine, Ukraine
- Dr. He Xiao, Cadence Design Systems, Inc, USA
- Dr. Ibraheem Shayea, Istanbul Technical University, Turkey
- Dr. Jency Rubia J, M.A.M College of Engineering and Technology, Anna University, India
- Dr. Jonny Paul Zavala De Paz, Professor, Universidad Politécnica de Querétaro, Mexico
- Dr. K. Prahlada Rao, Gulbarga University, India
- Dr. Koffka Khan, Department of Computer and Information Technology The University of the West Indies, West Indies
- Dr. K. Senthil Kumar, Associate Professor, Department of ECE, Rajalakshmi Engineering College, India
- Dr. Li Xiang, Associate Professor, Guilin University of Electronic Technology, China
- Dr. Lu Leng, Professor, Nanchang Hangkong University, China
- Dr. Mudassar Raza, University of Science and Technology of China (USTC), China
- Dr. Nagesh Deevi, Associate Professor, Malla Reddy College of Engineering & Technology, Secunderabad, India
- Dr. Nguyen Cong Phuong, Hanoi University of Science and Technology, Vietnam
- Dr. Nguyen Phu Thuong Luu, HUTECH Institute of Engineering, Vietnam
- Dr. P. Kuppusamy, Professor, VIT- AP University, Andhra Pradesh, India
- Dr. Raveendra K, Koneru Lakshmaiah Educational Foundation, India
- Dr. Serdar SOLAK, Information System Engineering, Kocaeli University, Turkey
- Dr. Shamganth Kumarapandian, Department of Engineering, University of Technology and Applied Sciences, Oman
- Dr. Smt. Rachana C R, Associate Professor, DoS in Computer Science, PG Wing of SBRR Mahajana First Grade College (Autonomous), Pooja Bhagavat Memorial Mahajana Education Centre, India
- Dr. Subrato Bharati, Institute of Information and Communication Technology, Bangladesh University of Engineering and Technology, Bangladesh
- Dr. S.Suresh, Professor, Department of Computer Science and Engineering, P. A. College of Engineering and Technology, India
- Dr. Suresh Raikwar, Associate Professor, Department of Computer Engineering and Applications, GLA University, India
- Dr. Tan Sin Jin, School of Engineering, UOW Malaysia KDU, Malaysia
- Dr. Tarik A. Rashid, Professor, Computer Science and Engineering, University of Kurdistan Hewler, Iraq
- Dr. Xie Gang, Associate Professor, Beijing University of Posts and Telecommunications, China
- Dr. Urvesh Rathod, National Institute of Technology Surathkal, India
- Dr. Wei Lu, Air Force Early Warning Academy, China

Dr. Weihua Mou, Department of Electronic Science and Technology, National University of Defense Technology, China

Dr. Yifei Zhao, Mettler-Toledo Safeline Ltd, UK

This page intentionally left blank

Contents

Preface	v
<i>Antonio J. Tallón-Ballesteros</i>	
About the Conference	vii
Attack and Improvement of a Hidden Vector Encryption Scheme	1
<i>Ke Wang, Zhikun Wang, Song Luo and Zhi Guan</i>	
Performance Analysis of Aerial Base Station Cellular Network	10
<i>Xue Ding, Gongbin Qian and Chunlong He</i>	
Lightweight Application of SM2 Co-Signature Algorithm in the Power IOT	18
<i>Yanrong Zhang, Feng Yang and Yanfang Yuan</i>	
Research of Communication Protocols for Energy Metering Devices	24
<i>Huaxu Song, Xin Xia, Mi Zhang, Huiipo Yuan and Shouzhi Wang</i>	
A Method for Exchanging Data Between Master Station and Terminal Based on Key Agreement Mechanism	32
<i>Qingqin Fu, Zhengquan Ang, Fan He, Guanglun Yang, Yingchun Fu, Pingjiang Xu, Jia Liu, Ling Yi, Haifeng Xu, Zhaoyu Lu and Benyang Liu</i>	
A Method for Scientific Cultivation Analysis Based on Knowledge Graphs	40
<i>Aiyan Wu, Yongmei Zhang and Shang Yang</i>	
Warning of Dangerous Driving Behavior Caused by Drivers and Road Environmental Factors	48
<i>Yuhui Lin, Hao Lin and Zhiyi Lu</i>	
A Low Power Test Data Compression Scheme for Scan Test	56
<i>Bo Ye</i>	
Traffic Flow Imputation Based on Multi-Perspective Spatiotemporal Generative Adversarial Networks	62
<i>Guojiang Shen, Nali Liu, Yinghui Liu, Wenfeng Zhou and Xiangjie Kong</i>	
Kernel Data Evaluation System and Modeling Based on ABC-BP Hybrid Algorithm	74
<i>Kuozhi Xu and Yangbo Nie</i>	
PIXDet: Prohibited Items X-Ray Image Detection in Complex Background	81
<i>Mingyuan Li, Bowen Ma, Tong Jia and Yichun Zhang</i>	
Research on Cultivating Senior High School Students' Innovative Thinking in Mathematics Based on Bloom's Taxonomy of Educational Objectives	91
<i>Yujie Wang and Zhiqin Huang</i>	
Anti-Jamming Method of Cognitive Radio Based on Q-Learning	97
<i>Yichen Xiao, Haiyu Ren, Shan Wu, Lixiang Liu, Xiandong Meng and Pengcheng Ding</i>	

Real-Time Detection and Early Warning System for Public Security Key Places Based on Human Posture Characteristics <i>Xiaohui Bai, Zhenyu Shou and Tianhang Yuan</i>	105
Study Analysis of Printed Monopole Antenna for C and X Band Application <i>Samom Jayananda Singh, Rajesh Kumar and M.M. Dixit</i>	112
A Method for Power Amplifier Distortions Compensation at the RX Side for the 5G NR Communication Systems <i>Alexander Maltsev, Alexander Shikov, Andrey Pudeev, Seonwook Kim and Suckchel Yang</i>	119
Intelligent Patrol Route Visualization Design Based on Police Big Data <i>Weiyang Hao, Deming Guo, Qi Zhou and Xinyi Sha</i>	130
Advantage Analysis of MBSE in the Context of Multi-Historical Development Trends <i>Yuqiang Guo, Shiyan She, Jun Zhao and Junxian Guo</i>	138
Analysis of the Mainstream MBSE Methodologies from the Modeling Practice View <i>Yuqiang Guo, Hui Zhao, Keke Qi and Junxian Guo</i>	146
Quantitative Inversion Radar Imaging: A Physical Remote Sensing Modality of High Resolution <i>Shilong Sun and Dahai Dai</i>	155
A Lowpass-Bandpass Diplexer Using Common Lumped-Element Dual-Resonance Resonator <i>Shan Jin</i>	165
Low Time-Complexity Chaotic Image Encryption Algorithm Based on Plaintext Information <i>Nianhang Tang, Zeming Wu and Peng Guo</i>	172
Research on Security Sharing Model System of Power Digital Spatial Data <i>Aijun Wen, Zesan Liu, Di Liu, Chenghua Fu and Ziting Gao</i>	182
Chicken and Egg Food Traceability System Based on NFC and QR Code Technology <i>Yiqin Bao and Yulu Bao</i>	191
The Light and Image Synchronous Method Based on Adaptive Color Segmentation Algorithm <i>Qiuwei Deng, Nianhang Tang, Mingyue Su and Jianguang Zhai</i>	198
A Generative Learning Architecture Based on CycleGAN for Steganalysis with Unpaired Training Images <i>Han Zhang, Zhihua Song, Feng Chen, Xiangyang Lin, Qinghua Xing, Qingbo Zhang and Yongmei Zhao</i>	213
Multi-Path Propagation Prediction of 433MHz Wave in the Ship Environment Based on the Ray-Tracing Model <i>Wanli Tu, Hong Xu, Yiqun Xu and Qing Zhou</i>	219

A Study on the Strategy of Vocational English Digital Teaching Materials Development in the Context of Internet+ – Taking the Integrated Course of English as an Example	226
<i>Hui Sun, Huaizhong Zhu and Lisha Wang</i>	
Approach for Cryptography Digital Ecosystem Deployment	236
<i>Inara Opmane and Rihards Balodis</i>	
Citrus Appearance Quality Grading System Based on OpenCV Image Processing	244
<i>Yiqin Bao, Qin Liu and Yulu Bao</i>	
A Design of Hierarchical Bloom Filter	251
<i>Tao Ma and Bin Wang</i>	
Constellation Configuration Analysis Based on Angle Condition Number for Tri-satellite TDOA Geolocation System	260
<i>Bo Liu, Xiaoyang Chen, Ming Li, Shuai Li, Jie Ren and Lede Qiu</i>	
A Discrete Clutter Reduction Method for Drone Detection with High Resolution Radars	267
<i>Tran Vu Hop, Nguyen Van Loi, Pham Van Tien and Phung Dinh Thang</i>	
Algorithm Based on Deep Learning to Improve the Logistics Management of a Company That Distributes Reading Material	281
<i>Bruno Kevin-Flores Aquino, Ángel Eduardo-Córdova Baquijano and Christian Ovalle</i>	
Performance Analysis of 256-QAM Demodulation for 5G NR Sidelink	287
<i>Alexander Maltsev, Igor Serunin, Andrey Pudeev, Jin-Yup Hwang and Sang-Wook Lee</i>	
Application of SCMA Based on LoRaWAN Architecture	295
<i>Minhao Jin, Libo Fan, Shaojie Luo and Xiaotian Guo</i>	
Efficient Security Detection Strategy Based on K-Means Algorithm in LPWAN	301
<i>Minhao Jin, Shaojie Luo, Jiabin Huang and Xincheng Zhou</i>	
Research on the Construction and Evolution Model of Cloud Ecosystem	307
<i>Guolong She, Mengdi Yao and Guohua Deng</i>	
Artificial Intelligence Project Practice Based on K210	318
<i>Yijin Shi, Bin Chen, Guisheng Tan and Guiliang Zhang</i>	
Research on Intelligent Research Model of Clues in Cases of Production and Sale of Counterfeit Drugs	325
<i>Linfeng Gu, Sisi Li, Yutian Wang, Zhihui Lin and Jingsong Wu</i>	
Low Complexity and High Spectrum Efficiency Hybrid Precoding for Massive MIMO Systems	334
<i>Gang Xie and Zhixiang Pei</i>	
The Continuous Time Dynamical Analysis of Heart Rate Asymmetry	342
<i>Yi-Horng Lai, Jiahua Yu, Kun Su, Lin Lan, Zexin Li, Zequn Zhang and Zifeng Zhuang</i>	

Continuous-Speech Spoken Dialogue System Based on Joint Decision-Making of Audio and Semantics <i>Qiuwei Deng, Qiang Peng, Zhifang Ma, Pei Zhao and Di Wang</i>	348
A One-to-Two Filter Power Divider Based on LTCC <i>Yuan Yuan Li, Xianliang Wu, Yunfeng Hu, Mengying Dong, Yue Ma, Xiaolei Geng and Rongzhen Fang</i>	357
Tiny Deep Convolution Recurrent Network for Online Speech Enhancement with Various Noise Types <i>Qiuwei Deng, Di Wang, Tianxiang Luan and Bin Hao</i>	364
Degradation-Oriented Adaptive Network for Blind Super-Resolution <i>Shuo Wang and Lifang Chen</i>	375
Spin Sensitivity and Magnetic Response Analysis of Nano-SQUIDS <i>Zejun Shi, Huachuan Wang and Jianxin Lin</i>	383
Research and Evaluation of Early Warning Models for Crowd Density Monitoring Based on Drones <i>Hao Li, Yining Liu, Jiongfai Chen and Mingxuan Chen</i>	391
A Method of Anti-Nonsynchronous Short Pulse Jamming Based on Waveform Entropy <i>Zijun Hu, Xinliang Chen, Leizhen Zhou and Zhennan Liang</i>	400
Measuring the State of ECN Readiness in Mail Servers on the Internet <i>Chun-Xiang Chen, Tetuya Shigeyasu and Kenichi Nagaoka</i>	411
Intelligent Judgment Method of Superimposed Label Recognition Technology Based on a Deep Learning Target Detection Algorithm for Detecting Wiring Errors in Current Transformer Tests <i>Jia-Heng Xu, Lian-Song Yu, Wei-Wei Yang, Xiao Rong, Wei Luo, Na Song and Hua-Feng Hu</i>	417
Coherent Accumulation Algorithm for Maneuvering Weak Target Based on Angular-Stepped-GRFT <i>Yuxian Sun, Shaoqiang Chang, Gang Wang, Zhennan Liang, Jinpeng Guo and Quanhua Liu</i>	424
Analysis of Artificial Intelligence Applied in Virtual Learning Environments in Higher Education for Ecuador <i>Segundo Moisés Toapanta Toapanta, Eriannys Zharayth Gómez Díaz, Oscar Marcelo Zambrano Vizuete and Edith Elizabeth Ordoñez Chávez</i>	436
Content Connectivity Based Polyhedron Protection Against Multiple Link Failures in Optical Data Center Networks <i>Xin Li, Yu Liu, Hong Wang, Wei Xu and Shanguo Huang</i>	444
RL-Based Load Balancing for Software-Defined WiFi Networks <i>Jun Li</i>	450

3D Point Cloud and BIM Component Retrieval for Subway Stations via Deep Learning	457
<i>Yongfei Shi, Wei Ye, Bo Qu, Hong Jia, Zhanying Fu, Xinming Lv, Chenglu Wen and Weiquan Liu</i>	
Emulation of the Updated CANARIE Backbone Network Topology Under IPv6 Up to 2022	465
<i>Jose-Ignacio Castillo-Velazquez and Nelly-Guadalupe Velazquez-Cruz</i>	
Cost-Efficient Service Function Chaining with CoMP Zero-Forcing Beamforming in Mobile Edge Networks	472
<i>Yuan Gao, Hai Fang and Kan Wang</i>	
Study on Fault Prognostics and Health Management for UAV	484
<i>Jihui Pan, Wenqing Qu, Hao Xue, Lei Zhang and Liang Wu</i>	
Online and Offline Analysis of Planck Constant Measurement	492
<i>Zhongqi Luan, Lina Wang, Yanjun Wang, Haifeng Gu and Yaxiang Bai</i>	
Comparison of Deep Learning Methods and a Transfer-Learning Semi-Supervised GAN Combined Framework for Pavement Crack Image Identification	499
<i>Kai-liang Lu, Guo-rong Luo, Ming Zhang, Jin-feng Qi and Chun-ying Huang</i>	
A Massive-Cargo Transportation Routing Model Based on Reinforcement Learning	509
<i>Yi-shun Li and Ming Wei</i>	
Robust Estimation Method Using Successive Approximation Algorithm to Correct Errors	518
<i>Xiao-Ming Ye</i>	
Uncertainty Measurement of Variable Precision Fuzzy Soft Rough Set Model	533
<i>Xinyi Wang and Qinghai Wang</i>	
Prediction and Analysis of Stock Logarithmic Returns Based on ARMA-GARCH Model	544
<i>Hao Qi and Yuanshen Wang</i>	
Time-Domain Feature Parameter Extraction Algorithm of Pulse Wave Based on Morphological Features	555
<i>Xingguang Geng, Yitao Zhang, Jun Zhang, Yunfeng Wang and Haiying Zhang</i>	
Image Restoration of an Object Viewed Through a Polycapillary X-Ray Lens with Square Channels Using the Concept of a Space-Variant Point-Spread Function	567
<i>Mo Zhou, Yiming Wu, Kai Pan, Zelin Du, Tiancheng Yi, Tianxi Sun, Zhiguo Liu and Yude Li</i>	
Deep Learning Based Method for the Estimation of Patient's Angles from Lateral Skull Radiographs	575
<i>Kazuma Nakazeko, Shinya Kojima, Hiroyuki Watanabe and Hiroyuki Kudo</i>	

Stability Evaluation of Computational Intelligence-Based Subset Feature Selection Methods on Breast Cancer Data Analysis <i>Shaode Yu, Boji Liu, Bingjie Li, Mingxue Jin, Junjie Wu and Hang Yu</i>	587
Research on Radar Burn-Through Range Under Noise Jamming Based on Radar Equation <i>Hua Zhang, Yuntao Chen, Yi Wang, Litao Wang and Gen Qin</i>	595
Classification of Characteristic Factors of Brain Functional Network Using Decision Tree <i>Peng Yuan, Zuogang Zheng, Xinshuo Yuan, Lanhua Zhang, Mei Wang, Xiaoyan Wang and Xucui Ji</i>	599
A Stability Evaluation of Feature Ranking Algorithms on Breast Cancer Data Analysis <i>Shaode Yu, Bingjie Li, Boji Liu, Mingxue Jin, Junjie Wu and Hang Yu</i>	606
A Distribution Network Reconfiguration Continuous Method Based on Efficient Solution Space Coding <i>Wei Tang, Baohua Sun, Rongqiang Feng, Chenxi Huang and Lei Zhao</i>	614
Tribological Property Behavior of Sinusoidal Texture with Various Intervals Under Scarce Oil Supply <i>Jian Ma, Yancong Liu, Na Zhang, Xiaoshuang Yang and Hongyu Jia</i>	628
Research on Spatial Distribution in Power Frequency Magnetic Field Immunity Test <i>Yang Jiang, Chenxi Liao, Shisheng Fu, Fan Zheng, Limin Wang and Ming Li</i>	634
Design and Application of Fully Hydraulic Intelligent Screw Clearing Machine for Grain Silos <i>Jianping Luo and Zhiping Jia</i>	644
Integrated Management System of Expressway Intelligent Service Area <i>Jianxian Duan, Yanyan Li, Qingqing Yu, Anqi Li and Yongjun Shao</i>	653
Analysis of Expressway Intelligent Service Area for Better Vehicles/Passengers Service <i>Jianxian Duan, Yanyan Li, Qingqing Yu, Yongjun Shao and Anqi Li</i>	659
Optimizing IEEE 802.11a Preamble Design for Vehicle-to-Vehicle Communication <i>Jianghai Xu, Hao Zheng, Huaiyuan Liu and Heng Liu</i>	664
Subject Index	671
Author Index	675

Attack and Improvement of a Hidden Vector Encryption Scheme

Ke WANG^{a,b}, Zhikun WANG^c, Song LUO^c and Zhi GUAN^{d,1}

^aKey Laboratory of High Confidence Software Technologies (Peking University), MoE, Beijing, China

^bDepartment of Computer Science and Technology, EECS, Peking University, Beijing, China

^cSchool of Computer Science and Engineering, Chongqing University of Technology, Chongqing, China

^dNational Engineering Research Center for Software Engineering, Peking University, Beijing, China

Abstract. Hidden Vector Encryption (HVE) is a new kind of attribute-based encryption in which a vector is hidden in the ciphertext or linked with the secret key. In ESORICS 2014, Phuong et al. proposed an HVE scheme with constant-size ciphertext which is constructed in the prime order setting. In this paper, we show that Phuong et al.'s scheme is not vector-hiding due to public parameters in their scheme leak some information about vectors. Furthermore, an improved HVE scheme is proposed in the prime order setting and its security is proven in the security model. Comparison shows our scheme has more efficient in decryption than current other HVE schemes.

Keywords. Hidden vector encryption, constant-size ciphertext, prime order setting, bilinear group, security

1. Introduction

Hidden Vector Encryption (HVE) [1] is a new kind of attribute-based encryption [2, 3] in which the message is encrypted to a hidden vector while a user holds a secret key linked with a vector. Wildcard can be used in either secret key or ciphertext, the former is called key policy HVE and the latter is called ciphertext policy HVE [4]. When both vectors match, the ciphertext can be decrypted. For example, in a ciphertext policy HVE scheme, two secret keys linked with $(1, 2, 3)$ and $(1, 2, 5)$ respectively can decrypt a ciphertext associated with $(1, 2, *)$. Vector-hiding in HVE means the decryptor cannot know the concrete target vector except his vector matches the target vector. HVE can be used to do some operations on encrypted data such as comparison, range queries, conjunctions and subset queries, so it is very favorable in many applications requiring privacy protection such as cloud computing.

In ESORICS 2014, Phuong et al. [5] proposed two efficient ciphertext policy HVE schemes. They used composite order bilinear groups to construct the first HVE scheme.

¹Corresponding Author: guan@pku.edu.cn

Their scheme has constant-size ciphertext and is proven selective security in the standard model. They then transformed the first scheme to get the second prime-order scheme. However, their prime-order construction is not secure.

Our Contribution. In this paper, we give an attack on Phuong et al.'s prime order HVE scheme (PYS-HVE in short) and show their scheme is not secure. We construct a special ciphertext and prove that PYS-HVE scheme doesn't have vector-hidden property by testing the ciphertext. Furthermore, we construct a new HVE scheme on the prime order bilinear groups. We also prove its selective security in the standard model. Experiment shows our scheme has better performance than current HVE schemes.

Related Works. Boneh and Waters [1] first introduced the notion of HVE and they gave a construction in composite order groups. Katz et al.'s study [6] found that inner-product encryption implies HVE so we can naturally derive fully secure HVE schemes from fully secure inner-product encryption schemes [7]. Hattori et al. [4] proposed the first ciphertext policy HVE scheme which was based on the anonymous HIBE [8] and the wildcarded IBE [9]. The ciphertext size in Hattori et al.'s CP-HVE scheme is linear to vector length and Phuong et al. [5] proposed the first HVE scheme with constant-size ciphertext. Liao et al. [10] presented a ciphertext policy HVE scheme supporting multiuser keyword search. Lee [11] presented a conversion method which can transform composite-order setting HVE schemes into prime-order setting schemes. Bartusek et al. [12] proposed a new function-private predicate encryption scheme in the public key setting which supports point functions, conjunctions, d -disjunctions with read-once conjunctions and d -CNFs with a constant d . Recently, HVE is extended to ABE with hidden policy. Murad et al. [13] proposed a new kind of CP-ABE with in which access structures for AND or OR gates with wildcards are partially hidden. In fact, an access structure using partially hidden AND-gates with wildcards equals to a hidden vector.

Organization. The rest of this paper is organized as follows. We provide some necessary background knowledge in Section 2. We analyze the PYS-HVE scheme in Section 3 and propose our improved construction with security proof in Section 4 respectively. Next a brief comparison is given in Section 5. Finally the paper is concluded with future work in Section 6.

2. Preliminaries

Definition 2.1. Let p be a prime and \mathbb{G}, \mathbb{G}_T be two multiplicative groups of order p . Let g be a generator of \mathbb{G} . $e : \mathbb{G} \times \mathbb{G} \rightarrow \mathbb{G}_T$ is a bilinear map which satisfies the following two properties:

- (i) *Bilinearity:* $\forall x, y \in \mathbb{Z}_p, e(g^x, g^y) = e(g, g)^{xy}$.
- (ii) *Non-degeneracy:* $e(g, g) \neq 1$.

We call \mathbb{G} a bilinear group if the group operation in \mathbb{G} and the bilinear map $e : \mathbb{G} \times \mathbb{G} \rightarrow \mathbb{G}_T$ can be efficiently computed.

Definition 2.2. Let g be a random generator of \mathbb{G} . Let h and Z are chosen randomly from \mathbb{G} and \mathbb{G}_T respectively. Let $\vec{g}_{g, \alpha, d}$ be $g_1, \dots, g_d, g_{d+2}, \dots, g_{2d} \in \mathbb{G}^{2d-1}$ where $g_i = g^{\alpha^i}$ and $\alpha \in \mathbb{Z}_p^*$ is unknown.

We define the advantage for an algorithm \mathcal{A} to break the decision d -BDHE assumption as

$$|\Pr[\mathcal{A}(g, h, \vec{g}_{g, \alpha, d}, e(g_{d+1}, h)) = 1] - \Pr[\mathcal{A}(g, h, \vec{g}_{g, \alpha, d}, Z) = 1]|.$$

If no probabilistic polynomial-time algorithm has non-negligible advantage to break the decision d -BDHE assumption, we say the decision d -BDHE assumption holds.

An HVE scheme consists of the following four algorithms: **Setup** algorithm for system setup, **Key Generation** algorithm for secret key generation, **Encrypt** algorithm for message encryption, and **Decrypt** algorithm for ciphertext decryption. The security model used for our HVE is called selective security model with six stages: **Init**, **Setup**, **Query Phase 1**, **Challenge**, **Query Phase 2** and **Guess**. The adversary should submit two challenging vectors at the **Init** stage and all queried identities in **Query Phase 1, 2** cannot match these two challenging vectors.

3. Attack on PYS-HVE Scheme

We first review the public parameters and ciphertext of PYS-HVE scheme. Suppose the maximum number of wildcards that are allowed in an encryption vector be N and the vector length is L . The public parameters include $L + 1$ random elements $V, H_1, \dots, H_L \in G$, three random generators $g, f, w \in \mathbb{G}$, a pairing $e : \mathbb{G} \times \mathbb{G} \rightarrow \mathbb{G}_T$ and $Y = e(g, w)$.

Let $\vec{v} = (v_1, \dots, v_L) \in \Sigma_L^*$ be a vector with $\tau \leq N$ wildcards. To encrypt a message M with \vec{v} , the **Encrypt** algorithm chooses a random $s \in \mathbb{Z}_p$ and sets

$$C_0 = MY^s, C_1 = g^{\frac{s}{t}}, C_2 = f^s, C_3 = \prod_{i=1, i \notin J}^L (H_i^{v_i} V)^{\frac{\prod_{j \in J} (i-j)s}{t}} \quad (1)$$

where $J = \{j_1, j_2, \dots, j_\tau\}$ is the set containing the indexes of wildcards in \vec{v} and $t = (-1)^\tau j_1 j_2 \dots j_\tau$. The ciphertext is $CT = (C_0, C_1, C_2, C_3, J)$.

In PYS-HVE scheme, the elements linked with vectors, i.e., $V, H_1, \dots, H_L \in_R G$ are both used in encryption and decryption. This allows us to create elements similar to secret key. These elements cannot be used to decrypt but can be used to test the target vector. In fact, given the public parameters and a ciphertext, we can easily check whether a vector $\vec{z} = (z_1, \dots, z_L)$ is used to encrypt the message. We first construct $K = \prod_{i=1, i \notin J}^L (H_i^{z_i} V)^{\prod_{j \in J} (i-j)}$ and check whether the equation

$$e(C_1, K) = e(C_3, g) \quad (2)$$

holds. If the equation holds, we can conclude the encryption vector is \vec{z} . Hence, the vector-hiding property in PYS-HVE scheme is broken.

4. Our Improved Scheme

4.1. Description

- **Setup**($1^k, \Sigma, L$): Assume that at most $N(N \ll L)$ wildcards are allowed in a vector for encryption. Then the algorithm generates a pairing $e : \mathbb{G} \times \mathbb{G} \rightarrow \mathbb{G}_T$, randomly chooses $L + 1$ elements $V, H_1, \dots, H_L \in G$, two generators $g, w \in G$ and four integers $t_1, t_2, t_3, t_4 \in \mathbb{Z}_p$. Then it sets $U_1 = g^{t_1}, U_2 = g^{t_2}, U_3 = g^{t_3}, U_4 = g^{t_4}$ and $Y = e(g, w)^{t_1 t_2}$. The algorithm sets the public key $\text{PK} = (\text{PP}, V, (H_1, \dots, H_L), U_1, U_2, U_3, U_4, Y)$ and the master secret key $\text{MSK} = (w, t_1, t_2, t_3, t_4)$ where $\text{PP} = \{g, p, \mathbb{G}, \mathbb{G}_T, e\}$.
- **Encrypt**($\text{PK}, M, \vec{v} = (v_1, \dots, v_L) \in \Sigma_L^*$): Assume that $\vec{v} = (v_1, \dots, v_L)$ contains $\tau \leq N$ wildcards and $W = \{j_1, j_2, \dots, j_\tau\}$ is the set of the positions of wildcards in \vec{v} . The algorithm randomly chooses three integers $s, s_1, s_2 \in \mathbb{Z}_p$. It then computes $C_0 = M \cdot Y^s, C_1 = \prod_{i=1, i \notin W}^L (H_i^{v_i} V)^{\prod_{j \in J} (i-j)^s}, C_2 = U_1^{s-s_1}, C_3 = U_2^{s_1}, C_4 = U_3^{s-s_2}, C_5 = U_4^{s_2}$. The ciphertext CT is set as $(C_0, C_1, C_2, C_3, C_4, C_5, J)$.
- **Key Generation**($\text{MSK}, \vec{z} = (z_1, \dots, z_L) \in \Sigma_L$): Given a vector $\vec{z} = (z_1, \dots, z_L)$ for key generation, the algorithm randomly chooses $r_1, r_2 \in \mathbb{Z}_p$, then it computes $K_1 = g^{r_1 t_1 t_2 + r_2 t_3 t_4}$,

$$\begin{pmatrix} K_{2,0} = w^{t_2} \prod_{i=1}^L (H_i^{z_i} V)^{r_1 t_2} \\ K_{2,1} = \prod_{i=1}^L (H_i^{z_i} V)^{i r_1 t_2} \\ \dots \\ K_{2,N} = \prod_{i=1}^L (H_i^{z_i} V)^{i^N r_1 t_2} \end{pmatrix}, \begin{pmatrix} K_{3,0} = w^{t_1} \prod_{i=1}^L (H_i^{z_i} V)^{r_1 t_1} \\ K_{3,1} = \prod_{i=1}^L (H_i^{z_i} V)^{i r_1 t_1} \\ \dots \\ K_{3,N} = \prod_{i=1}^L (H_i^{z_i} V)^{i^N r_1 t_1} \end{pmatrix},$$

$$\begin{pmatrix} K_{4,0} = \prod_{i=1}^L (H_i^{z_i} V)^{r_2 t_4} \\ K_{4,1} = \prod_{i=1}^L (H_i^{z_i} V)^{i r_2 t_4} \\ \dots \\ K_{4,N} = \prod_{i=1}^L (H_i^{z_i} V)^{i^N r_2 t_4} \end{pmatrix}, \begin{pmatrix} K_{5,0} = \prod_{i=1}^L (H_i^{z_i} V)^{r_2 t_3} \\ K_{5,1} = \prod_{i=1}^L (H_i^{z_i} V)^{i r_2 t_3} \\ \dots \\ K_{5,N} = \prod_{i=1}^L (H_i^{z_i} V)^{i^N r_2 t_3} \end{pmatrix}$$

The corresponding key is $\text{SK} = (K_1, K_{2,t}, K_{3,t}, K_{4,t}, K_{5,t}, t \in \{0, \dots, N\})$.

- **Decrypt**(CT, SK): Suppose that CT is encrypted to \vec{v} and SK is associated with \vec{z} respectively. If $v_i = z_i$ for $i \in \{1, \dots, L\} \setminus J$, the decryption algorithm decrypts the ciphertext as follows. It first applies the Viète formulas on $J = \{j_1, \dots, j_\tau\}$ and computes $a_{\tau-k} = (-1)^k \sum_{i_1 < i_2 < \dots < i_k \leq \tau} j_{i_1} j_{i_2} \dots j_{i_k}$, for $0 \leq k \leq \tau$. Next it computes

$$K_2 = \prod_{t=0}^{\tau} K_{2,t}^{a_t}, K_3 = \prod_{t=0}^{\tau} K_{3,t}^{a_t}, K_4 = \prod_{t=0}^{\tau} K_{4,t}^{a_t}, K_5 = \prod_{t=0}^{\tau} K_{5,t}^{a_t},$$

and then outputs

$$M = \left(\frac{e(C_1, K_1)}{e(C_2, K_2)e(C_3, K_3)e(C_4, K_4)e(C_5, K_5)} \right)^{a_0^{-1}} \cdot C_0 \quad (3)$$

4.2. Security

Theorem 4.1. *Assume the decision L-BDHE assumption hold in \mathbb{G} , then our improved scheme is secure.*

We prove Theorem 4.1 through a series of experiments similar to that of [14]. We define the following games based on the security model with different challenge ciphertexts:

- G_1 : The challenge ciphertext is normal, i.e., $CT = (C_0, C_1, C_2, C_3, C_4, C_5)$.
- G_2 : This game is similar to G_1 but C_0 is replaced with a random element Z in \mathbb{G}_T , i.e., $CT = (Z, C_1, C_2, C_3, C_4, C_5)$
- G_3 : This game is similar to G_2 but C_2 is replaced with a random element Z_1 in \mathbb{G} , i.e., $CT = (Z, C_1, R_1, C_3, C_4, C_5)$
- G_4 : This game is similar to G_3 but C_4 is replaced with a random element Z_2 in \mathbb{G} , i.e., $CT = (Z, C_1, Z_1, C_3, Z_2, C_5)$

In G_4 , the elements of the challenge ciphertext are all random, so it will leak no information about the message or the vector. Therefore, if these four games are indistinguishable, the security of our HVE scheme is proven.

Lemma 4.1. *Under the decision L-BDHE assumption, G_1 and G_2 are indistinguishable.*

Proof. Suppose that the advantage of the adversary \mathcal{A} for distinguishing between G_1 and G_2 is ε which is non-negligible. Then the decision L-BDHE problem can solved by an algorithm \mathcal{B} based on \mathcal{A} . Given an L-BDHE challenge $(g, \vec{y}_{g, \alpha, L} = (g_1, g_2, \dots, g_L, g_{L+2}, \dots, g_{2L}), h, Z)$, where $g_i = g^{\alpha^i}$ and $\alpha \in \mathbb{Z}_p^*$ is unknown. \mathcal{B} should determine whether $Z = e(g_{L+1}, h)$ or not.

Let $W(\vec{v})$ be $\{1 \leq i \leq L \mid v_i = *\}$ and $\overline{W}(\vec{v})$ be $\{1 \leq i \leq L \mid v_i \neq *\}$, and $W(\vec{v} \upharpoonright_j^k)$ be $\{i \in W(\vec{v}) \mid j \leq i \leq k\}$. \mathcal{B} executes with \mathcal{A} as follows:

- **Init:** \mathcal{A} sends two challenge vectors $\vec{v}_0^* \in \Sigma_L^*$ and $\vec{v}_1^* \in \Sigma_L^*$ where $W(\vec{v}_0^*) = W(\vec{v}_1^*)$. \mathcal{B} randomly chooses $\mu \in \{0, 1\}$. Let \vec{v}_μ^* be $(v_1^*, v_2^*, \dots, v_L^*)$ for simplicity.
- **Setup:** \mathcal{B} randomly chooses integers $\gamma, y, t_1, t_2, t_3, t_4, u_1, \dots, u_L \in \mathbb{Z}_p$, then it sets

$$Y = e(g^\alpha, g^{\alpha^L} g^\gamma)^{t_1 t_2}, U_1 = g^{t_1}, U_2 = g^{t_2}, U_3 = g^{t_3}, U_4 = g^{t_4},$$

$$V = g^y \prod_{i \in \overline{W}(\vec{v}_\mu^*)} g^{\alpha^{L+1-i} v_{\mu,i}^*}, \{H_i = g^{u_i - \alpha^{L+1-i}}\}_{i \in \overline{W}(\vec{v}_\mu^*)}, \{H_i = g^{u_i}\}_{i \in W(\vec{v}_\mu^*)}$$

The element w in public parameters is $g^{\alpha^{L+1} + \alpha\gamma}$. Since $g^{\alpha^{L+1}}$ is unknown to \mathcal{B} , w cannot be computed by \mathcal{B} directly.

- **Query Phase 1:** \mathcal{A} sends a vector $\vec{\sigma}_u = (\sigma_1, \sigma_2, \dots, \sigma_u)$ without matching the challenge vectors for key query. Let $k \in \overline{W}(\vec{v}_\mu^*)$ which is the smallest integer for $\sigma_k \neq v_{\mu,k}^*$. \mathcal{B} generates the corresponding key as follows. We start from $K_{2,i}$.

$$\begin{aligned} K_{2,0} &= w^{t_2} \left(\prod_{i=1}^L H_i^{\sigma_i} V \right)^{r_1 t_2} \\ &= (g^{\alpha^{L+1} + \alpha \gamma})^{t_2} \left(\prod_{\overline{W}(\vec{v}_\mu^*)|_1^k} g^{u_i - \alpha^{L+1-i}} \prod_{W(\vec{v}_\mu^*)|_1^k} (g^{u_i})^{\sigma_i} \cdot g^{\frac{y + \sum_{\overline{W}(\vec{v}_\mu^*)} \alpha^{L+1-i} v_{\mu,i}^*}{\overline{W}(\vec{v}_\mu^*)}} \right)^{r_1 t_2} \\ &\stackrel{\text{def}}{=} (g^{\alpha^{L+1} + \alpha \gamma})^{t_2} (g^X)^{r_1 t_2} \end{aligned}$$

where $X = \sum_{\overline{W}(\vec{v}_\mu^*)} \alpha^{L+1-i} v_{\mu,i}^* + y + \sum_{\overline{W}(\vec{v}_\mu^*)|_1^k} (u_i - \alpha^{L+1-i}) \sigma_i + \sum_{W(\vec{v}_\mu^*)|_1^k} u_i \sigma_i$ Since $\sum_{\overline{W}(\vec{v}_\mu^*)|_1^k} (u_i - \alpha^{L+1-i}) \sigma_i + \sum_{\overline{W}(\vec{v}_\mu^*)|_1^k} u_i \sigma_i = \sum_{\overline{W}(\vec{v}_\mu^*)|_1^k} (-\alpha^{L+1-i} \sigma_i) + \sum_{i=1}^k u_i \sigma_i$ and recall $\sigma_i = v_{\mu,i}^*$ for $i \in \overline{W}(\vec{v}_\mu^*)|_1^{k-1}$ and $\sigma_k \neq v_{\mu,k}^*$. Hence, we have

$$X = \alpha^{L+1-k} \Delta_k + \sum_{\overline{W}(\vec{v}_\mu^*)|_{k+1}^L} \alpha^{L+1-i} v_{\mu,i}^* + \sum_{i=1}^k x_i \sigma_i + y$$

where $\delta_k = v_{\mu,k}^* - \sigma_k$. Then we choose \hat{r}_1 randomly in \mathbb{Z}_p , and implicitly set $r_1 = \frac{-\alpha^k}{\delta_k} + \hat{r}_1$. $K_{2,0}$ can be represented as

$$\begin{aligned} &\left[g^{\alpha^{L+1} + \alpha \gamma} \cdot g^{-\alpha^{L+1}} \cdot g^{\sum_{i \in W(\vec{v}_\mu^*)|_{k+1}^L} \frac{-\alpha^{L+1-i+k} v_{\mu,i}^*}{\Delta_k}} \cdot g^{\alpha^k \left(-\frac{\sum_{i=1}^k x_i \sigma_i + y}{\Delta_k} \right)} \cdot \left(V \prod_{i=1}^K h_i^{\sigma_i} \right)^{\hat{r}_1} \right]^{t_2} \\ &= \left[g^{\alpha \gamma} \cdot g^{\sum_{i \in W(\vec{v}_\mu^*)|_{k+1}^L} \frac{-\alpha^{L+1-i+k} v_{\mu,i}^*}{\Delta_k}} \cdot g^{\alpha^k \left(-\frac{\sum_{i=1}^k x_i \sigma_i + y}{\Delta_k} \right)} \cdot \left(V \prod_{i=1}^K h_i^{\sigma_i} \right)^{\hat{r}_1} \right]^{t_2} \end{aligned}$$

For $\hat{k} = 1$ to N , we compute $K_{2,\hat{k}}$ as

$$\left[g^{\frac{y + \sum_{\overline{W}(\vec{v}_\mu^*)} \alpha^{L+1-i} v_{\mu,i}^*}{\overline{W}(\vec{v}_\mu^*)}} \cdot \left(\prod_{\overline{W}(\vec{v}_\mu^*)|_1^{k-1}} g^{u_i - \alpha^{L+1-i}} \cdot \prod_{W(\vec{v}_\mu^*)|_1^{k-1}} (g^{u_i})^{\sigma_i} \right)^{\frac{-\alpha^k \hat{k}}{\Delta_k} + \hat{r}_1 i^{\hat{k}}} \right]^{t_2}.$$

Note that $K_{3,i} = K_{2,i}^{\frac{t_1}{t_2}}$, so we can compute $K_{3,i}$ easily from $K_{2,i}$. Next we choose random $r_2 \in \mathbb{Z}_p$ and compute $K_{4,k} = \prod_{i=1}^L (H_i^{z_i} V)^{i^k r_2 t_4}$ and $K_{5,k} = \prod_{i=1}^L (H_i^{z_i} V)^{i^k r_2 t_3}$ for $k = 0, \dots, N$ since V, H_0, \dots, H_L are known.

At last we can simulate the first element in the key:

$$K_1 = g^{r_1 t_1 t_2 + r_2 t_3 t_4} = (g^{\alpha k})^{-t_1 t_2 / \Delta_k} \cdot g^{\hat{r}_1 t_1 t_2 + r_2 t_3 t_4}$$

- **Challenge:** Two message M_0, M_1 are submitted to \mathcal{B} by \mathcal{A} . \mathcal{B} randomly chooses $s_1, s_2 \in \mathbb{Z}_p$ and computes:

$$C_0 = M_\mu \cdot Z^{t_1 t_2} \cdot e(g^\alpha, h)^{t_1 t_2 \gamma}, C_1 = \left(h^{y + \sum_{i=1}^L u_i v_{\mu, i}^*} \prod_{k=1}^{\bar{\epsilon}} (i - j_k) \right),$$

$$C_2 = h^{t_1} U_1^{s_1}, C_3 = U_2^{s_1}, C_4 = h^{t_3} U_3^{-s_2}, C_5 = U_4^{s_2}.$$

Here we implicitly set $g^s = h$. If $Z = e(g, h)^{\alpha^{L+1}}$, it is a valid ciphertext encrypted to M_b . Otherwise, if T is a random element of \mathbb{G}_T , the challenge ciphertext is an encryption to a random message.

- **Query Phase 2:** Query Phase 1 is repeated.
- **Guess:** \mathcal{A} outputs $\mu' \in \{0, 1\}$. \mathcal{B} outputs 1 when $\mu' = \mu$ then, otherwise it outputs 0.

If $\mu' = \mu$, then the simulation equals to the real game. Therefore, the probability of \mathcal{A} to guess μ correctly is $\frac{1}{2} + \epsilon$. If \mathcal{B} outputs 1, then Z is random in \mathbb{G}_T , then the probability of \mathcal{A} to guess b correctly is $\frac{1}{2}$. Therefore, the advantage of \mathcal{B} to solve the decision L -BDHE assumption is exactly ϵ . □ □

Lemma 4.2. *Under the decision linear assumption, G_2, G_3 and G_4 are indistinguishable.*

The proof of Lemma 4.2 will be provided in the full version of this paper due to space limitation.

Proof of Theorem 4.1. It is straightforward from Lemma 4.1 and Lemma 4.2. □

5. Comparison

We give a brief comparison for efficiency in the following Table 1. We compare our HVE scheme with some current ciphertext policy HVE schemes, including Hattori et al.'s scheme [4], Liao et al.'s scheme [10], Phuong et al.'s scheme [5]² and Murad et al.'s scheme (restricted to AND-gate policy). All the schemes are implemented in Intel Core i5-8250U 1.60GHz, 8G RAM and Ubuntu 16.04. We consider the times of Setup, Key Generation, Encryption and Decryption in these schemes. We can see that decryption in our scheme is much quicker than other schemes. The weakness in our scheme (also in Phuong et al.'s scheme) is that we need a long time to generate a key. Since many applications need instant decryption, our scheme may have great advantage in those instant applications.

6. Conclusion

Hidden Vector Encryption can hide the information of vector used to encrypt the message. Phuong et al. proposed two HVE schemes with constant ciphertext size in composite order and prime order groups respectively. We give an analysis on Phuong et al.'s

²We only compare Phuong et al.'s first scheme in composite order groups because the second scheme is not secure as we show in Section 3.

Table 1. Efficiency Comparison (ms)

Scheme	Group	Setup	Key Generation	Encryption	Decryption
Hattori et al.[2011] [4]	Composite	1,033	17,710	13,405	332,629
Phuong et al.[2014] [5]	Composite	622	499,032	805	22,669
Liao et al.[2015] [10]	Prime	307	2,415	462	13,586
Murad et al.[2019] [13]	Prime	243	1,635	305	1,721
Our scheme	Prime	151	50,387	93	947

Note: we assume that the length of a vector is 1000 and the number of wildcard is 100.

prime order HVE scheme and show their scheme doesn't satisfy the vector-hiding property. Furthermore, we propose an improved construction which also has constant ciphertext size. The security of proposed scheme is proven under the L-BDHE assumption. Future work may be finding more efficient or secure HVE schemes under simple assumptions.

Acknowledgements

This work is supported by the National Key Research and Development Program of China No. 2020YFB1005404, Ministry of Education-China Mobile Scientific Research Fund MCM20200104, and National Natural Science Foundation of China (Grant No. 61872051).

References

- [1] Dan Boneh and Brent Waters. Conjunctive, subset, and range queries on encrypted data. In S.P. Vadhan, editor, *TCC 2007*, volume 4392 of *LNCS*, pages 535–554. Springer-Verlag, 2007.
- [2] Vipul Goyal, Omkant Pandey, Amit Sahai, and Brent Waters. Attribute-based encryption for fine-grained access control of encrypted data. In *CCS '06: Proceedings of the 13th ACM conference on Computer and communications security*, pages 89–98, New York, NY, USA, 2006. ACM.
- [3] John Bethencourt, Amit Sahai, and Brent Waters. Ciphertext-policy attribute-based encryption. In *SP '07: IEEE Symposium on Security and Privacy*, pages 321–334, 2007.
- [4] Mitsuhiro Hattori, Takato Hirano, Takashi Ito, Nori Matsuda, Takumi Mori, Yusuke Sakai, and Kazuo Ohta. Ciphertext-policy delegatable hidden vector encryption and its application to searchable encryption in multi-user setting. In Liqun Chen, editor, *Cryptography and Coding - 13th IMA International Conference, IMACC 2011, Oxford, UK, December 12-15, 2011. Proceedings*, volume 7089 of *Lecture Notes in Computer Science*, pages 190–209. Springer, 2011.
- [5] Tran Viet Xuan Phuong, Guomin Yang, and Willy Susilo. Efficient hidden vector encryption with constant-size ciphertext. In Mirosław Kutylowski and Jaideep Vaidya, editors, *Computer Security - ESORICS 2014 - 19th European Symposium on Research in Computer Security, Wroclaw, Poland, September 7-11, 2014. Proceedings, Part I*, volume 8712 of *Lecture Notes in Computer Science*, pages 472–487. Springer, 2014.
- [6] Jonathan Katz, Amit Sahai, and Brent Waters. Predicate encryption supporting disjunctions, polynomial equations, and inner products. In N. Smart, editor, *Advances in Cryptology - EUROCRYPT 2008*, volume 4965 of *LNCS*, pages 146–162. Springer-Verlag, 2008.
- [7] Tatsuaki Okamoto and Katsuyuki Takashima. Fully secure functional encryption with general relations from the decisional linear assumption. In Tal Rabin, editor, *Advances in Cryptology - CRYPTO 2010*, volume 6223 of *LNCS*, pages 191–208. Springer-Verlag, 2010.
- [8] Jae Hong Seo, Tetsutaro Kobayashi, Miyako Ohkubo, and Koutarou Suzuki. Anonymous hierarchical identity-based encryption with constant size ciphertexts. In S. Jarecki and G. Tsudik, editors, *Public Key Cryptography - PKC 2009*, volume 5443 of *LNCS*, pages 215–234. Springer-Verlag, 2009.

- [9] Michel Abdalla, Dario Catalano, Alexander W. Dent, John Malone-Lee, Gregory Neven, and Nigel P. Smart. Identity-based encryption gone wild. In Michele Bugliesi, Bart Preneel, Vladimiro Sassone, and Ingo Wegener, editors, *ICALP 2006*, volume 4052 of *LNCS*, pages 300–311. Springer-Verlag, 2006.
- [10] Liao Zhenhua, Wang Jinmiao, and Lang Bo. A ciphertext-policy hidden vector encryption scheme supporting multiuser keyword search. *Secur. Commun. Networks*, 8(6):879–887, 2015.
- [11] Kwangsu Lee. Transforming hidden vector encryption schemes from composite to prime order groups. In Seokhie Hong and Jong Hwan Park, editors, *Information Security and Cryptology - ICISC 2016 - 19th International Conference, Seoul, South Korea, November 30 - December 2, 2016, Revised Selected Papers*, volume 10157 of *Lecture Notes in Computer Science*, pages 101–125, 2016.
- [12] James Bartusek, Brent Carmer, Abhishek Jain, Zhengzhong Jin, Tancrede Lepoint, Fermi Ma, Tal Malkin, Alex J. Malozemoff, and Mariana Raykova. Public-key function-private hidden vector encryption (and more). In Steven D. Galbraith and Shiho Moriai, editors, *Advances in Cryptology - ASIACRYPT 2019 - 25th International Conference on the Theory and Application of Cryptology and Information Security, Kobe, Japan, December 8-12, 2019, Proceedings, Part III*, volume 11923 of *Lecture Notes in Computer Science*, pages 489–519. Springer, 2019.
- [13] Miada Murad, Yuan Tian, and Mznah A. Rodhaan. Computationally efficient fine-grain cube cp-abe scheme with partially hidden access structure. In Yuan Tian, Tinghui Ma, and Muhammad Khurram Khan, editors, *Big Data and Security*, pages 135–156, Singapore, 2020. Springer Singapore.
- [14] Xavier Boyen and Brent Waters. Anonymous hierarchical identity-based encryption (without random oracles). In C. Dwork, editor, *Advances in Cryptology - CRYPTO 2006*, volume 4117 of *LNCS*, pages 290–307. Springer-Verlag, 2006.

Performance Analysis of Aerial Base Station Cellular Network

Xue DING^{a,1}, Gongbin QIAN^a and Chunlong HE^{a,b}

^a*Guangdong Key Laboratory of Intelligent Information Processing, Shenzhen University, Shenzhen, 518060, China*

^b*National Mobile Communications Research Laboratory, Southeast University, Nanjing, 211189, China*

Abstract. In this paper, we model the cellular network consisting of aerial base stations (ABSs) which follow homogeneous Poisson Point Process (PPP) and an independent collection of random users is considered. We assume that each user communicates with the closest ABS. In particular, we deal the interference signals with Laplace transform. As a result, we can obtain a tractable expression of the coverage probability. We have found that there is a maximum coverage probability which can be reached by an optimal ABS density and with low signal-to-noise ratio (SNR), the optimal ABS density gets larger when path loss exponent (PLE) increases. Simulations under high or low SNR condition have shown that the influence of PLE on coverage probability is quite different in spite of changing signal-to-interference-plus-noise ratio (SINR) threshold or ABS density.

Keywords. coverage probability, stochastic geometry, Poisson Point Process (PPP), air-to-ground (A2G) communication

1. Introduction

When it comes to deploying ABSs in the sky, unmanned aerial vehicles (UAVs) with the advantage of flexible deployment have aroused much interest among academia and industry [1]. Once the disasters, emergencies or some major events happen, which require rapid and stable network resources, it's of significance to provide wireless connectivity rapidly [2]. Hence, it's necessary to deploy ABSs in the sky to quickly provide connectivity and recover communication.

In the research of aerial cellular network, people have taken advantage of the distribution characteristics of nodes and stochastic geometry as the tool to study the performance of the network. In [3], a framework has been presented to study the coverage probability and achievable rate of the aerial cellular network. However, they simplified the analysis without considering the effect of interference. As is known to all, interference is a key factor to influence the performance. The author in [4] has neglected the small-scale fading to conduct a performance analysis where UAVs served as ABSs. [5]

¹Corresponding author, E-mail: 15910912606@163.com.

is beneficial to have an overall look of the cellular network, especially for a better understanding of the performance analysis. However, the obtained complex analytical results involving multiple nested integrals, can't offer clear and straightforward insights for the future network design. As mentioned above, there are some questions left about the performance of the aerial cellular network.

Firstly, because the A2G link is easier to form a LOS link, we assume that A2G channel experiences a LOS propagation. We later make use of the characteristic of Rayleigh fading channels to conduct a tractable calculation. Then a tractable and accurate coverage probability expression of the aerial cellular network is obtained where ABSs are located as a PPP. Based on the results which have been derived, the impacts of ABS density, SNR and PLE are investigated. The accuracy of our theoretical analysis is proved by comparing with the results of Monte Carlo simulations.

2. System Model

The aerial cellular network model is described as Figure 1, which consists of ABSs arranged according to homogeneous PPP Φ of intensity λ with height h above the ground. The random users under consideration are modeled as an independent stationary point process. The horizontal distance denoted as r is on the assumption of that each user communicates with the closest ABS. PLE of A2G links is α . The power gain of small scale fading g is characterized by Rayleigh fading where the mean of the random variable is unit. And the power of additive white Gaussian noise is characterized by a Gaussian random variable whose mean is zero and variance is N . We assume that ABSs transmit with power normalizing to 1. Therefore, a typical node receives power of value $gr^{-\alpha}$, where the node is away from its ABS with horizontal distance r . The interference power received by the typical user is denoted as I . Excluding the received power from the tagged ABS, the sum of all other ABSs' power forms I . Slivnyak's theorem makes it reasonable to conduct the analysis that a typical user is at the origin [6].

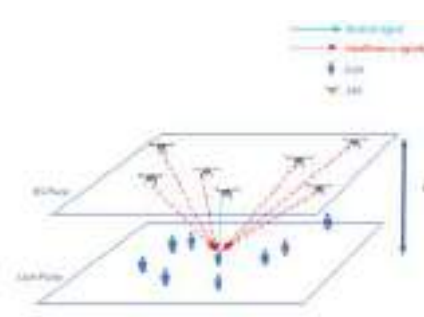


Figure 1. Air-to-ground (A2G) cellular network.

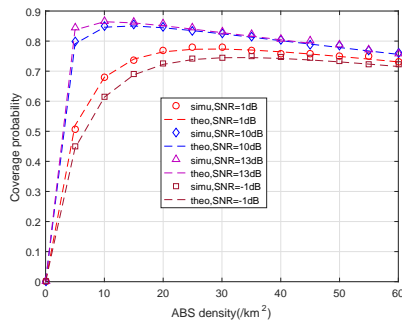


Figure 2. The coverage probability versus ABS density (km^2) with different SNR

3. SINR Coverage Probability

In this section, we derive the downlink coverage probability of the aerial cellular network. A SINR threshold required for the actual SINR of each user is defined. Only when the SINR threshold is lower than the actual SINR, can a user be regarded as being covered, otherwise it is not covered. Subsequently, we will consider the aggregate interference to obtain a closed form of SINR coverage probability when the serving area is assumed to be infinite.

When the actual SINR is larger than a predefined SINR threshold β , the user can be regarded as being covered while be dropped from the network for actual SINR below β . Therefore, we define the probability being covered as

$$P_c(\beta, \lambda, h, \alpha) \triangleq P[\text{SINR} > \beta]. \quad (1)$$

As mentioned above, a typical user is located at the origin. The effective SINR is $\text{SINR} = \frac{g_0 X_0^{-\alpha}}{I+N}$, where $I = \sum_{i \in \phi \setminus \{0\}} g_i X_i^{-\alpha}$. Excluding the received power from the tagged ABS, the sum of all other ABSs' power forms I . The distance between the typical user and interference ABS is denoted as X_i , where $X_i = \sqrt{r_i^2 + h^2}$. The fading is g_i . g_i follows $g_i \sim \exp(1)$.

In the following section, the subscript 0 refers to related parameters of the desired ABS and the subscript i refers to related parameters of the interference ABSs. The PLE is assumed to be a typical value of 4, which can be used to get a closed expression of coverage probability by some mathematical transformation. The coverage probability of a randomly located user can be derived as

$$P_c(\beta, \lambda, h, 4) = c \sqrt{\frac{\pi}{b}} \exp\left(\frac{a^2}{4b}\right) Q\left(\frac{a}{\sqrt{2b}}\right), \quad (2)$$

where $c = \pi \lambda \exp(-A h^2 - \beta N h^4 + \pi \lambda h^2)$, $a = A + \beta N 2 h^2$, $b = \beta N$ and $A = \pi \lambda [\sqrt{\beta} (\frac{\pi}{2} - \arctan(\frac{1}{\sqrt{\beta}})) + 1]$.

The proof of Eq. (2) is given as follows. We assume that a typical user is away from its nearest ABS with distance X_0 and the projection distance is denoted as r . So the conditional coverage probability is

$$\begin{aligned} P(\text{SINR} > \beta | r) &= P\left(\frac{g_0 X_0^{-4}}{I+N} > \beta | r\right) = P(g_0 > \beta (I+N) X_0^4) \\ &\stackrel{(a)}{=} E_I[\exp(-\beta (I+N) X_0^4)] = E_I[\exp(-\beta I X_0^4)] \exp(-\beta N X_0^4), \end{aligned} \quad (3)$$

denote $m = m(r) = \beta X_0^4 = \beta (\sqrt{r^2 + h^2})^4 = \beta (r^2 + h^2)^2$,

$$P(\text{SINR} > \beta | r) = L_I(m) \exp(-mN), \quad (4)$$

g owns unit mean and is exponential distributed, which contributes to the result of (a). With the definition of Laplace transform, we can get the Laplace transform of I . Moreover, if we take the concrete expression into I , we can obtain

$$\begin{aligned}
L_I(m) &= E_I[\exp(-mI)] = E_I[\exp(-m \sum_{i \in \Phi/\{0\}} g_i X_i^{-4})] \\
&= E_{\{g_i, \Phi\}}[\prod_{i \in \Phi/\{0\}} \exp(-mg_i X_i^{-4})] = E_{\{\Phi\}}\{\prod_{i \in \Phi/\{0\}} E_{g_i}[\exp(-mg_i X_i^{-4})]\} \\
&\stackrel{(b)}{=} E_{\{\Phi\}}\{\prod_{i \in \Phi/\{0\}} \frac{1}{1+mX_i^{-4}}\}.
\end{aligned} \tag{5}$$

where (b) follows from the properties of g_i including its independence from process Φ and its distribution characteristic.

As for PPP, the transformation of the expectation of the product of $f(x)$ in Φ is as follows.

$$E[\prod_{x \in \Phi} f(x)] = \exp(-\lambda \int_{R^2} (1-f(x))dx). \tag{6}$$

Due to the communication strategy of a typical user communicating with the nearest ABS, the distances of interference ABSs should be farther than the distance $X_0 = \sqrt{r^2 + h^2}$. Use the change of variables $v^2 + h^2 = y$. So $L_I(m)$ can be further derived as

$$\begin{aligned}
L_I(m) &= \exp(-\lambda \int_{R^2} (1 - \frac{1}{1+mX_i^{-4}})dx) = \exp(-2\pi\lambda \int_r^\infty (1 - \frac{1}{1+m(\sqrt{v^2+h^2})^{-4}})v dv) \\
&= \exp[-\pi\lambda \int_{r^2+h^2}^\infty (1 - \frac{1}{1+my^{-2}})dy] = \exp\{-\pi\lambda \sqrt{\beta}(r^2+h^2)[\frac{\pi}{2} - \arctan(\frac{1}{\sqrt{\beta}})]\}.
\end{aligned} \tag{7}$$

The coverage probability of the whole work is as Eq. (8). We get the function of distribution characteristic of horizontal distance r to the nearest ABS as $f(r)$. $f(r)$ follows $f(r) = 2\pi\lambda r e^{-\lambda\pi r^2}$.

$$\begin{aligned}
P_c(\beta, \lambda, h, 4) &= \int_0^\infty P(\text{SINR} > \beta | r) f(r) dr = \int_0^\infty L_I(m) e^{-mN} f(r) dr \\
&= \int_0^\infty \exp\{-\pi\lambda \sqrt{\beta}(r^2+h^2)[\frac{\pi}{2} - \arctan(\frac{1}{\sqrt{\beta}})]\} e^{-\beta(r^2+h^2)^2 N} 2\pi\lambda r \exp(-\pi\lambda r^2) dr.
\end{aligned} \tag{8}$$

Using the change of variables $r^2 + h^2 = u$, we obtain

$$\begin{aligned}
P_c(\beta, \lambda, h, 4) &= \int_{h^2}^\infty \exp\{-\pi\lambda \sqrt{\beta}u[\frac{\pi}{2} - \arctan(\frac{1}{\sqrt{\beta}})]\} e^{-\beta u^2 N} \pi\lambda \exp(-\pi\lambda(u-h^2)) du \\
&= \int_{h^2}^\infty \exp\{-\pi\lambda[\sqrt{\beta}(\frac{\pi}{2} - \arctan(\frac{1}{\sqrt{\beta}})) + 1]u\} \exp(-\beta N u^2) \pi\lambda \exp(\pi\lambda h^2) du \\
&\stackrel{(d)}{=} \int_{h^2}^\infty \exp(-Au) \exp(-\beta N u^2) \pi\lambda \exp(\pi\lambda h^2) du \\
&\stackrel{(e)}{=} \int_0^\infty \exp(-A(w+h^2)) \exp(-\beta N(w+h^2)^2) \pi\lambda \exp(\pi\lambda h^2) dw \\
&= \int_0^\infty \exp[-(A + \beta N 2h^2)w] \exp(-\beta N w^2) \pi\lambda \exp(-Ah^2 - \beta N h^4 + \pi\lambda h^2) dw.
\end{aligned} \tag{9}$$

In (d), $A = \pi\lambda[\sqrt{\beta}(\frac{\pi}{2} - \arctan(\frac{1}{\sqrt{\beta}})) + 1]$, where (e) uses the change of variables $u - h^2 = w$.

$$\int_0^{\infty} e^{-ax} e^{-bx^2} dx = \sqrt{\frac{\pi}{b}} \exp\left(\frac{a^2}{4b}\right) Q\left(\frac{a}{\sqrt{2b}}\right), \quad (10)$$

We call $Q(x)$ as standard Gaussian tail probability, where $Q(x) = \frac{1}{\sqrt{2\pi}} \int_x^{\infty} \exp(-y^2/2) dy$. Set $a = A + \beta N 2h^2$, and $b = \beta N$, gives

$$P_c(\beta, \lambda, h, 4) = c \sqrt{\frac{\pi}{b}} \exp\left(\frac{a^2}{4b}\right) Q\left(\frac{a}{\sqrt{2b}}\right). \quad (11)$$

where c is given by (2).

4. Numerical Results and Discussion

In this section, the simulation results regarding coverage probability with different system parameters are provided. Theoretical results are verified by comparing with the results from Monte-Carlo simulations. In the end, some system design guidelines to maximize the coverage probability are showed. The simulation process is as follows. We randomly generate the locations of ABSs according to a PPP in an area with a radius of 1000 m. The channel fading gain g between the receiver and transmitter nodes obeys exponential distribution with unit mean. The power of additive white Gaussian noise N is set by different value in different SNR environments. Path loss exponent α is from 2 to 5. We assume that the desired signal power is from the nearest ABS. After the desired power and interference power are obtained, we calculate the actual SINR. If the actual SINR surpasses some SINR threshold defined by our problem, the link is deemed to be successfully covered. Therefore, the successful connection times add one time. The simulations run for 100000 times.

We set SINR threshold=-10dB, $h=100\text{m}$, PLE=4 and theoretical results denoted by dotted lines fit well with Monte Carlo results denoted by different patterns in Figure 2. As we can see, there exists an optimal ABS density to maximize coverage probability. Because in a range of low ABS density, the probability of connecting a nearer ABS by the typical user will raise when increasing ABS density. As a result, communicating distance gets smaller and the received power gets larger which makes coverage probability larger. Once the ABS density exceeds a certain value, the coverage probability is inversely related to the increase of ABS density because users receive increasing interference. Owing that a higher SNR has a smaller noise power, it's obvious that a smaller noise power causes a higher coverage probability.

We set height=100m and $\lambda=10 \text{ ABSs}/\text{km}^2$ in Figure 3 and $\lambda=0.5 \text{ ABSs}/\text{km}^2$ in Figure 4. It shows that there is a positive correlation between PLE and the coverage probability when SNR=50dB in Figure 3. With the high SNR, the effect of noise power is negligible. The larger PLE, the more path loss both the desired signal and interference signal will suffer. However, the decay peed of the interference power and desire power

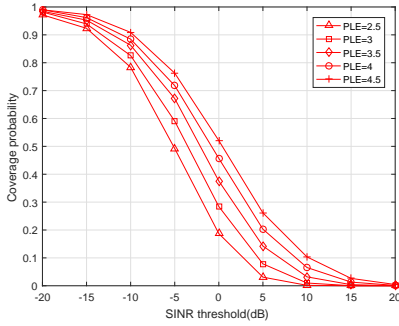


Figure 3. The coverage probability versus SINR threshold(dB) with SNR=50dB.

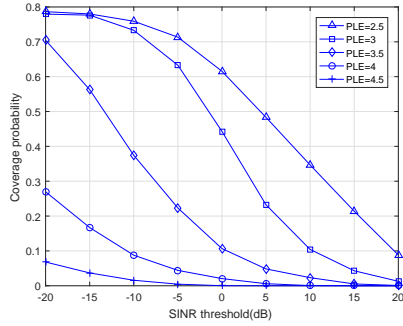


Figure 4. The coverage probability versus SINR threshold(dB) with SNR=1dB.

is quite different. Due to the larger propagation distance of interference ones, the attenuation degree of interference power is more severe than that of desired power. Therefore, the actual SINR is enhanced when increasing PLE which also improves the coverage. While the interference could be neglected with the low SNR condition as Figure 4 presents. The actual SINR is mainly depended on desired power and noise power. It's obvious that when the PLE gets larger, the desired power will become smaller. The noise power can be considered as a constant with the specific environment. Hence the coverage probability is reduced when increasing PLE.

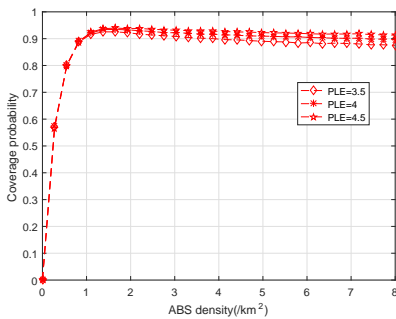


Figure 5. The coverage probability versus ABS density(km^2) with SNR=50dB.

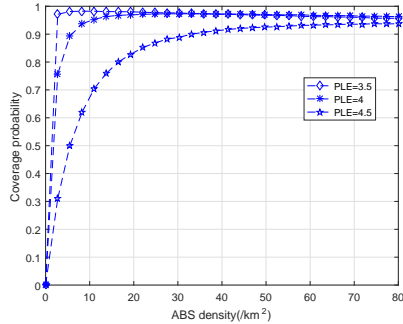


Figure 6. The coverage probability versus ABS density(km^2) with SNR=1dB.

As is demonstrated in Figure 5 and Figure 6, we set SINR threshold=-10dB and height=100m. With high SNR value of 50dB, the larger PLE corresponds to larger coverage probability. However, with low SNR value of 1dB, larger PLE leads to smaller coverage probability. The reason why there are two different results is as the reason of Figure 3 and Figure 4.

We can observe that the optimal ABS densities are very close with different PLEs in Figure 5. As the result of high SNR, the tiny noise power makes it possible to deploy a small number of ABSs to achieve maximum coverage. As for actual SINR, it's mainly

dominated by the ratio of signal power to aggregate interference power and so as the maximum coverage probability. Because the sparse ABS distribution leads to maximum coverage, the change of PLE to large communication distance and interference distances has little impact on the ratio. Therefore, the optimal ABS densities are almost the same under different PLEs. While it shows another phenomenon in Figure 6. As the PLE grows, the optimal ABS density gets larger. Because the SINR is mainly decided by the ratio of signal to noise with low SNR. The desired signal is bound to get smaller and so as SINR with the increase of PLE. Hence, it's necessary to deploy more ABSs to reach the maximum coverage.

5. Conclusion

In this paper, we presented a downlink coverage analysis with different parameters. We modeled the location of ABSs as a PPP. An exact expression of SINR coverage probability for the aerial cellular network under Rayleigh fading channel is obtained. The impacts of ABS density, SNR and PLE were investigated by analyzing the results. We have found that there is a maximum coverage probability which can be reached by an optimal ABS density and with low SNR, the optimal ABS density gets larger when PLE increases. Simulations under high or low SNR condition have shown that the influence of PLE on coverage probability is quite different in spite of changing SINR threshold or ABS density. Some performance trends of cellular parameters have been revealed with the analysis, which contributes to the future system design.

Acknowledgment

This work was supported in part by the Shenzhen Basic Research Program under Grant 20200811192821001 and JCYJ20190808122409660, in part by the Guangdong Basic Research Program under Grant 2019A1515110358, 2021A1515012097, 2020ZDZX1037, 2020ZDZX1021, in part by the open research fund of National Mobile Communications Research Laboratory, Southeast University (No. 2021D16).

References

- [1] C. -H. Liu, D. -C. Liang and R. -H. Gau, "A 3D Modeling Approach to Tractable Analysis in UAV-Enabled Cellular Networks," ICC 2021 - IEEE International Conference on Communications, 2021, pp. 1-6, doi: 10.1109/ICC42927.2021.9500441.
- [2] T. Kim and J. P. Choi, "Performance Analysis of Satellite Server Mobile Edge Computing Architecture," 2020 IEEE 92nd Vehicular Technology Conference (VTC2020-Fall), 2020, pp. 1-6, doi: 10.1109/VTC2020-Fall49728.2020.9348834.
- [3] A. AL-Hourani, S. Chandrasekharan, G. Kaandorp, W. Glenn, A. Jamalipour, and S. Kandeepan, Coverage and rate analysis of aerial base stations [letter], IEEE Transactions on Aerospace and Electronic Systems, vol. 52, no. 6, pp. 3077-3081, 2016.
- [4] M. Mozaffari, W. Saad, M. Bennis, and M. Debbah, Unmanned aerial vehicle with underlaid device-to-device communications: Performance and tradeoffs, IEEE Transactions on Wireless Communications, vol. 15, no. 6, pp. 3949-3963, 2016.
- [5] L. Zhou, Z. Yang, S. Zhou, and W. Zhang, Coverage probability analysis of uav cellular networks in urban environments, in 2018 IEEE International Conference on Communications Workshops (ICC Workshops), 2018, pp. 1-6.

- [6] J. G. Andrews, F. Baccelli, and R. K. Ganti, A tractable approach to coverage and rate in cellular networks, *IEEE Transactions on Communications*, vol. 59, no. 11, pp. 3122-3134, 2011.

Lightweight Application of SM2 Co-Signature Algorithm in the Power IOT

Yanrong ZHANG¹, Feng YANG and Yanfang YUAN
Beijing Smartchip Microelectronics Technology Company Limited, China

Abstract. The access of massive terminal devices at the perception layer poses security threat to the power Internet of Things (IOT) Of the State Grid Corporation. Due to lack of computing resources, the IOT perception layer terminal devices cannot embed the security chips. The lightweight authentication technologies are urgently needed to be developed to protect the authentication security of the IOT perception layer terminal devices. This paper proposes a lightweight identity authentication system based on the SM2 co-signature algorithm, which can be applied to the identity authentication of the IOT perception layer terminal devices. This system is implemented in software and characterized by low cost and strong compatibility, and most importantly, it can strengthen the identity authentication security of the power IOT which security protection capability will be improved consequently.

Keywords. SM2 algorithm, co-signature, lightweight, power IOT

1. Introduction

With the continuous deepening construction of the Power Internet of Things (IOT) of the State Grid Corporation, the continuous exploration and expansion of the power business, the continuous innovation of related technologies have brought new risks to the network security. In particular, the massive terminal devices connected to the network participate in the interaction of the power grid and generate a large amount of data, which brings severe challenges to terminal trust management and network access security. The perception layer terminal devices have become potential risks of invading the power IOT from the outside, which forming an important weakness of power grid security [1].

As the important modules for building the power IOT, the perception layer terminal devices are the key factors of the power IOT security. The data sensed by the terminal devices contain various important information such as personal privacy, economic development and national security. It may cause very dangerous consequences once the information is leaked. With the appearance and development of new technologies such as cloud computing, big data, and mobile applications, the network attacks are constantly being upgraded. It is impossible to completely prevent malicious attacks simply relying on the security design of the terminal devices. How to manage the secure access of massive terminal devices is the key issue to solve the current security protection problems of the power IOT. In response to this problem, the

¹ Corresponding author: Yanrong Zhang, Beijing Smartchip Microelectronics Technology Company Limited, China; E-mail: 474123226@qq.com.

existing research result is to make physical isolation among networks to some certain extent, which enhanced the security of information interchange. However, this measure is relatively single, and the power consumption of the physical isolation equipment is relatively large. Besides, the physical isolation equipment requires more computing resources. This cannot meet the requirements of low power consumption, low cost, and multi-distribution. The lightweight identity authentication technologies are urgently needed to be developed to ensure secure access control of terminal devices [1].

The computing resources of the IOT perception layer terminal devices are limited and the security chip cannot be embedded in. Thus, this leads to the existing identity authentication requirements cannot be met. The co-signature technology based on SM2 algorithm proposed in this paper is implemented in software, and it is characterized by low cost and strong compatibility, and can be widely used in the identity authentication of the IOT perception layer terminal devices to achieve secure access control.

2. SM2 Co-Signature Algorithm

2.1. SM2 Algorithm

SM2 algorithm is an elliptic curve public key cryptography standard issued by the State Cryptography Administration of China, and the relevant standard is "GM/T0003-2012 SM2 Elliptic Curve Public Key Cryptography". In 2018, the SM2 digital signature algorithm became an ISO/IEC international standard. Before SM2 algorithm is used, the following conventions are made for the symbols and operations in this paper: if P and Q are elements (elliptic curve points) in the elliptic curve point group, then $P+Q$ represents the point addition of P and Q ; $[k]P$ represents the point addition of k times P , that is $P+P+\dots+P$ (there are k times P in total); $\text{mod}(n)$ is the operation of modulo n ; " \cdot " represents the multiplication symbol. The public parameters of the SM2 algorithm include q, n, E and G , q is a large prime number; E is an elliptic curve defined on a finite field F_q ; $G = (x_G, y_G)$, is the base point of the n th order on E , and e is the message digest obtained by the signature preprocessing of the message M to be signed. SM2 algorithm consists of key generation, signature generation and signature verification [2][3].

2.2. SM2 Co-Signature Algorithm

SM2 co-signature algorithm is based on SM2 digital signature algorithm mentioned in the standard "GM/T0003-2012 SM2 Elliptic Curve Public Key Cryptography". The principle is as follows: a part of the private key is stored in the client and server respectively, and the two parties can only sign the message together. Neither party can obtain any information about the other party's private key. The signature cannot be forged no matter either party is attacked [4][5].

SM2 co-signature process consists of cooperative key generation and cooperative signature.

1. Cooperative key generation

The client and the server generate a private key component independently, the two parties transmit the auxiliary calculation data through interactive communication, and the sever combines the auxiliary calculation data to generate SM2 public key and publishes it.

The process is as follows:

- 1) The client generates the private key component $D1$.
- 2) The server generates the private key component $D2$, and then calculates the SM2 public key P according to $D1$ and $D2$. P is taken as the SM2 public key.

Figure 1 shows the detailed process of SM2 cooperative key generation.

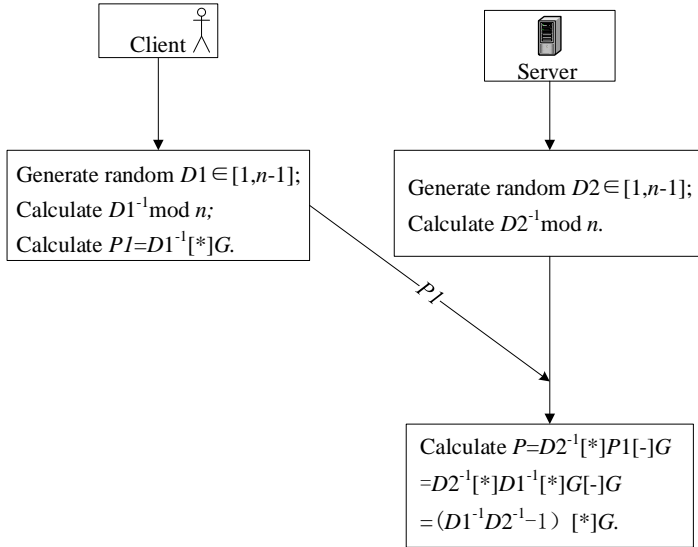


Figure 1 SM2 cooperative key generation

2. Cooperative signature

When the message needs to be signed, the two parties use their respective private key component to calculate the signature component, and then the two parties transmit auxiliary calculation data such as the signature component, and finally, the client combines and calculates the received data to get SM2 co-signature.

The process is as follows:

- 1) The client calculates the digest e of the message M to be signed and the first part of the signature $Q1$, then sends e and $Q1$ to the server;
- 2) The server calculates the second part of the signature r according to $Q1$ and e , and calculates the third part of the signature $s2$ and the fourth part of the signature $s3$ according to $D2$, then sends r , $s2$ and $s3$ to the client;
- 3) The client calculates the complete signature (r, s) according to $D1$, r , $s2$ and $s3$, then outputs it as SM2 co-signature;

Figure 2 shows the detailed process of SM2 co-signature.

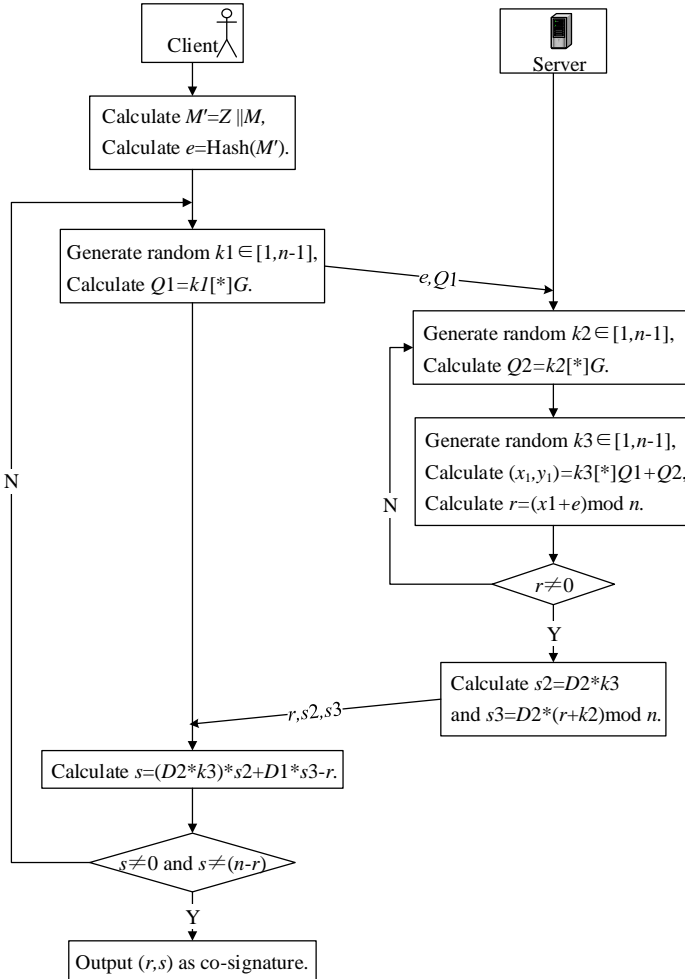


Figure 2 SM2 co-signature

3. Identity Authentication System Based on SM2 Co-signature

3.1. The System Model

The identity authentication system based on SM2 co-signature does not rely on the hardware cryptographic chip, and implements all functions such as reliable cryptographic operation and CA digital certificate operation in software, thereby it can replace the traditional USBKEY technology which implements the above functions in hardware. The system runs in the of the power IOT terminal devices and provides cryptographic computing support for the power IOT application. This system requires the integration of the software development kit (SDK) on the client and server, and the SDK provides the related functions of SM2 co-signature cryptographic operation [6][7].

The application process is as follows:

1) The application system initiates a signature request, and meanwhile pushes the signature request to the client and the server. The client and the server cooperate to calculate the user's public key and SM2 co-signature.

2) The server uses the public key to apply for a user certificate through the CA system, and then uses the user certificate to verify SM2 co-signature, and thus the identity of the client is confirmed.

It has been proved by practice that the SM2 co-signature result is correctly verified by the traditional SM2 signature verification method mentioned in the standard "GM/T0003-2012 SM2 Elliptic Curve Public Key Cryptography". So, the identity authentication system based on SM2 co-signature is reliable [8].

The application process is shown in Figure 3.

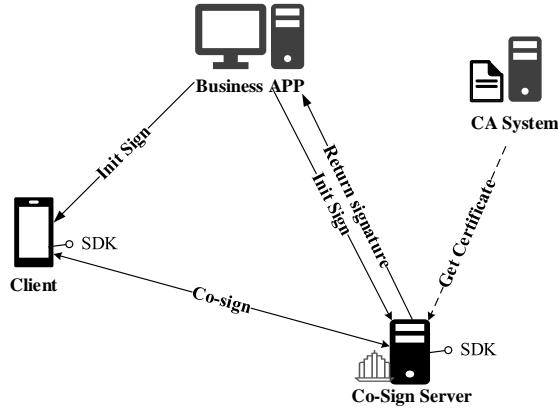


Figure 3 The identity authentication system based on SM2 co-signature

3.2. The System Features

1. Key split

The security design of the identity authentication system based on SM2 co-signature relies on the key split technology. The private key of the traditional SM2 algorithm is split into two parts: the client private key component and the server private key component. The client and the server store their own private key component separately so as to ensure the safe storage.

2. Two parties cooperate to sign

The client and the server calculate their own signature independently. Both of the signatures are used as intermediate results. No signature information can be deduced from the intermediate results. The server transmits the intermediate results to the client, and the client finally completes the final co-signature. The verification of the SM2 co-signature is completed by the server through the user certificate according to the traditional SM2 signature verification method mentioned in the standard "GM/T0003-2012 SM2 Elliptic Curve Public Key Cryptography".

3. Online signature

During the SM2 co-signature process, the client must maintain real-time interaction with the server, and both of them need to be online synchronously, thus the signature performance depends on the network environment.

4. Conclusions

Now the scale of the Power IOT terminal devices connected to the State Grid Corporation reaches tens of millions, and the terminal devices have the characteristics of wide variety, huge scale, wide application, diverse scenarios and complex networks. The identity authentication system based on SM2 co-signature does not rely on any additional hardware cryptographic module. It has strong compatibility, and can solve the security access problem of the diverse perception layer devices with limited computing resources effectively, thereby, an open, efficient and flexible power IOT cryptographic protection system will be built.

Compared with the traditional UKEY authentication technology, the security level of the lightweight identity authentication system based on SM2 co-signature is lower, because UKEY relies on the hardware cryptographic module. However, the authentication system based on SM2 co-signature adopts key split technique and various risk control measures. Only a part of the private key appears on the client or the server, and the complete private key does not appear at any time in the key cycle, which is different from UKEY authentication technology. This prevents the private key from the risk of exposure, and also there is no need for additional chip to store the private key. The chips are more expensive, especially when the number of devices is large, and this system is only to integrate SDK in the device. So, if this system is adopted, the cost will be reduced to a great extent, moreover, the application scenarios of the authentication system will be expanded greatly. The authentication system can also be applied to other fields such as finance, electronics and so on.

References

- [1] HU Zhaohui, LIANG Zhiqiang. Research on authentication technique in electric power information system [J]. *Computer Applications and Software*, 2013, 30 (12): 318-321
- [2] State Cryptography Administration. GM-T 0003-2012 Public Key Cryptographic Algorithm SM2 Based on Elliptic Curves[S]. Beijing: Standards Press of China, 2010.
- [3] Wang Zhaohui, Zhang Zhenfeng. Overview on public key cryptographic algorithm SM2 based on elliptic curves[J]. *Journal of Information Security Research*, 2016, 2 (11): 972-982.
- [4] Feng Qi, He DeBiao. Efficient Two-Party SM2 Signing Protocol for Mobile Internet. *Journal of Computer Research and Development*. 2020, 57 (10): 2136-2146.
- [5] Lin Jingqiang, Ma Yuan. Signature and decryption method and system based on SM2 algorithm suitable for cloud computing. Patent CN 104243456 B, 2014.
- [6] Zhang Yong, Zhang Huan. Secret sharing scheme based on elliptic curve[J]. *Computer Engineering and Applications*, 2014, 50 (8): 90-92.
- [7] Shang Ming, Ma Yuan, Lin Jingqiang. SM2 Elliptic Curve Threshold Cryptographic Algorithm [J]. *Journal of Cryptography*, 2014, 1(2): 155-166.
- [8] Zhang QiuPu, Peng Zhu. A method system of SM2 Cooperative Signature which can verify the client's identity. CN 109246129 A, 2019.

Research of Communication Protocols for Energy Metering Devices

Huaxu SONG¹, Xin XIA, Mi ZHANG, Huipo YUAN and Shouzhi WANG
Beijing Electric Power Science & Smart Chip Technology Co., Ltd., Beijing China

Abstract. In this paper, we will design a set of standard communication protocols that can be used in different electric energy metering device environments by analyzing the communication protocols of the most used electric energy metering devices in the context of IoT smart laboratory construction, so that the electric energy metering devices can automatically detect the inspected equipment. It achieves the purpose of promoting the construction of a smart laboratory, enhancing the management of electric energy metering devices, and improving the efficiency of metering activities. It provides strong support for forming an automated, intelligent and industrialized testing system.

Keywords. Internet of Things, smart laboratory, automatic detection, communication protocol

1. Introduction

Based on Internet technology, supplemented by network communication technology, a network bridge is established between the electrical energy metering device with certain digitalization and the wisdom laboratory, and through this bridge to achieve the function of extracting device data, automatic detection, automatic identification, and automatic control device. With the continuous development and progress of information technology, many occasions have realized the transformation of wisdom. The laboratory is important for carrying out quantity transmission and quality inspection business. It is crucial to recognize the smartness of the laboratory. A series of functions such as receiving tasks, automatic testing, and uploading testing data of energy measurement devices have become essential cornerstones of intelligent laboratories. Therefore, this paper conducts a study on the communication protocols of metering devices.

2. Status of research on communication protocols for energy metering devices

Electricity metering devices are mainly tested for various types of high-precision energy meters. The testing work is carried out with the manual participation of many laboratory personnel, which leads to significant errors in the testing data, incomplete data reporting, subjectivity and randomness, poor timeliness, low accuracy of metering equipment and high error rate. To ensure accurate data, need to repeat the test several times, resulting in

¹Corresponding Author, Beijing Electric Power Science & Smart Chip Technology Co., Ltd., Beijing HaiDian China,100192, E-mail: 1648733414@qq.com.

duplication of personnel efforts, and there are certain safety hazards when testing. Because of the above problems, the design detection process starts from the receiving task of the metering equipment to the end of the task. It performs operations such as automatic data collection, detection, feedback, control, data upload, and real-time monitoring to solve these problems.

In the research, it is found that there are many problems with the current electric energy metering device. First of all, each company's electric energy metering devices use their protocols. Secondly, due to different models and production dates of the same company, the communication protocols of electric energy metering devices will also be slightly different and incompatible, resulting in a large number of electric energy devices. The protocol needs to be parsed before use. The operation and maintenance of the communication protocol of the power metering device are significantly increased in realizing the smart laboratory. As time goes on, the communication protocol will be bloated, so it will take a lot of time, energy, and money to maintain the communication protocol of the electric energy metering device. It will also cause difficulties in integrating the resources of the entire metering industry.

3. Analysis of the current situation of the communication protocol of the power metering device and the design of the standard communication protocol

3.1. Research and analysis of communication protocols of power metering devices with high application volume at present

Taking the communication protocol messages of Sida, ZERA, Sanhui, and Kelu electric energy metering devices as an example to analyze: Sida controls the source cabinet, error cabinet, and standard meter through a communication serial port, and the control source cabinet, error cabinet and standard meter all execute the same Command protocol, the format is the same, the meaning is the same; ZERA controls the source cabinet through a communication serial port and controls the error cabinet through a communication serial port, and the error cabinet communicates with the standard meter. The control source cabinet, error cabinet, and standard meter are different. Command protocol, the format is the same, but the meaning is different; Sanhui controls the source cabinet through a communication serial port and a communication serial port control table, sharing the same set of command protocols; Kelu controls the source cabinet through a communication serial port, and handles the error cabinet through a network cable. A standard set of command protocols. It can be seen from the above four message communication methods that different manufacturers will derive other message communication methods, resulting in the problem of adaptation when connecting to other power metering devices when building a smart laboratory. The specific communication format of each manufacturer is as follows.

The Sida communication protocol is represented as a stream of hexadecimal bytes. The first byte is the functional unit category code. The second byte is the serial number of similar functional units (slaves). The first two bytes together constitute the address code. The third byte is the message length value. The fourth byte is the command code, the subsequent bytes are the specific values of the command code, and finally, the checksum byte is used to end. The checksum is the single-byte hexadecimal data obtained by adding up the contents of each byte of the message frame sent by each communication (excluding the address code, message length, and checksum itself) byte

by byte and discarding the rounding value. The message length is equal to the number of bytes in the message frame except for the "address code" and "frame length value" (including the checksum).

Address + Message Length + Command Code + Value + Checksum

The ZERA communication protocol is displayed in ASCII to hexadecimal, ending in 0D. A control protocol is created by splicing command codes and values.

Command Code+Value+0D

The Sanhui communication protocol is displayed in ASCII to hexadecimal and ends with 0D. Command codes and values are spliced into one control protocol.

Command code: Value+0D

The communication protocol of Kelu is displayed in a hexadecimal byte stream, which is divided into the fixed frame and variable frame. The fixed frame takes 10H as the frame start symbol, the second to fifth bytes are the terminal address, the sixth byte is the function code, and finally, the check code and the 16H frame end symbol are concatenated; the variable frame takes 68H as the frame Start symbol, the second to third bytes are the frame length, the fourth to seventh bytes are the terminal address, the eighth to eleventh bytes are the control field, plus the data field, check code and 16H terminator.

Fixed frame. 10H + terminal address + function code + check digit + 16H

Variable frame. 68H + frame length + terminal address + control field + data area
+ check digit+16H

By parsing and reassembling the communication protocols, the upper computer will receive tasks and then carry out automatic testing and upload test data after the testing is completed. The existing devices will also have the ability to carry out the entire testing process.

From the above, it is clear that the communication protocols of each device manufacturer are very different in detail, which makes it much more challenging to connect the energy metering devices to the smart lab, so it is urgent to unify the protocol messages.

3.2. Design of unified standard communication protocol for electrical energy metering devices

Faced with the existing situation, dismantling, analyzing, and integrating various types of protocols, following the object-oriented principle, and formulating a set of standard communication protocols for electric energy metering devices, require unified management of the communication protocols electric energy metering devices. The automatic detection is divided into the following steps. Each step includes actions such as start, stop, and the status query.

3.2.1. Device initialization

The initialization of the electrical energy metering device allows the device to have certain standardized initial values and resets the calibration parameters that were not restored in the last inspection test.

3.2.2. Initialization of Meter Bits

The initialization of the meter positions allows the device to identify which meter position has a device to be detected and which has no device to be detected.

3.2.3. Device output

The device's output voltage, current, frequency, phase line, and other parameters control powering up and powering down the source and meter.

3.2.4. Device output query

The current real-time status of the device, such as voltage, current, frequency, active power, reactive power, apparent power, three-phase phase voltage, and three-phase phase current, is obtained by querying the output of the device.

3.2.5. Testing test selection

Start the selected test by selecting the test item with the test item-specific parameters.

3.2.6. Test result query

The query of the test results queries the data of the test results.

3.2.7. Stopping the test

Ends the test by sending a stop test command.

3.2.8. Device shutdown

Force the current test to stop, resume initialization, and power down by sending a device shutdown command.

3.2.9. Real-time monitoring

Use the form of an external monitoring device. Monitor the device status in real-time, such as voltage, current, detected results, etc. Then, after the real-time state data model analysis, an automatic warning or forced stop after the device exceeds the limit to avoid damage to the device in the over-limit state. The real-time state data model is a data model for judging electric energy metering devices trained based on a large number of data sets under the framework of deep learning. The basic structure of the deep learning neural network is shown in the following figure.

Neurons. Each node in a neural network is called a neuron and consists of two parts.

Weighted sum. The Weighted sum of all inputs.

Nonlinear transformation (activation function). A nonlinear function transforms the result of the weighted sum to give the neuron computation a nonlinear capability.

Multi-layer connection. Many are arranged at different levels to form a connected multi-layer structure called a neural network.

Forward calculation. Calculating the output from the input, in order from before to after the network.

Calculation chart. Graphically presenting the computational logic of a neural network is also known as a computational graph, which expresses the computational graph of a neural network as an equation.

$$Y = f_3(f_2(f_1(w_1 \cdot x_1 + w_2 \cdot x_2 + w_3 \cdot x_3 + b) + \dots) \dots)$$

Loss Value. A value that measures the difference between the predicted and true values of the model.

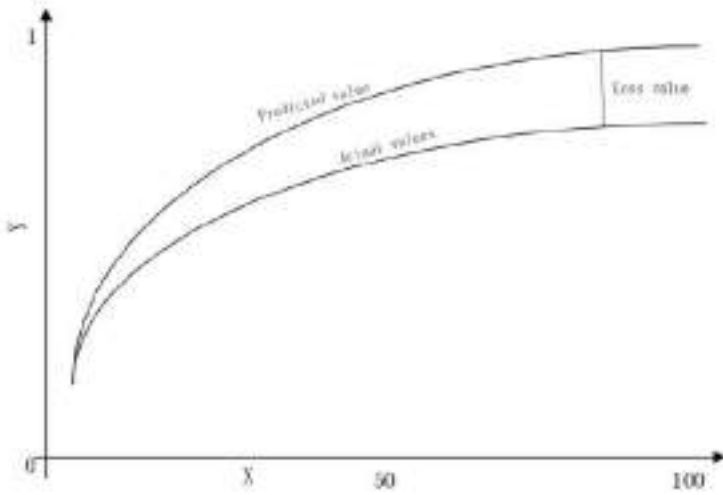


Figure 1. Loss Value chart

3.2.10. Testing process

According to the above design, a whole test process is constructed. In the basic error test, as an example, the device is initialized first. Then the epitope is initialized after the device is initialized. Then the source is upgraded, the error test is performed, and the error data generated in the error test is read simultaneously. And then lower the source, carry out the second set of error tests, repeat the test of all detection points until the detection is completed, and stop the test and turn off the device. The whole test process is equipped with an external real-time monitoring device to monitor the whole process of the electric energy metering device. The specific flow chart is shown in the following figure:

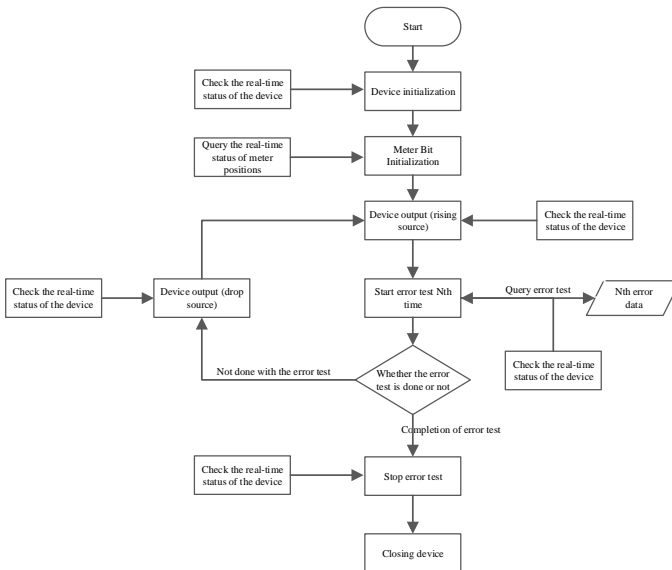


Figure 2. Detection flow chart

3.3. Communication protocol format of power metering device

Develop a unified device communication protocol to send commands to devices in JSON objects. Control of energy metering devices in attribute names and attribute values. Applying an object-oriented form can significantly improve the scalability of the protocol.

3.4. Metering device communication frame diagram design

In constructing the whole intelligent laboratory, the upper information system sends the testing task to the upper computer. The upper computer sends the testing instruction to the electric energy metering device for testing according to the dismantling of the testing task. The electric energy metering device transmits the testing result back to the upper computer, which is assembled into structured data to the information platform, forming a closed-loop data chain to realize the networking work of the electric energy metering device.

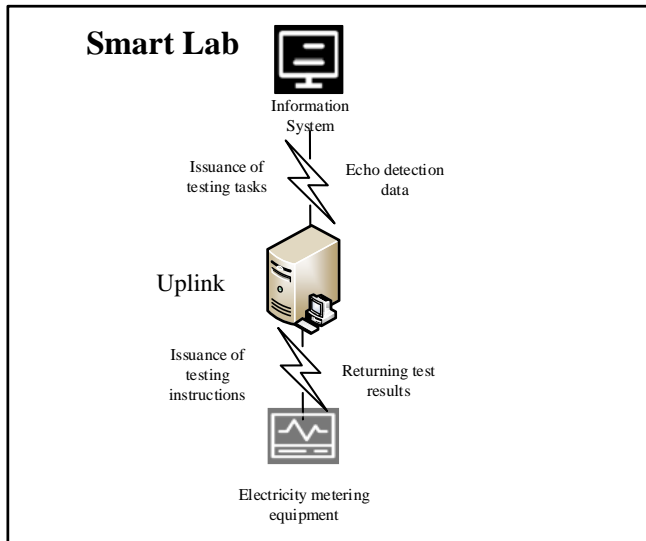


Figure 3. Metering device communication framework diagram

3.5. Design of automatic detection of metering devices

After 2.2-2.4, design, integration, and understanding can automatically detect the electric energy metering equipment. The testing task is sent by the testing personnel using the information system. After the upper computer analyzes and decomposes it into specific testing steps, as shown in 3.2, it sends particular testing instructions to the electric energy metering equipment to automatically test the inspected equipment. The electric energy metering equipment will send the process data back to the upper computer during the test. The electric energy metering equipment will send the test result data back to the upper computer. After analysis, integration, and processing, the upper computer will transmit all data to the information system.

3.6. Test results and analysis

Using 10 sets of electrical energy metering equipment to 1000 sets of tested equipment as a benchmark, for 54 days, 1 set of electrical energy metering equipment to test an average of 100 sets of tested equipment, each electrical energy metering equipment using the original test method and the current test method to test 500 sets of tested equipment respectively.

Efficiency. 500 units of inspected equipment with the original detection method to complete the time of about 20 days, 1 day can test about 25 units of equipment; 500 units of testing equipment with the current detection method to complete the time of about 16, 1 day can test about 30 units of design. The current detection method is 20% more efficient than the original.

Accuracy. The original test method will have 8 times of excessive deviation of error results in every 100 tests; the current process will have 2-3 times of excessive departure of error results in every 100 tests. The current testing method is 69% more accurate than the original.

In terms of personnel, the original detection method requires 5 people to use 10 electric energy measuring equipment, and one person operates 2 electric energy measuring equipment on average; the current detection method uses 2 people to prepare a plan, which can operate 10 electric energy measuring equipment, and one person operates an average of 5 electric energy measuring equipment metering equipment. The current detection method is 250% higher than the original detection method.

4. Advantages of the newly designed standard communication protocol

4.1. Reduce the workload of testing work

The information system automatically configures and issues inspection tasks. The inspection tasks contain the required inspection plans. The operator only needs to review the inspection plans to perform automatic inspections. After the detection test is completed, there is no need for staff to manually enter the detection data and then upload it to the information system. The device automatically uploads the data. This scheme greatly reduces the detection work for the bottom and the data entry work for the top.

4.2. Reduce operation and maintenance costs

Adopt standard communication protocols for new metering electric energy devices to facilitate management. There is no need to face different versions of communication protocols of each company, a set of standard communication protocols to manage all metering electric energy devices, reduce the duplication of development work, and reduce the cost of development.

4.3. To ensure the safety of testing personnel and equipment

Because the task is sent from a remote and operates the electrical energy metering device without personnel directly operating the metering equipment, it significantly reduces the danger to personnel in the detection test to protect their personnel safety. And it can

monitor the status of the equipment through real-time data reporting, timely processing of the equipment over the limit, and other functions to protect the safety of personnel and equipment.

4.4. Guarantee the scientific and accurate testing data

The standard test result data is extracted directly from various electrical energy metering equipment and transmitted to the information system through the channel. Compared with the previous practice of generating reports from electrical energy metering equipment and then manually entering data to upload to the information system, the error rate caused by manual entry is reduced, thus guaranteeing the scientificity and accuracy of the testing data.

5. Conclusion

The study of communication protocols for energy metering equipment provides solutions for solving data siloing and intelligent equipment solutions. It also provides the basis for the analysis of communication protocols for existing equipment and application and the development of standard specification communication protocols for subsequent new equipment. Thus, the laboratory's automation, wisdom, and intelligence ensure the safety of laboratory testing personnel and equipment. Improve the scientificity, accuracy, and traceability of testing work.

References

- [1] Fuentes-Velazquez Jose, Beltran Ernesto, Barocio Emilio, Angeles-Camacho Cesar. A fast automatic detection and classification of voltage magnitude anomalies in distribution network systems using PMU data. *Science Direct*.2022 March; Volume 192, 31. 10.1016/J.MEASUREMENT.2022.110816.
- [2] Zi Qi Yan; Chun Yue Zhou; Tong Xu. Research on the Structure of Smart Laboratory Based on the Internet of Things Technology. *Scientific.net*. 2013 September.Volumes 427-429, Issue 427-429. 2013. PP 2605-2608.
- [3] XU Yong-jun, LIU Yu, WANG Feng. The key technology of the Internet of things [M]. Publishing House of Electronic Industry, 2012. (In Chinese).
- [4] Yiyi Zhouzhou. Research on the Structure of Smart Laboratory Based on the Internet of Things Technology.2013 September. Volume 2748, Issue 427-429. 2013. PP 2605-2608.
- [5] L. Atzori, A. Iera, G. Morabito: *Computer Networks*. Vol. 54 (2010), p.2787–2805.
- [6] Liu Lijuan, Wang Lei, Tang Hong JJG 1085-2013 Standard Electricity Meter [D] Beijing: China Academy of Metrology 2013.
- [7] Ma Ruisong, Tang Hong, Shen Dongxiao JJG597-2005 AC Energy Meter Calibration Device [D] Liaoning: Liaoning Institute of Metrology and Science 2005.
- [8] Xie Xiaojun, Li Qingxian, Zhou Xinhua JJF 1779-2019 Electronic DC Energy Meters [D] Hunan: Hunan Provincial Institute of Metrology and Inspection 2019.

A Method for Exchanging Data Between Master Station and Terminal Based on Key Agreement Mechanism

Qingqin FU ^{a1}, Zhengquan ANG ^b, Fan HE ^a, Guanglun YANG ^a, Yingchun FU ^a, Pingjiang XU ^c, Jia LIU ^c, Ling Yi ^c, Haifeng XU ^a, Zhaoyu LU ^a and Benyang LIU ^a

^a*ZhongGuanCun XinHaiZeYou Technology Co.Ltd, Beijing 100094, China*

^b*Beijing aerospace flight control center, Beijing 100094, China*

^c*Beijing Chip Microelectronics Technology Co., Ltd., Beijing 100192, China*

Abstract. In order to ensure the security of data communication in the electricity consumption information collection system of power users, this paper proposes a security method for data exchange between the master station and the terminal data based on the key agreement mechanism. The method is mainly completed in three steps: first, the master station and the terminal A session channel is established between the two, and session key negotiation is performed to obtain the session key used in the subsequent data exchange process; then, the session key in the session key negotiation is used to perform the authentication operation of the master station to the terminal; finally, the terminal to the master station is used. station for authentication. At the same time, security policies such as encryption and signature are adopted in the process of data interaction. Through these three steps, the mutual authentication between the master station and the terminal is completed, a secure communication channel between the master station and the terminal is established, and the secure data exchange between the master station and the terminal is finally realized.

Keyword. Master station, terminal, session key, session key negotiation, certification, signature, certificate, encryption

1. Introduction

The electricity consumption information collection system of electric power users is a system that collects, processes and monitors the electricity consumption information of electric power users in real time. Metering abnormal monitoring, power quality monitoring, power consumption analysis and management, relevant information release, distributed energy monitoring, information exchange of intelligent power equipment,

¹ Corresponding author, email: fuqingqin@icrus.cn

etc., and ultimately achieve automatic meter reading, off-peak power consumption, power consumption inspection, and load forecasting and saving electricity costs.

In the construction of the electricity consumption information collection system, the main station and the terminal are two indispensable parts. The main station is used to process the data uploaded by the terminal; the terminal can be subdivided into electricity information collection terminal, special transformer Collection terminal, centralized meter reading terminal, distributed energy monitoring terminal and other types. Then, while ensuring the data acquisition and data transmission between the terminal equipment and the main station, realizing the security of the data exchange between the terminal equipment and the main station is a problem that must be solved by power [1-12].

2. Traditional data interaction methods

Before the data exchange between the master station (hereinafter referred to as master) and the terminal, the common practice is to perform internal authentication, external authentication or two-way authentication first. Through these authentications, both parties recognize the other party as a legitimate user, and then the two parties can conduct normal data exchange.

This authentication method, to a certain extent, can avoid illegal user intrusion operations. However, due to the single authentication method and many attack and cracking methods, it is necessary to adopt various means to strengthen communication security [13-29].

3. New data interaction methods

In order to strengthen the security of data exchange between the master and the terminal, to solve the problems of single traditional authentication method and low security, a data exchange method based on key agreement mechanism is proposed. The main implementation steps of this method are as follows:

- 1) The master and the terminal first negotiate the session key;
- 2) Use the negotiated session key to authenticate the terminal from the master;
- 3) The terminal authenticates the master.

The specific implementation method is as follows:

- 1) the master sends a first message to the terminal, and the first message is on the master side, using an asymmetric encryption algorithm to encrypt the master ID and the terminal ID to generate the first private information, and the first private information is encrypted. The information is combined with the IDs of the master and the terminal;
- 2) the master receives the first response message sent by the terminal, and the first response message includes the first random number generated by the terminal and the terminal generated based on the symmetric encryption algorithm and the asymmetric encryption algorithm. Second private information;
- 3) the master verifies the correctness of the second private information and the ID of the master, and after the verification is passed, uses a symmetric encryption algorithm to perform a key negotiation operation on the first

random number to generate a second session key, and in the first When the second session key is the same as the first session key, the first session key is saved.

Thus, the randomness, diversity and security of session key generation are ensured, which is beneficial to improve the security of data interaction.

3.1. Session key negotiation method

Figure 1 shows the session key negotiation process between the master and the terminal.

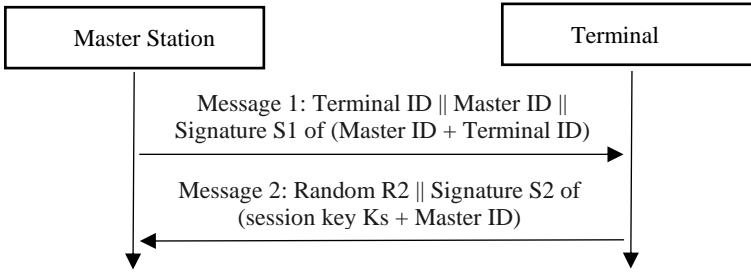


Figure 1. Session key negotiation method

The specific execution process is as follows:

1. The master generates message 1. The specific method for generating message 1 is as follows:

- a) Obtain the terminal ID;
- b) Get the master ID;
- c) Digitally sign with the private key pair (master ID + terminal ID) in the asymmetric key pair to obtain signature S1.

2. The terminal accepts message 1 and organizes message 2 to the master:

- a) Verify the correctness of the signature S1 with the terminal public key;
- b) The random number R2 is generated inside the terminal;
- c) Use the symmetric key to operate on R2 using the key agreement algorithm to generate the session key Ks;
- d) Sign with the terminal private key pair (session key Ks + master ID) to obtain signature S2;
- e) The terminal sends message 2.

3. The master processes packet 2 and negotiates the session key:

- a) Verify the correctness of the signature S2 with the terminal public key;
- b) Compare the correctness of the master ID;
- c) use the symmetric key to operate on R2 using the key agreement algorithm to generate the session key Ks';
- d) Compare Ks and Ks', if they are the same, save the session key Ks for subsequent mutual authentication.

The main implementation methods are as follows:

During session key negotiation, the terminal receives the first packet sent by the master station. The first packet carries the IDs of the master station and the terminal. The master station encrypts the master station ID and the terminal ID using a non-encrypted algorithm to generate the first packet. a private information.

The terminal verifies the correctness of the first private information, generates a first random number after the verification is passed, and uses a symmetric encryption algorithm to perform a key negotiation operation on the first random number to generate a first session key, and uses an asymmetric encryption algorithm to The first session key and the master station ID are encrypted to generate second private information, and the first random number and the second private information are combined to generate a first response message and send to the master station.

The master station performs a key negotiation operation on the first random number based on a symmetric encryption algorithm to generate a second session key. If the second session key is the same as the first session key, the first session key is saved to complete the session key negotiation.

During the session key negotiation, both symmetric encryption algorithm and asymmetric encryption algorithm are used. These two algorithms are used at the same time in the session key negotiation process to obtain the session key. This approach makes the session key more random, Security, which provides a security foundation for subsequent data interaction, which is conducive to improving the security of data interaction.

3.2. The authentication method of the master to the terminal

Figure 2 shows the specific flow and method of authentication of the terminal by the master.

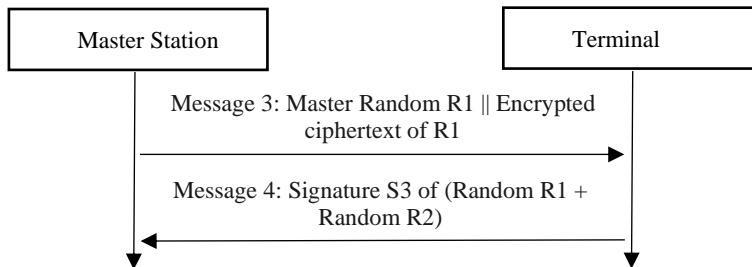


Figure 2. The method of the master to authenticate the terminal

The specific execution process is as follows:

1. The master organizes message 3 and sends it to the terminal:
 - a) Obtain the random number R1;
 - b) Encrypt R1 with the session key K_s to obtain the encrypted ciphertext of R1.
2. The terminal processes message 3 and organizes message 4:
 - a) Decrypt R1 with a symmetric key to get R1';
 - b) Compare R1 and R1', if they are the same, continue
 - c) Sign the data with the public key pair (R1+R2) in the asymmetric key pair to get the signature S3
 - d) Send message 4 to the master.
3. The master processes message 4 and authenticates the terminal:
 - a) Use R1 and R2 generated during session negotiation to verify the correctness of signature S3;

b) If the verification is passed, the master authenticates the terminal successfully, and subsequent messages use the session key generated in the session key negotiation process to perform related operations.

The main implementation methods are as follows:

1) After the terminal receives the third packet sent by the master station, the terminal first uses the preset symmetric encryption algorithm to decrypt the first encrypted ciphertext to obtain the third random number $R1'$. The text is decrypted to obtain a third random number $R1'$.

2) The terminal determines whether the first random number $R1'$ is the same as the first random number $R1$, and if they are the same, encrypts the first random number $R1$ and the second random number $R2$ with a preset asymmetric encryption algorithm to generate the third private information, such as using the private key in the asymmetric key pair to digitally sign the first random number $R1$ and the second random number $R2$ to form a signature $S3$, that is, the third private information.

3) The terminal generates a second response message according to the third private information and sends it to the master station.

4) The master station verifies the correctness of the third private information, and completes the authentication of the terminal by the master station after the verification is passed.

5) After the master station receives the second response message sent by the terminal, the master station verifies the correctness of the third private information, such as using the second random number $R2$ and the first random number $R1$ generated during session negotiation to verify the signature $S3$. correctness.

6) After the verification is passed, the master station authenticates the terminal successfully, and subsequently uses the first session key Ks generated in the session key negotiation to perform data transmission and so on.

3.3. Authentication method of terminal to master

The specific flow and method of the authentication of the terminal to the master are shown in Figure 3.

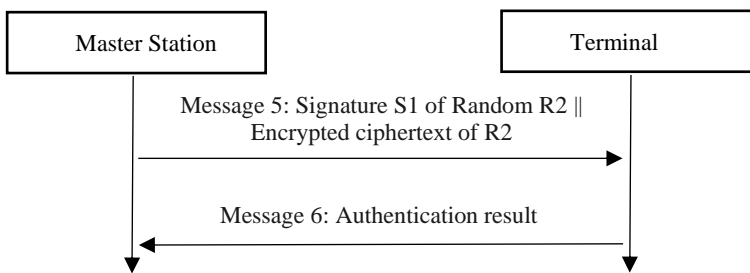


Figure 3. Authentication method of the terminal to the master

The specific execution process is as follows:

1. The master forms message 5 to the terminal:

- a) Sign the terminal random number $R2$ with the private key in the asymmetric key pair to obtain the signature data $S4$;
- b) encrypt $R2$ with the session key Ks ;
- c) Send message 5 to the terminal.

2. The terminal processes message 5 and authenticates the master:
 - a) Use the terminal public key to verify whether the signature S4 is correct;
 - b) The terminal uses the session key Ks to verify whether R2 is correct;
 - c) If the verification is passed, the authentication of the terminal to the master is completed.

The main implementation methods are as follows:

After the session key negotiation is completed, the terminal may perform an authentication operation on the master station by using the first session key Ks obtained through negotiation.

Referring to FIG. 2, at this time, the master station can first encrypt the first random number R1 with a preset asymmetric encryption algorithm to generate fourth private information, and use the first session key Ks to perform encryption on the first random number R1. The second encrypted ciphertext generated by encryption, for example, using the private key in the asymmetric key pair to digitally sign the first random number R1 to form a signature S4, that is, the fourth private information, and use the first session key Ks to perform a digital signature on the first random number R1. The second encrypted ciphertext generated by encrypting the number R1.

Combining the fourth private information and the second encrypted ciphertext to generate a third message and send it to the terminal device. After the terminal receives the third message sent by the master station, it first uses the preset asymmetric encryption algorithm to verify the correctness of the fourth private information, for example, using the terminal public key to verify whether the signature S4 is correct. The first session key Ks verifies whether the first random number R1 is correct.

After the verification is passed, the terminal successfully authenticates the master station, and can subsequently use the first session key Ks generated in the session key negotiation to perform data transmission and so on.

3.4. Data encryption processing method

After the authentication is completed, the data interaction method further includes the following steps: the master uses the first session key to perform data encryption and decryption processing, and judges whether the life cycle of the first session key reaches a preset life cycle; if so, the master Then re-initiate session key negotiation. Further, the primary station judging whether the life cycle of the first session key has reached a preset life cycle includes: the primary station judging whether the number of times of use of the first session key has reached a preset number of times; if so, judging the first session key The life cycle reaches the preset life cycle.

When using the session key generated in the session negotiation process to encrypt and decrypt data in the data interaction process, the number of times the session key can be used can be limited to enhance the security of the session between the master and the terminal. After the number of uses reaches a certain limit, the session key becomes invalid. At this time, the master needs to re-initiate the session key negotiation process to negotiate a new session key.

In practical applications, the number of communications between the master and the terminal can also be set. When the number of communications reaches the limit, the session key becomes invalid, and the master re-initiates the session key negotiation process.

3.5. Comparison of advantages of data exchange methods

This paper proposes a data exchange method based on a key negotiation mechanism. The advantages of this negotiation mechanism are as follows:

1) There are two security methods for establishing a connection between the master and the terminal, one is the authentication of the master to the terminal, and the other is the authentication of the terminal to the master.

2) The session key is obtained by combining the symmetric encryption algorithm and the asymmetric encryption algorithm, which improves the security of key generation.

3) After the session key is negotiated, the master and the terminal can use encryption, signature and other means to process data, which increases the security of data processing for both parties.

4) The method of limiting the number of times of use of the session negotiation key can effectively limit the timeliness of the two parties' sessions, thereby improving the security of use.

4. Conclusion

This paper implements a data exchange method between the master station and the terminal based on the key agreement mechanism. The method is mainly completed in three steps, so as to ensure the safe exchange of data between the master station and the terminal. The three steps of data processing between the master station and the terminal are session key negotiation, authentication of the master station to the terminal, and authentication of the terminal to the master station.

Before data exchange, session key negotiation between the two should be performed first. After the session establishment key negotiation is successful, the key negotiated in the session can be used for authentication and data encryption between the master station and the terminal. The number of communications between the master station and the terminal can be set. If the number of communications between the two reaches the limit, the two need to re-negotiate the session key. Only after the session key negotiation is successful, the data exchange operation can be performed again.

This method is currently applied to the power user's electricity consumption information collection system. In the process of using the system, security strategies such as encryption and signature are adopted to establish a secure communication channel between the two parties and realize the secure communication between the two parties. Different data interaction methods can be selected according to the security requirements of the application. By adopting this method, the security and confidentiality of data exchange can be realized in the electricity user's electricity consumption information collection system.

References

- [1] Xu Pingjiang. Design of smart card file system based on linked list method [J]. *Microcomputer Information*, 2011, 27 (11): 49-50.
- [2] Zhao Dongyan, Wang Yubo. Implementation of a smart card write protection mechanism [J]. *Electronic Technology Application*, 2014, 12: 32-34.

- [3] Fu Qingqin. Implementation of an improved smart card authentication method [J]. Computer Engineering and Science. 2014, 36 (1), 94-98.
- [4] Yuyang LAI. A grey lock method to support once pre-freezing mechanism in IC card[J]. Institute of Electrical and Electronics Engineers Inc. 2014, 1411-1414
- [5] Weibin LIN. A mechanism for patching ROM smart card[J]. Institute of Electrical and Electronics Engineers Inc. 2014, 1415-1417
- [6] Fu Qingqin. A grey lock method to support multiple pre-freezing mechanism in IC card[J]. CRC Press/Balkema, 2015,1395-1400.
- [7] Lai Yuyang. A high security network data transmission implementation [J]. Information Security and Communication Confidentiality, 2016, 2: 109-112.
- [8] Qing-qin FU. [A Novel Power-down Protection Mechanism for Secure Chip Based on CRC Check](#)[A]. EETA2017[C],2017,48-52.
- [9] Jia Liu. [Implementation of IC Card Authentication Method Based on Self-defined Algorithm](#)[A]. EETA2017[C],2017.
- [10] Fu Qingqin. A method for realizing secure chip multi-algorithm processing application[A]. Fuzzy Systems and Data Mining IV.2018,743-748.
- [11] Fu Qingqin. A new secure chip file access method based on security level information[A]. Fuzzy Systems and Data Mining IV.2018,749-756.
- [12] Pingjiang Xu. An Implementation of a Chip Security Mechanism[A]. Fuzzy Systems and Data Mining IV.2018,763-770.
- [13] Xu Pingjiang. State machine based chip access control implementation [J]. Microelectronics and Computer, 2019, 36(7): 98-102.
- [14] Xu Pingjiang. Implementation of a high reliability read/write mechanism for security chips [J]. Computer Application Research, 2019 (increase): 280-282.
- [15] Du Shuwei, Zhao Dongyan. Smart grid chip technology and application [M]. Beijing: China Electric Power Press, 2019.
- [16] Fu Qingqin. A chip data security transmission method based on command control word mode[A]. international conference on information systems, 2019.
- [17] Fu Qingqin. An improved security chip communication rate setting method[A]. international conference on information systems, 2019.
- [18] Fu Qingqin. Research on a Power Chip Power-off Test Method Based on MP300 Device, CECNet,2019.
- [19] Xu Pingjiang et al. System architecture design and roadmap of power chip technology standards [J]. Power Supply, 2020.3:39-44,57
- [20] Zhang Wei et al. A security chip operating system testing device [J]. Information and Computer (Theoretical Edition), 2020.
- [21] Xu Pingjiang et al. Analysis of the support of technical standards for enterprise R&D [J]. Standardization in China, 2021.
- [22] Xu Pingjiang et al. Analysis of the current situation of China's integrated circuit standards [J]. Standardization in China, 2021.
- [23] Xu Pingjiang et al. Analysis of the status quo of China's software industry standards [J]. Standardization in China, 2021.
- [24] Zhou Jing et al. Design of a security chip business test system adapting to multi-core scenarios [J]. Software Engineering and Application, 2021.
- [25] He Fan. A new security authentication method for master station and terminal, IEEE ICEI,2021.
- [26] Fu Qingqin. A new terminal and electric meter legality authentication method, Journal of Computer,2021.
- [27] He Fan. A master station and terminal data exchange method based on symmetric and asymmetric algorithms CECNet, 2021.
- [28] Pang Zhenjiang et al. Design method of security chip operating system [J]. Information Technology and Standardization, 2022.
- [29] Xu Pingjiang et al. Model and implementation of a general middleware for security chips [J]. Information Technology and Standardization, 2022.

A Method for Scientific Cultivation Analysis Based on Knowledge Graphs

Aiyan WU¹, Yongmei ZHANG and Shang YANG

School of Information Science and Technology, North China University of Technology, 100144, China

Abstract. The development of big data and artificial intelligence has improved the intelligence and informatization of scientific planting. A scientific cultivation analysis method based on knowledge graphs is proposed in this paper. First, the logical representation and the ontological representation are combined to realize the access of static cultivation information and dynamic cultivation experience, as well as their representation with graphs. Second, according to the characteristics of plant cultivation information, knowledge extraction is realized via relational computing. A relationship determination method based on the first derivative and a multi-level classification retrieval method based on a tree structure are proposed to extract cultivation experience from the experimental data. Then, multimedia technology is embedded in the RDF framework and implemented, which further realizes the display of decision suggestions after scientific cultivation information analysis. Finally, taking perennial flowers as an example, the realization and application performance of cultivation knowledge graphs are demonstrated.

Keywords. Scientific cultivation, knowledge graph, ontology, cross-media semantic

1. Introduction

With the development of big data and artificial intelligence, the informatization of the planting industry has developed rapidly. Especially in the past five years, planting informatization and sales informatization platforms have been widely used. At present, scientific cultivation driven by large databases has become popular in the field of planting. More and more scholars are interested in how to use big data methods to better diversify cultivation and disease control [1-3]. Therefore, how to control cultivation with advanced information technology has become an important research topic. Many researchers can acquire new knowledge about diverse cultivation and disease control with innovative experiments and analysis of data samples. However, this cultivation knowledge has been in the form of artificial experience. No intelligent analysis system has been formed [4]. Therefore, the universal application of scientific cultivation knowledge is poor. At the 6th International Plant Phenotyping Symposium, big data analysis was specifically discussed for scientific cultivation, promoting the application of big data technology in this area. Among many big data technologies, the knowledge graph has more advantages in mining and displaying the correlations of complex big data

¹Corresponding Author, E-mail: wuaiyan@ncut.edu.cn . The paper is supported by the R&D Program of the Beijing Municipal Education Commission (KM202110009002).

[5]. Therefore, it is used to analyze and display scientific cultivation knowledge, which is helpful to better understand and apply the knowledge.

The main work is as follows:

(1) In order to integrate static cultivation information and dynamic cultivation experience, this paper proposes a dynamic knowledge representation based on logical reasoning and a structured ontology model.

(2) In order to extract empirical knowledge from cultivation information, a relationship determination algorithm based on the first-order derivative is proposed, and a multi-level classification retrieval method based on a tree structure is also proposed.

(3) In order to realize the graphical display of cultivation knowledge, multimedia technology is embedded in the RDF framework and implemented.

(4) The validity of the above methods is demonstrated by taking perennial flowers as an example.

2. Framework Structure of Knowledge Graphs

A knowledge graph is a special graph structure. It uses an ontology to represent natural objects or abstract concepts and uses relationships to simulate the interaction between ontologies [6]. It is represented via the RDF framework, and the core structure is shown in Fig. 1. Its core storage mode is a triple. For example, there is a relationship r between object h and object t , which can be expressed as (h, r, t) . Here, h and t are ontologies in the structural model, and there is a relationship r between them. Many relationships can connect ontologies together. A triple is a subgraph by RDF and finally a complete industry semantic graph is achieved. An industry knowledge graph is a directed graph which contains both semantic information and graph structure information [7-8]. It can be represented by formula (1).

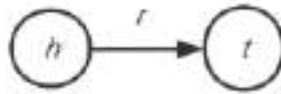


Figure 1. The core structure of the RDF framework.

G is an industry knowledge graph; H is the head ontology set; T is the tail ontology set, and R is the relationship set between ontologies. E is the collection of all ontologies of an industry graph, which contains H and T . In the knowledge graph, any two elements in the triple are known, and the other element can be known by reasoning. Here, the reasoning is actually the correlation effect generated by the various relations of the ontologies. So, the unknown relationships can be obtained by the inference of the known relationships.

$$G = (H, R, T) \quad \begin{cases} H = \{h_1, h_2, \dots, h_n\} \\ R = \{r_1, r_2, \dots, r_m\} \\ T = \{t_1, t_2, \dots, t_s\} \end{cases} \quad (1)$$

$$E = H \cup T \quad H \cap T \neq \phi$$

3. Knowledge Representation of Scientific Cultivation

A knowledge graph of scientific cultivation should show not only the basic attributes of plants, but also the cultivation experience of plant scholars. Plant attributes are static information which can be easily expressed by graphs. But the experience of scholars is dynamic, and this is difficult to express in existing knowledge structures. In this paper, a logical reasoning-based structured ontology model is proposed to represent the dynamic knowledge.

3.1. Dynamic knowledge representation based on logical reasoning and structured ontology model

Plant growth parameters include phenotypic parameters and physiological parameters. These will change with the change of the external environment. The growth environment can directly affect the physiological metabolism of plants and then change their growth behavior and shape. So, plant growth parameters can change with empirical measures, either increase or decrease. In a scientific cultivation experiment, if one phenotypic parameter and one physiological parameter increase or decrease together, there is a same direction relationship between them. On the contrary, there is a reverse relationship.

In order to express a dynamic knowledge system, the structured method of ontology is used to construct the cultivation knowledge graph, and logical reasoning is used to realize the representation of scientific cultivation experience. The ontology is used to express the entity concepts of a knowledge graph regarding cultivation, and the dynamic relationship between ontologies can be expressed by formulas (2) to (5). Here, f represents empirical measures; e and i are phenotypic parameters and physiological parameters, respectively. They are entities expressed by ontologies. R represents the change of ontology, including increase and decrease, which are represented with Δ and ∇ , respectively. Accordingly, the same direction relationship is represented as Δ' and the reverse relationship is represented as ∇' . Triples are used to represent the relationship between ontologies. A dynamic knowledge graph is a series of triple patterns.

$$\exists f_1 \vee f_2 \vee \dots \vee f_n \rightarrow R(e) \quad (2)$$

$$R = \{\Delta, \nabla\} \quad (3)$$

$$\exists \Delta(e) \vee \exists \Delta(i) \Leftrightarrow (e, \Delta', i) \quad (4)$$

$$\exists \Delta(e) \vee \exists \nabla(i) \Leftrightarrow (e, \nabla', i) \quad (5)$$

3.2. Cultivating knowledge extraction

The knowledge in scientific cultivation mainly includes two parts: the influence of scientific measures on physiological parameters, and the relationship between physiological parameters and phenotypic parameters. It is usually necessary to take measures according to the objectives and record the implementation degree and corresponding parameter values. From a scientific cultivation experiment, it is not difficult to find that the parameter values generated under different measures either increase or decrease, and generally show a linear trend. Therefore, a relational calculation method based on the first derivative is proposed, and the relational patterns are represented by triples, as shown in formulas (6) and (7) below.

$$\exists \frac{f'(x_s)}{f'(x'_s)} < 0 \Rightarrow (e_s, \nabla', i_s) \quad x_s \in [e_{s-1}, e_s], x'_s \in [i_{s-1}, i_s] \quad (6)$$

$$\exists \frac{f'(x_s)}{f'(x'_s)} < 0 \Rightarrow (e_s, \nabla', i_s) \quad x_s \in [e_{s-1}, e_s], x'_s \in [i_{s-1}, i_s] \quad (7)$$

Under the same measure, the value of a phenotypic parameter is expressed by e_s , and the value of a physiological parameter is expressed by i_s . The degree of the measures is gradually increased and new parameter values are constantly generated.

4. Realization and Application of the Scientific Cultivation Knowledge Graph

4.1. Definition of ontology conceptual model

Taking perennial flowers as an example, the conceptual model of a cultivation knowledge graph is given. In general, there are nine phenotypic parameters and nine physiological parameters in perennial flowers, and these physiological parameters are mainly photosynthetic parameters. Control measures can be roughly divided into four categories: light, shading, spray chemical reagent, and water control. Therefore, in order to clearly express the correlation between the internal and external parameters of different varieties of perennial flowers, the ontologies are defined with multiple layers in the cultivation knowledge graph. The ontologies and their attributes are defined as shown in Table 1.

Table 1. Definition of the ontologies conceptual model

ontology	sub ontology	attributes	constraints	
plant	non	species	character	
		variety	character	
	Plant height	unit	character	
		value	float	
	Stem diameter	unit	character	
		value	float	
	Number of blades	unit	character	
		value	float	
	Leaf yellowing number	unit	character	
		value	float	
	phenotype	Leaf area	unit	character
			value	float
		Specific leaf weight	unit	character
			value	float
		Bud length	unit	character
value			float	
Bud diameter		unit	character	
		value	float	
Number of flowers		unit	character	
		value	float	
physiology	Pn	unit	character	
		value	float	
	Gs	unit	character	
		value	float	
	Ls	unit	character	
		value	float	
	Ci	unit	character	
		value	float	
	LCP	unit	character	
		value	float	
LSP	unit	character		
	value	float		
Pmax	unit	character		
	value	float		

		value	float
		unit	character
	AQY	value	float
		unit	character
	Rd	value	float
		unit	character
	light	value	float
		effect	character
		unit	character
	shade	value	float
		effect	character
measure		unit	character
	spray chemical reagent	value	float
		effect	character
		unit	character
	control water	value	float
		effect	character

4.2. Implementation of knowledge extraction

Different plants have different growth needs. So, the effect of similar measures on different plants is quite different. Also, the same variety with different measures will get different growth shapes. For example, the shading method can be 75% or 50%, and different implementations can achieve different results. Considering the actual access cost and stability, this research uses a relational database to store cultivation information and triples.

In view of the above experimental characteristics, the experimental information is first stored according to the species of perennial flowers, and then stored according to the varieties in the same species. In the same variety database, the experimental information is first stored according to the category of measures, and then stored according to the implementation method in the same category. The cultivation knowledge mined from the information is stored in a separate database, which is still stored in the same multi-level storage structure. Obviously, this is a multi-level storage structure. For multi-level storage, the most efficient retrieval algorithm is based on a tree structure. Therefore, a multi-level classification retrieval method based on a tree structure is proposed to access the experimental data and extract relationships. The algorithm is described as follows:

```

Traversal(species.variety) /* access database by species.variety */
{
Node=measure; /* Locate the root node according to the measures */
Traversal(node) /* access database by measure */
{
Visit(node.method) /* then access parameter values by method of implementation
*/
While(not null)
{
X=the value of a phenotypic parameter;
X'=the value of a physiological parameter;
If(f'(x)/f'(x')>0)
Assign  $\Delta'$  to triples /* represented by triples */
else Assign  $\nabla'$  to triples
}
}

```

}
}

4.3. Implementation and application of the knowledge graph

The cultivating knowledge graph is dynamic. With the production of new experimental data, it will change. Therefore, the realization of the cultivating knowledge graph mainly includes information updating, knowledge mining, and knowledge retrieval displayed as a graph. The data is updated or accessed according to the above multi-level storage structure. The attribute of the stored information is consistent with the definition of the ontology. With the continuous updating of data, the amount of data will become larger and larger. Therefore, a temporary data table mechanism is set. These new data are first stored in the temporary data table for analysis. After the knowledge is extracted, they are stored in the fixed database. At the same time, the temporary data tables are released.

And the cross-media semantic representation of the knowledge graph is further explored. For example, after analysis, the proposed cultivation method and the main influencing parameters need to be highlighted in the cultivation knowledge graph. Cross-media representation can be achieved by defining related properties. In the realization of the cultivation knowledge graph, the color of the relevant nodes is automatically changed to highlight relevant ontologies. The cross-media semantic representation of knowledge graphs is researched to better display cultivation suggestions that meet the needs of cultivation goals in a unique graphical way. Finally, the Oracle database is used to store experimental information and triples, and Java is used to realize the development of the cultivation knowledge graph.

Taking Marco Polo as an example, the application effect of the cultivation knowledge graph is described. The aim is to have buds about five centimeters long and three flowers per plant. After retrieval and analysis with the cultivation knowledge graph, the recommended cultivation suggestion graph is shown in Fig.2.

Marco Polo

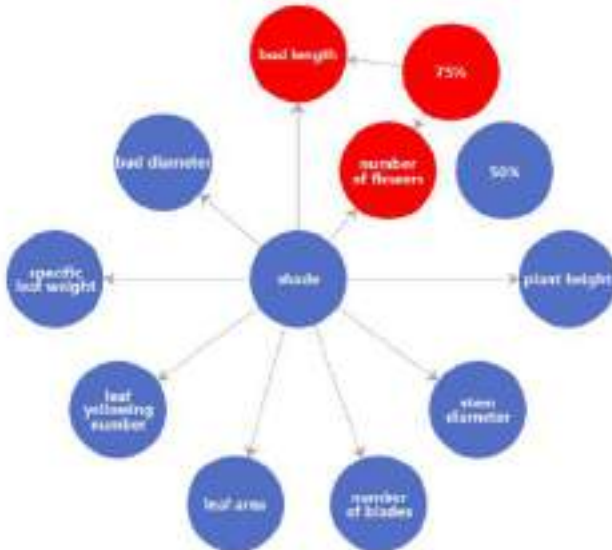


Figure 2. The cultivation analysis graph for Marco Polo.

According to the analysis of the knowledge graph, the 75% shading method can be used to achieve the desired cultivation effect. Fifty Marco Polo plants are experimentally cultivated, of which 25 plants are shaded by 75%. When each plant sprouts to 5 cm long, 25 of them shall be subject to the 75% shading treatment with a black shading net. During the experiment, the management of temperature, humidity, and cultivation are consistent. In the experiment, the bud length and number of flowers are measured, as shown in Fig. 3. As can be seen from this figure, most Marco Polo lilies have flower buds longer than five centimeters and have more than four flowers. Their photosynthetic metabolism can be weakened with the 75% shading method, which reduces their bud length to about five centimeters and number of flowers to three. The expected cultivation results are obtained.

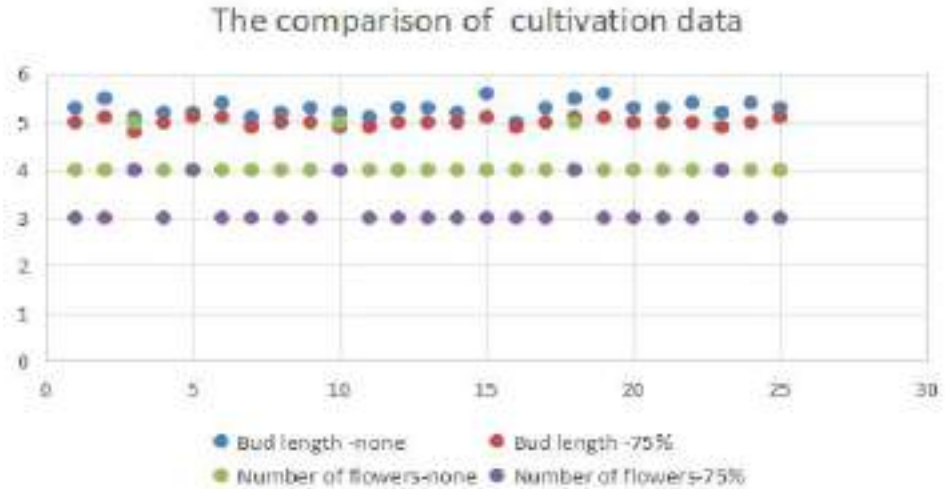


Figure 3. The comparison of cultivation data.

5. Conclusion

This paper presents a scientific cultivation analysis method based on a knowledge graph. It mainly addresses the extraction and display of dynamic experiential knowledge in the process of cultivation analysis. Finally, the scientific cultivation knowledge graph is realized which can provide intelligent analysis and diversified cultivation suggestions for flower cultivation. The effectiveness of this method is proved by the example of lilies cultivated in weak light. The research results will improve the intelligent development of scientific cultivation and the popularization of the cultivation experience.

In the future, the study will be improved from the following aspects. First, it will further discuss how to integrate the knowledge graph and the traditional knowledge representation to better meet the practical application needs of scientific cultivation. Second, the determination of complex relations will be further discussed to better realize intelligent search and accurate cultivation suggestions, and provide a comprehensive reference for the scientific cultivation of flowers with knowledge graph.

References

- [1] Shichao Jin, Xiliang Sun, Fangfang Wu. Lidar Sheds New Light on Plant Phenomics for Plant Breeding and Management: Recent Advances and Future Prospects, *ISPRS Journal of Photogrammetry and Remote Sensing*, 2021, no.171, pp. 202-223.
- [2] Patrick Hüther, Niklas Schandry, Katharina Jandrasits. Erratum to: ARADEEPOPSIS, an Automated Workflow for Top-View Plant Phenomics Using Semantic Segmentation of Leaf States, *The Plant Cell*, 2021, no.32, P. 3674-3688.
- [3] Sunil K. Kenchanmane Raju, Addie M. Thompson, James C. Schnable. *Advances in Plant Phenomics: From Data and Algorithms to Biological Insights, Applications in Plant Sciences*. 2020, vol.8, no.8, pp. 11386.
- [4] Luigi Gennaro Izzo, Matthew A. Mickens, Giovanna Aronne. Spectral Effects of Blue and Red Light on Growth, Anatomy, And Physiology of Lettuce, *Physiologia Plantarum*, 2021, pp. 1-12.
- [5] Zhonggui Ma, Runyu Ni, Kaihang Yu. Recent Advances, Key Techniques and Future Challenges of Knowledge Graph, *Chinese Journal of Engineering*, 2020, vol.42, no.10, pp. 1254-1266.
- [6] Aiyun Wu, Yongmei Zhang. Data Analysis Method of Talent Cultivation Based on Relational Graph, *Journal of Computers*, 2021, vol.32, no.6, pp. 168-175.
- [7] Hogan, Aidan, Eva Blomqvist. Knowledge Graphs, *ACM Computing Surveys*, 2021, vol.54. no.4, pp. 1-37.
- [8] Wiharja Kemas, Jeff Z.Pan. Schema Aware Iterative Knowledge Graph Completion, *Journal of Web Semantics*, 2020, no.65, pp. 100616.

Warning of Dangerous Driving Behavior Caused by Drivers and Road Environmental Factors

Yuhui LIN¹, Hao LIN and Zhiyi LU
Nanjing Forest Police College, Nanjing, China

Abstract. With the development of the supply-side reform of road transportation in China and the rapid development of public transportation, the pressure of public security management is also increasing. According to the statistics of public transport safety accidents, the number of public transport accidents and deaths accounts for about 1% of the total number of relevant road traffic accidents in China, among which 93% of bus accidents are caused by drivers' traffic violations. And, therefore, in order to predict the dangerous driving behavior of public transportation driver, this project combines the driver factors and environmental factors such as weather, road conditions, using the gradient promotion tree algorithm to forecast the risk in the process of public transportation to drive, to achieve the advance management and intervention of public traffic safety, to avoid major public traffic safety accidents, It provides ideas and deployment direction for public security traffic management.

Keywords. Transport, driver, police, security

1 Introduction

With the development of the supply-side reform of road transportation and the rapid and rapid development of public transportation, the pressure of public security management is increasing day by day. From the statistics of public traffic safety accidents, in the past six years, China's annual traffic accidents in about 200,000, the number of people who lost their lives in traffic accidents in about 60,000, the number of injured is as high as more than 200,000. The number of traffic accidents in China in 2019 was 248,000, up 11% year-on-year, with direct property losses of 1.346 billion yuan. Both the number of public traffic accidents and the number of deaths account for about 1% of the corresponding total number of road traffic accidents in China, among which 93% of bus accidents are caused by drivers' traffic violations. According to data from the Work report of the Supreme People's Procuratorate and the Supreme People's Court, dangerous driving is the most serious crime.

In the process of driving, drivers always get various information from the constantly changing traffic environment through their vision, hearing and touch, and make corresponding responses through information identification, information analysis,

¹ Corresponding Author: Nanjing Forest Police College, Nanjing, Nanjing China; Email: gaqb_lyh0520@163.com

information judgment and information decision-making [1]. Different information characteristics will produce different psychological reactions and decisions after analysis and judgment by different drivers. The different reactions and decisions of different drivers and the different combinations of road conditions and traffic conditions determine the level of road safety. It can be seen that controlling drivers' unsafe behaviors is an important way to reduce the frequency of accidents and improve driving safety coefficient.

In addition, the uncertainty of the road environment also increases the incidence of dangerous driving. For data display, the summer vacation and flood season are also the peak period of field management in agricultural production in summer, when people tend to go on intensive trips and travel for work and farming [2]. In addition, there are many rain weather and slippery road accidents in summer, which result in high road traffic safety risks and easily lead to fatigue driving, and are prone to mass death and casualty [3]. Therefore, how to timely prevent the occurrence of dangerous driving behavior according to the road environment factors is also worth the police to think.

At present, there are many studies at home and abroad that evaluate drivers' driving behaviors by detecting human physiological and cognitive states. For example, Katsis et al. from Loanina University demonstrated through experiments that drivers' driving fatigue can be significantly manifested by the signal fluctuation of their heart rate and skin conductance, then adjust the physiological condition of drivers to reduce the occurrence of traffic accidents.

In addition, there are also many studies on the impact of environmental factors on driving safety at home and abroad. For example, Satoshi et al. developed an accident severity assessment model based on ordered probit model in order to better understand the impact of weather on accident severity. In this model, traffic characteristics, road conditions, environment and factors related to multiple vehicles, single bikes and bicycles are considered. Combined with the actual data, the results show that in addition to traffic and road variables, several weather variables also have significant influence on the severity of accidents. Feng Zhongxiang et al. analyzed the influence of road environmental factors on the severity of traffic accidents based on the number of traffic accidents, and the analysis results showed that time period and weather had significant influence on the severity of traffic accidents.

The existing studies only select some dimensions of factors to predict and analyze the severity of accidents, and do not combine driver factors with road environment factors, which has certain limitations.

According to the recent studies mentioned above, existing studies do not combine driver factors with road environmental factors, and many domestic and foreign studies only emphasize the influence of one aspect on dangerous driving behavior [4]. And the existing public transport driver monitoring system is not perfect, lack of advance warning and incident records. In terms of policy supervision, relevant policies can not be formulated and implemented until major accidents occur. At the same time, the safety supervision failed to play the role of third-party supervision forces, and the investment in advanced instruments and equipment was low. Therefore, how to build an intelligent real-time warning system based on public transport drivers' emotional factors and road environment factors has become an important topic for police to prevent public traffic accidents in time.

This project will be the driver factors and environmental factors such as weather and road conditions, using the gradient promotion tree algorithm of public transport in the process of driving risk forecast, achieve the result that in time to prevent dangerous

driving behavior, in order to realize beforehand for public traffic security management and intervention, so as to avoid major public traffic safety accidents and provides ideas and deployment direction for public security traffic management.

2 Module Design

According to the needs above, this project intends to construct a based on driver factors and environmental factors of dangerous driving prediction system, through revitalizing the existing police internal data, this project finally confirmed that drivers' data such as mood states of drivers and fatigue driving state, as well as environmental data such as weather and road conditions are selected as data sources to build the model.

This project consists of three modules, namely, driver data acquisition module, environmental data acquisition module and dangerous driving prediction module, whose operation sequence is shown in Figure 1:



Fig. 1 Project Module Overview.

In the driver data acquisition module of this project, openCV, Dlib, Keras, Tensorflow and other modules in Python will be adopted to call the camera to achieve the acquisition of face data and collect real-time video images. In the environmental data acquisition module, real-time environmental data can be obtained through intelligent meteorological API and main environmental information can be extracted. After obtaining the data, the dangerous driving prediction model is imported to obtain the predicted value of whether dangerous driving is finally possible, and the dangerous driving coefficient is displayed. All the data obtained this time are imported into the database for further analysis.

At present, the mainstream prediction models in the market include Random Forest, Decision Tree, Neural Network, Logistic Regression and Support Vector machine [5], etc. Gradient Boosting Decision Tree (GBDT) in the Decision Tree is selected to build an algorithm model for model training and optimization by testing each model and comparing its prediction accuracy, prediction speed and prediction stability.

After model training, finally confirmed with “weather conditions”, “time (hours)”, “time (week)”, “time (months)”, “emotion”, “fatigue” and “speed” seven fields as input fields, whether “dangerous driving” as the target field, to extract the effective data, can be more objective and comprehensive to restore the truth of events, Improve data utilization.

Finally, the project plans to present an interface that can reflect the driver's driving state in real time, including dangerous driving coefficient, emotional state, eye, aspect ratio of mouth, mouth state and other parameters, which can intuitively reflect the current driving situation and remind the driver to adjust in time.

2.1 Data acquisition module

Based on the driver information acquisition module and environmental data acquisition module, the project builds a prediction model of dangerous driving behavior for drivers. Among them, "sequential fully-CNN" will be used for emotion recognition [6]. The schematic diagram of the model is shown in Figure 2:

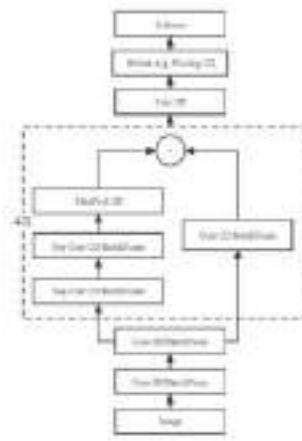


Fig. 2. Model for real-time classification. In FER2013 (35,000) data set of 7 expressions, the model recognition accuracy reached 66%, which can recognize and classify the facial movement features of eight basic expressions, namely, expressionless, happy, sad, surprised, afraid, fearful, angry and disgust, and finally achieve the classification of emotions [7].

The fatigue driving recognition part is to determine whether the driver has the fatigue driving behavior by monitoring the aspect ratio of the eyes and mouth on the basis of determining the key position of the face through the model of emotion recognition part [8]. When the aspect ratio of the driver's eyes is less than a certain threshold, the model will judge that the driver is in the state of eye closure. When the number of eye closing frames exceeds a certain threshold, the model determines that the driver is nodding off and makes corresponding judgment of fatigue driving. When the aspect ratio of the mouth is greater than a certain threshold, the model determines that the driver yawns, and when the number of yawns exceeds a certain threshold, the model makes the judgment of fatigued driving [9]. In addition, when the model can not recognize the driver's face, it is identified that the driver has abnormal driving conditions, and corresponding records are made.

In the module of environmental data acquisition, the project intends to determine the location through the IP address of the system, and at the same time obtain the accurate environmental data information such as weather and road conditions of the location in real time by using API calls.

2.2 Prediction module

The training data set of the prediction model adopts the internal data obtained by the public security system (about 240,000 pieces), including driver information, passenger information, weather conditions, road conditions and other fields (desensitization has been processed). We divided the data set by random allocation in a ratio of 3:7, with 30% of the data as test set and 70% as training set.

After confirming and dividing the data set, we used Gradient Boosting Tree (GBDT) in the Decision Tree to build the algorithm model, and improved the prediction accuracy of the model by adjusting parameters and continuously testing.

GBDT is an integration model, which can be regarded as the linear addition of many base models, among which the base model is CART regression tree [10]. CART tree is a decision tree model. Compared with ordinary ID3 and C4.5, the main feature of CART tree is that it is a binary tree, and the feature value of each node is “yes” and “no”. Such a decision tree recursively divides each feature and determines a unique output in each partition of the input space [11].

After desensitization and structured data processing, we have selected the “weather”, “time (hours)”, “time (week)”, “time (months)”, “emotion”, “fatigue” and “speed” and “accident” eight fields, and use the gradient promotion training tree algorithm of data and model building [12]. Finally, the prediction accuracy of training set and test set reached 82.20% and 81.69% respectively [13].

3 Results



Fig. 3 Program operation effect diagram

As shown in figure 3, “Blinks” are the number of Blinks, which are updated periodically as the program runs; “Blinktime” refers to the time when the eyes close (not blink); Mouth refers to the state of the Mouth, including open and closed. “EAR” refers to eye aspect ratio; “MAR” refers to aspect ratio of mouth; EMOTION refers to emotional states such as neutral and emotional. “No face_time” refers to the length of time when the face information is not detected; “HaqiNUM” is the cumulative number of yawns; “Dangerous_num” indicates the dangerous driving coefficient (0-100) predicted by the prediction model after real-time data is imported into the prediction model. It can be seen that the changes of each parameter will affect the prediction of the model's dangerous driving coefficient in real time. When the emotional state is neutral, the score of the dangerous coefficient is significantly lower than that of emotional.

Finally, the operation mechanism of the dangerous driving warning system proposed in this project is as follows: the driver installs the product on public transport and keeps the product running continuously; The police terminal can access the product, supervise the running state of the product in real time, and provide relevant data (driver information, road condition information, etc.) for the product. When the driver side product monitoring may be driving to the danger of the driver, the dangerous driving coefficient is more than the set value, alert the driver's driving condition, at the same time the data uploaded to the public security, the police after the data analysis, to decide whether the driver's driving condition of intervention, such as to pull over, its replacement driver, etc.; In addition, the data would be stored in a database, and constantly to update the model iteration, and gather more information, such as the driver whether happened traffic accident, whether to have criminal record, whether traffic congestion, etc., enrich and optimization model, the data scale after reaching a certain degree, in different regions using the model of training data in the region, Make products more in line with regional characteristics and related policy requirements. The overall operation logic of the system is shown in Figure 4:

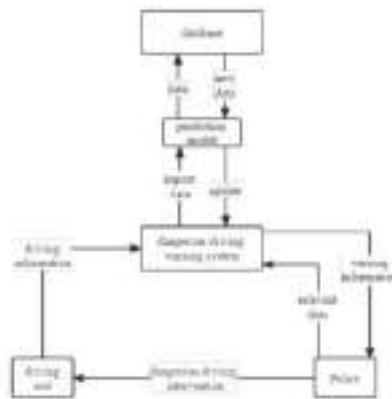


Fig. 4 Schematic diagram of operation mechanism of dangerous driving warning system.

4 Conclusions

Since the Deployment of the Ministry of Public Security to carry out the "four Construction", police organs around the country have seized the opportunity to strengthen information construction around basic information, to create a "big intelligence" work pattern. But up to now, in terms of public transport management, there are still some deficiencies in public transport danger warning research and intelligence collection from the perspective of public security, which makes it difficult to realize immediate supervision and intervention in public transport management.

To achieve public transportation for dangerous driving early warning, this project uses convolution neural network analysis of the driver whether dangerous driving, such as fatigue, emotional, and originally combines the driver factors and environmental factors such as weather and road conditions, and uses gradient ascending tree algorithm to predict the risk coefficient of public transport vehicles in the process of driving,

which provides a new idea for public transport safety management in the new era of police work and builds a management network of public transport vehicles [14].

In the police application, this project has a good application value, to achieve smart police. At the level of proactive regulation and supervision, the traffic management department can determine the driver's driving state and vehicle running condition according to the data returned by the project, as well as the risk coefficient calculated by the system, and determine the vehicle running track based on the road monitoring video to determine whether there is a possibility of danger, so as to implement real-time intervention. At the level of process control, when traffic accident occurs, the police can pass this project the data returned quickly to determine the accident site, quickly mobilize police to the scene to the wounded near the treatment for disposal, such as, the crowd evacuation, traffic channel to prevent casualties caused by treated not in time, or vehicles such as explosion accident caused by secondary damage; In hindsight, when the case is investigated, the data stored and uploaded in this project can record the driver's image information and relevant parameters of vehicle operation at that time, thus providing multidimensional reference data for the police's analysis and judgment, forming a complete chain of evidence, helping to solve the case and "saving" the police from the ambiguous judgment work. To achieve the goal of "Intensify the police by technology" and "Ask technology for police" intelligence policing, actively crack down on illegal and criminal activities, improve the efficiency of solving crimes, safeguard the safety of people's lives and property, maintain social stability.

Of course, there are some deficiencies in our research. Firstly, due to the limitation of data set size and field, we cannot cover all the subjective and objective factors that may affect the driving state of drivers, thus affecting the accuracy of the results to some extent. In addition, in the selection and use of the algorithm, considering the practicality of the system in police work and other needs, the algorithm we choose is relatively more stable, which can not take into account the innovation of the algorithm.

With the continuous advancement of social change and the increasingly frequent technological innovation, the use of surveillance video, artificial intelligence and big data for police forecasting will play a more important role in the future. When the data collected in this project reaches a certain scale, it can provide data support for the study of public traffic accidents by relevant police departments, deeply analyze the causes of public traffic accidents, and carry out corresponding rectification work to prevent public traffic accidents and improve passenger travel safety. At the same time, after the project is widely spread throughout the country, the public transport management network with provinces and cities as units can be constructed, and the database dedicated to each region can be constructed to make the model more consistent with regional characteristics, achieve more accurate prediction and analysis, and explore the factors affecting the smooth operation of public transport in different regions.

Acknowledgements

This research was support by the 2021 College Students Innovation and Entrepreneurship Training Program (Grant No. 202112213015Z). We also would like to express our sincere gratitude to the anonymous reviewers for their valuable comments, which have greatly improved this paper.

References

- [1] Ahmed Jubaer, Ward Nicholas, Otto Jay, McMahill Annmarie. How does emotional intelligence predict driving behaviors among non-commercial drivers?[J]. *Transportation Research Part F: Psychology and Behaviour*, 2022, 85.
- [2] Zhi Zhang, Yingshi Guo, Rui Fu, Wei Yuan, Guosong Yang. Do situational or cognitive factors contribute more to risky driving? A simulated driving study[J]. *Cognition, Technology & Work*, 2020 (prepublish).
- [3] Keonhee Min, Akira Ando. Analysis on Characteristics of Dangerous Driving Events via Recorded Data of Drive-Recorder[J]. *Transportation Research Procedia*, 2020, 48.
- [4] Xingcan Liang. Research on the correlation of dangerous driving behaviors based on naturalistic driving experiment[J]. *IOP Conference Series: Materials Science and Engineering*, 2020, 780(7).
- [5] Xiao Chen, Guoxiong Zhou, Aibin Chen, Ling Pu, Wenjie Chen. The fruit classification algorithm based on the multi-optimization convolutional neural network[J]. *Multimedia Tools and Applications*, 2021 (prepublish).
- [6] Ridza Azri Bin Ramlee, Yvonne Yap, Siva Kumar Subramaniam, Mohamad Harris Misran, Asem Khmag. Transfer learning using AlexNet Convolutional Neural Network for Face Recognition[J]. *International Journal of Innovative Technology and Exploring Engineering (IJITEE)*, 2020, 9(11).
- [7] Arriaga O, Valdenegro-Toro M, Plöger P. Real-time convolutional neural networks for emotion and gender classification[J]. *arXiv preprint arXiv:1710.07557*, 2017.
- [8] Tokarev K E, Zotov V M, Khavronina V N, Rodionova O V. Convolutional neural network of deep learning in computer vision and image classification problems[J]. *IOP Conference Series: Earth and Environmental Science*, 2021, 786(1).
- [9] Jafar Tavvoosi. Designing a new recurrent convolutional neural network for face detection and recognition in a color image[J]. *Iran Journal of Computer Science*, 2021 (prepublish).
- [10] Li Xiaochuan, Mba David, Lin Tianran, Yang Yingjie, Loukopoulos Panagiotis. Just-in-time learning based probabilistic gradient boosting tree for valve failure prognostics[J]. *Mechanical Systems and Signal Processing*, 2021, 150.
- [11] Lao Y, Qi F, Zhou J, et al. A Prediction Method Based on Extreme Gradient Boosting Tree Model and its Application[J]. *Journal of Physics: Conference Series*, 2021, 1995(1):012017-. Hatwell Julian, Gaber Mohamed Medhat, Azad R. Muhammad Atif. gbt-HIPS: Explaining the Classifications of Gradient Boosted Tree Ensembles[J]. *Applied Sciences*, 2021, 11(6).
- [12] Robotics - Robotic Systems; New Findings on Robotic Systems from Shandong University of Science and Technology Summarized (Depth Estimation for a Road Scene Using a Monocular Image Sequence Based On Fully Convolutional Neural Network)[J]. *Computers, Networks & Communications*, 2020.
- [13] Tamon Sadasue, Takuya Tanaka, Ryosuke Kasahara, Arief Darmawan, Tsuyoshi Isshiki. Scalable Hardware Architecture for fast Gradient Boosted Tree Training[J]. *IPSI Transactions on System LSI Design Methodology*, 2021, 14.
- [14] Lien Wu Chen, Hsien Min Chen. Driver Behavior Monitoring and Warning With Dangerous Driving Detection Based on the Internet of Vehicles[J]. *IEEE Transactions on Intelligent Transportation Systems*, 2020, PP(99).

A Low Power Test Data Compression Scheme for Scan Test

Bo YE¹

Shanghai Educational Technology Centre, Shanghai, China

Abstract. In this paper, an uncertain state filling method is proposed, which can not only effectively reduce the scan shifting power consumption, but also reduce the test time simultaneously for scan test. This method is based on the threshold algorithm of uncertain state filling, which can both reduce weighted transitions metric (WTM) and improve compression efficiency for test vectors. Experiments with ISCAS'89 benchmark circuits show that the proposed algorithm can make a good tradeoff between power consumption and compression efficiency.

Keywords. Low power, test data compression, scan test

1. Introduction

As integrated circuit design enters the nano stage, the scale is getting larger and larger, and the power consumption of design and test will bring serious problems [1]. Usually, the problem of test power consumption mainly includes excessive peak power consumption and average power consumption [2]. It is reported that the power consumption of the chip during the scan test is much higher than the normal working mode, which will damage the chip during the scan test, resulting in a reduction in yield [3]. Therefore, more attention should be paid to the power consumption during scan test, so that the test power consumption cannot exceed the threshold. With the increase of SoC's integration and complexity, the test time and cost will also increase significantly [4]. The amount of test data and test time are two other serious problems in SoC testing.

At present, there have been many researches on controlling the amount of test data, test time and power consumption. Test power consumption can be reduced by utilizing low-transition test pattern generators [1] [5-7], test vector reconstruction [8], modification of scan chains [9-10], and build-in-self test (BIST) [11-13]. The low-transition scheme reduces power consumption by assigning a fixed value to the uncertain position in the test channel, or mapping the don't cares to '0' or '1' according to special rules, thus reducing the number of transitions. Test vector reordering technology rearranges the scan latch and test vector, which can improve the power consumption. Scan chain modification technology reduces scan power by modifying structure of scan chains, thus it brings more extra hardware overhead. BIST structures are more suitable for IP core testing, with high fault coverage and low test cost [14].

¹ Corresponding Author, Ye Bo, Shanghai Educational Technology Centre, 1541, Da Lian Rd., Shanghai, China; E-mail: yebo925@126.com.

However, BIST takes a long test time, and it is mainly used for memory testing and is not suitable for general chips.

Test compact [15-16] and test compression techniques [17-20] can be used to reduce the amount of test data and test time. Test compaction technology can reduce the number of test vectors without reducing the fault coverage. But the compacted test sets may cause some physical defects to be undetectable [21]. Test compression technology can reduce the amount of test data and test time, but most of them can't reduce test power simultaneously.

With test data grows fast in large SoCs, the rapid growth of test data increases the test time and power consumption, which leads to the increase of chip test cost, and the increase of power consumption will damage the chip in the test process and bring reliability problems. However, rare methods can significantly improve compression efficiency and reduce power consumption at the same time.

This paper proposes an uncertain state filling algorithm, which can improve the compression efficiency and reduce the power consumption simultaneously. The algorithm can efficiently map the uncertain state to the appropriate determined state 0 or 1, and greatly reduce the test vector's switch activities. It provides a solution that can reduce the test volumes, test time and test power consumption.

2. Uncertain State Filling Algorithm

2.1. Switching Activity in EDT Environment

Scan test power consumption includes shift power consumption and response capture power consumption. Fig.1 shows the embedded deterministic test (EDT) structure.

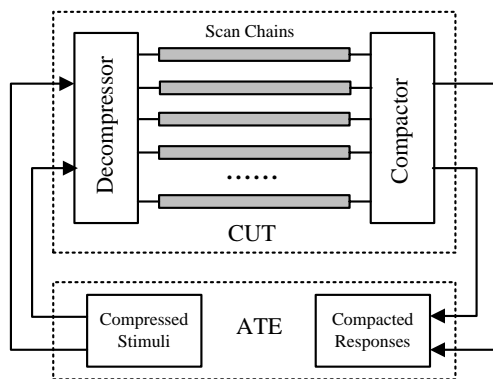


Figure 1. EDT structure.

As shown in Figure 1, the automatic test equipment (ATE) stores compressed test patterns and expected test responses. The compressed test vectors are transmitted to the de-compressor in a continuous manner through external channels during test. The circuit under test (CUT) compacts the test responses and then delivers them to ATE. The scan shifting power is directly dependent on the number of transitions that occur in the scan chains.

2.2. Power Dissipation Model

For CMOS circuits, most of the circuit power consumption is consumed in the conversion process of circuit components from logic 0 to 1 or from logic 1 to 0. During chip testing, the state change of circuit components is closely related to the change of test vectors. When the original inputs or scan flip-flops change the value, these components will switch [22]. Therefore, the scan test power consumption is closely related to the number of transitions of the test vector. Those with more transition times consume more power.

A model for estimating the power consumption of scan test is proposed in [16]. The scan power consumption is related not only to the number of transitions of the test vector, but also to the positions of 0 and 1 in the test vector. For example, for the test vector $v1v2v3v4 = 0100$, where $v1$ is the first vector, and the transition from 0 to 1 in this vector brings more switching behavior than the transition from 1 to 0. The shift power consumption during test can be estimated in the same way. More studies show that transition power consumption plays a major role in test power consumption.

For a scan test sequence $t_j = t_{j,1}, t_{j,2}, \dots, t_{j,l}$, where l is the length of the scan chain and $t_{j,1}$ is the first scan vector. The weighted transitions metric (WTM) [23] for t_j is given by

$$\text{WTM}_j = \sum_{i=1}^{l-1} (l-i)(t_{j,i} \oplus t_{j,i+1}) \quad (1)$$

For a given test set, the peak and average power consumption can be estimated by the following formulas:

$$P_{avg} = \frac{\sum_{j=1}^n \sum_{i=1}^{l-1} (l-i)(t_{j,i} \oplus t_{j,i+1})}{n} \quad (2)$$

$$P_{peak} = \max_{j \in \{1, 2, \dots, n\}} \left\{ \sum_{i=1}^{l-1} (l-i)(t_{j,i} \oplus t_{j,i+1}) \right\} \quad (3)$$

From equations (2), (3), it is obviously that the key to reducing power consumption is to reduce the number of transitions of the test vectors and the weight $l - i$.

2.3. Lower Power Uncertain State Filling Algorithm

For the alternate variable run-length coding [4], to lower the power dissipation and achieve high test compression efficiency, the mapping of don't cares need to consider the value of WTM, the longest length of runs of 1's and 0's, and the least number of consecutive 1's and 0's. The solution is like an N-P complete problem.

To solve the above problem, we introduce the concepts of run factor α and alternate factor β , and we will quickly get the better leverage of power dissipation and compression efficiency. The α is the ratio of real run-length and longest expected run-length. The $\alpha \in [0, 1]$, and α indicates that the 1's or 0's can get its longest run-length when it equals to value '1'. i.e., for test vectors "00XXX11XX10", run length of 0's is

mapped in expected manner, and the prime test sequence is then mapped to “000001,11110”. It is easy to get the longest run of 0’s is 5. But if the prime vector is mapped to “001,1111110”, then we get the longest run of 1’s and its value is 8. So if the prime test sequence is mapped to “00001,111110” during the algorithm executing process, then the run factor for 0’s is $\alpha_0=4/5=0.8$, and the run factor for 1’s is $\alpha_1=6/8=0.75$.

Alternate factor β indicates the alternating status of 0 and 1 in test sequence. If all 1 and 0 appear alternately, that is there are no consecutive 0’s or 1’s, then $\beta=1$, and no separator is needed. If the longest 0’s or 1’s after mapping is S , then $\beta=1/S$, and there are no consecutive 0’s or 1’s when $S=1$. The smaller the β , the higher efficiency the test data compression will be.

The don’t care mapping models can be shown as following:

$$C_{avg} = \frac{\beta P_{avg}}{\alpha_0 \alpha_1} = \frac{\beta \sum_{j=1}^n \sum_{i=1}^{l-1} (l-i)(t_{j,i} \oplus t_{j,i+1})}{n \alpha_0 \alpha_1} \quad (4)$$

$$C_{peak} = \frac{\beta P_{peak}}{\alpha_0 \alpha_1} = \frac{\beta \max_{j \in \{1,2,\dots,n\}} \left\{ \sum_{i=1}^{l-1} (l-i)(t_{j,i} \oplus t_{j,i+1}) \right\}}{\alpha_0 \alpha_1} \quad (5)$$

In (4), (5), C_{avg} is the evaluate parameter of average power and compression efficiency. C_{peak} is the evaluate parameter of peak power and compression efficiency. α_0 and α_1 are run factor for 0’s and 1’s respectively, and β is the alternating factor.

3. Experimental Results

ISCAS’89 full scan circuit is used to verify and compare the compression effect, test time and test power consumption. For the convenience of comparison, every circuit is designed by a single scan chain. Table 1 shows the comparison results for the ISCAS’89 benchmarks for test sets obtained from the Mintest ATPG program between the uncertain state filling technology, the FDR code [24] and the AVR algorithm [5] where T_D is the original test set.

Table 2 shows the comparison between the experimental results of test power consumption using the algorithm in this paper and TRP technology [25], including test peak power consumption and average power consumption. P_{peak} and P_{avg} are the peak and average power dissipation obtained with compacted test sets from the Mintest program. Compared with TRP [25] algorithm, the average reduction of peak power consumption of this algorithm is 38.49%, and the average reduction of average power consumption is 42.37%. It is obvious from Table 2 that this algorithm can not only significantly improve the compression effect, but also significantly reduce the test power consumption.

Table 1. Comparison of compression obtained using T_D

Circuit	Size of T_D (bits)	FDR code (bits) [24]	AVR Code (bits) [5]	This work	
				bits	Percentage Compression
S5378	23754	12346	9233	8856	62.72
S9234	39273	22152	16129	14476	63.14
S13207	165200	30880	23896	19080	88.45
S15850	76986	26000	19388	17761	76.93
S38417	164736	93466	51679	42074	74.46
S38584	199104	77812	57142	48621	75.58

Table 2. Comparison of scan-in power consumption

Circuit	TRP [25]			This work		
	P_{peak}	P_{avg}	P_{peak}	P_{peak}	P_{avg}	P_{avg}
				Reduction (%)		Reduction (%)
S5378	9531	2435	5651	40.71	1459	40.08
S9234	12060	3466	6158	48.94	1673	51.73
S13207	97606	7703	58765	39.79	4576	40.59
S15850	63478	13381	38973	38.60	8055	39.80
S38417	404617	112198	230046	43.14	61013	45.62
S38584	479530	88298	384691	19.78	56184	36.37
Average	-	-	-	38.49	-	42.37

4. Conclusion

We have presented an efficient don't care bit mapping algorithm which can effectively reduce SoC test power dissipation, test volume and test time simultaneously. By introducing the concepts of run factor α and alternate factor β to get the better leverage of the power dissipation and compression efficiency, the corresponding estimation models of power dissipation are also proposed. Experimental results indicate that the uncertain state filling technique is not only effective for the scan shifting power reduction, but also has better test data compression ratio.

Acknowledgment

This work was supported by 2021 Shanghai Educational Science Research Project (Project No.: A2021012).

References

- [1] Nourani M, Tehranipoor M, Ahmed N. Low-transition test pattern generation for BIST-based applications. *IEEE Trans. Computers*. 2008 Mar; 57(3):303-15.
- [2] Ye B, Li TW. A novel BIST scheme for low power testing. *Proc. 3rd IEEE International Conference on Computer Science and Information Technology*; 2010 July 9-11; Chengdu (China) : IEEE Press; Vol 1, p. 134-7.
- [3] Tzeng CW, Huang SY. QC-Fill: Quick-and-cool X-filling for multicasting-based scan test. *IEEE Trans. Comput.-Aided Design Integr. Circuits syst*. 2009 Nov; 28(11):1756-66.
- [4] Ye B, Luo M. A new test data compression method for system-on-a-chip. *Proc. 3rd IEEE International Conference on Computer Science and Information Technology*; 2010 July 9-11; Chengdu (China) : IEEE Press; Vol.1, p.129-33.

- [5] Ye B, Zhao Q, Zhou D, Wang X, Luo M. Test data compression using alternating variable run-length code. *Integration, the VLSI Journal*. 2011 Mar; 44(2):103-10.
- [6] Thubrikar T, Tejas, Kakde S, Gaidhani S, Kamble S, Shah N. Design and implementation of low power test pattern generator using low transitions LFSR. 2017 International Conference on Communication and Signal Processing (ICCSPP); 2017 Apr 6-8; Chennai (India); p.467-71.
- [7] Wang S, Gupta SK. LT-RTPG: A new test-per-scan BIST TPG for low switching activity. *IEEE Transactions on Computer Aided Design of Integrated Circuits and Systems*. 2006 Aug; 25(8):1565-74.
- [8] Bonhomme Y, Girard P, Landrault C, Pravossoudovitch S. Power driven chaining of flip-flops in scan architecture. In *Proc. IEEE International Test Conference*; 2002 Oct 7-10; Baltimore (MD); p.796-803.
- [9] Manikya DM, Jagruthi M, Anjum R, K AK. Design of Test Compression for Multiple Scan Chains Circuits. 2021 International Conference on System, Computation, Automation and Networking (ICSCAN); 2021 Jul; p.1-5.
- [10] Lee S, Cho K, Choi S, Kang S. A New Logic Topology-Based Scan Chain Stitching for Test-Power Reduction. *IEEE Trans. Circuits Syst. II*. 2020 Dec; 67(12):3432-6.
- [11] Sharan SG, Jeeshnu S, Annamalai PH, Rasheed SH, Prabhu E. Design and Implementation of a Power Efficient BIST. 5th International Conference on Computing Methodologies and Communication Computing Methodologies; 2021 Apr 8-10; Erode (India) ; p.555-61.
- [12] Malini M, Geethu RS, Ramesh B. Proposal for Design and Implementation of a Low Power Test Pattern Generator for BIST Applications. 2022 Second International Conference on Artificial Intelligence and Smart Energy (ICAIS); 2022 Feb; p. 1520–24.
- [13] Koneru A, Chakrabarty K. An Interlayer Interconnect BIST and Diagnosis Solution for Monolithic 3-D ICs. *IEEE Trans. Comput.-Aided Des. Integr. Circuits Syst*. 2020 Oct; 39(10):3056-3066.
- [14] Voyiatzis I, Paschalis A, Nikolos D, Halatsis C. An efficient built-in self test method for robust path delay fault testing. *Journal of Electronic Testing: Theory and Applications*. 1996 Apr; 8(2):219-222.
- [15] El-Maleh AH, Khursheed SS, Sait SM. Efficient static compaction techniques for sequential circuits based on reverse-order restoration and test relaxation. *IEEE Transactions on Computer Aided Design of Integrated Circuits and Systems*. 2006; 25(11):2556-64.
- [16] Sankaralingam R, Oruganti RR, Toubna NA. Static Compaction Techniques to Control Scan Vector Power Dissipation. *Proc. 18th IEEE VLSI Test Symp*; 2000 Apr 30-May 4; Montreal, Que (Canada) ; p.35-40.
- [17] Ye C, Zheng S, Tsai F, Wang C, Lee K, Cheng W, Reddy SM, Zawada J, Kassab M, Rajski J. Efficient Test Compression Configuration Selection. *IEEE Trans. Comput.-Aided Des. Integr. Circuits Syst*. 2022 Jul; 41(7), p.2323–36.
- [18] Eggersglus S, Milewski S, Rajski J, Tyszer J. On Reduction of Deterministic Test Pattern Sets. 2021 IEEE International Test Conference (ITC); 2021 Oct 8-15; Anaheim; p. 260–67.
- [19] Yang KC, Lee MT, Wu CH, Li JC. ATPG and Test Compression for Probabilistic Circuits. 2019 International Symposium on VLSI Design, Automation and Test; 2019 Apr 22-25; Taiwan (China) ; p. 1–4.
- [20] Lin SP, Lee CL, Chen JE, Chen JJ, Luo KL. A multilayer data copy test data compression scheme for reducing shifting-in power for multiple scan design. *IEEE Trans. Very Large Scale Integr. (VLSI) Syst*. 2007 Jul; 15(7):767–76.
- [21] El-Maleh AH. Test data compression for system-on-a-chip using extended frequency-directed run-length code. *IET Comput. Digi. Tech*. 2008; 2(3):155-63.
- [22] Pomeranz I, Reddy SM. Scan-BIST based on transition probabilities for circuits with single and multiple scan chains. *IEEE Trans. Computer-Aided Des. Integr. Circuits Syst*. 2006 Mar; 25(3):591–96.
- [23] Rosinger P, Gonciari PT, Al-Hashimi BM, Nicolici N. Simultaneous reduction in volume of test data and power dissipation for system-on-a-chip. *Electronics Letters*. 2001 Nov; 37(24):1434-6.
- [24] Chandra A, Chakrabarty K. Test data compression and test resource partitioning for system-on-a-chip using frequency-directed run-length (FDR) codes. *IEEE Trans. Comput*. 2003 Aug; 52 (8):1076–88.
- [25] Chandra A, Chakrabarty K. A unified approach to reduce SOC test data volume, scan power and testing time. *IEEE Trans. Comput.-Aided Design Integr. Circuits Syst*. 2003 Mar; 22(3):352-62.

Traffic Flow Imputation Based on Multi-Perspective Spatiotemporal Generative Adversarial Networks

Guojiang SHEN, Nali LIU, Yinghui LIU, Wenfeng ZHOU and Xiangjie KONG¹

College of Computer Science & Technology, Zhejiang University of Technology, Hangzhou 310023, China

Abstract. Traffic data occupies an important position in intelligent transportation systems (ITS). However, the collected traffic data is often incomplete. We propose a generative adversarial network (GAN) model based on multi-perspective spatiotemporal learning (MST-GAN) to repair data. To achieve the effect of interpolating data from three perspectives: temporal, spatial, and spatiotemporal, we utilize chained generator with independent parameters to progressively refine the learning of temporal and spatial features. In addition, we achieve high-level fusion of multi-perspective features by adversarial between multiple generators and one discriminator. We conduct experiments on two real datasets, showing that the imputation effect of the MST-GAN model is better than other baseline models under different missing patterns. For example, the root mean square error (RMSE) is less than 7.5% and the mean absolute error (MAE) is less than 5% in the random missing scenario, which is much lower than the best performance error of other models.

Keywords. Traffic flow imputation, Generative adversarial network, Multi-perspective spatiotemporal learning, Deep learning.

1. Introduction

With the rapid integration of big data analysis into ITS[1], the construction of intelligent cities has been promoted. Unfortunately, missing data can occur throughout a distributed urban network due to malfunctioning sensors or communication errors among the collection points[2]. Discarding records is the easiest way to deal with missing data. However, incomplete traffic information may seriously affect the prediction accuracy[3]. Therefore, it is crucial to propose an efficient traffic data imputation method. Most existing deep learning imputation models focus on a single road segment and only consider the temporal dependencies of the data. Most of these methods are based on recurrent neural network (RNN), like LSTM-M[4]. While these RNN-based methods ignore the spatial correlation between different roads. It is difficult to impute the traffic conditions of the entire road network. Recently, more and more works have applied graph-based deep learning techniques in various traffic tasks and have achieved excellent performances[5].

¹Corresponding Author: Xiangjie Kong, College of Computer Science & Technology, Zhejiang University of Technology, Hangzhou 310023, China, E-mail:xjkong@ieee.org.

However, graph-based methods are mainly used to deal with traffic flow prediction and rarely for traffic data imputation. The few existing graph-based imputation methods do not consider the temporal correlation of traffic flow, so the imputation effect is not ideal. The current spatiotemporal data generation work integrates spatiotemporal features to a certain extent. But most of them just use the simple linear superposition of the temporal and spatial model from separate perspectives of temporal and spatial, they do not consider high-level spatiotemporal fusion from multiple perspectives[6].

Missing patterns can seriously affect the performance of the imputation method. We classify the missing patterns in ITS into three categories in this paper: 1) Random missing (RM) (Fig.1(a)), where missing values are completely independent of each other and displayed as randomly scattered points for each sensor (or road); 2) Temporal correlated missing (TCM) (Fig.1(b)), where missing values are dependent in the time dimension and appear as a consecutive time interval for each sensor (or road); 3) Spatially correlated missing (SCM) (Fig.1(c)), where missing values are dependent in the spatial dimension and appear at neighboring sensors or connected road links for each time slot[7]. We will verify the performance of our model on the above three missing patterns.

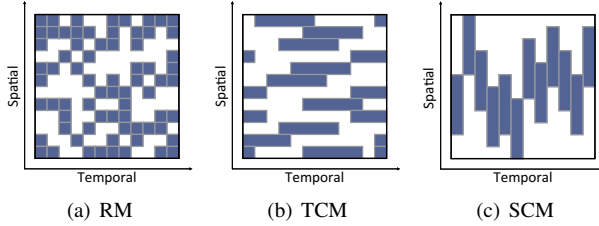


Figure 1. Patterns of missing data.

Our Contribution. To better estimate the lost traffic data, this paper draws on the idea of combining spatiotemporal interaction models and adversarial generative models. Compared with single-generator generative adversarial networks, we construct chained generators for multi-perspective fusion training based on iterated speech enhancement GAN (ISEGAN) and deep speech enhancement GAN (DSEGAN)[8]. Our contributions are as follows: (1) This is the first work to apply a chained generator to impute traffic data. We design a chained generator with independent parameters and one discriminator to capture spatiotemporal features in stages, achieving high-level fusion of spatiotemporal features during adversarial process. (2) We adopt a multi-perspective spatiotemporal learning strategy to impute traffic data by comprehensively analyzing spatiotemporal features from three perspectives: temporal, spatial, and spatiotemporal. (3)The model has been verified on two real large traffic datasets. The results show that the proposed MST-GAN model is much more efficient than other baseline models under different missing patterns.

Related Works. Missing data is inevitable in the Internet of Vehicles (IoV). At present, many methods have been proposed to impute data. Typical traditional imputation methods include support vector regression (SVR)[9], auto-regressive integrated moving average model (ARIMA)[10], etc. These methods ignore information with missing data and only use data before the missing data point, which can affect imputation accuracy because of not taking full advantage of the dataset.

Table 1. The limitations of these existing methods.

Category	Models	Limitations
Tradition	SVR	They ignore information with missing data and only use data before the missing data point.
	ARIMA	
RNN-Based	GRU-D	They only consider temporal information and ignore the global spatial dependencies in the traffic network.
	BRITS	
GAN-Based	GAIN	They focus on non-time-series datasets and do not take targeted measures to deal with spatiotemporal relationships.
	PC-GAIN	
Spatiotemporal	LSTM-AEs	They do not consider the effect of adversarial learning on the fusion of spatiotemporal features.
	GACN	

In recent years, the deep learning method for data imputation has gradually entered the public field. Che et al.[11] proposed the GRU-D model, GRU-D introduces two decay mechanisms so that the influence of the variable will gradually disappear over time when the variable is lost for a period of time. GRU-D uses two representations of the missing pattern, namely masking and time interval, and effectively integrates them into a deep model architecture. So it not only can capture the long-term time dependence in the time series but also use the missing mode to obtain better prediction results. In addition, Cao et al.[12] put forward BRITS model. The model can directly learn missing values in a bidirectional recursive dynamical system without the need for any specific assumptions. Both GRU-D and BRITS models are based on RNN, which only consider the temporal correlation of data, but do not fully consider the impact of spatial information on road network data.

Generative adversarial network is widely used in image data processing, it has been found to have good performance in data imputation in recent years. Yoon et al.[13] proposed the GAIN model based on GAN, they use the generator and discriminator adversarial learning to try to model the distribution of the original data and then achieve the effect of imputing the missing data. Wang et al.[14] proposed the PC-GAIN model, which adds a pre-training process based on GAIN. The PC-GAIN model is proposed to learn the potential category information contained in the subset of low-missing rate data, then it uses synthetic pseudo-labels to determine the auxiliary classifier, and improve the data imputation effect through the joint training of generator, discriminator and classifier. However, GAN-Based model does not consider the spatiotemporal correlation of data, so the imputation effect of traffic data is not very ideal.

Li et al.[15] proposed a deep spatiotemporal time-series missing data imputation model, called LSTM-AE_s, to enhance the imputation performance and handle multiple missing patterns. The proposed model combines deep auto-encoder (DAE) and long-short term memory (LSTM) for extracting spatiotemporal features to estimate missing values in multiple time series. Ye et al.[16] proposed a graph attention convolutional network model (GACN) for traffic-missing data imputation, which follows the encoder-decoder structure and introduces a graph attention mechanism to learn the traffic graph. The spatial correlation of traffic data is collected by adjacent sensors on the graph, and after the attention layer of the graph, a temporal convolutional layer is superimposed

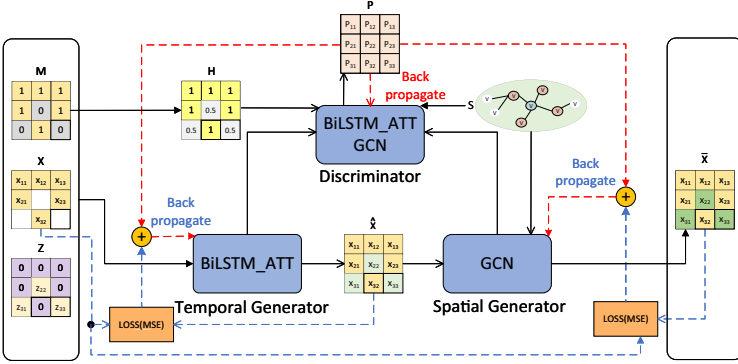


Figure 2. The MST-GAN framework.

to extract the relationship in the time series, so the traffic data can be imputed with higher quality by extracting the typical spatiotemporal features. However, time-domain convolution still has insufficient ability to obtain related information of different lengths in the extraction of time series information. Instead of a simple linear stack of spatial and temporal models, LSTM-AE_s and GACN implement spatiotemporal feature fusion learning through encoder and decoder. At last, we list the summary and limitations of these existing methods in Table 1.

Organization. The remainder of this paper is organized as follows. Section 2 describes the architecture and details of the proposed MST-GAN framework. Section 3 discusses the results of the experiment. Finally, the paper is summarized in Section 4.

2. System Model

2.1. The Overall Framework Analysis

In this section, we will introduce the proposed MST-GAN framework, as shown in Fig. 2. We adopt a learning strategy from three perspectives: temporal, spatial, and spatiotemporal. The temporal generator and spatial generator impute the missing data from the temporal and spatial perspective respectively. We embed temporal and spatial features into two different generators respectively, which can gradually refine the learning of temporal and spatial features in a staged manner. We design different generators with independent parameters so that the model can flexibly learn different spatiotemporal enhancement features at different stages [8]. In addition, the spatial generator inherits the enhanced features of the temporal generator. From the spatiotemporal perspective, the discriminator can combine the temporal and spatial generators to achieve a high-level fusion of spatiotemporal features in confrontation. Throughout the training process, the temporal and spatial generators strive to generate traffic flow data that is closest to the real distribution, and the discriminator judges whether the data is real or generated. The three networks achieve a dynamic balance in this confrontation. Specifically, we use bidirectional LSTM based on attention mechanisms (BiLSTM_ATT) to capture the time series features of traffic data and introduce graph convolutional network (GCN) to realize the spatial feature learning of the road network. Finally, the imputation of traffic data from three perspectives is achieved.

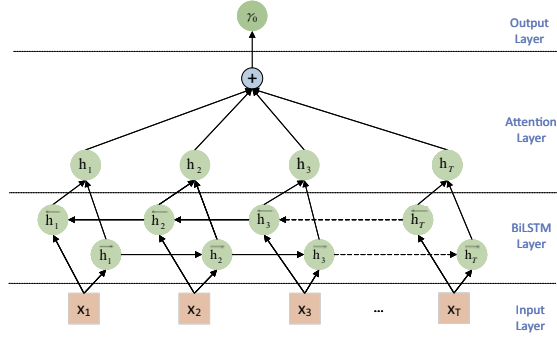


Figure 3. The network structure of BiLSTM_ATT.

2.2. Initial Input Data

The input to the model consists of five parts. Original observed traffic flow data matrix $X = (x_1, x_2, \dots, x_N) \in \mathbb{R}^{N \times T}$ represents the traffic flow of N intersections. $x_i = (x_{i1}, x_{i2}, \dots, x_{iT})$ represents the traffic flow of an intersection at T time gap, where x_{ij} represents the traffic flow situation of the i^{th} intersection in the road network at the j^{th} moment. Mask matrix $M \in \mathbb{R}^{N \times T}$ to characterize whether the road network data is missing, $M_{ij} = 0$ represents the lack of traffic flow data, otherwise $M_{ij} = 1$. The noise matrix Z is independent of other variables and makes the network produce a random distribution. To ensure the generator can generate samples based on the true underlying data distribution in the adversarial process, we introduce the indicator matrix H to provide additional information to the discriminator[13]. The road network matrix S maps the correlation information of different intersections in the road network.

2.3. Temporal Generator

The temporal generator (G_T) analyzes the characteristics of the road network from the temporal perspective. The G_T maps the initial random distribution to the real sample data. The core of G_T 's network structure consists of BiLSTM_ATT, as shown in Fig.3. LSTM is suitable for processing time series data with long intervals and delays, but it only relies on the information of the previous moment to predict the next moment. We introduce BiLSTM_ATT whose main goal is to increase the available information to the network by taking contexts in both directions into account. However, the traffic conditions of road segments change over time, which makes the modeling challenging due to the high dynamics. To address this problem, we compute dynamic weights between different time points by applying a self-attention strategy, that can capture dynamic temporal correlations. Specifically, we first calculate the weight of each time series. Then, we weight and sum the vectors of the all-time series as the feature vector, which produces the output of the temporal generator. The Attention layer is calculated as follows:

$$\begin{aligned}
 V &= \tanh(U) \\
 \alpha &= \text{softmax}(W_\alpha^T V) \\
 \gamma &= U \alpha^T
 \end{aligned} \tag{1}$$

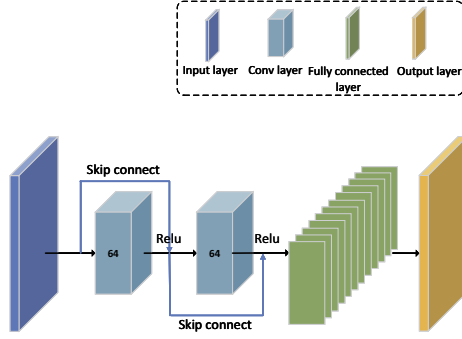


Figure 4. The network structure of GCN.

where the matrix $U = [u_1, u_2, \dots, u_T] \in d^{N \times T}$ (T is the length of time), $u_t = BiLSTM(x_t)$. $x_t = (x_{1t}, x_{2t}, x_{3t}, \dots, x_{Nt})$ denotes the observation of each intersection in the t -time interval. $W_\alpha \in d^N$ is learned as a training parameter. $\gamma = U\alpha^T \in d^N$ is actually a weighted sum of each hidden state based on the distribution of attention.

In summary, we define the above as $\gamma_k = x_{T+k+1} = Attention(BiLSTM(x_{T+k}))$, ($k = 0, 1, \dots, T-1, \gamma_k \in d^N$), then there is $X_{BiLSTM_ATT} = (\gamma_0, \gamma_1, \dots, \gamma_{T-1})$, the final output value \hat{X} of temporal generator is formulated as:

$$\begin{aligned} X_{BiLSTM_ATT} &= Attention(BiLSTM(X)) \\ \hat{X} &= X \odot M + X_{BiLSTM_ATT} \odot (1 - M) \end{aligned} \quad (2)$$

2.4. Spatial Generator

The spatial generator (G_S) analyzes the characteristics of the road network from the spatial perspective. G_S strives to capture hidden spatial information to generate outputs that are closer to the real sample feature distribution. We know that the traffic flow between different intersections will affect each other. The relationship adjacency graph formed by different intersections is a non-euclidean structure. Graph neural networks (GNNs) can capture spatial dependencies of non-Euclidean graph structures[17]. Therefore, the core of G_S 's network structure consists of GCN with two convolutional layers and a fully connected layer. The convolutional layer converts the input features into an internal hidden feature map and extracts local features. The fully connected layer reassembles these local features into complete features. Finally, we restore the feature maps to their original sizes. We know that as the depth of the network layer increases, it may bring about the problem of gradient dissipation. Therefore, we introduce skip connect to facilitate training deep networks in our model. In the G_S , we use ReLU as the activation function, which is relatively simple in gradient computation. As shown in Fig.4, both convolutional and fully connected layers are carefully designed to ensure that input and output spatial features are of the same size. At each time step of generation phase, G_S retains the position with the true value and populates the generated data into the missing position, thereby improving the guiding force of the observations to the model. After training with the spatial generator, we can impute missing values using the following equation:

$$\bar{X} = X \odot M + G_S(\hat{X}) \odot (1 - M) \quad (3)$$

2.5. Discriminator

The discriminator D achieves high-level fusion of spatiotemporal features from a spatiotemporal perspective. The generator strives to make the simulated data closer to the true value, and the discriminator strives to identify the observed and generated data, which is the process of two neural networks playing against each other. They eventually reach a dynamic equilibrium. In this paper, we achieve dynamic fusion of spatiotemporal features by confronting the discriminator with the spatiotemporal generator, abandoning the simple linear stacking scheme. We use a linear combination of the encoding loss and the adversarial loss to construct the generator loss according to a certain proportion, where the encoding loss function adopts the MSE function. We perform model optimization with two generators losses and a discriminator loss. The core structure of the discriminator network is composed of BiLSTM_ATT and GCN. The BiLSTM_ATT network structure is similar to the temporal generator. The GCN network contains two convolutional layers and a fully connected layer. Its structure is similar to the spatial generator. Besides, the indicator matrix H is introduced to provide additional information to the discriminator, where $H = X \odot M + 0.5 \odot (1 - M)$. The matrix H ensures that the generator generates samples based on the true underlying data distribution. The loss function of the discriminator can be expressed as:

$$L_D = -\frac{1}{n} \sum_{i=1}^n (M \cdot \log D(\bar{X}) + (1 - M) \cdot \log(1 - D(\bar{X}))) \quad (4)$$

We define the minmax goals for MST-GAN as:

$$\min_{G_T, G_S} \max_D E_{\bar{X}, M} [M \cdot \log D(\bar{X}) + (1 - M) \cdot \log(1 - D(\bar{X}))] \quad (5)$$

3. Experiments Settings and Performance Evaluation

3.1. Data Description

PEMS04 and PEMS08 datasets are from the California Department of Transportation Performance Measurement System. The data features include flow, occupy, speed, our paper only focuses on the flow data features for performance evaluation. PEMS04 dataset includes 307 detectors, the data range is 59 days, from January 1, 2018, to February 28, 2018. PEMS08 contains data collected by 170 detectors in a total of 62 days from July 1, 2016, to August 31, 2016. The time interval is 5 minutes, and 288 samples are generated at the same intersection every day.

3.2. Experiment Settings

In this paper, the first 50 days of the dataset are used as the training data, the remaining data is used as the test data. We choose $T = 576$ time steps (i.e., $5\text{min} * 576 = 48$ hours) as the imputation window. During training, we use the sliding window method to perform

imputation on $[t, t + T)$, $[t + T, t + 2T)$, $[t + 2T, t + 3T)$, etc. The model was trained using the Adam optimizer with an initial learning rate of 0.01 and a batch size of 48. We normalize the attention coefficients of time series using Softmax. The performance of the model is compared with other baseline methods at different missing rates of 30%-80%. We choose MAE and RMSE as evaluation indicators. Here's how the evaluation metrics are calculated:

$$MAE = \frac{1}{n} \sum_{i=1}^n \|\hat{y}_i - y_i\|$$

$$RMSE = \sqrt{\frac{1}{n} \sum_{i=1}^n (\hat{y}_i - y_i)^2}$$
(6)

where n represents the number of missing data, \hat{y}_i represents the prediction of missing value, and y_i represents the observed value.

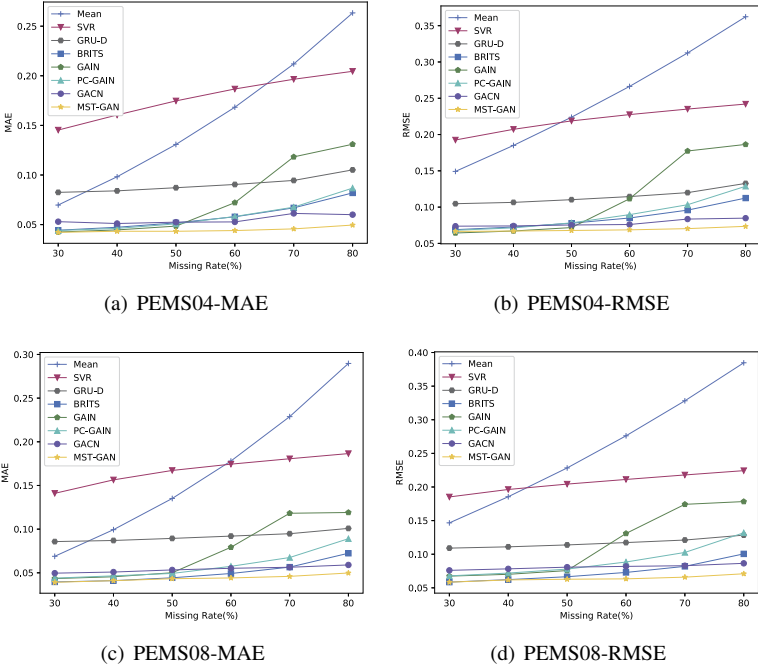


Figure 5. Performance comparison for imputation on PEMS04 and PEMS08 datasets in RM pattern. The abscissa represents different data missing rates, and the ordinate represents the loss of different models under different evaluation indicators.

3.3. Experiments Results and Evaluation

3.3.1. Baseline Analysis

Fig.5 shows the visualization results of data imputation errors under different evaluation metrics and different missing rates in RM pattern. We can draw the following conclu-

sions: First, only the performance of MST-GAN and GACN based on spatiotemporal feature information is relatively stable when the missing rate is higher than 50%. But according to Fig.5, the imputation error of our model is lower than the GACN model. Second, in both PEMS04 and PEMS08 datasets, the RMSE of the MST-GAN model is less than 7.5%, and the MAE is less than 5%, which is lower than the error of the best performance of other models. Third, the performance of Mean is the worst in all datasets, and the impact of data missing rate is also the greatest. The performance of SVR is better than Mean, but the imputation performance of machine learning is significantly lower than that of deep learning. Fourth, GRU-D and BRITS are data imputation models based

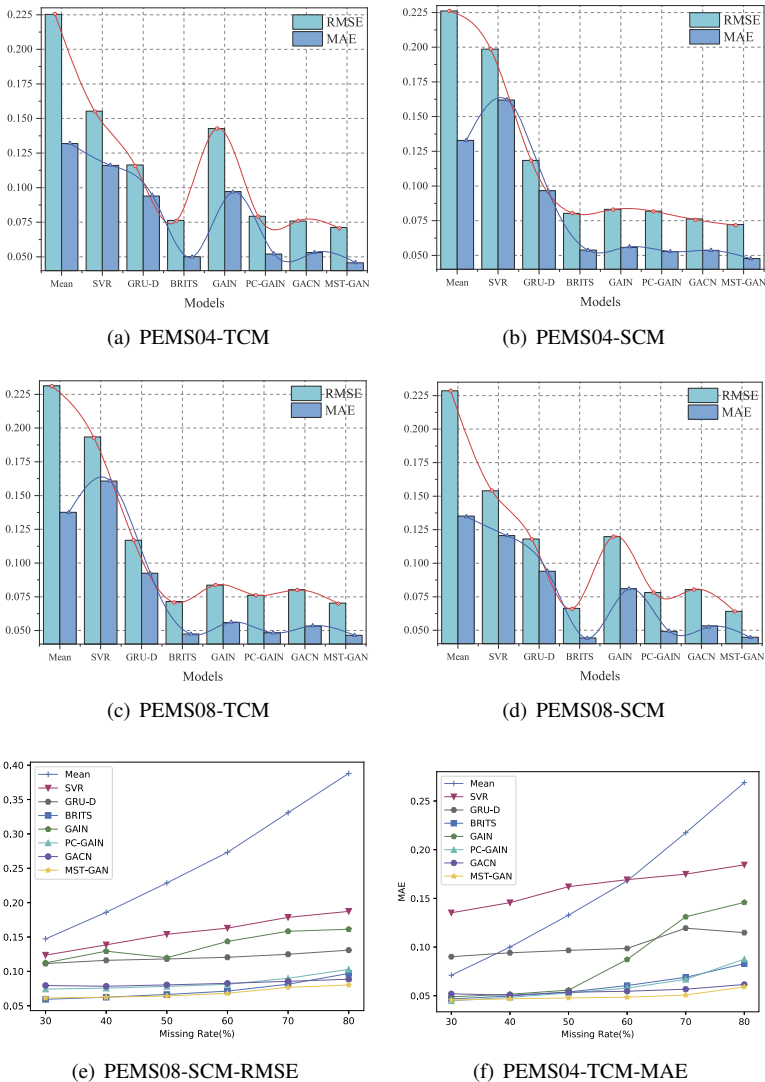


Figure 6. Performance comparison for imputation on PEMS04 and PEMS08 datasets in SCM and TCM patterns.

on time series features, and their performance is better than that of machine learning. Fifth, GAIN and PC-GAIN are data imputation models based on data distribution, they are difficult to apply to data imputation in the case of high missing rate, and their imputation error increases significantly when the missing rate is greater than 50%. This is because when the missing rate gradually increases, it is difficult for GANs based on learning data distribution to learn from historical data.

Fig.5 shows the performance of different models as the missing rate changes in the random missing mode. In Fig.6, we design the performance of each model in different missing patterns and datasets, where Fig.6 (a)-(d) are Typical of 50% missing cases. The abscissa represents different models, and the ordinate represents the evaluation indicators RMSE and MAE. We can find that our model has very stable traffic flow data imputation performance regardless of the evaluation metric. Fig.6 (e)-(f) are linear line charts of each baseline model under different datasets, missing patterns and evaluation metrics. It is evident that our model also outperforms other models in terms of TCM and SCM missing patterns. In conclusion, our method has better traffic data imputation performance than other baseline models in all missing cases.

3.3.2. Ablation Study

To verify that the multiple generators outperform the single spatiotemporal generator, we conduct ablation experiment MST-GAN-DG. Since RM is the most commonly studied missing type in literature, we use the RM scenario for experiments. MST-GAN-DG removes one generator and modifies both the generator and discriminator kernels to BiL-STM_ATT+GCN. The evaluation results are shown in Fig.7. According to the figure, we can know that the feature imputation method using temporal loss and spatial loss separation to train independent parameters is effective.

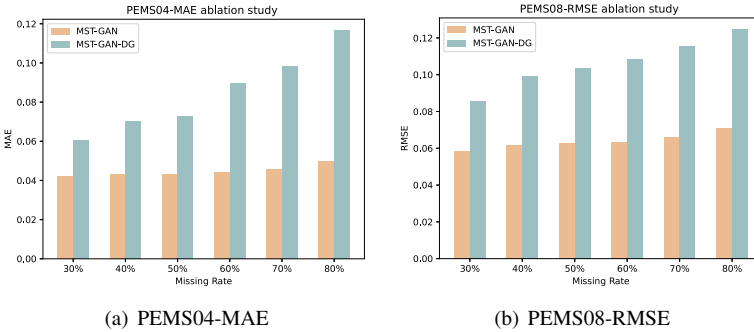


Figure 7. Ablation Study. Fig.7 represents the data imputation loss of the MST-GAN and MST-GAN-DG models under different conditions.

4. Conclusion and Discussion

Missing values in traffic data are an unavoidable problem in ITS. Although many studies are addressing this problem, there are two important limitations: first, most of the existing spatiotemporal imputation methods are only simple linear superposition of temporal

and spatial models, without considering high-level multi-perspective spatiotemporal fusion through chained generator adversarial learning; second, previous studies are mostly based on RM pattern and rarely consider other complex missing patterns. To fill these research gaps, we propose a deep learning model MST-GAN based on multi-perspective spatiotemporal learning to impute traffic data. MST-GAN adopts the strategy of analyzing and extracting road network features from three perspectives: temporal, spatial, and spatiotemporal, which makes our model learn the spatiotemporal information to the greatest extent. To achieve multi-perspective feature fusion, we employ adversarial between a chained generator and one discriminator to achieve high-level fusion of temporal and spatial information. The generator uses independent parameters to flexibly learn different enhanced features at different stages, making the overall model more flexible. Specifically, we capture the temporal and spatial correlations of traffic flow through bidirectional recurrent networks and graph convolutional networks, respectively. Furthermore, we introduce an attention layer to compute dynamic weights between different time points and focus on key temporal features. Finally, we conduct extensive experiments on real traffic datasets, comparing the performance of the MST-GAN model with other baseline models under three different missing patterns, showing that our results are all better than the baseline models. We validate the contribution of chained generators compared to single generator through ablation experiments, highlighting the superiority of the multi-generator module.

There are several directions for shortcomings and future works. First, the MST-GAN model does not consider the impact of other factors on traffic data imputation, such as weather factors, traffic accident information, etc. We plan to consider these external factors in our future work. Second, the MST-GAN model can be adapted to other spatiotemporal problems, such as route planning, traffic prediction, etc. Third, because deep learning methods are data-driven, models do not perform well without complete data. We consider combining tensor factorization method to improve the interpolation accuracy of the model. Fourth, the complex deep learning model has a slow convergence rate. We consider constructing a knowledge graph as a priori to improve the training efficiency and accuracy.

Acknowledgments

This work was supported in part by the "Pioneer" and "Leading Goose" R&D Program of Zhejiang under Grant 2022C01050, in part by the National Natural Science Foundation of China under Grant 62073295 and Grant 62072409, in part by the Zhejiang Provincial Natural Science Foundation under Grant LR21F020003, and in part by the Fundamental Research Funds for the Provincial Universities of Zhejiang under Grant RF-B2020001.

References

- [1] Han L, Zheng K, Zhao L, Wang X, Wen H. Content-aware traffic data completion in ITS based on generative adversarial nets. *IEEE Transactions on Vehicular Technology*. 2020;69(10):11950–11962.
- [2] Najafi B, Parsaeefard S, Leon-Garcia A. Estimation of missing data in intelligent transportation system. In: 2020 IEEE 92nd Vehicular Technology Conference (VTC2020-Fall). IEEE; 2020. p. 1–6.

- [3] Liu A, Li C, Yue W, Zhou X. Real-time traffic prediction: A novel imputation optimization algorithm with missing data. In: 2018 IEEE Global Communications Conference (GLOBECOM). IEEE; 2018. p. 1–7.
- [4] Tian Y, Zhang K, Li J, Lin X, Yang B. LSTM-based traffic flow prediction with missing data. *Neurocomputing*. 2018;318:297–305.
- [5] Ye J, Zhao J, Ye K, Xu C. How to build a graph-based deep learning architecture in traffic domain: A survey. *IEEE Transactions on Intelligent Transportation Systems*. 2020;23(5):3904–3924.
- [6] Li L, Zhang J, Wang Y, Ran B. Missing value imputation for traffic-related time series data based on a multi-view learning method. *IEEE Transactions on Intelligent Transportation Systems*. 2018;20(8):2933–2943.
- [7] Liang Y, Zhao Z, Sun L. Dynamic spatiotemporal graph convolutional neural networks for traffic data imputation with complex missing patterns. *ArXiv Preprint ArXiv:210908357*. 2021;.
- [8] Phan H, McLoughlin IV, Pham L, Chén OY, Koch P, De Vos M, et al. Improving GANs for speech enhancement. *IEEE Signal Processing Letters*. 2020;27:1700–1704.
- [9] Wu CH, Ho JM, Lee DT. Travel-time prediction with support vector regression. *IEEE Transactions on Intelligent Transportation Systems*. 2004;5(4):276–281.
- [10] Cetin M, Comert G. Short-term traffic flow prediction with regime switching models. *Transportation Research Record*. 2006;1965(1):23–31.
- [11] Che Z, Purushotham S, Cho K, Sontag D, Liu Y. Recurrent neural networks for multivariate time series with missing values. *Scientific Reports*. 2018;8(1):1–12.
- [12] Cao W, Wang D, Li J, Zhou H, Li L, Li Y. Brits: Bidirectional recurrent imputation for time series. *Advances in Neural Information Processing Systems*. 2018;31.
- [13] Yoon J, Jordon J, Schaar M. Gain: Missing data imputation using generative adversarial nets. In: *International Conference on Machine Learning*. PMLR; 2018. p. 5689–5698.
- [14] Wang Y, Li D, Li X, Yang M. PC-GAIN: Pseudo-label conditional generative adversarial imputation networks for incomplete data. *Neural Networks*. 2021;141:395–403.
- [15] Li D, Li L, Li X, Ke Z, Hu Q. Smoothed lstm-ae: A spatio-temporal deep model for multiple time-series missing imputation. *Neurocomputing*. 2020;411:351–363.
- [16] Ye Y, Zhang S, Yu JJ. Spatial-temporal traffic data imputation via graph attention convolutional network. In: *International Conference on Artificial Neural Networks*. Springer; 2021. p. 241–252.
- [17] Jiang W, Luo J. Graph neural network for traffic forecasting: A survey. *Expert Systems with Applications*. 2022;207:117921.

Kernel Data Evaluation System and Modeling Based on ABC-BP Hybrid Algorithm

Kuozhi XU¹ and Yangbo NIE

China Institute of Atomic Energy, Beijing 102413, China

Abstract. With the rapid development of the Internet, the demand for high-quality nuclear data services continues to grow. As the main carrier of network traffic, data centers face huge challenges in network resource management. In order to optimize the performance indicators of network flow (such as delay, jitter and packet loss rate, etc.), it is necessary to study the core data evaluation system and modeling. Through the theoretical introduction of nuclear data evaluation system and modeling and ABC-BP hybrid algorithm, this paper analyzes from three aspects: comprehensive data evaluation, nuclear data network modeling, and data evaluation system construction. Based on the relevant theoretical research of ABC-BP hybrid algorithm Based on the analysis of the feasibility of the nuclear data evaluation system and modeling research based on the algorithm theory, the existing nuclear data evaluation system and modeling system in the relevant literature are deeply discussed and studied. Scientific and operable evaluation index system to conduct nuclear data evaluation system and modeling for the ecological development of my country's government open data, so that it can truly understand its own system status. According to the existing problems of the system, reasonably coordinate and configure the relationship between the elements in the system, and finally realize the balanced, stable and efficient operation of the system. The final experimental results show that when the data fusion coefficients are 49.7, 31.6, 56.3, 73.9 and 60.5, the corresponding data compatibility degrees are 76.9%, 80.2%, 78.4%, 77.1% and 79.3%, respectively. And the compatibility of the nuclear data evaluation system is always maintained at the level of about 78%, indicating that the nuclear data evaluation system based on the ABC-BP hybrid algorithm has good feasibility in terms of data compatibility.

Keywords. ABC-BP Algorithm, hybrid algorithm, kernel data evaluation, modeling research

1. Introduction

The advent of the era of big data has brought more information to various fields, but also brought many challenges. Establishing a nuclear data evaluation system helps to extract useful information from massive data. In the field of data evaluation, a challenge often encountered is how to choose appropriate evaluation indicators to compare the performance of different classifiers [1]. In practical applications, the selection of evaluation indicators is more important due to the problem of category imbalance in a large number of datasets. Imbalanced datasets will not only affect the classification effect of the classifier, but also

¹ Corresponding author: xkz1999823@163.com

cause some commonly used classifier performance metrics to fail to truly reflect the Classifier performance.

In recent years, many researchers have explored the application of nuclear data evaluation system and modeling research, and achieved good results. For example, Iionen believes that the optimization of the BP algorithm is to use the complementary advantages of it and the genetic algorithm to improve the training efficiency of the network [2]. Oreski S believes that by using the genetic algorithm to optimize the initial weight and threshold of the BP hybrid algorithm, it can avoid falling into local extreme values and improve the training speed [3]. At present, scholars at home and abroad have carried out a lot of research on the nuclear data evaluation system and modeling research based on the ABC-BP hybrid algorithm. These previous theoretical and experimental results provide a theoretical basis for the research in this paper.

Based on the relevant theoretical research of the ABC-BP hybrid algorithm, this paper analyzes the feasibility of the kernel data evaluation system and modeling research based on the algorithm theory, and through a series of experiments to verify the kernel based on the ABC-BP hybrid algorithm. Whether the application of data evaluation system and modeling research is feasible. In the simulation analysis experiment of nuclear data modeling research, the experimental results show that in the simulation research and analysis of nuclear data modeling based on ABC-BP hybrid algorithm, the simulation of nuclear data modeling and the iteration coefficient of nuclear data change synchronously , the two are positively correlated.

2. Related Theoretical Overview and Research

2.1 Nuclear Data Evaluation System and Modeling

(1) Comprehensive evaluation of data

In the development process of comprehensive evaluation, there are many studies in the form of data. Comprehensive evaluation is a method of synthesizing various quantitative characteristics of the evaluation object. It can directly evaluate complex data forms effectively, so it is widely used in various social Research on economic phenomena [4-5]. With the increasingly complex social development and the rapid development of science and technology, a new data form has emerged—the nuclear data evaluation system based on the ABC-BP hybrid algorithm, which not only has interval characteristics, but also presents continuous function characteristics. Therefore, it is urgent to give the comprehensive evaluation process and method of interval function data are systematically analyzed.

(2) Modeling of nuclear data networks

Network modeling and network optimization are closely related, where network optimization is the purpose and network modeling is a prerequisite for network optimization [6]. In an SDN-based data center network, the general process of network routing optimization can be divided into three steps: (1) generate a set of candidate routing configurations, which includes multiple optional packet transmission paths; (2) based on the above The model obtained by the network modeling algorithm evaluates all routing configurations in the set; (3) According to the optimization goal given by the administrator, select a routing configuration that best meets the requirements for the current network flow.

(3) Construction of data evaluation system

With the advent of the era of big data, data has become a hot "treasure", and the development of nuclear data evaluation systems and modeling has become an inevitable trend [7]. At the same time, driven by the big data strategy, the pace of development of open

data is accelerated, and the full development and utilization of data resources can not only bring economic and social benefits to social development, but also strengthen governance capabilities. At present, although the level of open data construction is steadily improving, there are still some problems in its development process, such as personal data privacy and security issues and data resource sharing efficiency issues, which will be detrimental to the sustainable and healthy development of open data practices. Only by understanding the current state of its own open data ecosystem can it better achieve stable and sustainable development [8]. Therefore, it is urgent to build a scientific and effective open data ecosystem evaluation system to measure the state of its own ecosystem. According to the existing problems in the system, rationally coordinate and configure the relationship between the various elements in the system, and finally realize the balance, stability, and stability of the system. Efficient operation.

Through in-depth research on the existing nuclear data evaluation system and modeling system in the relevant literature, it is necessary to establish a scientific and operable evaluation index system suitable for my country's national conditions to verify the ecological development of my country's government open data. Data evaluation system and modeling, so that it can truly understand its own system state [9]. The research on the government nuclear data evaluation system and modeling ecologicalization facilitates government departments at all levels to fully understand their own data openness, find their development shortcomings, learn from the development experience of advanced cities, improve and optimize the way forward, and implement precise policies to promote the lasting work of open data. To provide operational support for the development of the government's open nuclear data evaluation system and modeling department.

2.2 Theoretical Introduction of ABC-BP Hybrid Algorithm

The BP algorithm is a supervised learning algorithm. Its learning process can be roughly divided into two stages. The first step is to calculate the output of each layer of neurons by determining the initial weights and thresholds of the input samples. The second stage is Refers to returning the error result from the output layer to the previous layer to modify the threshold and weight [10]. These two processes always alternate until the results of network training converge. Since the error is continuously propagated forward layer by layer, it is called the error back propagation algorithm. It can be generalized to the fact that the hidden layer in the middle contains many layers, and the BP algorithm of this multi-layer network is also called BP neural network [11]. The weight update direction of the standard BP algorithm is opposite to the performance error function.

Since the BP algorithm is a gradient descent search algorithm, it also has some defects to a certain extent. The most significant disadvantage is that the convergence speed is relatively slow, and it is easy to fall into the local minimum point of the error function. The optimization and improvement of the ABC-BP hybrid algorithm mainly starts from two aspects, one is the algorithm itself, and the other is combining it with other algorithms. The learning rate will greatly affect the training time of the network, and the methods to reduce this effect mainly include conjugate gradient/adaptive learning rate, optimizing the initial parameters of the network, and optimizing the parameters of the network learning algorithm [12]. There are four main ways to optimize the ABC-BP hybrid algorithm itself to improve the training efficiency of the network: modify the activation function and the squared error function; normalize the initialization parameters of the network, and use the year-on-year compression method to reduce the initial parameters. Normalize so that it is between 0-1.

3. Experiment and Research

3.1 Experimental Method

The most widely used evaluation metric for assessing classification quality is the accuracy rate ACC, also known as the overall accuracy rate or overall success rate. The accuracy rate is the ratio of the correct number of samples classified by the classifier to the total number of samples. In order to correct the defect that the ACC indicator only contains information on the diagonal of the confusion matrix, a new method that contains off-diagonal information and can be extended to any number is proposed. The performance evaluation index of the category - the class balance accuracy, its formula is expressed as:

$$ACC = \frac{\sum_{i=1}^C m_{ii}}{N} \quad (1)$$

$$CBA = \frac{1}{C} \sum_{i=1}^C \frac{m_{ii}}{\max(m_{i*}, m_{*i})} \quad (2)$$

In the above formula, the element m_{ii} in the matrix represents the number that actually belongs to the i -th class and is classified by the classifier, and C is a data analysis table that counts the classification of samples according to the classification results. m_{ii} represents the number of samples that the classifier predicted correctly for each class.

3.2 Experimental Requirements

The ACC indicator considers the overall classification result of the classifier predicting the category, and is another global evaluation indicator. Therefore, it can be used for both binary and multi-class problems. The value range of ACC is $[0,1]$. Similarly, the larger the value of ACC, the better the performance of the classifier. However, the ACC indicator only contains the information of the diagonal line of the confusion matrix, and cannot reflect the information of the off-diagonal line, that is, the information of misclassification. CBA seeks a balance between recall and precision for each category. When the recall rate and precision rate are unbalanced, the lower value of the two indicators is finally selected as the representative of the accuracy rate of the category. The value range of the CBA indicator is also $[0, 1]$. Similarly, the value of CBA is related to the classification is proportional to the performance of the device, and the higher the value, the better the performance.

4. Analysis and Discussion

4.1 Data Fusion Analysis of Nuclear Data Evaluation System

By comparing the relationship between the data fusion coefficient and the data compatibility degree in the five groups of nuclear data analysis research, the feasibility of the research on the nuclear data evaluation system based on the ABC-BP hybrid algorithm is judged. The experimental data are as follows:

Table 1. Data fusion analysis table of nuclear data evaluation system

Data analysis	Fusion coefficient	Compatibility(%)
One	49.7	76.9
Two	31.6	80.2
Three	56.3	78.4
Four	73.9	77.1
Five	60.5	79.3

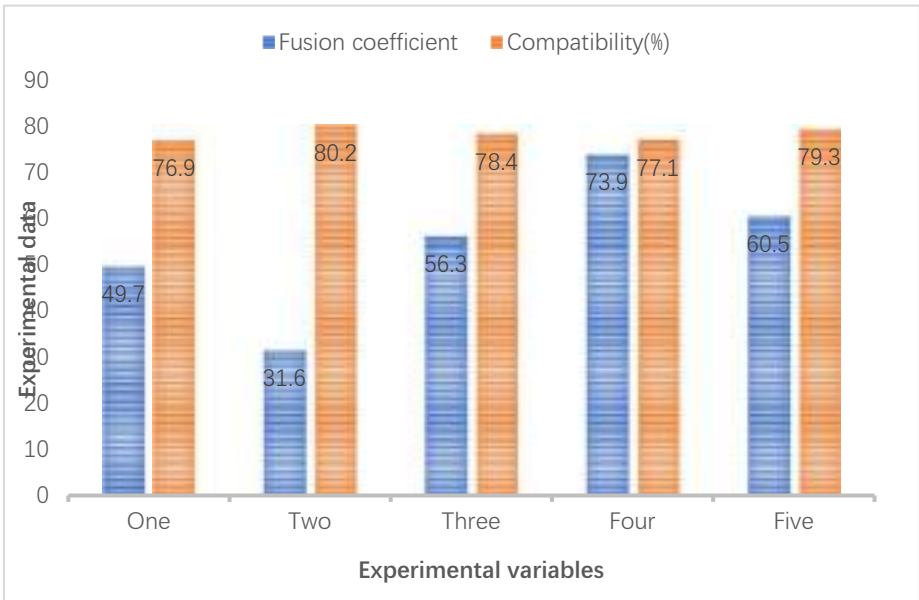


Figure 1. Data fusion analysis diagram of nuclear data evaluation system

From the data analysis in Table 1 and Figure 1, it can be seen from the results that in the five groups of nuclear data analysis studies participating in the experiment, when the data fusion coefficients are 49.7, 31.6, 56.3, 73.9 and 60.5, the corresponding data compatibility degrees are respectively were 76.9%, 80.2%, 78.4%, 77.1% and 79.3%. Through the data comparison, it can be seen that in the analysis and research of the nuclear data evaluation system based on the ABC-BP hybrid algorithm, the data compatibility degree of the nuclear data evaluation system is not related to the data fusion coefficient, and the compatibility of the nuclear data evaluation system is always maintained at 78%. It shows that the kernel data evaluation system based on ABC-BP hybrid algorithm has good feasibility in terms of data compatibility.

4.2 Simulation Analysis of Nuclear Data Modeling Research

By analyzing the simulation of the nuclear data modeling research based on the ABC-BP hybrid algorithm, the experimental data is shown in the following figure:

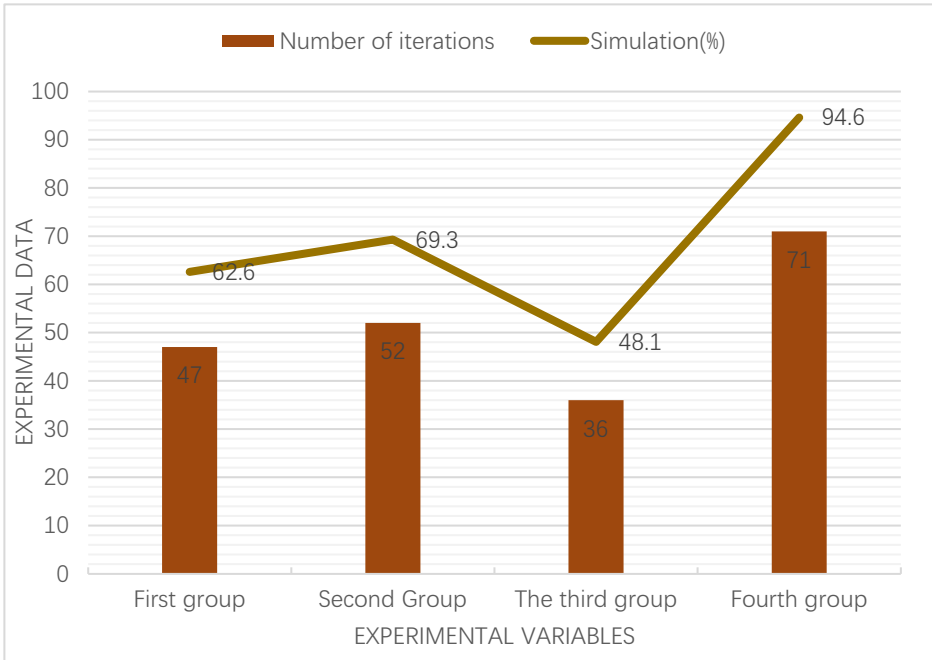


Figure 2. Simulation analysis diagram of nuclear data modeling research

As shown in Figure 2, for the simulation of the nuclear data evaluation system and modeling research based on the ABC-BP hybrid algorithm, when the iteration coefficients of the nuclear data are 47, 52, 36 and 71, the corresponding nuclear data modeling research The simulation performance is 62.6%, 69.3%, 48.1% and 94.6%, respectively. The experimental results show that in the simulation research and analysis of the nuclear data modeling based on the ABC-BP hybrid algorithm, the simulation of the nuclear data modeling and the iteration coefficient of the nuclear data change synchronously, and the two are positively correlated. It is concluded that the nuclear data evaluation system and modeling research based on the ABC-BP hybrid algorithm is feasible in terms of simulation.

5. Conclusions

Based on the relevant theoretical research of the ABC-BP hybrid algorithm, this paper analyzes the feasibility of the kernel data evaluation system and modeling research based on the algorithm theory, and through a series of experiments to verify the kernel based on the ABC-BP hybrid algorithm. Whether the application of data evaluation system and modeling research is feasible. In the simulation analysis experiment of nuclear data modeling research, the experimental results show that in the simulation research and analysis of nuclear data modeling based on ABC-BP hybrid algorithm, the simulation of nuclear data modeling and the iteration coefficient of nuclear data change synchronously , the two are positively correlated. In the analysis and research of the nuclear data evaluation system based on the ABC-BP hybrid algorithm, the results show that the degree of data compatibility of the nuclear data evaluation system is not related to the data fusion coefficient, and the compatibility of the nuclear data evaluation system is always maintained at about 78%. It shows that the nuclear data evaluation system based on ABC-BP hybrid algorithm has good feasibility in terms of data compatibility.

In this paper, the ACC index is used to consider the overall classification result of the classifier predicting the category, which is another global evaluation index. Whether this method really improves the model needs to be tested by relevant experts and in actual evaluation. In the current case of the nuclear data evaluation of the ABC-BP hybrid algorithm, the data asset transaction mainly focuses on several data trading platforms, whether the nuclear data evaluation calculated based on the ABC-BP hybrid algorithm can truly reflect the value of the data asset. ABC-BP algorithm, as a new intelligent algorithm, has good optimization degree, excellent algorithm mechanism, high fault tolerance rate and strong feedback. Artificial bee colony algorithm is one of the most promising intelligent algorithms at present. There is still a great prospect for improvement on the basis of the algorithm, which is worthy of further in-depth study.

References

- [1] R.S. Sexton, R.S. Sriram, H. Etheridge. Improving decision effectiveness of artificial neural networks: a modified genetic algorithm approach [J]. *Decis Sci*, 2020, 34(3):421-442.
- [2] Iionen, J.K. Kamarainen, J. Lampinen. Differential Evolution Training Algorithm for Feed-forward Neural Networks [J]. *Neural Processing Letters*, 2019, 17(1): 93-105
- [3] Oreski S, Oreski G. Genetic algorithm -based heuristic for feature selection in credit risk assessment. *Expert Systems with Applications*, 2020, 41(4):2052-2064.
- [4] Chadwick, et al. ENDF/B-VII. 1 nuclear data for science and technology: cross sections, covariances, fission product yields and decay data [J]. *Nuclear Data Sheets*, 2021, 112(12): 2887-2996.
- [5] Koning A J, Bauge E, Dean C J, et al. Status of the JEFF nuclear data library [J]. *Journal of the Korean Physical Society*, 2021, 59(2): 1057-1062.
- [6] Shibata, T. Kawano, T. Nakagawa et al. JENDL-4.0: A New Library for Nuclear Science and Engineering [J]. *Journal of Nuclear Science and Technology*, 2021, 48(1): 1-30.
- [7] Zabrodskaya, A.V. Ignatyuk, V.N. Koscheev et al. ROSFOND - Rossiyskaya Natsionalnaya Biblioteka Nejtronnykh Danykh [J]. *VANT, Nuclear Constants*, 2020:1-2.
- [8] MacFarlane, A. C. Kahler. Methods for processing ENDF/B-VII with NJOY [J]. *Nuclear Data Sheets*, 2020, 111(12): 2739-2890.
- [9] Paul K. Romano. The OpenMC Monte Carlo particle transport code [J]. *Annals of Nuclear Energy*, 2020, 51:274–281.
- [10] Leal L., Guber K., Wiarda D, et al. ORNL Resolved Resonance Covariance Generation for ENDF/B-VII.1 [J]. *Nuclear Data Sheets*, 2022, 113(12):3101-3119.
- [11] Herman M, Capote R, Carlson B V, et al. EMPIRE: nuclear reaction model code system for data evaluation [J]. *Nuclear Data Sheets*, 2020, 108(12): 2655-2715.
- [12] Koning A. J., Rochman D. Modern nuclear data evaluation with the TALYS code system [J]. *Nuclear data sheets*, 2022, 113(12): 2841-2934.

PIXDet: Prohibited Items X-Ray Image Detection in Complex Background

Mingyuan LI ^a, Bowen MA ^a, Tong JIA ^{a,1} and Yichun ZHANG ^b

^aCollege of Information Science and Engineering, Northeastern University, Shenyang, China.

^bChina Institute of Arts Science & Technology, Beijing, China

Abstract. In this paper, aiming at the complex background and overlapping characteristics in X-ray images, we propose an unique spatial attention mechanism based on the feedback of high-level semantic feature to guide low-level semantic features, named Feedback Guidance Mechanism (FGM). In addition, in view of the high probability of miss of small prohibited items, a feature aggregation method based on the fusion of high and low-level features and dilated convolution is proposed, named Feature Aggregation Module (FAM). Then, we combine FGM and FAM into a lightweight model SSD and get a new Prohibited Items Detector (PIXDet). Our experiments indicate that PIXDet is more lightweight, but it can achieve 90.36% mAP on PIXray dataset, exceeding SSD by 1.0% mAP, outperforming some state-of-the-art methods, implying its potential applications in prohibited items detection field.

Keywords. Deep Learning, security inspection, attention mechanism, feature aggregation

1. Introduction

With the growth of population in large cities and crowd density in public transportation hubs, security inspection has been playing an increasingly critical role in maintaining urban public safety[1]. In densely populated places such as stations or airports, the use of X-ray scanners to assist staff in checking passenger packages is one of the most extensive and effective security detection methods. The various objects in the detection image overlap each other with different shapes. It is difficult to find the prohibited items hidden in them, especially after the security inspectors have worked for a long time. With the development of deep learning technology, more and more research begin to use computer-aided technology based on object detection technology to assist human inspectors in security inspection[1,2,3,4,5]. Recently, some works using convolutional neural networks to detect the prohibited items in X-ray image have achieved rich results[1,4,5].

However, X-ray baggage images where objects are randomly stacked and heavily overlapped each other, resulting that background interfere with foreground detection and small prohibited items are easily missed. These characteristics bring great challenges to

¹Corresponding Author: Tong Jia, a Professor with the College of Information Science and Engineering, Northeastern University, Shenyang, China. E-mail: jiatong@ise.neu.edu.cn

both object detection methods and human inspectors[1]. We mainly focuses on the detection difficulties in X-ray security images, and propose a network framework based on Single Shot MultiBox Detector (SSD) algorithm[6] to adapt to prohibited items detection in X-ray images —PIXDet. The main contributions are as follows:

1) A new attention mechanism (FGM) is proposed, which uses high-level features to guide low-level features fusions in order to remove background information. By simulating the process of continuous feedback iteration, the network will pay more attention to the target area and remove redundant information. FGM effectively solves the problem of background interference in X-ray images, enables the network to efficiently and accurately detect prohibited items in X-ray images with complex backgrounds.

2) A feature aggregation method (FAM) is proposed to strengthen the expression of detailed features, integrate contextual information, and effectively improve the problem of missed detection of small prohibited items. It has a strong adaptability for contraband with different aspect ratio and scale change.

3) We combine SSD, FGM and FAM into a Prohibited Items Detector, named PIXDet. After a series of experiments and analysis, we come to the conclusion that our model is more lightweight while outperforming the state-of-the-art methods, implying its potential applications in prohibited items detection fields.

2. Related Work

2.1. Attention Mechanism

Attention mechanism can be understood as a kind of algorithm that helps computer to put the more computational resources into the most informative components of a signal[5]. Recently, there have been a series of studies incorporating attention mechanism improve the performance of computer vision tasks, including image classification, object detection and semantic segmentation[7,8,9,10]. SE-Net[9] proposes an effective attention mechanism utilizing channel attention for the first time and obtains promising results. But, it does not utilize spatial information, CBAM[10] based on SE-Net employs max pooling and average pooling to extract spatial feature. However, the pooling operations will result that the feature extraction network mix information of foreground and background. We use FGM solves this problem to some extent.

2.2. Methods of Feature Aggregation

FPN[11] is one of the most famous methods improve detection and segmentation performance by using features from different layers. PANet[12] proposes one bottom-up path augmentation mechanism to shorten information path and enhance FPN by more accurate localization signals in low-level feature. SSD[6], FSSD[13] and DSSD[14] utilize different feature levels to inference proposals. OPIXray[5] refines feature maps by operation named RIA for extracting more useful information from image better. However, RIA just uses the same size of convolution kernel, resulting that the feature extraction network ignores the information of the small objects in image. We propose a FAM mechanism solves this problem to some extent.

2.3. Object Detection Studies for Security Inspection

With the vigorous improvement of computer computing power and convolutional neural network technology, a large number of object detection algorithms emerge in an endless stream, i.e., Fast R-CNN[7], Faster R-CNN[8], SSD[6], DSSD[14], FSSD[13], YOLO[15], YOLOv3[16] and YOLOv4[17]. SSD is one of the most famous neural networks which is fast and high precision and our work is based on it. We boost it with FGM and FAM which are proposed according to the characteristics of X-ray image of security inspection. To the best of our knowledge about X-ray datasets of security inspection, there only three X-ray datasets are open for research purposes, i.e., SIXray[1], OPIXray[5] and PIXray[4]. SIXray[1] public a large-scale X-ray dataset including 105,931 X-ray images, but it just consists of six categories of prohibited items. OPIXray[5] just contains five kinds of knives, including folding knife, straight knife, scissor, utility knife, and multi-tool knife, lacking of resemblance to the real world. Therefore, we choose PIXray dataset which contains fifteen kinds of prohibited items and 5,046 X-ray images, in which 15 classes of 15,201 prohibited items[4].

3. Proposed Method

Challenge against the above, based on the single-stage object detector SSD network model, we propose a feedback guidance mechanism (FGM), which uses high-level semantic features to guide low-level semantic features after being processed by some modules, improving the feature representation of the region of interest, and thus realizing more accurate identification and positioning of overlapping prohibited items. In addition, in order to improve the detection of small prohibited items, feature aggregation module (FAM) is added to capture the lost information of local small targets in the global field of vision and reduce the missed detection rate of small prohibited items. Finally, we propose the PIXDet to combine the two modules and SSD to achieve the best result. The overall architecture is shown in Figure 1. In the following subsections, we first introduce the overall PIXDet, then elaborate on the proposed FGM, and finally describe FAM.

3.1. Overall Architecture

In fact, our PIXDet is independent of backbone, it can be easily applied to mainstream backbone networks, i.e., vgg-16[18], resnet-50[19] and densenet-121[20]. We just use the lightest vgg networks as backbone for validating our theory, which is the same as primary SSD[6]. The dataset $X = \{x_1, \dots, x_N\}$ has N training images, in Figure 1, each input image $x_n \in X$ will be fed into backbone of PIXDet to extract L different feature layers $x_n^{(l)}$, l represents the l -th of feature layer which will be directly used to detection module in primary SSD[6]. The larger the number of l , the higher the feature layer. One $FGM^{(l)}$ will be fed into two feature layers $x_n^{(l)}$ and $x_n^{(l+1)}$, outputting $\tilde{x}_n^{(l)}$, and the light green area in the Figure is where FGM plays a role.

Then, the guided feature layers $\tilde{x}_n^{(l)}$ and $\tilde{x}_n^{(2)}$ will be fused into $\hat{x}^{(1)}$ by FAM, and the light orange area in the Figure 1 is where FAM plays a role. Later, similar to SSD, we feed $\hat{x}_n^{(1)}, \tilde{x}_n^{(2)}, \dots, \tilde{x}_n^{(L)}$ to prediction layers to get classification and regression information, where L is 6 in our model. Finally, we paint the decode information predicted by PIXDet

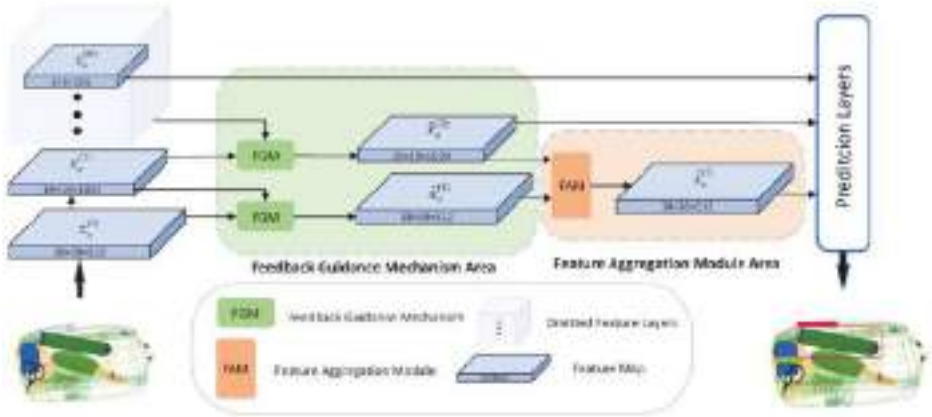


Figure 1. Prohibited Items X-ray Detector. The network adds a spatial attention mechanism of high-level semantic feature feedback to guide low-level semantic features and feature aggregation methods that combine high and low level features with dilated convolution.

on the input image to get output image. Summarizing PIXDet yields the following optimization problem:

$$\alpha^*, \beta^*, \gamma^* = \arg \min_{\alpha, \beta, \gamma} \sum_{n=1}^N Loss(y_n, y_n^*) \quad (1)$$

$$y_n = f(\hat{x}_n^{(1)}, \hat{x}_n^{(2)}, \dots, \hat{x}_n^{(L)}; \gamma) \quad (2)$$

$$\hat{x}_n^{(l)} = FGM^{(l)}(x_n^{(l)}, x_n^{(l+1)}; \alpha^{(l)}) \quad (3)$$

$$\hat{x}_n^{(1)} = FAM^{(1)}(\hat{x}_n^{(1)}, \hat{x}_n^{(2)}; \beta^{(1)}) \quad (4)$$

where $Loss(\cdot, \cdot)$ is a loss function which is the same as SSD[6]. Within this process, $\alpha^{(l)}$ and $\beta^{(1)}$ are parameters in $FGM^{(l)}$ and $FAM^{(1)}$, which will be updated according to ground-truth y_n^* , while γ is the other parameters automatically updated according to back propagation in model. $FGM^{(l)}(\cdot, \cdot)$ and $FAM^{(l)}(\cdot, \cdot)$ are the simplified equations of FGM and FAM, which are respectively discussed in Section 3.2 and Section 3.3.

3.2. Feedback Guidance Mechanism (FGM)

As shown in Figure 2, the FGM consists of a CR_{-1} and an up-sampling layer with bilinear interpolation, and then uses the SoftMax activation function for each channel to obtain a probability diagram for each channel. CR_{-1} is a module including convolution and Relu, and the kernel size and stride is 1. Specifically, the feature maps of Conv4_3 layer and FC7 layer are recorded as $x_n^{(1)}$ and $x_n^{(2)}$, respectively, where $x_n^{(1)} \in \mathbb{R}^{512 \times 38 \times 38}$, $x_n^{(2)} \in \mathbb{R}^{1024 \times 19 \times 19}$. We get the intermediate guidance weight chart to $\hat{x}_n^{(2)}$, where $\hat{x}_n^{(2)} \in \mathbb{R}^{512 \times 38 \times 38}$. We get $\hat{x}_n^{(2)}$ by calculating as follows:

$$\hat{x}_n^{(2)} = Relu(Conv_{1 \times 1}(x_n^{(1)})) \quad (5)$$

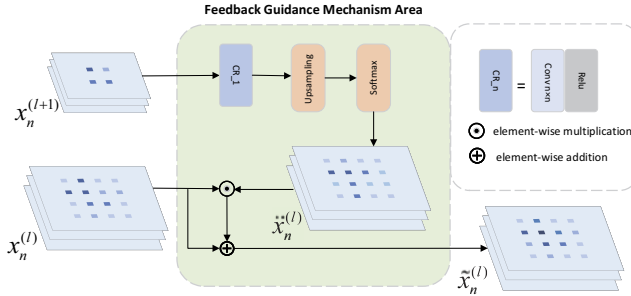


Figure 2. Feedback Guidance Mechanism: Higher-level semantic features are superimposed with the intermediate guidance weight $\check{x}_n^{(2)}$ to low-level semantic features.

$$\check{x}_n^{(2)} = SoftMax(UpSampling(\check{x}_n^{(2)})) \tag{6}$$

In order to obtain the same number of channels as $x_n^{(1)}$, $x_n^{(2)}$ is passed through a 1×1 convolution operation and activated by Relu, getting $\check{x}_n^{(2)} \in \mathbb{R}^{512 \times 19 \times 19}$. Then it will be upsampled by bilinear interpolation for changing feature map dimension, while the SoftMax function is used to normalize the feature values in order to optimize the weight of all channel feature expressions and strengthen the feature expression of contraband regions in low-level semantic features.

Finally, the intermediate guidance weight $\check{x}_n^{(2)}$ is fused with $x_n^{(1)}$, which serves as a correction. The fusion process can be expressed as:

$$\tilde{x}_n^{(1)} = \varepsilon^{(1)}(x_n^{(1)} \odot \check{x}_n^{(2)}) \oplus x_n^{(1)} \tag{7}$$

among them, \oplus indicates element-wise addition, \odot denotes element-wise multiplication, and $\varepsilon^{(1)}$ is an adaptive learning factor for 1st layer, which is used to auto-modify the power of influence of the higher-lever feature layer. Eqs. (5,6,7) can be simplified to Eq. (3).

Note that the FGM is developed in a unified framework that allows calculations to be trained end-to-end through back propagation of all layers. We just choose two layers to show its detail in Section 3.2, each FGM is not completely consistent due to the different dimensions of the data processed. It elegantly handles the main limitations of the existing one-stage object detector applied to prohibited items X-ray image detection. The proposed feedback guidance mechanism can effectively improve the interference of complex background in contraband detection, and at the same time allow the X-ray images to be varied, which further improves the performance of the detection.

3.3. Feature Aggregation Module (FAM)

Low-level features have a small receptive field, which can provide more detailed information for the recognition of small prohibited items (such as razor blades), but low-level features have no semantic feature information, and with the deepening of the network, the local small target information under the global vision will also be lost, which is the main reason for the high rate of missed detection of small targets. Therefore, we propose a feature aggregation module (FAM), whose structure is shown in Figure 3.

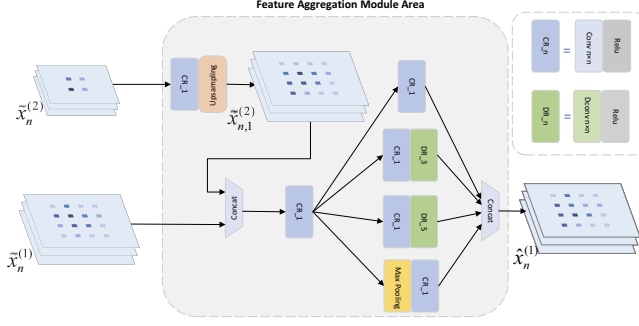


Figure 3. Feature Aggregation Module: Strengthen the expression of details and features and integrate contextual information.

Firstly, the higher level semantic feature FC7 layer $\tilde{x}_n^{(2)} \in \mathbb{R}^{1024 \times 19 \times 19}$, which has been processed by $FGM^{(1)}$ will be upsampled and convolved as the operation of Eq. (8):

$$\tilde{x}_{n,1}^{(2)} = UpSampling(ReLu(Conv_{1 \times 1}(\tilde{x}_n^{(1)}))) \quad (8)$$

The obtained feature map of Eq. (8) is denoted as $\tilde{x}_{n,1}^{(2)} \in \mathbb{R}^{512 \times 38 \times 38}$, while Conv4_3 layer $\tilde{x}_n^{(2)} \in \mathbb{R}^{512 \times 38 \times 38}$ will be fused with $\tilde{x}_{n,1}^{(2)}$ to get the transitional feature map $\tilde{x}_{n,2}^{(2)}$:

$$\tilde{x}_{n,2}^{(2)} = ReLu(Conv_{1 \times 1}(\tilde{x}_n^{(1)} || \tilde{x}_{n,1}^{(2)})) \quad (9)$$

where $||$ represents a concatenate operation, $\tilde{x}_n^{(1)} || \tilde{x}_{n,1}^{(2)} \in \mathbb{R}^{1024 \times 38 \times 38}$. We use 1×1 convolution kernels for dimensional reduction to obtain the associated feature map $\tilde{x}_{n,2}^{(2)} \in \mathbb{R}^{512 \times 38 \times 38}$.

In addition, dilated convolution[21] can increase the receptive field of convolution kernel while keeping the number of parameters unchanged, which is conducive to output more global feature information and help other algorithms learn global semantic feature information. At the same time, inspired by the inception architecture in GoogleNet[22], dilated convolution is added into the inception module to expand the visual field free of charge, which allows FAM to use multi-scale visual field to establish global and local connection to take into account the task of global positioning and local classification, effectively improving the detection rate of small prohibited items .

The latter half of the FAM is processed as follows:

$$\tilde{x}_{n,3}^{(1)} = ReLu(Conv_{1 \times 1}(\tilde{x}_{n,2}^{(1)})) \quad (10)$$

$$\tilde{x}_{n,4}^{(1)} = ReLu(Dconv_{3 \times 3}(ReLu(Conv_{1 \times 1}(\tilde{x}_{n,2}^{(1)})))) \quad (11)$$

$$\tilde{x}_{n,5}^{(1)} = ReLu(Dconv_{5 \times 5}(ReLu(Conv_{1 \times 1}(\tilde{x}_{n,2}^{(1)})))) \quad (12)$$

$$\tilde{x}_{n,6}^{(1)} = ReLu(Conv_{1 \times 1}(MaxPooling_{3 \times 3}(\tilde{x}_{n,2}^{(1)}))) \quad (13)$$

$$\hat{x}_n^{(1)} = \tilde{x}_{n,3}^{(1)} || \tilde{x}_{n,4}^{(1)} || \tilde{x}_{n,5}^{(1)} || \tilde{x}_{n,6}^{(1)} \quad (14)$$

where $\hat{x}_n^{(1)} \in \mathbb{R}^{512 \times 38 \times 38}$, $\hat{x}_{n,3}^{(1)} \in \mathbb{R}^{128 \times 38 \times 38}$, $\hat{x}_{n,4}^{(1)} \in \mathbb{R}^{256 \times 38 \times 38}$, $\hat{x}_{n,5}^{(1)} \in \mathbb{R}^{64 \times 38 \times 38}$ and $\hat{x}_{n,6}^{(1)} \in \mathbb{R}^{64 \times 38 \times 38}$. DR_{-n} is a module including dilated convolution and Relu, and the kernel size and dilation of dilated convolution is 'n' and 2 respectively. $FAM^{(1)}$ including Eqs. (8-14) can be simplified to Eq. (4) in section 3.1. Note that our model just has one FAM named $FAM^{(1)}$, '1' in equation represents the feature layers location of it.

4. Experiments

In this section, we carry on extensive experiments to evaluate FGM and FAM we propose. Firstly, the superiority in detecting prohibited items in X-ray images of PIXDet is verified through some comparative experiments. Secondly, the ablation experiment of the model is carried out for illustrating completely the effectiveness of each module we propose above. The experimental results demonstrate that the method proposed in this paper achieves satisfying results in the detection of contraband in X-ray images. Finally, we perform feature map visualization to show the effect of FGM. In the following experiments, the hardware and software environments of the experiment are PyTorch, Windows 10 system, and NVIDIA 3070 laptop GPU. All models are optimized by the SGD optimizer and the learning rate is set to 0.0001. The batch size is set to 8, and momentum decay and weight decay are set to 0.9 and 0.0005, respectively. What's more, we do not use pre-trained model of Imagenet 1000, because our detection task is based on PIXray dataset which is independent of natural images. For fairness, all models are trained for 300 epochs with the same hyper-parameter and training strategy.

4.1. Comparisons with State-of-the-art Methods

Taking SSD[6] as the basic architecture, in order to prove the effectiveness of the design of functional modules, we compare our PIXDet with some SOTA object detection models including SSD[6], YOLOv3[16] and FSSD[13] on the dataset PIXray with input size 300×300 . The ratio of training set and test set is 9:1 and mean Average Precision (mAP) was used as the index to evaluate the detection accuracy. The detection accuracy of prohibited items of X-ray images in each model is shown in Table 1. We evaluate the mean Average Precision (mAP) of the object detection to measure the performance of the model and the IOU threshold is set to 0.5.

Table 1. Complexity comparison of different models. PARAMs, SIZE and GFLOPs represent the total number of parameters, the model size and the Giga Floating Point operations, respectively.

Method	mAP	PARAMs	GFLOPs	SIZE(MB)
SSD[6]	89.36	25.48 $\times 10^6$	31.10	97.7
YOLOv3[16]	85.71	61.59 $\times 10^6$	19.42	235
FSSD[13]	90.20	33.05 $\times 10^6$	37.27	136
PIXDet(ours)	90.36	27.83 $\times 10^6$	33.03	106

PIXDet achieves 90.36% mAP on PIXray dataset with input size 300×300 , outperforming SSD, YOLOv3 and FSSD by 1.0% mAP, 4.65% mAP and 0.16% mAP, respectively. With regard to PARAMs and SIZE, PIXDet is only second to SSD. Our method

only brings a slight increase in computational cost(6.2% in GFLOPs), compared with SSD without any improvement. In brief, according to the experimental results, mAP of PIXDet is better than other state-of-the-art models. Both GFLOPs and model SIZE are lower than FSSD, meaning that it requires lower calculation power and can be more easily developed on embedded devices. However, comparing with SSD[4], there is a small increase in the demand for computing resources, i.e., the number of parameters, model size and the need of float point operation.

4.2. Ablation study

In this part, an ablation experiment based on SSD model is designed, which could more intuitively show the influence of FGM and FAM on the detection effect of PIXDET. The experimental parameters are consistent with the contrast experiment. The results of ablation experiment are shown in Table 2.

Table 2. Ablation studies of PIXDet. "+FGM" represents adding feedback guidance mechanism to SSD, "+FAM" represents adding feature aggregation module to SSD.

Method	mAP	Bat	Lighter	Pliers	Gun	PV	Scis	Hamm	Wren	Batt	Fires	Dart	Saw	Screw	Knife	Razor
vanilla model	89.36	100	96	98	96	96	97	95	93	90	91	76	82	80	82	69
+FGM	89.72	100	96	98	97	94	97	96	95	92	89	82	77	81	76	78
+FAM	90.05	100	96	96	98	97	96	95	94	94	87	83	79	78	82	77
+FGM+FAM(PIXDet)	90.36	100	98	98	96	95	94	93	94	92	90	83	78	80	85	79

FGM and FAM can improve detection performance by 0.36% and 0.71% on a basic detection network (SSD), respectively. It is concluded that when the detection network increases the corresponding feature weight through reverse connection, FGM is capable of completing the optimization of feature information adaptively, focusing the attention of the model more on prohibited items, reducing the interference degree of middle-level useless information and improving the detection accuracy. Compared to some other types of prohibited items, it is particularly difficult to detect the knife due to its small size. FAM has effectively improved the detection accuracy of small prohibited items, and the detection accuracy of dart has increased from 76% to 83%. PIXDet means adding module FGM and FAM on SSD. It can be seen that FGM and FAM are complementary to each other to achieve better performance. Therefore, mAP of PIXDet is the best of them. It is worth mentioning that although some kinds of prohibited items can not be detected perfectly by PIXDet, the detection results of them are not much worse than the vanilla model. In brief, the experimental results show that PIXDet has certain effectiveness in prohibited items object detection. However, PIXDet is not without its shortcomings, comparing with '+FGM' or '+FAM', the average precision of PIXDet has a slight drop, meaning that there is some overlap between FGM and FAM. Even so, they are functionally complementary because the mean average precision of PIXDet is higher than '+FGM' and '+FAM'.

4.3. Visualization Analysis

We display the detection results of PIXDet, as shown in Figure 4. SSD can only detect some characteristic objects, i.e., bat and pressure vessel. When it comes to small prohibited items razor blade and battery, the rate of missing or false detection is extremely

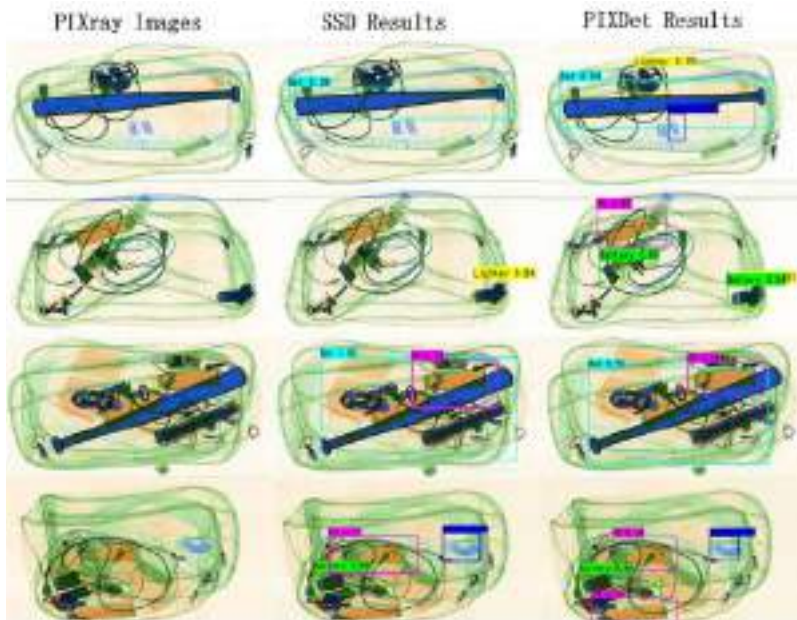


Figure 4. Detection examples using baseline model(SSD) and our model.

high. In contrast, our PIXDet can adapt to the X-ray images with complex background, and it can even recognize battery overlapped with electric wire. By comparing the experiments results, it can be demonstrated that our model can effectively improve the problems of background interference and small contraband missed detection in X-ray security images.

5. Conclusion

In this work, we explore in detail the application of deep learning in the object detection task of prohibited items in X-ray images. To facilitate research in this area, we propose the PIXDet detection model to solve the existing problems in contraband images, such as complex background and missed detection of small objects. Specifically, feedback guidance mechanism (FGM) and feature fusion module (FAM) proposed in this paper can effectively weaken the interference caused by complex background and improve the detection accuracy of small prohibited items. We have comprehensively evaluated our detection model on PIXray dataset, and proved that our module can effectively improve the detection performance and provided a new idea for the model improvement. Furthermore, our model is more lightweight while outperforming the state-of-the-art methods, implying its potential applications in prohibited items detection field. In the future, we will continue to study object detection of smaller prohibited items in more complex and real background.

References

- [1] Miao C, Xie L, Wan F, et al. Sixray: A large-scale security inspection x-ray benchmark for prohibited item discovery in overlapping images[C]//Proceedings of the IEEE/CVF Conference on Computer Vision and Pattern Recognition. 2019: 2119-2128.
- [2] Griffin L D, Caldwell M, Andrews J T A, et al. "Unexpected item in the bagging area": anomaly detection in X-ray security images[J]. IEEE Transactions on Information Forensics and Security, 2018, 14(6): 1539-1553.
- [3] Abidi B R, Zheng Y, Gribok A V, et al. Improving weapon detection in single energy X-ray images through pseudocoloring[J]. IEEE Transactions on Systems, Man, and Cybernetics, Part C (Applications and Reviews), 2006, 36(6): 784-796.
- [4] Ma B, Jia T, Su M, et al. Automated Segmentation of Prohibited Items in X-ray Baggage Images Using Dense De-overlap Attention Snake[J]. IEEE Transactions on Multimedia, 2022.
- [5] Wei Y, Tao R, Wu Z, et al. Occluded prohibited items detection: An x-ray security inspection benchmark and de-occlusion attention module[C]//Proceedings of the 28th ACM International Conference on Multimedia. 2020: 138-146.
- [6] Liu W, Anguelov D, Erhan D, et al. Ssd: Single shot multibox detector[C]//European conference on computer vision. Springer, Cham, 2016: 21-37.
- [7] Girshick R. Fast r-cnn[C]//Proceedings of the IEEE international conference on computer vision. 2015: 1440-1448.
- [8] Ren S, He K, Girshick R, et al. Faster r-cnn: Towards real-time object detection with region proposal networks[J]. Advances in neural information processing systems, 2015, 28.
- [9] Hu J, Shen L, Sun G. Squeeze-and-excitation networks[C]//Proceedings of the IEEE conference on computer vision and pattern recognition. 2018: 7132-7141.
- [10] Woo S, Park J, Lee J Y, et al. Cbam: Convolutional block attention module[C]//Proceedings of the European conference on computer vision (ECCV). 2018: 3-19.
- [11] Lin T Y, Dollár P, Girshick R, et al. Feature pyramid networks for object detection[C]//Proceedings of the IEEE conference on computer vision and pattern recognition. 2017: 2117-2125.
- [12] Liu S, Qi L, Qin H, et al. Path aggregation network for instance segmentation[C]//Proceedings of the IEEE conference on computer vision and pattern recognition. 2018: 8759-8768.
- [13] Li Z, Zhou F. FSSD: feature fusion single shot multibox detector[J]. arXiv preprint arXiv:1712.00960, 2017.
- [14] Fu C Y, Liu W, Ranga A, et al. Dssd: Deconvolutional single shot detector[J]. arXiv preprint arXiv:1701.06659, 2017.
- [15] Redmon J, Divvala S, Girshick R, et al. You only look once: Unified, real-time object detection[C]//Proceedings of the IEEE conference on computer vision and pattern recognition. 2016: 779-788.
- [16] Redmon J, Farhadi A. Yolov3: An incremental improvement[J]. arXiv preprint arXiv:1804.02767, 2018.
- [17] Bochkovskiy A, Wang C Y, Liao H Y M. Yolov4: Optimal speed and accuracy of object detection[J]. arXiv preprint arXiv:2004.10934, 2020.
- [18] Simonyan K, Zisserman A. Very deep convolutional networks for large-scale image recognition[J]. arXiv preprint arXiv:1409.1556, 2014.
- [19] He K, Zhang X, Ren S, et al. Deep residual learning for image recognition[C]//Proceedings of the IEEE conference on computer vision and pattern recognition. 2016: 770-778.
- [20] Iandola F, Moskewicz M, Karayev S, et al. Densenet: Implementing efficient convnet descriptor pyramids[J]. arXiv preprint arXiv:1404.1869, 2014.
- [21] Yu F, Koltun V. Multi-scale context aggregation by dilated convolutions[J]. arXiv preprint arXiv:1511.07122, 2015.
- [22] Szegedy C, Liu W, Jia Y, et al. Going deeper with convolutions[C]//Proceedings of the IEEE conference on computer vision and pattern recognition. 2015: 1-9.

Research on Cultivating Senior High School Students' Innovative Thinking in Mathematics Based on Bloom's Taxonomy of Educational Objectives

Yujie WANG and Zhiqin HUANG¹

School of Mathematical Sciences, University of Jinan, Jinan, Shandong, China

Abstract. Bloom's taxonomy of educational goals divides the educational goals in the cognitive field into different levels from low-level to high-level, and the highest level is innovation. Our country is stepping into the era of knowledge economy step by step, cultivating students' innovative thinking is the need of The Times development, the key to maintain the prosperity of national culture, and the development of national science and technology needs the promotion of education innovation. But the vast majority of middle school students lack of thinking in the learning process in our country, the lack of space imagination ability and logical thinking ability in the process of teaching, and teachers failing to cultivate students' various mathematical ability, based on this the paper in bloom education target on the basis of how to improve the students' mathematics creative thinking put forward the following Suggestions: Teachers should attach importance to preview before class and introduction, and students' learning methods should be reformed: skillfully use "flipped classroom", "group cooperative learning", attach importance to the cultivation of students' observation and analysis ability, attach importance to classroom summary and form knowledge system. And under the guidance of the classification of educational objectives, the teaching design of the sum of the first n terms of geometric progression is carried out.

Keywords. Bloom's taxonomy of educational objectives, high school students, innovative thinking in mathematics

1. Bloom's Taxonomy of Educational Objectives

In 1948, a group of testing experts first proposed the establishment of educational goal classification system at the Annual meeting of the American Psychological Society in Boston.

As shown in Table 1, the lower the level is, the more basic and critical the revised cognitive dimension goal classification is, and the higher the level is, the more complex it is [1].

¹ Corresponding author: 1454298423@qq.com

Table 1. Revised cognitive dimension target classification.

Memory	Understand	Application	Analysis	Evaluation	Create
identify	interpretation	implement	difference	check	produce
memory	For example	implementation	organization	comment	plan
	classification	attribution		generate	
	summarize				
	inference				
	compare				

2. Strategies for Cultivating Students' innovative Thinking

2.1. Pay Attention to Pre-class Preview and Classroom Introduction

The lowest and most basic level in Bloom's classification of cognitive dimension goals is memory. There are many different ways of memorizing, and the results are different. Rote, repetitive memorizing is far inferior to active exploration.

Teachers can set preview task to the students before the class, can be related to the next class a questions, can also be a preview of what part, students to preview before class not only can better grasp the difficult point of the whole class, to go to the lecture with questions can improve the teaching efficiency of the whole class, to explore knowledge actively, take the initiative to deepen our memory[2].

2.2. The Transformation of Students' learning Styles

On the basis of memory, further improve the level of cognition, to achieve the understanding and application of knowledge. The traditional teaching mode is teacher-student and teacher-student, although the classroom efficiency is high, it is not conducive to give play to the students' subjectivity. Teachers can reasonably divide the teaching content so that students can fully prepare before class and independently consult materials to learn the corresponding content. On the basis of "flipped classroom", students can communicate and discuss with each other. Teachers only play a guiding role in controlling the overall situation and return the initiative of learning to students [3].

2.3. Pay Attention to the Cultivation of Students' observation and analysis Ability

On the basis of understanding and applying knowledge, improve students' analytical awareness and ability to solve problems, and achieve the subdivision of analysis dimension in Bloom's cognitive dimension goal, namely distinction, organization and attribution. When students get a topic, they should not rush to apply the formula or theorem solution, but should guide students to analyze the context of the topic, make a distinction between key information and secondary information, and guide students to

draw the key information when reading the topic. Only by analyzing the topic thoroughly can we put forward creative questions on this basis. It can be seen that students can carry out innovation on the premise of careful observation and rigorous analytical ability.

2.4. Attach Importance to Classroom Summary and Form Knowledge System

A good lesson should begin and end, beginning with introduction and ending with summary. Guide students to evaluate their mastery of knowledge. Summary should not be limited to the end of the class, but can also be interspersed in the teaching process to establish the connection of various knowledge points. Teachers should clarify students' classroom subjectivity, guide students to summarize by themselves, make full use of mind mapping, gradually connect single knowledge points into lines, form knowledge blocks and transform them into complete knowledge areas, and establish a good knowledge system [4].

3. Teaching Design of "The Sum of the First N Terms of Geometric Progression " Under the Guidance of Educational Objective Classification

Taking "the sum of the first n terms of the arithmetic progression" as an example, this paper tries to integrate Bloom's theory of classification of educational objectives in cognitive field into practical high school mathematics teaching.

3.1. Textbook Analysis

The teaching period is divided into 2 periods, and this lesson is the first period. Before learning this lesson, students have learned the definition of arithmetic series, and can master the general term formula of arithmetic series, the first n term and formula and its derivation method, and the general term formula of arithmetic series, etc. All these knowledge lay a foundation for learning this lesson.

"Sum of the first n terms of geometric series" is widely used in real life, such as the calculation of housing loans, population growth rate and so on. In addition, some mathematical ideas and methods involved in the process of formula derivation, such as analogical reasoning, classification discussion, from special to general, are necessary mathematical ideas and methods for students [5].

3.2. Learning Situation Analysis

Students have learned the first n arithmetic progression and formula and its derivation process, from the level of the students' cognitive and thinking characteristics to infer, from the formula derivation method and application of the student union for an analogy, the consciousness of the students have the analogy is encouraging, but in this section, the formula derivation process in terms of quality and different from those of the arithmetic progression and referred to in the preceding paragraph, This will be a breakthrough for students' habits of thought n Besides, students tend to ignore this special situation $q = 1$.

3.3. Establishment of Teaching Objectives

(1) Knowledge and Skills

Master the first n terms and formulas of geometric sequence, understand their derivation process, and be able to apply the formulas to solve the corresponding problems.

(2) Process and Method

Understand the principle of dislocation subtraction and master the calculation method of dislocation subtraction. Develop mathematical thinking such as analogical reasoning, from special to general, classification discussion, improve logical thinking ability such as classification, inference and abstraction.

(3) Emotional Attitude and Values

Gain new knowledge through analogical reasoning, improve the ability to find, propose, analyze and solve problems. By independently exploring the derivation process of the formula, improve the awareness of exploration and innovation, enhance the mathematical thinking.

3.4. Teaching Key Points

Teaching emphasis: application of geometric progression's first n terms and formulas

Teaching difficulties: derivation of the formula of the sum of the first N terms of geometric progression

3.5. Analysis of Teaching Process

The teaching mode of this class is guided discovery, and the theoretical basis is Bloom's taxonomy of educational objectives. Teachers assign preview tasks to students before class, preview pages 35-37 of the textbook. In the classroom, teachers guide students to explore, in the form of group cooperation and exchange, provide students with opportunities to fully express, discuss and explore problems, so that students can obtain new knowledge through individual self-study, group discussion, collective explanation and other ways [6].

3.6. Teaching Process

Part 1: Introduce the story and explore new knowledge

Apple orchard apples are ripe, the farm long hired several workers to help collect apples, the farm long said, you work in the orchard for a month is 30 days, wages and so on to sell these apples to you. One of the workers said, "I don't want to be paid. I only want 1 apple on the first day, 2 apples on the second day, 4 apples on the third day, and then give me twice as many apples as the previous day. What do you say?" The farmer thought to himself, "If I give only one apple on the first day, two apples on the second day, and four apples on the third day, I can keep the workers working for a month with just one bag of apples." Think of here the farmer readily agreed. Can you help the farmer figure out how many apples he will have to pay the workers at the end of a month?

The student replied, "You have to pay the worker $1+2^1+2^2+2^3+\dots+2^{29}$ apples.

Design intent: After the questions are thrown out, the teacher guides the students to summarize the essence of the questions and seek the sum of the above geometric progression. The introduction of interesting stories related to real life can stimulate

students' desire to explore and interest in learning, thus deepening students' memory of this knowledge point. Teaching on the basis of students' preview, students coming into the classroom with questions, attending lectures in a targeted way, and answering doubts, is conducive to improving the efficiency of the classroom.

part 2: Analogical reasoning, explore the formula

Students discuss: how to solve it $S_{30} = 1 + 2^1 + 2^2 + 2^3 + \dots + 2^{29}$

Teacher guide: What are the rules? $S_{30} = 1 + 2^1 + 2^2 + 2^3 + \dots + 2^{29}$ If you multiply both sides of this equation by 2, you get, look at the similarities and differences on the right hand side of these two equations $2S_{30} = 2 + 2^2 + 2^3 + 2^4 + \dots + 2^{30}$

Students work together and communicate with each other in groups. The teacher gave the answer: This method is called dislocation subtraction, and it is a general method for us to find the sum of the first N terms of geometric progression.

Teacher: now if the first term of the geometric sequence is a_1 , the common ratio is q , how to find the sum of the preceding terms?

Teacher-student activities: students independently calculate and explore, teachers patrol, and give appropriate hints: for the example of the farmer giving apples to workers, how did you just eliminate some items in this geometric sequence? After the teacher's reminder, students analogize the method used in this example, multiply the common ratio first, and then use the dislocation phase subtraction.

$$S_n = a_1 + a_1q + a_1q^2 + \dots + a_1q^{n-1} \quad (1)$$

$$qS_n = a_1q + a_1q^2 + a_1q^3 + \dots + a_1q^{n-1} + a_1q^n \quad (2)$$

Formula (1) minus formula (2) can be obtained: $(1 - q)S_n = a_1(1 - q^n)$

After thinking, the students will answer, and the teacher will guide them step by step. When $q = 1$, what are the characteristics of the sequence?

After the students write on the blackboard, the teacher projects the correct results

$$S_n = \begin{cases} \frac{a_1(1 - q^n)}{1 - q}, & q \neq 1 \\ na_1, & q = 1 \end{cases} \quad (3)$$

Design Intention: The teacher guides the students through the process of understanding knowledge in Bloom's classification of educational objectives, grasping the students' thinking and making them follow the rhythm and route preset by the teacher, go through the process of independent inquiry, and gradually master the method of solving problems. Show the similar problem situation, induce the general formula by analogy, and realize the mathematical thought from the special to the general, which is helpful for students to break through the difficult points and master the key points in the future study. Students tend to take it for granted and ignore the situation $q = 1$ in the formula. Teachers question students and give students to explore, which is conducive to deepening students' understanding of the formula, improving their awareness of classification and discussion of problems, and developing rigorous thinking and problem-solving habits.

part 3: Tracking training, consolidation exercises

Design intention: Guide students to apply and analyze, and develop their analogical reasoning thinking. Let students' habit of solving problems gradually change from applying formulas to flexibly using deformation formulas, and solve problems not limited to fixed routines, encourage multiple solutions to a problem, and cultivate students' divergent thinking and innovative thinking.

Step 4: Summarize and form a knowledge system

Student activity: Guide the students to answer and summarize (teacher presents the frame in the form of mind map):

Design intention: Communicate with each other in groups, share the harvest of this lesson, check the omissions and make up for the deficiency, and the teacher makes up for the deficiency, reflecting the students' subjectivity and cooperation consciousness. In the form of mind mapping, show the knowledge system of this lesson and guide students to establish the whole knowledge vein of this chapter.

4. Conclusion

Throughout the teaching design of the whole lesson of the sum of the first terms of geometric sequence, it is based on the cognitive dimension objective classification of Bloom's educational objective classification. First, before teaching, according to the requirements of the new curriculum standard and based on Bloom's taxonomy of educational objectives, the educational objectives of the whole lesson are divided into three dimensions of cognition, emotion and motor skills, and then a series of teaching activities are designed according to the educational objectives of the cognitive dimension. With students as the main body and teachers as the auxiliary, let students experience the memory, understanding, application, analysis and evaluation of knowledge, and develop students' innovative thinking in mathematics on the basis of the first five dimensions. Let students learn in "activities", develop in "initiative", improve in "cooperation" and innovate in "exploration".

References

- [1] Chen Yanan. The guiding significance of Bloom's taxonomy to improve the metadata literacy of college students . *Journal of Jilin Institute of Education (late)*, 2014,30(01):17-19.
- [2] Tang Ruifen. Thoughts on Bloom's taxonomy of educational goals. *Journal of Mathematics Education*, 1993(02):10-14.
- [3] Xu Li. Research on the application of Bloom's mastery learning theory in junior middle school mathematics teaching. Shanghai Normal University, 2016.
- [4] Li Xiaohong. Research on the cultivation of high school students' innovative thinking ability in mathematics under the new curriculum standard. *Jiannan Literature (Classic Education Institute)*, 2011(07):258.
- [5] Tong Xiuying, Wo Jianzhong. Research on the characteristics of creative thinking development of senior high school students. *Psychological Development and Education*, 2002(02):22-26.
- [6] Cao Ju. On the cultivation of high school students' innovative thinking in mathematics. *Mathematics Teaching Newsletter*, 2013(30):21-23.

Anti-Jamming Method of Cognitive Radio Based on Q-Learning

Yichen XIAO^{a,1}, Haiyu REN^a, Shan WU^a, Lixiang LIU^a, Xiandong MENG^b and Pengcheng DING^b

^aScience & Technology on Integrated Information System Laboratory, Institute of Software Chinese Academy of Sciences Science, Beijing, China

^bTINNO Communications Co., Ltd, YiBin, Sichuan, China

Abstract. Due to the exposed nature of wireless links, the communication of wireless networks is vulnerable to jammers. And because the jammer models are usually unknown to communication users, particularly in military confrontation applications, how to ensure maintain communication under different jamming is an active research topic. In this paper, we take the anti-jamming task of cognitive radio as a Markov decision process and propose an anti-jamming method based on Q-learning. The method aim to learn an efficient policy for users to maximize the total channel transmission capacity in different typical jamming scenarios. The simulation results indicate that compared with the traditional anti-jamming methods, the anti-jamming method based on Q-learning can obtain better performance, and more effective against several kinds of typical jamming models.

Keywords. Cognitive Radio, Anti-jamming method, Q-learning algorithm

1. Introduction

The history of jamming attack can be traced back to the early 20th century. In the Second World War, jammers played an important role, interfering with the radio broadcasts of enemy countries and misleading pilots [1]. On the contrary, the development of anti-jamming technology has a long history.

In traditional anti-jamming methods, direct sequence spread spectrum (DSSS) and frequency hopping (FH) are widely used. A novel multiple parallel frequency-hopping (MPFH) communication system was proposed in [2], which prolongs processing time of jammers and finally nullifies follower jamming of interfering party. [3] proposed an anti-jamming method based on IIR and nonlinear compensation for anti-aliasing and out-of-band jamming in CFHR, which can reduce the implementation complexity when the BER performance is not declined. An index-modulation based joint mode-frequency-hopping (IM-MFH) scheme was proposed in [4], which activates several OAM-modes and carrier frequencies to hop simultaneously, thus resulting in low probability of legitimate signals jammed. In [5], a novel spread-spectrum communication theory which combined with the chaotic system and the anti-jamming applications were proposed.

In recent years, Cognitive Radio (CR) [6] has arisen as a potential solution to solve the spectrum shortage problem, where the sensing ability of cognitive users (CUs) helps

¹ Corresponding Author, Yichen Xiao, E-mail: yichen@iscas.ac.cn.

acquire knowledge of the environment. Thus, CUs could effectively use the ‘spectrum holes’ in spatial, time and frequency domain to reuse the idle spectrum, in order to avoid the effects of jammers. Game-theoretic modeling was a well-known technique used in CR to express the interaction between CUs and adversary jamming attackers since they have opposite objectives [7-8]. In [7], a game-theoretic learning anti-jamming (GTLAJ) paradigm is proposed, and its framework and challenges were introduced. [8] provided a machine-learning-based anti-jamming technique to avoid a hostile jammer, where both the jamming and anti-jamming processes are formulated based on the Markov game framework. However, these approaches of game theory need prior knowledge such as the jamming pattern, which is unpractical in actual usage scenario. Reinforcement learning can also be used to find optimal anti-jamming strategies for many fields of communication, such as Internet of things and UAV [9-10]. Cognitive radio anti-jamming based on the SARSA algorithm was proposed in [11], which took the spectrum energy efficiency of secondary users as a utility function.

Compared with conservative SARSA, Q-learning algorithm is more efficient. In this work, we consider Q-learning to determine optimal anti-jamming strategy. We build the CR anti-jamming model showing how Q-learning algorithm to choose optimal strategy to resist jamming, and via simulation to verify the anti-jamming performance of Q-learning algorithm, i.e. the improvement of total channel transmission capacity and SINR.

The remaining of the paper is organized as follows. In Section 2, we introduction the system model about cognitive radio network and types of jammers. In Section 3, we obtain Q-learning algorithm for anti-jamming. In Section 4 the simulation results are presented, followed by conclusion in Section 5.

2. System Model

Figure 1 shows a model of cognitive radio communication with jamming. There are a cognitive user (CU) and J jammers. The licensed frequency band is divided into K channels. In each time slot, both CU and jammer are allowed to access only one channel. The dotted line in Figure 1 represents the possible selected channel, and the solid line represents the actually selected channel. Assuming that the channel sensing part is known, the CU can observe the channel situation in real time .The jammer can only jam one channel in each time slot.

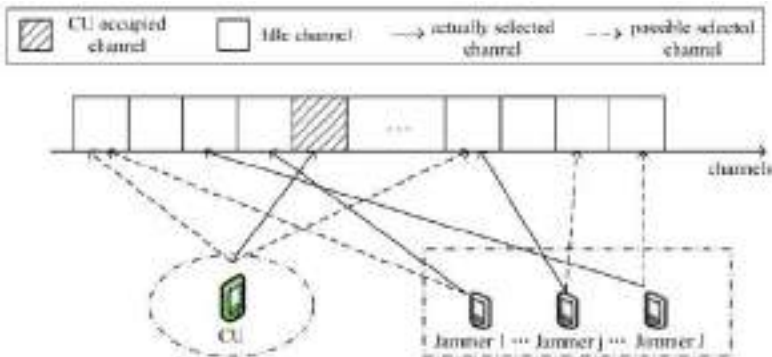


Figure 1. Cognitive Radio Communication with Jamming

The process of interaction between CU and jammers can be constructed into a reinforcement learning model. The jammer tries to block normal communication. If the channel accessed by CU is jammed, it will carry out anti-jamming strategy and select a new channel for data transmission. While avoiding jamming, CU tries to maximize its total transmission capacity. In the paper, the total transmission capacity of the channel is taken as the utility function of CU, which is denoted as

$$u^t = \sum_{k=1}^K B_k \log_2 \left(1 + \frac{|h_k|^2 \cdot p_c}{|g_k|^2 \cdot p_j \cdot f(x^t = y^t) + \sigma^2} \right) \quad (1)$$

where σ^2 is the noise variance, and B_k is the bandwidth of channel k . x^t and y^t are the selected channel in slot t of the CU and the jammer respectively. h_k and g_k are the gain of channel k for the CU and the jammer respectively. p_c and p_j are the transmission power of CU and jamming power of jammers respectively. $f(x)$ is an indicator function that equals 1 if x is true, 0 otherwise.

To analyze the impact of jamming attacks, we consider the following four popular kinds of jammers in military confrontation applications, and the jamming models are shown in **Figure 2**.

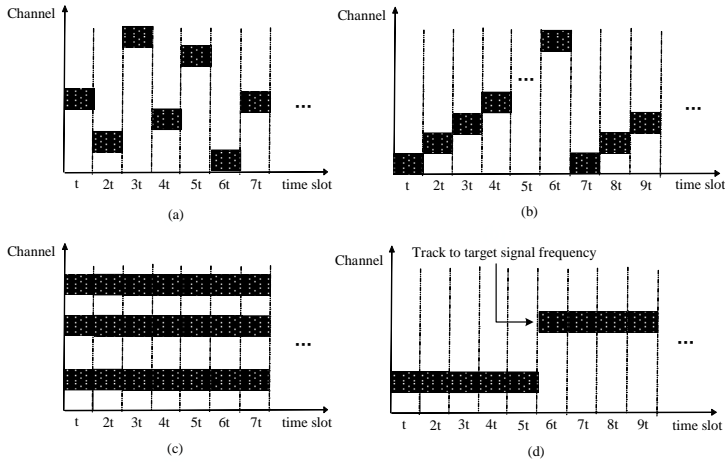


Figure 2. Random jamming model (a), Sweep jamming model (b), Comb spectrum jamming model (c) and Tracking jamming model (d).

- *Random jammer*, which randomly jams a channel in each time slot.
- *Sweep jammer*, which periodically scans the target frequency band. In a scanning period, the jamming frequency moves from the lowest frequency to the highest.
- *Comb spectrum jammer*, which superimposes multiple narrowband jamming signals within a certain bandwidth.
- *Tracking jammer*, which the jamming frequency follows the change of the target signal.

3. Anti-jamming Method based on Q-learning

Q-learning algorithm is a method to solve reinforcement learning control problem by using time sequence difference. In this article, we take the anti-jamming task of cognitive radio as a Markov decision process and propose an anti-jamming method based on Q-learning.

- State

In the interaction between CU and jammers, without knowing the jamming model and wireless channel model, CU can use Q-learning algorithm to determine its optimal strategy, that is, which idle channel is selected for signal transmission when the channel is jammed. The action selection of CU is based on the current state s^t . The state of CU is composed of the state of jammer and base station, which can be represented by SINR,

$$SINR = \frac{|h_k|^2 \cdot p_c}{\sigma^2 + \sum_{j=1}^J p_j \cdot |g_k|^2 \cdot f(x^t = y^t)} \quad (2)$$

- Action

In each time slot, CU and jammers take their own actions respectively. The idle channels among K channels defined as the possible actions x . In time slot t , CU selects channel $x(t) \in \{1, 2, \dots, K\}$ to determine the anti-jamming strategy of the current state, that is, to determine which channel is used to transmit data of the given power p_c .

Considering that at the beginning stage, CU don't know enough about the environmental information, and Q-value table of CU has not been updated a lot. So it is necessary to apply greedy strategy in exploring the results of different actions to update the Q-value table faster. In each time slot, CU has ε probability of exploration and $(1-\varepsilon)$ probability to select the action (i.e. channel) maximizing the Q value in the current state. In the previous iterations, CU has a high probability of exploration in order to understand the jamming strategy of the jammer as soon as possible, so ε is bigger. After a period of learning, the Q-value table has been greatly updated and reduced ε . ε is denoted as

$$\varepsilon = 1/\log(n+1) \quad (3)$$

where n is the number of iteration rounds.

- Reward

The utility function in (1) is taken as the real-time reward function of reinforcement learning algorithm. Through the interaction between CU and jammers, CU changes the anti-jamming strategy in real time to maximize the cumulative reward.

- Update

Set function $V_\pi(s)$ represents the expected reward that can be obtained if we continue to carry out strategy π after reaching a certain state s , which is given by

$$V_\pi(s) = E_\pi(G_0 | S_0 = s) = E_\pi\left(\sum_{t=0}^{\infty} \gamma^t R_{t+1} | S_0 = s\right) \quad (4)$$

where π is the mapping from state to action and γ is the discount factor that controls the impact of future rewards on the optimal decision.

In each time slot t , the goal of CU is to select an action x that maximizes the expected accumulated future reward $V_\pi(s)$. The Q-Learning algorithm can finding the optimal decision in each state based on iterative evaluations of possible actions for Q-table. So, CU updates Q-table by Bellman formula as follow,

$$Q(s^t, x^t) = (1 - \alpha)Q(s^t, x^t) + \alpha(u^t(s^t, x^t) + \gamma \max_x Q(s^{t+1}, x^t)) \quad (5)$$

The smaller γ , the more attention is paid to immediate income; the higher γ , the greater the weight of future rewards. α is the learning rate, the larger α , the fewer iterations, and vice versa. In our work, we set $\gamma = 0.7$.

The proposed method is summarized in Method 1.

Method 1 : Anti-jamming method based on Q-Learning

Initialize: $\alpha, \gamma, \varepsilon$

Initialize: $Q(s, x) = 0 \quad \forall s, x$

For $t = 1, 2 \dots$

Choose an initial state at random $s_0 = SINR^0$;

While do

Choose x^t via epsilon-greedy

Generate a random number r

If $\varepsilon < r$:

$x^t = \arg \max_x Q(s, x)$

Else:

Exploration, randomly choose a action;

End if

Use Channel x^t to send signals with power p_c ;

Obtain next state s^{t+1} ;

Obtain u^t

Update $Q(s, a)$:

$Q(s^t, x^t) = (1 - \alpha)Q(s^t, x^t) + \alpha(u^t(s^t, x^t) + \gamma \max_x Q(s^{t+1}, x^t))$

Update $s = s^{t+1}$;

End while

End for

4. Simulation and Results

The simulation is based on MATLAB to build a common scenario of cognitive radio communication with jamming. Table 1 shows the simulation parameters of the scenario. And we make the following settings to simplify the scenario:

- The channel gain obeys a uniform distribution over (a, b) and ignores the impact of distance;
- CU and jammers have the same numbers of channels and time slots, and the time slots are strictly aligned;
- The basic unit of time is time slot, and the basic unit of frequency is channel (apart from channel capacity).

Table 1. Simulation parameter settings

	Parameter	Value
Parameters of CU	number of channels	$K=256$

	number of slots	$T=512$
	channel gain	$h_k \sim U(0, 1)$
	bandwidth	$B=1\text{MHz}$
	power	$p_c=5$
	background noise power	$\sigma^2=1$
Major parameters of jammers	channel gain	$h_i \sim U(0, 1)$
	power(expect comb spectrum jammers)	$p_j=8$
	power(comb spectrum jammers)	$p_j=8/(K/\Delta f)$
	frequency interval (comb spectrum jammers)	$\Delta f=16$ channels
	sweep rate (sweep jammers)	1 channel per slot
	random rate (random jammers)	1 channel per slot
	response time (tracking jammers)	$T_i=16$ slots

In addition, the traditional anti-jamming methods, i.e. the DSSS method and the FH method, are used as the simulation comparison group. The spreading gain of the DSSS method is 4 and the frequency hop rate of the FH method is 1 hop/slot.

For jamming scenarios, we employ four typical jammers: Random jammers, Comb spectrum jammers, Sweep jammers and Tracking jammers, corresponding to scenario 1, scenario 2, scenario 3 and scenario 4, respectively.

From **Figure 3** to **Figure 6** show the performance when dealing with the four typical jammers respectively. And after the ant-jamming methods are stable, the results are shown in Table 2.

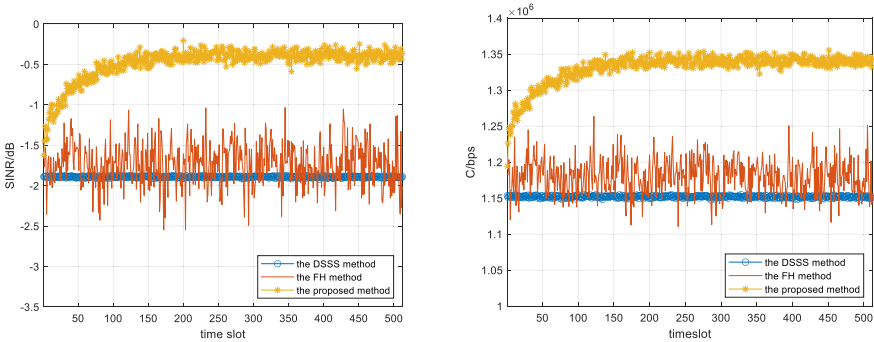


Figure 3. Performance against random jammers.

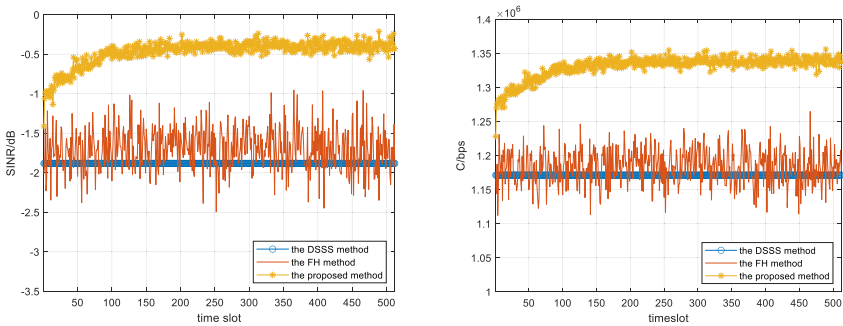


Figure 4. Performance against comb spectrum jammers.

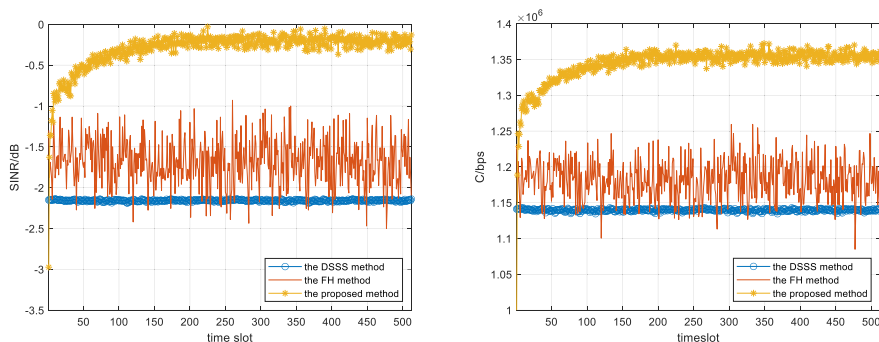


Figure 5. Performance against sweep jammers.

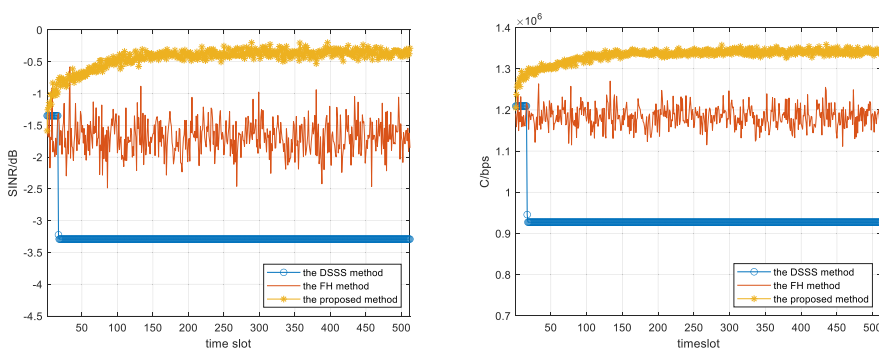


Figure 6. Performance against tracking jammers.

Table 2. Simulation results of the ant-jamming methods

Scenario	Performance	Mean of DSSS	Mean of FH	Mean of Proposed	improved (cp. DSSS)	improved (cp. FH)
Scenario 1	SINR	-1.892dB	-1.735dB	-0.391dB	1.501dB	1.344dB
	total channel capacity	1.152Mbps	1.180Mbps	1.340Mbps	16.37%	13.56%
Scenario 2	SINR	-1.882dB	-1.698dB	-0.394dB	1.488dB	1.304dB
	total channel capacity	1.171Mbps	1.184Mbps	1.339Mbps	14.35%	13.09%
Scenario 3	SINR	-2.157dB	-1.68dB	-0.203dB	1.954dB	1.478dB
	total channel capacity	1.14Mbps	1.182Mbps	1.355Mbps	18.86%	14.64%
Scenario 4	SINR	-1.882dB	-1.698dB	-0.394dB	2.931dB	1.325dB
	total channel capacity	0.927Mbps	1.183Mbps	1.341Mbps	44.66%	13.36%

Simulation and results show that:

- Under the different jamming models, the proposed method takes a certain time for iterative learning to stabilize the performance, but after that, it is more stable and better than the FH method. The SINR can be increased by 1.3-1.5dB, and the total channel capacity can be increased by 13%~15% specifically. That's because the proposed method effectively avoids the interference by learning, while the FH method still has the possibility of collision.
- Under the tracking jammers, the performance of DSSS method deteriorates rapidly since its frequency is fix and tracked by jammers, but the performance

of the proposed method remains good. Compared with the DSSS method, the SINR performance can be improved by 2.9dB, and the total channel capacity can be increased by 44.66%, while the improvement values under other jamming models are 1.4dB~2dB and 14%~19% respectively.

5. Conclusion

In this paper, one anti-jamming method of cognitive radio based on Q-learning is proposed. By applying the Q-learning algorithm, without knowing the channel model and the jamming model, proposed method can achieve anti-jamming communication with better performance of cognitive radio. To verify the effectiveness of the proposed method, the anti-jamming performance under four typical jammers is simulated. The result show that the proposed method has higher SINR and higher system transmission capacity compared with the traditional anti-jamming methods. In the future work, we plan to accelerate the convergence speed of the proposed method, and investigate multi CUs scenarios which exists the competition and collaboration among CUs.

References

- [1] Mpitziopoulou A, Gavalas D. An effective defensive node against jamming attacks in sensor networks. *Security and Communication Networks*, 2009, 2(2): 145-163.
- [2] Z. Chao, X. Zhu, W. He, Y. Ban and S. Chen, A Frequency-Hopping Communication System Based On Multiple Parallel Hopping, 2018 IEEE 3rd Advanced Information Technology, Electronic and Automation Control Conference (IAEAC), 2018 Oct 12-14; Chongqing, China:pp. 2163-2169.
- [3] Xiao Ma; Xuanhe Yang; Xin Jin; Xiaqing Miao; Shuai Wang. A Digital Coherent Frequency Hopping Anti-jamming Receiver Based on IIR, 2020 IEEE 4th Information Technology, Networking, Electronic and Automation Control Conference (ITNEC). 2020 Jun 12-14; Chongqing, China: 10.1109/ITNEC48623.2020.9084695.
- [4] X. Meng, R. Tao, L. Jia, Liping Liang, Wenchi Cheng, Hailin Zhang. Index Modulation Based Joint Mode-Frequency Hopping. *IEEE Communications Letters*, 2021, 25(6), pp.1810-1814.
- [5] Wenzhun Huang, Shanwen Zhang, Robert Hao Yan. Novel Spread Spectrum Communication Theory and the Anti-jamming Applications, 2021 6th International Conference on Inventive Computation Technologies (ICICT), 2021 Feb 20-22; Coimbatore, India: 10.1109/ICICT50816.2021.9358748.
- [6] J. Mitola. Cognitive radio for flexible mobile multimedia communications, 1999 IEEE International Workshop on Mobile Multimedia Communications (MoMuC'99) (Cat. No.99EX384), 1999 Nov 15-17; San Diego, CA, USA: pp. 3-10.
- [7] Luliang Jia, Nan Qi, Feihuang Chu, Shengliang Fang, Ximing Wang, Shuli Ma, Shuo Feng. Game-Theoretic Learning Anti-Jamming Approaches in Wireless Networks, *IEEE Communications Magazine*, 2022, 60(5), pp.60-66.
- [8] Khalid Ibrahim, Soon Xin Ng, Ijaz Mansoor Qureshi, Aqdas Naveed Malik, Sami Muhaidat. Anti-Jamming Game to Combat Intelligent Jamming for Cognitive Radio Networks, *IEEE Access*, 2021, Oct 04; pp.137941-137956
- [9] Ximing Wang, Yuhua Xu, Jin Chen, Chunguo Li, Xin Liu, Dianxiong Liu, Yifan Xu. Mean Field Reinforcement Learning Based Anti-Jamming Communications for Ultra-Dense Internet of Things in 6G. 2020 International Conference on Wireless Communications and Signal Processing (WCSP), 2020 Oct 21-23; Nanjing, China: 10.1109/WCSP49889.2020.9299742.
- [10] Jinlin Peng, Zixuan Zhang, Qin hao Wu, Bo Zhang. Anti-Jamming Communications in UAV Swarms: A Reinforcement Learning Approach, *IEEE Access*, 2019, 7, pp.180532-180543.
- [11] ZHU Rui, MA Yongtao, NAN Yafei, ZHANG Yunlei. Cognitive Radio Anti-Jamming Decision Algorithm Based on Improved Reinforcement Learning. *Journal of Frontiers of Computer Science and Technology*, 2019, 13(4): 693-701.

Real-Time Detection and Early Warning System for Public Security Key Places Based on Human Posture Characteristics

Xiaohui BAI¹, Zhenyu SHOU and Tianhang YUAN

School of Information Technology, Nanjing Forest Police College, Nanjing 210023, China

Abstract. Detention places, as an important part of police's safe of law enforcement, are receiving more and more research attention. We are aiming to apply advanced information technology to the field of detention places and build an early warning prediction model that can improve the security of detention places. This research can accumulate some experience for follow-up technological development in the field of detention places' supervision.

Keywords. Places of detention, security surveillance, risky behavior prediction, personnel control

1. Background Introduction

The need to continuously improve the level of social stability has become increasingly strong. Detention place, as a specific place to detain people who affect social stability, is particularly important in the perspective of security [1]. Only by establishing a set of effective and advanced security system, can we effectively manage the detainees in the daily work of detention place [2].

In response to some abnormal behaviors in Detention place, most of the detention places in China have solved the problem by providing full coverage of surveillance video, which needs to spend the massive manpower, material and financial resources.

2. A review of the literature on security systems for places of detention

2.1. Advances in security algorithms for custodial settings

For the security system of detention places, the core algorithm is mainly pedestrian detection and Human Pose Estimation algorithm.

From the very beginning to 2002, researchers have borrowed and quoted some mature methods in the field of image processing and pattern recognition.

In 2005, Dalal and others [3]. In 2011, Zhu proposed CENTRIST, namely the central transform histogram feature [4]. Several powerful algorithmic frameworks have been proposed so far, including R-CNN, YOLO, and SSD.

¹Corresponding author: Bai Xiaohui, E-mail: 444340687@qq.com.

In 2013, the research of pose estimation gradually started to shift from the traditional research to the research of deep learning Human Pose Estimation [5]. Alexander Toshev and others further combined DeepPose with CNN. By 2016, Convolutional Pose Machine (CPM) was introduced into Human Pose Estimation algorithms [6]. In the current field of Human Pose Estimation, classical algorithm structures such as CPN, HRNet, etc.

2.2. Selection of algorithms for security systems in detention facilities

2.2.1 Comparison of the advantages of different algorithms

2.2.1.1 Pedestrian detection

The mainstream pedestrian detection are mainly as follows.

RCNN has high precision under specific network model and data set, as shown in Figure 1. However, due to its large number of convolutional neural network computation, RCNN runs slowly and takes up a lot of space to run [7].

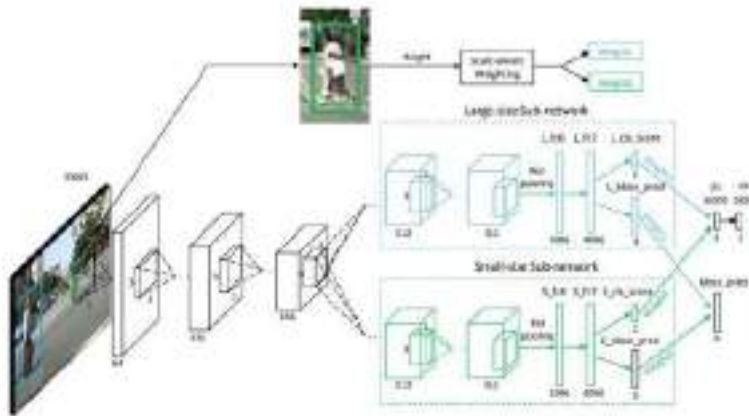


Figure 1. RCNN

SSD balances the advantages and disadvantages of YOLO and RCNN. However, SSD requires manual settings during debugging and cannot be automatically learned, which makes the debugging of SSD model very dependent on experience [8].

YOLO, like SSD, has the characteristics of accuracy and high speed. YOLO has excellent performance in overall detection by end-to-end testing. The YOLO uses CNN networks for target detection, which is very simple and fast [9].

2.2.1.2 Human Pose Estimation

The mainstream of Human Pose Estimation includes MediaPipe, OpenPose, HRNet and so on. MediaPipe has good accuracy and operation speed for Human Pose Estimation, but its gross defect is that cannot recognize the posture of multiple people. Although it can combine with other algorithms to realize the estimation function of multi person posture, the final result lags behind and the accuracy will be greatly reduced [10].

OpenPose integrates the models of mediapipe and posenet, and has high stability. It has good accuracy in most cases and can adapt to different environments by changing

the convolution core weight [11]. However, it is difficult for openpose to avoid misjudgment of actions in videos with complex backgrounds.

The biggest advantage of HRNet is that it can maintain the high resolution of images during operation. However, the operation process of HRNet is very complex and non real-time because it lacks the process of down sample.

2.2.2 Advantages of YOLOv3 and OpenPose algorithms

2.2.2.1 Pedestrian detection

Among the pedestrian detection, we have chosen the YOLOv3.

In this project, the algorithm of pedestrian detection is required to sensitively detect people in detention places. Comparing the mainstream algorithms, RCNN has very high accuracy and very sensitive perception for small targets, but it will consume a lot of time and memory space due to the complexity of its convolutional neural network. Thus, RCNN is not suitable for this project. Similarly, although SSD has a good performance of detection accuracy and running speed, its debugging process not only requires lots of manual settings, but also requires too much experience for the project team. YOLOv3 is much better than SSD variants and comparable to state-of-the-art models on the AP₅₀ metric, as shown in Figure 2. Therefore, it is not suitable for this project in all aspects. YOLOv3 is simple, fast, and sensitive to global video detection. Meanwhile, the layering of object detection makes YOLOv3 more effective for small targets, which is more suitable for this project's simple and efficient requirements [12]. Besides, YOLOv3 has good real-time performance, which can well meet the effect of real-time monitoring in this project [13]. So, we selected YOLOv3 to complete the figure detection in this project.

	backbone	AP	AP ₅₀	AP ₇₅	AP ₅₀	AP _M	AP _L
<i>Two-stage methods</i>							
Faster R-CNN++ [3]	ResNet-101-C4	34.9	55.7	37.4	15.6	38.7	50.9
Faster R-CNN w FPN [6]	ResNet-101-FPN	36.2	59.1	39.0	18.2	39.0	48.2
Faster R-CNN by G-RMI [4]	Inception-ResNet-v2 [10]	34.7	55.5	36.7	13.5	38.1	52.0
Faster R-CNN w TDM [18]	Inception-ResNet-v2-TDM	36.8	57.7	39.2	16.2	39.8	52.1
<i>One-stage methods</i>							
YOLOv2 [13]	DarkNet-19 [13]	21.6	44.0	19.2	5.0	22.4	35.5
SSD513 [9, 2]	ResNet-101-SSD	31.2	50.4	33.3	10.2	34.5	49.8
DSSD513 [2]	ResNet-101-DSSD	33.2	53.3	35.2	13.0	35.4	51.1
RetinaNet [7]	ResNet-101-FPN	39.1	59.1	42.3	21.8	42.7	50.2
RetinaNet [7]	ResNeXt-101-FPN	40.8	61.1	44.1	34.1	44.2	51.2
YOLOv3 608 × 608	Darknet-53	33.0	57.9	34.4	18.3	35.4	41.9

Figure 2. Algorithm comparison results.

2.2.2.2 Human Pose Estimation

Among the Human Pose Estimation, we chose OpenPose.

Although the MediaPipe has good accuracy and operation speed for motion recognition, its function can only estimate the pose of a single target and cannot meet the needs of this project. In terms of HRNet, it has the strongest function and is better than the other two algorithms in terms of prediction accuracy, but its function of maintaining image clarity during the operation is not necessary for this project. Besides, HRNet's poor real-time performance during the operation cannot meet the demand of timely alarm.

Therefore, we chose OpenPose. OpenPose as a real-time multi-person keypoint detection library allows simultaneous pose estimation of body, face and limbs [14].

3. Model Building

3.1. Personnel Standard Action Judgment System

The standard action judgment system uses posture evaluation algorithms and key frame action feature extraction to construct an innovative standard technical action data base in public security detention facilities. The core part is divided into 3 units - human key point prediction unit, key point data pre-processing unit, and standard action data database construction unit. The overall flow chart is shown in Figure 3.

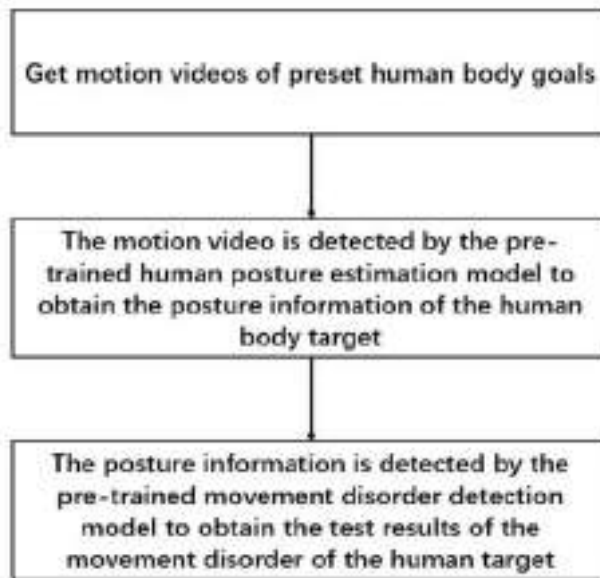


Figure 3. Overall flow chart of the unit.

When the video is input, the system extracts the video frame by frame and analyzes each frame of the video using the target detection algorithm, and then we use the OpenPose algorithm to extract the human bones in each frame, which is the human key point prediction unit.

The 2D or 3D coordinates of each human skeleton in each frame are usually used to represent the skeletal sequence. Previously, action recognition based on skeletal points was done by linking all the joint vectors in each frame into one feature vector. By adding the video to the algorithm and running it, the resulting JSON file is parsed as follows: position information of each body part (x, y, score), each part is an array containing the position information and detection confidence of each body part in the format = $x_1, y_1, c_1, x_2, y_2, c_2, \dots$ coordinates x and y can be normalized to the intervals [0,1], [-1,1], [0,source size], [0,output size], etc., and the skeletal information of the person can be obtained by concatenating each skeletal point. As shown in Figure 4.



Figure 4. Skeletal Coordinate Chart.

3.2. Character movement recognition

After the character localization and skeleton extraction operations, the system will define and recognize the actions of the annotated joint dynamic data training set by the st-gcn algorithm.

The hierarchical nature of ST-GCN eliminates the need for manual partitioning or traversal of rules. As shown in Figure 5 this not only results in greater expressiveness and higher performance (as shown in our experiments), but also makes it easy to generalize across different environments. Based on the generic GCN formulation, we also designed a new strategy for graph convolution kernels based on image model-inspired research. The main contributions of this work are threefold: 1) We propose ST-GCN, a graph-based approach for dynamic skeletal modeling, which is the first application of a graph-based neural network for this task. 2) We propose several principles for designing convolution kernels in ST-GCN, aiming to meet the specific requirements of skeletal modeling. 3) On two large-scale datasets based on skeletal action recognition, our model requires considerably less manual design and achieves superior performance compared to previously used methods that manually assign partial or traversal rules.

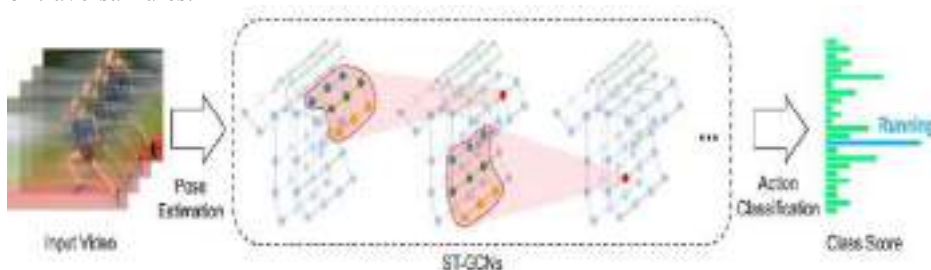


Figure 5. ST-gcn algorithm.

3.3. Motion acquisition subsystem

The motion capture subsystem uses the yolo object tracking detection algorithm and key frame motion feature extraction to build a human motion capture system. When an image

is fed into the yolo network, it is first scaled to a 416 by 416 size. After adding gray tones to the edges of the image to prevent distortion, yolo divides the image into $13 * 13$, $26 * 26$, and $52 * 52$ grids. $52 * 52$ grids are used to detect small objects since small features tend to disappear after multiple convolution and compression. $13 * 13$ grids are used to detect large objects. Since the cat is a relatively large object, it has a $13 * 13$ grid for detection, and each grid point is responsible for the detection of its lower right corner region. If the center point of the object falls in this region, the position of this object is determined by this grid point. yolo is nothing but dividing a picture into different networks, and each grid point is responsible for the prediction of its lower right region. As long as the object's center point falls in this region, this object is determined by this grid point.

When the video is fed into the system, the YOLO algorithm extracts detects and tracks the pedestrians in the video frame by frame. As shown in Figure 6.

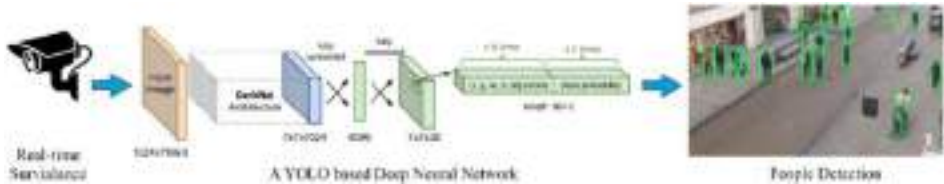


Figure 6. Yolo character extraction.

3.4. RFCOMM Bluetooth Protocol Alarm

Finally, the program will further test and evaluate the action posture of the identified object based on the training set of the annotated joint dynamic data, and then predict the possible abnormal behaviors of the suspect in the detention center, such as self-harm and fall, and define such actions as abnormal actions, if the action is defined as abnormal actions, the program will send out the warning message, and at the same time send the received abnormal warning message to the buzzer. If the action is defined as abnormal action, the program will send out a warning message, and at the same time will receive the abnormal warning information sent to the buzzer, that is, will be based on RFCOMM Bluetooth protocol based on communication programming connected to Bluetooth alarm, timely warning information to warn the police.

4. Conclusion

In this research, we focus on the key areas of social security work and the difficult areas of public security work under the condition of complicated public security situation. It revealed that the public security department does not have an excellent early warning and monitoring model for high-risk abnormal behaviors of specific personnel in detention places. Fortunately, most places of detention in our country are equipped with monitoring and other basic equipment during the process of public security informationization. On the basis of these conditions, we have added the recognition and alarm function of the person's movement to the monitoring to realize the judgment of high-risk abnormal behavior. The whole process is simple and easy to understand, suitable for use in places of detention.

Acknowledgements

This research was supported by the 2022 College Students Innovation and Entrepreneurship Training Program (Grant No. 202212213024Z).

References

- [1] Grethe Midtlyng. Safety rules in a Norwegian high-security prison. The impact of social interaction between prisoners and officers. *Safety Science*. 2022 May;149.
- [2] Zeping Zhang, Jing He, Zhiwei Zhang. Emotion Recognition Algorithm Based on Panorama-plane Mapping Dataset and VGG16 in Prison Monitoring System. *Journal of Physics. Conference Series*. 2020; 1627(1): 012010.
- [3] Tomoki Watanabe, Satoshi Ito, Kentaro Yokoi. Histograms of oriented gradients for human detection. *IPSJ Transactions on Computer Vision and Applications*. 2010; 2:39-47.
- [4] Wu Jianxin, Rehg James M. CENTRIST: A Visual Descriptor for Scene Categorization. *IEEE transactions on pattern analysis and machine intelligence*. 2011; 33(8): 1489-1501.
- [5] Alexander Toshev, Christian Szegedy. DeepPose. Human Pose Estimation via Deep Neural Networks. *IEICE Transactions on Fundamentals of Elect*. 2013.
- [6] Jian He, Cheng Zhang, Xinlin He, Ruihai Dong. Visual Recognition of traffic police gestures with convolutional pose machine and handcrafted features. *Neurocomputing*. 2020; 390(prepublish) : 248-259.
- [7] Yang Ai-min, Jiang Tian-yu, Han Yang, Li Jie, Li Yi-fan, Liu Chun-yu. Research on application of on-line melting in-situ visual inspection of iron ore powder based on Faster R-CNN. *Alexandria Engineering Journal*. 2022; 61(11) : 8963-8971.
- [8] Gao Xinbiao, Xu Junhua, Luo Chuan, Zhou Jun; Huang Panling, Deng Jianxin. Detection of Lower Body for AGV Based on SSD Algorithm with ResNet. *Sensors*. 2022; 22(5) : 2008-2008.
- [9] Ignacio Martinez-Alpiste, Gelayol Golcarenenji, Qi Wang, Jose Maria Alcaraz-Calero. A dynamic discarding technique to increase speed and preserve accuracy for YOLOv3. *Neural Computing and Applications*. 2021; 1-13.
- [10] Yasumuro Masanao, Jin'no Kenya. Japanese fingerspelling identification by using MediaPipe. *IEICE Communications Society Magazine*. 2022; 13(2) : 288-293.
- [11] Jiayuan Xing, Jun Zhang, Chenxing Xue. Multi person pose estimation based on improved openpose model. *IOP Conference Series: Materials Science and Engineering*. 2020; 768(7) : 072071.
- [12] Wang Zhihui, Zhu Houying, Jia Xianqing, Bao Yongtang, Wang Changmiao. Surface Defect Detection with Modified Real-Time Detector YOLOv3. *Journal of Sensors*. 2022.
- [13] He Xiaopei, Wang Dianhua, Qu Zhijian. An Improved YOLOv3 Model for Asian Food Image Recognition and Detection. *Open Journal of Applied Sciences*. 2021; 11(12) : 1287-1306.
- [14] Andi W. R. Emanuel, Paulus Mudjihartono, Joanna A. M. Nugraha. Snapshot-Based Human Action Recognition using OpenPose and Deep Learning. *IAENG International Journal of Computer Science*. 2021; 48(4).

Study Analysis of Printed Monopole Antenna for C and X Band Application

Samom JAYANANDA SINGH ^{a,1}, Rajesh KUMAR^a and M.M DIXIT^b

^aDept of Electronics and communication Engg, NERIST, Arunachal Pradesh, India

^bDept of Mathematics, NERIST, Arunachal Pradesh, India

Abstract. In this design, dimension of the proposed antenna is 20 X 25 X 1.6 mm³ with FR4 substrate having circular patch fed with co-planar waveguide (CPW) that operates at numerous resonance frequencies between 5 and 10 GHz. The proposed antenna can be used well for low range communication transceivers in the C and X bands, according to simulation results. The optimal parameters for UWB antenna are the fractional bandwidth, which should be greater than 85%, and VSWR, which is another parameter. For the best and most efficient technique of using printed monopole antenna, the range of Ultra wideband (UWB) bandwidth should be lower than 2. Simulate data suggest that the proposed antenna has outstanding impedance matching capabilities, achieving a peak gain of 8 dBi. Results indicate that the ground plane's dimensions of 15.9 mm and 11.4 mm are the most suitable for UWB due to its return loss of -41.86 dB, fractional bandwidth of about 89%, and Voltage standing wave ratio (VSWR) of less than 2 within the frequency spectrum. This modified prototype antenna has a decent, omnidirectional radiation pattern.

Keywords. Return loss, C and X bands, Ultra wideband (UWB), Voltage standing wave ratio (VSWR), Co-planar waveguide (CPW)

1. Introduction

Due to their inherent characteristics, such as their portable dimension, high speed signal over short distances, maximum bandwidth, low profile hardware, little power utilization, omnidirectional field pattern, and linearly shift, ultra-wideband systems have become necessary for many applications in recent years. The Federal Communication Commission (FCC) granted the radio spectrum upto 10 GHz to UWB in the year 2002 to overcome the flaw to pre existing narrow band communication [1]. The antenna system is highly desired in wireless communication due to its numerous characteristics, including short pulse length, wide frequency band, low distortion, multipath immunity, and low intercept probability. Monopole antennas are frequently employed as effective radiators in a wide range of applications, including radio receivers, mobile phones, mobile navigation, and communication. It is because of its key characteristics, including its cost effective, continuous conformal construction, light weight, simplicity of manufacture, integration with RF devices, etc. In recent years, wireless technology has advanced more rapidly. Through 3G and 4G, the technology advanced to the fifth generation (5G). In the past, planar microstrip

¹ Corresponding Author: Samom Jayananda Singh, Dept of Electronics and communication Engg, NERIST, Arunachal Pradesh, India; E-mail: jayanandmetal.inc@gmail.com.

antennas were used by 2G technology for sending and obtaining microwaves at the necessary centre frequency [2][3]. The working frequency of the cellular technology determines the antenna's size. For modern uses, the antenna gets progressively smaller, takes up very little room, and is simple to place. In contemporary wireless networks, such a small antenna is also favoured for low-power transceiver applications. The cellular band's spectrum allocation became congested as internet technologies advanced. Modern communication devices are a result of growing demand for wireless service in contemporary wireless communication networks.

Additionally, the antenna is crucial to the mobile communication system's ability to expand the coverage area, boost cellular system capacity, and simplify the network. The substrate's dielectric constant of printed antenna naturally affects the antenna's size [4-8]. Gangwar et al. [9] implemented slit and slot in the radiating element to accomplish multi-band operation. A thorough study by Carver et al. [10] revealed that changing the patch dimension from rectangular to another can provide impedance matching characteristic. Li et al. [11] created a wide range dual polarisation which is circular in nature, FR4 as substrate with CPW fed modifying the patch with slot.

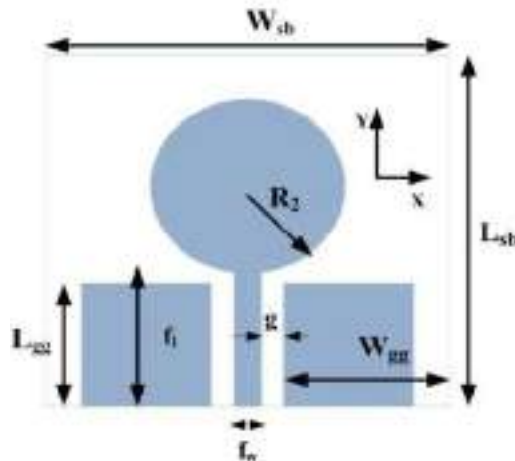


Figure 1. Proposed Antenna Design

2. Proposed Antenna Design

The design of the proposed monopole antenna with circular disc shaped patch can be found out from the following equations, Eqs (1) and (2) [12].

$$R_2 = \frac{R_{fe}}{\sqrt{1 + \frac{2h}{\pi \epsilon_r R_{fe}} \left[\ln \left(\frac{1.57 R_{fe}}{h} \right) + 1.78 \right]}} \quad (1)$$

$$R_{fe} = \frac{8.79 \times 10^9}{f_{rs} \sqrt{\epsilon_r}} \quad (2)$$

Where, h = substrate's height in mm, ϵ_r = dielectric constant of the substrate, f_{rs} = the resonating frequency.

The standard formulation given for estimating the lower band-edge frequency of printed monopole antennas can be used to evaluate the lower band-edge frequency of the antenna. With the right modifications, a cylindrical monopole antenna can be used [10-15]. These equations hold good for the antenna with planar model with monopole structure.

The lower band edge frequency is given in [11-15], if H represents height of the monopole antenna with cylindrical shaped and r denotes the effective radius of the corresponding antenna, the following equation describes the lower band edge frequency.

$$f_{fe} = \frac{c}{\lambda_l} = \frac{7.2}{(H+R_{ef}+f_l)} \text{ GHz} \quad (3)$$

When compared to planar antennas with circular shaped monopole properties with the printed layout having a single sheet of dielectric on the antenna. In this, f_l denotes feed length in order to match with 50Ω input impedance. The dielectric substrate act as to increase the effective size of the antenna thus decrease in the lower band edge frequency.

In Figure 1. the proposed antenna geometry is displayed. Substrate with FR-4 epoxy has the following dimensions: $L_{sb} = 30$ mm, $W_{sb} = 35$ mm, $h = 1.6$ mm, $\epsilon_r = 4.4$ and a patch circular radius $R_2 = 8.5$ mm is put on the upper portion of the substrate in order to matched 50Ω CPW fed line. The length and width of the stripline are $f_1 = 18$ mm, $f_w = 1.6$ mm respectively. Optimised dimension of ground plane is $L_{gg} = 19.5$ mm and $W_{gg} = 11.4$ m for better bandwidth.

3. Result and Discussion

The ground plane dimensions are an important design consideration for monopole antennas due to the significant influence of gain, bandwidth, and radiation pattern on ground plane size. When simulations are run for different ground plane dimensions, the effects of the ground structure on the centre frequency are seen in Figure 2.

Table 1. Simulated result of return loss(S_{11}) on various ground dimension

Ground plane dimension	Operating Centre frequency(GHz)	$ S_{11} $ dB	-10dB Bandwidth(GHz)	Fractional Bandwidth(GHz)
$L_{gg}=15.9$ mm $W_{gg}=13.4$ mm	$f_{cen1}=7.4$ $f_{cen2}=15.4$	-25.30 -17.97	(5.1-12.9) (14.2-19)	86.6 28.9
$L_{gg}=15.9$ mm $W_{gg}=12.4$ mm	$f_{cen1}=6$ $f_{cen2}=16$	-27.69 -31.9	(5.2-12.8) (14.0-18.0)	84 25
$L_{gg}=15.9$ mm $W_{gg}=11.4$ mm	$f_{cen1}=6$ $f_{cen2}=16$	-41.86 -39.91	(5.2-13.6) (14.1-18.2)	89 25
$L_{gg}=15.9$ mm $W_{gg}=10.4$ mm	$f_{cen1}=6$ $f_{cen2}=17.4$	-41.58 -26.68	(5.3-13.5) (14.4-19.7)	87 29.5
$L_{gg}=15.9$ mm $W_{gg}=9.4$ mm	$f_{cen1}=6$ $f_{cen2}=15.8$	-21.97 -21.97	(5.4-13.4) (14.6-17.0)	85 15

As seen in Table 1, the conventional prototype proposed antenna has dimensions of $L_{gg} = 15.9$ mm, $W_{gg} = 13.4$ mm, an impedance bandwidth of 5.1 GHz to 12.9 GHz, and a fractional bandwidth of 86.6%, or more than 10 GHz, which satisfies the requirement of UWB on its first resonance frequency, $f_{cen1}=7.4$ GHz. However, it does not meet the requirements for UWB at its second resonance frequency. Bandwidth, return loss, and VSWR can all be enhanced by altering the ground plane's length and width.

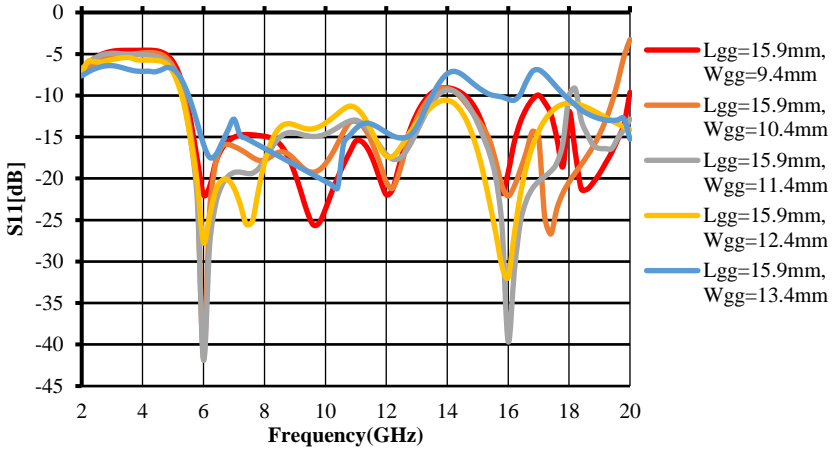


Figure 2. S_{11} [dB]vs Frequency response

According to Figure 3 and Table 1, the distance between the ground plane and the patch is a key factor in boosting bandwidth; the smaller the distance, the greater the bandwidth. Therefore, the optimal ground plane length is $L_{gg}=15.9$ mm, however decreasing the ground plane's width causes an increase in bandwidth and return loss. Further narrowing in breadth would result in inadequate bandwidth, hence the ground plane's width was tuned to be 11.4 mm. The conditions for UWB are met when $L_{gg}=15.9$ mm and $W_{gg}=11.4$ mm, which results in a bandwidth of 5.2GHz to 13.6GHz, return loss of -41.86dB, and fractional bandwidth of 89%.

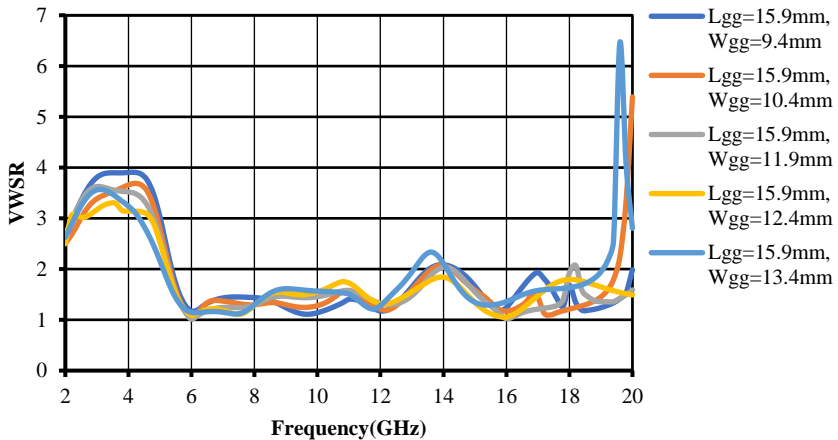


Figure 3. VSWR vs Frequency response

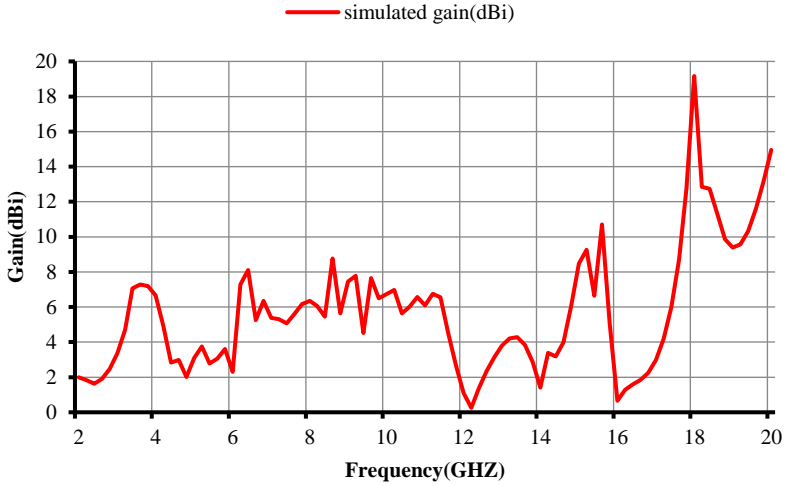


Figure 4. Gain(dBi) response of proposed antenna

The fluctuation of gain within the frequency ranges from 5 to 10 GHz is depicted in Figure 4. Additionally, it can be deduced that the suggested antenna achieves a maximum gain of 8.1 dBi at 6.4 GHz, first resonance frequency for the optimal ground plane dimension, and another significant gain of 8.77 dBi at 8.6 GHz, which is another resonance frequency for the next bandwidth. It is clearly seen that a good gain can be achieved with this modified ground plane.

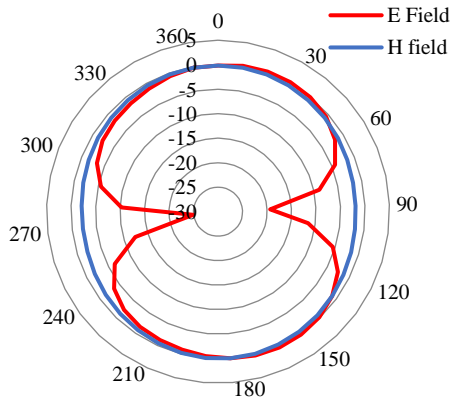


Figure 5. Radiation pattern of the proposed antenna

Figure 5. illustrates how the E-plane and H-plane radiation patterns of the suggested antenna behave, and it is obvious that it exhibits an omnidirectional pattern. It is reasonable to assume from this that it is transmitted uniformly in all directions by a printed monopole antenna.

Table 2. Comparison of performance for different proposed antenna

Ref	Dimensions (mm)	Bandwidth(GHz)	Gain(dBi)
[16]	60X56X1.6	1.3 to12	4 to7
[17]	50X50X1.575	2.6 to10.8	0.2 to 4
[18]	50X50X1.575	2.2 to11	0.2 to4
[19]	42X42X1.5	2.6 to10.6	2 to7
Proposed antenna	30X35X1.6	5.2 to12.8	4 to 8.77

Table 2. provides the literature of different proposed antenna, that cover the ultra wideband range. But in this proposed antenna, it focus on C and X band that is within the range from 4GHz to 12GHz. When compare to previous proposed antenna, the volume of the antenna is reduced as well as a better gain is obtained .

4. Conclusion

Proposed antenna provides impedance bandwidth greater than 10GHz, making it a good fit for C and X band applications. When the ground plane's size is reduced, the impedance bandwidth and return loss continue to grow. If the ground plane's size is still reduced, the bandwidth will eventually start to decline. The optimal ground plane dimension is the one at which the bandwidth is decreasing. Modified ground planes provide an efficient means of increasing bandwidth in comparison to standard prototype antennas. The electromagnetic and electric fields' radiation patterns closely resemble the dipole radiation patterns of the E and H planes. Regarding the gain response of the proposed antenna, it gives a gain of about 8dBi, which is better than the conventional prototype printed monopole antenna.

References

- [1] FCC Report and Order on Ultra Wideband Technology, Federal Commun. Commission, Washington, DC, USA, 2002.
- [2] Chinnagurusamy B, Perumalsamy M, Thankamony Sarasam AS. Design and fabrication of compact triangular multiband microstrip patch antenna for C- and X-band applications. *Int J Commun System* 2021.p.1-8.
- [3] Singh SJ, Kumar R, Dixit MM. Printed monopole antenna design with CPW fed for ultra wideband application. In *Journal of Physics: Conference Series 2022* (Vol. 2236, No. 1, p. 012010).
- [4] Balanis CA. *Antenna Theory: Analysis and Design*. 4th ed. New Jersey: John Wiley and Sons Wiley & Sons; 2016.
- [5] Mahendran K, Gayathri R, Sudarsan H. Design of multi band triangular microstrip patch antenna with triangular split ring resonator for S band, C band and X band applications. *Microprocess Microsystem*. 2020; 80:103400.
- [6] Kanagasabai M, Sambandam P, Mohammed GNA, et al. On the design of frequency reconfigurable tri-band miniaturized antenna for WBAN applications. *AEU-Int J Electron C*. 2020; 127:153450.
- [7] Desai A, Patel R, Upadhyaya T, Kaushal H, Dhasarathan V. Multi-band inverted E and U shaped compact antenna for digital broadcasting, wireless, and sub 6 GHz 5G applications. *AEU-Int J Electron C*. 2020; 123:153296.
- [8] Varshney G. Tunable terahertz dielectric resonator antenna. *Silicon*. 2021;13: p.1907-1915.
- [9] Gangwar AK, Alam MS. A miniaturized quad-band antenna with slotted patch for WiMAX/WLAN/WiMAX / WLAN/GSM applications. *AEU-Int J Electron C*. 2019.
- [10] Carver K, Mink J. Microstrip antenna technology. *IEEE Trans Antennas Propag*. 1981;29(1): p. 2-24.

- [11] Li Z, Zhu X, Yin C. CPW-fed ultra-wideband slot antenna with broadband dual circular polarization. *AEU-Int J Electron C*. 2019;98: p.191-198.
- [12] Kundu S. Experimental study of a printed ultra-wideband modified circular monopole antenna. *Microwave and Optical Technology Letters*. 2019 May;61(5): p.1388-1393
- [13] Elfergani IT, Rodriguez J, Otung I, Mshwat W, Abd-Alhameed RA. Slotted Printed Monopole UWB Antennas with Tuneable Rejection Bands for WLAN/WiMAX and X-Band Coexistence. *Radio Engineering* vol.27 no.3, p.694-702,2018,
- [14] Murugan NA, Balasubramanian R, Patnam HR. Printed planar monopole antenna design for ultra-wideband communications. *Radioelectronics and Communications Systems*. 2018 Jun;61(6): p.267-273.
- [15] Bakariya PS, Dwari S, Sarkar M. Triple band notch UWB printed monopole antenna with enhanced bandwidth. *AEU-International Journal of Electronics and Communications*. 2015 Jan 1;69(1): p.26-30.
- [16] Sharma, S. and Savita, M.K. Multi band circular antenna for ultrawideband wireless systems. In *2012 Nirma University international conference on engineering (NUiCONE)* (pp. 1-3) 2012.
- [17] Siddiqui, J.Y., Saha, C. and Antar, Y.M. Compact SRR loaded UWB circular monopole antenna with frequency notch characteristics. *IEEE Transactions on Antennas and Propagation*, 62(8), pp.4015-4020,2014.
- [18] Siddiqui, J.Y., Saha, C. and Antar, Y.M. Compact dual-SRR-loaded UWB monopole antenna with dual frequency and wideband notch characteristics. *IEEE antennas and wireless propagation letters*, 14, pp.100-103,2014.
- [19] Li, P., Liang, J. and Chen, X., 2006. Study of printed elliptical/circular slot antennas for ultrawideband applications. *IEEE Transactions on antennas and Propagation*, 54(6), pp.1670-1675,2006.

A Method for Power Amplifier Distortions Compensation at the RX Side for the 5G NR Communication Systems

Alexander MALTSEV^{a,1}, Alexander SHIKOV^b, Andrey PUDEEV^b, Seonwook KIM^c and Suckchel YANG^c

^a*Nizhny Novgorod State University, Nizhny Novgorod, Russia*

^b*LG Electronics Russia R&D Lab, Moscow, Russia*

^c*LG Electronics, Seoul, Korea*

Abstract. For the past years, the Internet of Things (IoT) supported by 5G technology, has been expanding rapidly across a wide range of services, enabling inter-object connectivity for the automotive industry, consumer electronics, transportation, logistics sectors, and manufacturing. With the increasing ubiquitous usage of various small-sized sensors, manufacturing cost of each element taken remains a critical aspect. Relatively low price of individual elements is the key for enabling tightly connected environment, but may severely affect RF chains quality as well as overall performance. With 5G expansion to the sub-THz bands, power amplifier nonlinearity may significantly limit system performance even in high-grade devices, due to power amplifier design limitations. Multiple studies were done to mitigate nonlinearity impact, both at the transmitter (TX) and receiver (RX) sides. Many solutions propose for evaluation and further compensation of the PA nonlinearity effects, via decision-directed feedback, training or even statistical processing of the received signal. However, with knowledge of the PA nonlinearity function at the receiver side, the processing may be simplified by the application of the reverse function to the equivalent signal in the time domain. In this paper we propose a method for PA nonlinear distortion compensation at the RX side, which can be adjusted for several signal waveforms adopted in 5G NR (New Radio) standard, such as CP-OFDM, DFT-S-OFDM, and others. The simulation results presented demonstrate performance improvement both for the sub-THz PA models and models for the 30-70 GHz band.

Keywords. 5G NR, OFDM, DFT-s-OFDM, mmWave, subTHz, power amplifier nonlinearity, PA models, PA pre-distortion

1. Introduction

Previous releases of the 5G New Radio (NR) standards Rel.15 and Rel.16 support carrier frequencies up to 52.6 GHz. Considering operations above 52.6 GHz in the next release of the 5G NR standard Rel.17, third generation partnership project (3GPP) radio access network (RAN) specification group already has investigated requirements for 52.6 GHz - 114.25 GHz [1] frequency band, with the main interest to first extend the current NR frequency range 2 (FR2) support to the frequency range 52.6 GHz - 71

¹ Corresponding author: Alexander Maltsev, e-mail: maltsev@rf.unn.ru. This work was partially supported by the Advanced School of Engineering of the Nizhny Novgorod State University.

GHz, with minimal changes to the system [2, 3]. Also, the possibilities of further expansion into the sub-THz band around 71-114 GHz have been considered. In this frequency band, despite recent technology advances in the PA design, they still demonstrate highly non-linear behavior for the typical allowed TX power [4]. Thus, PA distortions may become a significant performance limiting factor, especially for the highly efficient modulations like 64- and 256-QAM.

2. Problem and Previous Solutions

In the lower 5G NR frequency range 1 (FR1) below 6 GHz, and, partially, FR2, the effects of the PA can be neglected in most cases since the PA operation point may be safely placed in the linear region with minimal transmitted signal distortions. However, the problem of the PA nonlinearity distortion compensation may be very important for cheap transceivers with low-quality PA chains. It should be noted that the number of such devices can be very large, since cheap devices are a substantial part of Internet-of-Things (IoT) infrastructure. Therefore, this problem was addressed in a number of works [5-11], even for the lower bands.

In all these works, the Rapp model [12] of the power amplifier nonlinearity is widely used for description of the amplitude and phase distortions of the solid state power amplifiers (SSPA). In the 3GPP specification [1], the modified Rapp PA model, described by the equations shown in Eq. (1), was agreed as the baseline model in the 3GPP specification for simulations.

$$F_{AM-AM}(x) = \frac{Gx}{\left(1 + \left|\frac{Gx}{V_{sat}}\right|^{2p}\right)^{1/2p}}, F_{AM-PM}(x) = \frac{Ax^q}{\left(1 + \left(\frac{x}{B}\right)^q\right)}, \quad (1)$$

where $F_{AM-AM}(x)$, $F_{AM-PM}(x)$ are the amplitude-to-amplitude and amplitude-to-phase distortions, respectively, G is the small signal gain, p is the smoothness factor and V_{sat} is the saturation voltage. Coefficients A , B , q are phase distortion curve parameters.

Baseline characteristics of the typical power amplifiers in the 30-70 GHz bands were used to derive the PA model [13], viable in the corresponding bands. However, as it can be seen from the recent works [4, 14, 15], the sub-THz PA characteristics in 100-200 GHz bands are different. To evaluate the performance of the mobile communication systems in sub-THz, we have extracted parameters G , p , V_{sat} from the available experimental data [4, 14, 15] by fitting it with the Rapp AM-AM distortion model from Eq. (1). Then we derived a common PA model for 100-200 GHz bands by averaging these parameters. The $F_{AM-AM}(x)$ function for this sub-THz PA model and experimental curves from recent papers are presented in Figure 1. For comparison, the standard PA model used in the 30-70 GHz band is also shown in Figure 1. It can be seen that for the sub-THz PA model, the saturation voltage V_{sat} is about 3-4 dB less than for PA model used in the 30-70 GHz bands.

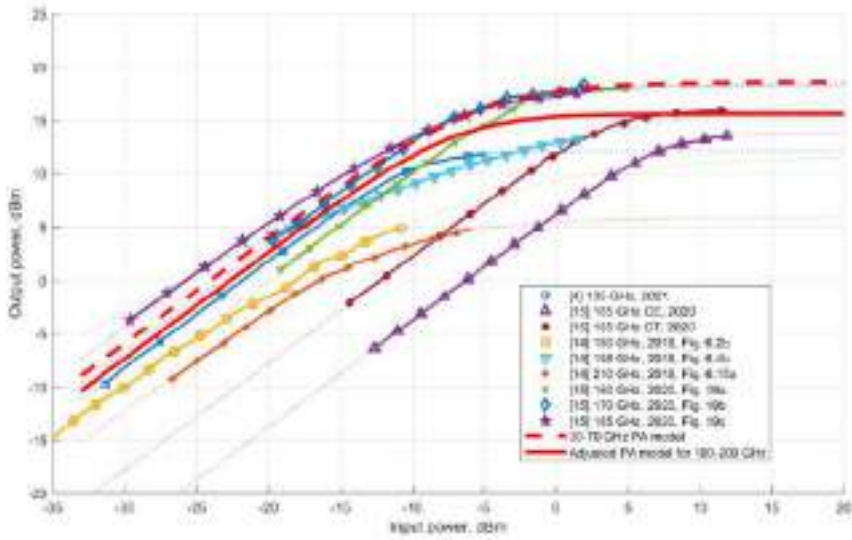


Figure 1. Comparison of SSPA characteristics based on the recent research papers. Dashed lines of the same color as the markers are curve fits of Rapp AM-AM distortion model in Eq. (1).

More detailed PA characteristics in sub-THz band (100-200 GHz), such as used technology, carrier frequency f_c , gain, bandwidth (BW), saturation power P_{sat} and power-added efficiency (PAE), available from literature and evaluated Rapp models parameters are presented in Table 1.

Table 1. Power amplifiers in sub-THz band (100-200GHz).

Parameters Source	Technology	f_c , GHz	Gain, dB	BW, GHz	P_{sat} , dBm	PAE, %	Rapp G	Rapp V_{sat}	Rapp p
[4]	28-nm CMOS	135	21.9	20	11.8	10.7	12.26	0.9	1.93
[14] Fig 6.2b	35-nm mHEMT	180	28	60	--	3.3	10.84	0.87	0.52
[14] Fig 6.4b	50-nm mHEMT	198	13.4	70	--	5	41.19	1.99	0.26
[14] Fig 6.15a	35 nm GaAs mHEMT	210	22.7	~100	--	6.4	7.89	0.44	0.9
[15] CT	130-nm SiGe BiCMOS CT	185	12.3	27	15.8	19.6	2.05	1.09	2.031
[15] CE	130-nm SiGe BiCMOS CE	185	6.3	27	13.5	20	4.08	1.41	1.91
[15] Fig. 19a	130-nm SiGe BiCMOS 3-stage CT	160	20.2	27	18.7	~3.9	9.88	1.81	2.75

[15] Fig. 19b	130-nm SiGe BiCMOS 3-stage CT	170	18.7	27	18.7	4.4	14.8	1.81	1.56
[15] Fig. 19c	130-nm SiGe BiCMOS 3-stage CT	185	25.9	27	18.7	3.5	19.29	1.86	0.87
100-200 GHz PA model	N/A	100-200	13.6	>20	15	3-20	13.59	1.35	1.41
30-70 GHz PA model	N/A	30-70	--	--	--	--	16	1.9	1.1

Figure 2 shows the effect of the PA nonlinearity impact on the different signal waveforms. It can be seen that for a single carrier (SC) system the effect is a straightforward amplitude distortion, which can easily be compensated. On the contrary, for OFDM symbols, PA nonlinearity causes inter-carrier interference (ICI), which is random and cannot be compensated easily at the RX side.

DFT spread OFDM (DFT-s-OFDM) modulation represents an intermediate case, where both deterministic and random components exist, and thus, compensation of the PA nonlinearity impact is visible. DFT-s-OFDM waveform generation practically matches that of the CP-OFDM waveform, with the key difference being an additional DFT operation prior to the subcarrier mapping and the main IFFT operation [16]. The additional DFT is usually referred to as transform precoding.

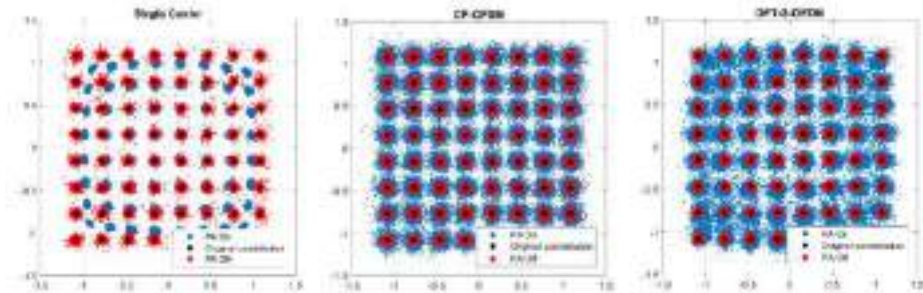


Figure 2. Examples of different constellation distortions on the receiver due to PA nonlinearity impact at the transmitter.

Two different approaches for PA nonlinearity mitigation have been proposed so far. The first is PA pre-distortion at the transmitter side, with preparation of the TX signals in such a way that minimizes PA nonlinearity negative effects. There are a number of such approaches, however they have a limited performance impact, and pre-distortion tends to have a poor performance at low input back-off (IBO) values [5-7]. Pre-distortion is also unavailable in small, low-cost devices like sensors, as it increases processing complexity and power consumption at the TX side.

Another way is the compensation of PA nonlinearity at the receiver. In paper [8], statistical processing of the received signals for the evaluation of the average PA distortion for further compensation was proposed. Works [5, 6, 9-11, 17, 18] considered a theoretical approach for PA nonlinearity compensation at the receiver side from a general point of view. In these papers a number of methods have been presented

for simple single carrier waveforms [5, 6, 9, 10], including hard-decision feedback, usage of the sequential Monte-Carlo method and inverse PA function. Several methods of the RX side nonlinearity compensation were considered for OFDM waveforms [11, 17, 18]. Therein, PA nonlinear distortion is represented as constant complex gain and a Gaussian noise component, with the main goal to obtain PA parameters (known or estimated with pilot signals) to compensate for the nonlinear distortion. In some papers [9-11] PA parameters are assumed to be known at the receiver to perform nonlinearity impact compensation. It is obvious that in cases when PA parameters need to be estimated, the system performance should be worse or at the same level.

3. Proposed RX-Side Compensation Approach

As it was shown for the SC modulations and, most importantly, in the DFT-s-OFDM case, the PA distortion has some deterministic component in addition to the ICI. With the knowledge of the TX PA nonlinearity function at the RX side, it is possible to compensate the deterministic component and thereby to improve the signal demodulation performance. This can be done by applying the RX processing, which is equivalent to the inverse function of the PA nonlinearity.

Generally, this function is not known at the receiver, not only because the PA characteristics are not known, but also due to the different TX power. The actual value of the TX power determines the working point of the PA and, thus, nonlinear distortions of the signal.

In several works, like [10, 11, 17], the decision-directed feedback is used for estimation of the power amplifier characteristics. Similarly, in [8] statistical processing is applied to adjust the demodulation algorithm to the received distorted signal. However, it is more effective to know the TX PA nonlinearity function and the working point for applying more precise inverse processing.

In this paper we present a receiver-side PA nonlinearity compensation method for the CP-OFDM and DFT-s-OFDM waveforms, based on usage of reverse signal processing, including an inverse PA distortion function. The communication system flow with PA compensation scheme (see Figure 3) consists of the basic TX processing at the transmitter side (1) that may include MIMO precoding and transform precoding (in the case of DFT-s-OFDM waveform), as well as standard OFDM IFFT block. The generated OFDM baseband signal is fed to one or more TX chains that may include CP insertion and frequency up conversion and finally come to the output power amplifiers (PAs) (2) operating at the carrier frequency. It should be noted, that for proper work of the proposed scheme, the signals on the different antennas should have the same amplitudes (but may have different phases). This limits the scheme's applicability to rank 1 (one data stream) transmission, even if several TX antennas are used. After propagating through the wireless channel, the signal comes to the RX chains (3) of one or more receive antennas for further baseline RX processing (4) that may consist of the FFT with maximum ratio combining (MRC), frequency domain (FD) equalization, and inverse transform precoding (in the case of DFT-s-OFDM waveform). Such processing effectively removes the impact of the frequency selective channel, and we may use this signal in the PA distortion compensation block (5). This block may consist of the IFFT operation (6) for returning the signal into the time domain (TD), the Inverse PA nonlinear function block (7) that actually performs the PA nonlinearity compensation, and an FFT block to return the compensated signal back to the FD. In

the case of DFT-s-OFDM modulation, additional transform precoding blocks (9) and (10) are used for proper signal processing.

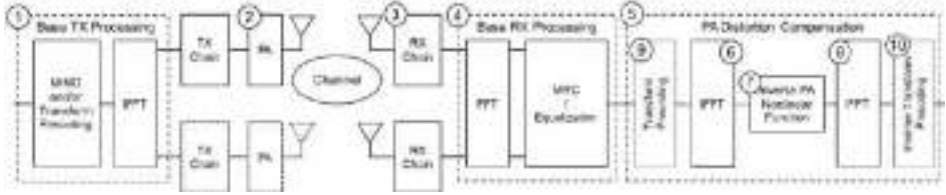


Figure 3. Schematic representation of the proposed receiver-side PA nonlinearity compensation scheme.

The inverse PA nonlinear function, which the signal is passed through inside of block (7), is obtained as an inverse of the Rapp AM-AM distortion in Eq. (1) with function value restrained, and is given in Eq. (2).

$$F^{-1}_{AM-AM}(x) = \begin{cases} \frac{x}{(1 - |x|^{2p})^{\frac{1}{2p}}}, & x < \alpha V_{sat} \\ \frac{\alpha V_{sat}}{(1 - |\alpha|^{2p})^{\frac{1}{2p}}}, & x \geq \alpha V_{sat} \end{cases}, \quad (2)$$

where F^{-1}_{AM-AM} is the inverse amplitude distortion function, α is a border-setting coefficient, which is required to prevent the function F^{-1}_{AM-AM} from reaching infinity at $x = V_{sat}$. The value of the coefficient α , used in the simulations, was $\alpha = 0.9$. It should be noted that it is important to constrain the inverse function with some ceiling, since allowing it to reach infinity may cause even more distortion to occur at the output of the compensation scheme.

4. Simulation Results

To prove the feasibility of the proposed approach for the receiver-side PA nonlinearity compensation method, link-layer simulations (LLS) were performed, comparing the proposed scheme with the cases of ideal PA and an uncompensated case for a given PA model. The PA model based on the parameters of the typical real power amplifiers in the 30-70 GHz band [13] was used, along with a newly developed PA model for the 100-200 GHz (see Table 1). Simulations were performed for different system parameters, such as subcarrier spacing (SCS), used waveform type, coding and modulation scheme, etc. The full list of LLS simulation parameters is summarized in Table 2. Simulation results, the block error rate (BLER) vs. signal-to-noise ratio (SNR), for the 30-70 GHz PA model are shown in Figures 4-6, and for the 100-200 GHz PA model in Figures 7-9.

To make an apple-to-apple system comparison, we have fixed the bandwidth (BW) to be 400 MHz. It leads to a change in the amount of resource blocks (RB) being used

in one slot in a simulation, depending on the SCS. The larger the SCS, the less RBs we can get for the given BW.

In the case of DFT-s-OFDM, transform precoding has been performed on the data-carrying subcarriers, which differs from the main IFFT. For example, if data is allocated into $N_{RB} = 64$ RBs, then the transform precoding DFT is performed on $N_{RB} \cdot 12 = 768$ subcarriers, whereas the main OFDM IFFT operation is performed on the closest power of 2 to the number of data subcarriers, in this case - 1024 subcarriers.

Table 2. System parameters and simulation assumptions.

Parameters	Assumption
Carrier Frequency	60 GHz / 180 GHz
Bandwidth	400 MHz
Waveform	CP-OFDM, CP-DFT-s-OFDM
PA Model & Parameters	30-70 GHz PA model [13], 100-200 GHz PA derived model
TX power	10 dBm
SCS	120 kHz / 480 kHz / 960 kHz
Resource blocks allocated	256 / 64 / 32 RBs
Channel Model	TDL-A, 5ns DS, 3 km/h (Doppler $f_D = 167$ Hz)
Transmission scheme	1x2 MRC
Modulation and coding	64-QAM, R=0.65 (MCS 22 Table 1) [19] 64-QAM, R=0.89 (MCS 27 Table 1) [19] 256-QAM, R=0.74 (MCS 22 Table 2) [19]
Impairments	Phase noise (BS and UE example 2 model, [20]), compensated with LS filter Channel estimation: LS fitting per precoding region (24 subcarriers)

4.1. Simulation Results for 30-70 GHz PA Model

Simulation results obtained for the 30-70 GHz PA model show that with the addition of the nonlinear PA, the performance decreases as expected. The use of the described algorithm improves the BLER metrics, compared with the uncompensated case for both CP-OFDM and DFT-s-OFDM waveforms.

For the SCS 960 kHz and 480 kHz (Figures 4, 5), the gain in performance can reach 3-5 dB on average. Since CP-OFDM has a greater PAPR value than that of DFT-s-OFDM, the performance drop from the PA nonlinearity for the CP-OFDM is much more noticeable compared to DFT-s-OFDM. Moreover, for considered impairments (PN + the PA nonlinearity) the 256-QAM modulation (MCS 22 T2) cannot be used for the CP-OFDM system at all.

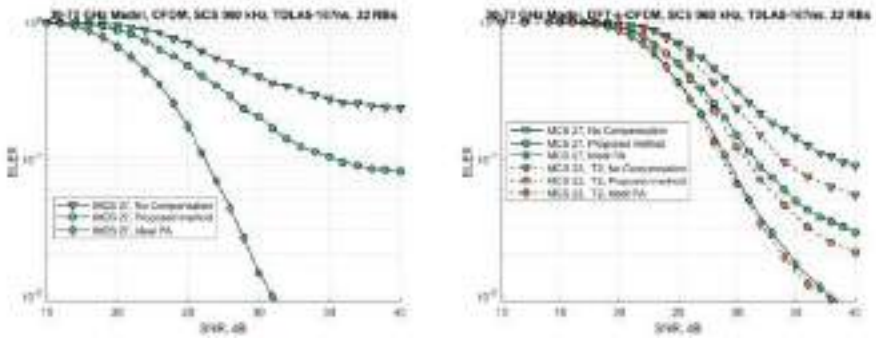


Figure 4. BLER for SCS 960 kHz, 64-QAM/256 QAM for OFDM (left) and DFT-s-OFDM (right).

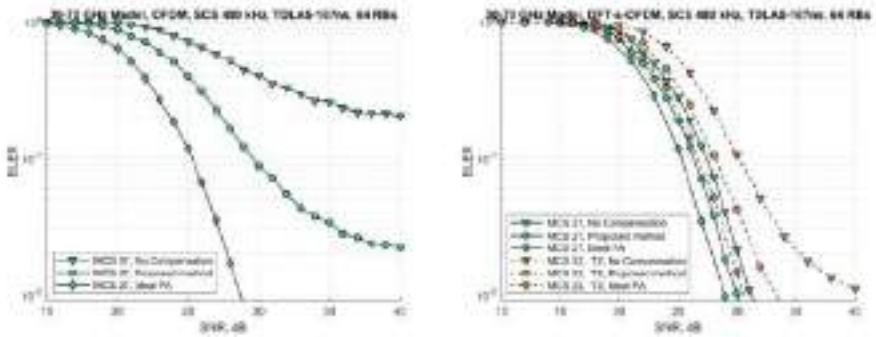


Figure 5. BLER for SCS 480 kHz, 64-QAM/256 QAM for OFDM (left) and DFT-s-OFDM (right).

As shown in [21], for the lower values of the SCS (15-120 kHz) the phase noise (PN) plays a dominant part in the system performance degradation due to the higher inter-carrier interference (ICI). That leads to a decrease of the PA nonlinearity impact on the whole system performance and, consequently, on the effectiveness of any PA nonlinearity compensation scheme. This effect is demonstrated in Figure 6 for both CP-OFDM and DFT-s-OFDM systems with SCS 120 kHz.

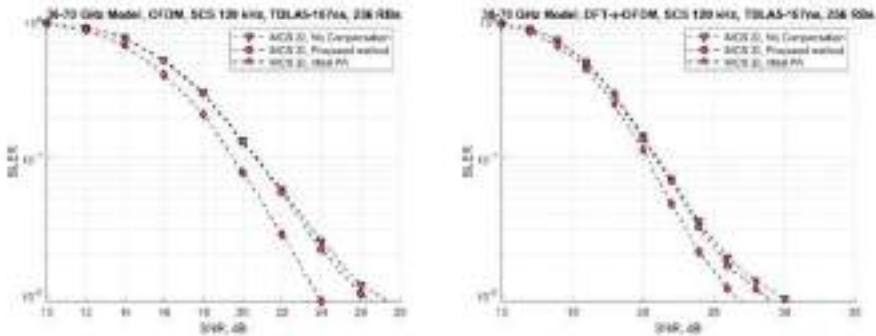


Figure 6. BLER for SCS 120 kHz, 64-QAM for OFDM (left) and DFT-s-OFDM (right).

4.2. Simulation Results for 100-200 GHz PA Model

For the derived 100-200 GHz PA model, the effects of the additional nonlinear distortion are even more pronounced (Figures 7-9). In this sub-THz band, most of the 256-QAM (MCS 22 Table 2) simulation results have ended up being unusable – the amount of errors in the data has reached a point, where the data is basically unrecoverable. Since the effect of the PA impairment has increased, the impact of the PN is now less dominant, which allows for the PA compensation schemes to be more effective.

For the CP-OFDM case, the increase of the PA nonlinearity effect allows for compensation to provide the desired performance gain for MCS 22 (Figure 7, left).

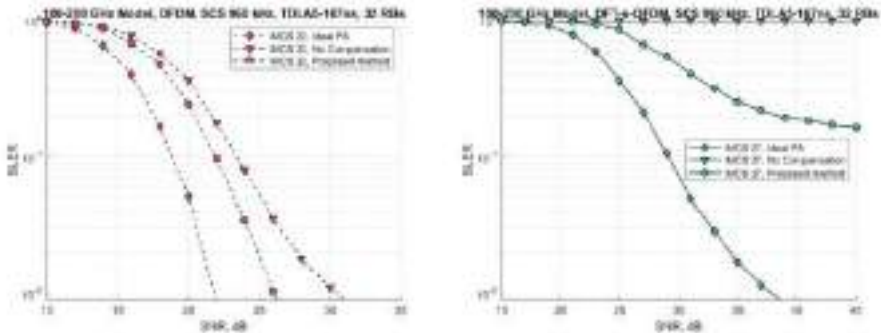


Figure 7. BLER for SCS 960 kHz, 64-QAM for OFDM (left) and DFT-s-OFDM (right).

For the DFT-s-OFDM with SCS 960 kHz (Figure 7, right), the PA nonlinearity has caused a significant decrease in performance to the point of data loss. The proposed compensation scheme has eliminated distortions in the received information and removed the BLER floor effect for MCS 27.

Figure 8 demonstrates similar system performances for the CP-OFDM and the DFT-s-OFDM cases for SCS 480 kHz.

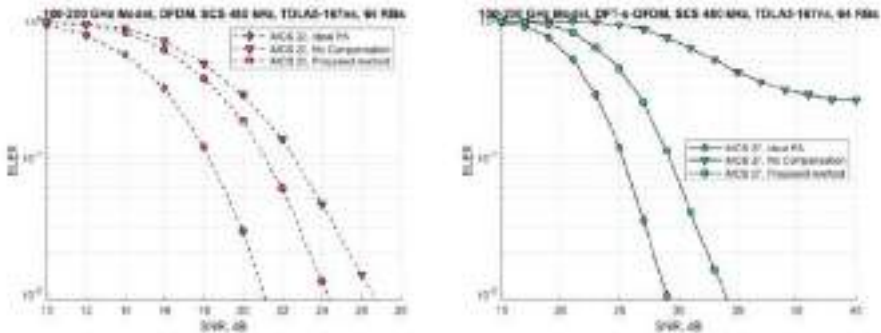


Figure 8. BLER for SCS 480 kHz, 64-QAM for OFDM (left) and DFT-s-OFDM (right).

For the CP-OFDM SCS 120 kHz (Figure 9, left), the effect of the PA nonlinearity is now more significant, and has a greater impact on the performance compared to the PN. This allows effective application of the proposed compensation scheme, since the system performance decrease is mostly related to the PA nonlinearity, and is slightly affected by the PN. DFT-s-OFDM is less affected by the PA nonlinearity due to low PAPR, and the PN is still the dominant impairment in that case (see Figure 9, right).

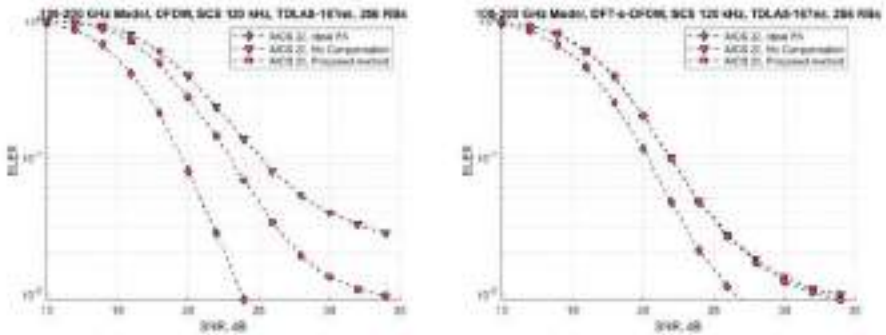


Figure 9. BLER for SCS 120 kHz, 64-QAM for OFDM (left) and DFT-s-OFDM (right).

4.3. Discussions

For the 30-70 GHz PA model analysis, the proposed PA nonlinearity compensation scheme demonstrates system improvement for the high modulations and coding schemes. For the SCS 960 kHz and 480 kHz, where the PN impact is non-dominant, the effect of the PA becomes the main system performance limiting factor and application of the proposed compensation scheme may provide several dB gain or even mitigate the BLER floor effect. For the SCS 120 kHz, the negative effect of the PN is dominant, and the use of any PA nonlinearity compensation scheme is not effective.

For the 100-200 GHz PA model, the impact of the PA nonlinearity increases considerably. Therefore, application of the proposed compensation scheme for 64-QAM modulation - MCS 22 and MCS 27 has shown a noticeable performance improvement compared with the uncompensated results. In several cases, the proposed compensation algorithm has even restored the data from being unusable and considerably improved the communication system performance. It should also be noted that in that case PN plays a less dominant role, allowing for efficient PA nonlinearity compensation at lower SCS values, like 120 kHz.

5. Conclusion

A method for compensation of the TX PA nonlinear distortion at the receiver side has been presented. The method at its core is based on the use of an inverse PA's distortion curve for compensation, it can be applied to different waveform types and can be adjusted for the task at hand. The method has been implemented and tested in a fully-fledged 5G NR link-level simulator for performance evaluation. Performance has been measured for the existing 30-70 GHz PA model, as well as a newly developed 100-200 GHz PA model, based on available recent research results. In both cases, the proposed method has shown the ability to significantly improve system performance in various scenarios (waveform, QAM constellation, PA model). As the method relies on the receiver-side compensation, this approach can be useful for communication systems with a large number of low-cost devices which use energy-efficient simple transmitters (e.g. in IoT case). This would allow the transmitter power consumption to be reduced

since there is no need to apply any kind of preprocessing for PA's nonlinearity compensation at the TX side.

References

- [1] 3GPP. Study on NR beyond 52.6 GHz. 3rd Generation Partnership Project (3GPP); 2019. 38.807. Version 1.0.0.
- [2] Intel Corporation. New SID: Study on supporting NR from 52.6GHz to 71 GHz. 3rd Generation Partnership Project (3GPP); 2019. RP-193259. TSG RAN Meeting №86.
- [3] Qualcomm. New WID on extending current NR operation to 71 GHz. 3rd Generation Partnership Project (3GPP); 2019. RP-193229. TSG RAN Meeting №86.
- [4] Zhang J, Wu T, Nie L, Ma S, Chen Y, Ren J. A 120–150 GHz Power Amplifier in 28-nm CMOS Achieving 21.9-dB Gain and 11.8-dBm P_{sat} for Sub-THz Imaging System. *IEEE Access*. 2021; 9: 74752-62.
- [5] Sharath M. Analysis and Compensation of Power Amplifier Distortions in Wireless Communication Systems [Ph.D. thesis]; 2015. Electronic Thesis and Dissertation Repository.
- [6] Shabany M, Gulak PG. Efficient Compensation of the Nonlinearity of Solid-State Power Amplifiers Using Adaptive Sequential Monte Carlo Methods. *IEEE Transactions on Circuits and Systems I: Regular Papers*. 2008; 55(10):3270-83.
- [7] Eda T, Ito T, Ohmori H, Sano A. Adaptive Compensation of Nonlinearity in High Power Amplifier by Support Vector Machine. *IFAC Proceedings Volumes*. 2001; 34(14):243-8. *IFAC Workshop on Adaptation and Learning in Control and Signal Processing (ALCOSP 2001)*, Cernobbio-Como, Italy, 29-31 August 2001.
- [8] Ermolaev GA, Bolkhovskaya OV, Maltsev AA. Advanced Approach for TX Impairments Compensation Based on Signal Statistical Analysis at the RX Side. In: 2021 Wave Electronics and its Application in Information and Telecommunication Systems (WECONF); 2021. p. 1-5.
- [9] Bhat S, Chockalingam A. Compensation of power amplifier nonlinear distortion in spatial modulation systems. In: 2016 IEEE 17th International Workshop on Signal Processing Advances in Wireless Communications (SPAWC); 2016. p. 1-6.
- [10] Qi J, Aissa S. Analysis and Compensation of Power Amplifier Nonlinearity in MIMO Transmit Diversity Systems. *IEEE Transactions on Vehicular Technology*. 2010; 59(6):2921-31.
- [11] Gregorio F, Werner S, Laakso TI, Cousseau J. Receiver Cancellation Technique for Nonlinear Power Amplifier Distortion in SDMA-OFDM Systems. *IEEE Transactions on Vehicular Technology*. 2007;56(5):2499-516.
- [12] Rapp C. Effects of HPA-nonlinearity on 4-DPSK/OFDM-signal for a digital sound broadcasting system; 1991. p. 179-184.
- [13] Nokia. Realistic power amplifier model for the New Radio evaluation. 3rd Generation Partnership Project (3GPP); 2016. R4-163314. TSG-RAN WG4 Meeting №79.
- [14] Amado Rey AB. Analysis, design, and experimental evaluation of sub-THz power amplifiers based on GaAs metamorphic HEMT technology [Ph.D. thesis]; 2018.
- [15] Ali A, Yun J, Giannini F, Ng HJ, Kissinger D, Colantonio P. 168-195 GHz Power Amplifier With Output Power Larger Than 18 dBm in BiCMOS Technology. *IEEE Access*. 2020; 8:79299-309.
- [16] Chen X, Cui J, Ni W, Wang X, Zhu Y, Zhang J, et al. DFT-s-OFDM: Enabling Flexibility in Frequency Selectivity and Multiuser Diversity for 5G. *IEEE Consumer Electronics Magazine*. 2020;9(6):15-22.
- [17] Bouhadda H, Zayani R, Shaiek H, Roviras D, Bouallegue R. Receiver Technique for Detection and Correction of Nonlinear High Power Amplifier Distortion Errors in OFDM Systems. In: 2015 IEEE 81st Vehicular Technology Conference (VTC Spring); 2015. p. 1-5.
- [18] Drotar P, Gazda J, Deumal M, Galajda P, Kocur D. Receiver based compensation of nonlinear distortion in MIMO-OFDM. In: 2010 IEEE International Microwave Workshop Series on RF Frontends for Software Defined and Cognitive Radio Solutions (IMWS); 2010. p. 1-4.
- [19] 3GPP. Physical layer procedures for data. 3rd Generation Partnership Project (3GPP); 2020. 38.214. Version 16.2.0.
- [20] 3GPP. Study on new radio access technology: Radio Frequency (RF) and co-existence aspects. 3rd Generation Partnership Project (3GPP); 2017. 38.803. Version 14.2.0.
- [21] Maltsev A, Pudev A, Kim S, Yang S, Choi S, Myung S. Phase Tracking Sequences for 5G NR in 52.6-71 GHz Band: Design and Analysis. *Proceedings of CECNet 2021*. 2021.

Intelligent Patrol Route Visualization Design Based on Police Big Data

Weiyang HAO¹, Deming GUO, Qi ZHOU and Xinyi SHA

School of information technology, Nanjing Forest Police College, Nanjing 210023, China

Abstract. In recent years, the public security department has insisted on technology to promote the high-quality development of public security work in the new era. It not only builds a three-dimensional patrol and defence system, but improve the level of patrol, defence and control management vigorously. At present, an intelligence-aided patrol system has been initially formed, and video patrols and law enforcement duty supervision have been carried out. However, the application of new technologies and the innovation of policing mechanisms in public security departments still have some problems. For example, unbalanced regional development, insufficient deepening of intelligent applications and insufficient systematization of applications, which greatly restrict the effectiveness of public security patrol and defence in practice. Based on this, our study identifies the crime hotspots in the city through EXCEL data analysis, and identifies them as patrol points. By applying the shortest route algorithm in the genetic algorithm, a precise patrol route is formed. Based on this, the precise patrol route is displayed on a map using a visualization tool and then fed back to the police terminal equipment. This project enables police patrols to be more accurate and patrol routes to be optimized. It improves the police patrol system and provides the basis for the construction of an intelligent patrol system.

Keywords. Patrol routes, planning research, data analysis, genetic algorithm

1. Introduction

1.1. Difficulty of patrolling the grassroots

The purpose of patrols is unclear because intelligence information cannot guide precise strikes and prevention and control. And the scale effect of intelligence information cannot be reflected in patrol work[1]. There're defects in the service operation mode on the grounds of insufficient police force. The current patrol work service mode is generally based on the patrol police as the main body to dynamically control the society.

1.2. Patrol plan is not scientific enough

Our country's current patrol methods are difficult to achieve "all-round" control. At present, among the 1.4 million police in our country, only 60,000 are engaged in street patrols, resulting in a low coverage rate of patrol police and weakening the ability to

¹ Corresponding author: Weiyang HAO, School of information technology, Nanjing Forest Police College, Nanjing 210023, China; E-mail:1105676420@qq.com.

control the society. As is to say, there are loopholes in the patrol scope [2]. This led to the emergence of a patrol vacuum, resulting in more crimes in some areas and out-of-control management [3,4].

1.3. Lack of effective dynamic patrol command system

The patrol command system is an indispensable part of the patrol system, and its modernization level determines the quality of the police patrol. However, so far, the command system of police patrol in our country has unbalanced regional development. And it is difficult to achieve real dynamic patrol command [5]. There are relatively mature patrol mechanisms in developed areas in our country, but in relatively backward areas, the construction of the command system is far behind. The 110 alarm podium is only limited to the issuance of 110 police orders, and does not have the overall command function of police patrols.

2. Accurate patrol route planning research

In this practice, our idea is to use dormant police data, with the help of big data technology, to build intelligent patrol automatic planning model. Through analyzing the public security crime data such as alarm address, crime data, personnel density data, monitoring data, special industry data, etc., data analysis and visualization of massive data, we plan to find high-crime area or key areas under public security control. When combining sensitive time data, weather data and other impacts on patrol routes, we can achieve prediction of the high incidence of preventable cases [6,7]. Also, we plan to remodel a new generation of accurate patrol and inventory mechanism to further improve the social security prevention and control system. Combining our existing police data sources and the actual situation, we try to use K-means clustering algorithm and heuristic genetic algorithm to achieve our goal of automatic patrol route plan, and use the online map api interface provided by the National Platform for Common Geospatial Information Services to display. As shown in Figure 1.



Fig. 1. Technical route

2.1. Data source

The source of data for this practice is the police data of a branch of Nanjing Public Security Bureau, with a total of 26,409 entries. Each police data contains a large amount of effective data information, such as "identity information, cell phone number, license plate, related person, account number, network communication tool, identity mark, address, etc[8]. After conversion, it can be obtained that only one branch of Nanjing

Public Security Bureau dynamically collects millions of pieces of fresh data and information every year by receiving and handling police affairs, which realizes "data is being collected every second". And these data have obvious advantages: the largest amount of Public Security data volume, the highest speed of updating, the widest source, the richest content, and the most vivid information. However, due to the confidentiality of data, the data used in this practice are desensitized data.

2.2. Clustering algorithm

After obtaining the population density, weather conditions and other related information, due to the wide distribution, the map has a larger area and may contain more locations, which is not conducive to the public security patrol work. The purpose of K-means algorithm is to solve the problem of scattered patrol locations and multiple locations. After the calculation and clustering of K-means algorithm, it can better fit the more aggregated points as the key areas of patrol, and its algorithm ensures the distance from the clustered points to other hot spots, which can ensure that more areas are taken into account when patrolling. It improves the efficiency of police handling and guarantees the effective implementation of public security work.

2.2.1 Data pre-processing

- Data deduplication

In the alarm situation, there are some cases that are duplicate, and the table shows that it is a duplicate alarm list. And these duplicate alarms are invalid for our analysis, so some duplicate alarms in the table are deduplicated.

- Information filtering

There is a part of the data that is incomplete, which is not meaningful for analysis. Also, there is a part of the data that has an unclear or non-existent address on the map, which also needs to be manually eliminated. After eliminating these data, the data that can be used is left.

- Coordinate conversion

Most of the data we get are Chinese addresses, which cannot be used directly. We need to convert the Chinese addresses into latitude and longitude coordinate points under the WGS84 coordinate system, and we use `arcg` is geocoding to decode the Chinese addresses to get a relatively accurate latitude and longitude data.

2.2.2 Application in the project

After processing the data into standard latitude and longitude coordinates, you can use the K-means algorithm to process them. Firstly, import the latitude and longitude coordinates. Secondly, convert them into the numpy array format that can be used in the algorithm to facilitate the import function for calculation. Thirdly, adjust the number of clustering points that need to be output and specify the location of the clustering points as points on the road in order to facilitate the map generation at a later stage and ensure the routes can be accurately mapped to the road surface. Then, we can ensure the accuracy of the patrol route. Then use the function in `sklearn` to get the labels of the clusters, get the clustering centers obtained by K-means algorithm, combine them with

the labels, write them to the csv file together, and finally save them to the csv file according to the vehicle id.

K-means clustering selects multiple locations as objects after calculation. Then compare the distances to all valid data points. According to the distance, it can be determined to be classified as which kind of position. Then we use machine to learn the algorithm. After many iterations, the calculation will be more and more appropriate, until the completion of clustering analysis.

2.3. Optimal route implementation based on heuristic genetic algorithm

After determining the patrol points in the area, the next step is to plan the optimal patrol routes. According to previous studies, police car patrols and foot patrols have a positive impact on the social control of security problems. By using foot patrols or police car patrols, a better quality route can be selected for a specific area to ensure a further reduction in crime incidents based on resource conservation. Both types of patrols have their own advantages in terms of patrolling methods, with foot patrols being able to effectively view all blind angles and police car patrols being able to patrol a wide area as long as they are carried out. In order to further use advanced technologies such as communication and information to take targeted initiatives to combat and prevent and control areas with a high incidence of incidents, this study focuses on how to develop a quality route in the police car patrol mode.

2.3.1 Application process

Step 1: Genetic encoding and initialization of the population. We use 1~n integers to encode the input n addresses one by one. An address is a gene, and a chromosome contains all the genes, which is a patrol route. The length of the chromosome is the number of addresses. The initialization of the population is also performed, and our program uses the method of randomly disrupting the genome arrangement to generate different chromosomes each time to initialize the population.

Step 2: Fitness function. Since populations need to evolve iteratively, we need to define a rule to evaluate which populations can survive in the current environment by scoring which routes require the shortest distance. Those with too long a distance will be eliminated, and we will call this rule the fitness function. We can design the fitness function for this project as: use the reciprocal of the total distance walked on a patrol route, to achieve the conversion between the maximum and minimum values. The smaller the value of the objective function, the greater the value of the fitness function. The stronger the adaptation, the better the individual, and vice versa the worse the individual.

Step 3: Selection of elite populations. After the previous step, we get the fitness function of each route, and we need to save the route with short distance, as is to say, let the elite population survive as long as possible. The probability that the population is selected to be defined as an elite population is proportional to its fitness, i.e., the higher the fitness of a patrol route, the higher the probability that the route will be selected as an elite chromosome. For the probabilistic approach to selecting elite populations, we use the optimal individual preservation strategy and the roulette wheel selection.

Step 4: Crossover, mutation and reversal of chromosomes. In genetic algorithms, the crossover operation involves swapping two random chromosomes for certain genes to produce two new combinations of genes, resulting in two new individuals. The pairing is based on the crossover probability, except for the first directly copied optimal chromosome. Two points were randomly selected to swap between the two calculated

patrol routes, that is the two patrol routes underwent crossover operations. However, we find that after swapping the route segments, the patrol points of the patrol routes are duplicated. For this reason, we need to solve this route conflict problem. And our method is to swap the punch points of the two patrol routes one by one, which can resolve the conflict to produce a new pair of chromosomes. And the new chromosome is a new patrol route. The above operation provides a new possibility to find the global optimal solution.

Variation of chromosomes. A mutation operation is a random selection of individuals in the population at mutated positions, where some individuals in that gene string are changed and one part of the chromosome changes accordingly, and the other part changes accordingly to ensure diversity and algorithmic convergence in the population. Our mutation operation occurs at two patrol points along a patrol route. The mutation of chromosomes makes the genes of chromosomes more stochastic, offering the possibility of jumping out of the local optimum solution.

Chromosome reversal operations. Reversal operations occur on a segment of a gene from a single chromosome. Two random sections of a patrol route are reversed and the fitness scores of the old and new patrol routes are compared. If the fitness score of the new route after reversal is greater than that of the old route, the reversal makes sense. If the new route has a smaller fitness score than the old route, then the reversal is not meaningful. After chromosome reversal, the reversed chromosome becomes superior and accelerates the quality of population evolution.

Step 5: Output the best patrol route.

2.4. Road matching and map visualization

This project realizes the mapping of genetic algorithm on roads by using python third-party tool library and relevant principles of gis to obtain the rasterized road network data of the desired area us. And this project uses the global common coordinate system WGS84, with an error of less than one meter. This is achieved so that our public security system can patrol using existing police cars, which cost little, and is fast and convenient.

We've got an approximate patrol route in the above process. We split the existing road network data according to the traffic intersection (road intersection) split. After that, we store each road's fold coordinate string according to the path ID, and use linear equations to calculate the diagonal intersection of these four points. Based on the intersection point split road network vector line, we record the intersection point connected to the road id in the point set. Then we can get the subdivided road data. Finally, the spatial index is established, realizing road matching. As shown in Figure2.

After implementing road matching, we use the folium open source library to add the base map and combine it with the rest of the data visualization to generate an interactive HTML file.

We use multidimensional data to construct three-dimensional patrol routes, and different patrol routes are planned for different time periods, as shown in Figure 3.

Our project can change different base maps for presenting data according to the actual work, as shown in Figure 4.



Fig. 2. Roadmap

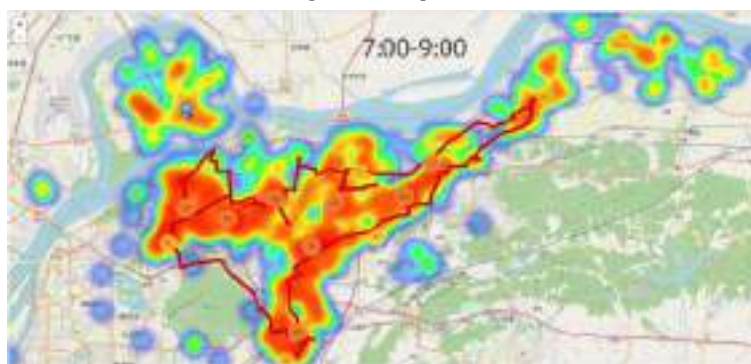


Fig. 3. Time dynamic chart



Fig. 4 Image marker map, topographic map, satellite

For a medium-large sized city, diversified patrol methods are essential. Therefore, we can choose three patrol methods in route generation, including foot patrol, vehicle patrol and riding patrol, which correspond to the most common public security patrol methods at present, making the public security patrol mechanism more perfect and scientific. As shown in Figure 5.



Fig.(a)



Fig.(b)

Fig. 5. Car patrol route and step patrol route design

The project all uses open source database, including map data, road data and so on. And the use of .csv files within the program to facilitate the police departments will be data access. Open source database can further reduce costs and save money. At the same time, when used in multiple police stations, you can string data to make patrol road routes to achieve full coverage and further accelerate the road of science and technology for the police.

2.5. Future prospects

Our model has advanced algorithmic ideas. With the in-depth promotion of "Internet+" action plan, the model follows the development trend of the times and responds to the call of General Secretary Xi Jinping "to take big data as a big engine to promote the innovation and development of public security work and to cultivate new growth points for combat force generation". And in response to the advancement of the social wave, developers have improved and optimized it by using data analysis and genetic algorithm, which has become a successful application recognized by the professional field in terms of big data technology being close to police combat. Our model design is close to a real application. The purpose of the model is to deepen the application of "data policing" in actual combat, to give full play to the subjective initiative of street patrol police, to make the information "move" and to make the data "live", and to strengthen the insight of public security organs. It strengthens the ability of public security organs to see and grasp the development of social security, and increases the efforts to combat illegal crimes. Our model is a social service application. Through the application of the intelligent patrol model, we can reduce the loss of human and material resources in the process of public security patrol and defense. The model realizes the reform of patrol mechanism through big data analysis. It reshapes the patrol system with clear responsibilities, smooth operation, integration of combat and defense, and high efficiency in combat. What's more, it improves the mode of "supervising and patrolling docking, police street, and moving preparation", further weaving the social security prevention and control system.

3. Concluding remarks

This paper designs a system that can be used to intelligently plan the optimal route for patrolling, based on Python basic data analysis, genetic algorithms and other technologies. It responds to the new requirements of economic and social development

for public security patrol work and effectively solves the traditional crude model of simply increasing the police force. Furthermore, it weaves an all-time, all-coverage "prevention and control network", helping to improve dynamic patrol capacity, instantly grasp the crime scene. It is also conducive to improving the dynamic patrol capability, grasping first-hand information on crime scenes, and taking immediate and effective targeted measures when encountering unexpected situations. Also, it is of benefit to comprehensively sort out and rectify urban patrol points, realize the technology of the police force, enhance the combat effectiveness and overall efficiency of the public security department, and achieve the goal of promoting the police with technology. It is more likely to gain more public recognition. Intelligent patrol routes are in line with the new requirements of economic society for public security work, but this work is still in the exploration stage. As long as we continue to improve and develop this new police patrol mechanism, we will be able to achieve the goal of promoting the police with technology.

Acknowledgements

This research was support by the 2022 College Students Innovation and Entrepreneurship Training Program (Grant No. 202212213014Z).

This research was support by the 2021 College Students Innovation and Entrepreneurship Training Program (Grant No. 202112213023Z).

References

- [1] Hongjie YE. Research on the basic work of grid-based professional patrol service [J]. Journal of Beijing People's Police Academy,2007(02):50-53.DOI:10.16478/j.cnki.jbjpc.2007.02.013.
- [2] Meicai ZHOU. "Stop-and-go" patrol to enhance the effectiveness of three-dimensional prevention and control [J]. Modern World Police, 2017(07):86-87.
- [3] Ying LIU, Xinglin XIE, Liping CHENG. Construction of police patrol path planning model in the context of big data[J]. Journal of the Chinese Academy of Criminal Police,2020(03):101-107.DOI:10.14060/j.issn.2095-7939.2020.03.014.
- [4] Shandong: Improving the Level of Rural Road Law Enforcement Management by Means of Science and Technology [J]. Automotive and Safety,2020(02):21-24
- [5] Liyi LIU. Research on optimizing countermeasures of urban and rural social security prevention and control system in Zhoushan City[D]. Zhejiang Ocean University, 2020. DOI:10.27747/d.cnki.gzjhy.2020.000068.
- [6] Guangyin GAO,Honggen CAO,Yang SHEN. Research on the application of neural network in patrol police prediction[J]. Computer and Digital Engineering,2020,48(06):1409-1412.
- [7] Haibo TAN. Research on social security prevention and control management in Guang'an City under the background of big data [D]. Sichuan Normal University, 2020. doi:10.27347/d.cnki.gssdu.2020.000998.
- [8] Jiancai LI. Development strategies of intelligent public security in the context of big data [J]. Electronic Technology and Software Engineering,2019(08):157.

Advantage Analysis of MBSE in the Context of Multi-Historical Development Trends

Yuqiang GUO, Shiyan SHE, Jun ZHAO and Junxian GUO¹

China Helicopter Research and Development Institute, Tianjin 300308, China

Abstract. Since INCOSE first proposed the Model-based System Engineering (MBSE) road map in 2007, the concept of MBSE has been well known, but the application results of MBSE in many companies have not been satisfactory. The implementation of MBSE is a considerable investment, including learning the top-level MBSE processes and the three pillars of MBSE, including the language, tool and methodology. The lack of understanding of MBSE's advantages makes it difficult for many complex equipment development enterprises to invest enormous time and economic costs to implement MBSE. In this paper, the advantages of MBSE are discussed in three developing trends, including written ideograms, human-machine communication language and human thinking. This is the first time to discuss the progressiveness of MBSE from these different views, which can help enterprises dispel the concerns about MBSE implementation and strengthen their confidence in MBSE's full implementation.

Keywords. MBSE, advantage, trend

1. Introduction

INCOSE released the MBSE roadmap (see Figure 1) and its aim was to build a distributed and secure model repository crossing multiple domains in 2020 [1]. But standing at the point of 2022, a large number of enterprises are still stuck in the document-based system engineering approach and have not completed the conversion to model-based system engineering.

¹ Corresponding author: Junxian Guo, General Management Department, China Helicopter Research and Development Institute, Tianjin 300308, China; E-mail: guojx@avic.com.

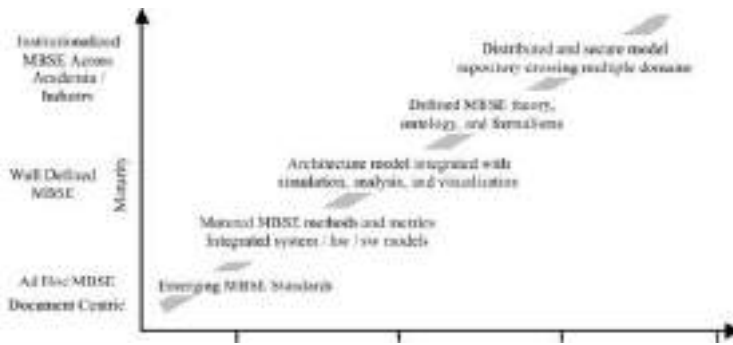


Figure 1. INCOSE MBSE roadmap

Implementing model-based systems engineering requires a breakthrough from learning the top-level system engineering processes described in the INCOSE SE handbook and mastering the three pillars of MBSE (see Figure 2), including the system modeling language, tool, and methodology, which involves a lot of time to learn and practice [2,3].



Figure 2. Three pillars of MBSE

Lack of understanding of the advantage of MBSE makes it difficult for companies to invest such a considerable amount of time and economic costs to carry out the implementation of MBSE. For this reason, this article systematically explores the advantages of MBSE from the perspective of the development trends of human written ideograms, computer programming languages and the way humans think. The second part of the article discusses the development trend of human writing and explores the SysML modelling language as an advanced language. The third part discusses the development of human-computer interaction language, i.e., computer programming language. It discusses that SysML is an object-oriented graphical modelling language with the potential for model-driven design and coding. The fourth part discusses the way humans think and figure out that MBSE is the application of modern complex systems thinking, based on recent computer and information technology, which uses multiple model views to build, check and manage system elements and the complexity between them. In the end, the article concludes with a summary.

This is the first time to discuss the progressiveness of MBSE from these different views and it can help enterprises dispel the concerns about MBSE implementation and strengthen their confidence in MBSE's full implementation.

2. The advantage analysis of MBSE from the view of human written ideograms development trend

SysML is the modeling language of MBSE. It is a graphical language to record and show model information [4,5]. We can analyse the progressiveness of SysML from the view of human written ideograms development trend.

As a carrier of human knowledge, the first stage of human writing evolved from narrative pictures. The first stage of writing was pictographs, as shown in Figure 3. Whether Chinese oracle, ancient Egyptian hieroglyphs, Naxi Dongba Pictographs or early Mesopotamian cuneiform writing belong to this category. This writing stage is clear, simple and easy to read and is a common form of the early development of writing.



Figure 3. Pictograms

The advantage of pictograms is that they are easy to read, but the disadvantage is that they are complicated to write and limited to express. It can describe only what can be seen visually, but it can't do anything for the definition of action and abstract concepts. For this reason, people used the ideographic method and simplified abstraction to express a wider range of concepts in the form of abstract symbols (see Figure 4). Nowadays, except for a part of Chinese characters that still retain the characteristics of pictographs, all other scripts in the world belong to the category of abstract hands. The technical specifications is mainly described by text in the traditional document-based system engineering.



Figure 4. Abstract text

In the next stage, to express the relationship between multiple elements, people began to use tables to classify and organize text information, forming a systematic text matrix so that the expression of information is more organized, readable and retrievable, as shown in Figure 5. Microsoft Word tables, Excel, and computer database technology are all based on the term of tables. In the systems engineering processes, requirements matrices, requirements management databases, N2 diagrams, and requirements traceability matrices are tabular.

First Name	Last Name	Department	Supervisor
Fareed	Awad	Marketing	Jane Doe, Vice-President
Adam	Doe	Custodial	Donna Martin, C.E.O.
Jane	Doe	Executive	Donna Martin, C.E.O.
Donna	Martin	Executive	None
John	Smith	Marketing	Jane Doe, Vice-President

Figure 5. Using table technology to organize and store textual information

Given the ambiguity and duality of words, textual descriptions cannot meet the needs of engineering communication exchange, so people began to use logic diagrams to express ideas, such as structure diagrams and flow charts (see Figure 6).

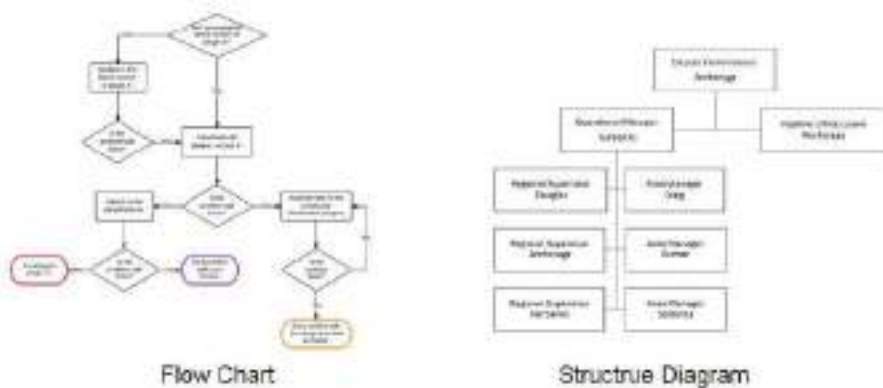


Figure 6. Logic diagram

MBSE uses graphical representations (both tabular and textual) to input and output information (see Figure 7), a formal logical description of the model, which can be read by a computer and transferred on the Internet based on a uniform format. It is an advanced form of ideogram development.



Figure 7. MBSE formal logic diagram

Combined with the above analysis, the development trend of human written ideograms can be shown in Figure 8.



Figure 8. The development trend of written ideograms

3. The advantage analysis of MBSE from the view of human-machine interaction language development trend

In the advanced application of MBSE, SysML model can be transmitted into coding directly [6]. SysML can be read by computer and is also a programming language. In the second part, we can analyse the progressiveness of SysML from the view of human-machine interaction language development trend.

As the language of human-machine interaction, computer programming languages have likewise undergone several developments. When computers were born, people used binary perforated cards to program computer operations, which was the most primitive form of programming, as shown in Figure 9.



Figure 9. Early perforated card binary programming method

To facilitate communication between people and machines, the assembly language was born as a text-based programming language (see Figure 10), and computer programming began to enter the era of programming languages [7]. Assembly language can be compiled into binary code by a compiler and executed with high efficiency.

```
data segment
string db 'dep(1),dep, dep, 1'
data ends

code segment
assume cs:code, ds:data
begin:mov ax,data
mov dx,ax
mov ah,ah
int 2h
lea dx,string
mov cx,09h
int 2h
mov ah,ah
int 2h
code ends
end begin
```

Figure 10. Text-based programming language

Although assembly language is more efficient in code execution, they are poorly readable and not easy to study and master. A process-oriented programming language, such as C, was invented to solve this problem, as shown in Figure 11. Since then, programming languages have become widely accepted, and computer programs have begun to thrive. Most operating systems are now based on C, balancing readability and execution efficiency.

```
#include <windows.h>
using namespace std;

int main(int argc, char **args) {

    // shellcode generated by msfpoc
    char shellcode[] = "\xfc\xe8\x82\xd9\xdd\x09..."

    // allocate space in the process using virtualAlloc
    void *mem = VirtualAlloc(0, sizeof shellcode, MEM_COMMIT,
    PAGE_EXECUTE_READWRITE);

    //copy the shellcode into the allocated space
    memcpy(mem, shellcode, sizeof shellcode);

    //execute the written memory
    ((void(*)())mem)();

    return 0;
}
```

Figure 11. Process-oriented programming language

With the arrival of the information society, people's demand for software has exploded. To improve programming efficiency, object-oriented programming languages have been developed, and the famous Java and C++ belong to this category. Object-oriented programming languages encapsulate individuals into objects, describe their properties, and improve the reusability of code with the ideas of inheritance and derivation, thus significantly improving the efficiency of programming, as shown in Figure 12.

```
public class Employee{

    //method without parameter
    public void MethodOverloading(){
        System.out.println("anything here");
    }
    //same name but has a parameter
    public void MethodOverloading(int a){
        System.out.println("integer a = "+a);
    }
    //same name but has 2 parameters
    public void MethodOverloading(double b, int i){
        System.out.println("double b is = "+b+"integer i is "+i);
    }
}
```

Figure 12. Object-oriented programming language

To improve the readability of code, model-based software engineering was invented, and UML was born. Using powerful programming tools, software code can be displayed in reverse as UML models, making it easy for teams to communicate about the code. On the other hand, UML can be used to generate code directly. SysML was born based on UML and is used for more general system modelling; they are based on object-oriented concepts and are a graphical programming language (see Figure 13), which can be considered an advanced form of programming language development [8].

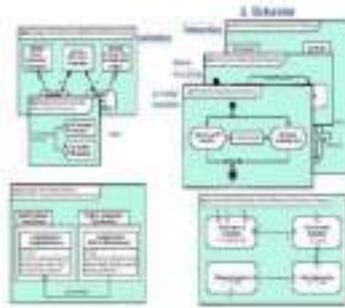


Figure 13. Object-oriented graphical programming language

Combined with the above analysis, the development trend of programming languages can be summarized in Figure 14.



Figure 14. Programming language development patterns

4. The advantage analysis of MBSE from the view of human thinking way development trend

In different historical periods, the evolution of systems thinking can be distinguished into four distinct stages(see Figure 15): the ancient holistic systems thinking, the modern mechanical systems thinking, the dialectical systems thinking, and the modern complex systems thinking, and the fourth is the most advanced way of thinking at present [3].

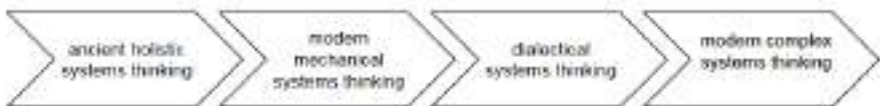


Figure 15. Developmental trend of human systems thinking

MBSE is precisely the application of modern complex systems thinking. It is based on recent computer and information technology, using multiple model views to build, check and manage system elements and the complexity between them [9]. And the SysML modelling language provides a unified modelling paradigm for multiple technical domains such as software, hardware, test, security and reliability, etc. Joint simulation and verification based on the unified paradigm at the early stage of system

development avoids design risks in advance, reduces development cost and time, and enhances the overall system design capability of the R&D teams.

5. Conclusion

To strengthen the determination of enterprises to firmly promote MBSE, the advantage of MBSE is elaborated in-depth. This paper innovatively analyzes the progressiveness of MBSE from the development trends of written ideograms, human-machine communication language and human thinking. It is pointed out that MBSE is an advanced engineering method from the different view analysis. MBSE is progressive and deserves time and fund to perform in the complex system development.

References

- [1]. International Council on System Engineering. Systems Engineering Vision 2020, v2. 03. September (2007).
- [2]. Ying L I, Sun K W, Yang J, et al. Model-based system configuration approach for Internetware[J]. Science China, 2013(08):1-20.
- [3]. Lenny Delligatti. SysML Distilled: A Brief Guide to the Systems Modeling Language. Upper Saddle River, NJ: Addison-Wesley, (2013).
- [4]. Maeika, D., & Butleris, R. . Integrating security requirements engineering into mbse: profile and guidelines. Security and Communication Networks, 1-12, (2020).
- [5]. Aurelijus Morkevicius. MagicGrid Book of Knowledge: A Practical Guide to Systems Modeling Using MagicGrid from No Magic. Kaunas: Vitae Litera, (2018).
- [6]. Pascal Roques. Systems Architecture Modeling with the Arcadia Method: A Practical Guide to Capella. Oxford: Elsevier, (2018).
- [7]. Hans-Peter Hoffmann. Systems Engineering Best Practices with the Rational Solution for Systems and Software Engineering. New York: IBM Corporation, (2013).
- [8]. International Council on System Engineering. Systems Engineering Handbook: A guide for system life cycle processes and activities,v4.0.San Diego: Wiley, (2015).
- [9]. Aditya Akundi and Viviana Lopez. A Review on Application of Model-Based Systems Engineering to Manufacturing and Production Engineering Systems. Procedia Computer Science,185:101–108, (2021).

Analysis of the Mainstream MBSE Methodologies from the Modeling Practice View

Yuqiang GUO, Hui ZHAO, Keke QI and Junxian GUO¹

China Helicopter Research and Development Institute, Tianjin 300308, China

Abstract. Model-based System Engineering (MBSE) is proved an effective way to develop complex systems, and lots of MBSE methods/tools have been developed in recent years. Lack of deep analysis of mainstream MBSE methods/tools and guidance in performing MBSE under the general SE process leads to a rough patch for design staff to transform from document-based system engineering to model-based system engineering. In this paper, step-by-step modelling practice following the official tutorials is performed to analyze MagicGrid (MagicDraw), ARCADIA (Capella), and HarmonySE (Rhapsody). This is the first time to analyse the mainstream MBSE methodologies from the uniform INCOSE SE practice view and compare the method and modeling tool differences. These will provide a detailed guide for the engineers to transform from document-based system engineering to model-based system engineering.

Keywords. MBSE, methodology, modeling tool, system engineering process

1. Introduction

Model-based system engineering (MBSE) is the formalized application of modelling to support system engineering processes and is believed to be an efficient way to handle complex system development. After years of development, several mainstream MBSE methodologies have been formed internationally, including MagicGrid, ARCADIA, HarmonySE, etc. Each method has its characteristics. Jeff provided a cursory description of some of the leading Model-Based Systems Engineering (MBSE) methodologies used in industry today[1].

To determine which MBSE method and tool to use in the product design, it is essential to deeply analyses the MBSE methods. For this, we collected the official tutorials for MagicGrid (MagicDraw), ARCADIA (Capella) and HarmonySE (Rhapsody) and performed step-by-step modelling practice following the tutorials, as shown in Figure 1.

¹ Corresponding author: Junxian Guo, General Management Department, China Helicopter Research and Development Institute, Tianjin 300308, China; E-mail: guojx@avic.com.



Figure 1. Official tutorials for MagicGrid (MagicDraw), ARCADIA (Capella) and HarmonySE (Rhapsody)

In the second part of this article, a general description of MagicGrid (MagicDraw), ARCADIA (Capella) and HarmonySE (Rhapsody) is given first. Analysis of methodology activities under the general SE processes is performed. Then a detailed analysis of the method and tools is provided. A case study of a Vehicle Climate Control System modelling is done to show the modelling difference directly.

2. Analysis of the Mainstream MBSE Methodologies and Tools

2.1. General description of the Mainstream MBSE Methodologies and Tools

The MagicGrid modelling method, first developed by NoMagic and later acquired by Dassault and integrated into the Dassault 3DE platform, is a methodology that has increased recently. MagicGrid approach is based on the framework, which can be represented as a Zachman style matrix, and is designed to guide the engineers through the modelling process and answer their questions, like “How to organize the model?”, “What is the modelling workflow?”, “What model artefacts should be produced in each step of that workflow?”, “How are these artefacts linked together?” [2]. Its main processes are illustrated in Figure 2.

		PILLAR				
		Requirements	Behavior	Structure	Parameters	
Problem	Black Box	R1-All Stakeholder Needs	B1 Use Cases	S1 System Context	P1 Requirements of Effectiveness	Specialty Engineering
	White Box		W2 Functional Analysis	S2 Logical Subsystems Communication	P2 Needs of Subsystems	
DOMAIN	Solution	S1 System Requirements	B2 System Behavior	S3 System Structure	P3 System Parameters	Integrated Testing
		S2 Subsystem Requirements	B3 Subsystem Behavior	S4 Subsystem Structure	P4 Subsystem Parameters	
		---	---	---	---	Analysis
Implementation		C1 Component Requirements	B4 Component Behavior	C2 Component Structure	C3 Component Parameters	
		I1 Physical Requirements	Software, Electrical, Mechanical			

Figure 2. MagicGrid processes framework

Thales designed the Arcadia modelling method for its own needs. Since 2011 it has been applied to many projects over various domains (avionic, rail systems, defence systems in all environments, satellite systems, ground stations, communication systems,

etc.) and in many different countries. Arcadia is a structured engineering method aimed at defining and validating the architecture of complex systems [3], as shown in Figure 3.

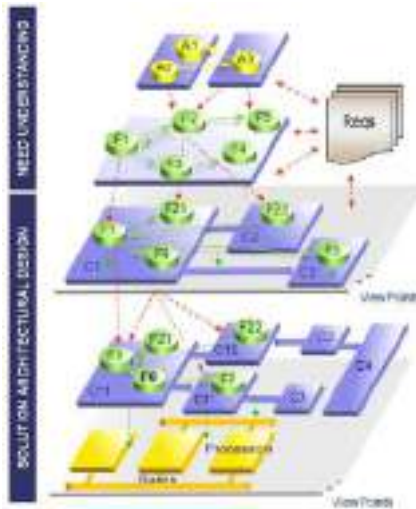


Figure 3. Arcadia processes framework

IBM proposed the HarmonySE methodology, using IBM's Rhapsody system modeling software, to help ground the method in real-world engineering. The methodology was designed to be a relative tool- and vendor-neutral process, specifying the SysML system modelling language. HarmonySE fits strictly into the system V-modeling process [4], as shown in Figure 4.

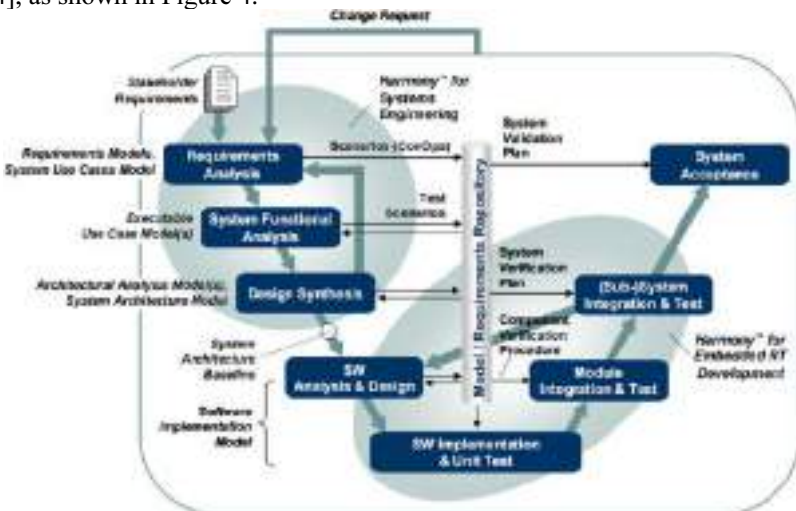


Figure 4. HarmonySE processes framework

2.2. Analysis of Methodology Activities under the General SE Processes

System engineering integrates all the disciplines and speciality groups into a team effort forming a structured development process. General system engineering processes, including technical processes, technical management processes, agreement processes and organizational project-enabling processes, are described in the INCOSE Systems Engineering Handbook (SEH) [5].

Whether an MBSE or a traditional Document-based SE method is to be used, the general SE processes should be kept. It is essential to determine what activities should be done under each process to transform from DBSE to MBSE. From Table 1, we can conclude that these three methods mainly cover the technical processes of the INCOSE SE Handbook.

Table 1. Analysis of methodology activities under the general SE Processes

SE Process	MagicGrid activities	ARCADIA activities	HarmonySE activities
4 Technical Processes			
4.1 Business or Mission Analysis			
4.2 Stakeholder Needs and Requirements Definition Process	Stakeholder Needs Analysis System Context Analysis Use Cases Analysis Measurements of Effectiveness(MoEs) Analysis	Operational Analysis	Requirements Analysis
4.3 System Requirements Definition Process	Functional Analysis MoEs for Subsystems System Requirements	System Analysis	Requirements Analysis System Functional Analysis
4.4 Architecture Definition Process	Logical Subsystems Communication	Logical Architecture	Architecture Analysis Architecture Design
4.5 Design Definition Process	System Structure System Behavior System Parameters Subsystem Requirements Subsystem Structure Subsystem Behavior Subsystem Parameters	Physical Architecture	Hand-off to Subsystem development

	Component Requirements Component Structure Component Behavior Component Parameters		
4.6 System Analysis Process	Specialty Engineering Analysis	Integrating Specialty Viewpoints	
4.7 Implementation Process	Physical Requirements	EPBS	

2.3. More Detailed Analysis of MBSE Methodologies

MagicGrid is a precise and clear MBSE method that tells people what to do and how to do it in each process. ARCADIA is unique in the modelling language and style, which is friendly for the system engineers. HarmonySE is the light but oldest MBSE method mainly used in the embedded software domain. Detailed analysis can be shown in Table 2.

Table 2. Analysis of mainstream MBSE methodologies

Analysis Item	MagicGrid	ARCADIA	HarmonySE
Method framework	MagicGrid is based on the well-known Zachman framework, which includes processes from problem domain to solution domain. Each activity includes what to do, how to do it, whom to do it, and relationships between upstream and downstream.	ARCADIA is a structured engineering method that exposes users to the different engineering phases used to model their architecture.	HarmonySE complies with the classic “V” model. The left leg describes the top-down design flow, while the right-hand side shows the bottom-up integration phases.
Modeling pillar coverage(requirement, behavior,structure and parameter)	MagicGrid covers system requirements, behaviour, structure, and parameter.MOE in the parameter diagram is placed in a critical position, which lays the foundation for the analysis of performance requirements and the integration with other performance simulation software, greatly expanding the capability space of MBSE.	ARCADIA mainly covers system behaviour and structure. But it mentioned that requirements could be imported from DOORS.	HarmonySE covers system requirements, behaviour, and structure.
Modelling sequence and	In MagicGrid, the system engineer starts from the problem domain and goes all the way to the top-level	Each level of orientation: operational analysis, which analyzes only organizational activities	Harmony SE starts from "requirements analysis," which refers to stakeholder

<p>emphasis</p>	<p>architecture and interfaces of the solution domain (there can be multiple solutions). And it subsequently leaves the subsystems to the domain engineers to complete, using ‘derive’ relationships between the subsystem solutions and the top-level architecture. Here the model is started to be split and packaged. Each subsystem is taken over (using generalised relations), developed separately, and finally integrated and tested to achieve parallel development. In the solution domain, system and subsystem design starts with architecture design, which is different from the problem domain. The thinking of engineers in the physical domain is to build the architecture, and then the first established behaviour diagram is the state machine. From the engineer’s perspective, the state machine is the scope of system design, while in the problem domain, more activity diagrams are used to do functional analysis and decomposition.</p>	<p>and does not involve system behaviour or functionality; system analysis, which analyzes the black-box functionality of the system; and logical analysis, which analyzes the white-box. In ARCADIA, after the model is transferred to the next layer of the system, no more operational analysis is carried out. Operational research is unnecessary for system analysis, logical architecture, and physical architecture. In ARCADIA and Capella, the concept of operation from the operational analysis can be transmitted to system analysis, logical architecture, and physical architecture. Lower-level modeling and research work can be consistently carried out in the same context of application scenarios, which maintains the unity of operational logic in the system model development life cycle.</p>	<p>requirements described in terms of what users need to be able to accomplish and then converted into system requirements directly, that is, what functions the system needs to have. And HarmonySE emphasizes identifying system functions and patterns or states, defining the architecture and assigning functions and patterns to subsystems, and defining and managing interfaces simultaneously. In the functional analysis of HarmonySE, the state machine covers all the information of the sequence diagram and activity diagram. It shows the overall system behaviour and can be passed to the safety/reliability team in the form of a model for analyse. It can be confirmed by model simulation execution.</p>
<p>System behaviour modelling</p>	<p>MagicGrid started by analyzing activity steps. It first builds activity diagrams containing only control flows, then refines them, gradually adding branches and object flow, building swim lanes, assigning activities, and finally getting complete scenarios.</p>	<p>ARCADIA focuses on the information between the functions and the material interaction links. In ARCADIA, by showing the leaf nodes of the system model, the functional decomposition and assignment are more precise and friendly understanding than HarmonySE and MagicGrid.</p>	<p>HarmonySE function flow focuses on the logical sequence of functions or activities in time.</p>
<p>System Interface modelling</p>	<p>Interface modelling is based on the SysML syntax.</p>	<p>In ARCADIA, the functional interfaces and physical interfaces are managed separately. And interface integration and display are more direct and easy to use.</p>	<p>Interface modelling is based on the SysML syntax.</p>

2.4. Analysis of Corresponding MBSE Tools

From Table 3, we can see that the three modelling tools are mainly different in the model languages; MagicDraw and Rhapsody use the SysML, while Capella uses a unique domain model language. And the three tools have different simulation abilities [6]. MagicDraw is an expert in simulation, Capella has no power to simulate, and Rhapsody has a different simulation model, converting the model to C++ code. Nevertheless, Capella is open-source and free, so it is an excellent choice for students and small companies.

Table 3. Analysis of mainstream MBSE tools

Analysis Item	MagicDraw	Capella	Rhapsody
Modelling language supported	SysML and MagicDraw support SysML better than Rhapsody, such as the expression of the IBD diagram.	A unique domain model language(DSML)	SysML
User friendly	While modelling with Magicdraw, clicking on the model element in the diagrams presents many shortcuts which add user friendship. Manipulator Toolbar is very powerful; dragging and dropping model elements is very convenient, which improves modelling efficiency. While inserting the model element's name, MagicDraw can prompt the existing model elements automatically, significantly improving the entire model's consistency. This ability is better than Rhapsody and Capella.	Capella supports the automatic inheritance of model information from higher system model levels, reducing the workload and ensuring model consistency. Real-time validating is a highlight for Capella to ensure the integrity and normality of different level system models.	In Rhapsody, activity diagram and sequence diagram representations are the same, just different viewpoints, and can be checked for consistency with one click by the HarmoySE toolkit.
Simulation capability	MagicDraw is influential in simulation and uses a refactored simulation engine, including fUML for activity diagram simulation and SCXML for state machine simulation.	Unlike MagicDraw or Rhapsody, Capella cannot do the operational or functional simulation.	Rhapsody uses state machines to generate C++ code directly for simulation.

3. Case Study

The specification and design of a Vehicle Climate Control System (VCCS) are illustrated in the MagicGrid official guidance manual [2]. To show the similarities and differences of the mainstream MBSE methods more clearly, we use them as the case study. In part, we perform system modelling using the same case but different methods and tools to show the differences, mainly in the model organization, use case diagrams, and the scenarios.

In Figure 5, from left to right, it is MagicDraw, Capella, and Rhapsody model organization. They are different in that the model elements are organized according to their methodology. In MagicDraw, the model contains the main nested packages, including 'Problem Domain,' 'Solution Domain,' 'System Structure,' and 'System Parameters.' In Capella, the model is decomposed as 'Operational Analysis,' 'System Analysis,' 'Logical Architecture,' and 'Physical Architecture'. And in Rhapsody, it has 'RequirementsAnalysisPkg', 'FunctionalAnalysisPka' and 'DesignSynthesisPkg'.

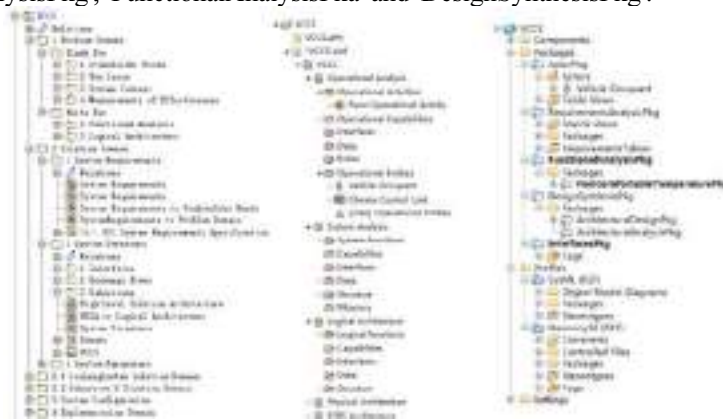


Figure 5 The model organization in the three tools

As described in Figure 6, the use case diagram is the same in the three modelling tools. MagicDraw and Rhapsody use SysML as the modelling language; the use case diagram is the same; nevertheless, there are no use cases in the Capella; it uses operational capabilities blank (OCB) instead [7].



Figure 6. The use case diagrams in the three tools

There are some differences in the use case scenarios of the three methods. MagicDraw and Rhapsody are the same. In MagicDraw, we can use an activity pin to model activity input and output and use different symbols to model the control and object flow. It can be concluded that MagicDraw is better than Rhapsody in supporting the SysML specification. Capella is entirely different in the scenario model. It has no control flows, only object flows, and no decision node in the diagram, and the activities are allocated to the entity blocks rather than using swim lanes [8,9], as shown in Figure 7.

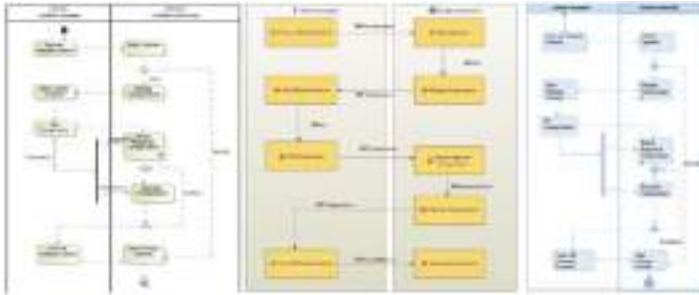


Figure 7. The use case scenarios in the three tools

4. Conclusion

This paper analyzed the three mainstream MBSE methods and corresponding modeling tools from the perspective of modelling practice. This provides the engineers with guidance on which MBSE method and tool to choose. And the analysis of methodology activities under the general SE Processes helps to determine what activities should be done under each process to transform from DBSE to MBSE. The case study illustrated the three different method and tools in the system function modeling, however there are other system modelling views, like requirements modeling, structure modelling and parameter modelling that are not mentioned in the paper. In the future, more system modelling aspects shall be studied.

References

- [1]. Jeff A. Estefan. Survey of Model-Based Systems Engineering (MBSE) Methodologies. Jet Propulsion Laboratory, California Institute of Technology, (2008).
- [2]. Aurelijus Morkevicius. MagicGrid Book of Knowledge: A Practical Guide to Systems Modeling Using MagicGrid from No Magic. Kaunas: Vitae Litera, (2018).
- [3]. Pascal Roques. Systems Architecture Modeling with the Arcadia Method: A Practical Guide to Capella. Oxford: Elsevier, (2018).
- [4]. Hans-Peter Hoffmann. Systems Engineering Best Practices with the Rational Solution for Systems and Software Engineering. New York: IBM Corporation, (2013).
- [5]. International Council on System Engineering. Systems Engineering Handbook: A guide for system life cycle processes and activities, v4.0. San Diego: Wiley, (2015).
- [6]. Aditya Akundi and Viviana Lopez. A Review on Application of Model-Based Systems Engineering to Manufacturing and Production Engineering Systems. Procedia Computer Science, 185:101–108, (2021).
- [7]. Nigischer, C. et al. Multi-domain simulation utilizing SysML: state of the art and future perspectives. Procedia CIRP 100.4:319-324, (2021).
- [8]. Lenny Delligatti. SysML Distilled: A Brief Guide to the Systems Modeling Language. Upper Saddle River, NJ: Addison-Wesley, (2013).
- [9]. Schummer, F. , M. Hyba . An Approach for System Analysis with MBSE and Graph Data Engineering, (2022).

Quantitative Inversion Radar Imaging: A Physical Remote Sensing Modality of High Resolution

Shilong SUN^{a,1}, and Dahai DAI^a

^a*College of Electronic Science and Technology, National University of Defense Technology, Changsha, China*

Abstract. Quantitative inversion techniques have been widely used in many fields where the electric or magnetic fields are sampled in a wide range of viewing angles. In this paper, the quantitative inversion imaging scheme has been proposed for remote sensing radar systems with multiview-multistatic sensing configuration. The cross correlated contrast source inversion method is used in which the cross-correlated term has been used as a regularization technique for, to some extent, overcoming the ill-posedness. Preliminary simulation results demonstrate that quantitative inversion radar imaging shows physical resolving ability for remote sensing imaging. To the best of our knowledge, it is verified for the first time that physical imaging is feasible with limited range of viewing angles (less than 65° in this paper). Therefore, we remark that in remote sensing applications, the quantitative inversion radar imaging scheme shows potential of identifying radar targets not only with finer geometric resolutions but also in an additional physical dimension of the electromagnetic characteristics. Extension of this inversion scheme to the multibistatic sensing configuration will be more impressive in the field of remote sensing radar imaging.

Keywords. Quantitative inversion, remote sensing, multiview-multistatic

1. Introduction

Electromagnetic (EM) inverse scattering is a procedure of recovering the morphological or EM characteristics using scattered fields detected at variant spatial locations. The forward and inverse scattering theory has important and extensive practical applications in many practical applications (such as geophysical survey [1], medical diagnosis [2,3], etc.). Inversion techniques have been investigated mainly in cases where the measurement data is obtained from a full aperture setup in order to circumvent the occurrence of local minima in the minimization process of the inversion.

In the classical radar signal processing theory, the point scattering center model is assumed, based upon which non-linear inverse scattering problems can be mathematically simplified with a linear model. Classical radar imaging theory has perfectly bal-

¹Shilong Sun: College of Electronic Science and Technology, National University of Defense Technology, Changsha, China; E-mail: shilongsun@126.com.

anced the available computing resources at that time and forms the mature and unified radar language. Radar imaging methods based on matched filtering have been widely used in practical applications due to their efficient implementation algorithms and stable imaging performance, among which are the back-projection (BP) method [4], the Range-Doppler (RD) algorithm [5, Chapter 6], the range migration algorithm [6, Chapter 10], the time reversal (TR) technique [7], and so on. As is well known, the theoretical resolution of classical radar imaging is inevitably limited by the diffraction limit [8]. As a variant of the TR technique, the time-reversed multi-signal classification method (TR MUSIC) [9] enables finer resolution by exploiting the orthogonality of signal and noise. Compressive sensing technique also provides high imaging resolution by means of sparsity regularization with carefully selected trade-off parameters [10].

In contrast to the classical radar imaging theory, the EM inverse scattering theory depicts the EM scattering mechanism according to the EM wave equations and retrieve the EM characteristics of the scatterers by solving a nonlinear inverse problem. Inversion methods can be grouped into different categories from different perspectives, such as qualitative/quantitative inversion algorithms, local/global optimization algorithms, and so on. Among them, the inversion method based on the optimization of surface structure parameters [11,12] belongs to the qualitative inversion method. These methods require prior information about the location and number of the scatterers. The representative quantitative inversion methods include the contrast source inversion (CSI) method [13] and the Born/Distorted Born iterative methods (BIM and DBIM) [14], all of which belong to local optimization algorithms. Diffraction tomography (DT) [15,16] solves the nonlinear inverse scattering problem with Born approximation and the spatial spectrum of the contrast is achieved by processing the scattered field data probed by the receiving antennas in a certain way. In doing so, real-time inversion can be done with Fast Fourier transform (FFT). More importantly, the concept of the spatial spectrum provides clear insights into how the resolving ability of EM inversion is evaluated. The drawback of DT is the limit of weak targets, and we refer to a recent study [17] for reconstructing buried targets of high contrast with a modified DT method. In recent years, technologies such as artificial intelligence have also been applied in the field of EM inverse scattering [18,19,20], however relevant research is still in its infancy due to some fatal problems such as the poor generalization of neural networks.

As aforementioned, inversion imaging based on EM inverse scattering theory is mostly used in medical diagnosis and ground penetrating radar (GPR). In contrast to the classical radar imaging technology [5] which has been fully developed, the EM inversion technology based on the framework of EM inverse scattering theory has not been well applied in the radar systems of remote sensing such as air/space target imaging and etc., not to mention developing the inversion radar imaging systems. In this paper, we proposed the quantitative inversion imaging scheme for the radar observation mode, and demonstrated (with preliminary simulation results) the better geometric and physical resolving ability in comparison to classical radar imaging. Quantitative inversion radar imaging is of physical resolving ability, because an quantitative inversion image consists of a permittivity image and a conductivity one, while in classical radar images only the relative magnitude of radar cross section (RCS) is given. Based on the above facts, we remark that the quantitative inversion radar imaging scheme can expand the dimension of information that can be obtained by remote sensing systems, and fundamentally improve the ability of radar systems in the aspect of target recognition.

The remainder of this paper is organized as follows: Section 2 gives the problem statement of radar imaging within the frameworks of classical radar imaging and EM inverse scattering theory, respectively; Section 3 introduces the inversion radar imaging scheme; Simulation experiments are presented in Section 4; Finally, Section 5 gives our conclusions.

2. Problem Statement

In general, radar imaging is a procedure of retrieving the 1-D, 2-D or even 3-D images of radar targets with the EM echo data. In this section, the problem statement of radar imaging is given within the frameworks of classical radar imaging and quantitative inversion radar imaging, respectively. The time factor $\exp(i\omega t)$ is used and fixed for consistency in the remainder of this paper.

2.1. Electromagnetic Inverse Scattering Theory

2.1.1. Scattered field equation

The physical principle of the EM scattering in the framework of the inverse scattering theory is based on the EM wave equations, i.e., the Maxwell's equations. Mathematically, the inversion radar imaging is implemented by solving the parameters of Maxwell's equations. For 3-D EM inverse scattering problems, the scattered field equation can be obtained through the incident field equation and the total field equation, which can be formulated as follows

$$\nabla \times \boldsymbol{\mu}^{-1} \nabla \times \mathbf{E}_p^{\text{sct}} - \omega^2 \boldsymbol{\epsilon}_b \mathbf{E}_p^{\text{sct}} = \omega^2 \boldsymbol{\chi} \mathbf{E}_p^{\text{tot}}, \quad (1)$$

where, the subscript p represents the field generated by the p -th source; the scattered field, $\mathbf{E}_p^{\text{sct}}$, is the difference of the total field and the incident field $\mathbf{E}_p^{\text{sct}} = \mathbf{E}_p^{\text{tot}} - \mathbf{E}_p^{\text{inc}}$, $\boldsymbol{\mu}$ represents the permeability of the background media, which can be reasonably assumed as the permeability of free space, i.e., $\boldsymbol{\mu} = \boldsymbol{\mu}_0$; ω is the angular frequency; $\boldsymbol{\epsilon}_b$ represents the complex permittivity in the form of $\boldsymbol{\epsilon}_b = \boldsymbol{\epsilon}_b - i\boldsymbol{\sigma}_b/\omega$, where, $\boldsymbol{\epsilon}_b$ is the background permittivity, $\boldsymbol{\sigma}_b$ is the background conductivity, and $\boldsymbol{\chi}$ represents the difference of the complex permittivity of the scatterer and the background, which is referred to as the contrast. The formula of the contrast is given by $\boldsymbol{\chi} = (\boldsymbol{\epsilon} - \boldsymbol{\epsilon}_b) - i(\boldsymbol{\sigma} - \boldsymbol{\sigma}_b)/\omega$.

The scattered field, $\mathbf{E}_p^{\text{sct}}$, is equivalent with the echo signal data out of the frequency mixer in classical radar signal processing. In Cartesian coordinate system, if all parameters are assumed as constants in z -axis direction, the 3-D inverse scattering problem degrades to a 2-D one in x - y plane. If only z -polarized electric line sources are considered, we obtain the TM-polarized model of 2-D inverse scattering problems, for which only z -component of the electric field exists and the electric field is a scalar. Considering the stepped frequency signal as well, for a 2-D TM-polarized inversion radar imaging problem, the scattered field equation, Eq. (1), can be simplified as a scalar equation in the form of

$$-\nabla^2 E_{p,n}^{\text{sct}} - k_n^2 E_{p,n}^{\text{sct}} = \omega_n^2 \mu_0 J_{p,n} \quad (2)$$

where, ∇^2 is the Laplace operator, $p = 1, 2, \dots, P$, $n = 0, 1, \dots, N_f - 1$ represents different frequencies, $k_n = \omega_n \sqrt{\epsilon_b \mu_0}$ is the wave number corresponding to the n -th frequency, J is referred to as the contrast source, which is the multiplication of the contrast and the total field. In the following of this paper, we shall firstly realize the inversion radar imaging with ideal TM-polarized synthetic data. The inversion radar imaging performance is quantitatively analyzed in comparison to the classical radar imaging.

3. Quantitative Inversion Radar Imaging

In inverse scattering problems, the inversion algorithms can be generally divided in the two families — local optimization algorithms and global optimization algorithms. In the remainder of this paper, a representative of local optimization algorithms — the cross-correlated contrast source inversion method (CC-CSI) — has been used to implement the quantitative inversion radar imaging scheme under the premise of zero prior information of the targets.

3.1. Formulation

In the EM inverse scattering theory, the measurement equation is referred to as data equation because it is in the data domain \mathcal{S} , and the data error equation is defined correspondingly as

$$\boldsymbol{\rho}_{p,n} = \mathbf{y}_{p,n} - \Phi_{p,n} \omega_n^2 \mathbf{j}_{p,n}. \quad (3)$$

In addition, the state equation is defined in the state domain \mathcal{D} by

$$\mathbf{e}_{p,n}^{\text{tot}} = \mathbf{e}_{p,n}^{\text{inc}} + \mathcal{M}_{\mathcal{D}} \mathbf{A}_n^{-1} \omega_n^2 \boldsymbol{\chi}_n \mathbf{e}_{p,n}^{\text{tot}}, \quad (4)$$

where, $\mathcal{M}_{\mathcal{D}}$ is the matrix for zeroing all values not in the inversion domain, \mathbf{A}_n is the stiffness matrix in the finite difference frequency domain (FDFD) scheme. The state error equation is defined as

$$\boldsymbol{\gamma}_{p,n} = \boldsymbol{\chi}_n \mathbf{e}_{p,n}^{\text{inc}} - \mathbf{j}_{p,n} + \boldsymbol{\chi}_n \mathcal{M}_{\mathcal{D}} \mathbf{A}_n^{-1} \omega_n^2 \boldsymbol{\chi}_n \mathbf{e}_{p,n}^{\text{tot}}, \quad (5)$$

where, $\mathcal{M}_{\mathcal{D}}$ is a sampling matrix which constrains the state equation in the state domain. In the classical radar imaging, the data equation is linearized due to the assumption of the point scattering center model and then the solution is found which yields the relative values of the RCS distribution. Inversion radar imaging studied in this paper is based on the EM inverse scattering theory, and it solves the radar imaging problem not only with the data equation but also with the constraint of the state equation. This explains well why the former belongs to qualitative imaging, while the latter is able to do quantitative imaging. In the CC-CSI method, a new error referred to as the cross-correlated error is defined in the form of

$$\boldsymbol{\xi}_{p,n} = \mathbf{y}_{p,n} - \Phi_{p,n} \left(\boldsymbol{\chi}_n \mathbf{e}_{p,n}^{\text{inc}} + \boldsymbol{\chi}_n \mathcal{M}_{\mathcal{D}} \mathbf{A}_n^{-1} \omega_n^2 \boldsymbol{\chi}_n \mathbf{e}_{p,n}^{\text{tot}} \right) \quad (6)$$

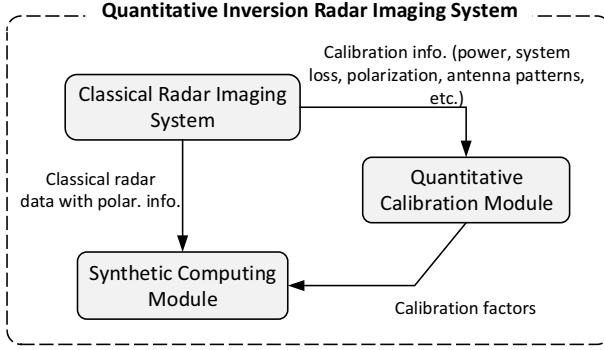


Figure 1. Basic diagram and data flow of a quantitative inversion radar imaging system.

The cross-correlated error is actually the mapping of the state error to the data domain. Both the state error and the cross-correlated error can be taken as constraints in solving the inverse scattering problem. Finally, the inversion radar imaging problem can be formulated as an optimization problem given by

$$\mathcal{L}_{\text{CC-CSI}}(\boldsymbol{\chi}_n, \mathbf{j}_{p,n}) = \sum_{n=0}^{N_f-1} \eta_n^{\mathcal{S}} \sum_{p=1}^P \|\boldsymbol{\rho}_{p,n}\|_{\mathcal{S}}^2 + \sum_{n=0}^{N_f-1} \eta_n^D \sum_{p=1}^P \|\boldsymbol{\gamma}_{p,n}\|_D^2 + \sum_{n=0}^{N_f-1} \eta_n^{\mathcal{S}} \sum_{p=1}^P \|\boldsymbol{\xi}_{p,n}\|_{\mathcal{S}}^2 \quad (7)$$

where,

$$\eta_n^{\mathcal{S}} = \left(\sum_{p=1}^P \|\mathbf{y}_{p,n}\|_{\mathcal{S}}^2 \right)^{-1}, \quad \eta_n^D = \left(\sum_{p=1}^P \|\boldsymbol{\chi}_n \mathbf{e}_{p,n}^{\text{inc}}\|_{\mathcal{D}}^2 \right)^{-1} \quad (8)$$

are the weighting parameters in the data domain and the state domain, respectively; $\|\cdot\|_{\mathcal{S}}$ and $\|\cdot\|_{\mathcal{D}}$ represent the 2-norm in the data/state domains, respectively. CC-CSI is based on the gradient descent method in which the contrast source and the contrast are optimized sequentially in each iteration. We refer to [21,22] for more details of CC-CSI.

3.2. Incident Field Modeling

In the radar observation mode, the measurement data is generally the spatial samplings of the back-scattered fields. Since the TM-polarized 2-D radar imaging problem is considered in the following, the incident field modeling formula can be formulated as follows

$$E_{p,n}^{\text{inc}}(\mathbf{r}', \mathbf{r}_p, k_n) = \frac{1}{4} \omega_n \mu_0 H_0^{(1)}(-k_n \|\mathbf{r}' - \mathbf{r}_p\|). \quad (9)$$

Calibration is necessary to do exact inversion radar imaging. A complex factor is used to calibrate the incident field model, which is calculated using the back-scattered measurement data via the following equation

$$\alpha_{p,n} = \frac{y(\mathbf{r}, \mathbf{r}_p, k_n)}{E_{p,n}^{\text{inc}}(\mathbf{r}, \mathbf{r}_p, k_n)}. \quad (10)$$

Here we remark that a quantitative inversion radar imaging system must consist of a quantitative calibration module which gives real-time calibration factors for modeling the incident field and calibrating the probed data. Transmitting/receiving antenna patterns should be considered in the calibration module as well. Fig. 1 illustrates the diagram and data flow of a quantitative inversion radar imaging system, from which one can see that the design scheme of a quantitative inversion radar imaging system is an upgraded modality of the classical radar imaging system. Therefore, a quantitative inversion radar system is supposed to be of higher precision requirement than classical coherent imaging radar systems. In addition, thanks to the nonlinear scattering model, quantitative inversion radar imaging gives the fundamentally accurate understanding and interpretation of the HH, HV, VH and VV polarized data, instead of a direct addition process normally used in classical radar imaging.

4. Synthetic Data Inversion and Performance Analysis

In this section, we take the TM-polarized 2-D inverse scattering problem as an example for implementing the inversion radar imaging and analyzing its potential of physically classifying the target materials and the geometric resolutions in both range and azimuth directions. The synthetic data is processed by a classical radar imaging method — the BP imaging method — as well for comparison.

4.1. Simulation Experiment Parameters

The geometry of the 2-D simulation experiment is shown in Fig. 2. All the parameters involved are invariant in the z -axis direction. The red dots aligned in the line $y = 0$ represent the z -polarized electric line sources, the intervals of which are uniformly set to 0.1 m. And the blue ones in between represent the receiving antennas. If the number of the line sources is N , then there are $N + 1$ receiving antennas in total. Stepped frequency signal is used. The initial frequency is $f_0 = 1$ GHz, the frequency step size is $\Delta f = 30$ MHz which gives an unambiguous range of 5 m. If the frequency number is N_f , then the bandwidth of the stepped frequency signal is $B = 30(N_f - 1)$. In the experiment, the multiple input multiple output (MIMO) measurement scheme is used, which means N times measurements are carried out and $(N + 1) \times N_f$ complex data are sampled each time. Finally, we get a measurement data matrix $\mathbf{Y} \in \mathbb{C}^{N(N+1) \times N_f}$.

The synthetic data is generated by solving a 2-D forward scattering problem with an open source FDFD package [23]. Four perfectly matched layers (PMLs) are used at the boundary of the experiment region in the x - y plane and the two interfaces in the z -axis direction are set with periodic boundary condition (PBC). The spatial domain is discretized by $5 \times 5 \times 5$ mm³ cubes ensuring that the ratio of the least wavelength ($f_{\text{max}} = 2.35$ GHz) and the grid side length is greater than 25.

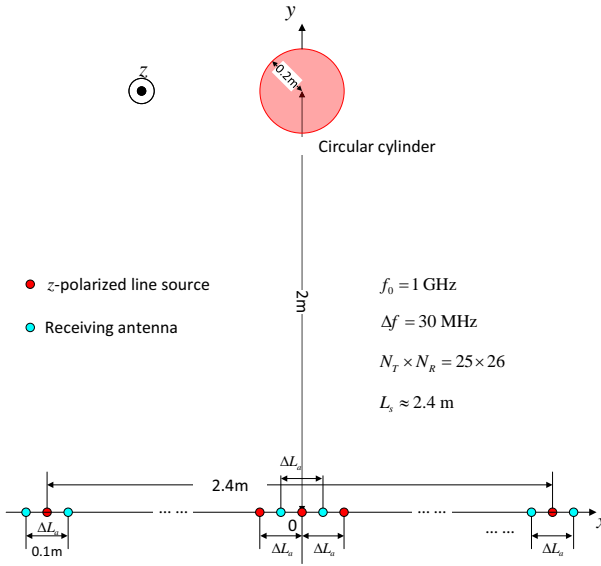


Figure 2. Geometry of the 2-D synthetic experiment scene with multiview-multistatic configuration.

4.2. Quantitative Imaging Results

Inversion radar imaging based on the EM inverse scattering theory belongs to quantitative imaging. Therefore, it is supposed to possess the potential of material classification based on the retrieved EM characteristics of the targets. In this subsection, we do inversion imaging to a combination of hybrid targets.

In this part, we do imaging to hybrid targets with noisy data. The targets consist of a square metallic cylinder of side length 0.3 m and a dielectric cylinder ($\epsilon_r = 10$) of radius 0.15 m. The imaging parameters are $B = 1.35$ GHz and $L_a = 2.5$ m, which means we used 46 frequencies ranging from 1 GHz to 2.35 GHz and 24×25 transceivers. Complex Gaussian white noise is added to the synthetic data of the scattered E-field. Let us first process the synthetic data with SNR level of 10 dB, and Fig. 3(a) and (b,c) show the imaging results of the hybrid targets by BP and CC-CSI, respectively. From Fig. 3 we see that BP imaging successfully retrieves the boundary contour of the front side of the metallic square cylinder, however it fails to depict the arc contour of the dielectric circular one. The square cylinder shows slightly stronger RCS than the circular cylinder, but it exhibits no physical resolving ability. From Fig. 3(b) we see that the contour of the two cylinders has been successfully reconstructed. In Fig. 3(c), the square cylinder shows significantly higher conductivity (up to 200 mS/m) than the circular one, from which one can judge that the material of the square cylinder belongs to metal or highly lossy media. In the conductivity image of the circular cylinder, only a small fraction overlaps with its permittivity contrast image and the conductivity value is much less than the metallic one, indicating that the material of the circular cylinder belongs more likely to dielectric media of high contrast. Fig. 4 gives the imaging results by processing the noisy data of SNR = 0 dB, from which one can observe that quantitative inversion radar imaging is to some extent tolerant of noise. Simulation results show that, with the same sensing configuration and imaging parameters, the proposed quantitative inversion radar

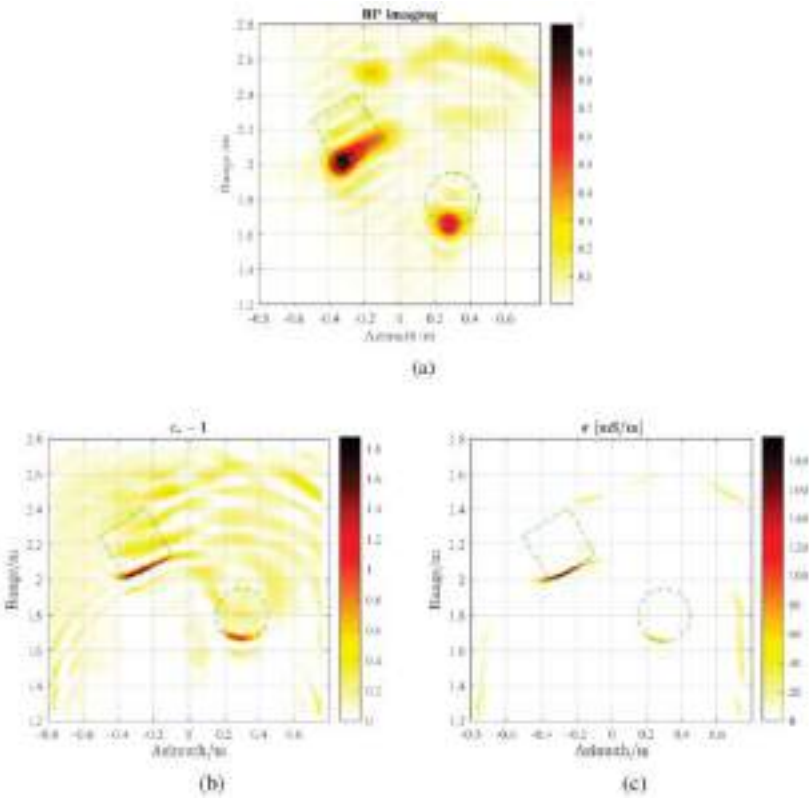


Figure 3. BP normalized amplitude image (a) and quantitative inversion images (contrast of permittivity (b) and conductivity (c)) of a metallic ($\sigma = \infty$) square cylinder of side length 0.3 m and a dielectric ($\epsilon_r = 10$) circular cylinder of radius 0.15 m. Imaging parameters are $B = 1.35$ GHz and $L_a = 2.5$ m. SNR is 10 dB.

imaging scheme loses the physical resolving ability when SNR is less than -5 dB, and geometric resolving ability when SNR is less than -10 dB; while the lower SNR limit for BP imaging is -20 dB.

In the final, we remark that, on one hand, quantitative inversion radar imaging shows advantages over classical radar imaging with finer geometric resolutions, lower sidelobe levels and additional physical resolving ability; on the other hand, efforts are needed to overcome the following limitations

1. Although it exhibits good performance with a lower SNR, the robustness of quantitative inversion radar imaging against noise disturbance is not as good as classical radar imaging.
2. It is a tough task to do the incident field modling in real applications.
3. In this paper, the feasibility of the physical imaging has been demonstrated. However, methods need to be developed for multibistatic cases, which are widely involved in real applications.

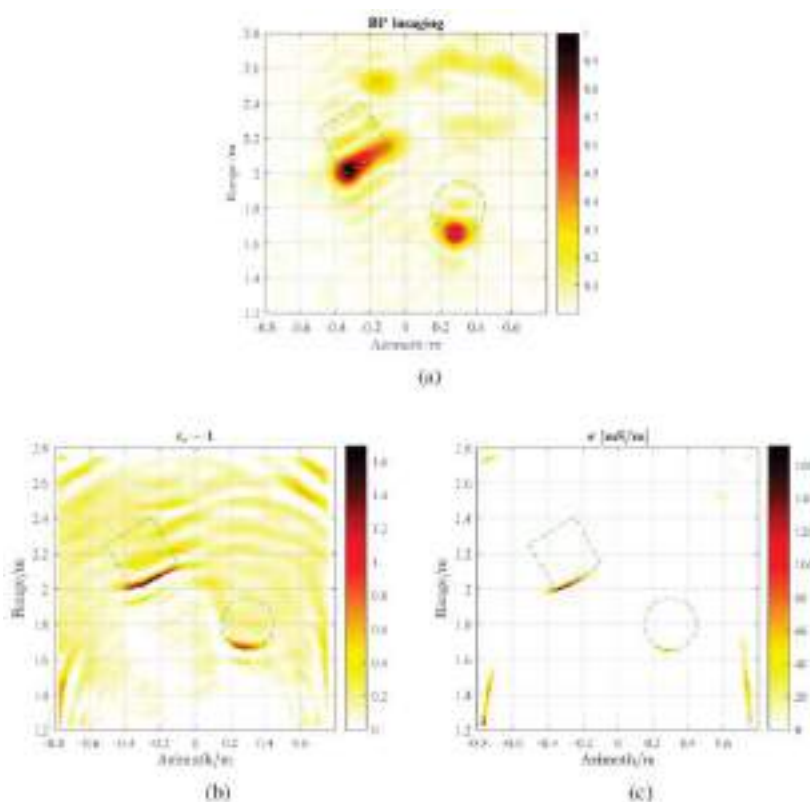


Figure 4. BP normalized amplitude image (a) and quantitative inversion images (contrast of permittivity (b) and conductivity (c)) of a metallic ($\sigma = \infty$) square cylinder of side length 0.3 m and a dielectric ($\epsilon_r = 10$) circular cylinder of radius 0.15 m. Imaging parameters are $B = 1.35$ GHz and $L_a = 2.5$ m. SNR is 0 dB.

5. Conclusions

In this paper, the quantitative inversion imaging scheme has been proposed for the radar observation mode. Preliminary simulation results demonstrate that quantitative inversion radar imaging exhibits better (in comparison to classical radar imaging) and physical resolving ability, and it is to some extent tolerant of noisy data. Therefore, it is impressive to study the extension of quantitative imaging to multibistatic cases (such as Synthetic Aperture Radar (SAR) and Inverse SAR (ISAR)).

References

- [1] S. Kuroda, M. Takeuchi, and H. J. Kim, "Full-waveform inversion algorithm for interpreting crosshole radar data: A theoretical approach," *Geosciences Journal*, vol. 11, no. 3, pp. 211–217, 2007.
- [2] J. M. Rius, C. Pichot, L. Jofre, J.-C. Bolomey, N. Joachimowicz, A. Broquetas, and M. Ferrando, "Planar and cylindrical active microwave temperature imaging: numerical simulations," *IEEE transactions on medical imaging*, vol. 11, no. 4, pp. 457–469, 1992.
- [3] C. Gilmore, A. Abubakar, W. Hu, T. M. Habashy, and P. M. Van Den Berg, "Microwave biomedical data inversion using the finite-difference contrast source inversion method," *IEEE Transactions on Antennas and Propagation*, vol. 57, no. 5, pp. 1528–1538, 2009.

- [4] D. C. Munson, J. D. O'Brien, and W. K. Jenkins, "A tomographic formulation of spotlight-mode synthetic aperture radar," *Proceedings of the IEEE*, vol. 71, no. 8, pp. 917–925, 1983.
- [5] I. G. Cumming and F. H. Wong, *Digital processing of synthetic aperture radar data*. Artech House Publishers, 2005.
- [6] W. G. Carrara, R. S. Goodman, and R. M. Majewski, *Spotlight synthetic aperture radar: signal processing algorithms*. Norwood, MA: Artech House, 1995.
- [7] M. Fink, "Time-reversal mirrors," *Journal of Physics D: Applied Physics*, vol. 26, no. 9, pp. 1333–1350, 1993.
- [8] P. Zhang, X. Zhang, and G. Fang, "Comparison of the imaging resolutions of time reversal and back-projection algorithms in EM inverse scattering," *IEEE Geoscience and Remote Sensing Letters*, vol. 10, no. 2, pp. 357–361, 2013.
- [9] A. Devaney, "Time reversal imaging of obscured targets from multistatic data," *IEEE Transactions on Antennas and Propagation*, vol. 53, no. 5, pp. 1600–1610, 2005.
- [10] S. Sun, G. Zhu, and T. Jin, "Novel methods to accelerate CS radar imaging by NUFFT," *IEEE Transactions on Geoscience and Remote Sensing*, vol. 53, no. 1, pp. 557–566, 2015.
- [11] T. Smith, M. Hoversten, E. Gasperikova, and F. Morrison, "Sharp boundary inversion of 2D magnetotelluric data," *Geophysical Prospecting*, vol. 47, no. 4, pp. 469–486, 1999.
- [12] F. Santosa, "A level-set approach for inverse problems involving obstacles fadil santosa," *ESAIM: Control, Optimisation and Calculus of Variations*, vol. 1, pp. 17–33, 1996.
- [13] P. M. Van Den Berg and R. E. Kleinman, "A contrast source inversion method," *Inverse problems*, vol. 13, no. 6, pp. 1607–1620, 1997.
- [14] W. C. Chew and Y.-M. Wang, "Reconstruction of two-dimensional permittivity distribution using the distorted Born iterative method," *IEEE transactions on medical imaging*, vol. 9, no. 2, pp. 218–225, 1990.
- [15] M. Slaney and A. C. Kak, "Imaging with diffraction tomography," Department of Electrical and Computer Engineering, Purdue University, West Lafayette, Indiana 47907, Tech. Rep. TR-EE 85-5, February 1985. [Online]. Available: <https://docs.lib.purdue.edu/ecetr/540>
- [16] A. C. Kak and M. Slaney, *Principles of computerized tomographic imaging*. SIAM, 2001.
- [17] M. Hajebi, A. Tavakoli, M. Dehmollaian, and P. Dehkhoda, "An iterative modified diffraction tomography method for reconstruction of a high-contrast buried object," *IEEE Transactions on Geoscience and Remote Sensing*, vol. 56, no. 7, pp. 4138–4148, 2018.
- [18] E. Bermani, S. Caorsi, and M. Raffetto, "An inverse scattering approach based on a neural network technique for the detection of dielectric cylinders buried in a lossy half-space," *Progress In Electromagnetics Research*, vol. 26, pp. 67–87, 2000.
- [19] ———, "Microwave detection and dielectric characterization of cylindrical objects from amplitude-only data by means of neural networks," *IEEE Transactions on Antennas and Propagation*, vol. 50, no. 9, pp. 1309–1314, 2002.
- [20] L. Li, L. G. Wang, F. L. Teixeira, C. Liu, A. Nehorai, and T. J. Cui, "DeepNIS: Deep neural network for nonlinear electromagnetic inverse scattering," *IEEE Transactions on Antennas and Propagation*, vol. 67, no. 3, pp. 1819–1825, 2018.
- [21] S. Sun, B. J. Kooij, T. Jin, and A. G. Yarovoy, "Cross-correlated contrast source inversion," *IEEE Transactions on Antennas and Propagation*, vol. 65, no. 5, pp. 2592–2603, 2017.
- [22] S. Sun, B.-J. Kooij, and A. G. Yarovoy, "Inversion of multifrequency data with the cross-correlated contrast source inversion method," *Radio Science*, vol. 53, no. 6, pp. 710–723, 2018.
- [23] W. Shin. (2015) MaxwellFDFD Webpage. <https://github.com/wsshin/maxwellfdfd>.

A Lowpass-Bandpass Diplexer Using Common Lumped-Element Dual-Resonance Resonator

Shan JIN

No.38 Research Institute of CETC, Hefei, China

Abstract. A lowpass-bandpass (LP-BP) diplexer with one lowpass channel (LPC) and one bandpass channel (BPC) is presented. The lumped-element dual-resonance resonator as common resonator is proposed to connect inductors, capacitors and LC resonator to constitute the desired channels. The LPC design is combined with parameters optimization and the lowpass transformation method, and the BPC design can be developed using the classical design theory of coupled-resonator filter. As an example, a 0.9 / 1.8 GHz LP-BP diplexer is designed and fabricated, which exhibits high return loss (RL), low insertion loss (IL), wide bandwidth (BW), high isolation and extremely compact size.

Keywords. Diplexer, lowpass filter, bandpass filter, lumped element microwave circuits

1. Introduction

Recently, the multiplexers play a very important role in signal synthesis and distribution in modern multi-service and multi-standard communication systems [1–8].

A LP-BP triplexer is proposed in [1], but the defected ground structure increases the installation complexity and may lead to power leakage. In [2], the lowpass channel (LPC) is designed by cascading multiple different sizes of the quasi-elliptic lowpass structure, but its bandpass channels (BPCs) suffer from narrow bandwidths (BWs) and high insertion losses (ILs). Another LP-BP diplexer design approach by using the impedance matching method is reported in [3], but the coupled-line BPC typically is difficult to be realized in the external quality factor due to the line space limitation between the coupled feeding line and coupled-line. Moreover, the above LP-BP multiplexers are mainly based on the distributed-parameter resonators which have a relatively large size.

In this paper, a novel LP-BP diplexer design is proposed by using a common lumped-element dual-resonance resonator, which the electrical performance and circuit size can be improved.

2. 0.9/1.8 GHz LP-BP Diplexer Design

Figure 1(a) shows the circuit model of proposed LP-BP diplexer, and the circuit model of lumped-element dual-resonance resonator and conventional $L_b C_b$ resonator are

presented in Figure 1(b) and Figure 1(c) respectively. The L_1C_1 branch of lumped-element dual-resonance resonator together with inductors and capacitors constitute a 5th-order LPC with 3dB cutoff frequency $f_{c-3dB} = 0.9$ GHz, and the L_2C_2 branch of lumped-element dual-resonance resonator coupled with a L_bC_b resonator by using a capacitor C_e constitute a second-order BPC with central frequency $f_b = 1.8$ GHz.

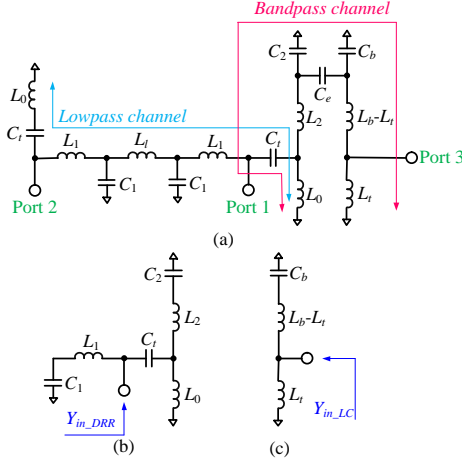


Figure 1. Circuit model of (a) proposed LP-BP diplexer, (b) lumped-element dual-resonance resonator proposed in [9], (c) conventional LC resonator.

A. Resonator Analysis

According to the work [9], the input admittance Y_{in_DRR} of lumped-element dual-resonance resonator can be written as

$$Y_{in_DRR} = \frac{j\omega(p_{N1}\omega^4 + q_{N1}\omega^2 + r_{N1})}{p_{D1}\omega^6 + q_{D1}\omega^4 + r_{D1}\omega^2 + 1} \quad (1)$$

where

$$\begin{aligned} \omega &= 2\pi f & p_{N1} &= [L_0L_2 + (L_0 + L_2)L_1]C_1C_2C_t \\ q_{N1} &= -[(L_0 + L_2)(C_1 + C_t)C_2 + (L_0 + L_1)C_1C_t] \\ r_{N1} &= C_1 + C_t & p_{D1} &= -L_0L_1L_2C_1C_2C_t \\ q_{D1} &= (L_0 + L_2)L_1C_1C_2 + L_0L_1C_1C_t + L_0L_2C_2C_t \\ r_{D1} &= -[(L_0 + L_2)C_2 + L_0C_t + L_1C_1] \end{aligned}$$

When $q_{N1}^2 - 4p_{N1}r_{N1} > 0$ is built, its natural resonant frequency with higher frequency f_{DRR2} is given by

$$f_{DRR2} = \frac{1}{2\pi} \sqrt{\frac{-q_{N1} + \sqrt{q_{N1}^2 - 4p_{N1}r_{N1}}}{2p_{N1}}} \quad (2)$$

The external quality factor Q_{e_DRR2} of lumped-element dual-resonance resonator at f_{DRR2} can be expressed by

$$Q_{e_DRR2} = Z_0 \pi f_{DRR2} \left. \frac{\partial [\text{Im}(Y_{in_DRR})]}{\partial f} \right|_{f=f_{DRR2}} \quad (3)$$

where $Z_0 = 50 \Omega$ is the port impedance.

The input admittance Y_{in_LC} of $L_b C_b$ resonator can be derived as

$$Y_{in_LC} = \frac{1 - \omega^2 L_b C_b}{j\omega L_l [1 - \omega^2 (L_b - L_l) C_b]} \quad (4)$$

The natural resonant frequency f_{LC} of $L_b C_b$ resonator is calculated by

$$f_{LC} = \frac{1}{2\pi \sqrt{L_b C_b}} \quad (5)$$

The external quality factor Q_{e-b} of $L_b C_b$ resonator can be written as

$$Q_{e-b} = Z_0 \pi f_b \left. \frac{\partial [\text{Im}(Y_{in_LC})]}{\partial f} \right|_{f=f_b} \quad (6)$$

B. LP-BP Diplexer Design

Step 1: 0.9 GHz LPC Design. The circuit model of ideal 5th-order lowpass filter (LPF) is shown in Figure 2, and the $L_2 C_2$ branch in Figure 1(a) is not included for analysis simplicity.

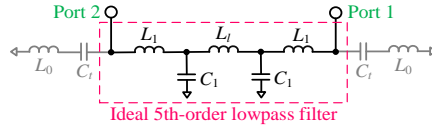


Figure 2. Circuit model of ideal 5th-order LPF.

First of all, the series $L_0 C_1$ circuit is temporarily removed from this 5th-order LPF, then the values of L_1 , C_1 and L_l are calculated by

$$L_1 = \frac{\Omega_c \gamma_0 g_1}{\omega_c} \quad (7a)$$

$$C_1 = \frac{\Omega_c g_2}{\omega_c \gamma_0} \quad (7b)$$

$$L_l = \frac{\Omega_c \gamma_0 g_3}{\omega_c} \quad (7c)$$

where $\Omega_c = 1 \text{ rad/s}$, $\gamma_0 = 50$, $\omega_c = 2\pi f_c$, which f_c is the cutoff frequency and g_{1-3} are the lumped circuit element values of the lowpass prototype filter referred to [10]. This 5th-order LPF is designed for a Chebyshev frequency response and a 28 dB return loss (RL), $f_c = 0.675 \text{ GHz}$ is chosen to acquire f_{c-3dB} around 0.9 GHz. $L_1 \approx 8.4 \text{ nH}$, $C_1 \approx 6 \text{ pF}$ and $L_l = 18 \text{ nH}$ can be then derived as using the lowpass transformation method [10]. The frequency response of 5th-order LPF without series $L_0 C_1$ circuit is shown in Figure 3 by the dash line.

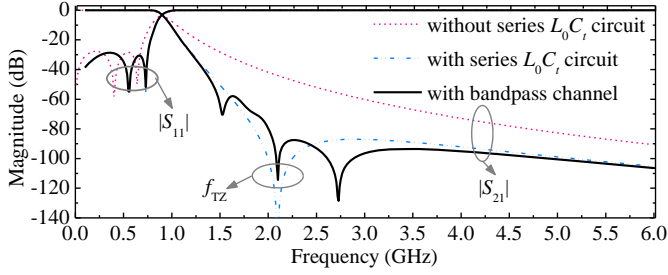


Figure 3. Frequency response of 5th-order LPF with or without series L_0C_t circuit, and LPC of LP-BP diplexer.

After the series L_0C_t circuit, which produces the virtual grounds at the connected points is considered in the 5th-order LPF. It will result in a transmission zero (TZ). The frequency location of this TZ, f_{TZ} is determined by

$$f_{TZ} = \frac{1}{2\pi\sqrt{L_0C_t}} \tag{8}$$

$C_t = 2.4$ pF can be calculated after $L_0 = 2.4$ nH is preset and $f_{TZ} = 2.1$ GHz is set in this design. The frequency response of 5th-order LPF is affected by series L_0C_t circuit. It is verified that the values of L_1 and C_1 can be optimized to acquire the desired 5th-order LPF performance. In this design, firstly $L_1 = 14.4$ nH is selected so that the corresponding return loss (RL) is better than 20 dB within lowpass passband, and then $C_1 = 6.6$ pF is selected to meet the return loss (RL) requirement of better than 28dB. Interestingly, we find that 3dB cutoff frequency (f_{c-3dB}) is obtained around 0.9 GHz in the present case. The final frequency response of 5th-order LPF with series L_0C_t circuit is plotted in Figure 3 by the dash-dot line.

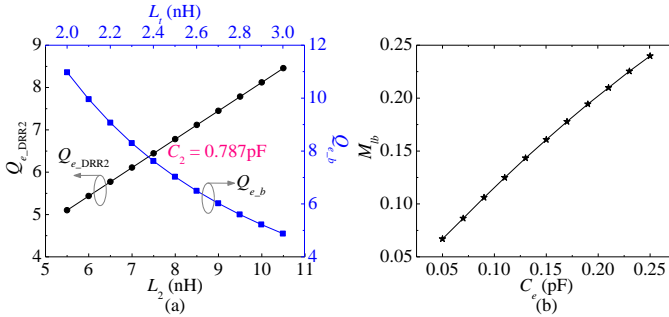


Figure 4. Extracted Q_{e_DRR2} , Q_{e_b} and M_{lb} of lowpass-bandpass diplexer.

Step 2: 1.8 GHz BPC Design. The lumped-element dual-resonance resonator and L_bC_b resonator will build the passband with bandpass response by the coupling capacitor C_e which is actually served as a J -inverter in this case. The ripple bandwidth (RBW) and return loss (RL) of BPC is specified as $RBW = 225$ MHz and $RL = 20$ dB. For an ideal second-order BPF, the external quality factor Q_e^{lb} and the coupling coefficients M_{lb} can be acquired as $Q_e^{lb} = 6.83$ and $M_{lb} = 0.12878$ [10]. There are various combinations of L_2 and C_2 which can meet the $f_{DRR2} = 1.8$ GHz. Figure 4(a) shows the extracted Q_{e_DRR2} versus C_2 with fixed $f_{DRR2} = 1.8$ GHz. $L_2 = 8$ nH and $C_2 = 0.787$ pF are calculated to meet $Q_e^{lb} = Q_{e_DRR2}$ and $f_b = f_{DRR2}$. After $C_b = C_2$ is preset, $L_b = 9.9339$ nH can be calculated by Eq. (5). The relationship between the variation of Q_{e_b}

and L_t is also shown in Figure 4(a), to meet the condition that $Q_e^{lb} = Q_{e-b}$, $L_t = 2.54$ nH is chosen. The variation trend of extracted M_{lb} relative to C_e is plotted in Figure 4(b) and $C_e = 0.12$ pF is preselected to acquire the required M_{lb} . In addition, considering the influence of parallel negative capacitances in the J -inverter, the design parameters of proposed LP-BP are further optimized. The values of these parameters summarized as $L_0 = 2.4$ nH, $L_1 = 14.4$ nH, $C_1 = 6.6$ pF, $L_l = 18$ nH, $C_l = 2.4$ pF, $L_2 = 8$ nH, $C_2 = C_b = 0.667$ pF, $L_b = 11.1$ nH, $C_e = 0.119$ pF and $L_t = 3$ nH. The solid line in Figure 3 plots the LPC of proposed LP-BP diplexer. It can be observed from Figure 3 that the out-band performance of LPC is improved with extra two TZs introduced by the BPC due to the increased signal transmission paths, and the effect of BPC on LPC is minor because the responses of $|S_{11}|$ and $|S_{21}|$ are basically the same with or without BPC.

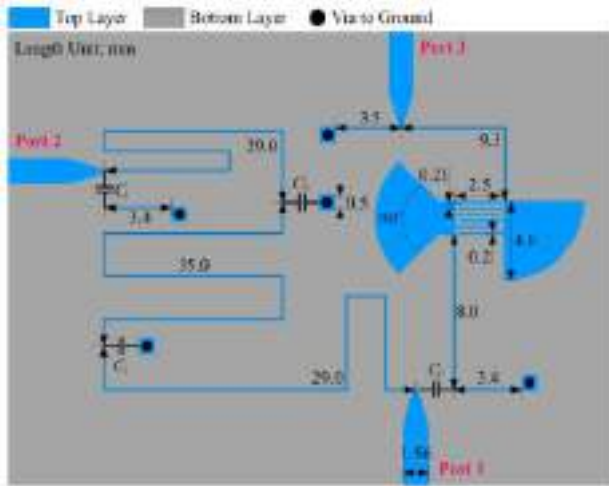


Figure 5. Physical layout of designed LP-BP diplexer (not to scale).

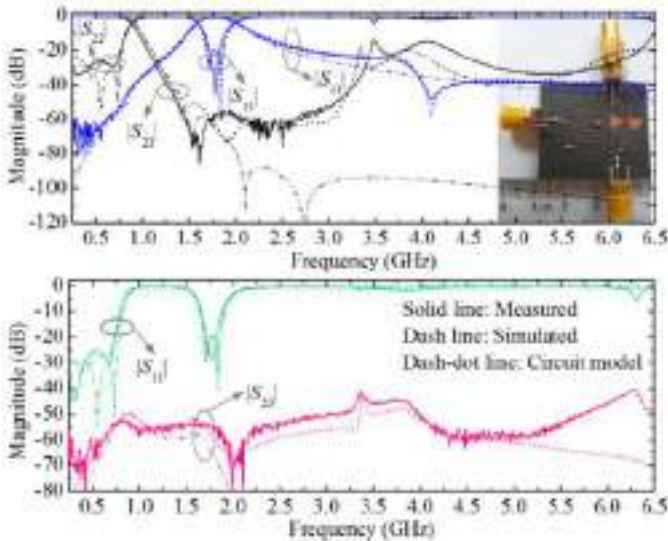


Figure 6. Simulated and measured results of fabricated LP-BP diplexer.

3. Simulated and Measured Results

Figure 5 shows the physical layout of designed LP-BP diplexer. This design was fabricated on a Rogers RT/duroid 5880 substrate, which $h = 0.508$ mm, $\epsilon_{re} = 2.2$ and $\tan\delta = 0.0009$. Its circuit realization approach can refer to the work [11]. Figure 5 also notes the physical dimensions of the final optimization. The illustration is shown in top right of Figure 6 is the photograph of fabricated LP-BP diplexer, it occupies the circuit area of $0.103 \times 0.063 \lambda_{gd}^2$ excluding the feeding lines, and the physical dimensions is $34 \times 21 \text{mm}^2$. λ_{gd} is the wavelength of 50Ω microstrip line at 0.9 GHz on the Rogers RT/duroid 5880 substrate.

Figure 6 plots the simulated and measured results of fabricated LP-BP diplexer. The LPC measured results of 3dB cutoff frequency (f_{c-3dB}) is 0.87GHz, in-band insertion loss (IL) is 0.3dB, return loss (RL) is better than 20dB. The BPC measured results of central frequency (CF) is 1.78GHz, 3dB fractional bandwidth (FBW) is 20.1%, in-band insertion loss (IL) is 0.65dB, and return loss (RL) is 20dB. The common port return loss (RL) is also better than 20 dB within two passbands, and the isolation between lowpass and bandpass channels are better than 52dB. Table 1 shows a comparison performance between the references [1~3] and this work.

Table 1. Comparison between the references and this work

	[1]	[2]	[3]	This work
fc_3dB and CF (GHz)	1.07/2.45	1.0/1.7	1.5/2.4	0.87/1.78
3dB FBW (%)	7.7	8.5	7.6	20.1
IL of LPC / BPC(dB)	0.8/2.1	0.53/2.08	0.25/2.42	0.3/0.65
Isolation(dB)	40	37	35	52
Circuit size (mm ²)	70×42	74×40	97×62	34×21

4. Conclusion

A 0.9 / 1.8 GHz LP-BP diplexer is presented by using lumped-element dual-resonance resonator and LC resonator, and the design procedures are introduced in detail. The proposed LP-BP diplexer exhibits high return loss (RL), insertion loss (IL), high isolation and compact circuit size. Owing to these excellent electrical performances, the proposed structure has a bright prospect in the fields of signal synthesis and distribution.

References

- [1] Chen FC, Qiu JM, Hu HT, Chu QX, Michael JL. Design of microstrip lowpass-bandpass triplexer with high isolation. *IEEE Microwave and Wireless Components Letters*, 2015 Dec; 25(12):805-7.
- [2] Tu WH, Wu CL. Design of microstrip low-pass-bandpass multiplexers using distributed coupling technique. *IEEE Transactions Components, Packaging and Manufacturing Technology*, 2016 Nov; 06(11):1648-1655.
- [3] Deng PH, Tsai JT. Design of microstrip lowpass-bandpass diplexer. *IEEE Microwave and Wireless Components Letters*, 2013 Jul; 23(7):332-4.
- [4] Yang T, Chi PL, Itoh T. High isolation and compact diplexer using the hybrid resonators. *IEEE Microwave and Wireless Components Letters*, 2010 Oct; 20(10):551-553.
- [5] Chen CF, Huang TY, Chou CP, Wu RB. Microstrip diplexers design with common resonator sections for compact size, but high Isolation. *IEEE Transactions on Microwave Theory and Techniques*, 2006 May; 54(5):1945-1952.

- [6] Zeng SJ, Wu JY, Tu WH. Compact and high-isolation quadruplexer using distributed coupling technique. *IEEE Microwave and Wireless Components Letters*, 2011 Apr; 21(4):197-199.
- [7] Carceller C, Soto P, Boria V, Guglielmi M, Gil J. Design of compact wideband manifold-coupled multiplexers. *IEEE Transactions on Microwave Theory and Techniques*, 2015 Oct; 63(10):3398-3407.
- [8] Wu JY, Hsu KW, Tseng YH, Tu WH. High-isolation microstrip triplexer using multiple-mode resonators. *IEEE Microwave and Wireless Components Letters*, 2012 Apr; 22(4):173-175.
- [9] Xu J, Wu W, Wei G. Novel dual-band bandpass filter and reconfigurable filters using lumped-element dual-resonance resonators. *IEEE Transactions on Microwave Theory and Techniques*, 2016 May; 64(5):1496-1507.
- [10] Hong JS, Michael JL. *Microstrip Filters for RF/Microwave Applications*. New York: Wiley, 2001.
- [11] Bahl IJ. *Lumped Elements for RF and Microwave Circuits*. Boston: Artech House, 2003.

Low Time-Complexity Chaotic Image Encryption Algorithm Based on Plaintext Information

Nianhang TANG^{a,b,1}, Zeming WU^c and Peng GUO^a

^a*School of Electronic Information and Communications, Huazhong University of Science and Technology, China*

^b*State Key Laboratory of Digital Household Appliances, China*

^c*Electronic Engineering College, Heilongjiang University, China*

Abstract. Based on plaintext information, a dynamic chaotic color image encryption algorithm is proposed as a solution for the security problem in image data transmission. Comparatively, the existing one has the characteristics of high key acquisition complexity and low encryption speed. Firstly, normalize the RGB components of the images so as to obtain the dynamic key associated with the plaintext, which encrypts images with any shape by rearranging and combining pixels from the original image. Secondly, the parameter offset key is introduced as the initial parameter of the logistic map to generate a high-precision chaotic encryption sequence. The chaotic value sequence is stored for disordered pixels according to the image size, and enlarged and rounded to enhance the pixel value diffusion of the original image. Finally, RGB components are fully fused and uniformly distributed to form a completely encrypted image. According to the experimental results and security analysis, the proposed algorithm is effective against differential attacks, with low complexity, high efficiency, and faster encryption speed.

Keywords. Chaotic System, Dynamic Keys, Arbitrary image encryption, Plaintext correlation, Low time-complexity

1. Introduction

It is convenient for people to use cloud computing and Internet of Things technology because of its rapid development, for example, people can retrieve the needed information from many images easily and quickly. However, with a large amount of data transmission in the network, privacy information leakage and other security issues, the study of how to protect images and transmit information quickly becomes an important topic. To protect digital image transmission security, it is commonly used as a digital image encryption method, such as traditional RSA and DES encryption algorithms that are to encrypt text information [1, 2]. Nevertheless, the technology doesn't apply to video and

¹Corresponding Author: Nianhang TANG, State Key Laboratory of Digital Household Appliances, Qingdao 266101, China; School of Electronic Information and Communications, Huazhong University of Science and Technology, Wuhan 430074, China; E-mail: tangnianhang@163.com

image information that contain a lot of data, nor does it guarantee its security [3]. Hence, chaos theory is extensively implemented in image encryption since it is non-periodic, sensitive to initial values, and unpredictable. So far, there have been many encryption results that combine chaos with other algorithms, such as the encryption algorithm that combines a chaotic system with DNA coding in order to make encrypted images more secure [4–6]. Nonetheless, after various studies, it is shown that the performance of encrypting images by DNA coding alone is relatively low and cannot resist selective plaintext attacks. To enhance image processing speed, the image can be compressed before it is encrypted, because compression and encryption are tightly coupled [7, 8], but image encryption algorithms, including the compression step encryption algorithm, are not suitable for schemes that require high data accuracy.

To solve some problems, an image encryption algorithm is proposed based on the above documents, which is highly secure and has a low complexity. In this way, a discrete Logistic chaotic map is designated to make the encryption algorithm more efficient and faster. Image encryption relies on both the plaintext image, as well as the offset key introducing some initial parameters to the logical chaotic map. It is possible to significantly increase the key space of the encryption algorithm without increasing the chaotic system's size, as well as improve its performance against differential attacks. Scrambling and diffusion of images are performed with the key generated by a chaotic system, which dramatically reduces the number of encryption keys to be obtained and makes the encryption algorithm more efficient. Since the image pixels are rearranged during the encryption process, the proposed encryption algorithm can encrypt images of any shape.

2. Basic theory and encryption algorithm

2.1. Logistic Chaotic Mapping

This section introduces the logical chaotic system used in the paper [9], which is also called an unimodal image. Described by a quadratic polynomial map (recursive relationship), it is often used to demonstrate how chaotic phenomena can derive from nonlinear dynamic equations. According to Eq.(1), logical mapping can be expressed mathematically as follows :

$$X_{n+1} = \mu X_n (1 - X_n) \quad (1)$$

in this case, $\mu \in [0, 4]$ is called the Logistic parameter. It is shown that when $X_n \in [0, 1]$, and $3.5699 < \mu \leq 4$, the logical map is in a chaotic state, this means that the sequence generated by the logistic mapping is acyclic and non-convergent. The generated sequence $\{X_k, k = 0, 1, 2, 3, \dots\}$ is noncyclic and non-convergent when it is outside this range. Therefore, image encryption requires a more random algorithm, which is sensitive to the initial value.

2.2. Encryption Algorithm

To achieve a better encryption effect and fully use plaintext information and a Logistic chaotic map, a color image chaotic encryption algorithm is proposed in this paper that has low complexity and high security when compared to plaintext encryption. With the

following algorithm steps, the proposed encryption algorithm is able to encrypt any size shape. The encryption process is shown in Figure 1.

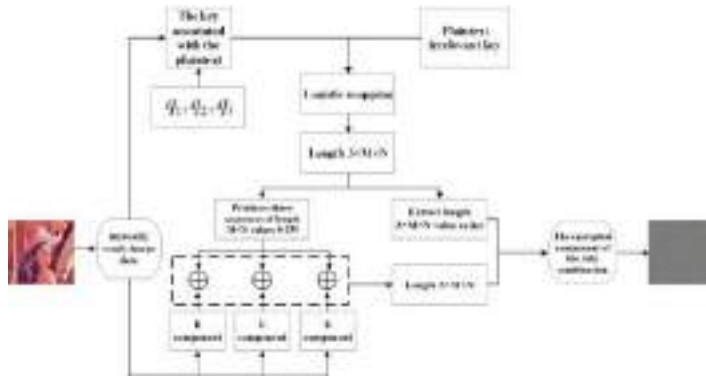


Figure 1. Encrypted block diagram

Step 1: Extract the RGB component of a color image of an $M \times N (M \neq N)$ size, and convert the extracted RGB to a matrix of three 8-bit binary numbers: I_1, I_2, I_3 .

Step 2: Normalize the generated matrix to generate three plain-text related keys: a_1, a_2, a_3 , and these three values are multiplied by each other to form the plain-text key. The key obtained here is the dynamic key. Depending on the read images, the obtained key changes dynamically, i.e., it changes with the image.

Step 3: Convert the matrix generated by the color image into 1 row $M \times N$ column and save it as I_R, I_G, I_B .

Step 4: μ', a'_0 are the keys independent of the plaintext of the chaotic system. The logistic mapping is initialized with values and parameters generated by (2) and (3). According to the above conditions, a chaotic order x with a length of $(M \times N \times 3 + \text{floor}(a_3 \times 10000))$ is generated, which will be generated in this step and in the above steps, $\mu', a'_0, a_1, a_2, a_3, q$ are transmitted to the decryption end as symmetric keys.

$$\mu'_1 + q_1 a_1 = \mu \tag{2}$$

$$a'_0 + q_2 a_2 = a_0 \tag{3}$$

Step 5: For the sequence x generated after step 4, a chaotic sequence has a length of $M \times N \times 3$ is intercepted from the $\text{floor}(a_3 \times 10000)$ -th bit of the chaotic sequence x , and this chaotic sequence scrambles the pixel positions with a value order of $L(i)$.

$$[A, L] = \text{sort}(x) \tag{4}$$

Step 6: There are three sequences, $R(i), G(i)$ and $B(i)$, with length of $M \times N$ divided by the chaotic sequence which the length is $M \times N \times 3$ obtained in step 5. After taking the these three segments' values according to Eq.(5), they are respectively used as the sequence of RGB components of encrypted color image.

$$(a(i) \times p) \bmod 256 \tag{5}$$

where, the value of a(i) is R(i), G(i), B(i); Considering that the value of the encryption sequence between 0-255, the value of p should be greater than 1000. In this paper, the value of p is 10000.

Step 7: XOR the sequences R(i), G(i), B(i) generated in step 6 with the corresponding I_R, I_G, I_B to the encrypted image data E_1, E_2, E_3 .

Step 8: Connecting E_1, E_2, E_3 produces a sequence E with length $M \times N \times 3$.

Step 9: Use the position sequence L(i) generated in step 5 to scramble the position of the data in sequence E (if the transmission problem is considered, it can be transmitted after this step), and convert the scrambled sequence into three $M \times N$ matrices in order.

Step 10: Will get three matrices merged to form the final encrypted image.

2.3. Decryption Scheme

An algorithm for image encryption is proposed based on symmetric cryptography, and the decryption algorithm belongs to the inverse process encryption algorithm. In this decryption process of the encrypted image, it is crucial to obtain the chaotic sequence to determine the pixel position. Here, we use $[A, B] = \text{sort}(x)$ twice to generate the sequence of restoring the original image position.

3. Simulation Experiments and Performance Analysis

After encrypting and decrypting a plurality of color images according to the steps shown in Sect. 2.2, image encryption algorithm enactment is examined in Windows 10 environment with an operating system of 2.5 GHz Intel CPU I5-4200U, 4 GB RAM, and Matlab 2020b.

3.1. Encryption and Decryption Analysis

In this section, Lena (512x512) and a portion of Splash (260x512) are used to evaluate the mentioned algorithm's performance. In the encryption and decryption process, the keys are chosen as $a'_0 = 0.02456$ and $\mu'_0 = 3.015$, with the constant $q_1 = q_2 = q_3 = 1$, and show these encryption and decryption results using this algorithm. In Figures 2-3, we show how it encrypts and decrypts an images of any size, obscuring the original image's information completely, which indicates its high security.

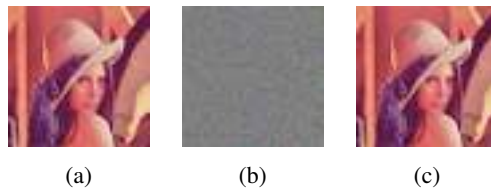


Figure 2. The Lena (512 × 512) image consists of a set of the original image (a) , encryption image (b), and decrypted image (c).

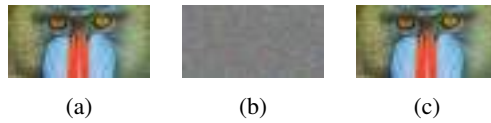


Figure 3. The Splash (260 x 512) image consists of a set of the original image (a) , encryption image (b), and decrypted image (c).

3.2. Histogram Analysis

In Figure 4 and 5, they show the histograms of Lena images, Splash and their corresponding cryptograms, respectively. They also show that the histogram pixel values of the original image will be centered within a specific range of values. Compared with the histogram of the original image, that of the encrypted image is more uniform, which shows that the proposed encryption method has a good performance in resisting statistical attacks.

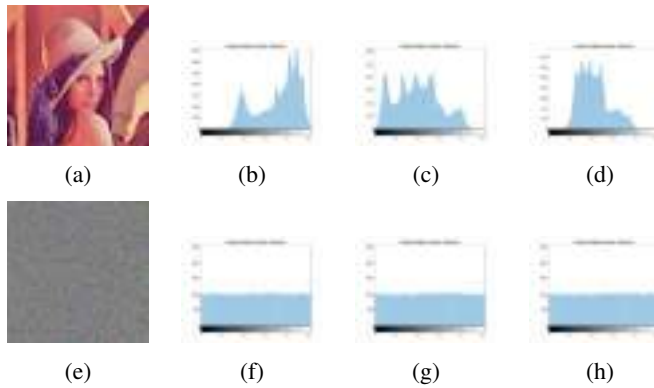


Figure 4. Original histograms of Lena (a) in the red (b), green (c), and blue (d) components; Encrypted histograms of Lena (e) in the red (f), green (g), blue (h) components.

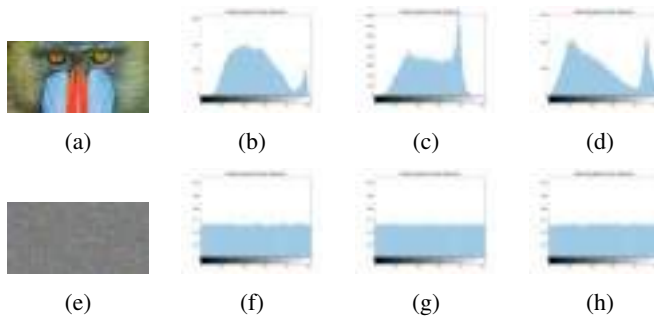


Figure 5. Original histograms of Splash (a) in the red (b), green (c), and blue (d) components; Encrypted histograms of Splash (e) in the red (f), green (g), blue (h) components.

3.3. Correlation Analysis

The image encryption algorithm could improve the correlation by dislocating and diffusing images with chaotic logistic sequences, and good permutation is measured by the correlation coefficient. This section analyzes a before and after image of encryption by Eq.(6).

$$r(X, Y) = \frac{cov(X, Y)}{\sigma(X)\sigma(Y)} \tag{6}$$

There is a covariance among X and Y, and $\sigma(\cdot)$, determined by $cov(X, Y)$. Accordingly, Y is composed of horizontal, vertical, and diagonal pixels, and $r(x)$ is composed of the horizontal, vertical and the diagonal correlation coefficients. $r(x)$ is used to determine the correlation coefficient for two adjacent pixels. The correlation is high if $r(x)$ approaches 1, and very low if $r(x)$ approaches 0. The correlation of encrypted images is shown in Table 1.

Table 1. Correlation comparison of adjacent pixels of RGB components of the original image and the encrypted image

		Horizontal correlation	Vertical correlation	Diagonal correlation
Lena	R	-0.0038989	0.0091044	0.008476
encrypted image	G	0.0023145	-0.0053152	-0.0056106
(512 × 512)	B	-0.008546	-0.0081218	-0.0072199
Splas	R	0.0016928	-0.0071815	0.0037677
encrypted image	G	0.0032405	-0.0078424	0.0055903
(260 × 512)	B	0.01608	0.0063418	0.003174
Lenas	R	0.0016	0.0041	-0.0089
Literature [4]	G	-0.0071	0.0043	-0.0071
(512 × 512)	B	-0.0031	-0.0023	-0.0047
Literature [8]	Average correlation	0.0116133	0.0125545	0.0218114

3.4. Information Entropy

In this section, this information entropy is calculated for a genuine image pixel value before and after encryption. Information entropy increases as the illness level of the image increases, and vice versa. Chaos level, on the other hand, increase the encryption effect and make algorithms more secure. As a result, information entropy can be expressed as tails.

$$H = - \sum_{i=0}^L p(i) \log_2 p(i) \tag{7}$$

where L is the image's gray level and $p(i)$ is the probability of occurrence of gray value i . It can be seen in Table 2—information entropy of the original image of Lena image and the encrypted image.

Table 2. Information entropy comparison of RGB components of original image and encrypted image.

Information entropy	R	G	B
Lena(512×512)	7.9993	7.9992	7.9993
Splas(260×512)	7.9987	7.9987	7.9986
Literature [6]	7.9900	7.9900	7.9901
Literature [7]	Average	information entropy	7.9989

As shown in Table 2— information entropy of the original Lena image and the encrypted image, L is the gray level, and $p(i)$ is the probability that gray value i will occur. In Table 2, it illustrates that as pixels increase, the encryption image's information entropy increases as well. From the information comparison in Table 2, by encrypting the exact sized image, this paper's encryption algorithm has higher information entropy than other algorithms in the literature.

3.5. Encryption Speed

Time complexity is a significant tool for evaluating the efficiency of encryption algorithms [10]. The total time calculation includes the time of chaotic sequence generation and the time of image dislocation and diffusion. In Table 3, encryption and decryption time, the comparison with the running time of other algorithms and itself are shown in the literature. It can be seen from the literature that with the steady improvement of the hardware processing capability, the operating cycle and processing speed of the encryption algorithm will be improved.

Table 3. Comparison of encryption and decryption time for images of different sizes and algorithms.

	Encryption time	Decryption time
Tree(256 × 256)	0.231710	0.239642
Lena(512 × 512)	0.360589	0.399276
Splas(260×512)	0.262001	0.290575
literature [8] gray image (512 × 512)	0.296	-
literature [11] Lena	2.090	-
literature [12] (512 × 512)	0.62	-
literature [10] color image (512 × 512)	1.76	1.54

From Table 3, as the time of encryption and decryption in the image encryption system varies with the environment, hardware or software, and system configuration, which directly compares with the encryption time of different algorithms is not rigorous. Therefore, this paper analyzes all steps of the computational complexity of the proposed image

encryption algorithm, including pseudo-random sequence generation, scrambling, and diffusion steps during encryption/decryption. Table 4 compares the calculations in this paper and other literatures.

Table 4. Computational complexity comparison

Algorithm	Computation complexity
Proposed	$O(3 \times M \times N)$
literature [13]	$O(24 \times M \times N)$
literature [14]	$O(24 \times M \times N)$
literature [15]	$O(8 \times M \times N)$
literature [16]	$O(4(M \log N + M + N))$

4. Security Analysis

In this section, different methods of verifying the security of our method of image encryption are shown in this section. Using the same encryption algorithm, the encryption results of images of different sizes are the same. As shown in Section 3, this section selects the familiar Lena graph as the image for the study of encryption algorithm security.

4.1. Key Space Analysis

When the key Space is more extensive, brute-force cracking can be excluded more easily, and the time required to crack the key becomes greater. Using the algorithm submitted, there are two domains of key space: one associated with the logistic chaos mapping a system and another with plain-text keys associated with the image. Keys of the logistic chaos system are μ', a'_0 ; and the one related to the plain-text consist of $q_1, q_2, q_3, a_1, a_2, a_3$. As the computer has a precision of (10^{15}) , and there are 8 keys in total, the key space proposed in this paper is $(10^{15})^8 = 10^{120}$, which is greater than 2^{100} . As a result, brute force cracking can actually be avoided by the algorithm.

4.2. Key Sensitivity Analysis

The more sensitivity the key, the more secure the algorithm. This paper chooses key μ' in order to test the encryption algorithm's key sensitivity. Since the key effect of the sensitivity test is the same for any image, in this section, select the Lena image (512 x 512). Since the computer can handle the accuracy of 10^{-15} , the value of μ is increased by 10^{-15} in this paper, and the decrypted image is observed as shown in Figure 6. The images show that any slight modification of the key cannot be decrypted accurately, suggesting that the encryption algorithm has restorative key sensitivity.



Figure 6. A key sensitivity test is performed on the following images: (a) The original image; (b) The encrypted image; (c) Decrypting the image correctly; (d) Decrypting the image after the key has been changed.

4.3. Differential Attacks

In this section of the proposed algorithm, differential attack resistance is tested. NPCR that is Number of Pixel Change Range and UACI that is Uniform Average Change Intensity are used to perform experiments on multiple image, defined as follows:

$$\begin{cases} NPCR = \frac{1}{M \times N} \sum_{i=1}^M \sum_{j=1}^N D(i, j) \\ UACR = \frac{1}{M \times N} \sum_{i=1}^M \sum_{j=1}^N \frac{|C1(i, j) - C2(i, j)|}{255} \end{cases} \quad (8)$$

Here, according to the examination manner check in publication. [17]. Firstly, the initial image is encrypted to accept a cryptographic image C1. Next, specify and modify a value in the initial image to be C2. Finally, the NPCR and UACI are estimated by Eq.(8) estimates the NPCR and UACI. As shown in Table 5, this paper's encryption algorithm has NPCR values greater than 0.9965 and UACI values in the range of (0.3335, 0.3352). From Table 5, it can be seen that the encryption algorithm provided in this paper has

Table 5. Differential attack analysis

	NPCR			UACI		
	R	G	B	R	G	B
Lena(512×512)	0.9961	0.9962	0.9960	0.3335	0.3343	0.3342
Tree(256*256)	0.9960	0.9961	0.9956	0.3339	0.3335	0.3341
Splas(260×512)	0.9962	0.9960	0.9962	0.3342	0.3339	0.3352
Literature [17] Lena (256×256)	0.99611	0.99627	0.99616	0.33400	0.33329	0.33483
Literature [18] Tree (256×256)	0.9962	0.9963	0.9962	0.3353	0.3343	0.3339
Literature [5] Baboon (256×256)	Average	NPCR	0.99617	Average	UACI	0.33474

NPCR values greater than 0.9960 and UACI values within the range of (0.3335, 0.3352). The ideal values of UACI and NPCR for image encryption anti-attack test are 33.4635% and 99.6094%, respectively, for the image encryption anti-attack test. Hence, this paper presents an image encryption algorithm that can resist the differential attack, indicating that it is effective at preventing that.

5. Conclusion

Using plaintext data for image encryption with attached size, a low-time-complexity chaotic encryption algorithm is presented in this paper. In addition, the key space of

reaches 10^{120} . Since the initial values and parameters of logistic mapping are connected with the plaintext, this algorithm has higher security than other algorithms. As a result, the encryption key is generated dynamically, and it is possible to create nonlocal keys for each image, enhancing the algorithm's resistance to differential attacks significantly. Through simulation experiments and investigations, we found that this algorithm not only ensures the security of the encryption algorithm, but also ensures the efficiency of encryption. In the future, through the modification and optimization of the algorithm and the continuous improvement of the hardware processing qualification, color image encryption will be used to transmit real-time images with high security requirements in this paper.

References

- [1] Zhang Li, Wu Wenling, Zhang Lei, Zheng Yafei, Key recovery attack based on exchange equivalence reduction round AES-128, *Computer research and development*, 58 (10): 2213-2221(2021)
- [2] Gao F . Data encryption algorithm for e-commerce platform based on blockchain technology, *Discrete and Continuous Dynamical Systems*,12(4 and 5),1457-147(2019)
- [3] Zhang X, Wang L, Cui G ,et al. Entropy-Based Block Scrambling Image Encryption Using DES Structure and Chaotic Systems, *International Journal of Optics*, 2019(5),1-13(2019)
- [4] Yuan Li, Xie Li, long Ying, Hu chungiang, Jiang Taojin, Color image chaotic encryption algorithm based on hash and DNA coding, *Journal of Chongqing University*, 44 (07), 55-63(2021)
- [5] Cun Q, Tong X, Wang Z, et al. Selective image encryption method based on dynamic DNA coding and new chaotic map, *Optik-International Journal for Light and Electron Optics*, 2021(3),167286
- [6] Niu Ying, Zhang Xun CAI, Image encryption based on variable step Joseph traversal and DNA dynamic coding, *Journal of electronics and information*, v.42 (06), 84-92(2020)
- [7] Es A, Rw B, Aks B, Securing color image transmission using compression-encryption model with dynamic key generator and efficient symmetric key distribution, *Digital Communications and Networks*, 2020
- [8] Zhang Miao,Tong Xiaojun,Wang Zhu,Chen Penghui, Joint Lossless Image Compression and Encryption Scheme Based on CALIC and Hyperchaotic System, *Entropy*,23(8), 2021
- [9] Belazi A, El-Latif A, Belghith S, A novel image encryption scheme based on substitution-permutation network and chaos, *Signal Processing*, 128(Nov.), 155-170(2016)
- [10] T J anani, Brindha M . A secure medical image transmission scheme aided by quantum representation, *Journal of Information Security and Applications*, 59(1-3), 102832(2021)
- [11] Khan, M., Alanazi, A.S., Khan, L.S. et al. An efficient image encryption scheme based on fractal Tromino and Chebyshev polynomial. *Complex Intell. Syst.* 7, 2751-2764 (2021).
- [12] Wang X , Gao S , Image encryption algorithm based on the matrix semi-tensor product with a compound secret key produced by a Boolean network, *Information Sciences*, 539(9),195-214(2020)
- [13] Panwar, K., Purwar, R.K., Jain, A.: Cryptanalysis and improve- ment of a color image encryption scheme based on DNA sequences and multiple 1D chaotic maps. *Int. J. Bifurc. Chaos* 29(08), 1950103 (2019)
- [14] Wu, X., Kan, H., Kurths, J.: A new color image encryption scheme based on dna sequences and multiple improved 1d chaotic maps. *Appl. Soft Comput.* 37, 24-39 (2015)
- [15] Mondal, B., Behera, P.K. and Gangopadhyay, S. A secure image encryption scheme based on a novel 2D sine-cosine cross-chaotic (SC3) map. *J Real-Time Image Proc* 18, 1-18 (2021).
- [16] Zhongyun Hua, Fan Jin, Binxuan Xu, Hejiao Huang, 2D Logistic-Sine-coupling map for image encryption, *Signal Processing*, 149, 148-161(2018)
- [17] Wu Zeming,Pan Ping,Sun Chunyang,Zhao Bing. Plaintext-Related Dynamic Key Chaotic Image Encryption Algorithm, *Entropy*, 23(9), 2021
- [18] Zhou Shuang,Wang Xingyuan,Wang Mingxu,Zhang Yingqian. Simple colour image cryptosystem with very high level of security, *Chaos, Solitons and Fractals*, 141(2020)

Research on Security Sharing Model System of Power Digital Spatial Data

Aijun WEN, Zesan LIU, Di LIU, Chenghua FU¹ and Ziting GAO
State Grid Information and Telecommunication Group Co., Ltd., Beijing, 100032,
China

Abstract. Digital transformation will promote the rapid progress of power digital space construction led by power data. Through the use of new digital information technology, we will give full play to the function of data integration and effectively support the construction of new power system. Data interconnection is the key link to release the value of data, but at present, there are still many urgent problems to be solved in the power digital spatial data sharing, such as the mismatch between data demand and data supply, weak security guarantee and so on. In order to study the security protection of power digital spatial information data sharing, according to the concept of privacy computing, a power digital spatial data security sharing model system based on privacy computing is designed. This model system has strong research and practical significance for realizing the secure circulation and sharing of new power system data.

Keywords. Power digital space, new power system, data security sharing, privacy-preserving computation.

1. Introduction

Through the application of a new generation of digital technology, the power digital space plays the role of data integration, realizes real-time mapping of new power systems, flexible and efficient allocation of power grid resources, and extensive aggregation of massive resources. How to effectively manage power grid data, do a good job in power grid data sharing, and give full play to the maximum value of new power system information resources is the basis for promoting the construction of power digital space. In data resource sharing, there are still problems such as difficulty in mutual trust between shared participants, high data security risks, weak protection of private information, and unclear data ownership [1]. The large limitation has become a key problem that urgently needs to be solved in the current data resource sharing [2]. In order to achieve a balance between data sharing applications and data privacy security protection, privacy computing has gradually entered the vision of the data industry. The privacy computing technology [3-7] guarantees the "available and invisible" of data in the process of circulation and fusion, so as to meet the needs of industrial development for the circulation of data elements under the premise that the private data is fully protected.[8-13]

¹ Corresponding author: Chenghua FU, State Grid Information and Telecommunication Group Co., Ltd., Beijing, 100032, China;E-mail:fuchenghua@sgitg.sgcc.com.cn.

By analyzing the challenges faced by power digital spatial data security sharing, combined with the theory of privacy computing technology, this paper proposes a model system of power digital spatial data security sharing based on privacy computing technology.

2. Research on Security Sharing of Power Digital Spatial Data

2.1. Challenges Faced by Power Digital Spatial Data Security Sharing

The demand of new power system for data fusion, sharing, development and circulation is increasing day by day, and the importance of power data security construction is also increasing. The security sharing of power digital spatial data mainly faces the following challenges:

(1) Challenges of various data types

Power enterprise data comes from development, transmission, transformation, distribution, regulation and other activities. It is different from multi-source heterogeneous data with different format standards, frequencies and definitions related to power supply operation, equipment management, business services and enterprise information management. There are a large number of enterprise data, a variety of data caliber, differences in professional caliber data, and the data are scattered in different units, different professional application systems, the data base is not unified, and the quality is uneven.

(2) Challenges of lack of process specifications

The management of power grid companies did not have detailed compliance guidance in all links of the whole process of sharing and opening up. The standards and methods of various institutions for the sharing needs of power grid related information were different, there was no clear understanding of the overall structure of power consumption information, and the information application mechanism after information circulation was not perfect.

(3) Challenges of immature technical solutions

Power grid information data has the characteristics of large volume and fast growth. With the continuous accumulation of power grid data information, the social demand for the ability of data information public sharing security protection technology will be higher and higher. At present, a relatively mature set of privacy protection technology scheme has not been established.

The use of privacy computing technology can realize the fusion and sharing of data from different data sources, and solve the dilemma of fusion and utilization of a wide variety of data sources that cannot be efficiently used; the use of privacy computing technology can realize the sharing and use of data under the condition that the data does not exceed the threshold, and the process of data circulation "Available is invisible, but it is not desirable" to ensure data privacy and security.

2.2. Application Prospect of Privacy Computing Technology in Secure Sharing of Power Digital Spatial Data

Data security in data sharing and circulation has become the focus of extensive attention in the academic circles [14], and privacy computing has also created a strong technical foundation for the development of modern security technology[15-19]. Privacy

computing, which has the dual characteristics of privacy protection and data application, has broad prospects in the field of data circulation. The use of privacy computing can effectively solve the data security problems in the sharing of power digital spatial information, and carry out the statistics and classification of information while protecting and securing the original data. In the process of multi-party information exchange and fusion, privacy computing technology has important advantages in ensuring security.

Through the application of new generation digital technology, power digital space plays a role in data integration, promotes the development of power grid digitalization and supports the construction of new power systems. Data sharing is also the development trend of the new power system at present. Privacy computing technology has become the main guarantee of security, and has a good and broad prospect in the power digital space. The secure multi-party computing and privacy computing technology in the power digital space data sharing and financing can solve the problems of information privacy and information security such as multi-party information exchange, resource interaction, privacy protection, use rights, etc., so that a large amount of information can be used effectively, which has laid a credible security cornerstone for the construction of China's power digital space. Combined with traditional digital desensitization technology and confidentiality means, it can effectively break through information security barriers, and effectively ensure the authenticity, perfection and information security of information under the cooperation of all parties.

In the future, privacy computing technology will be widely used in the secure sharing of power digital spatial data. Using the privacy computing technology of secure multi-party computing and trusted operating environment, it can carry out efficient statistical analysis without breaking away from the private domain of power digital spatial information, so as to ensure the security of private information and achieve the safe sharing of information across domains. Through the federal learning network, the power digital spatial data can realize highly trusted joint computing, and the information can be safely shared and used. Build a cross industry resource sharing system, provide data privacy protection measures to participating enterprises, establish a good information environment, and improve the overall security management level of power digital space.

3. A New Power System Data Security Sharing Model System Based on Privacy Computing Technology

3.1. A New Power System Data Security Sharing Model System Based on Privacy Computing Technology

While carrying out data fusion and sharing and establishing power digital space business collaboration, it is necessary to ensure the security of power digital space data and maintain the rights and interests of all participants in information and data sharing. Based on privacy computing technology, build a manageable, safe and efficient power digital spatial information sharing model system (as shown in Figure 1), realize the calculation of data in encrypted state, and protect the privacy data security of all participants. The model system of power digital spatial information sharing based on privacy computing adopts a secure multi-party computing framework. Multi party computing includes various roles such as task initiator, computing party, data user, data provider, etc. in actual use, each entity can concurrently serve two or more roles. In Figure 1, the task

initiator and data user can be merged into one party, and the roles of algorithm provider, calculator and dispatcher are all played by the privacy computing platform. This model system is mainly divided into three participants: data provider (input party), data user (result user), and privacy computing platform (Computing party). All systems, platforms, units and departments of the power system, as participants in the process of data sharing and circulation, are both data providers and data users; The privacy computing platform is responsible for providing and managing data security sharing space and providing data security sharing services based on privacy computing for power digital space. In addition to data circulation and sharing among systems within the power grid, data fusion and sharing can be realized between the power grid and social third-party platforms and government platforms by relying on the privacy computing basic platform, giving full play to the value of data elements and enabling the development of digital economy.

The implementation process of multi-party security computing consists of data input, task calculation and result analysis. The participating nodes of each data provider participating in the collaborative computing task will search the required data information in the local database system according to the requirements of the computing logic, and work together to carry out collaborative computing among the dense data information flows for the secure multi-party computing task. However, in the overall process, all their plaintext data information is saved locally and not submitted to other nodes. The security of the transmitted data is ensured by the combination of multiple security protocols, and the data information is kept secret through homomorphic encryption algorithm, so that under the premise of no trusted third party, multiple main participants will not disclose the secret data information while getting the correct calculation results. Among the main participants, the term "calculation result factor" is defined. The calculation result factor refers to the signal output by the data information provider after completing a key conversion. Its essence is to protect the secret security of data.

The data analysis service provider analyzes the data read from the local database system, generates the calculation result factor (input factor) after MPC data input processing, and uploads the entry factor to the operation node of the privacy statistics platform. Each operation node performs collaborative calculation based on the entry factor, and finally submits the secret calculation result factor (output factor) to the data user. The data user decrypts the calculation result and uses it.

The privacy computing platform includes core computing system, data quality management system and computing assistant management system.

(1) Core computing system

The core algorithm system is also an important computing party in the application of privacy computing, which realizes the "input privacy" and "output privacy" that should be paid attention to in private computing. Input privacy refers to the input information and intermediate results that the main participants cannot extract and analyze without permission, and output privacy refers to the fact that the main participants cannot reverse the data results to sensitive data. The privacy computing technology adopted here is secure multi-party computing technology. [20-21]

(2) Data quality management system

Data analysis quality supervision and management provides data quality control services at all stages of data provision, analysis and application, including data analysis specification management, quality plan management, data analysis quality index management, data analysis quality evaluation, and data analysis standardization,

perfection, accuracy, unity, timeliness, uniqueness and usability shall be supervised and managed.

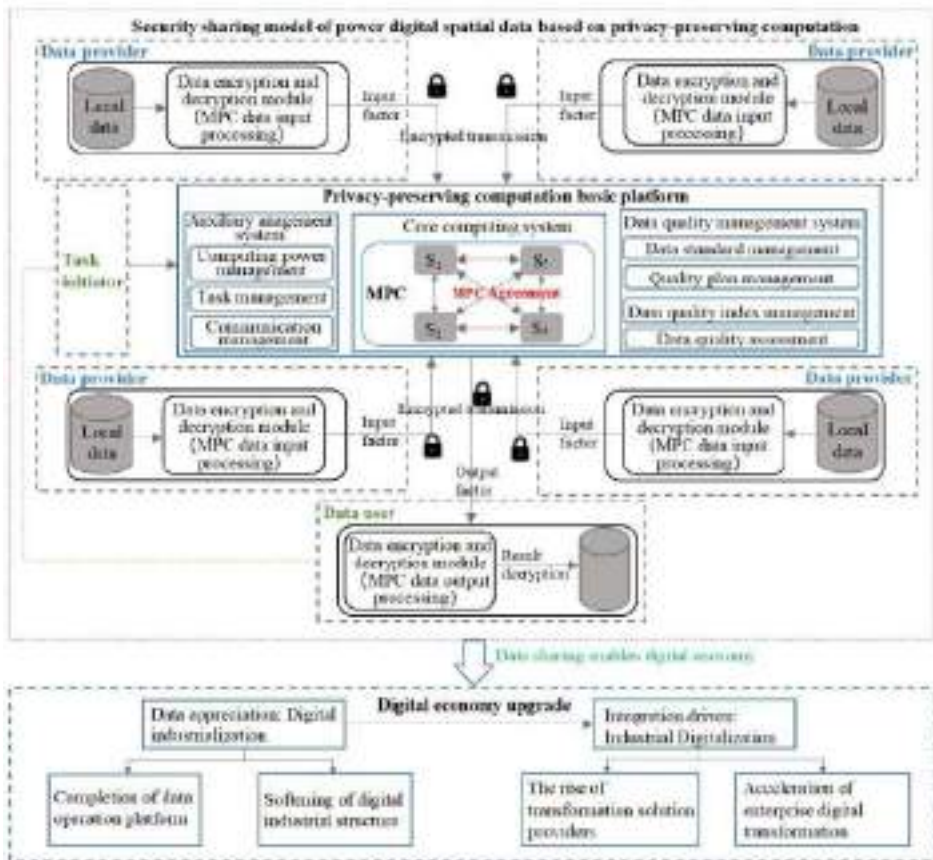


Figure 1. A model system of electric power digital spatial data safe sharing based on privacy-preserving computation

(3) Computer aided management system

Computer aided management system includes computing power management, task management and communication management. Privacy computing requires a lot of computing power. Computing power management realizes the optimal match between computing power demand and computing power resources through intelligent monitoring resources. Task management realizes task scheduling, and calculates task resources and computing resources in a balanced manner, while network control realizes scheduling control between cross platform process communications. The task scheduling part realizes the parallelization of the system, thus reducing the resource time used to complete the task [22]. Load balancing is achieved through task scheduling, and more efficient communication mechanism is used for communication scheduling, which reduces the processing time of transactions between cross platforms, thus improving the efficiency of the platform [23].

The new power system information resource sharing mode based on privacy computing technology uses the basic platform of privacy computing technology as the

intermediate medium to realize the secure cooperative resource sharing between data providers and data applications, and enable the development of digital economy.

3.2. Core Security Technology

The core information security technology used in this paper is secure multi-party computing. Secure multi-party computing (MPC)[24], the main purpose of information security multi-party computing is to overcome the problem of the ability of untrusted participants to work together under the condition of ensuring the information security of both sides [25]. The advantage of secure multi-party computing is that all participants have absolute control over their basic data to ensure the disclosure of basic data and personal information. Figure 2 is the logic diagram of secure multi-party computing. User C1 has private data x , and user Cn has private data y , and they do not know each other's data. In order to achieve cooperation between the two users, they distribute encrypted data fragments ($x_1, x_2... x_n, etc.$) to the server through secret sharing protocol; The server has several computing nodes ($S_1, S_2, etc.$) to calculate the encrypted data fragments according to the privacy computing protocol, and the calculation results are returned to the user. Secret sharing refers to the concept of hiding secret value by dividing secret value into random shares, and then giving these shares to different parties.

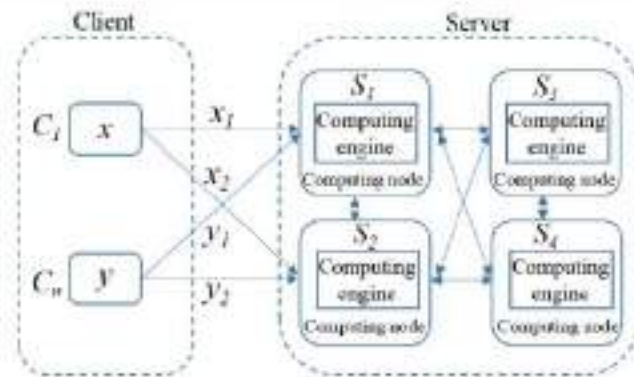


Figure 2. Logic diagram of secure multi-party computation

3.3. Application of Power Digital Spatial Data Security Sharing Based on Privacy Computing

The power digital space with secure multi-party computing technology and its data sharing mode are mainly used in order to realize joint data analysis. Due to the vigorous development of big data analysis technology, the amount of various data information and materials formed and obtained in the economic society has increased significantly. The acquisition of sensitive information data analysis, the cooperation of cross-border organizations and the business operation of cross-border enterprises have provided new challenges to the traditional data analysis algorithms, and the existing data analysis algorithms may cause a lot of privacy exposure. Therefore, privacy and information security in data mining have also received great attention. Introducing secure multi-party computing technology into the field of traditional data mining can alleviate this problem to a certain extent. By using multi-party data source collaborative data analysis algorithm, a large number of sensitive information data analysis can not be disclosed.

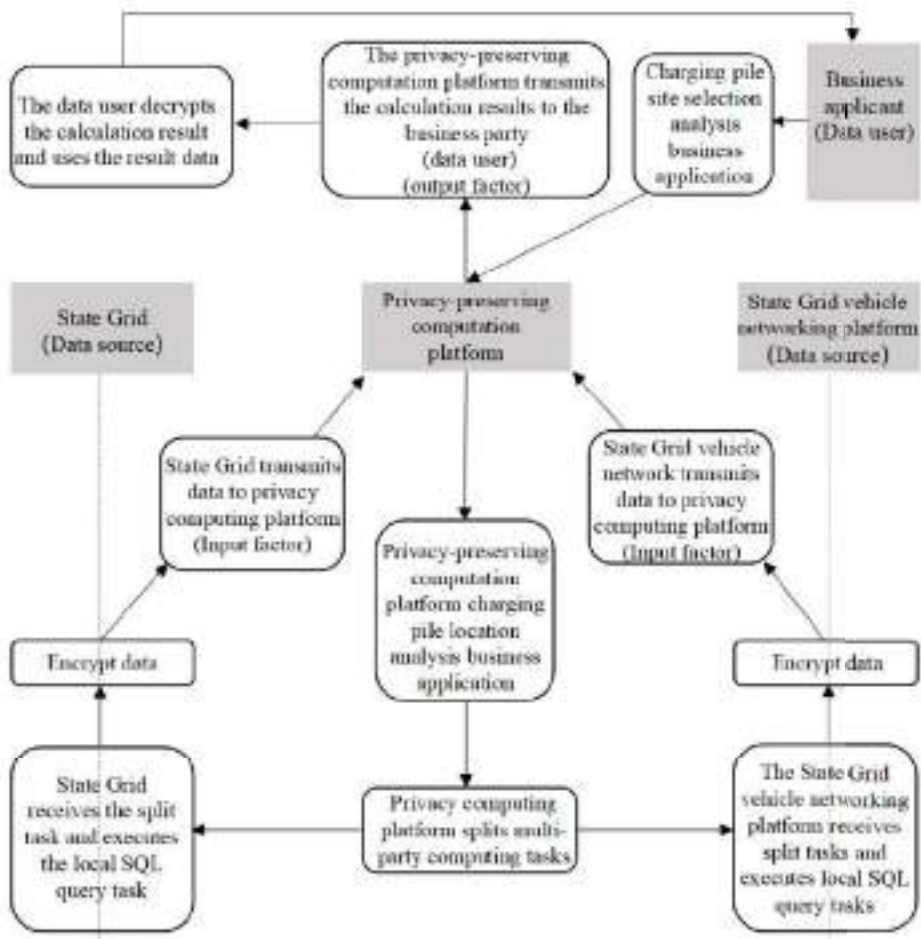


Figure 3. Business process of charging pile site selection

In the new power system design under the digital transformation of power digital space, the application of data sharing and fusion analysis is increasingly prominent. The application of using the information of multiple information providers to realize fusion data analysis and make power grid investment decisions is very extensive. Such as: intelligent operation of power grid, refined demand side management, internal and external data fusion and sharing of state grid energy big data center, business data sharing among provincial energy big data centers, information interaction and sharing between electric vehicles - charging piles - operators - power grid and other scenarios. Typical scenario analysis is as follows:

Using privacy computing technology in charging pile marketing, location and other scenarios, and with the support of proprietary data such as activity range, driving trajectory, driving habits, charging habits, etc., we can help the construction party determine the location without disclosing user sensitive data, and carry out customized marketing and bidding marketing in combination with owner data in subsequent charging pile operations, Improve the utilization rate of charging piles and improve the overall benefits; In the use of charging piles, account verification can be carried out in

combination with the owner's track and other information to prevent the occurrence of malignant events such as user account theft.

The business process is shown in Figure 3, and the key steps are described as follows:

(1) The privacy computing platform receives the application of charging pile location analysis business, which is disassembled into multiple multi-party computing tasks according to the business joint statistics and computing task request;

(2) The State Grid and the State Grid vehicle networking platform need to perform local SQL query tasks and obtain local query results according to the query tasks split by the privacy computing platform;

(3) The State Grid and the State Grid vehicle networking platform encrypt the local query results and transmit the encrypted results to the privacy computing platform;

(4) The privacy computing service platform performs the calculation and feeds back the calculation results to the business demander.

Data sharing and fusion analysis involves data interaction between multiple departments of the State Grid, and even with other industries. Data sharing and circulation are faced with privacy protection issues, so it is necessary to build a safe and reliable computing environment to ensure that all participants cannot obtain data outside their authority, so as to achieve the purpose of obtaining results through secure computing.

4. Conclusion

In this paper we analyze the challenges faced by the safe sharing of power digital spatial data, summarizes the application prospects of privacy computing technology in the safe sharing of electrical digital spatial data, and proposes a model system for the safe sharing of electrical digital spatial data based on privacy computing technology. Under the new power system, data elements are shared and exchanged more frequently between power and related social enterprises, departments and regions, and the circulation of data elements is wider. Through collaboration with external data, power data can not only empower and upgrade the power grid business itself, improve quality and efficiency, but also play a major role in promoting the economic development of the whole society, national governance, pollution prevention and carbon reduction, etc. However, with the increasing number of external cooperation and open sharing environment, serious deficiencies in data production factor governance capability and privacy protection capability have been exposed. Building a privacy computing service platform is a necessary way to reasonably use sensitive information of the power grid to solve related problems, and it is an effective way to rationally use the sensitive information of the power grid. The State Grid big data center, the data centers of various network provinces, and the energy big data center involve internal and external data interaction scenarios, and privacy computing technology can be applied to the current multi-level big data center scenarios. The platform can access multiple data sources or business demand platform data such as data from various platforms of the power grid, social platform data, and government system data.

References

- [1] Bian WL. Privacy-preserving computation: Industry Applications have Huge Potential. 21st Century Business, 2021-11-11(012).
- [2] Xu W, Wang Y, Jin C, et al. Thoughts on interconnection of data circulation platform based on privacy-preserving computation. *Financial Computerizing*, 2021, 9:72-73.
- [3] Kubicek H, Cimander R, Scholl HJ. Organizational interoperability in E-Government: Lessons from good practice cases all over Europe. Berlin: Heidelberg, 2011:135-141.
- [4] China M. White paper on privacy-preserving computation Applications. China Mobile, 2021.
- [5] Privacy-preserving computation alliance, Institute of Cloud Computing and Big Data, China Academy of Information and Communications Technology. White paper on privacy-preserving computation. China Academy of Information and Communications Technology, 2021.
- [6] Konecny J, McMahan HB, Felix XY, et al. Federated learning: strategies for improving communication efficiency. [2021-03-10]. <https://arxiv.org/abs/1610.05492>.
- [7] Tian L, Sahu AK, Talwalka A, et al. Federated learning: challenges, methods, and future directions. *IEEE Signal Processing Magazine*, 2020. <https://arxiv.org/abs/1908.07873>.
- [8] China Information and Communication Institute. Research report on computing applications of data value release and privacy protection[R]. China Information and Communication Institute, 2021.
- [9] Yan GX, Liu B, Cheng, H, et al. Research on data sharing security framework. *Information Security Research*, 2019, 5(2):309-317.
- [10] Zhu H, Liu JY. Research on the privacy-preserving computation model of users' online disclosure of personal information in the sharing era. *Books and Information*, 2019(2):76-82.
- [11] Dong, X.Q., Guo, B., Shen, Y., et al. An efficient and secure decentralized data sharing Model[J]. *Chinese Journal of Computers*, 2018, 41(5): 1021-1036.
- [12] Zhang, Y.T., Xia, L.X..Research on the integration model of E-Government information *Information*, 2009, 8(7): 161-165.
- [13] Zhang CY. Outlook on the development trend of key technologies in privacy-preserving computation. *Science & Technology Industry of China*, 2021, 10:16-22.
- [14] Yang J.. Research on data security application based on privacy-preserving computation technology. *China Technology Industry*, 2021, 10:61-63.
- [15] Mao YL, Hong WB, Wang H, et al. Privacy-preserving computation offloading for parallel deep neural networks training. *IEEE Transactions on Parallel and Distributed Systems*, 2021, 32(7):1777-1788.
- [16] De Cristofaro E, Tsudik G. Practical private set intersection protocols with linear computational and bandwidth complexity. [2021-03-10]. <https://eprint.iacr.org/2009/491.pdf>.
- [17] De Cristofaro E, Tsudik G. On the performance of certain Private Set Intersection protocols, 2012. <https://eprint.iacr.org/2012/054.pdf>.
- [18] Freedman MJ, Nissim K, Benny P. Efficient Private Matching and Set Intersection, 2004. <https://iacr.org/archive/eurocrypt2004/30270001pmeurocrypt04-Incs.pdf>.
- [19] Johnson T, Dasu T. "Data quality and data cleaning." *ACM SIGMOD International Conference on* 2003.
- [20] Hardy S, Henecka W, Ivey-Law H, et al. Private federated learning on vertically partitioned data via entity resolution and additively homomorphic encryption. [2021-03-10]. <http://arxiv.org/abs/1711.10677>.
- [21] Yang S, Ren B, Zhou X, et al. Parallel distributed logistic regression for vertical federated learning without third-party coordinator. [2021-03-10]. <http://arxiv.org/abs/1911.09824>.
- [22] Duan XY, Han XL, Wu XL. Non-real-time buffer information based scheduling algorithm in LTE system. *Journal of Harbin Institute of Technology*, 2016, 48(11):142-146,154.
- [23] Lv PP, Zhao JQ, Li DC, et al. A consensus-based collaborative algorithm for realtime dispatch of island microgrid in cyber physical system. *Proceedings of the CSEE*, 2016, 36(6):1471-1480.
- [24] Yao A, "Protocols for secure computations". 23rd Annual Symposium on Foundations of Computer Science (sfcs 1982).1982 Nov; 1(1):160-164.
- [25] Smart NP. *Cryptography sade simple*. Berlin:Springer, 2016:439-450.

Chicken and Egg Food Traceability System Based on NFC and QR Code Technology

Yiqin BAO^{a1} and Yulu BAO^b

^a College of Information Engineering of Nanjing XiaoZhuang University, China

^b Nanjing RuiHuaTeng Intellectual Property Co., Ltd., China

Abstract. Chicken and egg food traceability system based on NFC and QR code technology was designed. The traceability system registers and uploads the information of raised chickens through the chicken foot ring embedded with NFC tag. The system generates egg QR code according to the registered information and prints it on the eggs corresponding to the raised chickens. It is used for consumer users to scan and query the relevant information of the eggs and the raised chickens, including the breeding address, breeder and breeding record of the raised chickens. The system is designed based on the classic three-layer mode of the Internet of things and the B / S architecture. The system mainly realizes the traceability of chickens through NFC tags and eggs through QR codes. It has high stability and great application and promotion value.

Keywords. NFC, QR code, RFID, IoT

1. Introduction

With the increasing improvement of living standards, people's view of food health has risen to an unprecedented height, and the safety of chicken and egg food has been the concern of the public. At present, there is no complete system and method for the safety traceability system, nor can it run through the whole process from production to consumption. The current traceability system generally uses one-dimensional bar code technology for product identification, and then scans from delivery, storage and transportation to sales to record the circulation process, so as to achieve the purpose of traceability. However, due to the non uniqueness of one-dimensional code and its easy duplication, the traceability does not have real credibility, and the intermediate link is easy to be forged, so consumers can not really rest assured.

Radognat et al. [1] studied the framework for enhancing food safety and traceability, Zhao et al. [2] studied the impact of health risk perception on the purchase willingness of traceable fresh fruits in the Chinese blockchain, and adamashvili et al. [3] studied the wine supply chain based on the blockchain. However, these studies are only aimed at a certain circulation link, which can not be connected before and after, and can not achieve the purpose of real traceability. In addition, the verification and query methods provided by these traceability systems for consumers are generally network query or voice phone query, which greatly increases the possibility of fraud, and the enthusiasm and query convenience of consumers are also poor. Therefore, it is necessary to establish a complete set of chicken and egg food traceability system.

¹ Corresponding author: Yiqin BAO, email: 392335241@qq.com

This paper designs a chicken and egg food traceability system based on NFC and QR code, which includes information input equipment set in 1) breeding, 2) processing, 3) storage, 4) transportation and 5) sales. The input information is respectively connected to the host of each link. In the breeding production link, the NFC tag is used to identify the identity information of livestock and production raw materials. In all links, the CPU card is used to identify the subject identity, legal identity information, transaction records, history records, purchase information and sales information; Wherein, the identity information is scanned and uploaded to the production link host through the information input device, and each link host is wirelessly connected to the management terminal and the market query terminal through the Internet. The system also includes a backup server, a data server, an application processing server and a remote access server that are connected in sequence. The server is wirelessly connected to the management terminal and the market query terminal through the firewall and the Internet, the handheld terminal query machine is wirelessly connected with the application processing server.

The contributions and innovations of this paper are summarized as follows:

- 1) Designed the food traceability system architecture.
- 2) NFC and QR code technology are implemented in the system.
- 3) The service application of system is realized.

The rest of the paper is organized as follows: the second section designs the system architecture, the third section realizes the key technologies of the system, the fourth section realizes the application of system services, the fifth section carries out experiments and compares with manual traceability, and the sixth section summarizes the full text.

2. The System Overall Structure

The system adopts the classic three-layer design mode of the Internet of things, namely, the perception layer, the network layer and the application layer; The system adopts B / S architecture and takes the database as the center to build the system. The system block diagram is shown in Figure 1.

In this system, the perception layer is mainly embodied in the data interaction between smart phones, NFC tag foot rings and egg QR codes. Smart phones with NFC function can contact and scan the foot rings with NFC tag function worn on the chicken feet in the chicken farm to register all chickens in real time; At the same time, the corresponding egg two-dimensional code is generated according to the registered and uploaded data, which is used for printing the two-dimensional code of the egg shell produced by the chicken to realize the correspondence between the egg and the chicken.

The network layer is mainly used to transfer data between the perception layer and the application layer. It is composed of Internet, mobile operator network, network management module, etc. the network layer can realize large-scale and long-distance communication, and is an indispensable part of the whole system [4].

The application layer mainly serves users. In this system, users are mainly divided into two groups: chicken farm management personnel and consumer users. The chicken farm management personnel can realize the chicken registration and information query through the interface information interaction between the smart phone and wechat applet; The chicken farm staff can also view and manage the corresponding data on the

system data service platform. The consumer users can scan the QR code on the eggs through the wechat small program specially released for them to trace the source, so that the consumer users can find it and eat at ease.

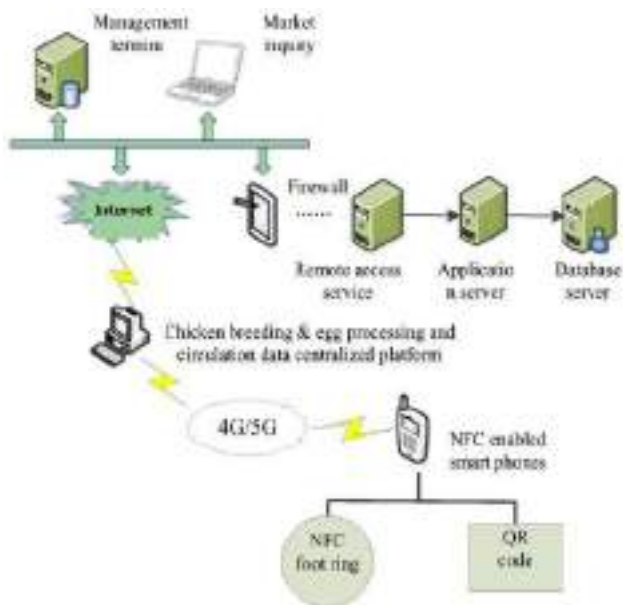


Figure 1. System architecture diagram

3. System key technology

3.1 Short range wireless communication technology

Near field communication (NFC) is an important part of the sensing layer. NFC technology is evolved from the integration of contactless radio frequency identification (RFID) and interconnection technology. It has the advantages of low power consumption, low cost and high security. At the same time, with the rapid upgrading of smart phones, most of them have NFC reading and writing functions, which is very convenient. NTAG chip is adopted as NTAG216, with a capacity of 888 bytes, which is sufficient to store relevant registration information [5]. The entire NFC tag is embedded in the chicken foot ring. The structure of NTAG216 is shown in Figure 2.

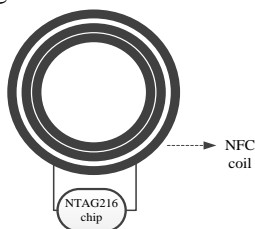


Figure 2. NTAG216 architecture diagram

When the chicken farm staff reads and writes the chicken ring information, open the smart phone with NFC function and set the phone to NFC card reader mode using app or wechat applet [6]. After the setting is completed, the NFC chicken ring data can be read and written by leaning into the chicken ring. The information is mainly used to identify the identity information of chickens in the process of chicken breeding and production. During the process, various process records can be added, such as breeding address, breeder, breeding record, etc., but they cannot be tampered with by others, thus ensuring the authenticity, reliability and uniqueness of the original source information. Its operation is shown in Figure 3.



Figure 3. Chicken ring information reading and writing

3.2 QR code technology

Two dimensional code is a product derived from one-dimensional code technology. Compared with the previous one-dimensional code, the two-dimensional code has the advantages of high storage density, error correction capability, wide application in combination with other technologies, and can store various kinds of information such as Chinese characters, letters and numbers [7]. QR code, code 16K and code one are common two-dimensional code formats [8]. In this system, QR code is in the format of QR code.

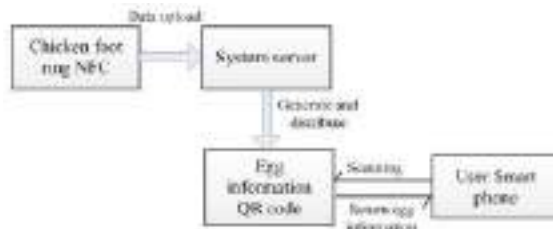


Figure 4. Generation and use of QR code

The QR code label is used for egg identification. That is, during the laying process of the chicken to which the egg belongs, the original NFC tag information plus the egg information (laying time, inspection mark, etc.) are converted into information codes into two-dimensional codes. Each egg has a unique two-dimensional code, which records the identity ID, source, batch, inspection qualification information, subcontracting time, secondary processing industry information, etc. of the food. The two-dimensional code can be used as the traceability code of the product, and it can be scanned and checked in all links. Every time it is transferred and disassembled, a new two-dimensional code will be generated for subsequent traceability until the final consumer. The two-dimensional code is encrypted by the encryption algorithm and

encoded. It can not be copied and reconstructed at will. Consumers can query the source and circulation of the product anytime and anywhere through smart phones, which is very convenient and the system deployment cost is extremely low. The two-dimensional code generation and use process is shown in Figure 4.

4. Application service

The system adopts B/S architecture, and its service architecture is shown in Figure 5. The service part is mainly divided into three modules, namely, the basic module, the application module and the data storage module.

The basic module is the construction foundation of the whole application service, including the function erection of the network service end, the erection of the mqtt service, the erection of the protocol processing service and the establishment of the data storage driver interface.

The function of the application module is: Based on the pure data obtained by the basic module, perform corresponding logic processing according to the required business, and display the data to the user; The application module performs corresponding linkage to the other two modules in the service architecture according to the user's operation at the B-side, that is, the browser side.

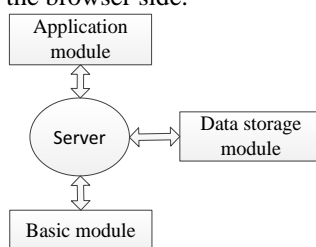


Figure 5. Application service architecture

The data storage module is mainly composed of a database server, which is used to store the information generated in the system, including the user information of the chicken farm management personnel and consumers, the upload registration information of the chicken foot ring collected by the perception layer and the egg two-dimensional code information generated according to the registration information, the process information of the egg from generation to market circulation, the consumer user query related information, the system operation log information and other data. The system itself is the collection of information, and the data storage module provides data support for the whole system, which is the core part of the system. In this system, MySQL database is used. MySQL is a multi-user and multi-threaded database management system. As the current mainstream database, it has the advantages of transaction security, on-demand scalability, high availability, high reliability, fast start and so on.

5. Experimental results and comparison

The main hardware component of the chicken and egg food traceability system based on NFC and QR code is the foot ring. The physical diagram of the foot ring development is shown in

Figure 6, the physical simulation diagram is shown in Figure 6 (a), and the actual diagram of the foot ring is shown in Figure 6 (b).



(a) Simulation picture of development board



(b) Actual picture of foot ring

Figure 6. Pictures of foot ring development

Compared with manual source tracing, the system is fast, easy to operate, highly reliable and powerful. It can identify the chicken breeding address, breeder, breeding record and other information, so that users can eat safely.

6. Conclusions

The large-scale application of the system makes the process of chicken and egg production more transparent and open. The management personnel of the chicken farm scan the foot rings on the chicken feet of the chicken farm through the smart phone with NFC function and upload the information of the registered chickens; The system generates the egg QR code according to the uploaded registration information and prints it on the egg. The QR code printed on the egg can allow the consumer to use the smart phone to scan and trace the source, including the chicken breeding address, breeder and breeding record corresponding to the egg. As a passive tag, the NFC tag embedded in the foot ring has the characteristics of short distance, low energy consumption and high bandwidth. Moreover, most smart phones in the market integrate the NFC card reader function, so it is easier, safer and faster to use. The chicken and egg food traceability system based on NFC and QR code technology has high application and promotion value.

Acknowledgement

This work is supported by Key topics of the ‘13th five-year plan’ for Education Science in Jiangsu Province (B-b /2020/01/18).

References

- [1] Radogna, A.V.; Latino, M.E.; Menegoli, M.; Prontera, C.T.; Morgante, G.; Mongelli, D.; Giampetruzzi, L.; Corallo, A.; Bondavalli, A.; Francioso, L. A Monitoring Framework with Integrated Sensing Technologies for Enhanced Food Safety and Traceability. *Sensors* 2022, 22, 6509.
- [2] Zhai, Q.; Sher, A.; Li, Q. The Impact of Health Risk Perception on Blockchain Traceable Fresh Fruits Purchase Intention in China. *Int. J. Environ. Res. Public Health* 2022, 19, 7917.
- [3] Adamashvili N, State R, Tricase C, Fiore M. Blockchain-Based Wine Supply Chain for the Industry Advancement. *Sustainability*. 2021; 13(23):13070.
- [4] Wei Ya Design and research of pork traceability system [J] *Modern salt chemical industry*, 2019, 46 (5): 2.

- [5] Wu Yihao, he Minghao, Peng Xiaohong, Chen Yuhan, Wu Huimin. Smart pet collar design integrating narrowband Internet of things and NFC technology [J]. *Sensors and Microsystems*, 2022,41 (02): 86-89.
- [6] Shen Xi, Kong Li. Mobile payment system based on NFC technology [J]. *Computer knowledge and technology*, 2021,17 (03): 254-256.
- [7] Yu Chengli, Hu Wanli. The past and present life of QR code [J]. *Confidential science and technology*, 2017 (12): 57-62.
- [8] Liu Dijia. The principle of two-dimensional code and its application in the management of expressway electromechanical engineering equipment [J]. *Engineering technology research*, 2021,6 (24): 96-98 + 134.

The Light and Image Synchronous Method Based on Adaptive Color Segmentation Algorithm

Qiuwei DENG^{a,b}, Nianhang TANG^{b,c,1}, Mingyue SU^b and Jianguang ZHAI^b

^aSchool of Computer Science, Chongqing University, China

^bState Key Laboratory of Digital Household Appliances, China

^cSchool of Electronic Information and Communication, Huazhong University of Science and Technology, China

Abstract. With the development of Internet of Things technology and the people's pursuit of high-quality life, the development of smart homes is becoming more and more diversified, paying more attention to reducing costs, increasing benefits and user experience. For the scene where lights and images change synchronously in smart homes, the current technology used in related products is a solution for external hardware processing equipment, which has problems such as high hardware cost, complex configuration, only supporting external HDMI sources, etc.. Combined with the above situation, this paper proposes a smart home lighting linkage system that is suitable for market demand, easy to promote, apply and implement. Through ZigBee, Bluetooth networking technology, color segmentation technology, signal processing technology, etc., this solution designs and implements an adaptive lighting linkage smart home system based on the color change of the TV screen. The scheme has been proved to have the characteristics of low cost, good experience and stable effect in practical application, and achieved the expected research goals.

Keywords. Lighting Changes with Movies Scenario, Image Processing, Color Space, Smart Home, Lighting Linkage System

1. Introduction

The initial development of smart home is mainly based on remote control lighting, home appliances and electric curtains. With the development of the industry, the functions of intelligent control are becoming more and more abundant. Like the linkage scene of control, smart home can cover almost all traditional weak current industries, and the market development prospects are promising. For the

¹Corresponding Author: Nianhang TANG, State Key Laboratory of Digital Household Appliances, Qingdao 266101, China; School of Electronic Information and Communication, Huazhong University of Science and Technology, Wuhan 430074, China; E-mail: tangnianhang@163.com.

scene in which the lighting and the image change synchronously in the smart home, this life scene is mainly based on the hardware solution. In literature [1], color extraction and synchronized display are implemented by external hardware boxes. The technology adopted by the existing products has problems such as high cost, complicated operation and only applicable to HDMI external input sources, which seriously hinders the promotion, application and development of the product. A music lighting algorithm based on spectrum analysis is proposed in the literature [2]. It is easy to use, but it needs to network lights separately, which is relatively complicated. While in literature [3], a simple equipment and a method for lights to follow music are proposed, but the lighting effect is not ideal. This topic aims to solve the technical shortcomings of existing products, and propose a smart home lighting linkage system that is suitable for market demand, easy to promote, apply and implement. Based on the image processing algorithms, Internet of things, ZigBee, Bluetooth Mesh and other technologies, this paper designs and implements a lighting linkage smart home system based on the color change of TV images.

2. The Design of The System

This paper proposes a lighting linkage system scheme based on the color of the TV screen. The system monitors the subtle changes of the TV screen in real time, and drives the LED smart lights around the TV according to the screen content, so that it presents brilliant and colorful colors. At this time, the TV screen extends beyond the LCD (TV) screen, and the changes of light and shadow break through the limitations of the screen, forming a wider range of visual appreciation, making it echo the TV screen, creating a cinema-like immersive visual enjoyment.

The lamp strip devices form a controllable network through ZigBee technology and Bluetooth Mesh technology. The TV calculates the color of the light strip in real time according to the image color, and sends it to each light strip through the network for control and adjustment, so as to achieve the effect of light linkage. The software interaction process of the whole system is shown in Figure 1. The system consists of two modules, a software application on the TV and network communication. The software applications on the TV are developed in the Kotlin language, known as Swift in the Android world. It collects real-time TV broadcast screen data and extracts valid data except for the black border area. The valid data is divided into color blocks by image algorithm and the main color of each color block is extracted, which the main color block is sent to the light strip device using the local network environment to realize the real-time linkage of the light and color of the TV screen.

The network communication module of the device is mainly constructed through ZigBee technology and Bluetooth Mesh technology. The advantages of this scheme are as follows: 1) low cost, 2) high flexibility, 3) easy to expand. If a new device is added, it only needs to be configured on the network.

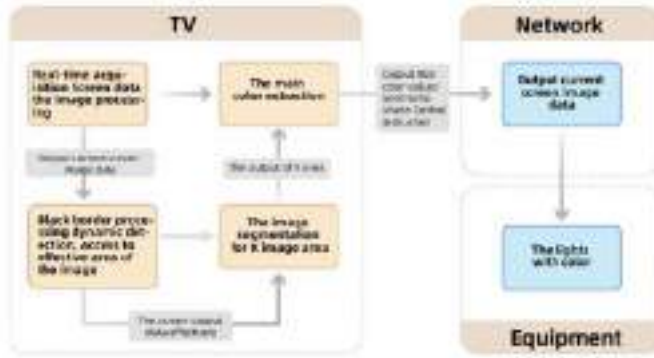


Figure 1. Flow Chart of System Software Interaction

3. Research on the Scheme of Adaptive Change of Light with Image

3.1. Overall Scheme

The overall scheme consists of six modules: real-time TV image acquisition, image compression, video black box detection, image segmentation, main color value extraction and light strip control protocol encapsulation and transmission. The specific workflow is shown in Figure 2:

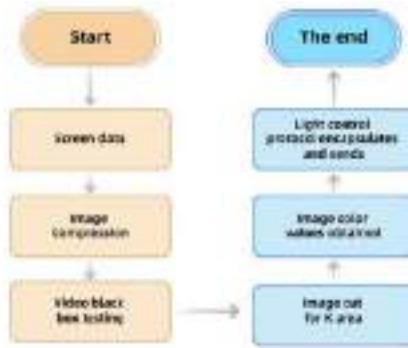


Figure 2. Software Flow Design Diagram

3.2. Design and Implementation of TV Real-Time Image Acquisition and Compression Module

The module is mainly responsible for acquiring TV screen data in real time. Before data collection, it is necessary to initialize the frame rate and screen resolution of the collected screen data, and set the parameters of the screen collection area and the type of collected data. The screen image data acquisition module including the osd layer (graphics layer of the smart TV system for common applications,

such as boot animation) and video layer (video layer, TV layer). According to the real-time video playback progress, the image is selected and sent to the subsequent image compression and processing module for calculation.

The module compresses the data obtained by the TV real-time image acquisition module. The color value algorithm is used to extract the image, the larger the image data, the longer the image processing time. In this scheme, images are compressed by K-fold smooth Bresenham scaling algorithm. On the premise of not affecting the extraction of the main color value, it simplifies and reduces the subsequent image processing time to the greatest extent. The smooth Bresenham scaling algorithm is an adaptation of the linear Bresenham algorithm [4], which is used to scale images with quality close to linear interpolation, with optimal scaling factor intervals between 50% and 200%.

3.3. Design and Implementation of Image Black Box Detection Algorithm Module

The commonly used image black-box detection algorithm is based on luminance information. Another black-edge video detection algorithm based on convolutional neural network [5,6], which has high accuracy, but requires more system resources and takes longer inference time on the CPU.

In this paper, a dynamic image black edge detection algorithm based on parameter update is designed and proposed. The algorithm is mainly used to deal with the upper and lower black borders of video images, we remove the black frame, keep the valid data area, and reduce the influence of the black frame on the extraction of main color values. The design idea of black edge detection is to set the maximum black edge threshold (e.g., 1/4 of the image height). Within the threshold, the image is cut into $M \times W \times K$ rectangular images (W is the width of the image, K is the height of the overlay), it is judged from top to bottom whether the rectangular area is black. If it is black, move on to the next one. This detection will eventually maintain a dynamic balance of advancing and retreating near the black frame of the video, so as to achieve the purpose of dynamically updating the parameter information of the black frame. The processing flow of this part is shown in Figure 3:

3.4. Design and Implementation of Image Adaptive Color Segmentation Module

Image color segmentation algorithms [7, 8] are mainly used to extract different color regions in an image, and then perform subsequent color extraction. In this paper, by comparing the effect and performance of three mainstream segmentation algorithms, we summarize the advantages and disadvantages of each algorithm, and propose an image adaptive color segmentation algorithm, which can achieve better segmentation results and take into account the performance. The three algorithms are the region growing-based color segmentation algorithm, the threshold-based color segmentation algorithm and the clustering-based color segmentation algorithm, respectively.

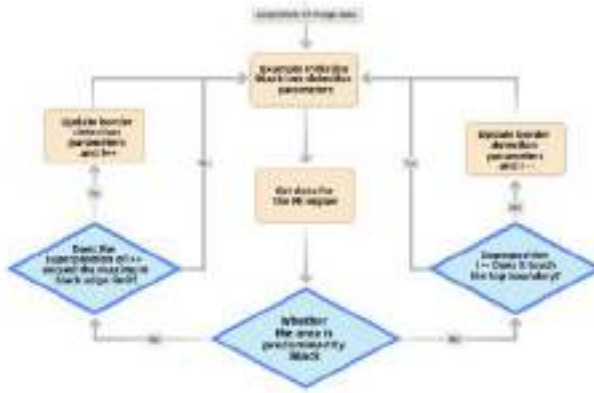


Figure 3. Flowchart of Image Black Box Detection Algorithm

3.4.1. Region Growing Based on Color Segmentation Algorithm

The region-growing-based color segmentation algorithm [9, 10] starts from a pixel or a small region, and judges whether adjacent pixels belong to the same region according to preset rules, thereby gradually growing into regions with the same attributes. The growth of the algorithm is terminated when no pixels meet the specified rules. In this way, this algorithm only considers whether the current pixel belongs to the region, without considering the fusion information of the whole image. The general steps are as follows:

1. Select the appropriate rules and area seeds. The rules can be features such as grayscale, color, texture, gradient, etc. The selected seeds can be a single pixel or a small area containing multiple pixels;
2. Determine the calculation and comparison method of different pixel features in the neighborhood (4-neighborhood or 8-neighborhood);
3. Determine the conditions under which growth stops. The advantages and disadvantages of the algorithm are obvious. On the one hand, the idea of this algorithm is relatively simple, and it can segment the closed area and it will have a good segmentation effect in a complex environment. On the other hand, it is sensitive to noise and prone to holes, so it needs to select seed pixels or regions and fusion rules in advance. Also, too many parameters settings result in high time and space complexity.

3.4.2. Threshold-Based Color Segmentation Algorithm

Another commonly used segmentation algorithm is the threshold-based color segmentation algorithm [11, 12], as shown in Figure 4. According to a large amount of video data, the aspect ratio coordinates of the general color segmentation area are summarized, and the entire picture is artificially divided into ten areas of different sizes. The algorithm is too simple, works best on the reference video set and has the fastest processing speed. However, for the non-reference video set, when the color regions of the pictures is irregular, the segmentation effect is poor. The segmentation area cannot be updated dynamically, and the user experience is poor.

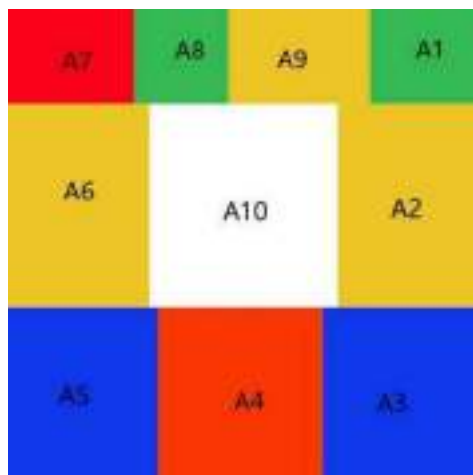


Figure 4. Schematic Diagram of Threshold-Based Region Cutting

3.4.3. Clustering-Based Color Segmentation Algorithm

The color segmentation algorithm based on clustering [13, 14] mainly divides the sample points of the vector space into K subspaces according to a certain distance measure, and the result of the clustering feature is the membership degree of the data to the cluster center. It will make the points in the subspace as close together as possible and the adjacent subspaces as far apart as possible.

In this algorithm, we use the RGB three channels of the color images as the X, Y and Z axes to establish a spatial Cartesian coordinate system, and then establish a one-to-one correspondence between each pixel on the image and the spatial Cartesian coordinate system. K points are randomly selected from the spatial Cartesian coordinate system as the centers of the K subspaces. The distances from all pixels to K centers are calculated, and all pixels into the subspace with the smallest distance are divided to achieve the clustering effect. Clustering distance can be defined as Euclidean distance:

$$\sqrt{(r_1 - r_0)^2 + (g_1 - g_0)^2 + (b_1 - b_0)^2} \quad (1)$$

The advantage of cluster-based color segmentation algorithm is that it has good local convergence and is more suitable for pixel classification in high-dimensional feature space. The disadvantages are also obvious. When there are unequal colors in the image, random selection of cluster centers can lead to misclassification. When the distribution information of each point shows the characteristics of the class, the image may be over-segmented, resulting in the segmentation effect not meeting the expected requirements, and even causing the segmentation to fail. The quadratic clustering algorithm is an iterative algorithm, which requires a large amount of computation and occupies too much CPU resources for high-resolution images.

3.4.4. Image Adaptive Color Segmentation Algorithm

Based on the advantages and disadvantages of the above algorithms, an adaptive color segmentation algorithm is proposed in this paper. The design idea of the adaptive color separation algorithm is to interpolate and scale the image after removing the black edge, and then retain the edge width of N pixels, and set the remaining pixels to 0 to reduce the processing time and impact on the final segmentation. The top, left and right edges of the image are processed. Taking the upper edge of the image as an example, the HSV color space component value of each pixel is obtained by looping. The conversion formula is as follows:

$$\begin{aligned} R' &= R/255 & G' &= G/255 & B' &= B/255 \\ C_{\max} &= \max(R', G', B') \\ C_{\min} &= \min(R', G', B') \\ \Delta &= C_{\max} - C_{\min} \end{aligned} \quad (2)$$

$$H = \begin{cases} 0^0, & \Delta = 0 \\ 60^0 \times \left(\frac{G' - B'}{\Delta} + 0 \right), & C_{\max} = R' \\ 60^0 \times \left(\frac{B' - R'}{\Delta} + 2 \right), & C_{\max} = G' \\ 60^0 \times \left(\frac{R' - G'}{\Delta} + 4 \right), & C_{\max} = B' \end{cases} \quad (3)$$

$$S = \begin{cases} 0, & C_{\max} = 0 \\ \frac{\Delta}{C_{\max}}, & C_{\max} \neq 0 \end{cases} \quad (4)$$

$$V = C_{\max} \quad (5)$$

Pixels are classified according to the established HSV color space threshold table, and S sets are obtained. There are outliers and smaller subsets in the set. Then, the region fusion is performed to merge the outliers and the regions whose range is less than the threshold H , and finally obtain the continuous color interval set at the upper edge of the image. According to the color interval setting, map to the original image through coordinates and then segment the image. The detailed processing process is shown in Figure 5, and the experimental simulation results are shown in Figure 6.

3.5. Design and Implementation of Main Color Value Extraction Module

3.5.1. Extraction of Conventional Primary Color Samples

The main color extraction algorithm is also known as the color quantization algorithm, the main purpose is to select the most representative or common 256 colors from the approximately 16M colors that can be represented by a true color image. Common color quantization algorithms include median segmentation algorithm, octree algorithm [15], clustering algorithm [16], etc. Aiming at the large amount of color component data in true color images, this paper, and optimizes the median segmentation algorithm. The algorithm processing idea is shown in Figure 7: For RGB888 image data, each RGB color component occupies for 8 bits. If all are used, the number of recorded colors is about 16M color counter. In



Figure 5. Hierar-DRL



Figure 6. Color Extension Diagram of Image Adaptive Color Segmentation Algorithm



Figure 7. Extraction Process of Conventional Primary Color Sample

order to reduce the space occupied, this scheme compresses each RGB component into 5 bits, that is, RGB555 image data, so that the number of color counters is

reduced to about 32Kb. Although precision is lost, the processing speed is greatly improved and the memory space of the program is used.

Before extracting the main color value samples, it needs to set the number of output theme color samples, which determines the final output theme color number in this area. The higher the number, the longer the processing time. In this scheme, the number of theme color samples is set to M. After the parameters are configured, the compressed RGB555 image data is processed, the color histogram is constructed to count the number of each color. The Median cut method is used to calculate the number of subject color samples.

The median segmentation method is to map all pixels into the RGB space, repeatedly slice the subspace in this three-dimensional space, and finally calculate the mean of the pixels in the segmentation space as the extraction result of the algorithm. Firstly, a spatial Cartesian coordinate system is established with three colors as the endpoints to ensure that all pixels are within the cube, and then set the median of the longest side of RGB in color statistics to 2, so that the two cuboids contain the same number of pixels. Next, repeat the above steps until the final number of cuboids equals the number of theme color samples. Finally, the average RGB color of each cuboid is calculated as the color value of the sample, and the number of cuboid samples is the number of main colors extracted from the area.

In this paper, the median segmentation method is optimized on the basis of a large number of experiments. According to the color frequency of the image and the distribution of color components in the color space, the cuboids in the color space is first sorted based on the maximum color difference, and the color mean of the components is selected as the dividing point instead of the median used for segmentation. In this way, the result obtained by the algorithm is more accurate, the color level of the image is richer, and there is no color failure. Based on the above operations, we obtain M color value samples in this area and the number of pixels for each color value sample in the area. The proportional value P of this color value in this area can be obtained by calculation.

$$P = \frac{\text{Number of color value pixels}}{\text{Number of total color value}} \quad (6)$$

The RGB values of M color samples and the pure black RGB value #ff000000 are respectively used for calculation, and the weighted Euclidean distance, that is, the color similarity, is calculated as follows.

$$\begin{aligned} \bar{r} &= \frac{C_{1,R} + C_{2,R}}{2} \\ \Delta R &= C_{1,R} - C_{2,R} \\ \Delta G &= C_{1,G} - C_{2,G} \\ \Delta B &= C_{1,B} - C_{2,B} \\ \Delta C & \\ &= \sqrt{\left(2 + \frac{\bar{r}}{256}\right) \times \Delta R^2 + 4 \times \Delta G^2 + \left(2 + \frac{255 - \bar{r}}{256}\right) \times \Delta B^2} \\ s_i &= \Delta C \end{aligned} \quad (7)$$

The larger the s_i value, the lower the similarity to black; the smaller the s_i value, the higher the similarity to black. This value can be used to evaluate the color contrast between subject colors. Finally, the similarity matrix is generated:

$$S = \begin{bmatrix} S_{11} & S_{12} & \dots & S_{1m} \\ S_{21} & S_{22} & \dots & S_{2m} \\ \dots & \dots & \dots & \dots \\ S_{n1} & S_{n2} & \dots & S_{nm} \end{bmatrix} \quad (8)$$

N is the number of divided areas of the screen, and m is the number of subject samples in a single area.

After calculating the proportion and similarity of the theme color value in M , a two-dimensional space is constructed to calculate the weight according to the similarity S and the proportion P of the color value. The evaluation method is as follows:

$$Y = C_1 \times (S - \mu)^2 + C_2 \times S + C_3 \times P \quad (9)$$

Note: C_1, C_2, C_3, μ are constants, and μ value is the optimum similarity.

The one with the largest Y value among the M theme color samples are taken as the main color value of this area.

3.5.2. Extraction of Saltation Samples

To analyze the jumping color in the image, it is necessary to extract all the theme colors of the image, and judge the change of the number of pixels of the same theme color in each frame according to the analysis of multi-frame image data within a certain period of time. The color in which the number of pixels of the same color increases and changes the most in short period of time is regarded as the jumping color. In this paper, a skip color quantization algorithm based on multi-frame data fusion is proposed. The simulation test results are shown in Figure 8.



Figure 8. Schematic Diagram of Main Color Extraction Effect of Jump Color Change

4. Test Platform and Test Results

In this scheme, a debugging environment is built in the smart home laboratory. According to the design of the light strip, the light belt is fixed on the upper, lower, left and right sides of the back frame of the TV, and is connected to the same controllable network as the TV. The actual scenario is as follows in Figure 9.



Figure 9. Display Diagram of Solid Light Belt

4.1. Hardware and Software Development Environment

The detailed parameters of flat-panel TV, LED symphony RGB light strip, TV and light strip are shown in Table 1 and 2.

Table 1.: Detailed Parameters for Flat-Screen TVs

Table 2.: LED Phantom RGB Lamp Strip Detailed Parameters

Model	Casarte K65E50	Model	JRM70001
operating system	Android 9.0 system	Operating voltage	DC12V
CPU	Cortex-A55 1.9GHZ	power	12.2W/m (white light).
resolution	3840x2160	Angle of light	120°
RAM	4G	output	RGB
ROM	64G	luminous flux	300lm./m
Refresh rate	60Hz	Lighting effects	25lm/W

The environment required for system software development is shown in Table 3 below.

4.2. Comparison of Algorithm Test Results

The four different algorithms in Section 2.5 are tested on the Intel(R) Core (TM) I7-8700 CPU hardware test platform, with 300 videos in the test set, and the average processing time of a single frame is compared as follows in Table 4.

The color extension effect obtained by the four algorithms is shown in the Figure 10. The test team invited 10 people to evaluate and score 300 videos, and

Table 3. Software Development Environment

Development Environment	The Version Number
JDK Version	65 inches
Operating System	V1.8
Android Studio	V4.0

Table 4. Comparison of Processing Time of Segmentation Algorithms

Segmentation Algorithm	Time-Consuming Processing (Average single frame)
Segmentation algorithm based on regional growth	970ms
Based on threshold value segmentation algorithm	5ms
Based on clustering segmentation algorithm	1060ms(K=8)
Image adaptive color segmentation algorithm	23ms

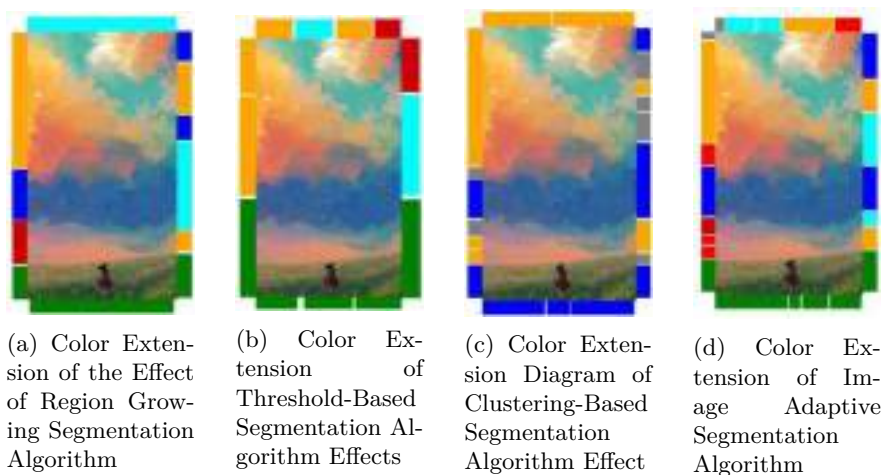


Figure 10. Color Extension Diagram Obtained By Four Algorithms

the subjective effect evaluation statistics are shown in Table 5. Threshold-based segmentation algorithms are the least time-consuming, but have poor subjective results. The algorithm with the best subjective effect are the clustering-based segmentation algorithm and the image adaptive color segmentation algorithm, but the clustering algorithm takes the most time. The adaptive color segmentation algorithm proposed in this paper achieves the desired effect with less time-consuming while taking into account the segmentation effect. In complex color scenes, the image adaptive color segmentation algorithm also performs well and can segment more color transformation domains.

Table 5. Evaluation Table of Subjective Effects of Segmentation Algorithms

Segmentation Algorithm	Subjective Experience (out of 10 out of 10)
Segmentation algorithm based on regional growth	6
Based on threshold value segmentation algorithm	5
Based on clustering segmentation algorithm	8
Image adaptive color segmentation algorithm	8

4.3. System Effect Display and Copy Test

At the TV side, the light and shadow effects can be switched on and off through the remote control. When it is turned off, the TV light strip is off and when the switch is turned on, it will automatically enter the light and shadow effect. The peripheral light strips will react according to the color of the TV screen as shown in Figure 11.

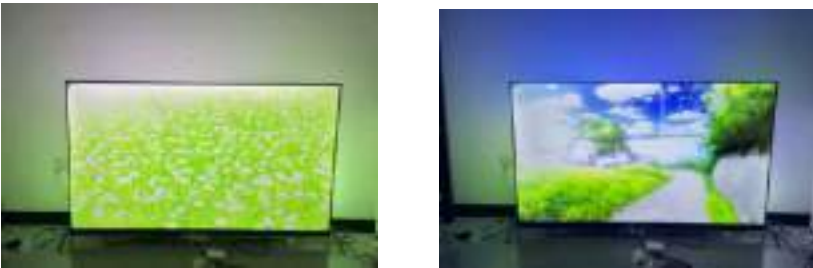


Figure 11. Display Renderings

The system has been continuously tested for 6 hours, and the average response time of the ribbon light and ribbon linkage is 40ms, which can capture the change of each frame of the video and meet the video requirements of 25 frames per second for ordinary network video. The actual test data is shown in Table 6.

Table 6. Copy Machine Test Data

Testing Phase	Total Number of Linkages	Average Time
2 hours	179,904	40.021ms
6 hours	539,020	40.073ms

5. Conclusions

5.1. Full Text Summary

This solution mainly realizes the synchronous linkage between the lighting equipment and the TV color in the life scene, and uses the image processing algorithm

to extract the color of the TV screen, then controls the color of the lights to extend the TV picture to the surrounding environment to achieve the effect of color overflow. In the process of color extraction, image color segmentation algorithm, color shift and conventional main color extraction strategy algorithm are used. In terms of device networking connection, ZigBee technology and Bluetooth Mesh technology commonly used in the Internet of Things are used to form a controllable IoT network for each light strip device in the home. Finally, a smart home lighting scene linkage scheme with TV equipment as the core is realized. The solution does not rely on hardware boxes, has low cost, high flexibility, and does not affect TV picture quality. In the current era of rapid development of IOT smart home and emphasis on immersive feeling and experience, the system has a good prospect and use value. The system has the following advantages:

- (1) Low cost. The cost of the hardware box is eliminated.
- (2) High flexibility and easy expansion. If a new indicator belt device is added, it only needs to be configured on the network.
- (3) It can play internal video source and external input video source, which is better than similar solutions in the market.
- (4) The video is not compressed. This scheme adopts the strategy of displaying first and then processing, which has no effect on the video resolution.
- (5) High stability and fast response.

5.2. Research Prospect

This paper focuses on TV equipment in smart homes, and introduces in detail the development and scene expansion of TV-based equipment, as well as the current technology applications between major brands. Through in-depth research on Internet of Things technology, image processing algorithm, ZigBee technology and Bluetooth Mesh technology, the optical linkage smart home system is realized. The system also has shortcomings. The first is the realization of system image acquisition, which relies too much on the method of chip manufacturers, cannot be used in other TV platforms and brand TV manufacturers, lacks versatility, so the image acquisition module needs to be adapted to the development. Secondly, the core of the system lies in image acquisition and algorithm processing, which also has certain requirements on the performance of TV equipment. The CPU must be above CortexA55 4 cores, otherwise the experience will be poor. The next step of the optical linkage smart home system is to optimize the image processing algorithm, decouple the software modules, and further improve the processing speed, so that it can still have a better visual experience on TV devices with low CPU.

References

- [1] Ma Yi, Zhang Shangchao, Dai Hui, Xie Wenjun System and method for realizing audio and image synchronization control of light, Guangdong Province: cn113286405a, August 20, 2021
- [2] Jin Wencan Multi lamp linkage music lighting system based on spectrum analysis , Hangzhou University of Electronic Science and technology, 2018

- [3] Zhang Hao, Qiu Qinghua, Luo Xiaolong, Bi Cheng A method, device, system and storage medium for light following music rhythm, Guangdong Province: cn113133165a, July 16, 2021
- [4] [4] Hong Chun. Bresenham circle drawing method to extract image information , Computer system application, 2014,23 (01): 128-131 + 27
- [5] Zhou Feiyan, Jin Linpeng, Dong Jun. review of convolutional neural networks , Journal of computer science, 2017,40 (06): 1229-1251
- [6] Zhou Junyu, Zhao Yanming. Overview of convolutional neural networks in image classification and target detection , Computer engineering and applications, 2017,53 (13): 34-41
- [7] Jca B, Lei C C, Yz B, Cryptanalysis of a DNA-based image encryption scheme - ScienceDirect, Information Sciences, 520, 130-141(2020)
- [8] Zhu Kaige, Wu Xiangjun, Ren Guanglong, Color image lossless encryption algorithm based on DNA dynamic coding and chaotic system, Computer application research, 37(S2), 230-233(2020)
- [9] Zhang Jianwei, Quan Qingle. A plane segmentation method of dense point cloud integrating regional growth and RANSAC, Journal of Xi'an University of science and technology, 2022,42 (02): 341-348. Doi: 10.13800/j.cnki.xakjdxsb.2022.0219
- [10] Wang Aichen, Zhang Min, Liu Qingshan, Wang Lili, Wei Xinhua. Extraction method of seedling crop rows based on regional growth mean shift clustering , Journal of agricultural engineering, 2021,37 (19): 202-210
- [11] Niu Ying, Zhang Xun CAI, Image encryption based on variable step Joseph traversal and DNA dynamic coding, Journal of electronics and information, v.42 (06), 84-92(2020)
- [12] Sun C, Wang E, Zhao B, Image Encryption Scheme with Compressed Sensing Based on a New Six-Dimensional Non-Degenerate Discrete Hyperchaotic System and Plaintext-Related Scrambling, Entropy, 23(3),291(2021)
- [13] Ma Xiaoyu, Zhang Jinsheng, Li Ting, Image compression and encryption method based on Chua's circuit and compressed sensing, System engineering and electronic technology, 43(09), 2407-2412(2021)
- [14] Es A, Rw B, Aks B, Securing color image transmission using compression-encryption model with dynamic key generator and efficient symmetric key distribution, Digital Communications and Networks, 2020
- [15] Zhang Miao,Tong Xiaojun,Wang Zhu,Chen Penghui, Joint Lossless Image Compression and Encryption Scheme Based on CALIC and Hyperchaotic System, Entropy,23(8), 2021
- [16] ZENG Jiexian, WANG Junting, FU Xiang. Multi-feature image retrieval method based on K-means clustering segmentation. Computer Engineering and Applications, 2013,49(2):226-230.

A Generative Learning Architecture Based on CycleGAN for Steganalysis with Unpaired Training Images

Han ZHANG ^{a*}, Zhihua SONG ^{b,1*}, Feng CHEN ^b, Xiangyang LIN ^b, Qinghua XING ^b, Qingbo ZHANG ^b and Yongmei ZHAO ^a

^a *Equipment Management and UAV Engineering College of Air Force Engineering University, Xi'an, China*

^b *Air and Missile Defense College of Air Force Engineering University, Xi'an, China*

Abstract. Steganalysis based on deep learning has made noticeable progress over the past few years where the training is all based on paired images. However, scenes without paired training data exist. We present an architecture for learning to generate corresponding pseudo stego image from a cover-image in the absence of paired training images. We seek a mapping G that can generate pseudo stego images indistinguishable from the real but unpaired stego images using an adversarial loss. Because this mapping is highly under-constrained, we designed a CycleGAN and introduce spectrum of stego images to reinforce the adversarial loss. Qualitative comparisons demonstrate the superiority of our approach.

Keywords. Steganalysis, generative learning, residual, CycleGAN

1. Introduction

Steganalysis and steganography are two sides of a coin and cannot be studied separately. In this communication game, the steganography player attempts to achieve communication by hiding secret message or image in a carrier image, which we named it cover as shown in Figure 1, through the public communication channel. The steganalysis player tries to anticipate the risk of misusing of the public communication channel by steganography, i.e., to calculate the probability that the images on the public communication channel are embedded with secret information.

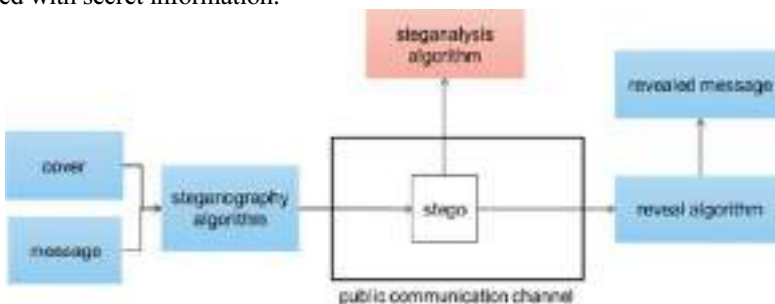


Figure 1: The architecture of the steganography and steganalysis game. The cover in the left stands for the carrier image to hide the secret message. The stego in the middle stands for the image generated by a steganographic algorithm using the cover and the secret message.

¹ Corresponding Author: Zhihua Song, E-mail: szhele@163.com, * indicates equal contribution

For the steganalysis player, paired cover and stego images are ideal to train the steganalysis neural network. But what if there are no paired cover images? Compared with stego image, the paired cover image is more difficult to get on the public communication channel as the cover image usually does not need to be transmitted to the receiver.

In this study, we are seeking to generate paired cover and pseudo stego images all in the absence of any paired training images: capturing special spatial and spectrum characteristics of the stego image collection and translating them to a cover image collection to generate corresponding pseudo stego image collection.

This problem can be described as an unpaired image-to-image translation problem[1]. Unlike the other image-to-image translation applications, such as style transfer[1], object transfiguration[2], and image synthesis[3], the cover-to-stego image translation must work between two extremely similar image collections, while the minimization of distortion loss is a relentless pursuit goal for the steganography player.

We therefore focused on cycle-consistent generative adversarial network (CycleGAN) [1] which is a state-of-the-art unpaired image-to-image translation architecture. In theory, the CycleGAN prevents mode collapse, where all input images map to the same output image, and can add stego styles to a cover image to make a pseudo stego image if the styles are obvious enough to be captured. But in reality, it is usually difficult to distinguish the style of a brilliant stego image from that of an ordinary image. Our early experiments also proved this conjecture, the generated images were not good enough to train any of the baseline steganalysis neural networks and they tend to be the same as the cover. This indicates that the CycleGAN cannot grasp the style difference between the two collections. Such a result is consistent with the nature of the problem, the two image collections are highly similar in the texture and visual effect, while these are the features that the convolution layers at the CycleGAN are good at.

The next thing we need to do is add more detailed and distinguishable information to our network. Therefore, we exploit the spectrum disequilibrium property, that the steganography distribution over different frequency is generally uneven. The rest of the paper is arranged as follows: after a brief review of related works in Section 2, we describe the architecture of the proposed network in Section 3. In Section 4, the experimental results are presented. Finally, Section 5 discusses the conclusion and future work.

2. Related Works

CycleGAN[1] was presented by Jun-Yan Zhu in 2017 for the problem of unpaired image-to-image translation and achieved impressive results in object transfiguration, season transfer, collection style transfer, and photo enhancement. The key to CycleGAN's success is the idea of cycle-consistent loss that encourages the bijection mapping between the generated image and the real source image and forces the generated image to be indistinguishable from images in the target domain. We adopt a cycle-consistent loss to our network. To the best of our knowledge, there is no study has reported using CycleGAN-generated images for the extensive training of steganalysis models.

In [4], a deep residual steganalysis architecture called SRNet is proposed to minimize the use of heuristics and externally enforced elements and it provides state-of-the-art performance for both spatial-domain and JPEG steganography. We borrows this architecture directly in our network as the steganalysis block.

Baluja[5] present an image-into-image steganography network, which can embed a full-sized image inside another image with minimal quality loss. There are three

components in the system, i.e., the preparation network, the hiding network, and the reveal network. These three components are trained simultaneously as a single network and the reveal network uses the stego images only. We call the network Baluja-Net for convenience and choose it as one of our baseline for our experiments.

3. Model

The key is to learn mapping functions between the cover image collection C and the stego image collection S , given unpaired training samples $\{c_i\}_{i=1}^N \in C$ and $\{s_j\}_{j=1}^M \in S$, using the CycleGAN. However, such an approach does not guarantee that the output y can embody the subtle feature difference between the cover and its corresponding stego. The CycleGAN is good at transfer texture difference and the texture distortion is usually what the steganography player is trying to minimize.

Moreover, in practice, we have found it difficult to optimize the adversarial objective: standard CycleGAN leads to the problem of mapping collapse, where input image is mapped to the same image as itself. Therefore, we exploit the spectrum information of the training samples.

The proposed model is shown in Figure2. The model includes two generators $G_s: C \rightarrow S$ and $G_c: S \rightarrow C$, and two discriminators D_s and D_c .

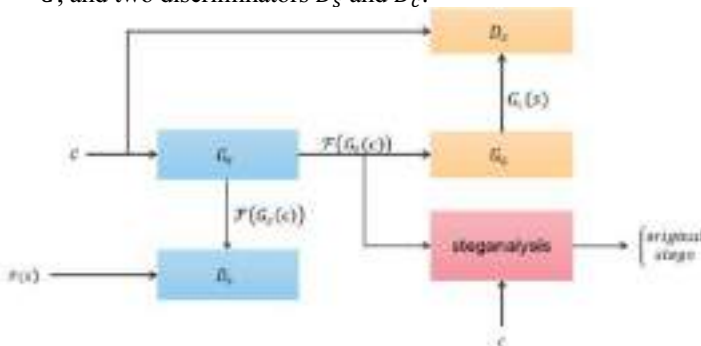


Figure2: Architecture of the proposed model

For the mapping function $G_s: C \rightarrow S$ and its discriminator D_s , we express the loss function:

$$L_{D_s} = [\mathcal{L}_{BCE}(D_s(\mathcal{F}(G_s(c))), 0) + \mathcal{L}_{BCE}(D_s(\mathcal{F}(s)), 1)] / 2$$

$$L_{G_s} = \mathcal{L}_{BCE}(D_s(\mathcal{F}(G_s(c))), 1)$$

where $\mathcal{L}_{BCE}(\cdot)$ is a binary cross entropy loss function, $\mathcal{F}(x)$ is the spectrum of image x . G_s tries to generate pseudo stego images that resemble unpaired real stego images in the frequency domain, while D_s aims to distinguish between the pseudo stego images and real stego images in the frequency domain.

For the mapping function $G_c: S \rightarrow C$ and its discriminator D_c , we express the loss function in the spatial domain as there is no need for the spectrum similar for the cover images:

$$L_{D_c} = [\mathcal{L}_{BCE}(D_c(G_c(s)), 0) + \mathcal{L}_{BCE}(D_c(c), 1)] / 2$$

$$L_{G_c} = \mathcal{L}_{BCE}(D_c(G_c(s)), 1)$$

where G_c tries to generate pseudo cover images that resemble corresponding real cover images in the spatial domain, while D_c aims to distinguish between the pseudo cover images and real cover images in the spatial domain.

Similarly, we introduced identity losses in the frequency domain of stego images and in the spatial domain of cover images:

$$L_{I_s} = \mathcal{L}_{BCE} \left(D_s \left(\mathcal{F}(G_s(s)) \right), 0 \right)$$

$$L_{I_c} = \mathcal{L}_{BCE} \left(D_c(G_c(c)), 0 \right)$$

The total GAN loss is

$$L_{GAN} = \alpha_1 L_{D_s} + \beta_1 L_{D_c} + \alpha_2 L_{G_s} + \beta_2 L_{G_c} + \alpha_3 L_{I_s} + \beta_3 L_{I_c}$$

where we can adjust their weights α_i and $\beta_i, i \in \{1,2,3\}$, to strengthen or weaken the desired domain.

The structures of generator and discriminator are shown in Figure3.

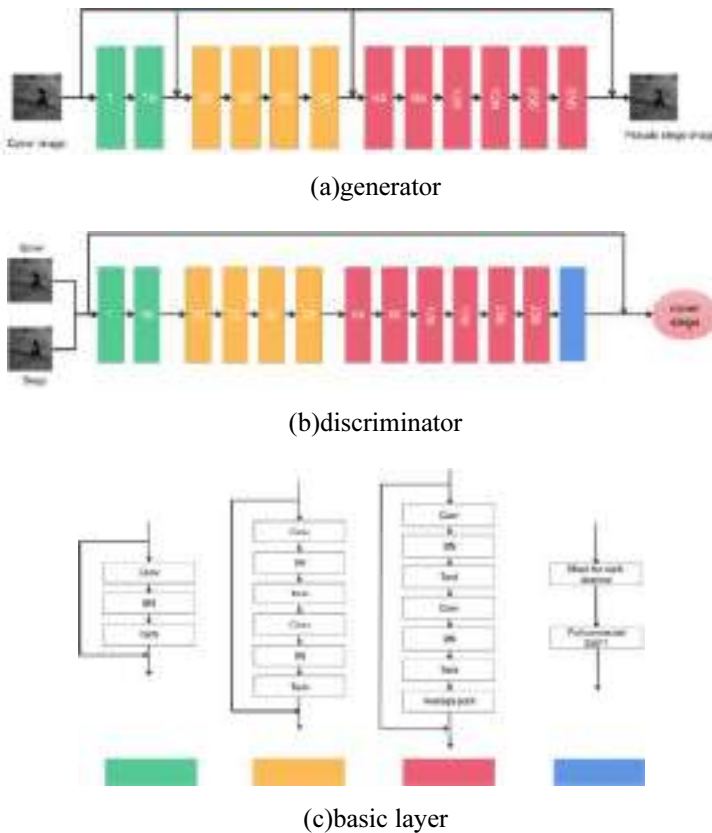


Figure 3. Structure of the generator (a) and the discriminator (b). There are four types of layers. The first type of layers is residual convolution layer with 3×3 -kernel as the first layer in (c). The second type of layer is convolution layer with 1×1 kernel as the second layer shown in (c). The third type of layer is convolution layer with 1×1 kernel as the third layer shown in (c). The number in each layer is its number of input channels. Unlike the SRNet, we use Tanh as the activation function. The fourth type of layer is a fully connected layer with a mean operation for each input channel as.

4. Experiments and Analysis

Our experiments are conducted on a commonly used publicly available sources BOSSBase v.1.01. The Baluja-Net [5] is used to embed a full-sized image into a cover image. We generate 2000 real stego images from the BOSSbase in such a way: for an image i in BOSSbase, we randomly select any other image $j \in \{k | 1 \leq k \leq 10000, k \neq i, k \in Z\}$ as secret image for steganography.

We conducted several experiments for performance comparison and show the results in Table 1. The Non in the second column stands for the steganalysis is trained with the real unpaired cover and stego images only.

Table1. Performance comparisons of proposed architecture

Steganography	generator	Training size		
		200	400	800
Baluja-Net[5]	RES	86.33%	91.61%	96.31%
	Non	93.33%	89.46%	93.11%
S_UNIWARD (0.2bpp)	RES	61.05%	70.19%	73.28%
	Non	50.00%	50.00%	50.00%
S_UNIWARD (0.4bpp)	RES	59.83%	72.60%	77.89%
	Non	50.00%	50.13%	50.58%
S_UNIWARD (0.6bpp)	RES	65.39%	74.88%	79.15%
	Non	50.540%	51.03%	51.85%

For the unpaired dataset composed of stego images generated by Baluja-Net, the generative learning framework proposed in this paper has certain advantages over the Non mode when the training size is 400 and 800. However, for the unpaired dataset composed of stego images generated by S-UNIWARD algorithm, the generative learning framework proposed in this paper has obvious advantages. If there is no paired dataset, the stego image generated by S-UNIWARD algorithm can be recognized by steganalysis module at about 50%, which is basically equivalent to random guess.

5. Conclusions and Future Work

In this paper, we proposed a generative learning network for steganalysis. The experiment results showed that the generative learning architecture improves the detecting accuracy of the steganalysis when the training images are unpaired. The generative learning framework proposed in this paper is a feasible and effective strategy for steganalysis training in the case of unpaired training dataset.

Although the generative learning framework proposed in this paper has achieved good results in the case of unpaired datasets, there is still much work to be done This architecture performance bad for other classic steganography algorithms such as WOW [6] and HUGO [7]. Future work includes exploring more unpaired training sets generated by different steganography algorithms, and trying to improve the performance of the generative learning framework from the aspects of network structure and learning algorithms.

Acknowledgement

This work was supported in part by the National Natural Science Foundation of China under Grant 71571190, 62002381.

References

- [1] J. Zhu, T. Park, P. Isola and A. A. Efros, "Unpaired Image-to-Image Translation Using Cycle-Consistent Adversarial Networks," 2017 IEEE International Conference on Computer Vision (ICCV), 2017, pp. 2242-2251, doi: 10.1109/ICCV.2017.244.
- [2] Chen, X., Xu, C., Yang, X., Tao, D. (2018). Attention-GAN for Object Transfiguration in Wild Images. In: Ferrari, V., Hebert, M., Sminchisescu, C., Weiss, Y. (eds) Computer Vision - ECCV 2018. ECCV 2018. Lecture Notes in Computer Science, vol 11206. Springer, Cham. https://doi.org/10.1007/978-3-030-01216-8_11
- [3] T. Park, M. -Y. Liu, T. -C. Wang and J. -Y. Zhu, "Semantic Image Synthesis with Spatially-Adaptive Normalization," 2019 IEEE/CVF Conference on Computer Vision and Pattern Recognition (CVPR), 2019, pp. 2332-2341, doi: 10.1109/CVPR.2019.00244.
- [4] M. Boroumand, M. Chen, and J. Fridrich, "Deep residual network for steganalysis of digital images," IEEE Trans. Inf. Forensics Security, vol. 14, no. 5, pp. 1181–1193, May 2019.
- [5] Shumeet Baluja. "Hiding images in plain sight: deep steganography". Proceedings of the 31st International Conference on Neural Information Processing Systems (NIPS'17). Curran Associates Inc., Red Hook, NY, USA, 2017. 2066–2076.
- [6] V. Holub and J. Fridrich, "Designing steganographic distortion using directional filters," in 2012 IEEE International Workshop on Information Forensics and Security (WIFS), 2012, pp. 234–239. doi: 10.1109/WIFS.2012.6412655.
- [7] T. Filler and J. Fridrich, "Gibbs Construction in Steganography," IEEE Trans. Inf. Forensics Secur., vol. 5, no. 4, pp. 705–720, 2010, doi: 10.1109/TIFS.2010.2077629.

Multi-Path Propagation Prediction of 433MHz Wave in the Ship Environment Based on the Ray-Tracing Model

Wanli TU¹, Hong XU, Yiqun XU and Qing ZHOU

Marine Engineering Institute, Jimei University, Xiamen, 361021, China

Abstract. Designing a stable wireless sensor network with reliable transmission is a key issue for wireless communication applied in the complex ship environment. The traditional network node deployment mainly relies on human experience along with multiple tests and leads to very long construction period. The current work established a three-dimensional ray-tracing model of the 433MHz wave transmission in an engineering ship. The multi-path propagation prediction results were compared with the on-site test of wireless channel using LoRa communication devices. Then the deployment scheme of the transmission and reception nodes was proposed to facilitate the signal stable transmission. It could provide an effective theoretical guidance for the network construction.

Keywords. Ship cabin, LoRa, ray-tracing method, multi-path propagation

1. Introduction

With the development of smart ships and unmanned ships, digital sensors and numerical control devices are widely used. Instead of the cable transmission, the application of wireless sensor networks based on the Internet of Things (IOT) for ship has been studied extensively over the past few years [1-2]. With low power, easily assemble devices and sensor modules, it becomes a potential low cost alternative for traditional cabling networks. So far, researchers mainly use Zigbee technology or LoRa (Long Range) technology to design the network [3-4].

The ship cabin is usually large and the equipment are placed in the relatively fixed position when the vessel is assembled. The monitoring sensors of cabin equipment are deployed with little change. Thus the wireless signal propagating in ship cabin mainly includes diffraction and reflection [5]. The longer the wavelength, the stronger the ability to diffuse the large obstacles. Besides, due to the abundance of metal equipment in the complex ship environment, the signal power loss could not be ignored.

LoRa is a kind of ultra-long-distance wireless transmission scheme based on spread spectrum technology. Compared to the Zigbee technology, it has unique advantage with longer transmission distance, longer battery life and better pass-through ability [6-8]. It has been proved its stable working performance for ship-based measurement system [9-10]. Thus it could be well employed in various cabins of the ship with a good application prospect. This paper analyzed the LoRa band (433MHz frequency band here)

¹ Corresponding Author: E-mail: wanlitu@163.com.

propagation in an engineering ship based on the ray-tracing method. It aims to provide the propagation prediction and some deployment guidance for the network design, different from the traditional way which mainly relies on human experience along with multiple on-site test and lack of effective theoretical analysis.

2. Multi-path Propagation Prediction of LoRa Band in Engineering Ship Cabin

2.1. Ship cabin model establishment based on the ray-tracing method

Prior simulation-based studies based on the indoor path loss model would help to predict the wireless channel propagation and would greatly reduce the cost of network construction. Ray tracing algorithms has computational advantages and high accuracy, and are used widely in graphics and mobile communication analysis. Details about the electromagnetic theory can be found in the published literatures [11]. It has been validated an effective method of the communication analysis in indoor complex environment [12]. The propagation prediction can be carried out by the comprehensive analysis of reflection, transmission, diffraction of each tracking ray. This group previously investigated the 2.4 GHz wireless channel propagation in the ship cabin and the simulated results were consistent with the experimental results [13]. In the present work, the 3D-dimensional model of the real engineering ship cabin “Zhaoming wheel” (shown as Figure 1) was established and the multi-path propagation prediction of wireless signal at 433MHz frequency band was carried out based on the ray-tracing method. All simulations reported here were performed using the Remcom Wireless InSite commercial software package[14].

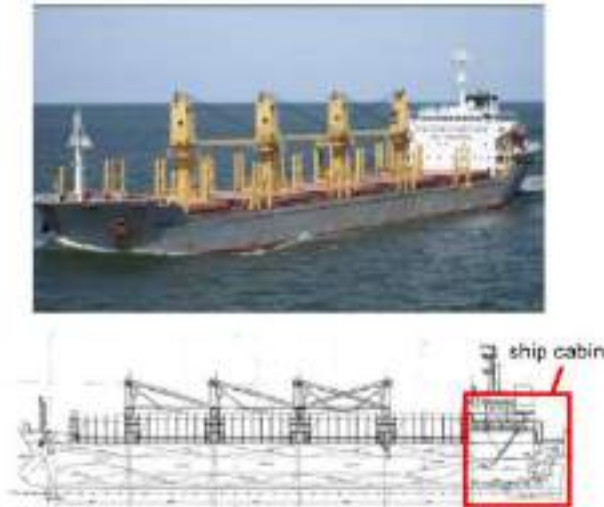


Figure 1. Side view of “Zhaoming Wheel”

The “Zhaoming wheel” is 169m length and 13.6m moulded depth with 43m maximum height. Figure 2 showed the ship cabin structure. The main engine was located at the middle area of the bottom floor, and the hollow staircase leading to the second platform was arranged on one side; The second-floor platform surrounded the main

engine and was arranged with a control room and the corridors, the ship auxiliary engine was located at the tail of this platform. The accommodation area was above the third platform and the ship wheelhouse was at the top. Figure 3 showed the deployment of the transmitter (Tx) and receiver (Rx). The transmitter was placed at the bottom platform of the main engine room. The receivers were placed at various areas including: bottom floor of cabin (Rx1, Rx2), outside the control room (Rx3), accommodation area1 (Rx4), accommodation area2 (Rx5), ship wheelhouse (Rx6) and the weather deck (Rx7). The receivers Rx3, Rx4 and Rx5 adopted 16 receiving nodes forming a rectangle shape, respectively.

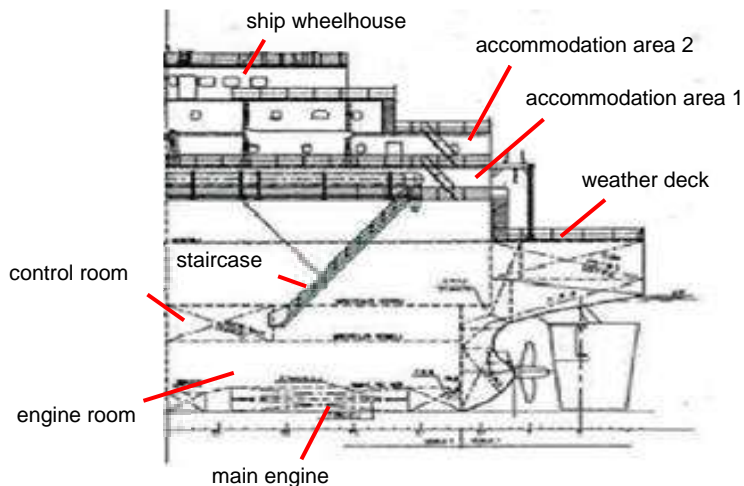


Figure 2. Ship cabin structure

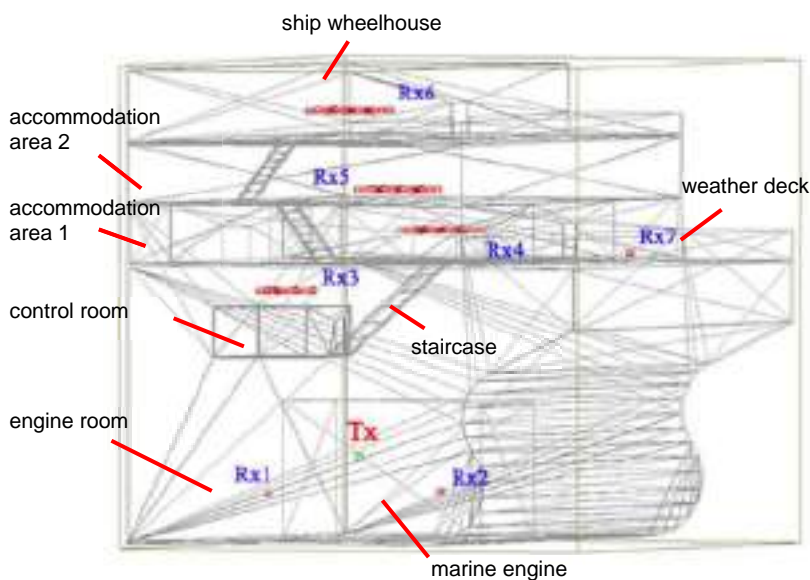


Figure 3. Deployment of the transmitter and receiver in ship cabin

The material of structure and equipment was set as steel. The doors between floors were open and set as fireproof material and were. The windows of the control room were made of glass. An omnidirectional monopole antenna working in vertical polarization mode was adopt with sinusoid wave shape of the transmitting signal. Other simulation parameters were shown in Table 1.

Table 1. Simulation parameter

parameter	value
Signal frequency	433MHz
Transmit power	20dBm
Transmitter	Linear monopole omnidirectional antenna
Receiver	Linear monopole omnidirectional antenna
Antenna gain	15dBi
Reflections	5
Transmission	2
Refraction	1

2.2. Propagation results

Both Rx1 and Rx2 have good reception since the receivers were located at the same layer as the transmitter. While the receiver Rx6 and Rx7 had bad reception because they were far from the bottom floor. And the Figure 4, Figure 5 and Figure 6 were the multi-path propagation results of Rx3, Rx4 and Rx5, respectively.

As can be seen from the results, while the floor height increases, the effective transmission path decreases significantly, as well as the signal strength. For the Rx3 located outside the control room, the minimum receiving power -30dBm occurred at the #1 receiving node, which represented the innermost position of the area. The multiple reflections caused the large energy loss. Except that, the other receiving node could get good reception due to the staircase which could provide the favorable transmission channel. For the Rx4 located at the accommodation area1, there were some receiving nodes (region 2) with poor reception because they were far from the hatch and several activity rooms and cubicles distributed in this floor. It obviously increased the reflections and consumed a lot of signal energy. For the Rx5 located at the restaurant in the accommodation area2, the fluctuation occurred on the various nodes (from the -13.5dBm to -250dBm). However, the receiver was relatively high and far from the transmitter at the bottom floor and most nodes had relatively poor reception. The region 3 even had no effective propagation path.

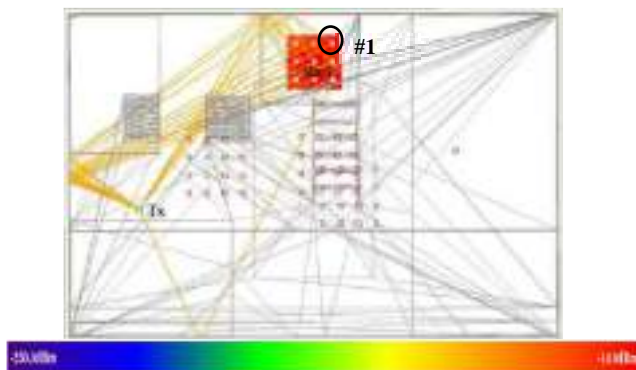


Figure 4. Propagation result of the receiving nodes of Rx3

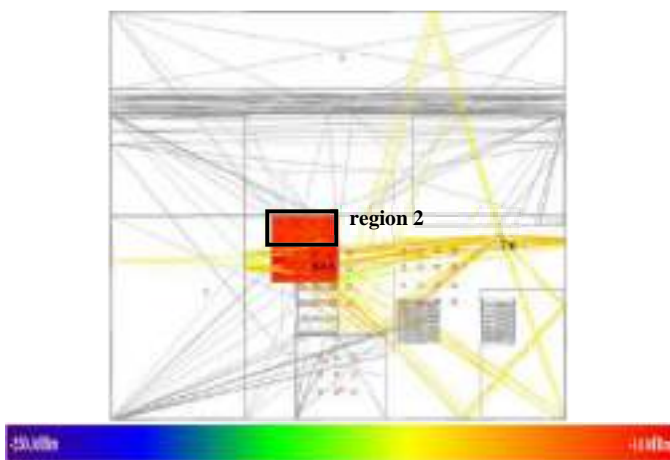


Figure 5. Propagation result of the receiving nodes of Rx4

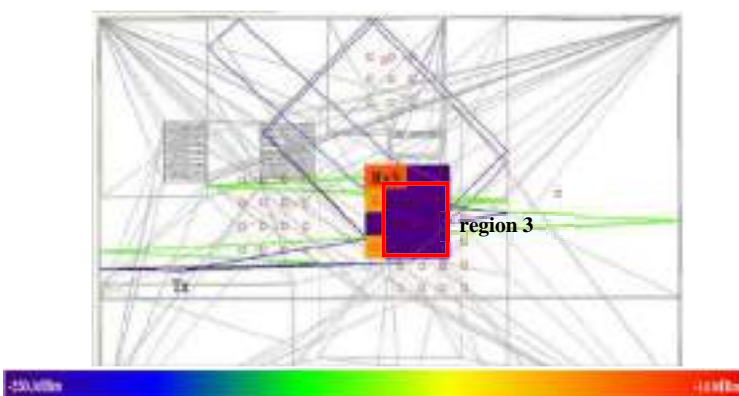


Figure 6. Propagation result of the receiving nodes of Rx5

The experimental point-to-point test using the LoRa communication devices was also carried out in the ship cabin of ‘Zhaoming Wheel’, shown as Figure 7. The measurement area was the same as the simulation[15]. The reception situation was shown in Table 2, as well as the simulated result. The comparison showed that although the model couldn’t fully represent the actual complicated ship structure, the simulation analysis was relatively consistent with the experiment. It means that propagation prediction based the proposed method could play effective guidance for real network.



Figure 7. Experimental test using the LoRa communication devices

Table 2. LoRa communication situation of the ship cabin

Receiver	Reception (simulation)	Reception (experimental)
bottom floor (Rx1、 Rx2)	good	good
control room (Rx3)	good	good
accommodation area1 (Rx4)	normal, partly no reception	normal
accommodation area1 (Rx5)	poor, partly no reception	normal, partly data packet loss
ship wheelhouse (Rx6)	no reception	poor, seriously data packet loss
weather deck (Rx7)	poor	poor, seriously data packet loss

From the simulated and experiment result, some deployment scheme of the transmission and reception nodes can be concluded to facilitate the signal stable transmission. The analysis can provide a good reference for the network deployment. Although the transmitter and the receivers was set at the different platforms, some receiving points within the adjacent layers could get good reception, especially with the help of the hollow staircase. However, it was still recommended that one gateway base station should be arranged on each cabin platform when constructing the network. It was only responsible for the communication with the nodes within this platform to ensure the stable signal transmission. In addition, in the same cabin platform, the location of the transmitter and the receivers should avoid the diagonal position of the large equipment obstacles. If it is really unavoidable, it was better to set another relay node for relay transmission of the collected data.

3. Conclusion

This work investigated the multi-path propagation of 433MHz wave transmission in an engineering ship cabin based on the ray-tracing method. According to the structure drawings combine with the cabin equipment measurement, the three-dimensional ray-tracing model of the 433MHz wave transmission in the ship cabin was established. The

transmitter and receivers were set at the various locations. And the propagation characteristics was investigated. Besides, the on-site point-point test of wireless channel using LoRa communication devices was carried out in the engineering ship and the reception was recorded. The comparison indicated that the propagation prediction based on the established model could be consistent with the experimental results of each cabin layer. The variance between the simulated model and the real ship unavoidable existed, however the simulated result would provide effective guidance for the practical signal transmission in the ship. For the complex ship environment, the prior simulation analysis was recommended because the network deployment could skip the unfavorable locations for the signal transmission. The simulation-based studies of wireless channel propagation in ship were an effective and low-cost way and would play an important role for the wireless sensor work construction.

References

- [1] Zhang H, Lu X, Vehicle communication network in intelligent transportation system based on internet of things. *Computer Communications*, 2020; 160: 799–806.
- [2] Dragulinescu AM, Halunga S, Zamfirescu C, Unmanned Vehicles' Placement Optimisation for Internet of Things and Internet of Unmanned Vehicles. *Sensors*. 2021; 21: 6984(38pp).
- [3] Wang MC., Research on data acquisition method of ship wireless sensor network node, *Ship Science and Technology*, 2018; 40(1A):144-146. (In Chinese)
- [4] Setiawan B, Putra ES, Siradjuddin I, Junus M, Dewatama D, Wiyanto S, Study of LoRa (Long Range) communication for monitoring of a ship electrical system. *Journal of Physics: Conference Series*. 4th Annual Applied Science and Engineering Conference. 2019; 1402(4), 044022 (6pp).
- [5] Xu YQ, Xu H, M LC, Tu WL. Research on network architecture and reliability of wireless communication system for full-scale ship. *Ship Engineering*. 2021; 43(6): 85-95. (In Chinese)
- [6] Sundaram JPS, Du W, Zhao Z, A Survey on LoRa Networking: Research Problems, Current Solutions, and Open Issues. *IEEE Commun. Surv. Tutor*. 2020; 22: 371–388.
- [7] Muhammad AU, Junnaid I, Arliones H, Richard DS, Hirley A, K-Means spreading factor allocation for large-scale LoRa networks. *Sensors*. 2019; 19: 4723.
- [8] Ji YH, Yang H, Applications of LoRa and NB-IoT in Internet of Things. *American Journal of Information Science and Computer Engineering*. 2019; 5(2):25-28
- [9] Sanchez-Iborra R, Liaño IG, Simoes C, Couñago E, Skarmeta AF, Tracking and Monitoring System Based on LoRa Technology for Lightweight Boats. *Electronics*. 2019; 8: 15.
- [10] Xu WD, Chen YH. A LoRa-Based ship data acquisition system. *Journal of shanghai ship and shipping research institute*. 2021 Sep; 44(3):16-21. (In Chinese)
- [11] Shikhantsoy S, Thielens A, Vermeeren G, Tanghe E, Demeester P, Torfs G, Martens L, Joseph W, Industrial indoor massive MIMO human EM-exposure evaluation. *Proceedings of the Joint Annual Meeting of the Bio Electromagnetics Society and the European Bio Electromagnetics Association*. 2018 p.403-406.
- [12] Maccartney GR, Rappaport TS, Sun S, Deng SJ, Indoor office wideband millimeter-wave propagation measurements and channel models at 28 GHz and 73 GHz for ultra-dense 5G wireless networks. *IEEE Access*, 2015, 2388-2424.
- [13] Tu WL, Xu H, Xu YQ, Ye QB, Shen MX, Research on 2.4 GHz Wireless Channel Propagation Characteristics in a Steel Ship Cabin. *International Journal of Antennas and Propagation*, 2021; Article ID 6623638(12pp).
- [14] REMCOM. *Wireless InSite 3.2.0 Reference Manual*. URL <http://www.remcom.com/>- Wireless InSite. 2017.
- [15] Callebaut G, Perre LV, der Characterization of LoRa Point-to-Point Path Loss: Measurement Campaigns and Modeling Considering Censored Data. *IEEE Internet Things J*. 2020, 7, 1910–1918.

A Study on the Strategy of Vocational English Digital Teaching Materials Development in the Context of Internet+—Taking the Integrated Course of English as an Example

Hui SUN^a, Huaizhong ZHU^b and Lisha WANG^{c1}

^a*Shanghai Technical Institute of Electronics & Information, China*

^b*Tianhua College, Shanghai Normal University, China*

^c*Shanghai Customs College, China*

Abstract. The advent of the age of intelligence has created a more urgent need for the digitisation of teaching materials in higher education institutions. The evaluation of English digital teaching materials is an extremely important and special window for the country to conduct cultural exchanges. [1] However, there are difficulties in digitising teaching materials in higher education institutions. The low importance attached to the construction of digital teaching materials, the lack of relevant teacher training, the insufficient investment in hardware funding, the low utilisation rate of resource libraries and the lack of effective inter-school communication and resource sharing have led to some repetitive development and waste. The relatively weak knowledge base, learning ability and willingness to learn of higher vocational students have always made the preparation of digital teaching materials for higher vocational English difficult. The author reconstructs the strategy of writing digital teaching materials for Integrated English Course based on three major dimensions: teaching materials, application of information-based learning software, and Internet+ exam, and explores five sub-dimensions: production team, a la carte lesson plan writing, cross-application of information-based learning software, knowledge base construction, and Internet+ exam. The use of digital teaching materials over two academic years has effectively improved the students' ability to systematically learn theoretical knowledge and intelligently apply information software.

Keywords. Higher education, Internet+, comprehensive English course, digital textbook, textbook development strategy

1. Introduction

With the development of computers, the Internet and other information technology, digital technology is increasingly used in school education as an effective supplement to classroom teaching through various new teaching modes such as MOOC, flipped classroom and online classroom etc. National Medium and Long-term Education Reform and Development Plan (2010-2020) places special emphasis on “integrating education

¹ Corresponding Author, Lisha WANG; E-mail: wanglisha@shcc.edu.cn.

informatization into the overall strategy of national informatization development[...]promoting the modernisation of education content, teaching methods and... and accelerating the popularisation of terminal facilities and promote the construction of digital campuses”.[2] According to the results of the 9th National Reading Survey published by China Publishing Network in 2012, the digital reading exposure rate of Chinese citizens aged 18-70 grew to 38.6% in 2011. [3] More and more teaching content is being moved digitally to the Internet, providing teachers, students and researchers with richer, more convenient and more vivid teaching resources, of which the need for digital construction of teaching materials has become more urgent. However, after analyzing the status quo of usage of digital teaching materials in our classrooms, it was found there exists great gaps among various majors.

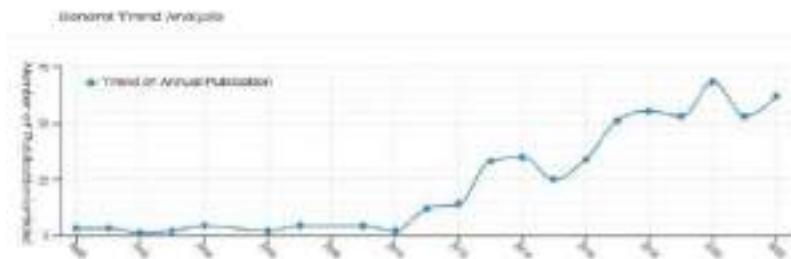


Figure1 General Trend of Digital Teaching Materials Research Analysis

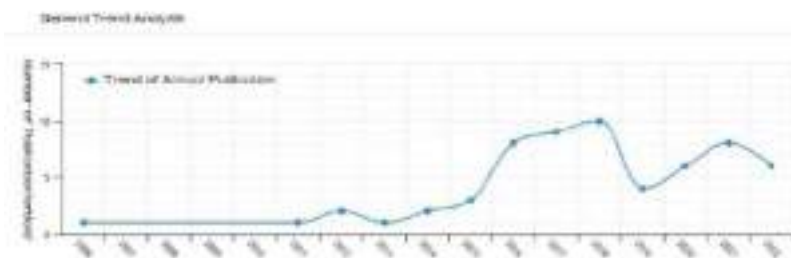


Figure2 General Trend of Digital Teaching Materials Research in English Analysis

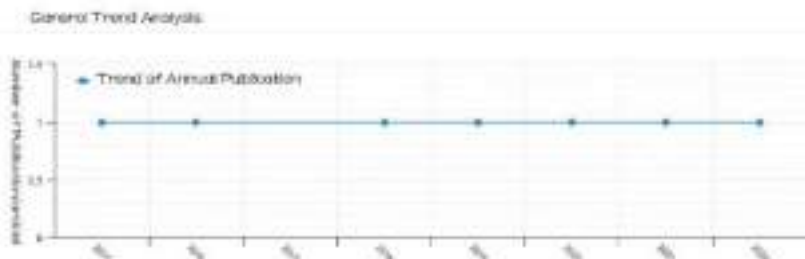


Figure 3 General Trend of Digital Teaching Materials Research in Vocational English Analysis

Analyzing the trend of digital teaching materials researches in the CNKI (China National Knowledge Infrastructure) in Figure 1, it was found it has shown powerful growth in China, covering 481 items. However, when we input “digital teaching materials in English” into the system, which tells us that there are only 56 items concerned about it in Figure 2. When we narrow down the topic into “digital teaching

materials in Vocational English”, the result shows only 7 items in Figure 3. Therefore, it was found the current research on Digital Teaching Materials in Vocational English still needs great attention, and it shows many gaps where we need to narrow down so as to improve vocational English teaching and research in a real sense.

The evaluation of English digital teaching materials is an extremely important and special window for the country to conduct cultural exchange. [1] At present, the theories and research results related to digital teaching materials in China are not perfect, and the development of digital teaching materials is basically at a preliminary stage, mainly in the form of electronic lesson plans, electronic teaching materials, related audio and video databases, online homework, question and answer platforms and other interactive platforms. The problems currently faced include the low level of attention paid by schools, the lack of relevant teacher training, insufficient investment in hardware, low utilisation of resource libraries, and the lack of effective inter-school communication and resource sharing, leading to some repetitive development and waste.

In addition, the knowledge base, learning ability and willingness to learn of students in vocational colleges are relatively weak, and the three-year teaching time further limits the teaching to more theoretical combing of students and more biased towards market application-based training. Students are less likely to concentrate in class but prefer video and audio digital materials to paper-based ones. At present, the digitalisation process of higher education textbooks in China has just started, and there is no perfect digital textbook that can perfectly combine with the paper version, not to mention replacing it. Therefore, in view of the characteristics of the current higher vocational education in China and the actual needs of the curriculum reform, how to design a set of digital teaching materials to meet the actual needs is a difficult task that higher vocational educators have to consider seriously.

Xiaotang, Cheng, published in 2010 by Foreign Language Teaching and Research Press, whose Integrated English Course for English majors in vocational colleges is widely used at present and edited by Professor Cheng Xiaotang. This textbook not only provides a systematic paper version of the teaching content, but also provides an accompanying MP3 material. Therefore, there is still room for further research and exploration on how to improve the quality of English teaching materials in higher education institutions under the background of Internet+ and how to make effective use of the new form of teaching materials, so that higher education students can actively participate in learning and truly promote teaching and learning.

2. Diachronic analysis of digital teaching materials both at home and abroad

Computer Internet information technology originated in Europe and the United States, where the research and practice of digitising textbooks is more mature. In the United States, the digitisation of textbooks is at its highest level, with scholars predicting as early as 2009 that paper textbooks in the USA might disappear (New York Times). After more than a decade of research and practice, the high cost of paper-based textbooks in the USA has prompted most USA schools to adopt paperless e-textbooks, and even two USA airline libraries have been forced to close and implement a completely electronic reading model. As of 2015, South Korea has fully digitised its textbooks; Germany is also actively promoting the pace of digital teaching; Malaysia, Indonesia, Turkey, Singapore and Portugal are also actively promoting the use of Kindle e-textbooks at primary and secondary school level, among others. The advantages of e-textbooks for students cannot

be overstated, and the profound changes and impact it has brought to publishers, libraries and others continue.

At present, the reviews of digital English textbooks in most Western countries are extremely optimistic, and they have not only experienced the advantages of convenience, speed and intuitiveness brought by new media and the Internet in digital English textbooks, but also improved the general education level of Western countries to a great extent. [1] A reading article in English IV dated 16 June 2018[4] describes the teaching application and commercial development of digital textbooks in the USA model of student feedback and dissatisfaction with publishers requiring students to pay high prices to complete assignments, showing a side-by-side look at the commercial promotion model of digital textbooks by USA publishers.

With the development of computer multimedia technology, domestic research on digital teaching materials began with electronic teaching materials in the late 1990s, and research on various types of electronic textbooks, e-textbooks and other “electronic” series increased. In the 21st century, the development of network information technology has brought about various kinds of “digital” research, among which the research on digital teaching materials has gradually become a hotspot since 2010, and various digital resource libraries have been established.

Zhong Cenzen’s[5] study pointed out that domestic research on digital teaching materials up to February 2016 mainly involved three major fields: education, publishing and technology, and was dominated by educational technology; although preliminary research has been developed, the amount of high-level literature and the depth of research still needs to be improved. Her research also found that the affiliations of digital teaching materials researchers were mainly focused on teachers with a background in educational technology research at universities, for example, Zhu Zhiting’s team at East China Normal University focused on the development of e-textbooks and e-schoolbags; Huang Ronghuai at Beijing Normal University focused on the systematic study of the generation, development, design and development of e-textbooks; Sun Zhong and others at Capital Normal University designed and built models to develop digital teaching materials and Sun Zhong from Capital Normal University designed models to develop digital teaching materials and resources, and explored issues such as teacher development and student technology acceptance in a digital environment. Research on digital teaching materials has also been a hot topic for publishers in recent years. For example, People’s Education Publishing House has conducted in-depth research on digital teaching materials from the perspective of educational publishing, from its own products such as English online teaching materials and digital teaching materials.

In terms of content, domestic and international research on the digitisation of teaching materials has focused on four main areas: basic research[6], design and development research[7], teaching application research[8] and business model research[9].

Li Yang[10] from Jiaotong University Press analyses the trend of digital publishing of higher vocational textbooks, giving the advantages and disadvantages of digitalization, and the great challenges and problems faced by higher vocational textbooks. Wu Lin and Yang Fangyong[11] continue to discuss the inevitable trend of digitization of higher vocational English textbooks and how to better solve the problems such as copyright, using higher vocational English audio-visual textbooks as a model.

3. Status quo of foreign language teaching materials publication in high vocational colleges

Digital materials should be designed to cater to students and be able to be easily presented in the classroom to capture their attention. A digital textbook has to choose the most appropriate means of presenting the project content to organise learning resources for learners to choose from according to their learning preferences. The project team will focus on designing adequate teaching and digital resources to gradually transform the previous teacher-centred English classes in higher education into a student-centred, task-completion oriented, student-led and self-motivated learning atmosphere. The two main areas of focus will be the following.

1. How to develop teaching resources and digital teaching materials for higher vocational education in the light of the characteristics of higher vocational education?
2. How to realize the deep integration of digital teaching materials and higher vocational teaching resources and the mutual promotion between them?

At present, under the background of Internet+, although the digital development and publication of foreign language teaching materials in colleges and universities have made certain achievements, the overall system is not yet perfect. There are many problems. [12]

3.1 Content homogenization

The three sets of Integrated English textbooks used by the first author's vocational college in recent years were found to have been developed to support the paper-based textbooks through the feedback of the teachers who taught them. This "copy" model limits the use of digital resources and does not reflect their advantages of personalisation, interactivity and information diversity. [13]

3.2 Monotonous format

Compared to the UNIPUS APP software of the Foreign Language Teaching and Research Press, Soochow University's Suda English Online, and Sichuan Foreign Studies University's English 84, English digital teaching materials in higher education institutions with mobile social software developed for foreign language corners are still rare, mobile APP content is not rich, and the development of digital teaching materials is relatively backward. With the increasing popularity of Internet+ learning methods, digital English teaching materials can be developed from multimedia courseware, online test banks, independent learning platforms, teaching websites and other aspects.

3.3 Disconnection between teaching and learning

Most of the current English e-textbooks in higher education institutions are matched with paper-based textbooks, but there are still shortcomings in the design of achieving the dimensions of teacher-student and student-student interaction. It is not uncommon to lose sight of this. This affects the consistency of teaching and learning to a large extent.

As such, technology brings with it the power to destroy and destroy the century, and young students are always most interested in and receptive to the latest technological products and applications. Therefore, using technology to motivate higher education students to learn English in the classroom is what the digital higher education English textbook hopes to accomplish. The digitisation of higher-level English textbooks can better suit the learning characteristics of higher-level students, stimulate their interest in learning and provide a useful complement to teachers' lectures. Therefore, the project team intends to document, summarise and make recommendations related to the construction of digital English textbooks for higher-level English by completing the e-

lesson plan and related digital resource library for Book 1 of the Comprehensive English Course.

3.4 Designing ideas of e-teaching materials for integrated course of English in a vocational college in Shanghai

Respondents of the first author’s experiment are Chinese students who come from Shanghai Technical Institute of Electronics & Information. As the e-learning programme and digital resource library of the Integrated English Course are intended to be reconstructed in three dimensions: teaching materials, information-based learning software applications, and Internet+ examinations, Figure 4 illustrates details.

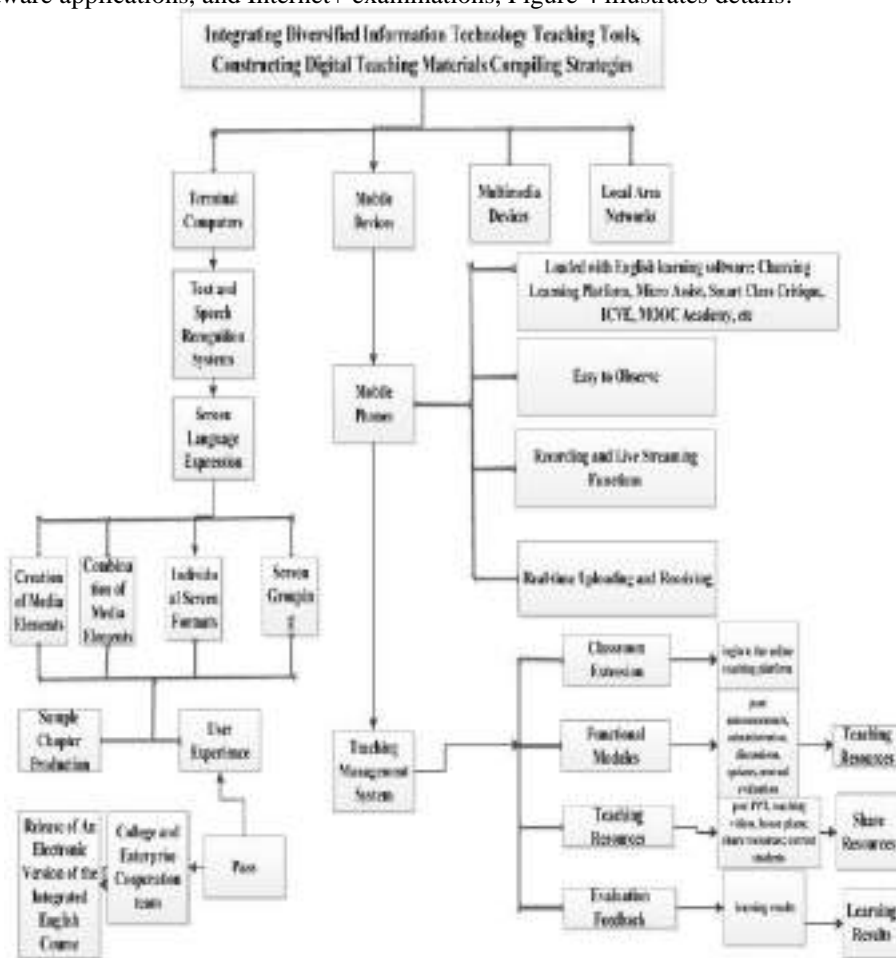


Figure 4 Strategies for writing digital materials

Integrating Diversified Information Technology Teaching Tools, Constructing Digital Teaching Materials Compiling Strategies is a relatively ideal tool which combines textbooks with online learning and offline learning. With the aid of the technical company, the teacher is equipped with the opportunity to release digital materials with detailed instructions for online learning in advance. In addition, the teacher can supervise online learning without any limitation, which reminds students what they need to do at various time and space. Ultimately, in order to narrow down the

gap between online and offline learning, the teacher, who has gained the latest information on students' performance online, can carry out his/her class purposefully. By doing so, class efficiency, to great extent, can be improved greatly.



Figure 5 Digital Materials for Integrated English Course

(1). Build a stable production team to work together to complete the task of digital development of this higher education textbook (see Figure 5). The teachers in this team are from a vocational college in Shanghai specialising in English and a teacher from Chaoxing company who is also an Internet+ professional team. The team includes front-line teachers who are familiar with image processing techniques, video editing techniques; software development skills; and the content of the Integrated English Course textbook. Teachers adopt a variety of digital representations and design different digital media formats so that students can selectively watch and learn according to their own preferences.

(2). Working together to complete the e-learning programme. The team members follow the task flow to decompose the digital meal and then reorganise it, setting up a search catalogue to facilitate students' query and retrieval of delayed knowledge points, thus allowing students to quickly and efficiently search for their preferred type of viewing media in order to maximise their independent learning.

(3). Cross-application of information-based learning software allows students to truly experience learning.

For example, for teaching Unit 6 *Job and Fun*, teachers can pre-assign the pre-reading topics in the micro-assist software. Create a group --> issue a task notice for students to complete the basic elements of the job interview (professional + moral) through pre-study --> check the students' pre-study assignments --> analyse the easy points in the students' assignments. During the course teaching the teacher is able to more effectively target the text and really have the material in his head and the students in his mind.

The development of Internet+ digital teaching materials also helps with classroom management. The mode of roll-call and sign-in at the author's university is still rather traditional. The time spent on roll-call in a class is quite a lot. The micro-assist software combines teaching materials, courseware, audio and video in one learning APP software.

It saves time and efficiency by giving students a 1-minute roll call and sign-in in class. Teachers can also follow up on student attendance in real time through the Chaoxing screen casting function. It effectively ensures classroom attendance and in-class teaching.

Table 1 Information-based Teaching Software that Your Teachers Use in Their Homework Assignments

Option	Total	Percentage
Chaoxing	77	17.46%
Zhike Pigai	18	4.08%
Wei Zhujiao	126	28.57%
Xiexie Weike	15	3.4%
Rarely Use	205	46.49%
Number of valid completions	441	



Figure 6 Highly-frequency of words list in Digitalized Teaching Platforms

Through the research, we found that on the question of whether teachers follow informative teaching software in the after-class homework assignment, 46.49% (see Table1) of students gave feedback that teachers hardly use it. However, on the question of whether you are willing to exchange your learning experience with the teacher of General English after class through the information technology platform? When asked this question, I found that 78.68% of students were still eager to implement the Internet+ learning model. (see Table1) However, many of our professional course teachers' information technology application ability is insufficient, and this is very much out of line with the background of our times. Ministry of Education of the People's Republic of China promulgated the Construction Plan for Modern Vocational Education System (2014-2020) in 2014: broadband and campus network to cover all vocational colleges by 2015, digital resources to cover all majors by 2020, and information technology application to reach the world's advanced level: accelerating the construction of digital professional curriculum system, extensive use of computer policy teaching in professional courses, digital practical training, and remote real-time education and other technologies[14]. Finally, the analysis of the word frequency of WorditOut shows that the third ranking word frequency is information technology. (see Figure 6) Although Internet+ exams change traditional paper-based exams that students have some difficulty

adapting for a while. However, big data tells us that this is an irreversible trend of the times. The authors suggest that teachers should continue to strengthen their professional training in informatisation in order to cope with the coming of the intelligent era with ease.

(4). Jointly building a library of relevant digital resources

Based on the research and practice of our predecessors, the project team has decided to start from five aspects: 1. making full use of and integrating the digital teaching resources already developed, such as *Integrated English Course*, Book 1, a high-quality resource sharing course; 2. developing the compatibility of digital resources running on different terminals and optimising the content of digital resources; for example, constructing knowledge maps, setting up knowledge points; 3. adding project-based scenarios and case studies to the digital resource library; 4. enhancing the fun of the digital resource library by adding digital games to create a good digital learning environment; 5. increasing the openness and inclusiveness of digital teaching materials.

(5). Internet + Examinations

In the process of implementing the digital construction of the Comprehensive English Course, the College of English Language and Culture, where I work, made 2 attempts to change the previous paper-based mid-term examination mode to a mobile phone terminal examination. Members of the team of professional course teachers produced numbered test questions in advance, and then the head of the teaching and research department entered the questions in the Chaoxing Learning App software and did the testing before the exam. Throughout, the students' examinations were basically smooth.

Table 2 Viewpoints on Mid-term Exams Held in An Information-based Format for Online Integrated English Course

Option	Total	Percentage
Time saving, Efficient; Worth Recommending	287	65.08%
Not much different from the traditional exam format	171	38.78%
Improving the validity of machine reading of subjective questions in order to better popularize information-based examinations	303	68.71%
Others (Your Suggestions)	147	33.33%
Number of valid completions	441	

As can be seen from the above Figures (see Table 2), 500 questionnaires were sent out, with 441 participants and an effective rate of 88.2%. How do you feel about the adoption of the information technology mode for the mid-term examinations of General English? 65.08% of the students think: it saves time and is efficient; it is worth promoting. However, we should also see our own shortcomings. 68.71% of the students think that the validity of the machine reading of the subjective questions is low. This is closely related to the system set-up. Subjective questions require extra time for teachers to mark and increase their workload. If Chaoxing could improve the technical aspects of the system, it might be more effective in improving the validity of the IT examinations.

4. Conclusion

From the construction of the e-lesson plan and digital resource library for the re-structured Comprehensive English Course in three dimensions: teaching materials, information-based learning software applications, and Internet+ examinations, we can see that the construction of digital teaching materials cannot be separated from the feedback from teachers of professional courses, corporate tutors, and even students. The team has now completed the first volume of the digital textbook, and work on the other three volumes is progressing in an orderly manner. Further research is needed to determine whether the research on this topic can be useful for the construction of digital teaching materials for small language majors. In conclusion, the improvement of the digital higher vocational Integrated English Course textbook needs to combine excellent digital resources and advanced new planned teaching methods to improve the effectiveness of higher vocational English classroom teaching and to write more reasonable digital textbooks to further promote the development of higher vocational English teaching.

Reference

- [1] Zhang Yunxia. Research on the Evaluation System of Digital Textbooks for College English[J]. *Journal of Heilongjiang Institute of Teacher Development*, 2018(5):142-144.
- [2] Gu Xiaoqing, Xu Zhe. How Can E-textbooks Support Changes in Teaching Styles [J]. *Modern Distance Education*, 2013(1):13-20.
- [3] Yang Dejun, Le Jinjun, Bao Shengjun, Wang Kai. Value and Problems of Promoting Digital Teaching Materials[J]. *Curriculum and Teaching Management*, 2011(3):2-4.
- [4] Pan Xiaoyan. Exam Guide for CET-4[M]. Shanghai: Xingjie Book Publishing Company, 2020.
- [5] Zhong Cencen. Research Status of Digital Textbook in China: A Literature Review[J]. *Digital Education*, 2016(5):7-12.
- [6] Hu Pan, Jiang Jiafu. A Study on the Technology Acceptance of Digital Teaching Materials by Primary and Secondary School Students and Its Influencing Factors [J]. *Modern Distance Education*, 2019(4):77-83.
- [7] Zhuang Kejun, He Baoxun. The Design of Electronic Teaching Materials Based on First Principles of Instruction[J]. *Modern Educational Technology*, 2012(4):21-24.
- [8] Gong Chaohua, Chen Guang, Huang Ronghuai. Re-examining the Value of Digital Teaching Materials Integrated into Daily Classroom Teaching in Primary and Secondary Schools [J]. *China Educational Technology*, 2014(2):60-66.
- [9] Jiang Xiaofeng. Marketing Model of E-books and Its Optimization Strategy[J]. *Journal of Library Science*, 2018(2):41-44.
- [10] Li Yang. On the Trends and Challenges of Digitalization of Teaching Materials Publication of Higher Vocational Education [J]. *Vocational and Technical Education*, 2013(23):85-87.
- [11] Wu Lin, Yang Fangyong. Trends in Digital Publishing of English Teaching Materials for Vocational College--A Review of A Course on Audio-visual English for Vocational College[J]. *View on Publishing*, 2015(16):112-113.
- [12] Wang Dong. Digital Publishing of Foreign Language Teaching Materials in Universities in the Internet+ Era [J]. *View on Publishing*, 2017(11):75-77.
- [13] Huang Min. Tendency and Countermeasures for Digital Publication of College English Teaching Material[J]. *Journal of Hunan University of Humanities, Science and Technology*, 2015(5):112-114.
- [14] Ministry of Education. Construction Plan for Modern Vocational Education System (2014-2020):2014, No.6[A].

Approach for Cryptography Digital Ecosystem Deployment

Inara OPMANE¹ and Rihards BALODIS

Institute of Mathematics and Computer Science of University of Latvia, Latvia

Abstract. The paper introduces the Cryptography Digital Ecosystem concept and describes the rationale for its implementation. A checklists approach is offered to ensure efficient and high-quality ecosystem deployment and helps to ensure consistency and completeness of necessary tasks. A collection of checklists are indicated, which have been analytically developed based on extensive analysis of public literature regarding the development of quantum encryption solutions and adequate compliance with the solution requirements.

Keywords. Checklist, methodology, cryptography, digital ecosystem deployment, quantum cryptography, quantum key distribution (QKD)

1. Introduction

An important research topic of the University of Latvia Centre for Quantum Computing Science is quantum computing: the theoretical aspects of quantum information including quantum algorithms, computational complexity, communications, and cryptography.

As solutions of the practical application of quantum computing are in the nearest future, the strategy of the Institute of Mathematics and Computer Science of the University of Latvia (IMCS UL) is to use quantum technologies that can be applied now and immediately.

The activity of IMCS UL was concentrated in quantum communications and encryption (quantum encryption) applications.

IMCS UL started the development of quantum cryptography research topics in 2019 with the purchase and operational testing of Clavis 3 from ID Quantique (<https://www.idquantique.com>). In order to develop the research of quantum cryptography at the institute, close research cooperation has been established with industry: the State Joint Stock Company “Latvijas Valsts radio un televīzijas centrs” LVRTC (www.lvrta.lv), mobile operator LMT (www.lmt.lv), telecommunication company TET (www.tet.lv), and the Electronic Communications Office of Latvia (www.vases.lv). Currently, QKD technology has been tested in LVRTC and LMT fibre infrastructure. The necessity of research is related to development of strategy for introducing a new comprehensive technology that could influence very different aspects and players of our everyday lives. The chosen research method is conceptual analysis. It includes data exploration gathered through literature research, in. The research strategy includes comparison and assessment of a different interpretation in theoretical research and its reflection on real situations analysed in the implementation of the European

¹ Corresponding Author, Inara OPMANE; E-mail: inara.opmane@lumii.lv

Regional Development Fund project “Applications of quantum cryptography devices and software solutions in computational infrastructure framework in Latvia”, Project ID number 1.1.1.1/20/A/106 (01.06.2021–30.11.2023).

In this paper authors describe in detail the topics and tasks for deploying a cryptography digital ecosystem strategy.

2. Digital Ecosystem Concept

The word ‘ecosystem’ was first used in print by A.G. Tansley in 1935 [1]. In literature, you can find different ecosystem establishing models: on the basis of business relations and services [2, 3], and ecosystem models in higher education [4].

Various Ecosystem Analogies are indicated in a summary report [3]:

- Biological Ecosystem
- Industrial Ecosystem
- Economy as an Ecosystem
- Digital Business Ecosystem
- Social Ecosystem.

The introduction of Digital Ecosystem concept started in 2000 at the World Economic Forum [5]. The concept was solidified in subsequent conferences and publications.

We follow the principles set forth by the World Economic Forum [5]:

- The digital renaissance and the global digital ecosystem
- Putting people at technology's heart
- Sustainability.

3. Cryptography Digital Ecosystem Concept

We deploy a Cryptography Digital Ecosystem model in connection with ICT cyber security and cryptography as a central technological solution for ICT security.

Cryptography Digital Ecosystem community cooperation partners are bound together by purposeful action, ensuring a higher level of cyber security in the environment, introduction of safer cryptography tools in the economy, and intensified replacement of classic cryptography solutions with post-quantum cryptography (PQC) secure tools.

We will distinguish three layers in the concept:

- Operational objectives layer: cybersecurity, cryptography
- Community and cooperation partners: research institutions, industry, cryptography use case, certification and accreditation standardization institutions (OSI, ETSI, NIST etc.), university education programs, technology producers (QKD, QRNG, chips, software)
- Ecosystem deployment orchestration and attracting an ecosystem partner layer: CERT, ENISA, legislation, PQC maturity assessment, best practice policy, survey, checklists collection

Cryptography Digital Ecosystem is characterized by the aspects required in [6]: Complexity, Self-organization, Emergence, Co-evolution, Adaptation. The model corresponds to the innovation ecosystem type.

4. Digital Cryptography Ecosystem Deployment Orchestrating

Cryptography digital ecosystem deployment orchestration requires several support activities to promote community partner collaboration. Analyzing the extensive literature and practice on cryptography, the authors identify the pillars of support activities: 1) follow CERT and ENISA recommendations, 2) follow standardization organizations ETSI, NIST requirements in cryptography, 3) follow and implement new innovative cryptography solutions, including technology mail stones as Quantum Key Distribution (QKD), Quantum Random Number Generation (QRNG), Post-Quantum Cryptography (PQC) solutions etc. We recommend to provide a maturity test of system readiness to PQC.

4.1. CERT, ENISA Recommendations Deployment Pillar

A computer emergency response team CERT (CERT or CSIRT with small differences) is a trademarked term to monitor and track security incidents in the country, industry or corporate networks. CERT units are networked for mutual coordinated cooperation, for example, in networks and cooperation partnerships such as the CSIRTs Network (CNW) (<https://csirtsnetwork.eu>), the European Government CSIRTs Group (EGC) (<https://egc-group.org>), FIRST (<https://www.first.org>), Trusted Introducer (<https://www.trusted-introducer.org>), EU ENISA, the EU Agency for Cybersecurity (<https://www.enisa.europa.eu>), and the NATO Computer Incident Response Capability (NCIRC) as a part of the NATO Communications and Information Agency (see: https://www.nato.int/nato_static_fl2014/assets/pdf/2021/4/pdf/2104-factsheet-cyber-defence-en.pdf).

Practically every member state of the European Union has one or more CERT units. CERT units promote information technology (IT) security solutions, including cryptography technology applications. The activity of CERT is a big umbrella for the development of cryptographic tasks and solutions for the cryptography digital ecosystem deployment.

ENISA, the EU Agency for Cybersecurity analyses the situation with cyber security in EU countries, evaluates technological solutions, including cryptography, and provides innovative recommendations for EU member states. Since 2013, ENISA has published an annual document “ENISA THREAT LANDSCAPE” [7] with summary news about the cyber security situation. In a similar way, the authors of the manual want to establish an overview of the use of cryptography as the main solution for ensuring cyber security in Latvia. ENISA has accumulated rich experience in the preparation of relevant documents over many years and has formalised the document preparation process by preparing a methodology intended for similar action [8].

ENISA provides recommendations for policy makers, risk managers and information security professionals in the field of cyber security up-to-date, but we focus more on one of the components of the implementation of cyber capability – cryptography.

4.2. Maturity Assessment Model

The concept of digital maturity is often used in ICT management. It is the basis of a methodology that aims to help people assess the effectiveness in a digital transformation process. Collapse of classical cryptography in the quantum computing era prompts us to hastily switch to quantum secure cryptography, and therefore we recommend to perform a maturity test for the readiness of the system for PQC solutions, for example, [9,10].

4.3. Institutional Cryptography Strategy, Risk Management, Good Practice Crypto Policy Development Pillar

Support for cryptography digital ecosystem deployment orchestration can be provided by institutional cryptography strategy, risk management, and good practice crypto policy [11].

In order to write a high-quality policy and good practice document, it is necessary to be familiar with cryptography, the experience gained in other institutions and their recommendations, the results of numerous questionnaires and monitoring of the situation.

4.4. Pillar of Checklists Approach as a Proof of Quality of Ecosystem Maturity Assessment Model

The Wikipedia explains the typical use of the term Checklist, “A checklist is a form of job support used to reduce failure by compensating for potential limitations of human memory and attention. This helps ensure consistency and completeness in the task. A basic example is an ‘to-do list’. The primary task of the checklist is to document the task and compare the documentation” [12].

The checklists approach is described in our manual for cryptography deployment as a tool to qualitatively implement necessary tasks.

Checklists help for Cryptography digital ecosystem deployment composition and decomposition, modelling organizational decision processes.

Checklists have been developed by analytically gathering the relevance (in the authors’ point of view) of documents available in the public space appropriately to crypto solutions and their implementation, requirements methodology and other issues.

The Digital Ecosystem Framework is organized around three separate, overlapping pillars: Digital Society, Rights, and Governance. And it encompasses four cross-cutting topics: Inclusion, Cybersecurity, Emerging technologies, and Geopolitical Positioning. Each checklist contains questions that cover cryptography application tasks and available WEB links to such specific checklists in detail. By thoroughly analyzing the public literature, the employee responsible for the cryptosystem implementation can adapt checklists to his needs and include the necessary tasks and executable topics.

Checklists cover tasks presented in the manual:

- Compliance of the cryptography solution with standards (ETSI, ISO, NIST)
- Cryptography solution accreditation tasks
- Migration of cryptographic solutions to post-quantum cryptography (PQC)
- Cryptographic solutions evaluation according to PQC Maturity Assessment Model
- Institutions crypto policy good practice evaluation
- Software security requirements checklist

- Checkpoint Microsoft Azure Security Best Practices checklist
- The University of Toronto checklists for cryptography and information classification and protection
- SANS, Amazon (AWS), Microsoft (Azure), Google (GCP) security checklists,
- Security checklists for system requirements
- Checklist for the cryptography designer at the institution
- Checklist when hiring a cryptography specialist.

Conceptually very close are a terms checklist, survey, and questionnaire. The questionnaire and the checklist applies to clarifying the situation on the subject under consideration, but the purpose of the checklist is to assess the current reality, while a questionnaire often gives clarity on the future [13], for example, discussion [14].

4.5. Digital Cryptography Ecosystem Deployment Manual

Cryptography covers an important and very broad spectrum of issues and tasks and cryptography digital ecosystem deployment must cover this wide range of tasks. To describe the existing situation in Latvia we developed the manual for Cryptography digital ecosystem deployment. www.lumii.lv uses a specific “Point of View” (POW) (users POW, industry POW, technology POW) according to the definition of Point of View terms in [15] and [16].

The content of the manual is described in the manner of “State of the Art” [17].

Ecosystem deployment and cryptography applications are expanding and improving the quality of practical ICT security. The manual contains recommended methodologies for Cryptography Digital Ecosystem deployment implementers.

In preparing the manual, we have widely used ENISA’s recommendations and publications, however, the content presentation style is more general, based on the above-mentioned approaches – changing the content presentation style from “landscape” to “point of view” and “state of the art”.

The considered manual does not follow the use of a checklist or questionnaire: it describes only a task/topic that can be transformed into either a questionnaire or a checklist.

5. Cryptography Digital Ecosystem Deployment Model Rationale

For justification, we will cite three arguments that indicate the practical possibility of Cryptography Digital Ecosystem deployment: geographic area (Latvia in EU), adequate level of knowledge in the cryptography field and available financing.

We define the digital ecosystem vertically (ecosystem status, in our case: EU level or national level) and horizontally – defining the boundaries that include technology (cryptography, in our case: ICT security and cryptography as practical instrument for security needs).

We will base the compliance model of the digital ecosystem of cryptography on the following features:

- Cryptography is widely used technology. With the growing importance of cyber security, the widespread use of cryptography in technological platforms and security solutions is predicted;

- There are several arguments to include cryptography in General Purpose Technology line [18]; Compliance of the cryptography solution with standards (ETSI, ISO, NIST) Migration of cryptographic solutions to post-quantum cryptography (PQC)
- Quantum cryptography as an EU development strategy has high priority, defined in the European Union (EU) Digital Europe Programme 2021–2027 (DEP) [19] and justification for sufficient knowledge and available financing source: QKD National Backbone Deployment and IPCEI on Next Generation Cloud Infrastructure and Services (IPCEI-CIS) Secure Priority.

We deploy a Cryptography Digital Ecosystem model in connection with ICT cyber security and cryptography as a central technological solution for ICT security.

In order to intensify the practical implementation of quantum cryptography in the country, we propose to base the development strategy on the Cryptography Digital Ecosystem concept.

5.1. QKD National Backbone Deployment

The objective of the Digital Europe Program (DEP) [19] is to ensure the wide use of digital technologies across the economy and society. DEP provides funding for projects in supercomputing, artificial intelligence, cybersecurity and advanced digital skills and the aim of the program is to connect digital technology research and market deployment. In this paper we will focus on cryptography, quantum cryptography and quantum communications as one of the methods to insure cyber security.

In 2019, EU countries signed a declaration to explore together and deploy a quantum communication infrastructure (QCI) within the initiative EuroQCI.

In 2022, the EU announced three Calls as part of the initiative:

- The digital renaissance and the global digital ecosystem. DIGITAL-2021-QCI-01-DEPLOY-NATIONAL
- Create a European industrial ecosystem for secure QCI technologies and systems, DIGITAL-2021-QCI-01-INDUSTRIAL
- Coordinate the first deployment of national EuroQCI projects and prepare the large-scale QKD testing and certification infrastructure, DIGITAL-2021-QCI-01-EUROQCI-QKD.

In the EuroQCI initiative, partners from Latvia (LVRTC, IMCS UL, TET and VASES) have presented Project LATQN and received an EU grant for development of a national QKD (Quantum Key Distribution) network backbone as secure/restricted networking part and deployment of public QKD backbone part.

5.2. IPCEI on Next Generation Cloud Infrastructure and Services (IPCEI-CIS) Secure Priority

The European Commission has set up a Strategic Forum for Important Projects of Common European Interest (IPCEI). IPCEI is an EU initiative of DEP and represents a very important contribution to economic growth, jobs and competitiveness for the Union's industry and economy. IPCEI aims is to create a common cloud and edge infrastructure and its associated smart services for the future. IMCS UL's interest is

directed at secure Cloud solutions, based on cryptography/quantum cryptography solutions.

The digital ecosystem concept is strongly related to society's needs. Development of national level digital ecosystem frame limits are influenced by society, the political and economic system of the EU.

The development of a large digital ecosystem depends on decisions made and funding tenders announced. As a rule, the creation of a national digital system is based on several (many) participations in tenders, funding sources and several technological components. We believe that the national ecosystem is created iteratively and is actually based on the evaluation of the EU society in advance, taking into account political and economic decisions.

6. Conclusions

1. The authors move forward the Cryptography national digital ecosystem deployment concept. In the view of the authors, this corresponds to DEP on QKD national backbone and international connectivity of these backbones.
2. An example of a national ecosystem readiness concept has been developed.
3. Recommended Cryptography digital Ecosystem deployment concepts that must be analysed: networking protocols, QKD networking, QKD in OSI layer protocols, research priorities, crypto in universities education curricula, PQC maturity, ecosystem deployment strategy and risks, standardisation rolling plan, checklists [20].
4. The checklists approach is offered to ensure efficient and high-quality ecosystem deployment, helping to ensure consistency and completeness of necessary tasks.

Acknowledgements

Publication was supported from European Regional Development Fund project "Applications of quantum cryptography devices and software solutions in computational infrastructure framework in Latvia", Project ID number 1.1.1.1/20/A/106 (01.06.2021–30.11.2023).

References

- [1] Tansley, A. G. "The Use and Abuse of Vegetational Concepts and Terms." *Ecology* 16, No. 3 (1935): 284–307. <https://doi.org/10.2307/1930070>.
- [2] Matthias Koch, Daniel Krohmer, Matthias Naab, Dominik Rost, Marcus Trapp, A matter of definition: Criteria for digital ecosystems, *Digital Business*, Volume 2, Issue 2, 2022, ISSN 2666-9544, <https://www.sciencedirect.com/science/article/pii/S2666954422000072>.
- [3] Peltoniemi, M. & Vuori, E. (2005). Business ecosystem as the new approach to complex adaptive business environments. Seppä, M. Hannula, A.M. Järvelin, J. Kujala, M. Ruohonen & T. Tiainen (Eds.), *Frontiers of e-Business Research 2004, Conference Proceedings*, Tampere, Finland (pp. 267–281) <http://www.ebrc.fi>
- [4] Ziyi Wang, Qingying Zhang, Higher-Education Ecosystem Construction and Innovative Talents Cultivating, *Open Journal of Social Sciences*, Vol. 7 No. 3, 2019, <https://www.scirp.org/journal/paperinformation.aspx?paperid=91072>.
- [5] Carly Fiorina, "The Digital Ecosystem", *World Resources Institute Conference: Creating Digital Dividends* Seattle, Washington, October 16, 2000, http://www.hp.com/hpinfo/execteam/speeches/fiorina/ceo_worldres_00.html, Accessed 29.09.2022
- [6] Järvihaavisto, Ulriikka & Riitta, Smeds. (2018). From Technology Platform to Innovation Ecosystem. *Academy of Management Proceedings*. 2018.

- [7] ENISA THREAT LANDSCAPE 2021. April 2020 to mid-July 2021, <https://www.enisa.europa.eu/publications/enisa-threat-landscape-2021>, last accessed 29.08.2022
- [8] ENISA CYBERSECURITY THREAT LANDSCAPE METHODOLOGY, JULY 2022, <https://www.enisa.europa.eu/publications/enisa-threat-landscape-methodology/@@download/fullReport>, last accessed 30.08.2022
- [9] Post Quantum Crypto Survey, DigiCert, 2019, <https://www.digicert.com/content/dam/digicert/pdfs/2019-digicert-post-quantum-crypto-survey-report-en.pdf>
- [10] Post-Quantum Cryptography (PQC) Maturity Model, DigiCert, 2020 <https://www.digicert.com/content/dam/digicert/pdfs/post-quantum-cryptography-maturity-model-whitepaper-en.pdf>, last accessed 29.08.2022
- [11] OECD, Recommendation of the Council concerning Guidelines for Cryptography Policy, OECD/LEGAL/0289, 2022, <https://legalinstruments.oecd.org/public/doc/115/115.en.pdf>, last accessed 29.08.2022
- [12] Checklist, Wikipedia, <https://en.wikipedia.org/wiki/Checklist>, last accessed 29.08.2022
- [13] Anna Georgiadou, Spiros Mouzakitis, and Dimitris Askounis, Designing a Cyber-Security Culture Assessment Survey Targeting Critical Infrastructures During Covid-19 Crisis, International Journal of Network Security & Its Applications (IJNSA) Vol. 13, No. 1, January 2021
- [14] Ali A. Naeem. What is the scientific difference between the checklist and the questionnaire? When and why is each tool used? <https://www.researchgate.net/post/What-is-the-scientific-difference-between-the-checklist-and-the-questionnaire>, last accessed 29.08.2022
- [15] Complete Guide to Different Types of Point of View: Examples of Point of View in Writing, Written by MasterClass, Last updated: Sep 2, 2021 <https://www.masterclass.com/articles/complete-guide-to-point-of-view-in-writing-definitions-and-examples>, last accessed 29.08.2022
- [16] Point of view Definition & Meaning – Merriam-Webster, <https://www.merriam-webster.com/words-at-play/point-of-view-first-second-third-person-difference>), last accessed 29.08.2022
- [17] State of the art Definition & Meaning – Merriam-Webster), <https://www.merriam-webster.com/dictionary/state%20of%20the%20art>, last accessed 29.08.2022
- [18] Richard Lipsey, Kenneth I. Carlaw, Clifford T. Bekhar (2005). Economic Transformations: General Purpose Technologies and Long-Term Economic Growth. Oxford University Press. pp. 131-218. ISBN 978-0-19-928564-8.
- [19] The Digital Europe Programme, <https://digital-strategy.ec.europa.eu/en/activities/digital-programme>, Accessed 29.08.2022
- [20] Marco Lucamarini, Andrew Shields, Romain Alléaume, Christopher Chunnillall, Ivo Pietro Degiovanni, Marco Gramegna, Atilla Hasekioglu, Bruno Huttner, Rupesh Kumar, Andrew Lord, Norbert Lütkenhaus, Vadim Makarov, Vicente Martin, Alan Mink, Momtchil Peev, Masahide Sasaki, Alastair Sinclair, Tim Spiller, Martin Ward, Catherine White, Zhiliang Yuan, Implementation Security of Quantum Cryptography, Introduction, challenges, solutions, ETSI White Paper No. 27, First edition – July 2018, https://www.etsi.org/images/files/ETSIWhitePapers/etsi_wp27_qkd_imp_sec_FINAL.pdf

Citrus Appearance Quality Grading System Based on OpenCV Image Processing

Yiqin BAO^{a1}, Qin LIU^a and Yulu BAO^b

^a College of Information Engineering of Nanjing Xiaozhuang University, China

^b Nanjing RuiHuaTeng Intellectual Property Co., Ltd., China

Abstract. The production technology of Citrus in China is still at the initial stage of development, and the classification of Citrus mainly depends on manual work, which is subjective and inefficient. To solve the problem of time-consuming, laborious and low efficiency of citrus classification, this paper uses the OpenCV image processing technology, Candy edge detection operator for edge detection and DP algorithm for contour extraction to find the two points with the largest distance in the contour to achieve citrus diameter detection; The RGB color space is converted into HSV color space, and the parameters of H component are extracted to obtain the citrus coloring rate, thus realizing the citrus appearance quality grading system. The experiment proves that the accuracy of diameter detection is more than 99%, reducing the artificial classification deviation.

Keywords. OpenCV, Image recognition, feature extraction, edge detection

1. Introduction

China is the largest fruit farmer in the world, and the planting area and output of its fruit rank first in the world. At present, China's fruit industry has become the main agricultural product next to grain and vegetables. China is the largest Citrus producing area in the world, with rich Citrus resources and excellent varieties. The planting history has exceeded 4000 years. China's Citrus output reached 23.31 million tons in 2008, surpassing Brazil and ranking first in the world [1]. Although China's Citrus output is large, the fresh Citrus exported each year only accounts for a small part of the global Citrus trading volume, and the prices of most varieties are very cheap. However, developed countries such as Europe and the United States have always monopolized the high-end market. This is mainly due to the backward post harvest inspection and grading technology in China and the low degree of post harvest commercialization, resulting in uneven varieties and varieties.

At present, the grading treatment of citrus before sales in China is mainly manual, which is time-consuming, labor-intensive and inefficient. The use of computer vision technology to classify fruits has become a development trend. There have been relevant studies, He et al. [2] has made a review of fruit quality detection based on machine vision, Xiong et al. [3] have made a study on the quality detection technology of litchi fruit during picking, Shi et al. [4] have studied the online grading detection of apple

¹ Corresponding author: Yiqin BAO, email: 392335241@qq.com

quality, and Rao et al. [5] have made a study on the external quality grading method of spherical fruits based on machine vision. However, there is no relevant data on citrus quality grading, and a complete detection system has also been formed.

In this paper, based on openCV image processing technology, Candy edge detection operator is used for edge detection and DP algorithm is used for contour extraction to find the two points with the maximum distance in the contour to achieve citrus diameter detection. The fruit area in each component channel image of RGB (red, green, blue), HSV (Hue, Saturation, Value) and other color spaces in the color space is extracted to extract the size, shape, color and other characteristics of the fruit, The citrus appearance quality classification system is realized.

The contributions and innovations of this paper are summarized as follows:

- 1) Design the structure of citrus grading system.
- 2) The related technology and citrus grading were studied.
- 3) The detection system is realized through QT.

The rest of the paper is organized as follows. The second section studies the relevant technologies, the third section designs the structure of the citrus grading system, the fourth section realizes the citrus quality grading, the fifth section conducts experiments and compares with manual work, and the sixth section summarizes the full text and prospects.

2. Related technology

2.1 OpenCV

OpenCV is a cross platform, lightweight and open source computer vision library, which supports various machine languages [6]. Opencv module covers all fields. Including character recognition, image processing and license plate recognition. OpenCV contains more than 300 C language function APIs in the middle and high levels. It has strong visualization ability and is suitable for the experimental environment of this paper. The advantages of OpenCV over other computer vision tools are shown in Table 1.

Table 1. Comparison of image processing and computer vision tools

Development tool	Developer	Application area	Is Free	Is the source code open
IPL	Intel	Image processing	Free	Not open
OpenCV	Intel	Image processing, computer vision	Free	Open
IPP	Intel	Image processing, signal processing	Not free	Not open
VisDSK	Microsoft	Image processing	Free	Open
Mattlab	Microsoft	Multidisciplinary	Not free	Not open

2.2 Freeman chain code

Chain code is a common graphic expression method, which can well express graphics [7]. Direction chain code is an effective coding method to describe the boundaries of graphics. It defines a direction and encodes the edges of an image on this basis, so as to form a set of connected sequences with a certain length and direction. At present, free chain codes and bribiska codes are more common.

In this paper, free chain codes are used to output curves. Free chain codes generally use eight directions, namely 0, 1, 2, 3, 4, 5, 6, 7 and 8. Starting from the starting point, the pixel values in the eight directions are detected counterclockwise and clockwise, as shown in Figure 1.

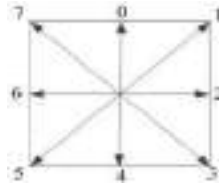


Figure 1. Eight directions of Freeman chain codes

Image detection is performed from top to bottom and from left to right. After the boundary point is detected, it is taken as the starting point of the detected edge and stored in the chain code. Then, it will go down until it returns to the starting position of the edge to complete its detection. And stores distribution information in eight directions in the chain code. Its expression is shown in Table 2.

Table 2. A contour free chain code table structure

(x_0, y_0)	n	B_0	B_1	B_2	B_{n-1}
--------------	-----	-------	-------	-------	-----	-----	-----------

In Table 2, (x_0, y_0) is the coordinate of the starting point of tracking along the boundary, n is the total number of points along the boundary, and B is the order of chain codes.

2.3 DP algorithm

Generally, Freeman chain code operation can be performed directly after contour extraction. Its feature is the contour feature, and its description is the description of the contour. Because the steps of chain code are very short, it is very difficult to describe the edges directly. In this paper, the DP algorithm is used to approximate the polygon, so as to obtain the initial shape of the polygon, find the optimal number of polygon sides, and then approximate other sides with the same number of sides to obtain the polygon with the same number of sides. So that the same feature points can be obtained as much as possible after polygon approximation.

2.4 Canny boundary detection algorithm

Canny boundary detection operator uses 2×2 The amplitude and direction of the image gradient obtained by the first order partial differential of the adjacent region through Gaussian filtering. The first order partial derivatives of X and Y directions can be expressed as formulas (1) and (2).

$$p_x(x, y) = \frac{[H(x,y+1)-H(x,y)+H(x+1,y+1)-H(x+1,y)]}{2} \tag{1}$$

$$p_y(x, y) = \frac{[H(x,y)-H(x+1,y)+H(x,y+1)-H(x+1,y+1)]}{2} \tag{2}$$

The amplitude and direction of the image gradient can be expressed in ways (3) and (4).

$$M(x, y) = \sqrt{p_x^2(x, y) + p_y^2(x, y)} \tag{3}$$

$$\theta(x, y) = \arctan\left(\frac{p_x(x, y)}{p_y(x, y)}\right) \tag{4}$$

In the system implementation, we use Canny operator to detect the boundary. Canny operator can achieve a good balance between false detection and missed detection, and has a good edge detection performance.

3. The System Overall Structure

3.1 System architecture

The system adopts the classic three-layer design mode of the Internet of things, namely, the perception layer, the network layer and the application layer; The system adopts B / S architecture and takes the database as the center to build the system. The system block diagram is shown in Figure 2.



Figure 2. System architecture diagram

3.2 Citrus Quality grading

3.2.1 Grading method

The grade indexes of fruit appearance quality include size, shape, color, surface defects, etc. According to the fruit grading standards issued by the state, fruit dealers divide them into different grades for packaging, so as to increase the added value of products. There are three main fruit classification methods: manual classification, mechanical classification and machine vision.

3.2.2 Grading standard

This paper studies the classification standard of citrus, mainly from the two aspects of fruit diameter and color, and gives the evaluation standard. The classification standard is shown in Table 3.

Table 3. Citrus grading standard

Grade	Fruit diameter	Coloration rate
Super grade	>=85	>80%
First grade	75-85	70%-80%
Second grade	65-75	60%-70%
Third grade	<65	<60%

3.3 Diameter detection

The Citrus diameter detection module can recognize and extract the outer contour of the Citrus fruit surface, and detect the diameter according to the two points with the largest distance in the contour. The diameter detection module is mainly composed of the original Citrus image, color space conversion, median filter denoising, threshold segmentation to obtain a three-dimensional image, morphological processing to remove noise, obtain an image, background segmentation, image extraction, adaptive threshold segmentation, edge removal processing, remove small areas, obtain contours, draw diameter contours, and calculate Citrus diameters. The flow chart is shown in Figure 3.



Figure 3. Diameter detection flow chart

3.4 Coloration rate detection

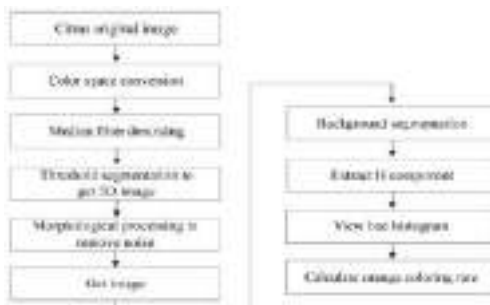


Figure 4. Color detection flow chart

Color is a major factor affecting the appearance quality of oranges. Oranges with uniform color and uniform color have high merchantability. In the process of post production commercialization of oranges, varieties with similar color and luster are often classified [8]. Therefore, in the classification of citrus, color is a big problem. The color detection module is mainly used to classify the color consistency of citrus. The

module describes the color of Citrus according to the distribution of hue characteristics of Citrus images, and divides Citrus into three color grades. The flow chart is shown in Figure 4.

4. System test and comparison

In order to achieve citrus and color grading, we have implemented the system and tested it. This paper uses Pycharm platform as the program deployment platform, and uses QT component programming interface. The operation effect is shown in Figure 5. It can be seen that the measured diameter of the orange is 36.2mm, which is verified to be correct through actual measurement with a ruler. The color shade is 57.6%, so the orange is tested to be Third grade.

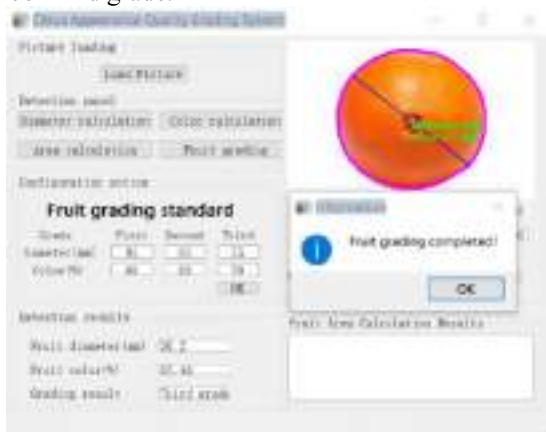


Figure 5. Citrus grading test interface

Through the comparison between manual and systematic tests, as shown in Table 4, the accuracy of citrus measurement can reach 99%, which can reach the level of practical application.

Table 4. Comparison of citrus diameter test results

Fruit No	Manual test results/mm	Repeat measurement results/mm					Maximum positive deviation/mm	Maximum negative deviation/mm	Accuracy
		1	2	3	4	5			
1	80.5	80.6	80.8	81.0	80.2	80.0	0.5	-0.5	99.4%
2	70.3	70.6	70.5	70.3	70	70.7	0.4	-0.3	99.3%
3	66.5	66.4	66.5	66.7	66.4	66.3	0.2	-0.2	99.6%
4	36.2	36.1	36.2	6.3	6.2	36.1	0.1	-0.1	99.7%

5. Conclusions

In view of the characteristics of artificial classification, low efficiency and poor accuracy of Citrus color detection in China, this paper uses image processing technology to classify the color of citrus, designs a Citrus appearance quality classification system based on image processing, studies the image pretreatment and feature extraction methods of citrus, and realizes the diameter and color classification of citrus.

This paper only realizes the citrus defect and color grading, which can combine the citrus shape, defect and other features with the color features. However, the next content to be studied is to achieve all-round citrus quality detection through depth learning methods.

References

- [1] Rao Xiuqin Research on Key Technologies of fruit quality real-time detection and grading production line based on machine vision [D] Zhejiang University, 2007.
- [2] He Wenbin, Wei Aiyun, Ming May Day, et al A review of fruit quality detection based on machine vision [J] *Computer Engineering and Application*, 2020, 56 (11): 7.
- [3] Xiong Juntao, Zou Xiangjun, Liu Nian, et al Quality detection technology of litchi fruit during picking based on machine vision [J] *Journal of Agricultural Machinery*, 2014, 045 (007): 54-60.
- [4] Shi Ruiyao, Tian Youwen, Lai Xingtao, et al Online apple quality grading detection based on machine vision [J] *China Agricultural Science and Technology Herald*, 2018, 20 (3): 7.
- [5] Rao Jian, Lu Ziyu Research on external quality grading method of spherical fruit based on machine vision [J] *Science, Technology and Innovation*, 2022 (000-005).
- [6] Liu Junwei. Design of graphic recognition system based on OpenCV [J] *Electronic Technology and Software Engineering*, 2019 (21).
- [7] Pei Shan, Zhang Teng Geometric figure recognition algorithm based on Freeman chain code [J] *Computing Technology and Automation*, 2018 (03).
- [8] Xie Jing Research on Automatic Apple Grading Method Based on Computer Vision [D] Anhui: Anhui Agricultural University, 2011.

A Design of Hierarchical Bloom Filter

Tao MA, Bin WANG¹

Information Engineering College, Yangzhou University, Jiangsu, China.

Abstract. Shifting Bloom filters use location offset to encode state values for a set of elements. In spite of its novelty, classification error rate inherent to shifting Bloom filters needs to be improved. In this paper, we design a hierarchical shifting bloom filter to address this issue. Firstly, state values of elements in a set are partitioned into disjoint groups. Each group is assigned a unique group number. Then these group numbers implicitly assigned to elements are encoded by a major shifting Bloom filter (*MShiftBF*). Each group is further associated with a secondary shifting Bloom filter (*SShiftBF*). State values of elements belonging to some group are encoded by the corresponding SShiftBF separately. Compared with standard Shifting Bloom filters, the advantage of the hierarchical structure of the proposed scheme is that we can improve both classification error rate and false positive rate. Finally, we provide theoretical analysis and conduct simulation experiments to demonstrate that the proposed scheme outperforms standard shifting Bloom filters.

Keywords. Shifting Bloom filters, Classification error rate, False positive rate, Hierarchical structure

1. Introduction

With the rapid development of computer network technology, many network functions require the use of compact online set representation and fast membership lookup functions. For instance, network caches first determine whether a queried element locates in fast on-chip memory. Only when a negative result is obtained, slow off-chip memory will be accessed to retrieve the element [1].

Traditional exact-match data structures such as binary search trees [2], trie [3] and hash tables [4] must store both keys and values. Some of them also need extra space to store pointers to facilitate maintaining the tree structure to resolve the hash collision problem [5]. These data structures are often considered too bloated and are usually difficult to implement in the processor's cache and memory due to their overly large memory footprint [6]. And in today's heavy network information transmission [7], traditional exact-match data structures can also take up a lot of traffic [8]. To solve this problem, more and more compact data structures are coming into view, such as the Bloom filter and its variants studied in this paper.

Bloom filters and their variants provide a probabilistic data structure to support fast approximate queries for set membership lookup [9] and can be naturally represented as

¹Corresponding Author: Bin Wang, Associate professor of Department of Electronics and Communication Engineering, Information Engineering College, Yangzhou University, Jiangsu, China; E-mail: bwang@yzu.edu.cn.

a binary array of bits to save memory space and computational overhead. At present, Bloom filters are increasingly used in various application fields such as DNA sequence data matching [10], network flow size estimation Classification [11], and network security [12]. The performance metrics for traditional Bloom filters are space usage, memory access, false positive rate. However, the classical design of Bloom filter suffers from the problem of non-zero false positive rate due to its randomized nature. Most of the variants of Bloom filters are designed to optimize some or all of the performance metrics for application-specific scenarios.

Traditional Bloom filters only consider the compact set membership representation. On the other hand, when each element of the set is associated with a state value (e.g., multiplicity of an element in a multi-set), Multi-set membership testing required that the state value of an element in the encoded set can also be returned. For instance, it is desirable for packet classification service to obtain an output ports for incoming packets based on their destination IP addresses [13]. There are a lot of research focused on Multi-set membership testing [14 – 17].

Hao et al. [14] present a combinatorial Bloom filter (COMB) design for Multi-set membership testing. The draw back of COMB is that the maximum state value is bounded by $\binom{\gamma}{\theta}$, and the lookup computational overhead is proportional to f . Chazelle [15] suggest the use of the Bloomier filter in which each cell is represented by multi-bits. The Bloomier filter requires that the knowledge of cells referenced by all elements should be used to find a matched cell for each element with high probability beforehand. Calderoni et al. [16] provide detailed definition and analysis for the Spatial Bloom Filter. The Spatial Bloom Filter also supports dynamic Multi-set membership testing by writing state values of elements into cells maintained by the Spatial Bloom Filter in sequence according to the prescribed increasing order of their priority. Both [15] and [16] require a cell of size $\lceil \log_2 g \rceil$, where g is the number of state values of the encoded elements. In addition, Spatial Bloom Filters have to handle an issue referred to as “classification error”.

Yang et al. [17] presents the Shifting Bloom Filter as a novel design for Multi-set membership testing. Their idea is to use the state value of an element as location offset to select k positions in the bit-array of the Shifting Bloom Filter and set the k bits to 1 to encode both the membership and state value of the element. In terms of memory efficiency, Shifting Bloom Filters outperform the schemes [15 – 16] since a cell of the Shifting Bloom Filter is represented by 1 bit. Shifting Bloom Filters also suffer from the problem of relatively high classification error rate since an incorrect state value may pass the test against the encoded Shifting Bloom Filter with a certain probability and return as valid for the element.

In this paper, we propose a hierarchical structure for Shifting Bloom filters to improve classification error rate. First, assume that there are γ state values assigned to all elements in a given set. These state values are partitioned into disjoint ρ groups. Each group consists of at most $\theta = \left\lceil \frac{\gamma}{\rho} \right\rceil$ distinct state values and is assigned a unique group number. Then these group numbers are encoded by a major shifting Bloom filter. For each group, elements whose state values belong to it are further encoded by the corresponding secondary shifting Bloom filter respectively. We provide theoretical analysis for performance of the proposed hierarchical Shifting Bloom filter. Compared with the the Shifting Bloom filter, the result of simulation experiments show that the proposed scheme reduces the false positive rate and classification error rate.

2. Related background

2.1. The Shifting Bloom filter

Let $o(e)$ represent the state value of an element e . The Shifting Bloom filter SBF operates as follows:

(1) To encode both membership and $o(e)$ of the given element e into the m -bit array B , SBF uses k hash functions to compute k positions $(h_1(e) + o(e)) \% m, (h_2(e) + o(e)) \% m, \dots, (h_k(e) + o(e)) \% m$ and set k bits $B(h_1(e) + o(e)) \% m, B(h_2(e) + o(e)) \% m, \dots, B(h_k(e) + o(e)) \% m$ in the array B to 1s. That is, state values of elements play the role of location offset to determine the positions in the array B to be written.

(2) Assume O_{max}, O_{min} are the maximum and minimum state values of elements respectively. Given an element e to be queried, SBF checks k bits $B(h_1(e) + o(e)) \% m, B(h_2(e) + o(e)) \% m, \dots, B(h_k(e) + o(e)) \% m$ in the array B for each $O_{max} \leq O_f \leq O_{min}$. If all of the above k bits in the array B are 1s, O_f is accepted as a candidate state value for the element e . When there is more than one candidate state values for element e , the maximum of the candidate state values will be returned.

2.2. Problem formulation

Let U be the universe of all elements. A set $X = x_1, x_2, \dots, x_n, X \subseteq U$. Each element $x_i \in X$ is associated with a positive integer value $v(x_i)$. For instance, $v(x_i)$ may be the multiplicity of x_i in a multi-set X . For ease of notation, we assume that $v(x_i)$ comes from a list $L = [1, y]$ with step size 1.

Given a $x \in U$, Multi-set membership testing requires to design a kind of probabilistic data structure such that a value $s(x) \in L$ will be returned when it decides that $x \in X$. The performance and accuracy requirements for Multi-set membership testing is generally listed as follows:

(1) Computation overhead: the number of hash computations for looking up an element;

(2) False positive : When $x \notin X$, make a wrong decision that $x \in X$, and return $s(x)$.

(3) Classification error : When $x \in X$, make a decision that $x \in X$, but return $s(x) \neq v(x)$.

3. The proposed Hierarchical Shifting Bloom filter

3.1. Encoding elements by the Hierarchical Shifting Bloom Filter

Grouping phase: Given an integer-valued parameter θ , set $\rho = \lceil \frac{y}{\theta} \rceil$. Divide the list $L = [1, y]$ into ρ groups, where θ is the number of state values in each group. Then we obtain the following groups for L :

$$V_1 = \{1, \dots, \theta\}, V_i = \{(i-1)\theta + 1, \dots, i\theta\}, \dots, V_\rho = \{(\rho-1)\theta + 1, \dots, y\}$$

Definition 1: For each group $V_i, 1 \leq i \leq \rho$ define $X_{V_i} = \{x | x \in X, v(x) \in V_i\}$, where $v(x)$ is the state value of an element x . $n_i = |X_{V_i}|$ represents cardinality of the set X_{V_i} . Given an element $x \in X$, $g(x)$ is the group number implicitly assigned to element x . Given an element x , we have $v(x) \in v_{g(x)}$.

Construction of the major shifting Bloom filter: Construct a m_s -bit array P_ShBF as the major shifting Bloom filter and initialize all of the bits in P_ShBF to 0. Let $h_1(\cdot), h_2(\cdot), \dots, h_k(\cdot)$ be k independent hash functions. Assume the output of each hash function is uniformly distributed over $0, 1, \dots, m_s - 1$. Given the group number $g(x)$ associated with an element $x \in X$, compute k positions $(h_1(x) + g(x)) \% m_s, (h_2(x) + g(x)) \% m_s, \dots, (h_k(x) + g(x)) \% m_s$, and set the corresponding k bits in P_ShBF to 1.

Construction of secondary shifting Bloom filters: Construct a m_i -bit array S_ShBF_i as the secondary shifting Bloom filter for each group $V_i, 1 \leq i \leq \rho$. Initialize all of the bits in S_ShBF_i to 0. Given an element $x \in X$, recall that $v(x)$ is the state value of an element x , and $g(x)$ is the group number associated with x such that $v(x) \in V_{g(x)}$. Compute k positions $(h_1(x) + v(x)) \% m_{g(x)}, (h_2(x) + v(x)) \% m_{g(x)}, \dots, (h_k(x) + v(x)) \% m_{g(x)}$, and set the k bits in the corresponding secondary shifting Bloom filter $S_ShBF_{g(x)}$ to 1.

3.2. Looking up elements by the Hierarchical Shifting Bloom Filter

Given an element $x \in U$, we should first look up the major shifting Bloom filter P_ShBF in order to obtain a list $w(x)$. By the looking up principle of shifting Bloom filters, the list $w(x)$ contains all candidate group numbers for the element x .

Taking $w(x)$ as input, for each $i \in w(x)$, we should check $s \in [\min(V_i), \max(V_i)]$ in the secondary shifting Bloom filter S_ShBF_i in sequence, where V_i is the group associated with S_ShBF_i . If all of the k bits with indices $[h_{j(x)} + s] \% m_i (1 \leq j \leq k)$ in S_ShBF_i are set to 1, s is considered to be a possible state value of x . We use a list $S_i(x)$ to record all possible state values for x returned by the secondary shifting Bloom filter S_ShBF_i .

When the major shifting Bloom filter P_ShBF return an empty list $w(x)$ or $S_x = \bigcup_{i \in w(x)} S_i(x)$ is empty, x is indicated not to be a member of the set X .

If S_x is not empty, return $s(x) = \max(S_x)$ as the state value for the queried element x .

4. Performance analysis of the Hierarchical Shifting Bloom filter

In this section, we provide theoretical analysis for the presented Hierarchical Shifting Bloom filter in terms of the computational overhead of encoding elements and looking up elements, false positive rate, classification error rate.

4.1. Analysis of false positive rate

Given an element $x \in U$ but $x \notin X$, first check the major shifting Bloom filter P_ShBF to obtain a list $w(x)$ as described in section 3.2 that contains the candidate group numbers for x .

The probability distribution of the length of the list $w(x)$ is given below:

$$Pr[|w(x)| = i] \approx C_\rho^i \cdot [1 - e^{-\frac{nk}{m_s}}]^{i \cdot k} \cdot \{1 - [1 - e^{-\frac{nk}{m_s}}]^k\}^{(\rho - i)} \quad (1)$$

When looking up an element, the false positive event FP occurs when the following two events occurs simultaneously:

(1) FP_1 : The major shifting Bloom filter P_ShBF returns a non-empty list $w(x)$;

(2) FP_2 :At least one of the secondary shifting Bloom filters S_ShBF_i with $i \in w(x)$ returns a non-empty list $s_i(s)$ that contains the candidate state values for x .

Let $\overline{FP_1}$ be the complementary event of FP_1 ,then:

$$Pr[\overline{FP_1}] \approx \{1 - [1 - (1 - \frac{1}{m_s})^{nk}]^k\}^\rho \approx \{1 - [1 - e^{-(\frac{nk}{m_s})}]^k\}^\rho \quad (2)$$

When we choose m_s as follows:

$$m_s = \frac{n \cdot k}{\ln 2} \quad (3)$$

It is easy to see that $e^{-(\frac{nk}{m_s})} = 0.5$.

Let $\overline{FP_2}$ be the complementary event of FP_2 ,

$$Pr[\overline{FP_2} \mid |w(x)| = t] = \prod_{i \in w(x)} \{1 - [1 - (1 - \frac{1}{m_i})^{n_i k}]^k\}^\theta \approx \{1 - [1 - e^{-(\frac{n_i k}{m_i})}]^k\}^{\theta \cdot t} \quad (4)$$

For ease of analysis,we assume that $n_i = \frac{n}{\rho}$ such that we can choose that the same m_i for all of the secondary shifting Bloom filters. By the formula of total probability and equations (4), we obtain:

$$Pr[\overline{FP_2}] \approx \sum_{t=1}^{\rho} Pr[|w(x)| = t] \{ [1 - e^{-(\frac{n_i k}{m_i})}]^k \}^{\theta \cdot t} \quad (5)$$

When we choose $m_i = \frac{n \cdot k}{\rho \cdot \ln 2}$, it is easy to see that $e^{\frac{n_i k}{m_i}} = 0.5$.

By the above discussion and the setting of parameters:

$$Pr[FP] = 1 - Pr[\overline{FP_1}] + Pr[\overline{FP_2}]$$

$$Pr[FP] \approx 1 - \{(1 - 2^{-k})^\rho + [\sum_{i=1}^{\rho} C_{\rho}^i (2^{-i \cdot k}) \cdot (1 - 2^{-k})^{(\rho-i)} (1 - 2^{-k})^{\theta \cdot i}]\} \quad (6)$$

4.2. Analysis of classification error rate

When looking up an element $x \in U$, FV denotes the classification error event, whose complement event is CV. CV means that $v(x) = s(x)$ holds, where $s(x)$ is the value returned by the Hierarchical Shifting Bloom filter.

Given $x \in X$, recall that $g(x)$ is the corresponding group number. We have $v(x) \in V_{g(x)}, V_{g(x)} = (g(x) - 1)\theta + 1, \dots, g(x) \cdot \theta$. Then we define two sets T_x, Y_x as follows:

$$T_x \triangleq \{i \mid g(x) \leq i \leq \rho\}, Y_x \triangleq \{y \mid v(x) \leq y \leq g(x) \cdot \theta\}$$

The set $T_x \cap w(x) \triangleq \{i \mid i \in w(x) \cap g(x) \leq i \leq \rho\}$ contains the group numbers in $w(x)$ that are strictly larger than $g(x)$.

$$Pr[|T_x \cap w(x)| = z] \approx C_{\rho-g(x)}^z \cdot [1 - e^{-\frac{nk}{m_s}}]^{z \cdot k} \cdot \{1 - [1 - e^{-\frac{nk}{m_s}}]^k\}^{(\rho-g(x)-z)} \quad (7)$$

$v(x) = s(x)$ requires that the following two events occurs simultaneously:

(1) $CV_1: \forall i \in T_x \cap w(x)$, the corresponding secondary shifting Bloom filter S_ShBF_i returns an empty list $s_i(x)$.

$$Pr[CV_1 | |T_x \cap w(x)| = z] = \{1 - [1 - (1 - \frac{1}{m_i})^{nk}]^K\}^{\theta \cdot z} \approx \{1 - [1 - e^{-\frac{nk}{m_i}}]^k\}^{\theta \cdot z} \quad (8)$$

$$Pr[CV_1] = \sum_{z=0}^{\rho-g(x)} Pr[CV_1 | |T_x \cap w(x)| = z] \cdot Pr[|T_x \cap w(x)| = z] \quad (9)$$

(2) CV_2 : When looking up the secondary shifting Bloom filters $S_ShBF_{g(x)}$, S_x is returned such that $v(x) = \max(S_x)$, where S_x is defined in section 3.2.

CV_2 means that $\forall y \in Y_X, y \notin s_{g(x)}(x)$ holds, where $s_{g(x)}(x)$ is the list returned by the secondary shifting Bloom filter $S_ShBF_{g(x)}$.

$$Pr[CV_2] = \{1 - [1 - (1 - \frac{1}{m_{g(x)}})^{n \cdot k}]^k\}^{[\theta \cdot g(x) - v(x)]} \quad (10)$$

$$Pr[CV] = Pr[CV_1] \cdot Pr[CV_2]$$

$$Pr[FV] = 1 - Pr[CV]$$

4.3. Storage and computational overhead of the Hierarchical Shifting Bloom filter

The bit-length of the major shifting Bloom filter P_ShBF is m_s . The total bit-length of ρ secondary shifting Bloom filters S_ShBF_i is $\sum_{i=1}^{\rho} m_i$.

Assume each secondary shifting Bloom filter S_ShBF_i encodes state values for $n_i = \frac{n}{\rho}$ elements. By equation (3), we obtain:

$$m_s + \sum_{i=1}^{\rho} m_i = \frac{2n \cdot k}{\ln 2} \quad (11)$$

To encode an element in the set X , k hash operations for the major shifting Bloom filter and k hash operations for the corresponding secondary shifting Bloom filter are needed. As a result, $2k$ hash operations are carried out to encode an element.

When looking up an element $x \in X$, $\rho \cdot k$ positions in the major shifting Bloom filter P_ShBF are first checked to return a non-empty list $w(x)$.

The probability distribution of the length of the list $w(x)$ is given below:

$$Pr[|w(x)| = i] \approx C_{\rho-1}^{i-1} \cdot [1 - e^{-\frac{nk}{m_s}}]^{(i-1) \cdot k} \cdot \{1 - [1 - e^{-\frac{nk}{m_s}}]^k\}^{\rho-i} \quad (12)$$

Then $\theta \cdot |w(x)| \cdot k$ positions in the $|w(x)|$ secondary shifting Bloom filters are checked to return a list $S_x = \bigcup_{i \in w(x)} S_i(x)$.

To sum up, the expected number of memory access for looking up an element can be expressed by :

$$(\rho + \theta \cdot E[|w(x)|]) \cdot k \quad (13)$$

$$E[|w(x)|] = \sum_{i=1}^{\rho} (i \cdot Pr[|w(x)| = i]) \quad (14)$$

5. Performance evaluation

In this section, we compare with the Shifting Bloom Filter [10] in terms of False positive rate, Classification error rate, the number of memory access when looking up an element, etc. For a fair comparison, the proposed scheme consumes the same memory overhead as the standard Shifting Bloom Filter.

We set the number of hash functions to 3, the number of state values to 16, and the number of groups to 4.

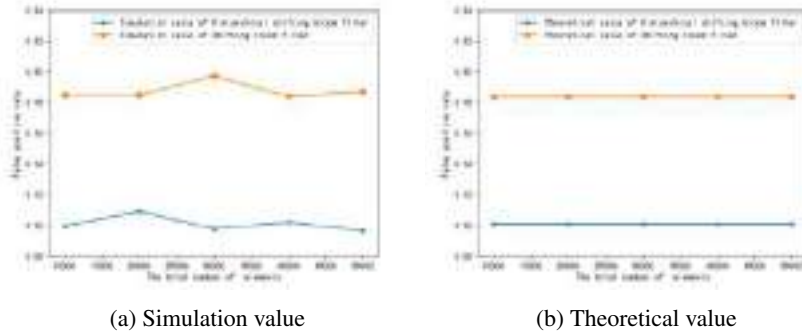


Figure 1. False positive rate comparison

As we can see from Fig.1, the false positive rate of the standard Shifting Bloom filter is around 0.184, while the false positive rate of the Hierarchical Shifting Bloom filter is around 0.10. The false positive rate of the Hierarchical Shifting Bloom filter is reduced by nearly 45%. The performance improvement is due to the fact that the major shifting Bloom filter first picks out the possible candidate groups for the queried element, then searches in the corresponding secondary shifting Bloom filters. Fig.2 also shows that the theoretical value of this paper is close to the simulation result, which proves the validity of the theoretical analysis.

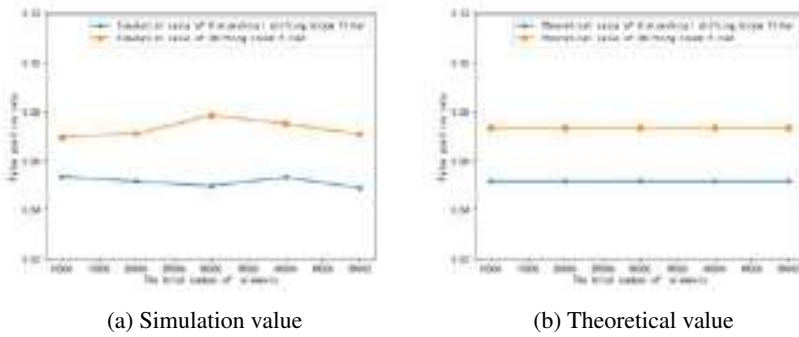


Figure 2. Classification error rate comparison

As we can see from Fig.2, the classification error rate of the Hierarchical Shifting Bloom filter is 0.052, which is 30% of the Shifting Bloom filter. The simulated classification error rate is close to the theoretical value. This is also due to the fact that the major shifting Bloom filter helps to reduce the number of state values to be tested. The hierarchical structure makes our scheme more suitable for Multi-set membership testing to yield better performance.

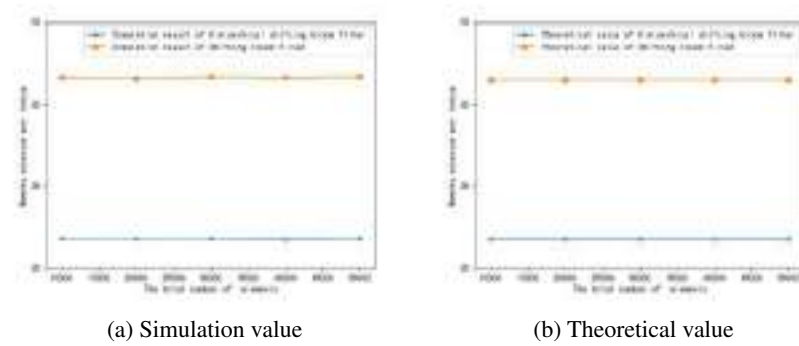


Figure 3. Memory accesses comparison

When the number of hash functions is 3, the number of state values is 16, and the number of groups is 4, from Fig. 3, we can see that the number of memory accesses when looking up an element of the hierarchical shifting bloom filter are around 28.5 and the shifting bloom filter is 48. The memory accesses reduction is also due to the reduced number of state values to be tested .

6. Conclusion

In this paper, we propose a kind of Hierarchical Shifting Bloom filter based on the standard Shifting Bloom filter for Multi-set membership testing. We provide theoretical analysis for performance of the presented scheme and show the impact of the number of

groups on the the expected number of memory access by numerical computation. In comparison with the Shifting Bloom filter, simulations shows that the presented scheme reduces the false positive rate, the classification error rate, and the number of memory access when looking up an element. The key point is that the major shifting Bloom filter first picks out the candidate groups for the queried elements and then searches the corresponding secondary shifting Bloom filters. This reduces the number of state values to be tested.

References

- [1] Haoyu Song, Sarang Dharmapurikar, Jonathan Turner, John Lockwood. Fast hash table lookup using extended Bloom filter: An aid to network processing. *ACM SIGCOMM Computer Communication Review*. Volume 35. Issue 4; 2005. p. 181-192.
- [2] J. Brodtkin. A wireless router that tracks user activity—But for a good reason. *Ars Technica*, Jan. 2013. [Online]. Available: <http://arstechnica.com/gadgets/2013/01/a-wireless-router-that-tracks-user-activity-but-for-a-good-reason/>
- [3] Y. Lu and B. Prabhakar. Robust counting via counter braids: An error-resilient network measurement architecture. In: *Proc. IEEE INFOCOM*, Apr. 2009, p. 522–530.
- [4] S. Dharmapurikar, P. Krishnamurthy, and D. E. Taylor. Longest prefix matching using Bloom filters. In: *IEEE/ACM Trans. Netw.*, vol. 14, no. 2, 2006, p. 397–409.
- [5] B. Chazelle, J. Kilian, R. Rubinfeld, and A. Tal. The Bloomier filter: An efficient data structure for static support lookup tables. In *Proc. ACM-SIAM SODA*, 2004, p. 30–39.
- [6] H. Wang, H. Zhao, B. Lin, and J. Xu. DRAM-based statistics counter array architecture with performance guarantee. In: *IEEE/ACM Trans. Netw.*, vol. 20, no. 4, 2012, p. 1040–1053
- [7] H. Song, F. Hao, M. Kodialam, and T. V. Lakshman. IPv6 lookups using distributed and load balanced Bloom filters for 100 Gbps core router line cards. In: *Proc. IEEE INFOCOM*, Apr. 2009, p. 2518–2526.
- [8] A. Z. Broder and M. Mitzenmacher. Using multiple hash functions to improve IP lookups. In: *Proc. IEEE INFOCOM*, Apr. 2001, p. 1454–1463.
- [9] X. Tian , Y. Cheng. Bloom filter-based scalable multicast: methodology, design and application. In: *IEEE Network*, vol. 27, no. 6; 2013. p.89-94.
- [10] W. Xue, D. Vatsalan, W. Hu and A. Seneviratne. Sequence Data Matching and Beyond: New Privacy-Preserving Primitives Based on Bloom Filters. In: *IEEE Transactions on Information Forensics and Security*, vol. 15; 2020. p. 2973-2987.
- [11] O. Rottenstreich, P. Reviriego, E. Porat and S. Muthukrishnan. Avoiding Flow Size Overestimation in Count-Min Sketch With Bloom Filter Constructions. In: *IEEE Transactions on Network and Service Management*, vol. 18, no. 3; 2021, p. 3662-3676.
- [12] X. Li, L. Peng and C. Zhang. Application of Bloom Filter in Grid Information Service. In: *2010 International Conference on Multimedia Information Networking and Security*; 2010, p. 866-870.
- [13] F. Chang, Wu-chang Feng and Kang Li. Approximate caches for packet classification In: *IEEE INFOCOM 2004*, vol.4; 2004, p. 2196-2207.
- [14] F. Hao, M. Kodialam, T. V. Lakshman and H. Song. Fast Dynamic Multiple-Set Membership Testing Using Combinatorial Bloom Filters. In: *IEEE/ACM Transactions on Networking*, vol. 20, no. 1; 2012, pp. 295-304.
- [15] B. Chazelle, J. Kilian, R. Rubinfeld, and A. Tal. The Bloomier filter: An efficient data structure for static support lookup tables. In: *Proc. ACM-SIAM SODA*; 2004, p. 30-39.
- [16] L. Calderoni, P. Palmieri and D. Maio. Probabilistic Properties of the Spatial Bloom Filters and Their Relevance to Cryptographic Protocols. In: *IEEE Transactions on Information Forensics and Security*, vol. 13, no. 7; 2018, p. 1710-1721.
- [17] T. Yang, A.X. Liu, M. Shahzad, Y. ZHONG, Q. Fu, Z. Li. A Shifting Framework for Set Queries. In: *IEEE/ACM Transactions on Networking*, vol. 25, no. 5; 2017, p. 3116-3131.

Constellation Configuration Analysis Based on Angle Condition Number for Tri-satellite TDOA Geolocation System

Bo LIU^a, Xiaoyang CHEN^{a,b,1}, Ming LI^{a,b}, Shuai LI^{a,b}, Jie REN^{a,b} and Lede QIU^a

^a*Institute of Telecommunication and Navigation Satellites, China Academy of Space Technology, Beijing 100094, China*

^b*Innovation Center of Satellite Communication System, CNSA, Beijing 100094, China*

Abstract. The geolocation performance of tri-satellite system based on time difference of arrival (TDOA) is significantly affected by the constellation configuration. In this paper, an angle condition number based method is proposed for constellation configuration analysis. First, the coefficient matrix of constellation configuration is derived by geolocation error analysis. Second, the angle condition number is adopted to measure the ill-condition of the coefficient matrix. Based on the measurement, the influence of constellation configuration on geolocation is deeply analyzed. The effectiveness of angle condition number on constellation configuration analysis is verified by simulations.

Keywords. Time difference of arrival, constellation configuration, angle condition number

1. Introduction

The geolocation of unknown radiation source is a hot research topic in satellite electromagnetic spectrum sensing. Time difference of arrival (TDOA) method is widely used to obtain the target location [1][2][3][4]. When the TDOA estimation accuracy is known, the geolocation accuracy is determined by the constellation configuration [5][6][7][8][9]. Therefore, many methods have been put forward to analyze the influence of constellation configuration on geolocation. The expressions of geolocation bias for TDOA geolocation system are derived in [10]. The geometry dilution of precision factor (GDOP) is derived for tri-satellite TDOA localization system in [11]. The optimum configuration, which minimize the geolocation error of single point, is derived in [12][13]. The relationship between GDOP and the triangle area formed by three satellites is derived in [14], which proved that the tri-satellite triangle area is inversely proportional to GDOP when the distances from radiation source to three satellites are equal. The ill-condition of coefficient matrix is preliminarily introduced to the geolocation error assessment in [15], but it is not discussed in detail.

In this paper, an angle condition number (ACN) based method for constellation configuration analysis is proposed. First, the coefficient matrix of constellation

¹ Corresponding author: Xiaoyang Chen, Institute of Telecommunication and Navigation Satellites, China Academy of Space Technology, Beijing, 100094, China; E-mail: chenxiaoyang_paper@163.com.

configuration is calculated by geolocation error analysis. In the following, the angle condition number is introduced to measure the ill-condition of the coefficient matrix. Based on the measurement, the influence of constellation configuration on geolocation is deeply analysed.

2. Geolocation error model

The tri-satellite TDOA geolocation solution equations are:

$$\begin{cases} r_2 - r_1 = c\tau_{12} \\ r_3 - r_1 = c\tau_{13} \\ x^2 + y^2 + z^2 = R_e^2 \end{cases} \quad (1)$$

where $r_i = \sqrt{(x_i - x)^2 + (y_i - y)^2 + (z_i - z)^2}$, $i=1,2,3$ is the distance between the i th satellite and the radiation source. (x, y, z) denotes the coordinate of radiation source. (x_i, y_i, z_i) is the coordinate of the i th satellite. R_e denotes the radius of the earth. c denotes the light speed. τ_{12} is the TDOA measurement about satellite 1 and 2, τ_{13} is the TDOA measurement about satellite 1 and 3. The error equation can be obtained by differentiating the Eq. (1):

$$Cdu = d\tau + dR_e \quad (2)$$

where $du = [dx \ dy \ dz]^T$, $d\tau = [cd\tau_{12} \ cd\tau_{13} \ 0]^T$, $dR_e = [0 \ 0 \ dR_e]^T$. The matrix C denotes the partial differential matrix of the radiation source, expressed as:

$$C = \begin{bmatrix} g_{x2} - g_{x1} & g_{y2} - g_{y1} & g_{z2} - g_{z1} \\ g_{x3} - g_{x1} & g_{y3} - g_{y1} & g_{z3} - g_{z1} \\ x/R_e & y/R_e & z/R_e \end{bmatrix} \quad (3)$$

where $g_{xi} = (x - x_i)/r_i$, $g_{yi} = (y - y_i)/r_i$, $g_{zi} = (z - z_i)/r_i$, $i=1,2,3$. Therefore, the geolocation error can be measured by GDOP, which is calculated by:

$$GDOP(x, y, z) = \sqrt{tr(P)} \quad (4)$$

where matrix $P = E[du][du^T]$ is the radiation source geolocation error covariance matrix. From the Eq. (2) and (4), it is found that the matrix C reflects the geometric constellation configuration relationship among three satellites and the radiation source, $d\tau$ is the TDOA estimation error, dR_e is the elevation error. For the definite signal, the $d\tau$ is determined when the TDOA estimation method is determined. For radiation source at sea level, the dR_e is determined meanwhile. Therefore, the geolocation error depends on

the error propagation characteristics of the matrix C at this time [15], which can be calculated by condition number:

$$cond(C) = \|C^{-1}\| \|C\| \tag{5}$$

where $\|\cdot\|$ denotes the norm. The condition number reflects the influence of the perturbation. The condition number of matrix C reflects the disturbance degree of the constellation configuration on the geolocation error. When the condition number is too large, the system is ill-conditioned, which means the geolocation accuracy will decline.

3. Constellation configuration analysis based on angle condition number

Although the condition number can effectively analyze the geolocation accuracy, the interpretation is poor. For example, the condition number calculated by the 2-norm is related to the eigenvalue of matrix $C^T C$, which is not directly related to constellation configuration. To solve this problem, the concept of angle condition number is adopted, which can analyze the constellation configuration more easily. The detail is described in the following.

3.1. Concepts of angle condition number

For matrix $A \in R^{n \times n}$ with $\det(A) \neq 0$, $\alpha_i (i = 1, 2, \dots, n)$ is the i th row vector, $A(i)$ is the Euclidean space composed of the row vectors $\alpha_1, \alpha_2, \dots, \alpha_{i-1}, \alpha_{i+1}, \dots, \alpha_n$, ξ is the orthogonal projection of α_i on $A(i)$, $w = \alpha_i - \xi$. So $\theta_i = \arcsin(\|w\|_2 / \|\alpha_i\|_2)$ can be called as the i th characteristic angle. The angle condition number of matrix A is [16]:

$$cond(A)_a = \min_{1 \leq i \leq n} \{\theta_i\} \tag{6}$$

For n -order nonsingular linear algebraic equations $AX = B$ and a given positive number $\varepsilon (0 < \varepsilon \leq \pi / 2)$, if

$$cond(A)_a \leq \varepsilon \tag{7}$$

then, $AX = B$ is an ill-conditioned system with respect to ε .

3.2. Geometry configuration analysis based on angle condition number

This part analyzes the error propagation characteristics of coefficient matrix C based on angle condition number. In order to simplify the expression, C can be rewritten as:

$$C = \begin{bmatrix} g_{x2} - g_{x1} & g_{y2} - g_{y1} & g_{z2} - g_{z1} \\ g_{x3} - g_{x1} & g_{y3} - g_{y1} & g_{z3} - g_{z1} \\ x/R_e & y/R_e & z/R_e \end{bmatrix} = \begin{bmatrix} \alpha_1 \\ \alpha_2 \\ \alpha_3 \end{bmatrix} = \begin{bmatrix} \beta_2 - \beta_1 \\ \beta_3 - \beta_1 \\ \alpha_3 \end{bmatrix} \tag{8}$$

where $\beta_i = [(x-x_i)/r_i \quad (y-y_i)/r_i \quad (z-z_i)/r_i], i = 1, 2, 3$ is the unit vector from the i th satellite pointing to the radiation source, and α_3 is the unit vector from the earth's core pointing to the radiation source. In the east-north-up (ENU) coordinate which is based on the radiation source, the three satellites can be marked as $s_i, i = 1, 2, 3$, and the six vectors $\alpha_1, \alpha_2, \alpha_3, \beta_1, \beta_2, \beta_3$ are shown in the Figure 1.(a).

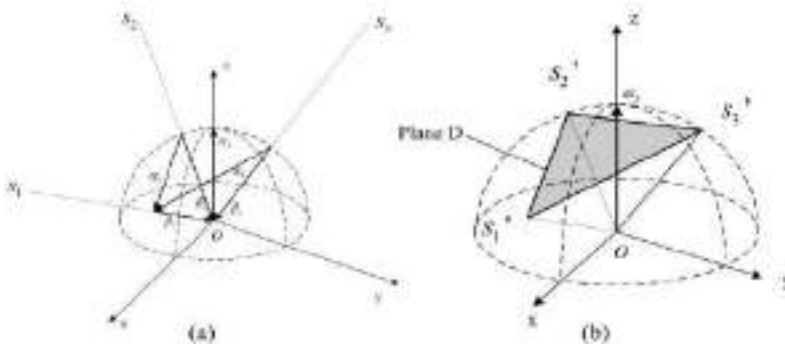


Figure 1. Geometry diagram: (a) the six vectors, (b) the Plane D

According to the concept of angle condition number, the angle between α_i and the plane composed of the remaining two vectors is used to analyze the geolocation error. Obviously, the vector α_3 is fixed, as the unit vector in the Z direction. The vectors α_1, α_2 change continuously with the motion of three satellites. Therefore, the plane composed by vectors α_1, α_2 (marked as plane D) should be discussed. Plane D is defined by three points $s_i, i = 1, 2, 3$, which are the projections of three satellites on the unit sphere centered on the radiation source, just as shown in the Figure 1.(b). Thus, only the angle between Plane D and Z axis is required to be analyzed. When $cond(C)_a \leq \epsilon$, the system is ill-conditioned. It can be deduced that the plane D is almost perpendicular to plane XOY, while the constellation configuration is the worst at this time.

4. Numerical simulations

In this section, MATLAB and STK simulation are used to verify the proposed method. The simulation uses three satellites for radiation source geolocation. The orbital paraments at the initial time of three satellites are shown in the Table 1. The TDOA estimation error is 50 ns, the elevation error is 10 m. The radiation source is located at longitude 90 degrees west and latitude 10 degrees north. The condition number is calculated by the 2-norm.

Table 1. Simulation parameters of three satellites

	Satellite 1	Satellite 2	Satellite 3
Apogee Altitude (Km)	600	600	600
Perigee Altitude (Km)	600	600	600
Inclination (deg)	50	50	50
Argument of Perigee (deg)	0	0	0
Lon. Asc. Node(deg)	-105	-100	-95
True Anomaly (deg)	5	3	5

As the satellites moving, the relative position between the radiation source and the tri-satellite constellation changes, as well as the geolocation error changes. The relationship of GDOP, condition number, angle condition number (ACN) and the reciprocal of ACN with time are shown in the Figure 2. It can be found that when $t = 256s$, GDOP is the largest, which means the constellation configuration has the greatest impact on the geolocation accuracy. At this time, the condition number reaches the maximum value, and the angle condition number is close to zero, which both reflect the system ill-condition.

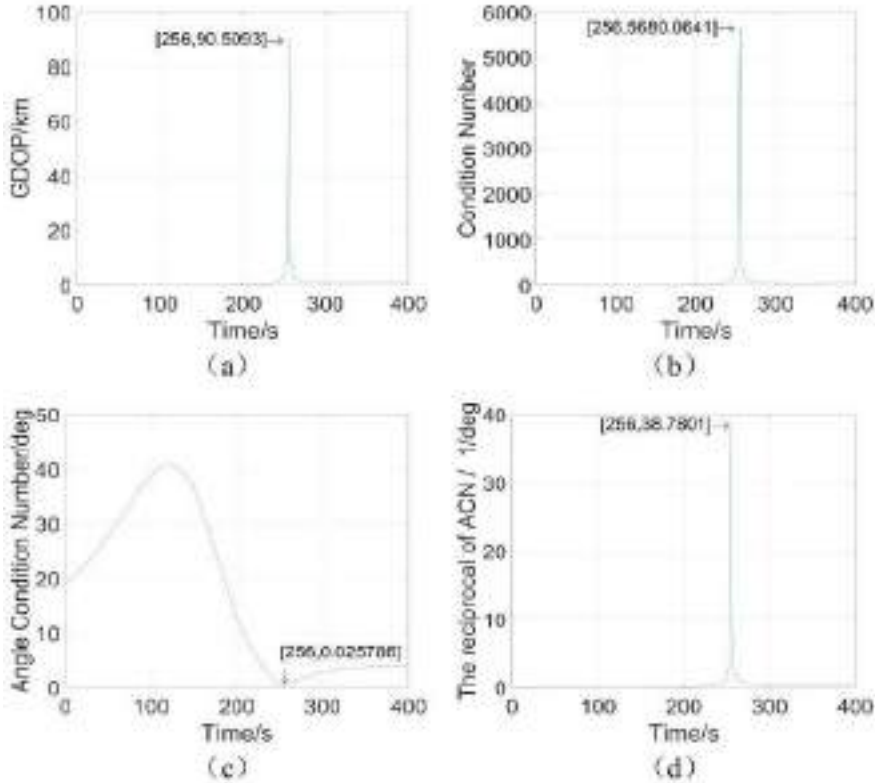


Figure 2. (a) GDOP with time, (b) condition number with time, (c) angle condition number with time, (d) the reciprocal of angle condition number with time

In order to further discuss the constellation geometric configuration when the geolocation accuracy is the worst, the three satellites coordinates can be obtained. The satellites' positions (in earth-centered earth-fixed coordinate system) and six vectors $\alpha_1, \alpha_2, \alpha_3, \beta_1, \beta_2, \beta_3$ (in ENU coordinate system) are shown in the Table 2 and 3.

Table 2. Three satellites coordinate at $t = 256s$

Radiation source (Km)	[0 -6281.9 1100.2]
Satellite 1 (Km)	[-315.0 -6704.2 1910.3]
Satellite 1 (Km)	[126.2 -6757.7 1735.5]
Satellite 1 (Km)	[854.5 -6656.5 1912.0]

Table 3. Six vectors coordinate at $t = 256s$

Vector β_1	[0.3259 -0.7497 -0.5760]
Vector β_2	[-0.1571 -0.6756 -0.7203]
Vector β_3	[-0.6909 -0.5938 -0.4123]
Vector α_1	[-0.4830 0.0741 -0.1443]
Vector α_2	[-1.0169 0.1558 0.1637]
Vector α_3	[0 0 1]

After that, the six vectors geometric configuration can be got, as shown in the Figure 3. In this figure, the blue dotted line vector corresponds to $-\beta_1, -\beta_2, -\beta_3$, while the red solid line vector corresponds to $\alpha_1, \alpha_2, \alpha_3$. It can be seen that the plane D , where the vectors α_1, α_2 are located, is perpendicular to the XOY plane. In the physical sense, it corresponds that the plane composed of three points, which is projected by the three satellites on the unit sphere with the radiation source as the origin, is perpendicular to the XOY plane. That is consistent with the above analysis conclusion.

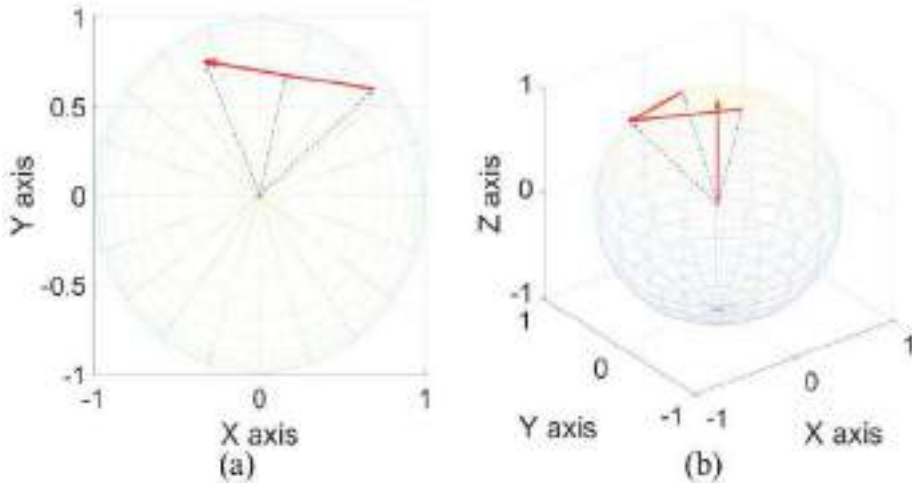


Figure 3. Six vectors geometric configuration: (a) view direct above, (b) view at an oblique 45°

5. Conclusion

This paper proposed a constellation configuration analysis method based on the angle condition number for tri-satellite TDOA geolocation system. This paper derived the constellation configuration coefficient matrix from geolocation error analysis model. Then the angle condition number is adopted to assess the ill-condition of the coefficient matrix. Finally, the influence of constellation configuration on geolocation is deeply analyzed. The simulation results showed that the angle condition number can effectively measure the influence of constellation configuration on geolocation accuracy.

References

- [1] Su T, Gao Y. TDOA estimation of dual-satellites interference localization based on blind separation. *Journal of System Engineering and Electronic*. 2019;30(4):696-702.
- [2] Velasco J, Pizarro D, Macias-Guarasa J, Asaei A. TDOA matrices: algebraic properties and their application to robust denoising with missing data. *IEEE Transactions on signal processing*. 2016;64(20):5242-54.
- [3] Pham-Viet H, Tran VH, Nguyen CT, Van NT, Cuong NM. Performance Assessment of Marine Vessel Positioning Method Using AIS Signals Based on Time Difference of Arrival. 2020 IEEE 8th International Conference on Communications and Electronics; 2021 Jan 13-15; Phu Quoc Island, Vietnam. p. 297–301.
- [4] Khyzhniak M, Malanowski M. Localization of an Acoustic Emission Source Based on Time Difference of Arrival. 2021 Signal Processing Symposium; 2021 Sep 20-23; LODZ, Poland. p. 117-121.
- [5] Fokin G, Kireev A, Al-Odhari AHA. TDOA positioning accuracy performance evaluation for arc sensor configuration. 2018 Systems of Signals Generating and Processing in the Field of on Board Communications; 2018 March 14–15; Moscow Russia. p. 1-5.
- [6] Wang WJ, Bai P, Wang YB, Liang XL, Zhang JQ. Optimal sensor deployment and velocity configuration with hybrid TDOA and FDOA measurements. *IEEE Access*. 2019; 7:109181–94.
- [7] Wang WJ, Bai P, Liang XL, Wang YB, Zhang JQ. Optimal deployment of sensor-emitter geometries for hybrid localisation using TDOA and AOA measurements. *IET Science, Measurement and Technology*. 2019;13(5):622–31.
- [8] Yang C, Kaplan L, Blasch E, Bakich M. Optimal placement of heterogeneous sensors for targets with gaussian priors. *IEEE Transactions on Aerospace and Electronic Systems*. 2013;49(3):1637–53.
- [9] El-Ghoboushi M, Ghuniem A, Gaafar A, Abou-Bakr HE. Geometry effect on a multilateration air traffic Surveillance System Performance. 2017 Japan-Africa Conference on Electronics, Communications and Computers ;2017 December 18-20; Alexandria, Egypt. p. 136–43.
- [10] Ho KC, Chan YT. Solution and performance analysis of geolocation by TDOA. *IEEE Transactions on Aerospace Electronic Systems*. 1993;29(4):1311-22.
- [11] Wang HL, Ren X, Chen L. Localization precision analysis of three satellites cluster for time-difference localization. *Chinese Space Science and Technology*. 2000;(05):26-31.
- [12] Yang B, Scheuing J. Cramer-Rao bound and optimum sensor array for source localization from time difference of arrival. *IEEE International Conference Acoustic, Speech, Signal Processing*; 2005; Philadelphia, USA. p. 961-64.
- [13] Zhou C, Huang GM, Gao J. Optimum Sensor Array for Passive Localization from Time Differences of Arrival. *Applied Mechanics and Materials*. 2014; 721:411–5.
- [14] Zhu WQ, Huang PK. Constellation shape of tri-station geolocation system using TDOA. *Modern Radar*. 2010; 32(1):1-6.
- [15] Li WH. Research on configuration of tri-satellites and location precision of TDOA. *Journal of Astronautics*. 2010;31(3):701-706.
- [16] Xu YH, Gao J, Wang YQ, Zhang L, Zeng XW. Angle condition number of real matrices. *Journal of Sichuan Normal University (Nature Science)*. 2000; 23(5):491-492.

A Discrete Clutter Reduction Method for Drone Detection with High Resolution Radars

Tran VU HOP, Nguyen VAN LOI¹, Pham VAN TIEN and Phung DINH THANG
Radar Center, Viettel High Technology Industries Corporation, Hanoi, Vietnam

Abstract. The paper deals with a problem of noise reduction for drone detection with high range resolution radars. The considered discrete clutter includes land vehicles, birds, etc. This clutter involves in the radar echo signals and could not be rejected by using classical methods, for example moving target indicator (MTI) and moving target detection (MTD). As a result, this clutter forms the false alarms on the radar screen. To reduce clutter we propose a new method which is based on the target's Doppler dispersion and moving characteristic. The study is integrated on a drone detection radar and is tested with a variety of drones in different moving scenarios. The test results show that the proposed method achieves a better performance than that one recently published.

Keywords. Radar signal processing, clutter reduction, drone detection radar, high resolution radar

1. Introduction

A radar is a complicated system that uses the radio waves to detect objects (targets). In the radar signal echoes, beside the signals from considered objects there are signals from unwanted objects, for example, for a drone detection radar with a high range resolution (HRR) (see [1, ch. 9]) unwanted objects are land (or surface) clutter (grasses, trees, ground), volume clutter (precipitation and chaff) and discrete (or point) clutter (birds, insects, land vehicles, wind turbines, buildings, water tanks). These clutters form false alarms on the radar screen and degrade the system performance (see Figure 1).

Two most popular methods for radar clutter reduction are the MTI and MTD. The MTI was firstly discussed by Ridenour (see [2]) and Grisetti et al. (see [3]) and it contains a delay line and a subtraction circuit which takes the difference between consecutive pulses (see Figure 2). For a moving target, the Doppler shift of the carrier frequency will change the phase of the received pulse whereas a ground or building echo will leave it essentially unchanged. Therefore, the clutter will be cancelled in the output pulse.

The subsequent studies are extended to the case of digital MTI (see [4]), MTI with the staggered pulse repetition frequency (see [5], [6]). However, there are many causes such as small movements of trees on the ground, rotation of the radar antenna that lead to inefficiency of the MTI.

¹ Corresponding Author; E-mail: loinv12@viettel.com.vn, loinv14982@gmail.com.

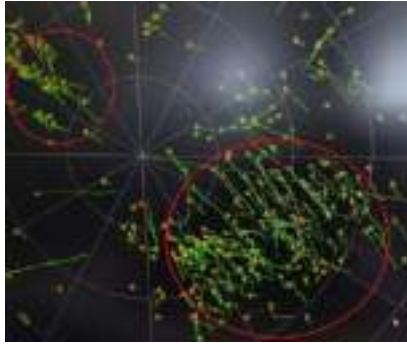


Figure 1. Illustration of false alarms (in the circles) from volume clutter on a high range resolution radar

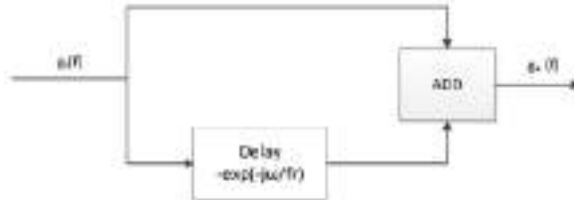


Figure 2. Block diagram of an MTI system [3]

The MTD is the newer approach for detection of moving targets than the MTI (see [7], [8]). One of the main blocks of the MTD system (see Figure 3) is the block “Doppler Filter Bank” that separates objects into different velocity levels (or equivalent, different Doppler banks) in order to reduce clutter (see Figure 4).

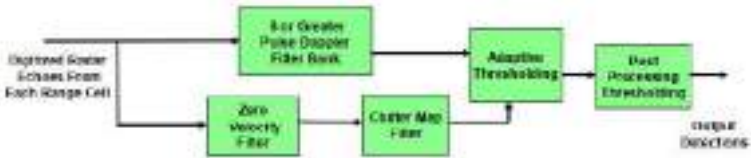


Figure 3. Block diagram of an MTD system [8]

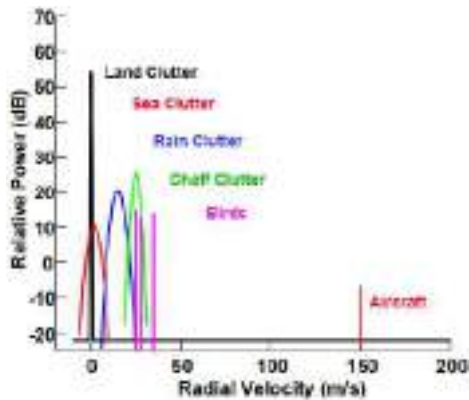


Figure 4. Example of clutter spectra [8]

For 2D (or even 3D) drone detection radars, it is hard to reduce discrete clutter (such as land vehicles and birds) because its Doppler is similar to that one of drones which fly slowly or at a low altitude. In this situation the use of MTI and MTD cannot help. Therefore, there is a need to explore new methods to avoid these difficulties.

Among a large number of works concerning to radar discrete clutter suppression, let us recall the work of Martin and Shapiro (see [9]) with a method for discrimination of birds and insects for high resolution weather radars using a combination of estimated radar cross section and density of targets, the work of Zaugg et al. (see [10]) studied a problem of automatic identification of bird targets from insects and ground clutters for radars using wing flapping patterns and support vector classifiers, the work of He et al. (see [11]) investigated a problem of wind farm discrete clutter suppression for air surveillance radar based on clutter map and a generalizing algorithm of K-means clustering process, the work of Jatau et al. (see [12]) for detecting birds and insects in the atmosphere using machine learning on pattern of bird and insect echoes based on dual polarization variables. The reduction methods for another type of radar discrete clutters reflected from buildings was studied in [13-16].

In this paper, we propose a new method to recognize drones from discrete clutter. The method is based on the target's Doppler diversion and the moving characteristic. The paper is organized in the following way. In the next section, we take a statistical analysis on target's Doppler and moving properties. In section 3, the proposed design and algorithms are described. Then, the test results show the efficiency of the study. The last section deals with the conclusion and future works.

2. Analysis

In this section by using a HRR radar (see Figure 5 and Table 1) we analyze the characteristics of drone (Inspire 2, Phantom 4, Mavic 3) and discrete clutter (such as land vehicles, birds) based on their radar signal echoes.



Figure 5. The radar used for the study

Table 1. Radar parameters

Parameter	Value
Radar type	FMCW, 2 dimensions
Frequency	X-band
Instrumented range	12km
Range resolution	1.5m
Scan rate	01Hz

2.1. Doppler characteristic

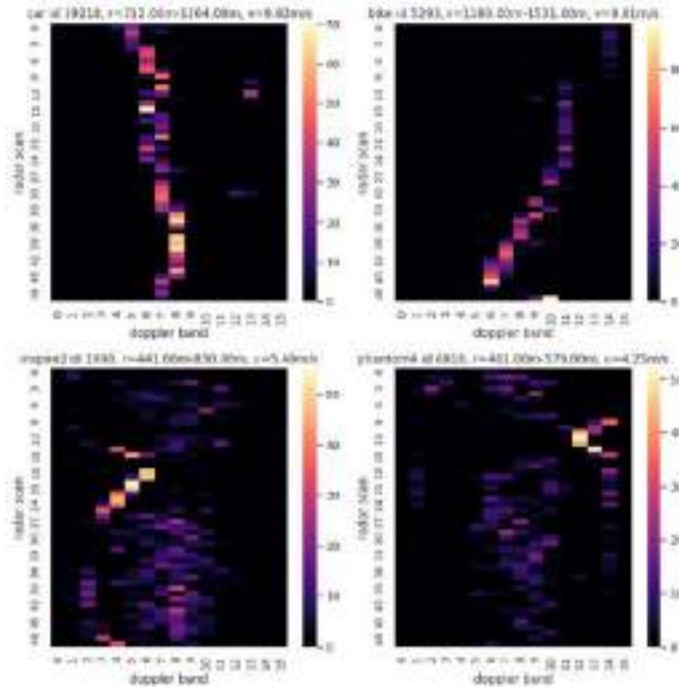


Figure 6. Doppler characteristic of different targets

There are 16 Doppler bands using for coherent integration in this study. The number “16” of Doppler bands is followed from the radar parameters (see Table 1). At each radar scan, a target will be detected as a group of plots. Each plot characterizes an echo pulse from a part of the target and has its own Doppler. Counting the plots which have the same Doppler and displaying the results with consecutive scans we obtain the target’s Doppler characteristic picture (see Figure 6).

The target’s Doppler dispersion is featured by $(\overline{\Delta f_D}, \sigma_{\Delta f_D})$:

$$\overline{\Delta f_D} = mean\{\Delta f_{D1}, \Delta f_{D2}, \dots, \Delta f_{DM}\} \tag{1}$$

$$\sigma_{\Delta f_D} = std\{\Delta f_{D1}, \Delta f_{D2}, \dots, \Delta f_{DM}\} \tag{2}$$

where Δf_{Di} is the target’s Doppler spread at i -th scan and $mean$ and std denote the mean and standard deviation, M is number of scans and the target’s Doppler spread on the Doppler banks.

Analyzing data from radar targets with range less than 1,7km we obtain the following statistic of targets Doppler dispersion (see Figure 7 and 8)

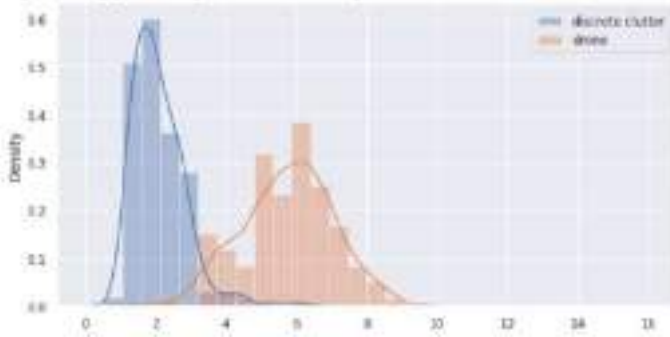


Figure 7. Distribution of $\overline{\Delta f_D}$ of discrete clutters and drones

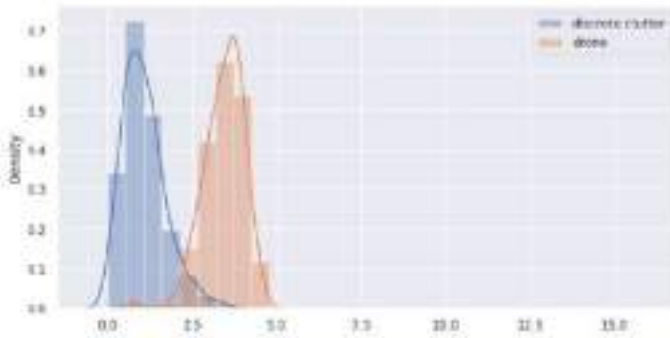


Figure 8. Distribution of $\sigma_{\Delta f_D}$ of discrete clutters and drones

2.2. Moving characteristic

As given in the previous section, the targets Doppler dispersion feature is not enough to reduce the discrete clutters because of its dependence on the range from the radar to the targets. For a small drone moving far from the radar, its Doppler dispersion feature is the same as discrete clutter. Therefore, in this section we introduce a street data which is used to extract targets moving characteristic for clutter reduction.

A street data is taken from www.openstreetmap.org and it contains a list of elements (or equivalent streets). Each element (or street) is constructed by connecting adjacent nodes (or points) together. For illustration, Figure 9 shows an element in a street data.

To perform a street map, we need the well-known following converting formula.

For a point A with range d (m) and azimuth α (rad), its latitude and longitude are defined as:

$$lon_A = lon_{root} + \frac{d \times hs \times \sin \alpha}{\cos^{\frac{lat_{root} \times \pi}{180}}} \tag{3}$$

$$lat_A = lat_{root} + d \times hs \times \cos \alpha \tag{4}$$

where (lat_{root}, lon_{root}) is the latitude and longitude of the radar position and

$$hs = \frac{1}{\frac{2\pi}{360} \times R}, R = 6378.137 \text{ (}^\circ\text{/m)} \tag{5}$$

```

* elements [352]
  * : [0]
  * : [0]
    type : way
    id : 130061693
  * boards [4]
  * nodes [17]
  * geometry [17]
    * : [2]
      lat : 28.9903916
      lon : 105.5290392
    * : [2]
      lat : 28.9904214
      lon : 105.5287271
    * : [2]
      lat : 28.9904714
      lon : 105.5284758
    * : [2]
      lat : 28.9905173
      lon : 105.5283310
  
```

Figure 9. An element with its first three nodes

For a point A (lat_A, lon_A), its coordinates (x_A, y_A) in the Cartesian coordinate are

$$x_A = \left(\frac{lat_A - lat_{root}}{hs} \right) / scale \tag{6}$$

$$y_A = \left(\frac{lon_{root} - lon_A}{hs} \right) / scale \tag{7}$$

where $scale$ (pixel/m) is a parameter.

Now let us present the method to construct a street map with (approximately) the same range resolution with the radar. In fact, the radar used in this study has the range resolution 1,5m (see Table 1), hence we can use the value $scale = 1,5/\sqrt{2} \approx 1(\frac{pixel}{m})$, i.e. the street map has resolution 1,0m in the Cartesian coordinate (see Figure 10).

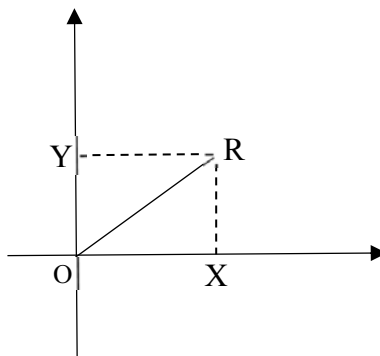


Figure 10. Illustration of different resolutions: range resolution OR and resolution in Cartesian coordinate OX, OY

The process is as following.

Step 1. From www.openstreetmap.org load the street data where the radar set up. The street data is determined by a square shape with length $2R_{\text{ins}}$ (m) and center in the radar position (see Figure 11), where R_{ins} is the radar instrumented range.



Figure 11. Illustration of the radar position and the loaded street data (the square shape)

Step 2. Using formulas (2) and (3) calculate the latitude and longitude of Point A (see Figure 12) with $(lat_{\text{root}}, lon_{\text{root}})$ is the latitude and longitude of the radar.

Step 3. For each street in the loaded data, convert coordinates of all nodes into Cartesian coordinate using formulas (5), (6), the latitude and longitude of Point A as $(lat_{\text{root}}, lon_{\text{root}})$.

Step 4. Connect consecutive nodes of a street and interpolate values (coordinates) for other points in the street (in order of resolution 1m of the street map). Repeat for all other streets we obtain the street map with (approximately) the same range resolution with the radar (see Figure 12).



Figure 12. A street map (red color) displayed on the radar screen

For analyzing of moving characteristic of radar discrete clutters with respect to the street map we collect 10676 distance samples and 9311 moving direction samples from 380 discrete clutter (cars, motorbikes, birds) and take the statistic of the distance and moving direction of targets to the nearest street on the street map. The statistic results are given in Figure 13.

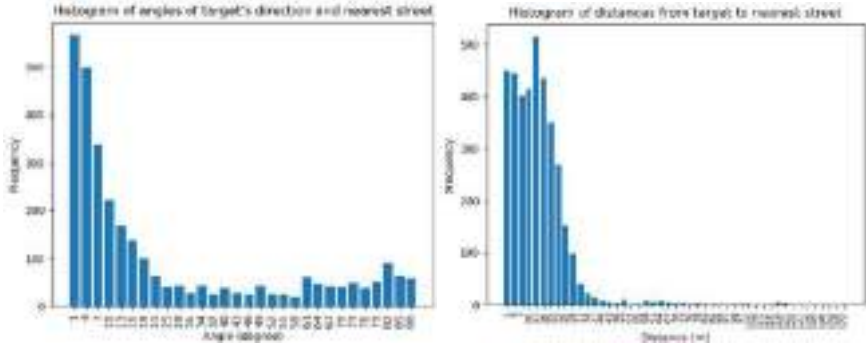


Figure 13. Statistic results of radar target trajectories

3. Proposed method and test results

3.1. Proposed method

We propose a system design and algorithms for module “Discrete clutter reduction”. The principle of the module is included in the classification of discrete clutters and drones. The design of the module is represented in Figure 14.

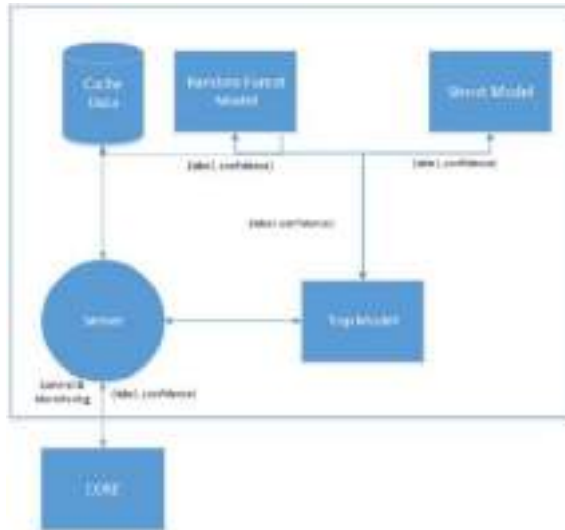


Figure 14. System design of module “Discrete clutter reduction”

The data flow is as follows.

Step 1: From “Core” the target parameters (such as ranges, azimuths, moving direction) is transferred into “Random Forest Model” and “Street Model” via “Server” and “Top Model”.

Step 2: Each of submodules “Random Forest Model” and “Street Model” will predict the targets as “drone” or “discrete clutter” and sends the label with confidence score (probability of classification) back to the “Top Model”.

Step 3: At the “Top Model” a decision for each target is confirmed and the results are back in “Core” to display on the radar monitor.

The algorithms for “Random Forest Model”, “Street Model” and “Top Model” are described in Algorithm 1, Algorithm 2 and Algorithm 3 respectively.

Algorithm 1 (Random forest model).

Input: Doppler dispersion of targets;

Output: targets label (“drone” or “discrete clutter”);

Model: random forest with 20 trees;

Dataset for training: we collect 20.000 samples with 10.000 samples of drones and 10.000 samples of discrete clutter.

The structure of a decision tree is given in Figure 15.

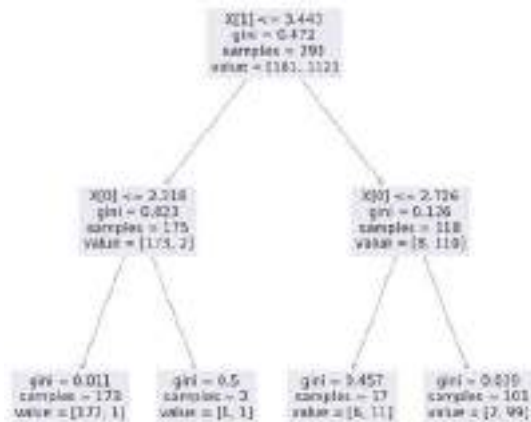


Figure 15. Structure of a decision tree ($X[1]$ is $\overline{\Delta f_D}$ and $X[0]$ is $\sigma_{\Delta f_D}$)

Algorithm 2 (Street model).

Input: target’s trajectory from radar;

Output: target’s label (“drone” or “undefined”).

Step 1: For a radar target, convert its ranges and azimuths to latitude and longitude coordinates using formulas (2) and (3). Then using formulas (5) and (6) with the root at Point A (Figure 12) we obtain target’s positions in the street map (see Figure 16).

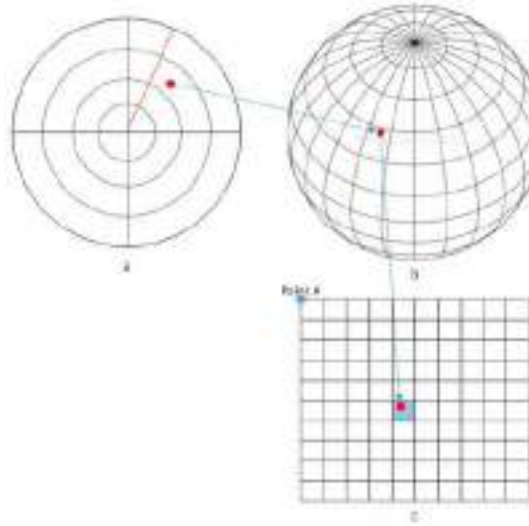


Figure 16. Illustration of the coordinate conversions in Step 1: target's position on radar screen (a), geographic coordinate (b) and street map (c)

Step 2: From the target's current position (in the street map) open a square gate with center at target's position and radius r (see Figure 17). If there is a node (point) in the gate which belongs to a street, then target's current position is considered as "near street".

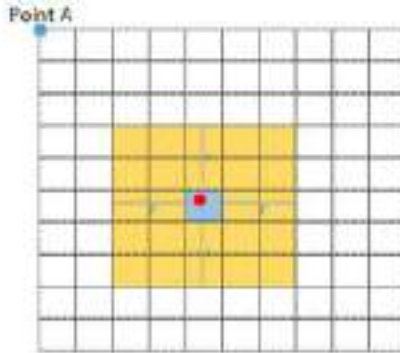


Figure 17. An example of a square gate on the street map

Step 3. Repeat Step 2 for N consecutive radar scans, if there are at least M scans at which target's position is near street and $M \geq N \times \text{nearStreetRate}$, then we decide that the target is near street.

Step 4. For a near street target, consider N last radar scan ($n-N+1, n-N+2, \dots, n$) where n is the current radar scan. A window with length k ($k < N$) is used to calculate $N-k+1$ angles $\{angle_1, angle_2, \dots, angle_{N-k+1}\}$ between target's moving direction and the nearest street. If $\text{median}\{angle_1, angle_2, \dots, angle_{N-k+1}\} < \text{angleMax}$, then we conclude that the target is moving along the street.

Step 5. If a target is moving along the street we classify it as "undefined", else classify as "drone".

The parameters used in this study for algorithm 2 are given in Table 2.

Table 2. Parameter values for Algorithm 2

Parameter	Value
<i>r</i> (radius of square gate)	30m
<i>N</i> (number of consecutive scans)	15
<i>nearStreetRate</i>	0.5
<i>k</i> (window size)	5.0
<i>angleMax</i>	30degree

Algorithm 3 (Top model).

The top model uses rule-based method to confirm a target as “drone” or “discrete clutter”.

Input: target’s labels from submodules “Random Forest Model” (for short: RFM) and “Street model” (for short: StM); active ranges of models (1,7km for random forest model and 12km for street model as given in section 2);

Output: target’s confirmed label (“drone”, “discrete clutter” or “undefined”).

The main logic rules of the top model are as follows (see Figure 18 for more details).

If RFM is inactive, i.e. the target’s range is greater than 1,7km, then StM is used.

If target’s predicted label (PRED) is different with “UNDEFINED”, then use MN logic (in this study M = 6, N = 10) to confirm target as “drone” or “discrete clutter”.

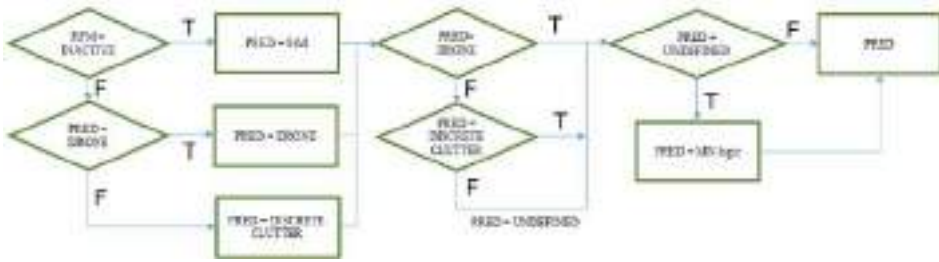


Figure 18. Diagram of Top model

3.2. Test results

The module was integrated in the radar system and tested with different drones (inspire 2, phantom 4, mavic 3) in different moving scenarios (such as radial flight, tangent flight). For the performance evaluation we use the following metrics:

$$\text{True Rate of Clutter Reduction (TRCR)} = \frac{\text{number of true clutters classified}}{\text{number of all discrete clutters}} \quad (8)$$

$$\text{True Rate of Drone Recognition (TRDR)} = \frac{\text{number of true drone classified}}{\text{number of all drones}} \quad (9)$$

$$\text{MRDR} = \text{Maximum Range for Drone Recognition} \quad (10)$$

The results are given in Table 3 and Figure 19-21.

Table 3. Test results

Parameter	Value
TRCP	0.95
TRDR	1.0
MRDR for drones moving across the streets	3.0km
MRDR for drones moving along the streets	1.7km

For comparison, Table 4 shows the results of our study and of Robin [17].

Table 4. Comparison with the same module on Robin drone detection radar

Parameter	Robin radar	Proposed module
TRCP	-	0.95
TRDR	-	1.0
MRDR	2.2km	3.0km



Figure 19. “Discrete clutter” and “Drone” on radar screen (recognize a drone from 3km)



Figure 20. Test results with different moving scenarios: drone moves in a sinusoidal trajectory (above) and along the street (below)



Figure 21. Three drones (inspire 2, phantom 4 and mavic 3) and a bird (inside the circle) in a test

4. Conclusion and future works

The paper presented the new approach for discrete clutter reduction with drone detection radars. A machine learning and a street model is combined to reduce discrete clutter and recognize a drone based on Doppler diversion moving trajectories. The tests show that 95% discrete clutter was rejected while 100% drones were exactly recognized.

In future works we will extend the study to recognize more different types of targets such as drones, helicopter, UAV from discrete clutter.

References

- [1] Barton DK. Radar Equations for Modern Radar. Artech House. 2013.
- [2] Ridenour L. Radar System Engineering. McGraw-Hill, New York. 1947.
- [3] Grisetti R, Santa M, Kirkpatrick G. Effect of internal fluctuations and scanning on clutter attenuation in MTI radar. IRE Trans. – Aeronautical and Navigational Electronics. 1955 March; 2(1):37-41.
- [4] Ewell GW. Design of Digital Moving Target Indication. PhD thesis. Georgia Institute of Technology. 1974.
- [5] Ispir M, Candan C. Least square and Min-Max design of MTI filters with nonuniform interpulse periods. Proceeding of 2013 IEEE Radar Conference; 2013 29 April – 03 May; Ottawa, Canada.
- [6] Ispir M, Candan C. On the design of staggered moving target indicator filters. IET Radar, Sonar & Navigation. 2015; 10(1):1-11.
- [7] Skolnik MI (Edi.). Radar Handbook. McGraw-Hill. 3rd Edition. 2008.
- [8] O'Donnell RM. Introduction to Radar Systems. Massachusetts Institute of Technology: MIT OpenCourseWare, <http://ocw.mit.edu>. 2007.
- [9] Martin WJ, Shapiro A. Discrimination of bird and insects radar echoes in clear air using high-resolution radars. J. Atmospheric and Oceanic Technology. 2007 July; 24:1215-1230.
- [10] Zaugg S, Saporta G, van Loon E, Schmaljohann H, Liechti F. Automatic identification of birds targets with radar via patterns produced by wing flapping. J. R. Soc. Interface. 2008 March; 5:1041-1053.
- [11] He WK, Zhang X, Bi FH, Yang L. Wind farm clutter suppression for air surveillance radar based on a combined method of clutter map and K-SVD algorithm. IET Radar, Sonar & Navigation. 2020; 14(9):1354-1364.
- [12] Jatau P, Melnikov V, Yu TY. Detecting birds and insects in the atmosphere using machine learning on NEXTRAD radar echoes. Environ. Sci. Proc. (Proceeding of 4th International Electronic Conference on Atmospheric Sciences); 2021 June; 8(1).

- [13] Verma P, Gaikwad A, Singh D, Nigam M. Analysis of clutter reduction techniques for through wall imaging in UWB range. *Progress in Electromagnetics Research*. 2009; 17:29-48.
- [14] Gaikwad A, Singh D, Nigam M. Application of clutter reduction techniques for detection of metallic and low dielectric target behind the brick wall by stepped frequency continuous wave radar in ultra-wideband range. *IET Radar, Sonar & Navigation*. 2011; 5(4):416-425.
- [15] Sévigny P. Clutter reduction using an image-based thresholding approach for 3-D through-wall synthetic aperture radar. *Scientific Report*. Defence Research and Development Canada. 2015 Dec.
- [16] Liu H, Huang C, Gan L, Zhou Y, Truong TK. Clutter reduction and target tracking in through-the-wall radar. *IEEE Transaction on Geoscience and Remote Sensing*. 2020 Jan; 58(1):486-499.
- [17] <https://www.robinradar.com/press/news/machine-learning-software-upgrade-announcement>

Algorithm Based on Deep Learning to Improve the Logistics Management of a Company That Distributes Reading Material

Bruno Kevin-Flores Aquino, Ángel Eduardo-Córdova Baquijano and Christian Ovalle¹
Private University of the North, Peru

Abstract. Companies in the field of sales and distribution of reading material, which have the problem of great variability in the demand for their products, which causes higher costs and customer dissatisfaction. Deep Learning, which is a branch of Machine Learning which is responsible for training a computer to learn on its own, works by recognizing patterns using many processing layers and learns through repetition in its training. Using the KDD methodology, we have implemented a deep learning algorithm to improve the logistics management of a reading material distribution company through demand forecasting and other aspects of logistics. It was shown that with the use of certain functions in the neural network of the algorithm it can be predicted with a low deviation and a minimum level of error, giving us results for 85% of improvement in demand prediction, also an 80% of improvement in material devolution, increasing the precision of the company on buying material aiming to get the exact amount of material to distribute. However, we can improve the results for a more accurate prediction by adapting the algorithm to the situation. Also, we share our challenges, and other opportunities for future research. This paper can help other investigators being a guide for beginners in deep learning application in logistics management.

Keywords. Deep learning, machine learning, value chain

1. Introduction

Despite the ravages of the pandemic due to covid-19, Latin American companies showed an 8.5% growth in the technology market during 2021 and new trends have arrived like IoT, big data and artificial intelligence with the digitalization on the 4.0 industry [1].

Authors Zhou, Yang and Fu's article [2] talks about pricing and ordering, which they say is very important, as benchmark prices have a significant impact on customer buying behaviors and companies' operational strategies. Therefore, we believe that this aspect will help the logistics management of book distribution companies.

Authors Kun and Hongliang [3] mention in their paper that smart purchase prediction is about predicting when a consumer may buy a new product or service based on their purchase history. This type of prediction has been applied in online advertising, search engines, recommendation systems and inventory control.

¹ Corresponding author: denis.ovalle@upn.pe

Therefore, intelligent prediction helps distribution companies to reduce the rate of customer abandonment, determine the deficiency in business plans and in the processes of operation and logistics [4]. Likewise, in the article by Yiwey, Lin & Bo [5] it is said that accurately forecasting sales is a major challenge faced by almost all companies.

Overestimation can directly affect inventory, cash flow, the company's business reputation, and profits. Therefore, in the business world the predictive algorithm has attracted a lot of attention, which are mainly based on autoregressive models.

2. Methodology

According to Kanwal, Lau, Ng, Sim and Chandrasekaran [6] for the purpose of the algorithm which will be the prediction is considered complex by various market factors adding incomplete and sometimes confusing information, so a precise prediction model must be made using different input variables as it ensures [7].

All methodologies seek to convert data into information through organized work together with stakeholders (people affected or involved by the project), to turn it into resources that facilitate decision-making in the company [8].

The KDD is an interactive process that involves a series of steps, usually, we can find that this is divided into 6 steps: Mastery of the Study and Establishment of Objectives, Collection or obtaining of data, Cleaning and processing of data, Data mining, Interpretation of patterns, Use of the acquired knowledge.

For the domain of study, it is sought to take prior knowledge of the context in which we manage ourselves, to have a deep mastery of the subject understanding the problem to be solved and the objectives that we must achieve [8].

Subsequently, one of the categories was taken that will serve as test data for use in the development of the model. This data was arranged in a ".csv" file to make its manipulation by the software in which the algorithm will be developed more convenient.

Multilayer perceptron:

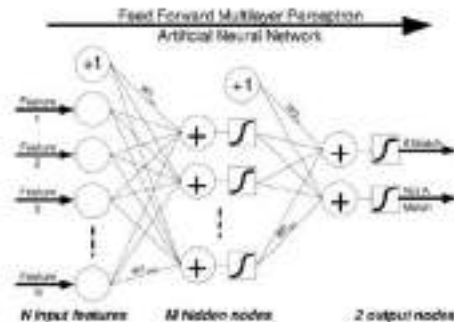


Figure 1. Feed forward multilayer perceptron artificial neural network.

The multilayer perceptron is one of the most used designs in the section of neural networks, unlike machine learning, the neural network does not need to be trained with individual features, but by training algorithms such as back-propagation the weight of each node in the layers is adjusted like in the fig. 1, in this way a more accurate precision is reached as Mentioned by Broussard and Kennell [9].

The indicators and metrics that we will use for this research are the following:

MAD (Mean Absolute Desviation): Represents the average deviation of the forecast in absolute values.

MSE (Mean Square Error): Average of the squares of the deviations of the estimate in the N periods.

RMSE (Root Mean Square Error): It is the root of the average of the squares of the differences of the estimate in the N periods.

MAE (Mean Absolute Error): The different errors are not weighted, but the scores increase linearly with the increase in errors. This is measured as the average of the absolute error values.

3. Results

For this section, the demand prediction was determined as a solution, for this we based on a sales and distribution dataset of the company, and we took it to the multilayer perceptron model with embeddings, we obtained the following results:

And in the metrics chosen for the prediction of demand we have the MSE, which shows us values that even reach 0.05 which indicates a very good result since there is no deviation in the prediction as shown in Fig. 2.



Figure 2. MSE Indicator.

And according to Fig. 3 in the case of MAD we have values close to 0.17 that indicate a good percentage for the absolute deviation of the predictions.



Figure 3. MAD Indicator

In the metrics chosen for the prediction of the withdrawal of merchandise we have the RMSE, which shows us that the values descend considerably fig. 4 to 0.20, which is a big improvement due to the low error rate per average root.

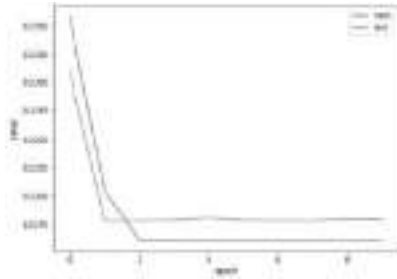


Figure 4: RMSE Indicator

And finally for the MAE we can see according to fig. 5 that the value of the absolute error drops to average values of 0.35

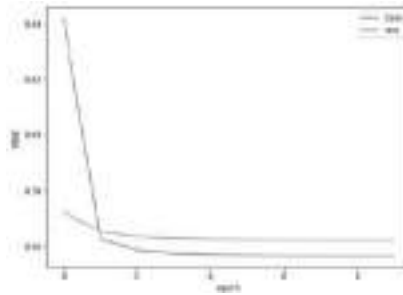


Figure 5: MAE Indicator

4. Discussion

In the present research work aimed at the development of a mobile application based on Deep Learning for the prediction of the demand for books per season of bookstores, in this way it will be possible to prevent what type of reading material will be a trend at each time of the year, so they will know what products they should distribute, consequently, this will give the administrative area of the company the opportunity to select the work with certain publishers based on the tastes of the end customer.

Likewise, the following question was asked: Will the development of a predictive algorithm carried out with Deep Learning help improve the logistics of supply in a company that distributes reading material?

Widely we can answer with a yes , since experimental/practical studies usually produce models, systems, frameworks, approaches, algorithms, methods or methodologies, and that logistics belongs to the experimental/practical type [10], so it demands an algorithm, which is our predictive algorithm which gives an accuracy of 80% to 85% for the continuous improvement of the end customer.

We have based on 3 dimensions which are Supply, Return and Withdrawal of merchandise. For each one, different neural network models were applied based on the multilayer perceptron and varying properties of the same model such as batch size, learning rate, loss functions, activation functions and Epochs. We even use embeddings for supply prediction, from which we get a loss of 17%, which indicates a low deviation in our predictions in contrast to real values.

For the prediction of the withdrawal of merchandise it was identified that we have a low percentage of deviation since we reached success values of 70%.

5. Conclusion

On what has been investigated based on the methodology and results of the experiments carried out, we can conclude that through the use of neural network models, predictions of different dimensions of the logistics of a book distribution company can be reached, resulting in an 85% improvement in the prediction of demand, also an 80% improvement in the return of material, increasing the accuracy of the company in the purchase of material with the aim of obtaining the exact amount of material to be distributed.

In addition, the KDD methodology helped us to propose the study from an application panorama, following the steps of research and elaboration of the algorithm to reach the results obtained.

In turn, the use of the algorithm sought to improve the prediction of demand to obtain accuracy in purchases and improve the total cost of acquiring new reading material for the company.

6. Limitations and implications

On the present work we can observe that we had limitations to be explicit in the details of the research, such as the state of the art, the elaboration of the algorithm and its comparison with others.

Due to the few works on the field of the distribution of reading material, we have decided to explain in an integral way the operation of the algorithm and its results in practice, to demonstrate that it has use in the field and is of help to the client.

In addition, our research has some implications in the aspect of the use of the algorithm, since its effectiveness depends on its characteristics and properties, which must be modified if they are used for different data sets.

7. Future research

Although deep learning in the reading material companies sector is new, all prediction algorithms share with each other the use of different learning models and neural network design, just as we use the multilayer perceptron and back-propagation.

To improve the results and reduce the scientific vacuum, other machine learning and deep learning models could be integrated, such as Random Forest, recognition and classification patterns or other models applied in prediction with images, in order to solve problems in integration of the distribution of the reading material.

References

- [1] C. Ovalle, «Predictive model based on Machine Learning for the Supply Chain and its influence on the logistics management of car sales company.» 2022
- [2] Zhou, Q., Yang, Y., & Fu, S. (2022). Deep reinforcement learning approach for solving joint pricing and inventory problem with reference price effects. *Expert Systems with Applications*, 195.
- [3] X. Kun, F. Hongliang, H. Jianguang, W. Hanyu, R. Junxue, J. Qin y W. Dafang, «An Intelligent Self-Service Vending System for Smart Retail,» *Sensors*, vol. 21, n° 10, p. 3560, 2021.
- [4] M. Torrens and S. Parra, "Artificial Intelligence. The Road to Ultrainelligence," *RBA Collectibles*, 2017.
- [5] Y. Liu, L. Feng y J. Bo, «Future-Aware Trend Alignment for Sales Predictions» *MDPI*, vol. 11, n° 558, 2020.
- [6] A. H. Moghaddam, M. H. Moghaddam y M. Esfandyari, «Stock market index prediction using artificial neural network,» *Journal of Economics, Finance and Administrative Science*, vol. 21, n° 41, pp. 89-93, 2016.
- [7] R. H. Ballou, *Logistics: Supply Chain Management*, Pearson Education, 2004.
- [8] J. S. Burgos Vargas and K. L. González Cubero, "Implementation of a Management System Based on Methodology," *Guayaquil*, 2020.
- [9] R. P. Broussard y L. R. Kennell, «An artificial neural network based matching metric for iris identification,» *Proceedings of SPIE - The International Society for Optical Engineering*, vol. 6812, n° 1, 2008.
- [10] Toorajipour, R., Sohrabpour, V., Nazarpour, A., Oghazi, P., & Fischl, M. Artificial intelligence in supply chain management: A systematic literature review. *Journal of Business Research*, 122, 502-517. (2021).

Performance Analysis of 256-QAM Demodulation for 5G NR Sidelink

Alexander MALTSEV^{a,1}, Igor SERUNIN^b, Andrey PUDEEV^b, Jin-Yup HWANG^c and Sang-Wook LEE^c

^a*Nizhny Novgorod State University, Nizhny Novgorod, Russia*

^b*LG Electronics Russia R&D Lab, Moscow, Russia*

^c*LG Electronics, Seoul, Korea*

Abstract. Higher order modulations are the key elements to the throughput and spectral efficiency increase, especially important for the limited bandwidth scenarios. In this paper, we present a detailed analysis of the 256-QAM signal demodulation performance for the novel sidelink (SL) mode of the 5G NR communication systems. The performance is frequency offset (CFO). It was shown that the CFO has critical impact on the system performance, along with channel mobility. The simple and effective CFO studied in the non-stationary, frequency selective channel in the presence of the carrier compensation algorithm based on the slot-by-slot time-domain signal processing is proposed and investigated. Obtained simulation results have shown the feasibility of the 256-QAM modulation in applications to the main 3GPP sidelink scenarios and parameters, with the proposed CFO compensation method applied even in the case of significant user mobility.

Keywords. 5G NR sidelink, SL, 256-QAM, demodulation, CFO compensation, Doppler effect

1. Introduction

Industry requests for direct communication between large numbers of devices without using base stations eventually lead to the development and implementation of the sidelink (SL) protocols within the framework of the LTE communication systems. Further development of these protocols continued within the next generation of the communication standards, the 5G NR specification. In Rel.16 of the 5G NR, the V2X (Vehicle-to-everything) capabilities based on the air interface were introduced for the first time. Among the new usage models, we should especially note remote driving scenarios in the rapidly changing environment with the high Doppler spread channels. Nevertheless, in most aspects, 5G NR SL in Rel.16 and Rel.17 follow the basic capabilities and options from LTE Rel.15. However, many basic communication elements and options may require additional performance analysis before being implemented in 5G NR SL for the new scenarios and requirements.

Currently, 256-QAM modulation has not yet been adopted for data transmission using the SL protocol. So, at the 3GPP TSG RAN4 (3rd Generation Partnership Project

¹ Corresponding author: Alexander Maltsev, e-mail: maltsev@rf.unn.ru. This work was partially supported by the Advanced School of Engineering of the Nizhny Novgorod State University.

Technical Specification Group Radio Access Network) meeting, the possibility of using 256-QAM modulation in SL together with other modulations was discussed [1]. In particular in [2], it was proposed to introduce a test scenario for analyzing the performance of 256-QAM demodulation and to set requirements for it. The extension of the V2X service was defined as the main argument for the introduction of 256-QAM modulation in SL protocol. At the initial consideration stage, this proposal was declined, due to necessity to have relatively high SNR levels for successful 256-QAM demodulation, which may not be typical for V2X scenarios.

The main purpose of this paper is to investigate the performance of 256-QAM demodulation in SL framework based on the test scenario discussed and proposed as the baseline for analysis in [1]. The performance analysis is done by modeling the 5G NR SL communication system with the help of the link level simulator (LLS). During the initial analysis, the critical impact of carrier frequency offsets on the 256-QAM demodulation performance was proven. For this reason, we introduce a new approach for CFO compensation based on the slot-by-slot time-domain signal processing, which is more suitable for SL protocol. The paper discusses the use of an additional CFO compensation block for signal processing in the time domain and shows its effectiveness for a 3GPP test scenario of 256-QAM demodulation performance analysis, as well as for cases of significant user mobility, when the Doppler frequency becomes comparable with the carrier frequency offset.

2. Cyclic-prefix based CFO compensation

CFO is one of the major impairments for the orthogonal frequency-division multiplexing (OFDM) communication systems. Basically, CFO is the result of the frequency mismatch in the RF oscillators at the transmitter and receiver. The negative effect of CFO consists in the destruction of the orthogonality properties of the subcarriers and creating interference between them. The CFO impact on the OFDM performance has been known for a long time from the first IEEE 802.11a OFDM systems. Many different solutions and schemes for CFO compensation have been proposed and studied for more than 25 years [3][4][5][6][7][8][9][10][11]. In our paper, we will focus on the consideration of the additional CFO compensation block for slot-by-slot signal processing in the time domain, which includes a combination of two relatively simple CFO estimation algorithms. The structure of the OFDM communication system, including a CFO compensation block, is shown in [Figure 1. Structure of the 5G NR sidelink communication system with the CFO compensation block.](#) The first stage of the CFO compensation includes a rough evaluation/compensation of CFO based on cyclic-prefix (CP) correlation analysis. The second stage includes fine residual evaluation/compensation of CFO using standard pilot (demodulation reference) signals (DM-RS).

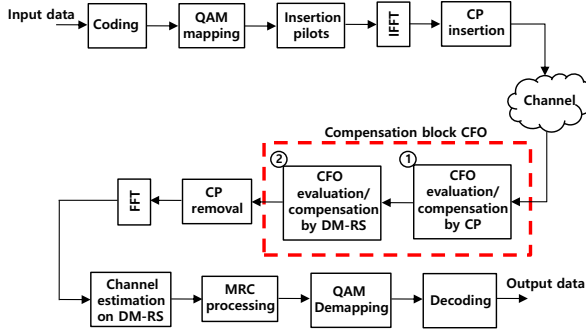


Figure 1. Structure of the 5G NR sidelink communication system with the CFO compensation block

The received signal model can be written as follows (Eq. (1)):

$$y[n] = \sum_{k=0}^{N_{Maxdelay}} h[k]x[n-k] e^{j2\pi\Delta f\Delta t n} + w[n], \quad (1)$$

where $x[n]$ is the transmitted signal, k is the sum index, n is the sample index, $y[n]$ is the received signal, $h[k]$ are the channel model coefficients, Δf is the CFO value, Δt is the duration of one sample, $N_{Maxdelay}$ is the number of samples corresponding to the maximum signal delay in multipath propagation, $w[n]$ are AWGN (Additive white Gaussian noise) samples. Rough evaluation is carried out using a correlation calculation unit (correlator) based on a cyclic prefix. The cyclic prefix is located at the beginning of each OFDM symbol and is a copy of the end of each symbol. Its main purpose is to decrease the inter-symbol interference created by the temporal dispersion of the transmission channel, but it can also be used to evaluate CFO. This is done by finding the phase difference between the cyclic prefix and the end of the symbol. The CFO evaluation using the CP-correlator for all available symbols in the frame can be written as follows (Eq.(2)):

$$\widehat{\Delta f}_{cp} = \frac{1}{2\pi} E \left\{ \sum_{p=0}^{p-1} \arg \left\{ \sum_{n=N_{Maxdelay}}^{\frac{N_{CP}+12}{2}} y_p^*[n] y_p[n+N] \right\} \right\}, \quad (2)$$

$$y_p[n] = \sum_{k=0}^{N_{Maxdelay}} h[k]x_p[n-k] e^{j2\pi(N_g p+n)\Delta f\Delta t} + w[n],$$

$$y_p[n+N] = \sum_{k=0}^{N_{Maxdelay}} h[k]x_p[n+N-k] e^{j2\pi(N_g p^{n+N})\Delta f\Delta t} + w[n],$$

where p is the symbol index, N is the symbol length without CP, $N_g = N + N_{cp}$ is the symbol length with CP, \arg is the argument of a complex number, E is the averaging. As can be seen from Eq.(2), not all CP samples are used to evaluate CFO. This is due to two negative factors that are taken into account in the corresponding scenario for analyzing the performance of 256-QAM. The first of them is multipath propagation of

the signal. Therefore, first CP samples and its replica samples at the end of the symbols are not included in the correlation window for evaluating CFO. The second factor is the synchronization error. This error is defined as timing offset and, for the sake of simplicity of the simulation, it is not modeled explicitly, but rather set to a fixed value. For this reason, the last CP samples and its similar samples at the end of the symbol are also not included in the correlation window when evaluating CFO. [Figure 2. Selecting a correlation window for evaluating CFO by CP.](#) shows an illustration of the OFDM symbol. In this figure, the area shaded in blue is the selected correlation window, taking into account the reasons indicated above.

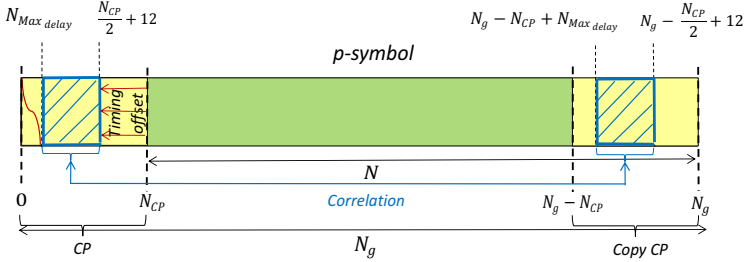


Figure 2. Selecting a correlation window for evaluating CFO by CP.

After the initial CFO evaluation using the CP-correlator, the first stage compensation is carried out in the time domain as shown in Eq.(3):

$$y_{comp1}[n] = y[n]e^{-j2\pi\widehat{\Delta f}_{CP}\Delta t n} \quad (3)$$

The residual CFO is evaluated using PSSCH (Physical Sidelink Shared Channel) DM-RS (Demodulation Reference Signal) pilot signals in the frequency domain, but compensation is carried out also in the time domain (see [Figure 1. Structure of the 5G NR sidelink communication system with the CFO compensation block](#)). If there are two symbols for the PSSCH with the DM-RS pilot signals spaced in time, it is possible to evaluate the phase difference between these two symbols. Next, we can transfer to the frequency domain at the position of the symbols PSSCH DM-RS using FFT (fast Fourier transform). We can write down the residual CFO estimate as follows (Eq.(4)):

$$\widehat{\Delta f}_{DMRS} = \frac{E\{\arg\{Y_1 Y_2^*\}\}}{2\pi\Delta T}, \quad (4)$$

where ΔT is the time duration between OFDM symbol centers with pilot PSSCH DM-RS, Y_1, Y_2 are demodulated received reference signals in the frequency domain on the first and second OFDM symbols with PSSCH DM-RS. The phase difference makes it possible to estimate precisely the average phase drift between two DMRS symbols. After the evaluation of the residual CFO, the second stage compensation is carried out as shown in (Eq.(5)):

$$y_{comp2}[n] = y_{comp1}[n]e^{-j2\pi\widehat{\Delta f}_{DMRS}\Delta t n}, \quad (5)$$

where y_{comp2} are finally corrected signals in the time domain.

3. Simulation assumptions for SL evaluations

The main parameters of the used scenario were discussed at the 3GPP meeting [1], for analyzing the performance of 256-QAM demodulation, and are shown in Table 1. Main scenario parameters for performance analysis of 256-QAM demodulation in Sidelink. In general, the parameters in Table 1. Main scenario parameters for performance analysis of 256-QAM demodulation in Sidelink. converge with the existing test scenario for 64-QAM in [2], except for the MCS (Modulation Coding Scheme) value and the effective code rate. In the investigated scenario, MCS = 20 [12] and the data transmission channel is a multipath TDL-A (Tapped Delay Line) model, which is described in [13].

Table 1. Main scenario parameters for performance analysis of 256-QAM demodulation in Sidelink.

Parameters	Assumption
Carrier Frequency	6GHz
Bandwidth	20 MHz
Waveform	CP-OFDM
SCS	30 kHz
Resource blocks allocated	10 RBs
Channel Model	TDL-A, 30ns DS, ~30 km/h (Doppler $f_D = 180$ Hz)
Transmission scheme	1x2 Low, MRC
Timing offset	CP/2 - $12T_s$
Frequency offset	600Hz
Modulation	256-QAM, MCS 20 from [12], Table 2
Coding	LDPC
PSSCH Allocation Size	732 REs
Number of DM-RS for PSSCH	120 REs
Transport Block Size of PSSCH	4608 bits
Effective code rate	0.79

The time-frequency structure of the SL subframe (one slot) consisting of 14 OFDM symbols is shown in Figure 3. Time-frequency structure of the SL frame.. As can be seen, in addition to the main PSSCH allocation, containing the data load, there are other channels, as well as standard special signals. They all perform their specific tasks. Similar functionality of these channels and signals can be found in [14]. It is also possible to find more detailed information in a number of review articles on sidelink [15] [16].

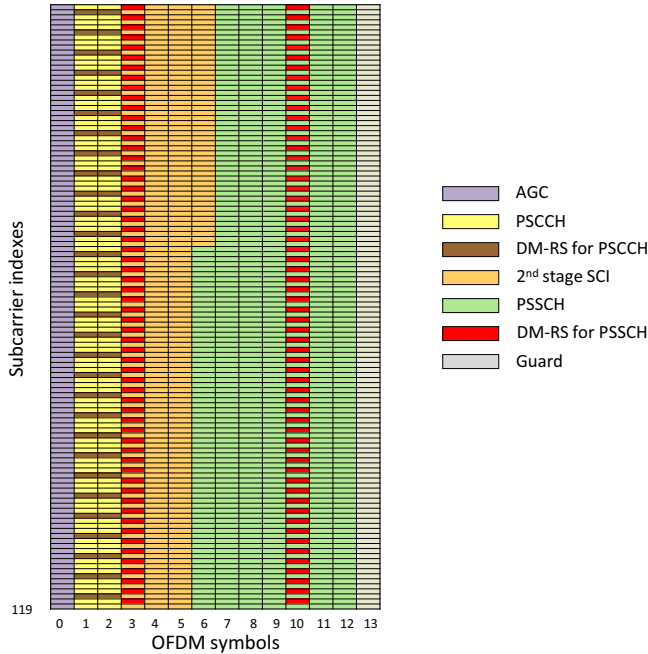


Figure 3. Time-frequency structure of the SL frame.

4. Simulation results

In this section, we present the simulation results obtained using the Matlab-based LLS for 5G NR sidelink. The LLS includes all the necessary elements of the sidelink communication system as shown in [Figure 1. Structure of the 5G NR sidelink communication system with the CFO compensation block](#). In addition, LLS includes all relevant impairments: modeling carrier frequency offset, fixed timing offset and frequency selective offset, as well as time-variant channel with the Doppler spread modeling in accordance with Jakes approach.

[Figure 4. Performance results of 256-QAM demodulation in sidelink](#), shows the 5G NR SL performance results for the 256-QAM modulation in the form of BLER (Block Error Rate) vs. SNR curves. As it can be seen from the presented results, the uncompensated CFO makes 256-QAM transmissions completely impossible (black curve, stationary case). Further, the results show the effectiveness of the CFO compensation block (presented in [Figure 1. Structure of the 5G NR sidelink communication system with the CFO compensation block](#)) depending on the channel mobility level in comparison with the ideal case (no CFO). The proposed CFO compensation block has proven to be sufficient for 256-QAM sidelink demodulation and has demonstrated a good efficiency for the cases of significant user mobility. For the main 3GPP scenario with user mobility of 30 km/h ($f_{\text{doppler}} = 180$ Hz), the use of the developed CFO compensation block provides almost full compensation of the CFO and guarantees a BLER level below 10^{-1} with an SNR of ~ 24 dB. A more detailed study of this scenario has shown that using only a CP-compensator (the first stage of the CFO

compensation, see Figure 1. Structure of the 5G NR sidelink communication system with the CFO compensation block) is sufficient to obtain high performance results (see curves for 30 km/h user mobility in Figure 4. Performance results of 256-QAM demodulation in sidelink.). Nevertheless, additional compensation with the use of PSSCH DM-RS gives a gain of ~ 0.5 dB for BLER level of $\sim 10^{-1}$ and about 1.0 dB for BLER level of $\sim 10^{-2}$.

However, it should be noted that the proposed method for the CFO compensation is based on the slot-by-slot time-domain signal processing, and therefore has several shortcomings. The first one is the necessity of data storage for each successive slot, and the second is its susceptibility to the inter-symbol interference in the case of the strong channel frequency selectivity. Consequently, the scheme may not work properly for the channels with the large delay spread. On the other hand, after the CFO evaluation and compensation block (see Figure 1. Structure of the 5G NR sidelink communication system with the CFO compensation block), the channel estimation procedure in the frequency domain is performed, followed by MRC (Maximum ratio combining) processing. This process can be regarded as another additional compensator of the residual CFO.

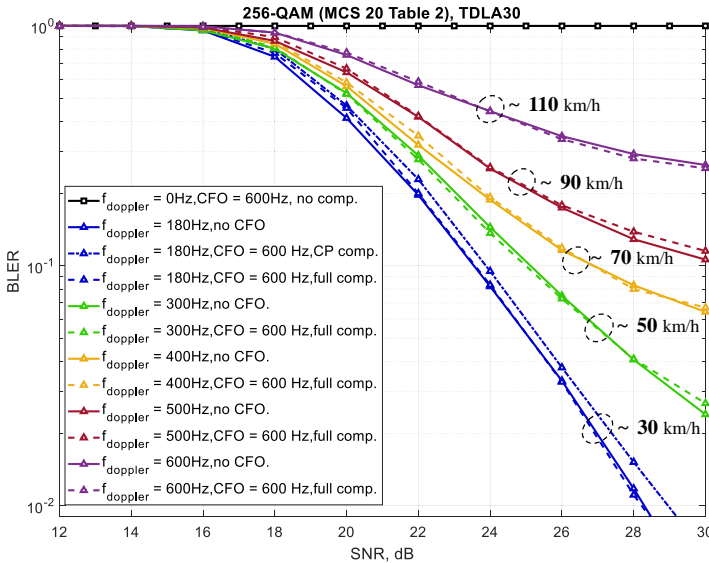


Figure 4. Performance results of 256-QAM demodulation in sidelink.

5. Summary

In this paper, we have shown the 5G NR SL performance results for the 256-QAM demodulation in sidelink mode for the baseline scenarios considered by 3GPP RAN4 meeting [1]. The main purpose of this analysis is to elaborate the requirements for 256-QAM modulation in RAN 4 specification. During the initial studies, the problem of the critical impact of CFO has been revealed. Normally, the CFO should be compensated during the initial acquisition process, on the base of primary and secondary synchronization signals [14]. However, for the purpose of developing the requirements

for sidelink mode, we have considered the synchronization and data channels as independent entities. The proposed CFO compensation method based on the independent slot-by-slot time-domain signal processing has shown high efficiency for the cases of significant user mobility and provided an acceptable level of 5G NR SL performance results for the 256-QAM demodulation. Consequently, the discussion about 256-QAM modulation feasibility for the SL mode may be reconsidered for the new Rel.18 sidelink protocol based on the results obtained in this paper.

At the same time, the proposed method for the CFO compensation works properly only for mobile users at speeds up to 70 km/h (see [Figure 4. Performance results of 256-QAM demodulation in sidelink.](#)). However, this approach, based on the independent slot-by-slot time-domain signal processing, also may be extended on the Doppler spread compensation in time-varying channels. We consider this line of actions as the next step for further investigations.

References

- [1] LG Electronics, "R4-2208318, Discussion on test cases for LS enhancement demodulation requirements", "3GPP TSG-RAN WG4 Meeting #103-e Electronic Meeting, May 9-20,2022"
- [2] 3GPP, "TS 38.101-4 NR; User Equipment (UE) radio transmission and reception; Part 4: Performance requirements (version 17.4.0 Release 17)" 3GPP, Tech. Spec., April 2022.
- [3] Yong-An Jung, Sang-Bong Byun, Han-Jae Shin, Dong-Cheul Han, Soo-Hyun Cho, Sung-Hun Lee. "Frequency and Symbol Timing offset Estimation Method for CP-OFDM based System", Citation information: DOI 10.1109/ICTC52510.2021.9621185, IEEE, December 2021.
- [4] Ziad Hatab, Hiroaki Takahashi, Michael Gadringer. "OFDM Symbol-timing and Carrier-frequency Offset Estimation Based on Singular Value Decomposition", Citation information: DOI 10.1109/CoBCom55489.2022.9880699, IEEE, July 2022.
- [5] Dinh Van Linh, Vu Van Yem. "Carrier Frequency Offset Estimation and Compensation Technique for Massive MIMO-OFDM Wireless Communication System", Citation information: DOI 10.1109/ICECET55527.2022.9872995,IEEE, July 2022.
- [6] Hongbao Zhang. "A Joint Scheme for Carrier Frequency Offset Estimation, Carrier Phase Correction and Timing", Citation information: DOI 10.1109/CEECT198.2021.9672646, IEEE, December 2021
- [7] Mohamed S. AbdRaboh, Hatem M. Zakaria, Abdel Aziz M. Al Bassiouni and Mahmoud M. El Bahy. "Carrier frequency offset (cfo) estimation methods, a comparative study", 16th International Conference on Aerospace Sciences & Aviation Technology (ASAT-16), 2015.
- [8] Abdul Gani Abshir and M. M. Abdullahi "A comparative study of carrier frequency offset (CFO) estimation techniques for OFDM systems". IOSR Journal of Electronics and Communication Engineering, 9(4):1–6, 2014.
- [9] Hao Zhou, Amaresh V Malipatil, and Yih-Fang Huang. "Maximum-likelihood carrier frequency offset estimation for ofdm systems in fading channels". In Wireless Communications and Networking Conference, 2006. WCNC 2006. IEEE, volume 3, pages 1461–1464. IEEE, 2006.
- [10] Praween Kumar Nishad, P. Singh. "Carrier Frequency Offset Estimation in OFDM Systems", Citation information: DOI 10.1109/CICT.2013.6558220, IEEE,2013
- [11] Elnaz Ershadi, Hamidreza Bakhshi, "A Novel Pilot-based Frequency Offset Compensation Method in MIMO-OFDM Systems", Citation information: DOI 10.1109/ICIAS.2010.5716240, IEEE,2010
- [12] 3GPP, "TS38.214 NR; Physical layer procedures for data (version 17.1.0 Release 17)" 3GPP, Tech. Spec., April 2022
- [13] 3GPP, "TS 38.901 NR; Study on channel model for frequencies from 0.5 to 100 GHz (version 17.1.0 Release 17)", 3GPP, Tech. Spec., April 2022.
- [14] 3GPP, "TS 38.211 NR; Physical channels and modulation (version 17.1.0 Release 17)", 3GPP, Tech. Spec., April 2022
- [15] Jie Chen, Jun Tan, "NR V2X: Technologies, Performance, and Standardization". ACSSC 2020: 1012-1016
- [16] Mario H. Castañeda Garcia, Alejandro Molina-Galan, Mate Boban, Javier Gozalvez, Baldomero Coll Perales, Taylan Şahin and Apostolos Kousaridas, "A Tutorial on 5G NR V2X Communications", Citation information: DOI 10.1109/COMST.2021.3057017, IEEE

Application of SCMA Based on LoRaWAN Architecture

Minhao JIN^{a,1}, Libo FAN^a, Shaojie LUO^a and Xiaotian GUO^b

^aState Grid Zhejiang Electric Power Company, China

^bBeijing University of Posts and Telecommunications, China

Abstract. Low-power Wide-Area Network (LPWAN), as a wireless connection technology of the Internet of things, has met the requirements of power consumption of network providers and operators, network coverage and Internet of things equipment. As the main technology of LPWAN, Long Range (LoRa) has entered the stage of scale deployment. However, in the MAC protocol of LoRa, multiple end nodes send data to the gateway at the same time, which will cause serious collision problems. When data collision occurs, the gateway will no longer receive collision data, and the data packet needs to be retransmitted after a certain time. In order to solve this problem and improve the throughput of the whole system, this paper proposes to introduce the sparse code multiple access (SCMA) technology of 5G non-orthogonal multiple access (NOMA) into Long Range Wide Area Network (LoRaWAN) architecture from the perspective of code domain. The theory and simulation results show that SCMA can effectively solve the problem of data collision and improve the system throughput.

Keywords. LoRaWAN, SCMA, throughput

1. Introduction

Low-power Wide-Area Network (LPWAN), is a wireless connection technology suitable for machine communication and Internet of things equipment, which appeared in 2013. LPWAN has met the requirements of power consumption of network providers and operators, network coverage and Internet of things equipment. So it has become the connection option of most Internet of Things (IoT) devices. LPWAN technology has appeared in recent years. Among them, LoRa is a technology that works in unlicensed frequency bands [1].

LoRa is a modulation technology in the physical layer, which can be applied to different protocols, such as Long Range Wide Area Network (LoRaWAN) protocol, China LoRa Application Alliance (CLAA) network protocol, LoRa private network protocol [2], etc.

As a MAC protocol, LoRaWAN 's communication protocol and architecture are mainly designed for LoRa long-distance communication network. The official white paper of LoRa alliance, what is LoRaWAN, provides a schematic diagram of LoRaWAN architecture, as shown in Fig.1.

¹ Corresponding author: Jin Minhao, State Grid Zhejiang Electric Power Company. E-mail: 1715414560@qq.com.

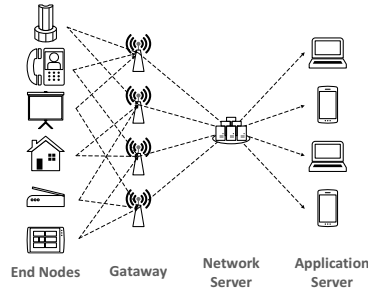


Fig. 1. LoRaWAN Architecture.

In Fig.1, LoRaWAN architecture includes four parts: end nodes, gateway, network server and application server. In LoRaWAN, multiple end nodes can send data information to the gateway at the same time, which often leads to serious collision problems. In addition, LoRa network mainly uses ALOHA protocol for simplicity and energy saving, which further aggravates data collision. When the data collides, the gateway no longer receives the collision data, and the data packet needs to be sent again after a certain time.

In wireless communication technology, the solutions to data collision mainly include conflict avoidance strategy and conflict resolution strategy. The conflict avoidance strategy first needs to detect the channel state, and then adjust the link scheduling according to the channel state. However, the key of this scheme is real-time monitoring and accurate synchronization, which will cause additional overhead. The conflict resolution strategy is to use the unique time-domain characteristics (such as fixed waveform shape) or the power difference between data packets in wireless communication technology to decode the data packets with collision, so as to improve the throughput and system efficiency [3] [4] [5]. However, the LoRa time-domain waveform shape is different, so this scheme is not suitable for LoRa collision packet decoding. In order to effectively solve the problem of data collision and improve the throughput of the end nodes of the whole system sending data to the gateway, this paper proposes to introduce the sparse code multiple access [7] (SCMA) technology of 5G non-orthogonal multiple access [6] (NOMA) into the node access location of LoRaWAN architecture from the perspective of code domain. SCMA is similar to the idea of Tanner graph in back propagation (BP) decoding of low density parity check code (LDPC) channel coding. With this idea, data collision can be effectively avoided when a single resource unit carries multiple user information. In addition, the reference of NOMA technology can effectively improve the throughput of end nodes accessing the network.

2. System Model

SCMA belongs to a multi-carrier non-orthogonal multiple access technology in the code domain. SCMA is based on code division multiple access (CDMA) [8] spread spectrum method low-density signatures (LDS). For a multi-user SCMA system with an overload factor of $\lambda = J/K$, K resource blocks in the system support access to J users ($J > K$), where each user occupies N resource blocks ($N < K$). For the SCMA system with $K = 4$ and $J = 6$, its structure is shown in Fig.2 by the factor graph. Each

resource block is shared by $d_f = 3$ users, and each user is connected to $N = 2$ resource blocks.

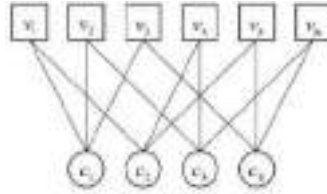


Fig. 2. Factor Graph.

In Fig. 2, each layer node represents a user, and each resource node represents a carrier resource block. It is expressed as $\mathbf{F} = (\mathbf{f}_1, \mathbf{f}_2, \dots, \mathbf{f}_J)$ by a factor matrix and represents that the user J is connected to the resource block K when $\mathbf{f}_j(k) = 1$.

$$\mathbf{F} = \begin{bmatrix} 1 & 1 & 1 & 0 & 0 & 0 \\ 1 & 0 & 0 & 1 & 1 & 0 \\ 0 & 1 & 0 & 1 & 0 & 1 \\ 0 & 0 & 1 & 0 & 1 & 1 \end{bmatrix} \tag{1}$$

2.1. Sender

The transmitter first performs multidimensional modulation on the bit stream input by each user. Taking user J as an example, the modulation order is M_j and the input bit stream is \mathbf{b}_j . The N -dimensional complex codeword generated after multidimensional modulation is $\mathbf{z}_j = (x'_1, \dots, x'_N)^T$. The mapping from bits to N -dimensional codewords is as follows:

$$\mathbf{z}_j = g(\mathbf{b}_j) \tag{2}$$

Second paragraph. Then K -dimensional complex codeword $\mathbf{x}_j = (x_1, x_2, \dots, x_K)^T$ is generated through the mapping matrix, which contains N non-zero elements. The mapping matrix [9] of each user is:

$$diag(\mathbf{V}_j \mathbf{V}_j^T) = \mathbf{f}_j \tag{3}$$

The user J has its specific codebook \mathbf{C}_j , which is generated by the rotation and expansion of the mother constellation [10] \mathbf{A} corresponding to the modulation selected by the user J . The rotation matrix [11] and the mapping matrix of the user further make the codebook of each user different.

$$\mathbf{C}_j = \mathbf{V}_j \mathbf{A}_j \mathbf{A} \tag{4}$$

Where $\mathbf{C}_j \in \mathbb{C}^K$ contains M_j symbols and Δ_j is $N \times N$ dimensional rotation matrix.

2.2. Receiver

After the SCMA joint codeword passes through the channel, the received signal \mathbf{y} can be expressed as:

$$\mathbf{y} = \text{diag}(\mathbf{h}) \sum_{j=1}^J \mathbf{x}_j + \mathbf{n} = \text{diag}(\mathbf{h}) \sum_{j=1}^J \mathbf{V}_j f_j(\mathbf{b}_j) + \mathbf{n} \tag{5}$$

Where $\mathbf{h} = (h_1, \dots, h_K)^T$ is the channel vector and $\mathbf{n} = (n_1, n_2, \dots, n_K)^T$ is the additive Gaussian white noise.

After receiving the signal, the receiver can use the MPA algorithm to decode. The flowchart of the decoding process is shown in Fig. 3.

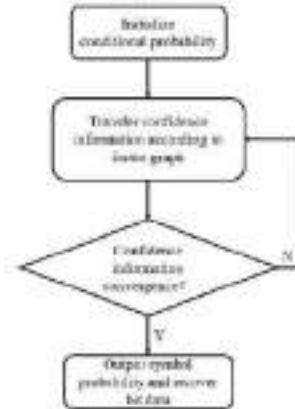


Fig. 3. Flowchart of MPA Algorithm.

The main idea of the receiver's MPA algorithm is to use the information observed by the receiver, that is, the information carried by the received signals of each resource node, to estimate the probability distribution of the symbols of the user node through multiple iterations.

3. Simulation Results

This section presents the simulation results and analysis to illustrate the bit error rate (BER) and throughput performance of the SCMA system. Channel coding is not added to the simulation SCMA system. The performance of bit error rate directly determines whether the problem of data collision can be effectively improved. In the simulation of BER performance, we consider the transmission in AWGN channel. The modulation methods included in the simulation are QPSK and 16QAM. The number of transmitted symbols is 10^7 , and the average energy of each codeword is normalized to 1. The SCMA modulated signal is carried on OFDM subcarriers for transmission, including 4096

subcarriers. The sampling frequency is 60KHZ and the frame length is 20 (the number of OFDM symbols per frame is 20). The throughput is calculated according to the correct number of bits transmitted by the system and the transmission time statistics. Data frames whose BER does not meet the transmission quality requirements are directly discarded and are not included in the system throughput.

Fig. 4 shows the BER performance of SCMA for different modulation modes in AWGN channel. Fig. 5 shows the throughput performance of SCMA for different modulation modes in AWGN channel.

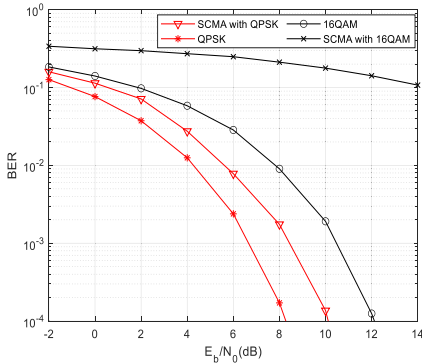


Fig. 4. BER performance in AWGN channel.

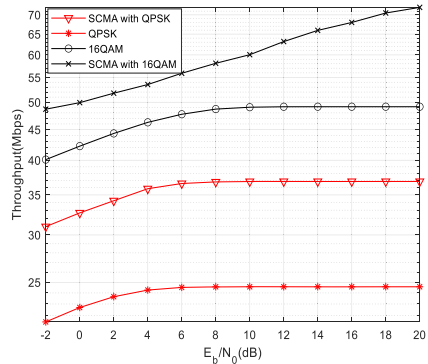


Fig. 5. Throughput performance in AWGN channel.

From Fig. 4 and Fig. 5, we can see that for QPSK, MPA iterative decoding is used to effectively solve the problem of data collision in a single resource unit. SCMA greatly improves the throughput of the whole system at the cost of losing BER performance close to 2dB. The improvement in throughput performance tends to be saturated after E_b / N_0 reaches 6dB, which is about 148%. For 16QAM, the BER performance loss of SCMA is large. But the BER performance is getting better with the gradual increase of signal-to-noise ratio (SNR), which is also confirmed in the throughput curve. Hence when the channel is ideal or the SNR is high, SCMA can also solve the data collision problem. From the throughput performance curve of 16QAM, we can see that the throughput of SCMA system whose gain is still increasing rapidly with the increase of E_b / N_0 can be improved even when the BER is poor. When E_b / N_0 is 20dB, the throughput gain of SCMA reaches 146%.

4. Conclusion

From the perspective of code domain, this paper proposes to introduce SCMA technology into the end nodes access location of LoRaWAN architecture, which effectively solves the problem of LoRaWAN data collision and improves the overall system throughput. In the process of codebook design, we use the codebook energy normalization to meet the low power consumption requirements of LPWAN.

The simulation results show that SCMA system improves the throughput of the transmission system at the expense of a certain BER performance. With the increase of E_b / N_0 , the negative gain of BER of SCMA decreases and the system throughput tends

to be saturated when the E_b / N_0 reaches a certain critical value. According to Shannon's theorem and the simulation results in this paper, it is proved that when the throughput curve is saturated, its gain is infinitely close to the overload factor λ of SCMA system.

However, there are also some problems in this technology. As mentioned above, the design of λ directly affects the overall system throughput improvement. If λ is too large, the BER performance loss will increase and the complexity of the whole system will increase exponentially. Hence the increase of throughput results in the decrease of transmission bit quality. How to choose between long-distance, high throughput and high-quality transmission is a problem that can be studied at present. For example, the better modulation mode and multiple access can be selected according to different channel parameters and SNR. In addition, whether LoRa technology can use higher-order modulation determines whether SCMA has advantages over previous ones. Considering the current LoRa modulation, SCMA is mainly used in the direction of future LoRa using QPSK modulation. Compared the SCMA with 16QAM, the SCMA with QPSK is a technical reference that can be considered at present to both solve collisions and effectively improve throughput. To sum up, SCMA focuses on improving the throughput of the end nodes access LoRaWAN. The use of SCMA in the LoRaWAN structure is still at the exploratory stage, which is a technology reference that LoRa is expected to use in the future.

Acknowledgment

This work was supported by the project of State Grid Zhejiang Electric Power Company (B311HZ220001).

References

- [1] Sanchez-Gomez J, Dan G C, Sanchez-Iborra R, et al. Integrating LPWAN technologies in the 5G ecosystem: A survey on security challenges and solutions [J]. *IEEE Access*, 2020.
- [2] Park J, Park K, H Bae, et al. EARN: Enhanced ADR with Coding Rate Adaptation in LoRaWAN[J]. *IEEE Internet of Things Journal*, 2020, PP (99): 1-1.
- [3] L. Kong and X. Liu, mZig: Enabling multi-packet reception in zigbee[C]. *Proceedings of the 21st annual international conference on mobile computing and networking*. ACM, 2015, pp. 552–565.
- [4] S. Gollakota and D. Katabi, Zigzag decoding: combating hidden terminals in wireless networks[C]. *ACM*, 2008, vol. 38, no. 4.
- [5] Liao C H, Zhu G, Kuwabara D, et al. Multi-Hop LoRa Networks Enabled by Concurrent Transmission [J]. *IEEE Access*, 2017, 5:21430-21446.
- [6] Y. Saito, A. Benjebbour, Y. Kishiyama, et al. System-level performance evaluation of downlink non-orthogonal multiple access (NOMA) [A]. //2013 IEEE 24th Annual International Symposium on Personal, Indoor, and Mobile Radio Communications (PIMRC) [C], 2013: 611-615.
- [7] H. Nikopour and H. Baligh. Sparse code multiple access [A]. //2013 IEEE 24th Annual International Symposium on Personal, Indoor, and Mobile Radio Communications (PIMRC) [C], 2013: 332-336.
- [8] Feng-Tsun Chien, Chien-Hwa Hwang and C.-C. J. Kuo. Analysis of asynchronous long-code multicarrier CDMA systems with correlated fading [J]. *IEEE Transactions on Communications*, 2005, vol. 53, no. 4: 666-676.
- [9] M. Gao, W. Ge, P. Zhang, et al. An Efficient Codebook Design for Uplink SCMA [J]. *IEEE Access*, 2020, vol. 8: 211665-211675.
- [10] L. Yu, P. Fan, D. Cai, et al. Design and Analysis of SCMA Codebook Based on Star-QAM Signaling Constellations [J]. *IEEE Transactions on Vehicular Technology*, 2018, vol. 67, no. 11: 10543-10553.
- [11] L. Yu, P. Fan, X. Lei, et al. BER Analysis of SCMA Systems With Codebooks Based on Star-QAM Signaling Constellations [J]. *IEEE Communications Letters*, 2017, vol. 21, no. 9: 1925-1928.

Efficient Security Detection Strategy Based on K-Means Algorithm in LPWAN

Minhao JIN^{a,1}, Shaojie LUO^a, Jiabin HUANG^a and Xincheng ZHOU^b

^a State Grid Zhejiang Electric Power Company, China.

^b Beijing University of Posts and Telecommunications, China.

Abstract. With the development of multi-element integration and high elastic power grid construction, digital sensing of transmission, transformation and distribution equipment in many new energy sources, virtual power plants and load aggregators will be widely used. In this environment, it is urgent to build a reliable sensing network to support its digital sensing applications such as operation state sensing, data collection and demand management. However, due to the large number and wide distribution of distribution equipment, there may be errors in the uploading results of sensors. This paper proposes an efficient security detection strategy based on K-Means algorithm, which greatly improves the information integration and decision ability of the data center.

Keywords. Digital perception, efficient, security, LPWAN

1. Introduction

As the traditional transmission, transformation and distribution equipment is designed and deployed with less consideration of upgrading and transformation needs, problems such as inability to supply power for new modules, complex electromagnetic environment and limited internal space of equipment appear in the process of transformation and upgrading. As pointed out in the vision reference model IEEE smart grid control vision: reference model for 2030 and beyond, in order to realize this vision, research needs to be conducted to address all these challenges[1]. At present, there is an urgent need for a communication means with extremely low power consumption, strong anti-interference ability and flexible deployment to transform the traditional transmission, transformation and distribution equipment and help improve the power system.

Wireless sensor network has been widely used in recent years. It can be applied to military[2], environmental monitoring and forecasting[3], building state monitoring [4]and other fields. At the same time, the new generation of living smart home system developed based on smart home wireless technology makes the green home network gradually form a complex system to handle various tasks[5]. Scientific research using wireless sensor networks for habitat or animal monitoring is used to generate a large amount of data that needs to be analyzed and normalized to help researchers and other people interested in information. Managing these data and comparing it with information from other sources and systems can help the decision-making process and trigger other

¹ Corresponding author: Jin Minhao, State Grid Zhejiang Electric Power Company; E-mail: zhouxc@bupt.edu.cn

experiments again[6]. A large number of wireless sensor networks are also used in the fields of warehouse management, security monitoring of airports and large industrial parks[7].

LPWAN (low power wide area network) with characteristics of low bandwidth, low power consumption, long distance and large capacity meets the requirements of Internet of things applications[8]. The two major LPWAN technology representatives, NB-IoT and LoRa, are better known. Developing low-power wide area network (LPWAN) solutions for efficient adoption, deployment and maintenance is crucial for smart cities[9][10].

In [11], the author reviewed the rapid growth of research subjects using different graph based deep learning models (such as graph convolution and graph attention networks) in various problems of different types of communication networks (such as wireless networks, wired networks and software defined networks). In [12], the author proposes two new graph based intrusion detection solutions, which integrate the remaining learning into GNN using the available graph information. In[13], the author proposes a novel hierarchical adversarial attack (HAA) generation method for GNN based intrusion detection in IoT system. An E-GraphSAGE algorithm is proposed for network intrusion detection of the Internet of Things in[14].

This paper studies the efficient and accurate information collection of power transmission and distribution equipment nodes based on LPWAN, and proposes an efficient security detection strategy called ESDS based on K-Means algorithm, which greatly improves the information integration and decision ability of the data center.

The chapter II of this paper briefly describes the network model of the proposed algorithm strategy application, the chapter III describes the details of the algorithm in detail, the chapter IV shows the simulation results of the algorithm, and the chapter V is the summary of this paper.

2. System Model



Figure 1. Schematic diagram of power Internet of things

Figure 1. is a basic schematic diagram of a city level power IoT network, which divides different production work areas, deploys sensor network terminals respectively, and plans technical coverage and human management according to the coverage radius of the wireless gateway and the management area of the work area. The LPWAN wireless gateway is connected to the LPWAN IoT core network through the internal transmission

network of the power grid. In some remote areas, such as covering the edge suburbs, where the internal transmission network cannot reach, the VPN network of the operator can be connected to the LPWAN control network through 3G/4G wireless VPN tunnel technology. And establish the IoT monitoring server to manage the data collected by the IoT, and the information security server to manage all the data information to ensure the information security of the monitoring network. The monitoring center accesses the control network through the internal network to obtain the concerned equipment state information and environment state information in real time.

The power system digital sensing network is composed of a large number of wireless sensor nodes deployed in the monitoring area. It is a multi hop self-organizing network system formed by wireless communication. Its purpose is to monitor, sense and collect the information of various sensing objects in the network coverage area and process the information. Because there are many nodes in the wireless sensor network and the setting range is wide, in the power grid application, the data transmission needs to ensure the accuracy of the data, and at the same time, considering the impact of security, the data judgment center is designed at the central node to comprehensively judge the data uploaded by each node, so as to eliminate the sensor nodes that have failed or been attacked.

3. Data Fusion Algorithm Based on K-Means Introduction

Because there are many nodes in the power system digital sensor network, and the setting range is wide, and it is necessary to maintain the long-term stable operation of the system. At the same time, in power grid applications, the data transmission equipment is required to work normally in extreme weather environments such as cold or hot weather, so the accuracy of the new power system digital sensor network is extremely high, especially in the case of equipment overheating. In order to ensure the efficiency and accuracy of the system, the system classifies and eliminates the sensor terminals that have failed and have low accuracy in the process of information collection and transmission.

3.1. Reputation value establishment

Firstly, the detection level of each sensor node is obtained by comparing the results uploaded by each sensor node with the actual results, and the beta reputation system is used to evaluate it. Beta reputation system allocates reputation to members through beta distribution function. Use x to indicate that the sensor has correctly transmitted the collected information, y to indicate that the sensor has not successfully collected the information or transmitted the wrong collection results, let r denote the number of times of event x and s denote the number of times of event y , then the probability of occurrence of x in the two events follows the beta distribution, and the probability density function is:

$$f(p | \alpha, \beta) = \frac{\Gamma(\alpha + \beta)}{\Gamma(\alpha)\Gamma(\beta)} p^{\alpha-1} (1-p)^{\beta-1} \tag{1}$$

where, $\Gamma(\square)$ is the gamma function, $\alpha = r + 1$, $\beta = s + 1$ in the beta distribution, and the expectation of event x is

$$E[x] = \frac{\alpha}{\alpha + \beta} \tag{2}$$

3.2. The implementation of K-Means algorithm

The historical information uploaded by each sensor node is summarized and counted through the beta reputation system, and then the K-Means clustering algorithm is used to classify each sensor node, so as to eliminate the sensor nodes that have failed and have low accuracy. Figure 2. shows the implementation steps of K-Means algorithm.

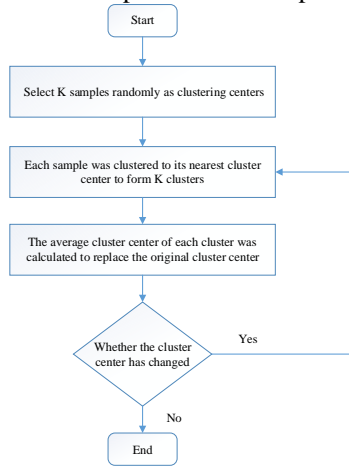


Figure 2. The implementation steps of K-Means algorithm

The specific description of the above steps is as follows:

Step 1: For spatial data set $X = \{X_1, \dots, X_i, \dots, X_n\}$, k values $C_1, C_2, \dots, C_j, \dots, C_k$ are randomly selected as the initial clustering center, and the data shall meet the following conditions:

$$X = \cup C_i (i = 1, 2, \dots, k) \tag{3}$$

$$C_i \neq \emptyset (i = 1, 2, \dots, k) \tag{4}$$

$$C_i \cap C_j \neq \emptyset (i = 1, 2, \dots, k; i \neq j) \tag{5}$$

Step 2: Calculate the Euclidean distance from sample X_i to each cluster center C cluster each sample to its nearest cluster center C_i , and form k clusters.

$$D_i = \min_{i < j < k} \left\{ \sum_i^n (x_i - c_j)^2 \right\} \tag{6}$$

Step 3 : Recalculate the average cluster center of K clusters, and replace the original cluster center with the new average cluster center.

$$C_j = \frac{1}{N(C_j)} \sum_{i \in C_j} X_i \tag{7}$$

Step 4 : Repeat steps 2 and 3 until the clustering center is unchanged or basically unchanged.

4. Simulation Result

In this paper, MATLAB software is used to simulate and design an ad hoc network with 10 wireless sensor nodes. Among them, 8 sensor nodes can still be used normally, but 2 sensor nodes cannot collect information. Due to the damage and transmission environment, the collected information transmitted by 2 sensor nodes to the data center is wrong. The data center collects the information uploaded by all sensor nodes, performs data fusion, compares it with the actual state of each environment, obtains the final detection probability, and evaluates the working state and detection level of each sensor. The simulation diagram is as follows:

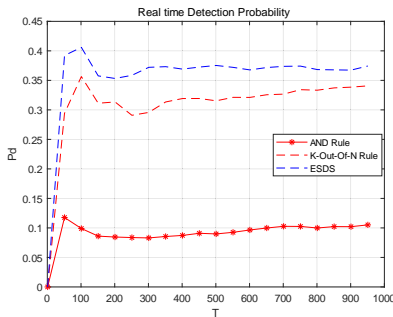


Figure 3. Real time Detection Probability Simulation Result(10 nodes)

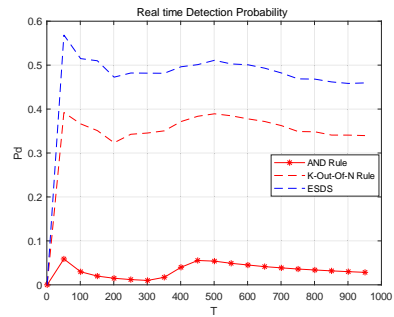


Figure 4. Real time Detection Probability Simulation Result(15 nodes)

In Figure 3., due to the existence of sensing nodes that fail and upload erroneous data, when the traditional "AND" criterion is used to fuse the statistical data, the accuracy is low, and the detection probability is only 10%. When using the "K-Out-Of-N" criterion to judge in the data center, the detection level of the system can be greatly improved. The detection algorithm using K-Means algorithm for classification proposed in this paper is improved by 10% on the basis of "K-Out-Of-N" criterion algorithm. This is because before the data judgment, the K-Means algorithm is used to classify the failed and low accuracy perceptual nodes and normal perceptual nodes by summarizing and classifying the historical collected information of each perceptual node, and different judgment weights are given in the final data fusion, so as to achieve efficient and accurate digital perception.

It can be found from the simulation in Figure 4. that when the number of sensor nodes in the core network reaches 15, the complexity of information to be processed increases due to the large number of loaded nodes, the difficulty of data center decision increases. At this time, the algorithm proposed in this paper still has advantages in the final data decision.

5. Conclusion

In this paper, the K-Means algorithm is used to eliminate the sensor nodes that have failed or have low accuracy, thus increasing the decision level of the final data center. By using the digital sensing network model proposed in this paper, the operation state

and information collection of transmission, transformation and distribution equipment in the power system can be effectively and accurately sensed, so as to improve the intelligent level of the power system.

Acknowledgment

This work was supported by the project of State Grid Zhejiang Electric Power Company (B311HZ220001).

References

- [1] A. Annaswamy, "IEEE Vision for Smart Grid Control: 2030 and Beyond Roadmap," in *IEEE Vision for Smart Grid Control: 2030 and Beyond Roadmap*, vol., no., pp.1-12, 24 Oct. 2013, doi: 10.1109/IEEEESTD.2013.6648362.
- [2] Lixianli, P. Wei, A. Jianyong and W. Ping, "The Application Research on Military Internet of Things," 2020 17th International Computer Conference on Wavelet Active Media Technology and Information Processing (ICCWAMTIP), 2020, pp. 187-191, doi: 10.1109/ICCWAMTIP51612.2020.9317321.
- [3] F. Wu, C. Rüdiger, J. Redouté and M. R. Yuce, "Live Demonstration: An IoT Platform for Environmental Monitoring Using Self-Powered Sensors," 2018 IEEE SENSORS, 2018, pp. 1-1, doi: 10.1109/ICSENS.2018.8589904.
- [4] S. Sarkar, K. U. Rao, J. Bhargav, S. Sheshaprasad and A. Sharma C.A., "IoT Based Wireless Sensor Network (WSN) for Condition Monitoring of Low Power Rooftop PV Panels," 2019 IEEE 4th International Conference on Condition Assessment Techniques in Electrical Systems (CATCON), 2019, pp. 1-5, doi: 10.1109/CATCON47128.2019.CN004.
- [5] H. Wei-Dong and Z. Bo-Xuan, "Smart Home Wireless System Using ZigBee and IEEE802.15.4," 2016 Sixth International Conference on Instrumentation & Measurement, Computer, Communication and Control (IMCCC), 2016, pp. 858-863, doi: 10.1109/IMCCC.2016.168.
- [6] R. A. G. da Costa and C. E. Cugnasca, "Use of Data Warehouse to Manage Data from Wireless Sensors Networks That Monitor Pollinators," 2010 Eleventh International Conference on Mobile Data Management, 2010, pp. 402-406, doi: 10.1109/MDM.2010.72.
- [7] Wei Xia, S. X. Yang, Xiaofang Li, Huibing Wang, Xijun Yan and Xiaodong Wei, "Design of wireless sensor networks for safety monitoring at civil engineering construction sites," 2011 Second International Conference on Mechanic Automation and Control Engineering, 2011, pp. 6418-6421, doi: 10.1109/MACE.2011.5988511.
- [8] S. Y. Mane, "LPWAN's – Overview, Market Scenario and Performance Analysis of Lora, Sigfox Using NB-Fi Range Calculator," 2021 International Conference on Smart Generation Computing, Communication and Networking (SMART GENCON), 2021, pp. 1-4, doi: 10.1109/SMARTGENCON51891.2021.9645902.
- [9] A. Ramoutar, Z. Motamedi and M. Abdulla, "Latency of Concatenating Unlicensed LPWAN with Cellular IoT: An Experimental QoE Study," 2021 IEEE 94th Vehicular Technology Conference (VTC2021-Fall), 2021, pp. 1-6, doi: 10.1109/VTC2021-Fall52928.2021.9625483.
- [10] M. L. Liya and D. Arjun, "A Survey of LPWAN Technology in Agricultural Field," 2020 Fourth International Conference on I-SMAC (IoT in Social, Mobile, Analytics and Cloud) (I-SMAC), 2020, pp. 313-317, doi: 10.1109/I-SMAC49090.2020.9243410.
- [11] Jiang, W. (2021). Graph-based deep learning for communication networks: A survey. *Computer Communications*.
- [12] Chang, L., & Branco, P. (2021). Graph-based Solutions with Residuals for Intrusion Detection: the Modified E-GraphSAGE and E-ResGAT Algorithms. *arXiv preprint arXiv:2111.13597*.
- [13] Zhou, X., Liang, W., Li, W., Yan, K., Shimizu, S., Kevin, I., & Wang, K. (2021). Hierarchical adversarial attacks against graph neural network based IoT network intrusion detection system. *IEEE Internet of Things Journal*.
- [14] Lo, W. W., Layeghy, S., Sarhan, M., Gallagher, M., & Portmann, M. (2022, April). E-GraphSAGE: A Graph Neural Network based Intrusion Detection System for IoT. In *NOMS 2022-2022 IEEE/IFIP Network Operations and Management Symposium* (pp. 1-9). IEEE.

Research on the Construction and Evolution Model of Cloud Ecosystem

Guolong SHE^a, Mengdi YAO^{b1} and Guohua DENG^c

^a*College of Social Science, University of Ottawa, Ottawa, Canada*

^b*School of Literature, Law and Economics, Wuhan University of Science and Technology, Wuhan China*

^c*Business School, Jiang Han University, Wuhan China*

Abstract. Clarifying the positioning of participants in the cloud ecosystem and analyzing the competition and cooperation among subjects are important for the sustainable and healthy development of cloud ecosystem. This paper analyzed the structure and the evolution law of the participants in the cloud ecosystem. The results show that, in a certain degree of competitive environment, companies with different positions and competitive relationships have different competitiveness. Cooperation is conducive to the coexistence of individuals. The stronger the cooperative relationship, the greater the enterprise's profit. These findings give a beneficial motivation for the coordinated relationship and development strategy for cloud providers.

Keywords. Cloud ecosystem structure, evolution model, competition and cooperation

1. Introduction

As cloud computing development enters a period of high growth, supporting service segments such as third-party application developers, system integration, cloud consulting services become more and more important [1]. Establishing a cloud ecosystem becomes the key to cloud service provider competition. More and more companies, such as Microsoft and Google, are working together to build cloud ecosystems by expanding their business scope and cultivating partners [2-4]. Competition among enterprises in cloud industry has gradually evolved into the competition among cloud ecosystems. In relation this shift, it is an important issue to promote the development of a healthy cloud ecosystem by building a cloud ecosystem, analyzing the competing relationships of member companies in the ecosystem, and promoting the sustainable development of the cloud ecosystem.

A well-developed cloud ecosystem must be balanced and stability, which is achieved through the development and interaction of participants. Although researchers have mentioned the interrelationship between enterprises in cloud ecosystem, there is no clear answer the interactive relations and deep research on evolution law among the participants. Therefore, the paper analyses the structure of cloud ecosystem, establishes the evolution model for the participant's cooperation and competition. Finally, taking the

¹ Corresponding author: Mengdi YAO; Email address: 1126983967@qq.com

CPs in Ali cloud ecosystem as an example for empirical analysis, this paper explores the evolution mechanism by simulation. Through the understanding of the internal membership and the evolution mechanism of cloud ecosystem, the relationship among members can be better coordinated, the healthy development strategy of ecosystem can be formulated and maintained.

2. Related Works

Many scholars have extended the concept of business ecosystem from traditional industries to the emerging cloud computing industry, and put forward different perspectives on the cloud ecosystem [5-9]. The University of Melbourne research team believed that there are multi-CPs and multi-tenants (cloud users) in the cloud market [1]. Gupta and others regarded cloud ecosystem as the resource sharing ecosystem among cloud providers [6]. Kushida et al. proposed a "cloud service framework" analysis tool which includes two dimensions of provider type and cloud architecture layer [9]. From a market view, Kushida K E summarized the cloud ecosystem into three key components: the demand side (individual, organization, and enterprise users), the cloud (IaaS, PaaS, and SaaS) and the provider [9]. Deng et al. put forward the value structure model of cloud ecosystem, which is composed of CPs, agencies, consumers and external environment [4]. In the evolution of cloud ecosystems, scholars have conducted studies from the perspective of cooperation and competition [10-13]. In the early stage of cloud ecosystem formation, usually multiple subjects choose to cooperate among themselves to build a dynamic cloud ecosystem with a generic value network to jointly provide high-value cloud services to users [11], while Paya et al. argue that cooperation among subjects in a cloud ecosystem can reduce the cost of energy consumption for both parties [12]. Subramanian et al considered the elasticity of cooperation between logistics and cloud providers from the perspective of innovation diffusion [13]. As cloud computing ecosystems grow and evolve, competition becomes more intense [2].

At present, the research on the evolution and internal mechanism of cloud ecosystem is mainly carried out from the qualitative point of view, lacking the construction of mathematical models. Therefore, this paper explores the sustainable development law of cloud ecosystem by constructing a framework of cloud ecosystem and analyzing the dynamic competition and evolutionary game relationship between multiple subjects.

3. The construction of cloud ecosystem

Cloud computing ecosystem is subordinate to business ecosystem, which is the expansion and extension of business ecosystem theory in cloud computing industry, so cloud ecosystem also has the general structure of traditional business ecosystem. This paper uses Moore's business ecosystem structure model, combined with the characteristics of the cloud computing industry chain, to divide the cloud ecosystem into five parts: core cloud ecosystem, extended cloud ecosystem, competitive system, support system and environmental system.

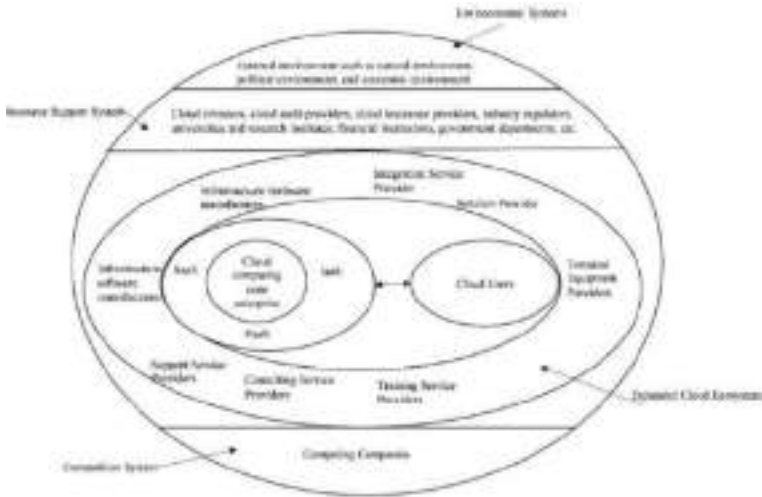


Figure 1. The structure of Cloud ecosystem

As shown in Figure. 1, in the cloud ecosystem structure model, the core cloud ecosystem is generally built by a certain core cloud computing enterprise or platform, which is the core layer of the cloud ecosystem and dominates the development direction of the whole ecosystem. After the core cloud ecosystem matures, it attracts a large number of upstream and downstream enterprises to join the ecosystem, gradually forming a broader range and richer species of extended cloud ecosystem, which is a supplement and extension of the core cloud ecosystem, and the two together build the core business system of the cloud ecosystem. The resource support system provides the basic resources needed for the survival of the cloud ecosystem, and is an important support for the core business. The development of the cloud ecosystem is also inseparable from the support of the external environment. The environmental system is the basis for enterprises to provide services to users, and provides environmental and spatial support for enterprises in the ecosystem

4. The Evolution Model of Competition and Cooperation of Main Enterprises

The main enterprises of the cloud ecosystem cooperate and interconnect with each other to provide users with high-quality, high-value cloud services and jointly promote the development and evolution of the cloud ecosystem. This paper establishes the evolution model of subject interaction in the cloud ecosystem based on the competing symbiotic relationship. Here, the evolution model of competition and cooperation between CP A and B can be shown as follows

$$\begin{aligned}
 \frac{dy_1}{dt} &= r_1 y_1 \left(1 - \frac{y_1}{K_1} - \frac{\alpha_{12} y_2}{K_2} + \frac{\beta_{12} y_2}{K_2} \right) \\
 \frac{dy_2}{dt} &= r_2 y_2 \left(1 - \frac{y_2}{K_2} - \frac{\alpha_{21} y_1}{K_1} + \frac{\beta_{21} y_1}{K_1} \right)
 \end{aligned}
 \tag{1}$$

α_{12} , α_{21} refer to the competition coefficient, β_{12} , β_{21} present the cooperation coefficient.

Here, let set $c_{12} = \alpha_{12} - \beta_{12}$, $c_{21} = \alpha_{21} - \beta_{21}$, c_{12} , c_{21} refer to the coincidence coefficient, so the Eq(3) can be transferred into :

$$\begin{aligned} \frac{dy_1}{dt} &= r_1 y_1 \left(1 - \frac{y_1}{K_1} - \frac{c_{12} y_2}{K_2}\right) \\ \frac{dy_2}{dt} &= r_2 y_2 \left(1 - \frac{y_2}{K_2} - \frac{c_{21} y_1}{K_1}\right) \end{aligned} \tag{2}$$

According to the evolution model, when the competition and cooperation of enterprises A and B reach to the balance, the equation is as follows:

$$\begin{aligned} \frac{dy_1}{dt} &= r_1 y_1 \left(1 - \frac{y_1}{K_1} - \frac{c_{12} y_2}{K_2}\right) = 0 \\ \frac{dy_2}{dt} &= r_2 y_2 \left(1 - \frac{y_2}{K_2} - \frac{c_{21} y_1}{K_1}\right) = 0 \end{aligned} \tag{3}$$

Therefore, the contours of the change rate of service transaction volume of enterprises A and B respectively are obtained.

$$L_1 : 1 - \frac{y_1}{K_1} - \frac{c_{12} y_2}{K_2} = 0, L_2 : 1 - \frac{y_2}{K_2} - \frac{c_{21} y_1}{K_1} = 0$$

Here, the coefficients of competition and cooperation c_{12} , c_{21} are different, enterprises A and B also show different evolution results. So, the evolution models of competition and cooperation between A and B under different conditions are discussed separately.

Case 1: $c_{12} = 0, c_{21} = 0$

When $c_{12} = 0, c_{21} = 0$, the negative effects of competition and the mutually beneficial effects of cooperation offset each other. It indicates that in the process of competition and cooperation, the evolution of the niche of enterprises A and B follows the Logistic law. Both enterprises make the best use of resources, then the equilibrium state equation is established.

$$\begin{aligned} \frac{dy_1}{dt} &= r_1 y_1 \left(1 - \frac{y_1}{K_1}\right) = 0 \\ \frac{dy_2}{dt} &= r_2 y_2 \left(1 - \frac{y_2}{K_2}\right) = 0 \end{aligned} \tag{4}$$

As shown in Figure. 2, the equilibrium point $E(K_1, K_2)$ is the best symbiotic point of the two enterprises. The result of the competition and cooperation shows that the niche of

them is adjacent and coexists with their maximum niche breadth, namely, both enterprises reach their maximum service transaction volume K_1, K_2 .

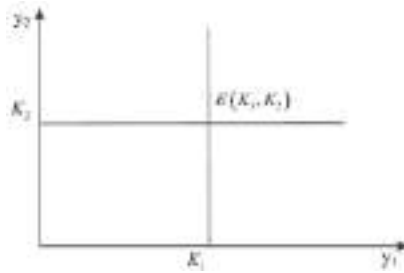


Figure.2. Case 1: The equilibrium state of the evolution model of the competition and cooperation when $c_{12} = 0, c_{21} = 0$

Case 2: $c_{12} = 0, c_{21} > 0$ or $c_{12} > 0, c_{21} = 0$

When $c_{12} = 0, c_{21} > 0$, for enterprises A, the negative effects of competition and the mutually beneficial effects of cooperation with enterprises B offset each other. Enterprises A can maximize the use of resources to reach the upper limit of service transaction volume. For enterprises B, the negative effects of competition caused by partial niche overlap are greater than the mutually beneficial effects. Consequently, the niche breadth of enterprises B is decreasing. Thus, the growth rate of service transaction volume is decreasing. However, the evolution model has two equilibrium states according to the different value ranges of the service transaction volume.

1) When $c_{21} > 1$, the result shows in Figure.3 (a). The final result of competition and cooperation is that the niche breadth of enterprise A occupies the enterprise B's. The bigger the resource utilization of enterprise A, the bigger the coefficient of competition and cooperation of enterprise B. Enterprise A is more likely to be in a dominant niche in competition symbiosis. Its balance point is $(K_1, 0)$, but the two enterprises can not reach a symbiotic balance.

2) When $c_{21} < 1$, the result shows in Figure.3 (b). The niche breadth of enterprise A remains unchanged while the enterprise B's decreases continuously. Under this condition, the smaller the competition coexistence coefficient is, the more conducive to the coexistence of the two enterprises are. Thus, the symbiotic equilibrium point is $E(K_1, K_2 - c_{21}K_2)$. This symbiotic state has no effect on enterprise A while is harmful to enterprise B, so it is a symbiotic state of partial harm.

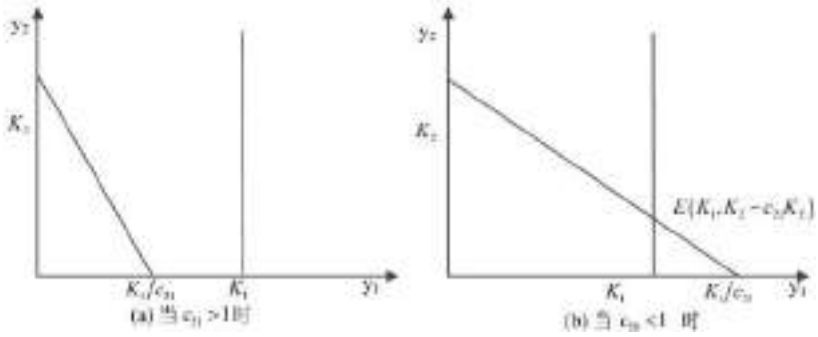


Figure.3 Case 2: The equilibrium state of the evolution model of the competition and cooperation when

$$c_{12} = 0, c_{21} > 0$$

If $c_{12} > 0, c_{21} = 0$, the model is similar to the above situation, and the paper will not discuss it here.

Case 3: $c_{12} = 0, c_{21} < 0$ or $c_{12} < 0, c_{21} = 0$

If $c_{12} = 0, c_{21} < 0$, the result shows in Figure.4. The negative effect of competition and the effect of cooperation between B and A offset each other, while the effect of cooperation between enterprise A and B is greater than the negative effect of competition. Therefore, the niche breadth of enterprise A keeps unchanged, while the enterprise B's keeps increasing, and the growth rate of service transaction volume keeps increasing. Finally, the two enterprises reach a symbiotic state, and their symbiotic equilibrium point is $E(K_1, K_2 - c_{21}K_1)$. This symbiotic state has no influence on enterprise A and is beneficial to enterprise B, so it is a symbiotic relationship of preference and benefit.

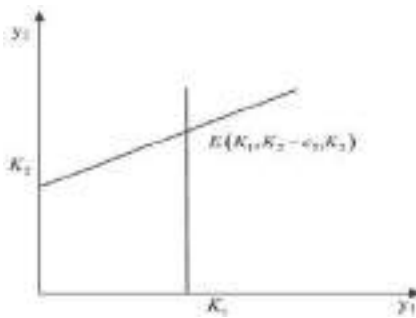


Figure.4 Case 3: The equilibrium state of the evolution model of the competition and cooperation when

$$c_{12} = 0, c_{21} < 0$$

If $c_{12} < 0, c_{21} = 0$, the model is similar to the above situation, and the paper will not discuss it in detail here.

Case 4: $c_{12} > 0, c_{21} < 0$ or $c_{12} < 0, c_{21} > 0$

If $c_{12} > 0, c_{21} < 0$, for enterprises A, the negative competition effect caused by partial niche overlap is greater than the mutually beneficial effect caused by cooperation. Therefore, the resources used by enterprises A are decreasing, the niche breadth is decreasing, and the growth rate of service transaction volume is decreasing. However, the effect of cooperation between enterprises A and B is greater than the negative effect of competition. So, the niche breadth of enterprise A remains unchanged, while that of enterprise B keeps increasing. For enterprise B, the utilization of resources continues to increase, and the growth rate of service transaction volume continues to increase. The equilibrium state of the competitive and cooperative has two conditions according to the different value ranges of the service transaction volume.

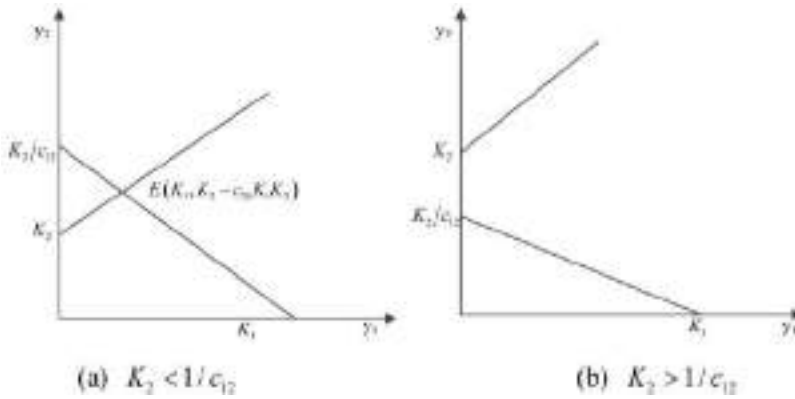


Figure.5 Case 4:The equilibrium state of the evolution model of the competition and cooperation when $c_{12} > 0, c_{21} < 0$

1) When $K_2 < K_2/c_{12}$, as shown in Figure.5 (a), the initial service transaction volume of Enterprise A is larger than that of B. While the niche breadth of enterprise A decreases and enterprise B uses part of the resources of enterprise A to increase the niche breadth, the niche of the two enterprises is separated to achieve the competitive symbiosis equilibrium point, and the two enterprises realize the symbiosis state $E(K_1, K_2 - c_{21}K_1K_2)$. This symbiosis state is harmful to enterprise A and beneficial to B, so it is a similar predatory or parasitic relationship.

2) When $K_2 > K_2/c_{12}$, as shown in Figure. 5.(b), enterprise B's niche increased continuously. The greater the competition coefficient for enterprise A, the further occupied the niche of enterprise A. The increasing service transactions volume of B was achieved at the expense of enterprise A's resources, so the two could not achieve a symbiotic balance.

If $c_{12} < 0, c_{21} > 0$, the model is similar to the above situation, and the study will not discuss it here.

Case 5: $c_{12} > 0, c_{21} > 0$

When $c_{12} > 0, c_{21} > 0$, the negative effect of competition between the two enterprises is greater than the mutually beneficial effect of cooperation.

When $K_1 > K_1/c_{21}, K_2 < K_2/c_{12}$, the enterprise A is in the dominant niche in the competition and cooperation between the two enterprises. By occupying the niche of enterprise B, enterprise A finally reaches the equilibrium point $(K_1, 0)$. However, when enterprise B is eliminated, the two enterprises can not achieve symbiosis.

When $K_1 < K_1/c_{21}, K_2 > K_2/c_{12}$, enterprise B wins in the competition symbiosis and finally reaches the balance point $(0, K_2)$. However, when enterprise A is eliminated, the two enterprises can not achieve symbiosis. $(0, K_2)$.

When $K_1 > K_1/c_{21}, K_2 > K_2/c_{12}$, The niche overlap of the two enterprises is relatively large, showing a strong competitive relationship. Enterprises with competitive advantages want to occupy the niche of another enterprise, and the two are not mutually compatible. $(K_1, 0)$ and $(0, K_2)$ is the maximal goal of the service transaction volume sought by enterprises A and B. Therefore, the two enterprises can not achieve the symbiotic state and may win in the unstable competitive symbiotic state.

When $K_1 < K_1/c_{21}, K_2 < K_2/c_{12}$, both A and B enterprises are in a weak competitive state, and they can reach a symbiotic equilibrium, with a symbiotic equilibrium point of $E\left(\frac{(1-c_{12})K_1}{1-c_{12}c_{21}}, \frac{(1-c_{21})K_2}{1-c_{12}c_{21}}\right)$.

Case 6: $c_{12} < 0, c_{21} < 0$

If $c_{12} < 0, c_{21} < 0$ the mutual benefit effect of the cooperation between A and B is greater than the negative competition effect. The two enterprises pay more attention to the coordination and cooperation through resource sharing and complementary advantages. As a result, the niche breadth of each other is increasing. The growth rate of resource utilization and service transaction is increasing. The niche separation degree is greater than their overlap degree. The two enterprises realize mutually beneficial symbiosis, and their symbiosis equilibrium point is $E\left(\frac{(1+c_{12})K_1}{1-c_{12}c_{21}}, \frac{(1+c_{21})K_2}{1-c_{12}c_{21}}\right)$

5. The simulation analysis for the evolution model in cloud ecosystem

Here, we assume that there are six representative CPs from a cloud ecosystem. Then, the evolution model of competition and cooperation for the enterprises are simulated by using MATLAB.

Scenario 1:Competitive Evolution

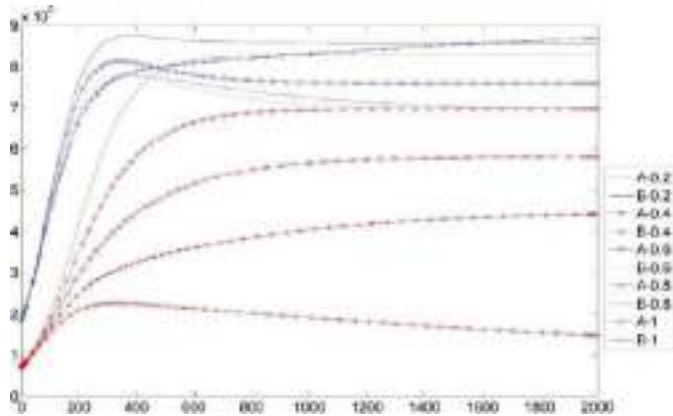


Figure 6. Individual evolutionary trends of service providers with different competition coefficients

From Figure.6, it can be seen that the initial state and ecological niche width of cloud service provider B within the cloud ecosystem are more advantageous compared to A. Therefore, cloud service provider B has ecological niche advantage compared to A. Comparing and analyzing the development evolution trend of cloud service provider A and B under the change of competition coefficient, cloud service provider A and B reach the maximum service transaction volume respectively when the mutual competition between enterprises within the ecosystem is the weakest. With the increase of competition coefficient, the competition between cloud service providers A and B for resources within the ecosystem intensifies, and the change of competition factors within the ecosystem has less impact on B with ecological niche advantage, while it has a significant impact on the development evolution of A.

Scenario 2: Cooperation Evolution

As shown in Figure.7, cloud service providers B and D form complementary advantages and value co-creation through mutually beneficial cooperation, and then reach a mutually beneficial symbiotic state, and the actual service transaction volume of both cloud service providers exceeds the upper limit of their service transaction volume in normal state. From the evolution process of individual cloud service providers under the cooperation mode, the initial state of the individual has an important role in the early development of the individual, while the role is not obvious in the late development and evolution of the individual. When the cooperation coefficient is 0.2, 0.4, 0.6, and 0.8, the trend of the development and evolution of cloud service providers B and D, the greater the cooperation coefficient between B and D, i.e., the stronger the cooperation relationship, the greater the final service transaction volume under the equilibrium state of the evolution and development of the two service providers, i.e., the greater the profit of the two cooperative enterprises.

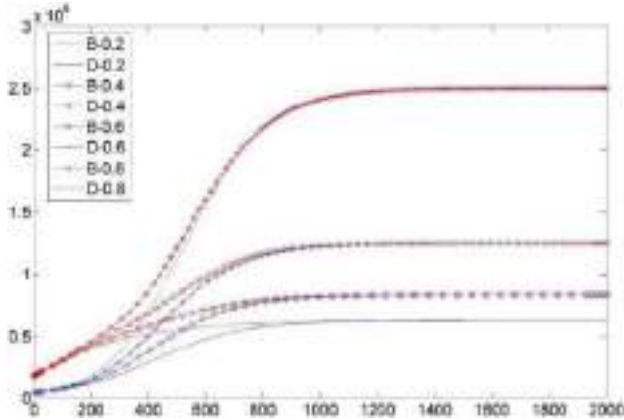


Figure 7. Individual evolutionary trends of service providers with different cooperation coefficients

Scenario3: Competition and Cooperation Evolution

As shown in Figure 8, they are gradually eliminated under the monopolistic competitive environment formed by the cooperation of A and B. The deeper the overlap between the ecological niche width and A and B, the more affected by their cooperation. The deeper the overlap between ecological niche width and A and B, the more it is affected by their cooperation, such as the overlap between E and A and B is low, so it is less affected by A and B cooperation; CP F has a higher degree of overlap than E, F, A and B, so F is more affected by A and B competition.

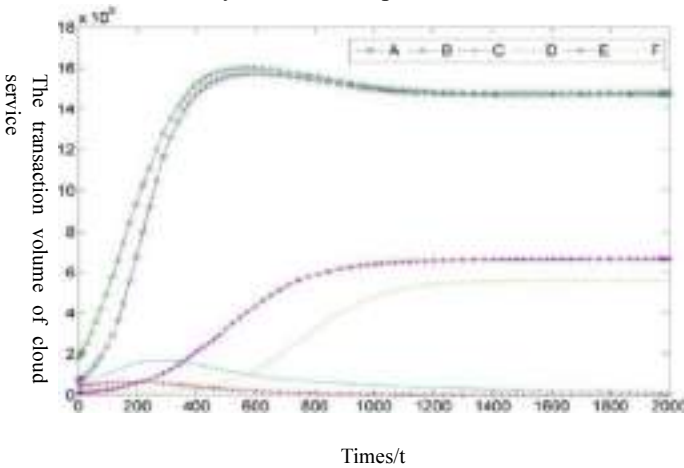


Figure.8 The Evolutionary Trend of CPs' Competition and Cooperation under the Cooperation of A and B

6. Conclusion

In this paper, we construct a cloud ecosystem structure and analyze the evolutionary model of competition and cooperation among subjects to explore the individual development laws under different circumstances. The results show that in a competitive

environment, cooperation is beneficial to the coexistence and development of both participants. This paper focuses on the evolutionary mechanisms of competition and cooperation in the cloud ecosystem. However, the main firm strategies assumed in this paper are fixed, i.e., competition, cooperation, and one of the competitions. Therefore, a further study can be the evolutionary pattern of dynamic strategies of the business entities in the cloud ecosystem. Considering the influence of the transaction process, the development and change patterns under the interaction of different firms can be analyzed.

Reference

- [1]. Buyya, R., Pandey, S. and Vecchiola, C. (2012), "Cloudbus Toolkit for Market-Oriented Cloud Computing", *Computer Science*, 5931: pp.24-44.
- [2]. Basole, R. C. and Park, H. (2018), "Interfirm collaboration and firm value in software ecosystems: evidence from cloud computing", *IEEE Transactions on Engineering Management*, pp. 1-13.
- [3]. Dahunsi, F. M. and Owoseni, T. M. (2015), "Cloud Computing in Nigeria: The Cloud Ecosystem Perspective", *Nigerian Journal of Technology*, 34(1):pp. 209-216.
- [4]. Deng, G., Chen, D., and Yao, M. (2015), "Value structure analysis for cloud service ecosystem", *International Journal of Services Technology and Management*, 21(4-6): pp.228-237.
- [5]. García-Peñalvo, F. J., Johnson, M., Alves, G. R., Minović, M. and Conde-González, M. Á. (2014), "Informal learning recognition through a cloud ecosystem", *Future Generation Computer Systems*, 32: pp.282-294.
- [6]. Gupta, A., Kapoor, L., and Wattal, M. (2010), "C2C (Cloud-to-Cloud): An Ecosystem of Cloud Service Providers for Dynamic Resource Provisioning", *International Conference*. DBLP, pp.501-510.
- [7]. Gentzoglani A. (2012) "Evolving Cloud Ecosystems: Risk, Competition and Regulation", *Communications & Strategies*, 1(85): pp. 87-107.
- [8]. Iorga, M. and Scarfone, K. (2016), "Using a capability-oriented methodology to build your cloud ecosystem", *IEEE Cloud Computing*, 3(2): pp.58-63.
- [9]. Kushida, K. E., Murray, J. and Zysman, J. (2012), "The Gathering Storm: Analyzing the Cloud computing industry ecosystem and Implications for Public Policy", *Communications & Strategies*, 1(85): pp.63-85.
- [10]. Loulloudes, N. et al. (2015), "Enabling interoperable cloud application management through an open source ecosystem", *IEEE Internet Computing*, 19 (3): pp. 54-59.
- [11]. Nieuwenhuis, L. J. M., Ehrenhard, M. L. and Prause, L. (2018), "The shift to cloud computing: the impact of disruptive technology on the enterprise software business ecosystem", *Technological Forecasting and Social Change*, 129: pp.308-313.
- [12]. Paya, A., and Marinescu, D.C. (2017), "Energy-aware load balancing and application scaling for the cloud ecosystem", *IEEE Transactions on Cloud Computing*, 5(1): pp.15-27.
- [13]. Subramanian, N., and Abdulrahman, M. D. (2017), "Logistics and cloud computing service providers' cooperation: a resilience perspective", *Production Planning & Control*, 28(11-12): pp.919-928.

Artificial Intelligence Project Practice Based on K210

Yijin SHI¹, Bin CHEN, Guisheng TAN, Guiliang ZHANG
Lijiang Culture and Tourism College, Lijiang, Yunnan, China

Abstract. Under the background of "New Engineering Course", aiming at the difficulty and lack of project resources in the practice course of "Introduction to Artificial Intelligence", the project design of practice course of Introduction to Artificial Intelligence based on K210 chip is proposed. Based on Python language, practical projects are designed with K210 chip to be applied to the introductory course of Artificial Intelligence. The results show that the students' final grades are improved and their interest and enthusiasm are increased through practical courses. The design of AI practical course based on K210 can provide reference for this course and other interdisciplinary introductory courses.

Keywords. Artificial intelligence, practical course, project design, K210 chip

1. Introduction

Artificial Intelligence technology is also a key development direction in developing new national infrastructure. The continuous development of technology requires a continuous supply of talents, which will lead to a surge in the number of Artificial Intelligence talents. Therefore, the state promulgated the "New Generation Artificial Intelligence Development Plan" and the Ministry of Education's "Several Opinions on "Double First-Class" Construction of Higher Education Institutions to Promote Discipline Integration and Accelerate the Training of Graduate Students in the Field of Artificial Intelligence" [1], are both to ensure the balance of supply and demand of talents, the reasonable structure of the training system, and the matching of talent quality. To cultivate innovative and compound talents with professional skills, knowledge, and engineering application ability. To give full play to the advantages of undergraduate education and carry out the teaching tasks of new concepts, we must break the experimental teaching scheme under traditional education. In particular, lower grade students are integrated into the teaching process, on the one hand, it can improve students' interest; on the other hand, it can improve students' learning efficiency, optimize the practical effect of Artificial Intelligence introduction, and achieve the expected teaching results in line with the talent training plan.

In the Artificial Intelligence professional personnel training process, the revision of personnel training programs is significant, reflecting that theoretical knowledge and practical links must be closely linked. However, many professional courses do not have

¹ Corresponding author: Yijin Shi (1985-), Associate Professor, research direction is Internet of Things Technology and Artificial Intelligence. E-mail: shiyijin1985@126.com

a complete practical planning scheme, which is relatively single, which brings problems to teaching. The first choice course for lower grade students to enter the Artificial Intelligence classroom is "Introduction to Artificial Intelligence." The teaching effect of the introductory course is directly related to the student's learning cognition and interest in this major. Therefore, creating a first-class course is the core and primary task of the teachers of this course.

2. Artificial Intelligence Major Status Quo Analysis

In 2019, the Ministry of Education selected 39 higher education institutions to offer Artificial Intelligence undergraduate majors. In 2022, 402 higher education institutions opened Artificial Intelligence majors, showing explosive growth in four years. Compared with the rapidly developing Artificial Intelligence industry, the talent training programs offered by the Artificial Intelligence majors offered by colleges and universities in my country are lagging behind. For example, the mismatch of teaching resources, especially the practical courses or useful links, is challenging to meet the teaching design requirements; in addition, the lack of professional teachers' ability, thus affects the progress of teaching and indirectly affects the development of the entire Artificial Intelligence profession. Students in the lower grades lack basic knowledge of programming, algorithms, pattern recognition, and machine learning. [2] The reality is that it is difficult for students to carry out a comprehensive Artificial Intelligence practice course when they study the introduction to Artificial Intelligence course. The course is mainly based on theoretical explanations, and students lack interest. Therefore, the course is not enough to cultivate students' cognition of Artificial Intelligence and improve their interest in learning in a particular program.

3. Introduction to Artificial Intelligence Practical Course Based on K210 Chip

In "Introduction to Artificial Intelligence", it is necessary to introduce the origin and development of Artificial Intelligence. Based on knowledge representation, it uses forms such as production representation, knowledge graph, first-order predicate logic, state space method, and reduction method to represent knowledge so that machines can understand it, and further use various algorithms to obtain machine imitation and machine decision-making. In the introduction course of Artificial Intelligence major, it is necessary to fully mobilize students' interest in learning and guide students to understand the development direction and application fields of Artificial Intelligence. Therefore, the design of practical course is particularly important. Practical courses need to rely on hardware equipment as the basis. With the technological development of Artificial Intelligence chips, K210 chip is a good choice. [3-5]

There are 115 pieces of research literatures on the introduction to Artificial Intelligence, of which there are more than 70 from 2018 to 2022, of which 48 are from 2020 to 2022. These literatures mainly study the teaching mode of courses, curriculum reform and practice, curriculum ideology and politics, Artificial Intelligence school-enterprise cooperation courses based on Baidu Paddle and AI Studio platforms, and preliminary exploration of practical teaching modes based on new engineering. [6-7] There are 84 works of literature on K210, mainly using K210 for Artificial Intelligence application research, including face recognition applications and designing and implementing of

various Artificial Intelligence application systems. [8-9] However, scholars have had no reports and research on combining the K210 chip and introduction to Artificial Intelligence practice. The application of the K210 chip in introduction to Artificial Intelligence course is studied to provide helpful reference for the teaching practice of the introduction to Artificial Intelligence course. To sum up, applying the K210 chip to the introduction to Artificial Intelligence course can explore a new model of Artificial Intelligence education, and solve the problem of lack of experimental conditions for Artificial Intelligence majors to a certain extent.[10]

3.1 Hardware System Construction

K210 is a chip with powerful reduced instruction set architecture, using RISC-V architecture. This AI chip mainly integrates a system-on-chip (SoC) with machine vision and machine hearing capabilities. It has a dual-core 64-bit processor and has better power consumption performance, stability and reliability. The chip can be deployed in the user's product in the shortest time, giving the product Artificial Intelligence.

Constructing a suitable hardware system is crucial for introducing Artificial Intelligence practice courses. On the one hand, it is necessary to consider the knowledge of students, and on the other hand, to consider the realization of Artificial Intelligence applications. K210 chip and Arduino chip (hereinafter referred to as "UNO") are used to build an Artificial Intelligence kit (hereinafter referred to as "Xiaozhi"). The smart chipset shown in Figure 1 consists of a K210 chip board and a UNO smart car. The body is disassembled and can be equipped with a K210 chip motherboard. The UNO single-chip microcomputer control chip is designed on the body, mainly used to control motors and other sensors. The main control chip K210 is responsible for completing Artificial Intelligence applications. The main frequency of K210 can exceed 600M to support conventional visual algorithms, compatible with most Openmv algorithms, and support neural network algorithms. The face detection speed (OVGA, RGB image) AI acceleration can reach more than 60 frames, 2.4-inch resistive LCD with a resolution of $240 \times (\text{RGB}) \times 320$, a high-definition camera with 2 million pixels, pluggable ultrasonic expansion, and support for Python open source programs.



Figure 1 Physical Map of AI Xiaozhi

The primary function of the smart car is to enhance the scalability and fun of the project. The LCD, microphone and camera on the K210 motherboard can complete the collection of graphics and sound, and provide materials for image recognition and speech recognition. The Python language is easy to use, which reduces the difficulty of learning to a certain extent, allowing students to be familiar with the tasks to be completed by Artificial Intelligence in the early grades.

3.2 Face Recognition Practice Project Design

As a relatively mature application of Artificial Intelligence, face recognition has always been the main direction of Artificial Intelligence research. Face recognition is similar to object recognition. It is a recognition technology based on facial features of the face. Image or video stream is collected through sensors, and the model library is used for automatic detection and tracking for further recognition. The core of face recognition is still based on the model library after training.

Among the Artificial Intelligence introduction practice projects, face recognition is a relatively comprehensive practice project and a typical application of Artificial Intelligence technology. The hardware equipment used in this project is the K210 chip, and the camera is used for data acquisition. The main teaching goal is to familiarize students with the development process of Artificial Intelligence technology applications. Because the lower grade students are not familiar with algorithm and model training, the model of this project has been trained. To complete face recognition, you only need to use Python code to write the camera driver and simultaneously complete the model call and anchor parameters.

Before applying face recognition, you need to use KFLASH software to import the trained face_3M model library to the 0x300000 position of the K210 chip. Face_3M is a library of trained face recognition models. The face recognition process includes initializing the camera for face image acquisition, initializing the LCD for displaying images, setting 10 face anchor point parameters, and loading the face model to identify whether it is a face. The detailed steps include four steps, one is to initialize the model, Two is to set the number of reference points, Three is that the anchor parameter is the variable anchor, and Four is to draw a rectangle and calculate the center point to draw a cross. The design of this case is mainly to let students understand the principles and processes of face recognition, and further increase their understanding of YOLO target detection and recognition. The model download and program flow chart are shown in figures 2,3, and 4.



Figure 2 Model Download Interface

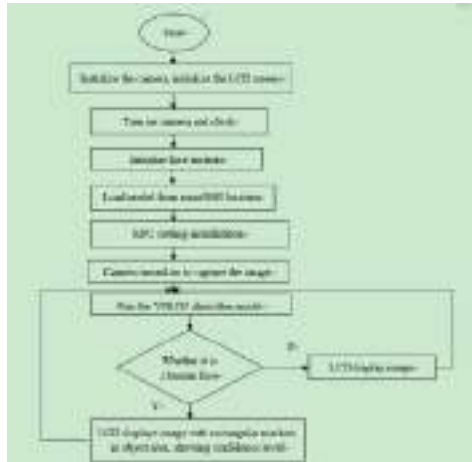


Figure 3 Face Recognition Effect



Figure 4 Face Recognition Program Flow Chart

Figure 5 below is part of the critical code for students to realize face recognition. Students can understand the process of face recognition, have a basic understanding of the YOLO2 algorithm, and achieve the guiding role of the introduction to Artificial Intelligence course. Meanwhile, students can also ask their questions about the setting of anchor points, and why these parameters can get better recognition effects. Through the explanation, practice and reflection of this project, a face recognition project has been completed, and the teaching effect of the task-driven has been achieved.

```

14  #YOLOv2 yolov2
15  #YOLOv2 yolov2
16  #YOLOv2 yolov2
17  #YOLOv2 yolov2
18  #YOLOv2 yolov2
19  #YOLOv2 yolov2
20  #YOLOv2 yolov2
21  #YOLOv2 yolov2
22  #YOLOv2 yolov2
23  #YOLOv2 yolov2
24  #YOLOv2 yolov2
25  #YOLOv2 yolov2
26  #YOLOv2 yolov2
27  #YOLOv2 yolov2
28  #YOLOv2 yolov2
29  #YOLOv2 yolov2
30  #YOLOv2 yolov2
31  #YOLOv2 yolov2
32  #YOLOv2 yolov2
33  #YOLOv2 yolov2
34  #YOLOv2 yolov2
35  #YOLOv2 yolov2
36  #YOLOv2 yolov2
37  #YOLOv2 yolov2
38  #YOLOv2 yolov2
39  #YOLOv2 yolov2
40  #YOLOv2 yolov2
41  #YOLOv2 yolov2
42  #YOLOv2 yolov2
43  #YOLOv2 yolov2
44  #YOLOv2 yolov2
45  #YOLOv2 yolov2
46  #YOLOv2 yolov2
47  #YOLOv2 yolov2
48  #YOLOv2 yolov2
49  #YOLOv2 yolov2
50  #YOLOv2 yolov2
51  #YOLOv2 yolov2
52  #YOLOv2 yolov2
53  #YOLOv2 yolov2
54  #YOLOv2 yolov2
55  #YOLOv2 yolov2
56  #YOLOv2 yolov2
57  #YOLOv2 yolov2
58  #YOLOv2 yolov2
59  #YOLOv2 yolov2
60  #YOLOv2 yolov2
61  #YOLOv2 yolov2
62  #YOLOv2 yolov2
63  #YOLOv2 yolov2
64  #YOLOv2 yolov2
65  #YOLOv2 yolov2
66  #YOLOv2 yolov2
67  #YOLOv2 yolov2
68  #YOLOv2 yolov2
69  #YOLOv2 yolov2
70  #YOLOv2 yolov2
71  #YOLOv2 yolov2
72  #YOLOv2 yolov2
73  #YOLOv2 yolov2
74  #YOLOv2 yolov2
75  #YOLOv2 yolov2
76  #YOLOv2 yolov2
77  #YOLOv2 yolov2
78  #YOLOv2 yolov2
79  #YOLOv2 yolov2
80  #YOLOv2 yolov2
81  #YOLOv2 yolov2
82  #YOLOv2 yolov2
83  #YOLOv2 yolov2
84  #YOLOv2 yolov2
85  #YOLOv2 yolov2
86  #YOLOv2 yolov2
87  #YOLOv2 yolov2
88  #YOLOv2 yolov2
89  #YOLOv2 yolov2
90  #YOLOv2 yolov2
91  #YOLOv2 yolov2
92  #YOLOv2 yolov2
93  #YOLOv2 yolov2
94  #YOLOv2 yolov2
95  #YOLOv2 yolov2
96  #YOLOv2 yolov2
97  #YOLOv2 yolov2
98  #YOLOv2 yolov2
99  #YOLOv2 yolov2
100 #YOLOv2 yolov2

```

Figure 5 Face Recognition Program Implementation

Face recognition applications with embedded hardware K210, so the use of YOLO algorithm, the algorithm is fast, based on the loading model inside the chip, easy to use. A comprehensive comparison of two popular algorithms: one is the R-CNN series based on the Region Proposal, which belongs to two stages and needs to be generated by using Selective Search or RPN Region (RPN Region) before classification and regression of the Region Proposal; the other is the YOLO used in this project, which uses only one CNN to directly predict the categories and locations of different targets. The precision of the first kind of method is higher, but the speed is slower, the precision of the second kind of method is lower than the first kind, but the speed is faster. So the YOLO algorithm introduced in this paper is more suitable for face recognition with hardware acquisition, and the hardware chip combining AI and IOT will be developed rapidly in the development of AI and IOT, thus promoting the wide application of AI technology.

4. Teaching Effect Evaluation

After using the K210 chip and case teaching in the introductory Artificial Intelligence course, student's interest in the introductory Artificial Intelligence course has increased, and the teacher is responsible for the case explanation and completing the task of "Giving Example". Students complete the "Draw Inference" requirements in the practical examination part after class and at the end of the term. Through three rounds of teaching practice, the case package has been perfected. Judging from the students' final practice assessment, the teaching effect has been improved, eliminating the dullness and poor effect of pure theoretical teaching of this course in the early stage. By introducing practical teaching through the Artificial Intelligence case package, students can complete a comprehensive practical case at the end of the semester. For example, recognizing numbers and speech signals can also raise new questions, such as how to recognize Dongba language, wild fungi, and Naxi language. In this way, students can be guided to explore, step by step, the knowledge map representation of wild fungi, the establishment of the wild fungi identification model library, the establishment of the Dongba language model library, and the establishment of the Naxi language model library. This also achieves the original intention of the Introduction to Artificial Intelligence course to guide students to increase their interest in solving problems.

Table 1 shows the final assessment results of the students. After using these case packages, the students' interest in learning has improved, and their scores have also improved compared with the previous pure theory courses.

Table 1 Students' Final Scores

Grade	Total Number	Average Score	Number of Failed	Number of Excellent (90-100)	Highest Score	Academic Affairs System Student Evaluation	Student Satisfaction
2017	55	68	3	8	88	90 (Excellent)	Average
2018	54	75	0	10	81	94 (Excellent)	High
2019	55	78	0	12	94	96 (Excellent)	High
2020	55	85	0	12	94	96 (Excellent)	High

5. Conclusion

The practical part of the introduction to Artificial Intelligence course plays a vital role in inspiring students and guiding them into the field of Artificial Intelligence. Through K210-based Artificial Intelligence suite design and case package design, teaching resources are enriched to a certain extent, while considering the weak foundation of students entering the field of Artificial Intelligence. Case design using face recognition, image recognition, object recognition, and speech recognition, to a large extent, covers the content of the introduction to Artificial Intelligence course. On the one hand, it enhances students' interest in learning and broadens students' horizons. Through the realization of cases in teaching, students can understand the application field of Artificial Intelligence, and gradually cultivate student's innovative abilities. While understanding the knowledge of Artificial Intelligence, you can have an overview of the knowledge field of Artificial Intelligence, which can also provide a specific reference for the practical teaching of the introduction to Artificial Intelligence course. Of course, the shortcoming is that students lack knowledge about model training. Model training based on YOLO-MARK can be added to subsequent case packages to improve the teaching effect of the entire case package.

Acknowledgment

Fund Project of Yunnan Provincial Department of Education(2022J1234);
Lijiang Science and Technology Project (2020ljhb01, 2020ZX10)

References

- [1] Fan Chao, Yang Tiejun, Hou Huifang, et al. Design of Core Experimental Teaching Projects for Artificial Intelligence Major under the Background of "New Engineering Course" [J]. *Experimental Technology and Management*, 2021, 38(8): 183-189.
- [2] Xu Yinyun, Jiang Ming, Li Yunfei, Wu Yunfei, Lu Guifu. Fruit Target Detection Based on Improved YOLO and NMS [J]. *Journal of Electronic Measurement and Instrumentation*, 2022, 36(04): 114-123.
- [3] Li Hui. Reform and Practice of Introduction to Artificial Intelligence for Local Universities [J]. *Computer Education*, 2021(11): 51-53
- [4] Liu Jinjiang, Li He, Ma Xiaopu, Zhang Xingang. A Preliminary Study on the Practical Teaching Mode of Introduction to Artificial Intelligence for New Engineering [J]. *Computer Times*, 2021(05):91-93.
- [5] Liu Kai, Yu Yingfu, Yan Wenjun. Hierarchical Progressive Experimental Case Design for Military Artificial Intelligence Course [J]. *Experimental Technology and Management*, 2022, 39(04): 186-189.
- [6] Ju Moran, Luo Haibo, Wang Zhongbo, He Miao, Chang Zheng, Hui Bin. Improved YOLO V3 Algorithm and Its Application in Small Target Detection [J]. *Journal of Optics*, 2019, 39(07): 253-260.
- [7] Gao Zong, Li Shaobo, Chen Jinan, Li Zhengjie. Pedestrian Detection Method Based on YOLO Network [J]. *Computer Engineering*, 2018, 44(05): 215-219.
- [8] Ihsanullah I.,Alam Gulzar,Jamal Arshad,Shaik Feroz. Recent advances in applications of artificial intelligence in solid waste management: A review[J]. *Chemosphere*,2022,309(P1).
- [9] Wong Hoo Keat,Estudillo Alejandro J.. Face masks affect emotion categorisation, age estimation, recognition, and gender classification from faces[J]. *Cognitive Research: Principles and Implications*,2022,7(1).
- [10] Hertrampf Katrin,Wenz Hans Jürgen,Goetz Katja. Covid-19: teaching and learning in practical courses under special regulations – a qualitative study of dental students and teachers[J]. *BMC Medical Education*,2022,22(1).

Research on Intelligent Research Model of Clues in Cases of Production and Sale of Counterfeit Drugs

Linfeng GU¹, Sisi LI, Yutian WANG, Zhihui LIN and Jingsong WU
School of information technology, Nanjing Forest Police College, Nanjing 210023, China

Abstract. This model takes the vigorous promotion of the construction of "smart policing" and the construction of a modern police system as the background, creates a data-based, technology-based, vigorously improves the analysis and mining capabilities of public security organs on the hot issues of counterfeit drug crimes, and transforms the traditional post-processing and passive response methods of police work to the direction of pre-prediction and active intervention. At the same time, drawing on the design ideas of the system architecture, the model system is layered and decoupled, creating a multi-channel data collection, to case text preprocessing and standard definition, forming a "four-category personnel database", and then classifying according to the theme of public security business to achieve a criminal model of production and sales of counterfeit drugs The overall framework is reused vertically in the field and flexibly extended horizontally.

Keywords. Counterfeit drug crime, research and judgment model, active discovery, knowledge base, system construction

1. Research background

1.1. Research status and development trends at home and abroad

Counterfeit drug crimes are economic crimes related to people's livelihood, which is a new type of crime derived from the development of social and commodity economies, which has a double harm to the public's life and health and property safety, as well as the national economic management order and social stability, seriously corrupt the commercial atmosphere, and lead to the phenomenon of "bad money expelling good money" from low-quality products expelling high-quality products on the market.[1]

In recent years, the crime of counterfeit drugs nationwide is still in a serious situation, but the academic community has done less research on it, and even the new direction that has not yet been excavated in the geographical study of crime is in huge contrast with the urgent reality. Although the public security organs have strengthened daily patrols, strengthened linkage and co-governance, and increased publicity and guidance, they have shown obvious results, but they are still based on long-term work experience, for some sudden or new types of counterfeit drug hotspots, it is difficult for us to find a better entry point to prevent in advance, which may cause negligence and leakage, and may also be ineffective and waste of manpower. Therefore, we hope to explore ways to take

¹ Corresponding author: GU Linfeng, E-mail: 1533601364@qq.com.

precautions and prevent problems before they occur, and there are still many pain points in the fight against counterfeit drugs.

1.2. Realistic pain points

- **The manufacturers and sellers of counterfeit drugs are very hidden and have certain anti-investigation capabilities, and it is difficult to collect all the evidence of the crime.** Pharmaceutical production enterprises produce counterfeit drugs by not investing or less in the main materials, valuable raw and auxiliary materials, etc., and sell fake and inferior drugs through legal channels, and their behavior is quite hidden.
- **Circulation management problems.** Those who manufacture and sell counterfeit drugs mainly complete the "flow of goods" through post offices and logistics companies. There are four reasons for this: First, mailing and express delivery to sell counterfeit drugs quickly; Second, the review is not strict, and safety is guaranteed; The third is to adopt the cash on delivery method, which has a certain fraudulent nature and convenient payment collection; Fourth, it is not in direct contact with patients, and it is highly concealed.[2]
- Police data resources are relatively limited, and it is difficult to reflect the hot spots of social governance of counterfeit drugs; The research results of counterfeit drugs have focused on solving a type of problem and have not formed a system.[3] As shown in Figure 1.

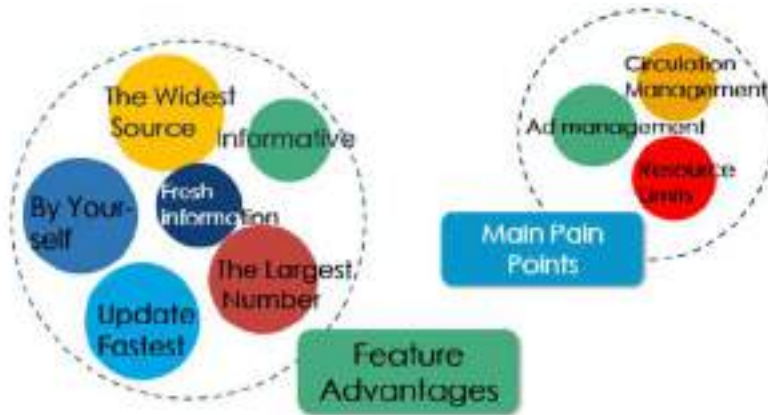


Figure 1. Feature Advantages and Main Pain Points

2. Technical realization

2.1. Multi-channel data access

In the selection of analysis samples, the idea of retrieving and collecting relevant data of counterfeit drug production cases involved in the whole country through the Chinese judgment documents and Openlaw legal document platform and local courts was determined, and then the division of labor was carried out according to different provinces, batch screening and downloading cases, and the data were integrated in

accordance with unified norms, and the results of case integration in different provinces were summarized separately for follow-up analysis.[4]

The research object of this project team is the criminal case of production and sale of counterfeit drugs recorded in the past five years in various provinces across the country recorded in the China Judgment Documents Network and Openlaw, and after data cleaning and preliminary review, 60,746 pieces of case data with complete data content and regular format are integrated and analyzed by case related variables. A total of 36 crimes and 60,746 cases were committed in four sections. The first part has 10 crimes against the production and sale of counterfeit and shoddy drugs, with a total of 18,182 case texts, the second part has 8 crimes of infringement of intellectual property rights, a total of 8,802 case texts, the third part has 2 crimes against public health, a total of 35 case texts, and the third part has 16 crimes against the protection of environmental resources, with a total of 33,727 case texts.

2.2. Definition of case text preprocessing and extraction standards

After using PivotTable function to preliminarily explore the correlation between various variables and case information, classify and sort the data according to provinces and case types, study the internal relationship between case frequency and time and space of each province, and complete the preliminary statistical analysis work. Through semantic analysis technology to realize the analysis of Internet social problems and police intelligence, realize the transformation of unstructured data to structured data.

This article extracts the key industries, key places, key parts, key personnel, main items, main species, and main crime methods involved in the case text in accordance with the standards. As shown in Table 1.

Example	According to the standard	Label the results
The suspect Tong is a pharmacist who colludes with Lin to sell counterfeit drugs	Key industry standards	Pharmaceutical manufacturing
Chen illegally obtained counterfeit drugs and shipped them to slimming pharmacies for sale	Standards for key places	Weight loss pharmacy
Under the pretext of beauty, Li sold counterfeit drugs to customers in the beauty shop he opened	Standard for key areas	Beauty shop
The suspect Wu mou is an individual and colludes with Lin to sell counterfeit drugs	Key personnel standards	individual
Ding illegally sold compound rheumatic capsules at outlets	The standard of the main items involved in the case	Compound rheumatic capsules
Sun illegally sold a cheap nine-valent vaccine	The criteria for the main species involved in the case	vaccine
Lin took the WeChat group as the starting point and sold counterfeit drugs through WeChat payment methods	Standards for the main modus operandi	Establish WeChat groups and sell online

Table 1. Label example table



Figure 2. Push The Process

On the basis of structured data, it further relies on deep neural network to realize intelligent mining of keywords of network social problems and police information. Tagging text extraction as follows: people, places, organizations, time, emotion is negative, similarity information, the main body, keyword information, information, publishing time, publishers, original forwarding information, field category information, sensitive category information, level of sensitive information, garbage label information such as hundreds of tags. In terms of text features, Word2VEC based and Bert based text semantic feature extraction techniques are respectively adopted according to different scenarios. As shown in Figure 2.

By classifying and labeling the historical data, the training data sample library of fake medicine text was constructed. The text semantic feature modeling based on Word2VEC method is implemented, and Text_CNN text classification technology is used to achieve the rapid extraction of local features, and the basic classification answer is output from the problem. The topic case, entity label, trigger word label and other important information are introduced for model fusion, and the accuracy of classification is further improved. Finally realize the classification of fake medicine text.

2.3. Integrate data sources and establish "Thesaurus of Four Types of Personnel Data"

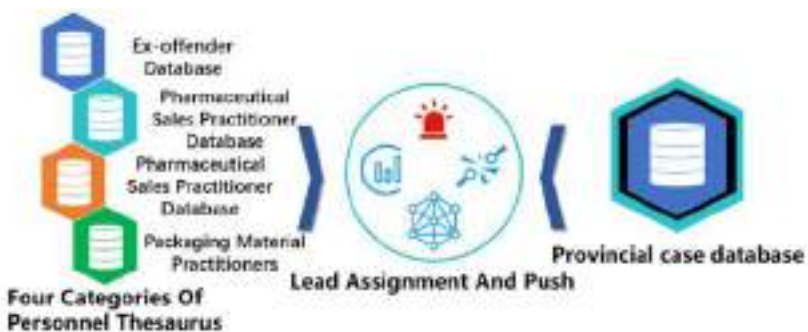


Figure 3. Thesaurus Building and Pushing

In the preparation process of manufacturing and selling fake drugs, raw materials such as inferior drugs, bottles, pill boxes, security codes and trademarks will be purchased from the suppliers of original wine and packaging materials. In the manufacturing process, to find production dens, hire packers to organize production; During the storage process, you need to find the storage dens. Temporary placement of unsold counterfeit medicines; In the sales process, it is necessary to contact the drug sales front line and support personnel for transportation and sales. Again, in this process, a large amount of relevant personnel information, funds, logistics and other key data will be generated, which can accurately depict and restore criminal activities, and formalize the evidence we need to combat such crimes. We use Word2VEC method to realize the semantic feature modeling of Text, and use text-CNN Text classification technology to achieve rapid extraction of local features, so as to output basic classification labels, and introduce multi-element information such as subject labels, entity labels and trigger word labels for model fusion, so as to further improve the accuracy of classification. Finally, the intelligent classification of police data is realized. We construct the required structured data thesaurus according to the following two points. As shown in Figure 3.

2.3.1 Aggregate and integrate internal and external data resources to establish "four types of personnel database" information

- Database of ex-offenders: In the text of the case, the public security organs punished and punished ex-offenders for manufacturing and selling counterfeit drugs; Persons at large and evacuated for the crime of manufacturing and selling counterfeit drugs throughout the country; Administrative punishment personnel for the manufacture and sale of counterfeit drugs by the Market Bureau; Information on the production and sale of counterfeit drugs seized by the major departments of pharmaceutical companies.
- Drug sales practitioner database: self-employed drug personnel registered in the case text; E-commerce platforms open pharmaceutical stores.
- Logistics employee database: logistics express employees
- Packaging materials employees: Employees of relevant printing plants and packaging material factories involved in the case

2.3.2 In response to the characteristics of the crime, clarify the elements of research and judgment, and collect "third-rate information"

- Capital flow information: account, online banking, alipay transaction information of the person involved in the case
- Communication flow information: spider web address book information, software address book information
- Logistics information: logistics delivery and delivery information

2.4. Clue assignment and push



Figure 4. The Assignment Of The Person Type

Through explicit and implicit two-dimensional reasoning, the model can reason social public opinion to the police topic, so as to achieve the automatic generation of social hotspots to police work goals, in the downstream of this model, is a steady stream of thematic business model, we for the time correlation, location correlation, character relevance, behavior correlation and other dimensions in accordance with the rules of the assignment, according to the total score value of the order, the branch is higher than 40 people are included in the scope of attention. According to the calculation results, according to the score level, the key objects are listed, the relationship chain is generated, and the associated personnel are included in the scope of early warning of the deployment control. Combined with its capital, logistics, communication upstream and downstream relationships to find out the sales port of counterfeit drugs and inferior drugs, test and buy identification, test the flow of funds, meet the standards for filing a case, and file a case for investigation. As shown in Figure 4.

3. Innovation highlights and practical results

3.1. Multi-channel construction of four types of personnel hot thesaurus, actively find and reduce human resource costs

By producing a large amount of data fusion of counterfeit crime subject keywords, combined with different associated personnel in each link of information data, to build a hot link library in the four types of personnel, through the model with the help of the public website relevant data real-time implementation of spiders crawling, real-time grasping library update supplement, realize the diversity of data source and thesaurus, For future cases to provide data support. This model carries out collision results of four types of personnel database data. After the results are generated, the data system of gang members, transaction record evidence and sales network is formed by using "third-rate information" to trace the source and relationship data, so as to further promote the investigation work. To find and collect clues of production and sales of fake drugs, and provide them to the corresponding functional departments in time, so as to provide safe and reliable technical support for law enforcement personnel. Daily police can pay attention to the real-time update of the keyword thesaurus, obtain the peak time and its

frequent areas, carry out timely actions, realize the process from passive attendance to active analysis, and greatly reduce the cost of human resources.

3.2. Intelligent analysis of public opinion and police intelligence to improve data processing efficiency

Using semantic analysis technology, the scheme of the collected from the network to produce counterfeit drugs related case analysis classification, sorting out and produce counterfeit crime cases related elements, implementation to produce counterfeit case flows, communication records, logistics information and other elements, and through the above elements to achieve a more accurate judgment, targeted projections for the criminal process. The collected massive texts related to counterfeit drug cases were independently classified, and the heterogeneous sub-structured texts were extracted as unified vector features to facilitate the subsequent correlation analysis and model fusion of the cases. The different links of the whole model system were connected in series to realize the end-to-end closed-loop computing process. Through the model modeling, the model calculated the number of personnel risk labels: place labels 4; 68 labels of individuals involved in high-frequency cases; 124 criminal tags using wechat or QQ; 569 low-cost drug labels; 1,663 labels for low-priced supplements; Health care product label 9207; Form 47 case association model instructions. Through manual research, judgment and screening, it was transferred to the public security business department 42 items. After the second research, judgment and verification of the materials, the correct rate of related cases was 71.43%. [5]

3.3. Social public opinion is linked to policing and improve data processing efficiency

This scheme draws on the design idea of the system architecture, decouples the model system in layers, realizes the vertical domain reuse of the overall model framework and the flexible expansion of the horizontal, and creates a "pyramid" model transmission system from the upstream problems of network public opinion mining to lead to social governance hotspots, to the processing factory that classifies the theme of public security business in the middle, and then to a series of corresponding practical solutions in the downstream. And through the thesaurus construction, the thesaurus will be the peak time of high-frequency words and their frequent occurrence of statistics, involving the production and sale of counterfeit drugs in the high incidence of crimes for rapid screening and screening, to achieve a complete closed loop from the discovery of problems to the solution of problems, for the police work intelligently proposed a complete set of solutions. To make up for the late start of police big data modeling applications in the field of public security, and the data related to counterfeit drug crimes is relatively complicated, which is not conducive to the efficient implementation of public security law enforcement work.

4. Summary and Prospect

In this study, the construction of a thesaurus of fake drug manufacturing and sales cases was completed, and the intelligent investigation model of fake drug manufacturing and

sales cases was realized based on semantic analysis, knowledge extraction and other big data technologies. Specifically, the following work was carried out:

- The crime model, research status and development trend of counterfeit drugs at home and abroad were studied.
- Go into the police grassroots business, think and summarize the pain and difficulty in the actual combat of the police grassroots, and formulate corresponding solutions.
- Refer to the policies and instructions related to police intelligence to determine the research direction
- Completed the text analysis project of food and drug ring investigation cases, investigated related databases, and completed the construction of the domain corpus
- Construct and design the experimental architecture according to the pain and difficulty of public security experimental business, and test the model system

4.1. Through the construction of a special thesaurus, improve the data utilization rate and the efficiency of the police's case handling

This model timely labels the data after statistics, classifies the keywords according to the frequency of occurrence, and sets the hot words with more occurrences as high-frequency words, which are used to show the peak period of high-frequency words and their frequent occurrence areas. Through the use of the thesaurus, the public security police can quickly screen and identify areas with a high incidence of the crime of designing, producing and selling counterfeit drugs, promptly crack down on the crime of producing and selling counterfeit drugs, and improve the efficiency of case handling. At the same time, the thesaurus will continue to inject new case data, enrich and optimize the model, and continuously improve the data utilization.

4.2. Through data intelligence, realize the transformation to science and technology to police force

Compared with the lag in the fight against counterfeit drug crimes in the past, which led to the infringement of the people's right to life and health and property rights, this model intelligently calculates the data, builds a real-time updated data thesaurus, continuously updates the thesaurus, liberates the police from redundant case data, realizes the innovative transformation to science and technology to police forces, and greatly reduces human resource costs.

Acknowledgements

This research was supported by the 2022 College Students Innovation and Entrepreneurship Training Program (Grant No. 202212213006Z).

References

- [1] Liu Lihua. Research on the Supervision of Drug Network Sales[C].Hainan University, 2020:33-37
- [2] Gong Lu, Zhu Zhengwang, Investigation of Online Sales of Counterfeit and Inferior Drugs[J], Jiangsu Police Officers College, Yancheng Municipal Public Security Bureau, 2017
- [3] Yang Xuzheng, Investigation of Internet-related food safety crimes [D], People's Public Security University of China,2022
- [4] Xu Fengsheng, Research on the Prevention and Control Countermeasures of Counterfeit and Shoddy Drugs Sold online in China[C].Chinese Min Public Security University, 2017:35-40
- [5] Zhang Yuying, Research on the Attributes of China's Online Public Opinion Crisis Events [D]. Hunan University,2018

Low Complexity and High Spectrum Efficiency Hybrid Precoding for Massive MIMO Systems

Gang XIE¹ and Zhixiang PEI

School of Information and Communication Engineering, Beijing University of Posts and Telecommunications, Beijing 100876, China.

Abstract. Recently, alternating minimization has been widely employed for hybrid fully-connected precoding schemes, whereas the complexity is too high. In order to further reduce the complexity while maintaining the performance of single user point-to-point millimeter wave multiple-input multiple-output (MIMO) systems, we propose an alternating minimization algorithm of inverse matrix's phase extraction based on orthogonal matching pursuit (AIPO). Firstly, both the analog and digital precoding matrices are obtained by orthogonal matching pursuit algorithm. Then, the analog precoding matrix is updated using the phase information extracted from the digital precoding matrix and the optimal digital precoding matrix. Finally, the local optimal solution can be iteratively obtained under the least squares criterion and the modulus constraint. Simulation results verify that the proposed algorithm is capable of dramatically decreasing the complexity by more than sixty percent without compromising spectrum and energy efficiencies.

Keywords. Hybrid precoding, alternating minimization, MIMO, AIPO

1. Introduction

The past few years have witnessed the rapid growth of global demand for wireless data traffic. However, due to limited spectrum resources, it is rather overwhelming for fifth-generation (5G) mobile communication systems to meet the increasing demands of users for an ultra-high data rate. Therefore, the exploitation of unauthorized millimeter wave band for communication has attracted widespread attentions from both domestic and foreign scholars. Thanks to the relatively short wavelength of millimeter wave, the physical size of antenna array is greatly reduced, thereby implying that large-scale antenna can be deployed at the base station. In line with this insight, it is intuitive to jointly combine millimeter wave with massive MIMO in an efficient manner.

Hybrid precoding technology is one of the most promising technologies in millimeter wave massive MIMO system [1]. So far, the research on hybrid precoding mainly focuses on two kinds of structures: fully connected structure [2-5] and partially connected structure [6-7]. For the fully connected hybrid precoding structure, each RF link connects to all antennas. The hybrid precoding for this structure can obtain all beamforming gains, which achieves comparable performance digital precoding.

¹ Corresponding author: Xie Gang, Beijing University of Posts and Telecommunications; E-mail: xiegang@bupt.edu.cn

Nevertheless, the disadvantages of this structure primarily include high complexity and power consumption. For the partially connected structure, each RF link merely connected to a part of the antennas. As a result, it only obtains incomplete beamforming gain, which thus compromises the performance. In order to improve the spectrum efficiency as much as possible, we consider full connection structure in this paper.

To improve the low spectral efficiency of existing communication systems, a hybrid precoding algorithm based on orthogonal matching pursuit (OMP) was proposed in [1]. The algorithm improved the spectrum efficiency to a certain extent. However, limited by the feasibility of the analog precoding matrix, performance loss is inevitable. To acquire a high spectrum efficiency, Yu. proposed propose a manifold optimization based AltMin (MO-AltMin) algorithm [8]. The spectrum efficiency was greatly improved under this algorithm, which is sufficiently close to the optimal digital precoding. However, it has to endure a heavy computational complexity to find the global optimal precoding matrix.

In order to reduce the unnecessary complexity, a phase extraction based alternating minimization (PE-AltMin) algorithm was proposed in [8]. Compared with MO-AltMin, this algorithm greatly reduces the complexity while maintaining the same spectrum efficiency. However, this algorithm can only guarantee a local optimal solution, and the convergence behavior over the iterations can be poor.

What this paper aims to do is to reduce the number of iterations after achieving a better result, and then reduce the complexity of each iteration by simple multiplication and division, thus reducing the computational complexity of the whole algorithm while maintaining the system performance.

2. System Model

2.1. Fully Connected Hybrid Precoding System

We exemplify the hybrid precoding by introducing a single user hybrid precoding structure of full connection in detail.

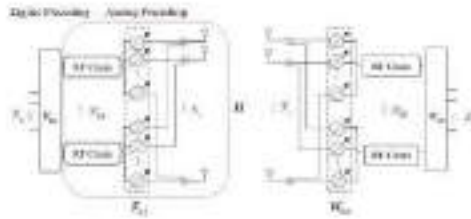


Figure 1. Hybrid Precoding System Model for Fully Connected Single User

As shown in Figure 1., we consider a fully connected single user hybrid precoding system model. The transmitter has N_t transmitting antennas and N_t^{RF} RF chains, and the receiver has N_r receiving antennas and the same N_r^{RF} RF chains as the transmitter.

The transmitter utilizes digital baseband precoder F_{BB} to process the received original data stream $\mathbf{s} \in \mathbb{C}^{N_s \times 1}$, where $E[\mathbf{s}\mathbf{s}^H] = \mathbf{I}$. Then, the processed data stream is upconverted to the intermediate frequency using the RF link. Next, the intermediate

frequency data stream is processed by analog precoder \mathbf{F}_{RF} . Finally, the processed data stream is transmitted over channel $\mathbf{H} \in \mathbb{C}^{N_r \times N_t}$ via transmitting antennas.

After receiving the signal, the antenna at the receiving end first utilizes the analog precoder \mathbf{W}_{RF} to process the received signal, and then downconverts the intermediate-frequency signal to baseband using the RF link. Next, the signal is further processed with the digital baseband precoder \mathbf{W}_{BB} . Finally, the received signal at the receiver is given by

$$\begin{aligned} \hat{\mathbf{s}} &= \mathbf{W}_{\text{BB}}^H \mathbf{W}_{\text{RF}}^H \mathbf{y} \\ &= \mathbf{W}_{\text{BB}}^H \mathbf{W}_{\text{RF}}^H \mathbf{H} \mathbf{F}_{\text{RF}} \mathbf{F}_{\text{BB}} \mathbf{s} + \mathbf{W}_{\text{BB}}^H \mathbf{W}_{\text{RF}}^H \mathbf{n} \end{aligned} \quad (1)$$

Accordingly, the achievable rate of the hybrid precoding system can be expressed as

$$R = \log \det \left(\mathbf{I} + \frac{\mathbf{W}_{\text{BB}}^H \mathbf{W}_{\text{RF}}^H \mathbf{H} \mathbf{F}_{\text{RF}} \mathbf{F}_{\text{BB}} \mathbf{F}_{\text{BB}}^H \mathbf{F}_{\text{RF}}^H \mathbf{H}^H \mathbf{W}_{\text{RF}} \mathbf{W}_{\text{BB}}}{\sigma^2 \mathbf{W}_{\text{BB}}^H \mathbf{W}_{\text{RF}}^H \mathbf{W}_{\text{RF}} \mathbf{W}_{\text{BB}}} \right). \quad (2)$$

2.2. Channel Model

We adopt extended Saleh Valenzuela (S-V) channel model [9,10] in this paper, where the signal transmitted from the base station will reach the user after a finite number of scatterings.

This model assumes that the number of scattering clusters is N_{cl} with each cluster containing N_{ray} transmission paths, and the inequality $N_{RF}^t \leq N_{cl} N_{ray} \leq \min(N_t, N_r)$ should be satisfied. Here, N_{RF}^t is the number of RF links at the transmitter, $\min(\bullet)$ is the obtained minimum, and N_t, N_r are the number of antennas at the transmitter and receiver, respectively. As a result, the narrowband discrete-time channel matrix [11] can be expressed as

$$\mathbf{H} = \sqrt{\frac{N_t N_r}{N_{cl} N_{ray}}} \sum_{i=1}^{N_{cl}} \sum_{l=1}^{N_{ray}} \alpha_{i,l} \mathbf{a}_r(\theta_{i,l}^r, \varphi_{i,l}^r) \mathbf{a}_t(\theta_{i,l}^t, \varphi_{i,l}^t)^H, \quad (3)$$

where independent and identically distributed $\alpha_{i,l}$ is the gain coefficient of the l -th transmission path of the i -th cluster yielding zero mean and $\sigma_{\alpha,i}^2$ variance, where $\sigma_{\alpha,i}^2$ is the average power of the i -th cluster. $\mathbf{a}_r(\theta_{i,l}^r, \varphi_{i,l}^r)$ and $\mathbf{a}_t(\theta_{i,l}^t, \varphi_{i,l}^t)$ represent the response vector of antenna arrays at the receiver and transmitter, respectively. $(\bullet)^H$ denotes the conjugate transposition of a vector. $\theta_{i,l}^r \in [0, 2\pi)$ and $\theta_{i,l}^t \in [0, 2\pi)$ are the horizontal arrival angle and departure angle of the l -th transmission path of the i cluster, respectively. Similarly, $\varphi_{i,l}^r \in [0, 2\pi)$ and $\varphi_{i,l}^t \in [0, 2\pi)$ denote the vertical arrival angle and departure angle of the l -th transmission path of cluster i , respectively.

In this paper, the antenna arrays at the transceivers are considered to be uniform square planar array (USPA)[8]. For a typical uniform planar array with \sqrt{N} horizontal elements and \sqrt{N} vertical elements, $a(\varphi, \theta)$ satisfies the following conditions:

$$\mathbf{a}(\varphi, \theta) = \frac{1}{N} \left[1, \dots, e^{j2\pi \frac{d}{\lambda} (m \sin(\varphi) \sin(\theta) + n \cos(\theta))}, \dots, e^{j2\pi \frac{d}{\lambda} ((\sqrt{N}-1) \sin(\varphi) \sin(\theta) + (\sqrt{N}-1) \cos(\theta))} \right]^T, \quad (4)$$

where λ is the single wave wavelength. For a uniform planar array, d_1 and d_2 are the horizontal and vertical spacing of the antennas, respectively. We suppose that $d = d_1 = d_2 = \lambda / 2$ is satisfied for the considered millimeter wave settings.

2.3. Optimization Problem

With reference to [12,13], the formulated problem can be expressed as

$$\begin{aligned} \min_{\mathbf{F}_{\text{BB}}, \mathbf{F}_{\text{RF}}} & \left\| \mathbf{F}_{\text{opt}} - \mathbf{F}_{\text{RF}} \mathbf{F}_{\text{BB}} \right\|_F \\ \text{s.t.} & \mathbf{F}_{\text{RF}} \in f_{\text{RF}} \\ & \left\| \mathbf{F}_{\text{RF}} \mathbf{F}_{\text{BB}} \right\|_F = N_s \end{aligned} \quad (5)$$

where f_{RF} is the set of all feasible simulated beam vectors.

3. Precoding Matrix Design

In a nutshell, the main task for designing a precoder is to solve a matrix factorization problem while satisfying specific constraints, as shown in equation (4).

In the hybrid precoding scheme, the columns in the digital precoding matrix are orthogonal with each other, which can be rewritten as

$$\mathbf{F}_{\text{BB}}^H \mathbf{F}_{\text{BB}} = \alpha \mathbf{I}_{N_s}. \quad (6)$$

Then, it is plausible to fix the digital precoding matrix and then obtain the optimal solution of analog precoding according to the least square criterion. Based on the analysis, the problem can be described as

$$\arg \min_{\mathbf{F}_{\text{RF}}} \left\| \mathbf{F}_{\text{opt}} - \mathbf{F}_{\text{RF}} \mathbf{F}_{\text{BB}} \right\|_F, \mathbf{F}_{\text{RF}} \in f_{\text{RF}}. \quad (7)$$

The matrix $\mathbf{F}_{\text{opt}} = \mathbf{F}_{\text{RF}} \mathbf{F}_{\text{BB}}$ in (7) can be transformed as

$$\mathbf{F}_{\text{opt}} \mathbf{I}_{N_s} = \mathbf{F}_{\text{RF}} \mathbf{I}_{N_s} \mathbf{F}_{\text{BB}}. \quad (8)$$

Right multiplying \mathbf{F}_{BB}^H at the both sides of equation (8), equation (6) is rewritten as

$$\mathbf{F}_{\text{opt}} \mathbf{F}_{\text{BB}}^H = \alpha \mathbf{F}_{\text{RF}} \mathbf{I}_{N_s}. \quad (9)$$

Based on equation (9), the analog precoding matrix can be obtained as

$$\mathbf{F}_{\text{RF}} = \frac{\mathbf{F}_{\text{opt}} \mathbf{F}_{\text{BB}}^H}{\alpha}. \quad (10)$$

Because of the modular constraint of \mathbf{F}_{RF} , the analog precoding matrix can be written as

$$\mathbf{F}_{\text{RF}} = \exp(i \cdot \arg\{\mathbf{F}_{\text{opt}} \mathbf{F}_{\text{BB}}^H\}). \quad (11)$$

Considering that the columns in the digital precoding are orthogonal to each other, we can finally find \mathbf{F}_{RF} based on equation (11), as given by

$$\mathbf{F}_{\text{RF}} = \exp(i \cdot \arg\{\mathbf{F}_{\text{opt}} (\mathbf{F}_{\text{BB}})^{-1}\}). \quad (12)$$

Accordingly, the digital precoding matrix can be solved by the following least square method:

$$\mathbf{F}_{\text{BB}} = (\mathbf{F}_{\text{RF}}^{\text{H}} \mathbf{F}_{\text{RF}})^{-1} \mathbf{F}_{\text{RF}}^{\text{H}} \mathbf{F}_{\text{opt}}. \quad (13)$$

Based the above analysis, the calculation formulas of digital precoding matrix and analog precoding matrix can be obtained, so the iterative solution can be obtained by alternating minimization method.

4. Algorithm Design

Firstly, the analog precoding matrix and the digital precoding matrix are obtained by preprocessing the orthogonal matching pursuit algorithm. Then, the analog precoding matrix is updated by the phase information extracted from the digital precoding matrix and the optimal digital precoding matrix. Finally, the local optimal solution is iteratively obtained under the least square criterion and modulus constraint.

The implementation process of AIPO algorithm is summarized in Algorithm 1.

Algorithm 1: Alternating Minimization of Inverse Matrix of Phase Extraction based on Orthogonal Matching Pursuit (AIPO) Hybrid Precoding Algorithm:

Require: $\mathbf{F}_{\text{opt}}, \mathbf{A}_t, N_{\text{RF}}^i$

Initialization: $\mathbf{F}_{\text{RF}} = \mathbf{0}_{N_{\text{RF}} \times N_{\text{RF}}}, \mathbf{F}_{\text{BB}} = \mathbf{0}_{N_{\text{RF}} \times N_s}, k = 0, \mathbf{F}_{\text{res}} = \mathbf{F}_{\text{opt}}$;

1: **for** $i = 1 : N_{\text{RF}}^i$ **do**

2: Get analog precoding vector \mathbf{F}_{RF}^i :count $\Psi = \mathbf{A}_t^{\text{H}} \mathbf{F}_{\text{res}} \rightarrow \mathbf{F}_{\text{RF}}^i = \mathbf{A}_t^{(\arg \max_{i=1,2,\dots,N_{\text{RF}}^i} (\Psi \Psi^{\text{H}})_{ii})}$;

3: Update analog precoding matrix: $\mathbf{F}_{\text{RF}} = [\mathbf{F}_{\text{RF}} \mid \mathbf{F}_{\text{RF}}^i]$;

4: Update digital precoding matrix: $\mathbf{F}_{\text{BB}} = (\mathbf{F}_{\text{RF}}^{\text{H}} \mathbf{F}_{\text{RF}})^{-1} \mathbf{F}_{\text{RF}}^{\text{H}} \mathbf{F}_{\text{opt}}$;

5: Update residual matrix: $\mathbf{F}_{\text{res}} = \frac{\mathbf{F}_{\text{opt}} - \mathbf{F}_{\text{RF}} \mathbf{F}_{\text{BB}}}{\|\mathbf{F}_{\text{opt}} - \mathbf{F}_{\text{RF}} \mathbf{F}_{\text{BB}}\|_F}$;

6: **end for**

7: Normalized digital precoding matrix: $\mathbf{F}_{\text{BB}} = \sqrt{N_s} \frac{\mathbf{F}_{\text{BB}}}{\|\mathbf{F}_{\text{RF}} \mathbf{F}_{\text{BB}}\|_F}$;

8: **while** the iteration condition is satisfied **do**

9: Update the analog precoding matrix: $\arg\{\mathbf{F}_{\text{RF}}^{(k+1)}\} = \arg\{\mathbf{F}_{\text{opt}} (\mathbf{F}_{\text{BB}})^{-1}\}$, where $\arg\{\cdot\}$ is the phase information of the matrix.

10: Update digital precoding matrix: $\mathbf{F}_{\text{BB}} = (\mathbf{F}_{\text{RF}}^{\text{H}} \mathbf{F}_{\text{RF}})^{-1} \mathbf{F}_{\text{RF}}^{\text{H}} \mathbf{F}_{\text{opt}}$;

11: $k = k + 1$;

12: **end while**

13: Normalized digital precoding matrix: $\mathbf{F}_{\text{BB}} = \sqrt{N_s} \frac{\mathbf{F}_{\text{BB}}}{\|\mathbf{F}_{\text{RF}} \mathbf{F}_{\text{BB}}\|_F}$.

14: **Return:** $\mathbf{F}_{\text{RF}}, \mathbf{F}_{\text{BB}}$

5. Simulation Result and Algorithm Complexity Analysis

5.1. Simulation Setup

The simulation parameters are listed in Table 1.

Table 1. Simulation Parameters

Parameter name	Parameter value
Number of transmitting antennas N_t	256
Number of receiving antennas N_r	36
Antenna spacing d	$\lambda/2$
Number of clusters N_{cl}	5
Number of scatterers N_{ray}	10
Average power of clusters	1
Average power of transmitter P_{common}	10W
RF link power P_{RF}	100mW
Phasor power P_{PS}	10mW
Power amplifier power P_A	100mW

5.2. Simulation Performance Analysis

For comparison, we consider the PE-AltMin algorithm proposed in reference [14] and OMP-PE-AltMin algorithm initialized by OMP as benchmarks.

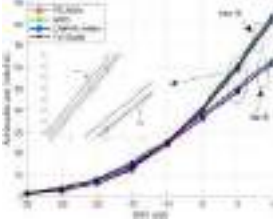


Figure 2. Spectrum Efficiency Curves with the Change of SNR.

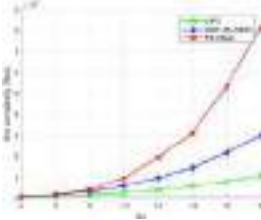


Figure 3. Algorithm Complexity Curves under Different Data Stream Numbers.

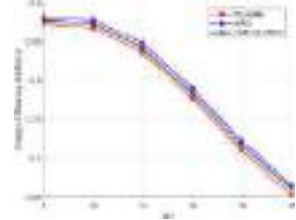


Figure 4. Energy Efficiency Curves under Different Data Stream Numbers.

In Figure 2, we show the spectrum efficiency versus SNR values of AIPO, PE-AltMin, optimal pure digital precoding, and OMP-PE-AltMin. The number of RF links at the base station and the receiving end equal to the number of data streams, i.e., $N_s = N'_{RF} = N''_{RF} = \{ 8, 16 \}$. It can be seen that the AIPO algorithm proposed in this paper achieves comparable achievable rate to the optimal pure digital precoding. Moreover, AIPO outperforms both PE-AltMin and OMP-PE-AltMin.

In Figure 3, we show the algorithm complexity of AIPO and the benchmarks under different data stream numbers, i.e. $N_s = N'_{RF} = N''_{RF} = \{ 4, 6, 8, 10, 12, 14, 16, 18 \}$. It is obtained that the algorithm complexity of the proposed AIPO is much lower than that of the benchmarks. This effectively validates the viability of AIPO.

In Figure 4, we plot the energy efficiency of AIPO and the benchmarks under different data stream numbers, i.e., $N_s = N'_{RF} = N''_{RF} = \{ 8, 10, 12, 14, 16, 18 \}$. It is

obtained that the energy efficiency of AIPO is significantly higher than PE-AltMin and OMP-PE-AltMin. Therefore, the proposed AIPO is capable of preserving more energy.

5.3. Complexity Analysis

In this paper, the AIPO algorithm is initialized by OMP, and then the analog precoding matrix is obtained by updating the phase information of the digital precoding matrix and the optimal precoding matrix. Based on the obtained analog precoding matrix, the digital precoding matrix is updated according to the least square criterion. The digital precoding matrix and the analog precoding matrix will be iteratively updated until the predefined convergence conditions are satisfied.

The complexity of OMP initialization algorithm is summarized in Table 2. The complexity of AIPO iterative algorithm is concluded in Table 3. The complexity of PE-Altmin iterative algorithm is shown in Table 4.

Table 2. The Complexity of OMP [1] Initialization Algorithm, where $L = N_{cl} \times N_{ray}$

Step	Operation	Complexity
1	$\Psi = \mathbf{A}_t^H \mathbf{F}_{res}$	$8L N_t N_s$
2	$k = \arg \max_{l=1,2,\dots,N_t N_{ray}} (\Psi \Psi^H)_{l,l}$	$8L^2 N_s$
3	$\mathbf{F}_{BB} = (\mathbf{F}_{RF}^H \mathbf{F}_{RF})^{-1} \mathbf{F}_{RF}^H \mathbf{F}_{opt}$	$2N_{RF}^{t^3} - 2N_{RF}^{t^2} + N_{RF}^t + 8N_{RF}^{t^2} N_t + 8N_t N_{RF}^t N_s$
4	$\mathbf{F}_{res} = \frac{\mathbf{F}_{opt} - \mathbf{F}_{RF} \mathbf{F}_{BB}}{\ \mathbf{F}_{opt} - \mathbf{F}_{RF} \mathbf{F}_{BB}\ _F}$	$8N_t N_{RF}^t N_s + 2N_t N_s$

Table 3. The Complexity of AIPO Iterative Algorithm

Step	Operation	Complexity
1	$\arg\{\mathbf{F}_{RF}^{(k+1)}\} = \arg\{\mathbf{F}_{opt} (\mathbf{F}_{BB})^{-1}\}$	$N_t N_{RF}^t + 8N_t N_{RF}^t N_s$
2	$\mathbf{F}_{BB} = (\mathbf{F}_{RF}^H \mathbf{F}_{RF})^{-1} \mathbf{F}_{RF}^H \mathbf{F}_{opt}$	$2N_{RF}^{t^3} - 2N_{RF}^{t^2} + N_{RF}^t + 8N_{RF}^{t^2} N_t + 8N_t N_{RF}^t N_s$

Table 4. The Complexity of PE-Altmin [8] Iterative Algorithm

Step	Operation	Complexity
1	$\Psi = (\mathbf{F}_{opt})^H \mathbf{F}_{RF}^{(k)}$	$8N_t N_{RF}^t N_s$
2	$\Psi = \mathbf{U}^{(k)} \Sigma^{(k)} (\mathbf{V}^{(k)})^H$	$72N_s^3 + 64N_{RF}^t N_s^2 + 32N_{RF}^{t^2} N_s$
3	$\mathbf{F}_{BB}^{(k)} = \mathbf{V}^{(k)} (:, 1 : N_s) (\mathbf{U}^{(k)})^H$	$8N_{RF}^t N_s^2$
4	$\arg\{\mathbf{F}_{RF}^{(k+1)}\} = \arg\{\mathbf{F}_{opt} (\mathbf{F}_{BB}^{(k)})^H\}$	$N_t N_{RF}^t + 8N_t N_{RF}^t N_s$

In Table 5, it is seen that AIPO not only achieves better performance than PE-AltMin and OMP-PE-AltMin, but requires much fewer iterations than the benchmarks to reach convergence. Quantitatively speaking, the proposed AIPO complexity is reduced by 66.90% regarding PE-AltMin and 86.32% regarding OMP-PE-AltMin.

Table 5. Comparison of required iterations, where $N_s = N_{RF}^t = N_{RF}^r = 18$

Algorithm	Initialization complexity	Single iteration complexity	Average number of iterations	Total complexity
AIPO	75853908	2006298	14.79	1.0553×10^8
OMP-PE-AltMin	75853908	2358144	103.0506	3.1886×10^8
PE-AltMin	4608	2358144	327.2079	7.71118×10^8

6. Conclusion

This paper investigated the problem of hybrid precoding for single user millimeter wave MIMO systems. We proposed AIPO hybrid precoding algorithm to solve the formulated problem. The proposed AIPO enjoyed significant improvement in both spectrum and energy efficiency, which achieved performance close to pure digital precoding algorithm. Besides, the complexity of the algorithm was far less than state-of-the-art benchmarks. Simulation results validated that AIPO can be effectively utilized as a hybrid precoding solution with relatively low complexity and satisfactory performance.

The algorithm proposed in this paper is not significant for the improvement of algorithm complexity when the system performance requirement is not high. In the future, we will focus on the computational complexity optimization for the case of relaxed iteration requirements.

Acknowledgements

This work was supported by the National Natural Science Foundation of China (NSFC, No.61531007)

References

- [1] Ayach O E, Rajagopal S, Abu-Surra S, et al. Spatially sparse precoding in millimeter wave MIMO systems. *IEEE Transactions on Wireless Communications*, 2014, 13(3):1499-1513.
- [2] M. A. Azam, A. K. Dutta and A. Mukherjee. Downlink Precoding for Hybrid Fully Connected Linear Subarrays in mmWave With Rainfall Scattering and Hardware Impairments. *IEEE Transactions on Vehicular Technology*, 2022, 71(5):5143-5155.
- [3] X. Qiao, Y. Zhang, H. Cao, Z. Xu and L. Yang. Hybrid Precoders and Combiners for Sub- Connected and Fully Connected Structures. *IEEE International Conference on Consumer Electronics - Taiwan (ICCE-TW)*, 2019:1-2.
- [4] X. Liu, W. Chen and J. Chu. Behavioral Modeling and Digital Predistortion for Fully-Connected Hybrid Beamforming Massive MIMO Transmitters. *2020 IEEE Asia-Pacific Microwave Conference (APMC)*, 2020:463-465.
- [5] Sohrabi Foad, Yu Wei. Hybrid digital and analog beamforming design for Large-scale antenna arrays. *IEEE Journal of Selected Topics in Signal Processing*, 2016, 10(3):501-513.
- [6] A. Osama, M. Elsaadany, S. I. Shams, A. M. A. Omar, U. S. Mohammed and G. Gagnon. Hybrid Precoder Design for mmWave Massive MIMO Systems with Partially Connected Architecture. *International Symposium on Networks, Computers and Communications (ISNCC)*, 2021:1-6.
- [7] L. Pang et al. Iterative Hybrid Precoding and Combining for Partially-Connected Massive MIMO mmWave Systems. *IEEE 92nd Vehicular Technology Conference (VTC2020-Fall)*, 2020:1-5.
- [8] X. Yu, J. Shen, J. Zhang and K. B. Letaief. Alternating Minimization Algorithms for Hybrid Precoding in Millimeter Wave MIMO Systems," in *IEEE Journal of Selected Topics in Signal Processing*, vol. 10, no. 3, pp. 485-500, April 2016.
- [9] Alkhateeb A, Ayach O E, Leus G, et al. Channel estimation and hybrid precoding for millimeter wave cellular systems. *IEEE Journal of Selected Topics in Signal Processing*, 2014, 8(5):831-846.
- [10] Bai T, Alkhateeb A, Heath R W. Coverage and capacity of millimeter-wave cellular networks. *IEEE Communications Magazine*, 2014, 52(9):70-77.
- [11] Samimi M K, Rappaport T S. 3-D statistical channel model for millimeter-wave outdoor mobile broadband communications. *IEEE International Conference on Communications*. London, UK: IEEE Press, 2015:2430-2436.
- [12] O. El Ayach, S. Rajagopal, S. Abu-Surra, Z. Pi, and R. W. Heath. Spatially sparse precoding in millimeter wave MIMO systems. *IEEE Trans. Wireless Commun.*, 2014, 13(3):1499–1513.
- [13] Y. Lee, C. Wang, and Y. Huang. A hybrid RF/baseband precoding processor based on parallel-index-selection matrix-inversion-bypass simultaneous orthogonal matching pursuit for millimeter wave MIMO systems. *IEEE Trans. Signal Process.*, 2015, 63(2):305–317.

The Continuous Time Dynamical Analysis of Heart Rate Asymmetry

Yi-Horng LAI, Jiahan YU¹, Kun SU, Lin LAN, Zexin LI, Zequn ZHANG, Zifeng ZHUANG

School of Mechanical and Electrical Engineering, Xiamen University Tan Kah Kee College, Zhangzhou 363105, China

Abstract. Heart rate asymmetry (HRA) can investigate the asymmetric characteristics that cannot be analyzed by traditional heart rate variability (HRV). The asymmetric pattern of heart rate acceleration and deceleration can be described by the projection of RR interval (RRI) series on the Poincaré plot. In this study, two new asymmetric variables of HRA are proposed. By using the moving window method, the dynamical analysis of HRA can be illustrated on the time series diagram. Two kinds of physiological experiments and an artificial chaotic RRI system are evaluated. The binomial experimental results (p-value: 0.004) verify that the proposed method can quickly and effectively respond to the HRA.

Keywords. Heart rate asymmetry, HRV, artificial chaos system, Poincaré plot

1. Introduction

Heart rate variability (HRV) is used to measure the variation of RR interval (RRI) of ECG. Previous studies proved that HRV can investigate the sympathetic-parasympathetic system and autonomic activity [1]. Recently, some new methods of HRV have been proposed to extract the asymmetrical information of heart rate acceleration and deceleration. By using Poincaré plot geometry, Heart rate asymmetry (HRA) can evaluate the asymmetrical energy distribution of heart rate acceleration and deceleration [2].

In [3], the authors consider the geometric distribution of the Poincaré plot of HRA. Two characteristic variables $SD1_{up}$ and $SD1_{down}$ are defined. The variables of HRA can correspond to the deceleration and acceleration variance of short-term HRV, respectively. The results of ECG experiments validated that the healthy adults existed a statistically significant asymmetry in heart rate. Furthermore, the authors introduced two long-term characteristic variables: $SD2_{up}$ and $SD2_{down}$. The experimental results showed that 76% of the subjects had long-term HRA [4].

The long-term correlation of bio-signals can be evaluated by Detrended Fluctuation Analysis (DFA). J. Piskorski proposed the Asymmetric Detrended fluctuation Analysis (ADFA) method and found that RRI had the global and local asymmetry scaling exponents. In addition, when the artificial synthetic signal is added with asymmetric noise, the asymmetric phenomenon can be observed by using ADFA [5].

¹ Corresponding Author, School of Mechanical and Electrical Engineering, Xiamen University Tan Kah Kee college; E-mail: yujiahan@stu.xmu.edu.cn

The bio-signal data analysis is a critical and useful method, especially for epidemic prevention and control [6, 7]. The previous studies validated that HRA can be used to evaluate the activities of the cardiovascular system [8, 9]. However, the previous study only discussed HRA on a fixed time scale. More exploratory and practical studies are needed to investigate the dynamic variation of HRA.

The motivation of this study includes three parts:

1. Design the binomial hypotheses experiment and evaluate HRA asymmetrical characteristics on the Poincaré plot.
2. By using the moving window method, observe and validate that the proposed asymmetric variables can reflect the dynamic variation of HRA.
3. Design an artificial chaotic RRI system and investigate whether the artificial RRI series has the same asymmetric characteristics as the real RRI series.

2. Experimental Method

When the RRI series is in a stable condition, the projection of RRI series on the Poincaré plot must be around a fixed attractor. The two energy variables (i.e. $SD1^2_{up}$ and $SD1^2_{down}$) can correspond to the variances of HR deceleration and acceleration, respectively. Furthermore, the asymmetry of HRA can be expressed that the variance of RRI series is not a normal distribution.

Poincaré plot is a nonlinear dynamic method to describe the variation of RRI series. Each RRI pair (i.e. RR n, RR n+1) can be marked on a two-dimensional phase space coordinate. On the plot, the standard deviation of the distance between each RRI pair to the straight line (L1): $y = x$ and (L2): $y = -x$ is defined as $SD1^2$, $SD2^2$, respectively (Fig. 1). $SD1^2$ corresponds to rapid variability and $SD2^2$ corresponds to long-term variability. The detailed quantitative method of HRA can be referred to [3].

In Fig. 1, with line L1 as the boundary, the RRI points falling above L1 are classified as $SD1^2_{up}$ area, representing the time of the next RRI becoming longer (i.e. the heart rate becomes slower). On the other hand, the points falling below L1 are classified as $SD1^2_{down}$ area, representing that the heart rate becomes faster. For healthy physiology, the heart rate always maintains at a stable interval. When RRI series are projected to the phase space plane, the statistics distributed in the up area seem should be consistent with that of the down area. In this study, the Binomial test is used to evaluate the asymmetric probability distribution on the Poincaré plot.

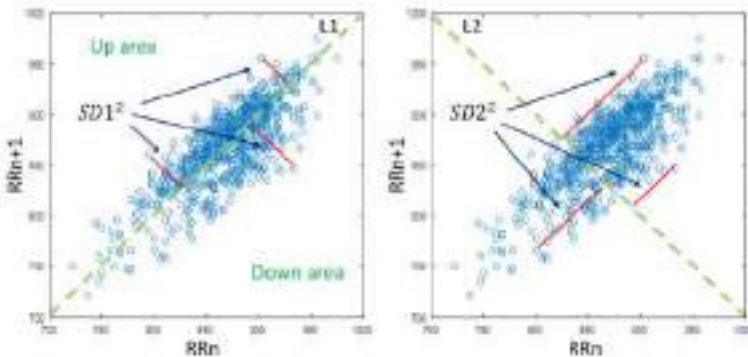


Figure 1. The projection of RRI series on the Poincaré plot.

2.1. Binomial Hypothesis of Heart Rate Asymmetry

Twenty-two healthy adults (21 males and 1 female, aged from 21 to 45 years) were measured by electrocardiography (ECG) in sitting posture for 5 minutes. After the automatic R wave detection process, the 300 RRI pairs were extracted from each subject's ECG. The RRI series were drawn on the Poincaré plot. The energy index ($SD1_{up}^2$ and $SD1_{down}^2$) were calculated, respectively.

Under the assumption of normal distribution and no interpersonal difference, half of the subjects should have $SD1_{up}^2 < SD1_{down}^2$ and vice versa. Therefore, the sample proportion P (i.e. the subjects with $SD1_{up}^2 < SD1_{down}^2$) should be 0.5. The binomial test of HRA is as follows (the significance level α is 0.05):

H_0 : The sample proportion $P = 0.5$; H_1 : The sample proportion $P \neq 0.5$.

2.2. The Continuous Time Dynamical Analysis of HRA

The previous studies only considered the asymmetrical characteristics of HRA at a specific time scale. To clarify the dynamic properties of HRA, the moving window method was used to explore the dynamic variation of HRA.

The asymmetry of HRA means that there will be more RRI points falling on the up area but less $SD1_{up}^2$ energy, and vice versa. To conveniently evaluate the results of dynamic analysis, two new asymmetric indexes of HRA are proposed:

$$SD1_{u-d}^2 = SD1_{up}^2 - SD1_{down}^2, \tag{1}$$

$$HRA_{P_{u-d}} = HRA_{P_{up}} - HRA_{P_{down}}, \tag{2}$$

where $HRA_{P_{up}}$, $HRA_{P_{down}}$ means the RRI points are located in the up area and down area, respectively. $HRA_{P_{u-d}}$ is the difference of RRI point number between up and down area.

By using the moving window and recursive method, move one RRI series at a time. The new asymmetric index can reflect the dynamical variation of HRA. The flowchart of the dynamical analysis of HRA and comparison diagram are in Fig. 2.

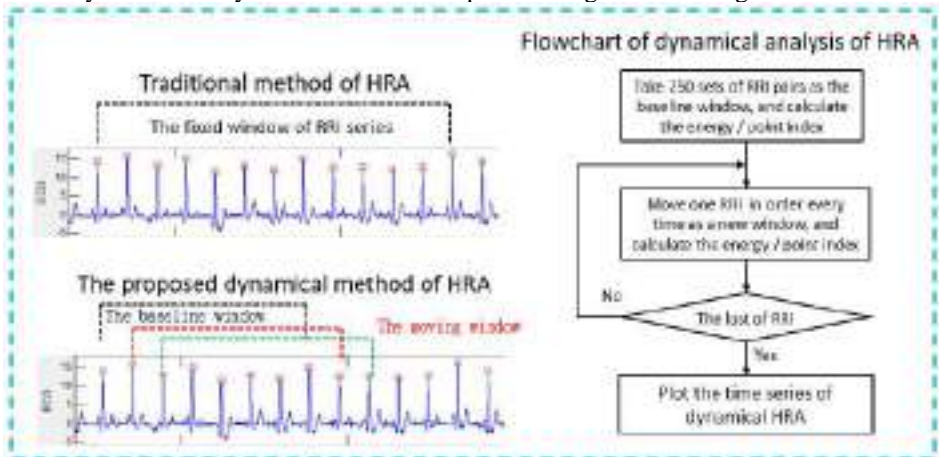


Figure 2. The flowchart of dynamical analysis of HRA and comparison diagram.

Two scenarios of physiological activities were designed to evaluate the dynamic analysis of HRA.

Scenario 1: Measure a 12-minute ECG of a healthy adult in a sober and sitting posture.

Scenario 2: Measure the ECG of a healthy adult taking a siesta. At the same time, record the start and end times of the siesta.

2.3. The Dynamical Analysis of HRA for artificial RRI series

Artificial bio-signals have great potential for application. Artificial bio-signals must have the same dynamic characteristics as real physiological signals.

In this study, the chaotic RRI system is designed. By adjusting the coefficients of Duffing equation, the artificial RRI series has the dynamic characteristics of self-similar. When the chaotic RRI series are projected on the Poincaré plot, the chaotic RRI signal appears the strange attractors similar to the real RRI series. The proposed dynamic analysis method is used to verify whether the chaotic RRI series has an asymmetric phenomenon similar to the real RRI series.

3. Experimental Results

3.1. The Experimental Result of Binomial test

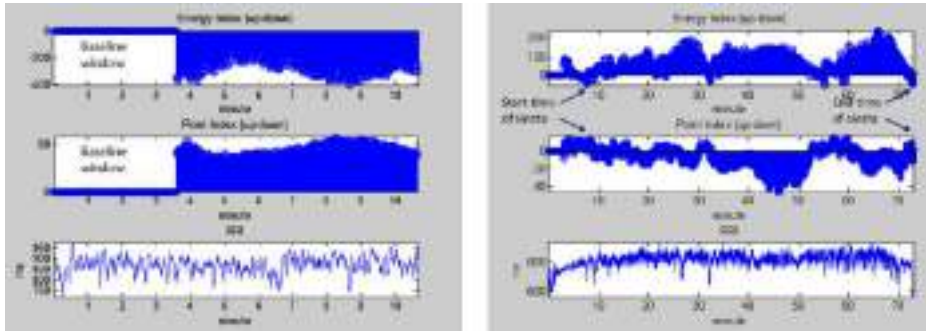
All variables of HRA in 22 subjects are listed in Table 1. Only three subjects (No. 10, 16, and 17) have higher $SD1^2_{up}$. Therefore, the sample proportion $P = \frac{19}{22} = 0.86$. Due to the $n=22$, binomial distribution $\mu = 11$ and $\sigma = \sqrt{nPQ} = 2.345$, the p -value is 0.004. The hypothesis of H_0 must be rejected. The p -value validates the asymmetry of HRA.

Table 1. HRA Characteristic Variables of 22 Subjects

No.	Mean of RRI (ms)	$SD1^2$	$SD1^2_{up}$	$SD1^2_{down}$	Points in the up area	Points in the down area
1	924.75	378.36	164.85	213.5	154	130
2	736.62	902.93	424.66	478.26	146	138
3	685.48	29.24	10.17	19.06	109	105
4	672.23	209.4	98	111.39	136	121
5	731.35	208.26	67.74	140.51	160	113
6	936.6	3474.6	1695.8	1778.7	156	139
7	907.77	591.12	240.72	350.39	168	122
8	824.64	417.83	186.63	231.19	154	136
9	685.29	20.19	9.61	10.57	110	104
10	772.16	809.3	437.47	371.82	137	140
11	861.77	850.06	424.27	425.79	152	143
12	897.26	761.18	365.58	395.59	150	140
13	973.62	762.97	362.75	400.22	154	138
14	860.08	368.33	128.6	239.72	181	101
15	818.4	692.78	266.35	426.42	174	119
16	866.6	317.69	159.05	158.63	143	139
17	968.32	2901.9	1463.2	1438.7	153	137
18	828.04	399.83	149.93	249.9	170	111
19	792.94	637.32	235.31	402	174	113
20	863.74	1271	601.9	669	161	128
21	943.54	683.33	295.08	388.24	164	129
22	996.14	430.23	210.28	219.94	142	143

3.2. The Experimental Result of Continuous Time Dynamical Analysis

The experimental results of the two scenarios are in Fig. 3. In Fig. 3 (a), the asymmetry variables of HRA appear stably in the time series diagram. In the sober condition, the energy of $SD1_{up}^2$ is steadily lower than $SD1_{down}^2$. The new index $SD1_{u-d}^2$ remains at a negative value, indicating that the asymmetric energy distribution is a persistent asymmetry. On the other hand, the Point index $HRA_{P_{u-d}}$ is always at a positive value, indicating that the RRI points falling in the up area are steadily higher than that of the down area.



(a) Scenario 1 experimental result (sober state). (b) Scenario 2 experimental result (siesta state).

Figure 3. Continuous time dynamical analysis of HRA.

In Fig. 3 (b), the proposed index shows another characteristic of HRA. When physiological activity transfers from a sober state to a sleeping state, the asymmetry changes in the opposite direction immediately. When siesta starting, the energy of $SD1_{up}^2$ is steadily higher than $SD1_{down}^2$. $SD1_{u-d}^2$ is a positive value in most moving windows.

Although the $HRA_{P_{u-d}}$ is not as stable as that of scenario 1, we can still observe that the RRI points fallen on the up area are fewer in the most moving windows. Scenario 2 experiment illustrated that the direction reverses of asymmetric took place immediately with physiological state transform. The proposed new asymmetric index can describe the different physiological states in real-time.

3.3. The Experimental Result of artificial RRI series

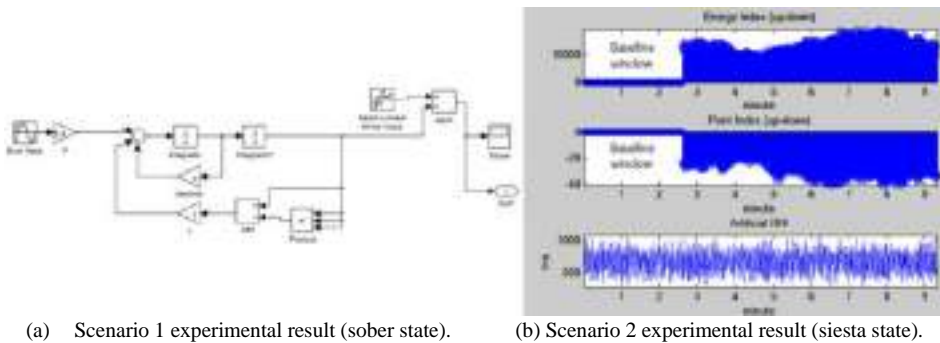
Duffing equation was used in the RRI chaotic system to generate an artificial RRI series. The Duffing equation is defined as follows:

$$\ddot{x}(t) + \gamma \dot{x}(t) - kx(t) + \zeta x^3(t) = F \cos \omega t, \tag{3}$$

where γ is the friction coefficient, F is the strength of the driving force with oscillate frequency ω , and k, ζ are constants.

Set $\gamma = 0.4, k = \zeta = 1, F = 1,$ and $\omega = 1,$ the Simulink model of the chaotic RRI system and the experimental result are illustrated in Fig. 4.

First, ten minutes of artificial RRI series are generated by the chaotic system (Fig. 4 (a)). By using the moving window method, the asymmetry of HRA appears stably in Fig. 4 (b). Just like the experimental result of scenario 2, the energy of $SD1_{up}^2$ is steadily higher than $SD1_{down}^2$. On the other hand, the Point index $HRA_{P_{u-d}}$ explains the artificial RRI points fallen on up area is steadily fewer than that of down area.



(a) Scenario 1 experimental result (sober state).

(b) Scenario 2 experimental result (siesta state).

Figure 4. HRA dynamical analysis of Artificial RRI.

4. Conclusion

In this study, the algorithm of continuous time dynamical analysis of HRA is proposed. By using the moving window method, two new HRA asymmetric variables ($SD1_{u-d}^2$, $HRA_{P_{u-d}}$) can effectively reflect the asymmetric characteristic of HRA on the Poincaré plot. Two real RRI series and an artificial RRI series are evaluated in the dynamical analysis of HRA. The proposed quantification method of HRA is also convenient for researchers to apply in different clinical environments.

Acknowledgment

This research was funded by Xiamen University Tan Kah Kee College (no. JGH2022005).

References

- [1] Voss, A., et al., Methods derived from nonlinear dynamics for analysing heart rate variability. *Philosophical Transactions of the Royal Society A: Mathematical, Physical and Engineering Sciences*, 2009. 367(1887): p. 277-296.
- [2] Piskorski, J., et al., Testing heart rate asymmetry in long, nonstationary 24 hour RR-interval time series. *Physiological Measurement*, 2019. 40(10): p. 105001.
- [3] Piskorski, J. and P. Guzik, Geometry of the Poincaré plot of RR intervals and its asymmetry in healthy adults. *Physiological Measurement*, 2007. 28(3): p. 287-300.
- [4] Piskorski, J. and P. Guzik, Asymmetric properties of long-term and total heart rate variability. *Medical & Biological Engineering & Computing*, 2011. 49(11): p. 1289-1297.
- [5] Piskorski, J., et al., Properties of Asymmetric Detrended Fluctuation Analysis in the time series of RR intervals. *Physica A: Statistical Mechanics and its Applications*, 2018. 491: p. 347-360.
- [6] Singh, P. and S.S. Bose, *A quantum-clustering optimization method for COVID-19 CT scan image segmentation*. *Expert Systems with Applications*, 2021. 185: p. 115637.
- [7] Singh, P. and S.S. Bose, Ambiguous D-means fusion clustering algorithm based on ambiguous set theory: Special application in clustering of CT scan images of COVID-19. *Knowledge-Based Systems*, 2021. 231: p. 107432.
- [8] Guzik, P. and J. Piskorski, Asymmetric properties of heart rate microstructure. *Journal of Medical Science*, 2020. 89(2): p. e436.
- [9] Shi, P., et al., The effect of passive lower limb training on heart rate asymmetry. *Physiological Measurement*, 2022. 43(1): p. 015003.

Continuous-Speech Spoken Dialogue System Based on Joint Decision-Making of Audio and Semantics

Qiuwei DENG^{abc,1}, Qiang PENG^{c,1}, Zhifang MA^c, Pei ZHAO^{c,1} and Di WANG^c

^aCollege of Computer Science, Chongqing University, Chongqing, China

^bState Key Laboratory of Digital Household Appliances, Qingdao, China

^cHaier Smart Home Intelligent Technology co. LTD, Beijing, China

Abstract. To avoid the frequent wakeups of general spoken dialogue systems, we studied continuous-speech spoken dialogue systems. The experiment results show that continuous-speech systems can efficiently enhance the success rate of interactions by 8%, in contrast with discontinuous ones. The full-duplex continuous-speech dialogue systems, which are continuously listening surrounding voices, are often interfered with by invalid sounds, such as the voice played on TV. Therefore, we have studied the audio recognition algorithm to reject those noises, and the experiments show that the recognition accuracy of this algorithm can reach about 94%. In this paper, we propose joint decision-making of audio and semantics, which can effectively reject invalid speech and further improve the success rate of interaction in continuous-speech spoken dialogue systems.

Keywords. Full-duplex, continuous-speech, broadcast sound, human voice, audio rejection

1. Introduction

In a general spoken dialogue system [1,2], the user wakes up a terminal device once, and waits for the terminal to turn on the listener. Then he speaks something, after which the audio data will be sent to the cloud service to do the subsequent procedures. During this process, users normally control the systems through their voices. However, the user must wake up the terminal every time before the real query is spoken [3]. Due to such frequent wakeups, it is rather challenging for users to control the timing, which may lead to interaction failure. Moreover, it is inconsistent with the natural dialogue pattern among human beings. As a result, we have developed continuous-speech dialogue technologies.

In Section 2 is a comparison experiment between continuous and discontinuous dialogue systems, which indicates that the interaction success rate of continuous dialogue system has a significant advantage over the discontinuous one.

Throughout the process of continuous dialogues, the device is in a sound-collecting state which may constantly collect invalid sounds in the environment [4] which can be classified into two categories:

¹ Corresponding Author, Qiuwei Deng, Qiang Peng, Pei Zhao, E-mail: {dengqiuwei, pengqiang.uh, zhaopei.uh}@haier.com.

1. Broadcast sounds: TV sounds, reply voices of speakers, etc.
2. Non-interactive order voices: chats among users, human voices when making phone calls, etc.

The correct way to deal with such invalid sound requests is to reject them through false rejection algorithms, which can reduce the disturbance to users.

Currently, the most commonly used algorithm of false rejection is to conduct semantic recognition based on texts transcribed from ASR. However, text semantic recognition is only capable of dealing with non-interactive orders, but is incapable of actions for broadcast sounds [5,6]. For instance, in a smart home scenario, queries containing hot words such as “air conditioner” or “fridge” are more likely to be parsed into “device control intentions”. If “it’s burning hot, turn on the air conditioner for me” is played on TV, the voice may be parsed into the intention of controlling the air conditioner. However, it’s not spoken by a real human, and thus shall be rejected [7]. Therefore, it is rather difficult for non-real-human sounds to be recognized at the level of text semantics.

Through analysis, it can be found that semantic recognition at the text level naturally lacks vital information in the process of spoken interaction: who is the speaker? We cannot make a judgment on who the speaker is from a text, nor tell whether it is from a real person or TV, while the audio contains that information.

Based on the above problems, we’ve put forward the algorithm of audio recognition (also called “audio rejection”) in continuous dialogues, in which speech orders can be divided into another two categories:

1. Human voices, including normal interactive human voices, human voices not interacting with devices, and clear human voices mingled with background sounds
2. Broadcast sounds (non-human voices), including media sounds, NLG reply audios of smart devices, and media sounds mingled with blurred human voices

In Section 3, a series of experiments on different parameters of the audio recognition model is conducted, and the results show that the recognition accuracy of human voice and broadcast sounds can reach 93.8% and 94.2% respectively.

By integrating the algorithms of semantic recognition and audio recognition, the continuous dialogue system can make effective rejection of both types of invalid speech, with the fluency and success rate improved to a certain extent.

At last, we make conclusions on this paper and propose further directions for future research.

2. Full-duplex Continuous-speech Spoken System

Continuous-speech dialogue is a highly integrated technology of speech interactions that involves multiple AI capabilities, which requires full-duplex communication technology for bi-directional information transmission, speech signal processing technology to tackle the noise problems of the device itself as well as its surroundings, and NLP (natural language processing) to accurately understand the intentions and conduct false rejection towards non-human voices [8]. By merely waking up the device once, users can continuously interact with it, which reduces the times of interactions as well as improves the success rate of interactions [9]. The main modules of the system can be referred to in Figure 1.

We conducted a series of simulation experiments to demonstrate the improved effectiveness of a continuous dialogue system compared to a discontinuous one.

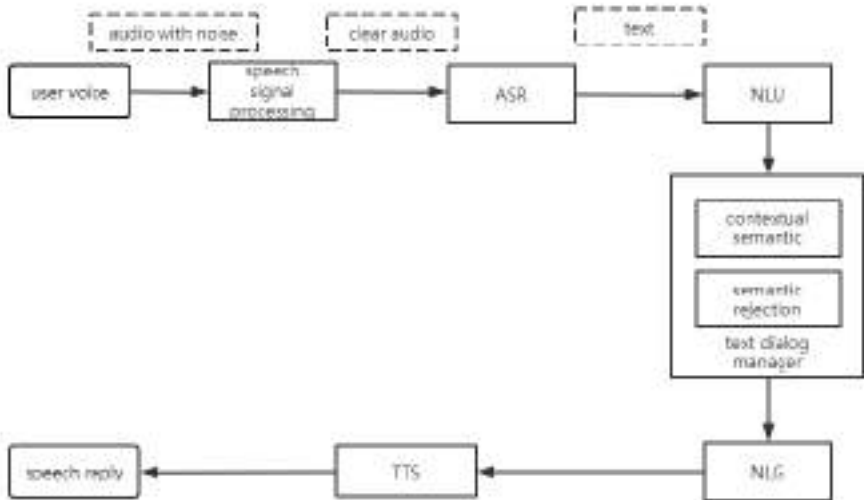


Figure 1. Modules of Continuous-Speech Spoken Dialogue System

2.1. Experiments

The mission data set of the simulation experiments are sorted out based on the data of real users, which chooses six most frequently-used functions of users, three functional data sets of home appliance control as well as three functional data sets of life services, including air conditioner control, fridge control, heater control, alarm schedule settings, song playing and weather inquiry. The basic principles for selecting data sets are:

1. Experimental tasks can be frequently used by users in their daily lives;
2. Users normally need to conduct continuous interactions for completing the tasks.

Basic principles of simulation experiments:

1. There is only one air conditioner, fridge and heater respectively which supports networking and voice control, excluding the number of additional interactions for device selection due to multiple devices that affect the accuracy and fairness of the experiment;

2. In order to avoid the interference of history data of contextual interactions among tasks, the simulation experiment is conducted in a serial manner;

In order to simulate the time fluctuation of quick answers and pauses between each round of interactions from real users, time fluctuations based on normal distribution are introduced into the simulation program:

$$X \sim N(\mu, \delta^2)$$

μ is the time length of reply messages played by the interactive system

δ is time deviation of users answering and pausing while the system plays the reply messages, with 1 second of assignment in the simulation program

Experiment procedures:

1. Initiate the speech interaction system service, with system data loading completed;
2. Initiate the simulation program, send requests to the speech interaction system service with HTTP protocol, and simulate the process of human-computer interactions;
3. The simulation program executes the task list cyclically:
 - (1) Load the data set of Task i ;
 - (2) Execute the data set of Task i ;
 - (3) Task execution is completed, and history interaction data is cleared;
 - (4) Execute the above step cyclically until all the tasks are completed;
4. Simulation tasks finish.

2.2. Experimental results

The statistics of the simulation experiment results are demonstrated in Table 1.

Table 1. Average Success Rate of Interactions in Experiment

Dataset	Amount	Non-continuous Dialogue (%)	Continuous Dialogue (%)
Air Conditioner	198	91.67	99.49
Fridge	126	92.06	100
Heater	215	91.86	100
Alarm	200	93.25	100
Music	201	88.06	100
weather	202	92.08	100

By comparing the average success rate of the two interaction modes and measuring the stability and friendliness of interactions of different systems, it can be concluded from the experiment that a higher value indicates a higher interaction success rate, while a lower value indicates a higher failure rate. As can be seen from Table 1, the interaction success rate of continuous dialogues is increased by about 8% relative to discontinuous dialogues.

The mode of non-continuous dialogue interaction requires users to wake up the device, wait for the system to reply and collect sounds, and send spoken orders. These four processes may fail without expected results as long as they are not paced correctly in time.

By contrast, users do not need to wake up the device frequently under continuous dialogue mode as the system is in the continuous full-duplex state of sound collecting. Therefore, there's no need for users to passively control the timing, with a more friendly interactive experience and lower error rates.

3. Algorithm and Model of Audio Recognition

In order to eliminate the interference of broadcast sounds in continuous dialogues, we did an analysis of human speech and broadcast sounds from the perspective of audio features.

There are comparisons of waveform and spectrum of two audio which are shown in Figure 2 and 3. The first audio is spoken by a real person, and the second one is a

record that the first audio played by the device. The recording parameters both are 16kHz sampling rate and a single channel.

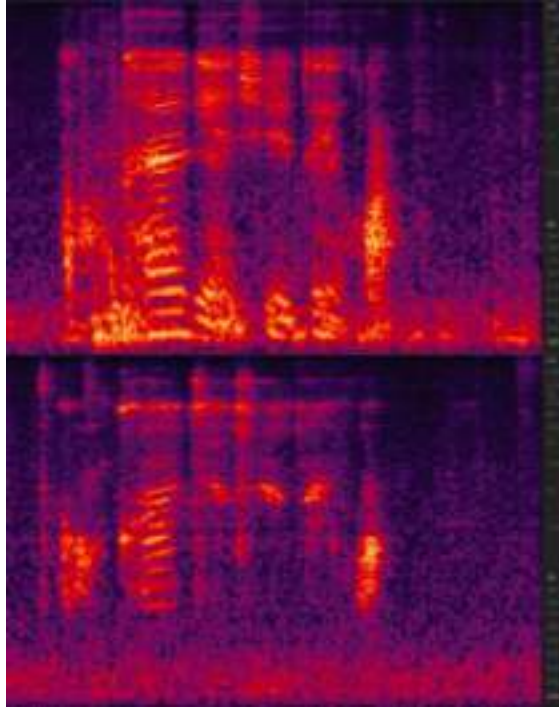


Figure 2. Spectrum Comparison of Two Audio Segments.

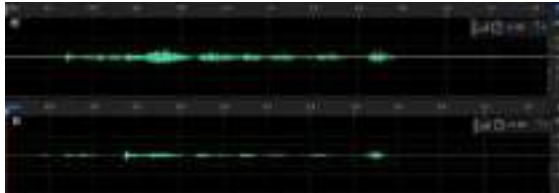


Figure 3. Waveform Comparison of Two Audio Segments.

It can be concluded from the comparison figures that the re-recorded audio lacks a lot of information in the bands of low and mid-high frequencies compared with the audio of the original human voice. Therefore, it is feasible to train models to identify non-human voices with audio features.

According to the difference between human voices and broadcast sounds, we choose MFCC features and GMM algorithm to build the model.

3.1. Model training and predicting

Model choosing:

By analyzing the comparison of the two audio segments above, it is easy to conclude that the spectrum is used as a training feature. However, since the original spectrum does not match the auditory properties of human ears, we chose MFCC (Mel-

scale frequency cepstral coefficients) as the training feature, which can better simulate the auditory processing of human ears compared to the original spectrum [10].

GMM (Gaussian mixture model) can theoretically fit an arbitrary distribution of samples by fusing multiple Gaussian distributions. From Figure 2 and 3, it can be seen that there is a distinct difference in the distribution of the two types of audio features, so a better classification effect can be achieved by using GMM which has fewer parameters and faster computing speed.

Below is the equation of GMM probability density for K Gaussian distributions:

$$P(x) = \sum_{k=1}^K \varphi(k)p(x|k)$$

$\varphi(k)$ is the weight of the kth Gaussian distribution, and satisfies $\sum_{k=1}^K \varphi(k) = 1$
 $p(x|k)$ is the probability that x is in the kth Gaussian distribution, which is calculated as

$$p(x|\mu_k, \sigma_k^2) = \frac{1}{\sqrt{2\pi}\sigma_k} e^{-\frac{(x-\mu_k)^2}{2\sigma_k^2}}$$

μ_k and σ_k^2 are the mean and variance of the kth Gaussian distribution respectively.

Training procedure:

1. Extract MFCC features from the same type of training datasets of audio data.
2. Randomly initialize N functions of Gaussian probability density.
3. Solve for the parameters of the N Gaussian distribution that best fit the training dataset MFCC with the EM method, and save the trained parameters.
4. Train human sounds and broadcast sounds once respectively to obtain two different GMM parameter models.

Predicting procedure:

Use two GMM models to calculate the probabilities from MFCC features of the same audio, and regard the class with higher probability as the final class.

3.2. Experimental results and conclusions

For different MFCC and GMM parameters, a series of comparison experiments were conducted with the above training sets and validation sets. The audio data are from real user logs in the online environment, and the number of training and validation sets is shown in Table 2:

Table 2. Number of Dataset

Dataset	Broadcast audio	Human-voice audio
Training Set	4743	2565
Validation Set	535	291

The predicting results of validation sets in different groups are as follows:

- (1) Group 1, different parameters: MFCC delta; same parameters: 16 Gaussian distributions, MFCC without frequency filter

Table 3. Results of Group 1

params	Data type	Predicted Human	Predicted Broadcast	
MFCC	without	Human-voice audio	84.53%	15.47%
	delta	Broadcast audio	10.29%	89.71%

MFCC with delta	Human-voice audio	89.00%	11.00%
	Broadcast audio	8.04%	91.96%
MFCC with delta & double delta	Human-voice audio	93.80%	6.20%
	Broadcast audio	5.80%	94.20%

Conclusion 1: As shown in Table 3, the MFCC delta has a substantial impact on prediction accuracy, which is probably because MFCC contains only static features, while delta contains dynamic audio features.

(2) Group 2, different parameters: number of Gaussian distributions; same parameters: with delta & double delta, MFCC without frequency filter

Table 4. Results of Group 2

params		Data type	Predicted Human	Predicted Broadcast
8	Gaussian Distributions	Human-voice audio	89.69%	10.31%
		Broadcast audio	5.05%	94.95%
16	Gaussian Distributions	Human-voice audio	93.80%	6.20%
		Broadcast audio	5.80%	94.20%
24	Gaussian Distributions	Human-voice audio	93.13%	6.87%
		Broadcast audio	7.67%	92.33%

Conclusion 2: As shown in Table 4, the number of Gaussian distributions is not as high as it should be. The more the Gaussian distribution is, the more time-consuming the training is, but with fewer gains. It can be judged from the experimental data that 16 Gaussian distributions can bring the best results.

(3) Group 3: different parameters: frequency filter; same parameters: MFCC with delta and double delta, 16 Gaussian distributions

Table 5. Results of Group 3

params		Data type	Predicted Human	Predicted Broadcast
Without frequency filter		Human-voice audio	93.80%	6.20%
		Broadcast audio	5.80%	94.20%
55hz low-frequency filter		Human-voice audio	91.40%	8.60%
		Broadcast audio	6.40%	93.60%
4.5khz high-frequency filter		Human-voice audio	91.07%	8.93%
		Broadcast audio	7.29%	92.71%
55hz-4.5khz band-pass filter		Human-voice audio	91.07%	8.93%
		Broadcast audio	7.48%	92.52%

Conclusion 3: As shown in Table 5, the addition of MFCC frequency filter does not improve the prediction accuracy, and it leads to a significant decrease in prediction accuracy of human-voice audios, which may be caused by the lack of a few features of human voices in low and high frequencies after being filtered.

In Summary, through the above-mentioned comparison experiments, we have found the optimal model parameters in our data sets: 16 Gaussian distributions, MFCC with delta and double delta, without frequency filters. With the optimal parameter model, the accuracy of human voices and non-human voices can reach 93.8% and 94.2% respectively. However, there are still few data at present, and we will make further optimization on models after collecting more labeled audios.

3.3. Application of audio recognition in continuous dialogues

The common continuous dialogue system of speech interactions merely has the module of dialogue manager based on the texts transcribed from ASR, which applies text semantics recognized by NLU, conducts cohesion on contextual semantics, and rejects invalid semantics.

Based on the clear audios processed by the speech signal processor, the module of audio dialogue manager that we added can extract the audio features, and identify the audio class which whether to reject.

Jointly managing the dialogue flow from two source, audio and text, can effectively reduce the interference of invalid requests and improve the interaction fluency of continuous dialogues [11,12]. System modules can be referred to Figure 4.

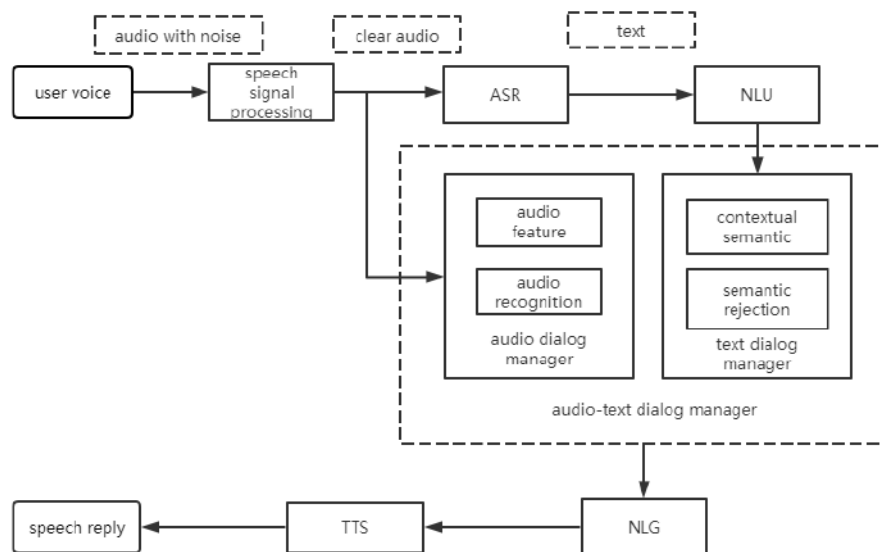


Figure 4. Modules of Continuous-Speech Spoken Dialogue System with Audio Dialog Manager.

4. Conclusion

In order to avoid frequent wakeups in the speech dialogue system, we have studied continuous speech dialogue systems. In this paper, we did a comparative experiment on continuous and discontinuous dialogue systems, and the results show that continuous dialogue technology can effectively improve the success rate of interactions.

However, a new problem arises in continuous dialogue systems: the interference of invalid speech.

Therefore, we divided the invalid speech into two categories and processed them separately. For the speech requests of non-interactive orders, we used text semantics to conduct false rejection; for the requests of broadcast sounds, we proposed an audio recognition algorithm based on MFCC and GMM, by which we can identify whether audio is from a human or broadcast. Through a series of experiments, we have explored the optimal parameters of the audio recognition model. The accuracy of broadcast sound recognition can reach up to 94.2%, which indicates that the algorithm can eliminate the interference of broadcast sounds.

The interaction success rate of continuous speech dialogue systems can be significantly improved by the joint decision-making of audio and semantics.

The current decision-making of the system is still based on the recognition results of audio and semantics separately, without a deep information fusion. In the future, we will further study the method of joint modeling of audio and texts.

References

- [1] Wen T H, Vandyke D, Mrkšić N, et al. A Network-based End-to-End Trainable Task-oriented Dialogue System[C] // Proceedings of the 15th Conference of the European Chapter of the Association for Computational Linguistics: Volume 1, Long Papers. 2017: 438-449.
- [2] Wu Yuexin, Li Xiujun, Liu Jingjing, et al. Switch-based active deep dyna-q: Efficient adaptive planning for task-completion dialogue policy learning[C]//Proceedings of the AAAI Conference on Artificial Intelligence. 2019, 33(01): 7289-7296.
- [3] Zhang Z, Takanobu R, Zhu Q, et al. Recent advances and challenges in task-oriented dialog systems[J]. *Science China Technological Sciences*, 2020, 63(10): 2011-2027.
- [4] Hakkani-Tür D, Tür G, Celikyilmaz A, et al. Multi-domain joint semantic frame parsing using bi-directional rn-ilstm[C] // Interspeech. 2016: 715-719.
- [5] Wu C S, Socher R, Xiong C. Global-to-local Memory Pointer Networks for Task-Oriented Dialogue[C] // International Conference on Learning Representations. 2018.
- [6] Wen T H, Gasic M, Mrkšić N, et al. Multi-domain Neural Network Language Generation for Spoken Dialogue Systems[C]//Proceedings of the 2016 Conference of the North American Chapter of the Association for Computational Linguistics: Human Language Technologies. 2016: 120-129.
- [7] Yangyang Zhao, Zhenyu Wang, Pei Wang, A Survey on Task-Oriented Dialogue Systems *Chinese Journal of Computers*,2020,43(10):1862-1896.
- [8] Li Y, Yao K, Qin L, et al. Slot-consistent nlg for task-oriented dialogue systems with iterative rectification network[C]//Proceedings of the 58th annual meeting of the association for computational linguistics. 2020: 97-106.
- [9] Dušek O, Jurcicek F. Sequence-to-Sequence Generation for Spoken Dialogue via Deep Syntax Trees and Strings[C]//Proceedings of the 54th Annual Meeting of the Association for Computational Linguistics. 2016: 45-51.
- [10] Peng B, Li X, Li L, et al. Composite Task-Completion Dialogue Policy Learning via Hierarchical Deep Reinforcement Learning[C]//Proceedings of the 2017 Conference on Empirical Methods in Natural Language Processing. 2017: 2231-2240.
- [11] Hu J, Yang Y, Chen C, et al. SAS: Dialogue state tracking via slot attention and slot information sharing[C]//Proceedings of the 58th Annual Meeting of the Association for Computational Linguistics. 2020: 6366-6375.
- [12] Lipton Z, Li X, Gao J, et al. Bbq-networks: Efficient exploration in deep reinforcement learning for task-oriented dialogue systems[C]//Proceedings of the AAAI Conference on Artificial Intelligence. 2018, 32(1).

A One-to-Two Filter Power Divider Based on LTCC

Yuanyuan LI¹, Xianliang WU, Yunfeng HU, Mengying DONG, Yue MA, Xiaolei GENG and Rongzhen FANG

^a Key Laboratory of Intelligent Computing and Signal Processing, Ministry of Education, Anhui University, Hefei 230001, China

Abstract. In order to miniaturize microwave devices in RF systems, a power divider with filtering performance is designed. The filter power divider is based on the LTCC process, and miniaturization is achieved by cascading a bandpass filter and a one-to-two power divider. The band-pass filter adopts a fourth-order comb-line structure, and the one-to-two power divider adopts an LC lumped structure. The size of the one-to-two filter power divider designed is 10mm×4mm×5mm, which is working in 3.3GHz-3.6GHz. The simulation results show that the insertion loss(S_{21} and S_{31}) are less than or equal to 4 dB, the return loss(S_{11}) is greater than 15 dB, the isolation(S_{23}) is greater than 17 dB, and the out-of-band suppression is greater than 18 dB in 3.8-4.3GHz and 22 dB in 0-3.2GHz and 4.3-6GHz.

Keywords. Filter power divider, LTCC, cascade

1. Introduction

With the continuous development of communication systems, miniaturized and high-performance microwave devices have become the focus of current research in the industry. Filters and power dividers are common microwave passive components, and their performance and size are critical to the overall system. There are usually two design methods. One is to design them separately and then cascade them together. The other is to carry out a comprehensive integrated design to make them have multiple performances such as power distribution, filtering, and frequency selection at the same time.

Xie Hanyu[1] designed a multi-channel filter power divider with a double-layer microstrip structure. The final overall size of the filter power divider is 28mm×30mm. Li Weijin[2] and others designed a filter power divider based on a stepped impedance resonator, the size of which is 22.6mm × 34.2mm. Wang Yujie[3] and others designed a dual-pass band filter power divider using the SIW, the size of which is 18.98mm × 19.05mm. LTCC has the characteristics of high integration and low loss. Dai Yongsheng[4] and others designed an LTCC filter with a center frequency of 60 GHz and a passband of 6 GHz whose overall size is 1.6mm×0.8mm×0.6mm. Fu Jiahui[5] and others designed a 1.27GHz-1.58GHz frequency band, LTCC three-way Wilkinson power divider, its size is 5.3mm×5mm×1.3mm.

Based on the characteristics of LTCC, this paper realizes an LTCC filter power divider by cascading the LTCC filter and the power divider, and its overall size is

¹ Corresponding Author: Yuanyuan Li; E-mail: liyuanyuan_hnxx@163.com.

10mm×4mm×5mm. Finally, the simulation of the filter power divider shows that:in the 3.3GHz-3.6GHz frequency band, the insertion loss(S_{21} and S_{31}) are less than or equal to 4 dB, the return loss(S_{11}) is greater than 15.7 dB, the isolation(S_{23}) is greater than 17.5 dB, and the out-of-band suppression is greater than 18 dB in 3.8-4.3GHz and 22 dB in 0-3.2GHz and 4.3-6GHz, meeting the given index requirements.

2. Design principle

The filter power divider designed is formed by cascading a fourth-order comb-line filter and a power divider.

2.1. LTCC comb-line filter

What shown in Figure 1 is the equivalent circuit schematic of the comb-line filter. The serial number N represents the N th resonator, and the serial number 0 and the serial number $N+1$ represent the input and output leads respectively. The energy is transferred between the resonators through side coupling. Each resonator is composed of a short-circuit transmission line connected to a lumped ground capacitor, which is equivalent to an LC parallel resonant. The resonant frequency can be tuned by adjusting the size of the transmission line and the size of the ground capacitance.

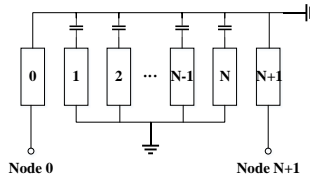


Figure 1. Equivalent circuit structure of comb-line filter.

In this paper, the three-layer broadside coupled stripline[6-7] is used as the resonator to design, and its structure is shown in Figure 2. The front end of the stripline in the middle layer is open and the back end is grounded, and the front ends of the upper and lower striplines are grounded and the back end is open, and they are symmetrical with respect to the stripline in the middle layer. The resonator is located in the center between the two ground plates. The distributed inductance of the three-layer broadside coupled stripline resonator is the distributed inductance of the single-layer stripline, and the distributed capacitance is the total capacitance formed by the distributed capacitance of the single-layer stripline and the two coupling capacitors.

The distributed inductance and distributed capacitance per unit length of the three-layer broadside coupled stripline[6] are expressed as:

$$\tilde{L} = \frac{\pi\mu_0}{8\text{arch}(e^{\pi w/2b})} \tag{1}$$

$$\tilde{C} = \frac{8\varepsilon\text{arch}(e^{\pi w/2b})}{\pi} + \frac{2\varepsilon w}{d} \tag{2}$$

The resonant frequency of the three-layer broadside coupled stripline resonator is:

$$f_0 = \frac{1}{2\pi\sqrt{LC}} = \frac{1}{2\pi\sqrt{(\bar{L}\bar{D})(\bar{C}\bar{D})}} = \frac{1}{2\pi\bar{L}\sqrt{\bar{L}\bar{C}}} \tag{3}$$

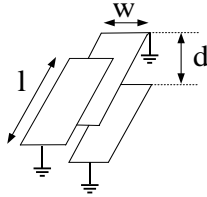


Figure 2. Geometry of a three-layer broadside coupled stripline resonator.

2.2. Wilkinson power divider

The Wilkinson power divider has a simple structure. By directly connecting an resistor between the output ports to absorb the reflected energy, the isolation between the ports is increased, and the effect of consuming the reflected power can also ensure the matching between the ports.

The use of quarter-wavelength transmission line in the power divider will make the physical size larger, so this paper uses the equivalent circuit of type π [8] to replace the quarter-wavelength transmission line to minimize the size.

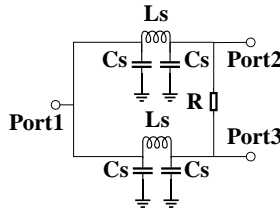


Figure 3. Circuit diagram of lumped-element one-to-two-way Wilkinson power divider.

Figure 3 is the circuit diagram of the lumped-element one-to-two-way Wilkinson power divider. The parameters in the figure can be calculated by equations (4)~(6).

$$L_s = \frac{Z_0 \sin \theta}{\omega} \tag{4}$$

$$C_s = \frac{1}{Z_0 \omega} \tan \frac{\theta}{2} \tag{5}$$

$$R = 2Z_0 \tag{6}$$

3. Models and Simulations

The filter power divider designed in this paper is composed of a LTCC filter and a power divider in cascade. Its indicators are shown in Table 1. In this paper, LTCC multi-layer metallized wiring is used in the design, and silver is used as the wiring conductor. The

dielectric constant of the ceramic dielectric used is 5.9 and its tangent loss angle is 0.0005, and the height between each stripline is 0.1 mm.

Table 1. Parameters of filter power divider

Indicator	Filter	Power divider	Filter power divider
Center frequency	3.45G	3.45G	3.45G
Bandwidth	300MHz	300MHz	300MHz
Insertion loss	1dB	3.5dB	4.5dB
Return loss	12dB	15dB	15dB
Isolation	-	15dB	15dB
Out-of-band suppression	15dB(0-3.1GHz,3.8-6GHz)	-	15dB(0-3.1GHz,3.8-6GHz)

3.1. LTCC fourth-order combline filter

The design steps of the distributed bandpass filter: First, the length, width and layer spacing of the stripline are preliminarily determined through the relationship between the center frequency and the physical quantities related to the stripline. Then use HFSS software for 3D modeling and simulation, and determine the bandwidth by optimizing the spacing between the resonators. Finally, between the first and fourth-order resonators, Z shape cross-coupling is added to introduce transmission zeros to enhance out-of-band suppression.

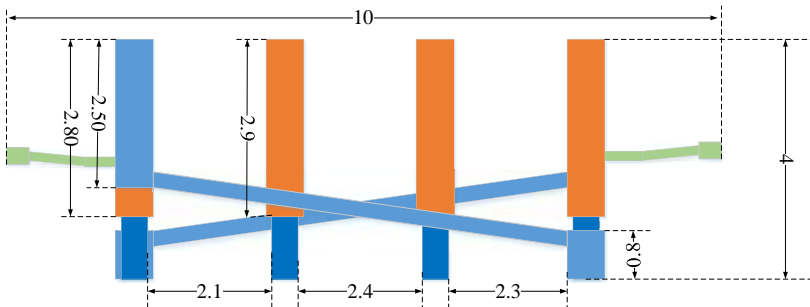


Figure 4. Top view of the fourth-order comb-line filter.

The model structure of the fourth-order comb-line filter is shown in Figure 4, and the data units in the figure are all millimeters. The filter size is 10mm×4mm×4.5mm.

In this design, Z shape cross-coupling is inserted above and below the first and fourth resonators[9], and the output signal of the main coupling channel is 180° out of phase with the output signal of the cross-coupling channel[10], so that cancel each other out and introduce transmission zeros near the upper and lower sidebands. Finally, by continuously fine-tuning the parameter variables, the simulation curve of the fourth-order comb-line filter with and without Z shape cross-coupling is finally obtained, which is shown in Figure 5.

From the simulation curve what can be seen is that the out-of-band suppression can be significantly enhanced by introducing transmission zeros through Z shape cross-coupling. In the operating frequency range of 3.3GHz-3.6GHz, the insertion loss(S_{21}) is less than 0.9dB, the return loss(S_{11}) is greater than 13dB, the out-of-band suppression is greater than 17dB in 2.8-3.1GHz and 3.8GHz-4.1GHz, and 19dB in 0-2.8GHz and 4.1-6GHz, which meets the given indicators.

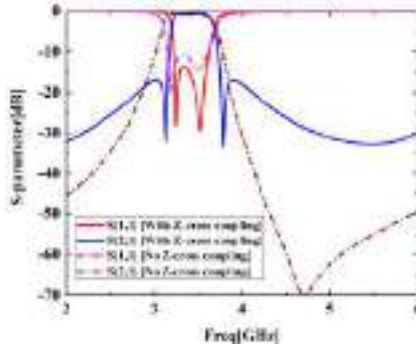


Figure 5. S-parameter curve of a fourth-order comb-line filter with and without Z shape cross-coupling.

3.2. LTCC Wilkinson Power Divider

In this section, based on the lumped Wilkinson-type power divider structure mentioned in Chapter 2, through the multi-layer advantage of the LTCC process, an LTCC one-to-two power divider is designed.

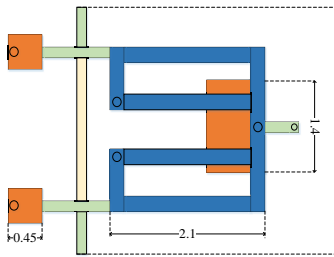


Figure 6. Top view of LTCC power divider.

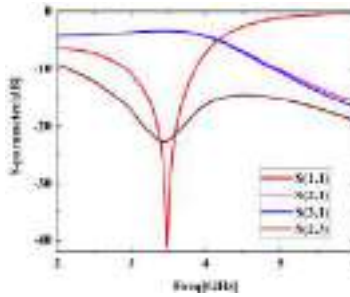


Figure 7. S-parameter curve of LTCC power divider.

Build the HFSS model and the model structure of the LTCC power divider is shown in Figure 6. The data units in the figure are all millimeters. The final size of the power divider is 4mm×4mm×0.5mm.

The parameters are continuously optimized, and the final simulation result can be seen in Figure 7. In the 3.3GHz-3.6GHz frequency band, the insertion loss(S_{21} and S_{31}) are less than 3.45dB, the return loss(S_{11}) is greater than 17dB, and the isolation(S_{23}) is greater than 20dB, which meets the design requirements.

3.3. LTCC filter power divider

The LTCC filter power divider adopts the cascade mode. The filter and power divider designed in the first two sections are cascaded. To reduce size, power divider is placed on top of filter and cascaded through metal post. Its structure is shown in Figure 8, whose data units are all millimeters, and the filter size is 10mm×4mm×5mm.

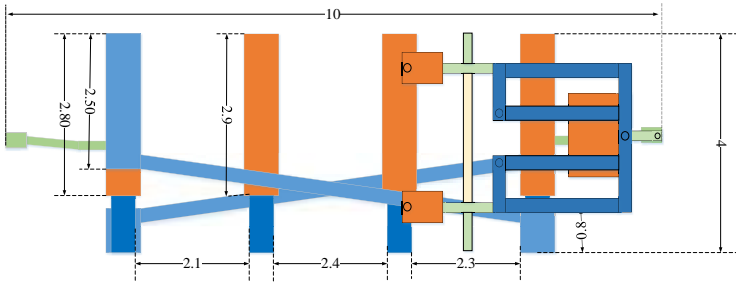


Figure 8. Filter power divider model.

By fine-tuning some parameters, the simulation results are presented in Figure 9. What shown in the figure is that in the 3.3GHz-3.6GHz frequency band, the insertion loss(S_{21} and S_{31}) are less than or equal to 4 dB, the return loss(S_{11}) is greater than 15.7 dB, the isolation(S_{23}) is greater than 17.5 dB, and the out-of-band suppression is greater than 18 dB in 3.8-4.3GHz and 22 dB in 0-3.2GHz and 4.3-6GHz, meeting the given index requirements.

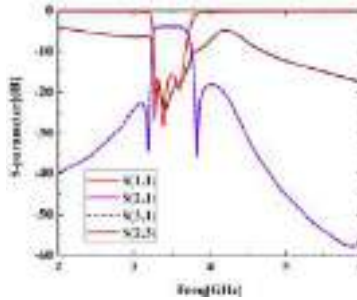


Figure 9. S-parameter curve of filter power divider.

3.4. Comparison of several filter power dividers

Table 2 shows the comparison of the filter power dividers designed in this paper with some references. It can be seen from the comparison that the design of the filter power divider using LTCC in this paper can greatly reduce the size and the insertion loss is small.

Table 2. Comparison of several filter power dividers

References	Center frequency	Structure	Insertion loss	Size
[1]	3.98GHz,6.44GHz	Microstrip line	5dB , 4.8dB	28mm×30mm
[2]	1.57GHz	Microstrip line	4.3dB	>22mm×34mm
[3]	7.5GHz,11.7GHz	SIW	3.811dB, 3.328dB	>18mm×19.mm
This work	3.45GHz	LTCC	4dB	10mm×4mm

4. Conclusion

Based on the characteristics of high integration and low loss of LTCC process, this paper designs a power divider with filtering performance. In this design, the working frequency band of the one-to-two filter power divider designed is 3.3GHz-3.6GHz. In order to reduce the overall size, a fourth-order comb-line structure bandpass filter and one-to-two power dividers are cascaded together, resulting in a final size of 10mm×4mm×5mm, and finally meet the performance of insertion loss less than or equal to 4 dB, return loss greater than 15dB, isolation greater than 17dB, and the out-of-band suppression is greater than 18 dB in 3.8-4.3GHz and 22 dB in 0-3.2GHz and 4.3-6GHz.

For further miniaturization, this paper has the following three suggestions: one is to use a ceramic dielectric with a higher dielectric constant, the other is to use an LC lumped structure, and the third is to use a comprehensive integration method to design the filter and power divider together.

Acknowledgment

This research is supported by the National Natural Science Foundation of China (61871001, 61971001).

References

- [1] Xie Hanyu, Tao Feng, Huang Qiman, Wu Bian. A double-layer microstrip structure multi-channel filter power divider[C]//. Proceedings of the 2019 National Microwave and Millimeter Wave Conference (Volume 2).[Publisher unknown],2019 :74-77.
- [2] Li Weijin, Wei Feng, Wang Xinhui, Shi Xiaowei. Design of Filter Power Divider Based on Step Impedance Resonator[C]//. Proceedings of the 2015 National Microwave and Millimeter Wave Conference., 2015:1008-1010.
- [3] Wang Yujie, Zhou Chunxia, Lin Binbin, Zhao Yanfei, Wu Wen. Design of dual-pass-band filter power divider based on substrate-integrated waveguide[J]. Microwave Journal, 2017,33(S1):148-151.
- [4] Y. -s. Dai, H. -h. Yin, H. -t. Sun, Y. Feng, Q. -y. Xie and M. Luo, "A miniaturized millimeter-wave bandpass filter with LTCC technology," 2012 IEEE MTT-S International Microwave Workshop Series on Millimeter Wave Wireless Technology and Applications, 2012, pp. 1-3, doi: 10.1109/IMWS2.2012.6338222.
- [5] J. Fu, Z. Wang, B. Lv, Z. Yang and Q. Wu, "A new compact three-way Wilkinson power divider based on LTCC technology," 2015 Asia-Pacific Microwave Conference (APMC), 2015, pp. 1-3, doi: 10.1109/APMC.2015.7411707.
- [6] Chang Yumin. Research and design of high-performance miniature filter based on LTCC [D]. Nanjing University of Science and Technology, 2020. DOI: 10.27241/d.cnki.gnjgu.2020.001635.
- [7] Zhang Xiangjun, Ma Xiaoping and Lai Qifeng, "Compact multilayer coupled stripline LTCC filter with defected ground structure," 2009 International Conference on Microwave Technology and Computational Electromagnetics (ICMTCE 2009), 2009, pp. 204-206, doi: 10.1049/cp.2009.1300.
- [8] Chen Peng. Research on miniaturized power divider and filter based on LTCC technology [D]. University of Electronic Science and Technology of China, 2022. DOI: 10.27005/d.cnki.gdzku.2022.004247.
- [9] Li Yongbin, Wang Ziliang, Cheng Kai. Design of tapped comb-line filter based on LTCC process[J]. Research and Progress in Solid State Electronics, 2017,37(01):36-39+44.DOI:10.19623/j.cnki.rpsse.2017.01.008.
- [10] Chao Sun, Yongsheng Dai and Bowen Li, "Design of four-order distributed band-pass filter based on LTCC technology," 2016 IEEE MTT-S International Microwave Workshop Series on Advanced Materials and Processes for RF and THz Applications (IMWS-AMP), 2016, pp. 1-3, doi: 10.1109/IMWS-AMP.2016.7588436.

Tiny Deep Convolution Recurrent Network for Online Speech Enhancement with Various Noise Types

Qiuwei DENG^{abc,1}, Di WANG^c, Tianxiang LUAN^c and Bin HAO^c

^aCollege of Computer Science, Chongqing University, Chongqing, China

^bState Key Laboratory of Digital Household Appliances, Qingdao, China

^cHaier Smart-Home Intelligent Technology co. LTD, Qingdao, China

Abstract. Nowadays, voice interaction is increasingly applied to smart home appliances. There are various types of noises in our real lives, which requires speech enhancement technology to deal with multiple noisy speech scenarios and to process them in real-time. Traditional technologies of speech noise reduction require estimating the noise power spectrum first, then estimating the spectrogram gain value of noise reduction, such as minima controlled recursive averaging (MCRA), which can only deal with stationary environmental noises but cannot estimate noises with serious fluctuations of the power spectrum within quite limited durations. A highly complicated deep-learning model can estimate the power spectrum of various types of noise, but it cannot meet the requirement of real-time processing due to the large number of parameters of these general models. In this paper, we proposed a method combining deep-learning technologies with traditional signal processing techniques to estimate the power spectrum of various types of noises by designing a new model with fewer parameters, tiny deep convolutional recurrent network (TDCRN), and computing the speech gain value with the power spectrum. The result of our experiment indicates that, compared with the traditional technology and complicated deep-learning model, the proposed method, with only 0.29M parameters, increases the PESQ by more than 0.6, the STOI by more than 0.2 and the wake-up rate by more than 6%.

Keywords. deep learning, real-time speech enhancement, noise power spectrum estimation, convolutional encoder-decoder

1. Introduction

The speech processing technology is increasingly applied in hearing aids, automatic speech recognition, and audio/video calls. Due to the interference of noise in actual scenarios, the quality of signals received by microphones is degraded, which seriously affects the subsequent use. Speech enhancement technologies can be used to improve the acoustic quality and speech intelligibility of speech signals whose quality has been degraded due to additive noise.

Traditional speech enhancement technologies include spectral subtraction [1], Wiener filter [2] and estimation based on noise spectrum [3], among which the more

¹Corresponding Author: Qiuwei Deng; E-mails: dengqiuwei@haier.com

well-developed and widely-used is the estimation based on noise spectrum. Cohen assumes that the Fourier transform of clean speech and noise satisfies a Gaussian distribution, using the optimally-modified log-spectral amplitude (OM-LSA) with minimum Bayesian estimation to solve for the optimal gain, during which the noise power spectrum is estimated with improved minima controlled recursive averaging (IMCRA) [4].

Recently, deep learning has made great achievements in the application of speech enhancement. The mainstream approach is to carry out speech enhancement in the TF domain. Xu[5] proposed the method of using DNN to directly learn the spectral mapping between the noise speech and the clean speech so as to obtain a clean speech spectrum, the training of which can be divided into two parts: the pre-training and the refined adjustment based on MMSE. One method is to conduct speech enhancement by masking[6][7][8]. We assume that both noise signal and speech signal exist in the noisy speech signal, and the speech signal can be left after masking out the noise signal. Currently, there are two masking methods: ideal binary mask (IBM) and ideal ratio mask (IRM). Recently, complex networks have also become popular, which can exploit phase information and have higher upper-performance limits theoretically[9][10][11] compared to real networks, but also require a large number of parameters.

The traditional technology cannot eliminate the noise that has a greater fluctuation in the power spectrum and short duration. Using deep learning to estimate the IRM, the enhanced signal obtained has speech distortion and aberration. If complex networks are used, a large number of parameters are required, which cannot meet the requirements of real-time processing. In this paper, we proposed a new method of speech enhancement, which is inspired by the method of speech processing based on DNN-mask[6][7][8]. The noise-reduction method we proposed introduces deep learning into the estimation of noise spectrum, using networks to output the mask value of noise components in the noisy speech signal, and making further estimation on priori SNR and posteriori SNR of the speech as well as the missing probability of priori speech, so as to obtain speech presence probability. As for the model result, we adjusted the CRN[12] structure and incorporated a convolutional encoder-decoder and long short-term memory. Compared with the LSTM model, CRN has better performance in objective speech intelligibility and quality.

The arrangements of this paper are as follows. In Section 2, we formulate the problem of speech noise reduction. In Section 3, we review the noise reduction method based on OM-LSA and IMCRA, and also describe its features and limitations. Section 4 introduces the noise-reduction method that we proposed. Section 5 provides the experimental results, and demonstrates the improvement of ASR by the noise-reduction method that we proposed in a real noise environment. Last but not least, we put our conclusions in Section 6.

2. Problem Formulation

In this section, we describe the problem of speech noise reduction in the TF domain. $d(t)$ and $n(t)$ stand for speech signal and additive noise signal respectively, and signal received by microphone $y(t)$ can be expressed as $y(t) = d(t) + n(t)$. With a short-time Fourier transform, it can be expressed as $Y(t, k) = D(t, k) + N(t, k)$, among which t and k stand for frame index and frequency bin index respectively.

As long as an accurate gain value $G(t, k)$ can be obtained, an estimated clean signal $\widehat{D}(t, k)$ can be obtained as well.

$$\widehat{D}(t, k) = G(t, k)Y(t, k) \quad (1)$$

2.1. Spectral Gain

The computing criterion of OM-LSA is to minimize the error in the optimally-modified log-spectral amplitude of actual clean speech and estimated clean speech $E\left\{\left[\log|D(t, k)| - \log|\widehat{D}(t, k)|\right]^2\right\}$. Assuming the statistical independence of spectral components[13], the log-spectral amplitude of clean speech is

$$|\widehat{D}(t, k)| = \exp\{E[\log|D(t, k)|] | Y(t, k)\}. \quad (2)$$

A binary hypothesis model is set, and $H_0(t, k)$ and $H_1(t, k)$ stand for the non-presence and presence of the speech respectively.

$$H_0(t, k): Y(t, k) = N(t, k),$$

$$H_1(t, k): Y(t, k) = D(t, k) + N(t, k). \quad (3)$$

The spectrogram gain value of OM-LSA[3] can be calculated as:

$$G(t, k) = \{G_{H_1}(t, k)\}^{p(t, k)} G_{min}^{1-p(t, k)},$$

$$G_{H_1}(t, k) = \frac{\xi(t, k)}{1+\xi(t, k)} \exp\left(\frac{1}{2} \int_{v(t, k)}^{\infty} \frac{e^{-t}}{t} dt\right). \quad (4)$$

In the above equation, $\xi(t, k) \triangleq \frac{\lambda_d(t, k)}{\lambda_n(t, k)}$, $\gamma(t, k) \triangleq \frac{|Y(t, k)|^2}{\lambda_n(t, k)}$, $v(t, k) \triangleq \frac{\gamma(t, k)\xi(t, k)}{1+\xi(t, k)}$. $\xi(t, k)$ and $\gamma(t, k)$ stand for priori SNR and posteriori SNR respectively. $\lambda_d(t, k)$ and $\lambda_n(t, k)$ stand for the power spectrum of clean signals and noise signals respectively. $p(t, k)$ and $q(t, k)$ stand for the priori probability of speech presence and non-presence respectively.

2.2. Speech Presence Probability

Assuming that the short-time Fourier transform coefficients of speech and noise conform to the complex Gaussian distribution and are incoherent, according to Bayes theorem, the presence probability of conditional speech is

$$p(H_1(t, k) | Y(t, k)) = \frac{1}{1 + \frac{q(t, k)}{1-q(t, k)} \times [1 + \xi(t, k)] \times \exp\{-v(t, k)\}}. \quad (5)$$

Among which priori SNR can be estimated based on historical smoothing information,

$$\hat{\xi}(t, k) = \alpha G_{H_1}^2(t - 1, k)\gamma(t - 1, k) + (1 - \alpha)\max\{\gamma(t, k) - 1, 0\}. \quad (6)$$

The first term on the right of Eq. (6) can be interpreted as the estimation of priori SNR on the last frame, the second term can be interpreted as the estimation of priori SNR on the current frame, and the final estimation of priori SNR can be obtained by smoothing the above two parts.

3. Conventional Method

To solve for the final spectrogram gain value $G(t, k)$, it is necessary to accurately solve for the spectrogram gain value when the speech is present $G_{H_1}(t, k)$, as well as the presence probability of conditional speech $p(H_1(t, k)|Y(t, k))$, during which the most vital unknown parameter is noise power spectrum $\lambda_n(t, k)$.

3.1. Formulation

The commonly used method for noise spectrum estimation, MCRA[3], combines recursive averaging and minimum value tracking to roughly estimate the speech presence probability based on minimum value tracking, eliminate the frequency points with high speech probability, filter out the noisy segments, and then update the noise spectrum only in the noisy segments. Cohen proposed to improve MCRA[4] by determining the frequency points with higher speech probability that need to be eliminated by two iterations, expanding the historical window of minimum tracking, and empirically compensating for the final estimated noise spectrum.

$$\hat{\lambda}_n(t, k) = \tilde{\alpha}_n(t, k)\hat{\lambda}_n(t - 1, k) + (1 - \tilde{\alpha}_n(t, k))|Y(t, k)|^2 \quad (7)$$

The noise spectrum estimation in Eq. (13) is all obtained by smoothing the historical power spectrum by adjusting the smoothing parameter based on the speech presence probability, and $\tilde{\alpha}_n$ is the smoothing factor obtained based on the speech presence probability.

3.2. Limitations of Conventional Method

The MCRA method of estimating the noise spectrum has the following limitations: 1. The problem of convergence; 2. It can only be used for estimating environmental noises which are rather smooth.

$$\tilde{\alpha}_n(t, k) = \alpha_n + (1 - \alpha_n)p_n(t, k) \quad (8)$$

In the above equation, α_n is a smoothing coefficient, and also a constant.

When the noise environment changes, the method of recursive averaging requires a certain number of frames to reach convergence. In Eqs. (6), (7), and (8), smoothing methods are used in estimating priori SNR, noise spectrum, and smoothing coefficient of the noise spectrum. Moreover, in the method of IMCRA, when tracking the minimum value of the power spectrum by two iterations, the minimum power spectrum saved during the smoothing process is calculated in the first iteration. In the second

iteration, the amount of windows D is divided into U shares, each with V sampling points, which also calculates the minimum power spectrum of the U shares. While this method improves the accuracy of noise spectrum estimation and eliminates those relatively strong speech components, it also increases the convergence time.

The accuracy of noise spectrum estimation depends on the estimation of the smoothing coefficient $\tilde{\alpha}_n$. The most ideal scenario is the frequency band with a high noise component and a small value of $\tilde{\alpha}_n(t, k)$. The first term on the right of Eq. (7) has a small proportion of historical values, and the second term has a large proportion of current noise spectral components. Frequency bands with higher speech components have higher values of $\tilde{\alpha}_n(t, k)$, and the accuracy of $\tilde{\alpha}_n(t, k)$ value depends on $p_n(t, k)$. In the method of IMCRA, Eq. (5) is used to estimate $p_n(t, k)$, and the minimum power spectrum S_{min} estimated with secondary iterations is regarded as λ_n . S_{min} calculates the minimum value of the power spectrum after time and frequency smoothing, and the computed $p_n(t, k)$ can only distinguish the frequency points with greater fluctuations in the power spectrum. We consider these points to be the frequency points with a higher probability of speech. The noise power spectrum $\lambda_n(t, k)$ obtained by Eq. (7) is rather smooth in the time dimension. Therefore, the method of OM-LSA & MCRA can only suppress the environmental noise that is relatively smooth, and cannot eliminate the noise that has a greater fluctuation in the power spectrum and short duration, such as keyboard tapping, knocking on tables and chairs, frying in the kitchen, etc.

4. Proposed Method: CRN-based Noise Spectrum Estimation

4.1. The Proposed Network Architecture

In order to solve the above problems, we proposed a new computing method to estimate the required noise power spectrum λ_n , instead of using the methods of recursive averaging and minimum tracking. Specifically, we proposed to use deep learning to estimate λ_n and apply it to estimate the priori SNR ξ , so as to compute the spectrogram gain value of noise reduction.

The CRN network structure proposed by Tan[12] uses CED (convolutional encoder-decoder) and long short-term memory (LSTM) in the model structure, which can be used for the real-time processing of speech signals. Choi[11] proposed a small UNET network that implements CED with one-dimensional convolution to reduce the number of trainable parameters.

In this paper, we proposed the tiny deep convolution recurrent network (TDCRN) based on previous network structures, using the loss function of mean squared error (MSE) to perform network optimization. This network model effectively combines the advantages of UNET and CRN methods, using LSTM to model the temporal dependencies. The encoder and decoder are implemented by one-dimensional convolution in the time domain, which can effectively reduce the number of trainable parameters and computing overhead.

A. Model input and output

The division of Bark band utilizes the perceptual characteristics of human ears to meticulously detail the low-frequency components of the signal. Setting fewer Bark bands can reduce the amount of computation and memory. The scale of Bark domain

nonlinearly maps frequencies to the perception domain of human ears. b stands for critical frequency band, and its relation with frequency f is,

$$b = 13 \times \arctan(0.76 \times f) + 3.5 \times \arctan\left(\frac{f}{7.5}\right)^2. \tag{9}$$

The amplitude spectrum of noisy speech signal is mapped to the Bark domain, and used as model input. Model output is the ratio of amplitude spectrum of clean signal to that of noisy signal in the Bark domain. $\mathcal{G}(\cdot)$ stands for model output, and $\mathcal{F}(nn)$ denotes the value mapped from the bark domain to the frequency domain. The estimated noise amplitude spectrum is,

$$\hat{\lambda}_n(t, k) = \mathcal{F}(nn)|Y(t, k)|^2. \tag{10}$$

B. Model structure

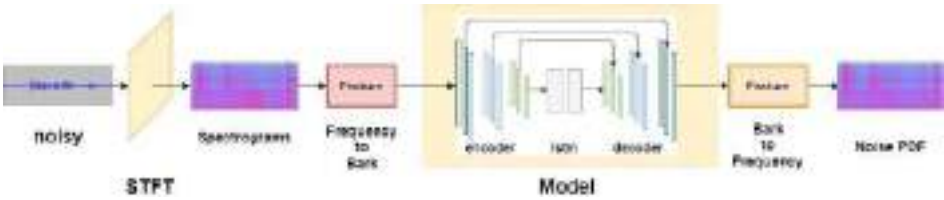


Figure 1. Flow Chart of TDCRN Estimation Noise Spectrum

The flow chart of our proposed TDCRN model for estimating the noise spectrum is shown in Figure 1. In this paper, we set up 3 layers of convolutional networks in encoder and decoder respectively, as shown in Figure 1. The output of each layer of encoder is used as part of the input of decoder layer with the method of res-net. Compared with [9][12], we use one-dimensional convolution instead of two-dimensional convolution. The convolution direction of [11] is the frequency direction of a frame, while the convolution direction that we proposed is the frame direction. What is shown in Figure 2 is the computing method of a convolution kernel in one-dimensional convolution. We set `in_channels`, a one-dimensional convolution parameter, as the feature number of input, and `out_channels` as the feature vector of output. This convolutional approach can extend the perceptual field of the network, and also count the influence among frequencies.

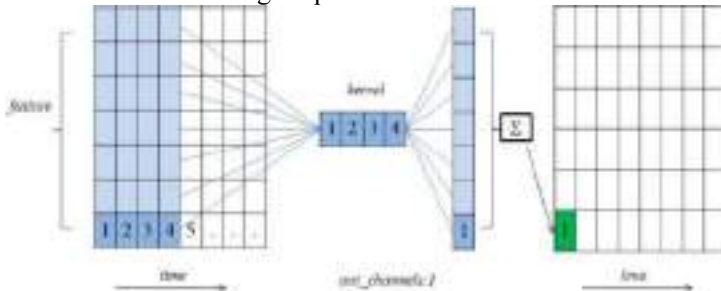


Figure 2. One-dimensional Convolution Diagram

4.2. Advantage of Proposed Method

Compared with the traditional method of estimating the noise spectrum, a major advantage of using the deep learning method to estimate the noise power spectrum λ_n is that it can estimate the change of noise in time and greatly reduce the convergence time of noise reduction. Besides, a reasonably trained model can learn the power spectrum of a wide variety of noises, and noise reduction is no longer limited to environmental noise that is rather smooth.

If the model output is used as the final output, a large number of parameters are often required to reduce speech distortion and aberration, which cannot meet the demand of real-time processing. In contrast, the method of combining TDCRN with OM-LSA only requires TDCRN to estimate the noise spectrum, without the need to consider the complex information of speech spectrum structure, so that it is advisable to design the model structure with fewer parameters.

Rnoise [14] is a hybrid method based on the improved traditional methods. In order to ensure the real-time performance of the algorithm, the network output is the 22 band in the bark domain. Although the computing resource of this method is low and the noise reduction ability is increased, the network output dimension is too small, some details are missing, and the speech distortion is relatively serious.

5. Experiment

5.1. Datasets

In the experiment, there are 62,810 noise data from Interspeech2021 DNS Challenge[15] dataset in the noise dataset, as well as 6.2 hours of free-sound noise and 42.6 hours of music in MUSAN[16] dataset. Besides, we recorded the 100-hour noise from an actual kitchen scenario with a microphone, including noises from frying and chopping food, hood, high-speed blender, etc.

In the clean speech dataset, there are 178 hours of human voice recorded by AISHELL-1[17]. We used the method of IMAGE to generate 1,000 rir with the clean data from Interspeech2021 DNS Challenge, and get the human voice data through convolution. Moreover, we also recorded 100 hours of human voice in an anechoic chamber with a microphone.

We generated 100,000 mixed data as the training dataset, each with 4s, which were 111 hours in total. We set SNR as $\{-5,0,5,10\}$ dB. We generated 15,000 as the test dataset, and 7,500 as the validation dataset, in which the percentage of real data is increased.

5.2. Training Setup and Baselines

The data are all with 16000Hz sampling rate, 32ms of STFT window length, 16ms of frameshift, and 512 of FFT length. The model was trained by Pytorch, optimizer Adam, with 0.001 initialized learning rate and 64 batch size.

The details of parameters of TDCRN model are shown in Table 1, with feature dimension of model output as 128, and the Hyper-parameters in Encoder and Decoder denote [in_channels, out_channels] and [kernel_size, stride, padding] respectively. In

Encoder, we chose to discard the first layer of data due to the output of T+1 per layer of zeros_padding. Similarly, in Decoder, we conducted zero-padding at the first layer due to the output of T-1 per layer of zeros_padding. The number of parameters for the whole model is 0.29M.

Table 1. Proposed TDCRN Structure. T stands for frames, and B stands for batch size.

	<i>Layer name</i>	<i>Input size</i>	<i>Hyper-parameters</i>	<i>Output size</i>
	Stft	[B, time]		[B, F, T]
	Frequency to Bark	[B, F, T]		[B, 128, T]
Encoder	Conv1d_1	[B, 128, T]	[128,96],[4,1,2]	[B, 96, T]
	Conv1d_2	[B, 96, T]	[96,64],[4,1,2]	[B, 64, T]
	Conv1d_3	[B, 64, T]	[64,48],[4,1,2]	[B, 48, T]
RNN	Lstm_1	[B, T, 48]	[48,64]	[B, T, 64]
	Lstm_2	[B, T, 64]	[64, 48]	[B, T, 48]
Decoder	Conv1dTranspose_1	[B, 48, T]+ [B, 48, T]	[48+48,64],[4,1,2]	[B, 64, T]
	Conv1dTranspose_2	[B, 64, T]+ [B, 64, T]	[64+64,96],[4,1,2]	[B, 96, T]
	Conv1dTranspose_3	[B, 96, T]+ [B, 96, T]	[96+96,128],[4,1, 2]	[B, 128, T]

We respectively chose IMCRA and LSTM models as the baselines.

LSTM: A semi-causal model consists of two LSTM layers, each containing 128 units. The output layer is a 128-unit fully connected layer with sigmoid activation function. The number of model parameters is 0.27M.

IMCRA: The coefficients are set according to[4].

At last, we compared the algorithm performance of IMCRA&OMLSA, LSTM out, TDCRN out, and TDCRN & OMLSA, among which LSTM out and TDCRN out models were trained when the target was with clean signals.

5.3. Results and Discussions

In this paper, we use PESQ and STOI and wakeup rate as evaluation metrics. The main purpose of the development of this algorithm is to be applied to noise reduction in kitchen scenarios of a smart home. We tested the effect of the algorithm in two scenes, All test dataset and Kitchen most, respectively. When testing PESQ, we used the above test dataset with 15,000 data. When testing the wakeup rate, we recorded the real-world data of a wakeup word with Smart Home Brain Screen². The wakeup word is a two-syllable Chinese pronunciation (“xiao U xiao U”), and the test dataset of wakeup words has ~56.3k positive examples (~30h) and ~60.4k negative examples (~72h).

² https://www.haier.com/business/smarthome/product/znckmb/20220610_182324.shtml?from=search&spm=cn.31493_pc.product_20200325.1

Table 2. Performance of PESQ on Test Dataset

Evaluation metrics	PESQ		STOI		(Acc. %)KWS Rate	
	All test dataset	Kitchen most	All test dataset	Kitchen most	All test dataset	Kitchen most
Origin	1.55	1.69	0.60	0.64	84.5	87.1
IMCRA&OMLSA[4]	1.668	1.94	0.63	0.69	89.1	89.9
LSTM out	2.03	2.11	0.71	0.73	92.3	93.7
TDCRN out	2.18	2.37	0.75	0.76	94.5	96.4
TDCRN & OMLSA	2.32	2.64	0.82	0.85	95.3	97.6

PESQ on the test dataset was calculated with different algorithms respectively, as shown in Table 2. Due to the concentration of the test, the short-time environmental noise which is smooth accounts for a relatively small percentage, mostly the type of noise with large power spectrum variation and short duration, which IMCRA cannot accurately estimate, and the enhancement of PESQ and STOI is minimized. The direct output of TDCRN has better performance than that of LSTM, indicating that the inclusion of CED results is favorable to complex target training. Although the direct output of the model improves PESQ and STOI to some extent, the speech quality can be further enhanced after being processed with OM-LSA.

Using the same wakeup engine, we set the false alarm to 1 time/24 hours, and distribute the wakeup rate of sound signals processed with different algorithms. Due to the poor performance in noise reduction of IMCRA, the result of wakeup rate is also unqualified. Although the direct output of the model can improve wakeup rate to some extent, it will lead to the loss, distortion, and aberration of noise speech. After being processed by OM-LSA, the wakeup rate can be continuously improved.

Table 3. PESQ on Test Dataset with different SNR

Evaluation metrics	-5dB	0dB	5dB	10dB	Avg.
Origin	2.20	2.31	2.36	2.52	2.35
IMCRA&OMLSA[4]	2.25	2.39	2.56	2.74	2.49
LSTM out	2.32	2.57	2.72	2.96	2.64
TDCRN out	2.38	2.62	2.77	3.03	2.70
TDCRN & OMLSA	2.47	2.70	2.85	3.10	2.78

PESQ on the test dataset with different SNR was calculated with different algorithms respectively, as shown in Table 3. It can be found that the performance of TDCRN&OMLSA is better than that of baseline IMCRA&OMLSA and LSTM, which proves the effectiveness of signal processing method combined with deep learning method.

Table 4. Calculation Cost of different algorithms

Evaluation metrics	Para.(M)	Time(ms)
IMCRA&OMLSA[4]	-	0.09
LSTM out	0.27	0.34
TDCRN out	0.29	0.31
TDCRN & OMLSA	-	0.36

With 2.90GHz i7-10700 CPU as the test machine, we calculate the average computation time of 200 audio files processed by different algorithms. Each file is 4 seconds long with 250 frames. As shown in Table 4, TDCRN runs 0.03ms faster than LSTM, indicating that although TDCRN parameters are slightly more than LSTM, its computation is slightly less than LSTM. The average time of TDCRN & OMLSA is 0.36ms per frame, which can be processed in real-time.

It is worth noting that the model proposed in this paper only supports 16000Hz data, and its effective frequency range is 0-8000Hz, which meets most use scenarios. For audios with other sample rates, we need to modify the model input dimension or resample the original data, which will increase the workload of model adaptation. Later, we consider that the model can be applied to data with different sample rates.

6. Conclusions

In this paper, we introduce deep learning into the estimation of noise spectrum, and use the conventional method of signal processing to estimate the spectrogram gain value of noise reduction, which can be used to suppress noises with greater fluctuations of the power spectrum and shorter durations. The TDCRN model implements one-dimensional convolution in the frame direction and achieves information exchange among frequencies by setting the number of output channels, which has better performance with fewer parameters. OMLSA&TDCRN that we proposed can achieve better performance than other algorithms in terms of PESQ and wakeup rate while satisfying the condition of real-time processing. In the future, we will deploy the proposed algorithm on smart devices, and also consider using the TDCRN model to improve the ability of noise rejection under reverberation conditions.

References

- [1] P. C. Loizou, *Speech Enhancement: Theory and Practice*, 2nd ed. ed. Boca Raton, FL, USA: CRC, 2013.
- [2] D.Wang and J. Lim, "The unimportance of phase in speech enhancement," *IEEE Transactions on Acoustics, Speech, and Signal Processing*, vol. 30, no. 4, pp. 679-681, 1982.
- [3] I. Cohen and B. Berdugo, "Speech enhancement for non-stationary noise environments," *Signal Processing*, vol. 81, no. 11, pp. 2403-2418, 2001.
- [4] I. Cohen, "Noise spectrum estimation in adverse environments: improved minima controlled recursive averaging," *IEEE Transactions on Speech and Audio Processing*, vol. 11, no. 5, pp. 466-475, 2003.
- [5] Y. Xu, J. Du, L. R. Dai, C. H. Lee, "An experimental study on speech enhancement based on deep neural networks," *IEEE Signal Processing Letters*, vol. 21, no. 1, pp. 65-68, 2001.
- [6] J. Heymann, L. Drude and R. Haeb-Umbach, "Neural network based spectral mask estimation for acoustic beamforming," *2016 IEEE International Conference on Acoustics, Speech and Signal Processing (ICASSP)*, 2016, pp. 196-200.

- [7] Y. Wang and D. Wang, "Towards Scaling Up Classification-Based Speech Separation," *IEEE Transactions on Audio Speech & Language Processing*, vol. 21, no. 7, pp. 1381-1390, 2013.
- [8] A. Narayanan and D. Wang, "Ideal ratio mask estimation using deep neural networks for robust speech recognition," *2013 IEEE International Conference on Acoustics, Speech and Signal Processing*, 2013, pp. 7092-7096.
- [9] Y. Hu, Y. Liu, S. Lv, M. Xing, S. Zhang, Y. Fu, J. Wu, B. Zhang and L. Xie, "Dccrn: Deep complex convolution recurrent network for phase-aware speech enhancement," *arXiv preprint arXiv:2008.00264*, 2020.
- [10] H.-S. Choi, J.-H. Kim, J., Huh, A., Kim, J.-W., Ha and K. Lee, "Phase-aware Speech Enhancement with Deep Complex U-Net," *arXiv preprint arXiv:1903.03107*, 2019.
- [11] H.-S. Choi, S. Park, J.-H. Lee, H. Heo, D. Jeon and K. Lee, "Real-time Denoising and Dereverberation with Tiny Recurrent U-Net," *arXiv preprint arXiv:2102.03207*, 2021.
- [12] K. Tan and D. Wang, "A convolutional recurrent neural network for real-time speech enhancement." in *Interspeech*, vol. 2018, 2018, pp. 3229-3233.
- [13] Y. Ephraim and D. Malah, "Speech enhancement using a minimum mean-square error log-spectral amplitude estimator," in *IEEE Transactions on Acoustics, Speech, and Signal Processing*, vol. 33, no. 2, pp. 443-445, April 1985.
- [14] J.-M. Valin, "A Hybrid DSP/Deep Learning Approach to Real-Time Full-Band Speech Enhancement," *arXiv preprint arXiv:1709.08243*, 2018.
- [15] A. Li, W. Liu, X. Luo, C. Zheng and X. Li, "ICASSP 2021 Deep Noise Suppression Challenge: Decoupling Magnitude and Phase Optimization with a Two-Stage Deep Network," *ICASSP 2021-2021 IEEE International Conference on Acoustics, Speech and Signal Processing (ICASSP)*, 2021, pp. 6628-6632.
- [16] D. Snyder, G. Chen and D. Povey, "MUSAN: A Music, Speech, and Noise Corpus," *arXiv preprint arXiv:1510.08484v1*, 2015.
- [17] H. Bu, J. Du, X. Na, B. Wu and H. Zhang, "AISHELL-1: An Open-Source Mandarin Speech Corpus and A Speech Recognition Baseline," *arXiv preprint arXiv:1709.05522v1*, 2017.

Degradation-Oriented Adaptive Network for Blind Super-Resolution

Shuo WANG¹ and Lifang CHEN

School of Artificial Intelligence and Computer Science, Jiangnan University, Wuxi, China

Abstract. Most of the super-resolution methods based on deep neural networks use a fixed image degradation model. However, when the real image degradation is inconsistent with the model assumptions, the performance of the network will be severely reduced. To address this issue, we propose a degradation-oriented adaptive network (DOANet), which can be used to solve multiple degradation super-resolution reconstruction. The network includes a degradation estimation network and an adaptive reconstruction network. The degradation estimation network extracts the abstract degradation of LR images using continuous residual blocks to provide necessary degradation information for reconstruction network. Then, the adaptive reconstruction network dynamically adjusts the parameters of the network layers based on the estimated degradation information using dynamic convolution and channel modulation to deal with various input images. Experimental results show that the proposed DOANet can cope well with multiple degradation and is superior to other recent blind methods in qualitative and quantitative comparison.

Keywords. Blind super-resolution, multiple degradations, attention mechanism, dynamic convolution

1. Introduction

Super-resolution (SR) as a basic low-level problem in computer vision has received widespread attention, which aims at recovering a high-resolution (HR) image from a low-resolution (LR). It has been widely used in many aspects such as image compression, medical imaging, remote sensing imaging and object recognition. Since SR is an ill-posed problem with multiple plausible solutions, it still faces great challenges.

Recently, convolutional neural networks (CNN) have been widely used in SR tasks. Compared with traditional methods, CNN-based methods have significant improvements in performance and end-to-end applications. Among them, Dong et al. first applied CNN to SR problems. The proposed SRCNN [1] surpassed the traditional method with a simple three-layer convolution network. After that, SR methods based on deep convolutional networks have been widely studied. VDSR [2] proposed by Kim et al. uses residual network to deepen the network depth to 20 layers and achieves better performance. EDSR [3] proposed by Lim et al. further deepens the network by removing the unnecessary BN layer in the SR network. RCAN [4] proposed by Zhang et al. uses residual in residual (RIR) structure to construct a very deep trainable network. However,

¹ Corresponding Author: Shuo WANG, School of Artificial Intelligence and Computer Science, Jiangnan University, China; E-mail: 1919099246@qq.com.

the above-mentioned methods are based on fixed degradation assumptions (such as bicubic interpolation [5]), when the actual image degradation does not match the assumptions, the performance of these networks will decrease rapidly.

So, some studies have proposed for blind SR. KernelGAN [6] uses the internal cross-scale recurrence to learn the internal distribution of image patches to estimate the blur kernel of LR image, but the accuracy of the estimated kernel needs to be improved. IKC [7] uses an iterative network to correct the estimated blur kernel, which improves the accuracy of prediction, but the running time increases significantly. DASR [8] obtains the implicit degradation information of LR images through comparative learning, which further improves the performance of blind SR.

In this paper, we propose a novel and efficient blind SR network to deal with images with multiple degradations. The main contributions of our work are summarized in the following:

- Image degradation is considered and estimated by designed sub-networks.
- The reconstruction network adaptively adjusts the network parameters using degradation information to deal with different degraded images
- Experiments show that our method has achieved advanced results compared with other methods

2. Methodology

2.1. Problem Formulation

In this paper, the degradation model of an image can be formulated as:

$$I^{LR} = (I^{HR} \otimes k) \downarrow_s \tag{1}$$

Where I^{HR} represents high-resolution (HR) image, I^{LR} represents low-resolution (LR) image, k represents the blur kernel, \otimes represents the convolution operation, \downarrow_s represents the down-sampling operation with the scale factor s .

Compared with the real image pairs that are difficult to obtain, although the synthetic data has a certain gap with the real images, it plays an important role in the research of blind SR methods. Following [7][8], isotropic Gaussian kernels and anisotropic Gaussian kernels are used to generate blur images.

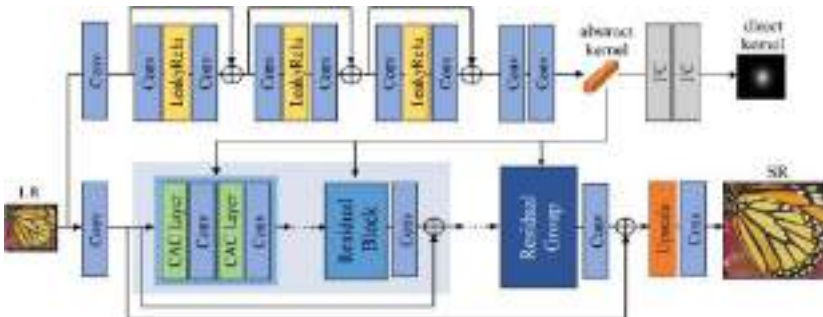


Figure 1. Overall structure of our DOANet

2.2. Structure of DOANet

As shown in Fig 1, proposed DOANet consists of two sub-networks: a degradation estimation network and an adaptive reconstruction network. The LR image is fed to the degradation estimation network to predict the abstract degradation information, and the output is expressed as $v \in \mathbb{R}^{1 \times 256}$. Then, the adaptive reconstruction network takes the LR image with its estimated degradation information to produce the SR result.

- Degradation estimation network

We first need to estimate the degradation of the input image to provide useful information for reconstructing the network. The degradation estimation network takes a degraded LR image I^{LR} as input, and aims to estimate its underlying degradation kernel. The input I^{LR} first undergoes a 3×3 convolutional layer to extract the shallow features, then deep features are extracted by successive three sets of residual blocks and each residual block consist of two 3×3 convolutional layer and one activation layer of Leaky ReLU. Another two 3×3 convolutional layer is placed later for feature reconstruction to generate degenerate information v .

Due to SR tasks are sensitive to kernel errors, the abstract kernel represents a better generalization ability for estimation errors. So underlying degradation information of the blurred image instead of the ground-truth kernel is predicted by degradation estimation network. After that, the underlying degradation information is fed to two fully connected layers and reshape a blur kernel. The reshaped blur kernel and the ground-truth kernel has the same size for loss calculation.

- Adaptive reconstruction network

Adaptive reconstruction network takes the LR image I^{LR} and its estimated degenerate information which is used to adjust network parameters to deal with the specific input image. Refer to RCAN [4], residual in residual (RIR) structure is used as the backbone of the network due to it can be built deeper network which is easy to train. The network contains several residual groups, and each residual group consists of several residual blocks, the number of groups and blocks is uniformly set to 5. The residual block is composed of two adaptive feature extraction blocks and two 3×3 convolution layers. Input images first undergo a 3×3 convolution for preliminary feature extraction, then the features are fed to RIR for deep feature refinement. The extracted features are up-sampled by the sub-pixel convolutional layer [9] and high-resolution images are reconstructed after a final convolutional layer.

- Adaptive Feature Extraction Block

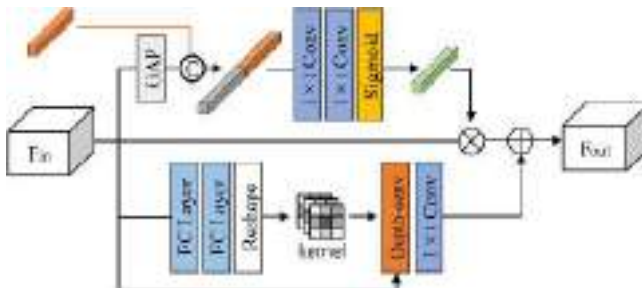


Figure 2. The structure diagram of CAclayer

As shown in Fig. 2, the key part of the adaptive reconstruction network is an adaptive feature extraction block, which consists of two branches: dynamic convolution branch and channel modulation branch.

Actually, dynamic convolution can be thought of as the attention of convolution kernel. In dynamic convolution branch, degradation information is fed to two full-connected layers and reshape a dynamic convolution kernel $k \in \mathbb{R}^{C \times 3 \times 3}$, C represents the number of channels, 3×3 represents the size of the dynamic convolution kernel. Then k is used to perform depth-wise convolution on the input feature maps.

Refer to the channel attention mechanism in SENet [10], the global information of the input feature map is compressed by global average pooling (GAP). The difference with SENet is that later the global information of the feature maps is concatenated with degradation information. After that, the concatenated vector goes through two 1×1 convolutional layers and sigmoid layer to generate channel modulation coefficients. Then the channel modulation coefficients are multiplied by the input feature maps.

The two branches use different attention mechanisms with degradation information to help the network adaptively adjust the network parameters to achieve better generalization capabilities.

2.3. Loss Function

The DOANet is optimized with loss function, which is the sum of the degradation estimation network loss and the adaptive reconstruction loss. The former is used to minimize the difference between the prediction kernel and the ground-truth kernel, and the latter is used to minimize the difference between the predicted SR image and the ground-truth HR image. As done in most previous work, L1 loss function is used to measure the difference for the both parts of the network. The loss function is formulated as follows:

$$loss = \frac{1}{N} \sum_{i=1}^N (\|k_i^p - k_i^{gt}\|_1 + \|I_i^{SR} - I_i^{HR}\|_1) \quad (2)$$

Where, k_i^p and k_i^{gt} represent the predicted kernel and the real kernel, respectively. I_i^{SR} and I_i^{HR} represent the SR image and the HR image.

3. Experiment

3.1. Settings

- **Datasets:** A total of 3450 high quality images from DIV2K and Flickr2K are used for network training. The datasets of Set5, Set14, B100 and Urban100 are used for testing. We degrade images in two ways: isotropic Gaussian blur and anisotropic Gaussian blur. Specifically, for the scale factors of $\times 2$ and $\times 4$, the kernel width ranges of isotropic Gaussian kernels are set to $[0.2, 2.0]$ and $[0.2, 4.0]$, respectively. The shapes of anisotropic Gaussian kernels are determined by parameters λ_1 , λ_2 , and θ . The ranges of λ_1 and λ_2 are set to $[0.2, 4.0]$, the ranges of θ are set to $[0, \pi]$.

- Evaluating indicator: In this paper, the peak signal to noise ratio (PSNR) is used for an objective evaluation index, the formula is expressed as:

$$PSNR = 10 \times \lg \frac{255^2 \times H \times W}{\sum_{i=1}^H \sum_{j=1}^W (I^{SR}(i, j) - I^{HR}(i, j))^2} \tag{3}$$

Where, H and W represent the height and width of the image, respectively. PSNR is measured in decibel (dB)

- Training details: During training, we first crop the input high-resolution (HR) images into 96×96 patches, and then apply random data enhancement to them, including random horizontals, vertical flips and 90° rotations. After that, the HR patches are blurred using random Gaussian kernels and down-sampling using bicubic interpolation to obtain the corresponding 48×48 low-resolution (LR) patches. The network is trained by the ADAM optimizer, the optimizer parameters $\beta_1=0.9$, $\beta_2=0.999$, $\epsilon=10^{-8}$, and the batch size is set to 32. The initial learning rate is set to 10^{-3} , and the learning rate is reduced by half every 125 epochs. We use PyTorch to implement our model, the training time on NVIDIA GTX2080 and Intel i7-8700 CPU platform is about 4 days.

3.2. Analysis of performance

- degradation estimation: To demonstrate that the degradation estimation network can effectively extract image blur kernels, we performed a visualization of the estimated blur kernels. Experiments were carried out on the image "baby" from the Set5 dataset, which is blurred with anisotropic Gaussian kernels of different shapes. The estimated result is shown in Fig.3. It can be seen that the degradation estimation encoder can effectively extract the blurred information of the image.

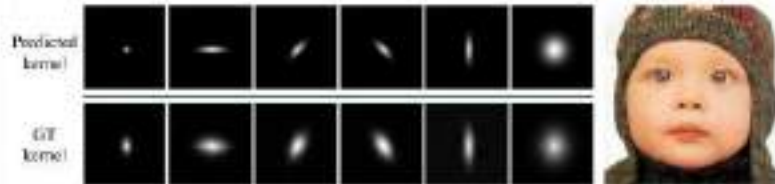


Figure 3. Visualization of the predicted blur kernel on "baby" image

- The plots of loss and PSNR in training: The training process of proposed DOANet is compared with DASR, as shown in Fig. 4. It can be seen from the figures that the loss of DOANet converges to a lower value and the PSNR of DOANet converges to a higher value compared with DASR, which illustrates that the network performance of proposed DOANet is better than DASR.

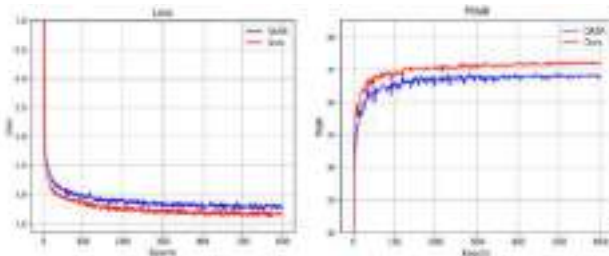


Figure 4. The plots of loss and PSNR in training

- Ablation of adaptive feature extraction block: To demonstrate the effectiveness of adaptive feature extraction block, we conducted ablation experiments on two of its branches. Specifically, we use vanilla convolution instead of dynamic convolution and use residual connection instead of channel modulation. The experiment is tested on B100 dataset with $\times 2$ scale factor, the kernel width is taken as 0 and 1.8 respectively. The experimental results are shown in Table 1:

Table 1. Ablation results of adaptive feature extraction block

model	dynamic convolution branch	channel modulation branch	Kernel width	
			0	1.8
1	✗	✗	32.03	30.54
2	✓	✗	32.16	30.66
3	✗	✓	32.13	30.75
4	✓	✓	32.19	30.87

Table 1 shows that the network without dynamic convolution and channel modulation has the worst performance. There will be improvement when only using dynamic convolution or channel modulation. The best results are obtained by using both, because the adaptive structural design can effectively improve the expression and generalization ability of the network.

3.3. Qualitative results

First, quantitative experiments were carried out on the model trained with isotropic Gaussian kernels, and a few representative methods were selected for comparison. RCAN is a SR method based for bicubic interpolation degradation model. We use the pre-trained model provided by the author for testing. IKC is a blind SR method through iterative blur kernel correction. DASR is a blind SR network by contrast learning to predict degradation information. For testing of scale factors $\times 2$ and $\times 4$, the kernel widths are set to [0.6, 1.2, 1.8] and [1.2, 2.4, 3.6], respectively. Quantitative (PSNR/dB) results are shown in Table 2:

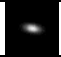

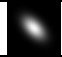
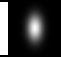

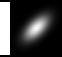
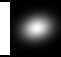
Table 2. Qualitative results on isotropic Gaussian kernel of different methods

Method	Scale	Set14			B100			Urban100		
		0.6	1.2	1.8	0.6	1.2	1.8	0.6	1.2	1.8
Kernel width		0.6	1.2	1.8	0.6	1.2	1.8	0.6	1.2	1.8
Bicubic		29.21	27.13	25.47	28.76	26.93	25.51	26.13	24.46	23.06
RCAN		32.31	28.48	26.33	31.16	28.04	26.26	29.8	25.38	23.44
DAN	$\times 2$	32.82	32.78	31.81	31.73	31.72	30.60	30.73	30.38	28.96
DASR		32.96	32.78	31.60	31.78	31.71	30.54	30.71	30.36	28.95
DOANet (Ours)		33.42	33.35	32.16	32.05	32.02	30.87	31.52	31.26	29.84
Bicubic		25.24	23.83	22.57	25.42	24.2	23.15	22.68	21.62	20.65
RCAN		27.48	24.93	23.41	26.89	25.09	23.93	24.71	22.25	20.99
IKC	$\times 4$	28.27	28.07	26.46	27.36	27.19	26.05	25.6	24.85	23.62
DAN		28.49	28.36	27.51	27.51	27.44	26.81	25.73	25.47	24.64
DASR		28.45	28.28	27.45	27.52	27.43	26.83	25.69	25.44	24.66
DOANet (Ours)		28.56	28.45	27.60	27.56	27.50	26.88	25.86	25.74	24.92

It can be observed from Table 1 that the performance of RCAN degrades severely as the kernel width increases, because it is based on bicubic interpolation model. IKC and DASR get a limited improvement due to the use of degradation information. Compared with the above methods, our DOANet achieves a significant improvement because it makes full use of the degradation information to adaptively adjust network parameters through the attention mechanism and dynamic convolution.

In addition, anisotropic Gaussian kernel were used for training data generation. We selected seven typical anisotropic Gaussian kernels for quantitative testing at the scale of $\times 4$ on the Set14 dataset. The experimental results are shown in Table 3, it can be seen that our method has achieved the best qualitative results compared to IKC and DASR.

Table 3. Qualitative results on anisotropic Gaussian kernel of different methods.

Method	Anisotropic Gaussian Kernel						
							
RCAN	26.55	24.61	24.34	24.4	24.31	24.01	23.49
IKC	28.27	27.53	27.31	27.13	27.22	27.01	26.87
DAN	28.28	27.66	27.75	27.82	27.77	27.63	27.21
DASR	28.25	27.81	27.73	27.70	27.63	27.55	27.15
DOANet (Ours)	28.46	28.03	28.03	27.95	27.81	27.81	27.42

3.4. Qualitative results

We also make an intuitive comparison of the visual effects for each method. The benchmark parameters are used for testing on the Urban100 dataset with a kernel width of 2.4 and a scale of 4. IKC takes the results of the last iteration.



Figure 5. The visual results on the image"083" of the urban100 dataset

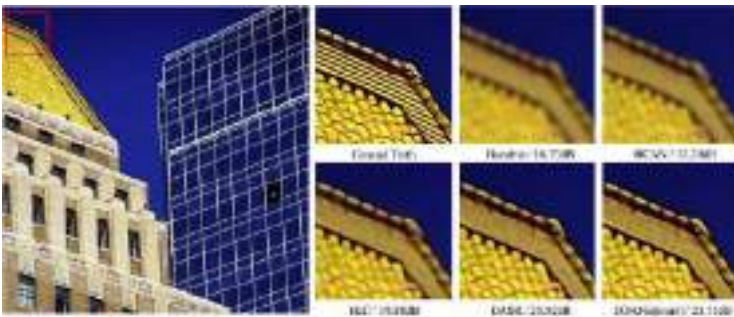


Figure 6. The visual results on the image"063" of the urban100 dataset

As shown in Fig.5 and Fig.6, it can be seen that the performance of RCAN has dropped sharply due to the change of the degradation model, resulting in a very blurred vision effect. IKC uses iterative blur kernel corrects to reduce the influence of different degradations but the results of each iteration of IKC are unstable. DASR achieves better performance than IKC. Compared to the above methods, our DOANet produces results with much clearer details, fewer artifacts and higher perceptual quality, because

conditional adaptive convolutional block can effectively use degradation information to adaptively adjust network parameters to cope with different types of degradation.

4. Conclusion

In this paper, we introduce a degradation-oriented adaptive network (DOANet) for blind SR. Specifically, we propose a degradation estimation network to predict the degradation from LR image and design an adaptive reconstruction network to complete high quality super-resolution reconstruction. It is demonstrated that our method can extract discriminative degradation information and use this information to improve network performance by dynamic convolution and channel modulation, which can effectively deal with different types of degraded images. Experimental results show that our method achieves advanced performance in qualitative and quantitative compared to recent blind super-resolution methods.

References

- [1] Dong C, Loy C C, He K, et al. Learning a deep convolutional network for image super-resolution[C]. European conference on computer vision. Springer, Cham, 2014: 184-199J. Clerk Maxwell, A Treatise on Electricity and Magnetism, 3rd ed., vol. 2. Oxford: Clarendon, 1892, pp.68-73.
- [2] Kim J, Lee J K, Lee K M. Accurate image super-resolution using very deep convolutional networks[C]. Proceedings of the IEEE conference on computer vision and pattern recognition. 2016: 1646-1654.
- [3] Lim B, Son S, Kim H, et al. Enhanced deep residual networks for single image super-resolution[C]. Proceedings of the IEEE conference on computer vision and pattern recognition workshops. 2017: 136-144.
- [4] Zhang Y, Li K, Li K, et al. Image super-resolution using very deep residual channel attention networks[C]. Proceedings of the European conference on computer vision (ECCV). 2018: 286-301.
- [5] Keys R. Cubic convolution interpolation for digital image processing[J]. IEEE transactions on acoustics, speech, and signal processing, 1981, 29(6): 1153-1160.
- [6] Bell-Kligler S, Shocher A, Irani M. Blind super-resolution kernel estimation using an internal-gan[J]. Advances in Neural Information Processing Systems, 2019, 32.
- [7] Gu J, Lu H, Zuo W, et al. Blind super-resolution with iterative kernel correction[C]. Proceedings of the IEEE/CVF Conference on Computer Vision and Pattern Recognition. 2019: 1604-1613.
- [8] Wang L, Wang Y, Dong X, et al. Unsupervised degradation representation learning for blind super-resolution[C]. Proceedings of the IEEE/CVF Conference on Computer Vision and Pattern Recognition. 2021: 10581-10590.
- [9] Shi W, Caballero J, Huszár F, et al. Real-time single image and video super-resolution using an efficient sub-pixel convolutional neural network[C]. Proceedings of the IEEE conference on computer vision and pattern recognition. 2016: 1874-1883
- [10] Hu J, Shen L, Sun G. Squeeze-and-excitation networks[C]. Proceedings of the IEEE conference on computer vision and pattern recognition. 2018: 7132-7141.

Spin Sensitivity and Magnetic Response Analysis of Nano-SQUIDs

Zejun SHI^{a,b}, Huachuan WANG*^{a,b} and Jianxin LIN*^{a,b}

^a*Qingdao Innovation and Development Center of Harbin Engineering University, Qingdao, 266404, China*

^b*College of Intelligent Systems Science and Engineering, Harbin Engineering University, Harbin 150001, China*

Abstract. This paper presents the spin sensitivity and magnetic response analysis of the nano-superconducting-quantum-interference devices (SQUIDs). We employed the computational study to understand the schemes of a nano-SQUID's detection capability according to the device's geometry and fabrication process. We find that the performance of the nano-device increased by decreasing the loop size of the SQUIDs, and it reached the maximum value at the corners of the loop. We then estimated the flux noise S_{Φ} of the SQUIDs in the thermal white noise regime and discussed the field amplification factor around the cross-section area. Furthermore, we fabricated $YBa_2Cu_3O_7$ (YBCO) based nano-SQUIDs with Josephson junctions at MgO biocrystal grain boundaries using the Pulsed Laser Deposition (PLD) and Focused Ion Beam (FIB) technique. By comparison with the estimated value of our calculation, the spin sensitivity evaluated by the experimentally fabricated devices coincides nicely with our estimation.

Keywords. Josephson junction, nanoSQUIDs, simulation, spin sensitivity, microfluidic technology

1. Introduction

Superconducting quantum interference devices (SQUIDs) with direct current (dc) are promising sub-micrometer dimension devices for probing quantum physical systems [1,2], such as small spin systems[3,4] and high sensitivity magnetometry[5]. High-temperature SQUID does not require expensive cryogenic refrigeration equipment, thus more capable as the building block for modern nanoscale applications [6,7,8,9].

A $YBa_2Cu_3O_7$ (YBCO) dc SQUID constitutes a thin film superconducting loop, and Josephson junctions interrupt the loop. It converts the magnetic flux into current or voltage. When the current is more extensive than the Josephson critical current I_0 , the junction switches to a resistive state, and the device's voltage will no longer remain zero due to the cooper pair-tunneling through the junction, shown in Figure. 1. A SQUID with high sensitivity can detect any form of energy that can convert into magnetic flux

*Corresponding Author
hcwang@hrbeu.edu.cn
linjianxin@hrbeu.edu.cn

within the loop of the SQUID. Recently, extremely low spin spectral density within the range of hundred nanometers has been reported[8,9]. The SQUID's sensitivity depends strongly on the device's design[10]. To increase the SQUIDs' detecting performance, the magnetic moment down to a single spin level, optimizing the SQUID's design to fabricate an appropriate SQUID sensor is necessary.

Simulation studies of a magnetic nanoparticle at any generic position above the SQUID loop and the corresponding influence to the magnetic flux were reported recently by Granata[2], Tilbrook[11] and Bouchiat[7]. The spin sensitivity of a SQUID layout is $S_{\mu}^{1/2} = S_{\Phi}^{1/2} / \Phi_{\mu}$ [12], in this function S_{Φ} is the magnetic flux noise and Φ_{μ} is the coupling factor. Given that the level of the inductance of the SQUID L is proportional to the magnetic flux noise S_{Φ} , it is necessary for us to reduce the inductance in order to increase the sensitivity [6,13]. In order to decrease the inductance, the dimension of the SQUID loop has to be reduced to submicron size. The details of the magnetic coupling between the SQUID device and the single spin need to be studied to predict the response of the SQUID corresponding to a single spin located at different positions within the device[14]. Moreover, this study can provide more perspectives regarding optimizing the SQUID single spin sensor [15].

This paper reports the detailed evaluation process of the SQUID's sensitivity and response relative to the single spin as a function of position within the SQUID loop. We then fabricated YBCO-based nano-SQUIDs with Josephson junctions at MgO biocrystal grain boundaries using the Pulsed Laser Deposition (PLD) and Focused Ion Beam (FIB) technique [16]. The electrical current, magnetic voltage, and noise are measured under liquid nitrogen temperature in an electrically and magnetically shielded environment to characterize the device's properties.

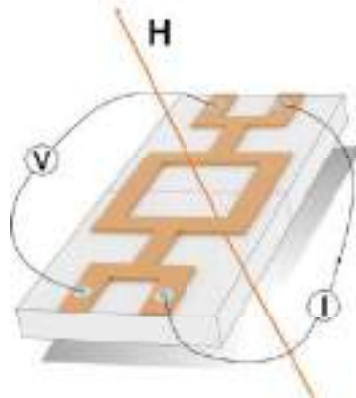


Figure 1. Schematic of the magnetic field passing through nanoSQUIDs.

2. Methodology

2.1. Spin sensitivity computation

To evaluate the spin sensitivity $S_{\mu}^{1/2}$ of the SQUID device, we need to know the coupling factor Φ_{μ} between the spin and SQUID [17]. Let us consider a single spin

($\mu_B = 9.3 \times 10 \exp -24J/T$) oriented along the z -axis, positioned within a rectangular geometry SQUID whose side length is a and width is b (shown in Figure. 2). The spin located at $P(x', y', z')$. Because the magnetic flux of the spin in the SQUID loop's direction does not contribute to the magnetic threading of the loop. The surface integral of the magnetic field threading by the magnetic moment μ_B over the loop is equal to the path integral of the potential vector of the spin tracing the loop of the SQUID, shown in Equation (5)

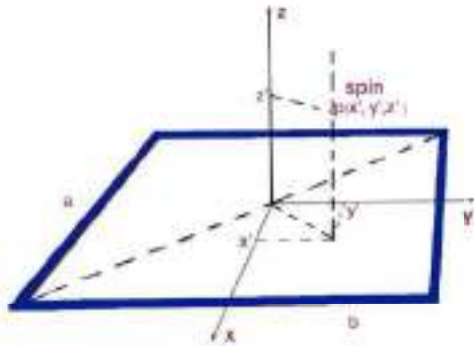


Figure 2. A spin located at a generic position within the SQUID loop.

$$\Phi_\mu = \oint \mathbf{A}(\mathbf{r}) \cdot d\mathbf{s} \tag{1}$$

Where $\mathbf{A}(\mathbf{r})$ is the magnetic vector potential. The x and y direction components of the magnetic vector potential at generic position $P(x', y', z')$ along the z -axis are [8],

$$\begin{aligned} A_x &= -\frac{\mu_0 \mu_B}{4\pi} \frac{y}{\mathbf{r}^3} \\ A_y &= \frac{\mu_0 \mu_B}{4\pi} \frac{x}{\mathbf{r}^3} \end{aligned} \tag{2}$$

Where \mathbf{r} is the distance between the spin and the plan of the SQUID loop, and μ_0 is the magnetic vacuum permeability. The magnetic flux of a spin as a function of its position within the loop is,

$$\begin{aligned} \Phi_\mu(x', y', z') &= -\frac{\mu_0 \mu_B}{4\pi} \left(\int_{-\frac{b}{2}}^{\frac{b}{2}} \frac{(a/2 - x')}{\mathbf{r}^3} dy + \int_{\frac{a}{2}}^{-\frac{a}{2}} \frac{(b/2 - y')}{\mathbf{r}^3} dx \right. \\ &\quad \left. + \int_{\frac{b}{2}}^{-\frac{b}{2}} \frac{(-a/2 - x')}{\mathbf{r}^3} dy + \int_{-\frac{a}{2}}^{\frac{a}{2}} \frac{(-b/2 - y')}{\mathbf{r}^3} dx \right) \end{aligned} \tag{3}$$

We further expand the above Equation (Equation 2.1) and revised the Equation as below,

$$\begin{aligned}
\Phi_{\mu}(x', y', z') = & -\frac{\mu_0 \mu_B}{4\pi} \left(\int_{-\frac{b}{2}}^{\frac{b}{2}} \frac{\frac{a}{2} - x'}{[(a/2 - x')^2 + (y - y')^2 + z'^2]^{3/2}} dy \right. \\
& + \int_{\frac{a}{2}}^{-\frac{a}{2}} \frac{\frac{b}{2} - y'}{[(x - x')^2 + (b/2 - y')^2 + z'^2]^{3/2}} dx \\
& + \int_{\frac{b}{2}}^{-\frac{b}{2}} \frac{-\frac{a}{2} - x'}{[(-a/2 - x')^2 + (y - y')^2 + z'^2]^{3/2}} dy \\
& \left. + \int_{-\frac{a}{2}}^{\frac{a}{2}} \frac{-\frac{b}{2} - y'}{[(x - x')^2 + (-b/2 - y')^2 + z'^2]^{3/2}} dx \right) \quad (4)
\end{aligned}$$

2.2. Magnetic flux noise

The other most critical factor of a SQUID device is the magnetic flux noise. We use the theoretical expression from Langevin simulations to determine the flux noise of the SQUID in the thermal white noise regime [18,19,20,21],

$$S_{\Phi} = f(\beta_L) \Phi_0 k_B T L / I_0 R \quad (5)$$

Here, the β_L is the screening parameter, I_0 is the critical current, and L is the inductance. For lower values of β_L , S_{Φ} increases. Furthermore, it is important to notice from this Equation that $S_{\Phi} \propto L$. The decreasing inductance will reduce the flux noise. We know that L will decrease with the contribution of miniaturization of the SQUID loop size and increase the thickness of the YBCO superconducting film, which means S_{Φ} is linearly dependent on the side length and film thickness of the SQUID.

2.3. Field amplification factor around the cross-section area

In this section, we discuss the magnetic amplification effect around the SQUID loop's cross-section area (constriction or junctions). The layout of the nanoSQUID (top view) is shown in Figure. 3(a). As shown in Figure. 3 (b), a and b are the width and thickness of the cross-section, respectively, d is the length of the constriction, λ is the London penetration depth, x and y are the widths, and the thickness direction of the cross-section, and z is the length direction of the cross-section [8,4]. Magnetic flux density at the x direction over the cross-section with a rectangular cross-section can be calculated using the Biot-Savart law.

$$B_x(x', y', z') = -\frac{\mu_0}{4\pi} \int_0^b \int_0^a \int_{-d/2}^{d/2} \frac{(y' - y)j(x)}{r^3} dx dy dz \quad (6)$$

Where $j(x)$ is the distribution of shielding current, $j(x, y) = j(x) = \frac{1}{2\lambda b} e^{(|x|-a)/\lambda}$.

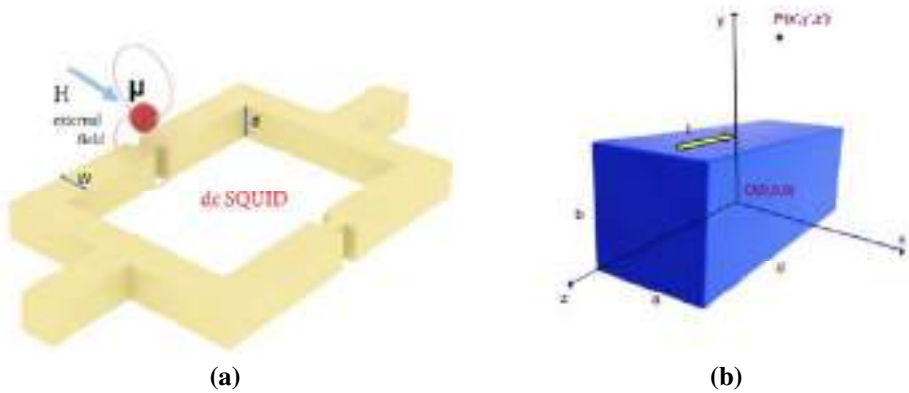


Figure 3. (a) Schematic diagram of magnetic nanoparticles on top of the cross-section area of a nanoSQUID. (b) Schematic diagram of the structure and coordinate systems of the cross-section area.

3. Results

Solving the analytically expressed Equation (2.1) numerically, we obtained the magnetic flux produced by a single spin as a function of its position within the SQUID loop. Figure. 4 reports the magnetic flux distribution of a single spin at the xy -plane, $10nm$ above the SQUID loop. The side length of the SQUID loop is $a = 380nm$ and $b = 220$. The highest values of the magnetic flux are obtained when the spin is close to the corner of the loop, as is shown in Figure. 4,.

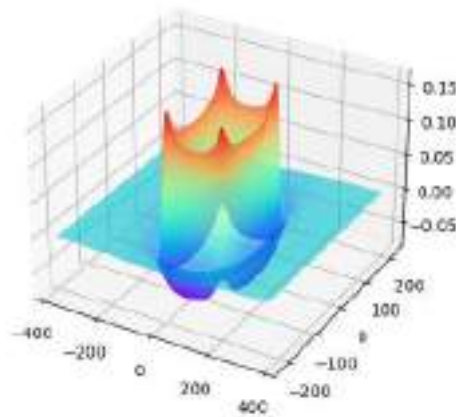


Figure 4. Distribution of the magnetic flux produced by a single spin within the SQUID loop. The side length of the loop is $a = 380nm$ and $b = 220nm$. The distance of between the spin and loop's xy -plane is $z' = 10nm$.

By modifying the distance z' value between the spin and the xy -plane of the SQUID loop, we find the dependence in the Equation within $-100nm \leq z \leq 100nm$ with abso-

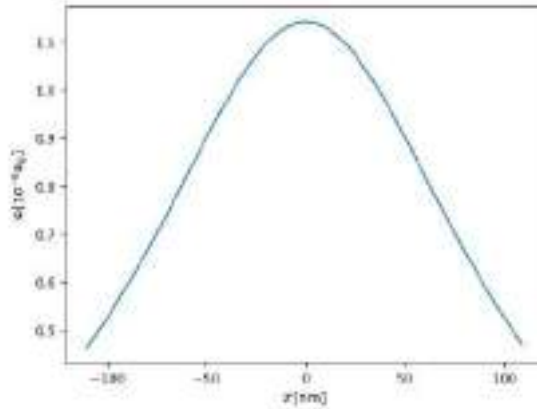


Figure 5. Calculating the coupling factor in the range of $-100\text{nm} \leq z \leq 100\text{nm}$.

lute values scaling like $\Phi_\mu \propto z^{-3/2}$, shown in Figure. 5. Decreasing z direction distance towards the SQUID loop, the values of the magnetic flux increase.

Figure. 6 (a) and (b) show the amplification factor variant along the x -direction. By reducing the width of the cross-section from 50nm to 10nm , the maximum amplification factor continuously increases. However, when the width of the cross-section area decreased, the peak of the amplification factor gradually transformed from two peaks on both sides to one peak at the center of the cross-section area. Meanwhile, the peak value of the amplification factor becomes larger. This result indicates that, in order to enhance the sensitivity of the nano-SQUID devices, the particle under test should be positioned above the center of the cross-section of the SQUID loop.

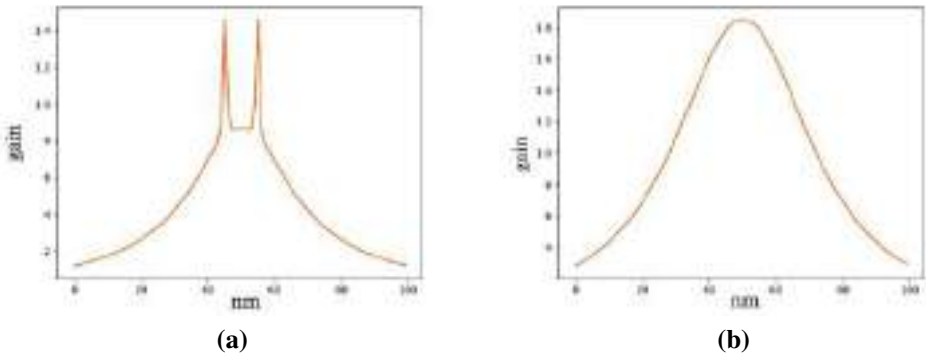


Figure 6. Field amplification factor distribution along the width direction of the cross-section. The distance above the SQUID's loop is 50 nm . (a) $a = 50\text{nm}$. (b) $a = 10\text{nm}$

YBCO films on MgO bicrystal substrates with a 24-degree misorientation angle. We use photolithography to define coarse structures, followed by Ar ion milling. Subsequently, FIB with 30 keV Ga ions in a dual beam Focused Ion Beam (FIB) system patterned the selected bridges into nanoSQUIDS[20,22,23]. We obtained a SQUID device

with a $220 \text{ nm} \times 380 \text{ nm}$ hole. Figure. 7 presents an SEM image of a YBCO nanoSQUID on a MgO bicrystal. Slightly enhanced white noise level down to $S_{\phi}^{1/2} = 175n\Phi_0/\sqrt{Hz}$ [16], we have made an improvement of the sensitivity of this nano-SQUID devices down to the level of single spin sensitivity, which agrees well with our simulation result.

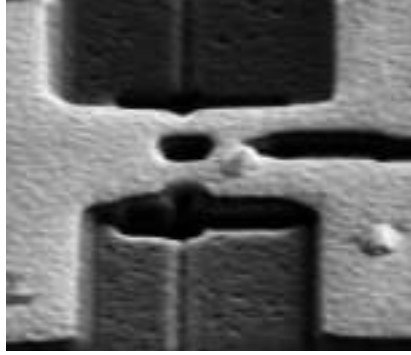


Figure 7. SEM image of a YBCO nanoSQUID on a MgO bicrystal substrate.

4. Conclusion

We illustrated the schemes of a nano-SQUID's detection capability according to the device's geometry and fabrication process. We demonstrated that the performance of the nano-device increased by decreasing the loop size of the SQUIDs, and it reached the maximum value at the corners of the loop. We estimated the flux noise S_{ϕ} of the SQUIDs in the thermal white noise regime and found S_{ϕ} is linearly dependent on the side length and film thickness of the nano-SQUID. We found that the field amplification factor around the cross-section area increases when shrinking the width of the cross-section area of the SQUID loop. We have successfully produced the YBCO-based nano-SQUIDs with Josephson junctions at MgO bicrystal grain boundaries. The spin sensitivity evaluated by the experimentally fabricated devices is comparable with our estimation.

5. Acknowledgment

This work was supported by the National Natural Science Foundation of China (Grant No. 12104112), the Natural Science Foundation of Shandong Province (Grant No. ZR2021QA036), and the Fundamental Research Funds for the Central Universities (3072022TS2602 and 79000012/011).

References

- [1] John Clarke and Alex I. Braginski. *The SQUID handbook. Vol. 1. Fundamentals and technology of SQUIDs and SQUID systems.* Wiley-VCH, Weinheim, 2004.

- [2] Carmine Granata, Antonio Vettoliere, P. Walke, C. Nappi, and M. Russo. Performance of nano superconducting quantum interference devices for small spin cluster detection. *Journal of Applied Physics*, 106(2), 2009.
- [3] John Clarke and Alex I. Braginski. *The SQUID Handbook Vol II: Applications of SQUIDs and SQUID Systems*. Wiley-VCH, Weinheim, 2004.
- [4] Robert Fagaly. Superconducting quantum interference device instruments and applications. *Review of Scientific Instruments*, 77:101101–101101, 2006.
- [5] W. Wernsdorfer, D. Mailly, and A. Benoit. Single nanoparticle measurement techniques. *Journal of Applied Physics*, 87(9):5094–5096, 2000.
- [6] M. M. Khapaev, M. Yu Kupriyanov, E. Goldobin, and M. Siegel. Current distribution simulation for superconducting multi-layered structures. *Superconductor Science and Technology*, 16(1):24–27, 2002.
- [7] Vincent Bouchiat. Detection of magnetic moments using a nano-squid: limits of resolution and sensitivity in near-field squid magnetometry. *Superconductor Science and Technology*, 22(6):064002, 2009.
- [8] Yue Wu, Liye Xiao, Shizhong Hou, Zhaoshun Gao, and Li Han. High tc tmr-superconducting mixed sensor: Fabrication and performance. *IEEE Transactions on Applied Superconductivity*, 29(1):1–5, 2019.
- [9] P. F. Vohralik and S. K. H. Lam. Nanosquid detection of magnetization from ferritin nanoparticles. *Superconductor Science and Technology*, 22(6):064007, 2009.
- [10] Aico G. P. Troeman, Hendrie Derking, Bert Borger, Johannes Pleikies, Dick Veldhuis, and Hans Hilgenkamp. Nanosquids based on niobium constrictions. *Nano Letters*, 7(7):2152–2156, 2007.
- [11] S. Lam and David Tilbrook. Development of a niobium nanosuperconducting quantum interference device for the detection of small spin populations. *Applied Physics Letters*, 82:1078–1080, 2003.
- [12] Natalia Sergeeva-Chollet, Hadrien Dyvorne, Hedwige Polovy, Myriam Pannetier-Lecoer, and Claude Fermon. *Magneto-resistive Hybrid Sensors for Simultaneous Low-Field MRI and Biomagnetic Measurements*, volume 28, pages 70–73. 2010.
- [13] Dieter Koelle. A tip for better sensing. *Nature Nanotechnology*, 8(9):617–618, 2013.
- [14] J. Nagel, A. Buchter, F. Xue, O. F. Kieler, T. Weimann, J. Kohlmann, A. B. Zorin, D. Ruffer, E. Russo-Averchi, R. Huber, P. Berberich, A. Fontcuberta i Morral, D. Grundler, R. Kleiner, D. Koelle, M. Poggio, and M. Kemmler. Nanoscale multifunctional sensor formed by a ni nanotube and a scanning nb nanosquid. *Physical Review B*, 88(6):064425, 2013.
- [15] Silvia Ruffieux. High-temperature superconducting magnetometers for on-scalp meg. 2020.
- [16] Lin Jianxin, Benedikt Müller, Julian Linek, Max Karrer, M. Wenzel, María José Martínez-Pérez, Reinhold Kleiner, and Dieter Koelle. YBa₂Cu₃O₇ nano superconducting quantum interference devices on mgo bicrystal substrates. *Nanoscale*, 2020.
- [17] Carmine Granata and Antonio Vettoliere. Nano superconducting quantum interference device: A powerful tool for nanoscale investigations. *Physics Reports*, 614:1–69, 2016.
- [18] Ling Hao, J. Macfarlane, J. C. Gallop, David Cox, J. Beyer, Dietmar Drung, and T. Schurig. Measurement and noise performance of nano-superconducting-quantum-interference devices fabricated by focused ion beam. *Applied Physics Letters*, 92:192507–192507, 2008.
- [19] S. Lam. Noise properties of squids made from nanobridges. *Superconductor Science and Technology*, 19:963, 2006.
- [20] Giuseppe C. Tettamanzi, Christopher I. Pakes, Simon K. H. Lam, and Steven Prawer. Flux noise in ion-implanted nanosquids. *Superconductor Science and Technology*, 22(6):064006, 2009.
- [21] M. Pannetier, C. Fermon, G. Le Goff, J. Simola, E. Kerr, and J. M. D. Coey. Noise in small magnetic systems—applications to very sensitive magneto-resistive sensors. *Journal of Magnetism and Magnetic Materials*, 290-291:1158–1160, 2005.
- [22] J. P. Cleuziou, W. Wernsdorfer, V. Bouchiat, T. Ondarçuhu, and M. Monthieux. Carbon nanotube superconducting quantum interference device. *Nature Nanotechnology*, 1(1):53–59, 2006.
- [23] C. P. Foley and H. Hilgenkamp. Why nanosquids are important: an introduction to the focus issue. *Superconductor Science and Technology*, 22(6):064001, 2009.

Research and Evaluation of Early Warning Models for Crowd Density Monitoring Based on Drones

Hao LI¹, Yining LIU, Jiongkai CHEN and Mingxuan CHEN

School of information technology, Nanjing Forest Police College, Nanjing 210023, China

Abstract. High-density crowd areas are receiving more and more research attention as a key area of concern for law enforcement agencies. This project focuses on combining emerging drones with crowd monitoring algorithms to build early warning prediction models that can be embedded into the backend systems of relevant departments to provide references for the holding of large events and the control of popular scenic spots.

Keywords. High density crowd area, People Flow Forecast, Abortion Management

1. Background Introduction

With the gradual emergence of the drone industry, it provides new ideas on how to effectively solve the problem of crowd control in dense areas. Drones have extremely high mobility, and by carrying high-definition camera equipment, they can synchronously collect and transmit relevant information, use algorithms to calculate the flow of people in real time, control and identify a large number of people, and effectively manage the crowd. At present, due to the large gap between domestic and foreign drones and other related technology research, although the domestic drone research on low and medium density crowd identification has been quite mature, but due to the impact of crowd occlusion and light changes in high-density scenes, the research on high-density crowd detection is still in the development stage. Therefore, there are still many difficulties in dense crowd control exist.

1.1. Insufficient Risk Assessment and Gaps in Management by the Organizers

In the context of an epidemic society, the shortage of manpower is particularly evident, and many efforts are limited. Secondly, the practice of video surveillance with human detection still cannot meet the requirements of overall comprehensive surveillance of key areas, limited personnel cannot control a large number of people, complex information about people is difficult to capture, and the management of scenic spots or large events unit awareness of high-risk behavior is weak, and dense crowds are prone to danger.

¹Corresponding author: Hao LI, E-mail: 1173980965@qq.com.

1.2 Traditional Measures Taken in the Work of Public Safety Issues Such as Dense Crowd Places

The main steps of the current control of high-density crowd places are: patrol - deploy personnel - dispatch personnel to the scene - carry out control work, resulting in the traditional crowd control mode of work response mode passive, greatly increasing the time for control personnel to arrive at the scene, it is difficult to deal with the problem in a timely manner. To do advance warning of the occurrence of danger, the control work in response to the sudden danger of passive into active, reduce the loss of large crowded places of danger is extremely necessary.

1.3 The Staff in the Inspection Process of High-risk Behavior Prediction of the Target is Weak

Dense crowd flow has a great randomness, it is difficult to predict its development, bringing great difficulties for personnel control. In the crowd control, strengthen the key links, key areas and important time of the site situation monitoring, how to achieve early warning, the passive into active, the effective use of science and technology to improve the traditional patrol prevention and control, control and disposal of the problem needs to be addressed.

2. Model Building

Our research idea is to build an intelligent aggregated hazardous event prevention model with the help of big data technology and image recognition algorithms. First we determine the data source, use the drone to collect the raw video data of the area, and then process the raw drone video with neural network and algorithm to realize the person counting and tracking. After that, we use openpose algorithm and st-gcn algorithm to analyze the behaviors in the returned video data and provide early warning of dangerous behaviors [1]. Finally, we continuously improve the accuracy of the model and the value of real-world applications through a large amount of data, and build a police prediction system to provide auxiliary decisions in the control background of relevant departments. The specific idea is shown in Figure 1.

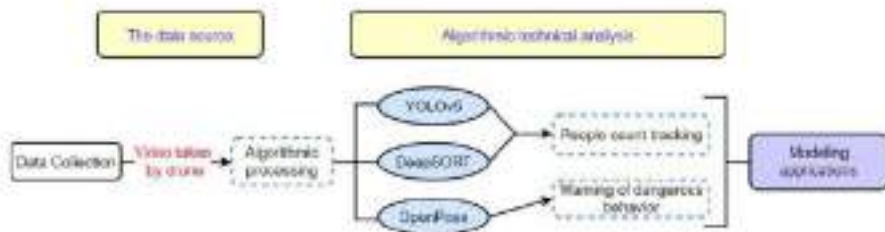


Figure 1. Specific thought diagram

2.1. Data Source

The data source is to collect the video data of dynamic distribution trajectory of people in Nanjing Qinhuai River scenic area by police drones with time slots and location allocation.

2.2 People Count Tracking Model

First, we use the open-source DOTA dataset from Wuhan University as the data source for the crowd density detection model, DOTA Dataset (A Large-scale Dataset for Object DeTection in Aerial Images) is an image dataset for object detection in aerial images, which is used to discover and DOTA-V2.0 contains a total of 2806 aerial images from different sensors and platforms, containing objects of different scales, orientations and shapes. These DOTA images are then annotated by experts using 15 common target categories. The fully annotated DOTA images contain 188,282 instances, each marked by an arbitrary quadrilateral. This is illustrated in Figure 2.



Figure 2. RCNN source of data set

SSD balances the advantages and disadvantages of YOLO and RCNN. However, SSD requires manual settings during debugging and cannot be automatically learned, which makes the debugging of SSD model very dependent on experience.

YOLO, like SSD, has the characteristics of accuracy and high speed. YOLO has excellent performance in overall detection by end-to-end testing. The YOLO uses CNN networks for target detection, which is very simple and fast.

For model construction we use deepsort tracking algorithm and yolov5 target detection algorithm to build the model [2].

The yolov5 target detection algorithm, YOLOV5 algorithm detects objects by dividing the image into a grid, and uses a modified GoogLeNet as the backbone network to extract features [3]. The feature map of the output layer is designed to output the coordinates of the target frame, the target frame score and the category score. yolov5 is a typical one-stage detector that only needs to be input to the network model once to produce detection and classification results. yolov5 target detection process is shown in Figure. 3.

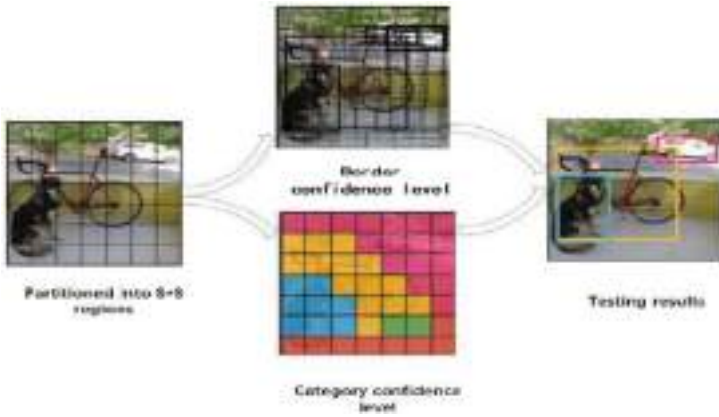


Figure 3. yolov5 target detection process

We use the yolov5 target detection network to analyze the UAV video transmitted in real time to obtain the location of each person in the video and mark them in the video. This is shown in Figure 4.



Figure 4. Implementation of the function of locating people on the video

We use a convolutional neural network to detect and track the pedestrians in the video. After the video frame is input, it first enters the network of YOLOv5 target detection, and after the Darknet-53 algorithm extracts the features, then performs regression analysis, and feeds the resulting prediction frame information into the SORT algorithm for target feature modeling, matching and tracking; finally, the output results. Figure 5 shows the algorithm flow design.

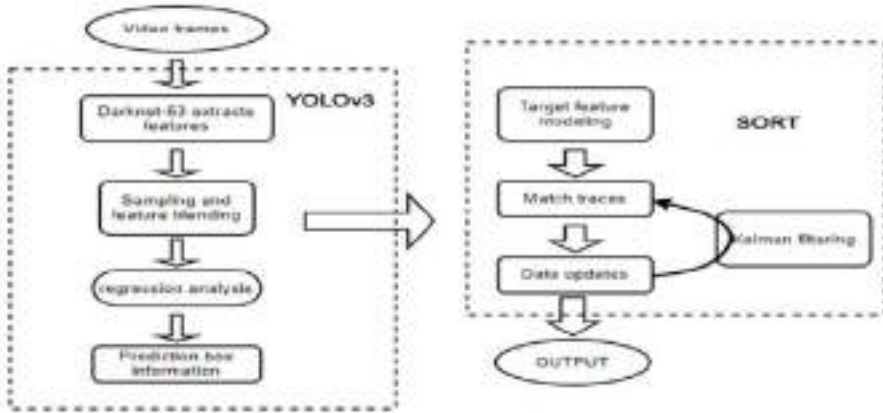


Figure 5. Algorithm flow design diagram

The steps of the character location tracking algorithm design are as follows:

The target detection algorithm analyzes each input frame and then determines the class of objects with specific attributes and gives the position of each coordinate. Next is the motion trajectory prediction phase: multiple feature extraction algorithms are used to extract features and a trajectory predictor is used to predict the next position for character localization. Then comes the similarity calculation phase, where the determined positions are compared with the images and the similarity is calculated. Finally, there is the association phase: based on the calculated similarity, detection objects belonging to the same target are associated with the trajectory, and the detection objects are given the same ID as the trajectory.

We encapsulate yolov5's target detection into a Person__detect class, through whose detect method every pedestrian target in the video can be detected. By setting a datum line in the video screen given the coordinates of the two ends of the line, we use this datum line as the axis to determine the forward direction of the pedestrian, and also determine the number of people entering and leaving both directions. At the same time, a tracker is created to track the targets detected by yolov5. This idea can be applied to track the movement trajectory of people in large scenic areas in real time.

2.3 Risky Behavior Warning

After the target detection algorithm analyzes the video, we apply the OpenPose algorithm to extract the human skeleton in each frame. By adding the video to the algorithm and running it, the resulting JSON file is parsed as follows: the position information of each body part (x,y,score), each part is an array containing the position information of each body part and the detection confidence in the format = x1,y1,c1,x2,y2,c2,... The coordinates x and y can be are normalized to the intervals [0,1], [-1,1], [0, source size], [0, output size], etc [4]., and each skeletal point is concatenated to obtain the human skeletal information.

After the character localization and skeleton extraction, the system will define and recognize the action of the annotated joint dynamic data training set through the st-gcn open source algorithm, in which the action definition uses the time series of human joint positions to represent the dynamic skeletal modality, and then defines the current human action by analyzing its action pattern [5]. Based on the dynamic definition, the machine recognizes the human action behavior, analyzes and judges what the human is doing at

this time, and defines the human's current action, and then visualizes the definition on the screen. This is shown in Figure 6.



Figure 6. The display diagram of personnel action after definition

Finally, the program will further test and evaluate the action posture judged by the st-gcn algorithm based on deep learning, and then predict the possible abnormal behaviors of specific people in the key places of public security, such as stabbing, stomping and fighting, and define such actions as abnormal actions, and if the action is defined as abnormal, the program will send an early warning message.

3. Model Innovation Highlight

The project proposes to use drones to monitor the crowded areas and transmit the data back to the background in real time, based on which the crowd density is calculated at the macro level with YOLOv5 and deepsort algorithm, and alarmed at the micro level with openpose algorithm for high risk actions such as stepping, to achieve the effect of reasonable control of key areas and reasonable allocation of manpower. The project features are as follows.

3.1 Combined with Drones to Build a New Model of Active Research and Analysis

The project to scientific control mode change, through the use of drones equipped with high-definition cameras, change the way of personnel control, through the drone shooting and real-time return of the video, take the means of video processing analysis, the number of people heat map and other related data and images, data integration and analysis, so as to enhance the initiative of personnel control work.

3.2 Drones and Patrol Synergy, The Establishment of Three-dimensional Control System

Relying on drones and backstage information platform, we can enhance the synergy between various departments, so as to improve efficiency, and the application of drones can collaborate with manpower for key control, real-time control of key areas, grasp the situation in key areas, improve the efficiency of manpower applications at the same time, and personnel control with each other, so as to establish a three-dimensional patrol and defense system.

3.3 Comparative Study of Recent Works to Highlight Project Strengths

The new DOTA dataset, DOTA-v2.0, was selected, and compared with DOTA-v1.0, DOTA-v2.0 has a total of 18 location categories labeled and aerial view images added. Compared with "YOLOv5-based UAV target image recognition" [5], this project UAV in remote sensing scenes The data scale for performing rotating target detection is large, small target sampling is not easily lost, and the accuracy is higher; in "Vehicle multi-target detection method based on YOLOv2 algorithm under Darknet framework " [6], which uses a joint optimized detector YOLOv5 and Deep-SORT for UAV multi-target tracking algorithm to achieve detection and tracking of targets, this project combines YOLOv5 and Deep-SORT algorithm is applied to macro level to calculate the density of human flow, and openpose algorithm is applied to micro level to alarm the high risk action, which is more perfect and comprehensive in the algorithm.

4. Conclusion

The system is more advantageous in terms of practical application of crowd monitoring, algorithm setting and promotion of operation. However, there are some shortcomings in terms of comprehensive consideration of UAV technology, equipment economics, and specific practicality. Based on our practical use experience the following advantages and limitations are summarized:

4.1. Model Advantage

4.1.1 Fits the Context of the Current Epidemic Environment

The use of drones can make the relevant departments more "intelligent" and "non-contact" control of personnel, which has a large application scenario in the current social context of the epidemic. In the current environment where drones are used in a large number of fields, it provides a good foundation for its rapid application nationwide.

4.1.2 Catering to the Need for Change in the Concept of a Strong Science and Technology Nation

In recent years, high-tech means to assist the work has become a new trend, drones have long been involved in the work of all sectors and play an important role. The combination of modern means of new work mode in also continue to deepen, showing a positive and active innovation prospects and development stage. Drones have a fairly high flexibility, mobility, functionality, in today's real-world aspects, become a successful application of the professional field recognized.

4.1.3 High Promotability of the Model System

The model is constructed based on the results of the YOLOv5, deepsort algorithm for UAV sampling, submitted to a Bayesian network for comprehensive analysis. These algorithms are mature, easy to maintain, and the model has a fast response time when

testing the data set, which can quickly produce realistic and feasible results with good results, meeting the requirement of efficiency.

4.2 Model Limitation

4.2.1 UAV Battery Life Problem to be Resolved

Because UAVs need to reduce takeoff weight as much as possible, they cannot carry heavier high-capacity batteries, and most UAVs must replace batteries or plug in charging cables after maintaining effective flight for twenty minutes, which results in UAVs only collecting local data on a small scale, and it is difficult to monitor the overall movement of people in the region.

4.2.2 Poor Interference Resistance of Drone Flight

UAV communication systems use public radio communication links, which have weak anti-jamming capability, especially co-channel interference cannot be avoided. In addition, civil UAVs generally use GPS and BeiDou dual-mode mode navigation. Navigation satellite signals are susceptible to terrain, weather, and the complexities of urban buildings and other objective conditions, resulting in a lack of accuracy and stability.

4.2.3 There Is Still Room for Optimization of the Model Algorithm

The model algorithms use artificial neural networks, which require a lot of training to improve the accuracy and stability of the system before they can be put into practical use, and the training of the models using big data requires high performance of hardware devices, which often brings various high hardware costs. In order to practice this technology better, reduce the cost of use, improve the economy and practicality, but also need for the optimization of the model algorithm.

Acknowledgements

This research was support by the 2022 College Students Innovation and Entrepreneurship Training Program (Grant No. 202212213040Z).

References

- [1] He Wentao,Huang Xueyu,Li Yao. Handheld object analysis algorithm based on OpenPose and YoLo[J].Journal of Air Force Engineering University (Natural Science Edition),2021,22(6).
- [2] Jia Doudou. Research on small target tracking method based on YOLOv5+DeepSort[C].North University of China, 2022:
- [3] HE Yu, LI Dan. Real-time subway passenger flow detection based on YOLOv5 and DeepSort[J]. Electronic Test.2022.
- [4] Zhang Zhimeng,Peng Jing,Jiang Xiaoping1,Shi Hongling. Human skeleton motion recognition based on Gaussian noise and ST-GCN[J].Journal of South Central University for Nationalities (Natural Science Edition), 2022,41(4).

- [5] Junyi Zhang YOLOv5-based UAV Target Image Recognition[J]. School of Electrical and Automation Engineering, Hefei University of Technology 2022,51-52
- [6] Li Xun, Liu Yao, Li Pengfei, et al. Vehicle multi-target detection method based on YOLOv2 algorithm under Darknet framework[J].Journal of Transportation Engineering,2018,18 (6):142-158.

A Method of Anti-Nonsynchronous Short Pulse Jamming Based on Waveform Entropy

Zijun HU^a, Xinliang CHEN^{a,b,c,1}, Leizhen ZHOU^d and Zhennan LIANG^a

^a*Key Laboratory of Electronic and Information Technology in Satellite Navigation (Beijing Institute of Technology), Ministry of Education, Beijing 100081, China;*

^b*Yangtze Delta Region Academy of Beijing Institute of Technology, Jiaxing 314019, China;*

^c*Chongqing Innovation Center, Beijing Institute of Technology, Chongqing 401135, China;*

^d*China Mobile Group Zhejiang Co., Ltd. Hangzhou 310016, China*

Abstract. In the condition of complex electromagnetic environment and multifarious methods of activate jamming, the anti-jamming approach has been highlighted. Anti-jamming method based on waveform entropy is used to counter nonsynchronous short pulse jamming because of its low compute complexity and easy implementation. This paper analyzes the anti-jamming performance, obtain the decision threshold value by taking use of kernel function, and exhibit the influence on radar system. The equivalent signal-to-noise ratio is improved by at least 12.2 dB compared with normal detector.

Keywords. Waveform entropy, nonsynchronous short pulse jamming, kernel function.

1. Introduction

With the development of science and technology, the working environment of radar is becoming more and more complex, especially rapid processing of ECM (electronic countermeasures), anti-jamming measures become necessary. In this condition, modern radar must be equipped with a variety of anti-jamming methods to ensure that the target information can be obtained effectively and quickly. The performance of anti-jamming of radar, which is kind of important sensor and data processor, has great meaning for its self-survival and battle performance[1][2].

Waveform entropy has been used in features recognition, ECM, and target detection fields due to its easy implementation and low compute complexity. Zhang[3] proposed a method to distinguish clutter and HRRPs (high resolution range profile) of targets in environment based on waveform entropy. In literature[4], to identify moving status of bird with waveform entropy variance is proposed via processing each HRRP from spectrogram. In addition, waveform entropy is also used in a variety of jamming scenarios, FANG[5]used frequency agility and waveform entropy to identify target and dense false target jamming which seriously affects the effectiveness of radar operations. Literature[6] take use of waveform entropy to obtain the profile of target which are

¹ Corresponding Author, Xinliang Chen, Beijing Institute of Technology. Beijing 100081, China.
E-mail: chenxinliang@bit.edu.cn;

covered by nonsynchronous short pulse jamming. However, the above literatures do not consider the value of decision threshold between target and jamming's waveform entropy and the influence on radar system after using waveform entropy.

This paper will clarify the principle of nonsynchronous short pulse jamming in chapter2, and then introduce the waveform entropy in chapter3. In chapter4, it will analyze performance of anti-jamming based on waveform entropy under jamming state, obtain the decision threshold by using kernel function, and then clarify the influence on the detection of radar system.

2. Jamming and entropy

2.1. Jamming model

As a common jamming model, narrow pulse jamming is often generated in high frequency to replace the cover-pulse jamming, so as to reduce the transmit power of jammer. In this condition, INR (interference to noise ratio) is quite high, and jamming can easily cover the echo of true target, so that radar cannot work anymore. When narrow pulse jamming is not stable in time domain relative to the radar system clock, it is called nonsynchronous short pulse jamming.

If the jammer transmits rectangular pulse as narrow pulse jamming, its time-domain signal expression can be written as:

$$j_{m_i}(t) = \sum_{i=1}^N \text{rect}\left(\frac{t - t_{m_i}}{\tau}\right) \tag{1}$$

Where τ is the pulse width of each narrow pulse jamming, t_{m_i} represents the i^{th} echo of narrow pulse jamming in m^{th} PRT (pulse repetition time), m is $1, 2, \dots, M$. So that the entire echo data of processed jamming can be expressed as:

$$j(t) = \sum_{m=1}^M \sum_{i=1}^N \text{rect}\left(\frac{t - t_{m_i}}{\tau}\right) \tag{2}$$

If jammer modulates the chirp which was sliced from echo of true target into rectangular pulse as transmitted wave, if echo of target in time domain is:

$$s(t) = \text{rect}\left(\frac{t}{T_p}\right) \exp(j2\pi f_0 t + k\pi t^2) \tag{3}$$

Where T_p is pulse width of transmitted signal from radar, f_0 is carrier frequency, k is ramp rate, $k = B/T_p$, B is band width of signal. So, Modulated jamming in the m^{th} PRT can be written as:

$$j_{m_i}(t) = \sum_{i=1}^N \text{rect}\left(\frac{t - t_0 - t_{m_i}}{\tau}\right) s(t - t_{m_i}) \tag{4}$$

Where t_0 is beginning of slicing time, and $0 < t_0 \leq T_p$. Similar with unmodulated jamming, the echo of modulated signal in M PRTs can be expressed as:

$$j(t) = \sum_{m=1}^M \sum_{i=1}^N \text{rect}\left(\frac{t - t_0 - t_{m_i}}{\tau}\right) s(t - t_{m_i}) \tag{5}$$

The response of jamming obtained after the passes through the matched filter can be expressed as:

$$j_o(t) = cs^*(\tau_0 - t) * j(t) \quad (6)$$

Where c represents constant, $s(t)$ is reference signal, if it is chirp signal, it can be seen in formulation(3), $s^*(t)$ is the complex conjugate of $s(t)$, τ_0 is achievable delay of physical filter.

2.2. Principle of waveform entropy

In 1984, the concept of information entropy is proposed by Shannon, which is used to express the uncertainty of describing the source[7]. The formula of information entropy is as follows:

$$H(\omega) = - \sum p \log(p) \quad (7)$$

The waveform entropy is proposed as a similarity concept to information entropy, which is used to characterize the stationarity of waveform. The higher the stationarity of signal, the bigger value of waveform entropy.

Suppose that radar signal after sampling is $x(m, n)$, where m represents the m^{th} PRT, its value can be $1, 2, \dots, M$. Besides, n represents the n^{th} sample data in a PRT, so that denote intermediate variable as:

$$\begin{cases} \|X(n)\| = \sum_{m=1}^M |x(m, n)| \\ P_n = \frac{|x(m, n)|}{\|X(n)\|} \end{cases} \quad (8)$$

Therefore, waveform entropy can be expressed as:

$$E(X) = - \sum_{n=1}^N P_n \ln P_n \quad (9)$$

We can know the properties of waveform entropy from formulation#(9), If the value of the n^{th} sample data in time domain change less from PRT to PRT, it will get a big value in waveform entropy, if it would not change absolutely, it can reach the maximum value $\ln M$.

3. Simulation and performance analyze

3.1. Simulation of nonsynchronous short pulse jamming

If primary parameters were set as **Table 1**, as the principle of nonsynchronous short pulse jamming in Chapter2.1, its echo in time-domain and its profile (result of pulse compress) can be seen in **Figure 1** and **Figure 2**.

Table 1. Primary parameters of nonsynchronous short pulse jamming tion.

Parameters	Value
Pulse width of jamming	5us
INR	30dB
Carrier frequency	2.7GHz
Pulse width of match filter	35us
Bandwidth of match filter	5MHz
Repeat numbers in a PRT	10

The echo and its profile of nonsynchronous short pulse jamming which was not modulated is shown as follows:

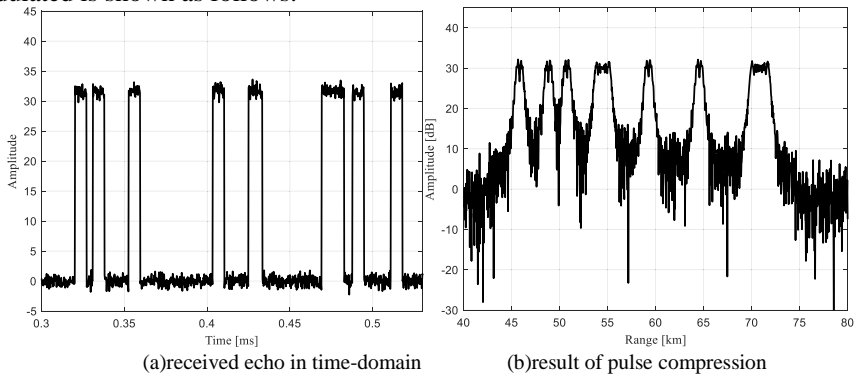


Figure 1. Simulation of nonsynchronous short pulse jamming which was not modulated

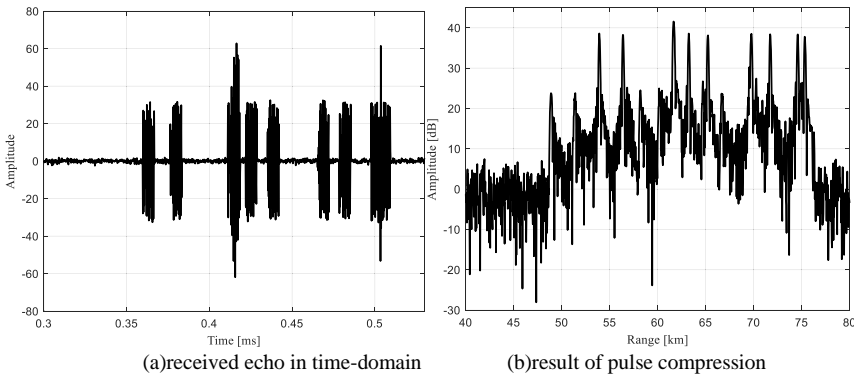
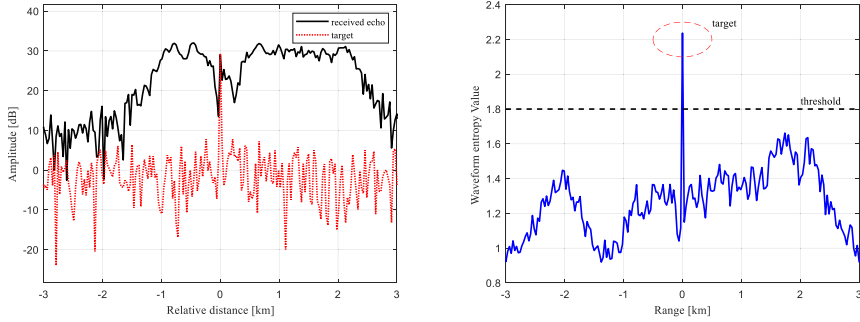


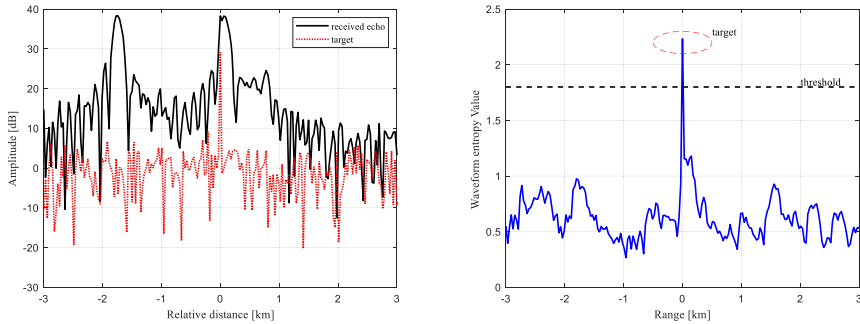
Figure 2. Simulation of nonsynchronous short pulse jamming which was modulated

The echo and its profile of nonsynchronous short pulse jamming which was modulated with chirp can be seen in **Figure 2**. We can find that INR after pulse compression increase about 0dB in **Figure 1** and about 8dB in **Figure 2**. Therefore, unmodulated jamming will hardly obtain gain after pulse compression, but jamming modulated with chirp can acquire a part of gain of match filter. The value of gain obtained by jamming depends on the match level. if it matches completely, the gain of match filter can be acquired absolutely.

If the echo of a stationary target was covered by jamming whose primary parameters are in **Table 1.**, one PRTs’ pulse compression can be seen in the left of Fig3, and waveform entropy is calculated with 10 PRT’s echo, the result can be seen in the right part of **Figure 3**.



(a) pulse compression and waveform entropy result of target echo covered with unmodulated jamming



(b) pulse compression and waveform entropy result of target echo covered with modulated jamming

Figure 3. Pulse compression and waveform entropy result

The calculated result of waveform entropy is obtained from 10 PRTs data of echo, we can find that target can be detected from nonsynchronous short pulse jamming in right pictures of **Figure 3**.

3.2. Decision criterion

As usual, radar will compare the results which are calculated after match filter with the threshold. If square-law detector is selected to achieve judgments, the decision criterion can be written as:

$$y(t) = \begin{matrix} H_1 \\ |x(t)|^2 \geq \gamma \\ H_0 \end{matrix} \tag{10}$$

Where H_1 means there is signal of target in received echo, H_0 means only noise in environment, the result of judgment can be presented as:

$$r_1(t) = \begin{cases} 1, y(t) > \gamma \\ 0, y(t) \leq \gamma \end{cases} \tag{11}$$

Threshold γ is determined by false alarm probability and distribute of noise. We combine the waveform entropy as the second threshold to replace the normal detect processing. So decision criterion can be corrected as:

$$r(t) = r_1(t)r_2(t) = \begin{cases} 1, there\ is\ target \\ 0, there\ is\ no\ target \end{cases} \tag{12}$$

Where $r_1(t)$ is the result of normal detect processing, $r_2(t)$ is the second threshold which is used to judge the statistical samples who's value over the first threshold. The method of proposed detector is similar with Generalized Likelihood Ratio Test (GLRT) detector[8] [9] and the detect method can be written as:

$$r_2(t) = E(t) > \epsilon = \begin{cases} 1, & \text{there is target} \\ 0, & \text{there is no target} \end{cases} \quad (13)$$

Where $E(t)$ is the power of waveform entropy which was mentioned in formulate(9).

Threshold ϵ can be obtained by distribute of jamming and signal of target under minimum error criterion[10], and then we take use of kernel density estimation method to acquire the distribute.

In summary, the flowchart of the proposed detection method under ISRJ scenario is shown in **Figure 4**.

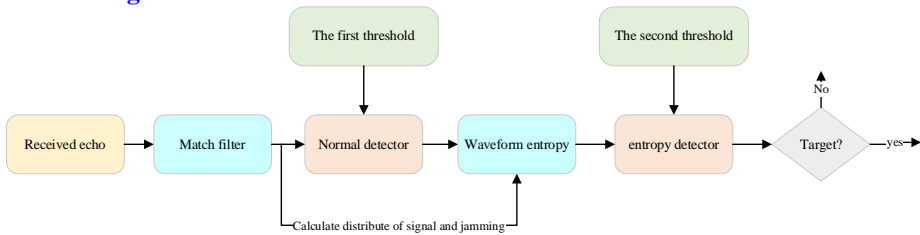


Figure 4. Flow chart of the proposed method

3.3. Kernel density estimation and detector performance

When we calculate waveform entropy, the signal features will be mapped to waveform entropy domain, threshold to distinguish target and others would be obtained by Monte-Carlo method again.

Unlike regular detecting, definition of waveform entropy makes its threshold not only related to the value of false alarm rate and power of noise, but also relevant to the calculated PRTs' number (M in formulation(8)). For convenience, if there is no special instructions, false alarm rate will be set as 10^{-6} , power of noise in each PRT is 0dbW. To ensure threshold and analyze detection performance, the distribution of noise and the distribution of signal plus noise in waveform entropy domain need to be known. In traditional detection processing, noise in environment is regarded as Gaussian white noise, and threshold can be calculated by precise mathematical expressions and hypothesis testing theory. But threshold in waveform entropy domain can only be acquired by Monte-Carlo method or approximate expression. The former uses statistical frequency instead of probability, which requires a large amount of calculation, the latter uses Gaussian distribution to obtain approximate distribution, which is not accurate. This paper will use kernel density estimation method to fit the distribution of noise and signal plus noise in waveform entropy domain.

Kernel density estimation (KDE) is an effective nonparametric estimation method which is also called Parzen window estimation[11]. Suppose a group of observations of the random variable z is $z^{(1)}, z^{(2)}, \dots, z^{(N)}$, so that probability density function $f(z)$ can be expressed as:

$$\hat{f}(z) = \frac{1}{Nh} \sum_{i=1}^N K\left(\frac{z - z^{(i)}}{h}\right) \quad (14)$$

Where N is number of samples, h is bandwidth of sample, $K(\cdot)$ is kernel function, and common kernel functions include uniform kernel, triangular kernel and Gaussian kernel, this paper take use of Gaussian kernel, which is:

$$K(u) = \frac{1}{2\sqrt{\pi}} e^{-\frac{u^2}{2}} \tag{15}$$

So that formulation(8) can be written as:

$$\hat{f}(z) = \frac{1}{Nh} \sum_{i=1}^N \frac{1}{2\sqrt{\pi}} \exp\left(-\frac{\left(\frac{z - z^{(i)}}{h}\right)^2}{2}\right) \tag{16}$$

Where bandwidth h can be approximately obtained by formulation(11), when we select Gaussian kernel:

$$h = \left(\frac{4\hat{\sigma}^5}{3N}\right)^{\frac{1}{5}} \tag{17}$$

Where $\hat{\sigma}$ is standard deviation of estimated samples. Further discussion can be found in Literature[12].

We compare the result of kernel density estimation method and Monte-Carlo method, the calculated samples are acquired from 7 PRTs whose SNR (signal to noise rate) is 7dB, the former take use of 26420 samples, and the latter take advantage of 2×10^7 samples. It can be shown in **Figure 5**.

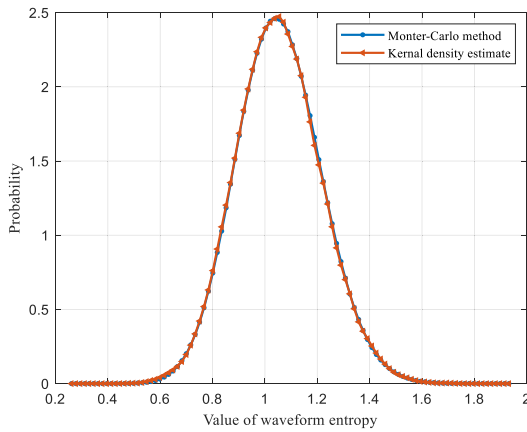
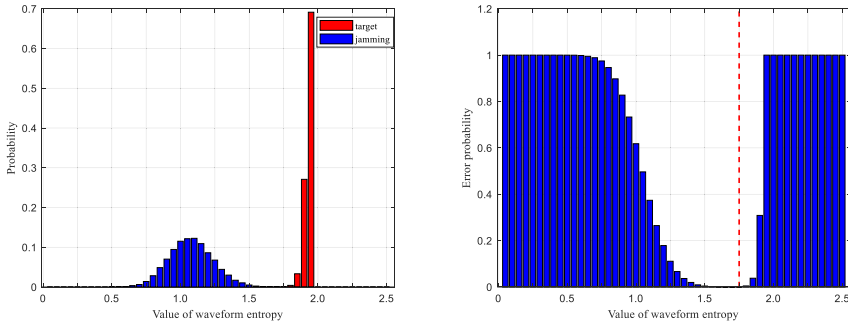


Figure 5. result of kernel density estimate method

It can be found that results are basically the same in **Figure 5**, using kernel density estimation can ensure high accuracy and reduce compute complexity. Similarly, the kernel density estimation method is used to obtain the probability density function of signal and jamming in **Figure 6**, it can be associated with **Figure 5** to acquire threshold.



(a) The probability distribution of waveform entropy (b) probability of error and identification threshold ϵ

Figure 6. distribution of jamming and signal in waveform entropy domain

Threshold ϵ can be obtained according to the distribution in **Figure 6**. When probability reach the minimum, threshold is 1.80. In this way, thresholds and detection probabilities in different SNR and JNR can be calculated, then we can know the performance of detector in using anti-jamming method based on waveform entropy.

In the condition of nonsynchronous short pulse jamming, when CA-CFAR is selected as detector, its performance will be worse than after taking anti-jamming measurement based on waveform entropy. The Details can be seen as follows:

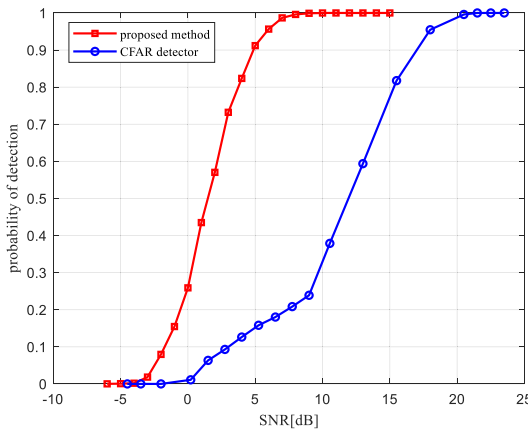


Figure 7. performance of CA-CFAR detector

X label in **Figure 7** means SNR of one PRT, and there are 7 PRTs are taken into calculate. We can find that proposed detector required SNR improvement about 12.2dB when probability of detection reaches 0.9.

If there is no jamming in electromagnetic environment, performance of normal detector and anti-jamming measurement detector are shown in **Figure 8**.

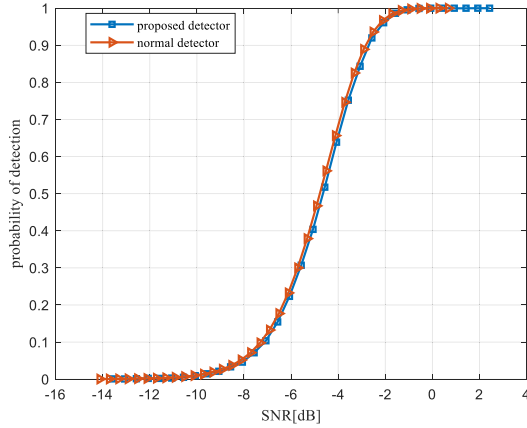


Figure 8. performance of CA-CFAR detector in no jamming environment

Two detection curves almost coincide in **Figure 8**, we can find that the detection performance of the proposed method has almost no loss in the simulation scenario.

4. Verification

This paper will verify performance of anti-jamming method based on waveform entropy and the correctness of threshold by taking using of measured data which was collected by a P-band radar. We can see pulse compression result of target’s echo covered with nonsynchronous short pulse jamming in **Figure 9**.

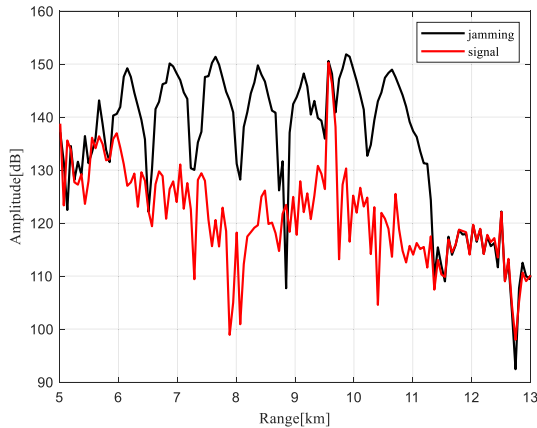


Figure 9. pulse compression result of measured data

The profile of target was obtained independently when jammer was turned off. We compare the amplitude with the first threshold and calculate the waveform entropy of measured data. Finally, we take use of the second threshold to judge the result.

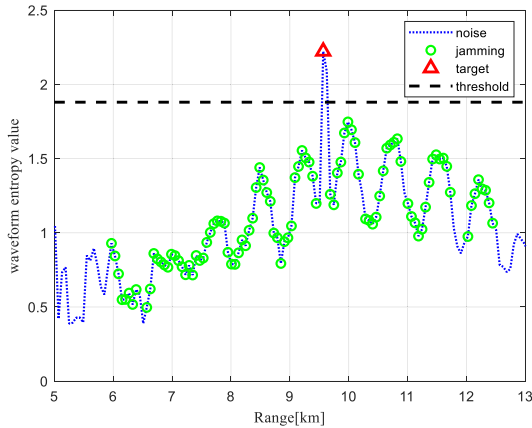


Figure 10. waveform entropy of measured data

The part of jamming whose value is over the first threshold are marked with green circle in **Figure 10**, and the second threshold is also presented, we can find that only the entropy of target's echo is over the second threshold. Therefore, the target can be detected correctly in waveform entropy domain.

5. Conclusion

On the basis of proving the effectiveness of anti-jamming measures based on waveform entropy, this paper takes advantage of kernel density function to fit the distribution of jamming and signal in waveform entropy domain, which reduce the compute complexity. Furthermore, the performance and gain of the detector under the condition of asynchronous narrow pulse interference are analyzed in this paper, we can find that proposed detector required SNR improvement about 12.2dB when probability of detection reaches 0.9. Finally, this paper proof that proposed detector will cause no influence on radar system, and measured data can also proof the effectiveness of proposed method. The method proposed in this paper can provide a new and easy to implement thought for radar anti-jamming, which is convenient to be applied in engineering practice.

References

- [1] LEI Zhengwei, WANG Xiaoli, Ji Xinwei, "Analysis on demand of anti-jamming design for modern radar system," *Journal of Modern Radar* 2020,42(02):85-90.
- [2] Y. Yan, H. Chen and J. Su, "Overview on anti-jamming technology in main lobe of radar," 2021 IEEE 4th International Conference on Automation, Electronics and Electrical Engineering (AUTEEE), 2021, pp. 67-71.
- [3] Zhang Zebing, Du XiaoYong, Hu Weidong, "Waveform Entropy-based Target Detection in HRRPs," *Journal of Aeronautical Computing Technique* 2007(06):51-54.
- [4] F. Zhu, Y. Feng, Y. Luo and Q. Zhang, "A novel method of identifying moving status of bird based on waveform entropy variance," 2008 International Conference on Communications, Circuits and Systems, 2008, pp. 922-926.

- [5] FANG Wen, QUAN Yinghui, SHA Minghui, et al "Dense false targets jamming suppression algorithm based on frequency agility and waveform entropy,"*Journal of System Engineering and Electronics* 2021,43(06):1506-1514.
- [6] Hao Ming, Guo Rujiang, "Asynchronous narrow pulse interference suppression based on waveform entropy," *Journal of Information Research* 2009,35(05):42-44+64.
- [7] X. Zhang, Y. Wang and L. Wu, "Research on Cross Language Text Keyword Extraction Based on Information Entropy and TextRank," 2019 IEEE 3rd Information Technology, Networking, Electronic and Automation Control Conference (ITNEC), 2019, pp. 16-19.
- [8] B. K. Chalise and K. T. Wagner. "Distributed GLRT-based Detection of Target in SIRP Clutter and Noise," 2021 IEEE Radar Conference (RadarConf21), 2021, pp. 1-6.
- [9] Y. Sun, J. Huang, J. Huang and P. Li, "Compressive GLRT detector for radar system," *IET International Radar Conference 2015*, 2015, pp. 1-4.
- [10] Kay Steven and Hall Prentice. *Fundamentals of Statistical Signal Processing: Detection Theory Volume II*. Englewood Cliffs, NJ, US, Prentice-Hall, Inc., 1998: 77-79.
- [11] SONG Yuanfeng,, WAN Lingyun et al "Coarse-to-Fine Detection for Nests on Pylon," *Journal of Power System and Clean Energy* 2016,32(06):85-88.
- [12] N. Suga, K. Yano, J. Webber, Y. Hou, T. Higashimori and Y. Suzuki, "Estimation of Probability Density Function Using Multi-bandwidth Kernel Density Estimation for Throughput," 2020 International Conference on Artificial Intelligence in Information and Communication (ICAIIIC), 2020, pp. 171-176.

Measuring the State of ECN Readiness in Mail Servers on the Internet

Chun-Xiang CHEN^{a,1}, Tetuya SHIGEYASU^a and Kenichi NAGAOKA^b

^a*Prefectural University of Hiroshima, Minami-ku, Hiroshima-shi, 734-8555, Japan*

^b*National Institute of Technology, Ishikawa College, Ishikawa, 929-0392, Japan*

Abstract. Congestion control on the Internet has been a challenge issue so far. Since there is no one-size-fits-all scheme for TCP congestion control, many various schemes have been developed to suit different kinds of communication environments. Among them, ECN (Explicit Congestion Notification) is the one which is able to feed the congestion state in the routers along a connection path back to the TCP transmitter. To promote the deployment of ECN and provide a concrete reference parameter to the Internet industry, in this paper, we actually measure the readiness of ECN in mail servers and analyze its deployment rate on the Internet. To clarify the characteristics of ECN in the mail servers, deployment rate of ECN is compared with that of ECN in major web servers. Based on the analysis results, we show some unique features of ECN in mail servers which are quite different from that of web servers.

Keywords. TCP congestion control, explicit congestion notification, deployment rate of ECN, email server, web server

1. Introduction

Over the last three decades, congestion control of TCP (Transmission Control Protocol) on the Internet still has been a challenge issue, especially in the super high-speed and/or ultra-dense heterogeneous networks. To solve this problem, a number of congestion control algorithms with TCP have been developed [1,2]. Due to the principles of TCP/IP (Internet Protocol), the TCP sender has no way to know about the traffic state along the connection path in real time. Therefore, all the schemes, such as the early TCP Tahoe, TCP Reno, TCP CUBIC [3] and then recent BBR (Bottleneck Bandwidth and Round-trip propagation time) [4,5], judge the congestion state in the intermediate network based on the packet loss and/or the transmission delay. However, their decisions probably diverge from the reality since traffic and connections might change rapidly within a short time.

To reflect the traffic state of a connection path in the sender, ECN was proposed and has been standardized in RFC 3168. To the authors' knowledge, ECN has been the only scheme that is able to successfully feed back an imminent congestion state along the connection path and greatly improve the throughput efficiency of the whole Internet. That is one of the reasons the authors have been committing to promoting the deployment of ECN [8]-[10]. However, the previous works have targeted only at major web servers. As an indispensable supplement to the previous works, in this paper, we conduct a set of empirical measurement and investigate the readiness of ECN in major mail servers on

¹Corresponding Author: Chun-Xiang Chen, Prefectural University of Hiroshima, Hiroshima, Japan;
E-mail:chen@pu-hiroshima.ac.jp

the Internet. Moreover, by analyzing the request-response of each SMTP (Simple Mail Transfer Protocol) connection, we clarify the deployment state of ECN on the Internet. Furthermore, we demonstrate some unique features of ECN in primary mail servers by comparing with that of leading web servers.

2. Related Works and Scope of this Work

ECN uses two bits in each of the IP and TCP headers. Its implementations have been stipulated in detail in RFC 3168. To clarify the benefit and risk of using ECN, a lot of previous works have been conducted [6]-[10].

RFC 8087 [7] expounds the potential benefits of ECN-Capable connections in terms of increased throughput and reduced delay. In [6], dynamic marking threshold algorithm for ECN was proposed. But it is limited in data center networks. In [8], the characteristics of ECN with regard to the connectivity, deployment rate were analyzed. Moreover, the latent risk of an ECN-Capable connection was evaluated quantitatively. To improve the connectivity of ECN, the sender would try to establish a not-ECN-capable connection when an ECN-Capable connection can't be established by timeout period. This process is called fallback. In [9], the effectiveness of the fallback regarding ECN was evaluated. Furthermore, features related to the deployment rate and connectivity were analyzed according to the regional distribution of the domains on the Internet.

However, all the previous works only focus on the major web servers on the Internet. As we know, email traffic based on SMTP is another traditional primary medium besides web services (based on HTTP and/or HTTPS). In recent years, the spread of SNS (Social Networking Service) has led to a decrease in the amount of email communication, but email, especially email with attachments, still plays an important role in the business world. In addition, many SNS use email addresses as authentication accounts. The number of email accounts continues to grow. Therefore, to reveal the deployment state of ECN over the Internet more precisely, measurement and analysis for major mail servers are also required. This paper aims to provide a concrete deployment rate of ECN for the Internet industry which have not been revealed so far. We analyze the readiness of ECN for major mail servers via a set of empirical measurement and clarify some unique features of ECN corresponding to mail servers.

3. Measurement Method

We firstly choose the mail servers targeted to be tested from the Internet. We use the major domains published by Alexa Global as the potential domains of mail servers [11] which are the same as the domain set used in the previous studies [8,10]. The process of our measurement is summarized as follows.

Download the Global Top one million domains from Alexa [11]; Query the DNS for the MX (Mail exchange) record of each domain. Here we use Google public DNS (8.8.8.8) to retrieve MX record and its IP (IPv4 and/or IPv6) address. For example, for domain {gmail.com}, we get its MX records as

```
gmail.com, gmail-smtp-in.l.google.com, alt1.gmail-smtp-in.l.google.com,
alt2.gmail-smtp-in.l.google.com,...
```

Then, we resolve their IP addresses of these MX records using the tool we developed. We get the entries of mappings as

```
gmail-smtp-in.l.google.com, 142.250.157.26, 2404:6800:4008:c13::1b
```

alt1.gmail-smtp-in.l.google.com, 142.250.141.27, 2607:f8b0:4023:c0b::1a

Note that, MX records and their IP addresses might be varying with the DNS server and the querying time. If a domain does not have its own MX record, it will be excluded from the domain entries. By removing the duplicated MX records of the domains, we finally obtained 220,367 and 210,440 entries of MX records (called *targeted server lists*) on 15 August 2021 and on 8 January 2022, respectively. Tools used to retrieve MX records and IP addresses and test SMTP connections, are developed in Python.

The measurements are performed by using a Linux host. Its specifications are as follows; CPU: Intel Xeon E5-1630v4, OS: CentOS 8.3 with kernel 4.18.0-240, Memory: 16GB, NIC: Intel 82574L Gigabit PCI interface. Measurements were conducted at the network of Prefectural University of Hiroshima. IPv6 network is connected through IPv4 tunnel provided by Hurricane Electric Internet Service. The tool used to test the targeted mail servers is developed according to the commands of SMTP. The procedures of measurements are similar to those in the previous studies [8,10]. `tcpdump` is used to capture all of the IP packets during the measurements. A simplified processes of the measurement are as follows.

1. Disable ECN by kernel setting `net.ipv4.tcp_ecn=0`; Pick up next entry from the *targeted server lists*; Initiate an SMTP connection (TCP port 25) with this server by setting flag SYN; Issue a `helo` and then quit the connection once the connection is established.
2. Enable ECN by setting `net.ipv4.tcp_ecn=1`; Initiate an SMTP connection (TCP port 25) with the targeted server by setting flags (SYN, ECN,CWR); Issue a `helo` and then quit the connection once the connection is established.
3. Repeat the above procedures 1 and 2 until all the targeted mail servers are tested.

The next task is to carefully and patiently analyze the readiness of ECN for each connection from the packets dumped by `tcpdump`.

4. Analysis and Results

In order to analyze the features of ECN in the mail servers, we need to collect these packets belonging to the same SMTP connection from all packets dumped by `tcpdump` and to extract the readiness of each connection. To do such hard work, we developed an analytical tool in Perl. We omitted the detailed analysis processes here due to space limitations.

This Section only presents the analysis results with regard to ECN deployment rate (shown by β_{ECN}) that is defined as the proportion of the targeted servers that are ECN-Capable to all valid servers. In order to do a comparison of the deployment rate of ECN on the web and mail servers, measurement about the web and mail server of the same TLD (Top Level Domain) are conducted at the same time.

Figures 1 and 2 show the deployment rate of ECN (β_{ECN}) by domains (IPv4) on mail servers measured on 15 August 2021 and on 8 January 2022, respectively. To compare with web servers, deployment rate of ECN on web servers is also measured and plotted in these figures. Note that the horizontal axis of Fig. 1 is sorted in descending order of β_{ECN} for mail servers in Aug. 2021. Subsequent figures are shown in the same order.

Figures 3 and 4 illustrate the variations of deployment rate of ECN on web and mail servers over a six-month period, respectively. From Figs. 1~4, we can see that, (1) β_{ECN} on most web servers is larger than that on mail servers. This feature is more noticeable for the domains on the right area of the figure. One exception is about domain `kr`; (2) β_{ECN} on mail servers keeps increasing (Fig. 4) while that on web servers increases slightly

(Fig. 3); (3) For domain kr , β_{ECN} on web servers is lower than that on mail servers (Fig. 1).



Figure 1. Deployment rate of ECN on mail servers vs. web servers (IPv4)

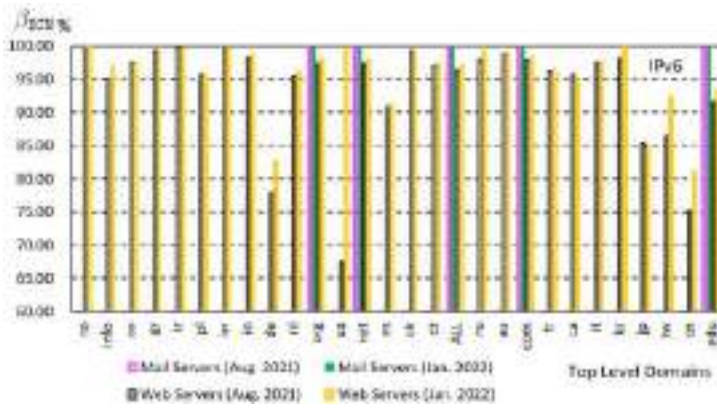


Figure 2. Deployment rate of ECN on mail servers vs. web servers (IPv6)

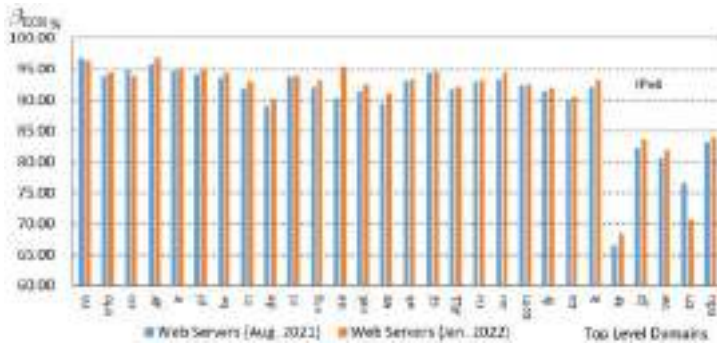


Figure 3. Deployment rate of ECN on web servers

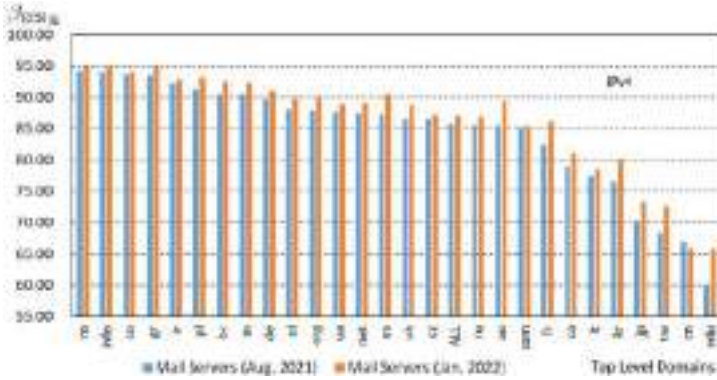


Figure 4. Deployment rate of ECN on mail servers

Deployment rates of ECN in IPv6 are illustrated in Fig. 5. It is clear that β_{ECN} on web servers keeps increasing. Especially, the range of increase on each of the domains de, ua, tw, and cn is significant. As for the deployment rate of ECN on the mail servers in IPv6, the percentage of β_{ECN} is 100% for each of domains org, net, com and edu, while it is 0% for the other domains. This means that there are very few mail servers which are running in IPv6. Furthermore, Table 1 details the number of the mail servers for those domains. Among 220,367 and 210,440 MX records of mail servers, only 16 and 14 mail servers were running in IPv6 at that time.



Figure 5. Deployment rate of ECN on mail and web servers (IPv6)

Table 1. Numbers of mail servers on the domains on IPv6

Time when measured	org	net	edu	com	all	Total MX records
Aug. 2021	2	1	1	12	16	220,367
Jan. 2022	1	1	1	11	14	210,440

5. Conclusion Remarks

In this paper, we measured and analyzed the state of ECN readiness in mail servers on the Internet. We also made a comparison of the deployment of ECN between mail and web servers. According to the analysis results, it is clear that (1) deployment rate of ECN in mail servers is mainly lower than that of web servers; (2) Deployment rates both on web and mail servers are increasing gradually; (3) β_{ECN} of domain jp, cn, tw and kr (in east Asia) are relatively low; (4) Unlike most web servers that work with IPv6, very few mail servers run in IPv6.

Compared to the previous studies [8,10], we also can see that deployment rates of ECN on web servers maintain stable growth over time. Therefore, it is obvious that the number of web and/or mail servers which are ECN-Capable on the Internet is increasing stably. As of Jan. 2022, deployment rates of ECN on web and mail servers at average were 92.18% and 87.16% (Fig. 2, A11), respectively. Based on these results, we can say that ECN is almost getting ready in server side. On the other hand, considering that ECN supported servers are probably in passive mode [8], this means that the use or non use of ECN depends largely on the communication client devices. Therefore, to take the advantage of ECN, we highly recommend that the developers of OSes and/or the vendors of networking equipment should launch their products with ECN enabled at initial settings.

References

- [1] R. Al-Saadi, G. Armitage, J. But, and P. Branch, "A Survey of Delay-Based and Hybrid TCP Congestion Control Algorithms," *IEEE Communi. Surveys & Tutorials*, vol.21, No.4, Feb. 2019. DOI:10.1109/COMST.2019.2904994
- [2] H. Huang, Z. Sun, and X. Wang, "End-to-End TCP Congestion Control for Mobile Applications," *IEEE Access*, vol. 8, pp.171628-171642, Sept. 2020. DOI:10.1109/ACCESS.2020.3024707
- [3] Ing. Marrone, Lic. Barbieri, and Mg. Robles, "TCP Performance - CUBIC, Vegas & Reno," *Journal of Computer and Technology*, Vol. 13, No. 01, pp.1-8, 2013.
- [4] N. Cardwell, Y. Cheng, C. S. Gunn et al, "BBR: Congestion-Based Congestion Control," *ACM Queue Networks*, pp. 20–53, Sept-Oct., 2016.
- [5] M. Claypool, F. Li, and J. Chung, "BBR - An Implementation of Bottleneck Bandwidth and Round-trip Time Congestion Control for ns-3," Technical Report WPI-CS-TR-18-01, Computer Science, Worcester Polytechnic Institute, Jan. 2018.
- [6] Y. Lu, X. Fan, and Lei Qian, "Dynamic ECN marking threshold algorithm for TCP congestion control in data center networks," *Computer Communications*, Vol. 129, pp. 197-208, 2018. DOI:10.1016/j.comcom.2018.07.036.
- [7] G. Fairhurst and M. Welzl, "The benefits of using explicit congestion notification (ECN)," RCF 8087, March 2017. DOI:10.17487/rfc8087
- [8] C.-X. Chen and K. Nagaoka, "Analysis of the State of ECN on the Internet," *IEICE Trans. on Inf. and syst.*, vol.E102-D, no.5, pp.910-919, May 2019. DOI:10.1587/transinf.2018NTP0006
- [9] L. Zou, C.-X. Chen, and K. Nagaoka, "An empirical study of the effectiveness of fallback on the ECN," *Proc. of NOMS 2020*, Budapest, Hungary, pp.1-4, April 2020. DOI:10.1109/NOMS47738.2020.9110403
- [10] L. Zou, K. Nagaoka, and C.-X. Chen, "An Evaluation of the Effectiveness of ECN with Fallback on the Internet," *IEICE Trans. on Inf. and Syst.*, vol.E104-D, no.05, pp.628-636, May 2021. DOI:10.1587/transinf.2020NTP0002
- [11] <https://s3.amazonaws.com/alexa-static/top-1m.csv.zip>

Intelligent Judgment Method of Superimposed Label Recognition Technology Based on a Deep Learning Target Detection Algorithm for Detecting Wiring Errors in Current Transformer Tests

Jia-Heng XU^a, Lian-Song YU^{b1}, Wei-Wei YANG^b, Xiao RONG^a, Wei LUO^b, Na SONG^a and Hua-Feng HU^b

^a *State Grid Co., Ltd. Technical College Branch, Jinan, China*

^b *State Grid Electric Power Research Institute Wuhan NARI Co., Ltd, Wuhan, China*

Abstract. This paper presents a novel method of intelligent detection of transformer wiring tests. It combines a new deep learning-based object detection algorithm with a tag code identification technique. Complex wiring in the current transformer error test scenarios implies a need for frequent human testing and judgment by digitizing the equipment terminals and the connected wires in the test. The automatic identification of the test connection lines is realized, relying on learning from the standard wiring and logically binding the standard wiring relationship. The proposed method is instrumental in greatly saving labor costs, reducing the possibility of human error, improving work efficiency, and developing a new concept of current transformer error test training for new employees.

Keywords. multi-target detection algorithm, current transformer, wiring judgment, deep learning.

1. Introduction

The error test of the current transformer is a relatively important work in the 24 field operations of the power marketing and measurement category, which is directly related to the fairness and feasibility of the electric power trade settlement. It is also a must-have skill for new employees of the State Grid Corporation of China. It is one of the electrical test training programs. During the training process, the trainer needs to check permanently whether their wiring is correct or not. Due to a large amount of training, trainers will inevitably experience fatigue during the inspection process, deteriorating the test efficiency and leading to various, which brings a more significant safety hazard to the training process. For this reason, this study proposes an automatic judgment method for the error test of current transformers based on the YOLO algorithm,

¹ Corresponding author. Email: Yuliansong@sgepri.sgcc.com.cn

significantly improving the wiring inspection efficiency. Besides, the workload is reduced, the possibility of misjudgment is diminished, and the safety of the training process is ensured.

2. Current transformer error test method

The comparison method is adopted in the error test of the current transformer. To measure the error of the current transformer under test, the standard current transformer with a high accuracy level should be compared with the test product, and the error of the current transformer under the rated load and the lower limit load should be measured. Consider the specific wiring in Figure 1.

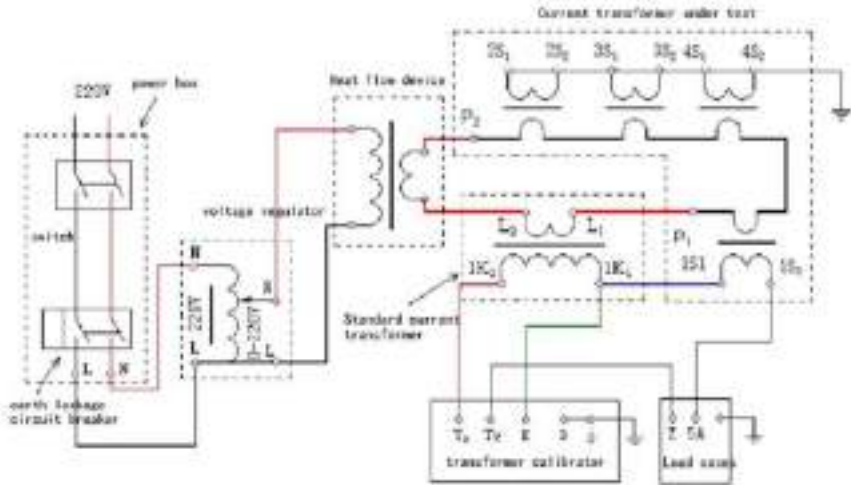


Fig. 1 Wiring diagram of the current transformer error test

Figure 1 comprises seven devices: the power box, voltage regulator, current lifter, standard current transformer, current transformer under test, load box, and transformer calibrator. A total of 16 wires are used, including twelve secondary wires, three ground wires, and one high-current wire. There are 16 pairs of terminals, among which wires 1K1-1S1 and 1K1-K share terminal 1K1.

3. Design ideas

Based on YOLOv4 target detection [1], intelligent barcode recognition [2], and data intelligent verification technology [3], an intelligent judgment system for the misconnection of the current transformer field error test is developed.

3.1. Digital preprocessing

(1) Digitization of test equipment

All the test equipment participating in the test undergoes pasting of the equipment asset code, entering the equipment information and barcode into the system through the data acquisition terminal that supports the camera function (hereafter referred to as the acquisition terminal).

(2) Terminal digitalization

One should digitize the terminals of the test equipment, adopt the recording method of pasting a two-dimensional code, and enter the system through the acquisition terminal (hereinafter referred to as the terminal code), and the terminal code is bound to the test equipment code, as shown in Figures 2 and 3.



Fig. 2 Terminal code

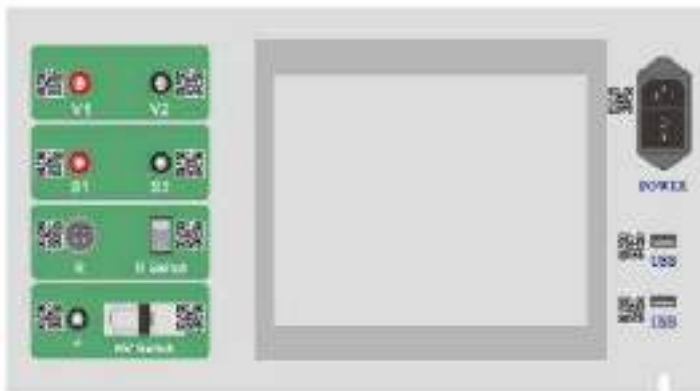


Fig. 3 Device terminal code digitization

(3) Digitization of the tested product

The wiring terminal of the test transformer is digitized by recording the acquisition terminal into the system, and the transformer terminal code is bound with the transformer device code.

(4) Digitization of test lines

The two terminals of the test line are coded in rings, used in pairs, and entered into the system through the acquisition terminal. Test line labeling digitization in Figure 4.

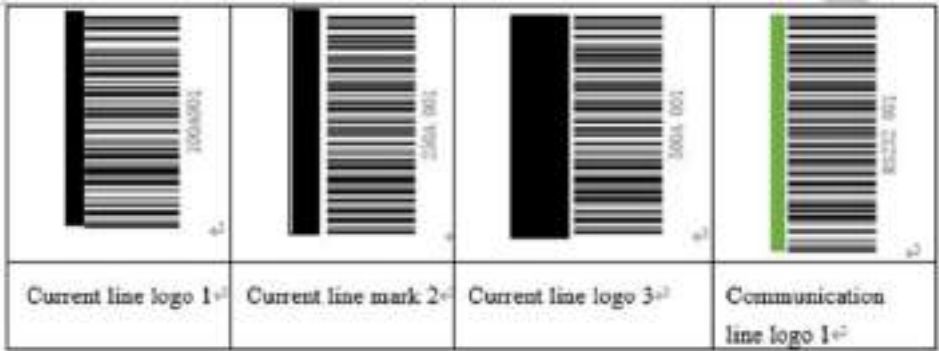


Fig. 4 Test line labeling digitization

3.2. Terminal Wiring Detection

Using the target detection method of YOLO v4[4], the terminal and wiring are set as the target identification area, multiple bar codes are collected in each identification box, and the barcode images are processed through the image processing function of the acquisition terminal. The computer reads the picture in the image file format and then identifies it through image preprocessing, binds the interconnected terminal codes and line codes, identifies the terminal codes and single or multiple line codes in the area, and records it in the temporary database. The detection and identification results are illustrated in Figure 5.

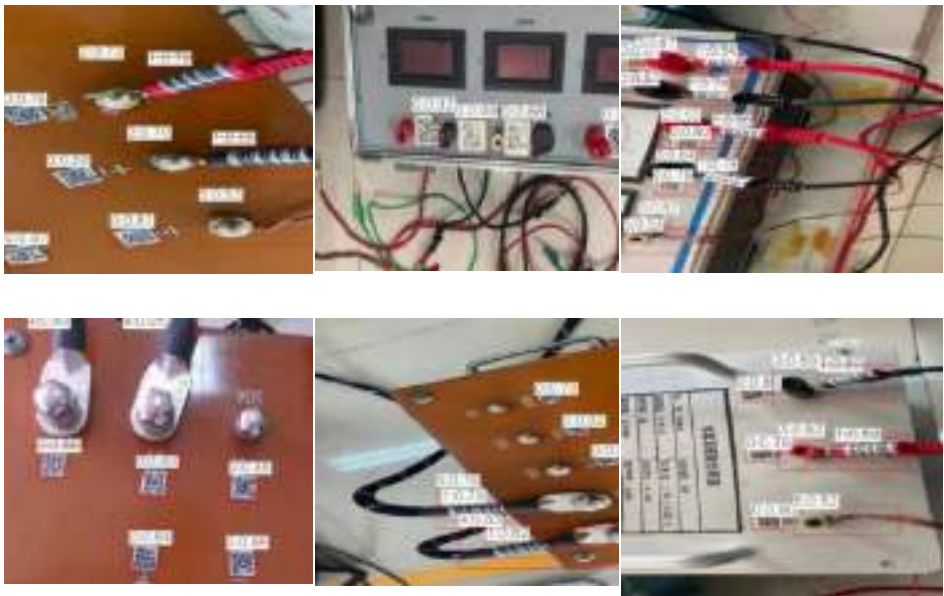


Fig. 5 Detection and identification results

The total training results achieved 90% correct recognition detection at IOU at 0.5.

By this method, all the terminals were photographed and identified successively. All the terminal codes and the corresponding lines of the terminals were identified successively and recorded in the alignment library. The YOLOv4 intelligence was required to distinguish the mutual binding relationship between terminals and line codes.

4. Intelligent judgment system of transformer wiring

This paper aims to realize the wiring intelligent judgment system of the transformer. First, the image (video) acquisition equipment, combined with the YOLOv4 target detection algorithm, sets the target identification area and collects all equipment, terminals, and wiring barcodes. Then, the computer is used, the relevant information is obtained and recorded to the temporary database for relationship binding, and the wiring connection rules are determined. After sending the pictures to be tested by the system for a series of analysis operations, and the actual connection relationship is compared with the information in the database, one can judge whether the connection is correct or not, and the intelligent judgment operation of the connection can be completed.

Specific function implementation involved the following components:

- (1) Data acquisition function: with microcomputer Nvidia NANO camera as a video picture acquisition terminal, using LINUX system, the OpenCV environment, implanted YOLOv4, barcode recognition, and information comparison algorithm [5].
- (2) Barcode information binding: computer implanted barcode recognition algorithm, for local data analysis, bar code analysis, corresponding relationship binding record to the temporary database.
- (3) Data detection function: the YOLOv4 algorithm is used to train the model, detect the pictures that need to be judged, interpret the bar code, compare the interpreted information with the database, and obtain the results. YOLO v4 algorithm was used for model training, as shown in Figure 6.[1]

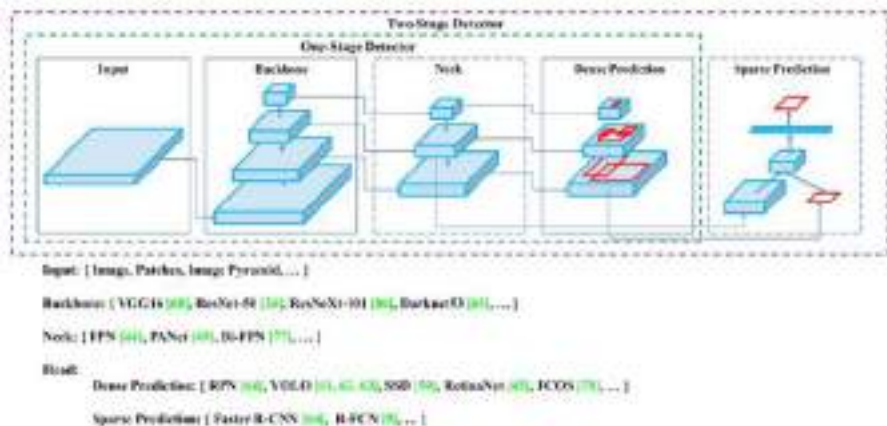


Fig. 6 The YOLOv4 algorithm usage to train the model^[1]

5. Application of intelligent wiring judgment

5.1 Standard wiring mode learning

In the standard wiring mode, the teacher holds the acquisition terminal, identifies and scans the code of the standard terminal code and the line marking code, obtains the corresponding relationship between the wiring ports, and saves the name as the standard wiring mode.

5.2 Wiring judgment and testing

The wiring detection procedure envisages that the trainees should watch the operation training video before connecting. After the trainees have completed the wiring, they should hold the acquisition terminal to perform target detection and identification on all the test instruments and transformers, in turn, automatically capture the equipment terminal code and line code, and detect the unscanned data. The missing terminals should be prompted until all scanning and verification are completed, the corresponding relationship between each port will be obtained, and it will be automatically compared with the standard wiring method of the test item. If it is not correct, it will display "wrong wiring" and display the name of the wrongly connected terminal, and the system will not be powered. This item is changed from manual inspection by on-site teachers to intelligent inspection by the software system.

6. Conclusion

This paper proposes a two-stage procedure to implement the intelligent judgment method of superimposed label recognition technology based on a deep learning target detection algorithm for detecting wiring errors in current transformer tests. The first stage envisages data collection through the acquisition terminal and binding the corresponding relationship. The second stage uses the YOLOv4 algorithm model, the recognition algorithm of bar code, and the intelligent data calibration algorithm to detect the terminal wiring. Bar code size, model parameters, and database size settings are combined with the actual scene and adjusted to the appropriate value. The method provides accurate target detection identification and timely recording of equipment information through intelligent detection system wiring inspection, improving detection efficiency and reducing misjudgment rate. Since it can reduce labor intensity and misjudgment rate, while enhancing the labor efficiency of users, the proposed method can also be extended to other kinds of electrical test wiring automatic determination, especially those involving training projects.

References

- [1] Bochkovskiy A, Wang CY, Liao HYM. (2020) YOLOv4: Optimal speed and accuracy of object detection. *Computer Vision and Pattern Recognition*, 17(9): 198-215.
- [2] Redmon J, Divvala S, Girshick R, et al. (2016) You only look once: unified, real-time object detection. *IEEE*, 2016: 779-788.
- [3] Bodla N, Singh B, Chellappa R, and Davis LS. (2017) Soft-NMS-improving object detection with one line of code. *Proc. IEEE International Conference on Computer Vision (ICCV)*, pp. 5561-5569.

- [4] Cao JL, Pang YW, Han JG, and Li XL. (2019) Hierarchical shot detector. Proc. IEEE International Conference on Computer Vision (ICCV), pp. 9705-9714.
- [5] Cai ZW and Vasconcelos N. (2018) Cascade R-CNN: Delving into high quality object detection. In Proc. IEEE Conference on Computer Vision and Pattern Recognition (CVPR), pp. 6154-6162.

Coherent Accumulation Algorithm for Maneuvering Weak Target Based on Angular-Stepped-GRFT

Yuxian SUN, Shaoqiang CHANG¹, Gang WANG, Zhennan LIANG, Jinpeng GUO and Quanhua LIU

*Key Laboratory of Electronic and Information Technology in Satellite Navigation
Beijing Institute of Technology, China*

Abstract. This paper proposes an improved angular stepped generalized Radon Fourier transform (angular-stepped-GRFT) algorithm for maneuvering weak target detection in synthetic wideband radar. The proposed method can achieve motion parameters estimation for the maneuvering weak target based on stepped frequency signal. On this basis, the motion compensation of maneuvering weak target and range profile focusing method are realized.

Keywords. Long-time coherent accumulation, GRFT, motion parameters estimation, range profile

1. Introduction

Small radar cross section (RCS) targets such as aircraft have brought severe threats and challenges to radar detection. At the same time, some small RCS targets also have strong maneuvering ability, which further increases the difficulty of radar detection. How to maintain high precision measurement of the motion parameters of small RCS maneuvering target is one of the difficult problems to be solved urgently by modern radar.

To solve the problem of estimating the motion parameters of weak targets, we can increase the observation time to realize the accumulation of target energy for a long time, so as to improve the radar echo signal to noise ratio (SNR) and improve the detection ability of weak targets[1-2]. In 1999, Perry R P et al. proposed Keystone transform[3], which corrected the phenomenon of high-speed target across range unit (ARU) through scale transformation on the slow time-fast frequency plane, and then used Fourier transform to accumulate the target energy in a coherent way. Based on Keystone transform, there are many early weak target coherent accumulation methods[4-5]. In 2011, J. Xu et al. analyzed the relationship between the target ARU phenomenon and the motion parameters of each order, combined the generalized Radon transform and Fourier transform. A long time coherent accumulation algorithm based on generalized Radon Fourier transform (GRFT) is proposed, which has achieved good detection results[6-8]. In 2021, J Guo et al. combined GRFT with stepped frequency signal and proposed a broadband coherent accumulation method based on stepped generalized Radon Fourier

¹ Corresponding Author, Shaoqiang Chang, Key Laboratory of Electronic and Information Technology in Satellite Navigation, Beijing Institute of Technology, Beijing, China; E-mail: changshaoqiang@bit.edu.cn.

transform (stepped-GRFT)[9]. Stepped frequency signal is an important high resolution radar signal[10], which is widely used in civil and military fields[11-16]. It uses a series of stepped carrier frequency narrowband pulses which are sequentially transmitted, and obtains the capability of range high resolution through synthetic broadband processing. Guo’s algorithm realizes weak target detection and radial motion parameters estimation based on long-term coherent accumulation, and then studies motion parameters compensation and target high resolution range profile (HRRP) focusing method, which effectively improves the ability of wideband radar to detect and measure weak targets.

Stepped-GRFT is limited in that it can only be used for the estimation of radial motion targets. When the weak target maneuvered, stepped-GRFT could not accurately estimate the motion parameters of the target, so that the correct range profile could not be obtained. In order to detect and image maneuvering weak targets in stepped frequency radar, angular-stepped-GRFT is proposed in this paper based on stepped-GRFT, which solves the problem of inaccurate estimation of motion parameters for maneuvering weak targets in stepped-GRFT. The coherent accumulation algorithm based on angular-stepped-GRFT can achieve correct motion compensation and range profile focusing. And effectively improve the SNR of the range profile after coherent accumulation processing.

2. Modeling and analysis of maneuvering weak target

The transmitted signal of stepped frequency radar can be expressed as

$$s(n, t_p) = \text{rect}\left(\frac{t_p}{T_p}\right) e^{j\pi k t_p^2} e^{j2\pi f_n t_p} \tag{1}$$

where, $n = (m-1)N + h + 1$ is the sub-pulse number, m is the frame number, $m = 1, 2, \dots, M$. N is the number of the sub-pulse in the frame. t_p is the fast time, T_p is the pulse width, and define $\text{rect}\left(\frac{t}{T}\right) = \begin{cases} 1, & 0 \leq t \leq T \\ 0, & \text{others} \end{cases}$. $k = \frac{B}{T_p}$ is the frequency modulation rate. $f_n = f_0 + h\Delta f$, where f_0 is the initial carrier frequency, Δf is the frequency step size, and $h \in [0, 1, \dots, N - 1]$ is the frequency coding sequence.

If a point target starts to maneuver when $t = 0$, its initial radial distance is R_0 , its velocity is v , and its initial velocity direction is radial. The target performs a turning maneuver with an angular turning velocity of ω . Assuming that the velocity of the target does not change during maneuvering, the instantaneous slant range of the target can be expressed as

$$\mathbf{R}_n = \sqrt{(2 - 2\cos \omega t + \cos^2 \omega t)R_0^2 - \frac{2vR_0}{\omega} \sin \omega t + \frac{v^2}{\omega^2} \sin^2 \omega t} \tag{2}$$

where, $t \in [0, MN * PRT)$, PRT is the pulse repetition time. This paper only discusses the case when the radial velocity of the target is positive, that is, the target moves towards radar. In this case, $0 \leq t < \frac{\pi}{2\omega}$.

3. Motion parameters estimation and range profile focusing algorithm based on angular-stepped-GRFT

3.1. Angular-stepped-GRFT algorithm principle

Based on the stop-and-go assumption, we have the down-converted baseband target echo in two-dimensional form as

$$s_R(n, t_p) = K_R \text{rect}\left(\frac{t_p - \mathbf{R}_n/c}{T_p}\right) e^{-j\frac{4\pi\mathbf{R}_n f_h}{c}} e^{j\pi k\left(t_p - \frac{2\mathbf{R}_n}{c}\right)^2} \quad (3)$$

where, K_R is the complex amplitude of target echo, c is the speed of light. Obtained by pulse compression of baseband echo target

$$s_{Rm}(n, t_p) = K_R T_p B \text{sinc}\left(\pi\left(t_p - 2\mathbf{R}_n/c\right)B\right) e^{-j\frac{4\pi\mathbf{R}_n f_h}{c}} \quad (4)$$

where, B is the stepped frequency signal sub-pulse bandwidth.

Let \mathbf{R} be the target slant range, $\mathbf{R} = ct_p / 2$, and Eq. (4) can be written as

$$s_{Rm}(n, t_p) = K_R T_p B \text{sinc}\left(\frac{2\pi B(\mathbf{R} - \mathbf{R}_n)}{c}\right) e^{-j\frac{4\pi\mathbf{R}_n f_h}{c}} = K_R T_p B \text{sinc}\left(\frac{\pi(\mathbf{R} - \mathbf{R}_n)}{\frac{c}{2B}}\right) e^{-j\frac{4\pi\mathbf{R}_n f_h}{c}} \quad (5)$$

where, $K_{Rm} = K_R T_p B$ is the target complex scattering coefficient. In practice, K_{Rm} is undulating and will bring phase noise. For simplicity, let's assume that K_{Rm} is a constant.

$\frac{c}{2B}$ is the range resolution before synthetic wideband processing. In order to achieve effective coherent accumulation of multi-frame signals, the phase term in Eq. (5) needs to be compensated, and the corresponding phase compensation factor is

$$\Phi_n = e^{j\frac{4\pi\mathbf{R}_n f_h}{c}} \quad (6)$$

In summary, a coherent accumulation algorithm for detecting maneuvering weak targets with stepped frequency signals can be obtained

$$G = \sum_{n=1}^{MN} s_{R_m} (n, \mathbf{R}_n) \Phi_n \tag{7}$$

A traversal search is performed for the motion parameters R_0 , v , ω of the target. The output of G is maximal if and only if the set of search parameters is equal to the actual motion parameters of the target. Considering the traversal of angular velocity, different from stepped-GRFT, which only traverses radial motion parameters, the detection algorithm for maneuvering weak targets defined in Eq. (7) for stepped frequency signals is called angular-stepped-GRFT in this paper.

3.2. Discrete angular-stepped-GRFT

Let the initial radial range of the target be $r \in [r_{\min}, r_{\max}]$, for data with range window, it is usually the case $r_{\min} = 0$, $r_{\max} = r_l$, r_l is the distance of range window. The velocity search range is $v \in [v_{\min}, v_{\max}]$, the angular velocity search range is $\omega \in [\omega_{\min}, \omega_{\max}]$. Because of the coherent accumulation time $T = MN * PRT$, the Doppler resolution of the doppler frequency filter can be written as

$$\rho_d = \frac{1}{T} \tag{8}$$

Therefore, the velocity search interval can be

$$\Delta_v = \frac{\lambda \rho_d}{2} = \frac{\lambda}{2T} = \frac{c}{2MNf_h PRT} \tag{9}$$

where, $f_h = f_0 + h\Delta f$, it can be found that the velocity search interval decreases with the increase of carrier frequency. For the convenience of calculation, the velocity search interval is selected as

$$\Delta_v = \frac{c}{2MNf_{aver} PRT} \tag{10}$$

where, $f_{aver} = f_0 + \frac{N-1}{2} \Delta f$ is the average carrier frequency. Then the velocity search number can be obtained as

$$N_v = \text{round}\left(\frac{v_{\max} - v_{\min}}{\Delta_v}\right) \tag{11}$$

where, round() denotes integer operation.

Assume that the system sampling rate f_s is given and the distance search interval is

$$\Delta_r = \frac{c}{2f_s} \quad (12)$$

Then the distance search number can be obtained as

$$N_r = \text{round}\left(\frac{r_i}{\Delta_r}\right) \quad (13)$$

The angular velocity search interval must meet

$$v \cos(\omega - \Delta\omega)T - v \cos \omega T \leq \Delta_v \quad (14)$$

That is, the search interval of angular velocity which reflect the change of radial velocity should less than that of velocity search interval. Let $\omega = \omega_{\max}$ ($\omega_{\max} \leq \frac{\pi}{4}$), $v = v_{\max}$. According to Eq. (14), the search interval of angular velocity is

$$\Delta\omega \leq \omega_{\max} - \frac{1}{T} \arccos\left(\frac{\Delta v}{v_{\max}} + \cos \omega_{\max} T\right) \quad (15)$$

Then the angular velocity search number can be obtained as

$$N_\omega = \text{round}\left(\frac{\omega_{\max} - \omega_{\min}}{\Delta_\omega}\right) \quad (16)$$

Velocity dimension, distance dimension and angular velocity dimension search vector can be expressed as

$$\begin{aligned} v(i) &= v_{\min} + i\Delta_v, \quad i = 0, 1, \dots, N_v - 1 \\ r(p) &= p\Delta_r, \quad p = 0, 1, \dots, N_r - 1 \\ \omega(q) &= \omega_{\min} + q\Delta_\omega, \quad q = 0, 1, \dots, N_\omega - 1 \end{aligned} \quad (17)$$

Substituting Eq. (17) into Eq. (6), the discretized phase compensation factor can be expressed as

$$\Phi(n, i, p, q) = e^{j \frac{4\pi f_s \sqrt{(2-2\cos \omega(q)t + \cos^2 \omega(q)t)r(p)^2 - \frac{2v(i)r(p)}{\omega(q)} \sin \omega(q)t + \frac{v(i)^2}{\omega(q)^2} \sin^2 \omega(q)t}}{c}} \quad (18)$$

Substituting Eq. (17) and Eq. (18) into Eq. (7), the expression of discretized angular-stepped-GRFT can be obtained as follows

$$G(n, i, p, q) = \sum_{n=0}^{MN-1} s_{Rm} \left(n, \begin{array}{l} \sqrt{(2 - 2 \cos \omega(q)t + \cos^2 \omega(q)t) r(p)^2} \\ - \frac{2v(i)r(p)}{\omega(q)} \sin \omega(q)t \\ + \frac{v(i)^2}{\omega(q)^2} \sin^2 \omega(q)t \end{array} \right) \Phi(n, i, p, q) \quad (19)$$

After the radar echo is processed by angular-stepped-GRFT, the estimation results of target motion parameters can be obtained by detecting the maximum value of range-velocity-angular velocity three-dimensional space.

3.3. Motion compensation and range profile focusing

Correct motion compensation is a prerequisite for range profile focusing. According to the motion parameters estimation result of angular-stepped-GRFT, motion compensation is carried out for maneuvering weak target in frequency domain

$$S_{Rm2}(n, f) = S_{Rm}(n, f) e^{-j4\pi f \left[\hat{r} - \sqrt{(2 - 2 \cos \hat{\omega}t + \cos^2 \hat{\omega}t) \hat{r}^2 - \frac{2\hat{v}\hat{r}}{\hat{\omega}} \sin \hat{\omega}t + \frac{\hat{v}^2}{\hat{\omega}^2} \sin^2 \hat{\omega}t} \right] / c} \quad (20)$$

where, $f \in [-f_s/2, f_s/2]$ is the fast time frequency, $S_{Rm}(n, f)$ is the fast time Fourier transform of Eq. (4) to the frequency domain.

$$\hat{t}_p = 2 \left(\hat{r} - \sqrt{(2 - 2 \cos \hat{\omega}t + \cos^2 \hat{\omega}t) \hat{r}^2 - \frac{2\hat{v}\hat{r}}{\hat{\omega}} \sin \hat{\omega}t + \frac{\hat{v}^2}{\hat{\omega}^2} \sin^2 \hat{\omega}t} \right) / c \quad (21)$$

\hat{t}_p is the range shift for each pulse.

After motion compensation based on angular-stepped-GRFT, broadband is synthesized by spectrum synthetic method to obtain the range profile of each frame signal. Since the target is a weak target with low SNR, the range profile of each frame signal can be summed in the slow time dimension to obtain the range profile after coherent accumulation. That is, the focus of the maneuvering weak target's range profile is realized.

4. Performance analysis by simulations

4.1. Simulation parameters

In order to verify the effectiveness of angular-stepped-GRFT algorithm proposed in this paper in detail, this section carries out simulation experiments based on the target motion

scene mentioned in section 2 and compares the performance with the similar coherent accumulation methods, stepped-RFT and stepped-GRFT.

The main parameters of radar system and target in simulation are shown in Table 1

Table 1. The parameters of radar system and target

Parameter	Value
Pulse Width	20 μ s
Bandwidth	16MHz
Pulse Repetition Time	1050 μ s
Coherent Processing Interval	2016ms
Initial Carrier Frequency	1.5GHz
Frequency Step Interval	8MHz
Step Number	64
Frames Number	30
Sampling Rate	25MHz
Initial Target Range	60km
Target Velocity	200m/s
Target Angular Velocity	0.2rad/s
SNR(After pulse compression)	-10dB

4.2. Performance analysis of angular-stepped-GRFT and similar algorithms

4.2.1. Performance analysis of stepped-RFT

Stepped-RFT is a range-velocity two-dimensional parameters search algorithm for radially moving targets in stepped frequency radar system. When using stepped-RFT, set the velocity search range to 100 m/s ~ 300m/s . The parameters estimation results obtained by stepped-RFT are shown in Figure 1. The initial radial distance of the target is estimated to be 58.404km, and the error is 1.596km. The target velocity is estimated to be 214.912 m/s with an error of 14.912 m/s . Figure 2 shows the target range profile obtained after motion compensation, synthetic broadband processing and coherent accumulation. It can be seen that the motion parameters of maneuvering weak targets cannot be accurately estimated and compensated by stepped-RFT. In the range profile after coherent accumulation, the target is submerged in noise, and the range profile cannot be correctly focused.

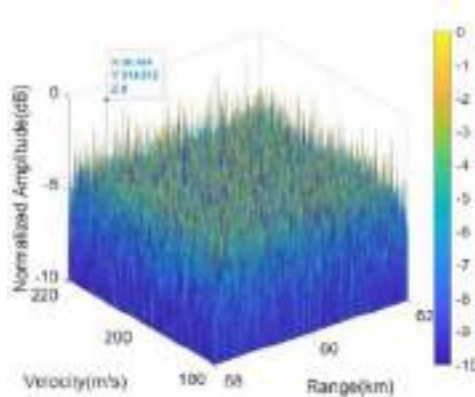


Figure 1. Stepped-RFT parameters estimation result

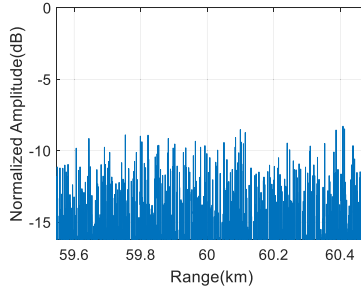


Figure 2. Range profile after motion compensation (Hamming Windows are used in the frequency domain)

4.2.2. Performance analysis of stepped-GRFT

Stepped-GRFT is a range-velocity-high order acceleration search algorithm for radially moving targets under stepped frequency radar system. In this paper, range-velocity-acceleration three-dimensional stepped-GRFT is selected for simulation which has the same search dimension as angular-stepped-GRFT. When three-dimensional stepped-GRFT is used, the velocity search range is set as $100 \text{ m/s} \sim 300 \text{ m/s}$, and the acceleration search range is set as $0 \sim 16 \text{ m/s}^2$, and ensure that the acceleration search range covers the variation range of radial acceleration during target maneuver. Figure 3 and Figure 4 show the estimation results of the initial radial distance, initial velocity and acceleration of the target using three-dimensional stepped-GRFT. The initial radial distance of the target is estimated to be 62.28 km , and the error is 2.28 km . The target velocity is estimated to be 250.934 m/s , and the error is 50.934 m/s . The target acceleration is estimated to be 1.2366 m/s^2 . Figure 5 shows the target range profile obtained after motion compensation, synthetic broadband processing and coherent accumulation. It can be seen that three-dimensional stepped-GRFT cannot achieve accurate estimation and compensation of the motion parameters of maneuvering weak target. In the range profile after coherent accumulation, the target is submerged in noise, and the range profile cannot be correctly focused. Three-dimensional stepped-GRFT algorithm approximates the motion parameters of the target by searching the range-velocity-acceleration parameters. However, when the target maneuvers, the radial acceleration changes, which leads to the incomplete motion compensation based on three-dimensional stepped-GRFT. And then the range profile can not be focused. Elected to take a higher order acceleration during stepped-GRFT parameters search, while it is possible to reduce the error of motion parameters estimation, the estimation results are more close to actual motion state. But the use of higher order radial acceleration to describe the target motion state means that the four-dimensional search and more multi-dimensional search. Compared with the three-dimensional search of angular-stepped-GRFT, multi-dimensional search will bring huge calculation burden which have no realizability.

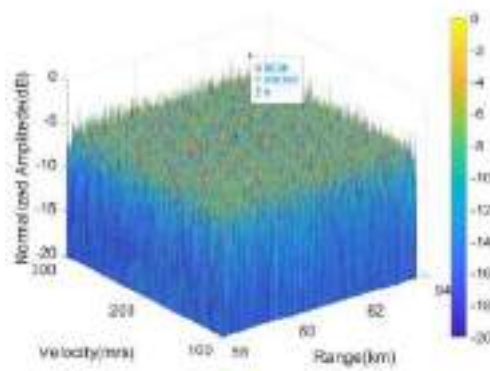


Figure 3. Stepped-GRFT parameters estimation result (range-velocity plane)

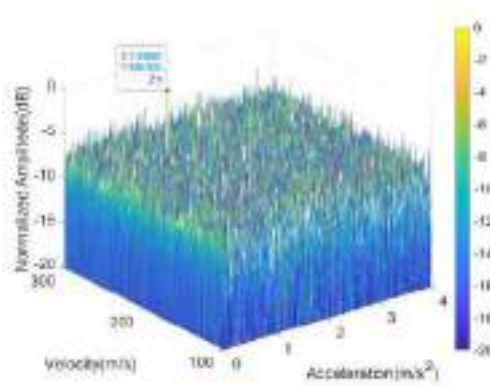


Figure 4. Stepped-GRFT parameters estimation result (acceleration-velocity plane)

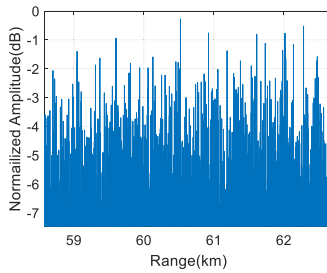


Figure 5. Range profile after motion compensation (hamming windows are used in the frequency domain)

4.2.3. Performance analysis of angular-stepped-GRFT

When angular-stepped-GRFT is used for parameters estimation, the velocity search range is set as 100 m/s ~ 300m/s , and the angular velocity search range is 0 ~ 0.3rad/s . As a comparison of stepped-RFT and stepped-GRFT, Figure 6 and Figure 7 show the estimation results of the initial distance, initial velocity and angular velocity of the target based on angular-stepped-GRFT. The initial distance of the target is estimated to be 60.0km, and the error is 0. The initial velocity was estimated to be 199.994 m/s with an error of 0.006 m/s . The angular velocity is estimated to be 0.19994 rad/s with error of

6×10^{-5} rad/s . Figure 8 and Figure 9 shows the coherent accumulation results of target range profile obtained by using the proposed angular-stepped-GRFT algorithm. The peak value of the target can be clearly observed from the result of range profile accumulation, and the initial distance is measured to be 60.0km, which is consistent with the simulation conditions. Obviously, when the stepped frequency signal is used to measure the motion parameters of maneuvering weak target, the target motion parameters estimation based on angular-stepped-GRFT and the range profile focusing algorithm proposed in this paper have better performance.

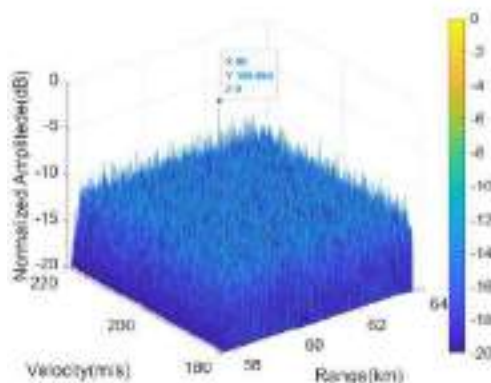


Figure 6. Angular-stepped-GRFT parameters estimation result (range-velocity plane)

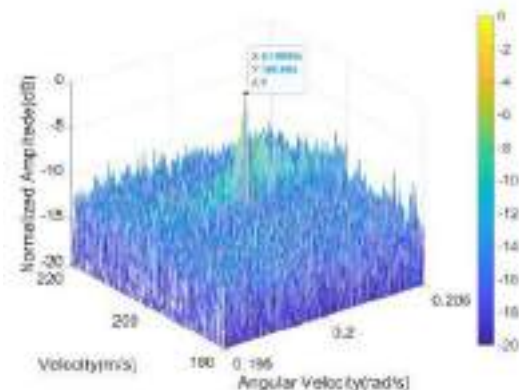


Figure 7. Angular-stepped-GRFT parameters estimation result (acceleration-velocity plane)

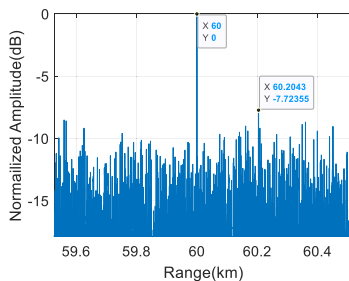


Figure 8. Range profile after motion compensation (hamming window is used in the frequency domain)

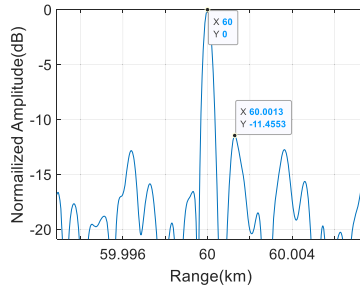


Figure 9. Enlarged range profile after motion compensation (hamming windows is used in the frequency domain)

5. Conclusion

In this paper, aiming at the problem of accurate estimation of motion parameters of maneuvering weak target by stepped frequency radar and range profile focusing, angular-stepped-GRFT is proposed, which realizes the estimation of motion parameters of weak target in circular maneuver scene with long time coherent accumulation. On this basis, the motion parameters compensation and target range profile focusing method are studied, and compared with stepped-GRFT and other methods. The comparative results are shown in Table 2. It is proved that angular-stepped-GRFT can effectively improve the range profile’s ability of stepped frequency radar for maneuvering weak target.

Table 2. The comparative results

Algorithm	Search dimension	Range Profile Result
Stepped-RFT	Range-Velocity	No Target
Stepped-GRFT	Range-Velocity-Acceleration	No Target
Angular-Stepped-GRFT	Range-Velocity-Angular Velocity	Clear Target

6. Acknowledgements

This study was supported in part by the Beijing Institute of Technology Research Fund Program for Young Scholars, in part by the National Science Fund for Distinguished Young Scholars under Grant 62201048.

References

- [1] Huang P, Liao G, Yang Z. Approach for space-based radar manoeuvring target detection and high-order motion parameter estimation. *IET Radar, Sonar & Navigation*. 2015; 9(6): 732-741.
- [2] Tian J. Study on Long-time Coherent Integration for Radar Maneuvering Targets. Beijing: Beijing University of Technology Press; 2014. 32p.
- [3] Perry R P, Dipietro R C, Fante R L. SAR imaging of moving targets. *IEEE Transactions on Aerospace and Electronic Systems*. 1999; 35(1): 188-200.
- [4] Zhang S, Zeng T, Long T. Dim target detection based on keystone transform. *IEEE International Radar Conference*. 2005; 889-894.
- [5] Zhang S, Zhang W, Wang Y. Multiple targets’ detection in terms of Keystone transform at the low SNR level. *2008 International Conference on Information and Automation*. 2008; 1-4.

- [6] Xu J, Yu J, Peng Y N. Radon-Fourier Transform for Radar Target Detection(I): Generalized Doppler Filter Bank. *IEEE Transaction on Aerospace and Electronic Systems*. 2011; 47(2): 1186-1202.
- [7] Xu J, Yu J, Peng Y N. Radon-Fourier transform for radar target detection (II): Blind speed sidelobe suppression. *IEEE Transactions on Aerospace and Electronic Systems*. 2011; 47(4): 2473-2489.
- [8] Yu J, Xu J, Peng Y N. Radon-Fourier transform for radar target detection (III): Optimality and fast implementations. *IEEE Transactions on Aerospace and Electronic Systems*. 2012; 48(2): 991-1004.
- [9] Liu Q, Guo J, Liang Z. Motion Parameter Estimation and HRRP Construction for High-Speed Weak Targets Based on Modified GRFT for Synthetic-Wideband Radar With PRF Jittering. *IEEE Sensors Journal*. 2021; 21(20): 23234-23244.
- [10] Wehner D R. *High-Resolution Radar*. Boston: Artech House Press; 1995. 68p.
- [11] Ingwersen P A, Lemnios W Z. Radars for ballistic missile defense research. *Lincoln Laboratory Journal*. 2000; 12(2): 245-266.
- [12] Myers H, Moore R, Butler W. Common aperture multiband radar (CAMBR). *Proceedings of the 1997 IEEE National Radar Conference*. IEEE. 1997; 143-148.
- [13] Ulander L M H, Frolind P O, Gustavsson A. Performance of the CARABAS-II VHF-band synthetic aperture radar. *IEEE 2001 International Geoscience and Remote Sensing Symposium*. 2001; 1: 129-131.
- [14] Hellsten H, Ulander L M H, Gustavsson A. Development of vhf carabas ii sar. *Radar Sensor Technology*. International Society for Optics and Photonics. 1996; 2747: 48-60.
- [15] Myers H, Moore R, Butler W. Common aperture multiband radar (CAMBR). *Radar Processing, Technology, and Applications*. 1996; 2845: 2-13.
- [16] Singh P. FQTSFM: A fuzzy-quantum time series forecasting model. *Information Sciences*. 2021; 566: 57-79.

Analysis of Artificial Intelligence Applied in Virtual Learning Environments in Higher Education for Ecuador

Segundo Moisés Toapanta Toapanta*, Eriannys Zharayth Gómez Díaz, Oscar Marcelo Zambrano Vizuete, Edith Elizabeth Ordoñez Chávez
Research Department, Instituto Tecnológico Superior Rumiñahui, Av. Atahualpa 1701 y 8 de febrero, Ecuador

Abstract. Artificial intelligence in virtual learning environments in higher education for Ecuador continues to be a problem because there is no adequate analysis. The objective of this research is to carry out the analysis of artificial intelligence applied in virtual learning environments for higher education. The deductive method and exploratory research were used to analyze the problems that arise from properly applying artificial intelligence in virtual environments. Turned out a Prototype of Virtual Environments based on AI, considering all the necessary processes for an adequate virtual environment. It was concluded that for an adequate solution of virtual environments based on artificial intelligence, the characteristics, capabilities, virtual community and IT infrastructure must be defined, where it will be applied, knowledge and digital material information, AI components, among others.

Keywords. Artificial intelligence, virtual environments, higher education, learning

1. Introduction

Artificial intelligence in education; today we find ourselves living in a new era which is based on the digital, this is how we are facing great scientific advances in the entire world. The great evolution, technological acceleration and the intensification of skills has forced us to evolve and the educational field has not been the exception, which is why the need has arisen to implement new policies in the educational area where the pedagogical aspect strongly prevails. and that it is framed more in this time than in previous times[1]. The use of digital technology is permeating and transforming all social systems, and education is no exception. In the last decade, the development of Artificial Intelligence has given new impetus to the hope of providing educational systems with "effective" and more personalized solutions for teaching and learning. Educators and researchers in the field of education and policy makers, in general[2]. In the nineties

when the first intelligent agents began to be built, such as supercomputers capable of performing extremely complex tasks such as heuristic algorithms, which even paved the way for artificial intelligence; scientific advances in AI have made a change in all paradigms and have been generated rapidly from 2000 to today, which has caused it to be included in the daily life of human beings. Given the challenge presented by the use

* Corresponding Author: Segundo Moisés Toapanta Toapanta,
Email:segundo.toapanta@ister.edu.ec

of AI tools and their relationship with education, it is important for the pedagogical leader teacher to know their impact on the pedagogical processes and the support they provide in the classroom for the development of their classes[3]. The Approach to Artificial Intelligence in distance education; it is born from different thoughts of various philosophers, such as Aristotle, who founded Syllogistic logic, which is based on a form of deductive reasoning; Leonardo Da Vinci, in 1495, built a robot capable of standing, sitting, walking, opening his mouth, moving his head and raising his arms, for this he used his studies in anatomy and kinesthetics; René Descartes proposes that the body of animals can be described as complex machines; Blaise Pascal, creates the first mechanical digital calculating machine, designed for addition and subtraction and many other Philosophers, mathematicians and scientists who stood out for their work and research carried out for several years and are still bases for Artificial Intelligence[4]. It is logical, in any case, that research on Information and Communication Technologies (ICT) takes into account, first of all, the multiplicity of interconnections and implications that are noted around the growing use of AI[5]. AI has strong potential to accelerate the process of achieving global education goals by reducing the difficulties of access to learning, automating management processes and optimizing methods that improve learning outcomes. This is why it is important to learn from these new innovations in teaching in order to improve and innovate classes[6]. The importance and challenges of the process in which knowledge and technology transfer are radically restructuring an environment in which knowledge, being increasingly accessible in a massive, open and low-cost manner, can be a solution. Information and communication technologies (ICT) give rise to a transfer of technology that easily permeates any geophysical point in a very accessible way, without major obstacles, such as the known barriers to the centralization of knowledge. The new paradigm of the decentralization of knowledge is the support of the new industrial revolution, no less important than the one that occurred after the invention of the Internet[7]. The impact of artificial intelligence (AI) in education. Based on the AI narratives and assessment frameworks identified from the preliminary analysis, the scope of the research is limited to the application and effectiveness of AI in management, teaching, and learning[8].

Why are the necessary artificial intelligence tools important in the teaching and learning process, does it enhance the opportunities it offers in the educational field?

For the strategies that teachers can implement in the teaching and learning process, relevant and that should be considered in the classroom. Various studies have managed to show that professionals in the area refuse to modify their practices and pedagogical strategies that have an impact on the immediate educational population, others because they find the training process difficult in new practices and others simply, they prefer to follow the same line.

The objective is to carry out the analysis of artificial intelligence applied in virtual learning environments in higher education for Ecuador, to define an adequate prototype.

Related references: Creation and Evaluation of a Pretertiary Artificial Intelligence (AI) Curriculum[9], Development of an AR-Based AI Education App for Non-Majors[10], Modern Artificial Intelligence Model Development for Undergraduate Student Performance Prediction: An Investigation on Engineering Mathematics Courses[11], Teaching machine learning in K-12 Classroom: Pedagogical and technological trajectories for artificial intelligence education[12], "Zhores" - Petaflops supercomputer for data-driven modeling, machine learning and artificial intelligence installed in Skolkovo Institute of Science and Technology[13], StEduCov: An Explored and Benchmarked Dataset on Stance Detection in Tweets towards Online Education

during COVID-19 Pandemic[14], Challenges and Opportunities in Game Artificial Intelligence Education Using Angry Birds[15], Cognition-Based Context-Aware Cloud Computing for Intelligent Robotic Systems in Mobile Education[16], Tooe: A Novel Scratch Extension for K-12 Big Data and Artificial Intelligence Education Using Text-Based Visual Blocks[17], Prediction of Physical and Mechanical Properties for Metallic Materials Selection Using Big Data and Artificial Neural Networks[18]. Application and theory gaps during the rise of Artificial Intelligence in Education[19].

The deductive method and exploratory research are used to analyze the problems that arise from properly applying artificial intelligence in virtual environments.

A Prototype of virtual environments based on IA is obtained, considering all the necessary processes for an adequate virtual environment.

It is concluded that for an adequate solution of virtual environments based on artificial intelligence, the characteristics, capacities, virtual community and IT infrastructure must be defined, where it will be applied, knowledge and digital material information, AI components.

2. Materials and Methods

In the first instance, in Materials, a search for information was carried out from different sources that allowed defining the situation of virtual environments based on artificial intelligence. Second, in the methods, the steps to achieve the results were defined.

2.1 Materials

The authors analyzed the implementation of a new assessment model based on an AI curriculum for the lower secondary school level using the co-creation process. This study presented two empirical findings and discussed its two main practical contributions to pre-tertiary AI education[9]. They present limitations of this study and considerations for future work. In the first place, the study is designed in a single group, it is necessary to carry out further studies with a complete experimental design. Second, to obtain generalized results, students who participated in the study must be taken into account. Finally, it is necessary to analyze education and its effect by designing a more sophisticated AR-based AI educational model[10]. They propose a modern educational decision support system adopted for prediction of student performance and academic program and implementation of quality assurance through practical, responsive course management, easy to use and learn. Platforms can promote a successful student learning journey, including student retention and progress, by adopting evidence-based models[11]. They describe some of the pedagogical elements computing educators need when considering machine learning in the K-12 classroom. This is a critical area for future citizens to be able to use the systems around them and put more emphasis on computer education research[12]. They are based on the properties of the group and we analyze the measured performance and modes of use of this new scientific instrument and is intended for cutting-edge multidisciplinary research in data-driven modeling and simulations, machine learning, Big Data and artificial intelligence (AI)[13]. They created and compared a new data set to analyze attitudes towards online education in the COVID-19 era. Data exploration was performed to provide summaries and insights about the dataset, such as topic modeling, tweet classification, and sentiment analysis[14]. They propose to experiment using the Angry Birds AI competition in a project-based

course as student groups explore computer vision, strategic decision making, resource management, and error-free coding of results[15]. The authors propose a system based on a context-aware cloud computing cognitive system for intelligent robotic systems in mobile education constant monitoring and present an adaptive context system, that is, a bridge connecting mobile recognition and AI services. Second, emotion recognition based on multimodal fusion is proposed to fuse multimodal emotional information[16]. They present a limitation in this study and that is that different types of instructional materials, such as teacher guides, lesson plans and rubrics, were not provided. So, in addition to eight sample apps and a ten-minute video tutorial, they planned to create and distribute more diverse resources that teachers can use in their classrooms. Since a new Scratch extension called Tooe was proposed allowing Scratch to communicate with text-based programming languages. Based on four design principles, the extension is made up of a minimum number of conversational blocks[17]. They performed predictive analysis, the predictive ability of a neural network improves as the data set grows, as it has more samples to learn from, and as a result, the network can learn more precise features (features that are closer to the reality of the problem)[18]. Growing importance of artificial intelligence (AIEd) in education and lack of comprehensive evaluation of it [19].

2.2 Methods

To carry out this research, the deductive method was used with the exploratory investigation and the review of official websites regarding AI.

In the first instance, the information related to the research topic is analyzed in order to support the results based on the trends of AI and virtual environments.

In the second phase, possible problems in the application of AI and virtual environments in higher education institutions are identified.

Table 1: Problems in the application of AI in virtual environments

Ord.	Issues	Ref.
001	The fundamental pillars of the education system must be expanded with non-cognitive skills.	[1]
002	Educators lack the necessary experiences to understand new technological systems.	[2]
003	Accelerating the development of digital technologies and their presence in everyday life.	[3]
004	Countries with limitations to be at the forefront of new technologies.	[4]
005	The need for innovation and the application of AI.	[5]
006	Ability to understand and solve everyday problems with AI within the area of education	[6]
007	Techniques and methods of AI and the challenges that can be caused for problem solving.	[7]
008	Impact of AI in different industries.	[8]

In table 1. It can be seen the frequent problems with the application of artificial intelligence in virtual environments, being one of the causes inappropriate selections.

3. Results

3.1 Proper prototype of virtual environments based on AI

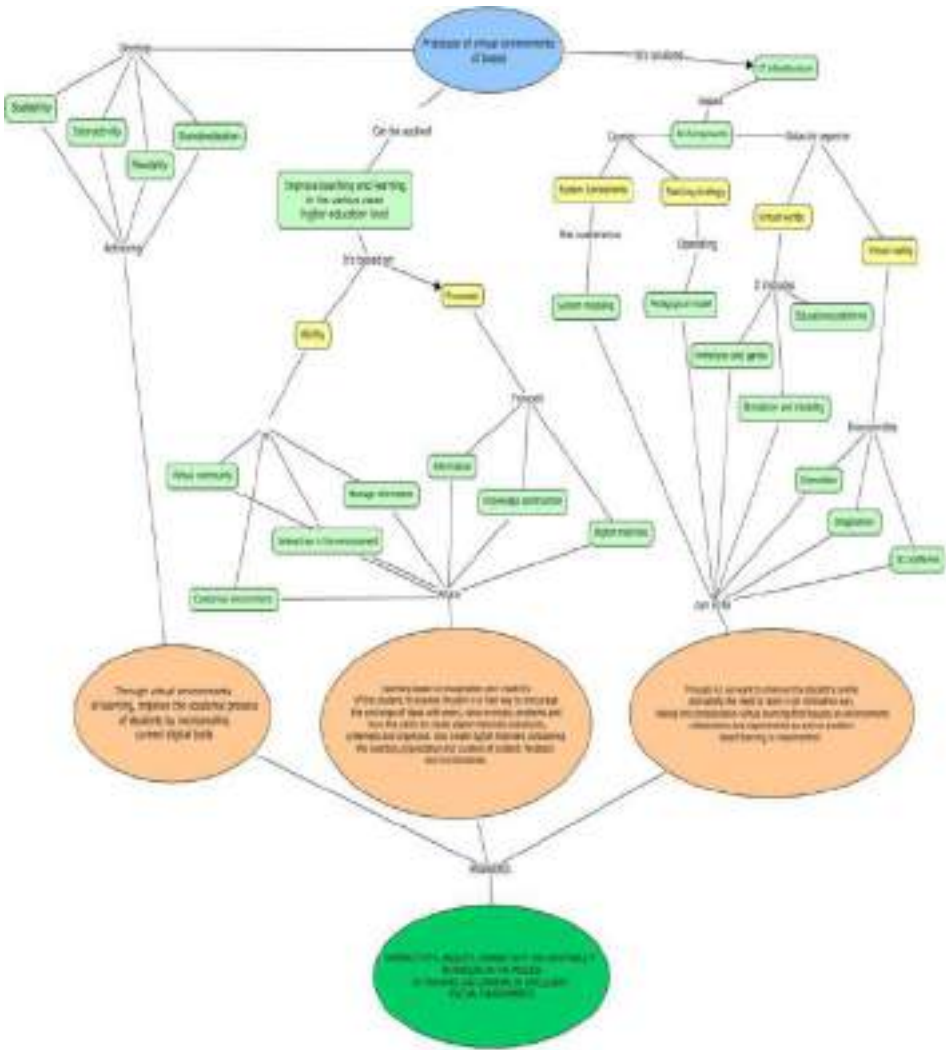


Figure 1. Proper prototype of virtual environments based on AI

Figure 1. In the Prototype for virtual environments based on AI, all the necessary processes that intervene to obtain as a result the techniques of interactivity, ubiquity, connectivity and adaptability in the teaching and learning process in intelligent virtual environments are visualized, that is a suitable prototype to improve virtual environments in higher education institutions.

3.2 A table of relevant indicators that will be used to carry out the different analyzes.

Table 2. Indicators and solutions defined by other authors.

ORD.	Indicator	Solution to the contribution	Ref.
001	Evaluation model.	New AI Curriculum.	[9]
002	Limitations of this study.	Design of an educational AI model based on AR.	[10]
003	Student performance.	Adopt evidence-based models.	[11]
004	Machine learning.	Computer education research.	[12]
005	Data-driven models.	Scientific instrument with AI and Big data.	[13]
006	Online education in the COVID-19 era.	Provide summaries and information on datasets.	[14]
007	High-level programming skills.	Software to help create user-created levels	[15]
008	Computational Cognitive System.	AI Mobile Recognition Services	[16]
009	Teacher Resource Distribution.	Scratch extension.	[17]
010	Artificial neural networks supported by big data.	computer aided tool.	[18]
011	Impact of AIED research.	Extensive review of AI-based material.	[19]

Table 2. Describes the indicators that other authors define for virtual environments that have allowed us to visualize in a better way to define the prototype of virtual environments based on AI.

4. Discussion

The solutions imposed by the authors of the references [9-19] are valid in virtual environments with their contribution to the investigation; the "Proper prototype of virtual environments based on AI" that is presented consists of defining the characteristics, capabilities, virtual community, IT infrastructure; where knowledge and information and digital material based on the reality of a higher education institution are applied.

The "Adequate prototype of virtual environments based on AI" can be applied in any higher education institution in Ecuador or countries with similar cultures and technological infrastructures similar to a developing country.

In this investigation, the implementation has not yet been carried out, an adequate prototype is presented so that it can be implemented in the future, considering the availability of the technological infrastructure.

5. Future Word and Conclusion

Carry out the implementation of this prototype in order to validate the applicability in a higher education institution.

It was concluded that for an adequate solution of virtual environments based on artificial intelligence, the characteristics, capabilities, virtual community and IT

infrastructure must be defined, where it will be applied, knowledge and digital material information, AI components, among others.

Artificial intelligence applied in virtual learning environments in higher education for Ecuador continues to be a problem because it has not been possible to standardize an adequate prototype based on the reality of the country.

Acknowledgments

The authors thank the collaboration of the authorities of the Instituto Tecnológico Superior Rumiñahui and the Secretary of Higher Education, Science, Technology and Innovation Senescyt.

References

- [1] V. R. García Peña, A. B. Mora Marcillo, and J. A. ÁvilaRamírez, “La inteligencia artificial en la educación,” *Brazilian J. Dev.*, vol. 6, no. 7, pp. 648–666, 2020, [Online]. Available: <https://www.brazilianjournals.com/index.php/BRJD/article/view/13539>
- [2] X. Giró-Gracia and J. M. Sancho-Gil, “La Inteligencia Artificial en la educación: Big data, cajas negras y solucionismo tecnológico,” *RELATEC Rev. Latinoam. Tecnol. Educ.*, vol. 21, no. 1, pp. 129–145, 2022, doi: 10.17398/1695-288x.21.1.129.
- [3] R. D. Moreno Padilla, “La llegada de la inteligencia artificial a la educación,” *Rev. Investig. en Tecnol. la Inf.*, vol. 7, no. 14, pp. 260–270, 2019, doi: 10.36825/riti.07.14.022.
- [4] M. A. N. Gómez and C. F. E. E. Y. A. Porras, “Aproximación a la Inteligencia Artificial en la educación a distancia,” pp. 45–58, 2021, [Online]. Available: www.fundacionavenir.net/revista
- [5] V. L. Salvador, X. Mamaqi, and J. V. Bordes, *Artificial intelligence: Theoretical, formative and communicative challenges of datification*, vol. 18, no. 1. 2020. doi: 10.7195/RI14.V18I1.1434.
- [6] P. N. E. Benavidez, C. V. V. Pérez, R. A. V. Pérez, and Others, “Inteligencia artificial como recursos educativos abiertos,” *Rev. Tecnológica Cienc. y Educ. Edwards Deming*, vol. 1, no. 4, 2019.
- [7] A. Acosta, V. Aguilar, R. Carreño, M. Patiño, J. Patiño, and M. a. Martínez, “Nuevas tecnologías como factor de cambio ante los retos de la inteligencia artificial y la sociedad del conocimiento,” *Espacios*, no. Tabla 1, p. 8, 2020, [Online]. Available: <http://www.revistaespacios.com/a20v41n05/20410525.html>
- [8] L. Chen, P. Chen, and Z. Lin, “Artificial Intelligence in Education: A Review,” *IEEE Access*, vol. 8, pp. 75264–75278, 2020, doi: 10.1109/ACCESS.2020.2988510.
- [9] T. K. F. Chiu, H. Meng, C. S. Chai, I. King, S. Wong, and Y. Yam, “Creation and Evaluation of a Pretertiary Artificial Intelligence (AI) Curriculum,” *IEEE Trans. Educ.*, vol. 65, no. 1, pp. 30–39, 2022, doi: 10.1109/TE.2021.3085878.
- [10] J. Kim and J. Shim, “Development of an AR-Based AI Education App for Non-Majors,” *IEEE Access*, vol. 10, pp. 14149–14156, 2022, doi: 10.1109/ACCESS.2022.3145355.
- [11] R. C. Deo, Z. M. Yaseen, N. Al-Ansari, T. Nguyen-Huy, T. A. M. P. Langlands, and L. Galligan, “Modern Artificial Intelligence Model Development for Undergraduate Student Performance Prediction: An Investigation on Engineering Mathematics Courses,” *IEEE Access*, vol. 8, pp. 136697–136724, 2020, doi: 10.1109/ACCESS.2020.3010938.
- [12] M. Tedre et al., “Teaching machine learning in K-12 Classroom: Pedagogical and technological trajectories for artificial intelligence education,” *IEEE Access*, vol. 9, pp. 110558–110572, 2021, doi: 10.1109/ACCESS.2021.3097962.
- [13] I. Zacharov et al., “‘‘Zhores’’ - Petaflops supercomputer for data-driven modeling, machine learning and artificial intelligence installed in Skolkovo Institute of Science and Technology,” *Open Eng.*, vol. 9, no. 1, pp. 512–520, 2019, doi: 10.1515/eng-2019-0059.
- [14] O. Hamad, A. Hamdi, S. Hamdi, and K. Shaban, “StEduCov: An Explored and Benchmarked Dataset on Stance Detection in Tweets towards Online Education during COVID-19 Pandemic,” *Big Data Cogn. Comput.*, vol. 6, no. 3, p. 88, 2022, doi: 10.3390/bdcc6030088.
- [15] D. M. Yoon and K. J. Kim, “Challenges and Opportunities in Game Artificial Intelligence Education Using Angry Birds,” *IEEE Access*, vol. 3, pp. 793–804, 2015, doi: 10.1109/ACCESS.2015.2442680.

- [16] J. Zheng, Q. Zhang, S. Xu, H. Peng, and Q. Wu, "Cognition-Based Context-Aware Cloud Computing for Intelligent Robotic Systems in Mobile Education," *IEEE Access*, vol. 6, pp. 49103–49111, 2018, doi: 10.1109/ACCESS.2018.2867880.
- [17] Y. Park and Y. Shin, "Tooee: A Novel Scratch Extension for K-12 Big Data and Artificial Intelligence Education Using Text-Based Visual Blocks," *IEEE Access*, vol. 9, pp. 149630–149646, 2021, doi: 10.1109/ACCESS.2021.3125060.
- [18] D. Merayo, a. Rodriguez-Prieto, and a. M. Camacho, "Prediction of Physical and Mechanical Properties for Metallic Materials Selection Using Big Data and Artificial Neural Networks," *IEEE Access*, vol. 8, pp. 13444–13456, 2020, doi: 10.1109/ACCESS.2020.2965769.
- [19] X. Chen, H. Xie, D. Zou, and G. J. Hwang, "Application and theory gaps during the rise of Artificial Intelligence in Education," *Comput. Educ. Artif. Intell.*, vol. 1, no. July, p. 100002, 2020, doi: 10.1016/j.caeai.2020.100002.

Content Connectivity Based Polyhedron Protection Against Multiple Link Failures in Optical Data Center Networks

Xin LI¹, Yu LIU, Hong WANG, Wei XU and Shanguo HUANG

School of Electronic Engineering, Beijing University of Posts and Telecommunications, China

Abstract. To further improve the resource efficiency of the p-polyhedron protection scheme against multi-link failures in optical data center networks (ODCNs), the content connectivity is considered when constructing the p-polyhedron structure. In this paper, the content connectivity-based polyhedron protection (CCPP) scheme is proposed. An ILP model and a heuristic algorithm are developed to realize the CCPP scheme. Numerical results show that the proposed CCPP scheme has a lower network redundancy. Moreover, the network redundancy of the CCPP scheme is positively correlated with the degree of content connectivity.

Keywords. Optical network, network survivability, p-polyhedron protection, content connectivity

1. Introduction

Survivability has always been an important research focus for optical networks. At present, the existing survivability techniques can be divided into two categories, i.e., the protection scheme and the restoration scheme. The restoration scheme such as link-based restoration, path-based restoration, makes best effort to establish recovery channels for interrupted working flows using the remaining available network resources after disasters. For the protection scheme, backup resources are usually reserved to achieve the uninterrupted service transmission. The backup spectrum resources are usually organized into a specific protection structure. To evaluate the resource efficiency of each protection structure, network redundancy which is defined as the ratio of the working resource consumption to the backup resource consumption is proposed [1]. In [2], we have proven that the *k-regular* and *k-edge* connected structure is the optimal protection structure against multi-link failures. Based on the *k-regular* and *k-edge* connected structure, the p-polyhedron protection scheme which has low resource redundancy is proposed [3, 4]. In optical data center networks (ODCNs), the required data or services can be replicated and maintained in multiple geographically distributed data centers. Based on this, the content connectivity which represents the reachability of the required content from each user is defined for ODCNs.

¹Corresponding author: Xin Li, School of Electronic Engineering, Beijing University of Posts and Telecommunications (BUPT), Beijing, 100876; E-mail: xinli@bupt.edu.cn.

Moreover, the degree of content connectivity can be improved by increasing the number of copies of content [5-7]. Besides, the artificial intelligence technology has been applied into optical networks. In [8], the authors reviewed the graph-based deep learning models in various problems from different types of communication networks. In [9], a deep reinforcement learning (DRL) model based on graph neural networks was proposed to solve the sub-problem of multicast session selection. In [10], a hierarchical deep reinforcement learning (DRL) model based on graph neural network (GNN) was proposed to orchestrate the allocations of IT resources in datacenters (DCs) and spectrum resources on fiber links dynamically. In ODCNs, the content connectivity can be integrated with the p-polyhedron protection scheme. With the help of content connectivity, the resource efficiency of the p-polyhedron protection scheme can be further improved. This paper proposes the content connectivity based polyhedron protection (CCPP) scheme to minimize the network redundancy of ODCNs. An ILP model and a heuristic algorithm are developed to realize the CCPP scheme under static and dynamic circumstances respectively. Numerical results show that the proposed CCPP scheme has a lower network redundancy. Moreover, the network redundancy of the CCPP scheme is positively correlated with the degree of content connectivity.

2. The CCPP Scheme

Figure 1(a) shows an ODCN which is composed of four data centers, four optical nodes. Contents C_1 , C_2 and C_3 are replicated and maintained in multiple datacenters. For each content, an aggregated topology is built. In this aggregated topology, data centers which store the same content are aggregated together into a content node. Then, the k -edge connected structure is extracted from this aggregated topology. The obtained CCPP structures are presented in Fig.1 (b).

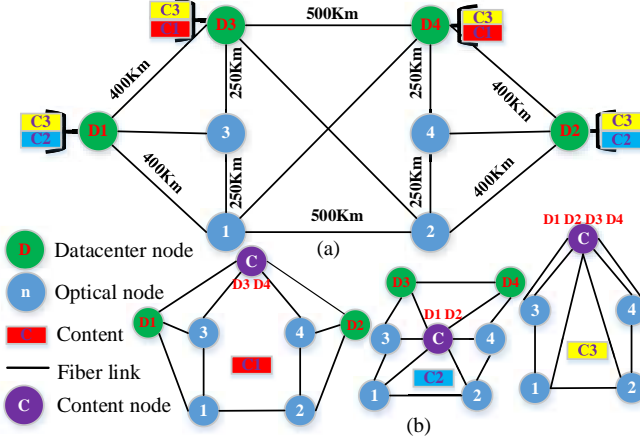


Figure 1. (a) The ODCN. (b) All built CCPPs.

$$RR_c = \frac{BLN_c * m}{(m + 1)^* |E| - m^* BLN_c} \tag{1}$$

$$RR_{CCPP} = \frac{\sum_{c \in C} RR_c * B_c}{\sum_{c \in C} B_c} \tag{2}$$

It can be seen that the number of on-body links (BLN) on the conventional polyhedron structure equals the total number of fiber links in this ODCN. The number of on-body links on each CCPP is not greater than that of the conventional polyhedron structure. For the CCPP, the proportional relation among the assigned working resources on on-body links, the assigned backup resources on on-body links, and the assigned working resources on stride links is 1:m: m+1, where m is the number of resisted failures. The network redundancy of the CCPP can be calculated by Eq. (1), where BLN_c is the number of used links on this CCPP and $|E|$ is the total number of fiber links. The consumed backup resources on each CCPP are determined by the bandwidth requirements of the corresponding content. The weighted mean of resource redundancies of all CCPPs can be obtained by Eq. (2), where B_c is the required bandwidth of content c. For the conventional protection structure, the lower bound of network redundancy is $m/(d-m)$, where d is the average node degree [11].

3. The ILP Formula and Heuristic Algorithm

In the developed ILP formula, the CCPP scheme does not need to fully satisfy the *k-regular* and *k-edge* connected constraint. The objective function is minimizing the total number of links used to achieve content reachability. The number of on-body links on each CCPP structure and the total number of on-body links on all CCPP structure are considered simultaneously.

Notations and Variables:

K: The number of independent paths, $k \in [1, K]$.

V: The set of optical nodes, $v \in V$.

D: The set of datacenter nodes, $d \in D$.

E: The set of links, $\langle i, j \rangle \in E$.

C: The set of contents, $c \in C$.

T^d : Initial content storage condition on datacenter d, $t_c^d \in T^d$.

Δ : A large integer constant.

$Y_{s,c}^{k, \langle i, j \rangle}$: Equals 1 if the k^{th} path uses link $\langle i, j \rangle$ to reach content c for node s.

$Z_s^{d,c}$: Equals 1 if node s reach content c on datacenter d.

$U_c^{\langle i, j \rangle}$: Equals 1 if link $\langle i, j \rangle$ is used on the CCPP for c.

$G^{\langle i, j \rangle}$: Equals 1 if link $\langle i, j \rangle$ is used on one CCPP.

Optimization Objective

$$Minimize(\sum_{c \in C} \sum_{\langle i, j \rangle \in E} U_c^{\langle i, j \rangle} + |C| * \sum_{\langle i, j \rangle \in E} G^{\langle i, j \rangle}) \tag{3}$$

Constraints:

$$\sum_{j: \langle i, j \rangle \in E} Y_{s,c}^{k', \langle i, j \rangle} - \sum_{j: \langle j, i \rangle \in E} Y_{s,c}^{k', \langle j, i \rangle} = \begin{cases} 1 & i = s, i \notin D \\ 1 - Z_s^{i,c} & i = s, i \in D \\ -Z_s^{i,c} & i \neq s, i \in D \\ 0 & else \end{cases} \tag{4}$$

$$\forall k' \in [1, K], s, i \in V, c \in C$$

$$\sum_{k \in K} Y_{s,c}^{k, \langle i, j \rangle} \leq 1 \quad \forall \langle i, j \rangle \in E, s \in V, c \in C \tag{5}$$

$$Z_s^{d,c} \leq t_c^d \quad \forall d \in D, c \in C, s \in V \quad (6)$$

$$\sum_{s \in S} \sum_{k \in K} Y_{s,c}^{k, \langle i, j \rangle} \geq U_c^{\langle i, j \rangle} \quad \forall \langle i, j \rangle \in E, c \in C \quad (7)$$

$$\sum_{s \in S} \sum_{k \in K} Y_{s,c}^{k, \langle i, j \rangle} / \Delta \leq U_c^{\langle i, j \rangle} \quad \forall \langle i, j \rangle \in E, c \in C \quad (8)$$

$$\sum_{c \in C} U_c^{\langle i, j \rangle} / \Delta \leq G^{\langle i, j \rangle} \leq \sum_{c \in C} U_c^{\langle i, j \rangle} \quad \forall \langle i, j \rangle \in E \quad (9)$$

Constraints (4-6) ensure that there are k link-disjoint paths used to achieve content reachability. Constraints (7-9) ensure that all links used to achieve content reachability must exist on the CCPP structure. The CCPP construction algorithm is developed to quickly get the CCPP structure based on the current content distribution. It aggregates the data center nodes stored content c as content node v_c and search the k -edge connected structure with the least on-body links in the aggregated topology.

The CCPP Construction Algorithm

INPUT: content c

OUTPUT: used links E_c on CCPP for c .

- 1: $G_c(V_c, D_c, E_c) == G(V, D, E)$
 - 2: build the datacenter nodes set $B_c, v_c \rightarrow V_c$
 - 3: **for** $b \in B_c$ **do**
 - 4: **for** $\langle b, i \rangle, \langle i, b \rangle \in E_c$ **do**
 - 5: $\langle v_c, b \rangle \rightarrow E_c, \langle b, v_c \rangle \rightarrow E_c$;
 - 6: **end for**
 - 7: **end for**
 - 8: $G_c = G_c / B_c$
 - 9: **for** $\langle i, j \rangle \in E_c$ **do**
 - 10: **if** ($G_c / \langle i, j \rangle$ is k -edge-connected) **do**
 - 11: $E_c = E_c / \{\langle i, j \rangle\}$;
 - 12: **end if**
 - 13: **end for**
 - 14: $G_c = G_c \cup B_c$;
 - 15: **for** $\langle i, v_c \rangle \in E_c$ **do**
 - 16: **for** $b \in B_c$ **do**
 - 17: **if** ($\langle i, b \rangle \notin E_c$ && $\langle i, b \rangle \in E$) **do**
 - 18: $\langle i, b \rangle, \langle b, i \rangle \rightarrow E_c$;
 - 19: $E_c = E_c / \{\langle i, v_c \rangle, \langle v_c, i \rangle\}$;
 - 20: **break**
 - 21: **end if**
 - 22: **end for**
 - 23: **end for**
-

4. Performance evaluation

Simulations are conducted in COST239. We assume each fiber link has 200 spectrum and 6 optical nodes are randomly selected as data centers. The initial number of copies of content ranges from 2 to 6 and each content are randomly distributed in data centers. The bandwidth requirement of each content is uniformly distributed between 1 and 10 slots. The degree of content connectivity is represented by cc and its value range can be determined by the ODCN topology ($cc \geq 4$ and $cc \leq 5$). The number of BLNs used by the CCPP under different content is different, so we calculate the average of BLNs on CCPPs to compare the performance with the conventional p-polyhedron protection (CPP) scheme and P-cycle. As shown in Fig. 2(a), the CCPP structure requires fewer on-body links against multi-link failures. Figure 2(b) shows that the network redundancy of the CCPP structure is less than that of the conventional polyhedron structure. Moreover, increasing the degree of content connectivity can further reduce the network redundancy of the CCPP structure.

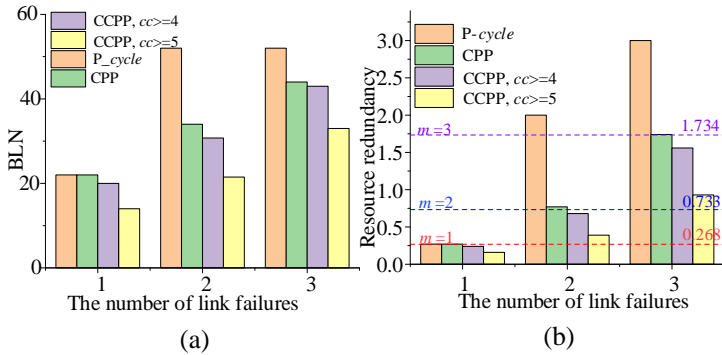


Figure 2. (a) BLN on each protection structure. (b) Resource redundancy of different protection structure.

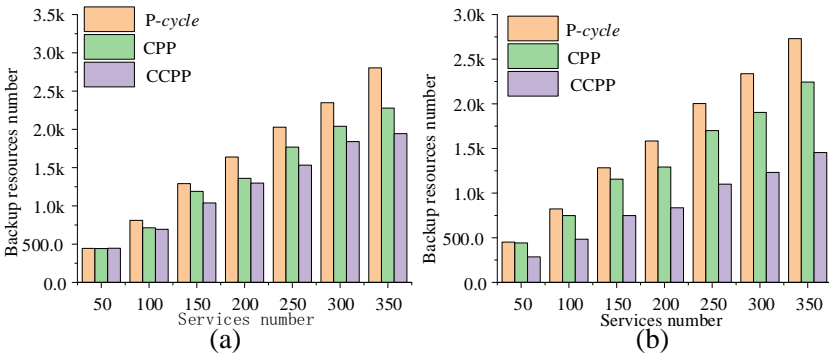


Figure 3. (a) Backup resources number under $cc=4$ and $m=2$. (b) Backup resources number under $cc=5$ and $m=2$.

Two kinds of content distributions with $cc=4$ and $cc=5$ are used to conduct the service simulation. The consumed backup resources are shown in Fig. 3 (a)-(b). Results show that increasing content connectivity has a small impact on the network redundancy of the conventional polyhedron structure. The slight change is mainly caused by the change of the service working path under different content distribution. However, it can greatly reduce the consumed backup resources on the CCPP structure. Under the two content distributions, CCPP can use the less backup resources to protect

the same number of working resources against double link failures than P-cycle and LCPP, and this advantage of CCPP emerges as services number increases.

5. Conclusion

This paper introduces the content connectivity into the construction of the polyhedron protection structure, and numerical results show this structure can effectively reduce the resource redundancy against multiple link failures.

Acknowledgements

This work was supported in part by National Natural Science Foundation of China (62125103, 62171050), Fund of Key Laboratory of Computer System and Architecture (CARCH201906) and Open Fund of State Key Laboratory of IPOC (BUPT) (IPOC2021ZT15).

References

- [1] X. Li, S. Huang, J. Zhang, Y. Zhao and W. Gu, "k-regular and k-(edge)-connected protection structures in optical transport networks," in *2013 Optical Fiber Communication Conference and Exposition and the National Fiber Optic Engineers Conference (OFC/NFOEC)*, Anaheim, USA, 2013, JW2A.03.
- [2] W. Zhang, J. Zhang, X. Li, "Theoretical analysis of preconfigured k-edge-connected structures in flexible bandwidth optical networks," *Optical Engineering*, vol.55, no.6, 066105, 2016
- [3] S. Huang, B. Guo, X. Li, J. Zhang, Y. Zhao, and W. Gu, "Pre-configured polyhedron based protection against multi-link failures in optical mesh networks," *Optics Express*, vol. 22, no. 3, pp. 2386-2402, 2014.
- [4] C. Ma, J. Zhang, Y. Zhao, J. Yuan, Y. Shi, S. Huang, and W. Gu, "Preconfigured Ball (p-Ball) Protection Method With Minimum Backup Links for Dual-Link Failure in Optical Mesh Networks", *IEEE Communications Letters*, vol.19, no.3, pp.363-366, 2015.
- [5] X. Li, S. Huang, S. Yin, Y. Zhou, M. Zhang, Y. Zhao, J. Zhang, and W. Gu, "Design of K-Node (Edge) Content Connected Optical Data Center Networks," *IEEE Communications Letters*, vol. 20, no. 3, pp. 466- 469, 2016.
- [6] X. Li, S. Huang, S. Yin, B. Guo, Y. Zhao, J. Zhang, M. Zhang, and W. Gu, "Shared end-to-content backup path protection in k-node (edge) content connected elastic optical datacenter networks," *Optics Express*, vol.24, no.9, pp.9446-9464, 2016.
- [7] X. Li, S. Yin, X. Wang, Y. Zhou, Y. Zhao, S. Huang, and J. Zhang, "Content placement with maximum number of end-to-content paths in K-node (edge) content connected optical datacenter networks," *Journal of Optical Communications and Networking*, vol.9, no.1, pp.53-66, 2017.
- [8] W. Jiang, "Graph-based deep learning for communication networks: A survey," *Computer Communications*, vol.185, pp. 40-54, 2022.
- [9] X. Tian, B. Li, R. Gu, and Z. Zhu, "Reconfiguring multicast sessions in elastic optical networks adaptively with graph-aware deep reinforcement learning," *Journal of Optical Communications and Networking*, vol.13, no.11, pp. 253-265, 2021.
- [10] B. Li and Z. Zhu, "GNN-based Hierarchical Deep Reinforcement Learning for NFV-Oriented Online Resource Orchestration in Elastic Optical DCIs," *Journal of Lightwave Technology*, vol.40, no.4, pp. 935-946, 2022.
- [11] W. Zhang, J. Zhang, X. Li, G. Luo, Y. Zhao, S. Huang, "Preconfigured k-edge-connected structures (p-kecs) against multiple link failures in optical networks," *Optik*, vol.138, pp.214-222, 2017.

RL-Based Load Balancing for Software-Defined WiFi Networks

Jun LI^{a,b,1}

^a*School of Computer and Information, Anhui Polytechnic University, China*

^b*Anhui Engineering Laboratory for Intelligent Applications and Security of Industrial Internet, China*

Abstract. Due to the popularity of mobile devices, more WIFI access points (APs) are being installed in public spaces, including train stations, airports, campuses, and shopping centers. Any station in WiFi networks will often connect to the AP that is closest to it based on the RSSI value that is the strongest. This user association approach will result in unfair bandwidth distribution and load imbalance when WiFi networks have many stations and an uneven distribution of those stations. By separating the control plane and data plane, software-defined networks (SDN) enable WiFi networks that are programmable, controllable, measurable, and manageable. This paper represents a novel load balancing mechanism based on reinforcement learning and SDN. In our proposed scheme, the center controller collects the number of associated stations with APs and traffic information on each AP's backhaul link. Then the controller decides the optimal station migration scheme to achieve load balancing among APs, based on collected information and reinforcement learning algorithm. The simulation results illustrate that our algorithm outperforms the RSSI method in terms of throughput of stations and average station number of each AP.

Keywords. reinforcement learning, user association, load balancing, SDN, WiFi networks

1. Introduction

Mobile voice and video traffic in the wireless network has grown significantly over the past few years as a result of the widespread use of smart mobile devices. For the increased mobile traffic, WiFi access points (APs) are widely used in public spaces (such as campuses, shopping malls, and airports). When WiFi APs are widely spread in a public space, the WiFi network's performance degrades as a result of interference or an unbalanced load.[1].

According to the IEEE 802.11 standard's user association method, stations choose the AP closest to them, with the highest Received Signal Strength Indicator (RSSI) value, to achieve a high data rate[2,3]. This association strategy will cause the load imbalance of the AP and congestion of the backhaul link since it ignores the load of the APs. Some APs have a high number of associated stations, and other APs may have fewer stations. The

¹Corresponding Author: Jun Li, School of Computer and Information, Anhui Polytechnic University, Wuhu, China; E-mail:edmondlee@ahpu.edu.cn

imbalance reduces network utilization, causes congestion at overloaded APs, and lowers the QoS of stations[4]. Due to IEEE 802.11 standard does not provide any solutions to mitigate the overload of APs caused by the imbalance of users, many schemes are proposed to solve this issue. In [5], a load balancing algorithm is proposed where stations do not connect the APs with the greatest transmission power. Literature [6] models the load balancing problem to a bipartite graph matching problem.

A revolutionary network architecture that separates the data plane and control plane is known as software defined networks (SDNs). In SDNs, a logically centered network controller can collect a global view of the whole network and make intelligent control decisions[7]. Recently, some studies have applied SDNs to the wireless network to make it programable, controllable, measurable, and manageable [8,9,10].In [8], OpenRoads is proposed to support heterogeneous wireless networks.Literature[9] implemented Odin, a WIFI management platform, handles scheduling wireless traffic.In [10], T. Zahid et al. proposed a software deinfied WIFI testbed.

Reinforcement Learning(RL) is a subfield of machine learning. As Fig. 1 shows, the agent observes the surrounding environment(state), takes action, and receives the environment’s reward, in which the RL agent continuously interacts with the environment to maximize the cumulative reward[11].Reinforcement learning can provide machine learning enabled scheme for issues in wireless network[12], such as rate controller[13],resource management in cell network[14],channel selection and power adaptation for cognitive radio network[15].



Figure 1. Reinforcement Learning Model

In this paper, we propose a novel load balancing algorithm based on reinforcement learning and SDNs. First, the SDN controller periodically collects the number of stations connected to per AP and traffic information per AP’s backhaul link. Then the optimal stations migration is decided by reinforcement learning algorithm according to the state of the system, including load information and traffic information of each AP. The simulation results show that the RL-based load balancing algorithm improves throughput of stations and average station number of each AP.

The rest of this paper is structured as follows: Section II presents the RL-based load balancing algorithm. The simulation and performance are evaluated in section III. Section IV end the paper by summarising conclusions and future works.

2. RL-based balancing algorithm

2.1. System Model

This study considers an SDN-based multi-station WiFi network for indoor communication with WiFi APs. N_A stands for the total number of APs, and N_S stands for the total number of stations. The associated stations list $STA_i^K = \{STA_1^K, STA_2^K, STA_3^K, \dots, STA_N^K\}$ defines the stations within the communication range of the AP K , where $K \in A = \{A_1, A_2, \dots, A_{N_A}\}$. We assumed an SDN controller center located in the network, which collects traffic and load information from each AP. A decision Agent make optimal AP assignement, using reinforcement learning algorithm, based on information from SDN controller.

We propose that the load of the AP, in contrast to the Least Load First (LLF) method, should take into account more factors, not only the number of stations connected to the AP but also the sorts of applications running on the stations that affect traffic flow on the AP's backhaul link. Few stations running high throughput applications, such as video on demand, live video, virtual reality, or augmented reality, have a larger chance of experiencing congestion on the connected AP than more stations running low throughput applications, like email, web pages, or messages. So we assumed the load of the AP mainly comes from two aspects: (i) the number of stations associated with the AP; (ii) the traffic on the AP's backhaul link. As Eq.1 shows, the load consists of the number of stations N_i and traffic T_i on AP's backhaul link. α and β are weight factors, the sum of α and β is 1. N_i is sum of stations connected the AP i . T_i is the sum of all traffic throughput on AP's backhaul link.

$$\begin{aligned}
 L_i &= \alpha \times N_i + \beta \times e^{T_i} \quad , \quad \alpha + \beta = 1 \\
 N_i &= \sum_{j=1}^n STA_j^i \quad , \quad i \in \{AP_1, AP_2, \dots, AP_{N_A}\}, \\
 STA &\in \{STA_1^i, STA_2^i, \dots, STA_n^i\} \\
 T_i &= \sum_{j=1}^n flow_j^i \quad , \quad flow \in \{flow_1^i, flow_2^i, \dots, flow_n^i\}
 \end{aligned} \tag{1}$$

In addition, the mean load of all APs controlled by an SDN controller:

$$\bar{L} = \frac{\sum_{i=1}^{N_A} L_i}{N_A} \tag{2}$$

The degree of imbalance of an AP is described by Eq.3. The bigger the positive value of IMD_i , the greater the overload of AP. Our method uses the degree of imbalance metric to find overload APs where this metric is greater than the threshold value.

$$IMD_i = \frac{L_i - \bar{L}}{\bar{L}}, i \in \{AP_1, AP_2, \dots, AP_{N_A}\} \tag{3}$$

The relative degree of imbalance between an AP and its adjacent AP within its communication range is described by Eq.4. The value of $RIMD_i$ is positive, which indicates

the load of AP i is greater than AP j , and vice versa. We use this metric to decide which AP to be selected to afford unassociated stations from overload AP.

$$RIMD_i = \frac{L_i - L_j}{\bar{L}_{i,j}}, i, j \in \{AP_1, AP_2, \dots, AP_{N_A}\} \quad (4)$$

In our method, the SDN controller collects the number of associated stations and traffic information from all APs in the WiFi network. By computing the degree of imbalance of each AP, we find the overload APs. Then we compute the relative degree of imbalance among overload AP and its adjacent APs to decide which we migrate stations to. The station migration algorithm, which we implement using the reinforcement learning algorithm.

2.2. RL-based station migration algorithm

Reinforcement learning can be modeled by Markov Decision Process(MDP), which is described by $(S, A, P, r, s_0, \gamma)$. S is the set of states. A is the set of actions. P is state transition probability. r is the reward function. s_0 is the initial state. At step t , an agent at state s_t , takes an action a_t , receives a reward $r_t = r(s_t, a_t)$, then transits to next state $s_{t+1} \sim P(\cdot | s_t, a_t)$. $\pi : a \rightarrow P(s)$ is the policy. The cumulative discounted reward under policy π is presented by Eq.5.

$$\mu(\pi) = \sum_{t=0}^{\infty} \gamma^t R_{t+1} \quad (5)$$

The goal of reinforcement learning is to maximum $\mu(\pi)$ to find an optimal policy π^* .

$$\pi^* = \arg \max_{\pi} (\mu(\pi)) \quad (6)$$

We formulate the station migration problem as a reinforcement learning problem. In our method, the set of state S includes the load information of overload AP and adjacent APs within its communication radius. A is a set of discrete actions, which is station migration which A station migrates from overload AP to its neighboring AP. $r \rightarrow S \times A$ is reward function, which is described by Eq. 7. \bar{L} is mean load of the whole network. L_t^{AP} is the current load of overload AP at step t ; L_{t+1}^{AP} is the current load of overload AP at step $t + 1$;

$$R(s, a) = \frac{L_{t+1}^{AP} - \bar{L}}{L_{t+1}^{AP} - L_t^{AP}} \quad (7)$$

3. Simulation and Performance

The simulation is performed by NS3-gym, which is a framework that integrates both OpenAI Gym and ns-3 in order to encourage usage of RL in networking research[16]. All the key parameters of the simulation are summarized by table 1.

Algorithm 1 station migration algorithm using RL

Input: current state s_t , including load of overload AP and other APs and optimal policy $\pi^*(a_t || s_t)$

- 1: using $\pi^*(a_t || s_t)$ for s_t to predict a_t
- 2: migrating a station from overload AP to other AP based on a_t
- 3: after migration, computing the current load of overload AP and mean load of whole network
- 4: obtaining r_{t+1} and s_{t+1}

Output: r_{t+1} and s_{t+1}

Table 1. Simulation Parameters

Parameters	Values
Area	$300 \times 300m^2$
Number of APs	10 WiFi
Location of APs	Uniform
Number of Stations	100
Request data rate of stations	0-50Mbps
RL algorithm	DQN
Episode length	1000
Learning rate	0.01
Discount factor	0.95

Figure 2 indicates the average station number of 10 APs in network. RSSI method results in imbalance of stations connected to APs, due to all stations prefer to associate the strongest signal AP. Our proposed RL-based method can balance the station number of all APs in network.

Figure 3 shows that the RL method can get higher throughput on most APs than the RSSI method because our proposed method can migrate stations from overload AP to light load AP so that stations can achieve higher throughput.

Figure 4 depicts the rewards of the RL method with respect to the number of iterations, which shows that rewards keep increasing over the iterations and our proposed algorithm converges fast as rewards are stable.

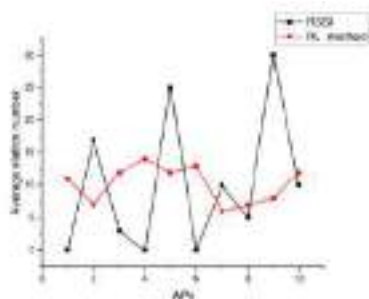


Figure 2. Average Station Number of Each AP

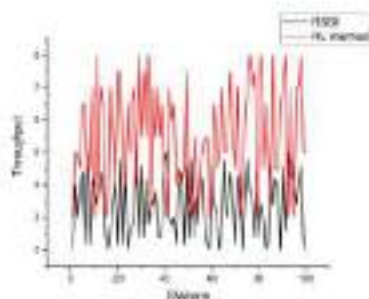


Figure 3. Throughput of Each Station

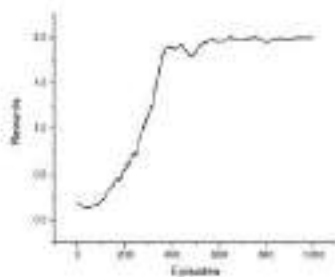


Figure 4. Training Curve of RL Method

4. Conclusions

This paper proposes a load balancing algorithm for a software-defined WiFi network. In the proposed scheme, the SDN controller first finds overload APs based on the global view of the network, load balancing, and traffic information. Then we use the RL-based stations’ migration algorithm to decide the optimal stations’ reassociation scheme to alleviate overload APs. Simulation results illustrate that our method achieve better performance than RSSI method in terms of throughput of stations and average station number of each AP.

5. Acknowledgement

This work is supported by the Natural Science Research Project in the Anhui Provincial Department of Education NO.KJ2020A0361 and the Open Fund of Anhui Engineering Laboratory for Intelligent Applications and Security of Industrial Internet under NO.IASII20-03.

References

[1] Wooi King Soo, Teck-Chaw Ling, Aung Htein Maw, and Su Thawda Win. 2018. Survey on Load-Balancing Methods in 802.11 Infrastructure Mode Wireless Networks for Improving Quality of Service. ACM Computing Surveys.2019,Mar;51(2):600-621.

- [2] O. Ercetin. Association games in IEEE 802.11 wireless local area networks. *IEEE Transactions on Wireless Communications*. 2008, Dec;7(12): 5136-5143.
- [3] Yigal Bejerano, Seung-Jae Han, and Li (Erran) Li. Fairness and load balancing in wireless LANs using association control. In *Proceedings of the 10th annual international conference on Mobile computing and networking*;2014, Oct 8-10;New York, NY, USA.p. 315–329.
- [4] O. Ercetin. Association games in IEEE 802.11 wireless local area networks. *IEEE Transactions on Wireless Communications*.2008 Dec;7(12):5136–5143.
- [5] Rohan Murty, Jitendra Padhye, Ranveer Chandra, Alec Wolman, and Brian Zill. 2008. Designing high performance enterprise Wi-Fi networks. In *Proceedings of the 5th USENIX Symposium on Networked Systems Design and Implementation*; 2008 Apr 16-18;San Francisco,USA.p. 73–88.
- [6] T. Lei, X. Wen, Z. Lu, and Y. Li. A semi-matching based load balancing scheme for dense IEEE 802.11 WLANs. *IEEE Access*.2017 July;5(2):15332–15339.
- [7] Nick McKeown, Tom Anderson, Hari Balakrishnan, Guru Parulkar, Larry Peterson, Jennifer Rexford, Scott Shenker, and Jonathan Turner. OpenFlow: enabling innovation in campus networks. *ACM SIGCOMM Computer Communication Review*. 2008, Apr;38(2): 69–74.
- [8] Kok-Kiong Yap, Masayoshi Kobayashi, Rob Sherwood, Te-Yuan Huang, Michael Chan, Nikhil Handigol, and Nick McKeown. OpenRoads: empowering research in mobile networks. *ACM SIGCOMM Computer Communication Review*.2010,Jan; 40(1) :125–126.
- [9] Lalith Suresh, Julius Schulz-Zander, Ruben Merz, Anja Feldmann, and Teresa Vazao. Towards programmable enterprise WLANs with Odin. In *Proceedings of the first workshop on Hot topics in software defined networks*;2012 Aug 13;New York, NY, USA.p.115–120.
- [10] T. Zahid, X. Hei and W. Cheng. Understanding the Design Space of a Software Defined WiFi Network Testbed. In *Proceedings of 2016 International Conference on Frontiers of Information Technology*; 2016 dec 19-21; Islamabad, Pakistan. p. 170-175.
- [11] R. S. Sutton and A. G. Barto. Reinforcement Learning: An Introduction. *IEEE Transactions on Neural Networks*.2018 sept;9(5): 1054-1054.
- [12] Weiwei Jiang. Graph-based deep learning for communication networks: A survey. *Computer Communications*.2022,Mar;2022(185):40-54.
- [13] G. Peserico, T. Fedullo, A. Morato, S. Vitturi and F. Tramarin. Rate Adaptation by Reinforcement Learning for Wi-Fi Industrial Networks. *Proceedings of 25th IEEE International Conference on Emerging Technologies and Factory Automation (ETFA)*; 2020 sept 8-11;Vienna,Austria.p. 1139-1142.
- [14] Y. Shao, R. Li, B. Hu, Y. Wu, Z. Zhao and H. Zhang. Graph Attention Network-Based Multi-Agent Reinforcement Learning for Slicing Resource Management in Dense Cellular Network. *IEEE Transactions on Vehicular Technology*.2021,Oct; 70(10) :10792-10803.
- [15] Zhao D, Qin H, Song B, et al. A graph convolutional network-based deep reinforcement learning approach for resource allocation in a cognitive radio network. *Sensors*.2020 Sep;20(18): 5216.
- [16] Gawłowicz, Piotr and Anatolij Zubow. ns3-gym: Extending OpenAI Gym for Networking Research. *ArXiv abs/1810.03943* (2018).

3D Point Cloud and BIM Component Retrieval for Subway Stations via Deep Learning

Yongfei SHI^a, Wei YE^c, Bo QU^a, Hong JIA^c, Zhanying FU^a, Xinming LV^b,
Chenglu WEN^c and Weiquan LIU^{c,1}

^a*Xiamen Rail Transit Group Co., Ltd., Xiamen, China*

^b*Xiamen Metro Technology Innovation Technology Co., Ltd., Xiamen, China*

^c*Fujian Key Laboratory of Sensing and Computing for Smart Cities,
School of Informatics, Xiamen University, Xiamen, China*

Abstract. It is urgent to digitize the subway equipment to detect the changes in the components in the subway station in time. In this paper, we use the 3D point cloud of the subway station as a benchmark, compare it with the completed BIM model of the subway station, find out the changes in the components of the subway station, and retrieve 3D point cloud and BIM model components. First, we obtained 3D point cloud and BIM model components in Xiamen Metro Station. Second, we labeled 140 pairs of matched 3D point cloud components and BIM model component point cloud. Third, we constructed a Siamese network which embedded triplet loss to learn the feature descriptors of 3D point cloud and BIM model components, and then retrieve 3D point cloud components to BIM model components. Experimental results show that our proposed method realize the retrieval of 3D point cloud components to BIM model components in the subway station environment.

Keywords. 3D point cloud, BIM, component retrieval, subway station

1. Introduction

Urban rail transit is the backbone of the urban public transportation system, with a huge investment scale, huge construction projects, and complex operation and management, which puts forward higher requirements for the digital construction of urban rail transit information. The proper management of data is a key business enabler and booster for companies [1]. The Building Information Modeling (BIM) methodology was proposed to unify projects around a Digital Twin of the information necessary for collaboration [2]. BIM model is the core data in the digital construction of urban rail transit informatization. It runs through the whole construction project management of feasibility analysis, investment decision-making, design, construction and completion [3]. However, BIM models cannot display the dynamic change information of the building.

Traditional methods usually use manual methods to manage subway equipment. In addition, manual management of subway equipment requires a lot of manpower and time,

¹Corresponding Author: Weiquan LIU, E-mail: wqliu@xmu.edu.cn.

and it is difficult to form digital subway management. However, there is a problem of inconsistent data representation between 3D point cloud and BIM model. It is necessary to unify the 3D point cloud and BIM model into the same data format. In this paper, we regard the data of BIM model as mesh data, and adopt the method of uniform surface sampling to convert the BIM model into the form of 3D point cloud data. Therefore, the retrieval problem of 3D point cloud and BIM model components becomes the retrieval problem of 3D point cloud components and BIM model components point cloud.

2. Research Objective

In this paper, we aim at the problem of digital management at the equipment component level of the subway station. First, we compare the difference between the 3D point cloud of subway station and the 3D point cloud data generated by the subway BIM model, and detect the areas of difference. Second, we construct a Siamese network which embedded triplet loss, to learn the consistent feature descriptors of the 3D point cloud and BIM model components. Experiments show that our proposed method realizes the retrieval of 3D point cloud components to BIM model components in the subway station.

The contributions of this paper are summarized as follows:

(1) We propose a Siamese network to jointly learn cross-domain descriptors of 3D point cloud components and BIM model components in the subway station environment. Meanwhile, the triplet loss is embedded to balance the consistency of the 3D point cloud and BIM model component feature descriptors.

(2) The local cross-domain feature descriptor learned by the proposed Siamese network has been applied in 3D point cloud components and BIM model retrieval, and has been demonstrated in the subway station environment.

3. Related Work

3.1. 3D feature descriptors

3D feature descriptors can be divided into handcrafted and deep learning based methods. Handcrafted 3D feature descriptors defined by geometric relationships between points, such as PFH [4] which describe the k-neighborhood geometric properties of points by parameterizing the spatial differences between query points and neighbor points and forming a multidimensional histogram, FPFH [5] which calculates the simplified point feature histogram (SPFH) of each point in the k-neighborhood of the query point separately, and then weights all SPFHs into the final fast point feature histogram through a formula.

Deep learning based methods use raw point clouds as input and output local 3D feature descriptors such as PointNet [6], PointNet++ [7], Paconv [8] and TopoSeg [9]. Some deep learning neural networks perform very well in extracting 3D feature descriptors, such as PerfectMatch [10] and D3Feat [11]. Furthermore, methods for extracting 3D feature descriptions have emerged from new perspectives. PVRCNN [12] combines the advantages of point-based and voxel-based methods to extract 3D feature descriptors more effectively and improve the performance of 3D object detection. PCTNet [13] uses Transformer [14] to encode the input point cloud into a new high-dimensional feature space.

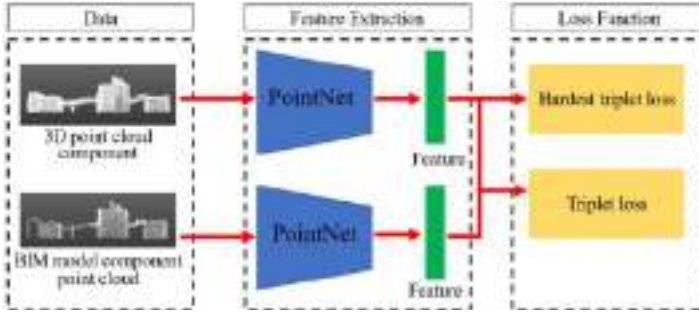


Figure 1. The constructed network structure of our method.

3.2. Deep similarity learning networks

Siamese network is commonly used for deep similarity learning networks, it uses two neural networks with shared weights to learn feature descriptors. The two neural networks convert the inputs into a vector respectively, the similarity is obtained by judging the distance. Metric learning networks achieve good performance by choosing to learn a nonlinear function to measure the similarity between feature descriptors, but require a lot of time and cost to calculate the similarity between feature descriptors. There are some Siamese networks for image patch matching based on feature retrieval such as MatchNet [15], SiamAM-Net [16], H-Net [17], Y-Net [18] and 2D3D-MVPNet [19].

4. Method

4.1. Network Structure

The constructed Siamese network structure is a two-tower structure, as shown in Figure 1. Each branch receives one type of data, resulting in a common feature descriptor. Subway 3D point cloud and BIM model point cloud belong to different domains of data, and it is difficult to match the two on the original data. Therefore, it is more reasonable to use feature descriptors based on different data for data matching. We use the Siamese network to process data from different sources and extract the cross-domain feature descriptors for 3D point cloud and BIM model components point cloud.

Each branch of the Siamese network adopts the Pointnet [6] structure. The parameters of the two branches are independent, which enables the branches to adapt to different data feature extraction. The structural parameters of Pointnet are: $conv1d(1, 64, 1) - conv1d(1, 64, 1) - conv1d(1, 64, 1) - conv1d(1, 128, 1) - conv1d(1, 1024, 1) - maxpool - fc(1024, 128)$, where $conv1d(k, d, s)$ is a one-dimensional convolution with convolution kernel k , output dimension d , and stride s , $maxpool$ represents the maximum pooling operation, $fc(p, q)$ represents a fully connected layer with input dimension p and output dimension q . Based on this structure, each branch receives a point cloud containing 8192 points and output a common feature descriptor with 128-dimensional.

4.2. Loss Function

To ensure that the matching network can distinguish matching samples from non-matching samples, we construct positive samples and negative samples for network train-

ing. Positive samples and negative samples constitute the constraints of the loss function. In this paper, triplet loss is used as a constraint, as shown in the Eq. 1, where p and c are the feature descriptors obtained by the subway 3D point cloud component P and the BIM component point cloud C after passing through the twin network, and $d(p, c)$ is the feature descriptor between the feature descriptors.

$$L(p, c) = \sum_{i=1, n} \max \{0, 0.2 + d(p, c) - d(p, c_{negative})\} \quad (1)$$

We use two methods to construct negative samples at the same time, namely, random sampling method and hardest sample method to construct negative samples. The random sampling method is to randomly sample a BIM model component in the range other than the matched BIM model component, in each pair of matching pair data of subway 3D point cloud components. Then the 3D point cloud component and the BIM model component form as a negative sample. The negative samples and positive samples obtained by this sampling method are substituted into triplet loss.

Difficult sample method, which finds samples that are indistinguishable by the network as negative samples in the batch of positive samples, thereby improving the network's ability to distinguish difficult samples. The specific process, for the training process with the number of batch samples n , first, based on n pairs of cross-dimensional feature vectors, construct an $n \times n$ distance matrix D , which is expressed as follows:

$$D = \begin{pmatrix} d_{1,1} & \cdots & d_{1,n} \\ \vdots & \ddots & \vdots \\ d_{n,1} & \cdots & d_{n,n} \end{pmatrix} \quad (2)$$

Second, the negative sample construction is performed. The sample sampling strategy selects the second nearest neighbor as a negative sample. For example, the positive sample (p_1, c_1) constructs the negative sample process: Assume that $d(p_2, c_1)$ and $d(p_1, c_4)$ in the distance matrix D are the minimum distances outside the positive sample; Compare $d(p_1, c_1)$ and $d(p_1, c_4)$, select the minimum value as the distance similarity corresponding to the negative sample, assuming $d(p_1, c_4) > d(p_2, c_1)$, then select p_2 as the negative sample of the sample (p_1, c_1) .

Therefore, the triplet loss can be written as:

$$L(p, c) = \frac{1}{n} \sum_{i=1, n} \max \{0, 0.2 + d(p_i, c_i) - \min [d(p_i, c_{j_{\min}}), d(p_{k_{\min}}, c_i)]\} \quad (3)$$

4.3. Training strategy

The training process constructs positive samples and negative samples at the same time, and optimizes the network parameters through the ternary loss proposed in Section 4.2. During the training process, the batch size of the sample is 8, and for each pair of positive samples of the 3D point cloud components, a total of two negative samples are obtained through the random sampling and difficult sample sampling methods proposed in Section 4.2, and are used in triplet loss.

The experiments are performed on a hardware device with NVIDIA RTX3090 GPU with 24GB memory. The learning parameters are set to 100 epochs, the optimizer SGD is the optimizer, the momentum parameter is 0.9, the learning rate is 0.001, and it is reduced by 0.05

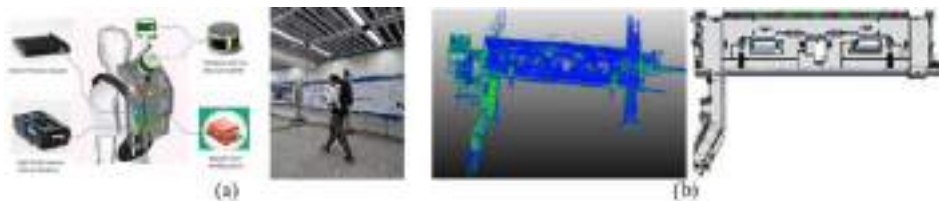


Figure 2. The backpack mobile LiDAR scanning equipment.

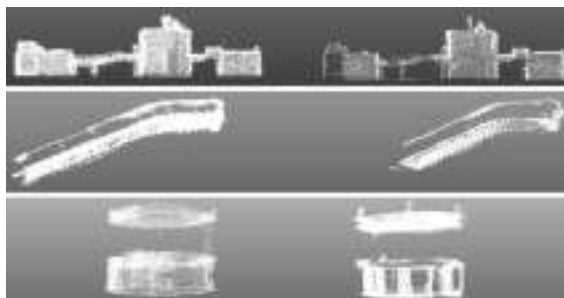


Figure 3. The matching 3D point cloud component and BIM model component point cloud. Left: 3D point cloud components. Right: BIM model component point cloud .

5. Experiments

5.1. Dataset

We use the backpack mobile LiDAR scanning equipment developed by the SCSC Laboratory of Xiamen University to collect 3D point cloud of subway stations, as shown in Figure 2 (a). We collected the 3D point cloud and the corresponding BIM model from Houcun Station, Shuangshi Station, and Huojuyuan Station of Xiamen Metro Line 3. Figure 2 (b) shows the 3D point cloud and the corresponding BIM model of Houcun Station of Xiamen Metro Line 3.

Specifically, we generated 3D point cloud from BIM model components of subway stations. Based on the acquired 3D point cloud and point cloud of BIM model, 140 pairs of matching 3D point cloud components and BIM model component point cloud were obtained by manual annotation. Figure 3 shows three pairs of matching 3D point cloud components and BIM model component point cloud. In this paper, the 140 pairs of matching samples are used for the experiment, among which 126 pairs of samples are used as the training set of deep learning neural network, and 14 pairs of samples are used as the test set. The training set and test set are guaranteed not to cross each other.

5.2. Difference detection between 3D point cloud and BIM model of subway station

We convert the BIM model into 3D point cloud data and perform registration processing with the real-time 3D point cloud of the subway station. We perform the same down-sampling process on the point cloud of the BIM model and the 3D point cloud of the subway station, so that the minimum distance between all points in the 3D point cloud



Figure 4. Left: 3D point cloud of subway station. Right: 3D point cloud generated by BIM model.

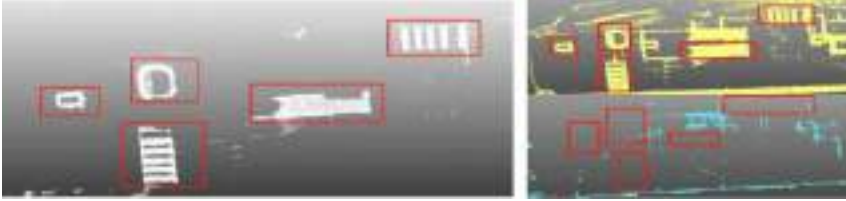


Figure 5. Left: The results of difference detection between 3D point cloud and BIM model of subway station. Upper right: 3D point cloud. Lower right: 3D point cloud generated by BIM model.

data is 2cm. After down-sampling processing, the ceiling and ground of the completed BIM model point cloud and the 3D point cloud are cut at the same time, and their internal component structure information is retained, so that the point cloud segmentation difference comparison algorithm [20] in PCL can detect and compare the areas of difference.

After processing the 3D point cloud of Xiamen Metro Line 3 Houcun Station Hall and the BIM model point cloud of Xiamen Metro Line 3 Houcun Station Hall, the results are shown in Figure 4. Using point cloud segmentation difference comparison algorithm to compare the point clouds above, and the detected difference area is shown in Figure 5.

5.3. 3D Point Cloud - BIM Component Retrieval

We use TOP1 retrieval accuracy and TOP5 retrieval accuracy as evaluation indexes to measure the retrieval results of 3D point cloud components and BIM model component point cloud. Among them, the TOP1 retrieval accuracy is defined as the proportion of the number of correct matches in the first result of retrieval confidence ranking in all queries, and the TOP5 retrieval accuracy is defined as the proportion of the number of correct matches in the TOP5 results of retrieval confidence ranking in all queries.

The TOP1 retrieval accuracy and TOP5 retrieval accuracy are $Accuracy_{TOP1} = \frac{k_1}{n} * 100\%$ and $Accuracy_{TOP5} = \frac{k_2}{n} * 100\%$, where, k_1 is the number of correct matches in the TOP1 retrieved confidence ranking result, k_2 is the number of correct matches in the TOP5 retrieved confidence ranking result, and n is the total number of queries.

Using our method, the final TOP1 retrieval accuracy in the test set is 78.57%, and the TOP5 retrieval accuracy is 92.85%. Figure 6 shows the visualization results of TOP5 retrieval of 3D point cloud to BIM model point cloud components. The BIM model point cloud components that are correctly retrieved are marked by red boxes.

From the experimental retrieval results in Figure 6, it can be found that our method successfully realizes the retrieval of 3D point cloud components to BIM model component point cloud. The first to third rows of Figure 6 show the correct TOP1 retrieval

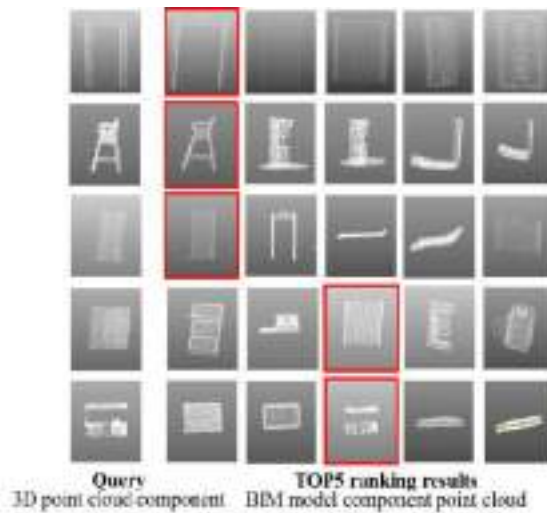


Figure 6. TOP5 ranking results. The queries are 3D point cloud components, and the ground truths and correct retrieval results of BIM model point cloud components are labeled with the red bounding boxes.

results, while the fourth and fifth rows show the wrong TOP1 retrieval results, but the correct TOP5 retrieval results. Although the fourth and fifth rows of Figure 6 are wrong TOP1 retrieval results, from the visualization results, we can find that the shape structure of BIM model component point cloud retrieved by our method is still similar to the query 3D point cloud components. In all the retrieval results, the shape and structure of BIM model component point cloud are similar to the query 3D point cloud components, which demonstrates the robustness of our proposed method.

6. Conclusion

In this paper, aiming at the problem of equipment parts-level digital management of subway stations, we compared the real-time acquired 3D point cloud of subway stations with the BIM model of subway stations to detect the area of change, and then detect the parts of difference, so as to update the BIM model components. To achieve this goal, we construct a Siamese network to extract consistent feature descriptors based on the obtained 3D point cloud components and BIM model components of subway stations. The experimental results demonstrate that the proposed method realizes the retrieval of 3D point cloud components to BIM model components in the subway station environment, and provide digital support for the digital management of equipment components in subway stations.

Acknowledgement

This work is supported by the China Postdoctoral Science Foundation (No.2021M690094); the FuXiaQuan National Independent Innovation Demonstration Zone Collaborative Innovation Platform (No.3502ZCQXT2021003) and the open fund of PDL (WDZC20215250113).

References

- [1] Bifulco I, Cirillo S, Esposito C, et al. An intelligent system for focused crawling from Big Data sources[J]. *Expert Systems with Applications*, 2021, 184: 115560.
- [2] Schiavi B, Havard V, Beddiar K, et al. BIM data flow architecture with AR/VR technologies: Use cases in architecture, engineering and construction[J]. *Automation in Construction*, 2022, 134: 104054.
- [3] Chen B, Jiang S, Qi L, et al. Design and implementation of quantity calculation method based on BIM data[J]. *Sustainability*, 2022, 14(13): 7797.
- [4] Rusu R B, Blodow N, Marton Z C, et al. Aligning point cloud views using persistent feature histograms[C]//*IEEE/RSJ International Conference on Intelligent Robots and Systems*. 2008: 3384-3391.
- [5] Rusu R B, Bradski G, Thibaux R, et al. Fast 3d recognition and pose using the viewpoint feature histogram[C]//*IEEE/RSJ International Conference on Intelligent Robots and Systems*. 2010: 2155-2162.
- [6] Qi C R, Su H, Mo K, et al. Pointnet: Deep learning on point sets for 3d classification and segmentation[C]//*Proceedings of the IEEE Conference on Computer Vision and Pattern recognition (CVPR)*. 2017: 652-660.
- [7] Qi C R, Yi L, Su H, et al. Pointnet++: Deep hierarchical feature learning on point sets in a metric space[J]. *Advances in Neural Information Processing Systems (NeurIPS)*, 2017, 30: 5099-5108.
- [8] Xu M, Ding R, Zhao H, et al. Paconv: Position adaptive convolution with dynamic kernel assembling on point clouds[C]//*Proceedings of the IEEE/CVF Conference on Computer Vision and Pattern Recognition (CVPR)*. 2021: 3173-3182.
- [9] Liu W, Guo H, Zhang W, et al. TopoSeg: Topology-aware Segmentation for Point Clouds[C]//*Proceedings of the International Joint Conference on Artificial Intelligence (IJCAI)*. 2022: 1201-1208.
- [10] Gojic Z, Zhou C, Wegner J D, et al. The perfect match: 3d point cloud matching with smoothed densities[C]//*Proceedings of the IEEE/CVF Conference on Computer Vision and Pattern Recognition (CVPR)*. 2019: 5545-5554.
- [11] Bai X, Luo Z, Zhou L, et al. D3feat: Joint learning of dense detection and description of 3d local features[C]//*Proceedings of the IEEE/CVF Conference on Computer Vision and Pattern Recognition (CVPR)*. 2020: 6359-6367.
- [12] Shi S, Guo C, Jiang L, et al. Pv-rcnn: Point-voxel feature set abstraction for 3d object detection[C]//*Proceedings of the IEEE/CVF Conference on Computer Vision and Pattern Recognition (CVPR)*. 2020: 10529-10538.
- [13] Guo M H, Cai J X, Liu Z N, et al. Pct: Point cloud transformer[J]. *Computational Visual Media*, 2021, 7(2): 187-199.
- [14] Vaswani A, Shazeer N, Parmar N, et al. Attention is all you need[J]. *Advances in Neural Information Processing Systems (NeurIPS)*, 2017, 30.
- [15] Han X, Leung T, Jia Y, et al. Matchnet: Unifying feature and metric learning for patch-based matching[C]//*Proceedings of the IEEE Conference on Computer Vision and Pattern Recognition (CVPR)*. 2015: 3279-3286.
- [16] Liu W, Wang C, Bian X, et al. Learning to match ground camera image and uav 3-d model-rendered image based on siamese network with attention mechanism[J]. *IEEE Geoscience and Remote Sensing Letters*, 2019, 17(9): 1608-1612.
- [17] Liu W, Shen X, Wang C, et al. H-Net: Neural Network for Cross-domain Image Patch Matching[C]//*Proceedings of the International Joint Conference on Artificial Intelligence (IJCAI)*. 2018: 856-863.
- [18] Liu W, Wang C, Chen S, et al. Y-Net: Learning Domain Robust Feature Representation for ground camera image and large-scale image-based point cloud registration[J]. *Information Sciences*, 2021, 581: 655-677.
- [19] Lai B, Liu W, Wang C, et al. 2D3D-MVPNet: Learning cross-domain feature descriptors for 2D-3D matching based on multi-view projections of point clouds[J]. *Applied Intelligence*, 2022: 1-16.
- [20] Rusu R B, Cousins S. 3d is here: Point cloud library (pcl)[C]//*Proceedings of the IEEE International Conference on Robotics and Automation*. 2011: 1-4.

Emulation of the Updated CANARIE Backbone Network Topology Under IPv6 Up to 2022

Jose-Ignacio Castillo-Velazquez¹ and Nelly-Guadalupe Velazquez-Cruz
Autonomous University of Mexico City, Mexico City, Mexico

Abstract. The National Research and Education Networks or Advanced Networks implemented in all countries in the world are the alternative Internet to the commercial Internet which was developed for education and experimental purposes beginning with the Internet 2. Our interest is to study the CANARIE topology after 27 years of the foundation of the pan-Canadian advanced network which now interconnects all the thirteen provinces and territories in the country. In this work a connectivity and management emulation for the updated 2022 backbone topology of CANARIE was developed under IPv6 protocols. So, emulator GNS3, Wireshark, iReasoning MIB browser, Virtual Box and Kali Linux were required to emulate CANARIE backbone infrastructure using the best possible approximation with the available resources, considering that real infrastructure is overly expensive and just supported by internet service providers. Results were successful for connectivity and management tests, showing no significative changes when Canada expanded its advanced network. Emulation uses a lot of CPU and RAM resources, but it also shows some limitations for GNS3 when comparing to real bandwidth scenarios. CANARIE maintains important connections to support international projects with other advanced networks GEANT in Europe, APAN in Asia, AFRICACONNECT through GEANT and CLARA in Latin America through Internet2 in USA. Emulating is the alternative for backbone networks for characterizing advanced networks around the world which uses expensive equipment only available by the Internet Service Provider companies.

Keywords. Advanced networks, backbone, Internet, network management.

1. Introduction

Last august 2020, Nunavut Territory joined to the Canadian Network for the Advancement of Research, Industry, and Education (CANARIE), or the National Research and Education Network (NREN) for Canada, fulfilling all thirteen provincial and territorial partners. This way, the dream of offering a pan-Canadian NREN when the Canadian Federal Government announced the born of CA*NET project in 1993 was completed. The Canadian NREN and Internet2 its equivalent in USA were interconnected in 1998, since then CANARIE has been evolving, and covering a broader area till interconnecting all the country. CANARIE members are also members of the Canadian Access Federation (CAF) which lets them access to “Edu roam” a secure Wi-Fi global roaming service and the Federated Identity Management service for researchers

¹ Corresponding Author, Jose Ignacio Castillo Velazquez, ADVNETLAB, UACM, Mexico City, Mexico; E-mail: ignacio.castillo@uacm.edu.mx.

and students. CANARIE is clue for the innovation, science, and economic development in Canada, from 2019 to 2020 data traffic grew around 26%, the highest rate in the 27 years of existence, maybe accelerated by the new normality imposed by COVID-19. Nowadays CANARIE supports national projects such as the research software program, research data management program, CAF, Digital Accelerator for Innovation and Research (DAIR) cloud platform, Ouranos for climate research, cybersecurity program and network development working as a team with the Centre of Excellence in Next Generation Networks (CENGN). CANARIE also maintains participation in worldwide projects such as International Cancer Genome Consortium (ICGC), ATLAS experiment for LHC at CERN and Square Kilometer Array (SKA) for cosmos study. The thirteen regional networks ACORN-NL, ACORN-NS, AURORA COLLEGE, BCNET, CYBERIA, MRNET, ECN, ORION, RISQ, SRNET, YUKON COLLEGE. CANARIE infrastructure supports nowadays more than 400 PB by year interconnecting their 770 national institutions to 125 NRENs in 100 countries [1-6]. Because GNS3 supports backbone routers, in previous works this emulator was used to study other backbone topologies but specifically the CANARIE for Canada one under IPv4, when all the thirteen provinces and territories were not covered, just only 12 of them, using 25 backbone routers in its topology [7]. It was in august 2020 when Nunavut Territory was included adding the first corresponding infrastructure to make reality the Canadian dream of offering a pan-Canadian advanced network after 27 years it was founded [8]. In this work GNS3 is used to emulate the full connectivity and management for the 2022 CANARIE topology under IPv6 protocols, using c7200 backbone routers [9-14]. For the most updated topology in 2022 CANARIE maintains connection to Internet2 in USA through routers from Toronto, Victoria, Windsor, Halifax, and Winnipeg. CANARIE maintains important connections to support international projects with other advanced networks GEANT in Europe, APAN in Asia, AFRICACONNECT through GEANT and CLARA in Latin America through Internet2 in USA.

2. Methodology

For the emulation of the 2022 CANARIE's backbone topology, the 28 backbone routers interconnecting the thirteen provinces and territories were configured using IPv6 addresses for all the 1Gbps optical fiber interfaces as shown in figure 1. Check that the new infrastructure at Nunavut was connected to CANARIE through the Yellowknife router. The physical equipment used for emulation was an icore 7 CPU and 16 GB, where the GNS3 2.2.20 was installed.

2.1. Connectivity configuration

All the 28 C7200 backbone routers were configured using IPv6 addresses and OSPFv3 under the IOS v12, for providing connectivity as shown in figure 2 as an example for the Whitehorse router. Then connectivity can be tested for all the 28 backbone routers in the advanced network, using ping and traceroute commands, but also by other tools as Wireshark.

2.2. Management configuration

For management emulation, first SNMPv3 was configured for each of the 28 backbone routers as indicated in figure 3, including the SHA security and parameters.



Figure 1. The backbone topology for CANARIE in 2022, using 28 backbone C7200 in GNS3 under IPv6 including the new infrastructure.

```
Whitehorse(config)#ipv6 router ospf 100
Whitehorse(config-rtr)#
May 3 21:51:06.499: %OSPFV3-4-NBRTZID: OSPFv3 process 100 could not pick a router
-ID.
Please configure manually.
Whitehorse(config-rtr)#router-id 1.1.1.1
Whitehorse(config-rtr)#exit
Whitehorse(config)#int p1/0
Whitehorse(config-if)#ipv6 ospf 100 area 0
```

Figure 2. IPv6 and OSPFv3 configuration for one of the 28 backbone routers

```
Victoria(config)#snmp-server group adv v3 auth read 113 write 456
Victoria(config)#snmp-server user nelly adv v3 auth sha amigo
```

Figure 3. The SNMPv3 configuration for BB router at Victoria Island.

Then also traps were enabled as shown in figure 4, in this example, configuration under another router is shown.

```

Fort-Simpson(config)#snmp-server view 123 iso included
Fort-Simpson(config)#snmp-server view 456 iso included
Fort-Simpson(config)#snmp-server host AAAA::1 version 3 auth nelly
Fort-Simpson(config)#snmp-server host 3456::1 v3
Fort-Simpson(config)#snmp-server host 2345::2 v3
Fort-Simpson(config)#snmp-server enable traps

```

Figure 4. The SNMPv3 configuration for enabling traps on Fort Simpson router.

Finally, the IReasoning MIB Browser was installed on the Kali Linux virtual machine attached to Victoria's router, which does the function as the Network Management System (NMS). For testing management activities, five managed variables were tested: "sysname", "syslocation", "ifnumber", "IfTable", "ipAddrTable" and "ipRouteTable" for monitoring the network at distance or changing the configuration just in case of read and write variables. SNMPv3 included the SHA secure algorithm at the configuration.

3. Results

3.1. Connectivity emulation

After configuring the 28 c7200 backbone routers using OSPFv3, the connectivity of the network was tested using ping among all routers but also using traceroute as shown in figure 5 as evidence when testing connectivity from the St John's router to the new infrastructure in Nunavut, using just 12 hops to get from east to Nunavut.

```

John#traceroute 5522::1
Type escape sequence to abort.
Tracing the route to 5522::1

 0  2514::1  184 msec 144 msec 108 msec
 1  1614::2   36 msec   8 msec  28 msec
 2  1415::1   68 msec  36 msec  36 msec
 3  1449::1   64 msec  52 msec  68 msec
 4  1258::1   92 msec  68 msec  68 msec
 5  1415::1   68 msec  72 msec  72 msec
 6  9181::2   76 msec  88 msec  84 msec
 7  5678::1   84 msec  104 msec 112 msec
 8  4587::1  108 msec  124 msec 108 msec
 9  3456::1  144 msec  144 msec 136 msec
10  2345::1  140 msec  124 msec 156 msec
11  5522::1  148 msec  152 msec 140 msec

```

Figure 5. Connectivity test using traceroute from ST John's to the new infrastructure in Nunavut.

Also, for testing connectivity it was used Wireshark in GNS3 for analyzing ICMPv3 and OSPFv3 packets, but not shown for extension.

3.2. Management emulation

Figure 6 shows the result from sending SNMP packets after a get request for the name of the router for Nunavut from the NMS next to ST John’s routers, using the IReasoning MIB Browser at the virtual machine. The “sysname” variable content was obtained through the entity or agent enabled at the router, this is a read and write variable, so changing the router’s name also was tested.

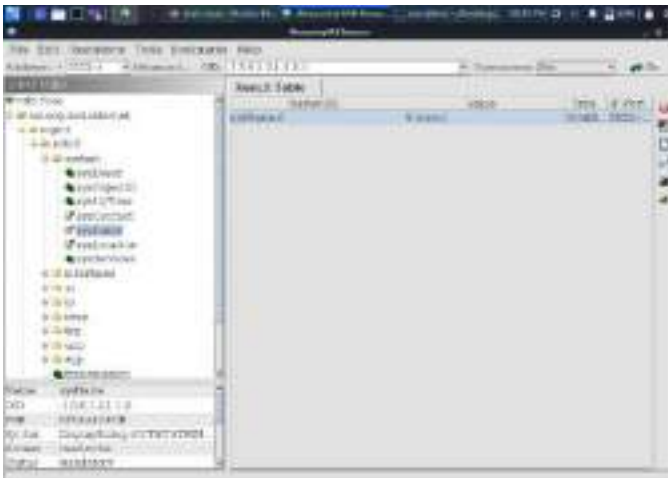


Figure 6. Management test SNMPv3 for getting the routers name for Nunavut.

Then “syslocation” and “ifnumber” were evaluated, not shown for extension and because they can be obtained using the get operation, but those kinds of test can be plotted just exemplified as the evidence shown in figure 5. So, to test *get bulk* operations, the “ifTable” was request, results are shown in figure 7, where index and descriptions are displayed.

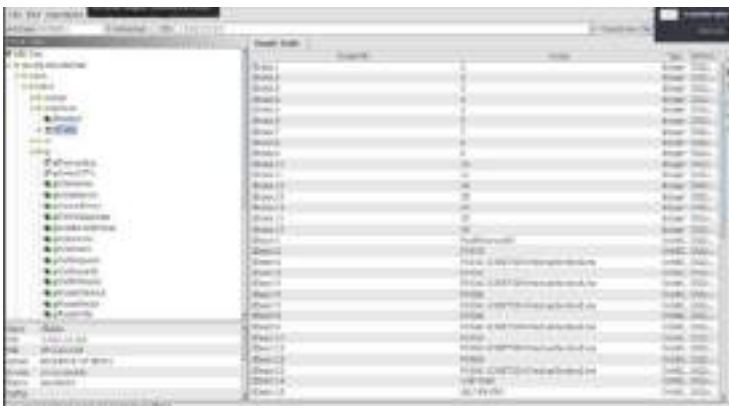


Figure 7. Management test for getting the table of interfaces for Nunavut router.

Also, for testing the *getbulk* operation a larger table was requested, the “ipAddrTable” as shown in figure 8, where some of the details are indicated. For all cases Wireshark was used to check SNMP packets sent and coming from the NMS.

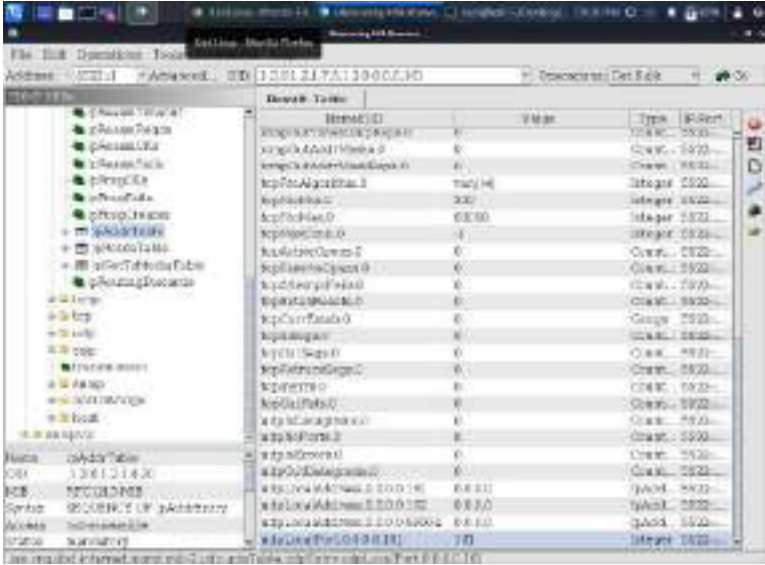


Figure 8. Management test for getting the addresses table for interfaces for Nunavut router.

3.3. Emulation resources consumption

Finally, table 1 shows the consumption of CPU and RAM by the different groups of processes when emulating tests for all the routers in the CANARIE backbone network. The average latency measured for all the connectivity tests was around 10 ms.

Table 1. CPU and RAM consumption for the CANARIE Emulation

Process	CPU % (Average)	RAM% (Average)
Connectivity	30.4+-0.1	90.2+-0.1
Management GET/SET	35.9+-0.1	90.5+-0.2
Management GET/BULK	42.4+-0.2	90.1+-0.1

4. Conclusions

This work shows the full connectivity and management of CANARIE as in 2022, including 28 backbone routers, where the OSPFv3 routing protocol, the IPv6 protocol and SNMPv3 were configured and tested. When configuring and testing connectivity, all tests were successfully, using 90.2% of RAM and 30.4% of CPU, but limited to 1Gbps links, far from real infrastructure links which support 100 to 300 Gbps. When configuring and testing management, by monitoring for GET and SET operations iReasoning MIB

browser functioned correctly using 35.9% of CPU and 90.5% of RAM. While when testing GET BULK operations the computational resources usage for RAM was 90.1%, but the CPU usage rises to 42.4%. The average latency was about 10 ms. On the other hand, it is important to mention that authors had a problem when asking for the entire IP Routing Table, due to the command “go”, must be used several times to get the entire routing table. This problem, which was solved at the indicated way, could be caused by the iReasoning MIB browser free version, but that must be proved. The main trouble authors faced was the activation of traps, for that test links among routers were evaluated making link down and link up tests, but problems persisted, the possible cause could be the iReasoning MIB browser free version, but that must be proved. So, in general, the connectivity and management for CANARIE topology as in 2022 was successful, although GNS3 still has two disadvantages, first, the limit of 1Gbps Bandwidth links and second, the only Cisco backbone router supported image is for c7200, this way emulating the full CANARIE’s function as advanced network is still a challenge for ISP companies. This updated work shows that when comparing to the previous analysis developed some years ago, no significative changes impacted the update of the CANARIE topology when Canada expanded its advanced network. Emulating is the alternative for backbone networks for characterizing advanced networks around the world which uses expensive equipment only available by the Internet Service Provider companies.

References

- [1] Petitti DB, Crooks VC, Buckwalter JG, Chiu V. Blood pressure levels before dementia. *Arch Neurol.* 2005 Jan;62(1):112-6.
- [2] Rice AS, Farquhar-Smith WP, Bridges D, Brooks JW. Canabinoids and pain. In: Dostorovsky JO, Carr DB, Koltzenburg M, editors. *Proceedings of the 10th World Congress on Pain*; 2002 Aug 17-22; San Diego, CA. Seattle (WA): IASP Press; c2003. p. 437-68.
- [3] Leslie Regan S., *Computer Networking in Canada: from CA*net to CANARIE*, Canadian Journal of Communication, Vol 19, N1, 1994.
- [4] Howard C. Clark, *Formal Knowledge Networks: A study of candian experiences*, 1998 Ed Int. Inst. for Sust. Dev., Canada, 1998: pp. 60-61.
- [5] CANARIE, *Scientific Research*, [online], 2022, [May 2022], Available: <https://www.canarie.ca/scientific-research/>
- [6] Canadian ICFA, Canadian Networks for Particle Physics Research, [online];2021[May 2021] Available:<http://hepnetcanada.ca/assets/themes/hepnet/documents/Canadian-ICFA-SCIC-Network>
- [7] J. -I. Castillo-Velazquez and A. Delgado-Villegas, "GNS3 Limitations when Emulating Connectivity and Management for Backbone Networks: A Case Study of CANARIE," 2020 IEEE Canadian Conference on Electrical and Computer Engineering (CCECE), 2020: pp. 1-4
- [8] CANARIE, NREN, Annual Report 2020:pp. 3-10.
- [9] S. Deering, Xerox PARC, R. Hinden, Ipsilon Networks. “Internet Protocol, Version 6 (IPv6) Specification”, RFC 1883, December 1995.
- [10] S. Deering, Cisco, R. Hinden, Nokia. “Internet Protocol, Version 6 (IPv6) Specification”, RFC 2460, December 1998.
- [11] R.Coltun, D.Ferguson, J. Moy, OSPF for IPv6, RFC 2740, December 1999.
- [12] R.Coltun, D.Ferguson, J. Moy, A.Lindem, OSPF for IPv6, RFC 5340, July 2009.
- [13] J. Case et al, Introduction to Version 3 of the Internet-standard Network Management Framework, RFC 2570, April 1999.
- [14] S. U. Masruroh, A. Fiade, M. F. Iman and Amelia, "Performance evaluation of routing protocol RIPv2, OSPF, EIGRP with BGP," 2017 International Conference on Innovative and Creative Information Technology (ICITech), 2017: pp. 1-7.

Cost-Efficient Service Function Chaining with CoMP Zero-Forcing Beamforming in Mobile Edge Networks

Yuan GAO^a, Hai FANG^a, and Kan WANG^{b,1}

^a*Xi'an Institute of Space Radio Technology, Xi'an 710100, China*

^b*Xi'an University of Technology, Xi'an 710048, China*

Abstract. As two promising paradigms in next generation cellular systems, service function chaining (SFC) and mobile edge computing (MEC) have attracted great interests, and would bring more delay-sensitive services to users in proximity. Nevertheless, owing to time-varying channel conditions and finite server resources, the SFC deployment in edge networks is nontrivial. In this work, leveraging both the coordinated multiple points (CoMP)-based zero-forcing beamforming and ℓ_p ($0 < p < 1$) norm-based successive convex approximation (SCA) methods, we investigate the SFC deployment in the edge. First, under the constraints of processing and link capacity, transmission power and service function ordering, we build a mixed-integer nonlinear programming (MINLP)-based cost optimization problem, to minimize both the flow and power cost. Then, using the dirty paper-based CoMP zero-forcing beamforming method, the interference among SFSs is canceled, and the original problem is recast as a interference-free one. Next, the ℓ_p ($0 < p < 1$) norm-based SCA method works to produce a series of convex subproblem, the iterative solution of which is proved to converge to optimal solution of original one at a linear convergence rate. Finally, numerical results are used to validate proposed method, showing that the wireless resource management deserves special interests in the SFC deployment in edge networks.

Keywords. service function chain, mobile edge computing, successive convex approximation, interference cancellation

1. Introduction

Next generation cellular systems are expected to experience the architecture innovation with network function virtualization (NFV), whereby service functions can be virtually instantiated in commodity servers, rather than deployed in specialized hardwares [1]. The cellular network operator can thus on-demand expand the architecture flexibly by supplementing more commodity servers and then instantiating service functions as software [2]. Besides, virtual network functions (VNFs) can be cascaded in a logical sequence through which the packet traverses [2]. Hence, such service function chaining (SFC) facilitates the flexible deployment of diversified services [3].

¹Corresponding Author: Yuan Gao, Xi'an Institute of Space Radio Technology, Xi'an 710100, China; E-mail: gaoy199034@126.com.

There have been many contributions made to the SFC or VNF deployment in traditional networks, e.g., large-scale networks [4], central cloud networks [5], and content delivery networks [6]. Meanwhile, as another one viable paradigm, mobile edge computing (MEC) is utilized to push caching and computation resources close to devices, without obtaining resources from the central cloud [1]. Integrating MEC with SFC would yield benefits. That is, by deploying SFCs in the edge, users can obtain services nearby, thereby promoting the computation-intensive or delay-sensitive services. Further, edge servers are directly programmable with NFV, and provide richer VNF combinations to build more complicated services [1,3].

Yet, deploying SFC in the edge poses more challenges in resource-constrained edge environment. First, the computing, caching, and networking resources in edge servers are typically insufficient than those of traditional core and cloud networks, and thus the resource allocation needs to be more regulated to save cost. Second, the fast fading of wireless channels in the edge asks for interference cancellation among SFCs [7]. Notice that, in the SFC of edge networks, the cached content needs to be visited before other service functions and thus caching dominates the SFC [8], while baseband unit (BBU) BBU provides signal processing ability, sends packets to users with remote radio heads (RRHs), and thus terminates the SFC [9].

Although there have been some outstanding works in the SFC deployment of edge networks, the channel conditions as well as interference cancellation schemes are not fully investigated [3,5,6]. Thus, assisted by recent advents in Gaussian codebook-based successive dirty paper encoding [10,11], we try to design an interference-free service function chaining method in the edge. First, we investigate the coordinated multiple points (CoMP) transmission-based zero-forcing method to cancel the interference across SFCs, thereby building a cost-efficient SFC deployment problem under the constraints of processing and link capacity. Then, ℓ_p ($0 < p < 1$) norm penalty is added to the mixed-integer nonlinear programming (MINLP)-based original problem, to build one equivalent counterpart with same optimal solutions. Finally, the successive convex approximation (SCA) method is utilized to solve the counterpart, approaching zero penalty at a linear convergence rate. The contribution can be summarized as follows:

- We investigate the cost-efficient SFC deployment problem in edge networks, by leveraging the CoMP-based zero-forcing beamforming method for interference-free SFCs. In the CoMP system, the effective zero-forcing beamforming matrices are designed to cancel the interference across SFCs, and then the cost is divided into edge server operating and wireless transmission power cost, under the constraints of processing and link capacity.
- To solve the MINLP-based SFC deployment, we then use the ℓ_p ($0 < p < 1$) norm-based SCA method to recast the problem as a series of convex subproblem. What is important, the equivalence on optimal solutions between original problem and its relaxed counterpart is proved, showing that the SCA converges to optimum with zero penalty at a linear rate.
- Finally, we evaluate the proposed method via simulation results, showing that the cost minimization benefits from not only the SFC routing across inter-connected edge servers, but also careful wireless power regulation. Meanwhile, proposed method shows its vitality with the increasing of SFC and service function number.

The rest is organized as follows. The network model as well as problem formulation are presented in Section 2. The zero-forcing beamforming is used in Section 3, and SCA

method is presented in Section 4. Simulation results are described to show the effectiveness of proposed method in Section 5, followed by conclusions in Section 6.

2. Network Model and Problem Formulation

For clarity, all mathematical notations throughout the paper are listed in Table 1.

Table 1. Mathematical Notations

$(\cdot)^\top$	Matrix or vector transpose
$(\cdot)^H$	Matrix or vector conjugate transpose
Upper-case bold letters	Matrices
Lower-case bold letters	Vectors
$\text{diag}\{\cdot\}$	Diagonalization
\succeq or \preceq	Componentwise inequality between vectors Matrix inequality between symmetric matrices
$\text{Tr}(\cdot)$	Sum of diagonal elements

Consider one MEC network composed of several MEC clouds, each of which includes multiple inter-connected edge servers and a group of RRHs [12]. Take one MEC cloud as a instance, and each edge server $n \in \mathcal{N} = \{1, 2, \dots, N\}$ in the MEC cloud can provide diversified VNFs. In particular, the edge server is inter-linked mutually via X2+ links to facilitate the interaction, and meanwhile empowers one RRH via vBBU. Thus, also let n be the index of RRH attached to server n interchangeably. Further, denote $\mathcal{M} = \{1, 2, \dots, M\}$ as the user set, and suppose that each user asks for one service at a time. Each service flow is endowed with one SFC, namely, any packet of the flow has to traverse through the sequenced service functions scattered in the MEC cloud, before the wireless transmission from the RRHs to user $m \in \mathcal{M}$. Denote such SFC associated with user m as $\mathcal{F}(m) = (f_1^m \rightarrow \dots \rightarrow f_l^m \rightarrow \dots \rightarrow f_{l_m}^m)$.

2.1. Signal Model and Data Rate

Each coefficient of user-RRH pair (m, n) 's channel coefficient matrix $\mathbf{H}_{m,n} \in \mathbb{C}^{L_n \times L_m}$ is drawn from the circularly symmetric complex Gaussian (CSCG) distribution. The received signal at each user m becomes as

$$\mathbf{u}_m = \mathbf{H}_m^H \mathbf{W}_m \mathbf{s}_m + \sum_{k < m} \mathbf{H}_m^H \mathbf{W}_k \mathbf{s}_k + \sum_{k > m} \mathbf{H}_m^H \mathbf{W}_k \mathbf{s}_k + \mathbf{n}_m, \quad (1)$$

where $\mathbf{H}_m = [\mathbf{H}_{m,1}; \mathbf{H}_{m,2}; \dots; \mathbf{H}_{m,N}]^H \in \mathbb{C}^{L \times L_m}$ is the channel matrix between RRHs and user m with $L = \sum_{n=1}^N L_n$, $\mathbf{W}_m \in \mathbb{C}^{L \times d_m}$ denotes the beamforming matrix from RRHs to user m with $d_m \leq L_m$ as the data stream number, $\mathbf{s}_m \in \mathbb{C}^{d_m}$ is the sampled Gaussian random codebook with zero mean and covariance \mathbf{I}_{d_m} [10], and \mathbf{n}_m acts as the additive Gaussian while noise with covariance \mathbf{I}_{L_m} . Then, via the Gaussian codebook-based successive dirty paper encoding, the second term in right-hand side (RHS) of (1) is removed [10,11], and data rate R_m turns into

$$R_m = \log_2 \frac{|\mathbf{I}_{L_m} + \sum_{k \geq m} \mathbf{H}_m^H \mathbf{W}_k \mathbf{W}_k^H \mathbf{H}_m|}{|\mathbf{I}_{L_m} + \sum_{k > m} \mathbf{H}_m^H \mathbf{W}_k \mathbf{W}_k^H \mathbf{H}_m|}, \quad (2)$$

which must be no less than its data rate requirement $R_{m,\text{th}}$, i.e.,

$$R_m \geq R_{m,\text{th}}. \quad (3)$$

2.2. Capacity Constraints

Assume that each virtual machine (VM) is capable of offering one VNF instance [13], and let \mathcal{N}_f denote the set of servers that could afford VNF f . To make each service function only get served on one node at a time, we have

$$\sum_{n \in \mathcal{N}_{f_l^m}} y_{f_l^m, n}^m = 1, \forall f_l^m \in \mathcal{F}(m), \forall m, \quad (4)$$

where $y_{f_l^m, n}^m \in \{0, 1\}$ indicates whether or not that the l -th service function for user m is served on n . Then, define $x_{f, n} \in \{0, 1\}$ to describe if server n opens VNF f , and we have

$$y_{f, n}^m \leq x_{f, n}, \forall f, \forall m, \forall n, \quad (5)$$

implying that only when $x_{f, n} = 1$ holds that can $y_{f, n}^m$ take 1; otherwise, $y_{f, n}^m = 0$ holds.

Next, let $R_{m,\text{th}}$ be the data rate requirement for user m , let \mathcal{F}_n be the set of VNFs readily embedded in n , and assume that processing one bit expends one processing unit in the VNF. Also, each VNF's being served flow rate must be no greater than its processing capacity $\mu_{f, n}$, i.e.,

$$\sum_m y_{f, n}^m R_{m,\text{th}} \leq \mu_{f, n}, \forall f \in \mathcal{F}_n, \forall n. \quad (6)$$

Meanwhile, the link capacity $\mu_{n, s}$ between n and s also needs to satisfy

$$\sum_m \sum_{f_l^m \in \mathcal{F}(m)} z_{f_l^m, n, s}^m R_{m,\text{th}} \leq \mu_{n, s}, \forall n, s, \quad (7)$$

where variable $z_{f_l^m, n, s}^m \in \{0, 1\}$ shows whether or not that f_l^m and f_{l+1}^m are serially offered by server n and s . Note in both (6) and (7) that the fixed data rate $R_{m,\text{th}}$ is set in the SFC routing across edge serves, since the backhaul data rate is typically assumed to be no greater than wireless data rate [14].

Finally, we have

$$z_{f_l^m, n, s}^m \geq y_{f_l^m, n}^m + y_{f_{l+1}^m, s}^m - 1, \forall f_l^m \in \mathcal{F}(m), \forall m, \forall n, s, \quad (8)$$

implying that $z_{f_l^m, n, s}^m$ can take 1 only when both $y_{f_l^m, n}^m = 1$ and $y_{f_{l+1}^m, s}^m = 1$ hold.

2.3. Problem Formulation

It is desired that service functions in one SFC are centralized in as few nodes as possible, to minimize the flow cost. Each edge server is nevertheless with restricted processing capacity, only accommodating finite service functions, and inevitably resulting in the flow routing cost. Further, not only the flow routing across servers, but also the VNF provisioning in edge servers do incur cost. Thus, the power cost includes both the wireless transmission power in the air and service function sustaining power in edge servers.

We aim to minimize the total service flow cost plus power cost in the edge. First, define $\sum_m \text{Tr}(\mathbf{W}_m \mathbf{W}_m^H)$ as the wireless transmission power. Further, let $P_{f_{\ell_m}^m, n}^m$ and $P_{n, \text{th}}^m$ be the vBBU processing and wireless transmission power budget for server n and RRH n to serve user m , separately, and $y_{f_{\ell_m}^m, n}^m \in \{0, 1\}$ denotes whether or not user m accesses server n 's vBBU. The beamforming matrix \mathbf{W}_m should satisfy

$$\text{Tr}(\mathbf{A}_n \mathbf{W}_m \mathbf{W}_m^H) \leq P_{f_{\ell_m}^m, n}^m y_{f_{\ell_m}^m, n}^m + P_{n, \text{th}}^m, \quad (9)$$

with

$$\mathbf{A}_n = \text{diag}\{\underbrace{0, \dots, 0}_{\sum_{n'=1}^{n-1} L_{n'}}, \underbrace{1, \dots, 1}_{L_n}, \underbrace{0, \dots, 0}_{\sum_{n'=n+1}^N L_{n'}}\}. \quad (10)$$

Next, denote $P_{f, n}$ and $P_{f, n}^m$ as the constant power consumption for server n to sustain VNF f and for n to supply user m with f , respectively, and the total cost becomes as

$$C = \sum_{n, s} \sum_m \sum_{f^m \in \mathcal{F}(m)} z_{f_l^m, n, s}^m R_{m, \text{th}} + \eta \left(\sum_n \sum_{f \in \mathcal{F}_n} x_{f, n} P_{f, n} + \sum_n \sum_m \sum_{f_l^m \in \mathcal{F}(m)} y_{f_l^m, n}^m P_{f_l^m, n}^m + \sum_m \text{Tr}(\mathbf{W}_m \mathbf{W}_m^H) \right), \quad (11)$$

where η is a positive trade-off factor between power and flow cost. In particular, the four different terms respectively denote service flow, supply power to sustain VNFs in servers, power consumption on service function provisioning for users, and wireless transmission power at the RRHs. Note in (11) that, we define that $\sum_m \text{Tr}(\mathbf{W}_m \mathbf{W}_m^H)$ also comprises the vBBU provisioning power. Thus, $\mathcal{F}(m) = \mathcal{F}(m) \setminus \{f_{\ell_m}^m\}$ holds in the third term.

Till now, considering the above link and service instance capacity constraints as well as data rate requirement and transmission power budget, the network cost minimization can be formulated as

$$\begin{aligned} \mathcal{P}_0 : \quad & \min_{[\mathbf{W}_m], \{x_{f, n}\}, \{y_{f_l^m, n}^m\}, \{z_{f_l^m, n, s}^m\}} C \\ & \text{s.t.} \quad (3) - (9) \end{aligned} \quad (12)$$

where constraint (8) together with the objective (11) implies that $z_{f_l^m, n, s}^m = 1$ makes sense only when both $y_{f_l^m, n}^m$ and $y_{f_{l+1}^m, s}^m$ take 1, and the minimization nature of (12) prevents the optimal solution from taking 1 on $z_{f_l^m, n, s}^m$, when only one of $y_{f_l^m, n}^m$ and $y_{f_{l+1}^m, s}^m$ equals 1.

Remark that \mathcal{P}_0 is actually one \mathcal{NP} -hard problem, since it is easy to prove that \mathcal{P}_0 reduces to the uncapacitated facility location (UFL) one (which is \mathcal{NP} -hard) [8].

3. CoMP-Assisted Beamforming to Cancel Interference

We try to utilize the zero-forcing beamforming in [10,11] at RRHs to cancel the interference on user m from other users $m + 1$ to M . First, stack the channel matrices for all users as $[\mathbf{H}_m]_{m=1}^M \in \mathbb{C}^{L \times \sum_{m=1}^M L_m}$, which is column full rank, and its QR decomposition is

$$[\mathbf{H}_m]_{m=1}^M = [\mathbf{Q}_m]_{m=1}^{M+1} \begin{bmatrix} \mathbf{R}_{1,1}, \dots, \mathbf{R}_{1,M} \\ \vdots \\ \mathbf{R}_{M,M} \\ \mathbf{0} \dots \mathbf{0} \\ \vdots \\ \mathbf{0} \dots \mathbf{0} \end{bmatrix}, \quad (13)$$

where $[\mathbf{Q}_m]_{m=1}^{M+1} \in \mathbb{C}^{L \times L}$ is the unitary matrix, and $\mathbf{R}_{m,m} \in \mathbb{C}^{L_m \times L_m}$ is the full-rank upper triangular matrix. From (13), we have $\mathbf{H}_m = \sum_{k=1}^m \mathbf{Q}_k \mathbf{R}_{k,m}$.

Thus, define $\mathbf{S}_m \in \mathbb{C}^{\sum_{k=m}^{M+1} L_k \times d_m}$ as the weight matrix, and the zero-forcing beamforming matrix for user m can be designed as $\mathbf{W}_m = [\mathbf{Q}_k]_{k=m}^{M+1} \mathbf{S}_m$, giving rise to

$$\mathbf{H}_m^H \mathbf{W}_k = \mathbf{0}, \forall k > m, \quad (14)$$

whereby the third term in (1) is also canceled.

Note that $\mathbf{H}_m^H \mathbf{W}_m = [\mathbf{R}_{m,m}^H, \mathbf{0}] \mathbf{S}_m$, and thus only the first L_m rows of \mathbf{S}_m could affect the data rate. The beamforming matrix of user m can reduce to $\mathbf{W}_m = \mathbf{Q}_m \bar{\mathbf{S}}_m$, with $\bar{\mathbf{S}}_m \in \mathbb{C}^{L_m \times d_m}$ and $\mathbf{S}_m = [\bar{\mathbf{S}}_m; *]$.

Afterwards, we define the positive semi-definite beamforming matrix as $\mathbf{\Sigma}_m = \mathbf{R}_{m,m}^H \bar{\mathbf{S}}_m \bar{\mathbf{S}}_m^H \mathbf{R}_{m,m}$, and the data rate (2) becomes as

$$R_m = \log_2 |\mathbf{I}_{L_m} + \mathbf{\Sigma}_m| \geq R_{m,\text{th}}, \quad (15)$$

Notice in (15) that, the interference among SFSs is canceled now, due to (14).

Till now, (9) can be recast as

$$\text{Tr}(\mathbf{A}_n \mathbf{W}_m \mathbf{W}_m^H) = \text{Tr} \left(\underbrace{\mathbf{R}_{m,m}^{-1} \mathbf{Q}_m^H \mathbf{A}_n \mathbf{Q}_m \mathbf{R}_{m,m}^{-H} \mathbf{\Sigma}_m}_{\bar{\mathbf{A}}_{m,n}} \right) \leq P_{f_{\ell_m}^m, n}^m y_{f_{\ell_m}^m, n}^m + P_{n,\text{th}}^m. \quad (16)$$

Finally, \mathcal{P}_0 is equivalently recast as

$$\begin{aligned} \mathcal{P}_1 : \quad & \min_{\{\mathbf{\Sigma}_m\}, \{x_{f,n}\}} C \\ & \{y_{f_l^m, n}^m\}, \{z_{f_l^m, n, s}^m\} \\ \text{s.t.} \quad & (4) - (8), (15), (16) \end{aligned} \quad (17)$$

4. Norm Penalty-based Iterative Solving

To solve \mathcal{P}_1 , we would like to relax $\{x_{f,n}\}$, $\{y_{f_l^m,n}^m\}$ and $\{z_{f_l^m,n,s}^m\}$. Yet, \mathcal{P}_1 is generally not equal to its relaxed counterpart, since the optimal solution in relaxed \mathcal{P}_1 cannot be insured to be binary. Thus, besides relaxation, we also add some ℓ_p ($0 < p < 1$) norm penalty terms to the objective, thereby forcing the relaxed variables binary.

For notational simplicity, let $\mathbf{x} = \{x_{f,n}\}$, $\mathbf{y} = \{y_{f_l^m,n}^m\}$ and $\mathbf{z} = \{z_{f_l^m,n,s}^m\}$ hereinafter, and then (4) can be recast as

$$\|\mathbf{y}_{f_l^m}^m\|_1 = 1, \forall f_l^m, \forall m, \quad (18)$$

with $\mathbf{y}_{f_l^m}^{m,t} := \left[y_{f_l^m,1}^{m,t}, y_{f_l^m,2}^m, \dots, y_{f_l^m,|\mathcal{N}_{f_l^m}^m|}^m \right]^\top$. Then, one instance problem is as follows:

$$\begin{aligned} \min_{\mathbf{y}_{f_l^m}^m} \quad & \|\mathbf{y}_{f_l^m}^m + \delta \mathbf{1}\|_p^p = \sum_{n \in \mathcal{N}_{f_l^m}^m} \left(y_{f_l^m,n}^{m,t} + \delta \right)^p \\ \text{s.t.} \quad & \|\mathbf{y}_{f_l^m}^m\|_1 = 1, \\ & \mathbf{0} \preceq \mathbf{y}_{f_l^m}^m \preceq \mathbf{1}, \end{aligned} \quad (19)$$

where δ takes one arbitrarily small positive value [15]. (19)'s optimal point is precisely 0-1 valued, i.e., only one server from $\mathcal{N}_{f_l^m}^m$ can afford f_l^m for user m , and thus (19)'s optimal value is $c_{\delta,f_l^m} = \left(|\mathcal{N}_{f_l^m}^m| - 1 \right) \delta^p + (1 + \delta)^p$.

Next, in addition to relaxation, we also add one L_p penalty term (with regulating parameter σ) onto \mathcal{P}_1 's objective, reformulating \mathcal{P}_1 as

$$\mathcal{P}_{1-L_p} : \min_{\{\Sigma_m\}, \mathbf{x}, \mathbf{y}, \mathbf{z}} C + \underbrace{\sigma \sum_m \sum_{f_l^m \in \mathcal{F}(m)} \left(\|\mathbf{y}_{f_l^m}^m + \delta \mathbf{1}\|_p^p - c_{\delta,f_l^m} \right)}_{P_\delta(\mathbf{y})} \quad (20)$$

$$\text{s.t.} \quad (4) - (8), (15), (16)$$

$$\|\mathbf{y}_{f_l^m}^m\|_1 = 1, \mathbf{0} \preceq \mathbf{y}_{f_l^m}^m \preceq \mathbf{1}, \mathbf{0} \preceq \mathbf{z}_{f_l^m}^m \preceq \mathbf{1}$$

with $\mathbf{z}_{f_l^m}^m = \left[z_{f_l^m,n,s}^m \right]_{n=1,s=1}^{|\mathcal{N}_{f_l^m}^m|,|\mathcal{N}_{f_l^m}^m|}$ and σ as a penalty parameter.

The asymptotic optimality of \mathcal{P}_{1-L_p} to \mathcal{P}_1 with increasing σ is already established in [15, Theorem 3], and we next prove its linear convergence rate to zero penalty by proposing one assumption.

Assumption 1. C is L_C -Lipschitz continuous and the maximum ℓ_2 norm distance between two solutions in \mathcal{P}_{1-L_p} is bounded by a constant R .

Under Assumption 1, we investigate the convergence rate of \mathcal{P}_{1-L_p} with the increasing $\{\sigma_v\}$, where v is the iteration index. Denote $P_\delta(\mathbf{y})$ in the v -th iteration as $P_\delta(\mathbf{y}^v)$.

Theorem 1. Assume Assumption 1 is satisfied. When the penalty parameter is updated as $\sigma_{v+1} = \tau\sigma_v$ with $\tau > 1$ and $\sigma_0 = 1$, the penalty term sequence $\{P_\delta(\mathbf{y}^v)\}$ satisfies

$$P_\delta(\mathbf{y}^v) \leq \frac{L_C R}{\tau^v}. \tag{21}$$

Proof. From the Appendix (proof of Theorem 3) in [15], we have

$$\sigma_v(P_\delta(\mathbf{y}^v) - P_\delta(\mathbf{y}^{v+1})) \leq C_{v+1} - C_v, \tag{22}$$

where C_v denotes the value of C in (20) at the v -th iteration for simplicity. Next, set $\sigma_{v+1} = \tau\sigma_v$, $\sigma_0 = 1$ and $\tau > 1$, and the following holds as

$$\tau^v(P_\delta(\mathbf{y}^v) - 0) = \tau^v P_\delta(\mathbf{y}^v) \leq C^* - C^v, \tag{23}$$

since the penalty term vanishes at optimal solutions, and C^* is the optimal value in \mathcal{P}_1 with binary \mathbf{x} , \mathbf{y} and \mathbf{z} .

Next, from Assumption 1, we further have

$$C^* - C_v \leq L_C R. \tag{24}$$

Till now, by substituting (24) into (23), we obtain

$$P_\delta(\mathbf{y}^v) \leq \frac{L_C R}{\tau^v}. \tag{25}$$

□

From (21), it follows that $\{P_\delta(\mathbf{y}^v)\}$ approaches 0 at a linear convergence rate. Till now, although the asymptotic optimality of \mathcal{P}_{1-L_p} to \mathcal{P}_1 is presented, \mathcal{P}_{1-L_p} is non-convex. We then have to leverage the SCA method [15], i.e., obtain the first-order Taylor approximation of penalty. As such, $P_\delta(\mathbf{y})$ can be upper bounded by $P_\delta(\mathbf{y}^v) \leq P_\delta(\mathbf{y}^v) + \nabla_{\mathbf{y}} P_\delta(\mathbf{y}^v)^\top (\mathbf{y} - \mathbf{y}^v)$, where the optimal point in the preceding SCA iteration is taken as \mathbf{y}^v , while $\nabla_{\mathbf{y}} P_\delta(\mathbf{y}^v)$ is the derivative of $P_\delta(\mathbf{y})$ on \mathbf{y}^v .

Finally, in the $(v + 1)$ -th SCA iteration, \mathcal{P}_{1-L_p} is recast as one convex problem as

$$\begin{aligned} \mathcal{P}_{1-S} : \quad & \min_{\{\mathbf{\Sigma}_{m,t}\}, \mathbf{y}, \mathbf{z}} \quad C_t + \sigma_{v+1} \nabla_{\mathbf{y}} P_\delta(\mathbf{y}^v)^\top \mathbf{y} \\ \text{s.t.} \quad & (4) - (8), (15), (16) \\ & \left\| \mathbf{y}_{f_t^m}^m \right\|_1 = 1, \mathbf{0} \preceq \mathbf{y}_{f_t^m}^m \preceq \mathbf{1}, \mathbf{0} \preceq \mathbf{z}_{f_t^m}^m \preceq \mathbf{1} \end{aligned} \tag{26}$$

which is readily solved via lots of algorithms, e.g., the Lagrangian dual [16].

Remark that, \mathcal{P}_{1-S} is indeed a one-slot SFC deployment problem. The dynamic SFC deployment in time-varying scenarios have also received lots of interests, via either deep reinforcement learning [17,18] or graph neural networks [19,20], which is yet beyond the scope of this work, and would be left in future work.

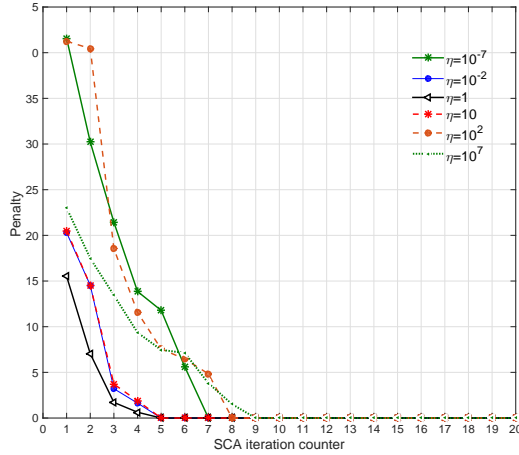


Figure 1. Convergence performance of penalty-based SCA iteration. (7 edge server and 6 SFCs exist in the system, and each SFC includes 4 service functions.)

5. Simulation Results

To simulate edge networks, the random network model [21] is used to create connections between any two edge servers n and s , with the connecting probability $\Pr(n, s) = \beta \exp\left(\frac{-d(n, s)}{\alpha R_d}\right)$, where $d(n, s)$ is the ℓ_2 norm distance, R_d denotes the maximum distance among all (n, s) -pairs, and both $\alpha \in [0, 1]$ and $\beta \in [0, 1]$ are control parameters. 7 edge servers with 8 antennas and 6 users with 3 antennas are distributed in a rectangular coordinate grid $300 \text{ m} \times 300 \text{ m}$. The fast fading is Rayleigh distributed, the log-normal shadowing fading per user is 8 dB, noise power spectrum density is -174 dBm/Hz, the path loss is $\text{PL}(\text{dB}) = 32.45 + 10 \log_{10}(d(m))$, and the maximum transmission power per RRH is 46 dBm.

Five different types services coexist, and their data rate requirements are separately 0.5 Mbps, 1 Mbps, 4 Mbps, 5 Mbps, and 10 Mbps. A total of seven different VNFs exist in edge networks, and each server have randomly accommodated three of them. The processing capacity of each VNF ranges from 5 Mbps to 15 Mbps, the link capacity between any two linked edge servers ranges from 10 Mbps and 50 Mbps, while both $P_{f,n}$ and P_{f1}^m in (11) range from 1 W to 4 W.

For performance comparison, three other benchmarks are presented as random SFC routing + CoMP zero-forcing beamforming (abbreviated as random zero-forcing), optimal SFC routing + unicast beamforming (abbreviated as optimal unicast), and random SFC routing + unicast beamforming (abbreviated as random unicast).

5.1. Numerical Results

Fig. 1 shows the convergence behavior of SCA iteration under different settings of η . We set error to zero duality as 0.01. All settings converge to zero penalty within 10 iterations, thus verifying the linear convergence rate of proposed ℓ_p ($0 < p < 1$) penalty-based SCA iteration.

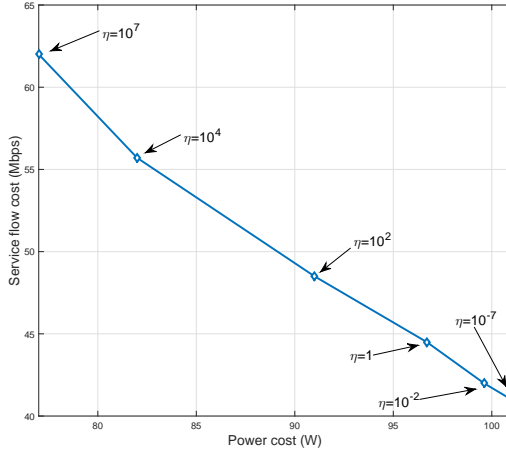


Figure 2. Tradeoff between power and service flow cost. (7 edge server and 6 SFCs exist in the system, and each SFC includes 4 service functions.)

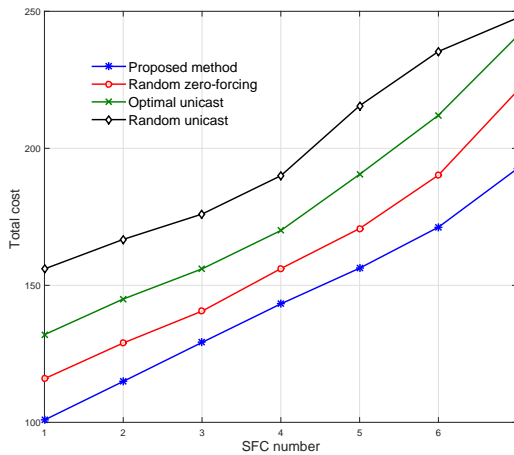


Figure 3. The impact of SFC number on total cost. (7 servers exist in the system, each SFC includes 4 service functions, and $\eta = 10^2$.)

Fig. 2 shows the tradeoff curve between power and service flow cost, under different η in (11). When $\eta = 10^7$, proposed method almost puts all emphases on power cost, and thus \mathcal{P}_0 reduces to the power minimization problem. The flow cost reaches above 60 Mbps, since no emphases are put on it. Conversely, when $\eta = 10^{-7}$, almost all emphases are imposed on service flow cost, \mathcal{P}_0 reduces to one service flow minimization problem, and thus power cost reaches above 100 W. Fig. 2 can provide empirical values of η for practical SFC deployment in next generation cellular systems.

Fig. 3 compares different methods regarding SFC number, in terms of total cost. As

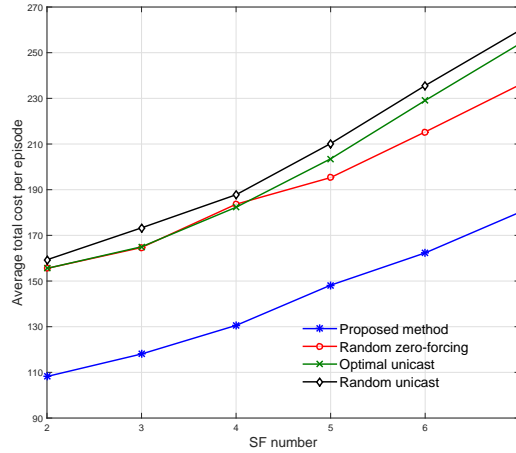


Figure 4. The impact of service function number on total cost. (7 servers exist in the system, each SFC includes 4 service functions, and $\eta = 10^2$.)

shown in Fig. 3, proposed method obtains the least system cost, due to its advantage in both SFC routing and wireless transmission exploitation. In addition, random zero-forcing gets less cost than optimal unicast, since the setting $\eta = 10^3$ gives more emphases on power cost, and random zero-forcing obtains less power cost via CoMP-based beamforming. More especially, proposed method respectively surpasses other three benchmarks on average by 38.1%, 55.3%, and 70.1%.

Fig. 4 shows the impact of service function number per SFC. As shown in Fig. 4, proposed method always has the least cost, due to its advantage in both optimal routing and optimal beamforming. In addition, random zero-forcing surpasses optimal unicast, since $\eta = 10^2$ setting would incur less power cost for the former. More especially, proposed method respectively surpasses other three benchmarks on average by 25.2%, 27.5%, and 30.1%.

6. Conclusion and Future Work

We investigated the cost-efficient SFC deployment in the mobile edge networks. First, both the flow routing and power sustaining costs were incorporated, and a SFC deployment problem was formulated to minimize the total cost, under the constraints of wireless interference, processing and link capacity, transmission power, as well as service function ordering. Then, to cancel the interference among SFCs, a dirty paper-based zero-forcing beamforming technique was used for interference-free SFC deployment. Next, to solve the MINLP-based original problem, the original one was relaxed, and the ℓ_p ($0 < p < 1$) norm penalty term was added onto the objective to make the optimal solutions of relaxed one also binary. Finally, simulation results verified the convergence behavior of proposed SCA method, as well as the importance of transmission power allocation in the SFC deployment in edge networks. In future work, we will study the dynamic SFC deployment in time-varying scenarios, using reinforcement learning.

References

- [1] Cabrera JA, Fitzek FH, Hanisch S, Itting SA, Zhang J, Zimmermann S, Strufe T, Simsek M, Fetzer CW. Intelligent networks. In: Fitzek FH, Li SC, Speidel S, Strufe T, Simsek M, Reisslein M, editors. *Tactile Internet*. San Diego, CA: Academic Press; 2021. p. 131–149.
- [2] Cui L, Tso FP, Jia W. Federated service chaining: Architecture and challenges. *IEEE Communications Magazine*. 2020 Mar; 58(3): 47–53.
- [3] Song S, Lee C, Cho H, Lim G, Chung J. Clustered virtualized network functions resource allocation based on context-aware grouping in 5G edge networks. *IEEE Transactions on Mobile Computing*. 2020 May; 19(5): 1072–1083.
- [4] Luo Z, Wu C, Li Z, Zhou W. Scaling geo-distributed network function chains: A prediction and learning framework. *IEEE Journal On Selected Areas In Communications*. 2019 Aug; 37(8): 1838–1850.
- [5] Alhussein O, Do PT, Ye Q, Li J, Shi W, Zhuang W, Shen X, Li X, Rao J. A virtual network customization framework for multicast services in NFV-enabled core networks. *IEEE Journal On Selected Areas In Communications*. 2020 Apr; 38(6): 1025–1039.
- [6] Dieye M, Ahvar S, Sahoo J, Ahvar E, Glitho R, Elbiaze H, Crespi N. CPVNF: Cost-efficient proactive VNF placement and chaining for value-added services in content delivery networks. *IEEE Transactions on Network and Service Management*. 2018 Jun; 15(2): 774–786.
- [7] Li J, Wang R, Wang K. Service function chaining in industrial Internet of Things with edge intelligence: A natural actor-critic approach. *IEEE Transactions on Industrial Informatics*. 2022, to appear, online. doi:10.1109/TII.2022.3177415.
- [8] Zheng G, Tsiopoulos A, Friderikos V. Optimal VNF chains management for proactive caching. *IEEE Transactions on Wireless Communications*. 2018 Oct; 17(10): 6735–6748.
- [9] Harutyunyan D, Shahriar N, Boutaba R, Riggio R. Latency and mobility-aware service function chain placement in 5G networks. *IEEE Transactions on Mobile Computing*. 2022 May; 21(5): 1697–1709.
- [10] Dong Y, Zhang H, Li J, Yu FR, Guo S, Leung VCM. An online zero-forcing precoder for weighted sum-rate maximization in green CoMP systems. *IEEE Transactions on Wireless Communications*. 2022 Sept; 21(9): 7566–7581.
- [11] Lu HF. Optimal sum rate-fairness tradeoff for MIMO downlink communications employing successive zero forcing dirty paper coding. *IEEE Communications Letters*. 2021 Mar; 25(3): 783–787.
- [12] Zhou Z, Wu Q, Chen X. Online orchestration of cross-edge service function chaining for cost-efficient edge computing. *IEEE Journal On Selected Areas In Communications*. 2019 Aug; 37(8): 1866–1880.
- [13] Pu L, Jiao L, Chen X, Wang L, Xie Q, Xu J. Online resource allocation, content placement and request routing for cost-efficient edge caching in cloud radio access networks. *IEEE Journal On Selected Areas In Communications*. 2018 Aug; 36(8): 1751–1767.
- [14] Tao M, Chen E, Zhou H, Yu W. Content-centric sparse multicast beamforming for cache-enabled cloud RAN. *IEEE Transactions on Wireless Communications*. 2016 Sept; 15(9): 6118–6131.
- [15] Zhang N, Liu YF, Farmanbar H, Chang TH, Hong M, Luo ZQ. Network slicing for service-oriented networks under resource constraints. *IEEE Journal On Selected Areas In Communications*. 2017 Nov; 35(11): 2512–2521.
- [16] Boyd S, Vandenberghe L. *Convex optimization*. New York: Cambridge University Press; 2004. 716 p.
- [17] Qi S, Li S, Lin S, Saidi MZ, Chen K. Energy-efficient VNF deployment for graph-structured SFC based on graph neural network and constrained deep reinforcement learning. In *Proceedings of 22nd Asia-Pacific Network Operations and Management Symposium (APNOMS)*; 2021 Sept 08-10; Tainan, Taiwan, China: IEEE Press; p. 348-353.
- [18] Wang T, Fan Q, Li X, Zhang X, Xiong Q, Fu S, Gao M. DRL-SFCP: Adaptive service function chains placement with deep reinforcement learning. In *Proceedings of International Conference on Communications (ICC)*; 2021 June 14-23; Montreal, Canada: IEEE Press; p. 1-6.
- [19] Jiang W. Graph-based Deep Learning for Communication Networks: A Survey. *Computer Communications*. 2022 Mar; 185:40-54.
- [20] Heo DN, Lange S, Kim HG, Choi H. Graph neural network based service function chaining for automatic network control. In *Proceedings of 21st Asia-Pacific Network Operations and Management Symposium (APNOMS)*; 2020 Sept 22-25; Daegu, South Korea: IEEE Press; p. 7-12.
- [21] Newman M. The structure and function of networks. *Computer Physics Communications*. 2022 Aug; 147(1): 40–45.

Study on Fault Prognostics and Health Management for UAV

Jihui PAN, Wenqing QU, Hao XUE, Lei ZHANG and Liang WU
ASN UAV Test Jingbian Co., Ltd., China

Abstract. With the improvement of automation and intelligence degree of unmanned aerial vehicle, its application scenarios and service scope continue to expand. The UAV system is complex and the task environment is changeable, which poses new challenges to its safety and reliability. Fault prediction and Health management (PHM) technology can effectively reduce the risk of mission interruption caused by faults, and improve the quality of UAV mission throughout its life cycle. Firstly, the framework of UAV PHM technology is proposed based on the basic concepts of UAV and PHM technology, and then the research status of UAV fault diagnosis and fault prediction technology is analyzed and summarized. Finally, the challenges of UAV fault diagnosis and prediction technology are discussed. In addition, the development trend of UAV PHM technology is summarized from four aspects: failure mechanism basis, condition monitoring technology, fault model construction and intelligent technology application, aiming to provide certain reference for the research and development of the new generation of UAV PHM technology.

Keywords. UAV, PHM technology, fault diagnosis, failure prediction

1. Introduction

UAVs, short for unmanned aircraft, are unmanned aircraft operated by radio remote control devices and preprogrammed controls. Because of their unique advantages over manned aircraft, drones tend to be better suited for "dull or dangerous" missions. At present, UAVs are mainly used in the military field to carry out corresponding combat missions and training. However, with the continuous development, UAVs are also gradually entering the civil fields such as aerial photography, observation and inspection [1].

UAV is a complex system which integrates aviation technology, computer control technology, sensing technology and electronic technology. With the development of UAV technology, the function of UAV is becoming more and more powerful, and its service mission is further extended. UAV mission diversity and service environment uncertainty pose new challenges to UAV mission success rate. To ensure that UAVs can successfully perform operations, training, transportation, mapping or other missions, and reduce the threat of mission disruption and substantial property damage caused by system component failures during UAVs service, the safety and reliability of UAVs need to be continuously improved. Traditional passive maintenance support methods, such as event-based post-maintenance and time-based periodic maintenance, are easy to cause unnecessary downtime, and there are maintenance damage risks, which can no longer meet the current demand for reliability and economy of UAVs.

The prognostics and health management technology are a state-based and prognostic maintenance method, which not only provides prognostics for system failure, but also provides prognostics for system health. Use of PHM technology for unmanned aerial vehicle key system and the important component to conduct a comprehensive monitoring, fault diagnosis and fault prediction, analysis of health status judgement and management, to enhance unmanned aerial vehicle the reliability of key components and the whole vehicle system, effective guarantee further UAV mission success rate, and reduce the operation of the whole life cycle maintenance cost. Therefore, the research on UAV PHM technology is of great significance for the development of UAV undertakings in China.

From unmanned aerial vehicle and the concepts of PHM technology, this paper elaborates the system framework of PHM technology for unmanned aerial vehicle, unmanned aerial vehicle both home and abroad are the key system of fault diagnosis and fault prediction technology research status, analysis and induction, further summarizes and discusses the unmanned aerial vehicle fault diagnosis and prediction technology research challenges and future development trend of existing, Try to provide reference for domestic UAV PHM technology research.

2. UAV PHM technology

2.1. Overview of PHM technology

In 2019, 392,000 drones were registered and 67,218 valid driver licenses were issued. In 2020, a total of 523,600 UAVs were registered, with 88,994 valid driver licenses. In 2021, 832,000 drones were registered and 120,800 valid driver licenses were issued. The development potential of civil UAVs is full, and the types of civil UAVs are changing from consumer to complex industrial. In the process of performing tasks, unmanned aerial vehicle each functional components in the critical systems or sensors in the event of failure, the light can affect the task quality, directly will cause unmanned aerial vehicle tasks fail, and may result in unmanned aerial vehicle equipment loss, even delay strategy and tactics for military drones layout, and might become serious consequences.

Because UAVs are detached from the ground and have various tasks, their mission environments are often characterized by strong vibration, multiple disturbances and alternating high and low temperatures, which increases the possibility of multiple failures such as progressive, abrupt and uncertain failures of key systems or functional components of UAVs. At the same time, limited by practical factors such as size, airborne capability and equipment power consumption, although the hardware redundancy technology of UAVs is adopted, it is difficult to reach the redundancy level of manned aircraft, and the failure of key systems or functional components of UAVs will have a more serious impact on the service performance and safety of UAVs. In addition, UAV has the characteristics of unmanned driving and data transmission delay. Due to the lack of pilot's state perception, quick judgment, flexible decision-making and real-time regulation of the aircraft, it is difficult to deal with unexpected situations and different faults. Therefore, while UAVs have good service performance, they must also have good health management ability to cooperate with them, so as to reduce

accidents caused by faults and ensure the continuity of the mission, so as to give full play to the practical value of UAVs in the whole life cycle.

PHM technology arises at the historic moment under the demand of information warfare for the combat effectiveness and precision support of weapons and equipment. The technology uses advanced sensors and various inference models and intelligent algorithms to realize the monitoring, prediction and management of devices. PHM technology can be divided into three levels: fault diagnosis, fault prediction and health management, which can be further subdivided into: real-time status monitoring, fault detection and isolation, remaining service life and fault prediction, maintenance and task assistance decision-making and resource management and other specific functions. PHM technology can timely monitor, diagnose and predict the occurrence of failure effectively, combining with all kinds of information resources to provide a series of safeguard measures so as to realize the situation and system maintenance, can avoid the accident and reduce the loss on the basis of manpower, financial resources, to get the most out of equipment efficiency, the high cost and maintenance cost of complex equipment has important engineering significance.

2.2. UAV PHM system architecture

The UAV PHM system is mainly composed of airborne sensor system, ground PHM processing system and maintenance support system. Airborne systems are wired or wirelessly transmitted to the ground processing system, which transmits the results to maintenance departments after processing. The maintenance unit determines the specific maintenance plan based on the results of the PHM system and the abnormal conditions observed by operators and maintenance personnel. Prepare required spare parts and materials according to the plan, select qualified maintenance personnel for maintenance, and update the technical data after maintenance. The main subsystems of PHM system are described below [2]. UAV PHM system architecture in Table 1.

Table 1. UAV PHM system architecture

Subsystem	Functions
Sensor installation	The sensors are distributed on each subsystem of UAV
Signal acquisition and processing Signal data acquisition	Digital to analog conversion, denoising, filtering, compression and other effective processing
Status monitoring status	Compare these data with the expected data value in the database, and provide fault alarm according to the predetermined parameter limit value
Fault prediction and diagnosis	Using the data of the previous system, historical statistical data and various parameters of the UAV system, based on algorithms, experience, modeling, trends and other methods and means to predict the failure situation, remaining life and future system health and stability trend of the UAV system
Health assessment	The health status of each subsystem and component is determined by the factory parameters, historical maintenance data and working status of the UAV system, using various comprehensive evaluation methods such as machine learning and deep learning
Decision making and maintenance	Use the information provided by each part of the PHM system to make maintenance decisions quickly and effectively and make maintenance plans

- Sensors are installed on each subsystem of the UAV in a distributed manner to build a whole-system sensor network, monitor real-time data of the operation status of the UAV system, master and evaluate the health of the UAV, and make UAV maintenance decisions based on the situation [3]. At present, sensors mainly transmit the acquired data to other parts of the PHM system through wired and wireless means.
- The collection of signal data is the premise and basis of the operation of PHM system, and the collected data needs to be processed effectively. There are many types and large quantities of UAV operation status data, which need to be sorted out and processed into computer-readable format through digital-to-analog conversion, denoising, filtering, compression and other methods [4]. Through to determine the status of unmanned aerial vehicle to extract fault features, due to malfunction and parameters that is not one to one correspondence, therefore need a variety of algorithms, such as: change fast Fourier (FFT), discrete wavelet transform (DWT), average filtering method, etc., to infer unmanned aerial vehicle fault condition, so as to achieve maximum PHM system fault diagnosis ability and precision.
- The condition monitoring system mainly receives the data from the data processing, and then compares these data with the expected data values in the database, so as to judge the state of the UAV system and provide fault alarm capability according to the predetermined parameter limit.
- Fault prediction and diagnosis of fault prediction and diagnosis is the main function of PHM system, the data of the front part mainly is to use the system and historical statistical data and the UAV system parameters, based on the algorithm, experience, methods such as modeling, trend method can be used to predict the failure condition of the UAV system, the residual life and future trend of the system of the healthy and stable, Provide effective information for subsequent decision making and maintenance.
- Health assessment in the part of receiving data from the other parts in the system, factory by unmanned aerial vehicle system parameters, history data and the maintenance work state, use all kinds of machine learning and deep learning comprehensive evaluation method to determine each subsystem and components such as health, the health data records, and determine whether there is the possibility of failure, It can provide information support for maintenance decision whether the UAV system can continue to perform the mission.
- Decision making and maintenance the part mainly USES PHM system information, the parts in unmanned aerial vehicle in the operation of the system can quickly and efficiently to make maintenance decision, make the maintenance plan, can quickly repair after the plane landed, ensure unmanned aerial vehicle can continue to flight mission, can improve the UAV system of continuous operational capability in wartime. The interface display is mainly to display the data of condition monitoring, fault diagnosis and health evaluation. The information is transmitted to the manufacturer, maintenance base and equipment unit through the network service system, so as to understand the status of the UAV system and facilitate the maintenance.

3. Present and future of UAV PHM technology in China

3.1. Major progress achieved

At present, stage research achievements have been made in UAV fault detection, fault diagnosis and fault prediction, as well as UAV PHM system framework design, and different degrees of engineering applications have been obtained. The main progress is summarized as follows :1) Domestic UAV PHM technology research is relatively comprehensive, involving sensors, actuators, data links, airborne equipment and other aspects, laying a solid foundation for further in-depth research. 2) Based on the foreign research results and domestic early research basis, it has a late-development advantage to carry out the research on UAV PHM technology in China. With the in-depth research of PHM technology in many fields and the continuous investment in China's aviation field, China's UAV PHM technology continues to improve, and the gap between China and foreign countries becomes smaller and smaller. 3) A variety of artificial intelligence methods have been gradually mature in the frontier research fields such as image recognition, speech processing and image enhancement. At present, the application research of UAV PHM technology based on artificial intelligence method has been in the preliminary development stage, which indicates that artificial intelligence method will bring infinite potential for the development of UAV PHM technology in China.

3.2. Challenges

China's UAV PHM technology has achieved fruitful theoretical and application results, but it still faces many problems and challenges. 1) UAV condition monitoring technology is not perfect. Due to multiple limitations such as UAV size, on-board capability and sensor technology, a large number of UAVs currently only integrate multiple feedback sensors for control purposes, without embedding sensors sensitive to fault or performance degradation characteristics. Therefore, the existing UAVs have not realized the comprehensive dynamic monitoring of UAVs, and the acquired dynamic information of UAVs service is incomplete, which cannot realize the full coverage of UAVs fault diagnosis. The absence of monitoring data also limits the advantages of AI methods in UAV fault diagnosis and prediction techniques. 2) The technical foundation of UAV PHM is relatively weak. Although UAV is widely used and the development momentum is strong at present, the UAV industry, especially industrial-grade UAV, is still in the initial stage of rapid development, and the failure form, failure mechanism and degradation process theory of key system and functional components of UAV are not deep enough. At the same time, as UAVs are mostly used in military strategic deployment, there are few literatures describing UAVs PHM technology in detail, and there is a lack of advanced experience for reference, so it is necessary to move forward in exploration. 3) It is difficult to analyze the coupling characteristics of faults in redundant structures. Unmanned aerial vehicle is a typical multiple redundant complex equipment, its structure and function are highly redundant features, unmanned aircraft system level different parts relationship is complex, reflected in the diversity of performance of a system parameter and nonlinear coupling characteristics between multi-source parameters, and the degree of coupling, sequence, different intensity, will have difficulties for system reliability and health assessment, The coupling relationship among various performance parameters, system behavior and

fault forms of UAVs needs to be sorted out in depth. 4) It is difficult to characterize the system performance degradation in finite sample space. Due to the high reliability of UAVs, they are characterized by rare fault samples, difficult to obtain samples, unbalanced samples, low sample information density and fragmentation in the operation and service process. Limited sample space brings great challenges to fault diagnosis, degradation behavior characterization, life prediction and health status assessment of critical systems and functional components of UAVs.

3.3. Development direction and trend

At present, China has a good research foundation of PHM technology, and has explored and accumulated some experiences of PHM technology in the fields of civil aircraft, helicopters, armored vehicles, high-speed railways and other equipment. It is believed that with the further application and popularization of UAV PHM technology in China will usher in a high tide of development. By analyzing the existing literature and the current demand of UAV PHM technology, the development direction and trend of the field can be preliminarily determined as follows:

- Fault mode and degradation mechanism analysis: fault modeling mechanism is the foundation of UAV PHM technology. The key systems and functional components of UAVs have some practical problems, such as failure uncertainty, unpredictability, coupling and multiplicity, which restrict the future improvement space of UAVs PHM technology. Based on failure physics research, random and cognitive uncertainty should be considered. Through multidisciplinary simulation technology and accelerated life experiment, the system should be expanded from functional components to subsystems and then to the whole UAV, and then to the super system. To realize the transparency of the transmission relationship between the failure mode, failure mechanism, fault propagation law and fault behavior of UAV system, so as to guide the basic layout of UAV PHM technology.
- Advanced sensor technology and condition monitoring technology: Perfect monitoring technology can provide data guarantee for UAV PHM technology. Monitoring means "see", and only when "see" is wide can "go" far. Intelligent sensor technology to support, relying on advanced lightweight sensors can solve each system component adaptation sensor and optimal distribution problems, and can realize unmanned aerial vehicle from functional components to all-round real-time monitoring and running of the system level situational awareness, eventually reach for unmanned aerial vehicle fault diagnosis, prediction and health management to provide complete and reliable source of data, To realize the full coverage of UAV fault diagnosis under complete monitoring. Then, the multi-dimensional data of the dynamic evolution of UAV from normal, degraded, ill-conditioned, faulty and other multi-state lifetime are collected to realize the accumulation of data and the construction of a complete UAV dynamic information database within the service cycle.
- Data mining and modeling technology under incomplete information: With the help of artificial intelligence methods, hidden information of data can be fully mined, data quality and value can be improved. Aiming at the uav

information incomplete, insufficient fault samples is difficult to obtain, a single scenario labels such as limited sample space problem, the possibility of a structure under the small sample distribution framework, at the same time, through deep learning network model such as access to agree with the original sample distribution twin samples in order to implement the data the expansion and diversity of ascension. Furthermore, artificial intelligence algorithms such as deep transfer learning and incremental learning are used for data mining and data fusion. This can solve the problem of cold start when UAV fault data is insufficient and single scene label is insufficient, and improve the modeling accuracy and generalization ability of UAV fault diagnosis and prediction under limited sample space and incomplete information.

- Intelligent diagnosis and prediction technology under the fusion of artificial intelligence and big data: As a representative of artificial intelligence, deep learning method has strong multi-layer nonlinear feature learning ability, which can automatically learn useful features in high-dimensional input data and achieve higher fault diagnosis accuracy. At present, intelligent diagnosis based on deep learning has achieved remarkable results [5], and the application of deep learning in UAV fault diagnosis has also achieved initial results. In the future, with the enrichment of various UAV monitoring data samples, the UAV PHM technology that integrates multi-source information and builds a deep learning model framework based on deep learning, extracts features and fits mapping relationships from time domain, frequency domain or time-frequency domain, and realizes intelligent fault identification and prediction will attract much attention.
- Life prediction and health assessment decision under complex network and variable working conditions: The UAV is composed of multiple key systems, and each system contains a large number of sensors, so the UAV can be regarded as a special complex network. By sorting out the logical relationship between data information features and fault modes and information fusion based on the topological properties of complex networks, the fault evolution process of key systems and functional components of UAVs can be clarified, and then the system performance degradation trend can be judged [6-8]. The service of UAVs under variable working conditions will make its performance degradation trend diversified. The prediction model constructed by deep learning, correlation analysis or multi-granularity model under variable working conditions will make the remaining life prediction of UAVs more accurate and reliable. Prediction, evaluation and decision-making in complex networks and variable operating conditions are conducive to the realization of UAV hierarchical mission planning, flight self-calibration and self-repair based on the residual accuracy of critical systems in the whole life cycle. In addition, differentiated life prediction for individual service task conditions of UAVs on the basis of global prediction can further improve the accuracy of prediction and bring better use experience [9-13].

4. Conclusion

Under the background of artificial intelligence technology and big data, the UAV PHM technology is reviewed. On the basis of introducing the concept of UAV and PHM technology, the PHM technology framework of UAV system is designed and described. The research status of UAV fault detection, diagnosis and prediction technology at home and abroad is further analyzed. The progress, existing problems and challenges of UAV PHM technology in China are summarized and summarized. Finally, it points out the overall development trend of UAV PHM technology based on accurate fault modeling mechanism, perfect monitoring technology as guarantee, information mining and modeling technology under the deep integration of artificial intelligence and big data as the core, and accurate diagnosis, prediction and task management under complex networks and variable working conditions as the goal.

References

- [1] Miao Jianguo, Wang Jianyu, Zhang Heng, et al. Review of the development of fault diagnosis technology for unmanned aerial vehicle[J]. Chinese Journal of Scientific Instrument, 2020, 41(9): 56-69.
- [2] LI Hailiang, CAI Jing, KANG Tingwei. Study on design of visual intelligent detection instrument for aviation cable fault [J]. Journal of Northwestem Polytechnical University, 2021, 39(4): 770-775.
- [3] Pan J H, Zhang S B, Zhang X L. Fault Diagnosis and Adaptive Reconfiguration for Multi-Redundancy Flight Control System [J]. Computer measurement and control, 2015. 23(48): 441-447.
- [4] ZHANG Yang, ZHOU Zhou, LI Xu. Effect of turbulence intensity and gradient of turbulence intensity on airfoil aerodynamic characteristics at low Reynolds number [J]. Journal of Northwestem Polytechnical University, 2021, 39 (4): 721-730
- [5] Pan J H, Zhang S B, Zhang X L. Design and Realization of Treble-Redundancy Management Method of Flight Control System [J]. Journal of Northwestem Polytechnical University, 2013, 31(5): 798-802.
- [6] Suo X J, Kang X D, Zhou Q. Application of Fault Injection Technique in Analog Signal Acquisition of Airborne Computer [J]. Computer Measurement & Control, 2016, 24(1) :304 -312.
- [7] YANG Lei, ZHANG Bainan, GUO Bin, ZUO Guang, SHI Yong, HUANG Zhen. Concept definition of new-generation multi-purpose manned spacecraft [J]. Acta Aeronautica et Astronautica Sinica. 2015 ,36(3): 703-713.
- [8] LEE J, KWON D, KIM N, et al. PHM-based wiring system damage estimation for near zero downtime in manufacturing facilities [J]. Reliability Engineering and System Safety, 2019, 184: 213-218.
- [9] WANG Danyang, TANG Jianjun, CHEN Ou, et al. Aerospace-cable fault location technology research based on time domain reflectometry (TDR) [J]. Aeronautical Manufacturing Technology, 2019, 62(Z2): 84-88, 96.
- [10] LI Lu. Simulation study on fault diagnosis of marine power cable [D]. Dalian: Dalian University of Technology, 2017.
- [11] CHUNG C C, LIN C P. A comprehensive framework of TDR landslide monitoring and early warning substantiated by field examples [J]. Engineering Geology, 2019, 262(28): 1-11.
- [12] LIU Yandong. Analysis of airworthiness requirement in EWIS design [J]. Journal of Shenyang Aerospace University, 2019, 30(4): 23-27.
- [13] MEI Z P, LI Q, WEN J Q. Research on optimization of wiring paths in airplane harness process [C]//2012 IEEE International Conference on Cyber Technology in Automation, Control, and Intelligent Systems, 2019: 485-488.

Online and Offline Analysis of Planck Constant Measurement

Zhongqi LUAN, Lina WANG¹, Yanjun WANG, Haifeng GU and Yaxiang BAI
School of Marine Science and Environment, Dalian Ocean University, Dalian, China

Abstract. The online virtual experimental platform and the laboratory photoelectric effect method were used to measure Planck's constant. Excel software was used for linear fitting, and Planck's constant and errors were analyzed and calculated. It was found that the offline experimental value was better than the online virtual observed value. However, the error of the online virtual experiment value is also within the controllable range. In the particular current period of frequent epidemics or for schools lacking experimental instruments, it is also a perfect choice to use the virtual experiment platform to measure the relevant empirical data.

Keywords. Planck constant, photoelectric effect, cut-off voltage

1. Introduction

Planck's constant was first proposed by Max Planck more than a hundred years ago when he solved the problem of black body radiation by assuming that energy is quantized and can only be emitted or absorbed by integer multiples of a small unit [1]. The energy according to a particular quantum is described by the equation:

$$E = h\nu \quad (1)$$

Where ν is the frequency of radiation and h is Planck's constant. Then in 1905, Albert Einstein extended Planck's black-body model by likening light as consisting of discrete quanta of photons with energy $h\nu$, where ν is expressed as the incident light's frequency [2]; however, this phenomenon is called the photoelectric effect. The photoelectric effect is explained according to Einstein's photoelectric equation, which is expressed as:

$$h\nu = \phi + E_{max} \quad (2)$$

Where ϕ is the work function of the metal, and E_{max} is the maximum kinetic energy of the ejected electrons. Since then, it has played an essential role in the proposal of Planck's constant in quantum physics and has become one of the constants commonly used in physics [3-4].

The most widely used method for determining Planck's constant is to use the photoelectric effect. This method is also a must-do experiment for science and engineering students in colleges and universities, especially for physics-related majors. The mode of processing students' experimental data offline in this experiment mainly adopts the method of manual drawing on graph paper, manually drawing a curve, creating a tangent at a point on the turn, finding the intersection of the two tangents, and performing linear fitting. All steps may lead to significant errors, and the amount of experimental data is large, so this processing method is very time-consuming [5,6].

¹ Corresponding author: l.n.w@163.com

Therefore, it is better to choose EXCEL or ORIGIN [7] to adopt the least squares method for the experimental data processing method. This paper uses EXCEL for direct linear fitting and data processing.

At the same time, due to the surge in demand for online virtual experiments due to the new crown epidemic in recent years, this experiment has also developed an online virtual experiment platform. The data processing of the online virtual experimental platform, the offline experiment practical measurement results, and the analysis of their errors and experiment practical and disadvantages can provide a better reference for selecting the Planck constant measurement method.

2. Experimental principle

Figure 1 in the following shows the photoelectric effect experiment diagram. In the figure, S is the photocell, the K pole is the cathode used to release electrons in the photocell, and A is the anode in the photocell. If there is no light irradiating the K pole plate, there will be no electrons escaping, and the A pole and the K pole are in an open circuit phenomenon, so there is no display in the galvanometer G, and no current flows. If we use a piece of monochromatic light with a short wavelength to irradiate the K plate, electrons will escape. Still, a photo current can be formed so that the galvanometer G will have an indication.

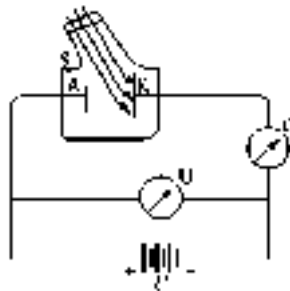


Fig.1. Schematic diagram of the photoelectric effect

When a photoelectron escapes from the K-pole metal plate, the photoelectron has initial kinetic energy and moves under the reverse force of the deceleration voltage; that is, the direction of movement of the photoelectron is opposite to the direction of the electric field force. The photoelectrons will move from the K pole plate to the A pole plate. However, if $U = U_0$ occurs, there will be no photoelectrons from the K pole plate to the A pole plate. The photocurrent decreases to zero, so the kinetic energy of the photoelectron is precisely equal to the work it does in the electric field to overcome the electric field force, that is the following equation:

$$\frac{1}{2}mv^2 = e|U_0| \quad (3)$$

Thus, we can learn from Einstein's hypothesis about the nature of light that light is a particle in motion, and light particles are also called photons. The energy of each photon is $E=h\nu$, and in this formula, h is Planck's constant, while ν is the frequency of the light wave. Therefore, the corresponding photons have different energies at different frequencies of light waves. After the photoelectron absorbs the photon energy $h\nu$, part of the energy is used to overcome the energy consumed when the electron escapes from the metal surface, called the escape work W_0 , and the other part of the energy is converted

into the kinetic energy of the electron moving in the electric field when it escapes from the metal surface. Finally, we will get the following equation from the law of conservation of energy.

$$h\nu = \frac{1}{2}mv^2 + W_0 \quad (4)$$

Eq. (4) is the famous Einstein equation for the photoelectric effect [8-10].

From the equation in equation (3) above and brought into equation (4) it can be seen:

$$h\nu = |U_0|e + W_0 \quad (5)$$

The equation that can then be obtained is

$$|U_0| = \frac{h}{e}\nu - \frac{W_0}{e} \quad (6)$$

This equation shows that the Planck constant h can be calculated from the slope of $U_{0-\nu}$, which can be expressed as

$$h = ek \quad (7)$$

The curb voltage U_0 is measured by the zero-current method. In the zero-current process, the curb voltage U_0 is the absolute value of the voltage U_{AK} corresponding to the zero current measured under each spectral irradiation. This method has a necessary prerequisite, that is, the corresponding anode reverse current, dark current, and background current are very small; only then the difference between the curb voltage U_0 and the theoretical value of the curb voltage measured by the zero-current method is minimal, and the difference ΔU of the curb voltage of each spectral line has little effect on the slope of the $U_0 - \nu$ curve and thus has no significant impact on the measurement of Planck h [11].

3. Experimental principle

3.1. Off-line experimental data analysis

The laboratory line experimental apparatus, as shown in Figure 2, includes a light source (mercury lamp), photocell, filter set, and photoelectric effect tester composition. Since the light source is a mercury lamp light source, which is a gas light source, it has the characteristics of a gas light source, such as the need to preheat for 15 minutes, does not have the instantaneous start characteristics, etc., and needs to be used as a critical instruction for students during the experiment.



Fig. 2. Underline Planck constant measuring instrument

Because the current generated in the experimental measurement process is tiny, and the size of the wind with the practical selection of the sensitivity of the phototube and the light source luminous intensity are closely related. Thus the off-line experimental

measurement process in the experimental instrumentation adjustment, the current detector gear needs to be adjusted at about $10^{-10} A/division$. As the curb voltage is the voltage corresponding to the photocurrent is zero, if the current amplifier is not sensitive enough or the stability is not good, it will bring a significant error in the measurement [12]. Table 1 shows the data which measured in the laboratory. To reduce the experimental error, the aperture of the diaphragm was chosen to be 4 mm [13].

Table 1. U_{0-v} data measured in the off-line laboratory

Wavelength λ/nm	265.0	415.0	436.0	546.0	578.0
Frequency $\nu/10^{14}hz$	8.216	7.410	6.882	5.491	5.196
Curb voltage U_0/V	1.734	1.443	1.214	0.663	0.524
Curb voltage U_0/V	1.732	1.441	1.212	0.656	0.515
Curb voltage U_0/V	1.726	1.429	1.216	0.655	0.513
Curb voltage U_0/V	1.731	1.421	1.203	0.651	0.522
Curb voltage U_0/V	1.735	1.423	1.202	0.644	0.511
Curb voltage U_0/V	1.731	1.415	1.191	0.641	0.513
Curb voltage average U_0/V	1.732	1.429	1.206	0.652	0.516

The data were processed as an Excel linear fit, and their slopes were obtained directly, i.e., the Planck constant h could be calculated.

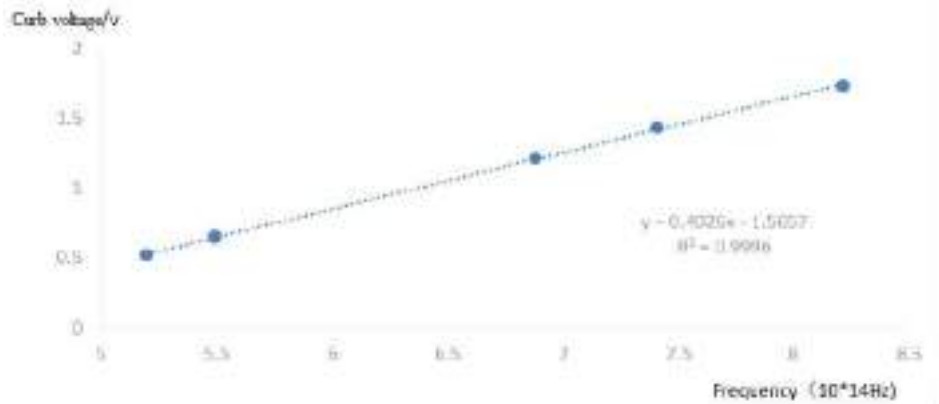


Fig. 3. Linear fit of offline laboratory measurement data

The slope $K = 0.4026$ of the linear fitting equation can be obtained from Figure 3, and h is calculated according to Equation (7).

$$h = k * e * 10^{-14} = 6.4416 * 10^{-34} J \cdot S \tag{8}$$

The theoretical value of Planck's constant is:

$$h_0 = 6.626 * 10^{-34} J \cdot S \tag{9}$$

so the error is calculated as

$$h_x = \frac{h-h_0}{h_0} * 100\% = 2.8\% \tag{10}$$

3.2. Online experimental data analysis

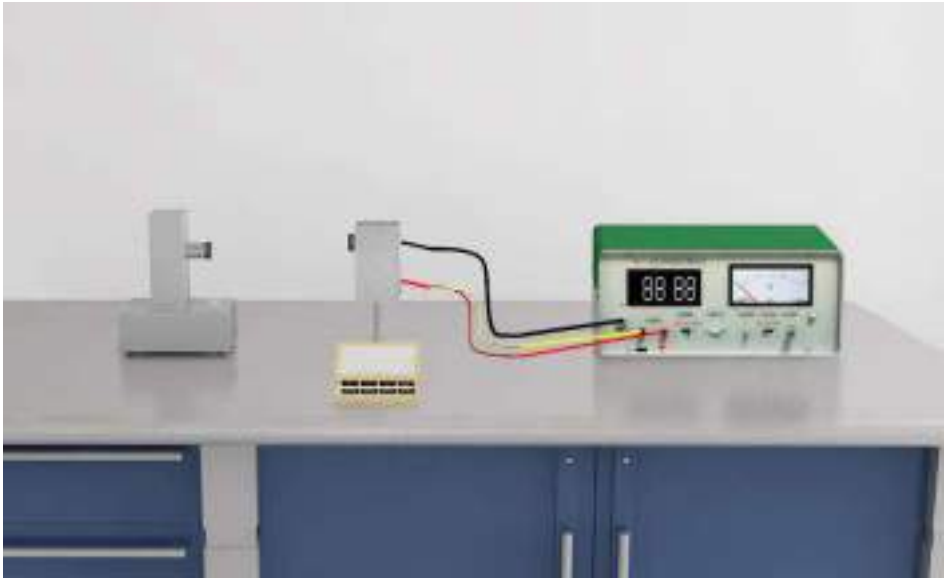


Fig. 4 Underline Planck constant measuring instrument

Online virtual experiment platform highly imitates offline experimental instruments, and in the practical operation, there will be error warning tips to avoid damage to the device due to incorrect operation. At the same time, the experimental instruments are easier and faster to adjust. They can be adapted to the best conditions in a concise period of time, thus saving much operating time. The data measured by the online virtual experiment platform are shown in Table 2.

Table 2. $U_{0-\nu}$ data measured in the online laboratory

Wavelength λ /nm	577	546	435.8	404.7
Frequency $\nu/10^{14}$ hz	5.198	5.492	6.88	7.41
Curb voltage U_0 /V	0.20	0.33	0.94	1.20
Curb voltage U_0 /V	0.20	0.30	0.90	1.20
Curb voltage U_0 /V	0.20	0.33	0.92	1.20
Curb voltage U_0 /V	0.20	0.32	0.92	1.18
Curb voltage U_0 /V	0.20	0.32	0.94	1.20
Curb voltage U_0 /V	0.20	0.34	0.91	1.10
Curb voltage average U_0 /V	0.20	0.323	0.922	1.18

The data processing method is also an Excel linear fit to obtain its slope and calculate its Planck constant h directly.

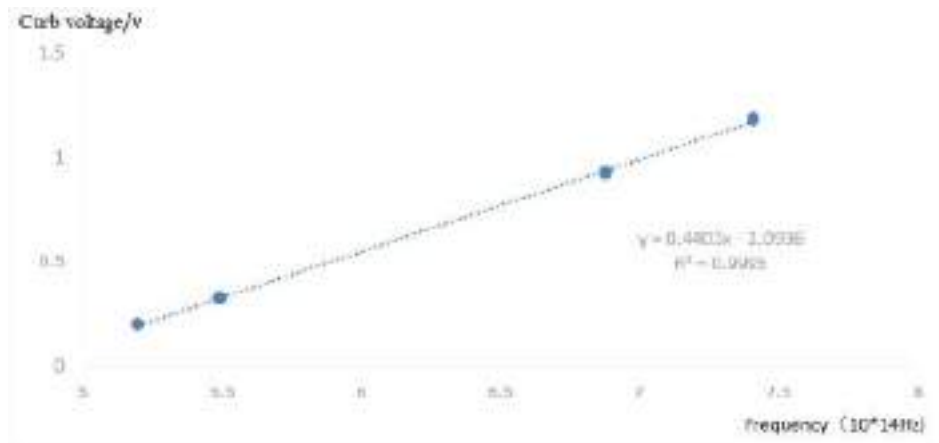


Figure 5 Linear fit of measurement data on the online virtual experiment platform

The slope $K = 0.4403$ of the linear fitting equation can be obtained from Figure 5, and the calculation of h according to Equation (7) yields.

$$h = k * e * 10^{-14} = 7.0448 * 10^{-34} J \cdot S \tag{11}$$

and its error is calculated as

$$h_x = \frac{h-h_0}{h_0} * 100\% = 6.3\% \tag{12}$$

A comprehensive analysis of the online and offline experiments results is shown in Table 3.

Table 3. Comprehensive analysis of online and offline experimental class data processing results

Measurement method	Offline laboratory data processing results	Online virtual experiment results
Planck constant/ $10^{-34}J \cdot s$	6.453	7.182
Relative error	2.8	6.3

4. Conclusion

In this paper, based on the analysis of the experimental principle, we measured the values of the curb voltage at different frequencies, measured the Planck constant using the offline laboratory photoelectric effect method and the online virtual experimental platform, and calculated and analyzed the experimental results, and finally obtained the value of Planck constant h . By analyzing the relative error, it was found that the data measured by the offline experimental apparatus were more detailed and reliable, and the calculation results were close to the theoretical value. In contrast, the experimental error obtained by the online experimental platform was more significant. Analysis of its causes may be.

(1) online experimental test platform voltage reading value sets fewer adequate numbers, only accurate to 0.01. In contrast, offline experimental instruments can be real to 0.001, and thus offline laboratory measurement results better than the virtual experimental platform. Still, this defect must only be set in the original program to improve its accuracy.

(2) online experimental operation is convenient and fast. However, the exercise of students' hands-on skills is not as good as offline operation but better than the faulty operation and damage to the instrument's service life; especially for valuable experimental tools, online virtual experiments have more significant advantages.

(3) online experimental platform values are taken for the database; the original data in the database of the experimental data error setting range may be relatively large, and thus there will be experimental results must have deviations.

Although there are specific errors in the online experimental results that exist in the current epidemic of the painful period or for the lack of testing equipment in schools, online practical classes assume more of how to let students successfully learn and complete the relevant experimental courses students complete their studies. Therefore, in the current environment, the online virtual experiment platform assumes an important teaching task in undergraduate practical teaching and has become an indispensable part of undergraduate teaching.

Acknowledgments

This work was financially supported by the Science Public Welfare Research Fund of Liaoning Province (No.2020JH4/10100039); Teaching Reform Project of Dalian Ocean University: Personalized Teaching Based on "Student-centered and Employment-oriented."

References

- [1] Wu LJ, Li Q. Three methods for measuring Planck's constant by the photoelectric effect. *University Physics Experiment*, 2007, 20(4): 49 -52.
- [2] Zhang JW, Yin SL. Measurement of Planck's constant by curvature method in photoelectric effect experiments. *Physics Experiments*, 2003, 23(11): 42- 44.
- [3] Li X, Zhu L. Measurement of Planck's constant with the aid of Matlab. *Physics Experiments*, 2008, 28(12): 33- 35.
- [4] Jin YY, Lu C, Li GQ. Application of Origin8.0 in the experiment of Planck's constant determination. *Physics and Engineering*, 2010, (6): 31- 34.
- [5] Ma DL, Du RJ. Application of Origin to Fermi-Dirac experiments. *Physics and Engineering*, 2009, 19(4): 34- 36.
- [6] Xie N, Zhang Y, Jiao YF, Liu JJ, Guo JW, Cao Y, Guo HMM. Analysis of experimental physics data with Origin software. *Laboratory Science*, 2007, (6) : 92- 93.
- [7] Li YQ, Zhi LL, Chen HM. Application of Origin to experimental data processing of Planck constant measurements. *Journal of Changji College*, 2014, (3):31-34.
- [8] Zhang JH, Hu WQ. Discussion of measurement methods in determining Planck's constant by the photoelectric effect. *Journal of Jiaying College*, 2006, (6):23-26.
- [9] Wang YZ, Zhao M. Data processing and error analysis of Planck constant measurement by the photoelectric effect. *University Physics Experiment*, 2011, (2):93-95.
- [10] Ma SB, Ding YQ, Zhao XM, Dai W. Experimental study of Planck's constant by photoelectric effect *Laboratory Research and Exploration*, 1999, (1):61-65.
- [11] Wang YZ, Zhao M. Data processing and error analysis of Planck constant measurement by the photoelectric effect. *University Physics Experiment*, 2011, (2):93-95.
- [12] Bai YX et al. eds. *Physics Experiments [M]*, Tsinghua University Press, 2016.
- [13] Deng ZX, Duan ZR. Inverse curb voltage method to measure Planck's constant *Value Engineering*, 2013, (13):59-60.

Comparison of Deep Learning Methods and a Transfer-Learning Semi-Supervised GAN Combined Framework for Pavement Crack Image Identification

Kai-liang LU, Guo-rong LUO, Ming ZHANG, Jin-feng QI and Chun-ying HUANG¹
College of Automation, Guangzhou Vocational University of Science and Technology, China

Abstract. The pavement crack identification performance of typical models or algorithms of transfer learning (TL), encoder-decoder (ED), and generative adversarial networks (GAN), were evaluated and compared on SDNET2018 and CFD. TL mainly takes advantage of fine-tuning the architecture-optimized backbones pre-trained on large-scale data sets to achieve good classification accuracy. ED-based algorithms can take into account the fact that crack edges, patterns or texture features contribute differently to the identification. Both TL and ED rely on accurate crack ground truth (GT) annotation. GAN is compatible with other neural network architectures, thus can integrate various frameworks (e.g., TL, ED), and algorithms, but the training time is longer. In patch classification, the fine-tuned TL models can be equivalent to or even slightly better than the ED-based algorithms, and the predicting time is faster; In accurate crack location, both ED- and GAN-based algorithms can achieve pixel-level segmentation. It is expected to realize real-time automatic crack identification on a low computational power platform. Furthermore, a weakly supervised learning framework (namely, TL-SSGAN) is proposed, combining TL and semi-supervised GAN. It only needs approximately 10%–20% labeled samples of the total to achieve comparable crack classification performance to or even outperform supervised learning methods, via fine-tuned backbones and utilizing extra unlabeled samples.

Keywords. Image identification, pavement crack, transfer learning, encoder-decoder, generative adversarial network, supervised and semi-supervised learning

1. Introduction

Compared with contact detection techniques, such as non-destructive testing (NDT) [1] or structural health monitoring (SHM) [2], pavement crack identification with visual images via deep learning algorithms [3-6] has the advantages of not being limited by the material of object to be detected, fast speed and low cost. Thus, it has wide application prospects in routine inspection and other preventive detection or monitoring scenarios, where accurate classification and (patch- or pixel-level) segmentation can be obtained to identify the existence, topology, and even size of cracks.

¹ Corresponding author: Chun-ying HUANG, E-mail: huangchunying@gkd.edu.cn

Historically, *hand-crafted feature engineering* algorithms, include edge/morphology algorithms such as Canny, Sobel, HOG, LBP and feature transformation algorithms such as FHT, FFT, Gabor filters. These algorithms do not have to learn from a data set, and most computations are mathematics analytical, lightweight thus fast. However, the shortcomings are the weak generalization ability to various random variable factors, once the scenario or environment changes, the algorithms must be fine-tuned or redesigned, and even fail.

Later on, *machine learning* (ML) algorithms, e.g., CrackIT [7], CrackTree [8], and CrackForest [9] were developed for pavement(concrete) crack image identification. Recently, *deep learning* (DL) has continuously achieved state of the art (SOTA) progress in various missions. DL extracts high-level features automatically from large-scale data sets mainly via non-convex optimization, with stronger generalization ability and higher accuracy, whereas ML is oriented towards lower-level features via convex optimization. However, the mathematical expression of ML is explicit and interpretable [10], [11], whereas that of most DL algorithms are still implicit, known as “Black Box” issue, though great efforts and progress [12-14] have been made to solve the interpretability problem.

We focused on typical DL methods including *transfer learning* (TL) [15], [16], *encoder-decoder* (ED) [3], [4], and *generative adversarial networks* (GAN) [5], [6] for pavement(concrete) crack identification in this study. The main contents and contributions include:

- The fundamental frameworks and characteristics of typical TL, ED, and GAN algorithms are presented. Recent developments of these algorithms on pavement crack identification are summarized. The common architecture, modules, and specific techniques that improve the identification performance are highlighted.
- The patch sample classification performance, full-size image segmentation and detection effect were tested on public pavement crack data sets such as SDNET2018 and CFD. The performance of different neural network models of a certain algorithm, and various algorithms of DL methods, were evaluated and compared within and between categories.
- A *weakly supervised learning framework*, named TL-SSGAN, combining TL and semi-supervised GAN, is proposed, which can maintain comparable crack identification performance to or even outperform the supervised learning algorithms while greatly reducing the number of labeled samples required, through the measures of (i) utilizing fine-tuned TL backbones, (ii) controlling the ratio of labeled and unlabeled samples, and (iii) adding extra unlabeled samples.

2. Deep Learning Methods

2.1. Transfer Learning

Overall Framework and Procedure of TL. TL learns the basic reusable features via CNN backbone models, which are typically SOTA models that have been architecture-optimized and pre-trained on large-scale generic datasets (e.g., ImageNet). Then, the weight parameters of the upper and/or output layers are fine-tuned on a specific data set

(e.g., pavement crack dataset). TL is suitable for small datasets, easy to adjust, with good generalization performance, and provides fast training. The overall procedure and detailed data flow and steps of TL can refer to Fig. 8 of [16].

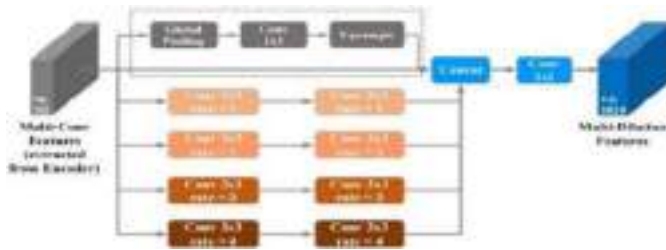
Common CNN Backbones. The evolution of common CNN backbone networks and the top-1/top-5 accuracy performance on ImageNet of typical backbone models for TL were illustrated.²

2.2. Encoder-Decoder

Motivation. The ED framework can compensate for the limitation of CNN [17] / FCN [18] algorithms for identifying complex crack topology (e.g., alligator cracks), that is, (i) pavement cracks have various morphology and topology. However, the CNN/FCN filters use specific kernels (3×3 , 7×7 , etc.), which limits the receptive field range and the robustness of crack identification. (ii) The fact that crack edges, patterns or texture features contribute differently to the identification has not been taken into account.

Architecture and Mechanism of Typical ED models. ED-based FPCNet [3] is one of the models with excellent accuracy and speed. It includes two sub-modules: a *multi-dilation* (MD) module and *SE-Upsampling* (SEU) module. Another model, U-HDN [4], similar to FPCNet [3], integrates MD module and *hierarchical feature* (HF) learning module based on U-net [19]. These two models are composed of similar or common sub-modules, such as the MD module (Fig. 1) based on the dilated convolution kernel operation, the SEU module (Fig. 2), and the U-net likewise main architecture (Fig. 3 and Fig. 4). Dilated convolution [20] enlarges the kernel's *context* window size, instead of using a sub-sampling operation or a larger filter with many more parameters.

As shown in Fig. 1, the MD module concatenates six branches, i.e., four dilated convolutions (double operations per branch) with rates of $\{1, 2, 3, 4\} / \{1, 2, 4, 8\} / \{2, 4, 8, 16\}$, which can be set according to the statistics of crack width, a global pooling layer, and the original crack multiple-convolution (MC) features. After concatenation, a 1×1 convolution is performed to obtain the crack MD features, which represent *contextual features ranging from pixel-level to global-level*, thus can detect cracks with different widths and topology.



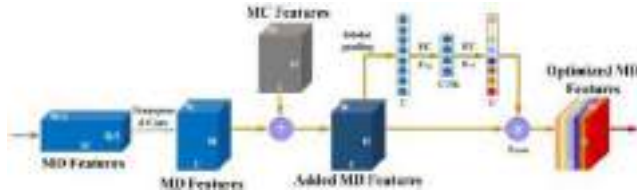
Remarks: The MC features and global pooling branches in the dashed rectangular box can also be integrated into the ED main architecture such as the design in U-HDN [4].

Figure 1. Multi-dilation module [3], [4].

The SEU module, as shown in Fig. 2, performs up-sampling operations in the decoder to continuously restore the resolution of the MD feature to the original size of input image, so that pixel-level crack identification can be realized. Through the *squeezing* and *excitation* learning, the SEU module adaptively assigns different weights

²<https://github.com/mikelu-shanghai/Typical-CNN-Model-Evolution>

to different crack features such as edges, patterns, and textures. The inputs of the SEU module are the MD features and MC features, and the output is the optimized MD features after weighted fusion.



The detailed implementation remarks: (a) The SEU module first restored the resolution of MD features via transposed convolution. Then, MC features were added to MD features to fuse the associated crack information concerning crack edge, pattern, and texture, etc. (b) Subsequently, the SE operation was applied to the added MD features to learn the weights of the different features. Global pooling was first performed to obtain global information on C channels. After *squeezing* F_{sq} and *excitation* F_{ex} (two fully connected layers), the weight of each feature for its channel was obtained. (c) Finally, each feature in the added MD features was multiplied by its corresponding weight F_{scale} .

Figure 2. SE-Upsampling module [3].

The overall architectures of FPCNet [3] and U-HDN [4] are shown in Fig. 3 and Fig. 4 respectively. FPCNet [3] embedded the above MD and SEU modules into a common semantic segmentation network. U-HDN [4] integrated the MD module (bounded by the red dotted rectangular box in Fig. 4) and the HF learning module (in the yellow dotted box) based on the modified U-net architecture (in the blue dotted box), and zero filling was adopted during the up- and down-convolution paths.



Implementation details: (a) four Convs (two 3×3 and ReLUs) + max pooling were used as the encoder to extract features. Next, the MD module was employed to obtain the information on multiple context sizes. Subsequently, four SEU modules were used as the decoder. (b) H, W indicate the original image size. The red, green, and blue arrows indicate max pooling, transposed convolution, and 1×1 convolution + sigmoid, respectively. MCF denotes the MC features extracted in the encoder and MDF denotes the MD features.

Figure 3. Overall architecture of FPCNet [3].

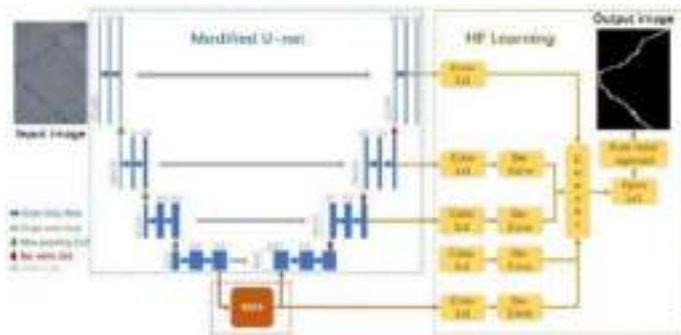


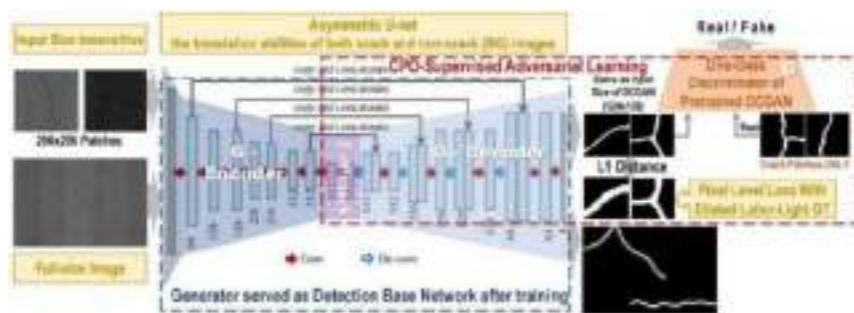
Figure 4. Overall architecture of U-HDN [4].

In addition, Li *et al.* [21], inspired by DenseNet, fused a densely connected convolution module and a deep supervision module to extract detailed crack features. Yu *et al.* [22] introduced CCapFPN, based on a capsule feature pyramid network (FPN) architecture. In summary, the aforementioned ED models [3], [4], [21], [22] contribute to common ideas, similar architectures, and fundamental modules.

2.3. Generative Adversarial Networks

Overview and Taxonomy. GAN makes the generated samples obey the distribution of real data via two networks (discriminator and generator) adversarial training. GAN has the advantages of (i) accurate estimation of the density function, (ii) efficient generation of required samples, (iii) elimination of deterministic bias, and (iv) good compatibility with various neural network architectures, algorithms, and techniques. Thus, GAN has received extensive attention and many GAN variants were derived [23-25]. The evolution diagram and main characteristics of some common GANs were shown in Fig. 7 of ³. It can be used for hard sample mining in semi-supervised/unsupervised learning.

Typical GAN algorithms for Crack Identification. ConnCrack [5] and CrackGAN [6] are representative GANs for highly accurate crack identification. However, the training and prediction times were longer in the earlier version. The improved CrackGAN [6], based on DCGAN and with encoder-decoder as the generator, proposed crack-patch-only (CPO) supervised adversarial learning and the asymmetric U-Net architecture to perform end-to-end training with partially accurate ground truth (GT) (i.e. 1-pixel curve manual labeling) labeled in a labor-light manner. The overall architecture of Crack-GAN [6] is illustrated in Fig. 5.



Remarks: (a) D is a One-class DCGAN discriminator that is pre-trained only by crack patches, which will enable the network to always generate crack images. It is a key module to conquer the “All-Black” issue. (b) Pixel-level loss is used to make sure the crack pattern generated is just the same as the input patches, which is achieved by optimizing the L_1 distance from Dilated Labor-light GT, e.g., 1 pixel dilated 3 times. The total loss is thus L_1 distance + adversarial loss generated by the DCGAN. Transfer learning is employed to train the prototype of the encoding network and transfer the knowledge from DCGAN to provide generative adversarial loss for end-to-end training. (c) An asymmetric U-net network is introduced to balance the crack and non-crack/background samples that are severely imbalanced. (d) After the training, the generator G will act as the detection network for new samples. (e) The whole network can handle arbitrary full-size images, since it’s a fully convolutional network (FCN). For more implementation details, refer to [6].

Figure 5. Overall architecture of CrackGAN [6].

CrackGAN [6] was developed to handle the practical problem named “All-Black” issue, i.e., the network converged to the state that the whole crack image was regarded

³ <https://arxiv.org/ftp/arxiv/papers/2112/2112.10390.pdf>

as the background, which is caused by (i) the data imbalance of crack and background/uncrack samples; and (ii) blurred boundaries of tiny long cracks that per-pixel accurate labeling is difficult or infeasible. CrackGAN [6] can significantly reduce the workload of GT labeling and achieve excellent performance when dealing with full-size images for pixel-level crack segmentation. The computational efficiency is also greatly improved (predicting a 4096×2048 image takes approximately 1.6 s on an NVIDIA 1080Ti GPU).

3. Evaluation and Comparison of the Crack Identification Algorithms

3.1. Public Crack Datasets ⁴

SDNET2018. It is a *patch-level annotated* dataset for training and benchmark test of crack-identification algorithms. There are 230 photographs, including 54 bridge decks, 72 walls, and 104 sidewalks. Each photo was cropped into 256×256 patches. In total, it contains 56,092 sample images. The crack sizes vary from 0.06 mm to 25 mm. Random variable factors (environmental, background, interference, etc.) in the images were listed ⁵, and many positive (crack) and negative (uncrack) samples are difficult to be recognized by human eyes.

Crack Forest Dataset (CFD). It is a *pixel-level annotated* pavement crack dataset that reflects the general situation of Beijing urban pavements. It is one of the benchmark baseline datasets. In total, 118 photos were collected and the samples contain noise or interference factors such as lane lines, shadows, and oil stains.

3.2. Crack Patch Classification Evaluation

The patch classification results of the TL algorithms were compared with FCN [18] (FCN is a one-stage pixel-level semantic segmentation algorithm that does not require window sliding), and the ED-based FPCNet [3], as listed in Table 1.

Table 1. Patch classification test performance comparison.

Algorithm/Model ^a	Accuracy	Precision	Recall	F_1 -score	Predicting Time @ GTX1080Ti ^b
TL-MobileNetV2	0.936 8	0.947 7	0.973 2	0.960 3	8.1 ms/patch
TL-InceptionV3	0.941 0	0.952 4	0.980 6	0.966 3	16.1 ms/patch
TL-Resnet152V2	0.956 1	0.961 3	0.981 7	0.971 4	50.2 ms/patch
Original FCN [18]	0.965 8	0.972 9	0.945 6	0.959 0	19.8 ms/patch
ED-FPCNet [3]	0.970 7	0.974 8	0.963 9	0.969 3	67.9 ms/patch

^a TL algorithms were tested on SDNET2018, whereas the FCN and ED algorithms were tested on CFD (statistical results at the pixel level), which is relatively more recognizable than SDNet2018. The results are the average of 10 runnings'. ^b The predicting time includes image loading, pre-processing, and inference time.

It can be seen from Table 1 that: (i) the testing accuracy of TL algorithms on SDNET2018/CFD has exceeded the ImageNet baseline of the backbones. (ii) The performance of fine-tuned TL algorithms is close to or even slightly better than (e.g., on recall & F_1 -score) that of the FCN and ED algorithms, which is attributed to the

⁴ Typical public pavement(concrete) crack datasets, their sample features, and download sources were collected and listed in [16].

⁵ <https://arxiv.org/ftp/arxiv/papers/2112/2112.10390.pdf>

architecture-optimized backbones pre-trained on large-scale datasets. Thus, the TL's predicting time is much lower than the 67.9 ms of FPCNet [3].

The TL algorithms are trained and tested on patch samples cropped from the original images. Owing to the limitation of the minimum size of the patches, they have a poor perform on full-size image segmentation [26], so are generally used for classification. The crack segmentation relies mainly on the ED and GAN algorithms.

On the other hand, the imbalance of crack and uncrack/background samples (SDNET2018 is approximately 1:5.6) may be compensated by the class weight or class-balanced loss function. However, owing to the ambiguous boundary of the topological complex cracks and thin cracks (e.g., pavement crack images collected by high-speed vehicle cameras, and defect images of the industrial products on an automatic assembly line), accurately per-pixel annotation is labor-intensive and even impossible, thus crack GT semi-accurate annotation (i.e., 1-pixel curve labeling, with 2 pixels labeling error) is usually adapted in practice, which will lead to bias in the evaluation via accuracy, precision, recall, or F_1 -score, and even worse, may cause to encounter the "All-Black" issue. Hence, the HD-score is advised as a quantitative evaluation indicator [6], [27] for crack pixel-level segmentation, with good discrimination when crack GT semi-accurate labeling [28].

3.3. Crack Segmentation Performance

A patch-level RCNN based method proposed in [26], cannot accurately locate the crack location owing to the limitation of the patch size. The prediction of full-size images required the usage of a sliding window, which increased prediction time a lot. It took approximately 10.2s for a single CFD sample. FCN-VGG [15] is a pixel-level identification algorithm that implements end-to-end training relying on accurate GT annotation at each pixel. When there is a deviation in the GT, thin cracks will not be detected. DeepCrack [29] achieves good performance with multi-scale hierarchical fusion, with HD-score of 94 and prediction time of 2.4s, but it also relies on the accurate GT.

As mentioned above (detailed in Fig. 5), by introducing CPO supervision and asymmetric U-net, CrackGAN [6] proposed a GAN architecture with a single-class discriminator. It successfully avoided the "All-Black" problem caused by the inherent imbalance of positive and negative samples, and significantly improved the ability of accurate crack segmentation, with HD-score as high as 96, especially good at the identification of thin cracks. And it only takes approximately 1.6s to predict a 4096×2048 image on an NVIDIA GTX1080Ti GPU.

4. A Weakly Supervised Learning Framework: TL-SSGAN

CrackGAN [6] utilized the semi-accurate labor-light annotation (i.e., 1-pixel curve manual labeling) to significantly reduce labeling difficulty and workload. On the other hand, *semi-supervised* GAN (SSGAN) can also significantly reduce the need for labeled samples from the perspective of semi-supervision [30], [31]. A weakly supervised learning framework (i.e., TL-SSGAN) that integrates TL and SSGAN, is proposed for classification, as shown in Fig. 6. TL backbone models can be pre-trained or fine-tuned. The ratio of labeled to unlabeled samples can be used as a variable parameter, and extra

unlabeled samples may also be added. The output of the TL-SSGAN is whether the test samples are generated or real, and whether a crack or not.

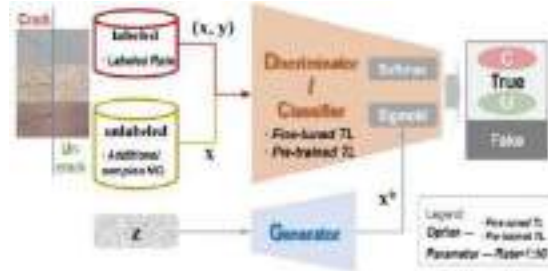


Figure 6. Pipeline of semi-supervised GAN embedded TL models as encoder (Discriminator/Classifier).

The evaluation tests were performed on SDNET2018, and results seen in Table 2.

Table 2. Test performance of TL-SSGAN on SDNET2018.

TL-SSGAN Framework with Different Models and Data						
Row	TL Backbone, fine-tuned or not	Labeled Rate + Extra Unlabeled Samples	Accuracy	Precision	Recall	F_1 -score
1	Resnet152V2, pre-trained	1:30	0.888 6	0.926 7	0.945 3	0.935 9
2	Resnet152V2, pre-trained	1:20	0.889 2	0.931 4	0.947 8	0.939 5
3	Resnet152V2, pre-trained	1:10	0.905 9	0.939 6	0.955 3	0.947 4
4	Resnet152V2, fine-tuned	1:30	0.901 6	0.929 3	0.956 7	0.942 8
5	Resnet152V2, fine-tuned	1:20	0.906 5	0.930 0	0.958 9	0.944 2
6	Resnet152V2, fine-tuned	1:10	0.924 5	0.941 9	0.974 9	0.958 1
7	InceptionV3, fine-tuned	1:10	0.917 0	0.945 5	0.961 0	0.953 2
8	MobileNetV2, fine-tuned	1:10	0.910 6	0.936 2	0.959 0	0.947 5
9	Resnet152V2, fine-tuned	1:10 + Extra 10k samples	0.931 4	0.946 9	0.972 1	0.959 3
10	Resnet152V2, fine-tuned	1:10 + Extra 20k samples	0.938 8	0.957 0	0.972 3	0.964 9
11	Resnet152V2, fine-tuned	1:5	0.946 0	0.972 1	0.970 1	0.971 1
12	Resnet152V2, fine-tuned	1:5 + Extra 10k samples	0.953 2	0.973 0	0.978 6	0.975 8

(1) In general, models of TL-SSGAN achieved good patch classification performance on SDNET2018. The best accuracy, precision, recall, and F_1 -score were 0.953 2, 0.973 0, 0.978 6, and 0.975 8 respectively when utilizing 1/5 labeled samples of the total plus extra 10k unlabeled samples via Resnet152V2, which can outperform the supervised TL and ED algorithms (refer to Table 1 & Table 2).

(2) Both the backbone model and fine-tuning mechanism in the TL framework contributed significantly to the improvement of accuracy. For instance, all other factors and parameters being the same, Resnet152V2-based algorithm is 1.5%, 0.6%, 1.7% and 1.1% better than MobileNetV2-based, respectively, on metrics of accuracy, precision, recall, and F_1 -score (i.e., Row 6 vs. 8 in Table 2); while the results of the fine-tuned algorithm increase by approximately 1.5–2.1%, –0.2–0.3%, 1.2–2.1%, 0.5–1.1% respectively, compared to the pre-trained algorithm, when both with Resnet152V2 as the backbone (i.e., Row 4-6 vs. Row 1-3 respectively).

(3) In the aspect of data usage, when the ratio of labeled/total sample number is 1:10, compared to 1:30 (Resnet152V2 as the backbone), the metric results increase by approximately 1.9–2.5%, 1.4%, 1.1–1.9%, 1.2–1.6% (i.e., Row 3 vs. 1 and Row 6 vs. 4). By adding extra unlabeled samples up to 2 times, an increase of approximately 0.7% can be achieved (i.e., Row 10 vs. 6). Therefore, the weakly supervised mechanism of the

proposed TL-SSGAN framework not only reduces the dependence on labeled samples but also improves the classification performance by using incremental unlabeled samples.

5. Conclusion

In summary, the patch classification accuracy performance of the fine-tuned TL algorithms on public crack datasets (e.g., CFD, SDNET2018), is comparable to or slightly better than that of ED algorithms; and the predicting time cost is less (approximately 8.1 – 50.2 ms/patch). In accurate crack location, both the ED and GAN can achieve pixel-level segmentation, furthermore, CrackGAN can achieve high-precision segmentation under labor-light partially accurate GT annotation (e.g., 1-pixel curve manual labeling). In terms of detection efficiency, CrackGAN only takes approximately 1.6 s to predict a 4096×2048 image on an NVIDIA GTX1080Ti GPU. It is expected to realize real-time crack detection on a low computational power platform.

We proposed a weakly supervised learning framework TL-SSGAN combining TL and semi-supervised GAN, through the measures of (i) utilizing fine-tuned TL backbones, (ii) controlling the ratio of labeled and unlabeled samples, and (iii) adding extra unlabeled samples, which can maintain comparable crack classification performance to or even outperform the supervised learning while greatly reducing the number of labeled samples (approximately 1/10 ~ 1/5 of the total) needed.

To conclude, the combination of various deep learning frameworks, such as TL, ED and GAN/SSGAN, can integrate the advantages of each mechanism and improve the performance of the overall architecture. Although pavement crack is taken as a case study, the algorithms discussed here can be easily modified for crack identification in other engineering structures.

Acknowledgements

This work was supported by NSFC (No.51405289) and Research Project of Education Department of Guangdong Province (No.2022KTSCX192).

References

- [1] K.L. Lu, W.G. Zhang, Y. Zhang, H. Huang, Y.S. Chen, W.Y. Li and C. Wang, "Crack analysis of multi-plate intersection welded structure in port machinery using finite element stress calculation and acoustic emission testing," *International Journal of Hybrid Information Technology*, vol. 7, no. 5, pp. 323–340, 2014.
- [2] A. Martone, M. Zarrelli, M. Giordano, and J. M. L'opez-Higuera, *Structural health monitoring in buildings, bridges and civil engineering*. New Jersey: Photonics for Safety and Security, World Scientific, 2013.
- [3] W.J. Liu, Y.C. Huang, Y. Li, and Q. Chen, "FPCNet: Fast Pavement Crack Detection Network Based on Encoder-Decoder Architecture," *arXiv:1907.02248*, 2019.
- [4] Z. Fan, C. Li, Y. Chen, J.H. Wei, L. Giuseppe, X.P. Chen and D. M. Paola, "Automatic crack detection on road pavements using encoder-decoder architecture," *Materials*, vol. 13, no. 13, pp. 1–18, 2020.
- [5] Q.P. Mei and M. G'ul, "A cost effective solution for pavement crack inspection using cameras and deep neural networks," *Construction and Building Materials*, vol. 256, p. 119397, 2020.
- [6] K.G. Zhang, Y.T. Zhang, and H.D. Cheng, "CrackGAN: Pavement Crack Detection Using Partially Accurate Ground Truths Based on Generative Adversarial Learning," *IEEE Transactions on Intelligent Transportation Systems*, vol. 22, no. 2, pp. 1306–1319, 2021.

- [7] O. Henrique and C. P. Lobato, "Automatic road crack detection and characterization," *IEEE Transactions on Intelligent Transportation Systems*, vol. 14, no. 1, pp. 155–168, 2013.
- [8] Q. Zou, Y. Cao, Q.Q. Li, Q.Z. Mao, and S. Wang, "CrackTree: Automatic crack detection from pavement images," *Pattern Recognition Letters*, vol. 33, no. 3, pp. 227–238, 2012.
- [9] Y. Shi, L.M. Cui, Z.Q. Qi, et al., "Automatic road crack detection using random structured forests," *IEEE Transactions on Intelligent Transportation Systems*, vol. 17, no. 12, pp. 3434–3445, 2016.
- [10] J. Wright and Y. Ma, *High-Dimensional Data Analysis with Low-Dimensional Models: Principles, Computation, and Applications*. Cambridge University Press, 2021.
- [11] C. Giraud, *Introduction to High-Dimensional Statistics*, 2nd ed. Chapman and Hall, CRC, 2021.
- [12] R. Ge, H. Lee, and J.F. Lu, "Estimating normalizing constants for log-concave distributions: Algorithms and lower bounds," in *STOC 2020: the 52nd Annual ACM Symposium on Theory of Computing*, 2020, pp. 1–46.
- [13] Y.D. Yu, K.H.R. Chan, C. You, C.B. Song, and Y. Ma, "Learning diverse and discriminative representations via the principle of maximal coding rate reduction," in *NeurIPS 2020: the 34th Conference on Neural Information Processing Systems*, 2020, pp. 1–28.
- [14] K.H.R. Chan, Y.D. Yu, C. You, H.Z. Qi, J. Wright, and Y. Ma, "Deep networks from the principle of rate reduction," *arXiv:2010.14765*, 2020.
- [15] X.C. Yang, H. Li, Y.T. Yu, X.C. Luo, T. Huang, and X. Yang, "Automatic Pixel-Level Crack Detection and Measurement Using Fully Convolutional Network," *Computer-Aided Civil and Infrastructure Engineering*, vol. 33, no. 12, pp. 1090–1109, 2018.
- [16] K.L. Lu, "Advances in deep learning methods for pavement surface crack detection and identification with visible light visual images," *Computer Engineering & Science*, vol.44, No.4, pp. 674-685, 2022.
- [17] Y. Fei, C.P.(Kelvin) Wang, A. Zhang, C. Chen, J.Q. Li, Y. Liu, G.W. Yang, and B.X. Li, "Pixel-Level Cracking Detection on 3D Asphalt Pavement Images through Deep-Learning- Based CrackNet-V," *IEEE Transactions on Intelligent Transportation Systems*, vol. 21, no. 1, pp. 273–284, 2020.
- [18] E. J. Long and T. D. Shelhamer, "Fully convolutional networks for semantic segmentation," in *Proceedings of the IEEE Conference on Computer Vision and Pattern Recognition (CVPR)*, 2015, pp. 3431–3440.
- [19] O. Ronneberger, P. Fischer and T., Brox, "U-net: convolutional networks for biomedical image segmentation," in *Proceedings of the Lecture Notes in Computer Science*, 2015, pp. 234–241.
- [20] F. Yu and V. Koltun, "Dilated residual networks," in *CVPR*, 2017, pp. 472–480.
- [21] H.F. Li, J.P. Zong, J.J. Nie, Z.L. Wu, and H.Y. Han, "Pavement Crack Detection Algorithm Based on Densely Connected and Deeply Supervised Network," *IEEE Access*, vol. 9, pp. 11 835–11 842, 2021.
- [22] Y.T. Yu, H.Y. Guan, D.L. Li, Y.J. Zhang, S.H. Jin, and C.H. Yu, "CCapFPN: A Context-Augmented Capsule Feature Pyramid Network for Pavement Crack Detection," *IEEE Transactions on Intelligent Transportation Systems*, pp. 1–12, 2020.
- [23] A. Creswell, T. White, V. Dumoulin, K. Arulkumaran, B. Sengupta, and A. A. Bharath, "Deep learning for visual understanding: Part 2 generative adversarial networks," *IEEE Signal Processing Magazine*, no. 1, pp. 53–65, 2018.
- [24] Y. Hong, U. Hwang and S. Yoon, "How generative adversarial nets and its variants work: An overview of GAN," *ACM Computing Surveys*, vol. 52, no. 1, pp. 1–43, 2019.
- [25] Z.W. Wang, Q. She and T.E. Ward, "Generative adversarial networks in computer vision: A survey and taxonomy," *ACM Computing Surveys*, vol. 54, no. 1, pp. 1–41, 2021.
- [26] Y.J. Cha, W. Choi and O. B'uy'uk'ozt'urk, "Deep Learning-Based Crack Damage Detection Using Convolutional Neural Networks," *Computer-Aided Civil and Infrastructure Engineering*, vol. 32, no. 5, pp. 361–378, 2017.
- [27] Y.C.(James) Tsai and A. Chatterjee, "Comprehensive, Quantitative Crack Detection Algorithm Performance Evaluation System," *Journal of Computing in Civil Engineering*, vol. 31, no. 5, p. 04017047, 2017.
- [28] Y. Inoue and H. Nagayoshi, "Crack detection as a weakly-supervised problem: Towards achieving less annotation-intensive crack detectors," in *ICPR*, 2020, pp. 1–10.
- [29] Q. Zou, Z. Zhang, Q.Q. Li, X.B. Qi, Q. Wang, and S. Wang, "DeepCrack: Learning hierarchical convolutional features for crack detection," *IEEE Transactions on Image Processing*, vol. 28, no. 3, pp. 1498–1512, 2019.
- [30] J. T. Springenberg, "Unsupervised and semi-supervised learning with categorical generative adversarial networks," in *International Conference on Learning Representations (ICLR)*, 2016, pp. 1–20.
- [31] Z.H. Dai, Z.L. Yang, F. Yang, W.W. Cohen and R. Salakhutdinov, "Good semi-supervised learning that requires a bad GAN," in *NIPS*, 2017, pp. 6511–6521.

A Massive-Cargo Transportation Routing Model Based on Reinforcement Learning

Yi-shun LI ^{a, b} and Ming WEI ^{c, d, 1}

^a *Transport Planning and Research Institute, Ministry of Transport, China*

^b *Laboratory for Traffic & Transport Planning digitalization, China*

^c *Key Laboratory of Flight Techniques and Flight Safety, CAAC, China*

^d *College of Air Traffic Management, Civil Aviation University of China, China*

Abstract. Considering the size (length, width, and height) and weight of massive cargos and on the basis of satisfying the throughput capacity of the road network, a massive-cargo transportation routing model was proposed to find the shortest transportation route based on the origin and destination. According to the characteristics of the routing problem, a reinforcement learning algorithm was designed to solve the problem and determine the strategy, reward function, value function, and environment model. Additionally, based on a case study, an optimized transportation plan was developed and the model sensitivity was analyzed to verify the validity and correctness of the proposed model and algorithm.

Keywords. Massive-cargo logistics transportation route, reinforcement learning, overload

1. Introduction

As a key part of highway transportation, massive-cargo transportation is often used for the transportation of key equipment used in national key construction projects, and the transportation process is required to be highly reliable and safe. Compared with normal cargo trucks, massive-cargo trucks are different in terms of the number of passing trucks, passage mode, and load distribution. To date, there is no unified and clear load control standard for massive-cargo transportation routing, which has brought difficulties for the approval and management of massive-cargo transportation by traffic authorities. Although the objectives, processes, and ideas of studies on massive-cargo transportation and conventional logistics are the same, the differences between their study objects determine that the transportation routes considering overloading are much more complicated than vehicle scheduling, which belongs to a class of NP-hard problems and has received wide attention from scholars at home and abroad.

Previous studies of vehicle routes focused on the related problems considering vehicle constraints and related problem variants [1]. Leng et al. [2] established a mathematical model for the vehicle routing problem of multiple distribution centers based on the logistics distribution system of urban rail transit and proposed a new

¹ Corresponding Author, Ming Wei, Key Laboratory of Flight Techniques and Flight Safety, CAAC, China; College of Air Traffic Management, Civil Aviation University of China, China; Email: mingtian911@163.com

concentration immune algorithm-based particle swarm algorithm to solve the vehicle routing problem by combining the concept of antibody concentration. Islam et al. [3] proposed a novel hybrid metaheuristic method combining particle swarm optimization algorithm and variable neighborhood search to solve the clustering vehicle route problem. Bdeir et al. [4] used Q-learning to solve the vehicle problem with capacity limitation and proved the correctness and rationality of the algorithm. However, there were few studies considering the capacity of stations and cargo constraints. Parsafard et al. [5] provided a practical framework to find the optimized route for fuel delivery trucks between bulk cargo wharves and bulk supply petrol stations considering the cost and safety on the road. Considering the complexity of road networks and time-varying traffic conditions, Bai et al. [6] studied the problems of low-carbon, cold chain logistics distribution and proposed a low-carbon, cold chain logistics route optimization model. Based on the constraints related to loading and restricted access, Pei et al. [7] established a dual-objective model considering the total travel cost and loading rate and proposed a genetic algorithm with efficient adaptive evaluation capability for solving the vehicle route problem of split delivery with three-dimensional loading constraints. Prado et al. [8] proposed a mathematical model for vehicle distribution at multiple warehouses, each of which has limited supply capacity, and solved the model by using a multi-stage method. Hessler [9] investigated the routing of vehicles with flexible compartment sizes, established a mathematical model with the objective of minimizing the total distance of all vehicle routes, and solved the problem by using a two-stage algorithm. Küçük et al [10] proposed an approach for solving the capacitated vehicle routing problem with three-dimensional loading constraints (3L-CVRP) that combines vehicle routing and three-dimensional loading and proved its rationality and effectiveness.

In summary, this paper investigated a class of reinforcement learning-based massive-cargo logistics transportation routing models. The main content includes: (1) establishing a mathematic model for massive-cargo transportation routing considering practical factors such as overloading, with the goal of minimizing transportation mileage; (2) designing a reinforcement learning algorithm for solving this problem and determining the strategy, reward function, value function, and environment model. Additionally, a simple example was used to verify the correctness of the model.

2. Massive-Cargo Logistics Transportation Routing Model

Compared with conventional logistics cargo, massive cargo shows unique sizes and weights. A massive-cargo logistics transportation network comprises nodes and sections. The nodes involve bridges and toll stations, while the sections consist of adjacent nodes. Apparently, the overload capacity of nodes restricts the capacity of massive cargos passing through road sections. Hence, it is important to clarify how to arrange a special vehicle, that is, select feasible nodes from all massive-cargo transportation nodes and determine the order of the vehicle visiting these nodes, so as to transport massive cargos from the origin to the destination. Without loss of generality, the model assumes that: (1) The random interference of the traffic network and the impact of the time window of massive cargos on massive-cargo transportation routes are not considered; (2) The conflicts between multiple massive-cargo logistics transportation routes are ignored; (3) The throughput capacity information of massive-cargo transportation networks is obtained in advance.

Table 1. Definitions of relevant variables in the lower-level model

Index:	Definition
m, n	Massive-cargo transportation nodes
Set:	
M	Massive-cargo transportation node set
Instrumental variables:	
i	Origin of massive cargo
j	Destination of massive cargo
l	Length of massive cargo
w	Width of massive cargo
h	Height of massive cargo
g	Weight of massive cargo
l_m	Length limit of massive-cargo transportation node m
w_m	Width limit of massive-cargo transportation node m
h_m	Height limit of massive-cargo transportation node m
g_m	Weight limit of massive-cargo transportation node m
d_{mn}	Distance between massive-cargo transportation nodes m and n
w_{mn}	Whether massive-cargo transportation nodes m and n are adjacent
Decision variable:	
s_{mn}^k	Whether drone k visits adjacent massive-cargo transportation nodes m and n in order

According to the problem description, the symbols and definitions of relevant variables are shown in Table 1, and the mathematical model is established as follows.

$$d_{ij}^k = \min \sum_{n, m \in M \cup i \cup j} s_{mn}^k \cdot d_{mn} \tag{1}$$

s. t.:

$$\sum_{m \in M} s_{mn}^k - \sum_{n \in M} s_{mn}^k = \begin{cases} 1, n = i \\ -1, n = j, \forall n \in M \cup i \cup j \\ 0, n \neq i, j \end{cases} \tag{2}$$

$$s_{mn}^k \leq w_{mn}, \forall n, m \in M \cup i \cup j \tag{3}$$

$$l \cdot s_{mn}^k \leq l_m, \forall m \in M \tag{4}$$

$$w \cdot s_{mn}^k \leq w_m, \forall m \in M \tag{5}$$

$$h \cdot s_{mn}^k \leq h_m, \forall m \in M \tag{6}$$

$$g \cdot s_{mn}^k \leq g_m, \forall m \in M \tag{7}$$

Herein, Eq (1) is the objective function of the problem, which minimizes the total mileage of the massive-cargo logistics transportation route, and Eqs (2)-(10) are the constraints. Eq (2) indicates the network flow constraints of the massive-cargo transportation route. For example, the origin allows going out but not going in, the destination allows going in but not going out, and the middle points allow both going in and out. Eq (3) ensures that the massive-cargo logistics transportation route only passes through adjacent nodes. Eqs (4)-(7) indicate that the massive-cargo transportation route must satisfy the load capacity limits of items and roads.

3. Two-Stage Hybrid Solution Algorithm Based on Deep Reinforcement Learning

Based on the characteristics of the problem, a reinforcement learning algorithm based on Q-learning was designed in this study. Q-learning is a kind of off-policy temporal difference control method, which shows good convergence in the case of solving an NP-hard problem. The Q table is updated as follows.

$$Q(s_t, a_t) \leftarrow Q(s_t, a_t) + \alpha(R_{t+1} + \gamma \max_a Q(s_{t+1}, a) - Q(s_t, a_t)) \quad (8)$$

where Q is the action value function, s_t is the state at moment t , a_t is the selected node at moment t , d_{t+1} is the penalty at moment $t+1$, that is, $R=d_{ij}$, where i and j are the node selected at moment t and the node selected before node i , α is the learning rate, and γ is the decay rate of gain.

According to the actual situation, ε -greedy algorithm was used to perform action selection so as to update the Q table. In other words, nodes were selected from the set ε of all available logistics nodes by means of the exploration probability ε . The nodes selected under different probabilities are:

$$a_t = \begin{cases} \operatorname{argmax} Q(s_t, a_t), & \tau > \varepsilon \\ \forall a_t \in A_t, & \tau < \varepsilon \end{cases} \quad (9)$$

where τ is a random number in the interval $(0, 1)$.

In summary, the problem was solved with the logistics node limit as the constraint and the shortest route as the objective, and the procedures of the algorithm are shown in Tables 2 and 3.

Table 2. Procedures of the Q-learning algorithm

Q-learning algorithm	
1:	Initialize logistics nodes, cargo, and vehicle information
2:	Initialize logistics connected graph, adjacency matrix, and route length information
3:	Initialize Q table and parameters,,
4:	For epoch =1, 2, 3, ...
5:	Set the origin of logistics distribution as the current node a_{t-1} at moment t-1
6:	while True:
7:	$\varepsilon > 0$, input a_{t-1} , and use ε -greedy algorithm to determine the selected node a_t at moment t
8:	$\varepsilon < 0$, input a_t , and use ε -greedy algorithm to determine the selected node a_{t+1} at moment t+1 under the current condition
9:	According to the current node a_{t-1} and the selected node a_t at moment t, compute the penalty $R=d_{ij}$
10:	$Q(s_t, a_t) \leftarrow Q(s_t, a_t) + \alpha(R_{t+1} + \gamma \max_a Q(s_{t+1}, a) - Q(s_t, a_t))$
11:	$a_{t-1} \leftarrow a_t$
12:	Add the selected node a_t into the route set
13:	Compute the total penalty R in the current state
14:	if: a_{t-1} is the destination of logistics distribution
15:	break
16:	return route set

Table 3. Procedures of the ϵ -greedy algorithm

ϵ -greedy algorithm	
1:	Input adjacency matrix, Q table, current node a_{t-1}
2:	According to the adjacency matrix and the current node a_{t-1} , determine the available node set A_t at moment t
3:	if $\tau > \epsilon$:
4:	Determine the Q values of all available nodes A_t in the current node a_{t-1}
5:	$a_t = \text{argmax}Q(s_t, a_t)$
6:	else:
7:	,
8:	return a_t

4. Case Study

4.1 Data Preparation

In this study, a certain massive-cargo transportation network was taken as an example. The network involves 30 nodes and is used to deliver a great number of massive cargos of different types. In the network, the connectivity and distance between two nodes are known and the length, width, height, and weight limits of each node are shown in Table 4. The data of the connectivity and distance between two nodes are shown in Figure. 1, where a circle represents a logistics node, a line represents the connectivity between two nodes without representing the actual geographical location or route, two connected points can pass in both directions, and the number on the line represents the actual distance between two nodes (unit: km).

Table 4. Cargo limitation of logistics nodes

Unit: (m, m, m, t)

No.	(l_m, w_m, h_m, g_m)	No.	(l_m, w_m, h_m, g_m)	No.	(l_m, w_m, h_m, g_m)
0	(150, 150, 30, 200)	10	(150, 150, 30, 200)	20	(150, 150, 30, 200)
1	(150, 150, 30, 200)	11	(120, 130, 20, 170)	21	(100, 90, 15, 150)
2	(100, 90, 15, 150)	12	(100, 90, 15, 150)	22	(100, 90, 15, 150)
3	(150, 150, 30, 200)	13	(80, 70, 10, 100)	23	(120, 130, 20, 170)
4	(120, 130, 20, 170)	14	(100, 90, 15, 150)	24	(80, 70, 10, 100)
5	(80, 70, 10, 100)	15	(80, 70, 10, 100)	25	(150, 150, 30, 200)
6	(150, 150, 30, 200)	16	(150, 150, 30, 200)	26	(100, 90, 15, 150)
7	(120, 130, 20, 170)	17	(120, 130, 20, 170)	27	(120, 130, 20, 170)
8	(10, 2.55, 3.5, 36)	18	(120, 130, 20, 170)	28	(150, 150, 30, 200)
9	(80, 70, 10, 100)	19	(80, 70, 10, 100)	29	(150, 150, 30, 200)

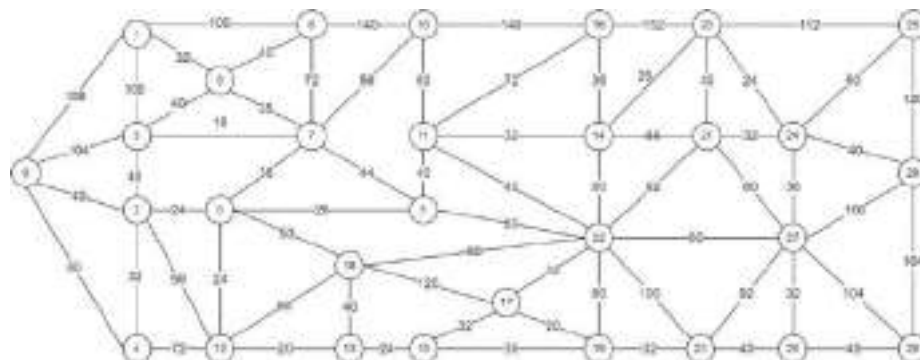


Figure. 1 Network of logistics nodes

4.2 Analysis of Experimental Results

In this study, Python 3.9 was used to code Q-learning algorithm to solve the model. With the number of iterations (epoch) as 200, learning rate α as 0.1, gain decay rate γ as 0.8, and exploration probability ϵ as 0.05, the transportation routes for different types of cargos were obtained. There are three types of to-be-distributed cargos, all of which were transported from Logistics Node 0 to Logistics Node 29. The cargo data were input into the algorithm to compute the optimized transportation route and the total traveling distance for each type of cargo, and the results and related cargo data are shown in Table 5.

Table 5. Properties of to-be-distributed cargos and their distribution routes

Cargo No.	$(l(m), w(m), h(m), g(t))$	Optimized route	Traveling distance (km)
Cargo 1	(120, 100, 25, 130)	0, 1, 6, 10, 16, 20, 25, 29	880
Cargo 2	(110, 100, 15, 150)	0, 3, 7, 10, 11, 16, 20, 25, 29	748
Cargo 3	(75, 65, 9, 100)	0, 4, 12, 13, 18, 22, 27, 29	452

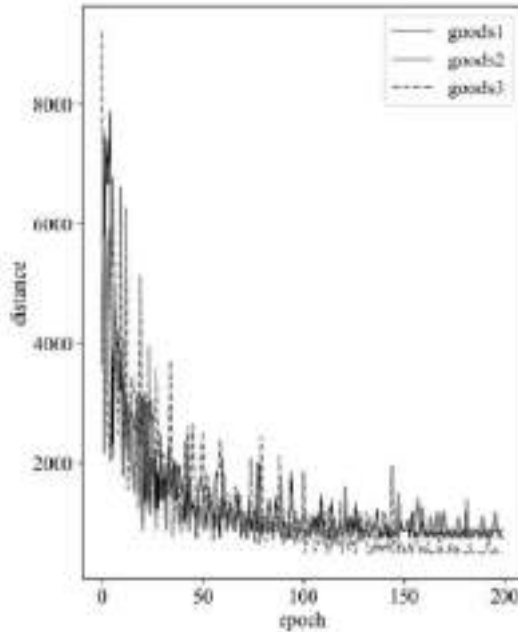


Figure 2. Optimized route planning process

As observed, the penalty value of the optimized solution found by the algorithm in each training process shows an overall decreasing trend and tends to flatten out, which verifies the effectiveness of the algorithm in solving this problem. Meanwhile, among the three types of to-be-distributed cargos, Cargos 3 has the shortest distribution route. This is because the volume and weight of the cargos are small so that the cargos can be transported in the entire logistics network and thus the shortest route can be selected. For the cargos with a large volume and weight (e.g., Cargo 1), however, only a few nodes in the logistics network are available. Hence, logistics nodes with a relatively long distance and a relatively high capacity are selected, resulting in an increase in the total traveling distance.

4.3 Analysis of Algorithm Sensitivity

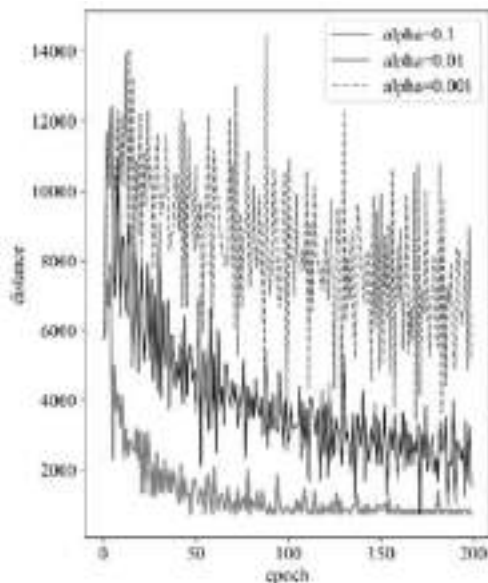


Figure. 3 The effects of learning rate α on the solution-solving performance of the algorithm

For the key parameters of the algorithm, that is, learning rate α and exploration probability ε , different parameter settings will affect the overall convergence of the algorithm. Cargos 2 was taken as an example for algorithm sensitivity analysis. Figure. 3 shows the optimized solution generating process of the algorithm under $\varepsilon = 0.05$. As observed, the model has the worst convergence effect when $\alpha = 0.001$, followed by the case when $\alpha = 0.01$ and then the case when $\alpha = 0.1$.

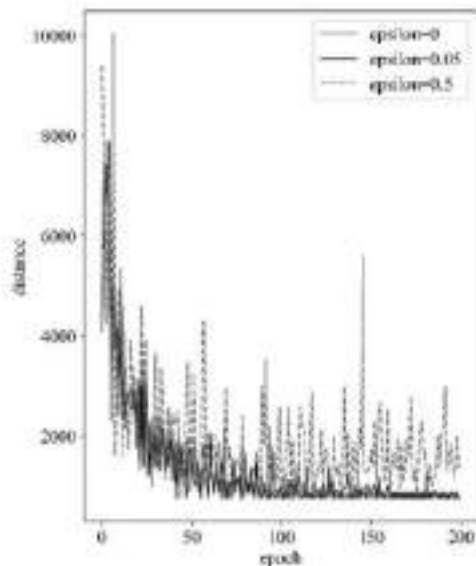


Figure. 4 The effects of exploration probability ε on the solution-solving performance of the algorithm

Figure. 4 shows the optimized solution generating process of the algorithm under $\alpha = 0.1$. As observed, when $\varepsilon = 0$, that is, the optimized node is selected from all available nodes each time without exploration, which will lead to the highest gain of the algorithm, the model converges the fastest, while in the case of no exploration, the algorithm may miss the opportunity to find a better solution; when $\varepsilon = 0.5$, since the ε -greedy algorithm does too much exploration in node selection, the model has poor convergence.

5. Conclusions

With the length, width, height, and weight of massive cargos into consideration and based on the origin and destination of massive-cargo logistics, a reinforcement learning-based massive-cargo logistics transportation routing model was proposed in this study to obtain a feasible optimized route. The results demonstrated that the proposed model can accurately compute the optimized plan and the computation results are consistent with the actual situation. Meanwhile, the learning rate of the reinforcement learning algorithm and the effect of exploration probability on the results were further analyzed to verify the effectiveness of the algorithm.

The shortcomings of this paper include: (1) the situation of multiple massive-cargo logistics transportation routes and the conflicts between the routes were not considered; (2) the massive-cargo logistics transportation routes were not integrated with the dynamic traffic condition. Therefore, the collaborative optimization of multiple massive-cargo logistics transportation routes considering the dynamic traffic condition will be our future direction of research.

Acknowledgement: To acknowledge all the people who have contributed to this paper in some manner.

Funding Statement: This paper is supported by Open Fund of Key Laboratory of Flight Techniques and Flight Safety, CAAC(No. FZ2021KF06).

Conflicts of Interest: The authors declare that they have no conflicts of interest to report regarding the present study.

References

- [1] Gutiérrez-Sánchez A, Rocha-Medina L B. VRP variants applicable to collecting donations and similar problems: A taxonomic review [J]. *Computers & Industrial Engineering*, 2021: 107887.
- [2] Leng K, Li S. Distribution Path Optimization for Intelligent Logistics Vehicles of Urban Rail Transportation Using VRP Optimization Model [J]. *IEEE Transactions on Intelligent Transportation Systems*, 2021, 23 (2): 1661-1669.
- [3] Islam M A, Gajpal Y, ElMekkawy T Y. Hybrid particle swarm optimization algorithm for solving the clustered vehicle routing problem [J]. *Applied Soft Computing*, 2021, 110: 107655.
- [4] Bdeir A, Boeder S, Demedde T, et al. RP-DQN: An application of Q-Learning to Vehicle Routing Problems [C]//German Conference on Artificial Intelligence (Künstliche Intelligenz). Springer, Cham, 2021: 3-16.
- [5] Parsafard M, Esmaeel A, Masoud K, et al. Practical approach for finding optimum routes for fuel delivery trucks in large cities [J]. *Transportation Research Record*, 2015, 2478 (1): 66-74.
- [6] Bai Q, Yin X, Lim M K, et al. Low-carbon VRP for cold chain logistics considering real-time traffic conditions in the road network [J]. *Industrial Management & Data Systems*, 2021.

- [7] Pei J, Hu C, Liu J, et al. Bi-Objective Splitting Delivery VRP with Loading Constraints and Restricted Access [C]//2021 IEEE Symposium Series on Computational Intelligence (SSCI). IEEE, 2021: 01-09.
- [8] Prado J, Moscatelli S, Piñeyro P, et al. Multi-Phase Methodology for Solving the Multi-Depot Vehicle Routing Problem with Limited Supply Capacity at the Depots [C]//International Conference on Metaheuristics and Nature Inspired Computing. Springer, Cham, 2021: 198-211.
- [9] Hessler K. Exact algorithms for the multi-compartment vehicle routing problem with flexible compartment sizes [J]. *European Journal of Operational Research*, 2021, 294 (1): 188-205.
- [10] Küçük M, Yıldız S T. Constraint programming-based solution approaches for three-dimensional loading capacitated vehicle routing problems [J]. *Computers & Industrial Engineering*, 2022, 171: 108505

Robust Estimation Method Using Successive Approximation Algorithm to Correct Errors

Xiao-Ming Ye¹

School of Geodesy and Geomatics, Wuhan University, Wuhan, China

Abstract. In measurement practice, the residuals in least squares adjustment usually show various abnormal discrete distributions, including outliers, which is not conducive to the optimization of final measured values. In this paper, according to the physical mechanism of deviation, dispersion and outlier of repeated observations, it can be seen that abnormal distribution and outlier are normal measurement phenomena, and weakening the influence of outlier is an incorrect research direction. Then, by revealing the advantages of functional model processing, this paper puts forward the error correction idea of using the approximate function model to approach the actual function model step by step, and forms a new theoretical method to optimize the final measured values, which greatly improves the quality of measured values. This is a new measurement theory idea that is completely different from mainstream robust estimation research.

Keywords. Robust estimation, Least square method, Gross error, Outlier, Function model.

1. Introduction

In measurement practice, the residuals obtained by the least squares adjustment usually show various abnormal discrete distributions, including outliers, so that the adjustment result is not an optimal result. In order to solve these problems, academia has carried out a lot of research and formed many robust estimation methods, and there are tens of thousands of relevant documents [1-4]. However, based on the error classification theory, these mainstream studies believe that outlier comes from wrong measurements and should weaken its influence, and no one cares about the real physical mechanism behind the phenomena of deviation, dispersion and outlier. Moreover, only considering precision but ignoring trueness, mainstream research inevitably sacrifices trueness, so as to obtain a false high accuracy and an unnecessary cumbersome mathematical process.

Different from the mainstream research aimed at weakening the influence of outliers, and starting from the error classless philosophy[5-13], this paper will analyze the actual physical mechanism that errors cause the phenomenon of deviation, dispersion and outlier, prove that outlier (abnormal distribution) is a normal measurement phenomenon and its influence should not be weakened, give a successive approximation algorithm using error's function model to realize error correction, and realize the

¹ Corresponding Author, Xiao-Ming Ye, School of Geodesy and Geomatics, Wuhan University, China; Email: xmye@sgg.whu.edu.cn

optimization of final measured values. Moreover, its mathematical process is simple and logical.

That is, the mainstream research of robust estimation is to weaken the influence of outliers, but this paper is to effectively use abnormal distribution and outliers. They are two completely opposite research directions.

Concerning the research method, this paper will use true values plus errors to simulate repeated observations, and verify the effectiveness of the algorithm by the ability that the final measured values respond to the true values. We will see that weakening the influence of outliers or eliminating outliers usually sacrifices trueness. Besides, we will also see the theoretical rigor and practical effectiveness of the successive approximation algorithm.

Next, through the regularity and randomness of errors, the author reveals the physical mechanism of deviation, dispersion and outlier of observation errors, and then derives the robust estimation algorithm that uses the function model to approximate successively.

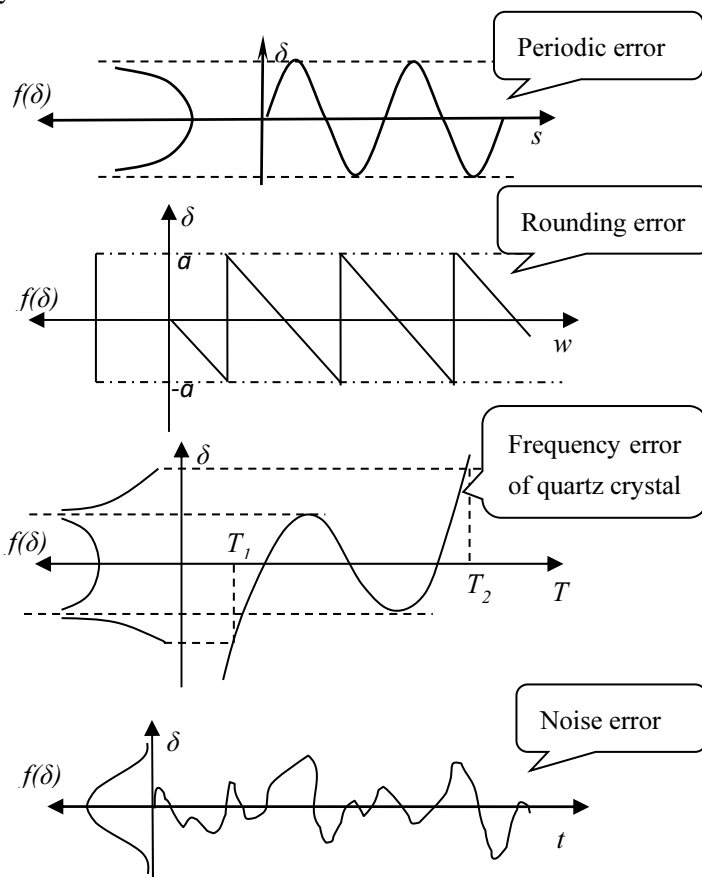


Figure. 1 Regularity and randomness of several different errors

2. Regularity and randomness of error

Let's review a new error epistemology from the regularity and randomness of errors.

The regularity of error means that there is a functional relationship between error and some measurement conditions. For example, the periodic error of geodimeter is a sinusoidal function of distance condition, the AC interference error in voltage measurement is a sinusoidal function of time condition, the frequency error of quartz crystal is a function of temperature condition, the rounding error is a sawtooth law function of true value, the electronic noise error is a random function of time condition, and so on.

The randomness of error means that all possible values of error form a random distribution, or the error exists in a limited probability interval. For example, periodic error and AC interference error follow U-shaped distribution, rounding error follows rectangular distribution, quartz crystal frequency error follows M-shaped distribution, electronic noise error follows normal distribution, etc., as shown in Figure 1.

That is, the regularity and randomness of errors are the results of observing errors from different perspectives, and errors are the unity of regularity and randomness. In other words, having both regularity and randomness, the error cannot be classified by regularity and randomness, the traditional classical error classification theory is a philosophical mistake, and we need to study the error processing method with an error classless epistemology [5-13].

3. Deviation, dispersion and outlier of observation error in repeated measurements

Now let's see the physical mechanism behind the phenomena of deviation, dispersion and outlier.

In measurement practice, repeated measurement conditions are in a changing state. For example, in leveling network survey, the instrument erection conditions (leveling, height, direction, temperature, etc.) of each route are different from each other; in traverse network survey, the instrument erection conditions and distance conditions observed by each traverse are also different from each other; in GNSS network survey, the positions of satellites in each observation period are different from each other, and the signal propagation conditions of each survey station are different from each other.

When the measurement conditions associated with the regular error change, it will inevitably drive the error to change, which is the physical mechanism of the dispersion caused by the regular error. For example, when the distance condition changes in repeated measurement, the periodic error will lead to the dispersion of observation error sequence; When the time condition changes in repeated measurement, the AC interference error will lead to the dispersion of observation error sequence; When the temperature condition changes in repeated measurement, the frequency error of quartz crystal will lead to the dispersion of observation error sequence; When the range conditions change in repeated measurement, the rounding error will lead to the dispersion of observation error sequence; When the time condition changes in repeated measurement, the noise error will lead to the dispersion of observation error sequence; and so on.

On the contrary, when the measurement conditions associated with the regular error

remain unchanged in the repeated measurement, the error will remain constant in the repeated measurement, resulting in the overall deviation of the observation error sequence.

However, the actual measurement conditions are usually neither even change nor absolutely unchanged, but an uneven change, which will inevitably drive the corresponding regular errors to produce uneven changes. This is the physical mechanism of abnormal distribution or even outlier of errors in measurement practice. For example, the serious imbalance of phase condition change of periodic error and AC interference error will cause them to form outlier distribution, the serious imbalance of discarding four and leaving five will cause outlier distribution of rounding error, the serious imbalance of temperature condition change will cause outlier distribution of quartz crystal frequency error, and so on.

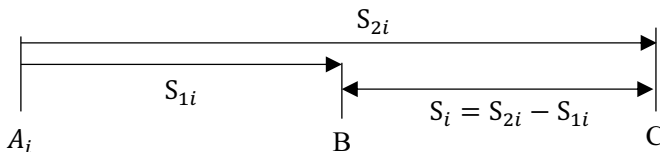


Figure .2 Measuring distance by difference method

For example, using difference method to measure distance, as shown in Figure.2, table 1 simulates a repeated differential observation data with a true value of $S_{A_iC} - S_{A_iB} = 8m$

by using the periodic error $\delta_i = 5 \sin(\frac{d_i}{20} \times 2\pi + \frac{\pi}{4}) (mm)$ of a geodimeter. It can be seen that each observation value S_i is different from each other, but the mean value is 8.0014m, indicating that both dispersion and deviation coexist, and its distribution is also uneven.

Table 1 Simulation observation values of periodic error of geodimeter

i	S_{A_iB}	S_{A_iC}	$S_{2i} = S_{A_iB} + \delta_i$	$S_{1i} = S_{A_iC} + \delta_i$	$S_i = S_{1i} - S_{2i}$
1	10	18	9.9965	18.0008	8.0043
2	12	20	11.9951	20.0035	8.0084
3	33	41	32.9951	41.0045	8.0094
4	27	35	27.0008	34.9965	7.9957
5	22	30	22.0049	29.9965	7.9916
6	28	36	27.9992	35.9977	7.9985
7	30	38	29.9965	38.0008	8.0043
8	36	44	35.9977	44.0045	8.0068
9	38	46	38.0008	46.0023	8.0015
10	26	34	26.0023	33.9955	7.9932
11	34	42	33.9955	42.0049	8.0094
12	16	24	15.9977	24.0045	8.0068
13	18	26	18.0008	26.0023	8.0015
14	19	27	19.0023	27.0008	7.9985
15	42	50	42.0049	49.9965	7.9916
$S_{A_iC} - S_{A_iB} = 8m$					

Moreover, when the number of samples is small, the random superposition of several errors can also appear outlier phenomenon.

4. Error processing with function model and random model

The dispersion and outliers of repeated observation errors come from regular errors, or even the superposition of a variety of different regular errors. Therefore, the observation error sequence can be regarded as both regular errors and randomly distributed errors. Naturally, both using the error function model to correct the error and incorporating the error into the random model to realize the self-compensation of the error are effective schemes to realize the adjustment.

Example 1: use the observation data in Table 1 to find the best measured value with random model and functional model respectively.

Assuming that the unknown true value is Y , the error equation treated according to the random model is:

$$V_i = S_{1i} - S_{2i} - Y \quad (4-1)$$

According to the least square method, the best measured value is:

$$y = \frac{\sum_{i=1}^n (S_{1i} - S_{2i})}{n} = 8.0014(m) \quad (4-2)$$

It can be seen that the final error is 1.4mm, which is much smaller than the 5mm amplitude of periodic error.

The function model of periodic error is:

$$\delta_i = A \sin\left(\frac{d_i}{20} \times 2\pi + \phi\right) = P \sin \frac{d_i}{20} \times 2\pi + Q \cos \frac{d_i}{20} \times 2\pi \quad (4-3)$$

The error equation treated according to the functional model is:

$$\begin{aligned} V_i &= S_{1i} - \delta_{1i} - (S_{2i} - \delta_{2i}) - Y \\ &= S_{1i} - S_{2i} - P(\sin \varphi_{1i} - \sin \varphi_{2i}) - Q(\cos \varphi_{1i} - \cos \varphi_{2i}) - Y \\ &= S_{1i} - S_{2i} - P\left(\sin \frac{S_{1i}}{20} \times 2\pi - \sin \frac{S_{2i}}{20} \times 2\pi\right) \\ &\quad - Q\left(\cos \frac{S_{1i}}{20} \times 2\pi - \cos \frac{S_{2i}}{20} \times 2\pi\right) - Y \end{aligned} \quad (4-4)$$

Making $S_i = S_{1i} - S_{2i}$, $A_i = \sin \frac{S_{1i}}{20} \times 2\pi - \sin \frac{S_{2i}}{20} \times 2\pi$, and

$B_i = \cos \frac{S_{1i}}{20} \times 2\pi - \cos \frac{S_{2i}}{20} \times 2\pi$, the error equation (4-4) becomes:

$$V_i = S_i - A_i P - B_i Q - Y \quad (4-5)$$

According to the least square method, the normal equations are:

$$\begin{pmatrix} n & \sum A_i & \sum B_i \\ \sum A_i & \sum A_i^2 & \sum A_i B_i \\ \sum B_i & \sum A_i B_i & \sum B_i^2 \end{pmatrix} \begin{pmatrix} y \\ p \\ q \end{pmatrix} = \begin{pmatrix} \sum S_i \\ \sum A_i S_i \\ \sum B_i S_i \end{pmatrix} \quad (4-6)$$

Substituting the data, the results are:

$$\begin{pmatrix} y \\ p \\ q \end{pmatrix} = \begin{pmatrix} 8.00000 \\ 0.00353 \\ 0.00353 \end{pmatrix} \tag{4-7}$$

In this way, the measured value returns to the true value, and the amplitude is $A = \sqrt{p^2 + q^2} = 0.00499 (m)$ and phase is $\phi = \arctan \frac{p}{q} = \frac{\pi}{4}$, which also return to the true values completely.

In short, the error can not only be corrected by its function model, but also be incorporated into the random model to realize its self-compensation.

5. The harm of eliminating outliers

However, in actual measurement, there are many and miscellaneous sources of errors, and it is impossible to fully understand the functional law of each error, so most of the functional model processing like example 1 is unrealistic. Moreover, some errors cannot be treated with a strict function model as example 1 to realize error correction. For example, the rounding error in Figure 1 is the sawtooth law of the true value, but the true value is precisely unknown. This is quite different from the periodic error in example 1, the random model seems to be the only way out, but the random model processing has to face the dilemma of unbalanced error distribution. The following is a simulation case to illustrate.

Example 2: The true mass values of three objects A, B and C are 5.1g, 4.2g and 7.2g respectively. Now, the readings of the precision balance are rounded to the gram bit for the combined measurement of the three objects. The original mass observation values must be as shown in Table 2. Now, we calculate the best measured value of each object mass according to the least square method to observe the response of the measured value to the true value.

Table 2. Combined observations simulated by the rounding error of the balance

Measuring method	A	B	C	A+B	A+C	B+C	A+B+C
Observed values (g)	5	4	7	9	12	11	17

Assuming that the masses of the three objects are X_1, X_2 and X_3 respectively, the error equations are:

$$\begin{pmatrix} V_1 \\ V_2 \\ V_3 \\ V_4 \\ V_5 \\ V_6 \\ V_7 \end{pmatrix} = \begin{pmatrix} 5 \\ 4 \\ 7 \\ 9 \\ 12 \\ 11 \\ 17 \end{pmatrix} - \begin{pmatrix} 1 & 0 & 0 \\ 0 & 1 & 0 \\ 0 & 0 & 1 \\ 1 & 1 & 0 \\ 1 & 0 & 1 \\ 0 & 1 & 1 \\ 1 & 1 & 1 \end{pmatrix} \begin{pmatrix} X_1 \\ X_2 \\ X_3 \end{pmatrix} \tag{5-1}$$

According to the least square method, the solution is:

$$\begin{pmatrix} x_1 \\ x_2 \\ x_3 \end{pmatrix} = \begin{pmatrix} 5.125 \\ 4.125 \\ 7.125 \end{pmatrix} \quad \text{and} \quad \begin{pmatrix} v_1 \\ v_2 \\ v_3 \\ v_4 \\ v_5 \\ v_6 \\ v_7 \end{pmatrix} = \begin{pmatrix} -0.125 \\ -0.125 \\ -0.125 \\ -0.25 \\ -0.25 \\ -0.25 \\ 0.625 \end{pmatrix}. \quad (5-2)$$

According to the cognition of mainstream research, v_7 in the equations (5-2) must be judged as a gross error, which is caused by wrong measurement and should be eliminated. After the elimination, the least square method is used again to obtain:

$$\begin{pmatrix} x_1 \\ x_2 \\ x_3 \end{pmatrix} = \begin{pmatrix} 5 \\ 4 \\ 7 \end{pmatrix} \quad \text{and} \quad \begin{pmatrix} v_1 \\ v_2 \\ v_3 \\ v_4 \\ v_5 \\ v_6 \end{pmatrix} = \begin{pmatrix} 0 \\ 0 \\ 0 \\ 0 \\ 0 \\ 0 \end{pmatrix}. \quad (5-3)$$

It can be seen that this is actually counterproductive. The residual looks very comfortable and can give a very high precision evaluation, but the error of the measured value is actually greater than that without elimination! That is, v_7 is actually a normal measurement error, the root cause of outliers is the imbalance of measurement data collection, and the high precision obtained by eliminating outliers is at the expense of trueness.

Example 3: Table 3 shows a set of simulated observation data of three-stage baseline measurement by geodimeter, assuming that points A, B, C and D are on the same straight line, the true values of three distances AB, BC and CD are all 15.0000m, and assuming that the geodimeter has only periodic error $5 \sin(\frac{d_i}{20} \times 2\pi + \frac{\pi}{3})$ (mm). Let's observe the harm of eliminating outlier by solving the best measured values of line segments AB, BC and CD.

Table 3. Observation values simulated by geodimeter's periodic error

<i>i</i>	Line segments	True values (m)	Error values (mm)	Simulated observations (m)
1	AB	15	-2.5	14.99750
2	BC	15	-2.5	14.99750
3	CD	15	-2.5	14.99750
4	AC	30	-4.3	29.99567
5	BD	30	-4.3	29.99567
6	AD	45	2.5	45.00250

1) Deal with periodic error with random model

Assuming that the true values of the three distances are Y_1, Y_2 and Y_3 respectively, the error equations are:

$$\begin{pmatrix} V_1 \\ V_2 \\ V_3 \\ V_4 \\ V_5 \\ V_6 \end{pmatrix} = \begin{pmatrix} 14.99750 \\ 14.99750 \\ 14.99750 \\ 29.99567 \\ 29.99567 \\ 45.00250 \end{pmatrix} - \begin{pmatrix} 1 & 0 & 0 \\ 0 & 1 & 0 \\ 0 & 0 & 1 \\ 1 & 1 & 0 \\ 0 & 1 & 1 \\ 1 & 1 & 1 \end{pmatrix} \begin{pmatrix} Y_1 \\ Y_2 \\ Y_3 \end{pmatrix} \tag{5-4}$$

According to the least square principle, the final measured values are:

$$\begin{pmatrix} y_1 \\ y_2 \\ y_3 \end{pmatrix} = \begin{pmatrix} 15.00000 \\ 14.99783 \\ 15.00000 \end{pmatrix} \tag{5-5}$$

Therefore

$$\begin{pmatrix} v_1 \\ v_2 \\ v_3 \\ v_4 \\ v_5 \\ v_6 \end{pmatrix} = \begin{pmatrix} 14.99750 \\ 14.99750 \\ 14.99750 \\ 29.99567 \\ 29.99567 \\ 45.00250 \end{pmatrix} - \begin{pmatrix} 1 & 0 & 0 \\ 0 & 1 & 0 \\ 0 & 0 & 1 \\ 1 & 1 & 0 \\ 0 & 1 & 1 \\ 1 & 1 & 1 \end{pmatrix} \begin{pmatrix} 15.00000 \\ 14.99783 \\ 15.00000 \end{pmatrix} = \begin{pmatrix} -2.5 \\ -0.33 \\ -2.5 \\ -2.17 \\ -2.17 \\ 4.67 \end{pmatrix} \tag{5-6}$$

According to the cognition of mainstream research, v_6 in the equation (5-6) is considered as a gross error, which is caused by wrong measurement operation and needs to be eliminated. In this way, the observation error equations become:

$$\begin{pmatrix} V_1 \\ V_2 \\ V_3 \\ V_4 \\ V_5 \end{pmatrix} = \begin{pmatrix} 14.99750 \\ 14.99750 \\ 14.99750 \\ 29.99567 \\ 29.99567 \end{pmatrix} - \begin{pmatrix} 1 & 0 & 0 \\ 0 & 1 & 0 \\ 0 & 0 & 1 \\ 1 & 1 & 0 \\ 0 & 1 & 1 \end{pmatrix} \begin{pmatrix} Y_1 \\ Y_2 \\ Y_3 \end{pmatrix} \tag{5-7}$$

According to the least square method, the final measured values are:

$$\begin{pmatrix} y_1 \\ y_2 \\ y_3 \end{pmatrix} = \begin{pmatrix} 14.99767 \\ 14.99783 \\ 14.99767 \end{pmatrix} \tag{5-8}$$

Substituting the measured values into the observation error equation, the residuals are:

$$\begin{pmatrix} v_1 \\ v_2 \\ v_3 \\ v_4 \\ v_5 \end{pmatrix} = \begin{pmatrix} -0.17 \\ -0.33 \\ -0.17 \\ 0.17 \\ 0.17 \end{pmatrix} \tag{5-9}$$

It can also be seen that after the "gross error" is eliminated, the residuals are indeed much denser, but the measured values y_1 and y_3 deviate more from the true value! This also proves that the so-called elimination of gross errors actually sacrifices trueness.

2) Deal with periodic error with functional model

The functional model of periodic error is:

$$\delta_i = M \sin\left(\frac{d_i}{20} \times 2\pi + \phi\right) = P \sin\frac{d_i}{20} \times 2\pi + Q \cos\frac{d_i}{20} \times 2\pi \quad (5-10)$$

Among equation (5-10), $P = M \cos\phi$, $Q = M \sin\phi$.

Making $a_i = \sin\frac{d_i}{20} \times 2\pi$, $b_i = \cos\frac{d_i}{20} \times 2\pi$, the observation error equations are:

$$\begin{pmatrix} V_1 \\ V_2 \\ V_3 \\ V_4 \\ V_5 \\ V_6 \end{pmatrix} = \begin{pmatrix} d_1 \\ d_2 \\ d_3 \\ d_4 \\ d_5 \\ d_6 \end{pmatrix} - \begin{pmatrix} 1 & 0 & 0 & a_1 & b_1 \\ 0 & 1 & 0 & a_2 & b_2 \\ 0 & 0 & 1 & a_3 & b_3 \\ 1 & 1 & 0 & a_4 & b_4 \\ 0 & 1 & 1 & a_5 & b_5 \\ 1 & 1 & 1 & a_6 & b_6 \end{pmatrix} \begin{pmatrix} Y_1 \\ Y_2 \\ Y_3 \\ P \\ Q \end{pmatrix} \quad (5-11)$$

Substituting the observed values, there are:

$$\begin{pmatrix} V_1 \\ V_2 \\ V_3 \\ V_4 \\ V_5 \\ V_6 \end{pmatrix} = \begin{pmatrix} 14.9975 \\ 14.9975 \\ 14.9975 \\ 29.99567 \\ 29.99567 \\ 45.0025 \end{pmatrix} - \begin{pmatrix} 1 & 0 & 0 & -1.00000 & -0.00079 \\ 0 & 1 & 0 & -1.00000 & -0.00079 \\ 0 & 0 & 1 & -1.00000 & -0.00079 \\ 1 & 1 & 0 & 0.00136 & -1.00000 \\ 0 & 1 & 1 & 0.00136 & -1.00000 \\ 1 & 1 & 1 & 1.00000 & -0.00079 \end{pmatrix} \begin{pmatrix} Y_1 \\ Y_2 \\ Y_3 \\ P \\ Q \end{pmatrix} \quad (5-12)$$

According to the least square principle, the final measured values are:

$$\begin{pmatrix} y_1 \\ y_2 \\ y_3 \\ p \\ q \end{pmatrix} = \begin{pmatrix} 15.00000 \\ 15.00000 \\ 15.00000 \\ 0.002498 \\ 0.004337 \end{pmatrix} \quad (5-13)$$

In this way, the amplitude of the periodic error is $m = \sqrt{p^2 + q^2} = 5(mm)$,

and the phase is $\phi = \arctan \frac{q}{p} = \frac{\pi}{3}$.

It can be seen that the periodic error is completely corrected, the measured values restore the true values, and the outlier here is also a normal error without any trouble.

6. Successive approximation algorithm

It has been confirmed that outliers should not be eliminated. Then, in order to benefit the final measured value, can we use the approximate function model of error? Of course, the answer is yes.

The periodic error in examples 1 and 3 can be treated by functional model because it is the function of phase, and the phase is the function of measurement serial number i , so its essence is that the error is the function of i . However, the error in example 2 is also a function of i , and the error in any measurement is a function of i , but the problem is only that their functional relationship cannot be expressed as an accurate mathematical model as examples 1 and 3. Although they cannot be expressed as an accurate mathematical model, it also should be effective to use approximate mathematical model.

According to this idea, let's see the distribution of V_i in example 2. After the adjustment, it is found that v_7 is 0.625, which is an outlier. The reason for the outlier is that the rounding error (rectangular distribution) with sawtooth regularity is unevenly sampled. Therefore, once there are two distinct residual groups, we can reasonably believe that there is a regular error component in the residuals, and its contribution to the two groups is the same, but the sign is opposite. Then, we can use the functional model of this error component to improve the observation error equations, so as to further approximate the two groups of residuals, whose principle is similar to Fourier series approximation. In this way, the observation error equations of example 2 are improved to:

$$\begin{pmatrix} V_1 \\ V_2 \\ V_3 \\ V_4 \\ V_5 \\ V_6 \\ V_7 \end{pmatrix} = \begin{pmatrix} 5 \\ 4 \\ 7 \\ 9 \\ 12 \\ 11 \\ 17 \end{pmatrix} - \begin{pmatrix} 1 & 0 & 0 & -1 \\ 0 & 1 & 0 & -1 \\ 0 & 0 & 1 & -1 \\ 1 & 1 & 0 & -1 \\ 1 & 0 & 1 & -1 \\ 0 & 1 & 1 & -1 \\ 1 & 1 & 1 & 1 \end{pmatrix} \begin{pmatrix} X_1 \\ X_2 \\ X_3 \\ C_1 \end{pmatrix} \tag{6-1}$$

According to the least square method, there are:

$$\begin{pmatrix} x_1 \\ x_2 \\ x_3 \\ c_1 \end{pmatrix} = \begin{pmatrix} 5.204545 \\ 4.204545 \\ 7.204545 \\ 0.318182 \end{pmatrix} \quad \text{and} \quad \begin{pmatrix} v_1 \\ v_2 \\ v_3 \\ v_4 \\ v_5 \\ v_6 \\ v_7 \end{pmatrix} = \begin{pmatrix} 0.11364 \\ 0.11364 \\ 0.11364 \\ -0.09091 \\ -0.09091 \\ -0.09091 \\ 0.06818 \end{pmatrix} \tag{6-2}$$

It can be seen that the residual is obviously approached, its distribution is improved, and the outlier phenomenon disappears. However, it is obvious that there are still two groups of positive and negative residuals. We can continue this idea and make the approximation algorithm again, so the error equations become:

$$\begin{pmatrix} V_1 \\ V_2 \\ V_3 \\ V_4 \\ V_5 \\ V_6 \\ V_7 \end{pmatrix} = \begin{pmatrix} 5 \\ 4 \\ 7 \\ 9 \\ 12 \\ 11 \\ 17 \end{pmatrix} - \begin{pmatrix} 1 & 0 & 0 & -1 & 1 \\ 0 & 1 & 0 & -1 & 1 \\ 0 & 0 & 1 & -1 & 1 \\ 1 & 1 & 0 & -1 & -1 \\ 1 & 0 & 1 & -1 & -1 \\ 0 & 1 & 1 & -1 & -1 \\ 1 & 1 & 1 & 1 & 1 \end{pmatrix} \begin{pmatrix} X_1 \\ X_2 \\ X_3 \\ C_1 \\ C_2 \end{pmatrix} \tag{6-3}$$

According to the least square method, the solutions are:

$$\begin{pmatrix} x_1 \\ x_2 \\ x_3 \\ c_1 \\ c_2 \end{pmatrix} = \begin{pmatrix} 5.2 \\ 4.2 \\ 7.2 \\ 0.3 \\ 0.1 \end{pmatrix} \quad \text{and} \quad \begin{pmatrix} v_1 \\ v_2 \\ v_3 \\ v_4 \\ v_5 \\ v_6 \\ v_7 \end{pmatrix} = \begin{pmatrix} 0 \\ 0 \\ 0 \\ 0 \\ 0 \\ 0 \\ 0 \end{pmatrix}. \tag{6-4}$$

Similarly, this method is also used for example 3. After going through two rounds approximation algorithm, there are:

$$\begin{pmatrix} y_1 \\ y_2 \\ y_3 \\ c_1 \\ c_2 \end{pmatrix} = \begin{pmatrix} 14.99963 \\ 14.99963 \\ 14.99963 \\ 0.00287 \\ 0.00073 \end{pmatrix} \quad \text{and} \quad \begin{pmatrix} v_1 \\ v_2 \\ v_3 \\ v_4 \\ v_5 \\ v_6 \end{pmatrix} = \begin{pmatrix} 0 \\ 0 \\ 0 \\ 0 \\ 0 \\ 0 \end{pmatrix}. \tag{6-5}$$

The authenticity of the measured values is obviously better than that treated according to the random model.

Now, this method is also applied to example 1. After four rounds approximation algorithm, the following results are obtained:

$$\begin{pmatrix} y \\ c_1 \\ c_2 \\ c_3 \\ c_4 \end{pmatrix} = \begin{pmatrix} 8.000032 \\ 0.005290 \\ 0.002386 \\ 0.001136 \\ 0.000326 \end{pmatrix} \tag{6-6}$$

Compared with the measured value of 8.0014 processed by the random model in the original example, the error of the measured value of 8.000032 is reduced by 45 times. The function model parameter value $c_1 \sim c_4$ shows obvious convergence, which also shows the effectiveness of the method.

In the three cases, the observed values are simulated by the true values plus errors,

and the effectiveness of the algorithm is tested by the ability of the final measured value to respond to the true value. In terms of effect, the final measured values of the three cases have been greatly improved compared with the pure random model. Now, let's see the application effect of a practical case.

Example 4: Table 4 is a set of observation data that using six segment baselines method calibrate additive and multiplicative constant error of a geodimeter, and the successive approximation algorithm is used to solve the best estimation of additive and multiplicative constant error.

Table 4. Observation data for calibrating the additive and multiplicative constant error of geodimeter

Instrument model: DTM-310 Serial number: 010086			
Test location: Wuhan baseline field for length calibration			
<i>i</i>	Baseline values	Observed values	Error values
	D_i (m)	D'_i (m)	y_i (mm)
1	264.23900	264.24038	-1.38
2	192.22441	192.22620	-1.79
3	312.32239	312.32532	-2.93
4	408.41467	408.41696	-2.29
5	432.43573	432.43840	-2.67
6	960.97569	960.97867	-2.98
7	456.46341	456.46539	-1.98
8	120.09798	120.09947	-1.49
9	216.19026	216.19136	-1.10
10	240.21132	240.21255	-1.23
11	480.50624	480.50906	-2.82
12	768.75128	768.75395	-2.67
13	576.56139	576.56419	-2.80
14	120.11334	120.11362	-0.28
15	360.40826	360.41033	-2.07
16	648.65330	648.65567	-2.37
17	24.02106	24.02290	-1.84
18	264.31598	264.31837	-2.39
19	552.56102	552.56371	-2.69
20	240.29492	240.29698	-2.06
21	528.53996	528.54266	-2.70

Assuming that the additive and multiplicative constant errors of the geodimeter are K and R respectively, the error equation is:

$$V_i = y_i - K - D_i R \tag{6-7}$$

According to the least square method, the measured values of the two errors are:

$$\begin{pmatrix} k \\ r \end{pmatrix} = \begin{pmatrix} -1.28mm \\ -2.16 \times 10^{-6} \end{pmatrix} \tag{6-8}$$

The standard deviations are:

$$\begin{pmatrix} m_0 \\ m_{\Delta k} \\ m_{\Delta r} \end{pmatrix} = \begin{pmatrix} \pm 0.52mm \\ \pm 0.23mm \\ \pm 5.1 \times 10^{-7} \end{pmatrix} \tag{6-9}$$

Now, according to the approximation algorithm, after four rounds of approximation algorithm, we get:

$$\begin{pmatrix} k \\ r \\ c_1 \\ c_2 \\ c_3 \\ c_4 \end{pmatrix} = \begin{pmatrix} -1.083mm \\ -2.589 \times 10^{-6} \\ 0.479mm \\ 0.271mm \\ 0.143mm \\ 0.094mm \end{pmatrix} \quad (6-10)$$

The standard deviations are:

$$\begin{pmatrix} m_0 \\ m_{\Delta k} \\ m_{\Delta r} \\ m_{\Delta c_1} \\ m_{\Delta c_2} \\ m_{\Delta c_3} \\ m_{\Delta c_4} \end{pmatrix} = \begin{pmatrix} \pm 0.073mm \\ \pm 0.033mm \\ \pm 7.3 \times 10^{-8} \\ \pm 0.017mm \\ \pm 0.017mm \\ \pm 0.017mm \\ \pm 0.017mm \end{pmatrix} \quad (6-11)$$

It can be seen that the quality of the results is greatly improved because the approximation algorithm corrects the regular errors such as the residual periodic error of the geodimeter, which greatly weakens their impact on the final measured values.

In short, the core of understanding this principle is to abandon the traditional thinking that the residual must be white noise, and recognize that the residual itself has regularity[7]. The theoretical basis of this method is that various regular errors are the root causes of dispersion and outlier, the residuals not only follow random distribution (including abnormal distribution) but also have regularity, and the error can be treated not only according to random model, but also according to function model. Its principle is to use the approximate function model of error to gradually approximate the actual function model of error to realize error correction. Its essence is to fit the error according to the function model $V(i) = C_1 f_1(i) + C_2 f_2(i) + \dots$, so it can effectively overcome the imbalance of sampling. Of course, the premise of the effectiveness of this method is that the overall characteristics of the error have been sampled and cannot be seriously missing (eliminated).

It should be pointed out that according to this algorithm, when the redundant observations are sufficient, the precision can be much higher than that of random model processing, because when there are enough redundant observations, the law details of the residuals can be displayed and the model fitting can be accurate; when there are few repeated observations, the regularity of the residuals cannot be fully displayed, the approximation times are limited, and the fitting effect will naturally be limited.

7. About the real gross error

Now, another problem is: how to distinguish the real gross errors caused by wrong

measurement? The answer is, to take the index of maximum permissible error (MPE) of the measuring instrument (sensor) as the judgment basis. When the standard deviation given by the least square method is consistent with this index, of course, it can be judged that all observed values are normal; on the contrary, due to wrong operation (including instrument failure), the error can reach thousands of times of the nominal tolerance index of the instrument, which is very easy to find in the adjustment and does not need too complex mathematical principles at all.

For example, there was a fault phenomenon of "ten meters" error in the early phase geodimeter, and its error value was an integral multiple of the precision ruler length (the precision ruler length of the early rangefinder was mostly 10 meters, which rarely appeared after improving the instrument design). The physical principle of its formation is that many electric rulers of different lengths are used in the phase geodimeter for measurement, when the measurement error of the long ruler is greater than $1/2$ of the length of the fine ruler, there will be errors in the connection between the measured values of the fine measurement and the rough measurement. However, this error can reach thousands of times of the nominal precision of the instrument, and can even appear in several observation equations of the traverse network many times. When the standard deviation given by the least square method reaches thousands of times of the nominal limit difference of the instrument, I believe anyone can know that there is a problem with the data. Therefore, this gross error in a traverse network can be easily identified without complex mathematical methods. The processing method is usually to send the instrument for repair, inspection and re measurement. I believe no one dares to use some mathematical method to save this kind of measurement data containing a large number of gross errors.

That is, there is no necessary relationship between outliers and gross errors, and outliers are not necessarily gross errors.

8. Conclusion

Through the physical mechanism of deviation, dispersion and outlier of repeated observations, this paper expounds that the discrete error sample sequence follows both random distribution and regularity, and can realize adjustment not only by self-compensation, but also by function model correction. Therefore, a function model correction algorithm using the approximate function model of error to realize successive approximation is derived, which greatly improves the quality of measured values, and can effectively overcome the influence of outlier error. Effectively using outliers and clearly opposing weakening their influence, this new theoretical idea challenges the mainstream robust estimation research, and completely changes the research direction of measurement theory.

References

- [1] N Cressie, DM Hawkins. Robust estimation of the variogram. *Journal of the International Association for Mathematical Geology*, April 1980, Volume 12, Issue 2, pp 115–125
- [2] S. J. Devlin, R. Gnanadesikan, J. R. Kettenring. Robust Estimation of Dispersion Matrices and Principal Components, *Journal of the American Statistical Association*, 1981, 76 (374) :354-362

- [3] De-ren LI. Gross Error Location by Means of the Iteration Method with Variable Weights. Journal of Wuhan University, 1984.
- [4] Yuan-xi YANG. Robust Estimation Theory and Its Application. Bayi Publishing House, 1993
- [5] Xiao-ming YE, Mo LING, Qiang ZHOU, Wei-nong WANG, Xue-bin XIAO. The New Philosophical View about Measurement Error Theory. Acta Metrologica Sinica, 2015, 36(6): 666-670.
- [6] Xiao-ming YE, Xue-bin XIAO, Jun-bo SHI, Mo LING. The New Concepts of Measurement Error Theory. Measurement, Volume 83, April 2016, Pages: 96-105.
- [7] Xiao-ming YE, Hai-bo LIU, Mo LING, Xue-bin XIAO. The New Concepts of Measurement Error's Regularities and Effect Characteristics [J]. Measurement, Volume 126, October 2018, Pages: 65-71.
- [8] Xiao-ming YE, Shi-jun DING. Comparison of Variance Concepts Interpreted by Two Measurement Theories. Journal of Nonlinear and Convex Analysis, Volume 20, Number 7, 2019, Pages: 1307-1316.
- [9] Hui-sheng SHI, Xiao-ming YE, Cheng XING, Shi-jun DING. Originand Evolution of Conceptual Differences between Two Measurement Theories, Fuzzy Systems and Data MiningVI, 2020.11.
- [10] Hui-sheng SHI, Xiao-ming YE, Cheng XING, Shi-jun DING. A New Theoretical Interpretation of Measurement Error and Its Uncertainty. Discrete Dynamics in Nature and Society, 2020. DOI: <https://doi.org/10.1155/2020/3864578>.
- [11] Xiao-ming YE, Shi-jun DING, Hui-sheng SHI. True Value Centered Theory and Measured Value Centered Theory in Measurement Error Theories, Metrology science and technology, 2021-3
- [12] Hai-bo LIU, Xiao-ming YE, Jia-bao LIU, Shi-jun DING. Mathematical Concepts of Numerical Value and Variable in the Interpretation of Measurement Theory, Journal of Nonlinear and Convex Analysis, Volume 23, Number 9, 2021-2034, 2022.
- [13] Xiao-ming YE. Measurement Error Theory Based on New Concepts. Wuhan: Hubei Science and Technology Press, 2017.

Uncertainty Measurement of Variable Precision Fuzzy Soft Rough Set Model

Xinyi WANG ^{a,b} and Qinghai WANG ^{a,b,1}

^aSchool of Computing, Qinghai Normal University, Xining, China

^bAcademy of Plateau Science and Sustainability, Xining, China

Abstract. Aiming at solving the uncertainty of knowledge in variable precision fuzzy soft rough set model. Firstly, from the perspectives of the approximated set and fuzzy equivalent soft approximation space, the uncertainty measurement methods of variable precision fuzzy soft rough set model are defined, such as information granularity, information entropy, rough entropy, etc; Secondly, many related theorems of the measurement methods are given and proved, the monotonicity of the measurement methods are obtained when the fuzzy equivalent soft relation satisfies the inclusion condition; Finally, the feasibility and validity of the definition are verified by an example.

Keywords. variable precision, soft rough set, measurement of uncertainty

1. Introduction

Because of the complexity, diversity and motion change of knowledge in practical problems, people are uncertainty about the expression of knowledge. There are two main reasons for the emergence of uncertainty: on the one hand, people's cognition of knowledge is limited; On the other hand, knowledge has a certain degree of randomness, fuzziness, instability and so on. To deal with the uncertainty problems, we should express and measure the uncertainty of knowledge through proper methods. Entropy is first used to describe the state of matter in a thermodynamic system, later it is used to describe the degree of irregular motion in a thermodynamic system. With the development of information theory, people found that entropy can be used to describe the uncertainty degree of knowledge, entropy combined with probability theory can also measure the uncertainty of knowledge. Inspired by this, Shannon proposed the concept of information entropy to measure the uncertainty of knowledge[1]. Many subsequent researchers defined different entropies to measure uncertainty problems according to different situations. For example, rough entropy is used to measure the roughness of rough set models, fuzzy entropy is used to measure the fuzziness of rough set models. Entropy is widely used in data processing[2], attribute reduction[5] and other fields.

Entropy is one of the methods to measure uncertainty. Compared with other uncertainty measurement methods, entropy has the advantages of simple definition, simple calculation and intuitive reflection of uncertainty. Combining probability theory with entropy, Liang et al. defined rough entropy to measure the roughness of rough set

¹ Corresponding Author, Qinghai WANG, School of Computing, Qinghai Normal University, Xining, China; E-mail: wangqinghai@qhnu.edu.cn.

models. They explored the relationship between different measurement methods, and verified that this measurement method based on entropy could also be used to measure the fuzziness of rough set models[8]. Liang et al. proved the relationship between rough entropy, information entropy and information granularity. They discussed the monotonicity of uncertainty problems in approximate space in this paper[9]. Qian et al. based on the relationship between two kinds of knowledge in the approximation space, proposed to measure the uncertainty in incomplete information systems using combinatorial entropy[10]. Yang et al. discussed the related properties of information entropy and the relationship between information entropy and other uncertainty measurement methods in intuitionistic fuzzy information systems[11]. Mi et al. discussed uncertainty measurement from the perspective of fuzziness. In the partition based on fuzzy rough set model, fuzzy entropy was defined to measure the fuzziness of knowledge, which reflected the degree of ambiguity of knowledge itself[12]. Chen et al. designed the rough entropy thresholding segmentation algorithm, constructed upper and lower approximate sets' rough uncertainty, and verified the effectiveness of the algorithm through experiments[13]. It can be seen that entropy is an effective mathematical method to measure the uncertainty of rough set model and its related models. The use of entropy measure is more suitable for solving the uncertainty problem of mathematical model of practical problems, which can help people to understand the nature and characteristics of data model objectively, also help to apply the model to solve practical problems.

Soft set theory is different from the existing parametric tools used to deal with uncertain data[14]. It uses the mapping between objects and attributes to express the relationship between them. In order to further combine soft set with rough set and fuzzy set to solve mathematical problems in real life, fuzzy soft set, soft rough set and other mathematical models have been proposed and popularized. Fuzzy soft set uses the parameterized feature of soft set to describe the relationship between objects and attributes in fuzzy environment[15]. Khan mentioned in the paper that fuzzy soft set can solve the problem of actual data decision-making in an imprecise environment[16]. Feng discusses the related properties and theorems of fuzzy sets in soft rough approximation space and verifies that the combination of soft sets and different mathematical models can be applied to solve more complex mathematical problems[17]. The advantage and limitation of fuzzy soft set model and fuzzy soft rough set model are shown in Table 1:

Table 1. The advantage and limitation of fuzzy soft set model and fuzzy soft rough set model

Set	Advantage	Limitation
Fuzzy soft set	It can express the relationship between objects and attributes in fuzzy environment.	It is not conducive to the processing of fuzzy environment data.
Fuzzy soft rough set	It is good for processing the data in fuzzy environment.	It is strict with the classification requirements for the processed data.

Variable precision rough set[18], as an extended rough set model using fault-tolerant mechanism, solves the problem of excessive classification requirements in classical rough set models in accurate environments. Subsequently, Katezberg and Ziarko[19] proposed a variable precision rough set model based on asymmetric boundaries u and l ($0 \leq l < u \leq 1$), which improved the original variable precision rough set model by using the upper and lower approximations of the asymmetric boundary limiting set. Xing et al. applied the variable precision rough set model combined with Bayesian method to the diagnosis of tumor cases[20]. Wu et al. proposed the image multi-threshold segmentation algorithm using variable precision rough set to solve the classification error problem of background subgraph and target subgraph[21]. In recent years, variable precision fuzzy

rough set model has become a mathematical tool to solve the problem of strict classification requirements in fuzzy environment. The model is beneficial to reduce the influence of noise data. A Mieszkowicz-Rolka and L Rolka used the research method of excluding objects that may affect the quality of the upper approximation and lower approximation results through cut-set when constructing the variable precision fuzzy rough set mode[22]. In the membership function approximated under the definition, the "better" objects are used instead of all objects; in the membership function of the upper approximation, the identification range of the upper approximation is expanded by some "good" objects after intercepting. Zhang et al. proposed a variable precision fuzzy rough set model based on coverage, extended the variable precision rough set model to cover fuzzy environment, discussed the properties of the model and cited examples to prove[23]. Gong et al. defined implicit operators and membership functions, explained the principle and application of operators, cited examples to prove the feasibility of the model[24]. Combining the knowledge expression characteristics of soft set theory with the robustness of variable precision fuzzy rough set model is helpful to analyze the mathematical model that built on the premise of fuzzy soft relation, solving the related mathematical problems of constructing fuzzy knowledge from actual fuzzy data.

Based on the variable precision fuzzy soft rough set model, this paper proposes many uncertainty measurement methods based on the idea of entropy, deeply studies the mathematical characteristics of the variable precision fuzzy soft rough set model, which is helpful to analyze and measure the uncertainty in the process of constructing fuzzy soft knowledge from actual fuzzy data. Firstly, from the perspectives of the approximated set and fuzzy equivalent soft approximation space, the uncertainty measurement methods of variable precision fuzzy soft rough set model are defined; Secondly, many related theorems of the measurement methods are given and proved, the monotonicity of the measurement methods are obtained when the fuzzy equivalent soft relation satisfies the inclusion condition; Finally, the feasibility and validity of the definition are verified by an example.

2. Preliminaries

Define 2.1[25] Let U be a finite universe of discourse. A fuzzy set A on U is described as: $A = \{(u, \mu_A(u)) | u \in U\}$, in which $\mu_A(u)$ denotes the possible membership degrees of the elements $u \in U$ to the set A , with the conditions: for $\forall u \in U$, $0 \leq \mu_A(u) \leq 1$. All fuzzy sets on U are represented as $F(U)$. $\forall A, B \in F(U) \forall u \in U$, there has $A \cap B = \frac{\mu_A(u) \wedge \mu_B(u)}{u}$. The cardinality of a fuzzy set A is defined as: $|A| = \sum_{u \in U} \mu_A(u)$. The α -level cut set of fuzzy set A , denoted by A_α , is defined as: $A_\alpha = \{u \in U | \mu_A(u) \geq \alpha\}$, for $\alpha \in [0, 1]$. Meanwhile, we call the set $\text{supp } A = \{u \in U | \mu_A(u) > 0\}$ is the support of set A .

Define 2.2[14] Let U be a finite universe of discourse, E be a set of parameters of U , $A \subseteq E$, $F(U)$ be all fuzzy sets on U . When the mapping f satisfies the condition $f: E \rightarrow F(U)$, the pair $\varepsilon = (f, E)$ is a fuzzy soft set over universe U . $R: U \times E \rightarrow [0, 1]$ is called a fuzzy soft relation from U to E , which is defined as $R = \{(u, e), \mu_R(u, e)) | (u, e) \in U \times E\}$, where $\mu_R: U \times E \rightarrow [0, 1]$ $\mu_R(u, e) = \mu_{f(e)}(u)$.

Define 2.3[26] Let U be a finite universe of discourse, E be a set of parameters of U , $A \subseteq E$, $F(E)$ be all fuzzy sets on E . When the mapping \tilde{f} satisfies the condition $\tilde{f}: U \rightarrow F(E)$, the pair $\varepsilon = (\tilde{f}, E)$ is a pseudo fuzzy soft set over universe U . $\tilde{R}: U \times E \rightarrow [0, 1]$

is called a pseudo fuzzy soft relation from U to E , which is defined as $\tilde{R} = \{ \langle (u, e), \mu_{\tilde{R}}(u, e) \rangle \mid (u, e) \in U \times E \}$, where $\mu_{\tilde{R}}: U \times E \rightarrow [0,1]$ $\mu_{\tilde{R}}(u, e) = \mu_{\tilde{f}(u)}(e)$.

Define 2.4[25] Let (f, E) be a fuzzy soft set on U , the set of all fuzzy soft relations from U to E is denoted as $F_S(U \times E)$. Let (\tilde{f}, E) be a pseudo fuzzy soft set on U , the set of all pseudo fuzzy soft relations from U to E is denoted as $\tilde{F}_S(U \times E)$. For $R_i \in F_S(U \times E)$, $R_j \in \tilde{F}_S(U \times E)$, if $(u_i, u_j) \in R$ indicated by $\exists v \in E$ let $(u_i, v) \in R_i$ and $(v, u_j) \in R_j$, which is called that the soft fuzzy relation R over U is synthetic by a fuzzy soft relation from U to E and a pseudo fuzzy soft relation from U to E , is denoted as $R = R_i \circ R_j$, $R = \{ \langle (u, u), \mu_R(u, u) \rangle \mid (u, u) \in U \times U \}$, where $\mu_R: U \times U \rightarrow [0,1]$ $\mu_R(u, u) = \mu_{f(u)}(u)$. If the fuzzy soft relation R over U satisfies reflexivity, symmetry and transitivity, R is called a fuzzy equivalent soft relation on U .

Define 2.5[22] Let U be a finite universe of discourse, $\forall A, B \in F(U)$, a fuzzy set A contained in a fuzzy set B is defined as: $A \subseteq B \Leftrightarrow \forall x \in U, \mu_A(x) \leq \mu_B(x)$. The fuzzy inclusion set of A in B is denoted by A^B , the membership function of fuzzy set A^B is defined as: $\mu_{A^B}(x) = \begin{cases} I(\mu_A(x), \mu_B(x)), & \mu_A(x) > 0 \\ 0, & \text{otherwise} \end{cases}$. We introduce the measure of α -inclusion error $e_\alpha(A, B)$ of any fuzzy set A in a fuzzy B : $e_\alpha(A, B) = 1 - \frac{\text{power}(A \cap A_\alpha^B)}{\text{power}(A)}$, among them, $\text{power}(A) = \sum_{i=1}^n \mu_A(u_i)$ is the cardinality of a fuzzy set A , the α -level cut set of fuzzy set A^B is denoted by A_α^B .

Define 2.6 Let U be a finite universe of discourse, E be a set of parameters of U , (f, E) and (\tilde{f}, E) are a fuzzy soft set and a pseudo fuzzy soft set from U to E , R_i and R_j are fuzzy equivalent soft relation and pseudo fuzzy equivalent soft relation from U to E , R is fuzzy equivalent soft relation on U which is synthesized by R_i and R_j , the pair (U, R) is called fuzzy equivalent soft approximation space. $\forall u_i \in U$, the fuzzy equivalent soft partition derived from u_i and R is represented as a fuzzy set, which membership function is defined as $U_i(u) = R(u_i, u)$ $i = 1, 2, \dots, n$. The boundary s, t satisfies the conditions: $0 \leq s < t \leq 1$, for any $A \in F(U)$, the s -lower approximation set of A and the t -upper approximation set of A in the fuzzy equivalent soft approximation space are defined as follows:

$$\begin{aligned} & \underline{R}_t^s(A)(u_i) \\ &= \begin{cases} \inf_{u \in S_{is}} I(U_i(u), A(u)) & \exists \alpha_s = \sup\{ \alpha \in (0,1] \mid e_\alpha(U_i, A) \leq 1 - s \} \\ 0 & \text{otherwise} \end{cases} \end{aligned} \tag{1}$$

$$S_{is} = \text{supp}(U_i \cap (U_i^A)_{\alpha_s}) \tag{2}$$

$$e_\alpha(U_i, A) = 1 - \frac{\text{power}(U_i \cap (U_i^A)_\alpha)}{\text{power}(U_i)} \quad i = 1, 2, \dots, n. \tag{3}$$

$$\begin{aligned} & \overline{R}_t^T(A)(u_i) \\ &= \begin{cases} \sup_{u \in S_{it}} T(U_i(u), A(u)) & \exists \alpha_t = \sup\{ \alpha \in (0,1] \mid e'_\alpha(U_i, A) < 1 - t \} \\ 0 & \text{otherwise} \end{cases} \end{aligned} \tag{4}$$

$$S_{it} = \text{supp}(U_i \cap (U_i \cap A)_{\alpha_t}) \tag{5}$$

$$e_{\alpha'}(U_i, A) = 1 - \frac{\text{power}(U_i \cap (U_i \cap A)_{\alpha})}{\text{power}(U_i)} \quad i = 1, 2, \dots, n. \tag{6}$$

Among them, T is the T-module operator and I is the implication operator, the pair $(\underline{R}_t^s(A), \overline{R}_t^s(A))$ is called variable precision fuzzy soft rough set of A .

3. The uncertainty measurements of variable precision fuzzy soft rough set

3.1. Uncertainty measure for fuzzy equivalent soft approximation space

Define 3.1.1 In the fuzzy equivalent soft approximation space, there exists an exact subset $U_s = \{u_1, u_2, \dots, u_m \mid m \leq n\}$ in the universe $U = \{u_1, u_2, u_3, \dots, u_n\}$, A subset U_s conditions to be fulfilled: $U_s = \text{supp}(U_i \cap (U_i^A)_{\alpha_s})$, where $F(U_s)$ denoted by all fuzzy sets on U_s . For any $A \in F(U_s)$, $\forall u_i \in U_s$, the fuzzy equivalent soft partitions derived from u_i and R are represented as fuzzy sets, their membership function are defined as $U_i(u) = R(u_i, u) \mid i = 1, 2, \dots, m$. In the following definitions, the symbol $U_i(u)$ is defined in the same way.

Define 3.1.2 In the fuzzy equivalent soft approximation space (U_s, R) , the information granularity of variable precision fuzzy soft rough set under fuzzy soft equivalent relation R is defined as: $GK(R) = \frac{1}{|U_s|^2} \sum |U_i(u)|$.

Theorem 3.1.1 Let $U_s = \{u_1, u_2, u_3, \dots, u_m\}$ is a finite universe, R and P are fuzzy soft equivalent relations. $\forall u_i \in U_s$, the fuzzy equivalent soft partition derived from u_i and P is represented as a fuzzy set, its membership function is defined as $P_i(u) = P(u_i, u) \mid i = 1, 2, \dots, m$. In the following definitions, the symbol $P_i(u)$ is defined in the same way. When $R \subseteq P$, $GK(R) \leq GK(P)$.

Proof: Because $R \subseteq P$, it can be known $\forall u_i \in U_s (U_i(u) \subseteq P_i(u))$, $\forall u_i \in U_s (|U_i(u)| \leq |P_i(u)|)$, then $GK(R) = \frac{1}{|U_s|^2} \sum |U_i(u)| \leq \frac{1}{|U_s|^2} \sum |P_i(u)| \leq GK(P)$.

Define 3.1.3 In the fuzzy equivalent soft approximation space (U_s, R) , the rough entropy of variable precision fuzzy soft rough set under fuzzy soft equivalent relation R is defined as: $E_r(R) = - \sum \frac{1}{|U_s|} \log_2 \frac{1}{|U_i(u)|}$.

Theorem 3.1.2 Let $U_s = \{u_1, u_2, u_3, \dots, u_m\}$ is a finite universe, R and P are fuzzy soft equivalent relations. When $R \subseteq P$, $E_r(R) \leq E_r(P)$.

Proof: Because $R \subseteq P$, it can be known $\forall u_i \in U_s (\log_2 |U_i(u)| \leq \log_2 |P_i(u)|)$, $E_r(R) = - \sum \frac{1}{|U_s|} \log_2 \frac{1}{|U_i(u)|} \leq - \sum \frac{1}{|U_s|} \log_2 \frac{1}{|P_i(u)|} \leq E_r(P)$.

Define 3.1.4 In the fuzzy equivalent soft approximation space (U_s, R) , the information entropy based on Shannon entropy of variable precision fuzzy soft rough set under fuzzy soft equivalent relation R is defined as: $H(R) = - \frac{1}{|U_s|} \sum \log_2 \frac{|U_i(u)|}{|U_s|}$.

Theorem 3.1.3 Let $U_s = \{u_1, u_2, u_3, \dots, u_m\}$ is a finite universe, R and P are fuzzy soft equivalent relations. When $R \subseteq P$, $H(R) \geq H(P)$.

Proof: Because $R \subseteq P$, it can be known, $\forall u_i \in U_s (-\log_2 |U_i(u)| \geq -\log_2 |P_i(u)|)$, then $H(R) = - \frac{1}{|U_s|} \sum \log_2 \frac{|U_i(u)|}{|U_s|} \geq - \frac{1}{|U_s|} \sum \log_2 \frac{|P_i(u)|}{|U_s|} = H(P)$.

Define 3.1.5 In the fuzzy equivalent soft approximation space (U_s, R) , the information entropy of variable precision fuzzy soft rough set under fuzzy soft equivalent relation R is defined as: $E(R) = \frac{1}{|U_s|} \sum \left(1 - \frac{|U_i(u)|}{|U_s|} \right)$.

Theorem 3.1.4 Let $U_s = \{u_1, u_2, u_3, \dots, u_m\}$ is a finite universe, R and P are fuzzy soft equivalent relations. When $R \subseteq P$, $E(R) \geq E(P)$.

Proof: Because $R \subseteq P$, it can be known $\forall u_i \in U_s (|U_i(u)| \geq |P_i(u)|)$, then $E(R) = \frac{1}{|U_s|} \sum \left(1 - \frac{|U_i(u)|}{|U_s|} \right) \geq \frac{1}{|U_s|} \sum \left(1 - \frac{|P_i(u)|}{|U_s|} \right) = E(P)$.

Define 3.1.6 The combined entropy and conditional entropy of the variable precision fuzzy soft rough set under fuzzy equivalent soft relation R and P are defined as: $E(P; R) = \frac{1}{|U_s|} \sum \left(1 - \frac{|U_i(u) \cap P_i(u)|}{|U_s|} \right)$, $E(P|R) = \frac{1}{|U_s|} \sum \left(\frac{|U_i(u)|}{|U_s|} - \frac{|U_i(u) \cap P_i(u)|}{|U_s|} \right)$.

Theorem 3.1.5 Let $E(R)$ is the information entropy of variable precision fuzzy soft rough set under fuzzy soft equivalent relation R in finite universe $U_s = \{u_1, u_2, u_3, \dots, u_m\}$, then $E(P|R) = E(P; R) - E(R)$.

Proof: $E(P|R) - E(P; R) = \frac{1}{|U_s|} \sum \left(\frac{|U_i(u)|}{|U_s|} - 1 \right) = -E(R)$.

3.2. Uncertainty measure for approximated set

Define 3.2.1 In the fuzzy equivalent soft approximation space (U_s, R) , $\forall u_i \in U_s$, the fuzzy equivalent soft partitions derived from u_i and R are represented as fuzzy sets, their membership function are defined as $U_i(u) = R(u_i, u) \ i = 1, 2, \dots, m$. For $\forall A \in F(U_s)$, variable precision fuzzy soft rough set of A is denoted by $(\underline{R}_i^s(A), \overline{R}_i^T(A))$, where $\underline{R}_i^s(A)$ represents the s-lower approximate set of A, $\overline{R}_i^T(A)$ represents the t- upper approximate set of A. The roughness of the variable precision fuzzy soft rough set under fuzzy equivalent soft relation R is defined as: $\rho_R = 1 - \frac{|\underline{R}_i^s(A)|}{|\overline{R}_i^T(A)|}$.

Theorem 3.2.1 Let $U_s = \{u_1, u_2, u_3, \dots, u_m\}$ is a finite universe, R and P are fuzzy soft equivalent relations. When $R \subseteq P$, $\rho_R \leq \rho_P$.

Proof: Because $R \subseteq P$, it can be known $\forall u_i \in U_s (U_i(u) \subseteq P_i(u))$. Assuming that the set S_{is} and the set S_{it} are the same under the fuzzy equivalent soft relation R and P, then according to the definition discussion:

Let $I(x, y) = \max(1 - x, y)$, $T(x, y) = \min(x, y)$. Because $\forall u_i \in U_s (U_i(u) \subseteq P_i(u))$, it can be known $\forall u_i \in U_s (1 - U_i(u) \supseteq 1 - P_i(u)) \ i = 1, 2, \dots, m$.

(1)When $\max(1 - U_i(u), A(u)) = A(u)$, $A(u) \geq 1 - U_i(u) \geq 1 - P_i(u)$, then $\max(1 - P_i(u), A(u)) = A(u)$.

(2)When $\max(1 - U_i(u), A(u)) = 1 - U_i(u)$, $1 - U_i(u) \geq A(u)$, $1 - U_i(u) \geq 1 - P_i(u)$, at this time, no matter what value $\max(1 - P_i(u), A(u))$ takes, it is less than or equal to $1 - U_i(u)$. In summary, $\underline{R}_i^s(A) \supseteq \underline{P}_i^s(A)$.

(3)When $\min(U_i(u), A(u)) = A(u)$, $A(u) \leq U_i(u) \leq P_i(u)$, $\min(P_i(u), A(u)) = A(u)$.

(4)When $\min(U_i(u), A(u)) = U_i(u)$, $U_i(u) \leq A(u)$, $U_i(u) \leq P_i(u)$, at this time, no matter what value $\min(P_i(u), A(u))$ takes, it is more than or equal to $U_i(u)$. In summary, $\overline{R}_i^T(A) \subseteq \overline{P}_i^T(A)$.

Accordingly, $\rho_R = 1 - \frac{|\underline{R}_i^s(A)|}{|\overline{R}_i^T(A)|} \leq 1 - \frac{|\underline{P}_i^s(A)|}{|\overline{P}_i^T(A)|} = \rho_P$.

Define 3.2.2 In the fuzzy equivalent soft approximation space (U_s, R) , $\forall u_i \in U_s$, the roughness based rough entropy of the variable precision fuzzy soft rough set under the fuzzy equivalent soft relation R is defined as $C(R) = \rho_R \cdot GK(R)$, where ρ_R is the roughness of the variable precision fuzzy soft rough set under fuzzy equivalent soft relation R, $GK(R)$ is the information granularity of the variable precision fuzzy soft rough set under fuzzy equivalent soft relation R.

Theorem 3.2.2 Let $U_s = \{u_1, u_2, u_3, \dots, u_m\}$ is a finite universe, R and P are fuzzy soft equivalent relations. When $R \subseteq P$, $C(R) \leq C(P)$.

Proof: From theorem 3.1.1 and theorem 3.2.1 we know that when $R \subseteq P$, $\rho_R \leq \rho_P$, $GK(R) \leq GK(P)$, then $C(R) = \rho_R \cdot GK(R) \leq \rho_P \cdot GK(P)$.

Define 3.2.3 In the fuzzy equivalent soft approximation space (U_s, R) , $\forall u_i \in U_s$, for $\forall A \in F(U_s)$, the rough membership degree of u_i with respect to A is defined as: $R(A)(u_i) = \frac{\sum_{u \in U_s} \min\{R(u_i, u), A(u)\}}{\sum_{u \in U_s} R(u_i, u)}$, where $A(u)$ represents the membership degree of element u in set A, then the fuzzy entropy of the variable precision fuzzy soft rough set under fuzzy soft equivalent relation R is defined as: $FR(A) = -\frac{2}{|U_s|} \sum_{u_i \in U_s} R(A)(u_i) \log_2 R(A)(u_i)$.

Theorem 3.2.2 In the fuzzy equivalent soft approximation space (U_s, R) , the fuzzy entropy of a definable exact set is 0.

Proof: There exists a definable exact set X in the fuzzy equivalent soft approximation space (U_s, R) . Since the set X is an exact set, $X(u)=1$ when $\forall u \in X$, $X(u) = 0$ when $\forall u \notin X$. For $\forall u_i \in U_s$, when $u \in X$, $R(X)(u_i) = \frac{\sum_{u \in U_s} \min\{R(u_i, u), X(u)\}}{\sum_{u \in U_s} R(u_i, u)} = 1$. For $\forall u_i \in U_s$, when $u \notin X$, $R(X)(u_i) = \frac{\sum_{u \in U_s} \min\{R(u_i, u), X(u)\}}{\sum_{u \in U_s} R(u_i, u)} = 0$. Accordingly, $FR(X) = -\frac{2}{|U_s|} \sum_{u_i \in U_s} R(X)(u_i) \log_2 R(X)(u_i) = 0$.

Theorem 3.2.3 In the fuzzy equivalent soft approximation space (U_s, R) , for any $A, B \in F(U_s)$, if $A \subseteq B$, $FR(A) \geq FR(B)$.

Proof: Because $A \subseteq B$, $\forall u_i \in U_s$, it can be known $R(A)(u_i) = \frac{\sum_{u \in U_s} \min\{R(u_i, u), A(u)\}}{\sum_{u \in U_s} R(u_i, u)} \leq \frac{\sum_{u \in U_s} \min\{R(u_i, u), B(u)\}}{\sum_{u \in U_s} R(u_i, u)} = R(B)(u_i)$, $-R(A)(u_i) \log_2 R(A)(u_i) \geq -R(B)(u_i) \log_2 R(B)(u_i)$, also $FR(A) \geq FR(B)$.

3.3. The relationship between uncertainty measures of variable precision fuzzy soft rough set

Theorem 3.3.1 In the fuzzy equivalent soft approximation space (U_s, R) , the information entropy based on Shannon entropy $H(R)$ of the variable precision fuzzy soft rough set under fuzzy equivalent soft relation R and rough entropy $E_r(R)$ of variable precision fuzzy soft rough set under fuzzy equivalent soft relation R have the following relationship: $H(R) + E_r(R) = \log_2 |U_s|$.

Proof: $H(R) = -\frac{1}{|U_s|} \sum \log_2 \frac{|U_i(u)|}{|U_s|} = -\frac{1}{|U_s|} \sum (\log_2 |U_i(u)| - \log_2 |U_s|) - \left(-\sum \frac{1}{|U_s|} \log_2 \frac{1}{|U_i(u)|}\right) + \sum \frac{1}{|U_s|} \log_2 |U_s| = -E_r(R) + \log_2 |U_s|$.

Theorem 3.3.2 In the fuzzy equivalent soft approximation space (U_s, R) , the information entropy $E(R)$ of the variable precision fuzzy soft rough set under fuzzy equivalent soft relation R and the information granularity $GK(R)$ of the variable

precision fuzzy soft rough set under fuzzy equivalent soft relation R have the following relationship: $E(R) + GK(R) = 1$.

$$\text{Proof: } E(R) + GK(R) = \frac{1}{|U_s|} \sum (1 - \frac{|U_i(u)|}{|U_s|}) + \frac{1}{|U_s|} \sum \frac{|U_i(u)|}{|U_s|} = \frac{1}{|U_s|} |U_s| = 1.$$

4. Example

Let $U = \{u_1, u_2, u_3, u_4, u_5, u_6\}$ represents the set of six different houses, $E = \{e_1, e_2, e_3, e_4, e_5, e_6\}$ represents the set of attributes possessed by each house, which respectively represent the price, location, basic decoration, lighting, surrounding environment and basic construction. In order to assess the six houses comprehensively, the fuzzy soft set (f, E) is used to represent the evaluation result of one of the experts as shown in Table 2, and the pseudo fuzzy soft set (\tilde{f}, E) is used to represent the evaluation result of the other expert as shown in Table 3.

Table 2. fuzzy soft set

U/E	e ₁	e ₂	e ₃	e ₄	e ₅	e ₆
u ₁	1	0.85	0.50	0.69	0.69	0.84
u ₂	0.85	1	0.50	0.65	0.65	0.84
u ₃	0.50	0.50	1	0.50	0.50	0.50
u ₄	0.69	0.50	0.50	1	0.61	0.69
u ₅	0.69	0.69	0.50	0.69	1	0.69
u ₆	0.84	0.84	0.50	0.69	0.69	1

Table 3. pseudo fuzzy soft set

U/E	e ₁	e ₂	e ₃	e ₄	e ₅	e ₆
u ₁	1	0.10	0.50	0.69	0.69	0.81
u ₂	0.35	1	0.50	0.40	0.40	0.69
u ₃	0.20	0.50	1	0.25	0.39	0.40
u ₄	0.62	0.69	0.34	1	0.50	0.69
u ₅	0.41	0.69	0.50	0.41	1	0.69
u ₆	0.30	0.50	0.50	0.30	0.60	1

Synthesizing fuzzy equivalent soft relation on U ,

$$R = \begin{pmatrix} 1 & 0.85 & 0.50 & 0.69 & 0.69 & 0.84 \\ 0.85 & 1 & 0.50 & 0.69 & 0.69 & 0.84 \\ 0.50 & 0.50 & 1 & 0.50 & 0.50 & 0.50 \\ 0.69 & 0.69 & 0.50 & 1 & 0.69 & 0.69 \\ 0.69 & 0.69 & 0.50 & 0.69 & 1 & 0.69 \\ 0.84 & 0.84 & 0.50 & 0.69 & 0.69 & 1 \end{pmatrix}$$

Let set $A \in F(U)$, $A = 0.60/u_1 + 0.65/u_2 + 0.65/u_3 + 0.70/u_4 + 0.80/u_5 + 0.85/u_6$ represents a collection of house that is rated as good, let $I(x, y) = \max(1 - x, y)$, $T(x, y) = \min(x, y)$, $s = 0.75$, $t = 0.55$, for example by u_3 , the s -lower approximate set of A and the t -upper approximate set of A are:

$$\underline{R}_s^{0.75}(A) = \{0.60/u_1, 0.65/u_2, 0.65/u_3, 0.65/u_4, 0.65/u_5, 0.65/u_6\}$$

$$\overline{R}_t^{0.55}(A) = \{0.84/u_1, 0.84/u_2, 0.65/u_3, 0.70/u_4, 0.80/u_5, 0.85/u_6\}$$

when $\alpha_s = 0.65$, $U_s = \{u_2, u_3, u_4, u_5, u_6\}$, in the fuzzy equivalent soft approximation space (U_s, R) , the fuzzy equivalent soft relation R over U_s is

$$R = \begin{pmatrix} 1 & 0.50 & 0.69 & 0.69 & 0.84 \\ 0.50 & 1 & 0.50 & 0.50 & 0.50 \\ 0.69 & 0.50 & 1 & 0.69 & 0.69 \\ 0.69 & 0.50 & 0.69 & 1 & 0.69 \\ 0.84 & 0.50 & 0.69 & 0.69 & 1 \end{pmatrix}$$

Let set $A \in F(U)$, $A = 0.65/u_2 + 0.65/u_3 + 0.70/u_4 + 0.80/u_5 + 0.85/u_6$ represents a collection of house that is rated as good, under this condition, the s -lower approximate set of A and the t - upper approximate set of A are:

$$\underline{R}_l^{0.75}(A) = \{0.65/u_2, 0.65/u_3, 0.65/u_4, 0.65/u_5, 0.65/u_6\}$$

$$\overline{R}^T_{0.55}(A) = \{0.84/u_2, 0.65/u_3, 0.70/u_4, 0.80/u_5, 0.85/u_6\}$$

In the fuzzy equivalent soft approximation space (U_s, R) , the information granularity of variable precision fuzzy soft rough set $GK(R) = 0.70$, rough entropy $E_r(R) = 1.81$, information entropy based on Shannon entropy $H(R) = 0.51$, information entropy $E(R) = 0.30$, roughness $\rho_R = 0.15$, roughness based rough entropy $C(R) = 0.11$, fuzzy entropy $FR(A) = 0.26$. If any $B \in F(U_s)$, $A \subseteq B$, $B = 0.70/u_2 + 0.70/u_3 + 0.70/u_4 + 0.80/u_5 + 0.85/u_6$, fuzzy entropy $FR(B) = 0.24$.

Let $U_s = \{u_1, u_2, u_3, \dots, u_m\}$ is a finite universe, R and P are fuzzy soft equivalent relations, and $R \subseteq P$, in the fuzzy equivalent soft approximation space (U_s, P) , the fuzzy equivalent soft relation P over U_s is

$$P = \begin{pmatrix} 1 & 0.50 & 0.69 & 0.69 & 0.84 \\ 0.50 & 1 & 0.50 & 0.50 & 0.50 \\ 0.69 & 0.50 & 1 & 1 & 0.69 \\ 0.69 & 0.50 & 1 & 1 & 0.69 \\ 0.84 & 0.50 & 0.69 & 0.69 & 1 \end{pmatrix}$$

Let set $A \in F(U)$, $A = 0.65/u_2 + 0.65/u_3 + 0.70/u_4 + 0.80/u_5 + 0.85/u_6$ represents a collection of house that is rated as good, under this condition, the s -lower approximate set of A and the t - upper approximate set of A are:

$$\underline{P}_l^{0.75}(A) = \{0.65/u_2, 0.65/u_3, 0.65/u_4, 0.65/u_5, 0.65/u_6\}$$

$$\overline{P}^T_{0.55}(A) = \{0.84/u_2, 0.65/u_3, 0.80/u_4, 0.80/u_5, 0.85/u_6\}$$

In the fuzzy equivalent soft approximation space (U_s, P) , the information granularity of variable precision fuzzy soft rough set $GK(P) = 0.72$, rough entropy $E_r(P) = 1.86$, information entropy based on Shannon entropy $H(P) = 0.46$ information entropy $E(P) = 0.29$, roughness $\rho_P = 0.17$, roughness based rough entropy $C(P) = 0.12$, the combined entropy $E(P; R) = 0.29$, conditional entropy $E(P|R) = 0$.

To sum up, the example results satisfy all the above theorems, which verifies the feasibility and effectiveness of the measurement methods.

5. Conclusion

With the in-depth study of different data models, the uncertainty of how to recognize and express knowledge has become the key to the study of mathematical models. The variable precision fuzzy soft rough set model is proposed. It combines the knowledge expression characteristics of the soft set theory with the robustness of the variable precision fuzzy rough set model, which is helpful to analyze the mathematical model

built on the premise of fuzzy soft relations, solving the problems of constructing the model based on actual fuzzy data. Based on the variable precision fuzzy soft rough set model, this paper proposes uncertainty measurement methods based on the idea of entropy, and deeply studies the mathematical properties of the variable precision fuzzy soft rough set model. The next step of this paper will be based on the variable precision intuitionistic fuzzy soft rough set model, carry out fuzzy extension research, so as to solve the problem of analyzing and processing fuzzy data under complex knowledge expression in practical application fields.

Acknowledgement

This research was supported by the Qinghai Key Laboratory of the Internet of Things (2020-ZJ-Y16) and the National Key Research and Development Project (2020YFC1523305).

References

- [1] Shannon CE. The Mathematical Theory of Communication. The Bell System Technical Journal. 1948 Jul;27(3):379-423.
- [2] Shi HT, Li YX, Ding MS, Li XB, Li ZX, Zhang ZF. Wind Power Prediction Based on Rough Set Conditional Entropy Weighted Markov Chain. Proceedings of the 2021 IEEE Sustainable Power and Energy Conference; 2021 Dec 23-25; New York, USA: IEEE Press; c2022. p. 169-72.
- [3] Sun L, Wang LY, Ding WP, Qian YH, Xu JC. Feature Selection Using Fuzzy Neighborhood Entropy-Based Uncertainty Measures for Fuzzy Neighborhood Multigranulation Rough Sets. IEEE Transactions on Fuzzy Systems. 2021 Jan;29(1):19-33.
- [4] Pal JK, Ray SS, Cho SB, Pal SK. Fuzzy-Rough Entropy Measure and Histogram Based Patient Selection for miRNA Ranking in Cancer. IEEE/ACM Transactions on Computational Biology and Bioinformatics. 2018 Mar;15(2):659-72.
- [5] Wang Z, Zheng X, Pan HG, Li DY. Information Entropy Multi-Decision Attribute Reduction Fuzzy Rough Set for Dust Particulate Imagery Characteristic Extraction. IEEE Access. 2020 Apr;8(1):77865-74.
- [6] Zhang QH, Xiao Y. New Attribute Reduction on Information Entropy. Journal of Frontiers of Computer Science and Technology. 2013 Apr;7(04):359-67.
- [7] Xiong JX, Wu JZ, Wang QH. Decision Cost Attribute Reduction of Hybrid Data Based on Neighborhood Mutual Information Entropy. Journal of Chinese Computer Systems. 2021 Aug;42(8):1584-90.
- [8] Liang JY, Chin KS, Dang CY, Yam CMR. A New Method for Measuring Uncertainty and Fuzziness in Rough Set Theory. International Journal of General Systems. 2002 Apr;31(4):331-42.
- [9] Liang JY, Shi ZZ. The Information Entropy, Rough Entropy and Knowledge Granulation in Rough Set Theory. International Journal of Uncertainty, Fuzziness and Knowledge-Based Systems. 2004 Jan;12(1):37-46.
- [10] Qian YH, Liang JY. Combination Entropy and Combination Granulation in Incomplete Information System. Lecture Notes in Computer Science. 2006 Jul;4062(1):184-90.
- [11] Yang WP, Lin ML. Information entropy in intuitionistic fuzzy information systems. Computer Engineering and Applications. 2014 Nov;50(11):130-34.
- [12] Mi JS, Leung Y, Wu WZ. An Uncertainty Measure in Partition-Based Fuzzy Rough Sets. International Journal of General Systems. 2007 Jan;34(1):77-90.
- [13] Chen BB, Fan JL, Lei B, Gao MF. SLIC superpixel granulation-based rough entropy image segmentation algorithm. Transducer and Microsystem Technologies. 2022 Feb;41(2):105-7.
- [14] Molodtsov D. Soft set theory—First results. Computers & Mathematics with Applications. 1999 Feb;37(4-5):19-31.
- [15] Maji P, Bis R, Roy A R. Fuzzy soft sets. Fuzzy Math. 2001 Jan;9(3):589-602.
- [16] Khan A, Zhu YG. A Novel Approach to Parameter Reduction of Fuzzy Soft Set. IEEE Access. 2019 Sep;7:128956-128967.

- [17] Feng F, Li CX, Dav BJ, Ali IM. Soft sets combined with fuzzy sets and rough sets: A tentative approach. *Soft Computing*. 2010 Jul;14(9):899-911.
- [18] Ziarko W. Variable Precision Rough Sets Model. *Journal of Computer & Systems Sciences*. 1993 Feb;46(1):39-59.
- [19] Katzberg JD, Ziarko W. Variable Precision Rough Sets with Asymmetric Bounds. *Rough Sets, Fuzzy Sets and Knowledge Discovery*. 1994 Oct;167-77.
- [20] Xing RF, Liu W, Fan YY. Research On Diagnosis of Tumor Based on Variable Precision Rough Set Theory. *Science & Technology Vision*. 2019 Jan;2019(03):43+7.
- [21] Wu SZ, Duan C, She ZY. Image Multi-Threshold Segmentation Algorithm Using Variable Precision Rough Set and Particle Swarm Optimization. *Journal of Northwest Normal University (Natural Science)*. 2019 Apr;55(02):65-72.
- [22] Alicja MR, Leszek R. Variable Precision Fuzzy Rough Sets. *Lecture Notes in Computer Science*. 2004 Dec;3100(1):144-60.
- [23] Zhang AQ, Ha MH, Fan YJ. Variable Precision Fuzzy Rough Set Model Based on Fuzzy Covering. *Proceedings of the International Conference on Innovative Computing Information & Control*; 2008 Jun 18-20; New York, USA: IEEE Press; c2008. p. 399-399.
- [24] Gong ZT, Zhang XX. Variable Precision Intuitionistic Fuzzy Rough Sets Model and Its Application. *International Journal of Machine Learning & Cybernetics*. 2014 Apr;5(2):263-80.
- [25] Li LH, Li S, Li Y, Yang YF. *Fuzzy sets and rough sets*. Beijing: Tsinghua University Press; 2015. 196 p.
- [26] Sun BZ, Ma WM. Soft Fuzzy Rough Sets and Its Application in Decision Making. *Artificial Intelligence Review: An International Science and Engineering Journal*. 2014 Jan;41(1):67-80.

Prediction and Analysis of Stock Logarithmic Returns Based on ARMA-GARCH Model

Hao Qi¹ and Yuanshen Wang

School of Mathematics and Big Data, Chongqing University of Arts and Sciences, China

Abstract. With the rapid development of economy, investment has become a hot word. Many people hope to find an investment method to make profits. Many investment methods such as stocks, wealth management and funds have emerged. In the process of investment, forecasting the trend of investment products is one of the most important links. This paper analyzes the time series of APPLE, AMERICAN AIRLINES and AMD based on ARMA-GARCH model, and evaluates the model according to AIC, BIC, HQIC and other indicators to select the optimal model. The research results show that ARMA (3,2) - GARCH (1,1) model is applicable to APPLE stock logarithmic profit Prediction, ARMA (2,2) model is applicable to AMERICAN AIRLINES stock logarithmic profit prediction, and ARMA (2,2) - GARCH (1,1) is applicable to AMD stock logarithmic profit prediction.

Keywords. Stock, Return, Prediction, ARMA, GARCH

1. Introduction

With the development of economy and the improvement of residents' income, residents hope to find an investment method that can be used as a sideline, such as stocks, funds and real estate. At the same time, investors are also very careful to choose the investment products, hoping to maximize profits (see [1]). Therefore, before investing, investors need to predict the price of the investment product in the future according to the price of the investment product in the past period to predict whether the purchase of the product will generate profits and evaluate the investment risk.

This paper mainly uses Autoregressive Moving Average Model and Generalized Autoregressive Conditional Heteroskedasticity Model(ARMA-GARCH) to predict the APPLE stock returns, American Airlines and Advanced Micro Devices(AMD). The ARMA model can predict stationary time series data, and it reduces the steps of difference in the ARIMA model proposed by Box, G. and Jenkins, G (see [2]). In 1982, the Model was proposed by Engle was ARCH, and this model was suitable for heteroscedastic financial time series. Bollerslev proposed a model called GARCH in 1986, and established a conditional heteroscedastic time series model of investment price and return in 1987 (see [3-5]).

¹ Corresponding Author, Hao Qi, *Chongqing University of Arts and Sciences, China*; Email: qih33333@163.com

2. Related Works

Stock is a very common option in investment. Many people hope to gain income by investing in stocks. The information measurement of expected investment is very important in stock trading. Shareholders need to know the daily closing price, increase and other important information of stocks in real time (see [6]).

As stock forecasting is a hot research field, Jörg Gottschlich and Oliver Hinz [7] use BFO and ABFO technologies to develop a prediction model with better accuracy and faster convergence than those based on genetic algorithm (GA) and particle swarm optimization (PSO) for stock prediction (see [7]). Using historical information of the stock closing price to predict the future stock price trend by using random walk model is very difficult. Therefore, Ritika Singh and Shashi Srivastava respectively built three kinds of neural networks, including deep neural network (DNN), to predict stock returns, and concluded that DNN has a better prediction effect than RBFNN and RNN (see [8]). Wenjie Lu et al. combined the Convolutional neural networks (CNN), bi directional long short term memory (BiLSTM) and Attention Mechanism (AM) to form the CNN-BiLSTM-AM stock price prediction. The experimental results show that CNN-BiLSTM-AM has the highest accuracy in predicting stock returns compared with the prediction results of eight methods, including MLP, CNN and RNN (see [9]). When selecting investment products such as stocks, traders need to use a variety of forecasting techniques to obtain information about the stock market, rather than a single method. Phichhang Ou discussed ten different data mining technologies, such as linear discriminant analysis (LDA), support vector machine (SVM) and least squares support vector machine, and applied them to the price trend prediction of Hang Seng Index in Hong Kong stock market. The experimental results show that support vector machine and least squares support vector machine have superior performance in predicting the price trend of Hang Seng Index in Hong Kong stock market (see [10]).

The ARMA-GARCH model has a wide range of applications, in which ARMA can predict stationary time series data. Before analyzing and predicting the time series data, it is necessary to perform unit root test (ADF test) on the data. When the data is verified to be a stationary time series, ARMA model can be used for prediction. Jingli Yang and Xiaofeng Zhou will apply ARMA model to PM 2.5. The results showed that the ARMA model can achieve the expected prediction effect (see [11]). Mohammad Valipour et al. used ARMA model and ARIMA model to predict the inflow of Dez Dam Reservoir every month from 1960 to 2007 (see [12]). J. L. Torres et al. verified that the wind speed prediction performance of ARMA is significantly better than that of the persistence model, especially in the long-term prediction (see [13]).

When ARMA model is used alone, the variance equation will be ignored and many parameters need to be estimated. The combination of ARMA model and GARCH model can overcome this shortcoming, and GARCH model can fully describe the volatility process of asset returns (see [14]). During the investigation of ARMA-GARCH model, we found that Heping Liu and Jing Shi used ARMA-GARCH model to forecast electricity prices (see [15]). Alicja Lojowska et al. used ARMA-GARCH model to predict wind speed (see [16]). ARMA-GARCH can capture the most important features of the data in a satisfactory way, such as distribution, time related structure and periodicity. The experimental results show that by simulating the wind speed with extremely high energy content characteristics, this model can help to consider the extreme situation of wind power generation (see [12]).

3. Methods

3.1 ARMA Model

ARMA (p, q) model is mainly aimed at stationary time series data. It is composed of AR (p) model and MA (q) model. p is the order of automatic regression process, and q is the order of the sliding average process. This model takes into account the values, prediction errors and random items of data in the past period. The basic model is shown in (1), α_m and β_n are autocorrelation coefficients and moving average coefficients, respectively.

$$R_t = \sum_{m=1}^p \alpha_m R_{t-m} + \varepsilon_t + \sum_{n=1}^q \beta_n \varepsilon_{t-n} \tag{1}$$

$\{R_t\}$ represents stock logarithmic returns time series data of logarithmic stock returns, $\{\varepsilon_t\}$ represents the error terms. The model can also be expressed in the form shown in (2).

$$R_t = \alpha_1 R_{t-1} + \alpha_2 R_{t-2} \cdots + \alpha_p R_{t-p} + \varepsilon_t + \beta_1 \varepsilon_{t-1} + \beta_2 \varepsilon_{t-2} + \cdots + \beta_q \varepsilon_{t-q} \tag{2}$$

The stationarity is a necessary condition for forecasting stock data with ARMA model. Therefore, before building the ARMA model, it is necessary to perform ADF test on the time series data of stocks (see [17]). After the test data is stationary time series data, ARMA can be used to analyze and predict the data. Since the average value of the logarithmic profit data of stocks is close to zero and the variance is constant, the logarithmic profit data of stocks are considered as stationary time series data (see [18]).

For the established model, we can evaluate the excellence of the ARMA model according to the value of AIC criteria (see [17]). The value of AIC calculation formula is shown in (3), L represents the maximum likelihood of the model, and k represents the number of variables.

$$AIC = -2 \ln(L) + 2k \tag{3}$$

In the process of establishing the model, multiple groups of p and q values can be selected for modeling, AIC of each model can be calculated, and the model with the lowest AIC value can be selected as the prediction model for the logarithmic return of stocks.

The flow chart of ARMA model for time series prediction is shown in Figure 1.



Figure 1. ARMA Flow Chart

3.2 GARCH Model

GARCH(i, j) is expressed by (4) and (5), a_p and b_q are coefficients, σ^2 represents the conditional standard deviation at time t , z_t represents the white noise with $\mu = 0$ and unit variance.

$$\sigma_t^2 = a_0 + a_1 \varepsilon_{t-1} + a_2 \varepsilon_{t-2} + \dots + a_i + b_1 \sigma_{t-1}^2 + b_2 \sigma_{t-2}^2 + \dots + b_q \sigma_{t-p}^2 \tag{4}$$

$$\varepsilon_t = z_t \sigma_t \tag{5}$$

$$0 < \sum_{m=1}^i a_m + \sum_{n=1}^j b_n < 1 \tag{6}$$

In order to select the optimal GARCH model, we can choose three criterion including Akaike Information Criterion (AIC) (see [17]), Bayesian Information Criterion (BIC), and Hannan Quinn Information Criterion (HQIC) to evaluate the GARCH model in this paper (see [19]). The calculation formulas of AIC, BIC, and HQIC are shown in (3), (7), and (8), k represents the number of variables, N represents the number of observations, L represents the maximum likelihood of the model.

$$BIC = \ln(N) k - 2 \ln(L) \tag{7}$$

$$HQIC = 2 \ln(\ln(N)) k - 2 \ln(L) \tag{8}$$

3.3 ARMA-GARCH Model

According to the model ARMA(p, q) and the model GARCH(i, j), we can build up the model ARMA(p, q)-GARCH(i, j). Before constructing the GARCH model, it is necessary to test the ARCH effect of the sequence. The GARCH model can be used when there is no ARCH effect. The standard test is the p value of chi square test. When the P value is less than 0.05, it indicates that the time series does not have ARCH effect, and GARCH modeling can be performed. ARMA (p, q) - GARCH (i, j) model models the mean and variance. ARMA (p, q) model models the mean, and GARCH (i, j) model models the variance.

4. Experimental Analysis and Results

4.1 Data Set

The data set used in the experiments involved in this paper is the stock closing prices of APPLE Inc(APPLE), AMERICAN AIRLINES and Advanced Micro Devices(AMD) from January 4, 2021 to September 30, 2022. The original data is shown in Table 1, and the data distribution and data trend are shown in Figure 2.

Table 1. Original Data

APPLE		AMERICAN AIRLINES		AMD	
Date	Closing Price	Date	Closing Price	Date	Closing Price
2021-1-4	129.41	2021-1-4	15.13	2021-1-4	92.30
2021-1-5	131.01	2021-1-5	15.43	2021-1-5	92.77
2021-1-6	126.60	2021-1-6	15.52	2021-1-6	90.33
2021-1-7	130.92	2021-1-7	15.38	2021-1-7	95.16
2021-1-8	132.05	2021-1-8	15.13	2021-1-8	94.58
.....		
2021-9-13	149.55	2021-9-13	19.31	2021-9-13	104.80
2021-9-14	148.12	2021-9-14	19.21	2021-9-14	105.73
2021-9-15	149.03	2021-9-15	19.38	2021-9-15	105.60
2021-9-16	148.79	2021-9-16	19.89	2021-9-16	106.22
2021-9-17	146.06	2021-9-17	19.73	2021-9-17	103.88
.....		
2022-9-26	150.77	2022-9-26	11.86	2022-9-26	66.30
2022-9-27	151.76	2022-9-27	12.27	2022-9-27	67.17
2022-9-28	149.84	2022-9-28	12.75	2022-9-28	68.36
2022-9-29	142.48	2022-9-29	12.25	2022-9-29	64.14
2022-9-30	138.20	2022-9-30	12.04	2022-9-30	63.36

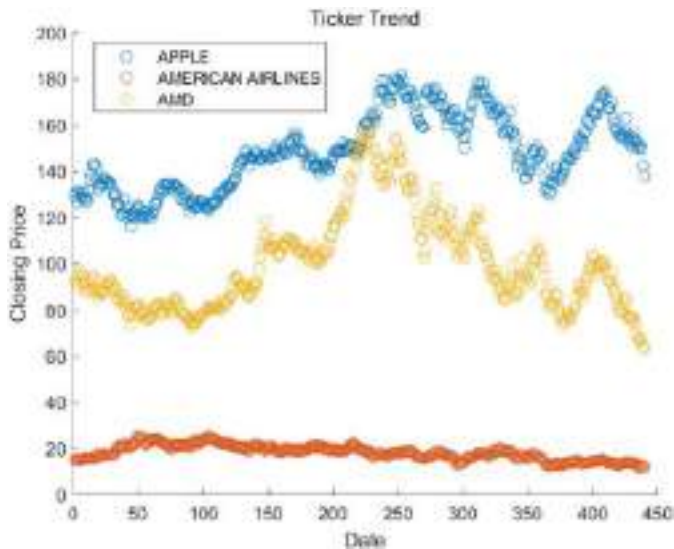


Figure 2. Data Distribution and Trend

4.2 Data Preprocessing

In order to make the data meet the assumptions of the linear model, we convert the stock closing price data into logarithmic income receipts, and apply ARMA-GARCH model to predict the logarithmic income of Apple, American Airlines and AMD. The logarithmic return formula is shown in (9), X_t represents the closing price on the t_{th} day.

$$R_t = \ln(X_t) - \ln(X_{t-1}) = \ln\left(\frac{X_t}{X_{t-1}}\right) \tag{9}$$

The trends of logarithmic return time series data of APPLE, AMERICAN AIRLINES and AMD are shown in Figure 3 to Figure 5, respectively.

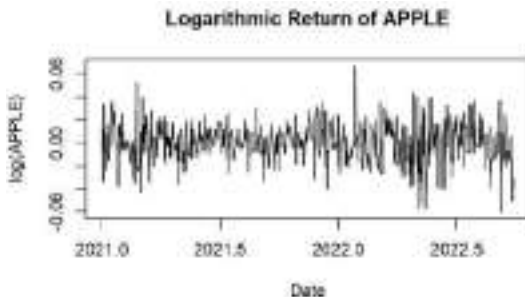


Figure 3. Logarithmic return of APPLE

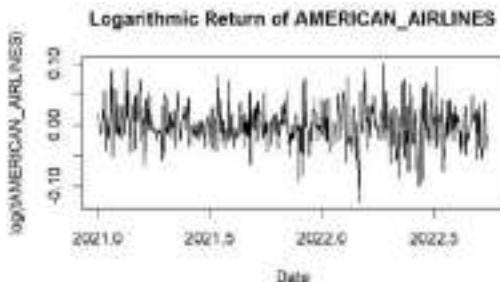


Figure 4. Logarithmic return of AMERICAN AIRLINES

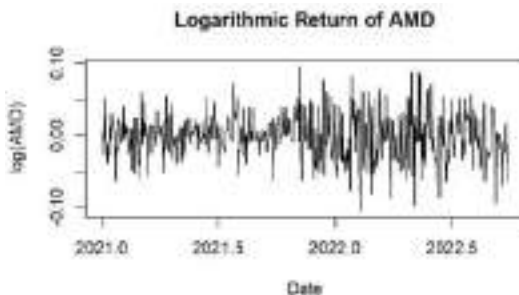


Figure 5. Logarithmic return of AMD

4.3 ARMA

Since ARMA model can predict and analyze stationary time series data, ADF test is required for data before ARMA model is applied to predict and analyze time series data. When the p-value obtained through the test is less than 0.01, the original assumption that the data is an unstable time series is rejected, indicating that the data is a stable time series data, which can be predicted and analyzed using ARMA model. The ADF Test Results table is shown in Table 2.

Table 2. ADF Test Results

	APPLE	AMERICAN AIRLINES	AMD
ADF Test			
p-value	<0.01	<0.01	<0.01

According to the ADF results shown in Table 2, the p-value of APPLE and AMERICAN AIRLINES is less than 0.01. The original assumption is rejected, which indicates that the logarithmic return data of the three stocks are stable time series data, and ARMA model can be used for prediction and analysis.

In order to ensure the accuracy of prediction and analysis, eight ARMA models are selected for data modeling and analysis, and the AIC of the model is calculated ($N = 440, k = p + q + 2$), p represents the autoregressive term, and q represents the number of moving average terms. The model with the minimum AIC is selected as the optimal model. All the AIC values of the eight models are shown in Table 3.

Table 3. AIC Values of ARMA(p, q)

	APPLE	AMERICAN AIRLINES	AMD
Model		AIC	
ARMA(0,1)	-2253.98	-1735.26	-1756.76
ARMA(1,1)	-2251.94	-1733.27	-1755.03
ARMA(1,2)	-2249.98	-1731.68	-1753.04
ARMA(2,1)	-2251.18	-1731.63	-1753.04
ARMA(2,2)	-2251.92	-1737.32	-1757.97
ARMA(3,1)	-2250.37	-1732.37	-1751.22
ARMA(3,2)	-2255.88	-1728.59	-1749.05
ARMA(3,3)	-2250.02	-1735.37	-1754.76

According to the AIC of the three stocks obtained by applying the ARMA model, select the ARMA (3, 2) model for APPLE stocks, ARMA (2, 2) model for AMERICAN AIRLINES, and ARMA (2, 2) model for AMD stocks. The prediction results are shown in Figure 6, Figure 7 and Figure 8.

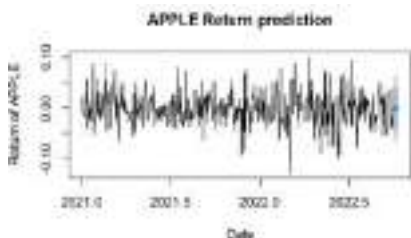


Figure 6. Prediction of APPLE Stock Return

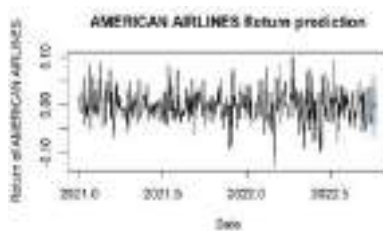


Figure 7. Prediction of AMERICAN AIRLINES Stock

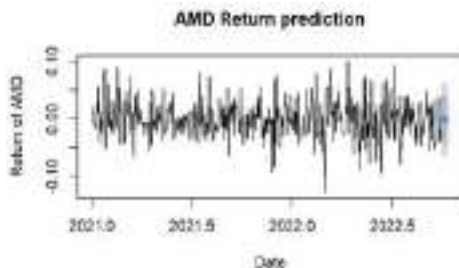


Figure 8. Prediction of AMD Stock Return

4.4 GARCH

Before establishing the GARCH model, it is necessary to test the data for the existence of the ARCH effect. If the p-value obtained through the test is less than 0.01, the original assumption that the data has the ARCH effect is rejected, indicating that the data does not have the ARCH effect, and the GARCH model can be established. The test results of ARCH effect are shown in Table 4.

Table 4. ARCH Test Results

	APPLE	AMERICAN AIRLINES	AMD
ARCH Test			
p-value	0.0006408	0.07996	3.436e-06

According to the test results of the ARCH effect, the p-value of the logarithmic return data of APPLE and AMD stocks is less than 0.01. Rejecting the original hypothesis, it can be explained that there is no ARCH effect in the logarithmic return data of APPLE and AMD stocks. GARCH model can be used to analyze the logarithmic return data of APPLE and AMD stocks. However, the p-value of the AMERICAN AIRLINES stock logarithmic return data is 0.07996, greater than 0.01, and the original assumption cannot be rejected. Therefore, it cannot be explained that there is no ARCH effect in the AMERICAN AIRLINES stock logarithmic return data, so the GARCH model cannot be used to analyze the AMERICAN AIRLINES stock logarithmic return data.

In order to test the accuracy of GARCH, the GARCH (1,1) model was established. GARCH (1,2) model and GARCH (1,3) model were used to model and analyze APPLE and AMD stocks. The AIC, BIC and HQIC obtained from the three types of models are gradually increasing, so GARCH (1,1) is selected to model and analyze two stocks.

The evaluation table for modeling and analyzing APPLE and AMD stocks using GARCH model is shown in Figure 5 and Figure 6. It can be seen intuitively that GARCH (1,1), GARCH (1,2) and GARCH (1,3) have the same evaluation results on the modeling and analysis of APPLE stock. In the evaluation results of AMD stock modeling and analysis, GARCH (1,1) is slightly better than GARCH (1,2) and GARCH (1,3). So we choose GARCH (1,1) model to model and analyze APPLE and AMD stocks.

Table 5. Model of APPLE

APPLE			
Model	AIC	BIC	HQIC
GARCH(1,1)	-5.215375	-5.178158	-5.200691
GARCH(1,2)	-5.215375	-5.178158	-5.200691
GARCH(1,3)	-5.215375	-5.178158	-5.200691

Table 6. Model of ADM

AMD			
Model	AIC	BIC	HQIC
GARCH(1,1)	-4.066688	-4.029472	-4.052005
GARCH(1,2)	-4.061805	-4.015284	-4.043451
GARCH(1,3)	-4.057147	-4.001316	-4.035116

4.5 ARMA-GARCH

To sum up, the model selected to predict the logarithmic returns of APPLE, AMERICAN AIRLINES and AMD stocks is shown in Table 7.

Table 7. Model Selection Results

Stock	Model
APPLE	ARMA(3,2) – GARCH(1,1)
AMERICAN AIRLINE	ARMA(2,2)
AMD	ARMA(2,2) – GARCH(1,1)

4.6 Model Accuracy

We can verify the accuracy of the model, by detecting the error of the prediction results. The error of the results selected by APPL, AMERICAN AIRLINES and AMD are shown in Figure 9 to Figure 11, respectively. Take standard deviation as the main error measurement standard, we can find that the prediction errors of APPLE and AMD is less than 0.03, and the prediction error of AMERICAN AIRLINES stocks is less than 0.1,

which indicates that the model is accurate and effective in predicting the logarithmic returns of stocks.

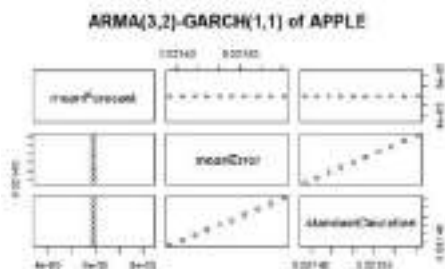


Figure 9. The Error of APPLE

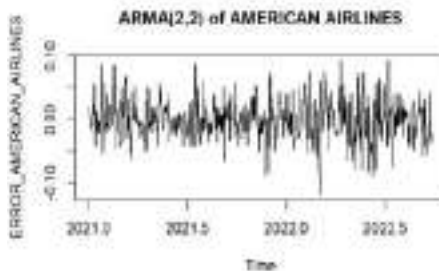


Figure 10. The Error of AMERICAN AIRLINES

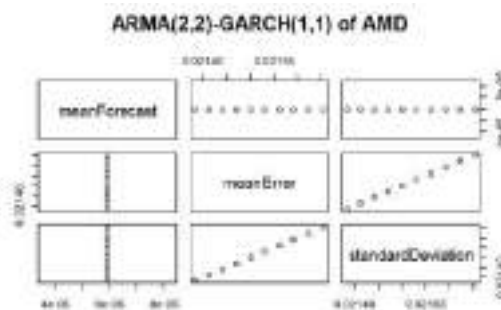


Figure 11. The Error of AMD

5. Conclusions

This study set out to apply time series analysis to predict and analyze APPLE, AMERICAN AIRLINES and AMD. This paper combines ARMA (p, q) model and GARCH (i, j) model for modeling and analysis. The results of time series analysis show that ARMA (3,2)-GARCH (1,1) model is applicable to APPLE stock, ARMA (2,2) model is applicable to AMERICAN AIRLINES stock, and ARMA (2,2)-GARCH (1,1) is applicable to AMD stock. In future work, we will continue to collect the closing price data of the three stocks to continuously improve the accuracy of the prediction.

Reference

- [1] Mak, M. K., & Ip, W. (2017). An exploratory study of investment behaviour of investors. *International Journal of Engineering Business Management*, 9, 184797901771152. doi: 10.1177/1847979017711520
- [2] Box, G. and Jenkins, G. (1970) *Time Series Analysis: Forecasting and Control*. Holden-Day, San Francisco.
- [3] Engle R F. Autoregressive conditional heteroscedasticity with estimates of the variance of UK inflation [J]. *Econometrica*. 1982, 50: 987-1008.
- [4] Bollerslev, Tim. Generalized Autoregressive Conditional Heteroscedasticity [J]. *Journal of Econometrics*, 1986, 31: 307-327.

- [5] Bollerslev. A Conditional Heteroskedasticity Time Series Model for Speculative Prices and Rates of Return [J]. *Review of Economics and Statistics*. 1987, 69: 542-547.
- [6] Lamont, O. A. (2000). Investment Plans and Stock Returns. *The Journal of Finance*, 55(6), 2719–2745. doi:10.1111/0022-1082.00304
- [7] Gottschlich, J., & Hinz, O. (2014). A decision support system for stock investment recommendations using collective wisdom. *Decision Support Systems*, 59, 52–62. doi:10.1016/j.dss.2013.10.00
- [8] Singh, R., & Srivastava, S. (2016). Stock prediction using deep learning. *Multimedia Tools and Applications*, 76(18), 18569–18584. doi:10.1007/s11042-016-4159-7
- [9] Lu, W., Li, J., Wang, J., & Qin, L. (2020). A CNN-BiLSTM-AM method for stock price prediction. *Neural Computing and Applications*. doi:10.1007/s00521-020-05532-z
- [10] Ou, P., & Wang, H. (2009). Prediction of Stock Market Index Movement by Ten Data Mining Techniques. *Modern Applied Science*, 3(12). doi:10.5539/mas.v3n12p28
- [11] J. Yang and X. Zhou, "Prediction of PM2.5 Concentration Based on ARMA Model Based on Wavelet Transform," *2020 12th International Conference on Intelligent Human-Machine Systems and Cybernetics (IHMSC)*, 2020, pp. 63-66, doi: 10.1109/IHMSC49165.2020.00022.
- [12] Valipour, M., Banihabib, M. E., & Behbahani, S. M. R. (2013). Comparison of the ARMA, ARIMA, and the autoregressive artificial neural network models in forecasting the monthly inflow of Dez dam reservoir. *Journal of Hydrology*, 476, 433–441. doi:10.1016/j.jhydrol.2012.11.017
- [13] Torres, J. L., García, A., De Blas, M., & De Francisco, A. (2005). Forecast of hourly average wind speed with ARMA models in Navarre (Spain). *Solar Energy*, 79(1), 65-77. doi: 10.1016/j.solener.2004.09.013
- [14] Zhang Dongxu, Empirical analysis of the fluctuation of the Shanghai Stock Index return rate based on the ARMA-GARCH models [D]. Tsinghua University, 2016
- [15] Liu, H., & Shi, J. (2013). Applying ARMA–GARCH approaches to forecasting short-term electricity prices. *Energy Economics*, 37, 152–166. doi:10.1016/j.eneco.2013.02.006
- [16] Lojowska, A., Kurowicka, D., Papaefthymiou, G., & van der Sluis, L. (2010). Advantages of ARMA-GARCH wind speed time series modeling. 2010 IEEE 11th International Conference on Probabilistic Methods Applied to Power Systems. doi:10.1109/pmaps.2010.5528979
- [17] J. Qin, Z. Tao, S. Huang and G. Gupta, "Stock Price Forecast Based on ARIMA Model and BP Neural Network Model," 2021 IEEE 2nd International Conference on Big Data, Artificial Intelligence and Internet of Things Engineering (ICBAIE), 2021, pp. 426-430, doi: 10.1109/ICBAIE52039.2021.9389917.
- [18] Wei-Min Li, Jian-Wei Liu, Jia-Jin Le, & Xiang-Rong Wang. (2005). The financial time series forecasting based on proposed ARMA-GRNN model. 2005 International Conference on Machine Learning and Cybernetics. doi:10.1109/icmlc.2005.1527274
- [19] Jia Chunmiao, Fu Zhongning, Ma Yaling, Li Jianguo, Chen Hulin. Freight Volume Forecast of Gan-Ning District Railway Based on ARMA Model and Multiple Regression [J]. *Comprehensive Transportation*, 2022,44 (09): 147-154

Time-Domain Feature Parameter Extraction Algorithm of Pulse Wave Based on Morphological Features

Xingguang Geng^{a,b}, Yitao Zhang^{a,b,1}, Jun Zhang^{a,b}, Yunfeng Wang^{a,b} and Haiying Zhang^{a,b,2}

^a*Institute of Microelectronics of Chinese Academy of Sciences, China*

^b*University of Chinese Academy of Sciences, China*

Abstract. Pulse wave's Time-domain characteristics have clear physiological and pathological significance, and are widely used in pulse recognition and disease prediction. At present, for different forms of pulse wave feature points, the accuracy of time-domain feature point extraction algorithms varies greatly. Therefore, this paper proposes a time-domain feature extraction algorithm of pulse wave based on morphological features. Firstly, the pulse wave is normalized and averaged by using normalization and correlation averaging methods. Secondly, the morphological characteristics of the main wave are divided into two states: extreme point and non-obvious feature. The characteristic morphology of the dicrotic front wave and the dicrotic wave are divided into three states: extreme point, non-obvious feature, feature fusion or disappearance. Finally, the location range of each feature point is determined, and the pulse wave feature points are identified by the curvature method and the difference method. The experiment shows that the algorithm can effectively identify the pulse wave characteristic points of common pulse waves, which creates conditions for the effective extraction of subsequent relevant human physiological and pathological information.

Keywords. pulse wave, time-domain characteristics, morphological characteristics, extreme point, dicrotic front wave, dicrotic wave

1. Introduction

Pulse wave carries important physiological and pathological information of human body[1-3]. At present, the methods of extracting pulse wave feature parameters mainly include time-domain, frequency-domain and time-frequency domain feature parameters. [4, 5] Because time-domain feature parameters are intuitive and each feature point has clear physiological significance. Therefore, they are widely used in pulse recognition and disease prediction [6, 7]. As shown in fig.1, the time-domain characteristics mainly

¹ Corresponding Author, Yitao Zhang (Institute of Microelectronics of the Chinese Academy of Sciences, Beijing 100029, China; University of Chinese Academy of Sciences, Beijing 100049, China) and E-mail: zhangyitao@ime.ac.cn.

² Corresponding Author, Haiying Zhang (Institute of Microelectronics of the Chinese Academy of Sciences, Beijing 100029, China; University of Chinese Academy of Sciences, Beijing 100049, China) and E-mail: zhanghaiying@ime.ac.cn.

include five feature points: the main wave peak (c), the dicrotic front wave valley (d), the dicrotic front wave peak (e), the dicrotic wave valley (f) and the dicrotic wave peak (g).[8]

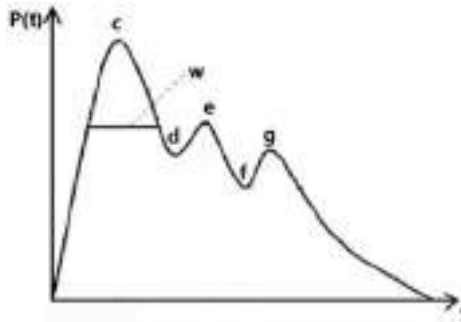


Figure1. Time-domain characteristic parameters of pulse wave

At present, the methods of extracting time-domain feature parameters mainly include slope method, slope and threshold combination method, differential method, extreme value method, wavelet method, sentence pattern method, etc. The slope method is mainly used to find the slope change point to determine the characteristic pulse wave. This method has poor recognition effect for waveforms with insignificant slope change or large pulse wave interference. The slope and threshold combination method is mainly based on the slope method to determine the location of feature points by determining the range of time-domain features[9]. This algorithm can only identify the feature points of a certain type of pulse wave. When the pulse wave is relatively gentle, the recognition effect is not ideal[10]. The differentiation method is to use the spline function to obtain the differential diagram of a single cycle pulse wave, set the threshold, and take the position of the first zero crossing point after differentiation as point c, and the rest are points d, e, f and g in turn. This method is only applicable to the case that both the dicrotic front wave and the dicrotic wave have wave peaks and valley, but the value of the first zero crossing point is not necessarily point c. The extreme value method is to calculate the maximum value in the pulse wave, take the first maximum point as point c, and then find the second largest and third largest extreme points as point e and point g in reverse order. Like the differential method, this method ignores that the maximum point is not necessarily point c, and the method has a large error when some people's the dicrotic front wave and the dicrotic wave are not obvious. Wavelet transform mainly uses wavelet transform to highlight time-domain feature points (such as Gaussian wavelet) and extract time-domain feature points. However, this method has poor recognition effect on d and e points [11, 12]. The main idea of syntactic pattern recognition is to classify and process the pulse wave signals, and then extract the characteristic parameters of the classified pulse wave signals. Therefore, it is necessary to establish an accurate classification standard for single cycle pulse waves, which has certain difficulties in the actual situation [13, 14]

In this paper, we summarize the morphological characteristics of pulse wave, and propose a time-domain feature extraction algorithm based on the characteristic morphology. Firstly, the pulse wave is normalized and averaged by using normalization and correlation averaging methods. Secondly, the morphological characteristics of the main wave are divided into two states: extreme point and non-obvious feature. The characteristic morphology of the dicrotic front wave and the dicrotic wave is divided into

three states: extreme point, non-obvious feature, feature fusion or disappearance. Finally, the location range of each feature point is determined, and the pulse wave feature points are identified by curvature method and difference method. The accurate identification of pulse wave feature points is helpful to the early prevention, diagnosis and follow-up treatment of diseases, which is of great clinical significance.

2. Materials and Methods

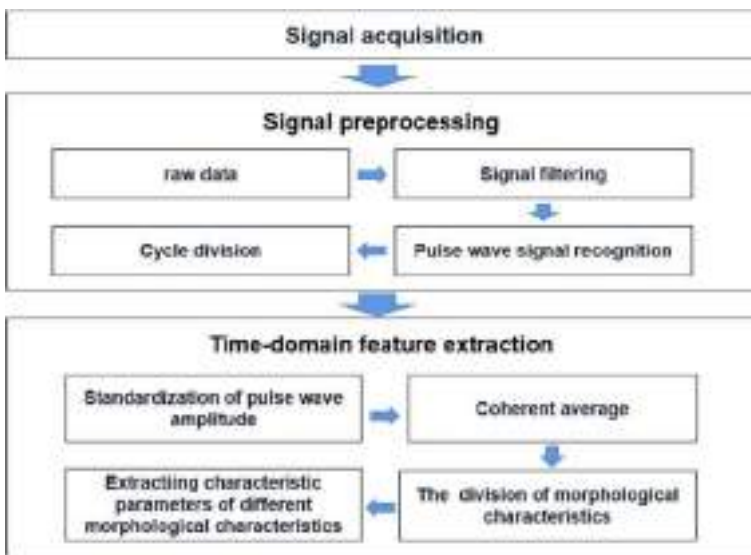


Figure2. Flow Chart of Pulse Wave Collection and Processing

This section mainly contains the following three parts. The first is signal acquisition, which mainly uses signal acquisition devices to collect pulse wave data. The second is signal preprocessing, which mainly uses filtering algorithms, pulse wave recognition algorithms, and cycle division algorithms to complete signal filtering, pulse wave signal recognition, and pulse wave cycle division. The last is time-domain parameter extraction, which is mainly used to standardize and average pulse waves, and classify pulse waves according to their morphological characteristics, Then the characteristic parameters of pulse wave are extracted by classification. Fig.2 shows the flow chart of pulse wave collection and processing.

2.1. Signal acquisition

As show in fig.3(a), in this paper, we use flexible bionic multi-channel pulse acquisition instrument to obtain pulse wave data. As show in fig.3-(b), the acquisition probe of the pulse diagnostic instrument contains compound pressure sensors, each of which is composed of a static sensor and a flexible dynamic sensor, and can complete the synchronous acquisition of static pressure and pulse wave. Through the way of air bag pressurization, simulating the pressurization technique of pulse taking in traditional Chinese medicine, the synchronous gradient pressurization and synchronous signal acquisition of the three positions can be realized. The sampling frequency is 225Hz. The

range of air bag pressurization is 10-150mmhg. And the pressurization gradient is 10mmHg. The static pressure signal and pulse wave signal in 10s are collected under each pressure. Fig.3-(c) shows single channel pulse sensor signal.

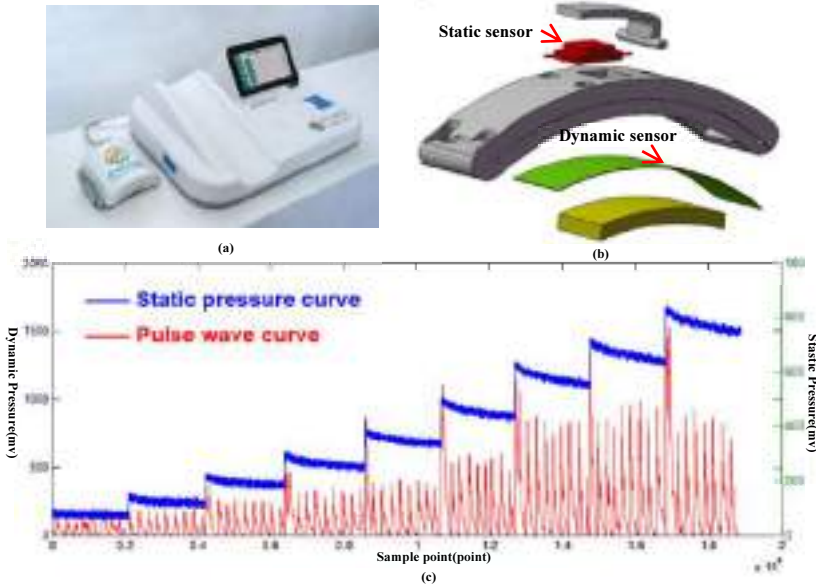


Figure 3. (a)Multi channel pulse wave acquisition device.(b)A compound pressure sensor Structural drawing(c) Single channel pulse sensor signal.

2.2. Signal preprocessing

The signal preprocessing algorithm is mainly composed of three parts: signal filtering, pulse wave signal recognition and period division. Firstly, 50Hz notch filter is used to remove power frequency noise, and wavelet transform is used to remove EMG noise and respiratory noise. The deep neural network algorithm is used to complete the pulse wave signal recognition [15]. And finally, the differential threshold method is used to complete the single cycle pulse wave.

2.3. Time-domain feature extraction method

(1) Standardization of pulse wave amplitude

As the pulse wave is an unstable signal, the amplitude of the pulse wave will be slightly different. In order to eliminate the influence of the amplitude, the pulse wave needs to be standardized. The pulse wave signal is described as a function $y(n)$. The formula for standardization is as follows:

$$z(n) = \frac{y(n) - y(1)}{\max[y(N)] - y(1)}, n = 1,2,3 \dots N \tag{1}$$

In the formula, $z(n)$ is the pulse sequence function obtained after standardization. N is the number of sampling points. Before and after standardization are shown in fig.4-(a) and fig.4-(b).

(2) Coherent average

Pulse wave is a quasi-periodic physiological signal. In general, the pulse wave carries noise of different frequency ranges, and the filter method cannot remove it well. The method of multiple signal superposition can be used to increase the signal gain. This paper sets $y_i(t)$ to represent a single cycle pulse wave signal with certain noise, then

$$y_i(t) = s(t) + n_i(t) \tag{2}$$

Where: $s(t)$ refers to the useful signal that occurs repeatedly. $n_i(t)$ represents random noise. As shown in fig.4-(c), in this paper, three spline interpolation method is used to unify the sampling points of pulse wave. According to the above formula, the single cycle pulse wave signal is superposed for many times, and the expression is as follows:

$$\bar{y}(t) = \frac{1}{N} \sum_{i=1}^N y_i(t) = \frac{1}{N} \sum_{i=1}^N [s(t) - n_i(t)] = s(t) + \frac{1}{N} \sum_{i=1}^N [n_i(t)] \tag{3}$$

Where: $\bar{y}(t)$ is the average signal. N is number of sampling points after triple bound spline interpolation

Assuming that the power is expressed as P and the variance of $n_i(t)$ is expressed as σ^2 , then for $y_i(t)$, its signal to noise ratio (SNR) can be expressed as:

$$SNR = \frac{P}{\sigma^2} \tag{4}$$

The formula shows that the noise variance will be reduced by N times by using the superposition averaging processing, and the pulse wave signal ratio will be increased by \sqrt{N} times after using the averaging processing. The waveform after coherent average is shown in fig.4-(d) (red curve).

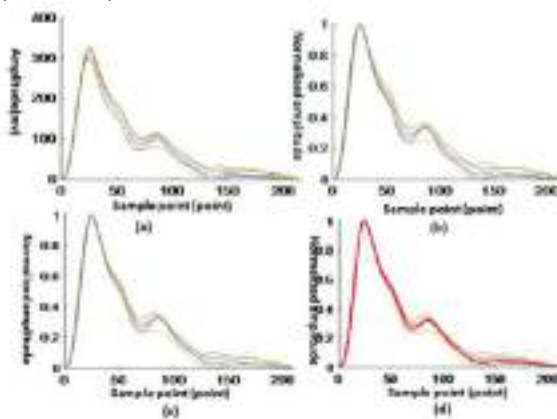


Figure 4. (a) Original pulse wave waveform (b) Amplitude standardized pulse wave waveform (c) Pulse wave waveform after resampling (d) Pulse wave waveform after coherent average

(3) The division of common pulse wave morphological characteristics

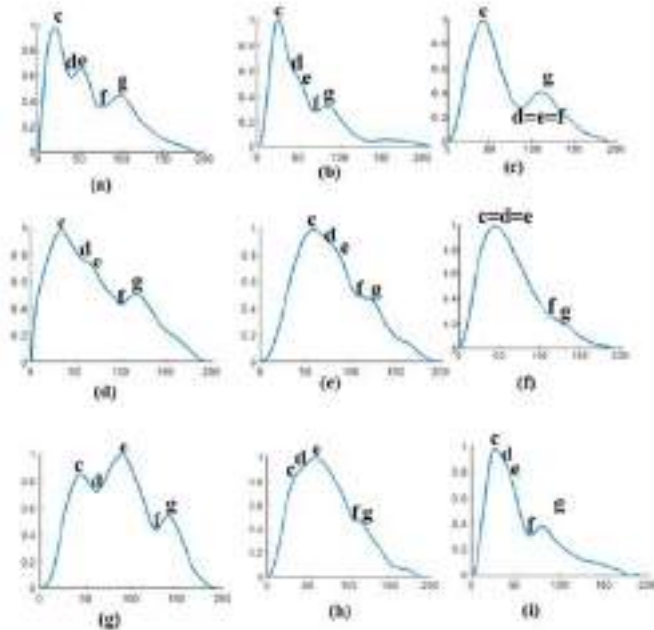


Figure 5. Common Pulse Wave Morphology

When the blood vessels have good elasticity and the human blood runs smoothly, generally speaking, the pulse wave of a complete cycle mainly includes three main characteristic waves: the main wave, the dicotic front wave and the dicotic wave, as shown in fig.5-(a). For some reason (such as high heat), the increase of blood flow in the cross-sectional area of the blood vessel within a unit time will enhance the local expansion and contraction ability of the human artery. The pulse wave shows that the dicotic front wave is close to the dicotic wave, as shown in fig.5-(b). When the blood vessel is further expanded, the dicotic front wave will fuse with the dicotic wave. At this time, the pulse wave presents double peaks, as shown in fig.5-(c). On the contrary, due to some reason (such as cold stimulation), the hardness of the human blood vessel wall increases. On the pulse wave, it is shown that the dicotic front wave is close to the main wave peak, as shown in fig5-(d). When the hardness does not increase, the dicotic front wave is fused with the main wave peak (as shown in fig.5-(e)), and even the position of the dicotic front wave exceeds the main wave peak (as shown in fig.5-(f)).

It can be seen from fig.5 that the characteristic morphology of the main wave can be divided into two states: extreme point, non-obvious feature. And the characteristic morphology of the dicotic front wave and the dicotic wave can be divided into three states: extreme point, non-obvious feature, feature fusion or disappearance. Therefore, in the time domain feature recognition, it needs to be discussed according to the situation.

(4) Extraction of time-domain characteristic parameters of different morphological characteristics

Firstly, obtain the position of the heart splash point (b). As shown in fig. 6, for a single cycle pulse wave, there is a first-order difference maximum point between the maximum peak point of the pulse wave and the starting point of the pulse wave, and the maximum point is the heart splash point (point b). The main wave, the dicotic front

wave and the dicrotic wave are all located on the right side. It is assumed that the data length of pulse wave $y(n)$ is N . The expression of first-order differential $d(n)$ is as follows:

$$d(n) = y(i + 1) - y(i), \quad i = 1, 2 \dots N - 1 \tag{5}$$

From the definition of each characteristic point, w is the width of the upper 1/3 of the main wave (expressed in g and k in the text). The effect is shown in fig. 6. The value of w_t is determined by the occurrence time of the dicrotic front wave and the peripheral resistance. Is calculated as follows,

$$w_t = \frac{y(k_x) - y(a_x)}{N}, \quad i = 1, 2 \dots N - 1 \tag{6}$$

In the formula, k_x and a_x are the abscissa corresponding to point k and point a on the pulse wave respectively.

Point b is located between the starting point of the pulse wave and point a . According to that point b is the maximum value point of the first order difference of the pulse wave, we can obtain the abscissa of the pulse wave position point. Then the abscissa b_x of point b meets the following requirements:

$$\begin{cases} d(b_x) - d(b_x - 1) > 0 \\ d(b_x) - d(b_x + 1) > 0 \\ b_x > 0 \\ b_x < a_x \end{cases} \tag{7}$$

In the formula, b_x is the abscissa corresponding to point b on the pulse wave .

Secondly, calculate the maximum peak value point c' , which is not necessarily the location of the main peak point. According to the definition, c' can be meet the following conditions:

$$\begin{cases} c'_x - c'_{x-1} > 0 \\ c'_x - c'_{x+1} > 0 \\ c'_x > b_x \\ c'_x < N \\ c'_y > y(n), n \neq c'_x \end{cases} \tag{8}$$

In the formula, c'_x is the abscissa corresponding to point c' .

Thirdly, obtain the position of f (the dicrotic wave valley) and g (the dicrotic wave peak) in the pulse wave.

Case1: If f and g are extreme points: when actually looking for f and g points, there are often multiple wave extreme points within the judgment range. In order to eliminate the influence of interference points, the maximum value of the difference between g and f 's ordinates is often selected. At the same time, the abscissa positions of g and f points should be greater than the abscissa positions of c points, and the abscissa position of f point should be less than the abscissa position of g point. From this, the judgment formula of g point and f point can be obtained as follows:

$$\begin{cases} x(g_x) - x(g_x - 1) > 0 \\ x(g_x) - x(g_x + 1) > 0 \\ g_x > k_x \\ g_x < N \\ (g_y - f_y) \geq (p_y - v_y) \end{cases} \tag{9}$$

In the formula g_x is the abscissa corresponding to point g . f_y is the ordinate corresponding to point f . v represents a valley under certain conditions. v_y is the ordinate corresponding to point v .

Point f is located at the first valley point on the left side of the point g .

Case 2: If the f and g characteristics are not obvious.

Obtain the curvature transformation expression of $x(n)$ according to the curvature definition.

$$k(n) = \left(\frac{y_2}{1 + y_1^2} \right)^{1.5}, n = 1, 2, \dots, N \tag{10}$$

In the formula, y_1 is the first derivative of y , y_2 is the second derivative of y . In order to remove the interference term in the curvature, the original curvature is smoothed by five points, which are determined by the sampling frequency of the original data. The filtering effect is shown in fig.6. In this paper, $fs = 225$. According to the characteristics of points g and f , if g and f are extreme points of curvature, then the positions of g and f will not exceed the maximum point c . At the same time, points f and g are located on the right side of point k . The corresponding point f should be the maximum point of curvature. To sum up, we can get the curvature judgment method of point f :

$$\begin{cases} k(f_x) - k(f_x - 1) > 0 \\ k(f_x) - k(f_x + 1) > 0 \\ f_x > k_x \\ f_x < N \\ f_y \geq k(i), i = k_x, k_x + 1, \dots, N \end{cases} \tag{11}$$

The minimum point of curvature wave crest on the right side of point f is point g . If there are no points g and f in the curvature, consider the third case, the dichroic wave and the dichroic front wave are merged.

Case3: the dichroic wave and the dichroic front wave are fusion or disappearance. According to the previous description, when the degree of vascular sclerosis increases, the dichroic wave will move to the dichroic front wave and even fuse. At this time, the position of the differential wave is merged with that of the heavy wave front wave.

$$\begin{cases} g_x = e_x \\ g_y = e_y \\ f_x = d_x \\ f_y = d_y \end{cases} \tag{12}$$

In the formula e_x and d_x is the abscissa corresponding to point e and d . e_y is the ordinate corresponding to point e .

Lastly, obtain the positions of c (main wave peak), d (the dichroic front wave valley) and g (the dichroic wave peak) in the pulse wave.

Case1: the dichroic wave exists: if the dichroic wave exists, the location of the dichroic front wave should be in front of the dichroic wave valley, which is mathematically expressed as the abscissa position of the dichroic front wave is less than the abscissa position of the dichroic wave valley. Since the differential front wave is an extreme point or the feature is not obvious

When the differential front wave takes wave crest and wave valley as extreme points

$$\begin{cases} c = c' \\ y(e_x) - y(e_x - 1) > 0 \\ y(e_x + 1) - y(e_x) < 0 \\ e_x > k_x \\ e_x < f_x \end{cases} \quad (13)$$

At the same time, it is considered that there may be multiple peak points between the dichroic front wave and the main wave peak c in the pulse wave. According to the relevant regulations of the pulse wave, the first peak is the main wave peak, the last peak is the dichroic front wave peak, and the nearest wave valley point in front of the dichroic front wave peak is the wave valley point d of the dichroic front wave.

When the differential front wave features are not obvious. If there is a peak curvature point between a and f , there is also a peak curvature point between a and f . Then determine the size of the curvature peak point on both sides: if the curvature peak point between a and d is smaller than the curvature peak point between d and f , or there is only a curvature peak point between a and f , then the judgment method for point c and point d is as follows:

$$\begin{cases} c = c' \\ k(d_x) - k(d_x - 1) > 0 \\ k(d_x + 1) - k(d_x) < 0 \\ d_x > k_x \\ d_x < f_x \end{cases} \quad (14)$$

Where point d is the maximum curvature point between point c' and point f , and point e is the minimum curvature point between point d and point f .

If the peak curvature point between a and c' is less than the peak curvature point between c' and f , or if there is only a peak curvature point between a and c' , if the minimum value of the peak curvature point is p , then

$$\begin{cases} c = p \\ k(d_x) - k(d_x - 1) > 0 \\ k(d_x + 1) - k(d_x) < 0 \\ d_x > p_x \\ d_x < c'_x \\ e = c' \end{cases} \quad (15)$$

Case2: The dichroic wave merges with the main wave peak. When the degree of arteriosclerosis is high, the dichroic wave and the main wave peak fuse. At this time, the crest and valley points of the digital wave disappear and merge in c . The expression is as follows:

$$c = d = e = c' \quad (16)$$

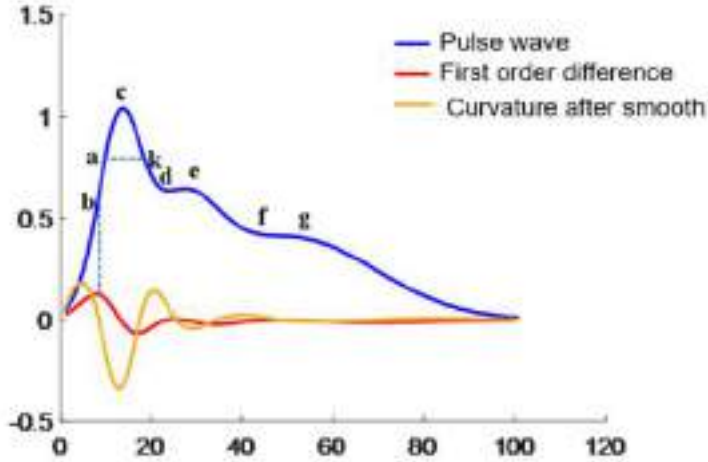


Figure 6. First order difference and smooth curvature of pulse wave

3. Experimental results

The students in our laboratory volunteered to participate in the experiment. Their age range is between 24 and 30 years old. In order to verify the accuracy of the time-domain feature extraction algorithm, we selected 9 groups of pulse waves as shown in fig.5. Use the manual calibration method to calibrate the pulse wave characteristics, and then use the algorithm in this paper to calculate. The comparison between the two is shown in table1. The number of data points is 190, and the sampling frequency is 225.

Table 1 Comparison between algorithm extraction and manual extraction (point=190, fs=225)

N	Algorithm identification results					Manual calibration results				
	T _{oc}	T _{od}	T _{oe}	T _{of}	T _{og}	T _{oc}	T _{od}	T _{oe}	T _{of}	T _{og}
a	20	41	52	77	101	20	41	52	77	101
b	26	45	51	71	87	26	42	51	71	87
c	28	71	71	71	96	28	71	71	71	96
d	33	53	66	99	117	33	52	66	99	117
e	59	73	81	113	119	59	72	82	112	119
f	44	44	44	114	129	44	44	44	114	128
g	45	62	89	126	141	45	62	89	126	141
h	35	47	59	109	114	33	49	59	108	111
i	27	37	44	66	80	27	34	42	66	80

It can be seen from fig.5 that (a) and (g) are the main wave peaks of the main wave, the dicrotic front wave and dicrotic wave. There is no difference in algorithm extraction

and manual extraction. It can also be seen from (g) that the main wave peak is not necessarily the highest point of the pulse wave peak in a cycle. In (b), (d), (e), (h) and (i), the characteristics of the dichroic front wave are not obvious, and there is no peak point. Then the accuracy of the identification algorithm extraction and manual extraction of point d and e is slightly different, with a maximum difference of two sampling points. The result is acceptable. In (f) and (h) the dichroic wave features are not obvious and there is no peak point, so the accuracy of the recognition algorithm extraction and manual extraction of f and g points is slightly different, with a maximum difference of two sampling points, and the results are acceptable. In general, the accuracy of the algorithm meets the requirements of data analysis.

4. Conclusion

In this paper, aiming at the time-domain characteristics of common pulse waves, combining curvature method and difference method, a time-domain feature extraction algorithm based on feature morphology is proposed. Experiments show that this method can effectively remove unnecessary interference and amplify the characteristics of signals through normalization and coherent averaging. Since the interval of the analysis waveform is gradually narrowed. The dichroic wave is divided into characteristic shapes. It can also well extract characteristic points for the main wave, the dichroic front wave, and the pulse wave shape that is not obvious in the dichroic wave. It has the characteristics of high recognition accuracy, wide application range, and strong anti-interference ability. It can provide direct and accurate basis for clinical applications, such as non-invasive blood pressure monitoring, central pulse pressure measurement, pulse wave shape characteristic quantity K, arterial reflection wave enhancement index, etc. It is of great significance for early prevention, diagnosis, treatment and prognosis evaluation of related vascular diseases. The algorithm proposed in this paper still uses manual recognition method to recognize pulse wave morphological features, with some errors. In the future work, we will use the deep learning algorithm to classify the pulse waves according to their morphological characteristics, and then extract the time-domain features of the classified pulse waves.

5. Funding and patents

Sichuan Major Science and Technology Projects (NO. 2022ZDZX0033) provides necessary financial support for data acquisition and algorithm verification.

References

- [1] Fei Cui, Xiaohui Chen and Jie Peng, A non-invasive blood viscosity detecting method based on pulse wave. MATEC Web of Conferences, 2020.
- [2] Keyu Meng, Jun Chen, Xiaoshi Li, Yufen Wu, Flexible Weaving Constructed Self-Powered Pressure Sensor Enabling Continuous Diagnosis of Cardiovascular Disease and Measurement of Cuffless Blood Pressure. ADVANCED FUNCTIONAL MATERIALS, 2018.
- [3] K Meng, X Xiao, W Wei, Highly Sensitive Flexible Iontronic Pressure Sensor for Fingertip Pulse Monitoring. ADVANCED HEALTHCARE MATERIALS, 2022.

- [4] ZhihuaChen, AnHuang, XiaoliQiang, Improved neural networks based on genetic algorithm for pulse recognition. *Computational Biology and Chemistry*, 2020.
- [5] N Li, J Yu, H Hu, The correlation study of Cun, Guan and Chi position based on wrist pulse characteristics. *IEEE Access*, 2021.
- [6] ZhixingJiang, ChaoxunGuo, DavidZhang, Pressure wrist pulse signal analysis by sparse decomposition using improved Gabor function. *Computer Methods and Programs in Biomedicine*, 2022.
- [7] DongmeiLin, AihuaZhang, JasonGu, Detection of multipoint pulse waves and dynamic 3D pulse shape of the radial artery based on binocular vision theory. *Computer Methods and Programs in Biomedicine*, 2018.
- [8] Tsai, Yun-Ning, Chang, Yu-Hsin, The use of time-domain analysis on the choice of measurement location for pulse diagnosis research. *JOURNAL OF THE CHINESE MEDICAL ASSOCIATION*, 2018.
- [9] ZHAO Zhi-qiang, ZHENG Guo-wei, SHEN Wei, LIAO Cheng, research on pulse wave signal noise reduction and feature point identification. *Electronic Design Engineering*, 2013.
- [10] Zhang Menglong, Li Xiaofeng Xu, Jinlin,Huang Wanfeng, Pulse wave feature extraction based on improved slop thresholding method. *ELECTRONIC MEASUREMENT TECHNOLOGY*, 2017.
- [11] Fufeng, Feature Point Recognition Method of Pulse Signal Based on Wavelet Modulus Maxima. *Computer Engineering*, 2019.
- [12] Wei Sun, Ning Tang, Guiping Jiang Study of Characteristic Point Identification and Preprocessing Method for Pulse Wave Signals. *Journal of Biomedical Engineering*, 2015.
- [13] Xiangjun Huang, Wu Xing, Feng Li, Application of Syntactic Pattern Recognition in Research on Pulse Wave's Characteristic Information. *Chinese Journal of Medical Instrumentation*, 2015.
- [14] Ji Zhong, Liu Xu, Study on feature points recognition of pulse wave based on waveform feature and wavelet. *Chinese Journal of Scientific Instrument*, 2016.
- [15] Huang L , Geng X, Xu Hao , Zhang Y, Li Zhi ,Zhang J, and Zhang H Interference Signal Identification of Sensor Array Based on Convolutional Neural Network and FPGA Implementation. *Electronics*.2022.

Image Restoration of an Object Viewed Through a Polycapillary X-Ray Lens with Square Channels Using the Concept of a Space-Variant Point-Spread Function

Mo ZHOU^{a,c}, Yiming WU^{a,c}, Kai PAN^{a,c}, Zelin DU^{a,c}, Tiancheng YI^e, Tianxi SUN^{a,c,d}, Zhiguo LIU^{a,b,c,d} and Yude LI^{a,b,c,d,1}

^aCollege of Nuclear Science and Technology, Beijing Normal University, Beijing 100875, China

^bBeijing Key Laboratory of Applied Optics, Beijing 100875, China

^cKey Laboratory of Beam Technology, Ministry of Education, Beijing 100875, China

^dBeijing Radiation Center, Beijing 100875, China

^eSpallation Neutron Source Science Center, Dongguan, 523803, Guangdong, China

Abstract. A polycapillary X-ray lens with square channels is a type of new X-ray optical device that is suitable for both X-ray focusing and imaging. Similar to micropore optics (MPO), the square matrix array of this lens contributes to the good correspondence between each individual channel and each pixel of a position-sensitive detector. The tiny difference in the curvature of each channel makes the point-spread function of this lens spatially variant. To realize image restoration of the raw data viewed through this lens, a Slice method called the Lucy-Richardson overlap-save method using total variation (LROS-TV) was used. In this work, a series of simulations were conducted to investigate at what flux and contrast levels the image features of an object can be resolved. A simple coaxial imaging experiment was also conducted to verify the LROS-TV method by changing the current of the X-ray tube from 300 to 600 μA . In this paper, it was found that the slice method is suitable for image restoration of an object viewed through a polycapillary X-ray lens with square channels.

Keywords. X-ray optics, polycapillary X-ray lens with square channels

1. Introduction

The polycapillary X-ray lens was first proposed by M.A. KUMAKHOV in 1986. [1] This device is a monolithic system fabricated from microstructure glass consisting of a large number of capillary channels. It can be used as an effective collection, focusing, and transfer optic based on the principle of total external reflection. [2] Traditional polycapillary X-ray lenses are not standardized optical imaging elements, although there have been reports on their application to imaging [3-4], especially combining the coded aperture concept, which was proposed recently [5-6]. Inspired by micropore optics (MPO), the optical structure of a polycapillary X-ray lens with square channels was

¹Corresponding Author: Yude LI, E-mail: liyude@bnu.edu.cn.

presented [7] to overcome the disadvantages caused by the triangular-shaped nonfunctional spaces between the circular channels. Then, slices with square channels that aimed to compose a novel lens using a stack-like arrangement were produced. The characteristic cruciform point-spread function (PSF) was demonstrated experimentally.[8]

Similar to an MPO, the square matrix array of capillaries in a square polycapillary X-ray lens contributes to the good correspondence between each individual channel of the optic device and each pixel of the position-sensitive detector. In this case, a square polycapillary X-ray lens has potential in X-ray imaging analysis applications. In 2000, Andrew G. Peele used the maximum likelihood method in the deconvolution of images viewed with a lobster-eye telescope, for an extended object. [9] For an MPO, the PSF remains consistent irrespective of manufacturing defects. However, for a polycapillary X-ray lens with square channels, individual square channels in different layers are bent, and the outline can be viewed as parabolic. This causes the PSF of this lens to be spatially variant. Various solutions for the restoration of images viewed through an optical system with spatially variant PSFs have been proposed, including sectioned methods [10-11], [12] and monolithic methods [13-14]. Combined with these methods, it is meaningful to demonstrate that image features can be recovered from the raw data collected by a polycapillary X-ray lens with square channels.

In this work, during the simulations, we selected a simple text as the test object. We sectioned the geometry of a thick lens slice and calculated the PSFs in different sections using our verified model. [7] Over the right modeled spatially variant PSFs, we completed the restoration of the raw images obtained using the square polycapillary X-ray lens with the Lucy-Richardson overlap-save method using total variation (LROS-TV). Several simulations were performed to research the influences of the ratio of the object luminous flux to the background and the entrance photon level on the recovered image quality. In addition, an image restoration experiment was implemented to verify the correctness of the simulations. The results of the simulations and experiment indicate that this method is suitable for image restoration when this type of X-ray optical device is used as a lens for imaging transmission.

2. Related Methods

2.1. Calculation of the spatially variant PSFs

The point spread function (PSF) is the response of an imaging system to a point source or point object. As Fig. 1(a) shows, the curvature of the outline of an individual bent channel changed slightly as the layer number increased. Computing the real PSFs of this optic would be very time-consuming. In this case, we simplified the problem by sectioning the geometry of the optic into $N \times N$ parts (Fig. 1(b)). For each section, the channels assumed to be associated with the same PSF kernel for tiny variations in their curvature are negligible. A window of size $r \times r$ was extracted around the center of each section to save the PSF. To calculate the spatially variant PSFs of a polycapillary X-ray lens with square channels, a point source was placed at the center of the transverse plane of each section and at a long distance from the entrance of the optic in the longitudinal direction. As shown in Fig. 2, the X-ray photons emitted from the source isotropic. Then, the process of the ray transmission through each section of the lens was calculated using

the mathematical model of our prior work. [15] The X-ray intensity distribution in the focal plane was finally summed on a uniform grid, and the results were obtained by tracing 10^9 photons using a Monte Carlo method. The bandwidth of the energy of the photons used was 0–330 keV.

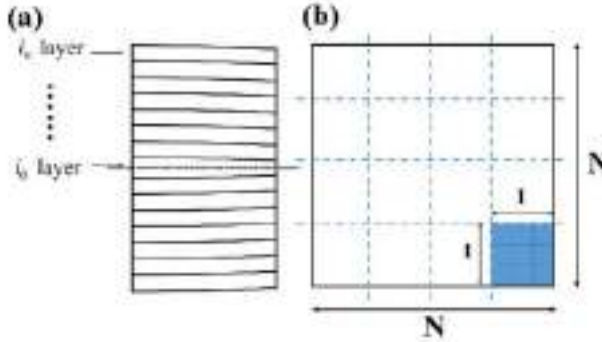


Figure 1. (a) Schematic structure of a polycapillary X-ray lens with square channels in the longitudinal direction; (b) Sectioned cross-section of the optic, $N = \{1, 2, 3, \dots, n\}$ is the number of sections with spatially variant PSFs and $I = \{1, 2, 3, \dots, i\}$ is the number of channels in one individual section.

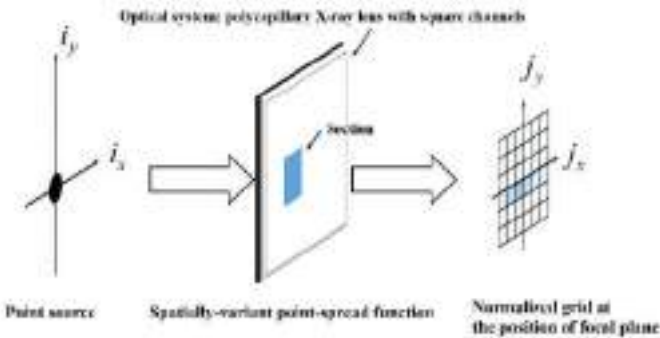


Figure 2. Calculation model of the spatially variant PSFs.

2.2. Simulation of the imaging experiment

The test object is shown in Fig. 3(a); it contains three letters, “BNU”, which is the abbreviation of Beijing Normal University. The whole object was set as an extended source of intensity of only the energy of interest. The contrast of the test object was

$$\frac{I_{\max} - I_{\min}}{I_{\max} + I_{\min}}$$

calculated using the Michelson formula [16]. It represents the count rates of the primary X-rays emitted from different parts of the object. For example, the ratio of the feature “BNU” to the background was set to 0.55:0.45, and the contrast value was 0.1. In terms of the geometric model of the optic, random channel tilts with a root mean square (RMS) value of 0.1 mrad and surface roughness with an RMS of 2 nm were considered. The manufacturing material was borosilicate glass. Further parameters of the simulation model are listed in Table 1. Our primary tool of investigation is based on the

Monte-Carlo ray-tracing method. The code has performed successfully in the numerical calculation of polycapillary X-ray lenses, as the results agreed well with experiments. [15],[17] Based on the code, a simulation of an imaging experiment was conducted. A schematic diagram of the simulation is shown in Fig. 3(b). The centers of the object, the lens and the confocal plane are coaxial. In the longitudinal direction, the object was positioned sufficiently far from the entrance of the lens. Therefore, the incident rays can be viewed as quasi-parallel in the case of paraxial approximation. The distance between the lens exits and the focal plane was determined using the optical properties of the lens. Table 2 shows the parameters of the simulation of the imaging experiment. In the simulation process, primary X-rays were emitted from random positions with a sampling frequency corresponding to the intensity of the object associated with the contrast value. Then, the rays struck the optic with random angles, and the final results were collected with a uniform grid in the focal plane after all the rays traced through the optic and exited.

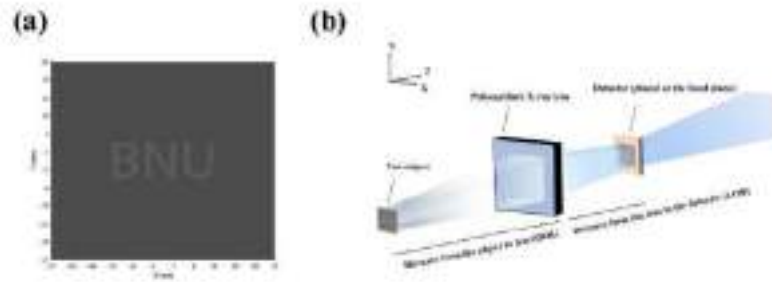


Figure 3. (a) Test object: the ratio of the feature BNU to the background was set to 0.55:0.45, and the contrast value was 0.1; (b) Schematic diagram of the simulation of the imaging experiment.

Table 1. Lens information

Type of glass	Borosilicate
Composition[wt%]	SiO ₂ -70, B ₂ O ₃ -25, Na ₂ O-2, Al ₂ O ₃ -2, K ₂ O-1
Density[g/cm ³]	2.28
Side length of the entrance[mm]	44
Side length of the exit[mm]	42
Thickness of the lens[mm]	10
Number of micro square channels	2200×2200
Channel diameter[μm]	20
Fractional open area	0.8

Table 2. Simulation of imaging experiment

Parameter	Value
OOL[mm]	10000
LOD[mm]	740
Ratio of feature to background (Contrast)	0.75:0.25 (0.5), 0.6:0.4 (0.2), 0.55:0.45(0.1), 0.505:0.495(0.01)
Number of rays	107, 108, 109, 1010
X-ray Energy	0–30 keV

2.3. Restoration method

As mentioned above, the sectioned method was selected in this work. The raw image viewed through the polycapillary X-ray lens with square channels was divided into tiles

of size $N \times N$ corresponding to the calculation of the spatially variant PSFs. Then, the restoration was performed for each tile individually. For a test object that emitted incoherent X-rays, the data collected in the detector plane satisfy a Poisson distribution. Taking no account of stochastic processes, the Poisson distributed signals can be expressed by:

$$Y(\mathbf{j}) = \sum_{\mathbf{i}} H(\mathbf{j}|\mathbf{i}) X(\mathbf{i}) \tag{1}$$

where $\mathbf{j} = \{j_1, j_2\}$ is the index of the pixels in the detector, $\mathbf{J} = \{\mathbf{j}_1, \mathbf{j}_2, \dots, \mathbf{j}_n\}$ is the number of pixels in the detector and $Y(\mathbf{j})$ represents the data acquired by the \mathbf{j}^{th} pixel of the detector. The term $\mathbf{i} = \{i_1, i_2\}$ is the index of the pixels in the plane of the test object, $\mathbf{I} = \{\mathbf{i}_1, \mathbf{i}_2, \dots, \mathbf{i}_n\}$ is the number of pixels in the plane of the test object and $X(\mathbf{i})$ is the object's true intensity. $H(\mathbf{j}|\mathbf{i})$ is the PSF of the optical system. The mean of $Y(\mathbf{j})$ is:

$$\mu(\mathbf{j}) = \varepsilon(\mathbf{j}) \sum_{\mathbf{i}} H(\mathbf{j}|\mathbf{i}) X(\mathbf{i}) \tag{2}$$

where $\varepsilon(\mathbf{j})$ is defined as the transmission efficiency of each section of the lens.

Then, based on the prior information offered by $Y(\mathbf{j})$, we employed a Lucy-Richardson overlap-save method using total variation (LROS-TV) to conduct the process of restoration. The basis of the LROS-TV method is the Lucy-Richardson deconvolution algorithm. In this work, the estimation of $X(\mathbf{i})$ can be obtained by iteration using the LR algorithm:

$$\hat{X}^{p+1}(\mathbf{i}) = \hat{X}^p(\mathbf{i}) \frac{1}{\sum_{\mathbf{j}} \varepsilon(\mathbf{j}) H(\mathbf{j}|\mathbf{i})} \sum_{\mathbf{j}} \frac{H(\mathbf{j}|\mathbf{i})}{\sum_{\mathbf{i}} H(\mathbf{j}|\mathbf{i}) \hat{X}^p(\mathbf{i})} Y(\mathbf{j}) \tag{3}$$

where p is the iteration number. In the regulation step of the Lucy-Richardson algorithm, total variation (TV) helps to preserve the borders and suppresses the noise. This results in dividing the image $\hat{X}^p(\mathbf{i})$ in Eq. (3) by a factor and Eq. (3) becomes:

$$\hat{X}^{p+1}(\mathbf{i}) = \frac{\hat{X}^p(\mathbf{i})}{1 - \lambda \operatorname{div} \left(\frac{\nabla \hat{X}^p(\mathbf{i})}{|\nabla \hat{X}^p(\mathbf{i})|} \right)} \frac{1}{\sum_{\mathbf{j}} \varepsilon(\mathbf{j}) H(\mathbf{j}|\mathbf{i})} \sum_{\mathbf{j}} \frac{H(\mathbf{j}|\mathbf{i})}{\sum_{\mathbf{i}} H(\mathbf{j}|\mathbf{i}) \hat{X}^p(\mathbf{i})} Y(\mathbf{j}) \tag{4}$$

After termination of the iteration, the estimation of the original intensity in each tile is stitched together using the overlap-save method.

3. Experimental measurement

A photograph of the experimental setup is shown in Fig. 4(a). The experimental setup was arranged as shown in Fig. 4(b). An X-ray tube with a Cu target [MCBM 50-0.6B, RTW] was controlled using a five-dimensional alignment stage, and the focal spot size of the X-ray was $50\ \mu\text{m}$. The polycapillary X-ray lens with square channels used in this experiment had 900×900 square channels, and the ratio of open area was 0.65. The side length of the entrance plane of the lens was 26 mm. To estimate the spatially variant PSFs of the lens, a $10\ \mu\text{m}$ pinhole was attached in front of the X-ray tube as a point object. The distance between the lens entrance and the Be window of the X-ray tube was set to 1000 mm. Then, the lens was sectioned to $N \times N = 9 \times 9$ with $I \times I = 100 \times 100$ channels in each section. The X-ray tube with the attached pinhole was moved at each step to ensure that the point object and the center of each section were coaxial. The images were recorded by an X-ray camera [C11440-42U30, HAMAMATSU]. The PSFs were obtained through deconvolution of these images and normalized to an energy of one. The test object of the simulation was replaced with an X-ray resolution chart [JIMA] in this experiment. A part of the chart was used, and the test object contained three $40\ \mu\text{m}$ width and three $30\ \mu\text{m}$ width stripes. The side length of the test object was $810\ \mu\text{m}$. The distance between the X-ray tube and the chart was 50 mm. The lens was placed 950 mm away from the chart, and the camera was placed in the focal plane at a distance of 200 mm away from the lens exit. The voltage of the tube was set to 30 kV, and the current was set to $300\ \mu\text{A}$, $400\ \mu\text{A}$, $500\ \mu\text{A}$ and $600\ \mu\text{A}$. The exposure time was set to 180 s for all of these cases.

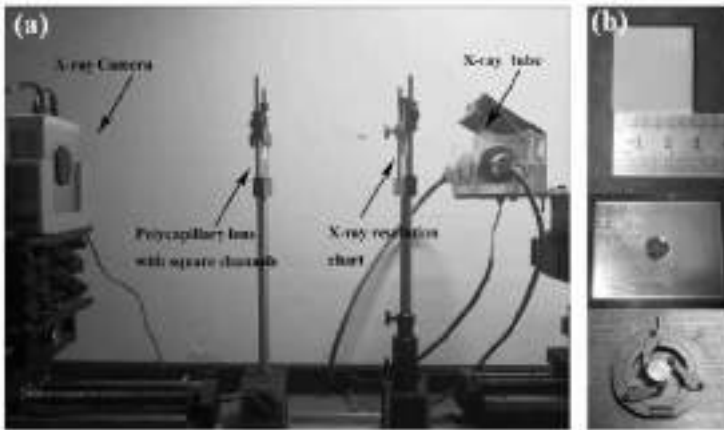


Figure 4. (a) Experimental setup; (b) From top to bottom: polycapillary X-ray lens with square channels, X-ray resolution chart and pinhole.

To test the feasibility of the LROS-TV method, a simple imaging experiment was conducted. Fig. 5(a) shows the estimated spatially variant PSFs. Fig. 5(b) shows the features of the resolution chart. Due to manufacturing errors such as dislocation and tilt of the channels, the PSFs cannot provide complete prior information for the process of restoration. In Fig. 6, (a)-(d) are the images of the resolution chart photographed directly by the camera, (e)-(h) are the raw images viewed through the lens and (i)-(l) are the deconvolved images using the LROS-TV method with 1000 iterations. With increased

current values, the contrast of the test object improved. The features of images projected back to the object plane can be better resolved. The PSNRs of Fig. 6(i)-(l) were 22.8382, 21.4842, 20.4325 and 19.8256, respectively. The X-ray source spot size increases with increasing current.

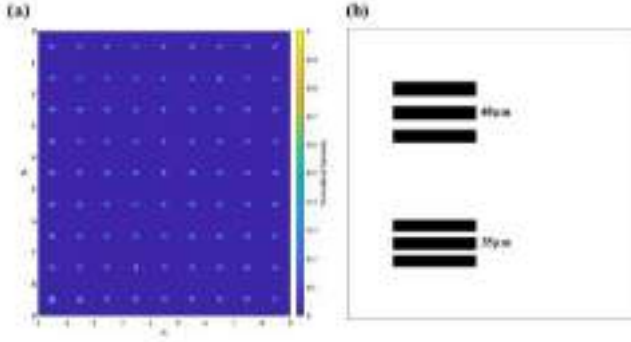


Figure 5. (a) Experimental spatially variant PSFs; (b) Pattern of the X-ray resolution chart JIMA.

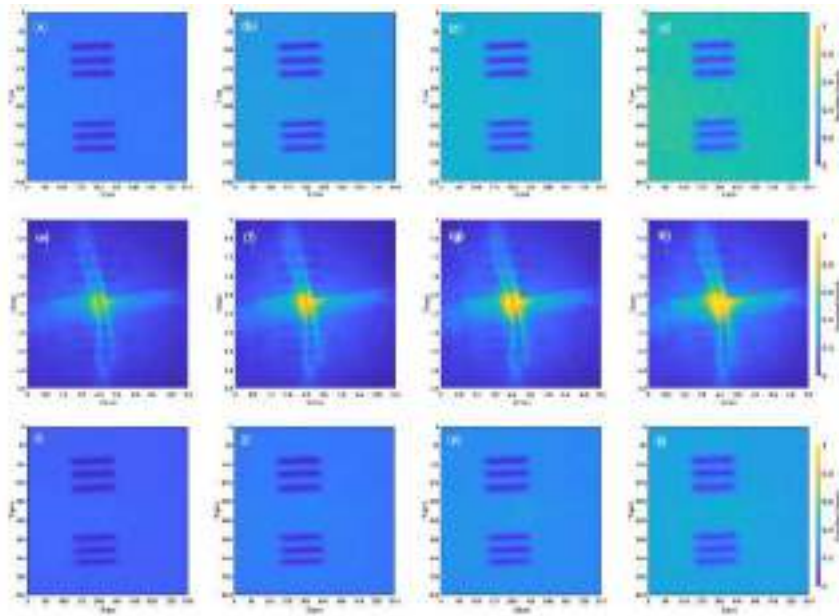


Figure 6. (a)-(d) Images of the resolution chart photographed directly by the camera; (e)-(h) Raw images viewed by the polycapillary X-ray lens with square channels recorded by the X-ray camera in the case of same voltage and different currents, from left to right the value is : 30kV 300 μ A , 30kV 400 μ A , 30kV 500 μ A , 30kV 600 μ A ; (i)-(l) Corresponding deconvolved images at the object plane.

4. Conclusion

In summary, we presented an idea to recover real images of an object from the raw data viewed through a polycapillary X-ray lens with square channels using the LROS-TV method. Because the curvature of each channel has tiny differences, the concept of a spatially variant point spread function was used in this work, and the whole lens was sectioned for simplified calculation. Using the prior information provided by the PSFs, imaging restoration was investigated by changing the numbers of photons that strike the lens and the contrast value of the test object. A feature can be clearly distinguished from the background when projected back to the object plane at the 109-photon level.

In addition, a simple coaxial imaging experiment was implemented to test the feasibility of the LROS-TV method. The results validated the method used in imaging restoration. The errors caused by lens manufacturing errors and the limited numbers of sections for simplified calculations make the next goal of our work clear. Methods to eliminate artifacts should also be investigated for better restoration quality. On the one hand, the manufacturing technique should be improved for a more satisfactory geometric structure. On the other hand, a more precise model for PSF estimation should be established, and parallel computing programs should be used. Furthermore, this work indicates that a polycapillary X-ray lens with square channels can be used as a lens for X-ray imaging transmission.

References

- [1] Kumakhov MA. Radiat EffDefect S. 1991. p. 329-363.
- [2] Shields PJ, Gibson DM and Gibson WM. Powder Diffr. 2002. p. 70-80.
- [3] Yonehara T, Yamaguchi M and Tsuji K. Spectrochim Acta B. 2010. p. 441-444.
- [4] Sun TX, Zhang ML and Liu ZG. J Synchrotron Radiat. 2009. p. 116-118.
- [5] Dabrowski KM, Dul DT and Wrobel A. Appl Phys Lett. 2013. p. 102.
- [6] Dabrowski KM, Dul DT and Korecki P. Opt Express. 2013. p. 2920-2927.
- [7] Qin M, Yi LT and Pan K. Opt Commun. 2018. p. 205-210.
- [8] Yi LT, Liu ZG. and Li ZB. Opt Commun. 2019. p. 139-142.
- [9] Peele AG. Nucl Instrum Meth A. 2001. p. 354-341.
- [10] Trussell HJ, Hunt BR. Ieee T Acoust Speech. 1978. p. 608-609.
- [11] Trussell HJ, Hunt BR. Ieee T Acoust Speech. 1978. p. 157-164.
- [12] Cobb ML, Hertz PL and Whaley RO. Digital Image Recovery and Synthesis II. 1993. p. 202-208.
- [13] Ozkan MK, Tekalp AM and Sezan MI. Ieee T Image Process. 1994. p. 450-454.
- [14] Marrugo AG, Millan MS and Sorel M. J Biomed Opt. 2014.
- [15] Peng SQ, Liu ZG and Sun TX. Chinese Phys B. 2016.
- [16] Pelli DG, Bex P. Vision Res. 2013. p. 10-14.
- [17] Peng SQ, Liu ZG and Sun TX. Nucl Instrum Meth A. 2015. p. 186-191.

Deep Learning Based Method for the Estimation of Patient's Angles from Lateral Skull Radiographs

Kazuma NAKAZEKO^{a, b, 1}, Shinya KOJIMA^c, Hiroyuki WATANABE^d and Hiroyuki KUDO^e

^a*Department of Radiological Technology, Faculty of Health Science, Juntendo University, 1-5-32, Yushima, Bunkyo-Ku, Tokyo, Japan*

^b*Graduate School of Systems and Information Engineering, University of Tsukuba, 1-1-1 Tennoudai, Tsukuba, Ibaraki, Japan*

^c*Department of Medical Radiology, Faculty of Medical Technology, Teikyo University, 2-11-1, Kaga, Itabashi-Ku, Tokyo, Japan*

^d*Graduate School of Health Sciences, Showa University, 1865, Tookaichibacho, Midori-ku, Yokohama, Kanagawa, Japan*

^e*Division of Information Engineering, Faculty of Engineering, Information and Systems, University of Tsukuba, 1-1-1 Tennoudai, Tsukuba, Ibaraki, Japan*

Abstract. Radiography is used for initial diagnosis and postoperative follow-up. If a radiograph is deemed unsuitable for diagnosis, it is rejected. Retaking a radiograph is disadvantageous for the patient because it prolongs the examination time and increases the radiation dose. Skull radiography is the position in which retaking occurs most frequently. In skull radiography, the patient's rotational direction is estimated from minute changes in the inner ear's structure in the lateral skull radiograph. When retaking, the amount of correction for patient positioning is generally estimated from the errors in the rejected image through empirical evidence. Therefore, considerable expertise is needed to correct the positioning appropriately, and inexperienced radiologic technologists take considerable time to estimate this error. This study aimed to estimate the patient's angle from lateral skull radiographs to compensate for radiologic technologists' lack of experience and reduce the burden on patients. The radiograph is a simulated 2-D line-integral projection of a 3-D CT image, and we developed an estimation method using deep learning with supervised training. The network is based on a re-scaled ResNet. The patient's angle was estimated in the lateral and superior-inferior directions. We evaluated the accuracy of estimation with the projected images of 256 simulated cases. The estimation errors were $0.48 \pm 0.41^\circ$ and $0.55 \pm 0.50^\circ$ in the lateral and superior-inferior angles, respectively. These findings suggest that a patient's angle can be accurately estimated from a radiograph using deep learning, compensating for the lack of experience and reducing retaking time.

Keywords. Deep learning, Radiography, Patient's angle, Retaking

¹ Corresponding Author: Kazuma Nakazeko, Department of Radiological Technology, Faculty of Health Science, Juntendo University; E-mail: k.nakazeko.tk@juntendo.ac.jp.

1. Introduction

Radiography is used for initial diagnosis and postoperative follow-up. Radiologic

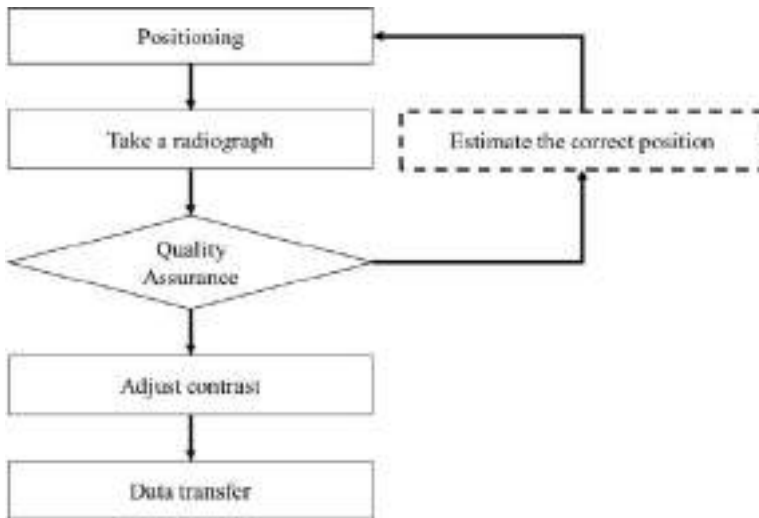


Figure 1. Workflow in taking a radiograph.

technologists must take radiographs suitable for diagnosis. Figure 1 shows the workflow of radiography. First, the radiologic technologist positions the patient and takes a radiograph. Subsequently, they send the contrast-adjusted radiograph to a doctor. However, the doctor might reject it if they find it unacceptable. The major sources of rejection are inappropriate positioning and image quality [1, 2]. The improperly positioned radiograph is not suitable for diagnosis because it cannot clearly show the region to be diagnosed. In addition, a radiograph that contains a lot of noise or has unclear contrast is also not suitable for diagnosis because the region to be diagnosed is unclear. Retaking a radiograph is disadvantageous for the patient because it prolongs the examination time and increases the radiation dose.

The causes of rejection are classified as inappropriate positioning and image quality. Currently, X-ray detectors used in many hospitals use digital radiography (DR). In screen/film systems, the dynamic range is small and does not provide adequate contrast in case of exposure errors (over- and underexposure). DR system has a larger dynamic range than the screen/film system, and adjusting the contrast of the radiograph and correcting it is feasible. Hence, the rejection due to image quality has been reduced. However, the rejection due to positioning is still frequent [3, 4]. The radiographs are positioned so that the diagnosed region overlaps as little as possible with other regions. Skull radiography are divided according to the area to be observed. In radiography, which requires observation of detailed areas, a slight deviation in angle makes the radiograph unsuitable for diagnosis. Therefore, skull radiography is the application in which the retaking occurs most frequently [5]. Proper positioning is determined based on the knowledge of anatomy and positioning in radiography. Additionally, experience in evaluating numerous radiographs enables the suitable positioning according to the

patient's physique, which requires appropriate radiographs. The patient's rotational direction needs to be estimated from minute changes in the inner ear's structure in the lateral skull radiograph. When retaking, the amount of correction for the patient positioning is generally estimated from the errors in the rejected image through empirical evidence.

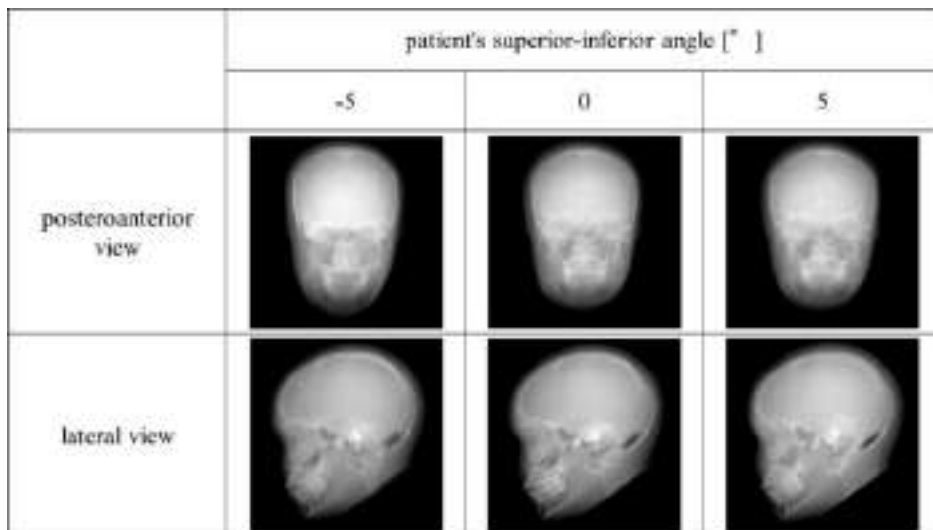


Figure 2. Differences in images depending on the positioning. Posteroanterior views and lateral views are shown and are compared.

Therefore, considerable expertise is needed to correct the positioning appropriately, and inexperienced radiologic technologists take a long time to estimate this error. This study is aimed at developing a method to estimate the patient's angle from lateral skull radiographs to compensate for radiologists' lack of experience and reduce the burden on patients.

Image processing can be used to estimate the angle of a subject in a photograph. In the field of face recognition, some methods recognize areas of high symmetry, such as faces [6, 7], and some use facial feature points and estimate face angles based on them. On the other hand, in radiography, Seah et al. extracted feature points from a radiograph of the lateral knee joint to estimate tube angles for another positioning [8]. In addition, Wu et al. estimated the rotation angle of the chest from asymmetric projection and validated it using a phantom [9]. However, there exist only two studies that used deep learning to estimate information about the patient's body position from radiographs.

- Ota et al. developed a method to estimate the knee joint rotation direction [10].
- Nakazeko et al. developed a method to estimate the patient's angle from a posteroanterior skull radiograph [11].

We mention that there exist very few previous studies on this topic, because there exist no image processing algorithms for estimating the angles in radiographs, unlike in photographs. A radiograph is a projection image, and feature points are depicted as changes in coordinates if the angle changes. These feature points cannot be represented in conventional image processing algorithms. In contrast, deep learning are powerful

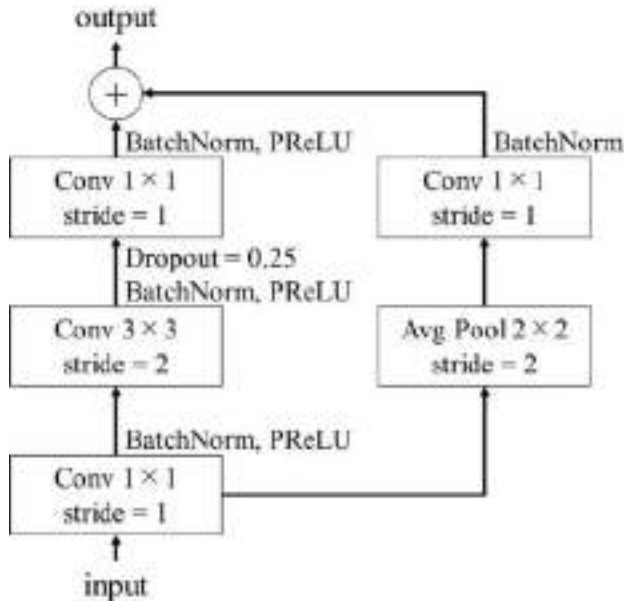


Figure 3. Structure of the residual block.

frameworks which solve the angle estimation problem, in which the mechanism of recognition is unknown, by using training data sets. This study developed a deep learning technique based on a rescaled ResNet (ResNet-RS). We used images of 256 simulated cases to evaluate accuracy of estimating the patient's angles.

Our previous work [11] also studied the problem of estimating the patient's angles from a skull radiograph. The major difference between [11] and this work is as follows. In [11], a radiograph taken from the posteroanterior direction was used. On the other hand, in this work, a radiograph taken from the lateral direction was used. It is known that an image change occurring by the patient rotation is relatively large in the posteroanterior radiograph, but is smaller in the lateral radiograph. Figure 2 compares the posteroanterior and lateral skull radiographs when rotated by $\pm 5^\circ$ in the superior-inferior direction. The posteroanterior skull radiograph shows some discrepancies in the image depending on the rotation direction, as shown in Figure 2. However, the differences in the lateral skull radiographs are not apparent. Therefore, the angle estimation from the lateral one is much more challenging than that from the posteroanterior one. Actually, the method developed in [11] did not work well in the original form for the lateral radiograph case. Therefore, we needed to improve the method in [11] in some parts to obtain successful results in the lateral radiograph case. This improved method is the major contribution of this paper.

2. Proposed Method

We use a deep learning technique to estimate patient angles. This method is based on a ResNet-RS [12]. Figure 3 illustrates the residual block in this model constructed using

Table 1. Architecture of ResNet-RS used.

Name	output size	Layer
stem	128×128	3×3, 64, stride = 2 3×3, 64, stride = 1 3×3, 64, stride = 1
conv 1	64×64	$\left[\begin{array}{l} 1\times 1, 64, \text{stride} = 1 \\ 3\times 3, 64, \text{stride} = 2 \\ 1\times 1, 256, \text{stride} = 1 \end{array} \right] \times 3$
conv 2	32×32	$\left[\begin{array}{l} 1\times 1, 128, \text{stride} = 1 \\ 3\times 3, 128, \text{stride} = 2 \\ 1\times 1, 512, \text{stride} = 1 \end{array} \right] \times 4$
conv 3	16×16	$\left[\begin{array}{l} 1\times 1, 256, \text{stride} = 1 \\ 3\times 3, 256, \text{stride} = 2 \\ 1\times 1, 1024, \text{stride} = 1 \end{array} \right] \times 23$
conv 4	8×8	$\left[\begin{array}{l} 1\times 1, 512, \text{stride} = 1 \\ 3\times 3, 512, \text{stride} = 2 \\ 1\times 1, 2048, \text{stride} = 1 \end{array} \right] \times 3$
C	2×1	Average Pooling, Linear

ResNet-D [13], which is able to suppress overlearning [14] and improve robustness. It uses the PReLU function, which can achieve higher accuracy in image classification [15]. The parameters of the dropout and PReLU functions are determined by trial and error. Table 1 lists the architecture of the network used in this paper. A radiograph is used as the input data; the stem layer downsizes the input data from 256 to 128, and increases the number of channels. Furthermore, the features of radiographs are extracted in convolution layers 1 to 4. Finally, the extracted features are converted into two real numbers representing the angles to be estimated in the last layer. The input data are simulated lateral skull radiographs, and the output data are the real values of the patient's angles in two directions. We explain about the input data in more detail in Section 3.1.1.

The rotation angles are normalized from 0 to 1 by setting the angle at which the patient's median sagittal plane is parallel to the detector to 0° and it takes the range from -10° to 9° in 1° increment. The approximate patient error is in this range, and any further errors can be checked by the radiologic technologist with the sight, so this range was used. The values obtained in the network output and supervised patient's angle are normalized by using the following equation.

$$\text{Normalized value} = \frac{\text{Patient's angle} + 10.0}{20.0} \tag{1}$$

Since the obtained estimated angle is normalized, we convert it into an actual angle by using the following equation,

$$\text{Estimated angle} = \text{Normalized output value} \times 20.0 - 10.0 \tag{2}$$

3. Experiment

3.1. Lateral skull radiograph

A lateral skull radiograph does not show noticeable differences with respect to the patient's rotation compared to a posteroanterior skull radiograph. In the first trial, we tried to estimate the patient's angles using the full lateral skull radiograph as the training

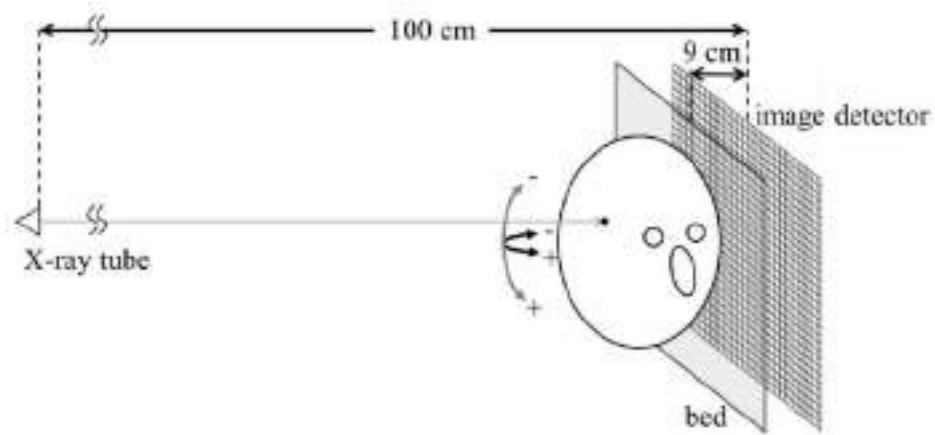


Figure 4. Illustration of simulating skull radiograph.

data. However, the method could not capture minute changes and incorrectly estimated the angles, resulting in a significant error. Since the structure of head is symmetric, the left and right structures overlap in the lateral skull radiograph. Consequently, remarkably similar images can be obtained even when the rotation direction is different. Radiologic technologists empirically estimate the direction of rotation of a symmetrical head based on differences in the magnification of the inner ear structures and temporomandibular joint. The inner ear and temporomandibular joint are located on the left and right sides of the skull, are at different distances from the detector. The differences in magnification make it possible to distinguish the left and right sides on the image. In this study, the estimation is based on the difference in magnification of the inner ear structures. Therefore, an improvement which is able to capture minute changes in the inner ear structure is necessary for accurate estimation. In this study, we propose to use only the region centered on the pituitary gland obtained by a pre-processing image cropping step. The cropping is performed in such a way that the pituitary gland coincides with the center of image, because the center point actually used in the radiograph positioning is approximately the pituitary gland.

3.1.1. Dataset

In our deep learning model, we use an image as the input and two angles as the output. Many image databases are currently available and have been actively used in radiology research. However, no datasets exist which combine the patient's angles with radiographs. Therefore, we constructed an image dataset consisting of simulated

radiographs for this work. Lateral skull radiographs were generated from 3-D CT images through numerical simulation. Figure 4 illustrates the geometric arrangement in skull radiography. In Fig. 4, the hatched and gray rectangular regions represent an image detector and a bed, respectively. A head rotates in the lateral (black arrow) and superior-inferior (gray arrow) direction to simulate a 2-D radiograph image. In the lateral direction, the direction corresponding to the anti-clockwise rotation in the top view was set as positive. In the superior-inferior direction, the direction corresponding to the extension was set as positive. The distances to the x-ray tube and the bed from the detector were 100 and 9 cm, respectively.

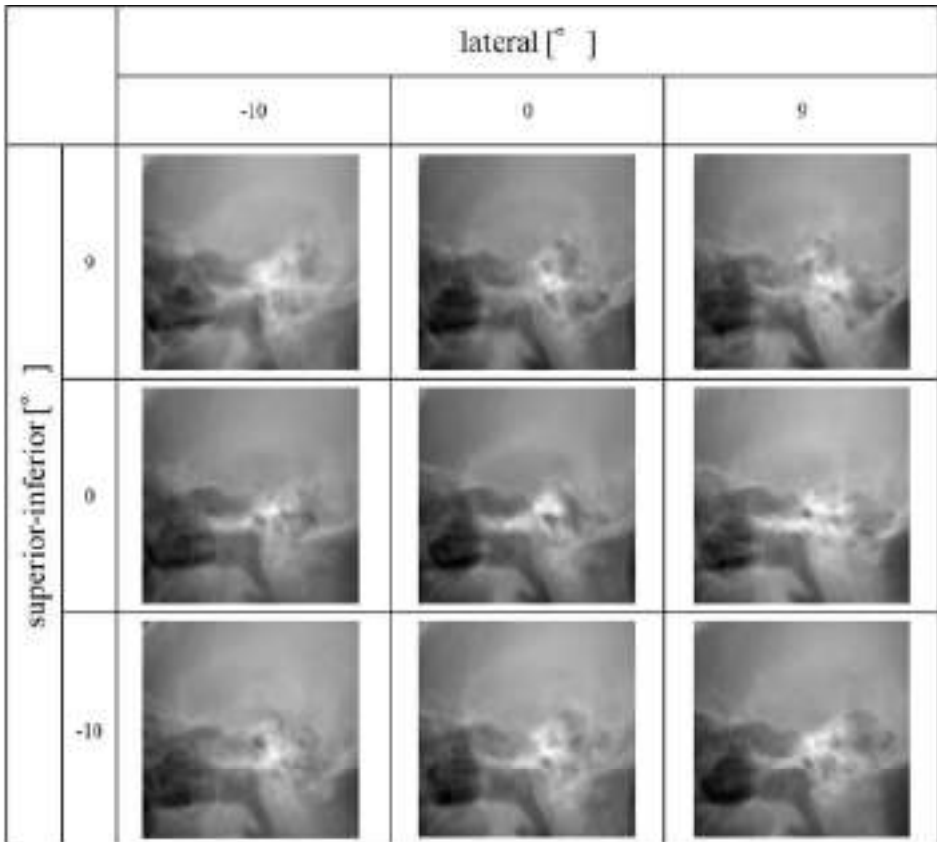


Figure 5. Illustration of simulating skull radiograph.

A lateral skull radiograph is taken with the setup of positioning the patient such that the middle sagittal plane and the detector plane are perpendicular to each other. Then, X-rays are radiated from the perpendicular direction to the detector. A dataset of 3-D CT images after cropping only the head region taken with a PET-CT scanner are provided

in the cancer imaging archive (TCIA) [16]. We used the 3-D CT images in this dataset to construct lateral skull radiographs. We use four different slice thicknesses: 0.6, 1.5, 2.5, and 3.0 mm. The dataset was initially created by setting the rotation angle to 0° in both the lateral and superior-inferior directions. Each radiograph was simulated as a ray-sum images with parallel-beam geometry. For this setting, three radiologic technologists set the angle at which the external auditory meatus overlaps the ray-sum images from multiple directions. Next, the point of X-ray incidence was determined such that the pituitary gland is approximately centered on the ray-sum image. The approximate position of the pituitary gland was used as the X-ray incidence point, because the incidence point is deviated from the radiograph obtained at each position in the clinic. Each radiograph was computed as a simulated 2-D line-integral projection of a 3-D CT image [17]. In more detail, each pixel value in the radiograph was computed by a summation of pixel values of 3-D CT image along the line through which the corresponding X-ray passes, which is expressed as

$$D(x, z) = \sum_{i=1}^N l_i \times p(x_i, y_i, z_i), \quad (3)$$

where $D(x, z)$, N , l_i , and p denote the value of 2-D line-integral projection, the number of pixels such that each X-ray passes, the length of line through each pixel, and pixel value of 3-D CT image, respectively. The matrix size of simulated image was 256×256 (pixels).

As only a portion of the lateral skull radiograph is used in this study, images containing metal artifacts in dental region could also be used. In addition, because changes in the inner ear structure are important features in the angle estimation, we also decided to use CT images without the parietal region. This resulted in the use of images from 256 cases. Figure 5 shows an example of a created lateral skull radiograph. Ota et al. used 60 cases in the previous work, whereas we used 256 cases. Therefore, we used a more significant number of cases in this study than in the existing previous study. Furthermore, in our previous work [11], the number of cases for training data was less than 50 so that we increased the number using a data augmentation, i.e. including images with rotations and images with grid distortion. However, adding the rotated images introduces errors in the relationship between the patient's angle and the simulated radiograph. Furthermore, a portion of the image was extracted in this work to capture minute changes. Using the grid distortion causes errors in the relationship between the minute changes and the patient's angles. Therefore, in this work, training data were used without the data augmentation, because the number of cases was more significant compared to our previous work [11].

3.2. Experimental settings

The construction of the image database was performed using C programming language, but a code to estimate the patient's angle using deep learning was developed using Python. The deep learning was implemented using PyTorch that is an open source machine learning framework on a GPU unit (NVIDIA GeForce RTX 3090). The training of the model was performed by using the Mean Squared Error (MSE) loss function and the Adam optimization method.

The number of training epochs was set to 50, and the weight decay rate was set to 0.00001. The learning rate was changed from 0.0001 to 0.00001 based on the number of iterations, and the batch size was eight, which were determined by trial and error.

3.3. Cross validation

In this study, we used 256 cases. In this 256-case study, 224 cases were used for training and 32 cases for test, i.e. 89,600 images were used for training and 12,800 images for test. These number of images are the number of training and test cases multiplied by 400, since there are 400 images for each case. Cross-validation was performed to validate 256 cases. We divided the 256 cases into eight groups, and performed eight times of testing 32 cases in each group.

Table 2. Summary of estimated error values of lateral and superior-inferior angles. Each value represents the average value of all the 256 cases.

	Average	Standard deviation
lateral	0.48	0.41
superior-inferior	0.55	0.50

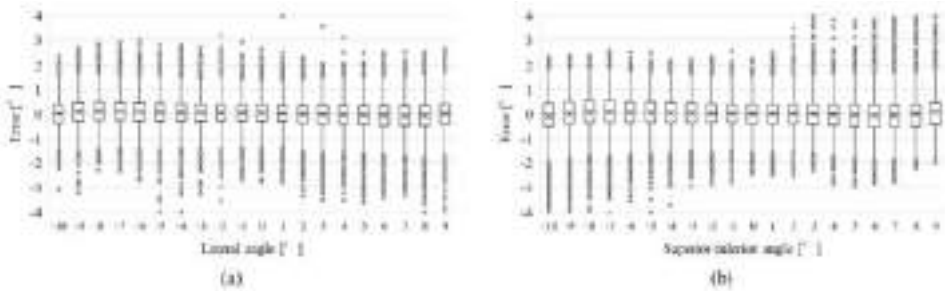


Figure 6. Error values of estimated angles averaged for all the cases.

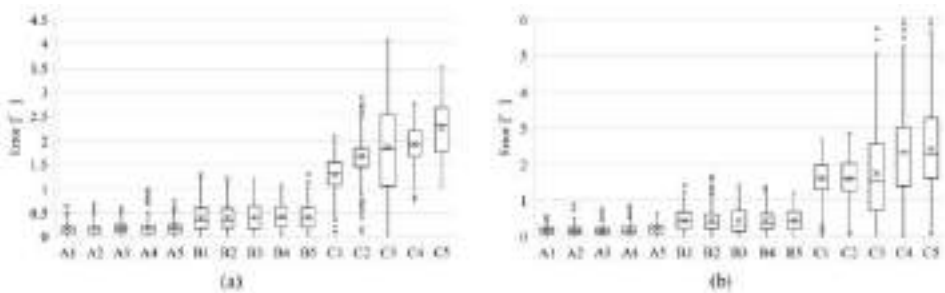


Figure 7. Five typical cases were selected for each group of small (A), medium (B), and large (C) errors.

Hereinafter, we refer to the two estimated patient's angles as “lateral” and “superior-inferior”, respectively.

4. Results

To evaluate accuracy of estimating the patient's angles from the lateral skull radiograph, we used estimation errors for the lateral and superior-inferior angles computed by

$$\text{The estimation error} = \frac{\sum_{i=1}^n |\theta_i - \theta'_i|}{n}, \quad (4)$$

where n , θ , and θ' denote the number of sample cases, the estimated angle, and the

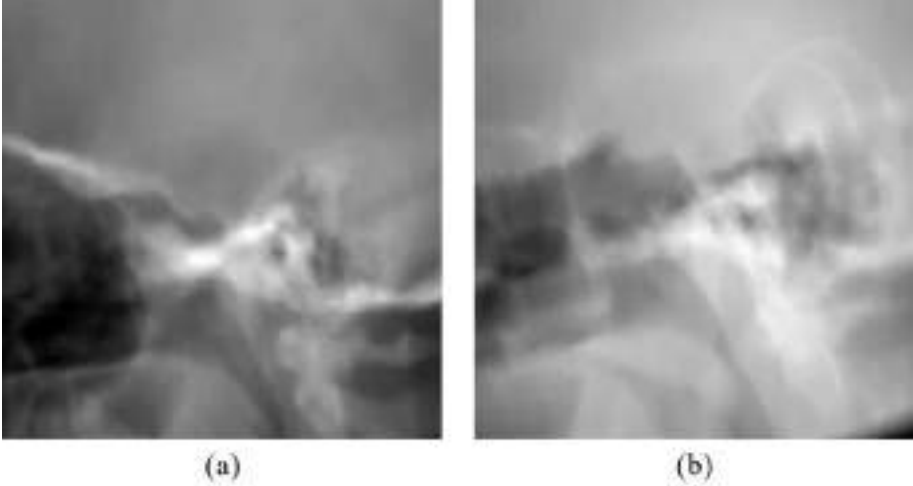


Figure 8. Representative samples with significant estimation error. (a) Case where the contrast between the bone and the other regions is high, (b) case where there was a large shift in the image coordinates.

correct angle, respectively. In Table 2, we summarize average and standard deviation of the errors obtained from all the results of 256 cases. Figure 6 illustrates the estimation errors for the lateral and superior-inferior angles in the corresponding directions. Figure 7 illustrates the estimation errors for each case. In Figs. 6 and 7, each graph shows the distribution of errors into quartiles. Boxes are drawn between the first and third quartiles. Lines in the box show the median value. Solid lines indicate the distribution outside the upper and lower quartiles, and any point outside those lines is considered an outlier. Cross marks and circle marks show the averages and outliers, respectively. Throughout the results, the most significant error found was $2.24 \pm 0.55^\circ$ in the lateral direction and $2.44 \pm 1.32^\circ$ in the superior-inferior direction.

5. Discussion

This work developed a method to estimate the patient's angles using a lateral skull radiograph. Before this development, we constructed an image dataset because no valid datasets with the annotation of patient angles were available in the existing open data. Table 2 summarizes the result of estimation for all the 256 cases. We believe that these results are promising in the following sense. The estimation results for each angle shown in Figure 6 are comparable to those in our previous work [11], in spite of the fact that the estimation from the lateral radiograph is more difficult compared to the

estimation from the posteroanterior radiograph. However, there was a change in error bias (increase or decrease) depending on the angle. This may be because more cases were used in the study than in the previous work.

Figure 8 shows two typical examples of cases with significant errors. Two factors are major sources of these large estimation errors. First, the image contrast in some images was higher than that in the other cases. In the case shown in Figure 8(a), the signal in the bone region is higher than that in the other cases, and the contrast between the bone and the other areas is also high. We suppose that this prevents capturing minute changes in the image due to changes in the angle, leading to a significant error. And, we believe that these errors can be reduced by adding a histogram equalization process to equalize the contrast as a process prior to estimating the angle. The second example is the case where the error becomes large due to the shift of X-ray incident point. In the case shown in Figure 8(b), the incident point is lower than that in the other cases, and there is a coordinate shift in the image. This leads to significant error because the image differs from the other cases. In this case, when the angle was estimated with the correct angle of incidence, the error decreased from $1.86 \pm 1.02^\circ$ to $0.91 \pm 0.58^\circ$ in the lateral direction and from $2.33 \pm 1.32^\circ$ to $0.95 \pm 0.78^\circ$ in the superior-inferior direction. To overcome these drawbacks, the following methods need to be developed to eliminate the factors that increase errors. First, it is necessary to develop a method that can handle various cases by increasing the number of cases. Second, the learning dataset is classified according to the characteristics of each image in the learning step. Then, the model training is performed dependent on each class. In the test step, a model which best matches the input image is selected to obtain output. A method that performs a classification as a pre-processing step enables the construction of such a method. Second, the first error factor will be reduced by developing a method that performs image processing to compensate for variations in image contrast. In addition, it is necessary to develop a pre-processing method that automatically extracts the area centered on the pituitary gland for clinical use. In addition, it is necessary to confirm that the data set is suitable for validation on a clinical device. It is essential to check the relationship between angular errors and image changes that occur when imaging with clinical equipment.

6. Conclusion

We developed a deep learning based method to estimate a patient's angles from a lateral skull radiograph. The estimation results were reasonable, with approximately 0.5° error in both the lateral and superior-inferior directions. Although the estimation from the lateral radiograph is more difficult compared to the estimation from the posteroanterior radiograph dealt in our previous work [11], the accuracy of estimation in this work (lateral) was comparable to that reported in [11] (posteroanterior). This may be thanks to using a significant number of cases in the training. However, there were cases where a considerable error occurred because of differences in the image contrast and the translation in the image coordinates. It is expected that this drawback will be resolved in the future by increasing the number of cases used for training and by using multiple models depending on the image characteristics. In addition, validating the proposed method with images taken from an actual clinical equipment is also an important future work.

7. Acknowledgements

We thank Editage (www.editage.com) for the English language editing.

References

- [1] Kjelle E, Schanche AK, Hafskjold L. To keep or reject, that is the question - A survey on radiologists and radiographers' assessments of plain radiography images. *Radiography (Lond)*. 2021 Feb;27(1):115-119. doi: 10.1016/j.radi.2020.06.020.
- [2] Atkinson S, Neep M, Starkey D. Reject rate analysis in digital radiography: an Australian emergency imaging department case study. *J Med Radiat Sci*. 2020 Mar;67(1):72-79. doi: 10.1002/jmrs.343.
- [3] Kjelle E, Chilanga C. The assessment of image quality and diagnostic value in X-ray images: a survey on radiographers' reasons for rejecting images. *Insights Imaging*. 2022 Mar 4;13(1):36. doi: 10.1186/s13244-022-01169-9.
- [4] Waaler D, Hofmann B. Image rejects/retakes--radiographic challenges. *Radiat Prot Dosimetry*. 2010 Apr-May;139(1-3):375-9. doi: 10.1093/rpd/ncq032.
- [5] Lin C-S, Chan P-C, Huang K-H, Lu C-F, Chen Y-F, Lin Chen Y-O. Guidelines for reducing image retakes of general digital radiography. *Advances in Mechanical Engineering*. 2016;8(4). doi:10.1177/1687814016644127.
- [6] Murphy-Chutorian E, Trivedi MM. Head pose estimation in computer vision: a survey. *IEEE Trans Pattern Anal Mach Intell*. 2009 Apr;31(4):607-26. doi: 10.1109/TPAMI.2008.106.
- [7] Borghi G, Fabbri M, Vezzani R, Calderara S, Cucchiara R. Face-from-Depth for Head Pose Estimation on Depth Images. *IEEE Trans Pattern Anal Mach Intell*. 2020 Mar;42(3):596-609. doi: 10.1109/TPAMI.2018.2885472.
- [8] Seah LJY, Seow D, Mahmood D, Chua EC, Sng LH. Can the measured angle ABC on the lateral projection of the knee be used to determine the tube angulation for an optimum skyline projection? *Radiography (Lond)*. 2022 May;28(2):407-411. doi: 10.1016/j.radi.2021.11.005.
- [9] Wu Z, Hou P, Li W, Zhu T, Wang P, Yuan M, Sun J. Estimating rotation angle from asymmetric projection of chest. *J Xray Sci Technol*. 2021;29(6):1139-1147. doi: 10.3233/XST-210990.
- [10] Ohta Y, Matsuzawa H, Yamamoto K, Enchi Y, Kobayashi T, Ishida T. Development of retake support system for lateral knee radiographs by using deep convolutional neural network. *Radiography (Lond)*. 2021 Nov;27(4):1110-1117. doi: 10.1016/j.radi.2021.05.002.
- [11] Nakazeko K, Kojima S, Watanabe H, Kudo H. Estimation of patient's angle from skull radiographs using deep learning. *J Xray Sci Technol*. 2022;30(5):1033-1045. doi: 10.3233/XST-221200.
- [12] Bello I, Fedus W, Du Xianzhi, Cubuk ED, Srinivas A, Lin T-Y, Shiens J, Zoph B. Revisiting ResNets: Improved Training and Scaling Strategies. *arXiv [Preprint]* arXiv:2103.07579. 10.48550/arXiv.2103.07579
- [13] He T, Zhang Z, Zhang H, Zhang Z, Xie J, Li M. Bag of tricks for image classification with convolutional neural networks. in: Lisa O'Conner, editor. *Proceedings of the IEEE conference on computer vision and pattern recognition*; 2019 June 16-17; Long Beach, CA. USA: Conference Publishing Services; pp.558-67. doi:10.48550/arXiv.1812.01187.
- [14] He K, Zhang X, Ren S and Sun J, Delving deep into rectifiers: Surpassing human-level performance on ImageNet classification. in: Lisa O'Conner, editor. *2015 IEEE international conference on computer vision*; 2015 Dec 7-13; Santiago, Chile: Conference Publishing Services; pp.1026-1034. doi: 10.1109/ICCV.2015.123.
- [15] Hinton GE, Srivastava N, Krizhevsky A, Sutskever I, Salakhutdinov RR. Improving neural networks by preventing co-adaptation of feature detectors. *ArXiv [preprint]*. arXiv: 1207.0580 doi:10.48550/arXiv.1207.0580.
- [16] Clark K, Vendt B, Smith K, Freymann J, Kirby J, Koppel P, Moore S, Phillips S, Maffitt D, Pringle M, Tarbox L, Prior F. The Cancer Imaging Archive (TCIA): maintaining and operating a public information repository. *J Digit Imaging*. 2013 Dec;26(6):1045-57. doi: 10.1007/s10278-013-9622-7.
- [17] Nakazeko K, Kajiwara H, Watanabe H, Kuwayama J, Karube S, Araki M, Hashimoto T, Shinohara H. [Development of computer assisted learning program using cone beam projection for head radiography]. *Igaku Butsuri*. 2012;32(1):2-11. Japanese. doi:10.11323/jjmp.32.1_2.

Stability Evaluation of Computational Intelligence-Based Subset Feature Selection Methods on Breast Cancer Data Analysis

Shaode YU^a, Boji LIU^a, Bingjie LI^a, Mingxue JIN^a, Junjie WU^b, and Hang YU^{c,1}

^a*School of Information and Communication Engineering, Communication University of China, Chaoyang, Beijing, China*

^b*Department of Radiation Oncology, University of Texas Southwestern Medical Center, Dallas, Texas, United States*

^c*School of Aerospace Science and Technology, Xidian University, Xi'an, Shanxi, China*

Abstract. The stability of computational intelligence based subset feature selection (CI-SFS) has not been explored. In this study, 44 methods are evaluated on BCDR-F03 using 5 stability estimators. Experimental results identify 3 methods achieving 0.55 or higher scores from two estimators, 7 methods leading to good classification (area under the curve ≥ 0.80) and 4 potential signatures helping cancer diagnosis. Conclusively, most of the CI-SFS methods seem sensitive to data perturbation and different estimators cause inconsistent results. In future work, attention should be paid to developing robust fitness functions to enhance feature preference and designing advanced estimators to quantify the feature selection stability.

Keywords. Stability, computational intelligence, subset feature selection, breast cancer diagnosis, signature discovery

1. Introduction

Own to the dramatic increase of variable dimension, feature selection (FS) is growingly important in pattern analysis [1–3]. To choose most relevant features, computational intelligence based subset feature selection (CI-SFS) algorithms have been developed [4], and their purpose is to imitate swarming behaviour, social hierarchy, foraging strategy and hunting mechanism to select a subset of features for user preference.

This study investigates CI-SFS stability on feature preference. Stability is important in machine learning, since it is correlated with experiment-level repeatability and pattern analysis [5]. Meanwhile, CI-SFS has made big progress in the past decades [4]. Thus, it is meaningful to present an evaluation of CI-SFS stability.

Few studies concern FS stability. In [6], algorithms are analyzed using correlation coefficient and Jaccard index. In [7], stability is assessed using two similarity-based es-

¹Corresponding Author: Hang Yu, Xidian University, Shanxi, China; E-mail: hyu@xidian.edu.cn.

timators. In [8], stability is estimated via adapted Tanimoto distance and correlation coefficients. In [9], stability is quantified via relative weighted consistency and correlation-based measures. In [10], 23 FR algorithms are evaluated using an advanced estimator. These studies pave the way for understanding the FS stability.

In this study, using 5 estimators, we investigate the stability of 44 CI-SFS algorithms on the BCDR-F03, a medical dataset with sufficient instances. The contributions of this study come from several points. Above all, the stability of a large number of bio-inspired CI-SFS algorithms is quantified. Secondly, five estimators are used to show experimental cues on estimator application. Thirdly, on BCDR-F03, several potential signatures are discovered that benefit medical image analysis and cancer diagnosis.

2. Materials and Methods

2.1. Data collection

BCDR-F03 [11] includes 230 benign and 176 malignant breast lesions of 736 mammograms². For representation, $p = 17$ features are computed from intensity (i_mean, i_median, i_std_dev, i_max, i_min, i_kurtosis and i_skewness), shape (s_area, s_perimeter, s_x_center, s_y_center, s_circularity, s_elongation and s_form) and texture (t_contrast, t_correlation and t_entropy). Since 310 cases are imaged twice [12], to avoid one lesion with multiple records, the first one of each lesion is used and 406 feature records remain.

Table 1 shows the dataset, and 141 records of each group are used in the variable selection procedure. Notably, t -test is conducted, and the features (i_min, i_kurtosis and s_x_center) with no significant difference are removed.

Table 1. Summary of the dataset BCDR-F03 used in this study

	benign (train/test)	malignant (train/test)	p	source
BCDR-F03	230 (141/89)	176 (141/35)	17 (14)	mammogram

2.2. CI-SFS algorithms

Forth-four algorithms are evaluated that use different heuristic optimization strategies³, including artificial bee colony (ABC) [13], artificial butterfly optimization (ABO) [14], ant colony optimization (ACO) [15], ant colony system (ACS) [16], atom search optimization (ASO) [17], bat algorithm (BA) [18], butterfly optimization algorithm (BOA) [19], cuckoo search (CS) [20], crow search algorithm (CSA) [21], differential evolution (DE) [22], equilibrium optimizer (EO) [23], emperor penguin optimizer (EPO) [24], firefly algorithm (FA) [25], fruit fly optimization algorithm (FFOA) [26], flower pollination algorithm (FPA) [27], genetic algorithm (GA) [28], genetic algorithm tournament (GAT) [29], generalized normal distribution optimization (GNDO) [30], gravitational search algorithm (GSA) [31], grey wolf optimizer (GWO) [32], henry gas solubility optimization (HGSO) [33], Harris hawks optimization (HHO) [34], human learning optimization

²<http://bcdr.inegi.up.pt>

³<https://github.com/JingweiToo/Wrapper-Feature-Selection-Toolbox>

(HLO) [35], harmony search (HS) [36], Jaya algorithm (JAYA) [37], Monarch butterfly optimization (MBO) [38], moth-flame optimization (MFO) [39], marine Predators Algorithm (MPA) [40], Manta ray foraging optimization (MRFO) [41], multi-verse optimizer (MVO) [42], poor and rich optimization algorithm (PARO) [43], pathfinder algorithm (PFA) [44], particle swarm optimization (PSO) [45], simulated annealing (SA) [46], satin bowerbird optimizer (SBBO) [47], sine cosine algorithm (SCA) [48], slime mould algorithm (SMA) [49], symbiotic organisms search (SOS) [50], salp swarm algorithm (SSA) [51], tree growth algorithm (TGA) [52], tree-seed algorithm (TSA) [53], whale optimization algorithm (WOA) [54], and weighted superposition attraction (WSA) [55].

2.3. Experiment design

Figure 1 shows stability estimation and classification performance. In each iteration, a dataset $\{(X, y)\}$ is divided for training $\{(X^{train}, y^{train})\}$ and testing $\{(X^{test}, y^{test})\}$, a CI-SFS yields a binary vector \vec{f}_i ($\vec{f}_i = \langle f_{i,1}, \dots, f_{i,k}, \dots, f_{i,p} \rangle$) after the i^{th} run of p features. Specifically, $f_{i,k} = 1$ indicates the k^{th} feature is selected, and classification metrics are computed. After $N = 500$ iterations, S values are estimated, and metrics are averaged.

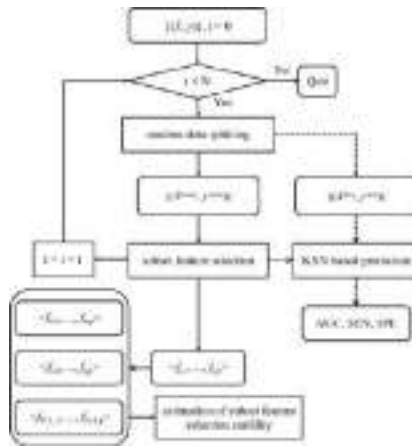


Figure 1. The procedure of estimating stability and classification performance.

2.4. Stability estimator

Five estimators are employed [56]. The computation of similarity based estimators Jacard, Dice and Ochi are defined as $J = \frac{\vec{f}_i \cap \vec{f}_j}{\vec{f}_i \cup \vec{f}_j}$, $D = \frac{2 \times (\vec{f}_i \cap \vec{f}_j)}{\vec{f}_i + \vec{f}_j}$ and $O = \frac{\vec{f}_i \cap \vec{f}_j}{\sqrt{\vec{f}_i \times \vec{f}_j}}$ respectively, in which \cap and \cup correspond to intersection and union parts of \vec{f}_i and \vec{f}_j . To the entropy estimator, it computes the normalized frequency of features, finds out the features with non-zero frequency $\hat{p}(s_i)$ and quantifies the entropy as $E = -\sum \hat{p}(s_i) \log_2 \hat{p}(s_i)$. The stability estimator (Nogueria) recasts the stability measure procedure as an estimation of a random variable [5], and allows for reliable comparison across different procedures.

2.5. Classification performance metrics

Three metrics of the area under the receiver operating characteristic curve (AUC), sensitivity (SEN) and specificity (SPE) are used to evaluate the performance of tumor classification [3]. Given the ground truth and predicted labels, AUC reveals the capacity of tumor differentiation based on the curve of prediction probability, SEN reflects the ability of a model to correctly recognize malignant lesions, and SPE shows the ability of a model to identify benign cases correctly. To each metric, a higher value indicates a better performance. In this binary problem ($y \in \{0, 1\}$), the label of malignant cases is $y = 1$.

3. Results

3.1. Estimated stability

Figure 2 shows the stability values of CI-SFS algorithms. The horizontal axis lists CI-SFS names, and the vertical axis is S values. It shows 3 algorithms achieve stable feature preference (DE, $S \geq 0.58$; FFOA $S \geq 0.55$; WSA, $S \geq 0.60$) identified by DICE (pink) and Ochi (black). The values using entropy- and Noguera-based estimators are low.

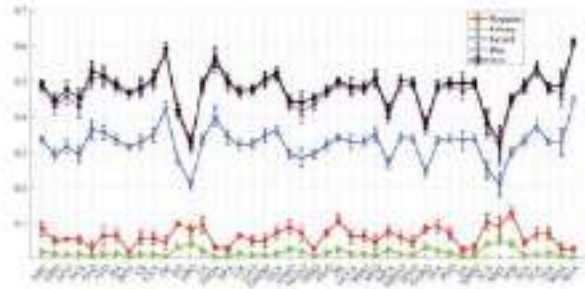


Figure 2. Stability values of CI-SFS algorithms from five estimators.

3.2. Prediction performance

Figure 3 shows the performance of tumor classification. The horizontal axis shows the CI-SFS names, the vertical axis shows the AUC values, and KNN is the classifier. It is observed that CI-SFS algorithms lead to good performance ($AUC \geq 0.70$) and 7 algorithms (ABC, FA, HLO, HS, MPA, PFA and SOS) achieve $AUC \geq 0.80$.

3.3. Potential signatures

Figure 4 shows the signatures discovered by CI-SFS algorithms. In the $N = 500$ iterations, when a feature is selected more than 250 times (*i.e.*, $\geq 50\%$ chance of selection), it is defined as a potential signature. Further, the number of CI-SFS algorithms that define features as signatures is summarized. It is observed that there are 44, 42, 28 and 34 algorithms that respectively identify `s_circularity`, `s_y_center`, `t_contr` and `s_form` as the potential signatures in BCDR-F03 data analysis, followed by `i_skewness` with 15 times of selection, and the other features are selected less than 6 times.

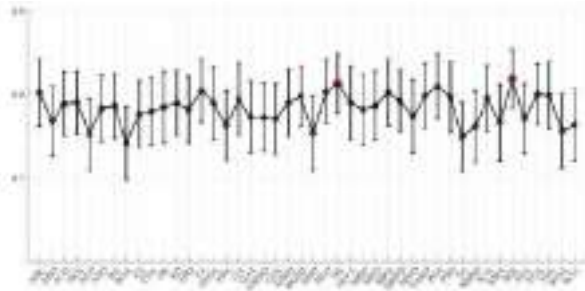


Figure 3. AUC values of CI-SFS-guided classification results.

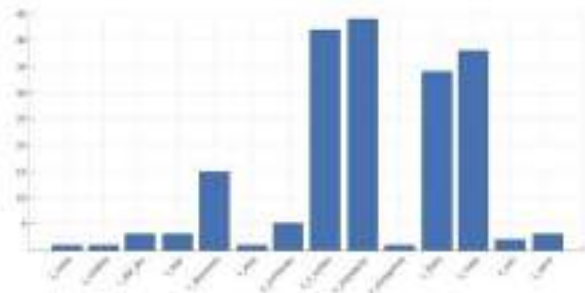


Figure 4. Potential signatures discovered by different CI-SFS algorithms.

4. Discussion

On the BCDR-F03 dataset with 406 samples of lesion cases, up to 44 CI-SFS algorithms are investigated using 5 stability estimators, and the breast tumor classification performance is also explored. All the algorithms achieve good prediction with $AUC \geq 0.70$, 4 potential signatures are identified consistently, while only 3 algorithms achieve stable feature preference ($S \geq 0.55$) when using Dice and Ochi as the estimator.

This study concerns CI-SFS stability. Five previous studies [6–10] explore the stability of FS methods by using different estimators. Notably, [10] focuses on FR stability, 23 methods are explored, while unfortunately, 3 methods generate stable feature ranks when using Noguera [5] as the estimator. In this study, 44 algorithms have been evaluated, and few methods (DE [22], FFOA [26], WSA [55]) shown in Figure 2 yield robust feature preference when using estimator Dice or Ochi [56]. The studies reveal that stability is an important characteristic and more attention should be paid to this topic.

Two similarity-based estimators (Dice and Ochi) identify three CI-SFS algorithms achieving good stability ($S \geq 0.55$, Figure 2). Firstly, 44 methods are evaluated using 5 estimators. Both the number of methods and estimators surpass that of previous studies [6–10]. Secondly, two similarity-based estimators find 3 stable algorithms. In details, among the five estimators, two estimators reveal the stability values of two methods are less than 0.2, and the Jaccard values of methods show similar value pattern as Dice and Ochi but much lower. It indicates that gaps exist among different estimators that should be well addressed in the future work.

CI-SFS algorithms lead to good prediction (Figure 3). These algorithms result in AUC values larger than 0.70, close to the baseline work [11]. Moreover, ABC [13],

FA [25], HLO [35], HS [36], MPA [40], PFA [44] and SOS [50] achieve AUC values larger than 0.80, better than the baseline [11]. It reveals that stability and effectiveness are important yet different characteristics of feature preference.

Moreover, four features are recognized as potential signatures by most CI-SFS algorithms (Figure 4) that may help cancer diagnosis and precision medicine. Among the four features, three features describe shape information (*s_circularity*, *s_y_center* and *s_form*), and one feature quantifies mass lesion texture (*t_contr*). In clinical practice, the breast imaging-reporting and data system descriptor (BI-RADS) recommends malignant lesions in MAM images are prone to show irregular shapes and inhomogeneous contrast, indicating that signatures discovered in the present study is in accordance to clinical guidelines [57].

Several limitations exist in the present study. Firstly, CI-SFS algorithms are investigated on one dataset, and for comprehensive stability analysis, more medical datasets should be used. Secondly, five estimators are used to quantify the CI-SFS stability, while the results from two estimators are much lower, that may induce controversy among different estimators [5]. Last but not the least, besides handcrafted features, deeply learned features will be studied in our future work to improve network explainability, robustness and generalization capacity [58].

5. Conclusions

Forty-four CI-SFS algorithms have been investigated on the BCDR-F03 dataset by using five stability estimators, and three algorithms are identified consistently exhibiting good stability from two similarity-based estimators, while the gap among different estimators should be considered in estimator design.

References

- [1] J. Cai, J. Luo, S. Wang, and S. Yang, "Feature selection in machine learning: A new perspective," *Neurocomputing*, vol. 300, pp. 70–79, 2018.
- [2] Z. Zhang, X. Liang, W. Qin, S. Yu, and Y. Xie, "matFR: a MATLAB toolbox for feature ranking," *Bioinformatics*, vol. 36(19), pp. 4968–4969, 2020.
- [3] L. Zou, S. Yu, T. Meng, Z. Zhang, X. Liang, and Y. Xie, "A technical review of convolutional neural network-based mammographic breast cancer diagnosis," *Computational and mathematical methods in medicine*, 2019.
- [4] K. Abu, I. Aljarah, A. Shariéh, E. Abd, R. Damaševičius, and T. Krilavičius, "A review of the modification strategies of the nature inspired algorithms for feature selection problem," *Mathematics*, vol. 10(3), pp. 464, 2022.
- [5] S. Nogueira, K. Sechidis, and G. Brown, "On the stability of feature selection algorithms," *Journal of Machine Learning Research*, vol. 18(1), pp. 6345–6398, 2017.
- [6] N. López, M. García-Ordás, F. Vitelli-Storelli, P. Fernández-Navarro, C. Palazuelos, and R. Alaiz-Rodríguez, "Evaluation of feature selection techniques for breast cancer risk prediction," *International Journal of Environmental Research and Public Health*. vol. 18(20), pp. 10670, 2021.
- [7] N. Cueto-López, M. García-Ordás, V. Dávila-Batista, V. Moreno, N. Aragonés, and R. Alaiz-Rodríguez, "A comparative study on feature selection for a risk prediction model for colorectal cancer," *Computer methods and programs in biomedicine*. vol. 177, pp. 219–229, 2019.
- [8] A. Kalousis, J. Prados, and M. Hilario, "Stability of feature selection algorithms: a study on high-dimensional spaces," *Knowledge and information systems*. vol. 12(1), pp. 95–116, 2007.

- [9] D. Derroncourt, B. Hanczar, and J. Zucker. "Analysis of feature selection stability on high dimension and small sample data," *Computational statistics & data analysis*. vol. 71, pp. 681–693, 2014.
- [10] S. Yu, B. Li, B. Liu, M. Jin, J. Wu, and H. Yu. "A stability evaluation of feature ranking algorithms on breast cancer data analysis," *Frontiers in Artificial Intelligence and Applications*. 2022.
- [11] J. Arevalo, F. González, R. Ramos-Pollán, J. Oliveira, and M. Lopez. "Representation learning for mammography mass lesion classification with convolutional neural networks," *Computer methods and programs in biomedicine*. vol. 127, pp. 248–257, 2016.
- [12] S. Yu, L. Liu, Z. Wang, G. Dai, and Y. Xie. "Transferring deep neural networks for the differentiation of mammographic breast lesions," *Science China Technological Sciences*. vol. 62(3), pp. 441–447, 2019.
- [13] D. Karaboga, B. Gorkemli, C. Ozturk, and N. Karaboga, "A comprehensive survey: artificial bee colony (ABC) algorithm and applications," *Artificial Intelligence Review*, vol. 42(1), pp. 21–57, 2014.
- [14] D. Rodrigues, V. de Albuquerque, and J. Papa, "A multi-objective artificial butterfly optimization approach for feature selection," *Applied Soft Computing*, vol. 94, pp. 106442, 2020.
- [15] M. Dorigo, M. Birattari, and T. Stutzle, "Ant colony optimization," *IEEE computational intelligence magazine*, vol. 1(4), pp. 28–39, 2006.
- [16] M. Dorigo and L. M. Gambardella, "Ant colony system: a cooperative learning approach to the traveling salesman problem," *IEEE Transactions on evolutionary computation*, vol. 1(1), pp. 53–66, 1997.
- [17] W. Zhao, L. Wang, and Z. Zhang, "Atom search optimization and its application to solve a hydrogeologic parameter estimation problem," *Knowledge-Based Systems*, vol. 163, pp. 283–304, 2019.
- [18] X. Yang and X. He, "Bat algorithm: literature review and applications," *International Journal of Bio-inspired computation*, vol. 5(3), pp. 141–149, 2013.
- [19] S. Arora and S. Singh, "Butterfly optimization algorithm: a novel approach for global optimization," *Soft Computing*, vol. 23(3), pp. 715–734, 2019.
- [20] X. Yang and S. Deb, "Cuckoo search: recent advances and applications," *Neural Computing and applications*, vol. 24(1), pp. 169–174, 2014.
- [21] A. Hussien, M. Amin, M. Wang, G. Liang, A. Alsanad, A. Gumaiei, and H. Chen, "Crow search algorithm: theory, recent advances, and applications," *IEEE Access*, vol. 8, pp. 173548–173565, 2020.
- [22] S. Das and P. M. Suganthan, "Differential evolution: A survey of the state-of-the-art," *IEEE transactions on evolutionary computation*, vol. 15(1), pp. 4–31, 2010.
- [23] A. Faramarzi, M. Heidarinejad, B. Stephens, and S. Mirjalili, "Equilibrium optimizer: A novel optimization algorithm," *Knowledge-Based Systems*, vol. 191, pp. 105190, 2020.
- [24] G. Dhiman, and V. Kumar, "Emperor penguin optimizer: a bio-inspired algorithm for engineering problems," *Knowledge-Based Systems*, vol. 159, pp. 20–50, 2018.
- [25] X. Yang, and A. Slowik, "Firefly algorithm," *Swarm Intelligence Algorithms*, vol. 62, pp. 163–174, 2020.
- [26] Q. Pan, H. Sang, J. Duan, and L. Gao, "An improved fruit fly optimization algorithm for continuous function optimization problems," *Knowledge-Based Systems*, vol. 62, pp. 69–83, 2014.
- [27] X. S. Yang, "Flower pollination algorithm for global optimization," *International conference on unconventional computing and natural computation*, pp. 240–249, 2012.
- [28] S. Mirjalili, "Genetic algorithm," *Evolutionary algorithms and neural networks*, pp. 43–55, 2019.
- [29] C. Ding, Y. Cheng, and M. He, "Two-level genetic algorithm for clustered traveling salesman problem with application in large-scale TSPs," *Tsinghua Science & Technology*, vol. 12(4), pp. 459–465, 2007.
- [30] Y. Zhang, Z. Jin, and S. Mirjalili, "Generalized normal distribution optimization and its applications in parameter extraction of photovoltaic models," *Energy Conversion and Management*, vol. 224, pp. 113301, 2020.
- [31] E. Rashedi, H. Nezamabadi-Pour, and S. Saryazdi, "GSA: a gravitational search algorithm," *Information sciences*, vol. 179(13), pp. 2232–2248, 2009.
- [32] S. Mirjalili, S. M. Mirjalili, and A. Lewis, "Grey wolf optimizer," *Advances in engineering software*, vol. 69, pp. 46–61, 2014.
- [33] F. A. Hashim, E. H. Houssein, M. S. Mabrouk, W. Al-Atabany, and S. Mirjalili, "Henry gas solubility optimization: A novel physics-based algorithm," *Future generation computer systems*, vol. 101, pp. 646–667, 2019.
- [34] A. A. Heidari, S. Mirjalili, H. Faris, I. Aljarah, M. Mafarja, and H. Chen, "Harris hawks optimization: Algorithm and applications," *Future generation computer systems*, vol. 97, pp. 849–872, 2019.
- [35] L. Wang, R. Yang, H. Ni, W. Ye, M. Fei, and P. M. Pardalos, "A human learning optimization algorithm and its application to multi-dimensional knapsack problems," *Applied Soft Computing*, vol. 34, pp.

- 736–743, 2015.
- [36] Z. W. Geem, J. H. Kim, and G. V. Loganathan, “A new heuristic optimization algorithm: harmony search,” *Simulation*, vol. 76(2), pp. 60–68, 2001.
- [37] E. H. Houssein, A. G. Gad, and Y. M. Wazery, “Jaya algorithm and applications: A comprehensive review,” *Metaheuristics and Optimization in Computer and Electrical Engineering*, pp. 3–24, 2021.
- [38] G. Wang, S. Deb, and Z. Cui, “Monarch butterfly optimization,” *Neural computing and applications*, vol. 31(7), pp. 1995–2014, 2019.
- [39] S. Mirjalili, “Moth-flame optimization algorithm: A novel nature-inspired heuristic paradigm,” *Knowledge-based systems*, vol. 89, pp. 228–249, 2015.
- [40] A. Faramarzi, M. Heidarinejad, S. Mirjalili, and A. H. Gandomi, “Marine Predators Algorithm: A nature-inspired metaheuristic,” *Expert systems with applications*, vol. 152, pp. 113377, 2020.
- [41] W. Zhao, Z. Zhang, and L. Wang, “Manta ray foraging optimization: An effective bio-inspired optimizer for engineering applications,” *Engineering Applications of Artificial Intelligence*, vol. 87, pp. 103300, 2020.
- [42] S. Mirjalili, S. H. Mirjalili, and A. Hatamlou, “Multi-verse optimizer: a nature-inspired algorithm for global optimization,” *Neural Computing and Applications*, vol. 27(2), pp. 495–513, 2016.
- [43] S. H. S. Moosavi and V. K. Bardsiri, “Poor and rich optimization algorithm: A new human-based and multi populations algorithm,” *Engineering Applications of Artificial Intelligence*, vol. 86, pp. 165–181, 2019.
- [44] H. Yapici and N. Cetinkaya, “A new meta-heuristic optimizer: Pathfinder algorithm,” *Applied soft computing*, vol. 78, pp. 545–568, 2019.
- [45] R. Poli, J. Kennedy, and T. Blackwell, “Particle swarm optimization,” *Swarm intelligence*, vol. 1(1), pp. 33–57, 2007.
- [46] D. Bertsimas and J. Tsitsiklis, “Simulated annealing,” *Statistical science*, vol. 8(1), pp. 10–15, 1993.
- [47] S. H. S. Moosavi and V. K. Bardsiri, “Satin bowerbird optimizer: A new optimization algorithm to optimize ANFIS for software development effort estimation,” *Engineering Applications of Artificial Intelligence*, vol. 60, pp. 1–15, 2017.
- [48] S. Mirjalili, “SCA: a sine cosine algorithm for solving optimization problems,” *Knowledge-based systems*, vol. 96, pp. 120–133, 2016.
- [49] S. Li, H. Chen, M. Wang, A. Heidari, and S. Mirjalili, “Slime mould algorithm: A new method for stochastic optimization,” *Future Generation Computer Systems*, vol. 111, pp. 300–323, 2020.
- [50] M. Cheng and D. Prayogo, “Symbiotic organisms search: a new metaheuristic optimization algorithm,” *Computers & Structures*, vol. 139, pp. 98–112, 2014.
- [51] S. Mirjalili, A. H. Gandomi, S. Z. Mirjalili, S. Saremi, H. Faris, and S. M. Mirjalili, “Salp Swarm Algorithm: A bio-inspired optimizer for engineering design problems,” *Advances in engineering software*, vol. 114, pp. 163–191, 2017.
- [52] A. Cheraghalipour, M. Hajiaghahi-Keshteli, and M. M. Paydar, “Tree Growth Algorithm (TGA): A novel approach for solving optimization problems,” *Engineering Applications of Artificial Intelligence*, vol. 72, pp. 393–414, 2018.
- [53] M. S. Kiran, “TSA: Tree-seed algorithm for continuous optimization,” *Expert Systems with Applications*, vol. 42(19), pp. 6686–6698, 2015.
- [54] S. Mirjalili and A. Lewis, “The whale optimization algorithm,” *Advances in engineering software*, vol. 95, pp. 51–67, 2016.
- [55] A. Baykasoğlu and S. Akpinar, “Weighted Superposition Attraction (WSA): A swarm intelligence algorithm for optimization problems—Part 2: Constrained optimization,” *Applied Soft Computing*, vol. 37, pp. 396–415, 2015.
- [56] A. Bommert and M. Lang, “stabm: Stability measures for feature selection,” *Journal of Open Source Software*, vol. 6(59), pp. 3010, 2021.
- [57] D. Spak, J. Plaxco, L. Santiago, M. Dryden, and B. Dogan, “Bi-rads fifth edition: A summary of changes,” *Diagnostic and interventional imaging*, vol. 98, pp. 179–190, 2017.
- [58] S. Yu, M. Chen, E. Zhang, J. Wu, H. Yu, Z. Yang, L. Ma, X. Gu, and W. Lu, “Robustness study of noisy annotation in deep learning based medical image segmentation,” *Physics in Medicine & Biology*, vol. 65(17), pp. 175007, 2020.

Research on Radar Burn-Through Range Under Noise Jamming Based on Radar Equation

Hua ZHANG^a, Yuntao CHEN^a, Yi WANG^a, Litao WANG^{a,1}, Gen QIN^a
^aArmy Engineering University of PLA, China

Abstract. Based on the characteristics of radar noise jamming and radar equation, the maximum operating range formula of radar under jamming condition is analyzed by using the logarithmic method, and the burn-through distance of radar under shield jamming and self-defense jamming is solved by taking examples, and the jamming effect is compared and analyzed.

Keywords. Electronic countermeasure, Noise interference, Burn-through distance

1. Introduction

Local wars and conflicts in recent years show that electronic jamming plays an increasingly important role with the development of information equipment technology applications. As an important part of the air defense system, the detection range of radar under disturbed conditions is an important parameter to measure its working efficiency. Therefore, it is of positive significance to analyze the maximum operating range of radar under noise jamming and determine the Burn-through range of radar under noise jamming.

2. Characteristics of noise interference

Radar jamming is mainly divided into suppression jamming and deception jamming, of which suppression jamming is the most widely used. Because radar detects the echo signal of the target to find the target and measure its parameter information, the main purpose of jamming is to reduce the radar's ability to find and track the target.

The mode of suppression jamming is mainly continuous and incoherent noise jamming. The best noise jamming signal should have the characteristics of receiver noise. According to information theory, Gaussian white noise (uniform spectral density) is the best noise jamming signal. When the average power is fixed, the Gaussian white noise has the maximum entropy value of any random waveform, that is, the maximum uncertainty. The main advantage of noise jamming is that it is not necessary to know the signal characteristics and signal processing links of the radar in detail, but only need to know the operating frequency of the radar. Therefore, noise

¹ Corresponding Author: Litao Wang, Army Engineering University of PLA, China
E-mail: wlтт@163.com.

jamming equipment is relatively simple. As long as the jamming frequency is consistent with the operating frequency of the radar and the power is large enough, the jamming effect on the radar receiving system will be good.

The noise jamming system is an ECM device designed to generate disturbance in the radar receiver so that it cannot detect the target. In order to make jamming effective, in the radar receiver, the jamming signal J generated by the jammer must have the strength that can cover the radar echo signal S . This strength can be calculated by using the radar equation, that is, the interference signal ratio must be high enough [1].

3. Calculation of the Maximum Operating Range of Radar under Noise Jamming

3.1. Electromagnetic propagation loss and atmospheric attenuation

When electromagnetic wave propagates in the air, it is subject to atmospheric attenuation and propagation loss. The attenuation loss is different for different propagation distances and different operating frequencies. If we take 10 logarithms on both sides of the radar equation, we can get the electromagnetic wave propagation loss formula as follows [2]

$$L_S = 32.4 + 20\lg D + 20\lg F \quad (1)$$

In the Formula (1): L_S is electromagnetic wave propagation loss, in dB; D is the propagation distance of electromagnetic wave, in km; F is the frequency of electromagnetic wave, in MHz.

3.2. Radar echo power and jamming signal power

The echo power received by the radar is [3]

$$S = P_T + 2G_{T/R} - 103 - 20\lg F - 40\lg D_T + 10\lg S \quad (2)$$

In the formula: P_T is radar transmission power (dB); $G_{T/R}$ is the gain of transmitting and receiving antennas (dB); F is the radar operating frequency (MHz); D_T is the target distance (km); S is the effective radar cross section of the target.

The jamming signal received by the radar is the electromagnetic wave directly sent by the jammer, and its propagation path is one-way. However, under the condition of supporting jamming, the direction of jamming signal arriving at the radar may be different from the direction of radar echo, so the gain of radar to jamming signal is different from that to echo. At this time, the jamming signal power received by the radar is

$$J = P_J + G_J - 32 - 20\lg F - 20\lg D_J + G_{RJ} \quad (3)$$

In the formula, P_J is the transmitting power of radar jammer (dB); G_J is the interference transmitting antenna gain (dB); F is the interference operating frequency (MHz); D_J is the target distance (km); G_{RJ} is the antenna gain of the radar in the jamming direction.

3.3. Interference signal ratio of radar receiver

The jamming effect of the jammer against the enemy radar is not measured by the absolute jamming power value of the jammer, but by the interference signal ratio at the

radar receiving end, that is, the ratio of the jamming signal power value to the radar echo signal power value, which is called interference signal ratio for short. In case of noise jamming, the operating frequency of the jammer is consistent with that of the radar. After the jamming signal power value (Formula 3) and the echo signal power value (Formula 2) at the radar receiving end are obtained, the interference signal ratio at the radar receiving end can be obtained as follows, which can be seen from the formula

$$\begin{aligned} J/S &= P_J + G_J - 32 - 20 \lg F - 20 \lg D_J + G_{RJ} - (P_T + 2G_{T/R} - 103 - 20 \lg F - 40 \lg D_T + 10 \lg S) \\ &= 71 + P_J - P_T + G_J - 2G_{T/R} + G_{RJ} - 20 \lg D_J + 40 \lg D_T - 10 \lg S \quad (4) \end{aligned}$$

Formula (4) shows that the jamming effect of the radar receiver is mainly related to the interference-to-signal ratio. The higher the interference-to-signal ratio, the better the jamming effect. The jamming effect is mainly related to the parameters such as the transmitter power and antenna gain of the jammer, the radar transmission power and antenna gain, the target distance, and the radar effective scattering area of the target. Therefore, the interference-to-signal ratio under specific parameters can be calculated by using this formula.

For example, for a radar transmitter with a peak power of 200kW, its antenna gain is 30dB. It detects a target 100km away, and the effective radar cross section of the target is 800m². Suppose that a radar jammer adopts the support jamming mode, transmits 200W jamming signal with 20dB antenna gain at a distance of 20km from the radar, and enters from 0dB radar antenna side-lobe to cover the target. Then according to formula (4), the interference-to-signal ratio when jamming is supported is

$$J/S = 71 + 53 - 83 + 20 - 2 * 30 + 0 - 20 \lg(20) + 40 \lg(100) - 10 \lg(800) = 26$$

If the radar jammer adopts self-defense jamming, the $D_T = D_J$, $G_{T/R} = G_{RJ}$, and Formula (4) can be simplified as

$$J/S = 71 + P_J - P_T + G_J - G_{T/R} + 20 \lg D_J - 10 \lg S \quad (5)$$

Formula (5) is the interference equation for self-defense jamming.

Under the same target, radar and jammer parameters above, the interference signal ratio during self-defense is

$$J/S = 71 + 53 - 83 + 20 - 30 + 20 \lg(100) - 10 \lg(800) = 42$$

Comparing the two results, it can be seen that the interference ratio of self-defense jamming is much larger under the same circumstances.

3.4. Maximum operating range of radar under noise jamming

When the radar operator can identify the real target signal and the jammer noise signal on his display, the maximum operating range of the radar in this case is called the radar "Burn-through range", that is, the maximum operating range of the radar under jamming conditions. It reflects the working ability of radar under jamming conditions, and this ability is reflected in the interference signal ratio of radar receiver.

In general, $J/S = 10\text{dB}$ is taken as the dividing point between normal and abnormal radar operation. If the interference signal ratio is greater than 10dB, the radar cannot work normally. If the interference signal ratio is less than 10dB, the radar can work normally. Similarly, for the jamming party, if the interference signal ratio to the radar is greater than 10dB, it indicates that the radar jamming is effective at this time; if the interference signal ratio to the radar is less than 10dB; it indicates that the radar jamming is invalid at this time.

Therefore, the formula (4) can be rewritten as

$$40 \lg D_T = -71 - P_J + P_T - G_J + 2G_{T/R} - G_{RJ} + 20 \lg D_J + 10 \lg S + J/S \quad (6)$$

In formula (6), D_T is the maximum operating range of the radar under the condition of supporting jamming.

In the case of the supporting jamming in the above example, using the formula (6), it can be obtained that the radar Burn-through distance is

$$40 \lg D_T = -71 - 53 + 83 - 20 + 60 - 0 + 20 \lg(20) + 10 \lg(800) + 10 = 62$$

$$\text{So, } D_T = 10^{62/40} = 35.48 \text{ (km)}$$

It shows that under the condition of supporting jamming, the radar can normally find and track the target when the target is close to the mine within 35.48 km.

When the radar detects the target with self-defense jammer, in the formula (6), $D_T=D_J$, $G_{T/R}=G_{RJ}$, the formula of radar Burn-through distance is:

$$20 \lg D_T = -71 - P_J + P_T - G_J + G_{T/R} + 10 \lg S + J/S \quad (7)$$

In the above example (Formula 7), if the jammer is configured to implement on the target, the maximum operating range of the radar is

$$20 \lg D_T = -71 - 53 + 83 - 10 + 30 + 10 \lg(800) + 10 = 18$$

$$\text{So, } D_T = 10^{18/20} = 7.94 \text{ (km)}$$

It can be seen that under the same noise jamming conditions, the radar's detection distance to targets with self-defense jammers is far less than the detection distance when they are under cover. At this time, the self-defense jamming effect is much better than the support jamming effect.

4. Conclusion

With the continuous development of radar and jamming technology, the struggle in the electromagnetic field will be more and more intense. While the radar is breaking through the traditional system, it is also constantly pursuing new progress in theory and technology, that is, to find and track targets as much as possible under the condition of jamming. This paper studies the calculation method of Burn-through distance under the condition of noise jamming through the radar equation, compares and analyzes the jamming effect, and draws the conclusion that self-defense jamming is much better than support jamming under the same noise jamming condition. Therefore, radar countermeasure should focus on the anti-jamming research of self-defense jamming.

References

- [1] L. F. Ding. Radar Principle. Xi'an: Xi'an University of Electronic Science and Technology Press, 2002.
- [2] Y. S. Liu, C.J. Xu. Radar countermeasure and counter countermeasure. Beijing: Electronic Industry Press, 1995
- [3] G. Q. Zhao. Principles of Radar Countermeasure. Xi'an: Xi'an University of Electronic Science and Technology Press, 1999.

Classification of Characteristic Factors of Brain Functional Network Using Decision Tree

Peng YUAN^a, Zuogang ZHENG^a, Xinshuo YUAN^a, Lanhua ZHANG^a, Mei WANG^a, Xiaoyan WANG^a and Xucai JI^{b,1}

^a*School of Medical Information and Engineering, Shandong First Medical University and Shandong Academy of Medical Sciences, Tai'an, 271016, China*

^b*School of Continuing Education, Shandong First Medical University and Shandong Academy of Medical Sciences, Tai'an, 271016, China*

Abstract. In order to explore the classification methods from imaging data, we propose to establish the feature classification order by building a classification tree with characteristic factors of brain functional network aided by calculating of network topology based on graph theory. By preprocessing the imaging data and modeling the networks with professional platform, we get the topology parameters as the input of the C4.5 decision tree, and then get the classification feature and classification tree by calculating the information gain ratio. The results show that the classification prefers holistic characteristics and quality characteristics. By programming and the samples test, it is feasible to extend the classification with network characters learning based on the processing results of multi-modal imaging data and machine learning algorithms.

Keywords. Decision tree, classification, brain functional network, characteristic factor

1. Introduction

With the development of imaging technology, brain nerve diseases were recognized more and more by neuroimaging data with higher time and space dimensions which provided big data for comprehensive researches and applications. Brain network provided a new view to recognize and comprehend the diseases, and anyone of them provided much information of function and structure for brain by images.

Artificial Intelligence provides a new tool for big data to mine the implied relation in information. Intelligent algorithms and models pushed the tools to find the disciplines behind the phenomena including the brain diseases with neuroimaging. Machine learning, one of fields of artificial intelligence, provides so many learning algorithms for field applications. In brain science, it can provide the advanced function of classification, recognition and prediction except the discovery and verification based on imaging data with intelligent algorithm, such as support vector machine, decision tree, deep learning.

¹ Corresponding Author: Xucai Ji, School of Continuing Education, Shandong First Medical University and Shandong Academy of Medical Sciences. E-mail: xywjxc@126.com.

For brain functional network, it can be set up by a serious process based on graph theory, and then to analyze the network topologies of the network to discover the inner disciplines of the disease, except that, independent component analysis, resting state functional connectivity and seed-based analysis also can give the functional networks, and they all analyzed the disease by function connection with many topology characters. It can get many characteristic meaning and evaluate the disease quantitatively from the imaging data such as for size, shape, or texture of images by degree, average path length and cluster of network with functional networks. Imaging and functional network contain so much information about disease and gave many results about nerve disease with the usual methods. The aim of them is to find the biomarker of the disease with the high time and space data model, together with the connectomics and machine learning. The machine learning provided four kinds of learning algorithm for brain imaging data to identify, evaluate and predict the disease characters with the advantage of data [1].

Classification is a form of supervised learning in machine learning with different algorithms. Decision tree is kind of classification algorithm belonging to machine learning including various classification algorithms, such as iterative dichotomiser3 (ID3), C4.5, classification and regression trees (CART), Chi-square automatic interaction detection (CHAID) and quick unbiased efficient statistical tree (QUEST) using discrete data. Selecting the largest information gain as the classification attribute, ID3 algorithm recursively expands the branches of the decision tree to complete the construction of the decision tree. CART algorithm implements classification and regression based on ID3 to predict the attribute or classification. C4.5 algorithm realizes continuous classification by improvement of ID3, and can prune and solve the default value. With the standard of Chi-square detection, CHAID algorithm expresses the multi-directional bifurcation classification [2].

Based on feature extraction, biomarker and classification model, more and more achievements implements the advanced function of brain nerve disease from data analysis view. Shahhosseini et al. put forward the individual difference in functional connectivity expressing the difference in cognition and behavior to classify for patients with functional magnetic resonance imaging (fMRI) data [3]. Vos et al. got three most distinguishing indicators by computing eight metrics as predictors for regression models and the classification results were assessed by area under curve (AUC) area with resting state fMRI (RSfMRI) data for Alzheimer (AD) patients [4]. Mudali et al. used C4.5 decision tree to classify the Parkinson's disease and healthy individuals union principal component analysis method with fluorodeoxyglucose positron emission tomography data [5]. Aoyagi et al. used the CART algorithm to classify the acute lumbar spondylolysis from non-specific low back pain patients [6]. In addition to using functional data, Zhang et al. use the gray matter volume and lateralization index to discuss the classification performances on the ADNI database with structural MRI (sMRI) data [7]. Zhu et al. combined CE-MRI radiomic feature to set up different machine learning models to predict the breast cancer patients [8]. The use of models is also one of the commonly used methods. Tang et al. demonstrated the classification and prediction in mild cognitive impairment and AD with brain MRI data by selecting the characteristic indexes so as to find the best model [9]. Provenzano et al. set up an assemble machine learning model to classify Gulf War Illness and Chronic Fatigue Syndrome with fMRI data [10]. Bashyam et al. develop a complex deep learning model and transfer learning to classify brain disease with MRI data [11]. Qiu et al. developed a convolutional neural networks to classify the cognitive state for Alzheimer's disease

with multimodal MRI imaging data [12]. Niu et al. provided a predictive model that can assist clinicians in individualizing the risk of bipolar disorder using routine biochemical testing for first-time admissions to patients with affective disorders [13]. Besides, more and more fields and applications combined the machine learning algorithms to explore the secrets of questions [14].

With the combination of imaging data and machine learning algorithms, more and more detailed information were mined based on classification requirement which provided the former information for patients and gave the help of the clinical remedy and predictions. In the middle of the results, connectome indexes acted more and more important roles from the network science view. We can get various network topologies indexes after handling the imaging data, and can it draw conclusions or deduce useful results directly from these parameters? Of course, we had got so many achievements from networks view [15].

Permana et al. have discussed the influential variable in so many diabetes variables by C4.5 decision tree algorithm [16]. Aim to test the effect of the indexes, in this paper we use the C4.5 decision tree to verify the classification in the imaging data.

In order to extend the function of network for data, we expanded the indexes of network topology to classify the samples except the role of network computing which provided the verification of the results and classified the sample directly. Meanwhile, we can give the index of network another explanation for the real world meaning.

2. Methods

2.1. Multi-modal imaging data and Machine learning

Imaging data with high time and space resolution provided clearer dimension information for the structure and function of patients. For the functional imaging, fMRI reflects brain dynamic action information by the blood oxygen on level depending (BOLD) signal with less anatomical information.

As the core of artificial intelligence, machine learning is a kind of technology to simulate human intelligence by computer algorithm and operations based on mathematical, probability, statistics, and computer science and so on. Four kinds of learning methods including various algorithms demonstrated the simulation process by supervised learning, unsupervised learning, semi-supervised learning and reinforcement learning. Computing closer to human learning, thinking and cognition, machine learning got new knowledge and ability with model, strategy and algorithm by simulating human brain and mathematical method. Decision tree, naive Bayesian, support vector machine, random forest, artificial neural network, boosting and bagging, association rules, expectation maximization, and deep learning are the common algorithms [1].

Classification aims to set up the classifier by training known samples so as to apply to the unknown samples with the model or strategy. Naïve Bayesian classifier judges attribute classification by calculating posterior probability with Bayesian formula. Logistic regress uses the eigenvalues of objects and their corresponding probabilities plus logical functions to judge, divide and evaluate the possibility of transaction attribution. Support vector machine finds a hyper-plane that maximizes the distance between objects to achieve classification results. Decision tree implements the classification by establishing an optimal classification decision tree. Article neural

network trains a set of input and output neurons continuously adjusting the weights for learning to achieve the ideal classification results [1].

As the supervised learning model, decision tree has its characteristic classification factor with feature selection, build tree and tree pruning for node classification and regression consisting of inner nodes and leaf nodes. Decision tree tries to find the classification rules from the data so as to approach to the value of a nearby function whose aim is to establish the high precision and small scale set as soon as possible by feature selection. ID3 is the basic and representative algorithm based on information theory computing by information entropy and information gain to classify the data. The information gain, deciding the degree of the feature selection, stands for the high precision with small uncertainty [2].

C4.5, a revision and optimization version of ID3, belongs to decision tree algorithm by substituting the information gain ration for information gain as the measure standards. C4.5 can alleviate sample shortage, solve the missing value, discrete continuous value and optimize over-fitting problem by pruning. Based on C4.5, C5.0 algorithm introduces the boosting technology to improve the sample recognition rate with lower complexity [2].

2.2. Work flow of our works

Getting the raw data of RS-fMRI, the first step is to process the imaging data. In order to satisfy the requirements of the machine learning test, we prepared three groups of fMRI imaging data. Before handle the imaging data, we did the preprocessing to uniform the data so as to suit for the software platform of statistical parametric mapping (SPM) based on Matlab embedded in the DPABI platform. The aimed file is dicom or nifti format [17].

With the DPABI, the RSfMRI data were processed by format conversion, removal of first n time points, temporal layer correction (slice timing), head motion correction (realign), spatial normalization, smoothing, de-linear drift (detrnd) and filtering in SPM software [17].

After preprocessing the data, the second step is to set up the networks. We got the matrix of the imaging, in order to strengthen the comparison, we applied the 90*90 brain partition atlas and 116*116 ones to compute the RSfMRI data. The brain area regarded as node and the correlation as the relationship. By the SPM in DPABI platform, we got two pairs of three groups networks, and then got the topologies from the GRETNA platform such as assortativity, centrality of betweenness, community, degree, hierarchy, efficiency, cluster, path length, rich club, small world and synchronization [18].

The third step is to design the classification algorithm. Based on the decision tree, we selected the C4.5 as the classification tool and the characters of network topology as the dataset. Based on the Python programming, the classification can be tested.

3. Results

Based on the algorithm and programming, we ran the test dataset with RSfMRI network by topologies. After the process of GRETNA, we got the network topologies as assortativity, centrality of betweenness, index of community, centrality of degree, hierarchy, efficiency of network, rich club, small world, synchronization and so on [18].

Before classification, we compute the network topologies of the three groups. From the results we can get the sample classification from the networks view which can give us verification for the classification algorithm.

In the test sample data and C4.5 decision tree (Fig. 1), we got quite a few points for classification. First, compared to individual parameter values, the holistic parameter is more suitable for classification feature. Second, as the parameter value increases, the classification accuracy improves. Third, there is no obvious difference between 90*90 and 116*116 atlas data. Fourth, in contrast to ID3, the C4.5 has a better classification effect. At last, the result of classification of the sample is feasible with the characteristic factor as identification index by C4.5 decision tree algorithm by brain functional network data.

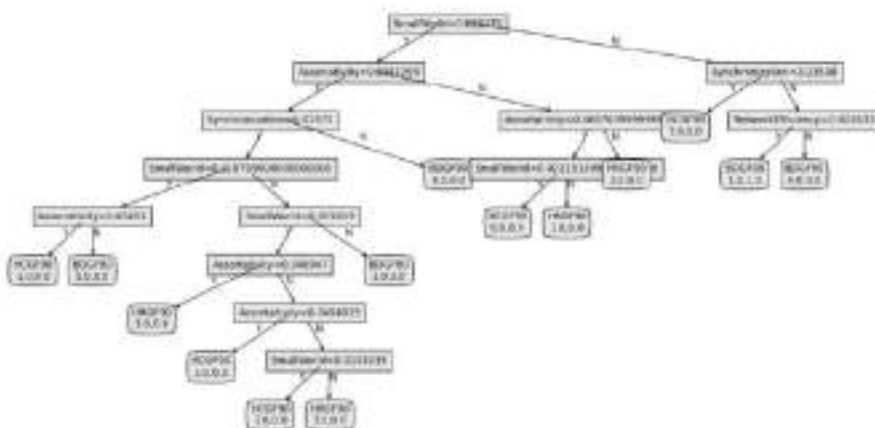


Figure 1. C4.5 decision tree of characteristic factors of brain functional networks.

4. Discussion

From the results of C4.5 decision tree and classification, the holistic in the network topologies implies more parameter meaning than the individual index. In complex network based on graph theory includes a host of indexes to measure the characteristic of the network with individual parameters and holistic parameters which are consist of individual parameters more or less, and the meaning of holistic ones represent more than the individuals that can be got by the feature selection results.

From the process of algorithm and programming, we test the number of parameters to classify the sample. As the number of parameters increases, the classification results get better and better, although one indicator can also complete the classification. That is, the function of classification does not depend on the number of parameters, but the accuracy of classification will become better as the number of parameters increases. However, when the amount of data increases, the increase of parameters will bring more time complexity to the calculation.

The Atlas between 90 and 116 is different by cerebellum which is brain tissue responsible for body balance. The disease of samples is not belonging to this disease type and brings little effect to the brain, so the effect of classification should be affected.

With the information gain of ID3, it did not perform as well as C4.5 implied that the gain ratio is more discriminating power. From the formula, we conclude that the odds are closer to connotation than numbers that is the meaning of data mining algorithm after a multitude of data handling and transformation. Also the missing value process played a role to some extent.

Of course, from the network topologies themselves, quite a few achievements can be obtained directly by the calculation based on graph theory. The results of the classification gave the research a new method for the disease and clinical application which made the focus on the data. Meanwhile, the classification results by characteristic factors of brain functional network show that it is possible to do deep research from the middle index of networks [16].

About the parameters of the network, everyone is pair to be selected. Randomly, we select five parameters to test the algorithm and get a tree with four parameters which tell us again that the factor of classification does not depend on number of the parameters. That is, comparing to the “Assortativity”, “NetworkEfficiency”, “SmallWorld”, and “Synchronization”, the “Hierarchy” index is less important for the samples to classify, and can also be seen as the classification results of “Hierarchy” has been contained in other four parameters. Moreover, the classification ability of “SmallWorld” is better than others which can be concluded from the graph theory and network science views.

5. Conclusions

In this paper, we tried to classify results with network parameters by machine learning methods. We got the same results as the network science and gave the classification decision tree which brought the connectome into a new application for the disease and clinical application. In addition to the calculation of topological feature parameters for network science, we can also use the network parameters as input for numerical computation-based reasoning or application. The C4.5 decision tree can classify the samples based on the network topology parameters and find the best classification factor to identify the individuals.

Of course, a sea of questions should be strengthened and solved so that the results can be promoted and applied. One is to test more samples and more type of data with different disease which make the tree model more stable, second is to test the sample with individual parameters so as to improve the contrast, third is to test the sample with more classification algorithms to increase its salience. Furthermore, we will continue to explore the characteristic factors with multi-modal imaging data individually and holistically.

Acknowledgements

This research was supported by the Natural Science Foundation of Shandong (No. ZR2020mf156), National Students' project for innovation and entrepreneurship training program (No. S202110439031).

References

- [1] Mechelli A, Vieira S. Machine Learning: Methods and Applications to Brain Disorders. Academic press, 2019.
- [2] Shamrat F, Ranjan R, Hasib KM, et al. Performance evaluation among ID3, C4.5, and CART Decision Tree Algorithms. Springer Nature, 2022:127-142.
- [3] Shahhosseini Y, Miranda MF. Functional Connectivity Methods and Their Applications in fMRI Data. Entropy, 2022,24(3):390.
- [4] Vos FD, Koini M, Schouten TM, et al. A comprehensive analysis of resting state fMRI measures to classify individual patients with Alzheimer's disease. Neuroimage, 2017, 167:62-72.
- [5] Mudali D, Teune LK, Renken RJ, et al. Classification of Parkinsonian syndromes from FDG-PET brain data using decision trees with SSM/PCA features. Computational and Mathematical Methods in Medicine, 2015, 2015(1):1-10.
- [6] Aoyagi M, Naito K, Sato Y, et al. Identifying Acute Lumbar Spondylolysis in Young Athletes with Low Back Pain: Retrospective Classification and Regression Tree Analysis. Spine, 2020, DOI: 10.1097/BRS.0000000000003922.
- [7] Zhang Q, Yang XL, Sun ZK. Classification of Alzheimer's disease progression based on sMRI using gray matter volume and lateralization index. PLOS ONE, 2022, 17.
- [8] Zhu Y, Yang L, Shen H. Value of the Application of CE-MRI Radiomics and Machine Learning in Preoperative Prediction of Sentinel Lymph Node Metastasis in Breast Cancer. Frontiers in Oncology, 2021, 11:4789.
- [9] Tang X, Liu J. Comparing different algorithms for the course of Alzheimer's disease using machine learning. Annals of palliative medicine, 2021(9):9715-9724.
- [10] Provenzano D, Washington SD, Rao YJ, et al. Machine Learning Detects Pattern of Differences in Functional Magnetic Resonance Imaging (fMRI) Data between Chronic Fatigue Syndrome (CFS) and Gulf War Illness (GWI). Brain Sciences, 2020, 10(7):456.
- [11] Bashyam VM, Guray E, Jimit D, et al. MRI signatures of brain age and disease over the lifespan based on a deep brain network and 14468 individuals worldwide. Brain, 2020(7):7.
- [12] Qiu S, Joshi PS, Miller MI, et al. Development and validation of an interpretable deep learning framework for Alzheimer's disease classification. Brain, 2020(6):6.
- [13] Niu Z, Wu X, Zhu Y, et al. Early Diagnosis of Bipolar Disorder Coming Soon: Application of an Oxidative Stress Injury Biomarker (BIOS) Model. Neuroscience Bulletin, 2022,9:1-13.
- [14] Zandvakili A, Barredo J, Swearingen HR, et al. Mapping PTSD symptoms to brain networks: a machine learning study. Translational Psychiatry, 2020, 10(1):195.
- [15] Stern P. Brain disease and network reorganization. Science, 2021, 371(6530):688.3-689.
- [16] Permana B, Ahmad R, Bahtiar H, et al. Classification of diabetes disease using decision tree algorithm (C4.5). Journal of Physics: Conference Series, 2021, 1869(1):012082.
- [17] Yan CG, Wang XD, Zuo XN, et al. DPABI: Data Processing & Analysis for (Resting-State) Brain Imaging. Neuroinformatics, 2016, 14: 339-351.
- [18] Wang J, Wang X, Xia M, et al. GREYNET: a graph theoretical network analysis toolbox for imaging connectomics. Frontiers in Human Neuroscience, 2015, 9(386):386.

A Stability Evaluation of Feature Ranking Algorithms on Breast Cancer Data Analysis

Shaode YU^a, Bingjie LI^a, Boji LIU^a, Mingxue JIN^a, Junjie WU^b, and Hang YU^{c,1}

^a*School of Information and Communication Engineering, Communication University of China, Chaoyang, Beijing, China*

^b*Department of Radiation Oncology, University of Texas Southwestern Medical Center, Dallas, Texas, United States*

^c*School of Aerospace Science and Technology, Xidian University, Xi'an, Shanxi, China*

Abstract. Stability of feature preference is a most vital yet rarely explored characteristics of feature ranking algorithms. In this study, 23 feature rankers are evaluated on 4 breast cancer datasets (BCDR-F03, WDBC, GSE10810 and GSE15852) using an advanced stability estimator (S), and 3 rankers are identified showing good stability ($S \geq 0.55$) consistently on the four datasets. It suggests that data sufficiency is crucial for the construction of feature importance measure, since more rankers are stable on medical imaging datasets (BCDR-F03 and WDBC) than on gene expression datasets (GSE10810 and GSE15852), and high-dimensional small-sample-size datasets are big challenges of stability estimation. In our future work, more attention should be paid to the topics of developing stable feature ranking algorithms and stability estimators to well tackle different sizes of medical datasets.

Keywords. Stability, feature ranking, breast cancer, data analysis, matFR

1. Introduction

Feature ranking (FR) becomes increasingly important in the fields of precision medicine due to the dramatic growth of feature dimension [1]. As one of FR's most crucial characteristics, stability quantifies how different training sets affect its feature preferences [2].

Four studies have evaluated the stability of feature selection algorithms. For breast cancer (BC) risk prediction, 6 algorithms are analyzed using correlation coefficient and Jaccard index [3]. For colorectal cancer risk forecasting, 6 methods are assessed with two similarity-based estimators [4]. On high-dimensional datasets, the stability of 5 methods is estimated via correlation coefficients and adapted Tanimoto distance [5]. Besides, relative weighted consistency, partially adjusted average Tanimoto index and some other correlation based similarity measures are employed [6].

This study focuses on FR stability and differs itself from three points. First, 23 algorithms are evaluated that surpasses previous studies. Second, an advanced estimator [2]

¹Corresponding Author: Hang Yu, Xidian University, Shanxi, China; E-mail: hyu@xidian.edu.cn.

is used to observe the dynamic change of stability. Third, stable algorithms are identified on 4 breast cancer datasets. The study could enrich our understanding of FR stability on diverse cancer data analysis.

2. Materials and Methods

2.1. Data collection

Four BC datasets shown in Table 1 are collected for FR stability analysis. BCDR-F03 includes 406 breast lesions (230 benign and 176 malignant)² and 17 features are provided [7]. To avoid one lesion with multiple records [8], the first feature record is used and 406 records are analyzed. WDBC contains 357 benign and 212 malignant instances³. For a digitized fine needle aspiration (FNA) image, based on multiple delineation, the mean, standard error and largest values of each feature are collected, and 30 features are formed [9]. GSE10810 provides 31 tumor and 27 control samples of valid specimens [10], and 18,382 genes are collected⁴. GSE15852 involves 43 tumor samples and 43 control samples of Malaysian women⁵, and 22,283 gene points are detected [11].

Table 1. Summary of the datasets used in this study

	benign (train/test)	malignant (train/test)	feature number (p)	data source
BCDR-F03	230 (141/89)	176 (141/35)	17	MAM
WDBC	357 (170/187)	212 (170/42)	30	FNA
GSE10810	27 (22/5)	31 (22/9)	18382	gene
GSE15852	43 (34/9)	43 (34/9)	22283	gene

2.2. Experiment design on stability estimation

Figure 1 shows the experiment design. In each iteration, a dataset $\{(X, y)\}$ is divided into two subsets and one is for training $\{(X^{train}, y^{train})\}$, and each method yields a feature rank in terms of feature importance. Here, vector $\langle f_{i,1}, \dots, f_{i,k}, \dots, f_{i,p} \rangle$ is the output of the i^{th} running of p features of an algorithm, and $f_{i,k}$ is the order of the k^{th} feature. In this study, $N = 100$, and 100 iterations of each algorithm are conducted.

The outcome is the stability value (S) when top- m features are selected. An algorithm generates a rank in descending feature importance order. When the number (m) is defined, it yields a subset of features. In this study, $N = 30$, and m ranges from 3 to 9 features. When $m = 3$ and $S \geq 0.55$, the algorithm is assumed to be stable.

²<http://bcdr.inegi.up.pt>

³<https://archive.ics.uci.edu/ml/datasets/>

⁴<https://www.ncbi.nlm.nih.gov/geo/query/acc.cgi?acc=GSE10810>

⁵<https://www.ncbi.nlm.nih.gov/geo/query/acc.cgi?acc=GSE15852>

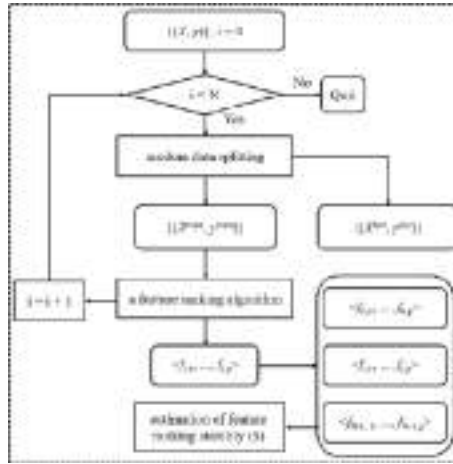


Figure 1. The procedure of stability estimation. (The figure can be enlarged for viewing.)

2.3. Feature ranking algorithms

Twenty-three methods in matFR⁶ are evaluated, since the others exceed time expectation (≥ 0.5 hour per iteration) on GSE15852. The core ideas of algorithms are based on absolute values of t -test [12], relative entropy [13], Bhattacharyya distance [14], area between the empirical receiver operating characteristic curve and random classifier slope [15], absolute values of Mann-Whitney test [16], ReliefF [17], least absolute shrinkage and selection operator [18], correlation analysis [19], generalized Fisher score (GFS) [20], Gini score [21], Kruskal-Wallis test [22], pairwise feature proximity (PWF) [23], min-max local structure information [24], local learning-based clustering [25], eigenvector centrality [26], probabilistic latent graph-based measure space [27], concave minimization and SVM [28], convergence properties of the power series of matrices [29], Laplacian score [30], $L_{2,0}$ -norm equality constraints (LNEC) [31], adaptive structure learning [32], robust spectral learning of the spectrum information of the graph Laplacian [33], and $L_{2,1}$ -norm minimization on processes of both label learning and feature learning [34].

2.4. Stability estimator

The estimator recasts the stability measure as a random variable estimation with explicitly embedded parameters⁷. After sampling distribution is identified, confidence intervals are estimated and hypothesis tests are performed. It allows for reliable comparison of stability across different procedures. Notably, S value above 0.75 represents excellent agreement and between 0.40 and 0.75 indicates intermediate to good agreement.

3. Results

Estimated stability is shown in Tables 2 and 3. The values with $S \geq 0.55$ when $m = 3$ are highlighted in red, indicating the algorithms are stable. Table 2 shows most algorithms

⁶<https://github.com/NicoYuCN/matFR>

⁷<https://github.com/nogueirs/JMLR2018>

achieve excellent stability. The S values of [12, 22, 23, 26, 30, 33, 34] are larger than 0.75 on both datasets. On contrast, [19] and [24] on BCDR-F03, and [19] and [28] on WDBC, are highly sensitive to data perturbations.

On gene expression datasets, Table 3 indicates few algorithms with good stability. On GSE10810, [14, 20, 23, 28, 31] are with $0.58 \leq S \leq 0.78$, and on GSE15852, [20, 22, 23, 26, 29–31] have values between 0.56 and 0.85. Notably, [13] and [23] achieve $S \geq 0.70$ on GSE10810 and [23] and [27] are with $S \geq 0.80$ on GSE15852, with good agreement when feature subsets change.

In summary, 19, 20, 5, and 7 algorithms show good stability ($S \geq 0.55$ when $m = 3$) on BCDR-F03, WDBC, GSE10810 and GSE15852, respectively. Further observation reveals that [13, 22, 26, 29, 30] are robust on 3 datasets, and 3 feature rankers (GFS [20], PWFP [23] and LNEC [31]) are consistently stable on all the datasets.

4. Discussion

The stability of 23 FR algorithms is investigated using an advanced estimator on 4 BC datasets. Stability is central in massive applications. Since higher stability increases user confidence in complex data analysis, a user prefers an algorithm that yields stable feature ranks even though perturbations exist in training data [2, 5].

Three algorithms show good stability consistently on the datasets. Initially, 19 methods cannot handle GSE15852 effectively. Besides high-performance hardware, these algorithms need massive time to process gene datasets (GSE10810 and GSE15850). Secondly, most of the remaining algorithms achieve stable feature ranks on BCDR-F03 and WDBC, while substantially fewer algorithms are stable on GSE10810 and GSE15850. It is found that more than 18 samples describe a feature on BCDR-F03 and on WDBC, while on gene datasets, samples are far from sufficient to express a feature. This might suggest that data sufficiency is vital to the construction of measure spaces before accurate estimation of feature importance [6]. Close observation finds that GFS [20], PWFP [23] and LNEC [31] are consistently robust on all the four datasets.

There are several reasons that the three algorithms generate stable feature ranks efficiently. To GFS [20], it first finds a subset of features jointly to filter out redundant and unrelated variables. In a reduced feature space, data subsets are optimized in regularized discriminant analysis. Second, in the data space spanned by selected features, the distances between samples in different classes will be expanded as large as possible, and that between samples in the same class will be reduced as small as possible. Finally, the feature ranking problem is formed as a multiple kernel learning problem in each iteration, and thus, time cost decreases and the computing is efficient. To PWFP [23], instead of looking at the samples in groups, it evaluate feature efficiency based on pairwise fashion, *i.e.*, a pair of samples is considered at a time. In particular, the features bringing the sample pairs closer or putting the pairs far away is selected as a good choice for feature ranking. And to LNEC [31], feature selection and data partition are considered in a joint manner that increases interdependence among data samples, cluster labels and selected features. Using $L_{2,0}$ -norm equality constraints of dependence guided terms, learned cluster labels are used to fill the information gap between data samples and selected features, and alternating direction method of multipliers is designed to solve the constrained minimization problem iteratively and efficiently.

Table 2. Stability of algorithms on medical image datasets

	top-3	top-4	top-5	top-6	top-7	top-8	top-9	
BCDR-F03	[12]	1.00	0.85	0.77	0.76	0.77	0.78	0.74
	[13]	0.85	0.81	0.80	0.69	0.66	0.68	0.64
	[14]	0.87	0.82	0.80	0.68	0.66	0.67	0.63
	[15]	0.80	0.79	0.89	0.79	0.73	0.71	0.71
	[16]	0.73	0.76	0.84	0.80	0.82	0.93	0.84
	[17]	0.46	0.39	0.37	0.39	0.39	0.40	0.39
	[18]	0.74	0.59	0.54	0.50	0.46	0.43	0.47
	[19]	0.06	0.08	0.07	0.10	0.11	0.14	0.14
	[20]	0.67	0.74	0.77	0.83	0.84	0.80	0.86
	[21]	1.00	0.82	0.77	0.73	0.63	0.59	0.59
	[22]	0.81	0.81	1.00	1.00	1.00	1.00	1.00
	[23]	1.00	0.89	0.90	0.91	0.92	0.92	0.99
	[24]	0.24	0.27	0.35	0.36	0.35	0.36	0.38
	[25]	0.72	0.89	0.85	0.91	1.00	0.92	0.91
	[26]	0.83	1.00	0.88	0.75	0.70	0.73	0.73
	[27]	0.52	0.62	0.63	0.62	0.62	0.54	0.48
	[28]	0.73	0.82	0.79	0.84	0.75	0.68	0.71
[29]	0.79	1.00	0.87	0.78	0.78	0.79	0.83	
[30]	1.00	1.00	0.93	0.89	1.00	0.99	0.92	
[31]	0.77	0.80	0.94	0.85	0.99	0.88	0.88	
[32]	0.79	0.80	0.82	0.78	0.82	0.79	0.69	
[33]	0.88	0.90	0.93	0.94	0.87	0.91	0.89	
[34]	1.00	0.85	1.00	1.00	1.00	0.96	0.89	
WDBC	[12]	0.81	1.00	1.00	0.95	0.92	0.89	0.92
	[13]	0.74	0.76	0.78	0.86	0.88	0.86	0.85
	[14]	0.56	0.71	0.84	1.00	0.88	0.95	0.94
	[15]	0.75	0.87	1.00	0.94	0.90	0.89	0.97
	[16]	0.89	1.00	0.88	0.86	0.80	0.86	0.91
	[17]	0.59	0.59	0.56	0.53	0.53	0.51	0.50
	[18]	0.67	0.63	0.57	0.54	0.50	0.47	0.47
	[19]	0.08	0.12	0.14	0.17	0.21	0.22	0.25
	[20]	0.81	0.98	0.97	0.91	0.92	0.95	0.97
	[21]	0.61	0.78	1.00	0.88	0.82	0.85	0.88
	[22]	1.00	0.97	1.00	0.89	1.00	0.94	1.00
	[23]	1.00	1.00	1.00	1.00	1.00	1.00	1.00
	[24]	0.82	0.95	0.96	1.00	0.91	1.00	0.98
	[25]	0.86	0.86	0.90	0.83	0.80	0.78	0.80
	[26]	0.96	1.00	0.88	0.99	1.00	0.96	0.98
	[27]	0.90	0.97	0.91	0.85	0.87	0.95	0.93
	[28]	0.19	0.22	0.23	0.23	0.23	0.23	0.25
[29]	0.98	1.00	0.88	0.98	1.00	0.96	0.97	
[30]	0.98	0.87	1.00	0.98	1.00	0.98	0.95	
[31]	1.00	1.00	0.90	0.90	0.96	1.00	1.00	
[32]	0.47	0.57	0.66	0.72	0.77	0.81	0.83	
[33]	0.98	0.87	1.00	1.00	1.00	0.98	0.92	
[34]	0.80	0.86	0.77	0.75	0.73	0.80	0.82	

Table 3. Stability of algorithms on gene expression datasets

	top-3	top-4	top-5	top-6	top-7	top-8	top-9	
GSE10810	[12]	0.44	0.55	0.54	0.52	0.52	0.51	0.50
	[13]	0.78	0.87	0.81	0.77	0.73	0.71	0.72
	[14]	0.44	0.52	0.52	0.49	0.49	0.50	0.50
	[15]	0.52	0.51	0.46	0.44	0.43	0.44	0.47
	[16]	0.21	0.26	0.25	0.25	0.25	0.25	0.25
	[17]	0.43	0.42	0.41	0.41	0.41	0.41	0.42
	[18]	0.15	0.20	0.20	0.20	0.21	0.23	0.24
	[19]	0.00	0.00	0.00	0.00	0.00	0.00	0.00
	[20]	0.58	0.50	0.49	0.48	0.48	0.47	0.49
	[21]	0.52	0.51	0.46	0.44	0.43	0.44	0.47
	[22]	0.31	0.40	0.39	0.39	0.37	0.39	0.39
	[23]	0.71	0.77	0.82	0.85	0.86	0.84	0.84
	[24]	0.11	0.12	0.13	0.16	0.18	0.21	0.22
	[25]	0.00	0.00	0.01	0.01	0.01	0.01	0.01
	[26]	0.46	0.51	0.59	0.66	0.73	0.78	0.80
	[27]	0.00	0.00	0.00	0.00	0.00	0.00	0.01
	[28]	0.63	0.56	0.52	0.50	0.46	0.45	0.44
[29]	0.46	0.50	0.59	0.66	0.71	0.78	0.80	
[30]	0.25	0.28	0.30	0.30	0.33	0.35	0.36	
[31]	0.73	0.64	0.64	0.65	0.67	0.66	0.66	
[32]	0.05	0.05	0.07	0.09	0.09	0.09	0.09	
[33]	0.51	0.52	0.50	0.48	0.51	0.54	0.57	
[34]	0.17	0.18	0.18	0.21	0.22	0.23	0.24	
GSE15852	[12]	0.40	0.49	0.51	0.52	0.59	0.61	0.61
	[13]	0.51	0.51	0.56	0.60	0.61	0.60	0.62
	[14]	0.47	0.51	0.57	0.59	0.58	0.57	0.57
	[15]	0.28	0.33	0.38	0.40	0.40	0.42	0.44
	[16]	0.48	0.52	0.59	0.65	0.70	0.73	0.76
	[17]	0.31	0.41	0.46	0.52	0.55	0.58	0.60
	[18]	0.16	0.21	0.21	0.20	0.20	0.21	0.21
	[19]	0.00	0.00	0.00	0.00	0.00	0.00	0.00
	[20]	0.57	0.56	0.57	0.61	0.66	0.71	0.75
	[21]	0.21	0.24	0.26	0.30	0.32	0.35	0.38
	[22]	0.59	0.62	0.62	0.67	0.73	0.78	0.81
	[23]	0.84	0.88	0.88	0.86	0.88	0.88	0.89
	[24]	0.24	0.26	0.24	0.26	0.27	0.28	0.30
	[25]	0.53	0.46	0.44	0.42	0.43	0.42	0.43
	[26]	0.87	0.97	0.89	0.88	0.85	0.87	0.86
	[27]	0.00	0.00	0.00	0.00	0.00	0.00	0.00
	[28]	0.25	0.28	0.27	0.29	0.31	0.31	0.32
[29]	0.85	0.96	0.89	0.89	0.86	0.86	0.88	
[30]	0.62	0.65	0.66	0.74	0.80	0.88	0.87	
[31]	0.56	0.54	0.56	0.57	0.59	0.60	0.61	
[32]	0.05	0.05	0.06	0.07	0.06	0.07	0.07	
[33]	0.54	0.58	0.56	0.55	0.55	0.55	0.55	
[34]	0.16	0.18	0.22	0.24	0.26	0.27	0.29	

Several limitations exist in this study. First, how the change of training sizes impacts on the stability estimation is interesting. However, due to insufficient samples of gene datasets, the training sample sizes of each dataset is fixed. Second, using one estimator to assess stability seems not convincing, even if the estimator possesses the properties of a good stability measure. One desirable approach is to use more stability estimators for a comprehensive evaluation [2]. In addition, besides handcrafted features, deeply learnt features will be in our future work to improve network robustness and generalization capacity [35]. In this kind of settings, deep networks perform as feature extractors [36, 37]. When using dropout [38] to determine which nodes are activated or selected, a subset feature selection method is formed, and its stability can be measured.

5. Conclusions

This study investigates the stability of 23 FR algorithms on four BC datasets using an advanced estimator, and three algorithms are identified as consistently exhibiting good stability on all the datasets. Stability is crucial for many decision-making applications. In our future work, experiments will be conducted by involving more algorithms, estimators and datasets to recognize stable algorithms for data analysis.

References

- [1] Z. Zhang, X. Liang, W. Qin, S. Yu, and Y. Xie, "matFR: a MATLAB toolbox for feature ranking," *Bioinformatics*, vol. 36(19), pp. 4968–4969, 2020.
- [2] S. Nogueira, K. Sechidis, and G. Brown, "On the stability of feature selection algorithms," *Journal of Machine Learning Research*, vol. 18(1), pp. 6345–6398, 2017.
- [3] N. López, M. García-Ordás, F. Vitelli-Storelli, P. Fernández-Navarro, C. Palazuelos, and R. Alaiz-Rodríguez, "Evaluation of feature selection techniques for breast cancer risk prediction," *International Journal of Environmental Research and Public Health*, vol. 18(20), pp. 10670, 2021.
- [4] N. Cueto-López, M. García-Ordás, V. Dávila-Batista, V. Moreno, N. Aragonés, and R. Alaiz-Rodríguez, "A comparative study on feature selection for a risk prediction model for colorectal cancer," *Computer methods and programs in biomedicine*, vol. 177, pp. 219–229, 2019.
- [5] A. Kalousis, J. Prados, and M. Hilario, "Stability of feature selection algorithms: a study on high-dimensional spaces," *Knowledge and information systems*, vol. 12(1), pp. 95–116, 2007.
- [6] D. Derroncourt, B. Hanczar, and J. Zucker, "Analysis of feature selection stability on high dimension and small sample data," *Computational statistics & data analysis*, vol. 71, pp. 681–693, 2014.
- [7] J. Arevalo, F. González, R. Ramos-Pollán, J. Oliveira, and M. Lopez, "Representation learning for mammography mass lesion classification with convolutional neural networks," *Computer methods and programs in biomedicine*, vol. 127, pp. 248–257, 2016.
- [8] S. Yu, L. Liu, Z. Wang, G. Dai, and Y. Xie, "Transferring deep neural networks for the differentiation of mammographic breast lesions," *Science China Technological Sciences*, vol. 62(3), pp. 441–447, 2019.
- [9] W. Street, W. Wolberg, R. Ramos-Pollán, and O. Mangasarian, "Nuclear feature extraction for breast tumor diagnosis," *Biomedical image processing and biomedical visualization*, pp. 861–870, 1993.
- [10] V. Pedraza, J. Gomez-Capilla, G. Escaramis, C. Gomez, P. Torné, J. Rivera, A. Gil, P. Araque, N. Olea, and X. Estivill, "Gene expression signatures in breast cancer distinguish phenotype characteristics, histologic subtypes, and tumor invasiveness," *Cancer: Interdisciplinary International Journal of the American Cancer Society*, vol. 116(2), pp. 486–496, 2010.
- [11] I. Ni, Z. Zakaria, R. Muhammad, N. Abdullah, N. Ibrahim, N. Emran, N. Abdullah, and S. Hussain, "Gene expression patterns distinguish breast carcinomas from normal breast tissues: the Malaysian context," *Pathology-Research and Practice*, vol. 206(4), pp. 223–228, 2010.
- [12] N. Cressie and H. Whitford, "How to use the two sample t -test," *Biometrical Journal*, vol. 28(2), pp. 131–148, 1986.

- [13] T. Cover and J. Thomas, "Entropy, relative entropy and mutual information," *Elements of information theory*, vol. 2(1), pp. 12–13, 1991.
- [14] T. Kailath, "The divergence and Bhattacharyya distance measures in signal selection," *IEEE transactions on communication technology*, vol. 15(1), pp. 52–60, 1967.
- [15] F. Hsieh and B. Turnbull, "Nonparametric and semiparametric estimation of the receiver operating characteristic curve," *The annals of statistics*, vol. 24(1), pp. 25–40, 1996.
- [16] N. Nachar, "The Mann-Whitney U: A test for assessing whether two independent samples come from the same distribution," *Tutorials in quantitative Methods for Psychology*, vol. 4(1), pp. 13–20, 2008.
- [17] M. Robnik-Šikonja and I. Kononenko, "Theoretical and empirical analysis of ReliefF and RReliefF," *Machine learning*, vol. 53(1), pp. 23–69, 2003.
- [18] R. Tibshirani, "Regression shrinkage and selection via the lasso," *Journal of the Royal Statistical Society: Series B (Methodological)*, vol. 58(1), pp. 267–288, 2003.
- [19] G. Roffo, "Feature selection library (MATLAB toolbox)," arXiv preprint, arXiv:1607.01327, 2016.
- [20] Q. Gu, H. Li, and J. Han, "Generalized fisher score for feature selection," arXiv preprint, arXiv:1202.3725, 2012.
- [21] J. Uitdehaag and G. Zaman, "A theoretical entropy score as a single value to express inhibitor selectivity," *BMC bioinformatics*, vol. 12(1), pp. 1–11, 2003.
- [22] P. McKight and J. Najab, "Kruskal-wallis test," *The corsini encyclopedia of psychology*, pp. 1–1, 2010.
- [23] S. Happy, R. Mohanty, and A. Routray, "An effective feature selection method based on pair-wise feature proximity for high dimensional low sample size data," *European signal processing conference*, pp. 1574–1578, 2017.
- [24] W. Hu, K. Choi, Y. Gu, and S. Wang, "Minimum–maximum local structure information for feature selection," *Pattern Recognition Letters*, vol. 34(5), pp. 527–535, 2017.
- [25] H. Zeng and Y. Cheung, "Feature selection and kernel learning for local learning-based clustering," *IEEE transactions on pattern analysis and machine intelligence*, vol. 33(8), pp. 1532–1547, 2010.
- [26] G. Roffo and S. Melzi, "Features selection via eigenvector centrality," *Proceedings of new frontiers in mining complex patterns*, 2016.
- [27] G. Roffo, S. Melzi, U. Castellani, and A. Vinciarelli, "Infinite latent feature selection: A probabilistic latent graph-based ranking approach," *IEEE international conference on computer vision*, pp. 1398–1406, 2017.
- [28] P. Bradley and O. Mangasarian, "Feature selection via concave minimization and support vector machines," *IEEE international conference on machine learning*, vol. 98, pp. 82–90, 1998.
- [29] G. Roffo, S. Melzi, and M. Cristani, "Infinite feature selection," *IEEE International Conference on Computer Vision*, pp. 4202–4210, 2015.
- [30] X. He, D. Cai, and P. Niyogi, "Laplacian score for feature selection," *Advances in neural information processing systems*, pp. 18, 2005.
- [31] J. Guo and W. Zhu, "Dependence guided unsupervised feature selection," *AAAI Conference on Artificial Intelligence*, vol. 32(1), 2018.
- [32] L. Du and Y. Shen, "Unsupervised feature selection with adaptive structure learning," *ACM SIGKDD international conference on knowledge discovery and data mining*, pp. 209–218, 2015.
- [33] L. Shi, L. Du, and Y. Shen, "Robust spectral learning for unsupervised feature selection," *IEEE International Conference on Data Mining*, pp. 977–982, 2014.
- [34] M. Qian and C. Zhai, "Robust unsupervised feature selection," *International joint conference on artificial intelligence*, 2013.
- [35] S. Yu, M. Chen, E. Zhang, J. Wu, H. Yu, Z. Yang, L. Ma, X. Gu, and W. Lu, "Robustness study of noisy annotation in deep learning based medical image segmentation," *Physics in Medicine & Biology*, vol. 65(17), pp. 175007, 2020.
- [36] T. Xiao, L. Liu, K. Li, W. Qin, S. Yu, and Z. Li, "Comparison of transferred deep neural networks in ultrasonic breast masses discrimination," *BioMed research international*, 2018.
- [37] L. Zou, S. Yu, T. Meng, Z. Zhang, X. Liang, and Y. Xie, "A technical review of convolutional neural network-based mammographic breast cancer diagnosis," *Computational and mathematical methods in medicine*, 2019.
- [38] N. Srivastava, G. Hinton, A. Krizhevsky, I. Sutskever, and R. Salakhutdinov, "Dropout: a simple way to prevent neural networks from overfitting," *Journal of machine learning research*, vol. 15(1), pp. 1929–1958, 2014.

A Distribution Network Reconfiguration Continuous Method Based on Efficient Solution Space Coding

Wei TANG¹, Baohua SUN, Rongqiang FENG, Chenxi HUANG and Lei ZHAO
NARI Technology Development CO., LTD, Nanjing 210000, Jiangsu Province, China

Abstract. This paper proposes a distribution network reconfiguration (DNR) continuous method to reduce network loss, balancing load, eliminating overload and improving power quality. When a certain coding rule reduces the dimension and reduces the radius of the variable confidence interval, the first type of non effective solution is avoided in probability through the coding rules and algorithm characteristics, and the second type of non effective solution is completely avoided compared with the expert base, so that the number of power flow calculations is greatly reduced. Through improved Crisscross optimization algorithm (CSO), the directionality is introduced into the horizontal crossing, and the fuzzy clustering idea is adopted to dynamically change the static vertical crossing factor, the simulation results show convergence speed and accuracy are improved, and verify the correctness and effectiveness of the method.

Keywords. Distribution network reconfiguration, crisscross optimization algorithm, network reconfiguration

1. Introduction

The distribution system is an important link at the end of power system, connecting the power supply system or power transmission and transformation system with user facilities, distributing and supplying electric energy to users. Network reconfiguration is not only an important means of distribution system operation and control, but also an important content of distribution management system. The main purpose of network reconfiguration is to change the network structure by changing the state of line switch, reduce the operation loss of the network and meet the constraints of capacity and voltage on the premise of realizing the balance of power supply and demand. With the continuous expansion of distribution network scale, a large number of distribution network reconfiguration methods came into the world [1]. The distribution network reconfiguration realizes the operation mode adjustment by switch the opening and closing states of the two types of switches, it can reduce the network loss and the number of switching actions, eliminate the overload, improved and the economy and reliability of the system operation [2].

¹Corresponding author, Wei Tang, NARI Technology Development CO., LTD, Nanjing 210000, Jiangsu Province, China; E-mail: 771866243@qq.com.

This research was financially supported by the NARI Technology Development CO., LTD's project of "Research and development of distribution operation and power supply service application based on SaaS layer of Internet of things cloud platform (524608210002)".

The distribution network reconfiguration problem is actually a combination optimization problem, the number of disconnectors or switches is huge. Therefore, the core of developing distribution network reconfiguration algorithm is to eliminate unnecessary combination search, reduce the amount of calculation, ensure sufficient optimization accuracy, and the optimization result reaches or approaches the optimal solution. At present, the methods used in distribution network reconfiguration mainly include analytical methods, heuristic methods, stochastic optimization methods and so on [3]. The traditional analytical method is not suitable for large-scale distribution system because of its large amount of calculation and slow speed, and most of the reconstruction algorithms are difficult to ensure the global optimal solution [4]. Heuristic methods mainly include branch exchange method (BEM) and optimal power flow (OPF) which can speed up reconstruction [5], but lack of rigorous and feasible mathematical theory to ensure the global optimality of the solution. Stochastic optimization methods include genetic algorithm [6], tabu search algorithm [7], simulated annealing [8], particle swarm optimization [9]. These algorithms have unclear physical meaning and slow convergence speed, but they are suitable for finding the global optimal solution, and more effective methods for solving large-scale nonlinear integer programming problems.

In this paper, the dimensional reduction and compression methods of solution space in distribution network reconfiguration are studied, and the coding method is improved. Firstly, the switching branch range is estimated by the approximate formula of network loss calculation to reduce the dimension and reduce the radius of variable confidence interval. Secondly, the dual population solution space with mapping relationship between continuous variable solution and discrete variable solution is established by combining real number coding and discrete coding. The real solution is mapped to the discrete solution space, and the switching between binary and decimal in the same dimension of the discrete solution is used to skillfully avoid the situation that the same branch set disconnects multiple branches to produce infeasible solutions. At the same time, the direct solution of discrete variables is avoided to reduce the difficulty of solution. Again, the first kind of non effective solutions are avoided in probability through coding rules and algorithm characteristics. Compared with the expert database, the second kind of non effective solution is completely avoided and the number of power flow calculation is reduced. In addition, the horizontal crossing operation and vertical crossing factor of Crisscross optimization algorithm (CSO) [10] are improved to make the optimization effect better.

2. Mathematical Model of Network Reconfiguration

2.1. Economic Restructuring Objective Function

$$\min F = \sum_{i=1}^T k_i r_i \frac{P_i^2 + Q_i^2}{U_i^2} \quad (1)$$

In this formula, T is the number of branches, k_i is the on / off (0 / 1) state of the switch on branch i , r_i is the resistance of branch i , u_i is the terminal node voltage

of branch i , p_i and u_i are the injected active and reactive power of node i respectively.

2.2. Power Flow and Network Topology Constraints

The Power flow constraint expression as follow:

$$f(P_G, Q_G, P_L, Q_L) = 0 \quad (2)$$

$$g(P_G, Q_G, V, S) \leq 0 \quad (3)$$

In this formula, P_G and Q_G , is the active and reactive output vector of the power node respectively, P_L and Q_L is the active and reactive power dissipation vector of load node respectively, V is the node voltage vector, S is the branch complex power vector.

The topological constraints expression as follow:

$$grid \in GRID \quad (4)$$

In this formula, grid is the topology of the current network, GRID is a set of all supporting trees, that means a set of network topologies for requirements of acyclic network and no island.

3. Coding Method and Definition of Non Efficient Solution

3.1. Network Simplification and Coding Method

When applying stochastic optimization method to distribution network reconstruction, if the coding method is unreasonable, a large number of infeasible solutions will be generated in the process of initialization and iteration. The following coding rules are adopted in this paper:

- Delete branches and nodes unrelated to the ring network, except power nodes.
- Merge branches with the same effect of unrolling into the same branch set.
- It is defined that each dimension (i.e. a variable) of the solution in the continuous solution space represents a branch set.
- The dimension is the number of estimated branch sets and is encoded by real numbers. It is defined that each dimension (i.e. a variable) of the solution in the discrete solution space represents a branch, the dimension is the number of all equivalent branch sets, and binary and decimal coding methods are adopted. In the first step, binary coding is used to select the estimated branch set. If the dimension is 0, it means that the branch set is not selected, and all branches in the set are closed. If the dimension is 1, it means that the branch set is selected. Note that all dimensions occupied by the set of unmeasured branches are set to zero. In the second step, the branch in the selected branch set is selected by

decimal coding. If the dimension is a positive integer n , it indicates that the n th branch in the branch set is disconnected.

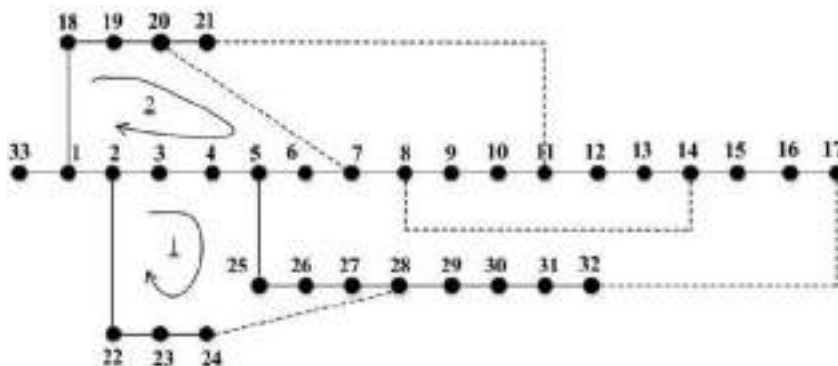


Fig. 1. Single-line diagram of IEEE-33 node distribution system.

As shown in Figure 1, if it is specified that a reconstructed single ring contains only one connecting branch, branches 2-3, 3-4, 4-5, 5-25, 25-26, 26-27, 27-28, 28-24, 24-23, 23-22, 22-2 form a single ring. From the perspective of ring solution, the effect of disconnecting branches 22-2 or 23-22 or 24-22 is the same. Therefore, all branches from node 2 to node 24 are merged into the same branch set and expressed in one dimension in the continuous solution space. If the connecting branches are classified into a branch set, there are only 10 branch sets, which means that the dimension of the solution variable is reduced. Here, the steepness parameter u takes an appropriate fixed value. In order to ensure the radial shape of the network topology, the number of disconnected branches cannot be changed, the five variables with the largest probability value determine that one branch of the branch set is disconnected and set to 1, and the others are set to 0. Then, branch n is randomly selected for the selected branch group in the discrete solution space. It is worth noting that each branch set does not contain all solution ring equivalent branches. This is because the branch exchange range estimated in the previous section determines the alternative branches, which is equivalent to quadratic dimensional reduction in terms of calculation.

3.2. Introduction of Continuity Thought

As the discrete optimization algorithm increases with the combination number, the difficulty of solution increases sharply and the convergence speed is difficult to ensure, this paper does not binarize or decimal the optimization algorithm suitable for continuous variables. The existing continuous method transforms the original discrete problem into a planning problem about continuous variables and then solves it.

For example, in reactive power optimization, the switching group of shunt capacitor and the tap position of transformer are discrete variables, and the generator active and reactive output are continuous quantities. The nearest rounding of multiple discrete quantities is likely to lead to the convergence of the whole solution.

Due to the iterative process of distribution network reconfiguration needs to convert continuous variables into discrete variables for power flow calculation and check constraints, this idea is not applicable. In literature [11], after the above process is similar, it is converted into continuous variables for iteration. In fact, the problem

lies in that when the variables in the same solution space are converted from continuous to discrete again, it is easy to fall into the infeasible region, it is difficult to escape, and the population diversity decreases sharply, which is not conducive to the solution of the problem.

In this paper, two mapping relations are established for the solutions of real number coding and discrete coding in Section 3.1, mapping from real number solution to binary solution, and then reflecting the original image integer solution in another mapping relationship. Therefore, the certainty from continuous solution to integer solution is deterministic in random, it is conducive to the application of continuous optimization algorithm to obtain the global optimal solution in the global optimization space containing the whole support tree set of distribution network, effectively reduce the variable dimension and ensure the solution speed.

3.3. Definition of Non Efficient Solution and Effective Avoidance

The constraint test and evolution criterion in network reconfiguration depend on power flow calculation. Due to power flow calculation accounts for the vast majority of the whole running time, if power flow calculation is carried out for each individual of each generation, unnecessary repeated power flow calculation is bound to prolong the convergence time. Therefore, it is necessary to put forward the concept of non effective solution.

Different from the definition of infeasible solution or invalid solution, the noneffective solution is feasible first, that is, it meets the radial shape and does not lose load. This paper defines two types of noneffective solutions: the first type of noneffective solution means that the reconstructed network loss is greater than that before the structure, or the solution generated in this iteration is worse than that generated in a previous iteration on the premise that the network loss value in the optimization process is smaller than the initial network loss, that is, the network loss is greater. The second kind of non efficient solution refers to the same solution generated by the n th iteration and the m ($m < n$) iteration.

Avoiding the first kind of non effective solution can only rely on good coding rules and algorithm characteristics to avoid probability. In fact, the second kind of non effective solution accounts for a large proportion under low dimensional coding, especially in the late stage of iteration, which leads to the extension of convergence time. By establishing an expert database ratio that meets constraints and has no repeated solutions, it is unnecessary to realize multiple repeated power flow calculations to avoid the second kind of non effective solution, then reduce the convergence time and avoid the following ideas:

- Firstly, the initialized real population is obtained in integer form according to the mapping relationship, and the topology constraints before power flow calculation, node voltage constraints after power flow calculation and line capacity constraints are tested. The individuals that do not meet the constraints are regenerated until the discrete population that meets the constraints is formed, the individuals of the discrete population are checked, and a new discrete population without repeated individuals is obtained, and the initial expert database is established.
- The new discrete population satisfying topological constraints generated by each iteration is compared with the expert database. Power flow calculation is

carried out only when the current individual has no record in the expert database.

4. Improved CSO Algorithm and Reconstruction Steps

4.1. Improved CSO Algorithm

CSO algorithm is a random search algorithm based on population. It adopts the double search mechanism of horizontal crossover and vertical crossover. The crossover results spread in the whole population in a chain reaction. This mechanism makes CSO algorithm have obvious advantages in global convergence ability and convergence speed compared with other swarm intelligent optimization algorithms in solving complex optimization problems [12]. The improved CSO algorithm flow chart is as shown in Figure 2:

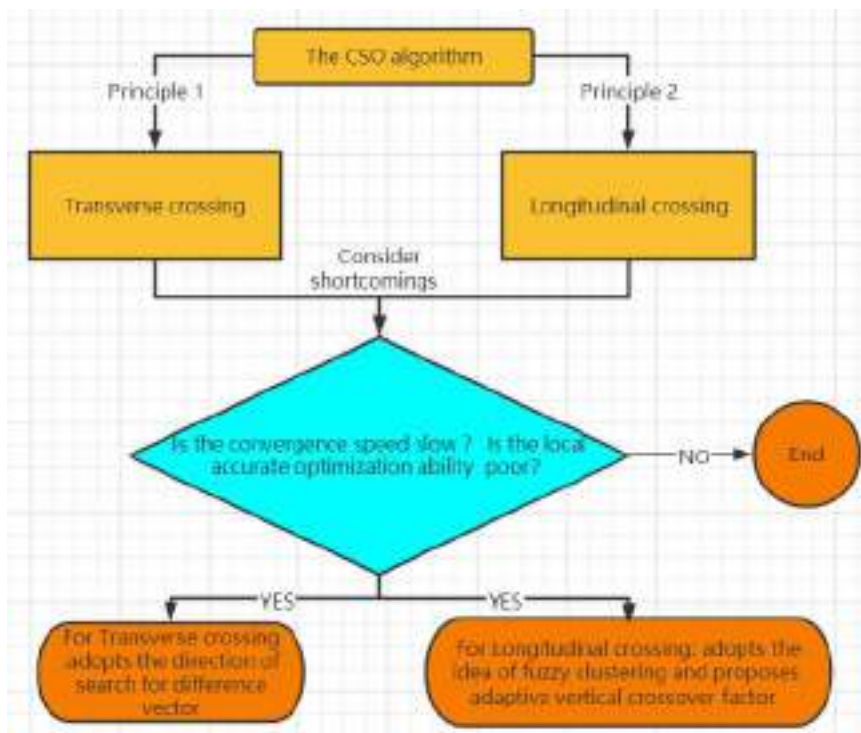


Fig. 2. The improved CSO algorithm flow chart.

The basic principle is as follows:

- Transverse crossing

It is an arithmetic crossing between all dimensions of two different and non repeating individuals selected with a certain probability in the population:

$$M_{hc}(i, d) = r_1 X(i, d) + (1 - r_1) X(j, d) + c_1 (X(i, d) - X(j, d)) \tag{5}$$

$$M_{hc}(i, d) = r_2 X(i, d) + (1 - r_2) X(j, d) + c_2 (X(i, d) - X(j, d)) \quad (6)$$

In this formula, i and j represent any two different individuals in the population, d stands for dimension, X and M_{hc} represents parent and child populations respectively, the uniform random number r_1 and $r_2 \in [0, 1]$, the uniform random number c_1 and $c_2 \in [-1, 1]$.

- Longitudinal crossing

Longitudinal crossing can make the dimension trapped in the local optimum have the opportunity to jump out. Once two different and non repetitive dimensions and are selected, all individuals of the population will make an arithmetic crossing on the dimension:

$$M_{vc}(i, d_1) = r_3 X(i, d_1) + (1 - r_3) X(i, d_2) \quad (7)$$

In this formula, the uniform random number $r_3 \in [0, 1]$.

Due to the optimization only depends on the crossover operation and does not take advantage of the unique properties of the problem, the convergence speed is slow and the local accurate optimization ability is poor. Now, the transverse crossover is improved as follows:

$$X_{con,i}^{k+1} = \omega_i^k (X_{con,b}^k - X_{con,i}^k) + X_{con,i}^k \quad (8)$$

Among that,

$$\omega_i^k = \omega_l + (\omega_u - \omega_l) \frac{F_b^k - F_i^k}{F_b^k - F_w^k} \quad (9)$$

ω_u and ω_l are the upper and lower limits of the disturbance factor ω_i^k , F_i^k is the fitness of the i -th individual in the k -th iteration, F_b^k and F_w^k are the fitness of the best and worst individuals in the k -th iteration population, $X_{con,b}^k$ and $X_{con,i}^k$ are the best and i -th individuals in the real coded population respectively.

The improved transverse crossing is no longer a complete random variation, but the base vector searches in the direction of search for $X_{con,b}^k - X_{con,i}^k$ as the difference vector. From the perspective of vector operation, searching in the individual direction with better fitness is conducive to faster convergence to the global optimum.

CSO algorithm vertical crossover factor P_{vc}^k , which directly determines how many dimensions participate in vertical crossover, thus affecting individual self cognitive behavior. If it is fixed according to the standard algorithm, the population information is not fully utilized. Therefore, this paper adopts the idea of fuzzy clustering and

proposes P_{vc}^k which changes adaptively with the population information. The equation is as follows:

$$P_{vc}^k = P_{vc\max} + \gamma^k (P_{vc\min} - P_{vc\max}) \quad (10)$$

Among that,

$$\gamma^k = \begin{cases} \frac{\sqrt{(F_i^k - \frac{1}{M-1} \sum_{j=1, j \neq i}^M F_j^k)^2}}{F_w^k - F_b^k}, & F_b^k \neq F_w^k \\ \gamma^{k-1} rand(), & F_b^k = F_w^k \end{cases} \quad (11)$$

In this formula, M is the population size, and $rand()$ is the uniform random number distributed in interval $[0,1]$.

4.2. Network Reconstruction Calculation Steps

The calculation of network reconfiguration is divided into the following seven steps:

Step1, read the original data of the distribution system, calculate the initial power flow of the whole network, and obtain the initial network loss and initial node voltage distribution.

Step2, call the subroutine of reduced dimension and compressed variable confidence interval radius to estimate the exchange branch of each ring.

Step3, determine the dimension of variable and constant (set of branches not estimated), as well as the interval number of continuous (real) coded and discrete (integer) coded variables of each variable.

Step4, according to various group dimensions and the mapping relationship between the two populations, the real population is initialized to form the initial discrete population, the power flow distribution of the latter is calculated, and the initial expert database is formed.

Step5, for the real population, the improved horizontal operation is carried out by using equation (8), the discrete population satisfying topological constraints is formed by mapping and reflection, and then compared with the expert database, the power flow calculation and constraint test of some individuals are carried out, the dominant solution is retained by the competition operator, and the expert database is updated.

Step6, for the discrete population after horizontal operation, calculate the P_{vc}^k of this iteration, change the previous crossover operation to vertical crossover, and repeat the subsequent process.

Step7, Judge whether the iteration is over. If yes, output the result. If not, go to step 5.

5. Simulations

The simulation environment is MATLAB R2010b, the basic parameters are population size $M_1=100$, $M_2=20$, transverse crossing factor $P_{hc} = 1$, static longitudinal crossing factor $P_{vc} = 0.7$, upper limit $\omega_u = 0.7$ and lower limit $\omega_l = 0.1$ of disturbance factor, upper limit $P_{vcmax} = 0.8$ and lower limit $P_{vcmin} = 0.2$ of adaptive longitudinal crossing factor, iteration times $D_1 = 100$, $D_2 = 20$ and $D_3 = 30$.

Now, two examples are simulated and analyzed. Example one is the ieee33 bus distribution system [12], with the population size of M_1 and the number of iterations of D_1 . Figure 3 shows the node voltage distribution of the system before and after reconstruction. It can be seen that the node voltage distribution is significantly improved after reconstruction. The lowest node voltage is changed from bus 17 to bus 31, and the unit value increases from 0.913 to 0.9378.

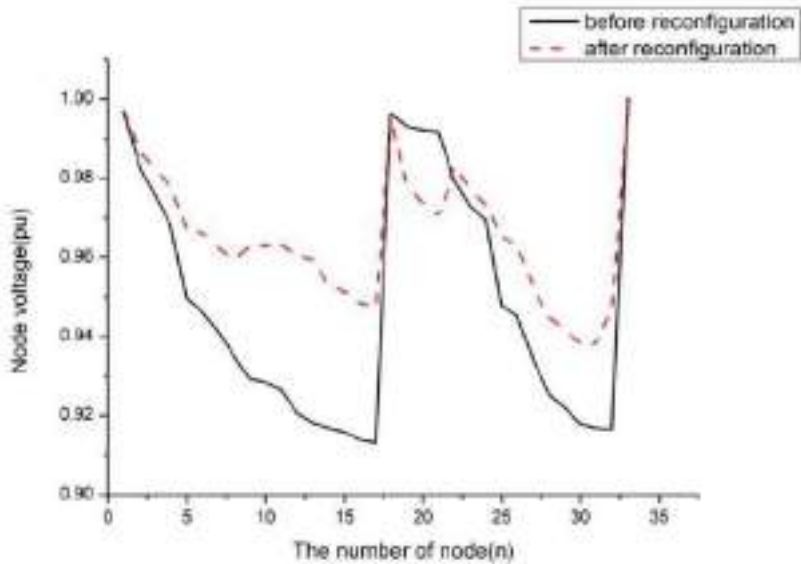


Fig. 3. Voltage profile for IEEE 33 node system before and after reconfiguration.

The Figure 4 shows the optimization convergence curves of different CSO. Dimension Reduction CSO(DRC SO) is the improvement of the standard CSO algorithm after dimensional reduction and interval radius reduction. Self adaption DRC SO(SADRC SO)is improved to adaptive longitudinal crossover on this basis, and Improved SADRC SO(ISADRC SO)is the improved algorithm after considering the non effective solution in this paper. It can be seen that its convergence speed has been significantly improved.

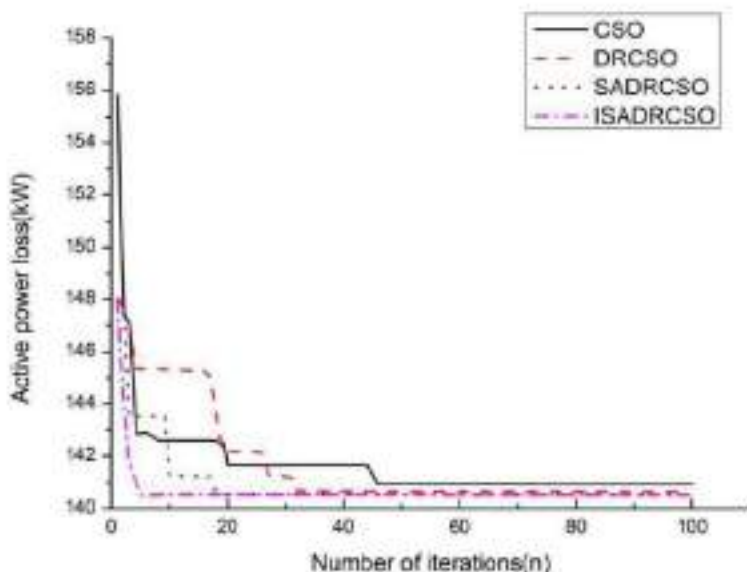


Fig. 4. Convergence curve of different CSO.

The above algorithms converge to the optimal solution under a given number of iterations. The open branches are 6-7, 8-9, 13-14, 24-28 and 31-32, and the network loss decreases from the initial value of 202.68kw to 139.55kw. Table 1 shows the performance comparison of the algorithm. In order to reduce the random error, each algorithm runs 20 times. After DRCSO reduces the dimension and reduces the interval radius, the average convergence time relative to CSO is reduced by 40%. After ISADRC SO considers avoiding the non effective solution, the average convergence time relative to SADRC SO is reduced by 74.9%, and the average number of convergence iterations is only 5 times. Obviously, the convergence speed is faster than that in literature [10], and it converges to the global optimum after 20 consecutive runs, and the robustness is better.

Table 1. Performance comparison among four CSO algorithms.

Name	Average convergence time	Average convergence iterations	Times of convergence to global optimum
CSO	68.361	46	17
DRCSO	46.506	32	20
SADRC SO	26.796	18	19
ISADRC SO	6.724	5	20

The example two is a part of PG &E distribution system, which is a 69 bus system [12]. Figure 5 compares the convergence of ISADRC SO with dimensional reduction and interval radius reduction in population size M_2 and iteration number D_2 with ISADRC SO without prior estimation of branch range operation. It is not difficult to find that ISADRC SO converges globally after 3 iterations, in which the convergence

time is 3.585s, while ISACSO needs 10 iterations for local convergence, in which the convergence time is 9.679s.

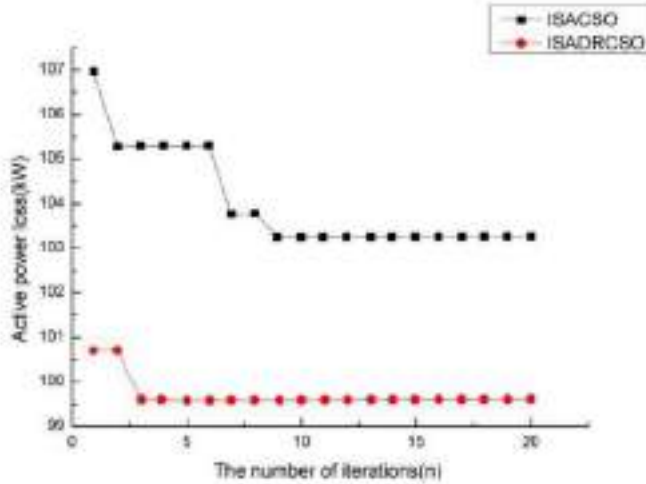
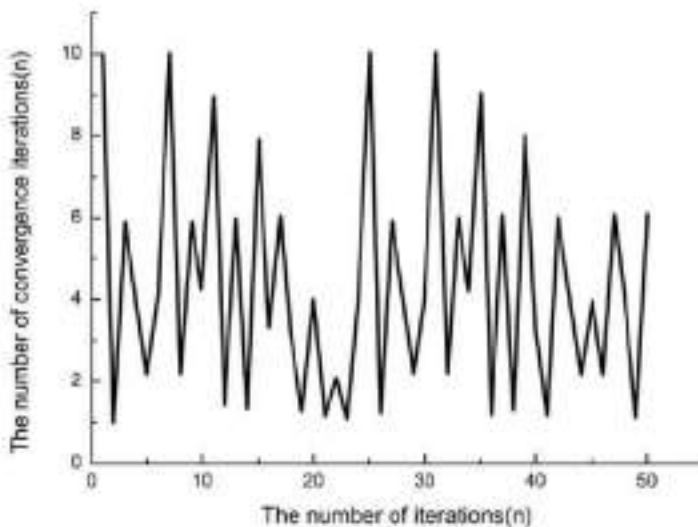


Fig. 5. Convergence curve of two CSO.

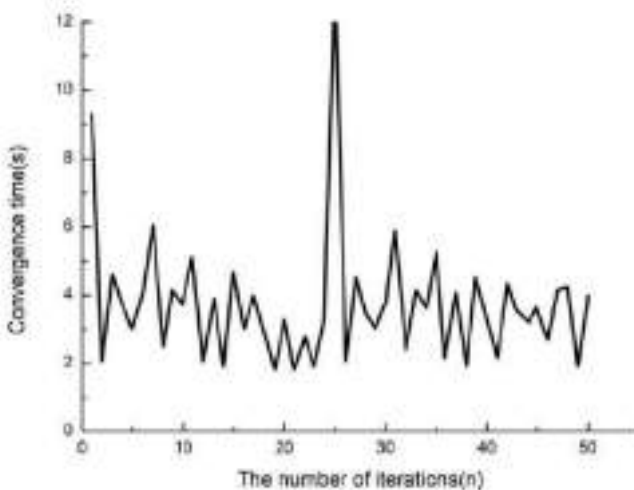
In order to ensure the global convergence of ISACSO, the population size is changed to M_1 and the number of iterations is changed to D_3 . However, the robustness is not strong. The global convergence is 14 iterations, in which the convergence time is 80.864s and the minimum network loss is 99.6032kw.

Taking the node number in reference [13] as an example, the reconstruction results of this paper show that the disconnected branches are 10-70, 12-19, 13-14, 46-47 and 50-51. Although other algorithms [14] are different from individual disconnected branches in this paper, the network loss and the lowest node voltage are the same. In essence, nodes 45, 46 and 47 are unloaded, so the effect of disconnecting branches 44-45, 45-46, 46-47 or 47-48 is the same. Therefore, the reconstruction results in this paper are consistent with most other algorithms. Among them, the immune algorithm [14] has an average number of convergence iterations of 34, while the fuzzy genetic algorithm [15] needs 300 iterations to converge when it runs for 50 consecutive times, and the hybrid particle swarm optimization algorithm [16] has an average number of convergence iterations of more than 10 times, with a convergence time of 7.609s. In this paper, it runs for 50 consecutive times, with an average number of convergence iterations of 4.4 times and an average convergence time of 3.781s. Obviously, the convergence speed is significantly improved. However, the broken branches of binary crossbar algorithm [11] are 11-66, 13-20, 12-13, 46-47 and 50-51, which are obviously sub-optimal solutions and are not difficult to verify.

Figure 6 shows the curve of convergence iteration times and convergence time of ISADRCO running for 50 consecutive times, in which the maximum number of convergence iterations is 10 and only 4 times, and only 3 times run local convergence.



(a)



(b)

Fig. 6. Number of iterations and convergence time of 50 times run.

In this coding method, after branch estimation, the number of search branches is reduced from 57 to 18, the variable dimension and interval radius are greatly reduced, and the convergence speed is further improved after effectively avoiding the non effective solution in the low dimensional solution space. The comparison with other algorithms fully shows the effectiveness of this method.

6. Conclusions

This paper studies the solution space dimensional reduction, compression and coding improvement methods of distribution network reconfiguration, and proposes a continuous optimization algorithm of reconfiguration. Firstly, the approximate formula of network loss calculation based on load current is derived to determine the minimum branch range of the optimal solution, compress the solution space, improve the optimization efficiency, and establish the mapping relationship between continuous variable solution and discrete variable solution. Secondly, a two-population solution space with mapping relationship between continuous variable solution and discrete variable solution is established to avoid directly solving discrete variables and prevent the amount of calculation from increasing exponentially with the increase of the scale of combination optimization problem. This method also has reference significance for exploring how to apply the effective mathematical method and optimization theory suitable for continuous variables to the discrete variable optimization model. Finally, the non effective solution is defined. By relying on the coding rules and algorithm characteristics, the first type of non effective solution is avoided probabilistic, and the second type of non effective solution is completely avoided compared with the expert database. The number of power flow calculation is greatly reduced and the calculation time is shortened.

The CSO simulation example used in this paper shows that the performance of the algorithm is improved by adding the directional guidance of horizontal crossing operation and dynamic vertical crossing factor, and the convergence speed is faster than other algorithms. It is proved that this method can effectively find the global optimal solution, and the calculation speed has obvious advantages.

References

- [1] Tan WY, Liu M, Luo YP, et, al. Review of research on algorithm and time division of dynamic reconfiguration of distribution network. *Electrical Measurement & Instrumentation*. 2020; 57(11):63-67.
- [2] Wu JX, Yu YJ. Multi-objective distribution network reconfiguration optimization harmony search algorithm. *Power Sys. Protection and Control*. 2021;49(19):79-85.
- [3] Wang YS, Sun JL, Cao MZ. Research on the optimization of the tie lines based on dynamic programming for distribution network. *Power Sys. Protection and Control*. 2016;44(10):30-36.
- [4] Ma Q, Gou L, Zhang HF, et, al. Multi-period dynamic reconfiguration of distribution network considering the number of switching actions. *Electrical Measurement & Instrumentation*. 2021;3(58):9-14.
- [5] Deng P, Liu M, Cao P, et, al. Research probabilistic power flow reconfiguration of distribution network based on improved heuristic algorithm elec. *Power Science and Engineering*. 2021;8(37):34-40.
- [6] Alsaf H, Kahouli O, Boutera Y, et, al. Power system reconfiguration in distribution network for improving reliability using genetic algorithm and particle swarm optimization. *Applied Sciences*. 2021;11(7):3092.
- [7] Ma CY, Sun ZZ, Yin ZC, et, al. Reconfiguration of distribution network based on double hybrid particle swarm algorithm. *Transactions of China Electrotech. Society*. 2016;31(11):120-128.
- [8] Zhang K, Lu L, Sun YL. Dynamic reconfiguration of distribution network based on membership partition of time intervals. *Power Sys. Protection and Control*. 2016;44(3):51-57.
- [9] Lu Y, Wu JY, Hao LL. Multi-objective distribution network reconfiguration with distributed generations based on improved MOBPSO algorithm. *Power System Protection and Control*. 2016;44(7):62-68.
- [10] Juan W, Tan YH, Lei KJ. Multi-objective optimization of distribution network dynamic reconfiguration based on intercoded quantum particle swarm optimization algorithm. *Power Sys. Protection and Control*. 2015;43(16):73-78.

- [11] Yin H, Zhou YL, Meng AB. Application of binary crisscross optimization algorithm to distribution network reconfiguration *Power Sys. Tech.* 2016;40(1):270-275.
- [12] Trakas DN, Hatziargyriou ND. optimal distribution system operation for enhancing resilience against wildfires. *IEEE Trans. on Power Sys.* 2017; 33(2):2260-2271.
- [13] Salkuti SR, Battu NR. An effective network reconfiguration approach of radial distribution system for loss minimization and voltage profile improvement. *Bulletin of Electrical Engineering and Informatics.* 2021;10(4):1819-1827.
- [14] Zhang ZL, He L, Wu S. Dynamic reconfiguration of distribution network based on improved NSGA-II. *Science Tech. and Engineering.* 2021;21(21):8916-8922.
- [15] Xu Z, Yang W, Zhang WQ, Chen SK. Multi-objective distribution network reconfiguration based on chain loops and improved binary particle swarm optimization. *Power Sys. Protection and Control.* 2021;49(6):114-123.
- [16] Tian SX, Liu L, Wei SR, Fu Y, Mi Y, Liu S. Dynamic reconfiguration of a distribution network based on an improved grey wolf optimization algorithm. *Power System Protection and Control.* 2021;49(16):1-11.

Tribological Property Behavior of Sinusoidal Texture with Various Intervals Under Scarce Oil Supply

Jian MA^a, Yancong LIU^{a,b,1}, Na ZHANG^a, Xiaoshuang YANG^a and Hongyu JIA^a
^a College of Mechanical and Electronic Engineering, China University of Petroleum, Qingdao, China

^b Shandong Institute of Petroleum and Chemical Technology, Dongying, China

Abstract. Reasonable texture area density can effectively form continuous oil film and improve the surface tribological properties. The combination of friction experiment and simulation analysis studied the influence of sinusoidal texture surface density on the surface friction performance, and also discussed its influence on the surface oil retention behavior. The experimental results and simulation analysis show that the texture synergistic lubrication has a significant positive correlation with the tribological properties. Moreover, it is noticed that tribological properties are more sensitive when the smaller texture interval is employed. And when the texture interval is 0.216 mm, the effect of sinusoidal texture on surface wettability and dynamic pressure lubrication is more significant. The results of this research contribute to better understanding of sinusoidal texture friction mechanism.

Keywords. Lubricated, starved lubrication, texture, hydrodynamic

1. Introduction

Sliding element surface geometry plays a crucial role in maintaining surface lubrication performance [1]. Sliding friction pair can form a continuous oil film under sufficient oil supply. However, oil waste can occur during the process. Surface texture can act as a micro-reservoir between the friction pair, which can store and release oil [2-4]. Micro-texture does not only regulate the amount of surface oil, but it also generates a hydrodynamic pressure between the friction pair, which results in additional lifting power [5-7]. When oil supply is insufficient, the influence of surface micro-texture morphology parameters on friction properties is more sensitive [8-10].

With the development of laser surface texture (LST) technology, more accurate control of micro-texture parameters is achieved [11, 12]. In recent years, a consensus has emerged which states that surface tribological properties can be improved by modifying the micro-texture morphology parameters. In the existing reports, micro-pits are applied extensively in the experimental research of piston ring friction reduction. It has already

¹ Corresponding author, Yancong Liu, College of Mechanical and Electronic Engineering, China University of Petroleum No.66 Changjiang West Road, Huangdao District, Qingdao 266580, China; E-mail: lycupc.609@gmail.com.

This study was supported by the Postgraduate innovation project foundation (No. YCX2019058), Shandong province agricultural major application technology innovation project (No. SD2019NJ018).

been proven that reasonable micro-pitting parameters can produce fluid dynamic pressure effects which reduce wear between the friction pair [13-15]. Furthermore, the antifriction effect of micro-texture is not only related to morphology, but also to operating conditions [11, 16, 17]. When subjected to different operating conditions, the micro-texture shows a specific optimal morphology [16, 18]. The uncertainty of micro-texture optimal morphology has promoted the research of asymmetric and bionic texture morphology. The research results indicate that under oil/water lubrication conditions, the micro-texture produces a wedge effect, which is a key to hydrodynamic lubrication.

In this paper, influence of sinusoidal texture interval on surface friction, wear properties are investigated both experimentally and numerically. Contrary to previous investigations, experimental data and simulation results are organically combined. Influence mechanism of sinusoidal texture interval on surface tribological properties is investigated. Research results provide a basis for friction reduction mechanism investigations.

2. Materials and Methods

2.1. Materials and Methods

Friction pair materials are 40Cr and GCr15. The upper specimens are a GCr15 cylindrical pin and the lower specimen is 40Cr. The base oil of polyalphaolephin (PAO6) was used as the lubricant. Sinusoidal textured surface with a width to depth ratio of 1.35 is selected for testing. Sinusoidal texture surfaces are fabricated by YLP-MP20 fiber-laser. In order to research the synergy between textures, surfaces with density of 5% (S1), 10% (S2), 15% (S3), 20% (S4), 25% (S5), and 30% (S6) are employed to calculate the texture interval.

Friction experiments equipment Comprehensive tester (CFT-I, Lanzhou Zhongke Kaihua Technology Development Co., Ltd., Lanzhou China) is selected and oil is supplied in a single time. Load pressure and speed are set to 15N and 0.05m/s respectively. The surface morphology of specimens is measured by SEM scanning electron microscope (SEM, JEOL JSM-7200F). In order to further explain the influence mechanism of different texture interval distances on surface friction and wear properties, surface oil film is simulated by ANSYS Fluent-18.0 software.

3. Results and Discussion

3.1. Effect of Texture Area Density on Friction Coefficient

Friction coefficient and average friction coefficient of various surfaces are shown in Figure 1. In general, the friction coefficient first fluctuates and then stabilizes. For different texture intervals, surface friction coefficient curve degree of fluctuation also varies. Except for S5 (density of 25%), the remaining five specimens all demonstrate large fluctuations in the early experimental stage. As the experiment progresses, continuous oil film is formed between the surfaces, which causes stabilization of friction coefficient. Surface S6 (density of 30%.) has a maximum interval distance of 1.08 mm, which helps friction coefficient curve to enter the stable stage.

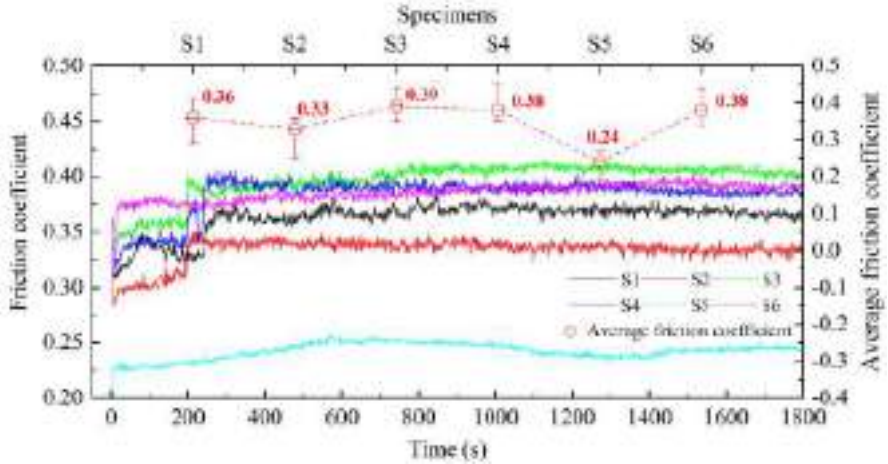


Fig. 1. Friction coefficient and average friction coefficient of various surfaces.

3.2. Analysis of Textured Surface Pressure Distribution

Pressure distribution and maximum positive pressure gradient of textured surface are exhibited in Figure 2. The oil film pressure forms a small positive pressure value or even a negative pressure at the groove valley (i.e., the divergence) and the flat area. A larger positive pressure may form at the crest of the groove, i.e., the convergence zone. Moreover, the texture causes the hysteresis of oil film internal pressure. This phenomenon is mainly due to the wedge effect that causes the backflow and squeezing at the texture. The above phenomena leads to the formation of a pressure gradient within the oil film. When the texture interval distance is between 0.36 mm and 1.08 mm, a negative pressure value appears in the flat area, as shown in Figure 2 (a-c). When the fluid passes through the flat plate area, the wedge effect is weakened, and the flow rate is reduced. This causes a formation of relatively weak wedge and backflow effects in the next texture area. However, when the texture interval distance is sufficiently small, progressive enhancement between textures plays a key role in forming a stronger wedge and recirculation effects in the next texture area. Consequently, the texture near the outlet forms large positive pressure value, as shown in Figure 2 (b-f).

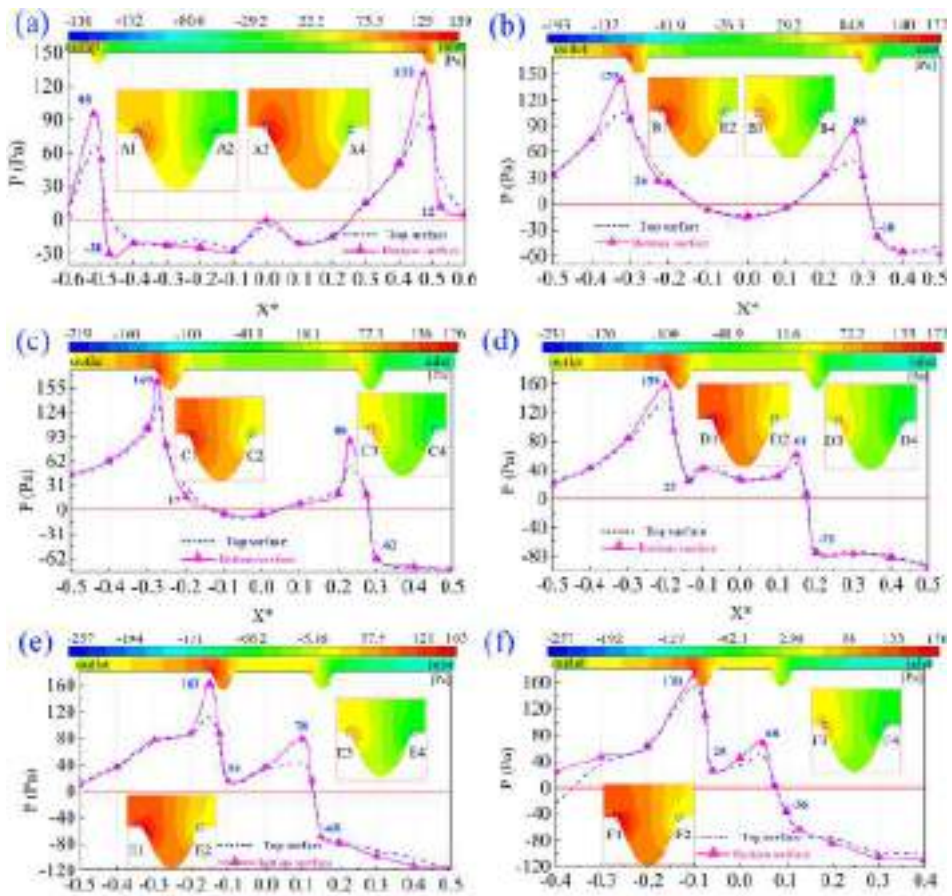


Fig. 2. Oil film pressure distribution on textured surface and maximum positive pressure gradient: (a) S1, $L = 1.08$ mm, (b) S2, $L = 0.5$ mm, (c) S3, $L = 0.36$ mm, (d) S4, $L = 0.27$ mm, (e) S5, $L = 0.216$ mm, (f) S6, $L = 0.18$ mm.

3.3. Effect of Texture Interval on Surface Wear

In Figure 3, results of wear quality and texture width reduction (at point A) are depicted. In general, the texture surface has different degrees of scratches and deformation, and they all occur within the flat area. Compared with other styles, scratches on S5 surface are relatively shallow. Therefore, as shown in Figure 3, S5 also demonstrates a smaller coefficient of friction. Moreover, the non-friction (N-F) area of S5 appears to simultaneously diverge and converge (peak area), while the surface of the remaining five patterns does not appear to converge. There is no N-F area on the surface of S1-S4 specimens, which means that a stable oil film cannot be formed on the pattern surface. This is mainly caused by excessively large texture spacing, which results in the inability to form continuous positive pressure in the flat area. Dynamic pressure lubrication cannot be formed between the friction pair, and friction can only be reduced by relying on the texture to store the wear debris, as well as the secondary oil release.

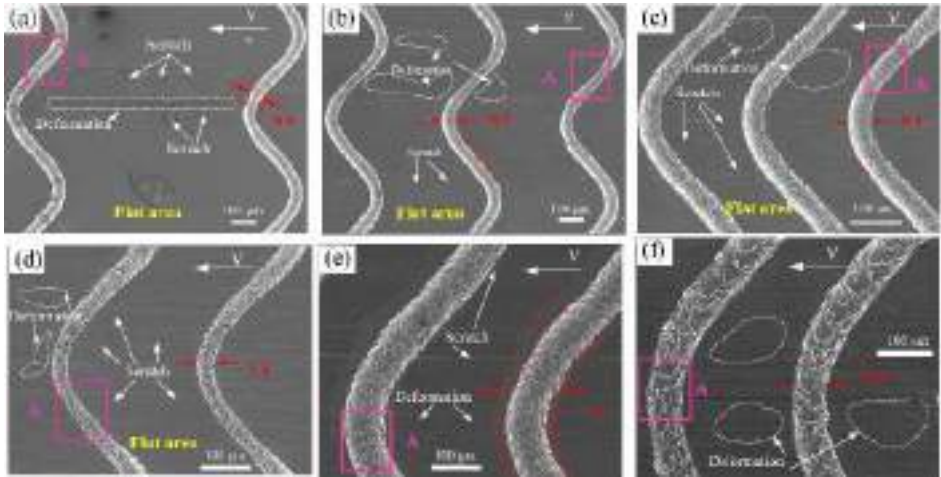


Fig. 3. Surface wear morphology and texture width reduction at point A: (a) S1, (b) S2, (c) S3, (d) S4, (e) S5, (f) S6.

4. Conclusions

The following conclusions were obtained from the work. Formation of the N-F area on the textured surface is mainly related to hydrodynamic lubrication. Further, texture interval distance also affects the texture width, which is mainly due to surface deformation and material migration. When the texture interval is greater than 0.36 mm, no corresponding relationship between oil spreading performance and tribological surface properties is observed. The research in this paper will provide experimental and data references for texture surface design and fluid lubrication.

References

- [1] Galda L, Sep J, Prucnal S. The effect of dimples geometry in the sliding surface on the tribological properties under starved lubrication conditions. *Tribol Int.* 2016; 99: 77-84.
- [2] Zhang D, Li Z, Zhao F, Guo F, Dong G. Study on tribological behavior of grooved-texture surfaces under sand-oil boundary lubrication conditions. *Tribol T.* 2020;1-11.
- [3] Wang J, Zhao H, Huang W, Wang X. Investigation of porous polyimide lubricant retainers to improve the performance of rolling bearings under conditions of starved lubrication. *Wear.* 2017;380: 52-58.
- [4] Zhang D, Gao F, Wei X, Liu G, Meng H, Li P. Fabrication of textured composite surface and its tribological properties under starved lubrication and dry sliding conditions. *Surf Coat Tech.* 2018; 350: 313-322.
- [5] Braun D, Greiner C, Schneider J, Gumbsch, P. Efficiency of laser surface texturing in the reduction of friction under mixed lubrication. *Tribol Int.* 2014; 77: 142-147.
- [6] Dumitru G, Romano V, Weber H P, Gerbig Y, Haefke H., Bruneau S, et al. Femtosecond laser ablation of cemented carbides: properties and tribological applications. *Appl Phys A-mater* 2004; 79: 629-632.
- [7] Gualtieri E, Borghi A, Calabri L, Calabri, L, Pugno N., Valeri S. Increasing nanohardness and reducing friction of nitride steel by laser surface texturing. *Tribol Int.* 2009; 42: 699-705.
- [8] Wojciechowski L, Kubiak K J, Mathia T G. Roughness and wettability of surfaces in boundary lubricated scuffing wear. *Tribol Int* 2016; 93: 593-601.
- [9] Nicolau A, Dias N, Mota M, Lima N. Trends in the use of protozoa in the assessment of wastewater treatment. *Res Microbiol* 2001; 152: 621-630.

- [10] Maheshwari DK, Kumar S, Maheshwari NK, Patel D, Saraf M. Nutrient availability and management in the rhizosphere by microorganisms. *Bacteria in agrobiolgy: Stress management*. Springer, Berlin, Heidelberg, 2012; 301-326. 978-3-642-23464-4.
- [11] Qiu Y, Khonsari MM. Performance analysis of full-film textured surfaces with consideration of roughness effects. *J Tribol*. 2011; 133: 021704.
- [12] Gropper D, Wang L, Harvey TJ. Hydrodynamic lubrication of textured surfaces: a review of modeling techniques and key findings. *Tribol Int*. 2016; 94: 509-529.
- [13] Etsion I. State of the art in laser surface texturing. *J. Tribol*. 2005; 127: 248-253.
- [14] Ibatan T, Uddin MS, Chowdhury MAK. Recent development on surface texturing in enhancing tribological performance of bearing sliders. *Surf Coat Tech* 2015; 272: 102-120.
- [15] Ye J, Zhang H, Liu X, Liu K. Low wear steel counterface texture design: a case study using micro-pits texture and alumina-PTFE nanocomposite. *Tribol Lett*. 2017; 65: 1-12.
- [16] Henry Y, Bouyer J, Fillon M. An experimental analysis of the hydrodynamic contribution of textured thrust bearings during steady-state operation: A comparison with the untextured parallel surface configuration. *P I Mech Eng J-J Eng*. 2015; 229: 362-375.
- [17] Wang X, Wang J, Zhang B, Huang W. Design principles for the area density of dimple patterns. *P I Mech Eng J-J Eng*. 2015; 229: 538-546.
- [18] Han J, Fang L, Sun J, Ge S. Hydrodynamic lubrication of microdimple textured surface using three-dimensional CFD. *Tribol T*. 2010; 53: 860-870.

Research on Spatial Distribution in Power Frequency Magnetic Field Immunity Test

Yang JIANG^{a,b}, Chenxi LIAO^c, Shisheng FU^{a,b}, Fan ZHENG^a, Limin WANG^a and Ming LI^{a,b,1}

^a*Zhejiang Institute of Metrology, Hangzhou 310007, China*

^b*Key Laboratory of Energy and Environmental Protection Measurement of Zhejiang Province, Hangzhou 310007, China*

^c*Nanyang Technological University, Nanyang Avenue 639798, Singapore*

Abstract. At present, the automation level in the power frequency magnetic field immunity test is relatively low. The placement and rotation of the tested equipment are manually done, which has health implications on lab technicians caused by long-term exposure to magnetic fields. This paper uses finite element simulation software to study the spatial distribution of the power frequency magnetic field. We started by building a simulation model of the power frequency magnetic field, then set up the air region, copper coil material, and magnetic field parameters. As a result of the simulation, we obtained the magnetic flux density model and the magnetic field arrow diagram. We then deduced the safe operation distance of test by referencing GB 8702-2014 and the simulation result. The simulation model's and algorithm's effectiveness are then verified by real-world measurement results of the spatial distribution of power frequency magnetic field.

Keywords. Power frequency magnetic field immunity test, spatial distribution, finite element simulation, safe operation distance

1. Introduction

An electric field and a magnetic field constitute an electromagnetic field together. Due to different features of a magnetic field and an electric field, they cause different biological health issues. According to prior researches, a magnetic field is far more harmful to the health of a living being than an electric field. A power frequency magnetic field is generated by the power-frequency currents in a conductor. The waveform of a test magnetic field is a power-frequency sine wave. The test magnetic field is imposed on the subject equipment by the immersion method.

During the power frequency magnetic field immunity test, the test equipment and the magnetic field coil are placed and rotated manually. Specific test equipment requires high strength of magnetic field and long staying period, e.g. electricity meter. According to OIML R46-1/-2:2012 [1], measure the error changes in the two load current conditions of $10I_{tr}$ and I_{max} upon a power factor of 1.0 and a continued magnetic field of 0.5mT; impose the magnetic field in 3 mutually-vertical directions of the meter upon a continued

¹ Corresponding author, Ming Li, Zhejiang Institute of Metrology, Hangzhou 310007, China; E-mail: liming_ah@163.com

Market Supervision Administration of Zhejiang Province scientific research project: Development of Intelligent Fixture System for Power Frequency Magnetic Field Test (20200303)

magnetic field of 0.5mT and a test period of 3s without load currents. The continued magnetic field is 1.25mT with 20x theoretical starting time. Therefore, the test period of a single electricity meter may be 1h or so. The impacts on the physical health of the test personnel can't be ignored due to long-term short-distance direct contact with the magnetic field. In the current standards, however, there is no specific requirement on the distance between the test personnel and the test equipment. Therefore, it is particularly important to research on the spatial distribution of the magnetic field during an immunity test of power frequency magnetic field and analyze and infer the safe operation distance of a test.

2. Status-Quo of Research at Home and Abroad

2.1. Status-Quo of Research

There are primarily two methods for the research on spatial distribution in a power-frequency magnetic field test. First, directly place the magnetic field probe on a test bed for measurement. If it is disabled due to difficulty in field measurement, an equivalent model will be established for the measurement. Second, perform modeling and simulation of the research subject, conclude on the necessity for research and finally make a comparison with the real experiment data to justify modeling.

Yu Hongwen, et al researched on the phase shift in the same frequency under a power-frequency magnetic field and proposed on immunity devices [2] in response to the latest standards on electricity meter. Due to complexity and diversity of the test subjects, there are limited researches on the power frequency magnetic field test of an electronic and electric product. The available researches on the power frequency magnetic field test of an electronic and electric product are primarily concentrated on the test equipment, the calibration method and the biological effects of power-frequency magnetic field. For instance, Zhao Shizhen et al researched on the design of coil upon electromagnetic compatibility, including the features and structure of a coil, as a reference for further research on power-frequency magnetic field tests [3]. Huang Wenguang et al used existing power-frequency magnetic field equipment to research on the basic principles, magnetic induction calculation and prior cases [4]. Han Bao et al analyzed the impacts of converter and coil in power-frequency magnetic field test equipment on the test results [5].

2.2. Research Work in the Thesis

Simulation software COMSOL Multiphysics is adopted to establish the spatial distribution model of magnetic field. The GSH250A power-frequency magnetic field test equipment of SIPAI from ZJIM is adopted as the reference. Simulation software is used for modeling and simulation of the spatial distribution of power-frequency magnetic field test. The equipment coil has an inner diameter of 150cm, an outer diameter of 164cm and a width of 7cm. the inner diameters of two parallel coils are 70cm from each other and their outer diameters are 84cm away from each other. The equipment is 200cm high. As the spatial distribution plan, the center of coil is taken as the origin and five planes are chosen at an interval of 0.4m (as Figure 1 shows). Twenty points at an interval of 0.375m are chosen on each plane (as Figure 1 shows) and a total of 100 points are chosen to establish the spatial distribution model. The magnetic field strength data of a spatial

position are obtained through simulation. Then a teslameter is used for practical measurement of the magnetic field data at 100 spatial points in the same position to verify the correctness of the simulated data. Finally, the safe operating distance during a power-frequency magnetic field test is concluded according to the electromagnetic environment control limits of the latest GB 8702-2014 [6].

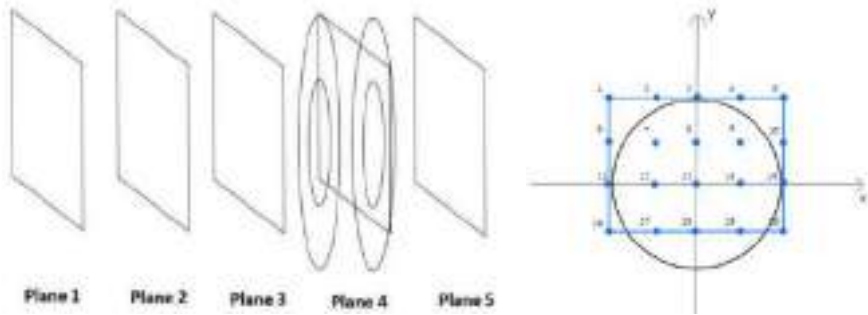


figure 1. Schematic diagram of spatial distribution test plan and measuring points within plane.

3. Simulation of Spatial Distribution in a Power-Frequency Magnetic Field Test

COMSOL Multiphysics is simulation software of physical fields based on finite element mathematical method. It includes using partial differential methods to research on and simulate physical fields.

The spatial distribution simulation of the power-frequency magnetic field test has Maxwell equation as the core; first, a 3D spatial module is established; choose electromagnetic field module in field volume and add it; choose the frequency domain via the solver and then analyze it. The steps are as follows:

- Establish the required geometric structure which basically comprises the external cubic structure and two parallel circular coils. First, obtain the basic coil structure through the establishment of a plane geometric circle and then set the parameters and tensile changes and z-ordinate parameters to obtain two parallel circles. Then produce the external cubic structure and make it transparent (as Figure 2 shows).
- Perform material operations, produce the air domain and the copper coil material and set their parameters.
- Set the structural magnetic field, choose even multi-coil wires, set AC input and define the AC input face. The figure shows the AC input face wherein physic field control network is adopted for the grid and the size of cell is set (as Figure 3 shows).
- The magnetic flux density mode and magnetic field arrow chart are acquired through calculation (as Figure 4 shows).

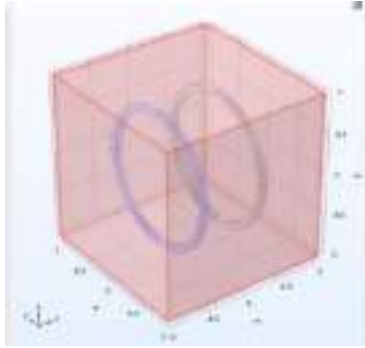


Figure 2. Establish the Structure Diagram.

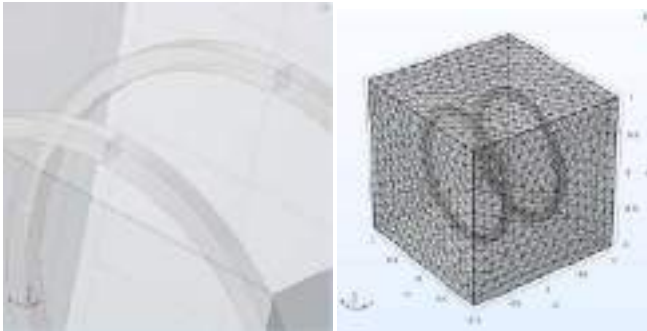


Figure 3. AC Input Face Diagram (left) Grid Section Diagram (right).

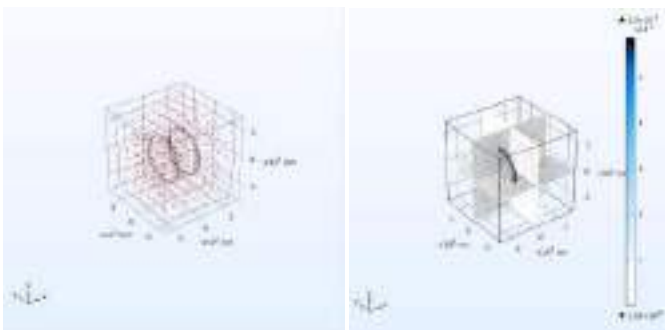


Figure 4. Magnetic field arrow chart (left) and magnetic flux density mode diagram (right).

3.1. Simulation Results

Use COMSOL Multiphysics to calculate and obtain the image of the magnetic flux density mode of the simulation results, as the figure shows. The lines in Figure 5 indicate magnetic induction lines. Darker color indicates greater strength of magnetic induction. The circle in the diagram is the Helmholtz coil. The magnetic induction lines excited by the coil demonstrate a plurality of closed curves on three planes. The density of magnetic induction lines indicates the strength of the magnetic field. The figure shows that the magnetic induction lines around the Helmholtz coil are dense while those farther away from the Helmholtz coil have a lower density.

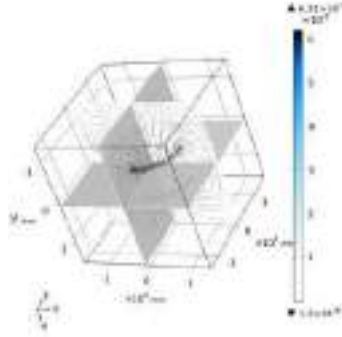


Figure 5. Image of Magnetic Flux Density Mode of Simulation Results.

The accuracy of the model can be verified according to the convergence diagram. As Figure 6 shows, convergence is concluded if the error is $0.0001 < 0.01$ upon the third iteration. Therefore, the simulation model satisfies the requirement.

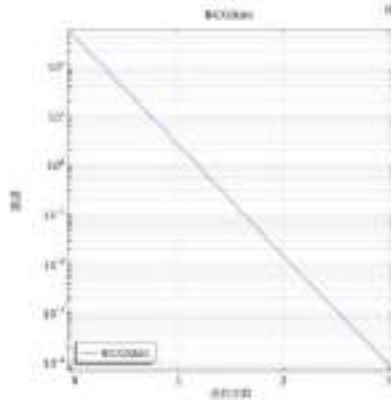


Figure 6. Convergence Diagram of Simulation Model.

Perform parametric scanning of the fixed points. Change the scanning step width successively to obtain the data of simulated magnetic flux density mode at a total of 100 points on 5 planes.

Point	1 Floor1 (mT)	Floor3 (mT)	Floor4 (mT)	Floor5 (mT)	
1	0.055	0.015	0.044	0.029	0.021
2	0.120	0.002	0.128	0.066	0.01
3	0.053	0.005	0.171	0.071	0.028
4	0.04	0.079	0.111	0.009	0.01
5	0.059	0.006	0.049	0.036	0.021
6	0.205	0.032	0.228	0.007	0.037
7	0.117	0.131	0.142	0.003	0.042
8	0.120	0.139	0.125	0.005	0.040
9	0.142	0.125	0.146	0.001	0.049
10	0.23	0.052	0.238	0.055	0.036
11	0.264	0.065	0.290	0.072	0.038
12	0.108	0.129	0.131	0.003	0.044
13	0.131	0.131	0.125	0.003	0.047
14	0.133	0.128	0.135	0.00	0.041
15	0.414	0.059	0.425	0.061	0.033
16	0.209	0.042	0.207	0.035	0.04
17	0.141	0.152	0.155	0.002	0.051
18	0.14	0.118	0.140	0.003	0.021
19	0.17	0.116	0.143	0.005	0.031
20	0.285	0.039	0.286	0.055	0.038

4. Measurement of Spatial Distribution of Power-Frequency Magnetic Field

The power-frequency magnetic field test device used for the measurement comprise external equipment and induction coils. External equipment supplies the required AC currents and the Helmholtz coil generates the magnetic fields and thus form the complete test equipment (as Figure 7 shows). AC currents in 50Hz and 1.1A are used for the test primarily to generate the magnetic induction strength of 0.125mT in line with the simulation software.



Figure 7. Power-frequency Magnetic Field Experimental Equipment(left) and Teslometer and Standard Probe(right).

In order to verify the correctness of the simulated model of spatial distribution of power-frequency magnetic field test, a teslameter is adopted to measure the magnetic field data at 100 points on 5 planes; and the simulation data are analyzed through comparison. The real-time magnetic field data are read by the 8053 electromagnetic radiation teslameter of Narda; EHP-50C standard magnetic field probe is adopted (as Figure 7 shows) which is connected to the teslameter via an optical fiber. The measurements of the teslameter are magnetic induction strength data in mT.

The measurement is performed in a lab of 20°C. For the purpose of this measurement, the spaces around the test equipment are divided into 5 planes (as Figure 1 shows) at an interval of 0.4m. Choose 4 points along one column on the same plane and a total of 5 columns and 20 points are defined, with an interval of 0.375m between two points. As such, a regular rectangle (as Figure 1 shows) is constituted. Totally 100 points are measured on 5 planes, thus constituting a regular cube.

Real measurements at 100 points on 5 planes

	Plane1 (mT)	Plane2 (mT)	Plane3 (mT)	Plane4 (mT)	Plane5 (mT)
1	0.049	0.036	0.05	0.032	0.018
2	0.32	0.071	0.318	0.058	0.025
3	0.01	0.092	0.544	0.082	0.027
4	0.335	0.071	0.334	0.06	0.025
5	0.052	0.008	0.052	0.033	0.018
6	0.25	0.042	0.249	0.053	0.024
7	0.131	0.12	0.133	0.078	0.013
8	0.125	0.124	0.126	0.075	0.006
9	0.14	0.123	0.136	0.077	0.015
10	0.228	0.04	0.229	0.055	0.025
11	0.24	0.059	0.24	0.06	0.026
12	0.12	0.123	0.119	0.077	0.006
13	0.113	0.12	0.114	0.074	0.018
14	0.12	0.122	0.121	0.076	0.017
15	0.416	0.153	0.417	0.081	0.026
16	0.191	0.132	0.191	0.081	0.022
17	0.145	0.141	0.144	0.073	0.01
18	0.131	0.003	0.133	0.073	0.004
19	0.151	0.008	0.152	0.072	0.002
20	0.195	0.153	0.195	0.046	0.023

5. Analysis of Errors and Results of Simulated and Measured Data

Produce a thermodynamic chart of the simulated and measured data. The horizontal ordinate is the serial number of planes and the longitudinal ordinate is the serial number of measuring points.

According to Figure 8 thermodynamic chart of simulation results: Point 15 of Plane 1 and Plane 3 is highly different from other points around in color primarily because Plane 1 and Plane 3 are the two planes closest to the Helmholtz coil and have similar data and thus are symmetric to each other. Compared with other points, Point 15 is closer to the coil and therefore has sharp color changes. As the figure shows, it gets brighter from Plane 2 to Plane 3, indicating data increase; it gets darker from Plane 3 to Plane 5, indicating data decrease. It means that the magnetic induction strength is lower when it is farther away from the Helmholtz coil. Thermodynamic chart of the measurements also has the same rule, which proves that the simulated spatial distribution rule of the magnetic field conforms to the de-facto measurement.

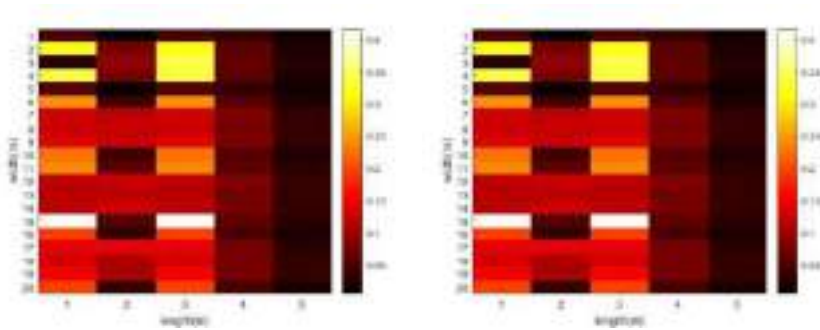


Figure 8. Thermodynamic Chart of Simulation Results(left)and measurements(right).

Take simulation and measurement methods as the independent variable and the obtained magnetic field data are the dependent variable for independent sample *t* test, Levene variance and other homogeneity test of the data of 200 points. If the Levene variance significance $P > 0.05$, the two groups of data may be deemed to have the same variance, indicating that the two methods are not significantly different; calculation shows that the *P* value of the two groups of data is 0.879 (see Table 1) and therefore the variances of the two independent samples can be taken to be homogeneous. Therefore, when variance homogeneity is satisfied and it is assumed the significance is higher than 0.05 in equal variance, mean value and other homogeneity *t* tests, it can be concluded that the two groups of data are not significantly different from each other in variance. As the significance is 0.473 which is higher than 0.05 based on the simulated and the measured data, it is thus believed that the two groups of data are not different from each other with a significance level of 0.05. It shows that the simulation model and the simulation algorithm are effective.

Table 1. Levene Variance Homogeneity Test and Mean Value Homogeneity *t*- test.

	F	Significance	2-tailed significance	Average value difference
Assume equal variance	0.017	0.879	0.473	-0.0093
Unassume equal variance	/	/	0.473	-0.0093

6. Analysis of the Safe Operating Distance

GB 8702-2014^[6] electromagnetic environment control limits specify the range of public exposure to an electromagnetic environment and the environment for the use of this standard. 50Hz AC current is adopted for the test and therefore the limit is 0.025kHz~1.2kHz. See formulae (1) for the formula to calculate the magnetic induction strength, which shall be lower than 0.1mT. A comparison of the simulation result and the de-facto measurement shows that the magnetic field of Plane 5 (0.8m from the Helmholtz coil) is basically lower than 0.1mT. Therefore, under the test of 0.125mT, it is safer to perform the test with a vertical distance of higher than 0.8m from the Helmholtz coil in order to ensure the health and safety of the test personnel.

$$B = 5 / f = 5000 / 50 = 100 \mu T = 0.1 mT \quad (1)$$

7. Conclusion

Software simulation is adopted in this paper, the spatial distribution of power frequency magnetic test is simulated with COMSOL Multiphysics software. Then, the validity of the simulation model and algorithm is verified by field measurement of power frequency magnetic field test spatial distribution data with a Tesla meter. Finally, according to the standard, the safe operating distance for tester is analyzed and deduced. In various laboratories, for different manufacturers, different sizes of power frequency magnetic field test equipment, and different levels of magnetic flux density it provides a method and idea to study the spatial distribution of magnetic field and analyze the safe operation distance of test personnel.

List of nomenclatures.

Terms	Definitions
GB	Chinese national standard
immersion method	Placed in the center of an inductive coil
$10I_{tr}, I_{max}$	Input value of load current tested by electric energy meter
ZJIM	Zhejiang Institute of Metrology
Helmholtz coil	In loop flows a current, generating a magnetic field of defined constancy in its plane and in the enclosed volume
Thermodynamic Chart	It is a statistical chart that displays data by shading color blocks
Levene Variance Homogeneity Test	In statistics, it is called homogeneity (equality) test of variance
Mean Value Homogeneity t- test	Compare whether there is difference in the overall mean of two different samples

References

- [1] International organization of legal metrology. international recommendation. OIML R 46-1/-2Edition 2012(E) Active electrical energy meters-Part 1: Metrological and technical requirements, Part 2: Metrological controls and performance tests [s]: International.

- [2] Yu HW, Zhao DY, Ke J. Research and development of standard device for the power frequency magnetic immunity with same frequency and phase shift of the smart meter. *Metrology & Measurement Technique*. 2018; 45(01):5-7+10.
- [3] Zhao SZ, Wu ZW, Ma X. Design and verification of Helmholtz coil in EMC test. *Shanghai Measurement and Testing*. 2012; 39(03):7-11.
- [4] Huang WG. Analysis of power frequency magnetic field measurement system and design of induction coil. *Medical Equipment*. 2010; 23(11):13-15.
- [5] Han B, Liu WG, Zhang H. Research on calibration of power frequency magnetic field immunity test device. *Electronic Measurement Technology*. 2013; 36(08):108-110.
- [6] State Administration for Market Regulation of the People's Republic of China, Standardization Administration of China. GB 8702—2014 Electromagnetic Environment Control Limits[s] Beijing: Standardization Administration of China,2014

Design and Application of Fully Hydraulic Intelligent Screw Clearing Machine for Grain Silos

Jianping LUO and Zhiping JIA¹

China Waterborne Transport Research Institute, Beijing, China

Abstract. In order to fundamentally solve the hidden danger of dust explosion in grain silos, a new fully hydraulic intelligent screw clearing machine for grain silos was studied. The rotation of the spiral shaft and the movement of the whole machine were controlled by the hydraulic system, which realized that there was no electrical component in the internal actuator and the safety was higher. This paper introduces the structure and composition of the fully hydraulic intelligent screw clearing machine for grain silos and studies its key technologies. Based on the above achievements, the first domestic fully hydraulic intelligent screw clearing machine for grain silos is developed and applied to the grain silos of Xiamen Port Hailong Wharf. The application further compares and analyzes the main performance parameters of the fully hydraulic intelligent screw clearing machine and the electric screw clearing machine for grain silos. The research shows that the fully hydraulic intelligent screw clearing machine for grain silos can effectively reduce the operation of personnel entering the warehouse and realize safer, intelligent and efficient clearing operations.

Keywords. Grain silos, hydraulic driven, screw clearing machine, dust explosion proof

1. Overview

Grain silos are the main types of grain storage silos for various grain reserves and grain-oil terminals in China. In the process of clearing and conveying the grain in the grain silo, a large amount of grain-associated dust will be generated. These dusts will continue to spread during the production process, which can easily cause dust explosions and cause great harm to the lives of personal and collective and property loss. Dust explosion has become a major threat to the grain processing and storage enterprises.

The screw clearing machine is one of the main clearing equipment for grain silos. At present, most of the screw clearing machines used for grain silos in China and abroad are mostly electric or pneumatic drives [1, 2]. The pneumatic-driven screw clearing machines has complex structure and high failure rate, and when used in humid and dusty environments, blockage of cylinders and various valves, water ingress and corrosion are often seen. Its market share is gradually decreasing. In addition, according to the explosion-proof zoning regulations of the national standard

¹ Corresponding author, Zhiping Jia, China Waterborne Transport Research Institute, Beijing, China; E-mail: jiazp@wti.ac.cn.

GB17440-2008 "dust explosion-proof safety regulations for grain processing, storage and transportation systems" [3], the interior of the silo is zone 20 explosion-proof level, and electrical equipment is not allowed to operate in such places. However, there is no motor with explosion-proof certification of zone 20. Therefore, the electric-driven clearing machine in the grain silo is contrary to the requirements of the national mandatory standards, and there are certain safety hazards. In recent years, explosion accidents have also occurred due to electric-driven clearing machine.

Some research on hydraulic drive clearing machines have been done. Huang Sulong of China University of Mining and Technology [4] researched and designed a multi-arm telescopic coal warehouse clearing robot system. The drive system is connected with the actuator of the clearing robot, and drives the actuator to work to realize the robot clearing operation. Zhong Lingling of Shandong Luban Machinery Technology Co., Ltd. disclosed a patent for a hydraulic system of a warehouse clearing machine and a cylinder hydraulic transmission conveyor [5]. The machine provides power, which can realize the smooth operation of the excavator and improve the efficiency of coal slime excavation or dredging. Fan Yang and Jiang Sihan of Wuxi Nuoliyanke Hydraulic System Co., Ltd. disclosed a patent for a screw conveying device and a clearing machine [6]. The screw conveying device in the patent includes a conveying shaft and a rotary power device that drives the conveying shaft to rotate. The power device is an electric cylinder, and a hydraulic cylinder is also set on the screw conveyor as a power booster, so that the screw conveyor can be driven by a power booster in addition to being driven by a rotary power device. When driving the conveying shaft, additional power is provided by the power assist device to ensure the continuous rotation of the conveying shaft, thereby ensuring the stability of material conveying. To sum up, at present, the research on the hydraulically driven warehouse clearing machine mainly focuses on providing power for local devices or mainly for use in coal bunker.

Therefore, in view of the above background, this paper proposes for the first time a fully hydraulic driven screw clearing machine for grain silos, which has better safety performance, stronger driving ability, and more intelligent control, can better ensure grain processing and storage and finally improve the capacity of grain storage and transportation system.

2. Design and Application of the Fully Hydraulic Driven Screw Clearing Machine

2.1. Structure Design

The fully hydraulic driven screw cleaning machine is mainly composed of body, hydraulic system and electric control system. The body mainly includes centering and rotating device, head transmission device, revolution drive device, structural support device, screw conveying device and revolution track. Among them, the centering and rotating device is installed on the center discharge port of the flat-bottomed silo, and the center of the silo is used as the rotary centering. The hydraulic system includes pump station motor, hydraulic pump [7], electro-hydraulic proportional multi-way valve, pressure sensor, screw drive motor, revolution drive motor, hydraulic filter, radiator, etc.

The screw drive motor is installed on the head transmission device and is used to drive the screw shaft in the screw conveying device to rotate, so as to achieve the

purpose of conveying and clearing materials. The revolution drive motor is installed on the revolution drive device, and is used to drive the whole machine to rotate and walk along the revolution track with the rotary centering as the center.

In the scheme, a sprocket is installed on the revolution drive device. Under the circular running track of the sprocket, a revolution track is installed, and the track is fixed and installed in the silo through embedded bolts. Each track has evenly distributed arc-shaped toothed sprocket holes of a specific size, and the whole machine can be propelled on the revolving track through the meshing between the sprocket and the sprocket holes. The revolution drive device and revolution track meshing technology ensure the compulsion, no slippage, no climbing, high reliability, and no need for manual warehousing auxiliary operations.

The screw conveying device of this scheme is mainly composed of screw shaft, screw blades, material trough, etc. Among them, the screw shaft adopts a multi-section + universal joint connection, which solves the problems of huge span, poor rigidity, and easy deformation of the screw shaft, and can realize multi-degree-of-freedom rotation adjustment and coaxiality self-adaptation. In addition, in order to reduce the stress concentration caused by the discontinuity of the structure, spherical bearings are arranged in the middle and tail sections of the screw shaft, and the two ends are connected to the screw shaft through flanges. There are keys between the flanges, which can effectively transmit the torque of the screw shaft.

The structural support device is installed on the trough of the screw conveying device, which has the effect of strengthening the longitudinal strength and rigidity of the cleaning machine. In addition, the structural support device is also provided with an up and down adjustment function to facilitate the adjustment of the gap between the screw conveying device and the local ground.

The hydraulic pump is directly driven by the pump station motor to generate high-pressure oil, which is adjusted by the electro-hydraulic proportional multi-way valve to control the direction and speed of the screw drive motor and the revolution drive motor. The hydraulic system is equipped with a large flow filter and a radiator in the oil return circuit to ensure the cleanliness and temperature of the hydraulic oil and prevent the hydraulic oil from deteriorating.

The hydraulic pump station and the electronic control system are arranged outside the belt conveyor corridor, and the screw drive motor and the revolution drive motor are driven to work by controlling the hydraulic system connected to them. The structure of the whole machine is shown in Figure 1, and the composition of the hydraulic and electronic control system is shown in Figure 2.

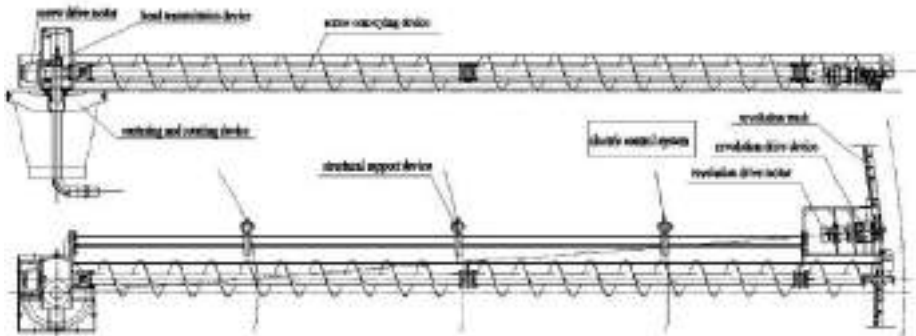


Figure 1. The structure of the fully hydraulically driven intelligent screw clearing machine.



Figure 2. Composition of hydraulic and electronic control system.

2.2. Working Process Introduction

When starting, the electronic control system controls the screw drive motor and the revolution drive motor to work. The screw drive motor transmits the torque to the screw shaft to rotate, and the screw blade cuts into the grain pile. Depending on the cutting action of the screw blade and the self-flow property of the grain itself, the grain continuously enters the material trough of the screw conveyor, following the principle of screw conveying. The grain will be sent into the central grain unloading port, so as to achieve the purpose of conveying materials. When there is no grain in front of the screw blade, the whole machine will take the rotation centering as the center under the push of the revolution drive device, rotate along the revolution track, and continue to clear the grain. The remaining grain will be cleared when whole machine complete one rotation.

2.3. Key Technologies of Fully Hydraulic Driven Screw Clearing Machine

(1) Fully Hydraulic Drive

The screw cleaning machine proposed in this paper adopts the full hydraulic drive. Since the driving shafts of the screw conveying device and the revolving propulsion device have low rotational speeds and complex driving loads, the motor will be directly driven by low-speed and high-torque hydraulic motor, which can provide the drive shaft low speed and high torque. In addition, the low-speed scheme is also easy to control and adjust, with flexible layout and less space. The hydraulic motor is directly installed on the drive shaft, eliminating various transmission links between the hydraulic motor and the drive shaft, avoiding additional power loss between them and reducing mechanical noise. At the same time, the moment of inertia of the drive shaft is reduced, which is conducive to improving the adjustment quality of the system and reducing the impact of the impact load on the screw structure and the traveling structure during the clearing operation.

(2) Load-Sensing, Constant-Power Control and Load Adaptive Control Technology

The load-sensing and constant-power control technology is adopted. With the same output power, the torque output characteristics of the clearing machine are improved, the energy consumption of the hydraulic system is reduced, and the efficient operation of the motor of the pump station is ensured. The hydraulic system provides flow according to the screw speed requirement, reducing energy consumption. At the same time, when the grain is hardened, the hydraulic system will automatically increase the working pressure, increase the screw driving torque, and reduce the flow output to ensure that the motor of the pump station always works in the high-efficiency area, and the system is more energy-saving.

In addition, this equipment also adopts the load adaptive control technology. The control system can automatically adjust the screw and revolution driving speed according to the load condition of the screw, which realizes the automatic execution of the clearing operation without the intervention of the staff. When the material flow is good, it can be switched to the "automatic" mode of operation. The automatic control system automatically adjusts the revolution action according to the load condition of the screw drive: when the material is quite limited, the revolution advances, the screw speed decreases, and the screw filling rate is increased; when the load increases, the automatic control system identifies that the material filling rate is high, and the revolution stops. The screw operates at maximum speed, enabling automatic clearing operations without the necessity of human intervention.

(3) Intelligent remote monitoring technology

At the same time, this clearing machine adopts newly developed intelligent remote monitoring system. For the first time, it realizes the full remote working mode of the whole life cycle remote debugging, remote maintenance, remote monitoring and remote control of the grain silo clearing machine. At the stage of machine installation, debugging and trial operation, system programmers do not need to visit the site in person, they can conduct system program modification, program uploading and downloading, and joint debugging of programs and equipment through the online cloud platform. Controlling various remote methods such as PC terminal, mobile APP terminal, online cloud platform terminal, etc., workers can obtain information such as equipment running time, main failure frequency, spare parts maintenance cycle, specific maintenance reminders, etc., and realize 24h all-weather monitoring of clearing machine real-time operating status and fault alarms, query historical data, accurately locate fault information, and reasonably arrange maintenance work according to the actual situation on site. The mentioned remote terminals can also be used to start, stop, reset, speed regulation, manual automatic switching on the clearing machine, realizing the "zero entry" of the staff, and ensuring the work safety and personnel health under the complex operation environment of grain silos. What's more, the operation and maintenance costs will be reduced and operation efficiency will be comprehensively improved.

2.4. Development and Application of the First Fully Hydraulically Driven Intelligent Screw Clearing Machine in China

Based on the above research results, the first fully hydraulic driven screw clearing machine in China was developed (as shown in Figure 3), and it has been applied to the grain silo of Xiamen Port Hailong Terminal Co., Ltd. Based on the dimension and capacity of the silo, combined with the severity of grain hardening, the clearing machine equips with 45KW pump station motor, hydraulic motors that can meet the

maximum driving torque of 6900Nm, and other supporting hydraulic components and joints.

The hydraulic components and hydraulic joints of the clearing machine are all made of the world's top hydraulic products to avoid the phenomenon of "running, bubbling, dripping and leaking" to the greatest extent. Meanwhile, food-grade hydraulic oil certified by the US authority has been adopted to avoid contamination of the grain in the silo. At present, the equipment operation status and clearing operation effect are good, which can meet the actual needs of users, and can realize safe, intelligent, efficient and reliable clearing operations, which has been strongly recognized by users. The main technical parameters of the equipment are shown in Table 1.

Table 1. Main technical parameters of the fully hydraulic driven intelligent screw clearing machine.

Item	Technical parameter
Conveying material	Soybeans, Wheat, Corn
Clearing Capacity	300t/h
Screw Diameter	500mm
Clearing duration	5-6h
Maximum pitch	500mm
Screw Length	11.55m
Maximum driving torque	6900Nm



(1) Clearing Operation



(2) Hydraulic Pump Station

Figure 3. Fully hydraulic driven intelligent screw clearing machine.

3. Comparative Analysis of Performance of Full Hydraulic Driven and Mainstream Electric Driven Screw Clearing Machine

3.1. Comparative Analysis of Output Characteristics

Figure 4 and Figure 5 are the output characteristic curve of the motor and the output characteristic curve of the hydraulic system, respectively. Comparing and analyzing the curves, when the working frequency is below 50Hz, the motor is in a constant torque control state. No matter how the speed is adjusted, the output torque of the motor is always constant. Only when the frequency is higher than the rated frequency, the constant power control is adopted, while the torque is reduced. For the hydraulic

system, constant power electro-hydraulic control can be performed within the allowable range of working pressure. For example, when the grain is hardened, that is, when the resistance torque increases, the output speed can be automatically reduced, thereby increasing the output torque and enhancing the driving ability. And in this working process, the motor of the pump station always works at the highest efficiency point with the lowest energy consumption.

As a summary, under the same output power, the hydraulic system can improve the torque output characteristics of the clearing machine, reduce the energy consumption of the hydraulic system, ensure the efficient operation of the pump station motor, and be more conducive to the efficient cleaning operation of the clearing machine under complex working conditions.

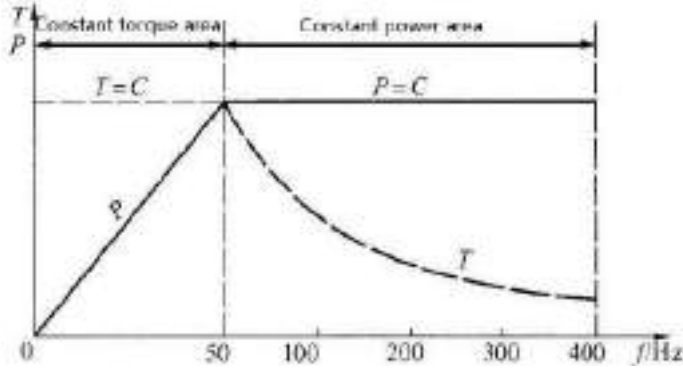


Figure 4. Motor output characteristic curve.

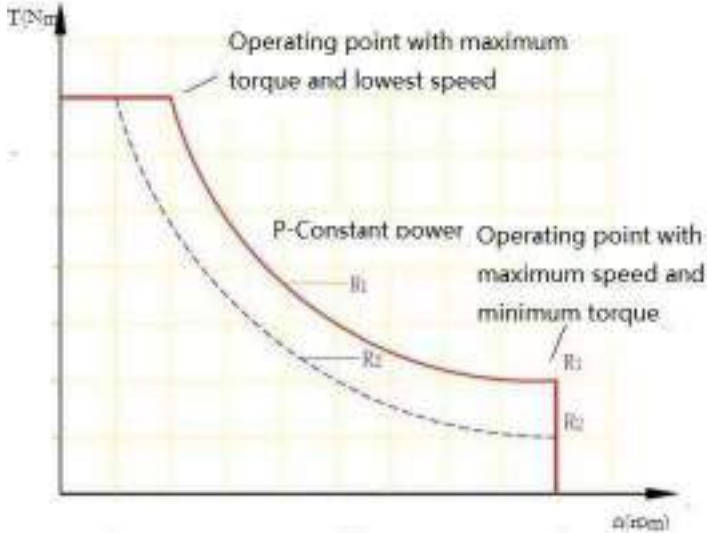


Figure 5. Output characteristic curve of hydraulic system.

3.2. Comparative Analysis of Main Technical Parameters

A comparative analysis of other technical parameters of the fully hydraulic driven screw clearing machine and the mainstream electric screw clearing machine is shown in Table 2.

Table 2. Performance comparison table of different driving modes of screw cleaning machine.

	Fully Hydraulic Driven	Electric Motor Driven
Torque under same power	Larger	Smaller
Crack breaking capacity	Unmanned clearing can be realized in light and moderate compaction conditions; in severe compaction, the rotating speed of the equipment is automatically reduced, the screw driving force is increased, and the compaction-breaking ability is enhanced.	Realize the clearing operation under separation of personnel and machine in the case of mild and moderate hardening
Transmission efficiency	Hydraulic motor direct driven, high transmission efficiency	Electric motor + gearbox drive system, loss of transmission efficiency, overall mechanical transmission efficiency is reduced
Structural form	Compact structure, flexible layout, light weight, small installation space, easy installation	Complex structure, large volume, large space occupation
Explosion-proof safety	No electrical components in the silo, the safety is high	low, potential safety hazards
Cleanliness and environmental protection	Easy to cause oil leakage, food-grade hydraulic oil must be used to avoid leakage and contamination of food.	Clean and pollution-free
Operation efficiency	Effectively improve operation efficiency and shorten the clearing time	The clearing efficiency is quite limited.
Operation and maintenance costs	Reduce the operation and maintenance of equipment such as motor reducers, which can effectively reduce maintenance costs	High operation and maintenance costs of motors and reducers

Through the above comparative analysis, the fully hydraulic intelligent screw clearing machine has the significant advantages of large torque, strong breaking capacity and high safety. However, in order to prevent problems such as "running, bubbling, dripping and leaking" in the hydraulic system, it is necessary to optimize the processing technology and solve the hydraulic sealing problem through proper selection of materials. PARKER, Rexroth and STAUFF as the world well-known brands are suggested. Their high-quality sealing materials and sealing technologies can ensure the reliability of product sealing. In addition, food-grade hydraulic oil certified by the American authority shall be used to ensure no pollution to Grain.

4. Conclusion

The research results of this paper fill the technical gap in this field in China, realize that the actuator inside the silo has no electrical components, solve the problem of dust electrical explosion-proof, and can effectively avoid serious casualties and property losses caused by dust explosion; It can reduce the number of people entering the silos, effectively reduce the long-term operation cost and labor cost, and improve the occupational hygiene level of the enterprise; at the same time, it realizes a safe, green, intelligent, efficient and reliable silo clearance operation, which can significantly improve the residual grain clearing efficiency of the grain silos, guaranteeing the normal operation of the grain processing and storage and transportation system, and further improve the turnover efficiency and storage and transportation capacity of the grain storage and transportation system. At the same time, the research results have a positive role in promoting the level of occupational hygiene in China's grain and port industries, and promoting the development of silo loading and unloading technology

and equipment industry. The research results of this paper have good social and economic benefits, and have broad prospects for market promotion.

References

- [1] Guo JT, Xin SJ, Sui S. Research and analysis of the clearance process equipment for the silo at home and abroad. *Modern Food*. 2016; (02):75-82.
- [2] Bai XF. New type of buried spiral clearance machine. *Grain Science and Technology and Economy*. 2006; (02):50-51.
- [3] General Administration of Quality Supervision, Inspection and Quarantine of the People's Republic of China, China National Standardization Management Committee. GB17440-2008. Safety regulation for dust explosion protection of grain processing, storage and transportation system. [S]. Beijing: China Standards Publishing House, 2009.
- [4] Huang SL. Design and research of multi-arm telescopic coal bunker clearance robot system [D]. China University of Mining and Technology. 2021.
- [5] Zhong LM, Song F, Song TF. Clearing machine hydraulic system, cylindrical hydraulic transmission conveyor [P]. China: CN 113148569A, 2021-07-23.
- [6] Fan Y, Jiang SH. Screw conveying device and clearing machine [P]. China: CN109703993A, 2019-05-03.
- [7] Jani DB, Mistry Y, Suthar M, Suthar A, Shah J, Patel P. An overview on cavitation in centrifugal pump. *International Journal of Innovative Research in Technology*. 2019; 6(5): 66-70.

Integrated Management System of Expressway Intelligent Service Area

Jianxian DUAN^a, Yanyan LI^{b,1}, Qingqing YU^c, Anqi LI^c and Yongjun SHAO^b

^a*Shaanxi Transportation Holding Services Management Group Co., Ltd, Xi'an 71075, China*

^b*Shaanxi Expressway Testing & Measuring Co., Ltd, Xi'an 71086, China*

^c*Shaanxi GSXZ Technology Co., Ltd, Xi'an 71086, China*

Abstract. Different from traditional service areas, intelligent service areas can better adapt to the construction of expressway networks and meet the high-level needs of the current society for service areas. Based on big data analysis and machine vision technology, a new intelligent service area management system for the expressway has built in this paper, which covers staff management, intelligent washroom, vehicle flow and passenger flow analysis and statistics, intelligent parking guidance, and senseless refueling payment, and other functions, which can promote the synchronous improvement of service area supervision and management and service quality.

Keywords. Expressway, service area, intelligent transportation, planning and design

1. Introduction

Due to the fully closed operation nature of expressway, the driver and passenger on the expressway are cut off from contact with the outside world [1-3], therefore the expressway service area as an important part and subsidiary facility of the expressway, assumes the important role of providing services for the passengers driving on the expressway and the expressway management personnel. With the construction of national and local expressway networks [4,5], the number of service areas is fast increasing, however, the traditional management of service areas is difficult to meet the current social needs, resulting in problems of congestion during peak periods or excessive staff in service areas during low peak periods.

According to the current social service needs, an integrated management system for smart service areas is proposed in this paper, which could be better improved the supervision ability and service level of service areas, facilitate standardized and intelligent management of staff, and enhanced the convenience for drivers and passengers.

¹ Corresponding author, Yanyan Li, Shaanxi Expressway Testing & Measuring Co., Ltd, Xi'an 71086, China; E-mail: 354634924@qq.com.

Supported by the Scientific research projects in 2021 of Shaanxi Provincial Transport Department (21 – 37X).

2. Service Area Intelligent Management Requirements

Service areas, whether as infrastructure or tourist destinations, need to take good management demand as the main reference factor to control the normal operation of a large number of people flow or traffic flow. Meanwhile, a better management can also improve the satisfaction of people who is driving on expressway with the service area, so the continuous improvement of information management, combined with resource conditions to seek the expansion of service area functions will further meet people's high-level demand for service areas.

2.1. Basic Information Management

The management of the service area is mainly to analyze the characteristics of staff and alarm to correct behavior problems, so as to achieve reasonable management and realize the intelligent operation of the service area.

Due to the particularity of the geographical location of each service area, resulting in the mobility of the service object will be different. Unlike foreign service areas, which are equipped with large shopping centers and other entertainment facilities, the domestic expressway service areas usually focus on convenience, so there are very few customers who go to the service areas to consume purely for the purpose of consumption, which determines the singleness and one-time service objects in the operation and management of service areas. At the same time, the passenger flow of the expressway changes with holidays and seasonal changes, showing an unstable development and periodic fluctuation trend, while the economic benefits of the service area mainly depend on the passenger flow of the expressway, and the economic expenditure mainly depends on the fixed wages of the employees. In general, if the passenger flow is large, the economic benefit of the service area is good, otherwise, the economic benefit is poor. The service content of each service area, such as business scope and service quality, is different, which also leads to the instability and volatility of service efficiency. Therefore, it is particularly important to record the basic information such as the name, address, time of use, management organization, contact person, merchant information and parking space information in detail, so as to support the function of adding, deleting, correcting and querying, so as to better manage each service area.

2.2. Staff Information Management

Reasonable management of the staff in the service area could be further improved the standardized operation of the intelligent service area. The basic information management function of the staff in the service area should include the personnel name, age, ID card, mobile phone number, face photo, work type, organization, and other information records. It should also support the addition, deletion, correction, and query of personnel information, as well as the import and deletion of batches.

In staff behavior regulation, for example, security guards, cleaning staff and restaurant health and restaurant service personnel outfit, behavior regulation and abnormal behavior, the traditional "man to man" regulatory system cannot real-time supervisory staff's behavior, leading to the behavior of the individual staff problems was not correct, it is difficult to meet the demand for service level.

The same problem also appears in the bathroom, the traditional regulatory system with fixed scheduling methods, cleaning personnel check-in, and cleaning washroom

sanitation. However, when there is more passenger flow, it occurs a shortage of staff, which leads to washroom sanitation being poorer. When there is less passenger flow, it results in the staff too much, which leads to a waste of resources. Therefore, rational intelligent management is needed to achieve the full scheduling and utilization of resources.



Figure 1. Technical solutions for the overall system.

3. The Focus of the Planning and Design of the Intelligent Service Area Based on the Hierarchy of Needs

Based on the above analysis of the demand for intelligent service area charging management and intelligent service, the intelligent upgrade of service area operation management, driver service, and commercial operation is realized in this paper through all-factor perception, big data analysis [6] and artificial intelligence [7] application, in order to improve the safety, efficiency and intelligence level of the service area. The overall system of technical solutions is shown in Fig. 1. In this paper, we focus on the part of expressway management, and the other part of overall system is introduced in our other paper.

3.1. Staff Behavior Analysis and Management

The staff of service area in the case of long-term work will inevitably appear personal behavior problems. It should be noticed that an appropriate amount of staff should be arranged to better serve when passenger flow group entering the expressway in the peak and low-peak periods of traffic flow in the service area.



Figure 2. Staff behavior trajectories.

Based on the application of visual intelligent analysis, the behavior supervision of staff such as security, cleaning, cooks, and restaurant service personnel will be strengthened. The system supports the dressing, behavior, behavior track supervision and abnormal behavior alarm functions of security personnel, restaurant sanitation and restaurant service personnel and cleaning personnel, as shown in Fig. 2. In terms of washroom operation management, the cloud platform is used to realize the statistics of the number of personnel in the cleaning area, real-time location displays, departure analysis, personnel information viewing and real-time alarm reminders.

3.2. Management of Intelligent Washroom

In management of washroom, the statistics of washroom passenger flow is realized based on infrared sensing, and the intelligent shift scheduling function for cleaning operations based on passenger flow data, as shown in Fig.3. It supports the face recognition check-in function of cleaning personnel, and supports the record and query of check-in information, including check-in date, check-in personnel, check-in time, etc. It can fully mobilize the enthusiasm of employees with the better solution in the integration of human resources, etc., which solves the drawbacks of our traditional management mode “man to man” and systems managing people.



Figure 3. Intelligent washroom technology solution.

Drivers and passengers can easily grasp the use of washroom and service quality in service areas along the route through third-party applications, which is convenient for reasonable planning of washroom time during the trip. On the guidance screen in the service area, a map is displayed to guide the user to easily find the nearest washroom. At the same time, it displays the quantity, distribution and occupancy of men's, women's, mother and baby rooms, third washrooms and disabled washrooms, environmental quality indicators, such as air temperature and humidity, air status, and green environmental protection status of overall sewage discharge standards, etc., for managers to grasp the internal situation of the washroom in real time and notify the staff to clean, clean, maintain, and supply consumables in time for the washroom. If users are dissatisfied with the washroom, they can scan the QR code in the washroom to raise opinions and complaints about the dirty and messy public washroom, and the responsible custodial service staff can be prompted in time and quickly corrected.

4. Conclusion

Expressway service area is a necessary result of the development and the supporting facility of expressway industry, it not only drives the expressway passenger vehicles and the highway law enforcement management personnel to provide service at the same time, but also increased the employment opportunities, and improves the area economic benefit and social effect, which is becoming the window of cities in the promotion. With the rapid development of computer technology, the service area that adopts intelligence operations could be further improved services, in order to provide quality services for all kinds of vehicles and passengers on expressways, which could be also reduced the peak unnecessarily crowded jam to ensure the safety of driving personnel, and increased the economic benefits of the expressway investment company. Based on big data analysis and machine vision technology, a new set of intelligent service area comprehensive service platform system has constructed in this paper, which could be further promoted

the supervision and management of expressway service area and improved the service quality.

References

- [1] Liu HQ, Wang L, Lou F, Guo DH and Peng L. Research on preparation and properties of multi-functional anti-corrosion coating used to inner wall of water pond in service area of express highway. 2011 International Conference on Remote Sensing, Environment and Transportation Engineering; 2011 June 24-26; Nanjing, IEEE Press; p. 1506-1509.
- [2] Jiao EL, Liu YJ, Gao CD and Wen Y. Experimental study on wastewater treatment of expressway service area in BAF. 2017 International Conference on Smart City and Systems Engineering (ICSCSE); 2017 November 11-12; Changsha, China, IEEE Press; p. 115-118.
- [3] Zhi P, Meng W, Wang JQ, Wu X, Zhou R and Zhou Q. Key technology and analysis of expressway intelligent service area. 2022 IEEE 25th International Conference on Computer Supported Cooperative Work in Design (CSCWD); 2022 May 04-06; Hangzhou, China, IEEE Press; p. 400-405.
- [4] Wei JG, Cao HT, Zheng JL and Chen ZY. Axle load and road conditions disease investigation and analysis of the expressway service area. 2010 International Conference on Intelligent Computation Technology and Automation; 2010 May 11-12; Changsha, China, IEEE Press; p. 846-849.
- [5] Guo QM, Liang H, Liao HW, Zhang LS and Ni D. Statistical analysis and research on energy consumption in highway service area. 2022 7th International Conference on Intelligent Computing and Signal Processing (ICSP); 2022 April 15-17; Xi'an, China, IEEE Press; p. 210-214.
- [6] Wang JQ, Zhang K, Zhi P, Xi GL, Tang XR and Zhou QG. Analysis and prediction transient population in expressway service area based long short-term memory. 2021 IEEE 23rd Int Conf on High Performance Computing & Communications; 7th Int Conf on Data Science & Systems; 19th Int Conf on Smart City; 7th Int Conf on Dependability in Sensor, Cloud & Big Data Systems & Application (HPCC/DSS/SmartCity/DependSys); 2021 December 20-22; Haikou, Hainan, China, IEEE Press; p. 1828-1832.
- [7] Shen X, Zhang F, Lv H, Liu J and Liu H. Prediction of entering percentage into expressway service areas based on wavelet neural networks and genetic algorithms. IEEE Access. 2019; 7:54562-54574.

Analysis of Expressway Intelligent Service Area for Better Vehicles/Passengers Service

Jianxian DUAN^a, Yanyan LI^b, Qingqing YU^{c,1}, Yongjun SHAO^b and Anqi LI^c

^a*Shaanxi Transportation Holding Services Management Group CO., LTD, Xi'an 71075, China*

^b*Shaanxi Expressway Testing & Measuring Co., Ltd, Xi'an 71086, China*

^c*Shaanxi GSXZ Technology Co., Ltd, Xi'an 71086, China*

Abstract. Expressway is known as a bridge for a country to modernize and is the only way to develop the modern transportation industry. Traditional expressway service area is difficult to meet the needs of current users, thus in order to improve the service level of the service area and meet the current high-level demand of the society for the service area, a set of highway intelligent service area integrated management system based on cloud computing and big data technology is proposed in this paper, which can fully and reasonably schedule resources, facilitate the use of user, and improve the user's experience of the service area.

Keywords. Expressway, service area, intelligent transportation, planning and design

1. Introduction

The expressway service area provides necessary travel services for passing drivers and passengers [1], which is one of the important infrastructure of expressways to ensure driving safety, smooth roads and relieves driver and passenger fatigue. With the rapid development of expressways, the functions of service areas have gradually improved, however, the construction and operation of expressway service areas in China are still in the stage of exploration and practice due to the short development process [2-4]. Meanwhile, there are still some problems in the construction and operation of individual service areas since the unbalanced regional development, the positioning and understanding of service areas in different regions and departments are not uniform.

Therefore, the cloud computing [5], big data [6] and internet of things (IoF) [7] are applied to the information construction of service areas in this paper, which is built a set of intelligent service area platforms based on cloud applications and Internet architecture. It will further improve the construction and operation of the service area, greatly improve the management level and economic benefits of the service area. Besides, it also provides specialized, humanized and high-quality services for travelers that give full play to the

¹ Corresponding author, Qingqing Yu, Shaanxi GSXZ Technology Co., Ltd, Xi'an 71086, China; E-mail: 617087614@qq.com.

Supported by the Scientific research projects in 2021 of Shaanxi Provincial Transport Department(21 – 37X).

economic and social benefits of the expressway, and better promote the development of expressway transportation.

2. Service Area Intelligent Management

2.1. Management of Passenger Flow

The needs of people who is driving on expressway for service areas are different from these in urban areas. Usually, the passenger flow on expressways is dominated by drivers, passengers and expressway managers, and they mainly use expressway service areas for short stops and rest. Therefore, in order to view the heat distribution data of the number of people in each area, it is necessary to realize the function of passenger flow statistics, and then the number of customers in supermarkets, restaurants, boiling water rooms, and toilets can be analyzed in real time. Through the intelligent management and scheduling of staff, the rationalization of resources can be achieved more accurately.

2.2. Management of Traffic Flow Characteristics

The traffic flow through the expressway service area should be the focus of the service area. Effectively identify the type, model, body color, license plate, vehicle category information of the entry and exit of each service area, and analyze whether it is a yellow-label vehicle and whether it is a dangerous vehicle, etc. If it is, the staff in the service area should be informed immediately and the corresponding measures must be taken. Besides, the traffic flow is counted and analyzed to obtain the heat distribution of the traffic flow in each province, city and section, which can provide business analysis for managers, it could be used for precise classification and management of service areas, and then providing basic business information for drivers and passengers, which is helping service area to improve the soft power of the business environment and upgrade service levels.

3. Key Technology and Method

3.1. The Whole Composition of Intelligent Service Area

In order to realize the analysis of vehicle/person flow, the intelligent management and intelligent platform of service area is constructed in this paper, as shown in Fig. 1, which is consisted of three layers, named application layer, transmission layer and perception layer. The perception layer refers to the data acquisition sublayer and the sensor network networking and collaborative information processing sublayer, which usually uses external hardware devices to collect information data. We set up high-definition (HD) cameras, vehicle monitoring equipment, structure monitoring equipment, ETC equipment and gas monitoring in the intelligent service area to collect data, and then transmit the collected data to the cloud platform through the network transmission layer, which can conduct big data analysis and provide the best decisions to the staff for application. Through the decision-making cloud platform, the operation management of the service area will be rationalized, the driver and passenger service will be further

commissioned. In addition, we can also provide certain business opinions for merchants in this intelligent service area, according to the characteristics of the flow of people and vehicles obtained from the analysis, so that the merchant operation can be expanded and better bring economic benefits to the service area. Therefore, a complete of intelligent service area IoT system is set, which mainly provides a more perfect management system and high-quality services for the management departments and drivers. It should be noticed that we are focus on the analysis of flow vehicle and person in this paper, the detailed method of drivers and passengers service in intelligent parking lot, changing for electric vehicles (EVs) and ETC refueling service is shown in our other paper due to the page limits.



Figure 1. Technical solutions for the overall system.

3.2. Passenger Flow and Traffic Flow Statistical Analysis

Based on machine vision technology and head-and-shoulder sequence pedestrian recognition technology, vehicles are identified and the vehicle/person dwell time and behavior trajectories are then analyzed, as shown in Fig. 2. The data is mainly derived from the HD camera of intelligent service area, which is mainly divided into three categories: trucks, passenger cars, and private cars to analyze the service needs of male and female passengers entering the service area, such as the length of stay in each area such as fueling, toileting, catering, supermarkets, and car repairs. It could be used to provide the customized services for drivers and passengers through statistical analysis of data, and generate corresponding data sets and service area sets according to the corresponding characteristics of merchants to help merchants accurately expand their scale and further improve the operating benefits of service areas.

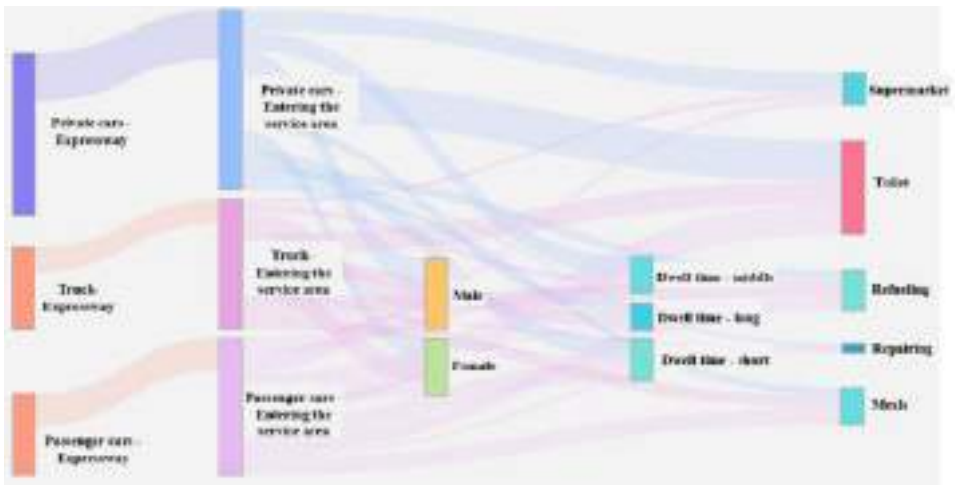


Figure 2. Vehicle/Person dwell times and behavior trajectories.

Besides, the analysis of vehicle/person dwell time and behavior trajectories can also be applied to intelligent security and the identification of dangerous behaviors. During the peak period of passenger flow in the service area, it is inevitable that unsafe factors will occur, resulting in uncontrolled behavior of personnel and conflict. Through the behavior recognition engine to provide positioning, analysis, screening, early warning capabilities, cooperate with the front-end capture engine to achieve real-time detection and analysis of video stream behavior. For abnormal behavior, including waving sticks and knives and other dangerous movements, raising hands to call for help, fighting, robbery, smashing, group fighting, mutual pushing, intrusion detection, tripwire detection, etc., it could be realized real-time alarm and notified on-site management personnel to deal with it, which improves the personal safety of drivers & passengers and reduces driving risks.

4. Conclusion

The expressway intelligent service area can further improve the service level of the service area and meet the high-level needs of users at this stage through reasonable

personnel scheduling. Based on cloud computing and big data technology to statistics and analysis of traffic/people flow, a set of intelligent highway service area integrated management system is constructed in this paper, which uses the analysis data to make reasonable suggestions to merchants to achieve contactless consumption, so as to form an intelligent business circle. At the same time, the system can also be well applied to peak hours, which could be reduced unnecessary congestion during peak hours, and further provide high-quality services for various vehicles and drivers and passengers on the highway to achieve the integration of communication and travel.

References

- [1] Jiang YM and Hou WJ. Research on expressway service area planning. 2010 The 2nd Conference on Environmental Science and Information Application Technology; 2010 July 17-18; Wuhan, China, IEEE Press; p. 1-3.
- [2] Jiao EL, Liu YJ, Gao CD and Wen Y. Experimental study on wastewater treatment of expressway service area in BAF. 2017 International Conference on Smart City and Systems Engineering (ICSCSE); 2017 November 11-12; Changsha, China, IEEE Press; p. 115-118.
- [3] Guo QM, Liang H, Liao HW, Zhang LS and Ni D. Statistical analysis and research on energy consumption in highway service area. 2022 7th International Conference on Intelligent Computing and Signal Processing (ICSP); 2022 April 15-17; Xi'an, China, IEEE Press; p. 210-214.
- [4] Wang JQ, Zhang K, Zhi P, Xi GL, Tang XR and Zhou QG. Analysis and prediction transient population in expressway service area based long short-term memory. 2021 IEEE 23rd Int Conf on High Performance Computing & Communications; 7th Int Conf on Data Science & Systems; 19th Int Conf on Smart City; 7th Int Conf on Dependability in Sensor, Cloud & Big Data Systems & Application (HPCC/DSS/SmartCity/DependSys); 2021 December 20-22; Haikou, Hainan, China, IEEE Press; p. 1828-1832.
- [5] Zhang FF, Sun HS, Wang XF and Wang L. Location and Route Optimization of Logistics Distribution Center Based on Beijing Expressway Service Area. 2020 4th International Conference on Robotics and Automation Sciences (ICRAS); 2020 June 12-14; Wuhan, China, IEEE Press; p. 137-141.
- [6] Zhao J, et al. Truck traffic speed prediction under non-recurrent congestion: based on optimized deep learning algorithms and GPS data. IEEE Access. 2019; 7:9116-9127.
- [7] Ahlgren B, Hidell M and Ngai ECH. Internet of things for smart cities: Interoperability and open data. IEEE Internet Computing. 2016; 20(6):52-56.

Optimizing IEEE 802.11a Preamble Design for Vehicle-to-Vehicle Communication

Jianghai XU¹, Hao ZHENG, Huaiyuan LIU, and Heng LIU

The 20th Research Institute of China Electronics Technology Group Corporation, China

Abstract. The popularity of the autonomous driving requires to establish a data communication path among vehicles. Due to its low price and easy deployment, the WiFi device is a possible approach. Motivated by this, in this paper, we study the performance of IEEE 802.11a for vehicle-to-vehicle communication. We especially focus on the impact of multi-path and Doppler spreading to the time synchronization, which is the main challenges in the vehicle-to-vehicle communication due to the high mobility. We also propose the possible approach to improve the time synchronization performance in the IEEE 802.11a by optimizing the preamble design. We evaluate the average synchronization error of our proposed methods through simulation. Simulation result shows that replacing the preamble with the Zadoff-Chu sequence can obtain the best time synchronization performance.

Keywords. IEEE 802.11a, Multi-Path, Doppler Spreading, Vehicle-to-Vehicle, Time Synchronization

1. Introduction

Autonomous driving has been becoming more and more popular in recent years [1]. To better support autonomous driving, a data communication path among vehicles has to be established such that the vehicle can be aware of the driving intent of its neighboring vehicles. Due to the low price and easy deployment, one possible approach is to install the WiFi device in the vehicle to support data communication.

However, the WiFi device is especially designed for the indoor communication [2]. In the indoor environment, due to the low movement of the pedestrian, the impairment from multi-path and Doppler spreading is much slight compared with the vehicle-to-vehicle environment, which typically has a much higher mobility. Thus, its communication performance in vehicle-to-vehicle communication has to be evaluated.

As a typical WiFi standard, IEEE 802.11a adopts the OFDM modulation in the physical layer design, and it is especially suit for the multi-path environment [3]. Thus, applying IEEE 802.11a for the vehicle-to-vehicle communication is a good option.

Motivated by the above, in this paper, we especially focus on the impairment from multi-path and Doppler spreading to the fine time synchronization of IEEE 802.11a. Considering the impairment from multi-path and Doppler spreading to the fine time syn-

¹Corresponding Author: Jianghai XU; E-mail: xujianghai2003@163.com.

chronization, we also give the possible approach to improve the time synchronization performance in the vehicle-to-vehicle environment and evaluate its performance.

The rest of this paper is organized as follows. In Section 2, we present the IEEE 802.11a preamble structure. In Section 3, we give the possible approach for optimizing IEEE 802.11a preamble to improve vehicle-to-vehicle communication performance. In Section 4, we evaluate the time synchronization performance for the proposed approach. We conclude this paper in Section 5.

2. IEEE 802.11a Preamble Structure

To assist for the frame detection, time synchronization, and frequency offset estimation, as in figure 1, the preamble of IEEE 802.11a consists of short training field (STF) and long training field (LTF). For the STF, it consists of 10 repeated sequences, and the sequence length is 12. Each symbol is mapped into the QPSK constellation and carried over 12 subcarriers in an OFDM symbol, and the subcarrier spacing is 1.25MHz. While for the LTF, it consists of 2 repeated sequences, the sequence length is 64. Each symbol is mapped into the BPSK constellation and carried over 64 subcarriers in an OFDM symbol, and the subcarrier spacing is 312.5kHz.

For the STF, it is designed for automatic gain control [4], frame detection, and coarse frequency offset estimation. Correcting the coarse time and frequency offset through the STF, the LTF can be further exploited for fine frequency and time synchronization.

Since IEEE 802.11a is especially designed for the indoor environment, if we apply it for a vehicle-to-vehicle communication scenario, its performance should be carefully evaluated.

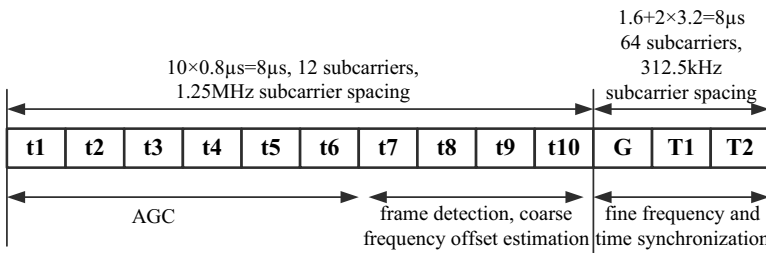


Figure 1. Preamble Structure of IEEE 802.11a

3. Optimizing IEEE 802.11a Preamble Design for Vehicle-to-Vehicle Communication

In this section, we first give the fine time synchronization method using LTF in the IEEE 802.11a, and then optimize the preamble design to improve the symbol synchronization performance.

3.1. Symbol Synchronization Method Using LTF

To achieve fine time synchronization, the cross-correlation $C(n)$ between the received signal $Y(n)$ and the LTF sequence $L(n)$ is calculated first as

$$C(n) = \sum_{m=0}^{63} Y(n+m) \otimes L^*(m),$$

where \star denote the complex conjugate. Since the LTF field has two repeated sequences, as in Figure 2, after calculating the cross-correlation, there should have two peaks. We denote the peak index as \hat{n}_1 and \hat{n}_2 separately. In the AWGN channel, since the LTF length is 64, such two peaks should have an index difference of 64. Further considering the error in locating the peak index, the index difference could be between 62 to 64, i.e., $62 \leq \hat{n}_2 - \hat{n}_1 \leq 64$. Using this rule, the receiver can precisely determine the start of the LTF sequence [5].

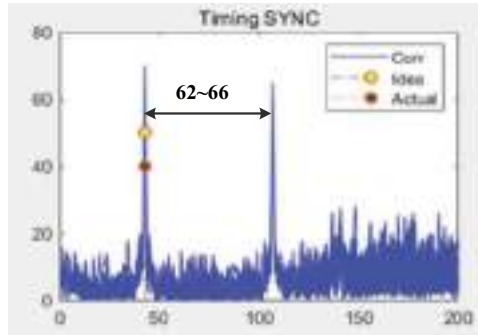


Figure 2. Cross-correlation for Fine Time Synchronization

3.2. Challenges for the Time Synchronization in Vehicle-to-Vehicle Communication

For the vehicle to vehicle communication, due to the high mobility, the challenges in the fine time synchronization come from the multi-path and Doppler spreading effects [6]. For the multi-path, especially when the gap between the first path and the non-first paths is small, the cross-correlation peak difference among paths is small. Combining the effect of Doppler spreading, which can severely disturb the peak in a small time period, the peak cannot be precisely determined, and this can degrade the time synchronization performance. Especially when the SNR is low, the time synchronization performance can be severely degraded.

3.3. Improving IEEE 802.11a Preamble Design

To improve the IEEE 802.11a performance in a vehicle-to-vehicle communication, we optimize the preamble design by three approaches as follows.

3.3.1. Increasing the LTF Sequence Length

To improve the time synchronization performance in the low SNR regime, we increase the LTF sequence length from 64 to 128, and extend the LTF from one OFDM symbol to two OFDM symbols. By increasing the LTF length, the matching gain can be increased, and this would increase the cross-correlation peak gap among paths, which may improve the fine time synchronization performance.

3.3.2. Skipping the Multi-path Effect in the Cross-correlation

To avoid multiple peaks induced by multi-path, one possible approach is to locate the last path, which cannot be impaired by other path. To achieve this, given the maximal path delay τ , we can derive its path delay in terms of the sampling point $\lceil \frac{\tau}{T_s} \rceil$, where $\lceil x \rceil = \min_{y \in \text{integer}} \{y \geq x\}$, and T_s is the sampling period.

Given $\lceil \frac{\tau}{T_s} \rceil$, after reaching the coarse time synchronization through the STF, before implementing cross-correlation to the LTF for fine time synchronization, we jump $\lceil \frac{\tau}{T_s} \rceil$ sampling points.

3.3.3. Replacing the Cross-correlation with the Auto-correlation

The benefit of using cross-correlation for fine time synchronization is that it can produce sharp peak, which can assist for the time synchronization. However, due to the multi-path and Doppler spreading effect, we cannot precisely locate the peak. While for the auto-correlation

$$A(n) = \sum_{m=0}^{63} Y(N+m) \otimes Y^*(m),$$

where N is the LTF sequence length, it can mitigate the multi-path effect. Thus, one possible approach for improving the fine time synchronization is to replace the cross-correlation with the auto-correlation.

3.3.4. Replacing the LTF Sequence by the ZC Sequence

Since the Zadoff-Chu(ZC) sequence has better correlation performance in terms of main-lobe and side-lobe, and it has been widely used in the LTE system, which is originally designed to support mobility [7]. Thus, we replace the LTF sequence with ZC sequence to expect better performance in dealing with the multi-path and Doppler spreading.

4. Simulation Results and Performance Evaluations

In this section, we evaluate the proposed fine time synchronization methods through simulation. We denote cross-correlation method as *XC N*, where N is the LTF sequence length, skipping multi-path effect method as *XC SKIP*, auto-correlation method as *AC Th*, and ZC sequence cross-correlation method as *zc XC*.

Table 1. Channel Multi-path Parameters

Path Delay (μs)	Relative Gain (dB)
0	0
0.5	-3
1	-6
1.5	-9

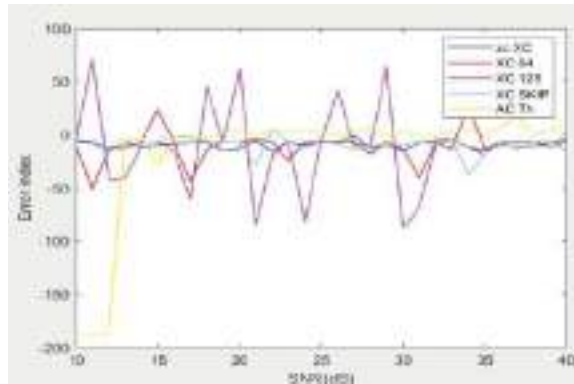
4.1. Simulation Setup

To evaluate the proposed algorithm performance, we set the channel model as in Table 1.

We set the Doppler spreading spectrum as Jake spectrum. We set the maximal Doppler frequency offset as 1000Hz, which corresponds to a velocity of 207km/h in the 5.2GHz band.

4.2. Performance Analysis

We evaluate the time synchronization error in Figure 3 versus the signal to noise ratio (SNR). We run each test 500 times, and give the averaged time synchronization error. We can observe that the *zc XC* method has the best performance. While for *XC 128*, it has the worst performance, and this demonstrates that increasing the LTF length is not an option. While for the *XC SKIP* and the *AC Th*, it has a better performance compared with the *XC 64* when the SNR is above 15dB.

**Figure 3.** Time Synchronization Error

5. Conclusions

We study the time synchronization performance of IEEE 802.11a for for vehicle-to-vehicle communication. Considering the impact of multi-path and Doppler spreading to the fine time synchronization, we propose three approaches to improve the fine time synchronization performance in the IEEE 802.11a by optimizing the preamble design. Simulation result shows that replacing the preamble with the Zadoff-Chu sequence can obtain the best time synchronization performance.

References

- [1] S. Chen et al., "Vehicle-to-Everything (v2x) Services Supported by LTE-Based Systems and 5G," in *IEEE Communications Standards Magazine*, vol. 1, no. 2, pp. 70-76, 2017.
- [2] L. Que, H. Ju, X. Fang, Y. Long, R. He and L. Huang, "Could IEEE 802.11bc Enhance Data Broadcast Performance for Moving Station: A Frame Loss Perspective," *2022 IEEE 95th Vehicular Technology Conference: (VTC2022-Spring)*, pp. 1-6, 2022.
- [3] Y. Wu, K. Yip and T. Ng, "ML frame synchronization for IEEE 802.11a WLANs on multipath Rayleigh fading channels," *2003 IEEE International Symposium on Circuits and Systems (ISCAS)*, 2003.
- [4] Y. Lee, D. Kang and W. Oh, "AGC Algorithm for IEEE 802.11a Based on Correlator and Threshold Detector," *2012 International Conference on Control Engineering and Communication Technology*, pp. 933-935, 2012.
- [5] Z. Wang, B. Zhao and F. Jeung, "Design and implementation of timing acquisition in IEEE 802.11a wireless LANs," *Fourth International Conference on Information, Communications and Signal Processing, 2003 and the Fourth Pacific Rim Conference on Multimedia*, pp. 554-558, 2003.
- [6] C. Gamier, M. Loosvelt, V. Le Thuc, Y. Delignon and L. Clavier, "Performance of an OFDM-SDMA based system in a time-varying multi-path channel," *IEEE 54th Vehicular Technology Conference. VTC Fall 2001*, pp. 1686-1690, 2001.
- [7] S. Kim, K. Joo and Y. Lim, "A delay-robust random access preamble detection algorithm for LTE system," *2012 IEEE Radio and Wireless Symposium, 2012*, pp. 75-78, 2012.

This page intentionally left blank

Subject Index

256-QAM	287	classification error rate	251
3D point cloud	457	cloud ecosystem structure	307
5G NR	119	clutter reduction	267
5G NR sidelink	287	co-planar waveguide (CPW)	112
ABC-BP algorithm	74	co-signature	18
abortion management	391	cognitive radio	97
active discovery	325	color space	198
advanced networks	465	communication protocol	24
advantage	138	competition and cooperation	307
AIPO	334	component retrieval	457
air-to-ground (A2G)		comprehensive English course	226
communication	10	computational intelligence	587
alternating minimization	334	constant-size ciphertext	1
angle condition number	260	constellation configuration	260
anti-jamming method	97	content connectivity	444
arbitrary image encryption	172	continuous-speech	348
ARMA	544	convolutional encoder-decoder	364
artificial chaos system	342	counterfeit drug crime	325
artificial intelligence	318, 436	coverage probability	10
attention mechanism	81, 375	crisscross optimization algorithm	614
audio rejection	348	cross-media semantic	40
automatic detection	24	cryptography	236
backbone	465	current transformer	417
bandpass filter	165	cut-off voltage	492
bilinear group	1	CycleGAN	213
BIM	457	data analysis	130, 606
blind super-resolution	375	data security sharing	182
Bloom's taxonomy of		decision tree	599
educational objectives	91	deep learning	62, 81, 281, 364, 417, 575
brain functional network	599	demodulation	287
breast cancer	606	deployment rate of ECN	411
breast cancer diagnosis	587	DFT-s-OFDM	119
broadcast sound	348	dicrotic front wave	555
burn-through distance	595	dicrotic wave	555
C and X bands	112	digital ecosystem deployment	236
cascade	357	digital perception	301
certificate	32	digital textbook	226
certification	32	Diplexer	165
CFO compensation	287	distribution network	
chaotic system	172	reconfiguration	614
characteristic factor	599	Doppler effect	287
checklist	236	Doppler spreading	664
classification	599		

driver	48	innovative thinking in mathematics	91
drone detection radar	267	intelligent transportation	653, 659
dust explosion proof	644	interference cancellation	472
dynamic convolution	375	internet	465
dynamic keys	172	Internet of Things (IoT)	24, 191
edge detection	244	Internet+	226
efficient	301	Josephson junction	383
electronic countermeasure	595	K210 chip	318
email server	411	kernel data evaluation	74
encoder-decoder	499	kernel function	400
encryption	32	knowledge base	325
evolution model	307	knowledge graph	40
explicit congestion notification	411	learning	436
expressway	653, 659	least square method	518
extreme point	555	lighting changes with movies	
failure prediction	484	scenario	198
false positive rate	251	lighting linkage system	198
fault diagnosis	484	lightweight	18
feature aggregation	81	load balancing	450
feature extraction	244	long-time coherent accumulation	424
feature ranking	606	LoRa	219
filter power divider	357	LoRaWAN	295
finite element simulation	634	low power	56
full-duplex	348	low time-complexity	172
function model	518	lowpass filter	165
GARCH	544	LPWAN	301
generative adversarial network	62, 499	LTCC	357
generative learning	213	lubricated	628
genetic algorithm	130	lumped element microwave	
grain silos	644	circuits	165
GRFT	424	machine learning	281
gross error	518	massive-cargo logistics	
heart rate asymmetry	342	transportation route	509
hidden vector encryption	1	master station	32
hierarchical structure	251	matFR	606
high density crowd area	391	MBSE	138, 146
high resolution radar	267	measurement of uncertainty	533
high school students	91	methodology	146, 236
higher education	226, 436	microfluidic technology	383
HRV	342	MIMO	334
human voice	348	mmWave	119
hybrid algorithm	74	mobile edge computing	472
hybrid precoding	334	modeling research	74
hydraulic driven	644	modeling tool	146
hydrodynamic	628	morphological characteristics	555
IEEE 802.11a	664	motion parameters estimation	424
image identification	499	multi-path	664
image processing	198	multi-path propagation	219
image recognition	244		

multi-perspective spatiotemporal learning	62	privacy-preserving computation	182
multi-target detection algorithm	417	project design	318
multiple degradations	375	pulse wave	555
multiview-multistatic	155	Q-learning algorithm	97
nanoSQUIDs	383	QR code	191
network management	465	quantitative inversion	155
network reconfiguration	614	quantum cryptography	236
network survivability	444	quantum key distribution (QKD)	236
new power system	182	radar signal processing	267
NFC	191	radiography	575
noise interference	595	range profile	424
noise power spectrum estimation	364	ray-tracing method	219
nonsynchronous short pulse jamming	400	real-time speech enhancement	364
OFDM	119	reinforcement learning	450, 509
ontology	40	remote sensing	155
OpenCV	244	research and judgment model	325
optical network	444	residual	213
outlier	518	retaking	575
overload	509	return	544
p-polyhedron protection	444	return loss	112
PA models	119	RFID	191
PA pre-distortion	119	risky behavior prediction	105
patient's angle	575	robust estimation	518
patrol routes	130	safe operation distance	634
pavement crack	499	scan test	56
people flow forecast	391	scientific cultivation	40
personnel control	105	SCMA	295
PHM technology	484	screw clearing machine	644
photoelectric effect	492	SDN	450
places of detention	105	security	1, 48, 301
plaintext correlation	172	security inspection	81
Planck constant	492	security surveillance	105
planning and design	653, 659	service area	653, 659
planning research	130	service function chain	472
Poincaré plot	342	session key	32
Poisson Point Process (PPP)	10	session key negotiation	32
police	48	shifting Bloom filters	251
polycapillary X-ray lens with square channels	567	ship cabin	219
power amplifier nonlinearity	119	signature	32
power digital space	182	signature discovery	587
power frequency magnetic field immunity test	634	simulation	383
power IOT	18	SL	287
practical course	318	SM2 algorithm	18
prediction	544	smart home	198
prime order setting	1	smart laboratory	24
		soft rough set	533
		spatial distribution	634
		spin sensitivity	383
		stability	587, 606

starved lubrication	628	time-domain characteristics	555
steganalysis	213	traffic flow imputation	62
stochastic geometry	10	transfer learning	499
stock	544	transport	48
subset feature selection	587	trend	138
subTHz	119	UAV	484
subway station	457	Ultra Wideband (UWB)	112
successive convex approximation	472	user association	450
supervised and semi-supervised learning	499	value chain	281
system construction	325	variable precision	533
system engineering process	146	vehicle-to-vehicle	664
TCP congestion control	411	virtual environments	436
terminal	32	Voltage Standing Wave Ratio (VSWR)	112
test data compression	56	waveform entropy	400
textbook development strategy	226	web server	411
texture	628	WiFi networks	450
throughput	295	wiring judgment	417
time difference of arrival	260	X-ray optics	567
time synchronization	664		

Author Index

Ang, Z.	32	Guan, Z.	1
Aquino, B.K.-F.	281	Guo, D.	130
Bai, X.	105	Guo, J.	138, 146, 424
Bai, Y.	492	Guo, P.	172
Balodis, R.	236	Guo, X.	295
Bao, Y.	191, 191, 244, 244	Guo, Y.	138, 146
Baquijano, Á.E.-C.	281	Hao, B.	364
Castillo-Velazquez, J.-I.	465	Hao, W.	130
Chang, S.	424	He, C.	10
Chávez, E.E.O.	436	He, F.	32
Chen, B.	318	Hu, H.-F.	417
Chen, C.-X.	411	Hu, Y.	357
Chen, F.	213	Hu, Z.	400
Chen, J.	391	Huang, C.	614
Chen, L.	375	Huang, C.-y.	499
Chen, M.	391	Huang, J.	301
Chen, X.	260, 400	Huang, S.	444
Chen, Y.	595	Huang, Z.	91
Dai, D.	155	Hwang, J.-Y.	287
Deng, G.	307	Jayananda Singh, S.	112
Deng, Q.	198, 348, 364	Ji, X.	599
Díaz, E.Z.G.	436	Jia, H.	457, 628
Ding, P.	97	Jia, T.	81
Ding, X.	10	Jia, Z.	644
Dinh Thang, P.	267	Jiang, Y.	634
Dixit, M.M.	112	Jin, M.	295, 301, 587, 606
Dong, M.	357	Jin, S.	165
Du, Z.	567	Kim, S.	119
Duan, J.	653, 659	Kojima, S.	575
Fan, L.	295	Kong, X.	62
Fang, H.	472	Kudo, H.	575
Fang, R.	357	Kumar, R.	112
Feng, R.	614	Lai, Y.-H.	342
Fu, C.	182	Lan, L.	342
Fu, Q.	32	Lee, S.-W.	287
Fu, S.	634	Li, A.	653, 659
Fu, Y.	32	Li, B.	587, 606
Fu, Z.	457	Li, H.	391
Gao, Y.	472	Li, J.	450
Gao, Z.	182	Li, M.	81, 260, 634
Geng, X.	357, 555	Li, S.	260, 325
Gu, H.	492	Li, X.	444
Gu, L.	325	Li, Y.	357, 567, 653, 659

Li, Y.-s.	509	Qin, G.	595
Li, Z.	342	Qiu, L.	260
Liang, Z.	400, 424	Qu, B.	457
Liao, C.	634	Qu, W.	484
Lin, H.	48	Ren, H.	97
Lin, J.	383	Ren, J.	260
Lin, X.	213	Rong, X.	417
Lin, Y.	48	Serunin, I.	287
Lin, Z.	325	Sha, X.	130
Liu, B.	32, 260, 587, 606	Shao, Y.	653, 659
Liu, D.	182	She, G.	307
Liu, H.	664, 664	She, S.	138
Liu, J.	32	Shen, G.	62
Liu, L.	97	Shi, Y.	318, 457
Liu, N.	62	Shi, Z.	383
Liu, Q.	244, 424	Shigeyasu, T.	411
Liu, W.	457	Shikov, A.	119
Liu, Y.	62, 391, 444, 628	Shou, Z.	105
Liu, Z.	182, 567	Song, H.	24
Lu, K.-l.	499	Song, N.	417
Lu, Z.	32, 48	Song, Z.	213
Luan, T.	364	Su, K.	342
Luan, Z.	492	Su, M.	198
Luo, G.-r.	499	Sun, B.	614
Luo, J.	644	Sun, H.	226
Luo, S.	1, 295, 301	Sun, S.	155
Luo, W.	417	Sun, T.	567
Lv, X.	457	Sun, Y.	424
Ma, B.	81	Tallón-Ballesteros, A.J.	v
Ma, J.	628	Tan, G.	318
Ma, T.	251	Tang, N.	172, 198
Ma, Y.	357	Tang, W.	614
Ma, Z.	348	Toapanta, S.M.T.	436
Maltsev, A.	119, 287	Tu, W.	219
Meng, X.	97	Van Loi, N.	267
Nagaoka, K.	411	Van Tien, P.	267
Nakazeko, K.	575	Velazquez-Cruz, N.-G.	465
Nie, Y.	74	Vizquete, O.M.Z.	436
Opmane, I.	236	Vu Hop, T.	267
Ovalle, C.	281	Wang, B.	251
Pan, J.	484	Wang, D.	348, 364
Pan, K.	567	Wang, G.	424
Pei, Z.	334	Wang, H.	383, 444
Peng, Q.	348	Wang, K.	1, 472
Pudeev, A.	119, 287	Wang, L.	226, 492, 595, 634
Qi, H.	544	Wang, M.	599
Qi, J.-f.	499	Wang, Q.	533
Qi, K.	146	Wang, S.	24, 375
Qian, G.	10	Wang, X.	533, 599

Wang, Y.	91, 325, 492, 544, 555, 595	Yu, H.	587, 606
Wang, Z.	1	Yu, J.	342
Watanabe, H.	575	Yu, L.-S.	417
Wei, M.	509	Yu, Q.	653, 659
Wen, A.	182	Yu, S.	587, 606
Wen, C.	457	Yuan, H.	24
Wu, A.	40	Yuan, P.	599
Wu, J.	325, 587, 606	Yuan, T.	105
Wu, L.	484	Yuan, X.	599
Wu, S.	97	Yuan, Y.	18
Wu, X.	357	Zhai, J.	198
Wu, Y.	567	Zhang, G.	318
Wu, Z.	172	Zhang, H.	213, 555, 595
Xia, X.	24	Zhang, J.	555
Xiao, Y.	97	Zhang, L.	484, 599
Xie, G.	334	Zhang, M.	24, 499
Xing, Q.	213	Zhang, N.	628
Xu, H.	32, 219	Zhang, Q.	213
Xu, J.	664	Zhang, Y.	18, 40, 81, 555
Xu, J.-H.	417	Zhang, Z.	342
Xu, K.	74	Zhao, H.	146
Xu, P.	32	Zhao, J.	138
Xu, W.	444	Zhao, L.	614
Xu, Y.	219	Zhao, P.	348
Xue, H.	484	Zhao, Y.	213
Yang, F.	18	Zheng, F.	634
Yang, G.	32	Zheng, H.	664
Yang, S.	40, 119	Zheng, Z.	599
Yang, W.-W.	417	Zhou, L.	400
Yang, X.	628	Zhou, M.	567
Yao, M.	307	Zhou, Q.	130, 219
Ye, B.	56	Zhou, W.	62
Ye, W.	457	Zhou, X.	301
Ye, X.-M.	518	Zhu, H.	226
Yi, L.	32	Zhuang, Z.	342
Yi, T.	567		

This page intentionally left blank